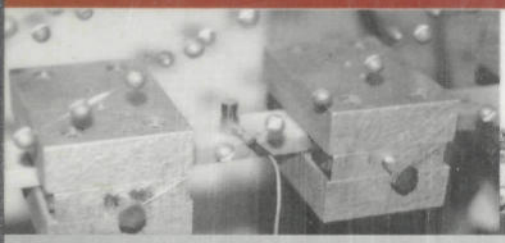
Universidade do Porto
Faculdade de Engenharia
FEUP





Elsa de Sá Caetano

Dynamics of Cable-stayed Bridges:

Experimental Assessment of Cable-Structure Interaction

Porto, 2000


Antônio de
Sousa Oliveira

Universidade do Porto
Faculdade de Engenharia
FEUP

Elsa de Sá Caetano

Dynamics of Cable-stayed Bridges:

Experimental Assessment of Cable-Structure Interaction

UNIVERSIDADE DO PORTO
Faculdade de Engenharia
BIBLIOTECA
N.º
CDU
Data / 20

A thesis submitted to the University of Porto in accordance with the requirements of the degree of Doctor of Philosophy in Civil Engineering, in the Faculty of Engineering

Porto, 2000

Enc./Ref./05

624(043)/CAEe/DYN

UNIVERSIDADE DO PORTO
Faculdade de Engenharia
BIBLIOTECA
N.º 56022
CDU 624(043)
Data 31 / 5 / 2001

Ao meu filho

Ricardo

ABSTRACT

The technological progress observed during the last decades contributed to the appearance and growing use of the modern cable-stayed bridge concept. Cable-stayed bridges are highly indeterminate and complex structural systems characterized generally by large flexibility, lightness and low damping coefficients, aspects that lead to a significant proneness to dynamic actions. In effect, a significant number of vibration problems have been reported in the literature, associated with the stay cables and/or with the deck and towers oscillations.

The topic of *Cable Vibrations* has been in general studied considering the stay cables isolated from the bridge structure, i.e., neglecting the effects of dynamic *Cable-Structure Interaction*. Although this interaction has been observed in several prototypes, the corresponding characteristics have not been fully understood yet, and apparently contradictory opinions can be found in the literature with respect to its effects in terms of the global dynamic behaviour of the bridge.

Under these circumstances, it is the purpose of the current dissertation to experimentally identify the phenomenon of *Cable-Structure Interaction* in cable-stayed bridges and to evaluate the corresponding effect in terms of the global response to dynamic excitations.

The research presented herein concentrates on the study of an existing physical model of a cable-stayed bridge constructed in South Korea, the Jindo Bridge. The physical model was modified in order to accurately reproduce at a given scale factor the dynamic behaviour of the stay cables. The corresponding dynamic properties and the dynamic *Cable-Structure Interaction* phenomenon were identified experimentally, based on the classical *Experimental Modal Analysis* and *System Identification* techniques, using the excitation produced both by an electrodynamic shaker and a shaking table. The bridge response to a set of artificial accelerograms used as input on the shaking table was also measured.

The results from the experimental tests were used to validate the numerical modelling. Additional numerical simulations were performed in order to emphasize the main aspects of the *Cable-Structure Interaction* phenomenon for limit cases of the excitation or of the dynamic structural properties.

The work based on the Jindo Bridge model involved analytical, numerical and experimental components. Since several of the studied subjects are relatively recent and involve knowledge in different domains, it was considered of interest to gather the most relevant information in the current dissertation.

The thesis starts then with the presentation of an updated state-of-art on the construction and structural characteristics of cable-stayed bridges. The main concepts and analytical formulations concerning the *Dynamics of Cables* are also reviewed. With respect to the *Numerical Modelling* of cable-stayed bridges, the various types and characteristics of

dynamic actions relevant to a dynamic analysis are described, as well as the available numerical formulations of analysis.

With regard to the experimental study of the dynamic behaviour of large cable-supported bridges, the following aspects are covered: (i) a presentation of the recent trends in instrumentation sensors and measurement systems; (ii) a description of the main characteristics of the classical *System Identification* techniques, referring in particular the recently developed *System Identification* techniques based on data from ambient vibration measurements; (iii) a presentation of the main results obtained during a campaign of measurements performed on the Vasco da Gama Bridge.

An extensive survey on the various phenomena that rule the occurrence of stay cable vibrations is then presented. Whenever possible, analytical/ empirical formulae for the evaluation of levels of cable vibration or for the prediction of the occurrence of instability phenomena are presented. In particular, various formulae developed by the author for evaluation of levels of amplification and increments of dynamic tension in the stay cables associated with oscillations of the cable anchorages (*external/parametric* excitation) are presented. These formulae were validated through the numerical modelling of a specific stay cable. Additional numerical simulations were developed in order to introduce to the phenomenon of *Cable-Structure Interaction* studied subsequently based on the physical model of the Jindo Bridge.

KEYWORDS

Cable
Cable-stayed bridges
Cable vibrations
Experimental techniques
Nonlinear geometric analysis
Shaking table
Cable dynamics
Wind excitation
Parametric excitation
Cable-structure interaction
Ambient vibration testing
Forced vibration testing

RESUMO

O progresso tecnológico registado nas últimas décadas deu lugar ao aparecimento e crescente utilização das pontes atirantadas ditas modernas. Estes sistemas estruturais altamente complexos caracterizam-se por um elevado grau de indeterminação e por uma grande flexibilidade e leveza. Os dois últimos aspectos, associados ao geralmente baixo amortecimento, fazem com que estas estruturas sejam muito vulneráveis a acções dinâmicas, o que tem suscitado variados problemas de vibração, tanto ao nível dos tirantes, como do tabuleiro e torres.

O problema das *Vibrações de Tirantes* de pontes tem sido em geral estudado considerando estes elementos isolados da estrutura, não se considerando portanto o efeito da *Interacção Dinâmica Tirante-Estrutura* que, embora evidenciada por algumas situações práticas, não foi ainda compreendida e completamente caracterizada, podendo de resto encontrar-se na literatura opiniões contraditórias no que respeita à sua importância do ponto de vista do comportamento dinâmico global da estrutura.

Neste contexto, a presente dissertação tem por objectivos fundamentais a identificação e caracterização do fenómeno de *Interacção Dinâmica entre Tirantes, Tabuleiro e Torres* em pontes atirantadas, assim como a avaliação da sua importância em termos da resposta estrutural a acções dinâmicas.

A investigação realizada centrou-se no estudo de um modelo físico já existente de uma ponte construída na Coreia do Sul, a ponte de Jindo. O modelo foi modificado com vista à reprodução à escala do comportamento dinâmico dos tirantes, tendo as suas propriedades dinâmicas e o fenómeno da *Interacção Dinâmica Tirante-Estrutura* sido experimentamente identificados e caracterizados utilizando técnicas clássicas da *Análise Modal Experimental* e *Identificação de Sistemas*, tendo por base a excitação introduzida por um excitador electrodinâmico e por uma mesa sísmica. Adicionalmente foi medida a resposta sísmica a um conjunto de acelerogramas gerados artificialmente, aplicados à plataforma sísmica.

Os resultados dos estudos experimentais foram utilizados na validação de modelações numéricas, tendo-se complementarmente realizado ainda simulações numéricas que evidenciaram os aspectos fundamentais do fenómeno de *Interacção Dinâmica Tirante-Estrutura* para situações extremas no que respeita às solicitações ou propriedades dinâmicas estruturais.

Os estudos realizados envolveram o desenvolvimento da investigação em três vertentes, analítica, numérica e experimental, tendo levado a uma incursão em domínios de grande actualidade e menor divulgação, que se considerou de interesse reunir na presente dissertação.

Assim, após a apresentação de uma estado da arte actualizado relativo à construção e aspectos estruturais associados às pontes atirantadas, sistematizam-se os principais conceitos e formulações analíticas relativos à *Dinâmica de Tirantes*. Sistematizam-se também

os principais tipos e características de acções a considerar no estudo dinâmico de uma ponte atirantada, assim com as formulações de análise numérica do comportamento dinâmico global.

No que respeita ao estudo experimental do comportamento dinâmico de estruturas de grande vão, procura-se apresentar os mais recentes tipos de sensores e equipamentos de medição, discutindo as respectivas potencialidades e interesse de aplicação. Apresentam-se também as diversas técnicas clássicas de *Identificação de Parâmetros Dinâmicos*, referindo-se em particular técnicas desenvolvidas muito recentemente com vista à identificação baseada em ensaios de vibração ambiental e livre, bem como os principais resultados obtidos durante uma campanha de medições na Ponte Vasco da Gama.

Realiza-se ainda uma extensa investigação dos diversos fenómenos que estão na base da ocorrência de oscilações em tirantes, apresentando-se sempre que possível expressões analíticas/ empíricas que permitam avaliar níveis de oscilação ou detectar a possibilidade de ocorrência de instabilidade. Refere-se em particular o estabelecimento pela autora de expressões matemáticas para avaliação das amplificações e incrementos de tensão dinâmica introduzidos pela oscilação das ancoragens (excitação *externa / paramétrica*). Estas expressões são validadas através da realização de um estudo numérico de um tirante, sendo desenvolvidas simulações numéricas adicionais com vista a introduzir os aspectos essenciais do fenómeno de *Interacção Tirante-Estrutura* estudados posteriormente com os ensaios experimentais sobre o modelo físico.

PALAVRAS-CHAVE

Tirante
Ponte atirantada
Vibrações em tirantes
Técnicas experimentais
Análise não-linear geométrica
Mesa sísmica
Dinâmica de tirantes
Vento
Excitação paramétrica
Interacção tirante-estrutura
Ensaios de vibração ambiental
Ensaios de vibração forçada

RÉSUMÉ

Le progrès technologique de ces dernières décennies a permis aux ponts haubanés d'affermir leur avantage. Leur construction s'est étendue partout dans le monde franchissant de plus en plus grandes portées.

Comparés a ses prédécesseurs, les ponts haubanés modernes sont généralement caractérisés par longues portées et profils de section très légère. Ces faits, combinés avec les relativement petits amortissements, rendent ces ouvrages très sensibles aux effects dynamiques. En conséquence, un nombre considérable de problèmes de vibration a été rapporté dans la littérature, concernant soit des vibrations des haubans, soit des tabliers et pylônes.

L'étude des vibrations des haubans de pont considère en général le hauban isolé de la structure du pont. L'interaction dynamique entre les haubans et le pont est donc négligée, bien qu'il ait été observé dans certains cas pratiques. En faite, ce phénomène n'est pas complètement compris toujours, et apparemment des opinions contradictoires peuvent être trouvées dans la littérature en ce qui concerne ses effets quant au comportement dynamique global.

Sous ces circonstances, le but de la dissertation courante est l'identification et caractérisation expérimentale du phénomène d'interaction dynamique hauban-pont, bien que l'évaluation de son effet dans la réponse globale aux excitations dynamiques.

La recherche ici présentée est concentrée sur l'étude d'un modèle physique existant d'un pont haubané construit en Corée du Sud, le Pont de Jindo. Le modèle physique a été modifié pour reproduire correctement à un facteur d'échelle donné le comportement dynamique des haubans. Les propriétés dynamiques correspondantes et le phénomène d'interaction hauban-pont ont été identifiés expérimentalement en employant les techniques classiques d'Analyse Modale Expérimentale et de l'Identification de Systèmes et en utilisant l'excitation produite par un excitateur electrodynamique et un banc de vibrations. La réponse du pont à un ensemble de registres d'accélération appliqués sur la table sismique a été aussi mesurée.

Les résultats des épreuves expérimentales ont été utilisés pour valider le modelage numérique. Des simulations numériques supplémentaires ont été exécutées pour mettre en évidence les aspects principaux du phénomène d'interaction hauban-pont dans certains cas limites de l'excitation ou des propriétés dynamiques structurelles.

Les études basés sur le Pont de Jindo ont couvert des composants analytiques, numériques et expérimentaux qui ont exigé la recherche dans plusieurs domaines récents et moins connus, que l'auteur a considéré d'intérêt pour assembler dans la dissertation courante.

Un premier aspect couvert par la thèse est un état-de-art actualisé sur la construction et caractéristiques structurelles des ponts haubanés. En ce qui concerne le modelage numérique des ponts haubanés, les différents types et caractéristiques des actions

dynamiques pertinents à une analyse dynamique sont décrits, aussi bien que les formulations numériques d'analyse disponibles.

Quant à l'étude expérimentale du comportement dynamique des ponts haubanés, les aspects suivants sont couverts: (i) une présentation des tendances récentes dans les capteurs et systèmes de mesure; (ii) une description des caractéristiques principales des techniques de l'identification de systèmes classiques, avec référence à un ensemble de techniques basés sur des épreuves de vibration ambiante; (iii) une présentation des résultats principaux obtenus dans une campagne de mesures sur le Pont Vasco da Gama.

Les différentes causes de vibration des haubans sont allors objet d'une recherche détaillée. Si possible, des formules pour prévoir la possibilité d'existence d'instabilité ou pour évaluer les amplitudes de vibration sont présentées. En particulier des formules développées par l'auteur pour l'évaluation des niveaux d'amplification et augmentation de tension dynamiques des haubans associées aux oscillations des ancrages sont présentées. Des simulations numériques supplémentaires ont été développées pour introduire le phénomène d'interaction hauban-pont étudié par la suite sur le modèle physique du Pont de Jindo.

MOTS-CLÉS

Hauban
Pont haubané
Techniques expérimentales
Analyse non-linéaire géométrique
Dynamique des haubans
Excitation du vent
Excitation des paramètres
Interaction hauban-pont
Essai de vibration ambiant
Essai de vibration forcé

CONTENTS

ABSTRACT v

RESUMO vii

RÉSUMÉ ix

CONTENTS xi

ACKNOWLEDGMENTS xvii

CHAPTER ONE: INTRODUCTION

1.1 General 1.1
1.1.1 Dynamic modelling of cable-stayed bridge response 1.7
1.1.2 Assessment of wind stability 1.9
1.1.3 Seismic analysis 1.15
1.1.4 Structural monitoring 1.16
1.1.5 Control of vibrations 1.20
1.2 Objectives 1.28

CHAPTER TWO: CABLE-STAYED BRIDGES

2.1 General 2.1
2.2 Historical review 2.1
2.3 Structural systems 2.30
2.3.1 Selection of bridge type 2.30
2.3.2 General layout 2.31
2.3.2.1 Span arrangement 2.32

2.3.2.2 Cable arrangement 2.33
2.3.2.3 Relative dimensions 2.38
2.3.3 The towers 2.41
2.3.4 The deck 2.46
2.3.5 The cables and anchorages 2.51
2.4 Major cable-stayed bridges in Portugal 2.54

CHAPTER THREE: THEORY OF CABLE DYNAMICS

3.1 General 3.1
3.2 Geometry and statics of a suspended cable 3.2
3.3 Dynamics of a suspended cable 3.12
3.3.1 Brief historical review 3.12
3.3.2 The linear theory of free vibrations of an horizontal cable 3.13
3.3.3 The linear theory of free vibrations of an inclined cable 3.23
3.3.3.1 The simplified approach from Irvine 3.23
3.3.3.2 The asymptotic approach from Triantafyllou 3.24
3.3.4 Nonlinear theory of cable vibration 3.28

CHAPTER FOUR: DYNAMIC ANALYSIS OF CABLE-STAYED BRIDGES: Design Loads and Numerical Formulation

4.1 General 4.1
4.2 The loads 4.2
4.2.1 Wind loads 4.3
4.2.1.1 Definition of mean wind 4.4
4.2.1.2 Definition of the site turbulence 4.7
4.2.1.3 Characterization of wind loads on a bridge structure 4.10
4.2.1.4 Instability phenomena 4.13
4.2.2 Moving loads 4.15
4.2.2.1 Traffic loads 4.15
4.2.2.2 Pedestrian loads 4.21
4.2.3 Earthquake loads 4.28
4.3 Numerical formulation 4.39
4.3.1 General 4.39
4.3.2 Brief state-of-the-art of static and dynamic analysis of cable-stayed bridges 4.42
4.3.2.1 Geometric nonlinearities 4.42
4.3.2.2 Geometric and material nonlinearities 4.45
4.3.2.3 Dynamic analysis of cable-stayed bridges 4.45
4.3.3 Finite element approach for the geometric nonlinear problem 4.47
4.3.3.1 Incremental equations of motion for static analysis 4.48
4.3.3.2 Governing finite element equations for static analysis 4.56

4.3.3.3 Governing finite element equations for dynamic analysis..... 4.62
4.3.4 Finite element modelling of a cable-stayed bridge..... 4.63
4.3.4.1 Modelling of the stay cables..... 4.64
4.3.4.2 Modelling of the girder and towers..... 4.70

CHAPTER FIVE: EXPERIMENTAL IDENTIFICATION OF THE DYNAMIC BEHAVIOUR OF CABLE-STAYED BRIDGES

5.1 General..... 5.1
5.2 Brief state-of-the-art on the experimental dynamic analysis of cable supported bridges.. 5.3
5.3 Recent trends in instrumentation systems for dynamic testing of cable supported bridges 5.9
5.3.1 Excitation devices..... 5.9
5.3.2 Input and response measurement devices..... 5.12
5.3.2.1 Input devices..... 5.12
5.3.2.2 Response measurement devices..... 5.16
5.3.3 Measurement and analysis systems..... 5.36
5.4 System identification techniques..... 5.38
5.4.1 General..... 5.38
5.4.2 Input-Output identification methods..... 5.40
5.4.2.1 Frequency domain methods..... 5.46
5.4.2.2 Tuned-sinusoidal SI methods..... 5.54
5.4.2.3 Time domain methods..... 5.55
5.4.3 Output-Only SI methods..... 5.60
5.4.3.1 Frequency domain methods..... 5.61
5.4.3.2 Time domain methods..... 5.65
5.4.3.3 Comparison of output-only SI methods..... 5.69
5.5 Dynamic tests on the Vasco da Gama cable-stayed bridge..... 5.70
5.5.1 Instrumentation system..... 5.71
5.5.2 Ambient vibration test..... 5.74
5.5.2.1 Test procedure..... 5.74
5.5.2.2 Levels of vibration..... 5.76
5.5.2.3 Identification of natural frequencies..... 5.77
5.5.2.4 Identification of modes of vibration..... 5.81
5.5.3 Free vibration test..... 5.83
5.5.3.1 Test procedure..... 5.83
5.5.3.2 Identification of natural frequencies and modes of vibration..... 5.86
5.5.3.3 Identification of modal damping factors..... 5.88
5.5.4 Dynamic measurements on stay cables..... 5.90
5.5.4.1 Instrumentation and setup..... 5.91
5.5.4.2 Identification of natural frequencies..... 5.91
5.5.4.3 Evaluation of cable tensions..... 5.92

5.5.5 Conclusions 5.94
5.6 Summary 5.95

CHAPTER SIX: CABLE VIBRATIONS

6.1 General 6.1
6.2 Direct excitation by wind and rain 6.4
6.2.1 Vortex-shedding 6.5
6.2.2 Galloping 6.15
6.2.3 Wake interference 6.18
6.2.4 Rain-wind induced vibrations 6.22
6.3 Indirect excitation 6.37
6.3.1 General 6.37
6.3.2 External excitation 6.39
6.3.3 Parametric excitation 6.51
6.4 Cable-structure interaction 6.58
6.4.1 General 6.58
6.4.2 Effect of cable-structure interaction in external excitation 6.61
6.4.3 Effect of cable-structure interaction in parametric excitation 6.62
6.5 Conclusions 6.63

CHAPTER SEVEN: THE JINDO BRIDGE: Experimental and numerical survey

7.1 General 7.1
7.2 The Jindo Bridge prototype 7.3
7.3 The physical model of the Jindo Bridge 7.6
7.3.1 Definition of scale factors 7.7
7.3.2 Description of the physical model 7.11
7.3.3 Tuning of cable tensions 7.15
7.4 Numerical evaluation of modal parameters of the model 7.16
7.4.1 Preliminary 2-D FEM analysis 7.17
7.4.2 3-D FEM analysis 7.22
7.4.3 Comparison between numerical analyses 7.40
7.5 Experimental modal survey 7.41
7.5.1 Electrodynamic shaker tests 7.42
7.5.1.1 Instrumentation 7.42
7.5.1.2 Multi-sine excitation tests 7.45
7.5.1.3 Sinusoidal tests 7.56
7.5.2 Tests at the EERC shaking table 7.65
7.5.2.1 Instrumentation 7.65
7.5.2.2 Multi-sine excitation tests 7.67
7.5.2.3 Damping tests 7.74

7.5.3 Tests at the ISMES shaking table 7.81
7.5.3.1 Modification of the Jindo Bridge model 7.81
7.5.3.2 Instrumentation 7.82
7.5.3.3 Multi-sine excitation tests 7.85
7.5.3.4 Damping tests 7.88
7.6 Ambient vibration tests on the bridge prototype 7.90
7.6.1 Monitoring system 7.91
7.6.2 Ambient vibration tests 7.91
7.7 Conclusions 7.96

CHAPTER EIGHT: THE EFFECT OF DYNAMIC CABLE-STRUCTURE INTERACTION IN THE GLOBAL RESPONSE TO SEISMIC EXCITATION

8.1 General 8.1
8.2 The Jindo Bridge model 8.3
8.2.1 Modal participation factors 8.3
8.2.2 Response to seismic excitation 8.5
8.2.2.1 Generation of artificial accelerograms 8.5
8.2.2.2 Measured response 8.6
8.2.2.3 Numerical response, *OECS* vs *MECS* 8.32
8.3 Numerical simulations 8.53
8.3.1 Internal resonance at the fundamental mode of vibration 8.53
8.3.1.1 Modified model 8.53
8.3.1.2 Numerical response, *OECS vs MECS* 8.55
8.3.2 Effect of severe cable excitation 8.57
8.3.2.1 Generation of accelerogram 8.58
8.3.2.2 Numerical response, *OECS* vs *MECS* 8.58
8.4 Conclusions 8.62

CHAPTER NINE: CONCLUSIONS

9.1 Summary 9.1
9.2 General conclusions 9.5
9.2.1 Dynamic testing of the Vasco da Gama Bridge 9.5
9.2.2 Indirect excitation 9.6
9.2.3 Dynamic cable-structure interaction 9.7
9.3 Perspectives of future research 9.9
9.3.1 Instrumentation of large structures 9.9
9.3.2 Application of System Identification techniques 9.10
9.3.3 Control of vibrations in cable-stayed bridges 9.11

REFERENCES

ACKNOWELEDGEMENTS

Dynamics of Cable-Stayed Bridges is a fascinating field of research in which the author had the pleasure and also the privilege of working during the last years. In this period, the author had also the opportunity to contact and work with various persons, whose contribution helped to enrich the work presented here and to whom wishes to express her gratitude:

- To Professor Álvaro Cunha who, in the quality of advisor, supported the developed research, creating material conditions for its pursue, providing fruitful discussions and a rigorous review of the dissertation;
- To Professor Colin Taylor, co-supervisor of the thesis, who proportionated the author the access to the facilities at the Earthquake Engineering Research Centre. His trust and helpful suggestions, as well as the final review of the thesis were very much appreciated by the author;
- To Professor Raimundo Delgado, leader of the Structural Dynamics Group of this Faculty, who provided the scientific framing for this research, by his encouragement and interesting suggestions during the preparation and review of the dissertation;
- To Professors Francisco Restivo, Armindo Lage, Augusto Gomes and Dias Rodrigues, who have kindly provided creative suggestions and help in the use of sensors, experimental devices and signal processing techniques throughout these years;
- To the colleagues António Pinto da Costa, John Macdonald, Barny Wainwright, and Ing. Ricardo Baldassari, who provided interesting information, discussions, help and assistance in theoretical developments and diverse experimental aspects;
- To Professors Habib Tabatabai, Uwe Starossek, Rune Brincker, Reto Cantieni, Angelo Luongo and Rui Carneiro de Barros, who provided helpful data, information and valuable suggestions during the course of this work;
- To Professors Yozo Fujino, Masaru Matsumoto, Jacques Mathivat, Martin Wieland, Christian Cremona, Nicholas Jones, Worsak Kanok-Nukulchai, Lan Hai, Trigo Barbosa, Laginha Palma, Carmelo Gentile and to colleagues Diego Cobo, and Jorge Rodrigues, who kindly sent the author diverse publications, information and photographs;
- To all the colleagues and staff of the Civil Engineering Department and to Mr. Dave Ward from the EERC of the University of Bristol, for their support, patience and kindness throughout all these years;
- To the author's parents, sisters and other family members, as well as the great friends who helped the author in various situations, creating an atmosphere of generosity, friendship, joy and opening in which the author is proud of living;
- To Álvaro, husband, friend and mate, and to Ricardo, our little Big Boy, who above all showed the author nothing of this is really so important.

Part of the present research was carried out at the EERC at the University of Bristol and funded from the Human Capital and Mobility Programme of the European Union, under the ECOEST Program (European Consortium of Earthquake Shaking Tables) and in conjunction with research contracts from the UK Engineering and Physical Sciences Research Council and from the Portuguese Foundation for Science and Technology (FCT). One component of the research was also developed at the Dynamic Testing Laboratory of ISMES, under the ECOEST Program. The author wishes to acknowledge the help of Professors Roy Severn and Franchioni, as well as the advice of Dr. A. Blakeborough, who provided the conditions for assessment to these facilities.

The author is also acknowledged by the grants attributed by the FCT, Gulbenkian and Fundação Luso-Americana para o Desenvolvimento, for the publication of the dissertation and participation in Congresses.

The diverse information supplied by Rendel Palmer & Tritton, Kajima Corporation, the Honshu-Shikoku Bridge Authority, Aas-Jakobsen, Schlaich Bergerman and Partner and Gattel is also very much appreciated by the author, as well as the authorization by Lusoponte in the person of Mr. Wastiaux, for publication of the results from the Vasco da Gama tests.

CHAPTER 1

INTRODUCTION



CHAPTER ONE

INTRODUCTION

1.1 GENERAL

The Strömsund Bridge, in Sweden, was open to traffic in 1956. The three-span cable-stayed bridge, with a total length of *332m*, and a main span of *182.6m*, the steel and concrete deck being suspended from each pylon by *4* pairs of diagonal stay cables (Figure 1.1), was considered the first cable-stayed bridge of the modern era. In effect, a systematic structural analysis was, for the first time, performed in connection with the bridge construction, which permitted a permanent control of the cable forces, assuring the efficiency of all cables in the final structure (Gimsing, 1983).

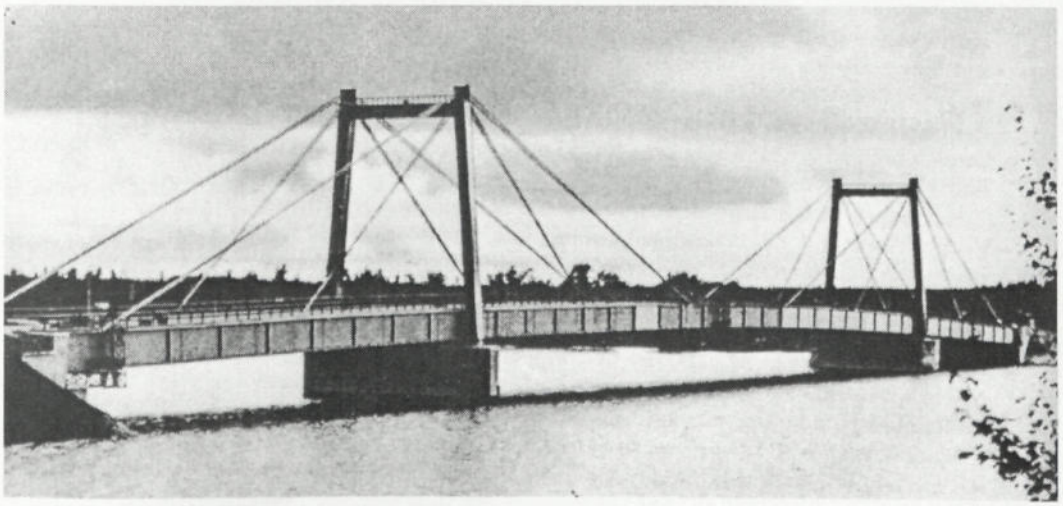


Figure 1.1. Strömsund Bridge (Sweden, 1956) (Troitsky, 1988).

In the short period of about *45* years, the design and construction of cable-stayed bridges showed a very deep evolution. In effect, the technological progress of the last decades, conjugated with the development of numerical methods of analysis, have permitted both to take advantage of improved material properties and to analyse more complex highly indeterminate structures. For technical, economical and also aesthetic reasons, cable-stayed bridges, that became very popular in Germany in the post-war reconstruction, have gained an increasing importance, establishing themselves as a new category amongst classical structural systems, and their use quickly spread all over the world, in a multitude of innovative solutions.

With the completion of the Normandy Bridge in France, in 1994, a multiple suspension bridge with a total length of *2141m* and a record main span of *856m* (Figure 1.2), it was even possible to prove that cable-stayed bridges, whose range of applications had been traditionally considered the *150m* to *500m* spans, can also be successfully applied, and with economic advantage, in the domain of the very long spans. The Tatara Bridge, which was completed in Japan in 1999, and has a main span of *890m* (Figure 1.3), enhanced this aspect. In fact, since no element in the bridge has reached a feasibility threshold yet, and since the ratio cost/span has not shown a steep increase with the increase of span, it is still possible to expect an increase in the span range (Taylor, 1991). The former proposals for cable-stayed bridges with main span larger than *1000m* are indeed older than *20* years.

Leonhardt and Zellner (1980) mentioned the limit of *700m* and *500m* for highway traffic and for railroad, respectively, in prestressed concrete cable-stayed bridges. As for steel cable-stayed bridges, they referred two proposals presented for the Messina Straits Crossing, with main spans of about *1300m* and *1500m* (*6* lanes highway and *2* tracks railroad) which, according to the designers, presented no structural difficulties and even were superior to a classical suspension bridge, not only in terms of the required amount of steel, but also with respect to deformations and dynamic behaviour.

Another proposal from Leonhardt, Andrä and Partner (1986) for the Messina Straits Crossing consisted in a steel cable-stayed bridge with a main span of *1750m* (Figure 1.4). The feasibility of a longer span suspension bridge, avoiding the necessity of founding one or more pylons on the large water depths of the Strait, favoured however the choice for a *3000m* single-span suspension bridge.

Still worth of reference is the proposal dated from 1989 for a *1204m* main span cable-stayed bridge, presented in the bid for the construction of the East Bridge, across the Great Belt. At that time, the largest existent cable-stayed bridge was the Annacis Bridge, in Canada, a composite bridge with *465m* main span. The cable-stayed bridge option was considered too risky for construction, and a suspension bridge with a main span of *1624m* was chosen instead (Gimsing, 1991).

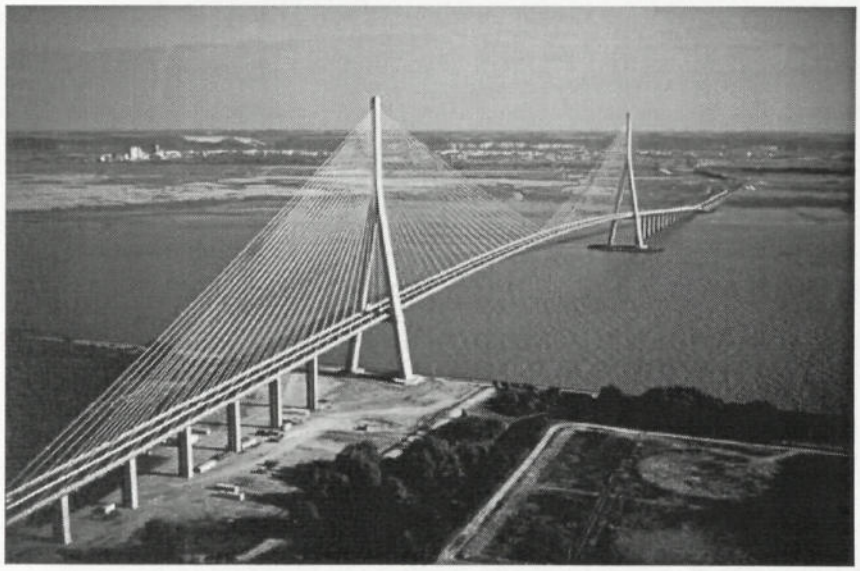


Figure 1.2. General view of the Normandy Bridge (France, 1994).



Figure 1.3. General view of the Tatara Bridge (Japan, 1999).

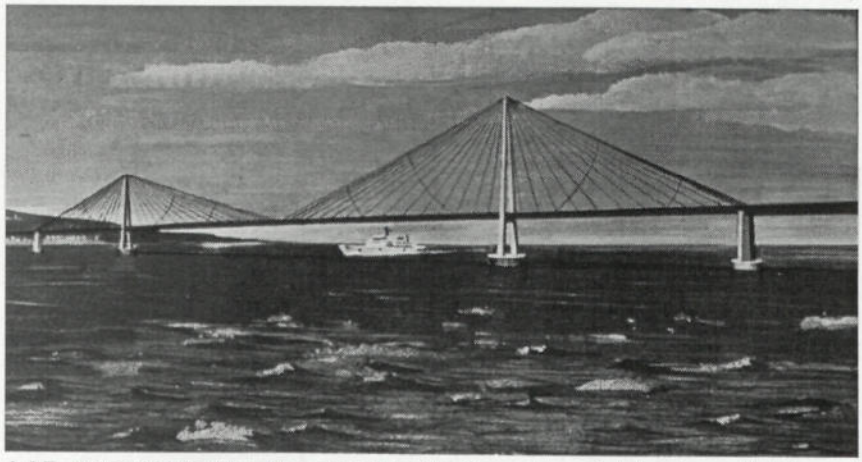


Figure 1.4. LAP proposal for the Messina Straits Crossing. Cable-stayed bridge with spans of *150-170-750-1750-750-150m* (Godden, 1980).

The most significant restriction to an increase of the span length of a cable-stayed bridge is associated with the development of high compression forces introduced in the deck by the stay cables. According to Mathivat (1994), this fact limits the main span length to about *1500m*. Above this length, it is normally assumed that the classical suspension type, with cables anchored to the ground, is the best solution.

But even in those large spans can the inclined stay cable suspension play an important role. In effect, the addition of inclined stay cables into a suspension bridge in the vicinity of the pylons provides a higher global stiffness for the bridge and, consequently, a better wind stability, and allows for a better control of static deformations, particularly important in the case of railroad bridges. This hybrid system was used in an empirical form by Roebling (Troitsky, 1988), in the railroad bridge across the Niagara River (1855), in the Ohio Bridge (1867) and in the Brooklyn Bridge (1883) (Figure 1.5). And it was several times proposed for the construction of recent bridges, as is the case of a *1500m* bridge across the Great Belt, presented in 1977 in an international bid (Figure 1.6). But no modern applications are known.

Another hybrid approach, presented by Lin and Chow (1991), consists in a double cantilever suspension system, where the main cable is suspended from the tips of inclined struts, which are themselves back stayed to the pylons. This structural system was one of the considered feasible schemes for a *5km* main span bridge to integrate a *14km* Crossing at the Gibraltar Strait. A more recent proposal by Menn (1998) employs the same concept of conjugating the inclined stayed system with classical suspension cables (Figure 1.7), achieving simultaneously the purposes of increasing the lateral stiffness of the bridge, and minimizing the construction time.



Figure 1.5. Brooklyn Bridge (1883). View along axis at the truss top level (Godden, 1980).

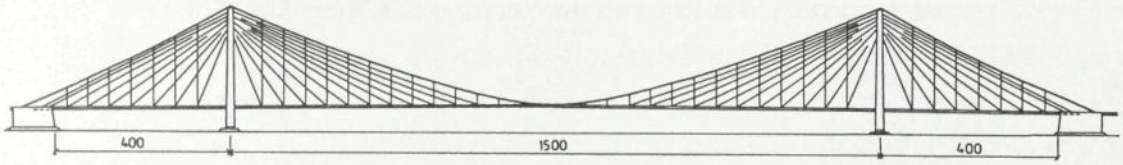


Figure 1.6. Hybrid suspension system studied for the Great Belt Crossing in 1977 (Gimsing, 1991).

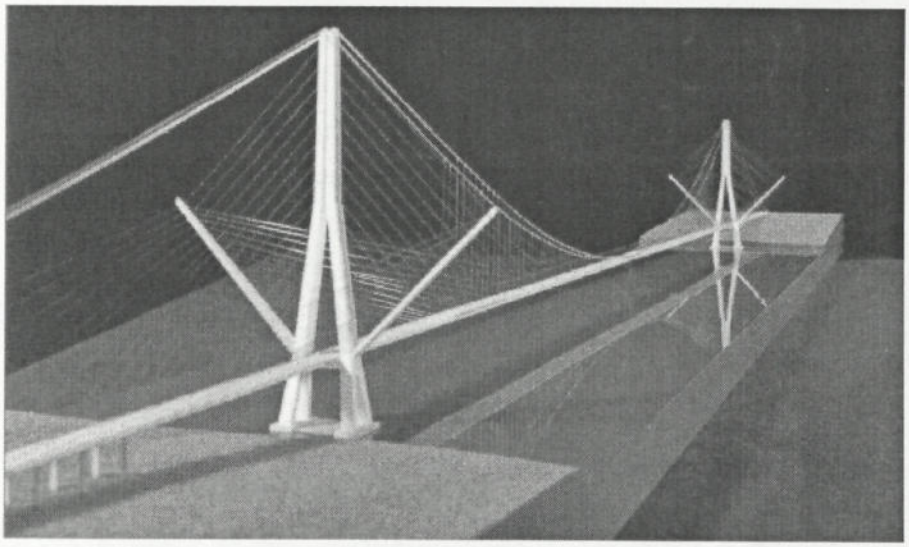


Figure 1.7. Hybrid structural system. Study for Gibraltar Crossing (Menn, 1998).

Most of the studies already performed for very long spans are based on the use of conventional materials, steel and concrete, whose properties were significantly improved during the last decades. But also during the last years investigation on the application of new high-strength lightweight materials has progressed a lot. Several small span girder bridges have already been constructed using the so-called Advanced Composite Materials (ACM), in the form of carbon fibers and plastics (Khalifa, 1992). These materials, whose strength-to-density ratio is about *5* to *10* times the corresponding strength-to-density ratio for steels, have an enormous potential for long span cable-stayed bridges applications, since the self-weight of the deck can represent a high percentage of the bearing capacity in a very long span.

The first reported application to cable-supported structures of these new materials is a small footbridge in Scotland, the Aberfeldy Bridge (1992), across the River Tay (Figure 1.8). With a total length of *113m* and a main span of *63m*, the bridge was designed by Maunsell Structural Plastics and erected without craneage by the final-year bridge engineering students of the Dundee University, from supercells made of Glass Reinforced Polymer (GRP) and Parafil Cables. Also a two-lane vehicular cable-stayed bridge, with a main span of *137m*, is being proposed for construction in San Diego, USA (Seible *et al.*, 1999). The application of fiber reinforced material as an outer shell to long span steel-concrete bridges, constitutes another application, which can enhance the torsional stiffness of the system, improve its aerodynamic profile, increase its durability and, eventually, provide a windshielding to vehicular traffic (Richmond & Sham, 1994).

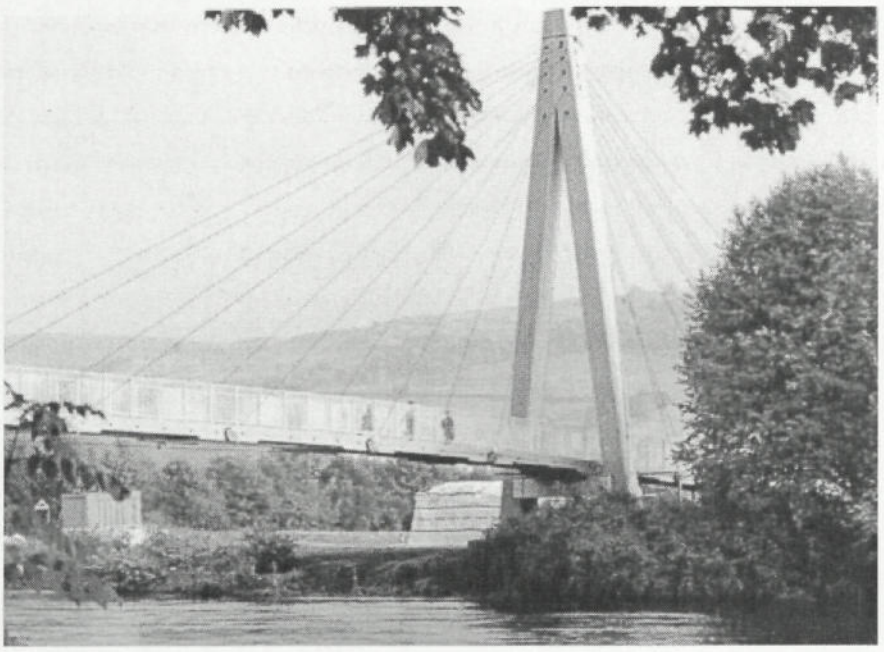


Figure 1.8. Aberfeldy Cable-Stayed Bridge (Scotland, 1992).

The Messina and, eventually, the Gibraltar Straits Crossings are challenging projects to accomplish during the next century. Other major projects in phase of construction, or still at a conception or design stage, like the Øresund Link, in Denmark, the Honshu-Shikoku, in Japan or the Rion Antirion, in Greece, will incorporate long span cable-stayed bridges. Although the span range application of cable-stayed bridges has also extended to the small spans (*60-150m*) during the last years (Reis *et al.*, 1998), the trend to an increase of the main span length is an evidence, as can be observed in the graphic presented in Figure 1.9, relating the span length with the year of completion for some of the most representative cable-stayed bridges around the world.

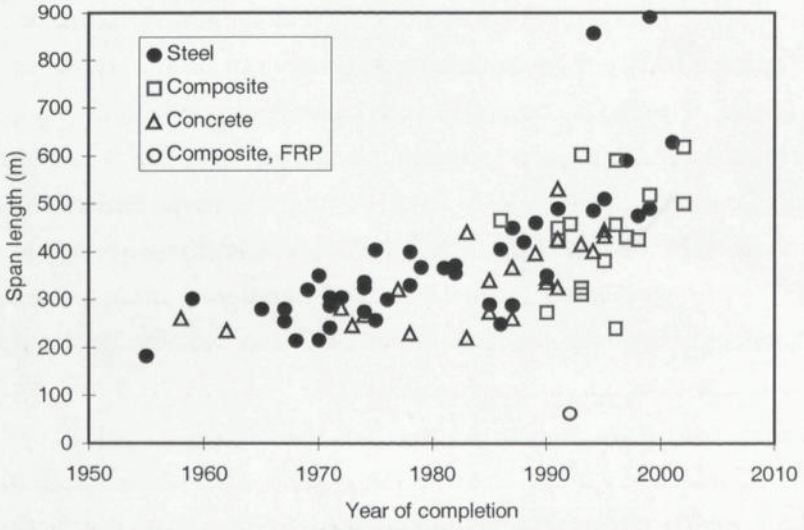


Figure 1.9. Evolution of span length with year of completion for cable-stayed bridges. Modified from (Karoumi, 1998).

The design of long span bridges is governed by their dynamic behaviour to wind and, for certain locations, to earthquake excitations. In spite of the tremendous progress achieved during the last decades in the areas of Dynamic Modelling, Seismic Analysis, Wind Stability, Structural Monitoring and Control of Vibrations, the vulnerability of these extremely complex systems to several types of dynamic actions has not been completely assessed yet.

The following Sections describe some of the main topics and current trends in the dynamic analysis of cable-stayed bridges.

1.1.1 Dynamic modelling of cable-stayed bridge response

Cable-stayed bridges are highly complex indeterminate systems marked by a large flexibility and low damping coefficients, properties that determine a significant vulnerability to dynamic loads.

The large flexibility of cable-stayed bridges, which is naturally augmented with the large span lengths achieved in recent years, is responsible for an accentuated geometric nonlinear behaviour, in addition to the nonlinearity associated with the cable sag, and with other nonlinearities related with the properties of the materials. These characteristics, combined with the various and complex types of actuating loads, are responsible for very demanding requirements of analysis and explain why only recently, during the last two decades, dynamic analysis has been incorporated on a regular basis in the design of cable-stayed bridges.

Historically, the dynamics of cable-supported bridges has first been investigated on the basis of continuous energy models.

One of the first studies employing this methodology was developed by Goschy (1961), who determined the first natural frequencies of a cable-stayed bridge.

A second level approach, employed by Baron and Lien (1971) in the design of a cable-stayed bridge, consisted in the use of a frame analysis based on the beam-column theory for the determination of the static configuration under permanent loads, and subsequent performance of a linear dynamic analysis by modal superposition, employing the tangent stiffness matrix calculated at the dead-load configuration, and considering a lumped mass approach. In this respect, it is interesting to refer the various studies performed by diverse authors in order to assess the degree of nonlinearity associated with the static and dynamic responses. One of the most clarifying studies in this topic was developed by Fleming and Egeseli (1980), who concluded that it is sufficient to perform a geometric nonlinear analysis for static loads and a linear dynamic analysis for live loads, as long as the later analysis departs from a tangent stiffness matrix calculated at the dead-load configuration of the bridge. It is important to note however that the mentioned study focused on a medium span cable-stayed bridge (centre span of *260m*) which is far away from the current trend in span length for a so-called long span cable-stayed bridge. Besides this fact, it is also relevant

to note that the step by step integration algorithm employed by Fleming and Egeseli as reference method for the assessment of the degree of nonlinearity did not consider the nonlinearity associated with the stay cables dynamics, but instead employed a simplified description of the sag effect, based on the definition of an equivalent Young modulus for the stay cables. Although this simplification is sufficient to describe the static behaviour of a cable-stayed bridge, it is certainly not suited to assess the corresponding dynamic behaviour, particularly when the bridge employs a very large number of stay cables, and when these cables are arranged in inclined planes.

A more recent contribution to the assessment of the degree of nonlinearity associated with the dynamics of a cable-stayed bridge is due to Nazmy and Abdel-Ghaffar (1990a; 1990b; 1990c), who extended the research by Fleming and Egeseli to larger spans, employing however the same level of simplifications in the idealization of the stay cables' behaviour. Nazmy and Abdel-Ghaffar confirmed the results previously obtained for the analysis of a cable-stayed bridge with a centre span of *335m*. However, for a centre span of *600m*, they realized that both static and dynamic analyses demanded the use of a geometric nonlinear formulation.

The third and last level of approach in the numerical modelling of a cable-stayed bridge consists in the use of the *finite element method*. One of the former applications to cable-stayed bridge response analysis is due to Kajita & Cheung (1973), who discretized the bridge deck into a number of small shell elements supported at the cable anchorages by equivalent springs, and performed a three-dimensional linear dynamic analysis, arriving at a set of torsional and bending vibration modes. More recent applications involve both linear and nonlinear static and dynamic analyses, using a variety of finite elements, and different possibilities for modelling joints and particular devices, such as cable dampers (Kanok-Nukulchai, 1992; 1993).

The progress in computer technology made the *finite element method* one of the most powerful tools for structural analysis, not only by offering a wide range of possibilities in terms of selection of finite element types and formulations, but also, by the possibility of running very large applications in PCs and workstations. In effect, most design companies have presently access to very sophisticated finite element software packages, allowing the performance of large displacement nonlinear material and geometric static and dynamic analyses, by idealization of the bridge as an association of several types of finite elements, like beam, shell and truss elements. The assessment of cable tensions and the control of displacements throughout the construction phase is also possible, by simple activation/de-activation of specific groups of finite elements in successive stages of the analysis. Moreover, the comparison between natural frequencies and modal shapes evaluated on the basis of these algorithms, and the corresponding measured values on the prototype, has proven that extremely good correlations can be obtained, what evidences the enormous sophistication that can be achieved in structural analysis.

An interesting aspect to emphasize is that, despite the various alternatives offered for the modelling of the stay cables, the most common numerical idealizations of cable-stayed bridges don't include an appropriate mass distribution for the stay cables, i.e., the dynamic behaviour of the stay cables is not included in the global dynamic analysis of the bridge, the problem of cable vibration being treated separately. The dynamic interaction between the cables and the structure, here designated as *cable-structure interaction*, has been investigated by several researchers, such as Kovács (1982), Maeda *et al.* (1983), Causevic and Sreckovic (1987), Abdel-Ghaffar and Khalifa (1991), Fujino (1993) and Tuladhar *et al.* (1995). Although different approaches have been followed, most authors stressed the importance of the performance of a global dynamic analysis, where the stay cables' dynamics is included in the global numerical model of the bridge. For this purpose, the distributed mass of the stay cables is required to be conveniently modelled, either by employing specific cable elements, like the two-node curved element (Gambhir & Batchelor, 1977), the elastic catenary element (Jayaraman & Knudson, 1981), or the four-node isoparametric truss element (Ali, 1991), or by discretizing the stays into series of truss elements.

With regard to the evaluation of the dynamic response and, assuming that the input excitation is fully characterized, two points should be stressed.

The first point relates to the amount of damping and type of damping present in the structural system. Most applications consider, for convenience, a damping of viscous type, proportional to a mass and/or a stiffness matrix. The measured damping coefficients on prototypes have evidenced however a large dispersion of values, which are very much dependent on the amplitude of vibration, specially for low amplitudes of the response in the first symmetrical bending mode (Okauchi *et al.*, 1997). Some attempts have been made in order to analytically estimate the structural damping (Yamaguchi *et al.,* 1997), permitting a better insight into the mechanisms of energy dissipation in cable-stayed bridges. However, as these structures have very small damping factors, slight errors in their characterization can originate significant errors in the evaluation of the dynamic response.

The second consideration in the evaluation of the dynamic response of cable-stayed bridges relates to the effect of dynamic *cable-structure interaction*. Leonhardt and Zellner (1980) introduced the concept of "*system damping*", considering that many cables vibrating at different natural frequencies produced an attenuation of the dynamic response. Several reported cases of cable and/or deck vibrations (Dumortier, 1990; Virlogeux, 1998; Yamaguchi & Fujino, 1998) have shown however that cable vibrations are not always beneficial to the global bridge structure, requiring, in certain cases, additional measures of vibration control.

1.1.2 Assessment of wind stability

Wind stability is a major aspect in the design of cable-stayed bridges. Several failures and important damages associated with wind effects occurred over the past *180* years in cable-

supported bridges (Podolny & Scalzi, 1976). The collapse of the Tacoma Narrows Bridge in 1940, due to divergent oscillation under moderate wind, marked the development of a new conscience on vibrational characteristics and aeroelastic phenomena and prompted most of the investigation on the aerodynamic stability of bridges. Basically, the results of the research in aeronautics and aerodynamics were applied equally to suspension and cable-stayed bridge structures, treating the deck section as an airfoil, like the wing-cross section of an aircraft. It should be pointed that, due to their geometry, cable-stayed bridges are more rigid and less vibration-sensitive than suspension bridges. They are thus less susceptible to the wind effects, which are in general controllable, but should always be evaluated.

The study of the wind effect on a particular cable-stayed bridge must address the following main aspects: *aerodynamic sensitivity* of the deck, *buffeting* and *cable vibrations*.

Aerodynamic sensitivity of the deck

The *aerodynamic sensitivity* of the deck is related with two main components, the cross section shape and the eigenfrequency constellation (Leonhardt & Zellner, 1991). These two components interact in the definition of the bridge proneness to aerodynamic instability, which is usually evaluated from wind tunnel tests. For long span bridges, the most important types of *aeroelastic phenomena* are *vortex shedding/lock-in*, *flutter* and, less likely, *vertical galloping*.

(i) Vortex-shedding/lock-in

The phenomenon of *vortex-shedding* is caused by the formation of vortices in the wake of the bridge deck, which shed at regular intervals, giving rise to sinusoidally varying vertical forces. In certain ranges of the wind speed, the frequency of these forces matches one of the bridge's natural frequencies of vertical or torsional vibration, exciting the correspondent mode into oscillation. Aeroelastic feedback tends to *lock-in* the shedding frequency to the natural frequency of the bridge deck, originating further amplification of the bridge forces. The wind tunnel tests using sectional models, consisting of the immersion in a wind flow of a representative length of the bridge deck elastically suspended at the ends and accurately shaped at a scale varying from *1:30* to *1:100* (Irwin, 1998), constitute presently the most appropriate form of establishing the *vortex-shedding* behaviour of the bridge deck, providing wind speed ranges of occurrence, as well as the maximum amplitudes of oscillation expected for various assumed damping values. These tests also help the development of improvements in the deck geometry in case the requirements for structural reliability are not satisfied.

(ii) Flutter

Flutter is a more dangerous form of instability whereby, in result of the structure's motion, the wind forces acting on the deck are changed, producing self-excited vibration. When the self-

excited vibration oppose the deck motion, a damping effect exists. The case of the so-called negative damping, corresponds to self-excited vibration adding the bridge motion and producing oscillations that can build up to the collapse of the structure at certain critical wind speeds. The classical description of *flutter*, associated with aircraft wings, comprehends the generation of a strongly coupled torsional and vertical motion. In bridge decks, however, the *flutter* occurs mainly for torsional oscillations, the coupling with vertical oscillations being in general weak. The performance of wind tunnel tests on sectional models of the bridge allows an evaluation of a critical *flutter* velocity, as well as of the values of aerodynamic derivatives to be introduced in multi-mode coupled-flutter theories (Katsuchi *et al.*, 1998). The performance of wind tunnel tests using partial elastic models, like the "taut strip" (Davenport *et al.*, 1992) or the "taut tube" (Irwin & Stone, 1986) models, which allow an approximate representation of the mode shape, permits the consideration of three-dimensional wind effects. Alternately, full aeroelastic models can be employed, constructed however at very small scales, say 1:150 to *1:300*, in view of the size limitation of the wind tunnels.

Buffeting

The *buffeting* of a bridge is caused by wind turbulence, and corresponds to a structural vibration around the deformed mean static configuration that results from the static component of the wind pressure. This vibration involves the contribution of various modes of vibration and has an essential influence on the dimensioning of cable-stayed bridges. The most unfavourable situation for *buffeting* frequently occurs during construction, when the deck extends on both sides of the tower supported only by the permanent cables.

Since the turbulence acts through gusts, which are random occurrences in terms of intensity and spatial distribution, a probabilistic approach should be employed in the evaluation of their dynamic effects. The classical method is based on the statistical theory of Davenport (1962), which involves a frequency description of the wind turbulence from series of wind time-histories, and a linear mode superposition analysis in the frequency domain, neglecting both the aeroelastic effects and the nonstationarity of the flow. Recent time-domain formulations overcome the main drawbacks of the Davenport theory and of other refined methods available, allowing the investigation of transient and nonlinear response (Katsuchi *et al.*, 1998). Experimental full-scale or wind tunnel tests (using full aeroelastic or partial elastic models) are alternative approaches to the problem, providing either a distribution of wind pressures on the surface of the structure, from which the dynamic response is evaluated analytically, or a direct measurement of the vibratory state.

Cable vibrations

Cable vibrations constitute a topic of investigation which only very recently, after the mid 80's, has deserved the attention of researchers. Yet, the first known report of observation of stay

cable oscillations, concerning the Brotonne bridge, in France, dates back from 1976 (Wianecki, 1979) and many cable-stayed bridges all over the world have been seriously affected by this problem, predominantly during the phase of construction (Yoshimura *et al.*, 1995a; Virlogeux, 1998). In effect, due to their small structural damping and high flexibility, cables are very easily excited, not only by wind and rain, but also by traffic (Wieland & Lukkunaprasit, 1990) and pedestrian actions (Pacheco & Fujino, 1993). Although the global integrity of the bridge is not in general affected, significant vibration of the stay cables has shown to cause fatigue problems at the anchor points of the cables, as well as to damage their external polyethylene (PE) coating tubes. Additionally, the consequent vibration of the towers and deck causes an insecurity feeling to the users. The suppression of cable vibration through the implementation of control devices is thus an important issue in the design and maintenance of cable-stayed bridges, requiring a full understanding of the corresponding generation mechanisms. Important research programs have been developed during the last years in various countries, namely in Japan, where a Committee for studying wind resistant characteristics of cables in cable-stayed bridges was created. This Committee actually identified *16*, among *55* cable-stayed bridges in Japan, where wind-induced cable vibrations were observed, and produced a systematic classification of the main observed characteristics and conditions of occurrence of vibration (Matsumoto *et al.*, 1989).

The main mechanisms of *wind-induced* cable vibration are: (i) *vortex-shedding*; (ii) *wake galloping*;(iii) *rain-wind* induced *vibration* and (iv) *indirect excitation*.

(i) Vortex-shedding

The phenomenon of *vortex-shedding*, as above described for the bridge deck, occurs in general for the shortest cables of the bridge and for small critical wind speeds, corresponding to very low wind energy and small amplitudes of vibration.

(ii) Wake galloping

The instability by *wake galloping* is a consequence of a disturbance of the wind flow around the cables by a structural element or a construction equipment. The classical situation corresponds to bridges with two planes of cables under oblique winds. Some of the downstream cables, which are in the wake of the upstream leg of the pylons, are excited by an increased turbulence. This phenomenon was observed on some of the shorter cables of the Normandy bridge once during construction, according to Virlogeux (1998). A more important form of *wake galloping* can occur when two or more stays are close. The adoption of the so-called "twin cables" is very popular in long span bridges in Japan and is motivated by the wish to accommodate high cable tensions in small diameter cables. The "twin cables" are arranged by pairs of parallel cables closely spaced (very few diameters) anchored at the same level in the tower and deck. *Wake galloping* may occur in the backward stay, as a

consequence of the vortices produced in the wake of the forward cable. The motion of this cable alters the flow around the forward stay, causing an interaction between the two cables. This type of vibration was observed at the Hitsuishijima and Iwakurojima Bridges, in Japan, for a wind speed of less than *5m/s*, causing amplitudes of vibration of *200-500mm*, which decreased after a certain wind speed (Ohashi, 1991). This phenomenon can be suppressed by proper spacing between cables.

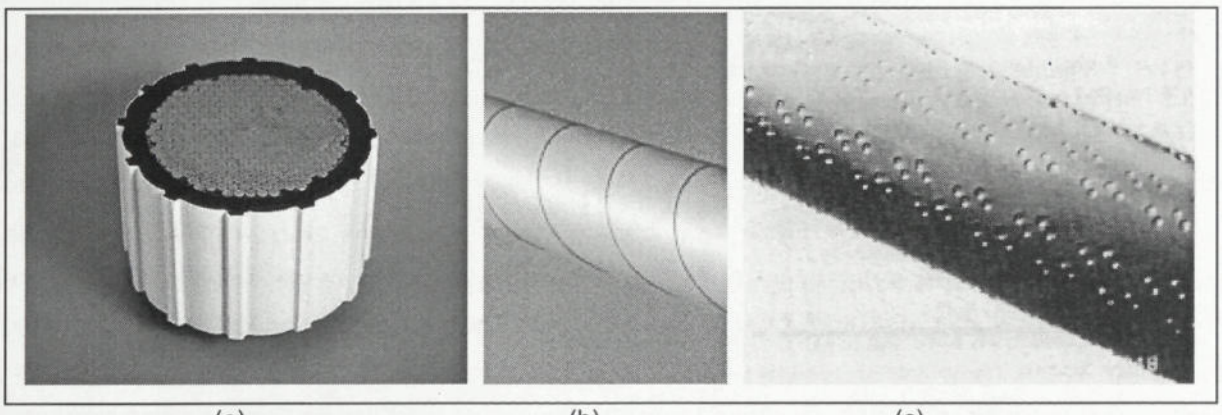
(iii) Rain-wind induced vibration

Rain-wind induced vibration was observed for the first time at the Meiko-Nishi Bridge, during the phase of construction (Hikami & Shirashi, 1988). Large amplitude vibrations developed for some of the *PE* coated cables located behind the tower, relative to the wind. These oscillations occurred in the cable plane, under combined action of wind and rain, at a natural frequency of *1-3Hz*. The monitoring of the bridge and the performance of additional wind tunnel tests showed that the cable vibrations were associated with the circumferential oscillation of two water rivulets which formed on the upper and lower surface of the cable for a particular wind velocity range (Hikami & Shirashi, 1988; Matsumoto *et al.*, 1995; Flamand, 1993; Verwiebe *et al.*, 1998). An attempt to analytically explain the phenomenon was made by Yamaguchi (1990), who developed a two-degree-of-freedom galloping model for the cable/upper rivulet system. As for the main characteristics of rain vibrations, observations in prototypes have shown that vibrations occur at a much lower frequency and much higher amplitude than *vortex-induced* vibrations. Matsumoto *et al.* (1989a) refer a frequency range of oscillation of *0.6-3Hz* and maximum observed oscillation amplitudes of about two cable diameters (*2D*). In later publications, Matsumoto and companion authors (1992, 1995, 1998) concluded that the phenomenon of *rain-wind* induced vibrations was in reality a complex combination of several forms of instability mechanisms, the presence of an upper water rivulet being only a factor to enhance aerodynamic instability. According to Matsumoto, the existence of an axial flow along the inclined cables motivates two types of instability: *velocity restricted galloping*, and *3-D vortex shedding* at high wind velocity. These phenomena are however not completely understood at present.

Rain-wind induced vibration is the most frequent form of cable instability in cable-stayed bridges, as can be evaluated from a long list of bridges all over the world, which in some phase during or after construction experienced this problem. This list includes namely the Brotonne Bridge, in France, the Farø Bridges, in Denmark, Ben Ahin and Wandre Bridges, in Belgium, the Glebe Island Bridge, in Australia, the Second Severn Crossing, in the United Kingdom, the Burlington Bridge, in the USA, the Erasmus Bridge, in Netherlands, and the Aratsu and Yobuko Bridges, in Japan.

Some simple measures can be taken in the phase of design, in order to avoid rain vibration, like the adoption of protuberated or rough coating surfaces for the cable tubes, which prevent the formation of water rivulets (see examples in Figure 1.10). The quantification

of cable forces generated by rain for use in a numerical analysis of the cable-stayed bridge response, already attempted in the study of cable vibrations at the Erasmus Bridge (Geurts *et al.*, 1998), is however a very complicated task which deserves further investigation.



(a) (b) (c)

Figure 1.10. Examples of non-smooth surfaces of cable coating to prevent *rain-wind-induced* vibration: (a) Protuberated, Higashi-Kobe Bridge; (b) Helical wire whirling, Vasco da Gama Bridge; (c) Dimpled, Tatara Bridge (Virlogeux, 1998).

(iv) Indirect excitation

The various forms of cable oscillations above referred result from direct excitation of wind and rain on the surface of the cable. It should be noted however that the oscillation of the cables induces motion at the end supports, which may also originate vibration of the deck and towers. On another hand, the vibration of the deck and towers caused by wind, traffic and earthquakes, produces an *indirect excitation* of the cables through motion of their anchorages. In certain circumstances, the induced cable vibrations attain very high amplitudes. Two phenomena can be identified under these circumstances, here designated as *external* and *parametric* excitation. The *external excitation* corresponds to an amplification of motion applied at some anchorage perpendicularly to the cable chord, while the *parametric excitation* corresponds to oscillations in the direction of the chord. The phenomena of *external* and *parametric excitation* have been observed in several bridges in the past (some examples are the Brotonne Bridge, in France, Ben-Ahin and Wandre Bridges, in Belgium, and the Annacis Bridge, in Canada). The literature in the topic of *indirect excitation* concentrates essentially in studies on the *parametric excitation* phenomenon, which is considered more important. The usual approach to the study of *parametric excitation* consists in an evaluation of the cable resonance condition from the dynamic equilibrium equations of a single cable under harmonic motion of the supports. A modified Mathieu-Hill type equation is obtained (Tagata, 1977; Nayfeh & Mook, 1979; Pinto da Costa *et al.*, 1996; Clement & Cremona, 1996), which is characterized by a set of secondary resonances, i.e., the response to an harmonic of frequency ω is not increased exclusively at resonance (when the natural frequency of the

cable system coincides with ω), but also at specific ratios between the exciting frequency and the system natural frequency: *½, 1/3, 2*, and *3*. It is possible then to define instability regions, i.e., intervals of frequency oscillation of the supports where high amplitudes of vibration occur and to characterize both the threshold amplitude for the occurrence of instability, and the maximum amplitude of oscillation inside the instability regions.

Cable structure interaction

The various phenomena of cable vibration have been most frequently studied considering the stay cables isolated from the bridge structure. It is important however to understand the type of interaction that these elements exert with the deck/towers system when integrated in the bridge structure, as well as the interaction between the various stay cables on a bridge.

The relatively restricted research performed in this particular issue was already referred in Section 1.1.1.

1.1.3 Seismic analysis

Earthquake resistance is a major issue in the design of cable-stayed bridges in seismically active regions, like Japan or the United States of America. Although many cable-stayed bridges have been built in regions of high seismic risk during the last decades, information concerning the performance of this type of structures under moderate to strong earthquakes is very scarce. In fact, to the author's knowledge, the only report of bridge damage associated with an earthquake refers to the Shipshaw Bridge, in Québec, Canada, which experienced the Saguenay earthquake (M_L=*6.0*) in November 1988, with an epicenter distant of about *40km* of the bridge, and suffered failure of one anchorage plate at the abutment (Filiatrault *et al.*, 1993).

In general, slender bridges are well able to accommodate deformation suffered in response to earthquake ground motion. The concern with cable-stayed bridges results from two main points. First of all, the structural damping observed on these bridges from ambient and forced vibration tests is extremely small (*0.3%-2%)* (Abdel-Ghaffar, 1991). A second aspect refers to the spatial variability of the earthquake ground motion. In effect, for long span bridges (span larger than *200m*, according to Abdel-Ghaffar), the phase-lag of ground motion at the two tower piers may be significant. Also, different foundation conditions originate different angles of incidence of the seismic waves and different travel paths, producing a very complicated correlation of the motion at the different supports, which can affect significantly the bridge response.

The seismic response of a cable-stayed bridge is highly affected by the form of connection of the girder to the towers. The seismic forces are reduced to a minimum whenever the deck is free to swing at the towers, the only connection to these elements being given by the stay cables. The inconvenience of such solution is however an increased

deformability of the bridge deck under service loads. On the contrary, a rigid connection at the towers is responsible for an increase of the seismic forces, but results in smaller deformation under service loads. It is thus of utmost importance to install special bearing devices at the deck-tower connections or at the abutments, which dissipate seismic energy at reduced displacements.

The estimation of the response of a cable-stayed bridge to an earthquake involves the following aspects: (i) Definition of design criteria and characterization of the input motion; (ii) Simplified preliminary analysis of the structure; (iii) Detailed analysis of the bridge.

The design criteria are defined taking into consideration that, in general, long span cable-stayed bridges are projects of great economical importance, which establish vital links in the transportation network. So, the required level of seismic protection is much higher than for ordinary structures. As an example, the new cable-stayed bridge over the Tagus River, in Lisbon, was designed for a ground acceleration of *0.5g*, with a spectral response peak of *1.15g*, *4* times greater than required for ordinary buildings in Lisbon (Capra & Leveille, 1998). Once a smoothed response spectrum has been defined, a preliminary analysis can be performed, using simplified methods, such as the multi-mode spectral method. A refined time-history analysis of the bridge can then take place using a set of previous records of ground motions or a set of accelerograms artificially generated based on the design input response spectrum. This analysis should incorporate three-dimensionality, nonlinearity (geometrical, material and of special damping augmentation devices), multiple-support seismic excitations and soil-structure interaction (Abdel-Ghaffar, 1994).

1.1.4 Structural monitoring

Long span cable-stayed bridges are usually highly complex unique prototypes. It is thus important, particularly for bridges located in zones of high environmental hazard, that both during the construction process and throughout their life time, these structures are monitored so that their structural behaviour is assessed and their safety for use is assured, the necessary repair and maintenance being performed in due time.

Although permanent observation of bridge structures has not been a common practice, the growing importance of these structures in terms of span length, construction and maintenance costs has made instrumentation and monitoring of bridges an important issue. So, it is a current practice that newly constructed bridges are equipped with a series of sensors for continuous measurements. These usually include a varying number of temperature sensors, strain gages, accelerometers and anemometers. More recently, optical devices based on laser technology have been employed for the measurement of velocities and displacements.

With regard to the recording of data, it is important to refer the new generation of acquisition systems, which can perform continuous measurements and on-line processing of

the collected signals and, consequently, provide on-line information on the structural status, allowing the detection of damage from variations in the dynamic properties of the bridge.

Considering the enormous amount of recorded data from continuous measurements, and the difficulty to store and process all the signals, different options are available for selecting the most relevant data and information. The systems developed by the Norwegian Geotechnical Institute (*NGI*), for example, which were employed in the instrumentation of the Helgeland and Skarnsundet Bridges, in Norway, sample continuously at *10Hz* and automatically perform statistics on *20* minute records (mean, maximum, minimum and standard deviation) for every sensor, storing the *72* logging periods statistics in a file for each day of operation. A ring buffer is used for storing *20* minute sampled records (*12000* samples per sensor), the data being sorted according to the average wind velocity and stored in such a way that the files associated with highest wind velocity are retained at the top of the stack.

The *OASIS* system, developed by Agbabian Associates in association with Kinemetrics Instruments (Nigbor & Diehl, 1997) and installed on the Rama IX Bridge, in Thailand, and on the Namhae Great Bridge, in the Republic of Korea, also records statistics of continuous measurements, sampling only extreme events, by means of a programmable threshold trigger.

A common characteristic of the two systems and of other modern acquisition systems, is the possibility of remote command and control of the monitoring operations, using graphic displays. In some cases, data is regularly compressed and sent via modem to the Laboratory.

But the usual practice in dynamic testing in the Civil Engineering field consists in the performance of short term tests at the end or after construction, employing simpler portable acquisition systems, which have less demands in terms of data management.

Short term dynamic tests of both physical models (Godden & Aslam, 1978; Sethia & Krishna, 1987; Garevski, 1990) and of full scale cable-stayed bridges (Ohlsson, 1987;Stiemer *et al.*, 1988; Murià-Vila *et al.*, 1991; Jakobsen *et al.,* 1995; Macdonald *et al.,* 1997; Okauchi *et al.*, 1997; Cunha *et al.*, 1998) have been performed during the last decades, with two main purposes: assessing the main dynamic structural parameters (natural frequencies, mode shapes and damping coefficients) for calibrating and eventual updating of numerical models, and identifying the current status of the structure in order to explain possible causes of damage or excessive vibration.

The techniques used in the dynamic testing of Civil Engineering structures are derived from *Experimental Modal Analysis* techniques, which were born and are commonly used in Mechanical Engineering and Aeronautics. The fact that these structures, in particular the long span bridges, are characterized by very small natural frequencies and damping factors, large dimensions, and high inertia, causes specific difficulties, which are responsible for a relatively restricted number of reported applications in this particular domain.

The direct application of *Modal Analysis* techniques to Civil Engineering structures consists in the performance of *Forced Vibration Tests* (*FVT*). This technique requires the application of a controlled excitation at one or more points along the structure, and the

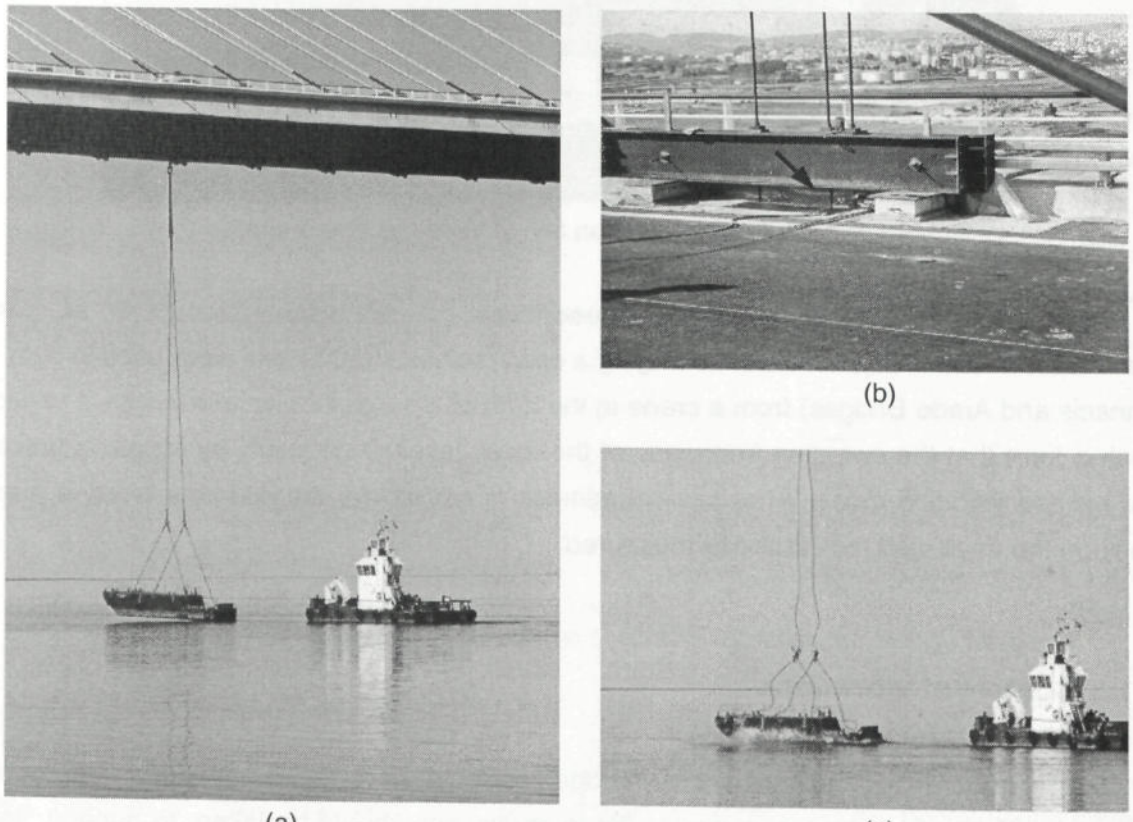
measurement of both the input and response signals. If all the measured responses are due to the controlled excitation, then well-established signal processing and system identification techniques can be applied in order to extract modal parameters. The *FVT* technique has proven efficient for small and medium size structures, using mechanical, hydraulic and electrodynamic shakers, which produce a level of response much higher than environmental actions (like wind, traffic and machinery (Flesch, 1990; Cantieni *et al.*, 1994). However, for large and flexible structures, such as cable-stayed and suspension bridges, very large shakers are required to produce a significant level of vibration. The *FVT* technique becomes then very costly and difficult to apply. One of the few known applications to a long span cable-stayed bridge respects the Hitsuishijima Bridge, one of the Honshu-Shikoku Bridges, in Japan, a continuous steel bridge with a main span of *420m*. Field tests were performed using two large shakers, with two main purposes (Okauchi *et al.*, 1997): to investigate damping properties at large amplitudes, and to investigate coupled vibrations between the girder and cables. The two shakers, with sliding masses of about *6000kg* and a stroke of about *0.16m*, delivering a maximum exciting force of *200 kN* at *0.7Hz*, and working in the range *0.36Hz-2.17Hz*, were operated simultaneously in-phase or out-of-phase at two opposite locations on each of two tested cross-sections, producing a maximum vibration amplitude of about *10cm*.

A derivation of *Modal Analysis* techniques consists in using environmental actions as source of dynamic excitation. Assuming that the excitation is smoothly distributed in the frequency band of interest, i.e., the input excitation can be idealized through a band limited "white noise", the amplitude of the frequency response functions is proportional to the spectral density of the response functions and, consequently, natural frequencies, mode shapes and damping coefficients can be estimated from spectral analysis of response measurements (Bendat & Piersol, 1980). This corresponds to the so-called *Ambient Vibration Testing* (*AVT*) technique. *AVT* has been applied rather successfully in suspension and cable-stayed bridges (Abdel-Ghaffar & Housner, 1978; Abdel-Ghaffar & Scanlan, 1985; Brownjohn *et al.*, 1987; Brownjohn *et al.*, 1989; Law & Ko, 1995, Fernandes *et al.*, 1996; Macdonald *et al.*, 1998; Rodrigues & Campos Costa, 1998; Cunha *et al.*, 1998).

The considerable development in electronics and instrumentation devices of the last decades has brought a new degree of confidence in *AVT*. In fact, the main drawback of this technique results from lack of resolution in amplitude and frequency of the measured response, which is due to the low level of excitation from ambient sources and typical high modal interference. Concerning the amplitude resolution, it should be pointed that *Force Balance Accelerometers* (*FBA*) are the most appropriate sensors for *AVT*, allowing amplitude measurements of acceleration as small as $1\mu g$ in the frequency range *DC-50Hz* . With regard to the acquisition systems, the common digitizing resolution was of *12* bits *10* years ago. Presently, it is considered that *16-bit* resolution is the minimum required for the performance of ambient vibration tests, although *32-bit* resolution systems are already available in the market. Moreover, a minimum frequency resolution of *0.01Hz* is required for flexible structures with very close natural frequencies. This leads naturally to the need of acquisition and storage

of very long records. Experience in this field has proven that a minimum recorded length of the response should be of *30* to *40* times the highest structural period, times a number of averages varying between *8* and *32*, what corresponds typically to about *32768* to *524288* samples per channel. As an example, the measurements at the Vasco da Gama Bridge (Cunha *et al.,* 1998), with a fundamental period of about *3s*, were performed from series of *16* minutes, recorded at a sample frequency of *50Hz* (*48000* samples per channel) at each of the *58* instrumented points (*2* per section along the deck). It is thus essential that the software that controls the Analog to Digital Converter hardware allows the acquisition of very long records, and also that large storage disks are available.

Finally, and considering that the damping coefficient estimates obtained from *AVT* present generally a significant dispersion, due to the large variation of this parameter at small levels of vibration amplitudes (Okauchi *et al.,* 1997) and also to the fact that it is not always possible to separate from *AVT* the characteristics of mode shapes that are strongly coupled, an intermediate technique of test has been applied in some structures, which consists in the sudden application of an excitation and measurement of the free vibration response. The level of induced vibration is commonly intermediate between *FVT* and *AVT*. The simplest type of test consists in the measurement of the impact response of a loaded truck passing repeatedly over a plank. Another form of free vibration testing consists in the measurement of the structural response that results from the sudden release of a suspended mass.



(a) (b) (c)

Figure 1.11. Free vibration test at Vasco da Gama Bridge: (a) Eccentrically suspended *60tf* barge; (b) Starting cut of hanging Dywidag bar; (c) Release of barge.

A test of this type was performed at the Normandy Bridge (Bietry & Jan., 1995). The procedure comprehended two sequences where a mass of *50t* and *100t* was released, vertically in the first test, and inclined at *14°* with horizontal, in the second test, so as to excite both the fundamental vertical and torsional vibration modes. At the Vasco da Gama Bridge, a simpler system was employed (Cunha *et al.*, 1998), consisting in the release of a *60tf* barge hanging eccentrically from the bridge deck at low tide, by forced failure of the Dywidag rope (see Figure 1.11). As a reference, the maximum vertical displacement of the deck in this test was about *25mm* (maximum acceleration of *30mg*), while *0.9mm* (maximum acceleration of *50mg*) had been achieved from the truck test, using a *30tf* loaded truck passing over a *4cm* thick plank (see Figure 1.12).

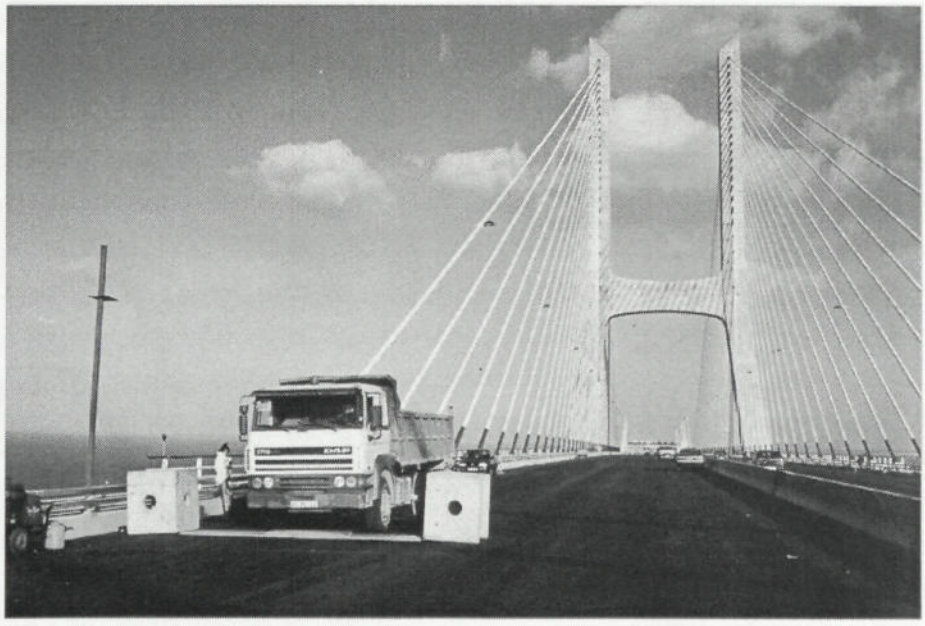


Figure 1.12. Impact vibration test at Vasco da Gama Bridge.

A different testing procedure, already used in the past (Stiemer *et al.*, 1998; Fernandes *et al.*, 1996), consists in hanging a concrete block (*2tf* blocks were used in both the Annacis and Arade Bridges) from a crane in the form of a pendulum, whose length is varied in such a form that the swinging frequency of the mass (excited manually by ropes) is tuned to the excited vibration mode. After several minutes of oscillation, the concrete block is placed back on the deck, and the response measured.

1.1.5 Control of vibrations

Once the generating mechanisms of bridge vibration have been identified, appropriate countermeasures to reduce or suppress large oscillations should be taken. In general, these measures can be classified in *3* categories, namely *aerodynamic*, *structural* and *mechanical control of vibrations*. These control measures belong to a category of so-called *passive*

techniques of control. Although extensively used around the world with proved effectiveness in the structural performance, these techniques have inherent limitations (Soong, 1988). In recent years, however, some attempts have been also registered in order to use *active* and *semiactive control* techniques, using some technological transfer from the area of Control Engineering to Structural Engineering. *Active* and *semiactive* control are, in effect, extensions of *passive control techniques* where the structural motion is controlled or modified by an actuator by action of a control system through external supply of energy. These systems may actually combine the three types of measures above associated with *passive control* devices.

Aerodynamic control of vibrations

The *aerodynamic control of* vibrations is performed by modification of the cross sectional configuration. For the bridge deck, some appendages are attached, as represented in Figure 1.13 (round fairings, triangular fairings, splitter plates, flaps), with the aim of disturbing the generation of vortices and achieving the streamlining effect.

For the bridge towers, either deflectors have been installed, or cutting of the corner edges applied (see Figure 1.14).

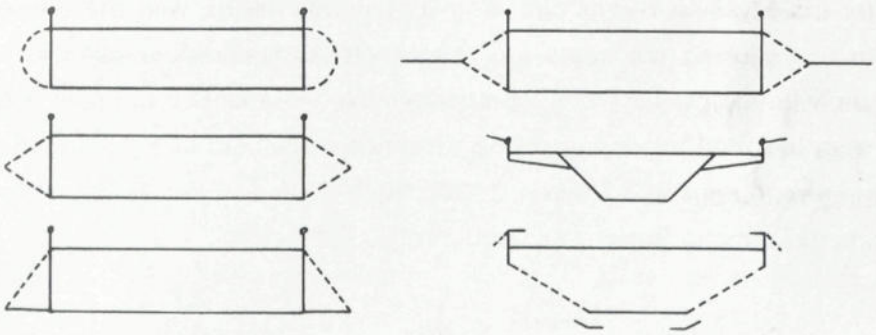


Figure 1.13. Examples of aerodynamic appendages for a bridge deck.

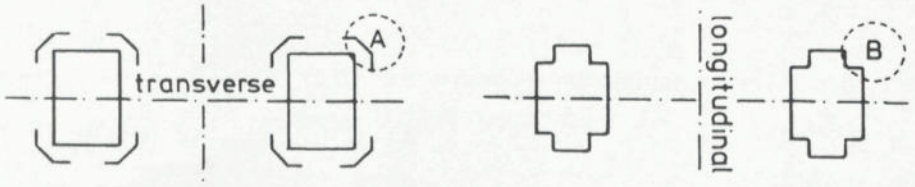


Figure 1.14. Examples of aerodynamic control of vibration for bridge towers.

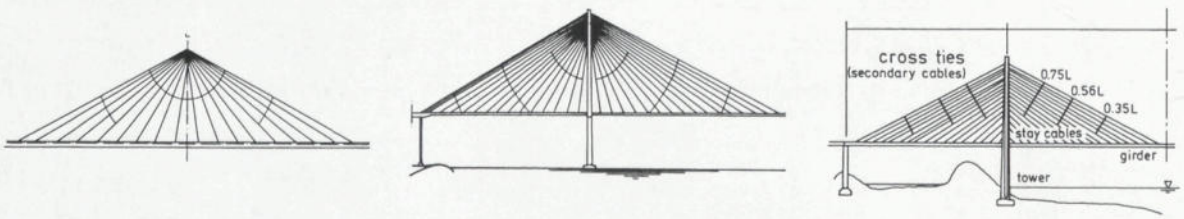
Although modification of the shape of cables is limited, recent studies (Miyata *et al.*, 1994; Saito *et al.*, 1994; Flamand, 1994) proved that, by roughening the polyethylene covered cable surface, the formation of water rivulets is prevented and, consequently, rain-wind induced vibration of the cables is suppressed. Examples of applications of this concept are

presented in Figure 1.10. The main drawback of this procedure is the risk of increasing the drag force for the design wind speed in comparison with the drag force on the normal smooth cable. This aspect is particularly relevant for long span cable-stayed bridges, as the wind load on the cable system is a significant part of the overall wind load. It is however possible to control the drag forces, if a convenient roughness arrangement is chosen. This was proved by Miyata *et al.* (1995) who performed series of wind tunnel tests on cable models with different densities and arrangements of dot surface roughness, arriving to the final dimpled surface presented in Figure 1.10 (c) for the cables of the Tatara Bridge.

Finally, another form of *aerodynamic control of vibrations* consists in adopting a specific cable arrangement. For PC cable-stayed bridges, a closely spaced arrangement significantly changes the flow around the cables. This solution was effective in preventing wake-induced vibration at the Ikara Island Bridge, in Japan (Fujino & Kimura, 1997).

Structural control of vibrations

The *structural control of vibrations* by interconnecting ropes has been used very frequently, either temporarily, before the installation of damping devices on the cables, or as a definite measure. The use of cross-cables was first proposed (although never used) by Leonhardt in the project for the Messina Straits Crossing (Leonhardt, 1986), with the aim of achieving a stiffer system by reducing the cable sag. Later, cross-cables were used in several cable-stayed bridges, with the purpose of suppressing cable vibrations. Examples of bridges where this system was installed according to the schemes presented in Figure 1.15, are the Farø Bridge, in Denmark (Langsoe & Larsen, 1987), the Helgeland Bridge (Jakobsen *et al.*, 1995), in Norway, and the Yobuko Bridge (Yamaguchi, 1995), in Japan.



(a) (b) (c)

Figure 1.15. Scheme of cable-cross systems installed at: (a) the Farø; (b) the Helgeland; (c) the Yobuko Bridge.

The addition of cross-ropes to the stay cable system creates intermediate supports at those elements and, consequently, increases their natural frequencies for vertical vibrations. With a proper design of these ropes, the fundamental frequency of the stay cables is shifted to relatively high values, thus reducing the possibility of internal resonance with global bridge modes at the fundamental mode shapes. Another effect of the installation of cross cables is an increase of the damping. A study by Yamaguchi (1995) showed that this increase is higher

for soft secondary cables than for taut ties. However, the initial tension on these cables should have a sufficiently high value, so that under extreme effects the cross cables are not detensioned, producing shocks and causing damage of the tie devices, as reported by Virlogeux in the Farø and some of the Honshu-Shikoku Bridges. In the case of the Normandy Bridge, the designers decided to use taut cross-cables made of ropes with a short pitch length (see Figure 1.16), which provide a high internal damping and a satisfactory resistance to fatigue (Virlogeux, 1998).

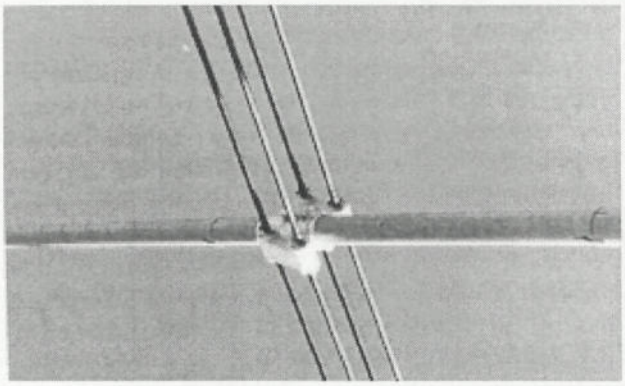


Figure 1.16. Cross-cables at the Normandy Bridge (Virlogeux, 1998).

Mechanical control of vibrations

The *mechanical control of vibrations* is achieved by installation of damping devices at certain locations along the bridge structure. The Forth Road Bridge, completed in 1964 in Scotland was the first, according to Narita and Yokoyama (1991), to install a damper, which consisted in a *16t* concrete block connected by rope wire at the tower top (*150m*), dissipating energy by Coulomb friction effect when moving on the ground. This type of damper was subsequently used during construction in several other bridge towers in Japan, such as the Kammon Bridge, the Innoshima Bridge and the Kita-Bisanseto Bridge. Oil dampers have been used in more recent applications, providing better results. Alternative devices for installation either at the bridge towers or inside the bridge deck are the *Tuned Mass Dampers* (*TMD*) and *Tuned Liquid Dampers* (*TLD*).

Tuned mass dampers are associations of sprung masses (typically *1%* to *2%* of the overall structure mass) and dashpot systems which, when properly tuned and attached at convenient locations along the bridge structure, reduce its dynamic response near resonance. The effectiveness of these systems, that were initially used in the aircraft and automobile industry, was first proved by Den Hartog (1956). Later applications to Civil Engineering structures include the road decks of the Kessock Bridge, in Scotland (Wallace, 1985), the Chao Phya Bridge, in Bangkok (Malhortra & Wieland, 1987), and the Normandy Bridge (during construction) (Conti *et al.*, 1994), and the towers of the Aratsu-Ohashi Bridge, Japan

(Yoshimura *et al.*, 1989), the Yokohama Bay Bridge (Saito *et al.*, 1988), the Chao Phya Bridge and the Meiko-Nishi Bridge (during construction) (Kawahito *et al.*, 1984). Figure 1.17 presents a photograph and scheme of the *TMD* installed at the Normandy Bridge deck during construction. A reduction of *35%* was observed for the bridge response under wind excitation using this device. Figure 1.18 presents the scheme and location of a set of *TMDs* installed at the Yokohama Bay Bridge.

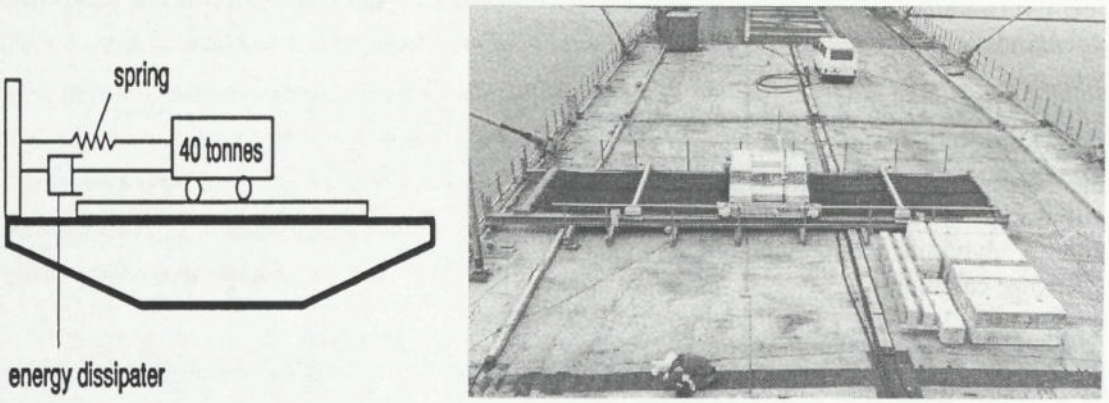


Figure 1.17. *TMD* of the Normandy Bridge, scheme and photograph (Conti *et al.*, 1994).

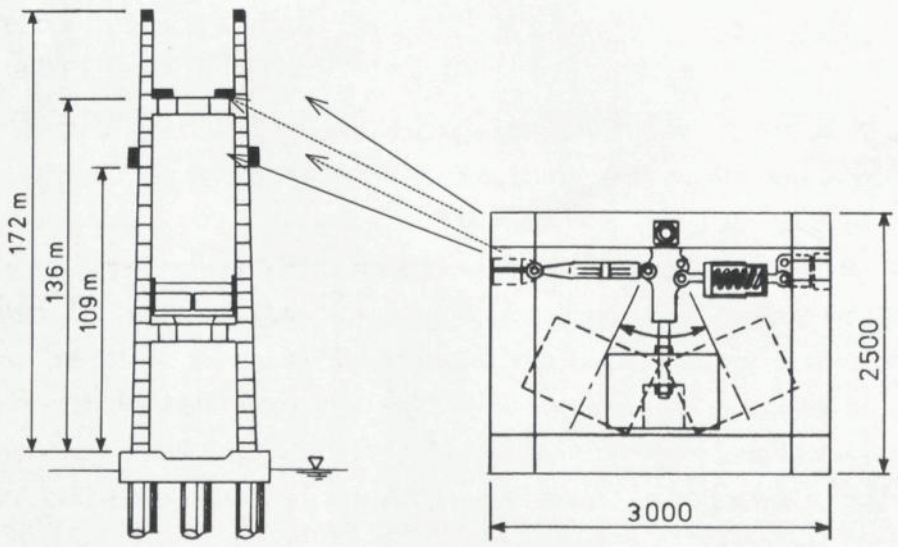


Figure 1.18. Location and scheme of TMDs installed at the towers of the Yokohama Bay Bridge (Saito *et al.*, 1988).

Tuned liquid dampers use the motion of liquid inside a container as energy dissipator. Although several applications of these devices are known (mainly for tall buildings and towers), the physical phenomenon of the liquid sloshing motion that reduces the structural response is not fully understood, particularly for large amplitude excitation (Reed *et al.*, 1998),

and the numerical modelling has not yet been completely assessed. Figure 1.19 presents an example of a building in Japan where a set of multi-layer *TLD*s were used.

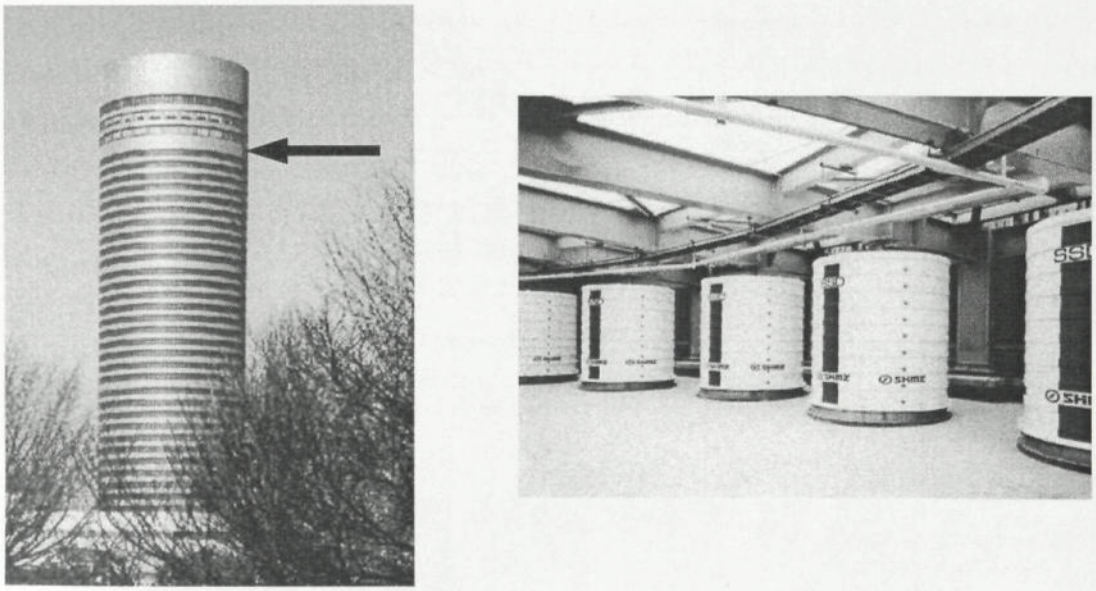
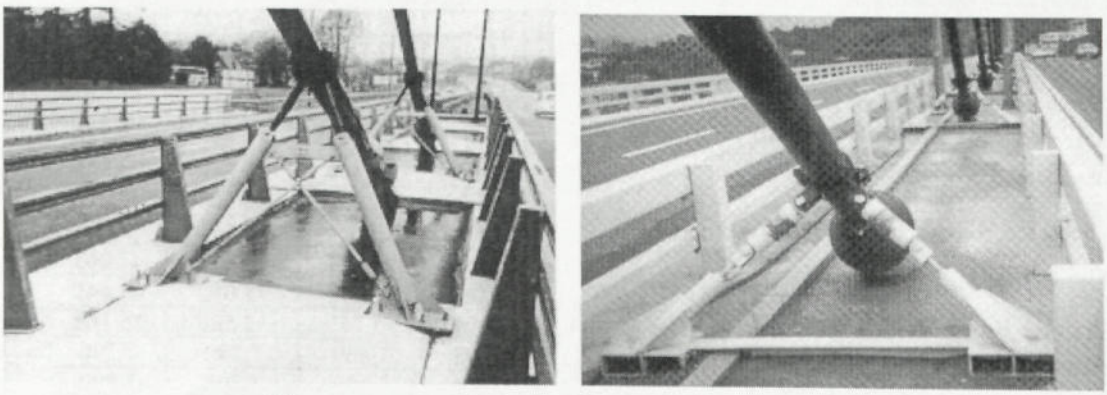


Figure 1.19. Multi-layer *TLD*s installed in a building in Japan (Tamura *et al.*, 1995).

The installation of mechanical devices at the stay cables is a classic solution for suppressing cable vibrations. The first known application in cable-stayed bridges respects the Brotonne Bridge, where two oil dampers were attached at an angle close to the lower cable anchorage of each stay cable. This system was used in several other bridges around the world. Figure 1.20 presents photographs of the devices employed at the Iroise (France) and Aratsu (Japan) Bridges.



(a) (b)

Figure 1.20. Hydraulic dampers at: (a) Iroise (Virlogeux, 1998) and (b) Aratsu Bridge (Ohashi, 1991).

Recent applications involve the installation of ring dampers made of neoprene, high damping rubber, or other viscous products inside a steel pipe (the deviator guide), at an appropriate distance from the lower and, eventually, the top anchorage. The scheme of a ring damper mounted at the lower end anchorage is shown in Figure 1.21.

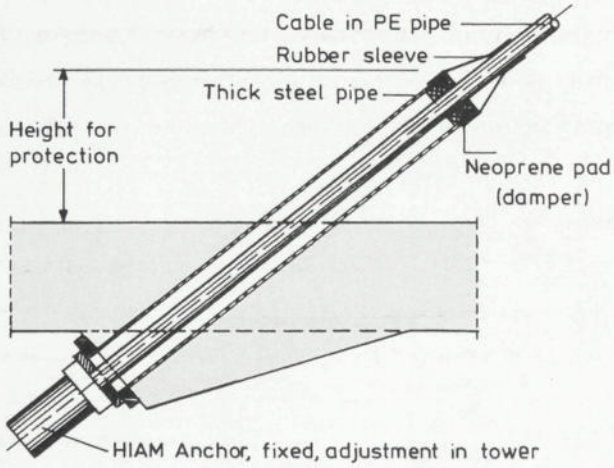


Figure 1.21. Scheme of ring damper.

Active control systems

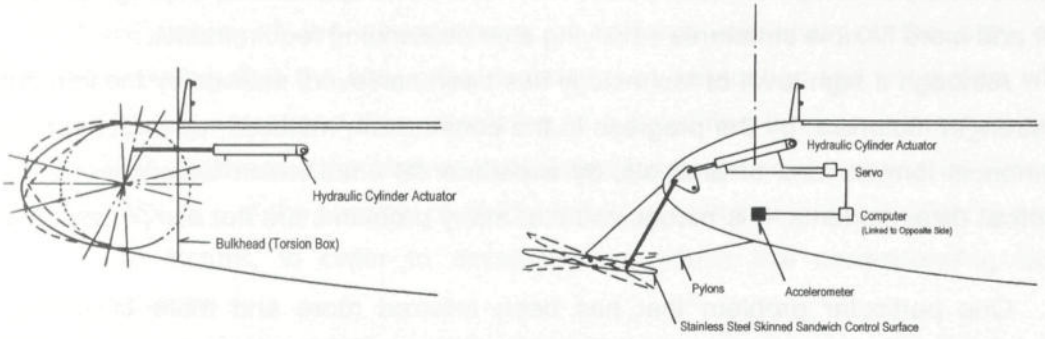
The basic scheme of an *active control system* comprehends the following components: (i) sensors located on the structure for measurement of external excitations and/ or structural responses; (ii) devices to process the measured information and compute the necessary control forces, according to a specified control algorithm (closed loop, open-loop, or open-closed loop); (iii) actuators, usually provided by external sources. Basically, the control system can follow two strategies, according to the chosen control algorithm, the first corresponding to a modification of the structural stiffness and damping so that the structure can respond favourably to the external excitations (closed-loop), and the second, consisting in the reduction or elimination of the external forces (open-loop).

The main control mechanisms studied for application in the specific domain of bridges are: (i) *active aerodynamic appendages*; (ii) *active mass dampers,* and (iii) *tendon control.*

(i) Active aerodynamic appendages

The idea of applying *active aerodynamic appendages* in ultra-long-span bridges was first introduced by Ostenfeld and Larsen (1992), inspired in principles used in the stabilization of surfaces in the aircraft industry. Two concepts were suggested, according to the representations of Figure 1.22. The first (Figure 1.22 (a)), consists in actively changing the geometry of the side of a streamlined box bridge deck, modifying the flow pattern around the girder to reduce wind-induced excitation. The second (Figure 1.22(b)) consists in the addition of control surfaces attached beneath the edges of the deck by aerodynamically shaped pylons at a convenient distance. The rotation of the surfaces by means of hydraulic actuators produces aerodynamic forces that stabilize the structure, increasing the critical wind speed. Recent studies (Wilde & Fujino, 1998) showed that a great advantage of this technique of

control over the structural methods is the fact that the source of stabilizing forces, the wind, is actually the same as the source of the aerodynamic forces that cause instability. However, the practical implementation is very complex, requiring the design of two or three parallel control systems, to ensure that the failure of a controller does not cause the collapse of the bridge.



(a) (b)

Figure 1.22. Suggestions for implementation of active control surface systems in streamlined bridge girders (Ostenfeld & Larsen, 1992).

(ii) Active Mass Dampers

On the contrary of *TMDs*, which are designed to reduce the response in only one mode of vibration, usually the fundamental one, *Active Tuned Mass Dampers* (*ATMDs*) can be effective over a wide frequency range. These devices have been studied in recent years with the purpose of application to tall buildings (Yamazaki *et al.,* 1992). Wind tunnel tests (Samali *et al.*, 1999) have shown in particular that the efficiency of a *TMD* can be achieved with an *ATMD* of *60%* mass using simple control algorithms. However, these devices are still in an experimental phase of research.

(iii) Active tendon control

Finally, *active tendon control* has been considered by several authors as a possible alternative technique to control cable vibrations, particularly for long span cable-stayed bridges, in which the application of passive dampers near the cable anchorage is less effective. Studies in *active tendon control* have been developed in two directions: the modal control, which uses the axial motion of the cable-support (Fujino & Susumpov, 1994; Susumpov & Fujino, 1995), and the wave-control approach, that applies transversal control forces in the cable span support (Yamaguchi & Dung, 1992). Given the number of cables on a typical cable-stayed bridge and the need for individual control of each cable using external power sources, either technique of active control may encounter many practical difficulties to be implemented. Very recent research is focusing on the so-called *semiactive damping* devices. On the contrary of active devices, that can induce unfavourable forces in the structure if not appropriately tuned, *semiactive dampers* can only exert dissipative forces (Johnson *et al.*, 1999).

1.2 OBJECTIVES

It was seen in the previous Section that, in a period of less than *50* years since the modern cable-stayed bridges established as a new category amongst the classical types of bridges, an extraordinary development took place, which led to the appearance of progressively larger, lighter and more flexible structures satisfying ever demanding requirements.

Although a high level of technology has been achieved, marked by the introduction of high strength materials, by the progress in the construction methods, by the generalized use of numerical formulations of analysis, by experimental observation techniques and also by theoretical developments, it is recognized that many problems are not completely understood yet.

One particular problem that has been referred more and more frequently in the literature relates to the excessive vibration observed in cable-stayed bridges, associated with the stay cables and/or with the deck and towers.

In many cases cable vibrations have been associated with the *direct* effects of wind excitation, namely with *vortex-shedding*, *wake effects* and the effects of the *combined action of rain and wind*. Another type of phenomena has been identified more recently, which concerns the *indirect* excitation of the cables by motion of the cable anchorages.

However, most of the formulations of dynamic analysis isolate the stay cable from the bridge structure, the corresponding interaction with the structure being neglected or considered in a very simplified form, whether the stay cable is subject to direct or *indirect* excitation.

Although some authors have already investigated the topic of *cable-structure interaction*, no experimental proof or characterization of the phenomenon was ever conducted on a real bridge, to the knowledge of the author. Moreover, the corresponding numerical approaches were never fully conclusive, pointing either to the possibility of the existence of favourable effects to the global bridge behaviour, or to the unfavourable amplification of vibrations.

Under these circumstances, given the previous background of the author in the field of Experimental Dynamics and System Identification, and making use of the opportunity to test an already existing physical model of a constructed cable-stayed bridge (the Jindo Bridge, in South Korea) at the Earthquake Engineering Research Centre at the University of Bristol, a research work centred on this physical model was developed, whose main objectives were:

- To experimentally identify and characterize the dynamic *cable-structure interaction* effect;
- To evaluate the effect of dynamic *cable-structure interaction* in the seismic response of a bridge structure.

This research program was developed in several phases, which are described as follows:

1- Literature survey in the topics of cable-stayed bridges and dynamics of cable-stayed bridges, considering in particular the subject of *cable vibrations*;
2- Investigation of the phenomenon of *indirect excitation* of the stay cables, considering first the stay cable isolated, i.e., neglecting the interaction with the bridge structure, and then simulating in a simplified form an interaction with the bridge structure, using both analytical developments and numerical analyses;
3- Modification of the physical model by redesign of the stay cables using appropriate scale factors, in order to accurately reproduce the corresponding dynamic behaviour;
4- *2-D* numerical modelling of the bridge model for identification of the cable-structure interaction phenomenon and for preparation of the experimental tests;
5- Performance of an extensive modal survey on the bridge model, using conventional Modal Analysis techniques and exciting the structure with an electrodynamic shaker;
6- Extension of the modal survey by additional performance of tests on the shaking table at the University of Bristol;
7- Measurement of the seismic response of the bridge model to artificially generated accelerograms that were used as input on the shaking table;
8- Signal processing of the measured data and identification of modal parameters from the constituted data base;
9- Validation and improvement of previously developed numerical models for assessment of *cable-structure interaction* and for evaluating the time response to various types of accelerograms;
10- Numerical simulation of the effects of *cable-structure interaction* either using particular severe excitation, or modifying the physical model properties in order to frame the problem for a general cable-stayed bridge.

It should be noted that, although the theme of the research is rather specific, the accomplishment of the various involved tasks demanded the development of an extensive literature survey and the complete understanding of different types of tools covering the analytical, the numerical and experimental fields of the Dynamics of Cable-Stayed Bridges that were focused in the previous Section. These were: (i) the numerical modelling of the dynamic behaviour of cable-stayed bridges; (ii) the experimental identification of the corresponding dynamic properties; (iii) the assessment of the various phenomena of instability in this type of bridges. Because most of these themes are relatively actual and involve concepts, information and new findings that are disperse in the literature, it was considered of interest to gather the most relevant information in the current dissertation.

The thesis is then organized in nine Chapters, the first and last containing respectively an *Introduction* and the *Conclusions* of the research. Besides these, the dissertation includes two groups of Chapters, one series of preliminary Chapters (*two, three, four, five)* that present an overview on the characteristics of cable-stayed bridges (*two*), and systematize the main analytical (*three*), numerical (*four*) and experimental (*five*) tools employed in the research, and a series of Chapters (*six, seven, eight*) that describe the main applied research developed by the author, which comprehend a survey of the cable vibrations phenomena, accompanied by a set of analytical developments made by the author in the particular issue of *indirect excitation* of stay cables (*six*), the description of the experimental survey developed on the physical model of the Jindo Bridge and of the main results concerning the *cable-structure interaction* phenomenon (*seven*), and an experimental and numerical evaluation of the corresponding effect in terms of the seismic response of the bridge (*eight*). A more detailed description of the various Chapters follows:

Chapter One

This Chapter focuses on the various particular issues covered by the thesis, presenting the main achievements and the major problems associated with each topic, and describing the objectives and organization of the thesis.

Chapter Two

In this Chapter a review of the evolution of the construction of cable-stayed bridges is presented, with reference to some of the most remarkable bridges and to the diverse structural systems. The various proportions involved in the design of a conventional bridge are also discussed and different possibilities for the construction of the main structural components (deck, towers and cables) are referred. A final Section describes some of the most important cable-stayed bridges constructed in Portugal, stressing particular features of these bridges that in several cases led to very innovative solutions.

Chapter Three

Chapter three provides a basic introduction to the deformational and vibrational characteristics of cables. The Chapter starts with the general equations of the static behaviour of suspended cables, considering the particular case of shallow and taut cables. Given the difficulty in applying analytical approaches to the solution of cable-stayed bridge problems, the simplified approach commonly employed in the dynamic studies of cable-stayed bridges, based on a linear finite element analysis of the full bridge using an equivalent modulus of elasticity for the stay cables, is referred and the expression of this modulus is derived. The linear theory of Irvine is then introduced for the dynamics of stay cables, and the refinement of Triantafyllou is

described. A final topic of this Chapter concerns the derivation of the general nonlinear dynamic equilibrium equations, which are relevant for the study of *indirect excitation* of stay cables presented in Chapter six.

Chapter Four

This Chapter relates to the various aspects involved in the mathematical modelling of the dynamic behaviour of cable-stayed bridges. The text is divided into two main parts, one that systematizes the various types of loads that are involved in the dynamic analysis of a cable-stayed bridge (wind, moving and earthquake loads) and the current state-of-art in the description of these loads and process of analysis, and another that describes the principal characteristics of the dynamic behaviour of a cable-stayed bridge, introducing a nonlinear geometric formulation of the problem either using the classical beam-column theory or a finite element approach. The most employed finite elements in the discretization of the various components of the bridge are presented, and the various possible levels of simplification in the analysis are discussed.

Chapter Five

This Chapter describes the main aspects associated with the experimental identification of dynamic parameters of cable-supported bridges. Starting with a state-of-art on the experimental testing of cable-supported bridge prototypes, some recent trends in the instrumentation of these structures are referred and the various types of excitation and sensing devices described. A Section concerning the application of System Identification algorithms is then presented, which summarizes the classical Modal Analysis methods and introduces recently developed powerful formulations for System Identification from ambient vibration measurements. Finally, given that during the course of this research the author had the opportunity of participating in the dynamic testing of a large cable-stayed bridge, the Vasco da Gama Bridge, in Lisbon, and given that the experience acquired was considered valid in the context of the present dissertation, it was decided to include a last Section describing the main aspects and results of these tests.

Chapter Six

The report of a chosen set of cases of cable vibrations observed in cable-stayed bridges is the starting point of this Chapter for the presentation of an extensive survey of the various sources of cable vibration. These are divided into two major groups, the *direct* sources, that comprehend essentially the excitation by wind, leading to different types of instability phenomena (*vortex-shedding*, *galloping*, *wake interference* and *rain-wind induced* vibrations), and the *indirect* sources, that are responsible for the so-called *external* and *parametric*

vibrations. All these phenomena are characterized and the conditions of occurrence specified. Observing in particular that the *external excitation* phenomenon has been only treated in the literature using linear approaches, and given the evidence of the involvement of a great nonlinear character of the induced vibrations by the finite element analysis of a particular stay cable, the author develops formulae that allow a more accurate characterization of the levels of amplification of the support excitation, as well as the increments of dynamic tension. Formulae of the same type are derived also for the case of *parametric excitation*, in the sequence of the research already developed by other authors, and the results of application to the analysis of a stay cable are compared with the results from a numerical analysis. A final Section introduces the *cable-structure interaction* phenomenon, starting to present a literature review of the research in this topic, summarizing the main findings, and presenting then an introductory numerical example in order to have a clear understanding of the involved phenomena.

Chapter Seven

This Chapter introduces the physical model of the Jindo Bridge, discussing the various scale factors involved and the modifications introduced in the stay cables in order to adequately reproduce the dynamic behaviour of these elements. The results of the *2-D* and *3-D* numerical analyses are presented and the characterization of the *cable-structure interaction* is performed. The modal survey developed using both the electrodynamic shaker and the shaking table of the University of Bristol are described, and the main results presented. Additional tests on the modified model of the Jindo Bridge performed at the ISMES are also described. In these tests the dynamic behaviour of the stay cables was not included as the distributed mass of the cables was concentrated at the anchorages. The comparison between the results of the two modal surveys is shown in order to confirm the *cable-structure interaction* pattern already identified from numerical analysis and from the former tests on the Jindo model. A final set of ambient vibration tests conducted on the Jindo Bridge prototype by an American consulting company is described. The limited character of the data to which the author had access did not allow the full identification of dynamic parameters of the bridge prototype, and in particular, the identification of the *cable-structure interaction* phenomenon. However, an indication of the prototype fundamental natural frequencies was achieved and the tensions installed in some of the cables were estimated.

Chapter Eight

Given the clear identification of the phenomenon of *cable-structure interaction* in the physical model of the Jindo Bridge, an additional set of shaking table tests was developed, in order to evaluate the effect of that interaction in terms of the bridge response to seismic excitations. This Chapter describes the performed tests and results, comparing with the results of the

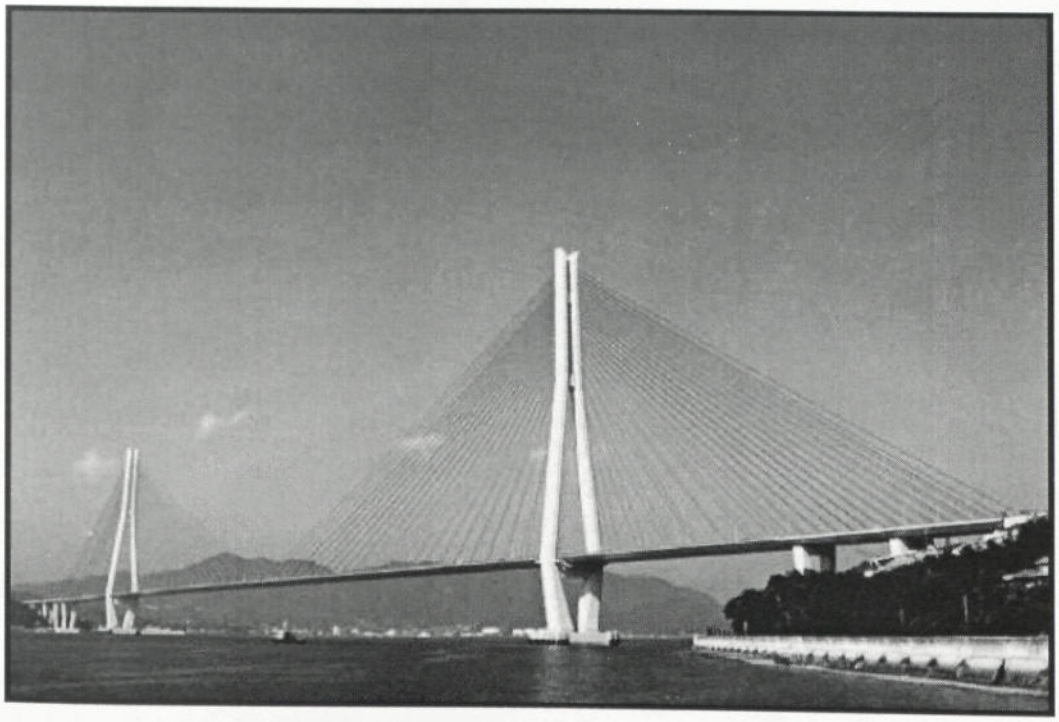
numerical evaluation of the bridge response to the artificial accelerograms measured on the shaking table. Given that a relatively good approximation is found between numerical and experimental results, it is considered that the numerical formulation is validated and further numerical analyses are performed, simulating or not the dynamics of the stay cables. Additional simulations are then developed, modifying either the dynamic properties of the Jindo model or the characteristics of the excitation, in order to extend the conclusions and frame the main results for particular cable-stayed bridges whose properties or actions lead to a more intense character of the *cable-structure interaction.*

Chapter Nine

This Chapter summarizes the main conclusions of the research and traces future lines of investigation in the context of the present work.

CHAPTER 2

CABLE-STAYED BRIDGES



CHAPTER TWO

CABLE-STAYED BRIDGES

2.1 GENERAL

The current Chapter starts to present a brief historical review of the construction of modern cable-stayed bridges, referring the characteristics of particular bridges that have constituted milestones in the history of cable-stayed bridge construction.

The various possible layouts for cable-stayed bridges are then described, and the typical ranges of variation of the several proportions involved discussed. Considering the three main components of a cable-stayed bridge, the deck, towers and stay cables, the diverse possibilities in terms of material, shape and constitution are also referred.

A final Section of the Chapter describes the main features of some of the most important cable-stayed bridges built in Portugal.

2.2 HISTORICAL REVIEW

The proposal of Verantius of a bridge system composed of a timber deck supported by inclined eyebars (Figure 2.1) is considered in the literature one of the first applications of the concept of supporting a bridge girder by inclined stays (Podolny & Scalzi, 1976; Troitsky, 1977). Another reported application respects a *32m* span pedestrian all-timber bridge (Figure 2.2), designed and constructed by Löscher, in Germany, in 1784.

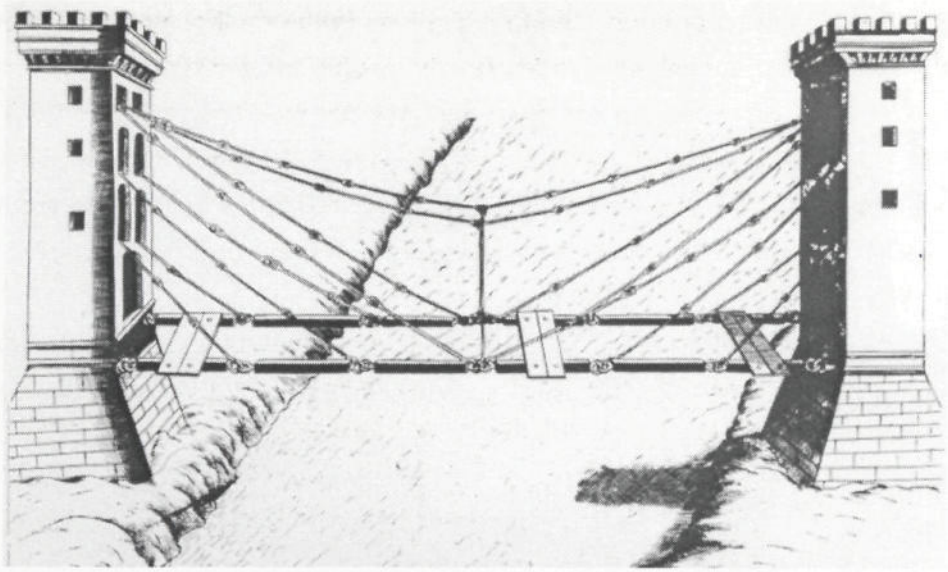


Figure 2.1. Verantius design of bridge stiffened by eyebars (Italy, 1617) (Brown, 1993).

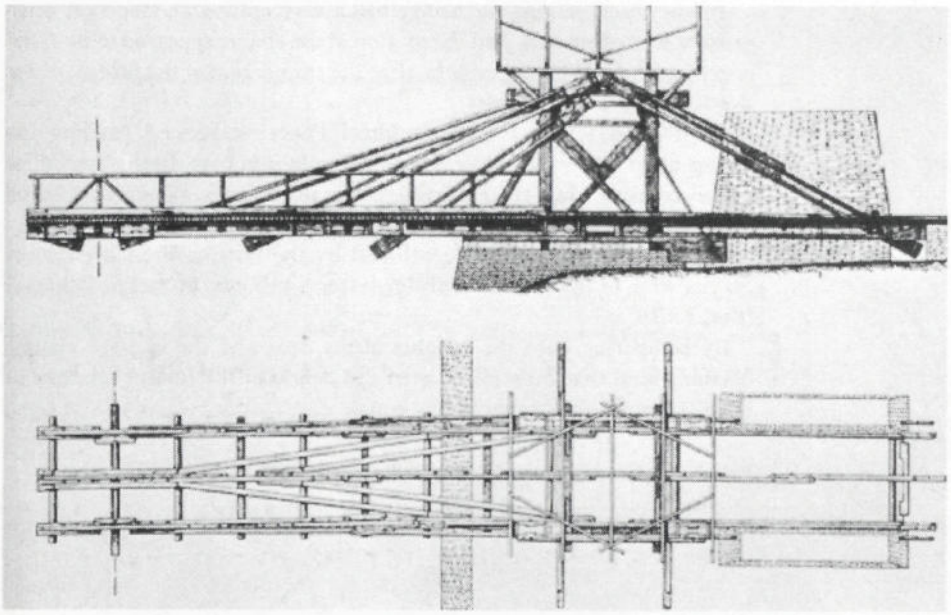


Figure 2.2. Design of Löscher for a pedestrian bridge stiffened by inclined timber stays (Germany, 1784) (Troitsky, 1977).

The King's Meadow Bridge (England, 1817), with a main span of *33.6m*, designed by Redpath and Brown for pedestrian use, was the first to employ wire ropes for the stay cables.

Several other stayed bridges were proposed and constructed along the nineteenth century, which was also marked by some failures. The collapse of the Dryburgh Bridge (England, 1817) (Figure 2.3) in consequence of a violent gale, and the failure of the bridge over the River Saale (Germany, 1824) (Figure 2.4) due to significant overloading (Walther *et al.*, 1988), for example, evidence the lack of full understanding of the actual structural behaviour of cable bridges, as well as defects and limitations in their construction at that time. In effect, the phenomenon of aerodynamic instability, apparently responsible for the failure of the Dryburgh Bridge, only received due care after the Tacoma Narrows suspension bridge

collapse, in 1940. On another hand, due to limitations in the methods of analysis, the cross-section adopted for the stay cables was frequently insufficient. Moreover, as the cables were not tightened during erection, the structure suffered large deformations before the stays started being effective (Troitsky, 1977). Cable-stayed bridges were thus considered extremely flexible and unsafe and, as a consequence, suspension bridges were preferred instead for several decades.

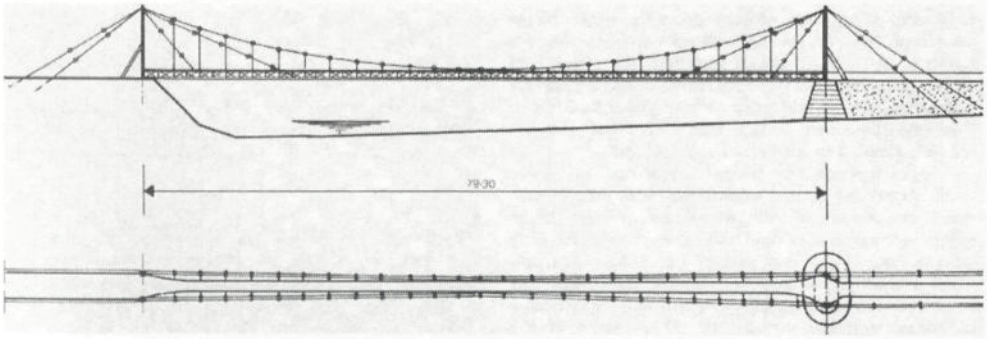


Figure 2.3. The Dryburgh Bridge (England, 1817) (Walther *et al.*, 1988).

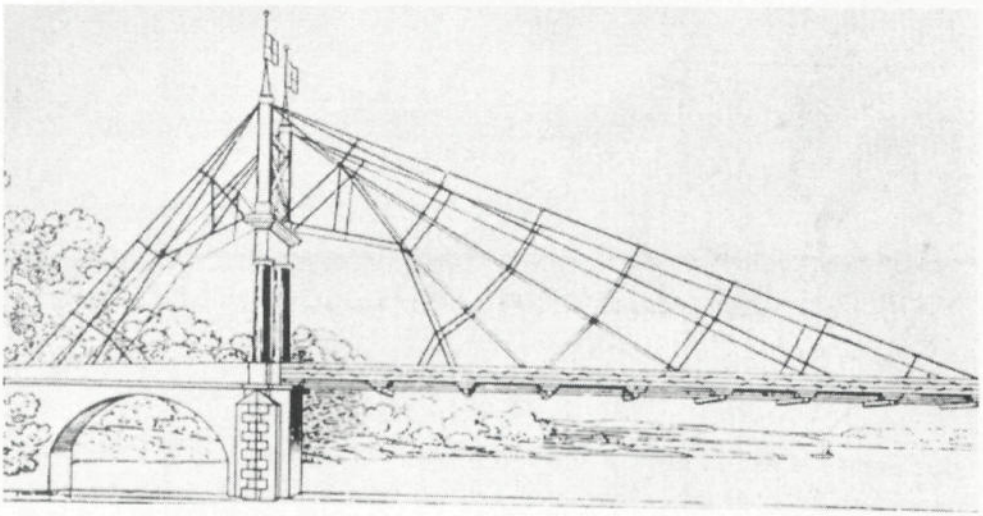


Figure 2.4. Bridge over the River Saale (Germany, 1824) (Troitsky, 1977).

During the second half of the nineteenth century, several bridges of hybrid type were constructed, combining inclined stays with catenary suspension cables. The Niagara Falls railway Bridge (United States, 1855), designed by J. Roebling and having a main span of *280m* (Figure 2.5), was the first large suspension bridge to employ radiating stays, which had the effect of increasing both the global stiffness of the bridge and the stability against the wind action. The same system was later employed by Roebling on the Ohio River Bridge (United States, 1867) and in several other bridges in Europe, such as the Albert Bridge (England, 1872), with a main span of *122m* (Figure 2.6), the Franz-Joseph Bridge (Czechoslovakia, 1868), with a main span of *100m* (Figure 2.7), and the bridge over the Saône River at Lyon (France, 1888), with a main span of *121m* (Figure 2.8). The famous Brooklyn Bridge (Figure

2.9), designed by Roebling and completed in 1883, having a total length of *1059.9m* and a main span of *486.5m*, is the major exponent of this hybrid system type of cable bridge and represents a milestone in the history of bridge construction. A relevant aspect is the use, for the first time in a large construction, of steel for cable wire instead of iron, at a time where this new material (with twice the strength of iron) was illegal for construction in England.

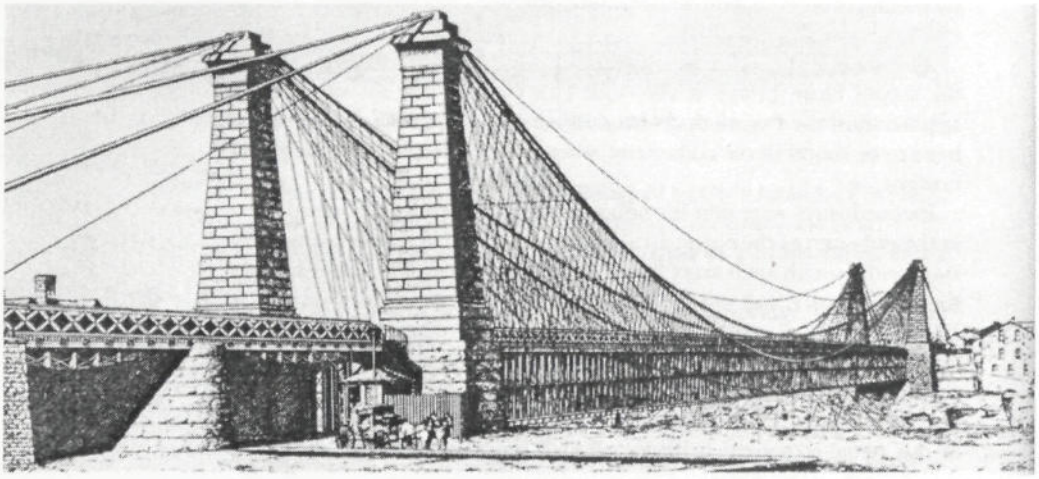


Figure 2.5. The Niagara Falls Bridge (United States, 1855) (Troitsky, 1977).



Figure 2.6. The Albert Bridge (England, 1872) (Godden, 1980).

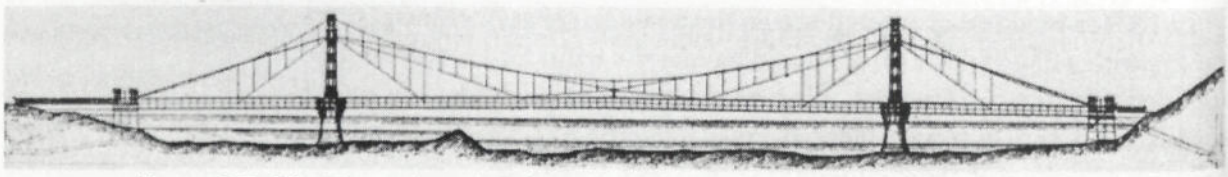


Figure 2.7. The Franz Joseph Bridge (Czechoslovakia, 1868) (Troitsky, 1977).

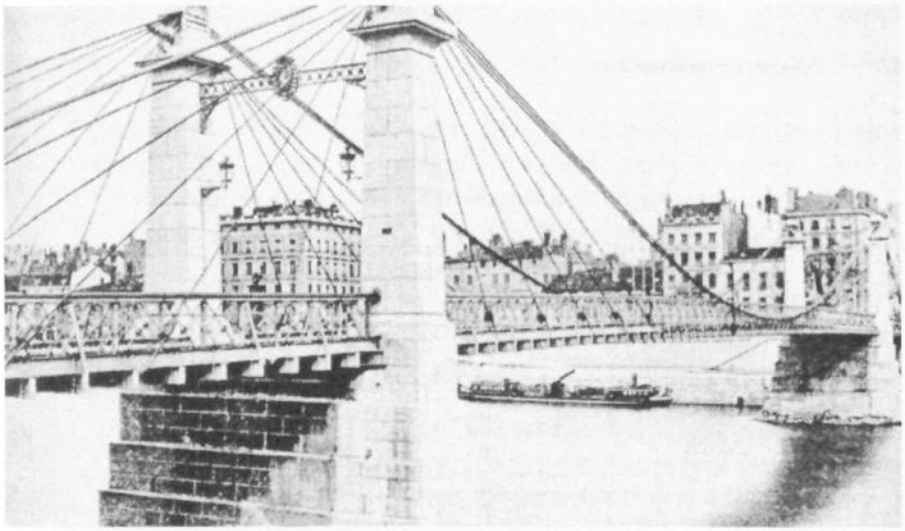


Figure 2.8. The Bridge over the Saône River at Lyon (France, 1888) (Troitsky, 1977).



Figure 2.9. The Brooklyn Bridge (United States, 1883) (Virtual Invention Factory, 1997).

The first rational approach for the actual concept of cable-stayed bridges was given by the French engineer A. Gisclard in 1899, who introduced a new cable system composed of inclined stays and almost horizontal cables (Figure 2.10). By absorbing the horizontal components of the forces set up by the inclined stays, the slightly inclined cables prevented the compression of the deck, thus avoiding deck instability. Furthermore, the direct transmission of loads provided an increased stiffness of the global structure, compared with traditional suspension bridges and constituted an economic and adequate solution for railroads. The Bridge at Cassagne (France, 1907), with a central span of *153m*, is one of the most notable works of Gisclard.

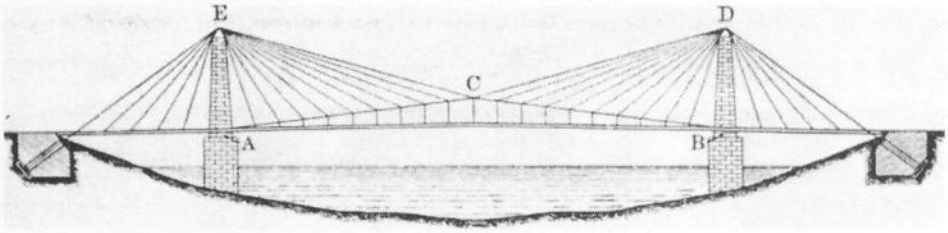


Figure 2.10. Typical Bridge of the Gisclard system (Troitsky, 1977).

Another French engineer, Leinekugel le Cocq, designed the Lezardrieux Bridge (France, 1925), with a central span of *111m*, which was actually based in the concept of Gisclard, although the compressive forces produced by the horizontal components of the inclined cable forces were transferred to the stiffening girder (Figure 2.11).

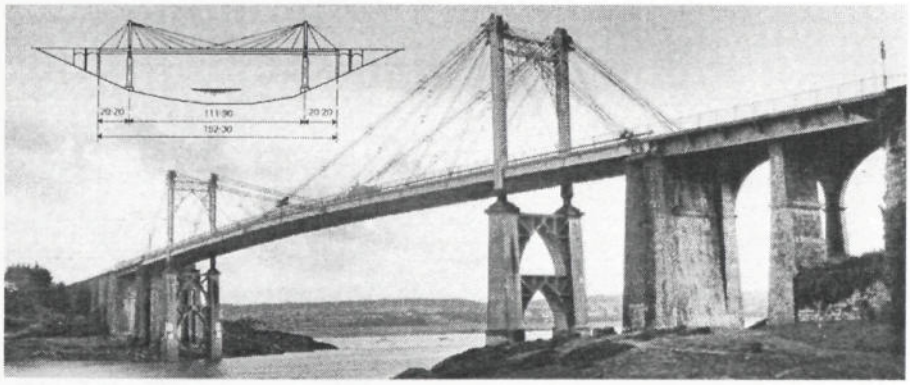


Figure 2.11. The Lezardrieux Bridge (France, 1925) (Walther *et al.*, 1988).

The small reinforced concrete aqueduct presented in Figure 2.12, built by E. Torroja over the river Guadalete at Tempul (Spain, 1925), is probably the bridge that most anticipated the modern concept of cable-stayed bridge. In effect, for the first time high strength steel was employed in the stays, which were made of tie-rods encased in concrete for protection against corrosion. These cables were prestressed by raising the heads of the pylons by jacks.

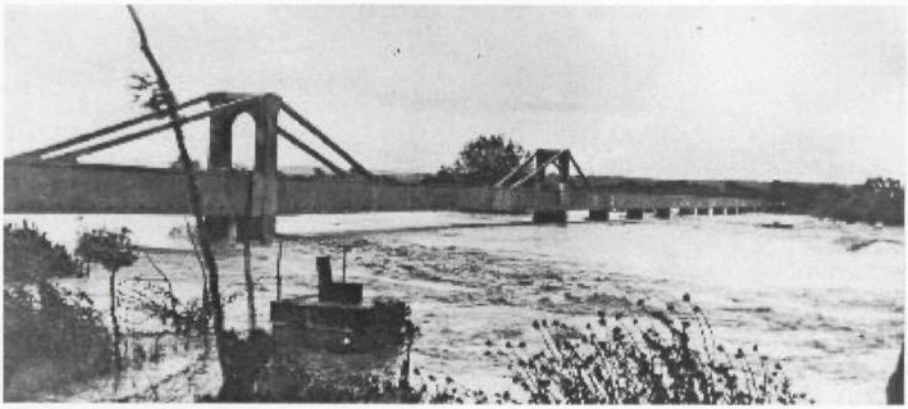
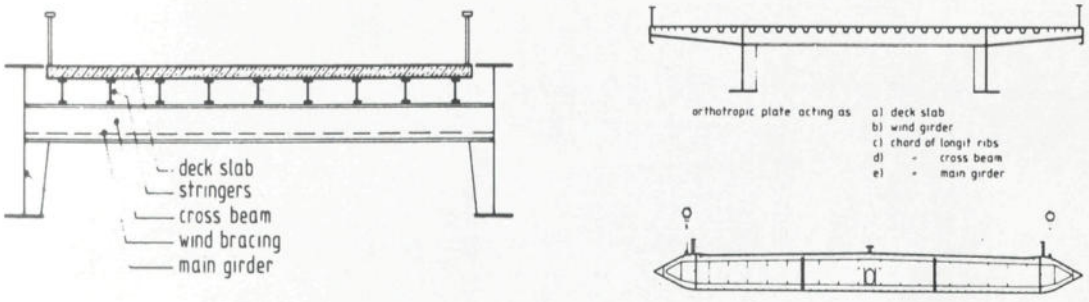


Figure 2.12. Aqueduct over the River Guadalete (Spain, 1925).
Courtesy of Instituto Eduardo Torroja, Spain.

But it was the investigation developed by Dischinger that opened the gate to the development of modern cable-stayed bridges (Leonhardt & Zellner, 1991). In 1938, Dischinger incorporated high strength steel prestressed stay cables in a railroad suspension bridge near Hamburg, in Germany, realising that higher stiffness and stability could be achieved if the cables worked at high stresses, as the softening effect of the sag of long stays was minimized.

Another aspect that contributed to the success of modern cable-stayed bridges, was the development of the superstructure as a jointless unit (Leonhardt & Zellner, 1991). This involved the continuity over intermediate supports, and the development of the so-called *orthotropic* steel decks, whose elements acted as a unit instead of being separated by joints (Figure 2.13).



(a) (b)

Figure 2.13. Cross-section of steel bridge. (a) Old practice: several members acting separately; (b) Leonhardt proposal: all members acting as a unit (Leonhardt, 1991).

The Bridge over the Donzère Canal (Figure 2.14), in France, constructed by Albert Caquot in 1951 and having a central span of *81m* was, according to Mathivat (1994), the first modern reinforced concrete cable-stayed road bridge. However, the Strömsund Bridge (Figure 1.1), constructed in Sweden in 1955, is presently considered the first modern cable-stayed bridge. The German engineer Dischinger designed this bridge, which was constructed by a German Company, Demag. And Germany was in fact the country of birth and development of cable-stayed bridges. As stated by Podolny and Scalzi (1976), approximately *15000* bridges were destroyed in West Germany at the end of World War II. The necessity of reconstructing those structures in a short time created the opportunity for the development of innovative solutions. Cable-stayed bridges, in particular, by combining an efficient use of the materials with aesthetic qualities and allowing a quick erection at comparatively low costs, soon were recognised as an interesting alternative to the classical bridge types, such as suspension and arch systems, mainly for medium spans (*150-300m*).

The Theodor Heuss Bridge, designed in 1955 by Leonhardt and completed in 1958, was the first modern cable-stayed bridge in Germany. This bridge, having a total length of *476m* and a central span of *260m*, was considerably larger than the Strömsund Bridge, and incorporated several innovations, namely in the cable arrangement, which was of harp type (comprehending parallel stays connected to the pylons at different levels), and in the design

of pylons, which were independent cantilevered masts (Figure 2.15). This bridge, together with the Knie Bridge and the Oberkassel Bridge, form a family of harp cable-stayed bridges that was conceived by the city of Dusseldorf for the crossing of the Rhine River, and were built during the period of 1956 to 1972 (Figure 2.16).

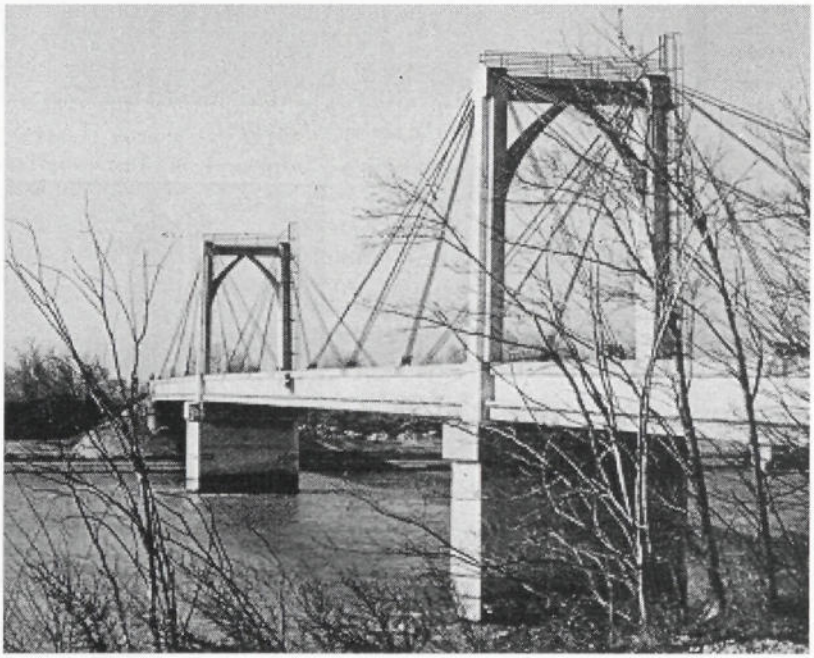


Figure 2.14. Bridge over the Donzère Canal (France, 1951). Courtesy of C. Cremona.

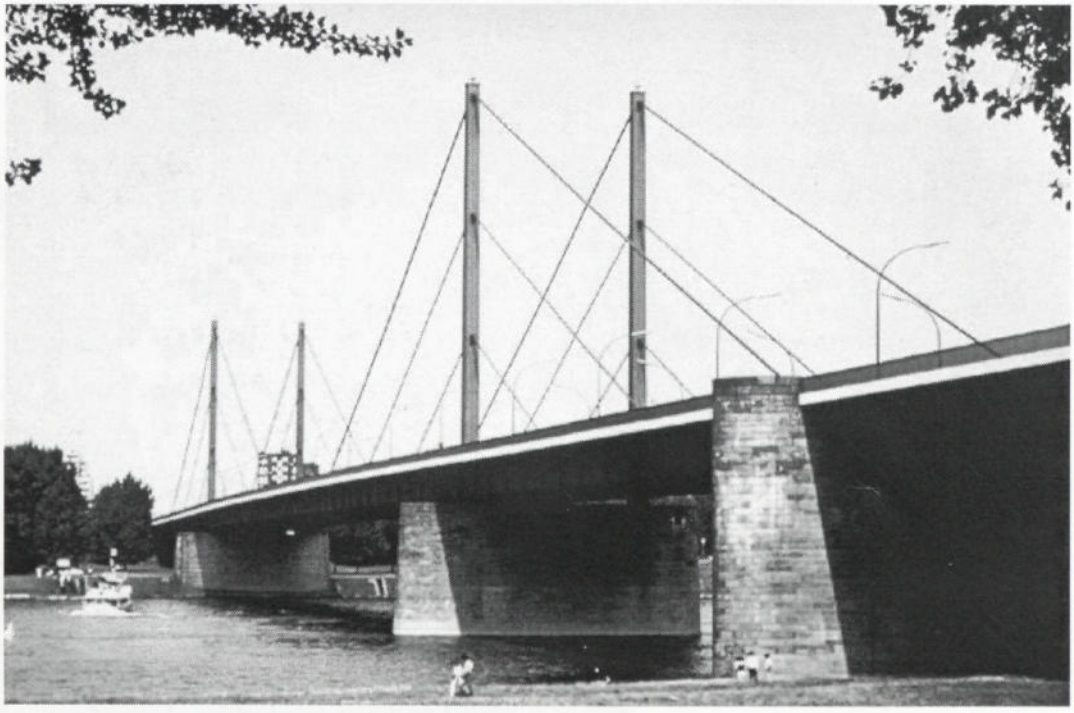


Figure 2.15. The Theodor Heuss Bridge (Germany, 1958). (Godden, 1980).

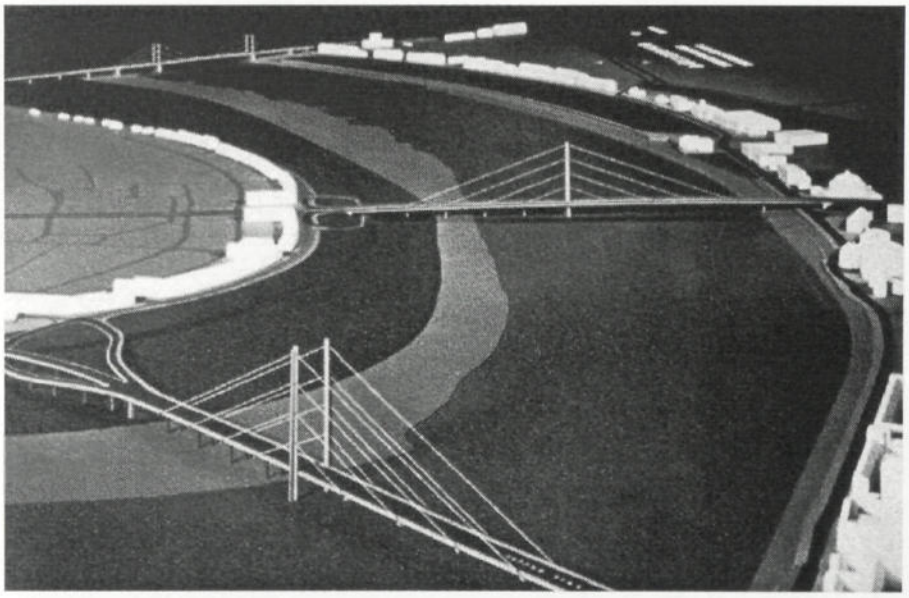


Figure 2.16. The Dusseldorf family of cable-stayed bridges (Godden, 1980).

Other important references to the history of cable-stayed bridges, are the Severin (1961) and the North Elbe Bridges (1962), in Cologne and Hamburg, respectively. Besides being the second and the third cable-stayed bridges built in West Germany, the two structures featured innovative aspects. In the case of the Severin Bridge, two asymmetrical spans (larger span of *302m*) were used for the first time, with only one pylon at one of the river banks. Moreover, the *A*-shaped pylon was combined with inclined cable planes and continuity was achieved along the *700m* long six-span girder (Figure 2.17). The North Elbe Bridge, with a main span of *172m*, constituted the first application with single-plane cables (Figure 2.18).



Figure 2.17. The Severin Bridge (Germany, 1960).

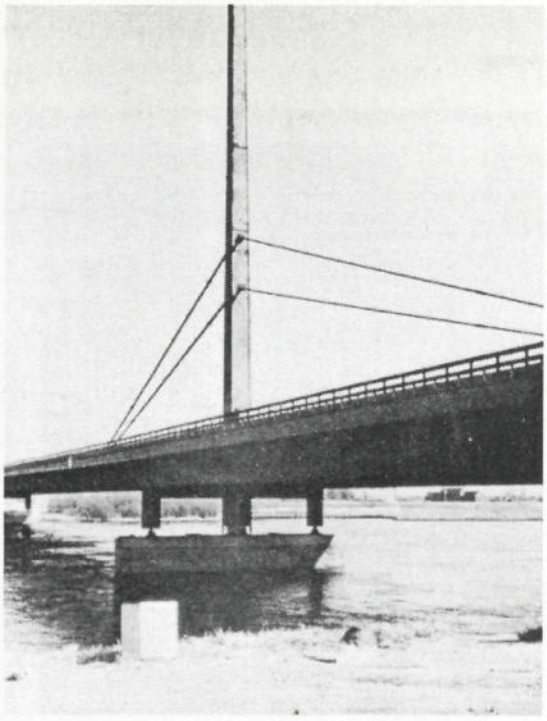


Figure 2.18. The North Elbe Bridge (Germany, 1962) (Troitsky, 1977).

The success of cable-stayed bridge construction in Germany rapidly extended to the rest of the world. Particular reference should be addressed to the Onomichi Bridge (1968), which was the first long (*215m* span) cable-stayed bridge constructed in Japan (Figure 2.19), and was also the first bridge almost entirely (*82%*) constructed of corrosion-resistant weathering steel (Podolny & Scalzi, 1976). Reinforced concrete applications were also developed, of which the multi-span Maracaibo Bridge, in Venezuela, designed by Morandi and constructed in 1962, is an outstanding example (Figure 2.20).

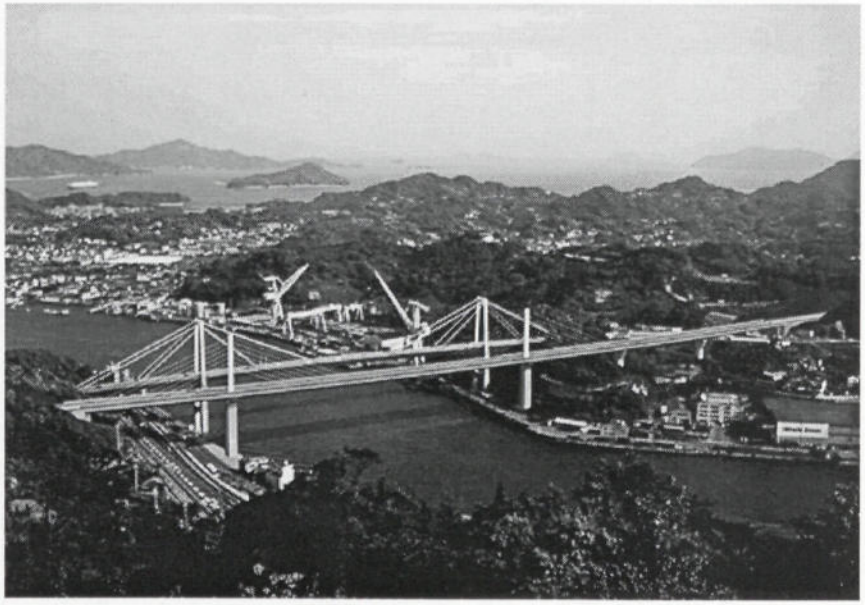


Figure 2.19. The Onomichi Bridge (Japan, 1968), behind the Shin-Onomichi Bridge. Courtesy of HSBA.

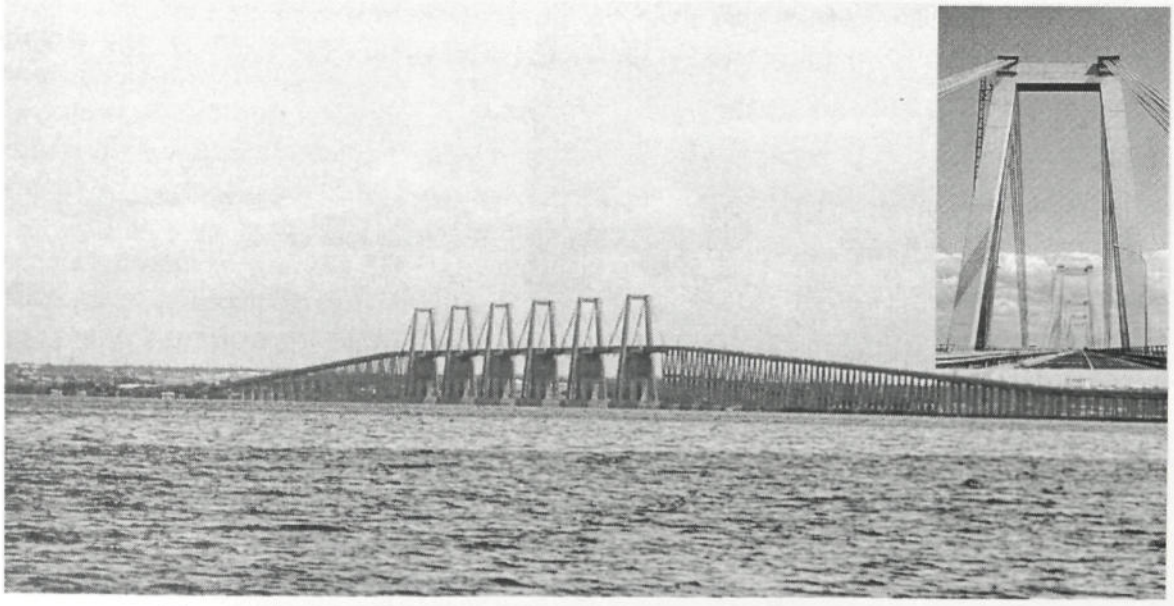


Figure 2.20. The Maracaibo Bridge (Venezuela, 1962) (Brown, 1993).

A common characteristic of the above described cable-stayed bridges and, generally, of the bridges of the so-called *first generation* (Mathivat, 1984), is the use of a limited number of stay cables, usually between *2* and *6* pairs of stays in the main span. These cables were separated by large distances, normally varying between *30m* and *80m*, what required a large bending stiffness of the deck (the usual depth varying from *3m* to *4m*) (Leonhardt & Zellner, 1991). Besides this, the cable tensions were so high, that several ropes were necessary to form each stay. This also originated complicated anchorages and important concentrated stresses. An additional difficulty was the need for auxiliary structures to erect these bridges.

The *second generation* of cable-stayed bridges came in the second half of the 1960s, with the introduction of computer analysis, consisting in the adoption of a partial suspension system, in which the deck was rigidly supported by the pylon and suspended by a high number of closely spaced stay cables. This system was introduced in Germany by Homberg, with the Friedrich Ebert Bridge over the Rhine, in Bonn, in 1967. According to Figure 2.21, this bridge, having a total length of *520m* and a central span of *280m*, was composed of two single pylons arranged in a plane, which gave support to *20* stay cables on each side of the steel deck. The use of this multiple-cable system type of suspension allowed two main achievements, namely the use of a moderated flexural stiffness for the deck, in view of the elastic support provided by the cables, and the reduction of concentrated forces applied to the deck, with the consequent use of simpler anchorages and avoidance of the need to strengthen the girder near the cable anchorages. The small spacing between deck anchorages (*2.24m*, in the case of the Friedrich Ebert Bridge) provided additional advantages in the construction phase, allowing a simpler free cantilever construction. It is still relevant in this bridge the introduction of a central suspension with only one plane of cables. This new concept resulted from the purpose of reducing the costs of the foundations, which employed the complicated and time-consuming pneumatic caisson method (Walther, 1994).

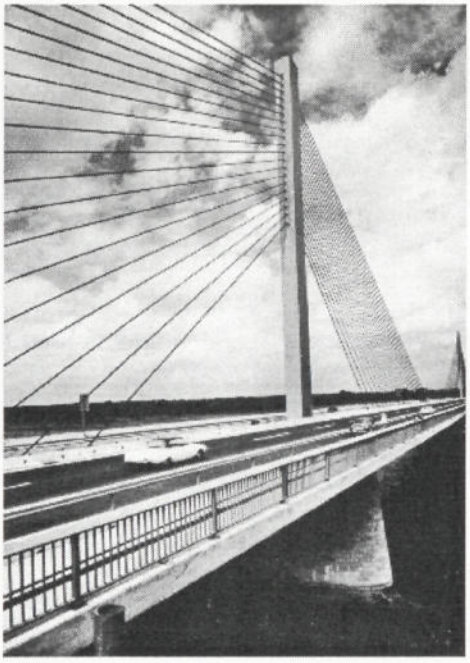


Figure 2.21. The Friedrich Ebert Bridge (Germany, 1967) (Troitsky, 1977).

Many other bridges of the so-called second generation were constructed, namely the Rhine Bridge at Rees (Germany, 1967), the Maxau Bridge over the Rhine (Germany, 1967), the Kohlbrand Bridge (Germany, 1974), the St. Nazaire Bridge (France, 1977), the Brotonne Bridge (France, 1977), the Rokko Bridge (Japan, 1977), the Sunshine Skyway Bridge (USA, 1986) or, more recently, the Normandy Bridge (France, 1994).

The Brotonne Bridge, presented in Figure 2.22, with a main span of *320m*, was the first application of the multiple-cable system type in a concrete cable-stayed bridge and is presently seen as the prototype of bridges of this *second generation*.

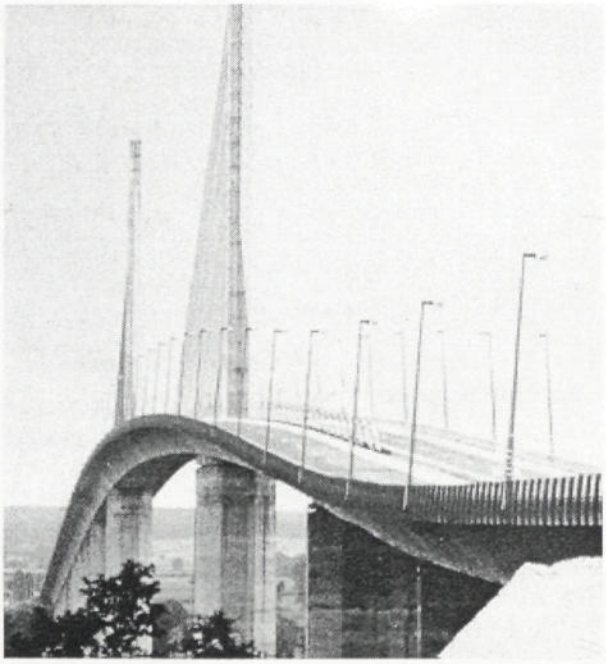


Figure 2.22. The Brotonne Bridge (France, 1977) (Gimsing, 1983).

The St. Nazaire Bridge, presented in Figure 2.23, was one of the first cable-stayed bridges built in France and was the world longest at that time, with a central span length of *404m*.

The Sunshine Skyway Bridge over the Tampa Bay, in Florida, was completed in 1987. The bridge extends for *6670m* (Figure 2.24) and is presently the second largest concrete span in North America (*366m*).

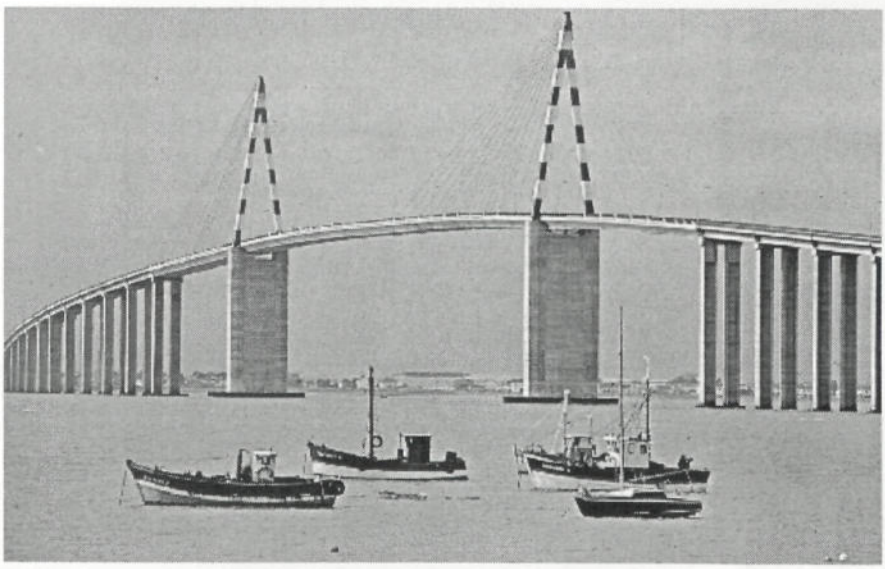


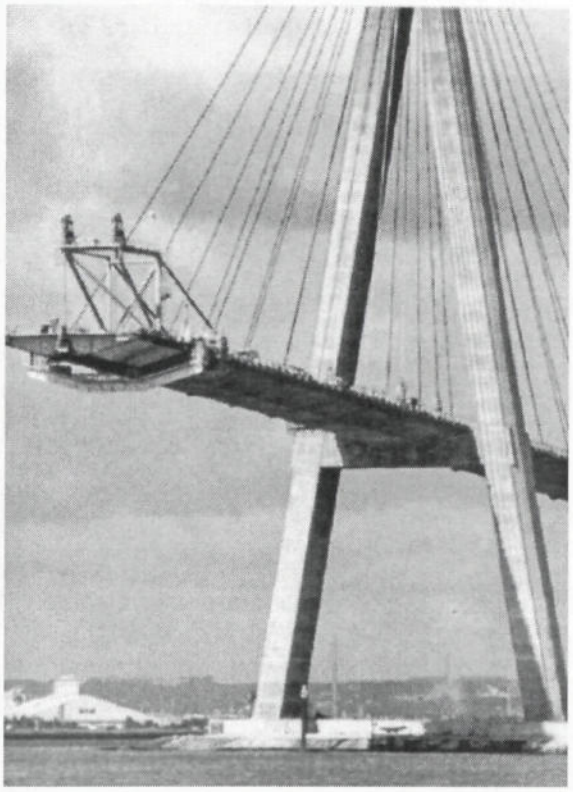
Figure 2.23. The St. Nazaire Bridge (France, 1978) (Brown, 1993).



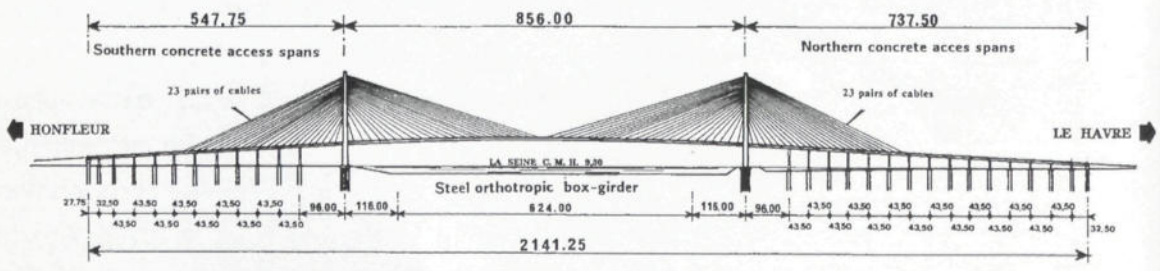
Figure 2.24. The Sunshine Skyway Bridge (USA, 1986) (Brown, 1993).

Finally, the Normandy Bridge, presented in Figure 2.25, the first cable-stayed bridge to enter the domain of very long span bridges, with a central span of *856m*, and presently the second largest cable-stayed bridge in the world, incorporates in its design specific aspects

that were achieved with the experience of *40* years of building cable-stayed bridges, namely: (i) a streamlined cross-section with only *3m* depth, which reduces the wind forces (dominant for the design in the North of France); (ii) a high torsional stiffness of the cross-section, combined with inverted Y-shaped pylons, which allow a separation of torsional and bending natural frequencies, therefore preventing instability by *flutter*; (iii) a fan arrangement of the two inclined planes of cables which, when combined with the *Y*-inverted shape of the pylons, provide an efficient distribution of stresses along these elements, as well as an increased stiffness for transverse wind forces; (iv) the use of two materials, concrete for the access spans and part of the main span (*116m* from each side of the pylon, according to Figure 2.25(b)), and composite (steel box girder and concrete slab) for the central span, with the advantage of obtaining simultaneously a lighter and stiffer structure and increasing the efficiency of back-staying the rear cables at reduced costs (Virlogeux, 1994).



(a)



(b)

Figure 2.25. The Normandy Bridge (France, 1994): (a) General view during construction; (b) Layout (Virlogeux *et al.*, 1994).

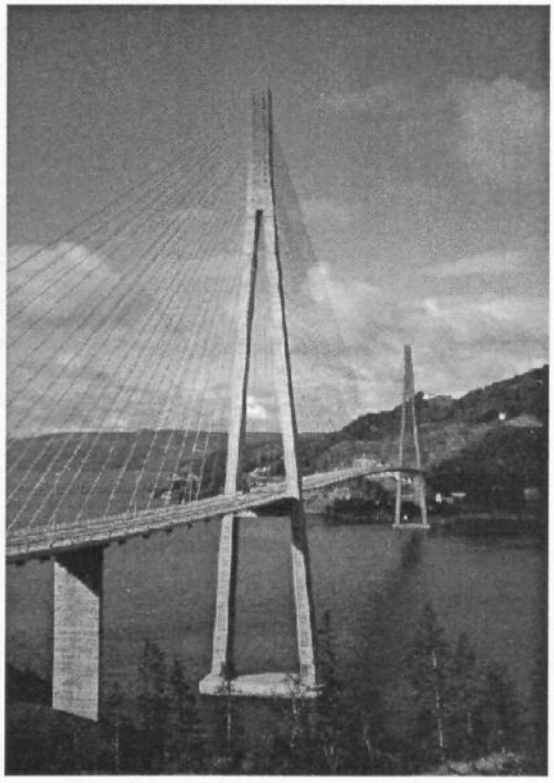
The bridges of the *second generation* established the transition to the so-called *third generation* of cable-stayed bridges that constitutes the current trend in large cable-stayed bridge design. Bridges of this *third generation* are characterized by the use of a large number of closely spaced stays (*8m* to *15m*, according to Leonhardt and Zellner (1980)), which entirely support the deck. A new type of structural behaviour is achieved with this form of suspension, where the deck acts as the compressive chord of a truss hung up to the towers by inclined stays. The fact that bending moments are very small makes the depth of the girder deck almost independent from the main span length, the required amount of longitudinal bending stiffness being governed by the safety against buckling and the necessity to limit local deformation under concentrated live load.

The Pasco-Kennewick Bridge, designed by Arvid Grant in collaboration with the consulting company Leonhardt, Andra & Partner and constructed in the USA in 1978, with a main span of *300m* and total length of *548m* (Figure 2.26), was the first concrete cable-stayed bridge built in the United States and also the first to employ total deck suspension. The deck, composed of two triangular edge box girders connected by transverse beams, is *2.15m* deep.

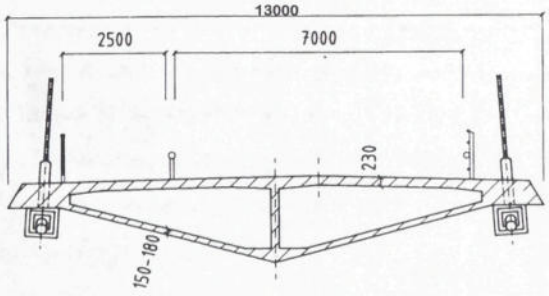


Figure 2.26. The Pasco-Kennewick Bridge (USA, 1978) (Godden, 1980).

The Barrios de Luna Bridge, constructed in Spain in 1983, and having a main span of *440m*, was also one of the first bridges of this new generation. At the time of construction, this bridge established a record for the largest main span in the world, which was only beaten in 1991 with the construction of the Skarnsundet Bridge, in Norway (Figure 2.27). The later bridge is actually one of the most remarkable bridges in the world, with a *530m* span and an extremely slender deck, composed of a concrete triangular box section *13m* wide and *2.15m* deep (Hansvold, 1994).



(a)



(b)

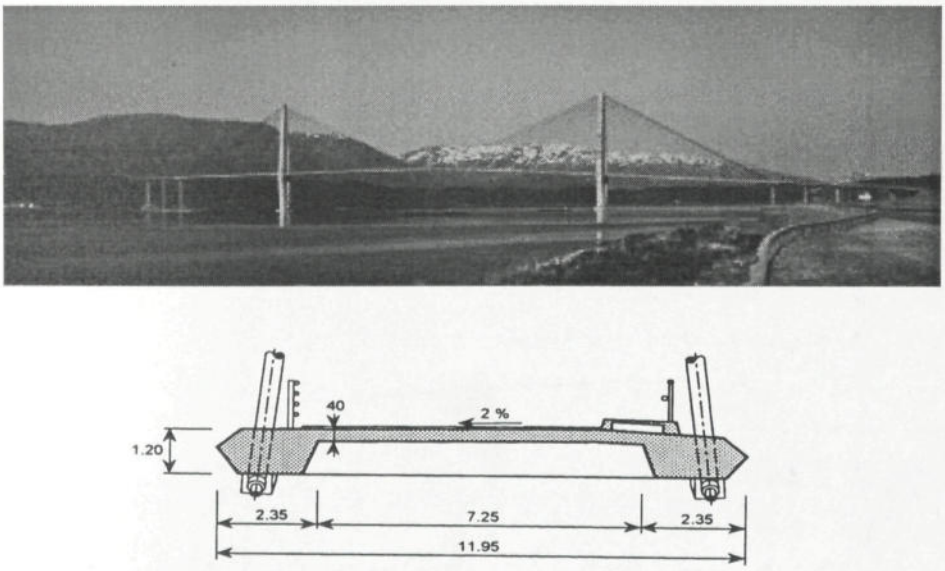
Figure 2.27. The Skarnsundet Bridge (Norway, 1991): (a) General view (NGI *et al.*, 1994); (b) Deck cross-section (Hansvold, 1994).

Another impressive cable-stayed bridge in Norway is the Helgeland Bridge (1991), with a total length of *1065m*, a main span of *425m*, and a deck width of only *11.95m*. Although the wind climate is very severe at the bridge location and the site is close to an active seismic zone in the Norwegian sea, a very slender open cross-section with relatively low torsional stiffness was employed, with only *1.20m* depth (see Figure 2.28).

It is still interesting to refer, amongst the enormous number of innovative large cable-stayed bridges of this *third generation*, the Annacis Island Bridge (Canada, 1986), the Evripos Bridge (Greece, 1988), the Yangpu Bridge (China, 1993) and, naturally, the Tatara Bridge (Japan, 1999).

The Annacis Island Bridge, presented in Figure 2.29, was the first large application of composites to the construction of a cable-stayed bridge, and beat the record for the world longest span at the time of construction, with a main span length of *465m*. The bridge deck was composed, as represented in Figure 2.29(b), of two longitudinal steel *I*-girders *2m* deep

connected every *4.5m* by steel floor beams, and a *26cm* deep concrete slab. This was also one of the first applications of solid slender slabs in cable-stayed bridges.



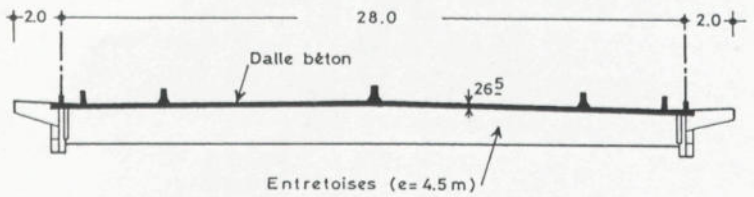
(a)

(b)

Figure 2.28. The Helgeland Bridge (Norway, 1991): (a) General view; (b) Deck cross-section (Walther, 1994).



(a)



(b)

Figure 2.29. The Annacis Island Bridge (Canada, 1986): (a) General view (Godden, 1980); (b) Deck cross-section (Mathivat, 1994).

The Evripos Bridge, with a main span of *215m*, was the first cable-stayed bridge built in Greece, according to Schlaich (1994). This concrete cable-stayed bridge is remarkable for the extremely slender deck (Figure 2.30), which is simply a solid slab of *45cm* thickness suspended between two cable planes at *13.5m* distance.

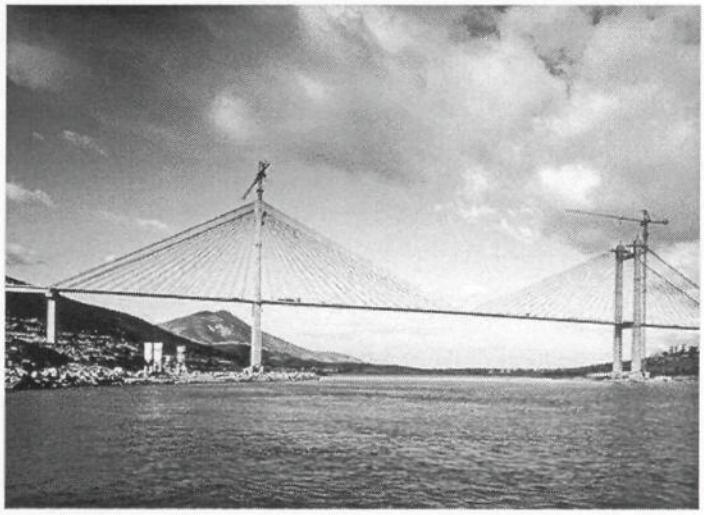


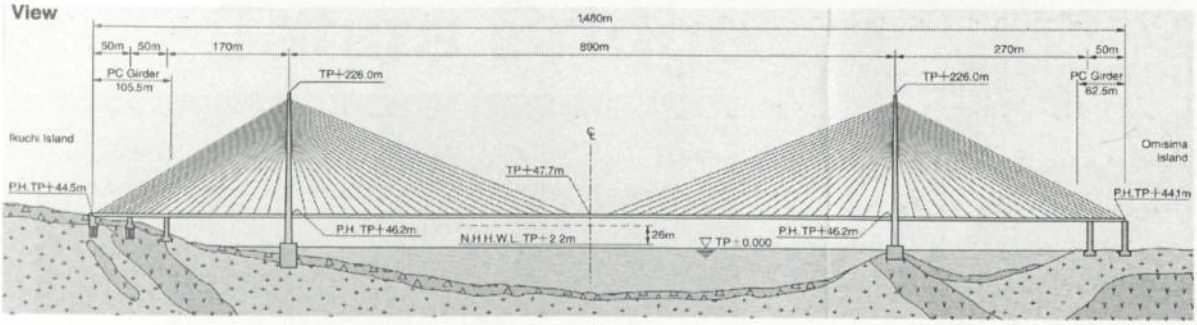
Figure 2.30. The Evripos Bridge. Courtesy of *Schlaich, Bergermann & Partner Consultants*.

The Yangpu Bridge (Figure 2.31), built over the Huangpu River in Shangai, with a centre span of *602m*, has presently the largest main span for a concrete cable-stayed bridge. This bridge was also a world span length record at the time of construction, fact particularly relevant for a country like China, where the construction of a significant number of large cable-stayed bridges (with centre spans varying from *400m* to *900m*) is expected for the next years (Xiang & Chen, 1998).



Figure 2.31. The Yangpu Bridge (China, 1993).

Finally, the Tatara Bridge, in Japan, the largest cable-stayed bridge in the world with a central span of *890m* and a total length of *1480m* (Figure 2.32), has just been completed in 1999 and is also the last bridge of the so-called *Honshu-Shikoku Bridge Project* (*HSBP*). Besides the various important aspects related to the bridge itself, such as the longest unrestrained cables (*460m* long), the slender steel box cross-section *2.7m* deep and the use of specific countermeasures against aerodynamic instability of the stay cables (dimpled cable sheathing), the construction of this large structure reflects the outstanding development of long-span bridge technology in Japan. In effect, the geographic situation of Japan, which incorporates *4* major islands and many other small islands, together with the growth of economy and need of reconstruction of destroyed and insufficient infrastructure facilities after World War II, led to the construction of many long-span bridges and, in particular, to the development of the *HSBP*. This Project aimed to connect the islands of Honshu and Shikoku by three road and rail links, according to the representations of Figures 2.33 and 2.34, the so-called Nishiseto, Seto-Chuo and Kobe-Awaji-Naruto Expressways.



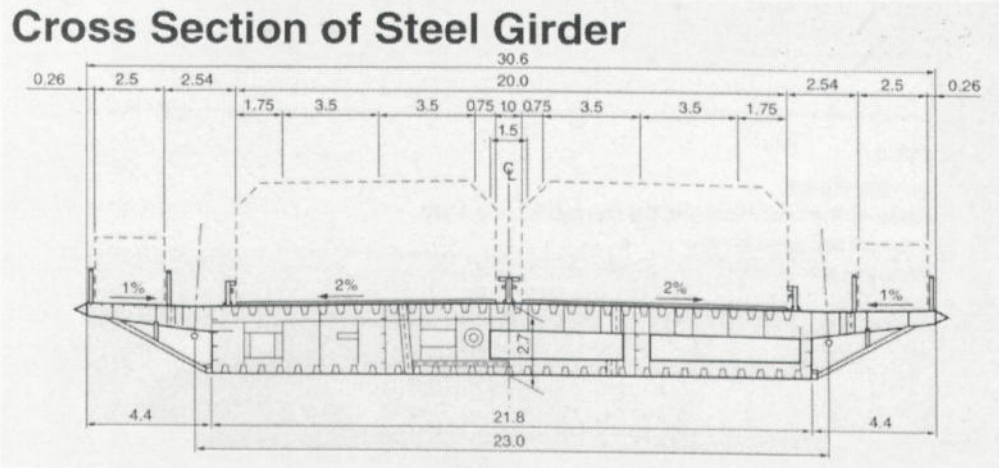


Figure 2.32. The Tatara bridge. Elevation and cross-section of the steel part of the deck. Courtesy of *HSBA*.

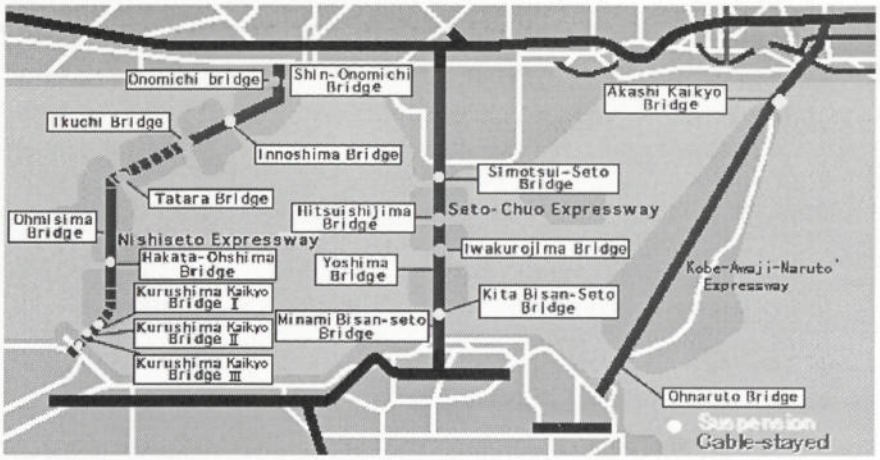


Figure 2.33. The Honshu-Shikoku Bridge Project. Scheme of three road-links connecting the islands of Honshu and Shikoku. Courtesy of *HSBA.*

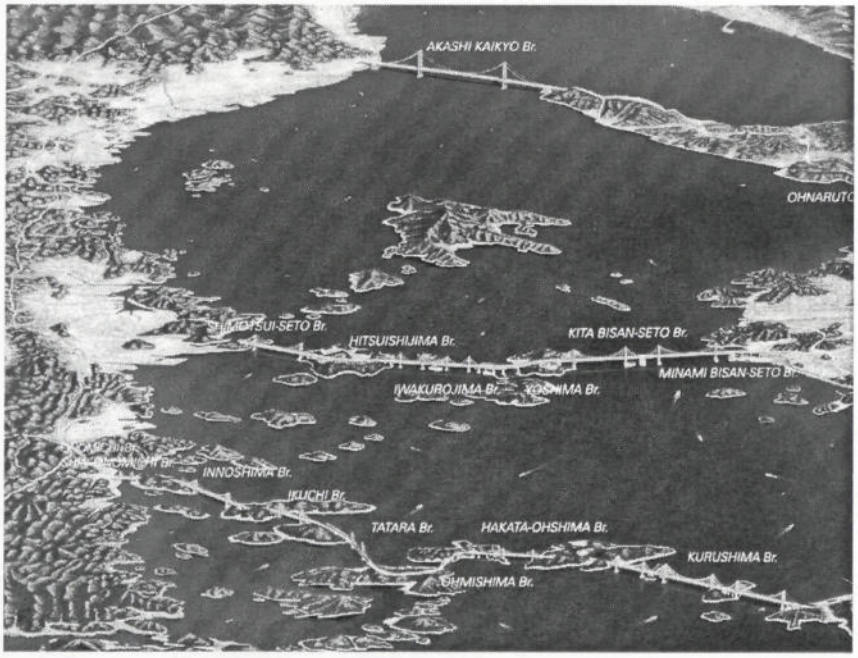


Figure 2.34. The Honshu-Shikoku Bridges: imaginary panorama (deformed illustration). Courtesy of HSBA.

The *HSBP* includes a total of *18* long span bridges, *10* of which are of suspension type, and *6* are cable-stayed. The Project was founded in 1970, the construction starting in 1976 with the Ohmishima Bridge and incorporating the Onomichi Bridge (already concluded in 1968), and ended during the year of 1999 with the completion of the Tatara Bridge. The main characteristics of the cable-supported bridges constructed in the context of the *HSBP* are listed in Table 2.1.

The fact that this table includes, among other very long span bridges, the two longest bridges in the world in their category, the Akashi-Kaikyo and the Tatara Bridge, together with the generally poor soil conditions and unfavourable climatic conditions in Japan (susceptibility to earthquakes and typhoons), illustrates the magnificence of this Project, which triggered in fact a very extensive research in several domains, such as *Bridge Aerodynamics*, *Seismic*

Engineering and *Construction Technologies*, and led inclusively to the development of specific codes for the Bridges of the *HSBP*. A view of some of the bridges of the Seto-Chuo Expressway is presented in Figure 2.35.

Table 2.1. Cable-supported bridges of the Honshu-Shikoku Bridge Project.

Bridge name	Year of completion	Type of suspension	Centre span (m)	Total length (m)	Girder material
Onomichi	1968	**cable-stayed**	215	385	steel
Innoshima	1984	suspension	770	1270	steel
Ohnaruto	1985	suspension	876	1629	steel
Shin-Onomichi	1999	**cable-stayed**	215	385	steel
Hakata-Oshima	1988	suspension	560	840	steel
Hitsuishijima	1988	**cable-stayed**	420	792	steel
Minami Bisan-Seto	1988	suspension	1100	1723	steel
Shimotsui-Seto	1988	suspension	940	1447	steel
Iwakurojima	1988	**cable-stayed**	420	792	steel
Kita Bisan-Seto	1988	suspension	990	1611	steel
Ikuchi	1991	**cable-stayed**	490	790	steel
Akashi-Kaikyo	1998	suspension	1990	3910	steel
Tatara	1999	**cable-stayed**	890	1480	steel
Kurushima I	1999	suspension	600	960	steel
Kurushima II	1999	suspension	1020	1515	steel
Kurushima III	1999	suspension	1030	1570	steel

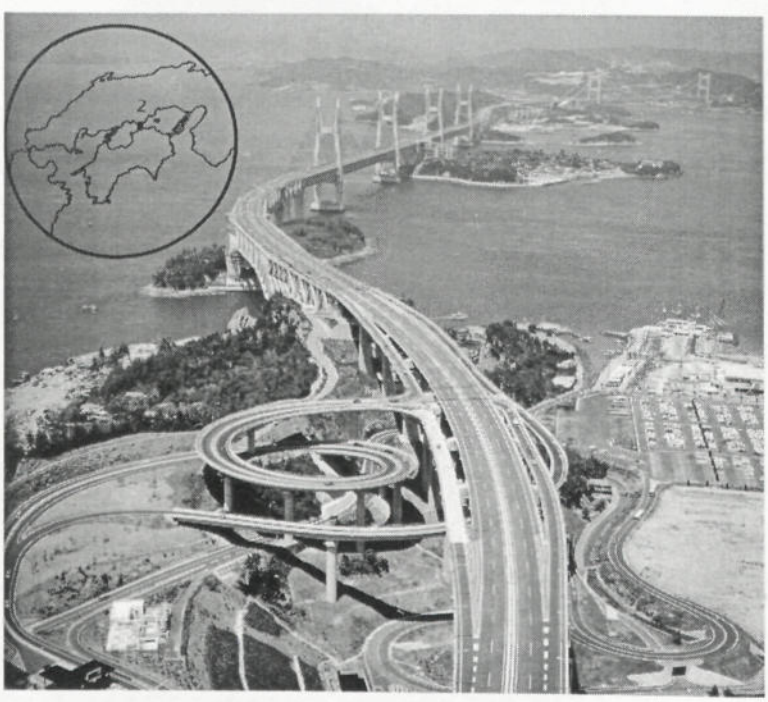


Figure 2.35. Seto-Chuo Expressway. View of Yoshima, Iwakurojima, Hitsuishijima and Shimotsui-Seto Bridges (Brown, 1993).

From the brief description and examples presented above, it is clear that the design and construction of cable-stayed bridges suffered a great evolution during the last *45* years, in which *3* main categories of bridges were identified, according to the structural type of behaviour. The prototypes described were some of the bridges that are generally considered milestones in the history of cable-stayed bridges. Although the author does not consider the span length the only parameter of interest in the characterization of bridges, it is undoubtedly, for the case of long span bridges, an index of the technological capacity and progress. For this reason, the span length was extensively referred and a list of major cable-stayed bridges constructed all over the world is presented at the end of this Section (Table 2.2).

It is important however to mention that most of the referred bridges are of classical type, in terms of their structural characteristics. In effect, these bridges are usually composed by one or two vertical pylons, which have a convenient structural shape. They are also self-anchored, that is, the cable anchorages are located along the deck and towers, and finally, the longitudinal axis is normally straight or at most, slightly curved. Yet, many variations to the classical type can be found in the literature, mainly for the short and medium spans. In some cases, this is a consequence of specific technical requirements and limitations of the site. In other cases, the purpose is to arrive at an aesthetically appealing solution, treating the bridge more as a sculpture. This is valid particularly for pedestrian bridges located in areas of great environmental value. Some examples of particularly interesting structures are presented bellow.

The first example refers to the possibility of anchoring the cables outside the deck girder. Although it is considered that one of the most important advantages of cable-stayed bridges is the possibility of construction of a self-anchored structure, several cable-stayed bridges have adopted a partial suspension, in which some or all of the stay cables are earth-anchored, transmitting both vertical and horizontal components of the installed force directly to the soil. This type of suspension has been used in several aqueducts and pipe bridges, such as the Tiber Bridge (Italy, 1967) and the Pipe Bridges over the Sele River (Italy, 1980) (Walther *et al.*, 1988). The first major road cable-stayed bridge employing an earth-anchored system was, according to Gimsing (1983), the Bridge across the Arno River, near Firenze, designed by Fabrizio de Miranda. The bridge comprises a *206m* long main span supported by two fans of cables radiating from the tops of slightly inclined pylons, and the backstays are anchored in two massive blocks located on both sides of the carriageway (Figure 2.36).

The Sancho el Mayor Bridge, across the River Ebro (Spain, 1978) is another example of an earth-anchored cable-stayed bridge. This bridge, designed by C. Casado, with an only span of *147m*, is composed of a single pylon aligned with the longitudinal axis of the road and three bundles of cables. The main bundle lies in the plane of symmetry of the bridge, and the two back sets make an angle of about *120°* with respect to the main one (Troyano *et al.*, 1998). The vertical component of the forces in the backstays is compensated by weight of the blocks of anchorage, while the horizontal component is absorbed by underground struts that connect those blocks to the tower foundation (Figure 2.37).

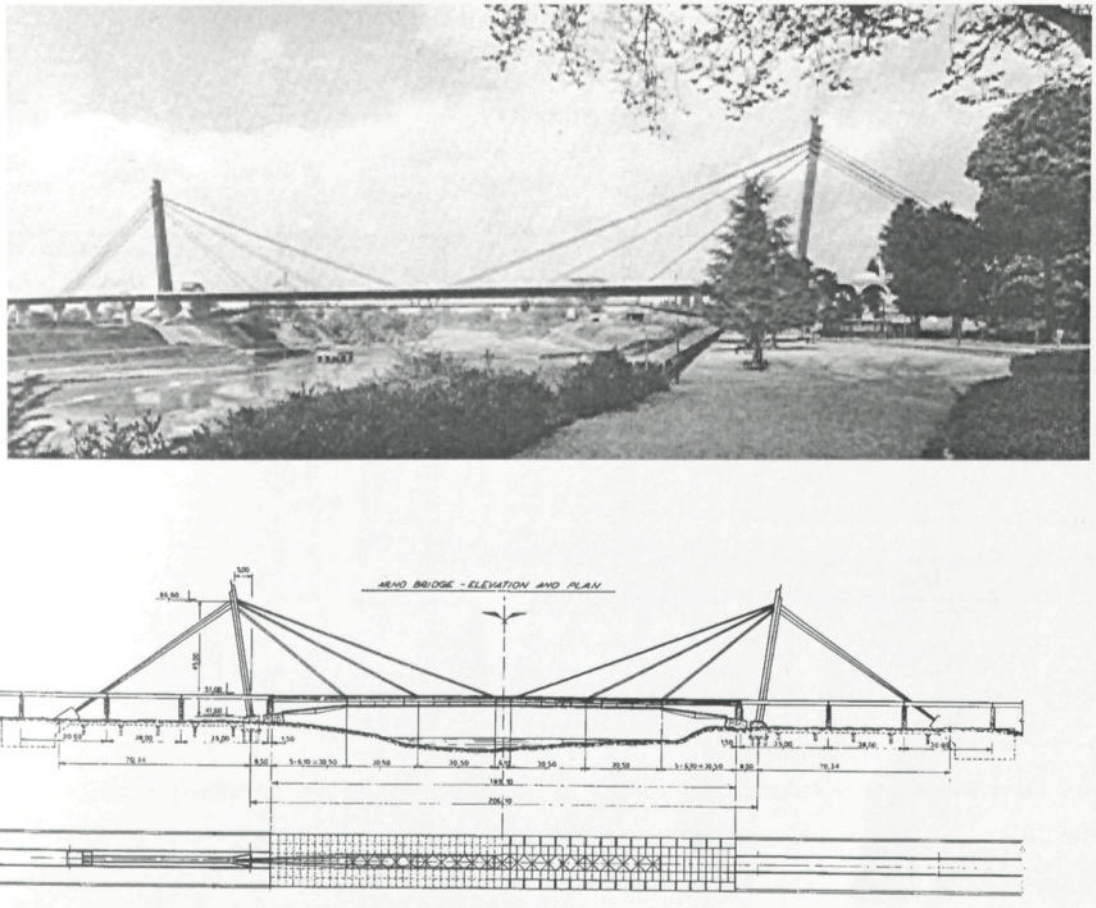
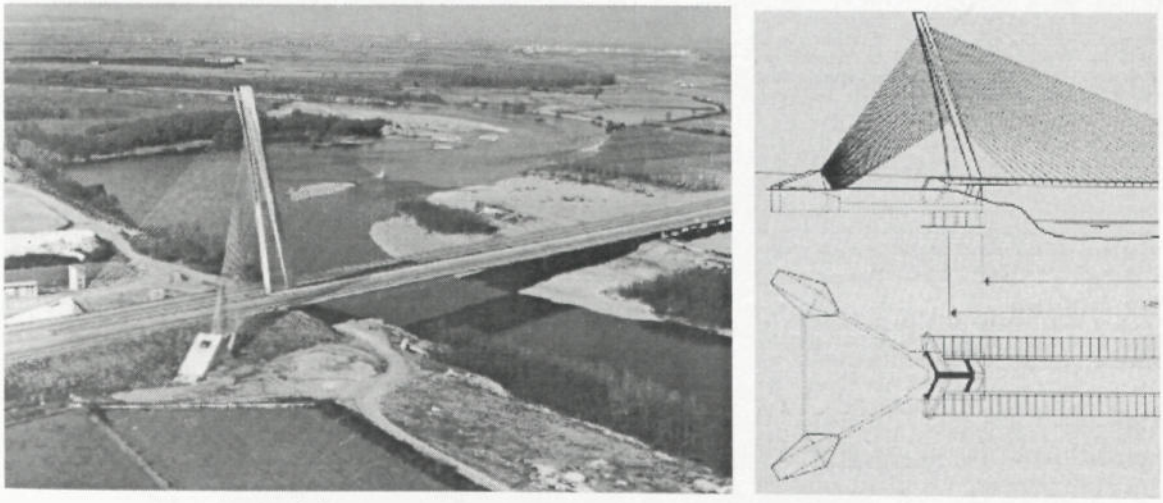


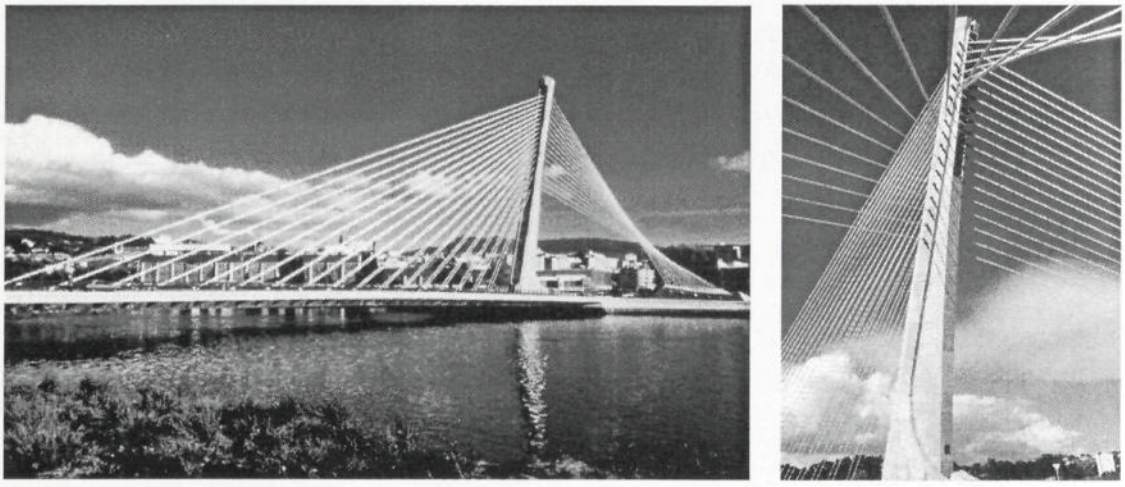
Figure 2.36. Bridge across the Arno River (Italy, 1978) (Miranda, 1978): (a) General view; (b) Structural scheme.



(a) (b)

Figure 2.37. Sancho el Mayor Bridge (Spain, 1978): (a) General view; (b) Elevation and plan showing detail of connection of anchor blocks to the tower foundation (Walther *et al.*, 1988).

Clearly inspired by the Sancho el Mayor, the Lerèz Bridge (Spain, 1995) employs a diverse arrangement of the back stays, which generate two impressive hyperbolic paraboloids, according to the representation of Figure 2.38.



(a) (b)

Figure 2.38. The Lerèz Bridge (Spain, 1995): (a) General view; (b) Detail of backstay arrangement (Troyano *et al.*, 1998).

But the most outstanding example of an earth-anchored cable-stayed bridge is the proposal for the Ruck-A-Chucky Bridge designed by T. Y. Lin International in 1978 (Figure 2.39). The bridge was designed to cross a narrow gorge, being composed of a *400m* span curved box girder supported by *48* cables individually anchored to the walls of the river canyon, in an arrangement conveniently studied in order to produce no moment or shear. This resulted in a sweeping fan curvature which approached the hyperbolic paraboloid, creating a pleasing effect (Lin, 1996). Unfortunately, although very extensive experimental and analytical studies were performed, the bridge was never built.

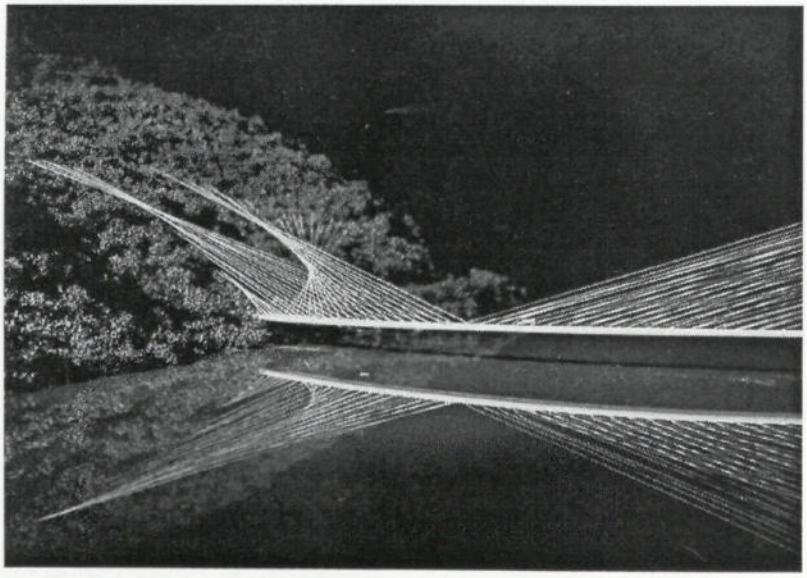


Figure 2.39. The Ruck-A-Chucky Bridge design (Godden, 1980).

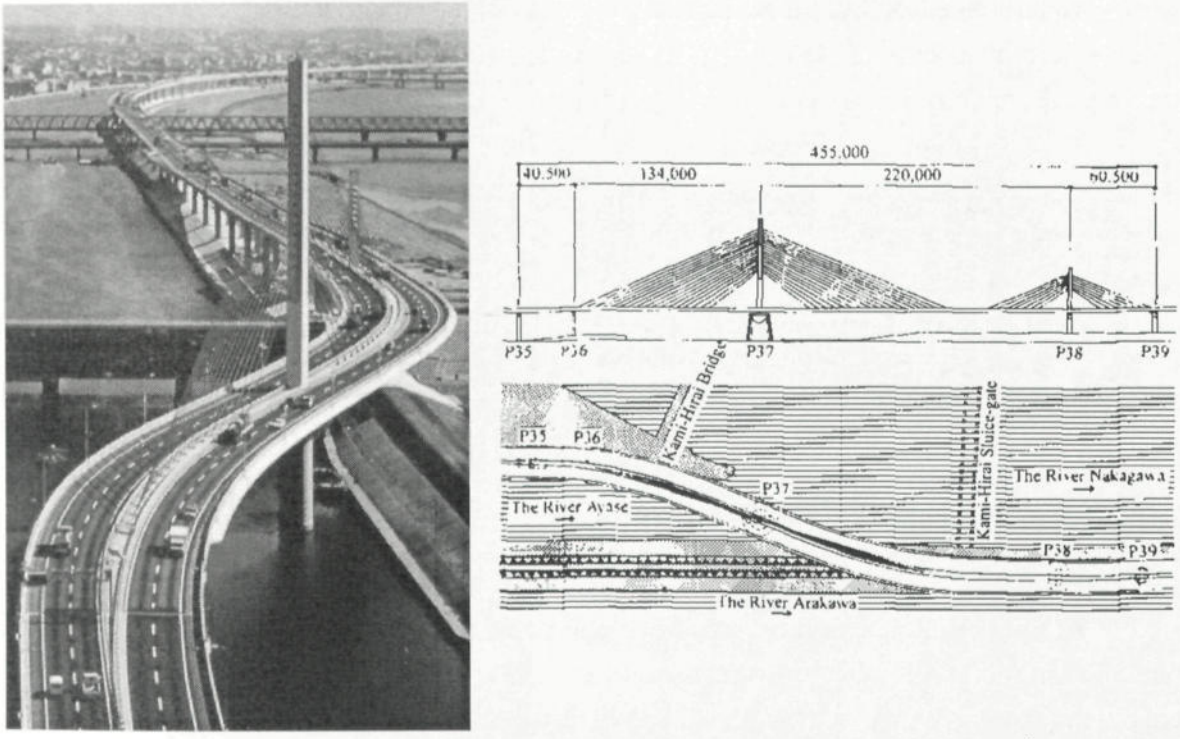


Figure 2.40. The Katsushika Bridge (Japan, 1987). General view and layout (Takenouchi, 1998).

The Ruck-A-Chucky and, generally, curved cable-stayed bridges originate very innovative and interesting solutions, with the advantage of allowing for an increased stability, due to the three-dimensional cable-support system. A singular *S*-curved solution was adopted in Japan for crossing a narrow river at an obtuse angle (Figure 2.40). The Katsushika Bridge (Japan, 1987) with a total length of *455m*, formed by four asymmetrical spans of length *40.5-134.0-220.0-60.5m*, is composed by a pair of pylons of different heights aligned with the center of the carriageway and employs a simple harp suspension type for the cables (Takenouchi, 1998).

When dealing with the architectural value of cable-stayed bridges, an important reference to consider is the Alamillo Bridge (Figure 2.41), designed by the architect and engineer Santiago Calatrava and built in Sevilla for the 1992 World Exhibition (Spain, 1992). The bridge, spanning *200m* across the Guadalquivir River, is composed by one single pylon aligned with the longitudinal axis of the road deck, which is supported itself by a set of *13* stay cables arranged in harp. The main innovative aspect of this bridge, also contrary to the structural behaviour concept, is the lack of backstays. In effect, the cable forces are compensated by a considerable leaning of the massive reinforced concrete pylon backward (*32°* from vertical), so that the resultant of its weight and cable forces is coincident with the direction of the pylon (Aparicio & Casas, 1997).



Figure 2.41. The Alamillo Bridge (Spain, 1992) (Keller, 1998).

At the end of this section, reference should be made to the Ganter Bridge, designed by Christian Menn and built in Switzerland in 1980 (Figure 2.42). The Bridge crosses a deep valley, the Ganter Valley, and is composed by two oppositely slightly curved lateral spans of *127m*, and a straight central span of *174m*. The depth of the valley required one of the pylons to be about *150m* high, thus demanding the use of massive hollow boxes for the towers. By choosing a very slender deck, Menn took advantage of this limitation, creating an extremely beautiful and original effect, further enhanced by the encasing of the stay cables in thin concrete walls, which was necessary for these elements to follow the curved deck profile. Incidentally, this encasing allowed a better corrosion-protection of the stay cables and reduced the stresses in these elements.

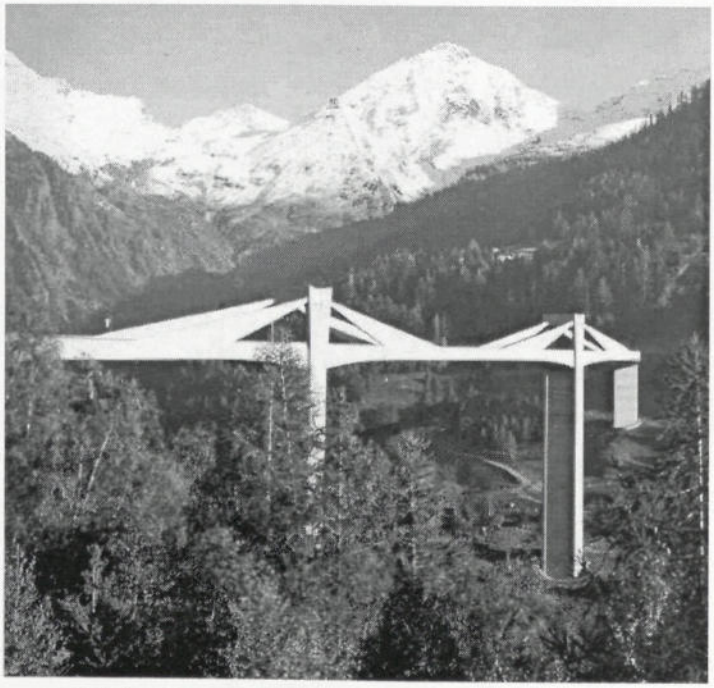


Figure 2.42. The Ganter Bridge (Switzerland, 1980) (Brown, 1993).

Table 2.2. Major cable-stayed bridges all over the world. Extended from (Karoumi, 1998).

Date	Span length (m)				Name	Arrangement of spans (m)	Extension of deck anchorage in side span (m)	Heigth above deck level	Deck width at centre span(m)	Country
	Steel	Composite	Concrete	Composite, FRP						
1999	890				Tatara	50-50-170-890-270-50	270	180.6	30.6	Japan
1994	856				Normandy	27.8-32.5-9x43.5-96-856-96-14x43.5-32.5	335.3	155.4	21.2	France
2001	628				Second Nanjing	305-628-305				China
2002		618			Third Wuhan					China
1993		602			Yangpu	81-162-602-162-81	243	165	32.5	China
1996		590			Xupu	45-3x39-40-590-40-3x39-45		175	71.9	China
1997	590				Meiko Central	290-590-290	290	141.3	37.5	Japan
1991			530		Skarnsundet	3x27-109-530-109-3x27-80	190	104.5	13	Norway
1999		518			Second Santou Bay					China
1995	510				Tsurumi Tsubasa	255-510-255	255	136.7	38	Japan
2002		500			Jingsha	200-500-200	200		29	China
1999	490				Oresund	141-160-490-160-141	230		30.5	Sweden
1991	490				Ikuchi	150-490-150	150			Japan
1994	485				Higashi Kobe	200-485-200	200	119.6	24	Japan
1998	475				Ting Kau	127-448-475-127*	127	130.5	2x21	Hong Kong
2000					Seohae					Korea
1986		465			Annacis Island	50-182.8-465-182.8-50	183	96.2	30	Canada
1989	460				Yokohama Bay	200-460-200	200	106	39	Japan
1992		457			Second Hooghly	182.9-457-182.9	182.9	99.4	35	India
1996		456			Second Severn	49.1-98.1x2-456-98.1x2-49.1	220.7	109	34	UK
1991		450			Queen Elizabeth II, Dartford					UK
1987	450				Rama IX	46.8-57.6-61.2-450-61.2-57.6-46.8	155.8	76.5	32.5	Thailand
1995			444		Chongking 2nd Bridge over Yangtze River	169-444-169	169	107.5	24	China
1983			440		Barrios de Luna	101.7-440-101.7	101.7	65	22.5	Spain
1995			432		Tongling	80-90-190-432-190-90-80	190		23.4	China
1997		430			Kap Shui Mun	80-80-430-80-80	160	93	32.5	Hong Kong
1991			425		Helgeland	177.5-425-177.5	177.5	91.4	11.95	Norway
1998		425			Vasco da Gama	62-70.7-72-420-72-70.7-62	204.7	95.3	30.9	Portugal

Date	Span length (m)				Name	Arrangement of spans (m)	Extension of deck anchorage in side span (m)	Heigth above deck level	Deck width at centre span(m)	Country
	Steel	Composite	Concrete	Composite, FRP						
1991		423			Nanpu	170-423-170	170		30.4	China
1988	420				Hitsushijima	185-420-185	185		27.5	Japan
1988	420				Iwakurojima	185-420-185	185		27.5	Japan
1993			414		Yunyang Hanjiang	86-414-86	86	90.6	15.6	China
1986	405				Meiko-Nishi Ohashi	175-405-175	175			Japan
1975	404				St. Nazaire	158-404-158	158	68	14.4	France
1994			400		Elorn	47.5-50.85-101.7-400-101.7-50.85-47.5	200	61.7	23.1	France
1978	400				Vigo-Rande					Spain
1989			396		Dame Point	198-396-198	198	89.4	30.5	USA (Florida)
1995		381			Baytown	146.9-381-146.9	146.9		23.83x2	USA (Texas)
1982	372				Luling, Mississippi	79-155-372-151-79	155/ 151	82	25.9	USA
1979	368				Flehe, Duesseldorf					Germany
1981	366				Tjörn (new)	124-366-156.6	124	72.7	15.8	Sweden
1987			366		Sunshine Skyway	165-366-165	165	76	29	USA (Florida)
1982	355				Yamatogawa					Japan
1970	350				Neuenkamp	240.5-350-240.5	240.5	49	36.3	Germany
1989	350				Ajigawa	170-350-120	170/120	152		Japan
1990	350				Tempozan					Japan
1990			345		Glebe Island	140-345-140	140	90.3	29.2	Australia
1985			340		ALRT Fraser	180-340-180	180		12.4	Canada
1974	336				West Gate, Melbourne					Australia
1990			335		Talmadge Memorial	143.2-335-143.2	143.2			USA(Georgia)
1978	330				Rio Parana (2 bridges)					Argentina
1993		325			Karnali	325-175*+	325/175	72.5	11.3	Nepal
1974	325				Köhlbrand	97.5-325-97.5	97.5	81	17.6	Germany
1991			324		Guadiana	36-135-324-135-36	135	75	18	Portugal
1969	320				Kniebruecke	5x48-5x48 **	240	95	29.3	Germany
1977			320		Brotonne	143.5-320-143.5	143.5	70	19.5	France
1993		311			Mezcala	79.4-311.4-299.5-83.8-57.9-39.4*		76.5	21	Mexico
1971	305				Erskine	110-305-110	110	38	19.8	Scotland

Date	Span length (m)				Name	Arrangement of spans (m)	Extension of deck anchorage in side span (m)	Heigth above deck level	Deck width at centre span(m)	Country
	Steel	Composite	Concrete	Composite, FRP						
1972	305				Bratislava	63.1-316-54**	63.1	80	20.8	Slovakia
1959	302				Severin	49.1-89-47.9-302-150.7-52.5**	150.7	152	29.6	Germany
1976	300				Kiev	85-300**	85	96.1	31.4	Russia
1978			229		Pasco Kennewick	123.9-299-123.9	123.9	72.9	24.4	USA
1985	290				Farö	120-290-120	120	70.7	22.4	Denmark
1987	288				Dongying	60.5-136.5-288-136.5-60.5	136.5	70	19.5x2	China
1971	287				Mannheim	287-125**	125	70		Germany
1972			282		Wadi-Kuff	97.5-282.97.5	97.5	53.9	12.9	Libya
1965	281				Leverkusen	106-281-106	106	44.8	37.2	Germany
1967	280				Bonn Nord	120-280-120	120	50	35.5	Germany
1974	275				Speyer					Germany
1985			274		East Huntington	185-274**	185	89.7	12.2	USA
1990		274			Quincy	134-274-134	134	54.3	14.1	USA
1974			267		River Waal, Tiel	94.9-267-94.9	94.9	46.3	30.9	Holland
1958			260		Theodor Heuss	107.9-260-107.9	107.9	40	26.6	Germany
1987			260		Yonghe	25.2-99.8-260.99.8.25.2	150	55	14.5	China
1975	258				Oberkassel	5x51.6-5x51.6**	258	60	35.1	Germany
1991			256		Arade	107-256-107	107	52	17	Portugal
1967	255				Rees-Kalkar	104-255-104	104	46	19.3	Germany
1986	250				Weirton-Steubenville	209.9-250**	209.9		28	USA
1973			245		Chaco/Corrientes	163.7-245-163.7	163.7	48	14.4	Argentina
1971	241				Papineau-Leblanc	89.9-241-89.9	89.9	38.4	26.4	Canada
1996		240			Kärkistensalmi	32.6-9x42-240-42x3	84/126	95.3/76.9	13.8	Finland
1962			235		Maracaibo	160-5x235-160	160	42.5	17.4	Venezuela
1983			220		Jinan Yellow River	48-94-220-94-40			29.5	China
1970	216				Toyosato-Ohashi, Osaka					Japan
1968	215				Onomichi Ohashi	85-215-85		10		Japan
1994			215		Evripos	90-215-90	90		13.5	Greece
1955	183				Strömsund	75-183-75	75	28.8	22.6	Sweden
1992			1992	63	Aberfeldy					Scotland

*- Multi-span bridge; ** - 1pylon

2.3 STRUCTURAL SYSTEMS

2.3.1 Selection of bridge type

The selection of a specific type of bridge to cross a river, a highway or a ravine, involves the evaluation of a significant number of factors, such as the span lengths of the various segments composing the bridge, the number and placement of the piers, aesthetic criteria for the site and, finally, the relative costs of several comparable bridge types with acceptable proportions.

A survey performed by Thul (1966), based on a comparative study of existing three-span continuous girder bridges, cable-stayed bridges and suspension bridges evidenced the economical range of applications associated with each type. According to this study, whose results are summarized in Figure 2.43, the upper limits for the centre span of continuous girder bridges are *213m* (*700 ft*), with ratios of centre span (*L*) to total length (*TL*), (*L/TL*), of *30%* to *50%*, while for suspension bridges the lower limit is *355m* (*1100 ft*), with *L/TL* ratios ranging from *60%* to *70%*. The range from *150m* (500 ft) to *335m* (*1100 ft*) associated with bridges with intermediate spans is covered by cable-stayed bridges with proportion *L/TL* ratios of *50%* to *60%*.

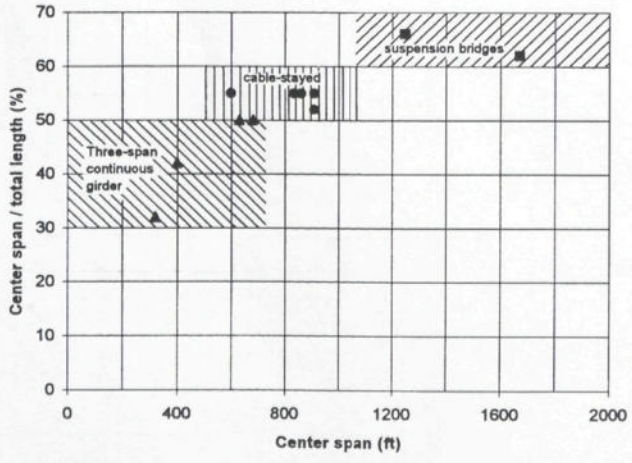


Figure 2.43. Bridge type span comparison (Thul, 1966).

The study developed by P. Taylor (1969) based on the comparison of weight of structural steel per unit area of the deck versus centre span length for the same three spans of steel orthotropic bridges, later complemented by Podolny (1973), evidenced similar results. Podolny and Scalzi (1976) also refer that cable-stayed bridges are most suited for pedestrian bridges with small centre spans, inferior to *150 m*.

The significant innovations in material properties and design and construction methods of the last three decades have shifted the upper limit of economical spans for cable-stayed bridges and suspension bridges, as is evident from Figures 2.44 and 2.45. These Figures represent, respectively, the evolution of centre span length with date of construction

for cable-stayed bridges, and the maximum *L/TL* ratio versus centre span for some of the major cable-stayed and suspension bridges all over the world.

Accordingly, spans over *500m*, which were achieved during the *90's* decade, were used already in the construction of several cable-stayed bridges. Moreover, two of those bridges, the Normandy and Tatara Bridges, have exceeded the *800m* span, entering the domain of very long spans previously covered only by suspension bridges.

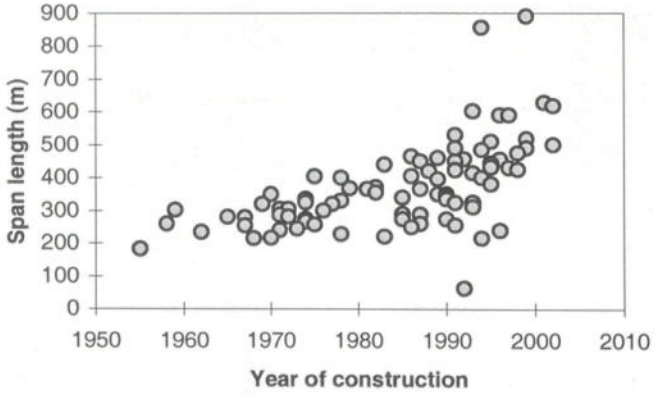


Figure 2.44. Evolution of cable-stayed bridge span length with date of construction.

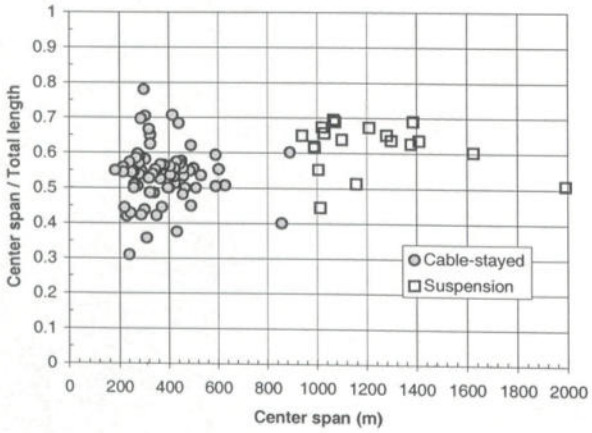


Figure 2.45. Centre span / Total length ratio for some of the major cable-stayed and suspension bridges all over the world.

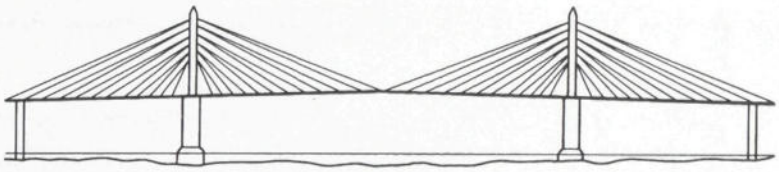
2.3.2 General layout

The cable-stayed bridge system is very flexible, allowing a large variety of geometrical configurations. The basic components of a cable-stayed bridge are the deck, the towers or pylons and the stay cables. This section describes the main types of span and cable arrangements, as well as the typical ranges of variation of several proportions, namely the tower height to span ratio, and the side span to center span ratio. Additionally, reference is made to the different types of towers and decks, and to the arrangements and constitution of cable stays.

2.3.2.1 Span arrangement

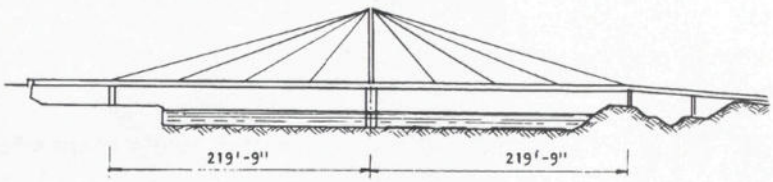
The majority of existing cable-stayed bridges are conventional three-span bridges, with one large central span and two shorter side spans, as shown in Figure 2.46(a). This type of bridges is typically used for long crossings. Common applications are also two-span symmetric or non-symmetric cable-stayed bridges, as represented in Figures 2.46(b) and 2.46(c). Other variations are one-span (Figure 2.46(d)) and multi-span (Figure 2.46(e)) cable-stayed layouts.

Sunshine Skyway Bridge, Florida, USA, 1986 (366m span)



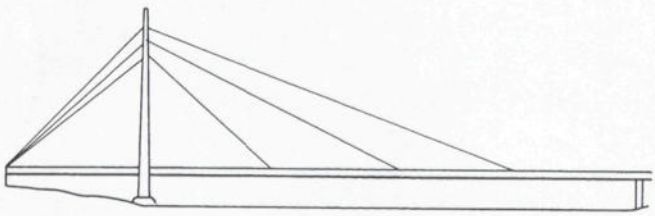
(a)

Canal du Centre Bridge, Belgium, 1966



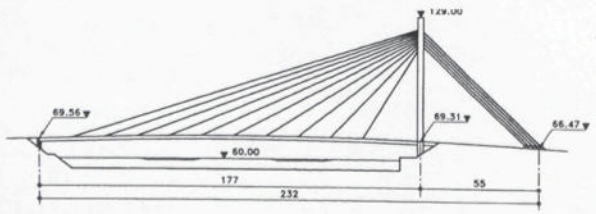
(b)

Kiev Bridge, Ukraine, 1976 (300m span)



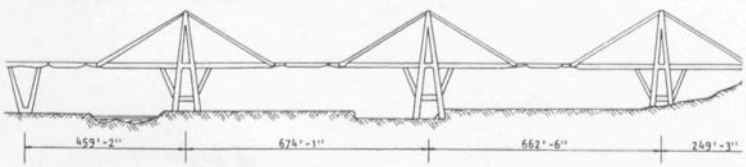
(c)

Lanaye Bridge, Belgium



(d)

Polcevera Creek Viaduct, Italy, 1967



(e)

Figure 2.46. Examples of existing span arrangements (a) Conventional three-span (b) Two-span symmetric (c) Two-span anti-symmetric (d) One-span (e) Multi-span.

2.3.2.2 Cable arrangement

The arrangement of cable stays is a determinant aspect of the design of cable-stayed bridges, in view of its strong influence in the structural performance and layout of the bridge. In effect, the arrangement in two planes of stays produces a torsionally stiff structural system, allowing the use of a slender bridge deck. In contrast, single plane arrangements require the use of a stiff box girder.

On the other side, the type chosen for the bridge deck constrains the spacing of the cable stays. An efficient cantilever construction with no use of temporary stays requires that the spacing between cables at the deck does not exceed the length of the deck segments. Furthermore, on the contrary of slender decks, which require a uniform distribution of the cables along the deck, the use of a heavy box girder required by a central suspension allows for a relatively extensive zone of the deck in the vicinity of the towers free of stay cables, forming an open triangular "window" in the cable plane. This is for example the case of the Friedrich Ebert and Brotonne Bridges presented in Figures 2.21 and 2.22.

Transverse arrangement of the stay cables

Concerning the transverse arrangement of stays, any number of cable planes is possible in principle, as represented in Figure 2.47. One and two plane arrangements are however the most common.

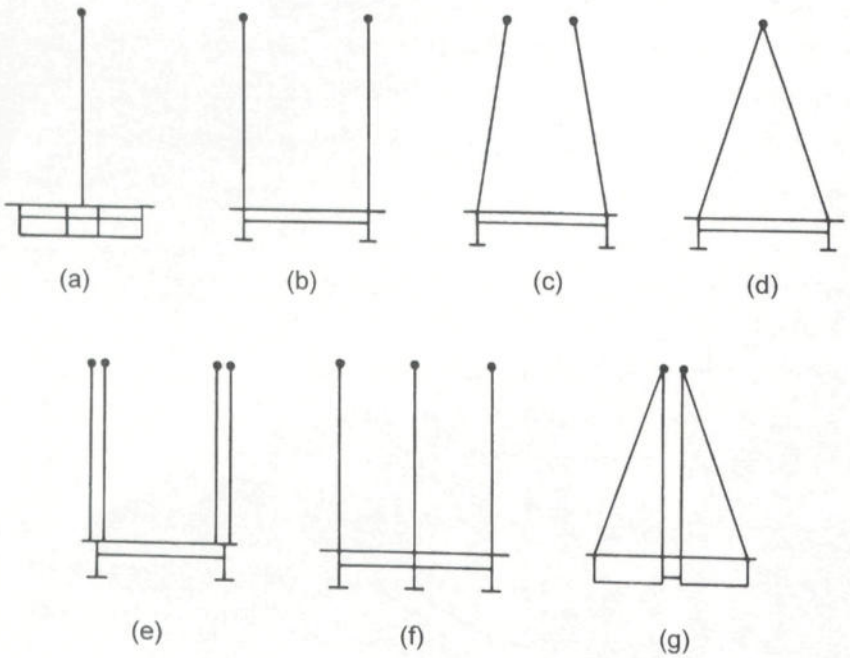


Figure 2.47. Transverse cable arrangement: (a) Single plane- vertical; (b) Double plane- vertical; (c) Double plane- inclined; (d) Double plane- intersecting; (e) Double plane- pairs of cables to avoid local eccentricity at anchorages; (f) Three planes of cables-vertical; (g) Four cable planes.

The arrangement in one plane of cables (Figure 2.47(a)) requires, as already stated, the use of a torsionally stiff box section for the bridge deck. Because of the central location of the pylon on the road deck, an increased width of the carriageway is required. This type of bridge has however better aesthetic quality, as a diagonal view at the bridge does not show a double line of cables as in the case of multiple cable planes.

The double plane or lateral suspension system is the most common type of stay arrangement, consisting of two planes of cables which are either parallel and vertical (Figure 2.47(b)), or inclined towards each other (Figure 2.47(c)). Eventually, these planes intersect above the longitudinal axis of the bridge at the top of an A-frame or inverted Y-frame tower (Figure 2.47(d)). The lateral suspension increases the torsional stiffness of the structural system, therefore improving the static and dynamic behaviour of the bridge, as well as its aerodynamic stability. This stiffening effect is improved when the cable planes intersect each other at the top of the tower, as the differential motion of the anchorages is prevented. The main drawback of the use of inclined cable planes concerns the possibility of creating vertical clearance problems for vehicular traffic, requiring an increased tower height or an extension of the transverse dimension of the bridge.

It should be also noted that the anchorages of the cables at the deck are usually attached to one side of the longitudinal girders, originating local eccentricities. This effect can be avoided using pairs of cables attached on either side of the girder (Figure 2.47(e)). A suspension system of this type was applied at the St. Florent Bridge (France, 1964).

The three and four cable plane systems, as represented in Figure 2.47(f) and (g), are less common types of suspension and meet application in bridges with very large carriageways, where the transverse bending forces would be greatly in excess of the longitudinal bending using the classical double plane suspension. The first proposal for a three-plane of suspension bridge is due to Walther and refers to the Riddes Bridge, in Switzerland, which crosses the Rhone River at an oblique angle. The design consisted in a set of three well separate masts on each bank, giving support to three vertical planes of cables (Figure 2.48), which suspended a *29m* wide and *0.31m* thick concrete slab. This solution was rejected, as it was considered too innovative, despite proving to be the most economical (Walther, 1988).

More recently, a four-cable plane bridge was constructed in Hong Kong, the Ting Kau Bridge (1998). According to Figure 2.49, this bridge is actually composed of two decks with a total width of *42m,* separated by a gap of *5m* and connected at the anchorage sections.

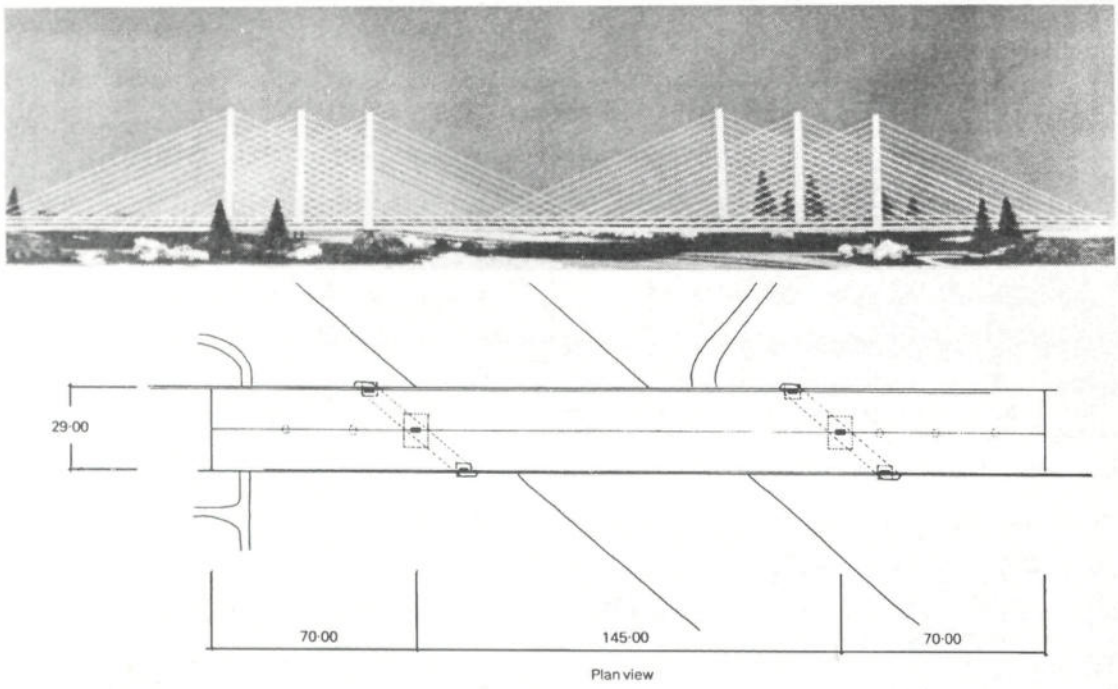


Figure 2.48. Proposal for the Riddes Bridge, Switzerland (Walther, 1988).

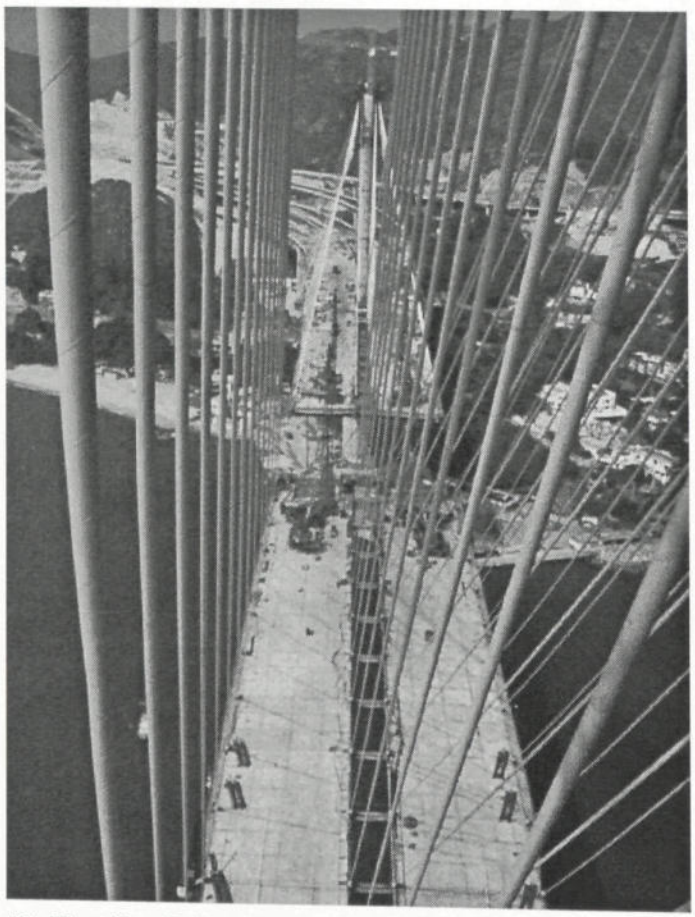


Figure 2.49. Ting Kau Bridge (Hong Kong, 1998), the four planes of cables.

Longitudinal arrangement of the stay cables

With regard to the cable arrangement in the longitudinal direction, three main configurations can be considered, namely the *harp*, *radial* and *fan patterns* (Figure 2.50).

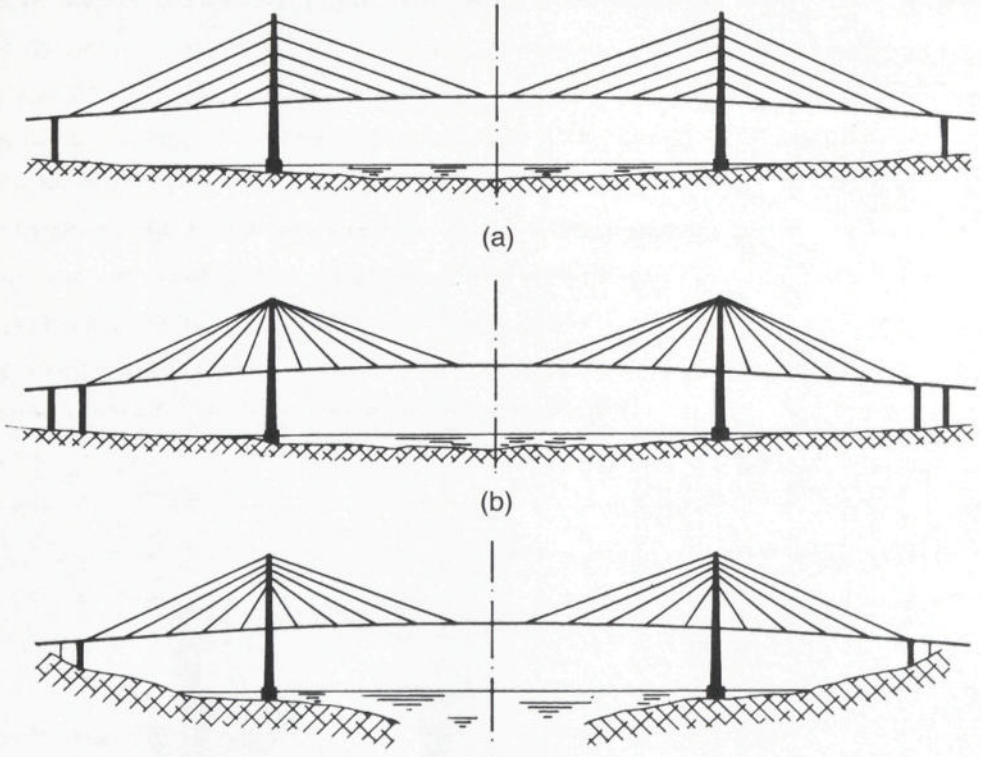


Figure 2.50. Longitudinal arrangements of cable stays: (a) Harp pattern; (b) Radial pattern; (c) Fan pattern.

The *harp* layout consists, according to the representation of Figure 2.50(a), in the arrangement of the cables parallel to each other. As a consequence, the anchorages are uniformly distributed along the height of the tower and along the bridge deck, aspect that leads to an easy installation of the cable stays during the construction of the bridge, as well as to an easy subsequent replacement of damaged stays. Despite the fact that this system is not the most adequate from the structural point of view, the *harp pattern* has been applied frequently in the construction of cable-stayed bridges, in view of the excellent aesthetic advantages that result from the constant angle of the cable stays. A unique example of application of this type of layout is the ensemble of bridges over the Rhine River at Düsseldorf, comprising three different bridges, namely the Knie, Oberkassel and Theodor Heuss Bridges (see Figure 2.16), which were constructed following this criterion, as specified by the architect F. Tamms.

The *radial pattern* (Figure 2.50(b)) concentrates all the anchorages at the top of the towers. This layout was used in several bridges, such as the Pasco-Kennewick Bridge (Figure 2.26), and constitutes the most efficient structural system. In effect, the slope of the cable

stays is maximized, resulting in a smaller weight of cables needed than the *harp pattern,* and transferring also a smaller horizontal force to the bridge deck. At the same time, as the primary force on the towers is axial compression, the longitudinal bending is minimized. The *radial pattern* is aesthetically less appealing than the *harp pattern*, in view of the optical effect of crossing cables at different angles when observed from different relative positions. The most important difficulty associated with the fan layout is however the difficulty in concentrating anchorages and the consequent formation of a heavily stressed zone whose construction can be rather complicated and costly.

The *fan pattern* (Figure 2.50(c)) is an intermediate layout where the cable anchorages are spread along the upper part of the towers. By combining the advantages of both the *harp* and *radial patterns*, a more efficient load carrying system is achieved. This type of layout is the most frequently employed in the construction of cable-stayed bridges, the Normandy and Tatara Bridges (Figures 2.25 and 2.32, respectively) being two outstanding examples.

A less common type, the *star pattern*, was employed only once, in the North Elbe Bridge (Figure 2.18), being characterized by the concentration of the cable anchorages at two single points on the deck. This type of layout goes against the purpose of reducing longitudinal bending forces by supporting the deck continuously along the longitudinal direction with multiple cable stays, and results in a costly and structurally less efficient system.

Cable spacing

The early cable-stayed bridges had a small number of stays, varying from one cable or pair of cables at each tower, as in the case of the Lake Maracaibo Bridge (Figure 2.20), to four cables or six pairs of cables, as used in the Knie and Oberkassel Bridges (Figure 2.16). The spacing between cable stays varied then from *30m* to *80m*, requiring the use of deck girders with large bending capacity.

With the construction of the Friedrich Ebert Bridge (Figure 2.21), Homberg evidenced the numerous advantages of the multiple suspension type: (i) the reduction of longitudinal bending moments by continuous support of the deck, which allowed the used of slender bridge decks, as well as the use of simpler and more economical construction procedures; (ii) a simplification in the installation of the cables and anchorages, which became lighter; (iii) easiness in the replacement of damaged stays.

The typical spacing used presently in multiple suspension systems varies from *8m* to *15m*, for steel and composite steel-concrete decks, and from *4m* to *10m*, for concrete decks, depending on the erection equipment available. Just as a curiosity, the depth *H* of the Lake Maracaibo Bridge, with main spans *L* of *236m* and adopting a cable spacing varying from *30m* to *73m*, is *5m*, giving a slenderness ratio *H/L* of *1:47*. On the opposite side, the Evripos Bridge (Figure 2.30), with a main span of *215m* and employing a multiple suspension system, has a concrete slab of *0.45m* for the deck, giving a slenderness ratio *of 1:477*.

2.3.2.3 Relative dimensions

The ratio between side spans and the main span (l/L)

Considering conventional three-span cable-stayed bridges, the usual ratio between the side spans, *l*, and the main span *L*, *l/L*, ranges between *0.4* and *0.5,* according to Mathivat (1983). Parametric studies developed by Mathivat and Leonhardt and Zellner (1986) have shown that both bending moments in the highly stressed sections and forces in the back stay cables suffer important changes with the variation of the ratio *l/L*. Mathivat refers in particular that the bending forces show a smaller variation for shorter side spans. The limit of *0.4* for the ratio *l/L* results from the fact that below this value, the lifting reactions associated to the back stay cables increase significantly the anchorage forces posing complex technical problems.

With respect to the material employed in the bridge construction, it is clear that, as concrete bridges are heavier than steel bridges, more significant changes in the back stay forces can occur for the later type due to variation of live loads. The definition of a fatigue strength limit leads then to smaller ratios *l/L* for steel than for concrete bridges. Leonhardt and Zellner recommend the use of an *l/L* ratio of *0.42* for concrete highway bridges and *0.34* for railroads of the same type. Furthermore they recommend that whenever only a short span or even no side span are practical, the back stay cables are anchored directly to the ground. This is the case of the Barrios de Luna Bridge, in Spain, where the *l/L* ratio is *0.23* (Figure 2.51).

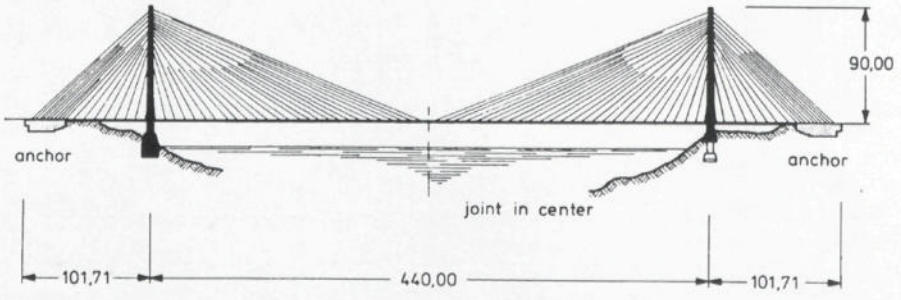


Figure 2.51 The Barrios di Luna Bridge (Spain, 1983). Example of grounded anchor of backstay cables for very short side spans (Leonhardt, 1991).

Leonhardt and Zellner also refer to the case of cable-stayed bridges where the main span is supported by one tower only. In this case, they consider advantageous the use of a heavy concrete deck with small spans for the approach spans, which are used as a long anchor zone for the back stay cables, while for the main span a light steel deck is employed. This solution was first employed for the Manheim Bridge over the Rhine River (Germany, 1971). This same concept has been used with slight variations in several modern three-span cable-stayed bridges, namely in the Normandy Bridge (Figure 2.25), with a ratio *l/L* of *0.39*, and in the Tatara Bridge (Figure 2.26), with a ratio *l/L* of *0.30*.

Figure 2.52 presents the *l/L* ratios of some of the most significant cable-stayed bridges all over the world.

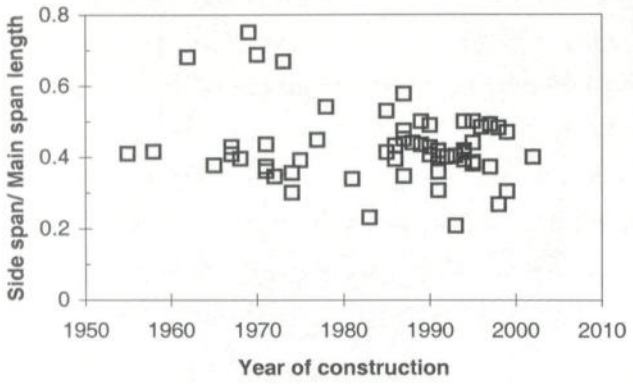


Figure 2.52. Side span to main span ratios of some of the most significant cable-stayed bridges all over the world.

The ratio between tower height and main span (h/L)

The height of the towers is normally controlled by the inclination of the longest cables and affects in a great extent the global stiffness of the bridge system. The angle of inclination of $45°$ is, according to Troitsky (1988), the angle of the cables that produces the smallest deflection of the stiffening girder. Troitsky recommends a variation of this angle within the range $25° - 65°$. Considering a side-to-main span ratio *l/L* of *0.4* to *0.5*, this leads to a ratio between tower height *h* and main span *L*, *h/L*, in the range *0.19* to *0.23*. This is in accordance with Podolny and Scalzi (1976), who consider that the most economical ratio *h/L* is approximately *0.2*.

Leonhardt, Mathivat and Gimsing (1980; 1983; 1983), using simplified considerations, evaluated the variation of steel weight, Π, needed for the three possible suspension systems (radial, harp and fan patterns) with the ratio *h/L*. The three curves presented in Figure 2.53 associated with a total suspension system (no deck support over the towers) evidence the following aspects:

- Minimum values of steel weight are achieved for the radial and harp patterns for *h/L* ratios of *0.29* and *0.50*, respectively;
- The radial system is more economical than the harp system for *h/L* ratios inferior to *0.3*;
- The fan and radial systems lead to almost identical values of steel weight in the range $0.2 < h/L < 0.25$.

Note that although the harp system in particular is more economical for *h/L* ratios of *0.4-0.5*, the increase in the tower height poses new aerodynamic stability problems that were not accounted for in the evaluation of steel weight Π. For this reason, Mathivat considers that the *h/L* ratio should generally vary in the range *0.15* to *0.25*. For small spans (*L<200m*),

Mathivat admits however that *h/L* ratios of *0.3* can be used. Figure 2.54 illustrates values of this ratio found in the longest and most significant cable-stayed bridges all over the world.

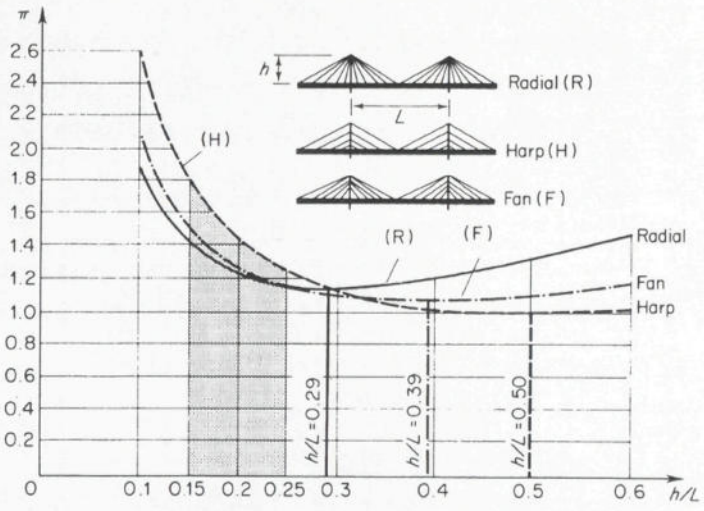


Figure 2.53. Variation of the quantity of steel needed for different forms of suspension with ratio *h/L*. Adapted from (Mathivat, 1983).

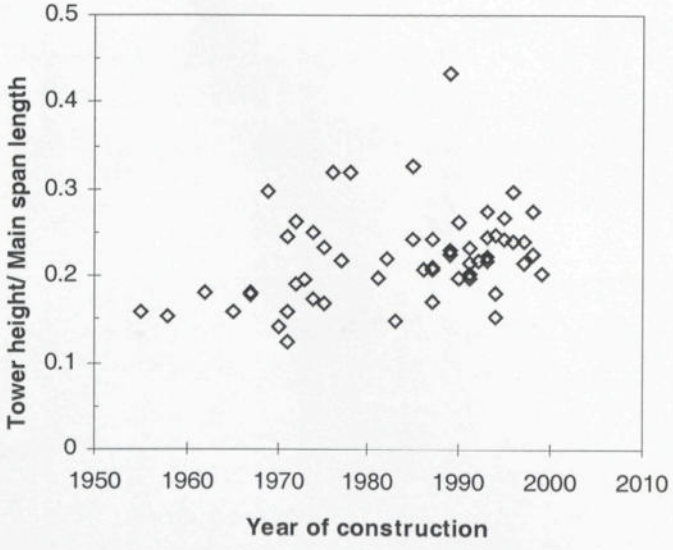


Figure 2.54. Ratio *h/L* between tower height above the deck and the span length for some of the most significant cable-stayed bridges all over the world.

The ratio between the deck width and the main span length (B/L)

The deck width *B* is normally governed by highway traffic requirements. For large spans however, this width is conditioned by lateral stability to wind forces. Leonhardt and Zellner (1991) consider that, in the case of concrete bridges, the aerodynamic stability is in general

assured provided that the deck width *B* is larger than *10* times the deck height *H*, or *1/30*th of the span *L*, or a "wind nose" is used. For steel bridges with spans above *400m*, the aerodynamic stability is assured with *A*-shaped towers and a width of *1/25*th of the main span or a "wind nose". As an example, the deck width to span ratio *B/L* and the deck width to deck depth *B/H* are, for the Normandy Bridge, of *1:39* and *7.3*, respectively, while for the Tatara Bridge these values are *1:29* and *11.3*, respectively. Figure 2.55 presents the *L/B* ratio found for some of the most significant cable-stayed bridges all over the world.

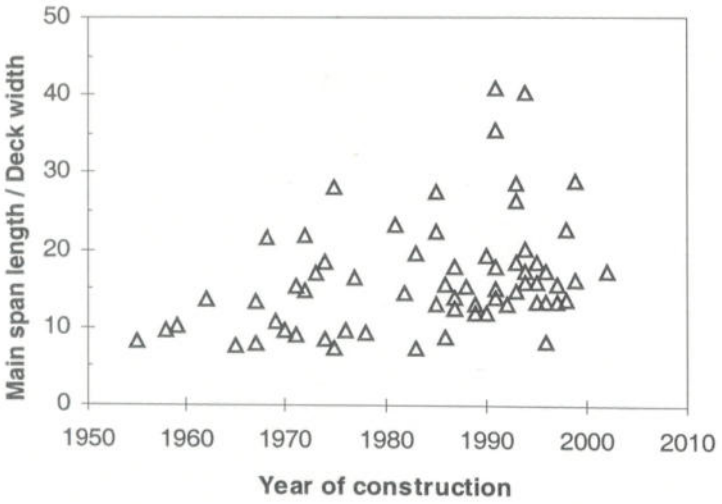


Figure 2.55. Main span length to deck width ratio, *L/B*, in some of the most significant cable-stayed bridges all over the world.

2.3.3 The towers

The basic function of the towers, also designated as pylons in certain cases, is the transmission of the vertical component of cable force to the foundation. The size and shape of these elements depends on the choice of suspension type, on the site conditions and also on aesthetic considerations. With regard to the material of construction, both concrete and steel can be employed. Leonhardt (1991) stated that concrete is the best material for the tower construction, in view of its most-effective cost and also of the more freedom allowed in shaping. Another solution, consisting in a composite steel-concrete construction of the upper part of the tower, has been employed very effectively lately. Examples of bridges employing this type of solution are the Normandy Bridge, in France, and the Vasco da Gama Bridge, in Portugal. In both cases the anchorage boxes were constructed in steel, assembled on site, and later embedded in concrete prestressed walls, as represented in Figure 2.56 for the Normandy Bridge. Two main advantages can be obtained from this system, namely the reduction of inner formwork at a considerable height of the tower, and the reduction of the pylon weight, which assures a better performance to seismic actions.

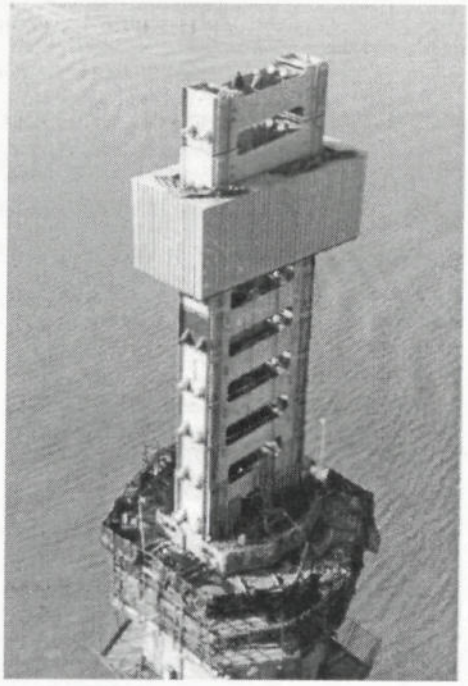


Figure 2.56. Composite construction of tower at the Normandy Bridge: installation of steel anchorage boxes on the pylon (Virlogeux *et al.*, 1994).

Arrangement in the longitudinal direction

Concerning the arrangement in the longitudinal direction, Leonhardt considered that the towers should be relatively flexible, in order to avoid the propagation of large bending moments to the foundations. Bad soil conditions may inclusively determine that hinges are employed at the tower foot. The hinged solution requires however a more complex method of construction.

The use of a *harp* suspension pattern leads, in principle, to higher longitudinal stiffness of the towers than the *radial* or *fan* suspension types. This is due to the need to reduce the deformability of the tower caused by the longitudinal bending moment generated by cable forces acting at different heights. On the contrary, in the *radial* or *fan* suspension, the convergence of the cable stays at the tower top restrains the movement at this point and originates smaller bending moments. Therefore, this tower is allowed a higher flexibility in the longitudinal direction and the main requirement in the analysis is the stiffness against buckling.

Arrangement in the transversal direction

With regard to the tower arrangement in the transversal plane, it is important to assure stiffness against wind loads.

Figure 2.57 presents the most common types of transversal arrangements. The simplest of these is the free cantilever tower, either a single mast, in the case of central

suspension (Figure 2.57(a)), or two independent cantilevers connected at the deck level or at the level of the foundation (Figure 2.57(b)), in the case of lateral suspension and cables arranged in vertical planes. Leonhardt (1986) considered that this solution is possible for maximum spans of *500m*. In effect a recent implementation of this scheme respects the Oresund Bridge, linking Denmark and Sweden, which was opened to traffic in July 2000 and has a main span of *490m* (Figure 2.58).

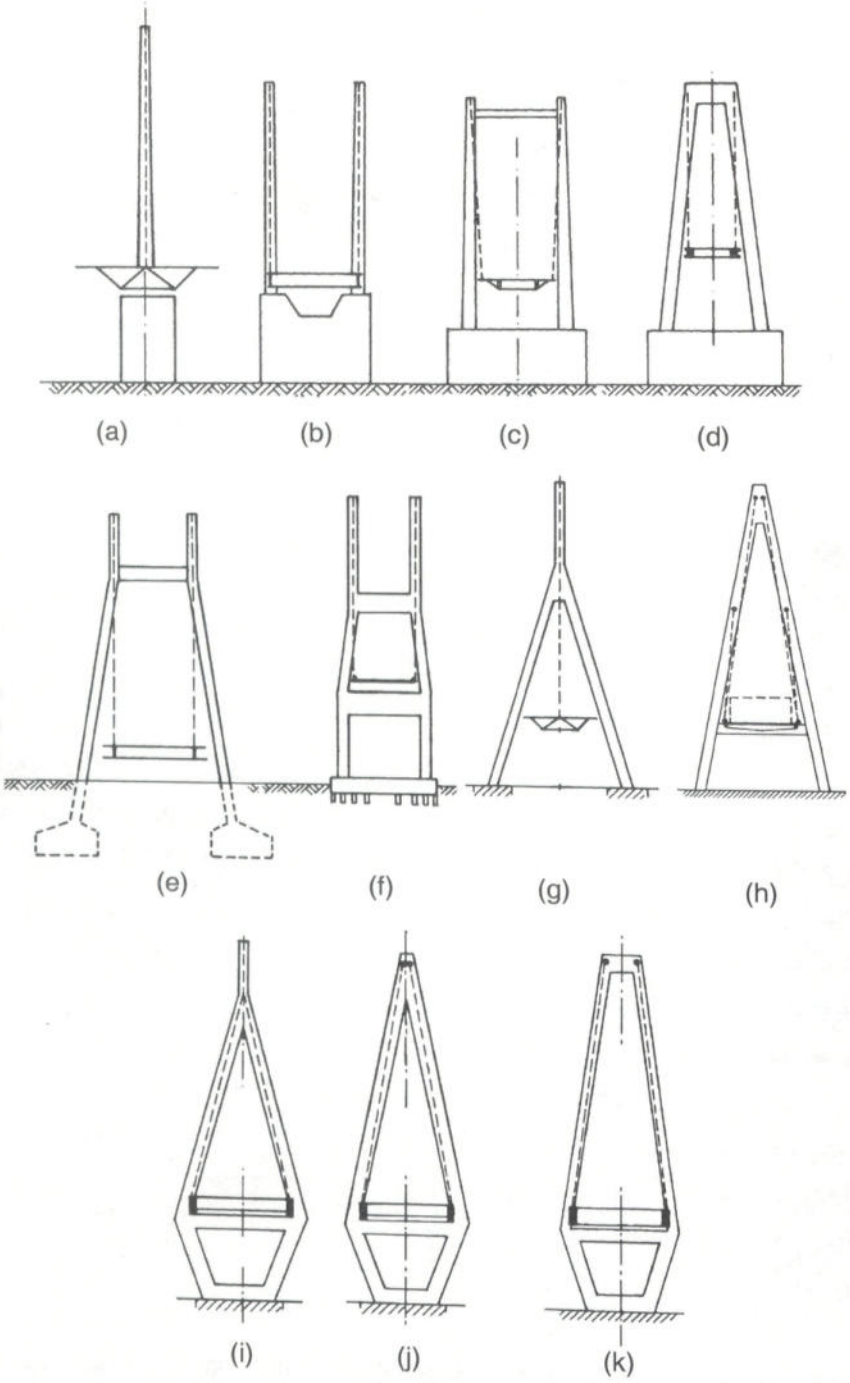


Figure 2.57. Transverse arrangement of towers: (a) Free cantilever; (b) Two independent cantilevers connected at deck level; (c) *H*-shaped; (d) (e) (f) Modified *H*-shaped; (g) inverted *Y*-shaped; (h) *A*-shaped; (i) δ-shaped; (j) diamond-shaped; (k) with bracing at the top.



Figure 2.58. The Oresund Bridge (Sweden-Denmark, 2000) (Gimsing & Nissen, 1998). Scheme of tower arrangement.

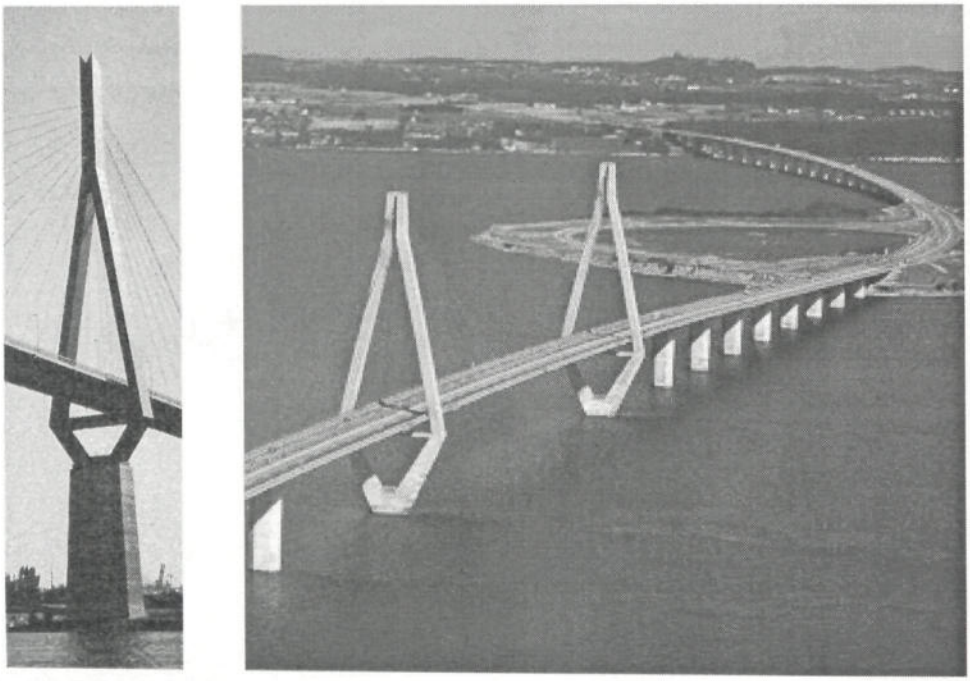
If the cables are not in vertical planes, then a transverse bracing between the cantilevers is necessary, leading to the so-called *H-shaped* arrangement, as represented in Figure 2.57(c). Several forms of variations in the tower legs' slopes are then possible for better accommodation of the deck (Figure 2.57(d) (e) (f)). In the limit, the *H-shaped* tower turns into an inverted *Y-shape*, or into an *A-shape* (Figures 2.57(g) and 2.57(h), respectively), if a bracing is added below the deck level. The two systems provide an increased stiffness in the transverse plane. The *A-framed* tower is in fact the most adequate solution for bridges located in regions that are susceptible to strong wind attacks, for very long spans or when the towers reach a considerable height (the towers of the Tatara Bridge, for example, reach *226.5m* above the sea level).

The need of large clearances below the deck is however a disadvantage for both the inverted *Y* and *A-shaped* towers, as the enlargement of the tower legs requires a large pier and, consequently, a large artificial island for ship impact protection. In this case, the tower legs can be joined under the deck level, as represented in Figures 2.57 (i) and 2.57(j), leading to the so-called δ and *diamond* types, respectively. Figure 2.59 presents the application of these two types to the Khölbrand (Germany, 1974) and Faro Bridges (Denmark, 1985).

Another alternative for large clearances, is the use of a short bracing element at the top of the tower (Figure 2.57(k)), which allows for a smaller enlargement of the tower legs. Additional bracing elements can be employed at intermediate levels along the tower height, in case of very high towers. Both the Meiko Central (Japan, 1998) and the Tatara Bridge towers presented in Figure 2.60 combine both lateral bracings at two levels along the tower, and the approach of the tower legs below the deck level.

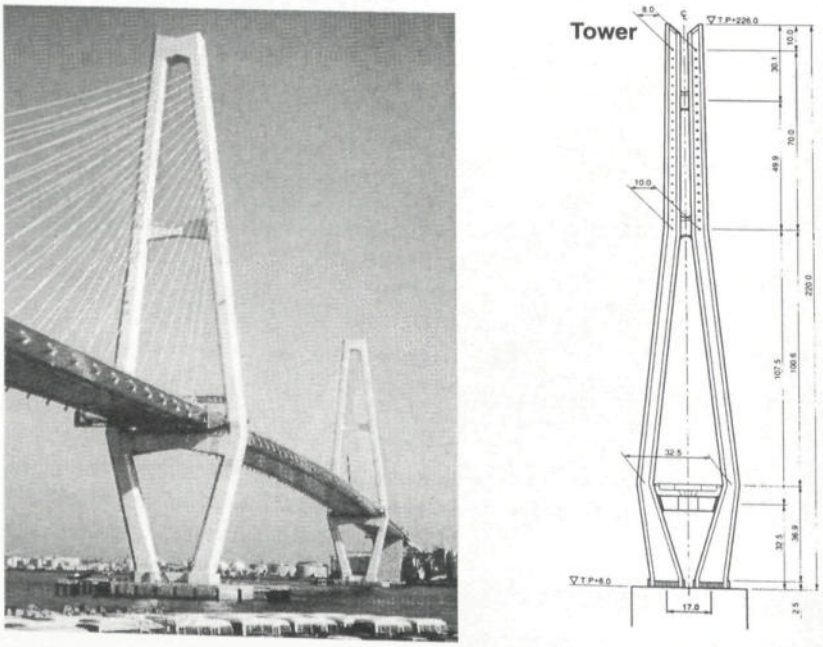
Finally the single stayed cantilever tower presented in Figure 2.61 was only employed at the Ting Kau Bridge (Hong Kong, 1998), designed by Schlaich and Bergermann (1998), and constitutes a significant innovation in cable-stayed bridge construction. In effect, by significantly reducing the aerodynamically shaped section with the use of a single semi-circular cross-section, the wind loads are reduced, aspect of major importance for the region where the bridge is located, susceptible to the occurrence of typhoons. Furthermore, the

stabilization of the mast by cables both in the transverse and longitudinal plane originates a behaviour similar to the masts of a sailboat, allowing for the suspension of four planes of cables to support the *42m* wide deck. At last, the reduced dimensions of the pier result in reduced dimensions and consequently in reduced cost of the necessary artificial islands for ship impact protection.



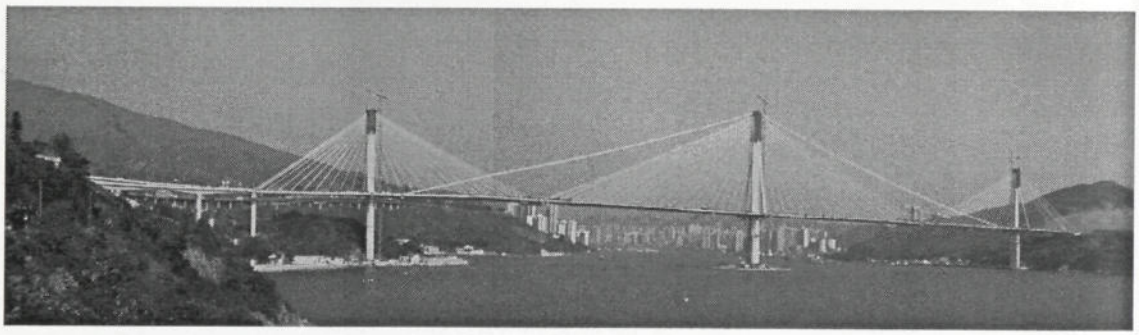
(a) (b)

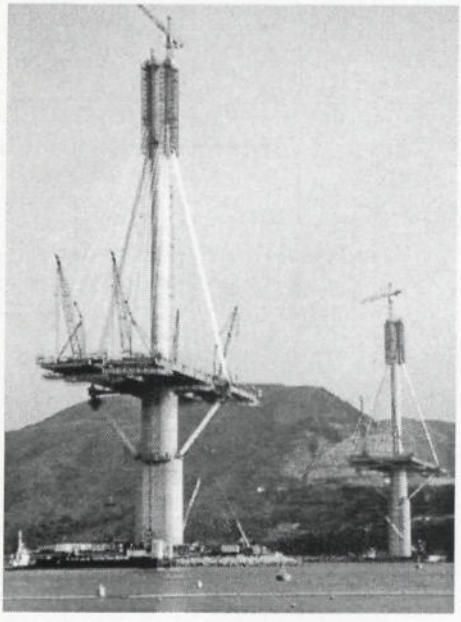
Figure 2.59 (a) The Khölbrand Bridge tower (*δ-shaped)* (Brown, 1993); (b) The Farö Bridge tower (*diamond shaped*) (www.monthor.dk).



(a) (b)

Figure 2.60 (a) The Meiko Central Bridge towers (Ito, 1998); (b) The Tatara Bridge towers. Courtesy of Honshu-Shikoku Bridge Authority.





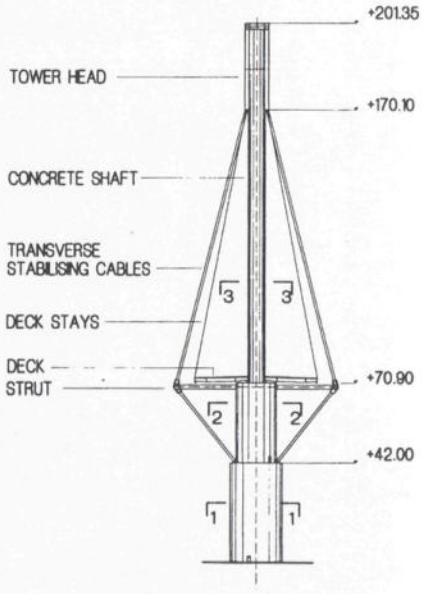


Figure 2.61. The Ting Kau Bridge. General view, view of towers during construction, and scheme of towers in transverse plane (Schlaich & Bergermann, 1998).

2.3.4 The deck

The bridge decks can be classified according to the material employed in construction, into steel, concrete and composite types.

Steel decks

Steel decks can be built with *I*-girders at the edges and a number of cover plates, as represented in Figure 2.62(a), or else can be composed of one or more box sections, as presented in Figure 2.62 (b) to 2.62 (f). Another possibility for steel solutions refers to the use of stiffening trusses (Figure 2.62 (g) to 2.62(i)). Trusses have been seldom used in the past in cable-stayed bridge construction, as they generally require significant costs in fabrication and maintenance and present usually an unfavourable visual appearance. However, for combined highway and railroad traffic, when usually two levels of the deck are of interest, trusses

provide an interesting solution, having additionally a good aerodynamic stability. A recently adopted trussed cross section refers to the Øresund Bridge, linking Denmark and Sweden (Figures 2.58 and 2.63). The steel truss is however combined with a transversely prestressed concrete top flange, which acts as a composite cross section.

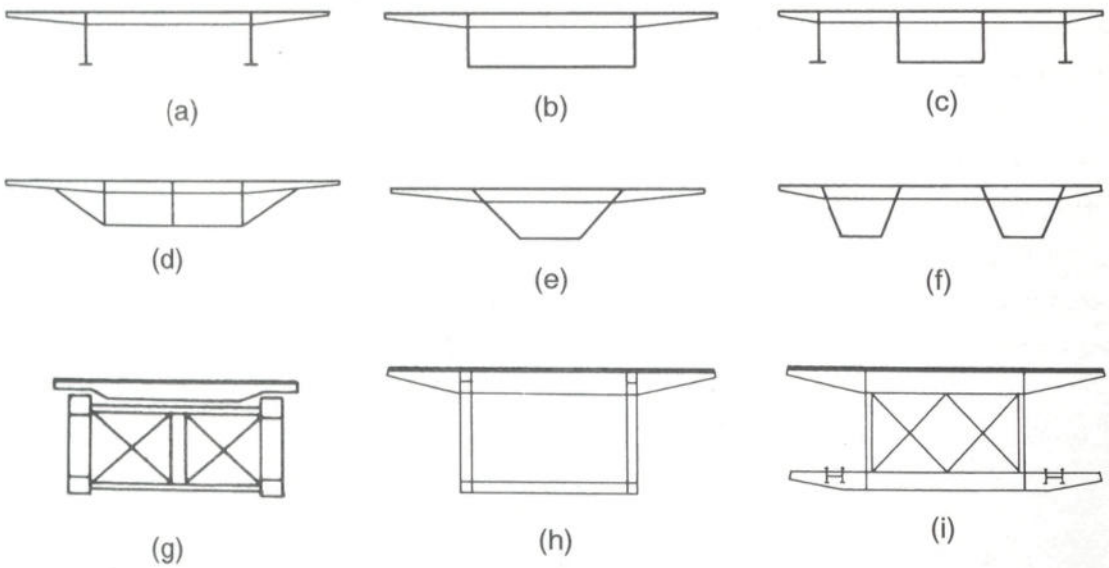


Figure 2.62. Types of steel bridge decks: (a) edge girders combined with cover plates; (b) to (f) box girders; (g) to (i) stiffening trusses (Troitsky, 1977).

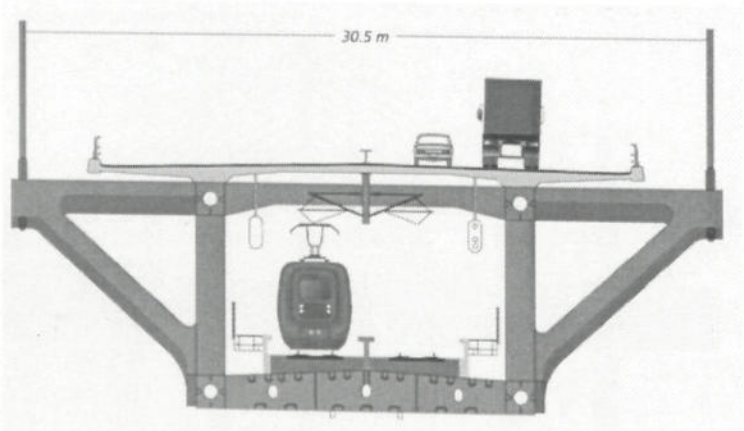


Figure 2.63. The Øresund Bridge cross-section, based on a stiffening truss (Øresund Konsortiet, 1998).

Concrete decks

Although the former cable-stayed bridges were mainly constructed in steel, concrete has been employed frequently during the last decades, the main advantages being a reduced cost and relatively high stiffness and damping. According to Leonhardt and Zellner (1991), for spans

with less than *150m* and for deck widths not greater than *20m*, a simple solid slab is the simplest and most adequate solution, the necessary thickness being determined by transverse bending moments. The solid slab solution was employed for the first time by R. Walther at the Diepoldsau Bridge, in Switzerland, with a main span of *97m*. This solution was later employed at the Evripos Bridge (Figure 2.30), with a main span (*L*) of *215m*, as already referred. In this case, a *0.45m* thick (*H*) solid slab was used for the deck, with a width of *13.5m*, leading thus to an extremely high slenderness characterised by an *H/L* ratio of *1:477*.

For deck widths larger than *20m* or spans in the range *150-500m*, Leonhardt and Zellner suggest the use of concrete slabs connecting edge solid beams stiffened transversely by *T*-beams or steel cross girders. A solution of the former type was employed in the deck of the Helgeland Bridge, in Norway, as represented in Figure 2.28. The deck of the Vasco da Gama Bridge, constructed recently in Portugal, is composed of a concrete slab *0.25m* thick supported by two edge solid beams *2.65m high*, stiffened transversely by steel *I*-girders every *4.4m*, as represented in Figure 2.64.



Figure 2.64. The Vasco da Gama Bridge deck.

The requirement of aerodynamic stability may oblige to the introduction of fairings in the cross section design, or even dictate the shape of the edge beams. In the Vasco da Gama Bridge, wind tunnel tests and *Computer Fluid Dynamic* (*CFD*) analysis determined a modification of the former design of the cross-section by addition of vertical baffles placed at the thirds of the deck width bellow the deck in the main span (Figure 2.65), conjugated with fairings at the edge beams. In the Pasco-Kennewick Bridge (Figure 2.26), a wind "nose" was formed with the edge girders, which assumed the form of triangular boxes, as represented in Figure 2.66.

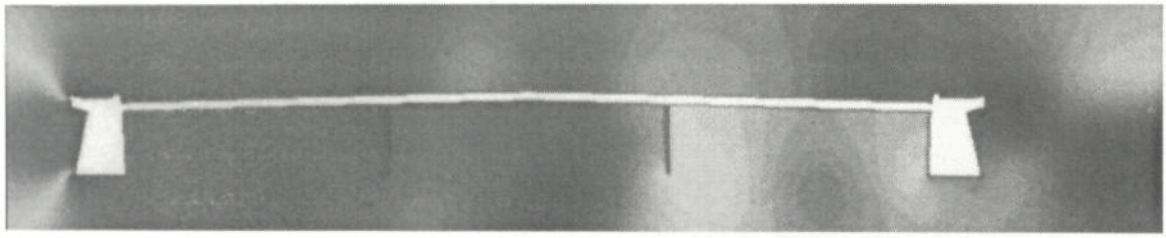


Figure 2.65. The Vasco da Gama Bridge deck. Addition of baffles bellow the deck for achievement of wind stability (Branco *et al.*, 1998).

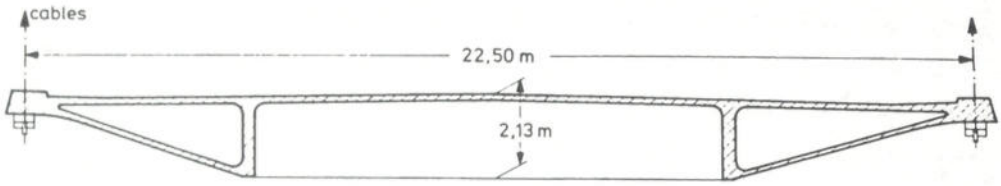


Figure 2.66. The deck cross-section of the Pasco-Kennewick Bridge (Leonhardt & Zellner, 1991).

In central suspension bridges, where a significant torsional stiffness is required for the deck, the concrete precast box girder is the ideal type of cross section. The Brotonne Bridge, presented in Figure 2.22, was one of the first cable-stayed bridges of axial suspension that employed a deck of this type, in which the transmission of cable forces is preformed by precast inclined struts, as represented in Figure 2.67. Other variations of concrete box sections are presented in Figure 2.68.

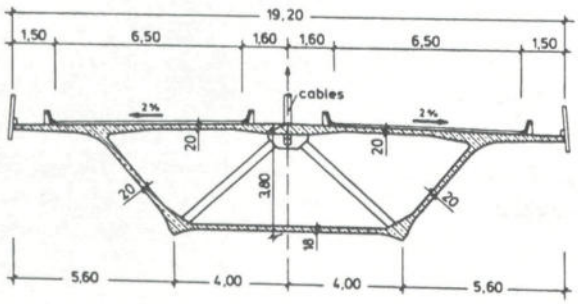


Figure 2.67. The Brotonne Bridge deck cross section (Leonhardt & Zellner, 1991).

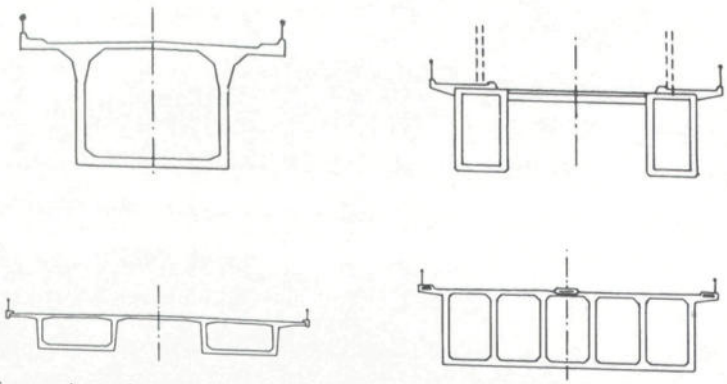


Figure 2.68. Examples of concrete box sections in cable-stayed bridges (Troitsky, 1977).

Composite decks

Composite cable-stayed bridge decks appeared only in the 1980's but they soon gained interest in applications to spans in the range *300m* to *500m*. The first major composite cable-stayed bridge to be built was the Annacis Bridge, in Canada, later called the Alex Frazer Bridge. A precast concrete slab 0.265m thick composes the deck of this bridge (Figure 2.29(b)) connected to steel *I*-girders by shear connectors. Steel cross beams support the concrete panels every *4.5m*. A recent application of composite deck construction refers to the Second Severn Crossing Bridge (UK, 1996), with a main span of *456m*. Figure 2.69 presents a view of the bridge during construction and a detail of the composite deck, where transversal framing was achieved with steel trusses.

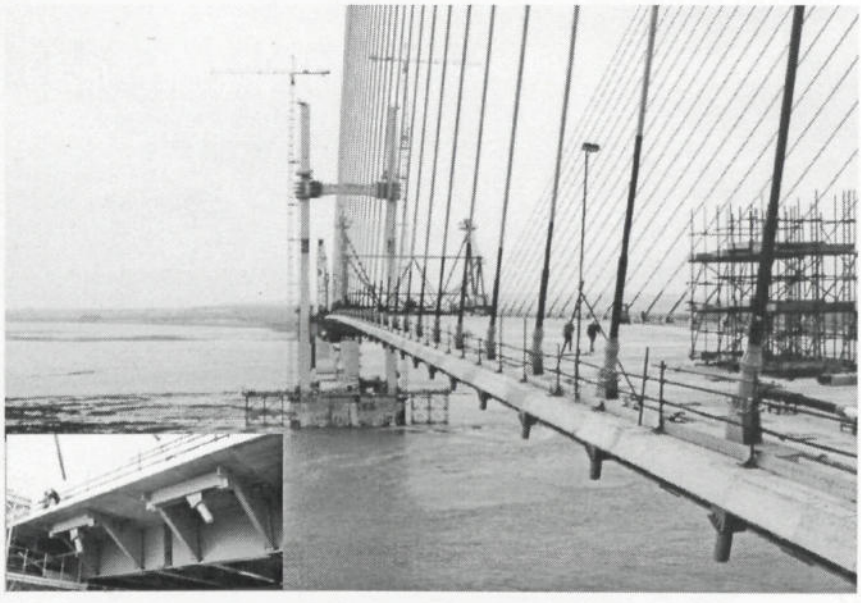


Figure 2.69. The Second Severn Crossing Cable-Stayed Bridge (UK, 1997). View during construction and detail of the composite deck.

Decks of wide and very long span bridges

Finally, for wider bridges (*B>25m*) and for very long span bridges (*L>500m*) steel solutions are considered most appropriate, in order to reduce the dead load. Leonhardt suggests the use of orthotropic steel decks, as the represented in Figure 2.70. Also shallow steel box cross sections of the type presented in Figure 2.71 have been lately employed in several cable-stayed and suspension bridges, where the wind 'nose' reduces the wind loads and increases the critical wind speed. Both the Normandy and Tatara Bridges employ steel box sections of this type, as can be observed in Figures 2.25(a) and 2.32, respectively. It should be noted however that in both bridges a part of the deck in the side spans (the whole side spans, in the case of the Normandy Bridge) is made of a concrete box, in order both to compensate for the

dead load imbalance between the centre span and the shorter side spans, and to allow for a more effective anchorage of the back stays.

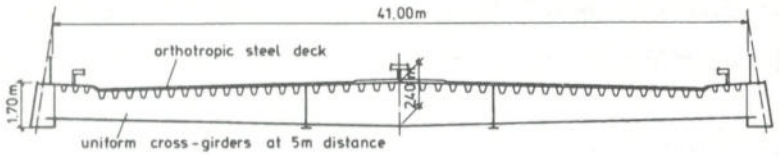


Figure 2.70. Example of orthotropic steel deck for very wide bridge in a span beyond *500m* (Leonhardt & Zellner, 1991).

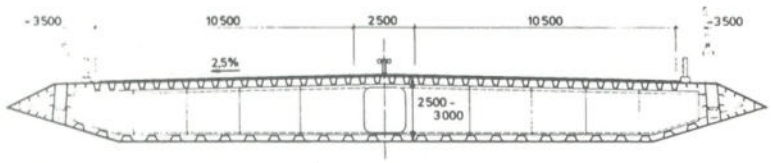


Figure 2.71. Example of shallow box section for a very long span bridge (Leonhardt & Zellner, 1991).

2.3.5 The cables and anchorages

The stay cables are members of utmost significance in the cable-stayed bridge design. The good performance of these elements is conditioned by the selection of materials and the quality of the manufacturing and should satisfy in particular the following requirements (Ohashi, 1991): (i) high load bearing capacity; (ii) high and stable Young's modulus; (iii) a compact cross section; (iv) high fatigue resistance; (v) ease in corrosion protection; (vi) ease in handling and installation; (vii) low cost.

A stay cable is basically composed of one or more *spiral strands*, *parallel wire strands*, *locked coil strands*, or *structural ropes*. The *strand* is generally an assembly of wires, which can be used as an individual carrying member, or as a component in the structural rope.

Spiral strands are composed of large diameter galvanised round wires helically spun together (Figure 2.72(a)). The wires are stranded in one or more layers, in order to achieve the required diameter, which typically varies in the range of *13mm* to *150mm*.

Parallel wire strands are composed of *5mm* to *7mm* galvanised round wires laid up in a hexagonal form, which are encased in a tight fitting *High Density PolyEthylen* tube (*HDPE*) (Figure 2.72(b)). The typical number of assembled wires ranges between *73* and *421*. The so-called *ultra-long lay parallel strands* introduced in the 1980's are an improved variant of the parallel wire strand and parallel cables, where the wires are twisted up to *3°* to *4°*. An interesting feature associated with this type of cables is the direct extruding of the *HDPE* coating onto the wire bundle, so that no void exists between the wires and the covering, increasing therefore the corrosion protection.

Locked coil strands are composed of a centre part of one or more layers of large galvanised round wires helically spun together, covered by one or more layers of large diameter *T* or *Z*-shaped wires (Figure 2.72(c)). Typical diameters vary between *30mm* and *150mm*. For increased corrosion protection, locked coil strands can be encased in *HDPE* tubes.

Finally, *structural ropes* combine *strands*, either spun around a steel core composed of smaller diameter wires that give the rope an increased flexibility (Figure 2.72(d)), or associated in a parallel wire bundle encased in *HDPE* tube (Figure 2.72(e)).

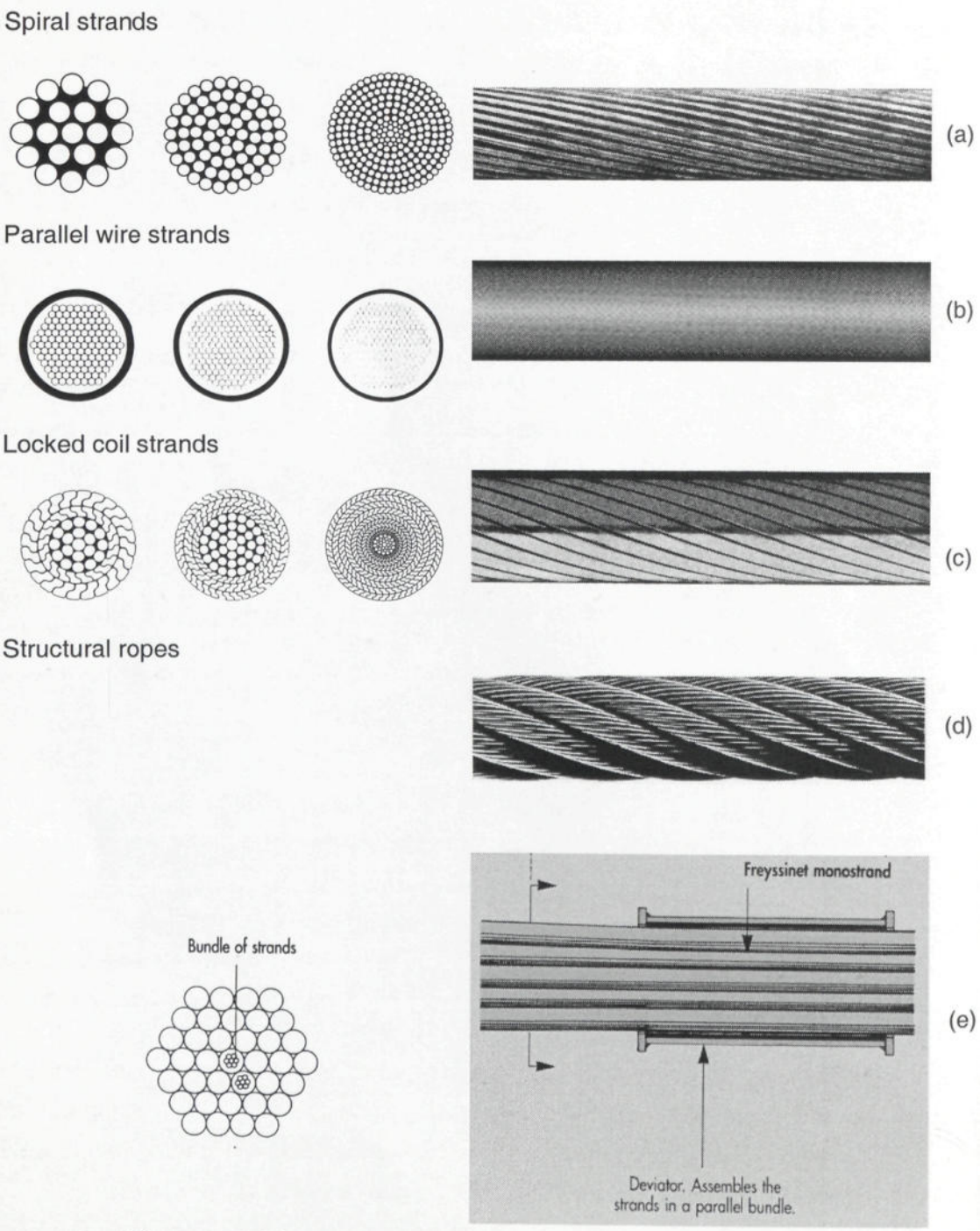


Figure 2.72. Types of stay cables (Bridon, 1998; Freyssinet, 1998)

Early steel cable-stayed bridges constructed in Germany employed locked coil strands or cables composed of smaller locked coil strands, which have a more compact cross section and a smooth surface and are generally more resistant against corrosion. Although locked coil cables have been recently used in some Norwegian suspension bridges, they are hardly used at present, due to the rather complicated anchorage details and difficulty of replacement (Ito, 1999).

On the other hand, spiral ropes have been traditionally used in the UK mainly because they are easier to handle, due to their flexibility. Spiral ropes are not popular elsewhere, because their properties are inferior to parallel wire strands. Japan and most countries have been using the *parallel wire cables* (more recently, the *long lay parallel cables*) in virtue of their increased mechanical properties.

Mechanical properties

With regard to the mechanical properties, and comparing with structural steel, the tensile strength of cable stays is much superior, although the ductility is lower. In *spiral ropes*, the guaranteed tensile strength is in the range *1500-1600MPa*. In *parallel wire strands* the strength varies in the range *1570-1765MPa*. Finally, in *locked coil ropes* the tensile strength is generally slightly lower. As for the Young's Modulus, it is generally known that for parallel wire strands its value is only slightly lower than that of the steel material. However, for helical strands, the twisting of the wires decreases the elasticity modulus. Typical values of Young's modulus are *160GPa* for *spiral ropes*, *180GPa* for *locked coil ropes*, and *190GPa* for *parallel wire ropes.*

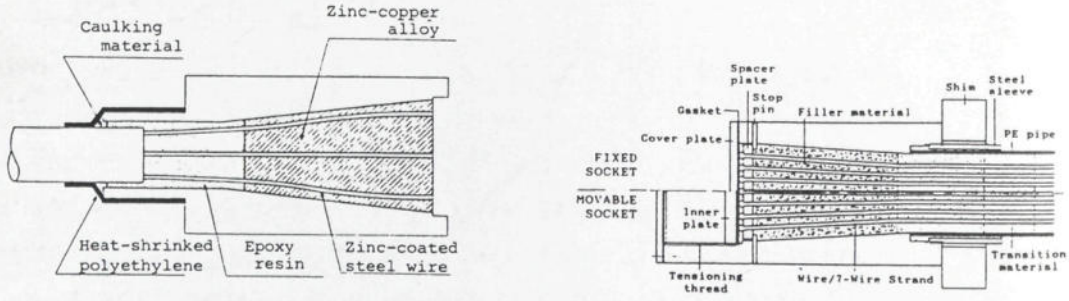
A reference should still be made to new composite materials, namely the *Carbon Fiber Reinforced Plastic* (*CFRP*), which appeared in the 1980's and that has been under experimental evaluation during the last years (Roos & Noisterning, 1999). The use of this material as tendons in cable-stayed bridges for very long span bridges is envisaged to have very interesting characteristics, like low weight (*1/3*rd of steel weight), high stiffness (tensile strength of *2700 MPa*) and resistance against corrosion, although lower elasticity modulus (*160MPa*) and higher price.

Anchorages

The connection of structural strands and ropes to the bridge girder and towers is performed through anchorages. Anchorages must transfer the breaking strength of the stay cables without exceeding the yield strength of the stay fitting and they must allow adjustment at one of the ends as well as the replacement of any damaged cable without interrupting the traffic. Also, given the large variation of cable stress in consequence of traffic loading (particularly for light girder bridges), anchorages must assure high fatigue resistance.

The main types of existing anchorages have been discussed by Leonhardt (1991) and Ohashi (1991) and are:

- The *zinc-socket*: this is the conventional type of anchorage, in which the conical cavity at the end of the cable is partially filled with an epoxy resin and with a zinc-copper alloy (Figure 2.73 (a)). This type of anchorage does not allow the full development of the cable fatigue strength because the wires are affected by the heat of the casting metal, and because corrosion between the wires and the zinc alloy occurs at the entrance of the socket;
- The *Hi-Am (High Amplitude) socket:* this anchorage was developed by the Swiss firm *BBR* with the aim of avoiding the decrease of fatigue strength by heat of the casting metals. According to Figure 2.73 (b), the anchorage uses the button heads at the wire ends bearing on a steel anchorage plate, the conic cavity of the socket being filled with a mixture of metals by pressure at normal temperature and closing the system with an epoxy resin.



(a) (b)

Figure 2.73. Cable anchorages: (a) Zinc-socket; (b) Hi-Am.

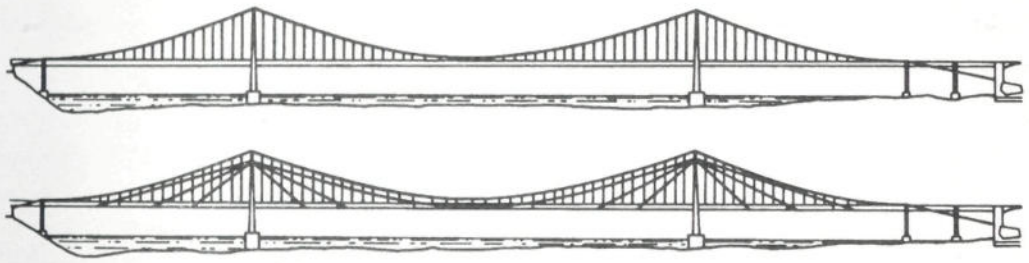
2.4 MAJOR CABLE-STAYED BRIDGES IN PORTUGAL

The first proposal for a combined suspension and stayed system bridge in Portugal dates from 1960, when the American D. Steinman won the original bridge project for the construction of a suspension bridge across the estuary of the Tagus River, in Lisbon.

In order to limit the investment, the bridge was conceived as an initially conventional suspension bridge with a total length of *2278m* and a main span of *1013m,* supporting a four-lane roadway (Figure 2.74(a)), and was prepared for a later addition of two railway tracks on a lower deck placed inside the stiffening girder, by strengthening both the cable system and the stiffening truss. According to Figure 2.74 (b), the solution consisted in the addition of a number of inclined stays and use of the railway stringers to transmit the horizontal component of the stay forces.

The design of the retrofit of the Tagus Bridge started in 1992, *26* years after the bridge construction. The considerable unexpected traffic demands and the necessity of carrying heavier long-distance freight trains instead of commuter trains motivated a more thorough intervention in the bridge structure. In order to preserve the scenic and historical nature of the bridge, the retrofit designers recommended the abandonment of the complementary stayed

system (Gesner & Jardim, 1998), in favour of the addition of two suspension cables parallel to the former cables located adjacent to the existing anchorages. Figure 2.75 presents a view of the former bridge, and of the final bridge after retrofit.



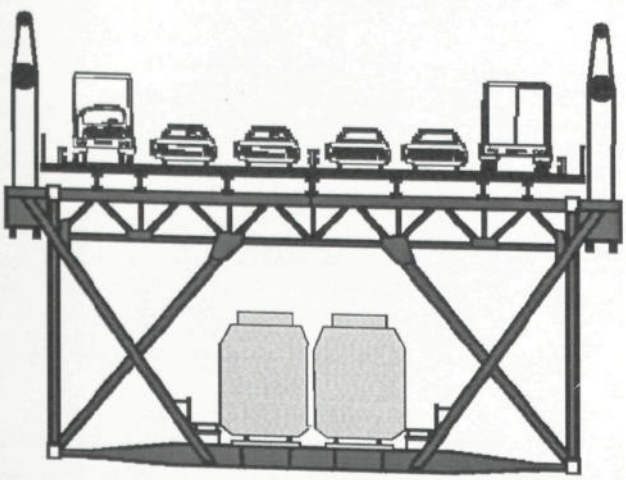
(a)

(b)

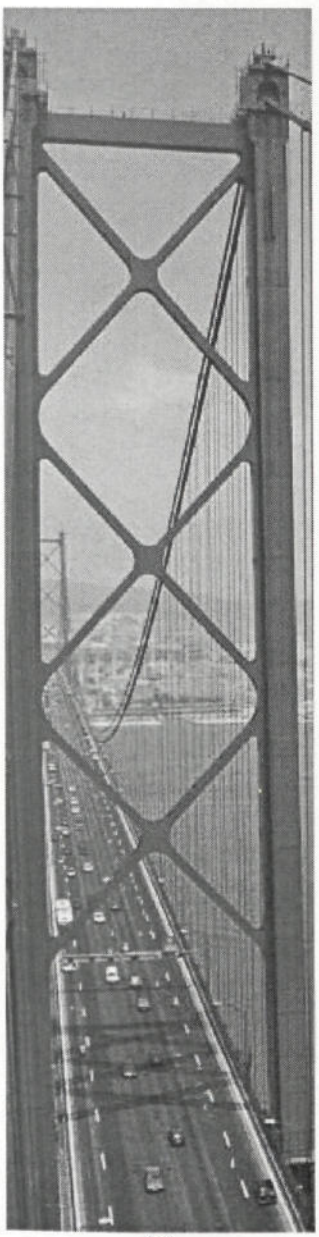
Figure 2.74 The Tagus Bridge (Lisbon, 1966): (a) former bridge; (b) proposal for the final bridge, including railway tracks (Podolny & Scalzi, 1976).



(a)



(b)



(c)

Figure 2.75. The Tagus Bridge: (a) before retrofit; (b) cross section after retrofit; (c) after retrofit (Gesner & Jardim, 1998).

Figueira da Foz Bridge

So it was only in 1982 that the first cable-stayed bridge was constructed in Portugal. The *Figueira da Foz* cable-stayed bridge presented in Figure 2.76, designed by the Portuguese E. Cardoso (1977), is part of a *1421m* long bridge in the central part of Portugal. The cable-stayed bridge, with an extension of *405m* over the River Mondego, has a main span of *225m* and two side spans of *90m* (Figure 2.77).

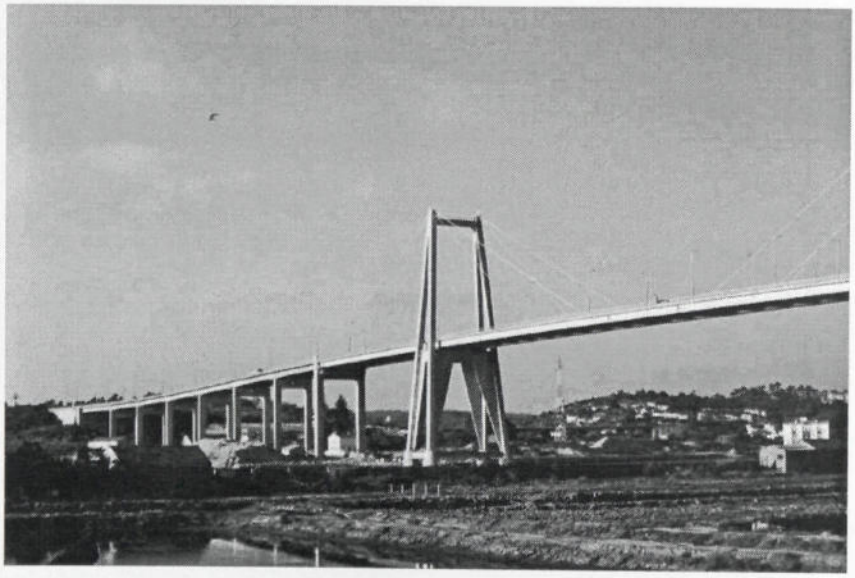


Figure 2.76. The Figueira da Foz Bridge. Partial view. Courtesy of J. Rodrigues.

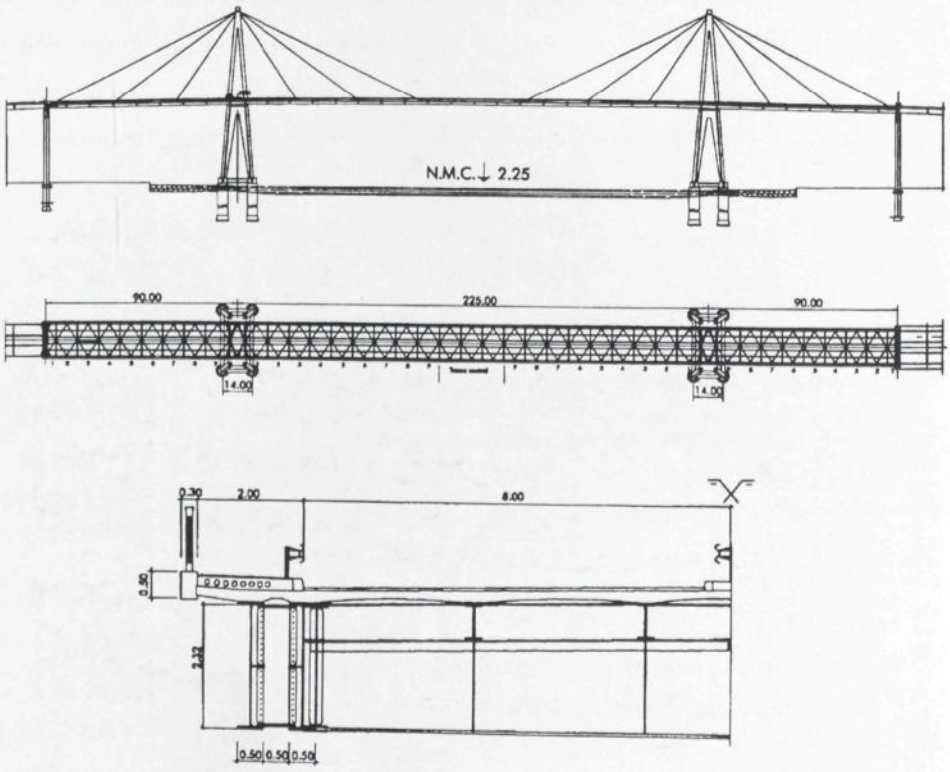


Figure 2.77. The Figueira da Foz Bridge. Elevation and cross section (Appleton & Rito, 1998).

The deck cross section (Figure 2.77) of this bridge is *20.6m* wide, and is composed of two main steel girders *2.30m* high, connected by transversal beams of the same height every *10m*. These girders support the stringers that carry a concrete slab with varying thickness (*0.13m-0.20m*). The towers (Figure 2.76), constructed in concrete, are composed of four inclined box section legs which are connected at the top by a transversal beam and that support the bridge deck by a set of transversal beams. The cable system comprehends three pairs of cables in a radial arrangement, which are composed of individual galvanized strands (*390* to *900* strands per cable) with a tensile strength of *1600MPa-1800MPa* connected to the towers through saddles and anchored at the deck every *30m*. The main span includes two joints spaced of *30m*.

International Bridge over the Guadiana River

The *International Bridge over the Guadiana River* (Figure 2.78) was designed by the Portuguese engineer Câncio Martins (1993) and constructed in 1992, and constitutes the main connection between Portugal and Spain at the Southern part of the two countries. The total length of the bridge of *666m* is divided into *5* spans, the three inner spans being suspended by a set of *64* pairs of cables (arranged in a fan) every *9m*. The main span is *324m*. The bridge deck consists of a pre-cast concrete box girder with a constant depth of *2.5m* and a width of *18m* stiffened by pre-cast diagonal struts every *4.5m*. The inverted *Y*-shaped concrete towers are *100m* high above the water level and support the deck partially. The stay cables are made of self-protected *15mm* strands, the number varying between *22* and *55*. Figure 2.79 illustrates the main characteristics of the bridge. Since it is located in an actively seismic zone, protection against seismic forces was needed. Special oil dynamic bearings were employed at one of the abutments in order to fully or partially restrain the longitudinal motion according to the intensity of the seismic action.

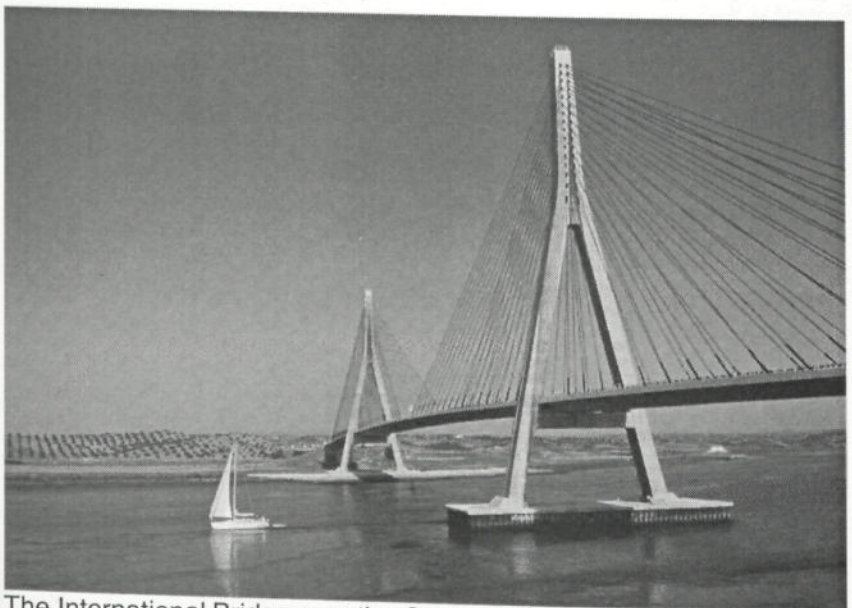


Figure 2.78. The International Bridge over the Guadiana River. General view (Freyssinet, 1994).

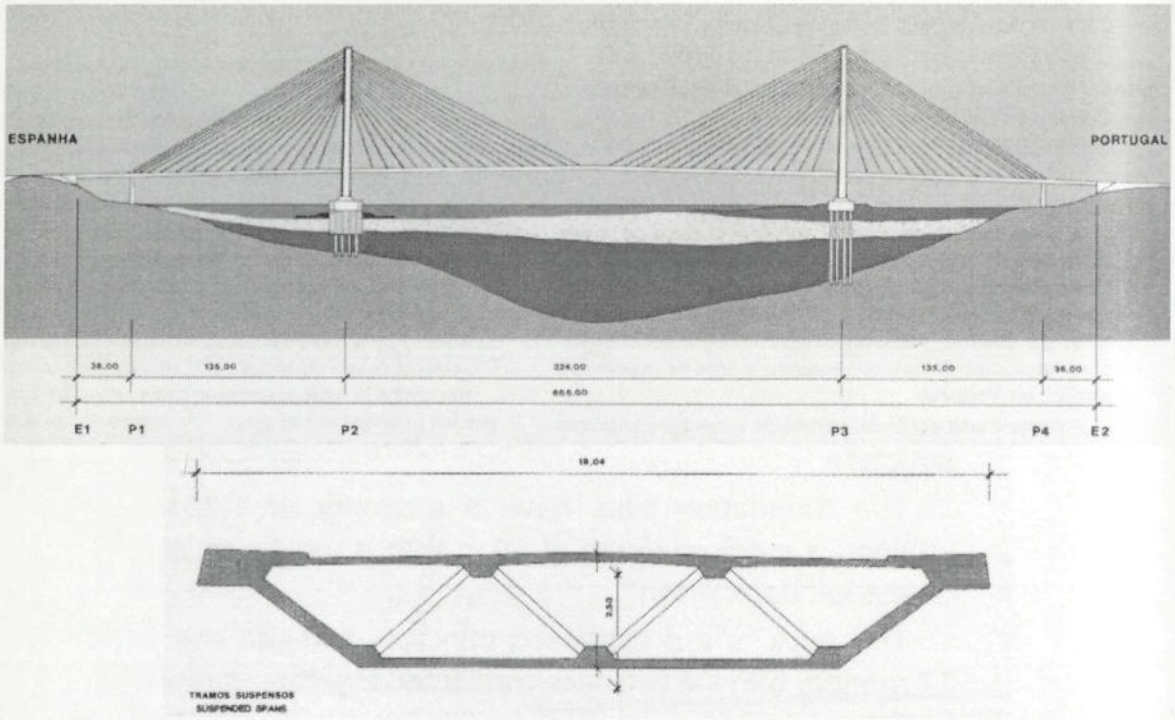


Figure 2.79. The International Bridge over the Guadiana River. Main characteristics (GPPE & FIP, 1994).

Arade River Bridge

The *Arade River Bridge* presented in Figure 2.80 is part of an *842m* long bridge over the Arade River and valley, near the coastal resort of Portimão in the Algarve. The bridge was designed by the Portuguese A. Rito (1993) and was constructed in 1992. It comprehends two approach viaducts with multiple spans of about *30m* and the main three-span cable-stayed bridge, with a total length of *470m* and a main span of *256m* (Figure 2.81).

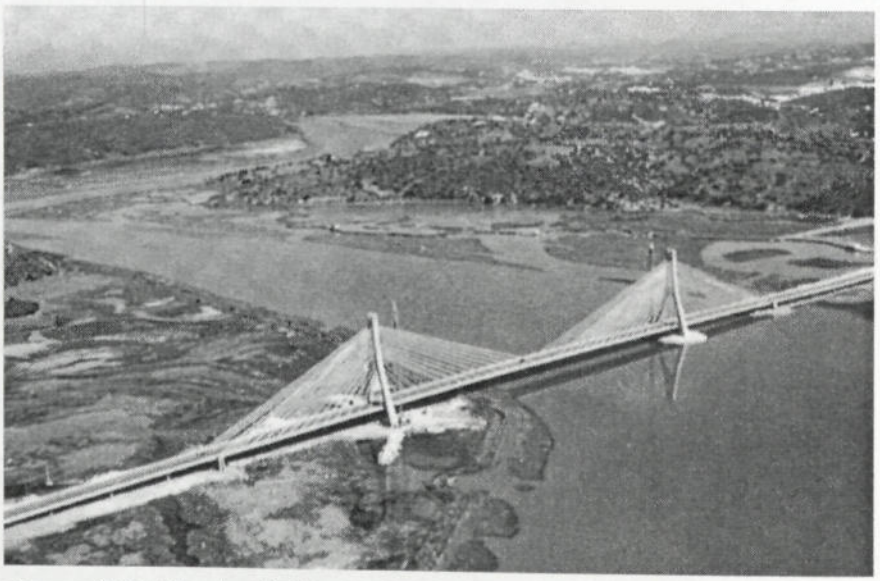


Figure 2.80. The Arade River Bridge. General view (GPPE & FIP, 1994).

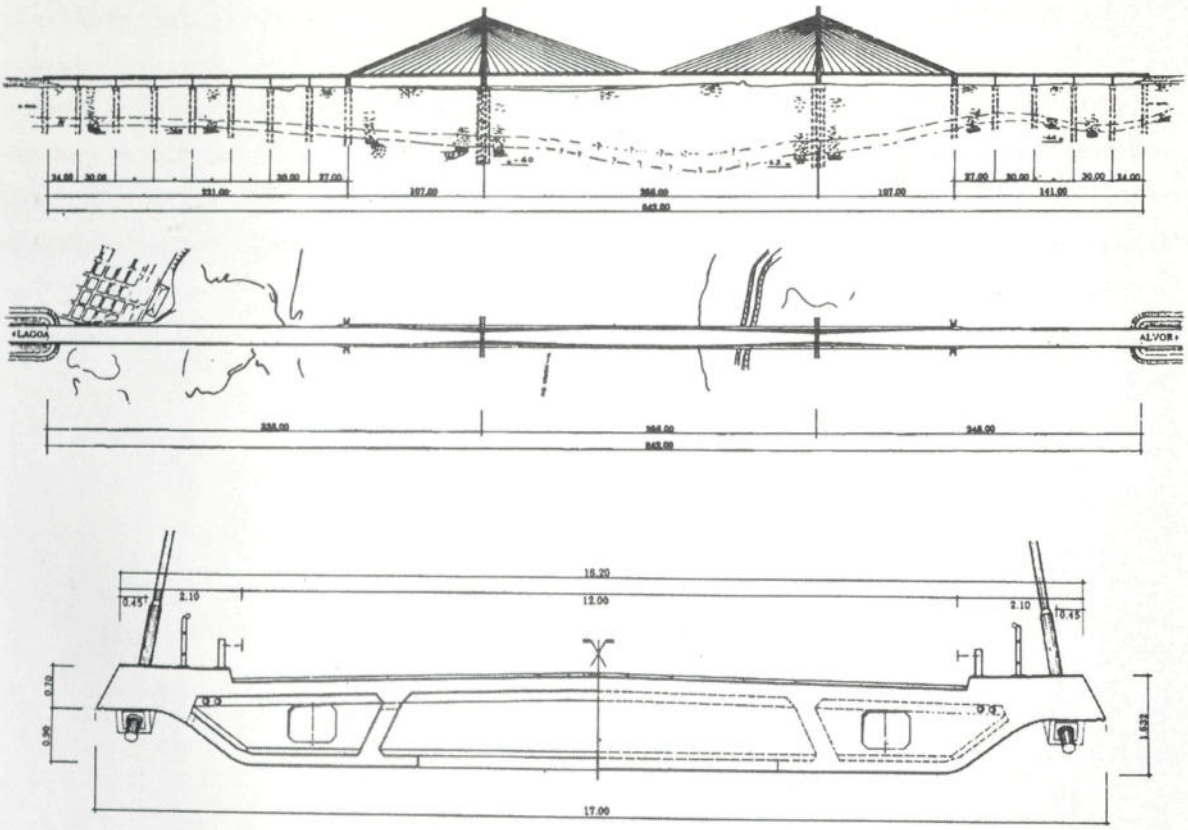


Figure 2.81. The Arade River Bridge. General characteristics (GPPE & FIP, 1994).

The main bridge and access spans form a continuous structure composed of a prestressed concrete deck with only two expansion joints at the abutments. The cable-stayed bridge is a full suspension bridge with two planes of cables arranged in a fan and anchored at the deck every *8m*, except for the backstays, that are spaced at *3.5m*. The concrete inverted *Y*-shaped towers are *62m* high above the water level and were designed to withstand a significant part of the seismic forces acting on the whole structure. The deck cross section is a prestressed concrete two cell box girder *17m* wide and *1.60m* deep, the two cells being connected by prestressed cross-beams every *4m*. The cables are composed of *15.2mm* parallel strands. Each strand is galvanised and individually protected by an extruded sheath of high-density polyethylene and injected with petrol wax. Innovative aspects of the stay cables are the use for a first time of this triple corrosion protection of the stays, and the white polyethylene sheath, required for achievement of an increased durability. Another particular aspect of the project is the foundation of the bridge in a soil composed of alluvial deposits of loamy sand and clay, which attain a depth of *40m* over a bedrock constituted by a shale formation with basaltic intercalations. This determined the necessity of founding the bridge pylons on piles that attain maximum depths of *63m*. Also the fact that the structure is located in an actively seismic zone required specific protection against earthquakes. In this case, the bridge is only fixed at the transition piers for horizontal motion and behaves as an oscillating pendulum under earthquake action for the longitudinal direction.

Socorridos Bridge

The *Socorridos Bridge* presented in Figure 2.82 is located in a deep valley in the island of Madeira and was open to traffic in 1993. The bridge, designed by the Portuguese A. Reis and A. Pereira (1994) and marked by a central suspension plane of cables embedded in a concrete wall *0.36m* thick, was very much inspired by the famous Ganter Bridge, designed by Christian Menn (Figure 2.42).



Figure 2.82. The Socorridos Bridge. General view (GPPE & FIP, 1994).

The elevation presented in Figure 2.83 evidences the particularly unfavourable geotechnical and local conditions that restrained the location of the piers, and shows the solution adopted for the *331m* long bridge, forming *4* spans of *54-85-106-86m*. Basically, the cable-stayed bridge was designed as a conventional cable-stayed bridge for construction, with a prestressed single cell box girder *20m* wide and *3.5m* deep rigidly connected to the masts and suspended by a central plane of cable stays. A total of *9* ordinary prestressing cables were employed for the stays, composed in general of *34-37* strands encased in thick walled corrugated plastic ducts injected with oil for protection against corrosion during the construction phase. Each stay cable passes through steel deviation saddles at the top of the mast and was stressed from both anchorages located at the centre line of the upper flange, the transmission of the stay loads to the webs being accomplished by *9* pairs of diagonal struts, as represented in Figure 2.83. After completion of the deck, the central cable plane was transformed into a prestressed concrete wall panel. The main piers, indicated as *P2* and *P3* in Figure 2.83, with box cross section, have a total height of *120m*.

A particular aspect related to the conception of the bridge was the study of the influence of the wind effects of the stay panels on vehicles running on the bridge. This was done by performance of wind tunnel tests on a *1/100* scale model (Borges & Delgado, 1990).

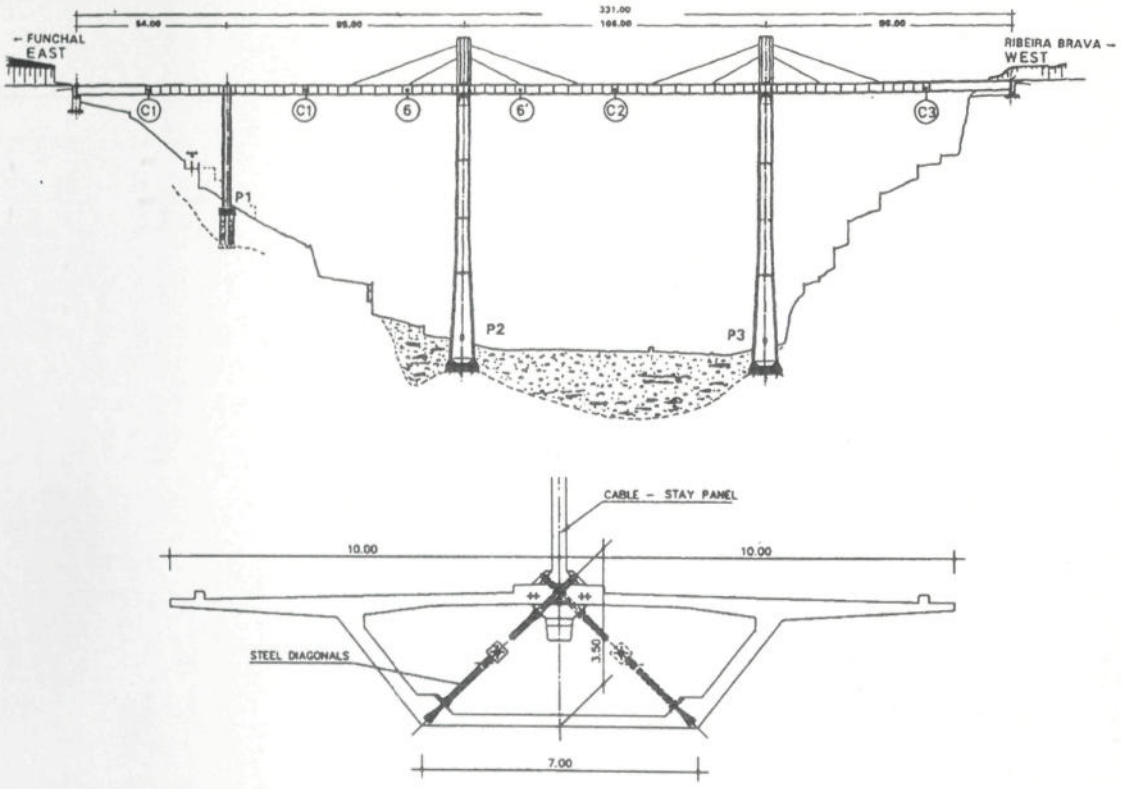


Figure 2.83. The Socorridos Bridge. General characteristics (GPPE & FIP, 1994).

Macau-Taipa Bridge

The new Macau-Taipa Bridge (Figure 2.84), connecting the former Portuguese city of Macau with the International Airport of Taipa and the People's Republic of China, was designed by Câncio Martins and constructed in 1994.

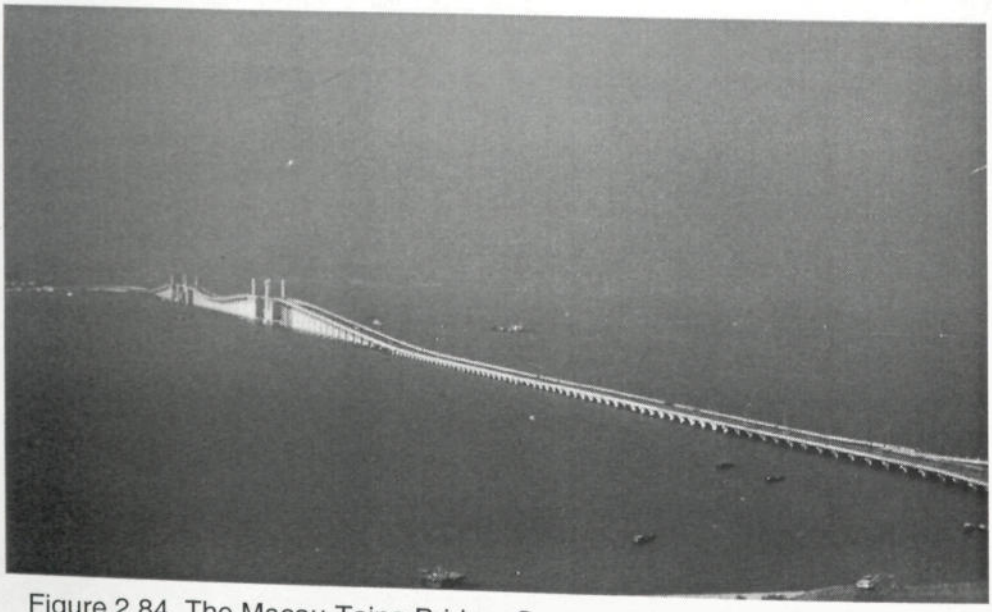


Figure 2.84. The Macau-Taipa Bridge. General view (GPPE & FIP, 1994).

The *4414m* long bridge comprehends three access viaducts with *35m* spans and a total length of *1855m*, two stretches of trestle structure on piles with *12m* spans and an approximate total length of *2000m*, and two main central cable-stayed bridges with spans of *112m* across the navigation channels, separated by a short span of *35m* (Figure 2.85).



Figure 2.85. The Macau-Taipa Bridge. View of main cable-stayed bridges (GPPE & FIP, 1994).

The short contract time awarded for the bridge construction and the unavailability of physical space for site construction motivated the massive use of precast elements in the conception of the bridge. A total number of *2531* precast elements were used in the construction. Referring to the central cable-stayed bridges, the two towers and adjacent piers were cast in situ. The deck, with a width of *19m*, is composed of a grid of precast stringers and cross beams that support the concrete cast in situ slab (Figure 2.86). The same structural elements were used along the entire deck of the bridge, although the main bridges spans are about three times longer than the span of the access viaducts. In effect, the only pair of stay cables replaces the suppressed support columns for each bridge.

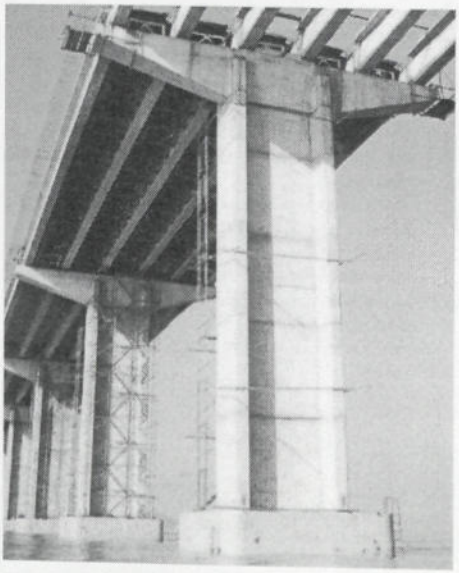


Figure 2.86. The Macau-Taipa Bridge. Detail of deck construction (GPPE & FIP, 1994).

Vasco da Gama Bridge

The *17300m* long new crossing of the Tagus river in Lisbon, the *Vasco da Gama Bridge*, opened to traffic in 1998. The bridge includes three interchanges, a *5000m* long section on land, a continuous *12300m* long bridge, and a cable-stayed bridge over the main navigation channel (Figure 2.87), with *420m* central span and three lateral spans (*62+70.6+72m*) on each side, corresponding to a total length of *829.2m* between transition piers (Figure 2.88).

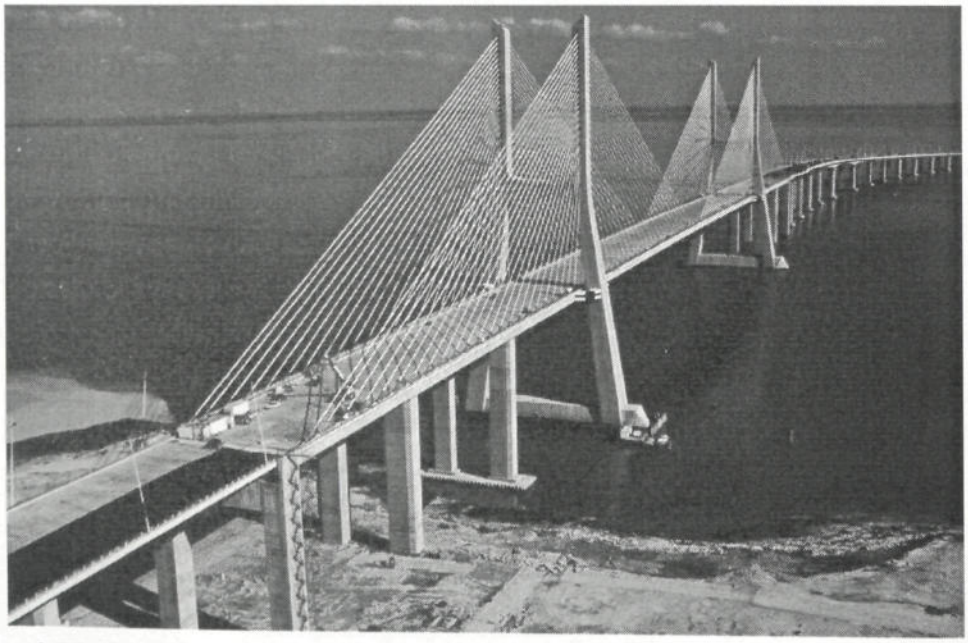


Figure 2.87. The Vasco da Gama Cable-Stayed Bridge. General view during construction.

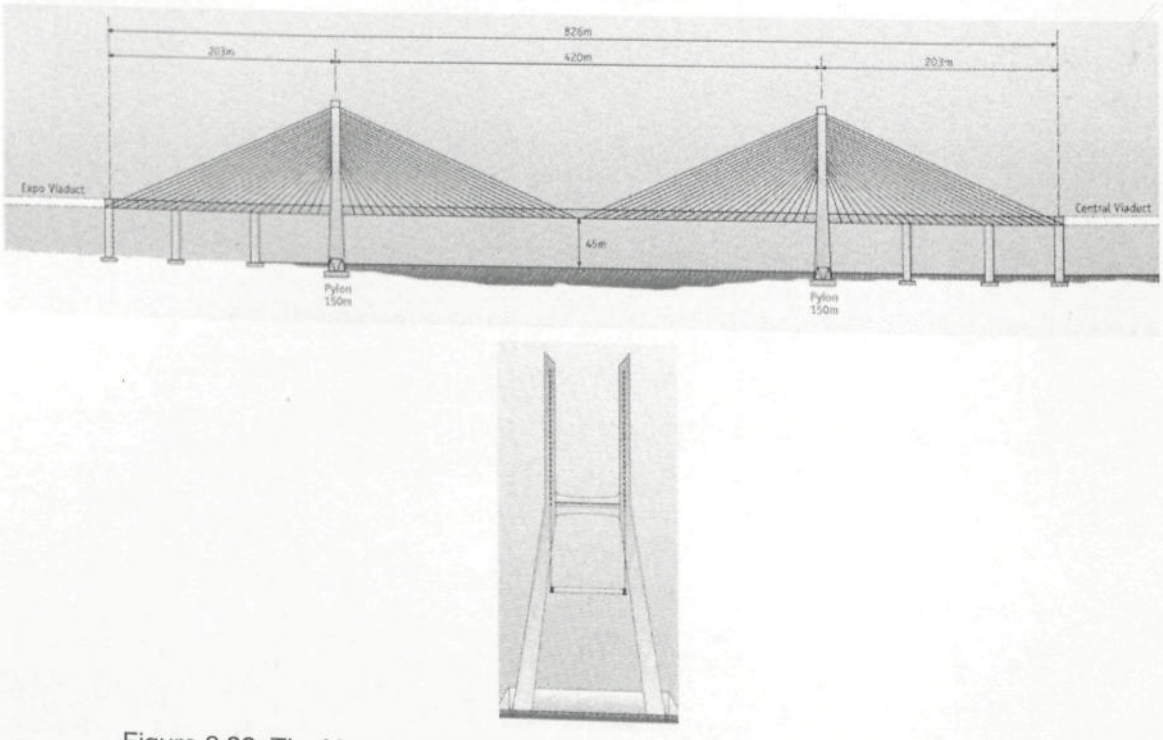


Figure 2.88. The Vasco da Gama Cable-Stayed Bridge. Main characteristics.

The cable-stayed bridge, in particular, was designed by LUSOPONTE/ Europe Études *SGE* and is composed by a *31m* wide deck formed by two lateral prestressed girders *2.60m* high, connected by a cast in situ slab *0.25m* thick and by transverse steel *I*-girders every *4.42m* (Figure 2.64). The bridge is continuous along the total length and is fully suspended at level *52.5m* by two vertical plans of *48* stays connected to each tower. The two *H*-shaped towers are *147m* high above a massive zone at their base as protection against ship collision. Each foundation consists of *88* reinforced concrete piles with diameter *2.2m* that are partially encased in steel tubes reaching down to *50m* in the North Tower, and to *65m* in the South Tower. Given the actively seismic location of the bridge site, specific measures were taken in the design of the bridge, namely the adoption of a full suspension deck from flexible towers (as in the case of Arade Bridge) in order to minimize the seismic forces. Additionally, a set of hysteretic steel dampers connecting the pylons and the deck were introduced (Figure 2.89), in order to limit the displacements. Under service loads, the transverse dampers work within the elastic range, acting as elastic supports, while the longitudinal dampers allow low speed displacements. In case of earthquake, use is made of the steel hysteresys to dissipate energy.

With regard to the stay cables, that consist of bundles of parallel self-protected strands covered by an *HDPE* sheath, specific protection against vibration was adopted, namely by inclusion of a double helical rib in the cable cover for prevention of rain wind vibration, and by use of innovative damper devices placed inside the steel guide pipe of the cables at the deck anchorages.

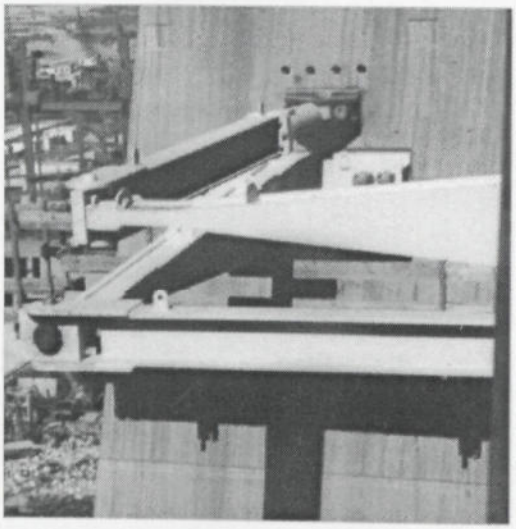


Figure 2.89. Hysteretic steel dampers connecting the deck and the pylons at the Vasco da Gama Bridge (Branco et al., 1998).

Salgueiro Maia Bridge

The Salgueiro Maia Bridge (Figure 2.90) is a new crossing of the Tagus River at the city of Santarém, about *60Km* upstream the Vasco da Gama Bridge. The bridge was completed in

June 2000 and was designed by Câncio Martins. It includes *10* standard viaducts with *10* spans of *42m*, and a main cable-stayed bridge, with a total length of *570m*, arranged in a central span of *246m* and three side spans of *78+42+42m* (Figure 2.91). The bridge employs a central suspension system of fan pattern composed of *18* pairs of cable stays suspended from each mast and anchored on the deck every *6m*. Both the deck and part of the masts are constructed in concrete. Beyond the first anchorage level, the later elements constitute composite steel and concrete structures, reaching *53m* above the piers. The deck comprehends a single cell box girder *2.62m* deep and two cantilevered slabs on each side, leading to a total width of *28.2m*. For an efficient transmission of stay cable forces, additional diagonal struts are introduced at the anchorage sections, as represented in Figure 2.92(a). A particular feature of this bridge, is the fact that the masts are rigidly connected to the bridge deck, the system being fully isolated from the foundation by interposition of high rubber damping devices (Figure 2.92(b)), in order to reduce the seismic forces on the bridge.

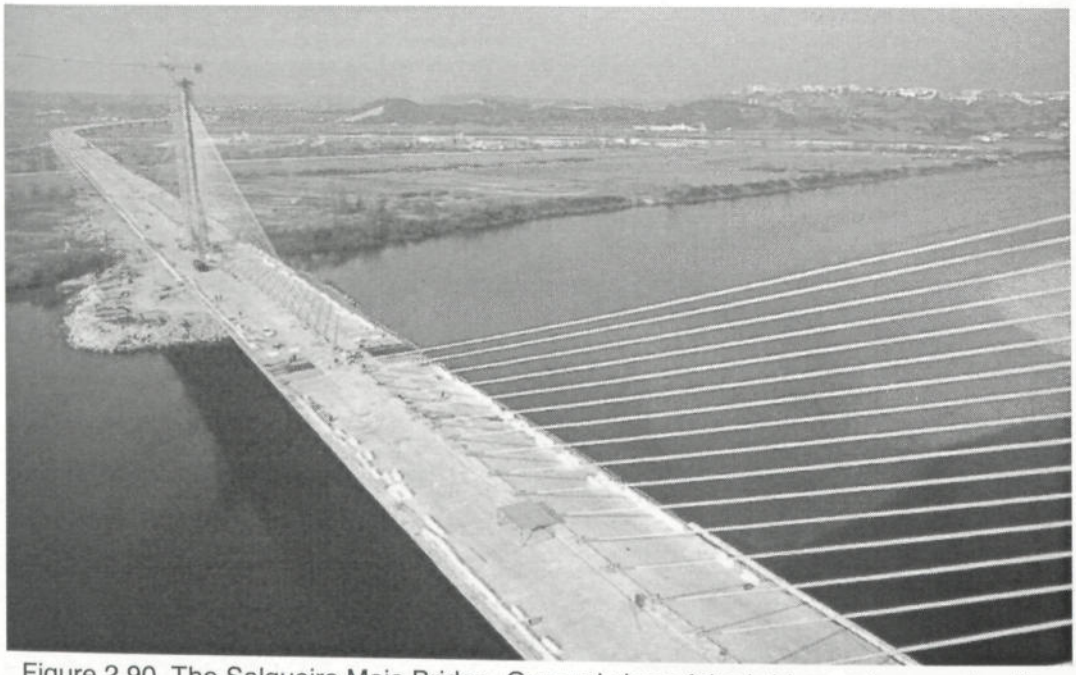


Figure 2.90. The Salgueiro Maia Bridge. General view of the bridge under construction (Vigouroux, 2000).

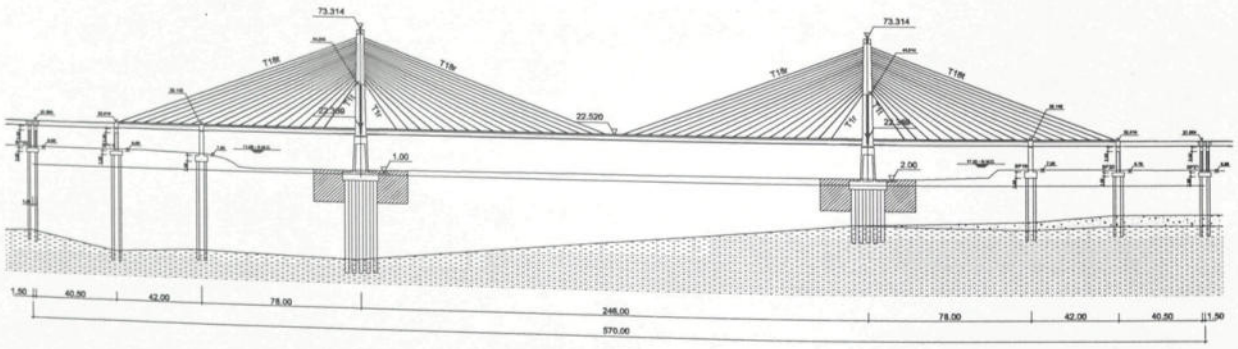


Figure 2.91. The Salgueiro Maia Bridge. Elevation.

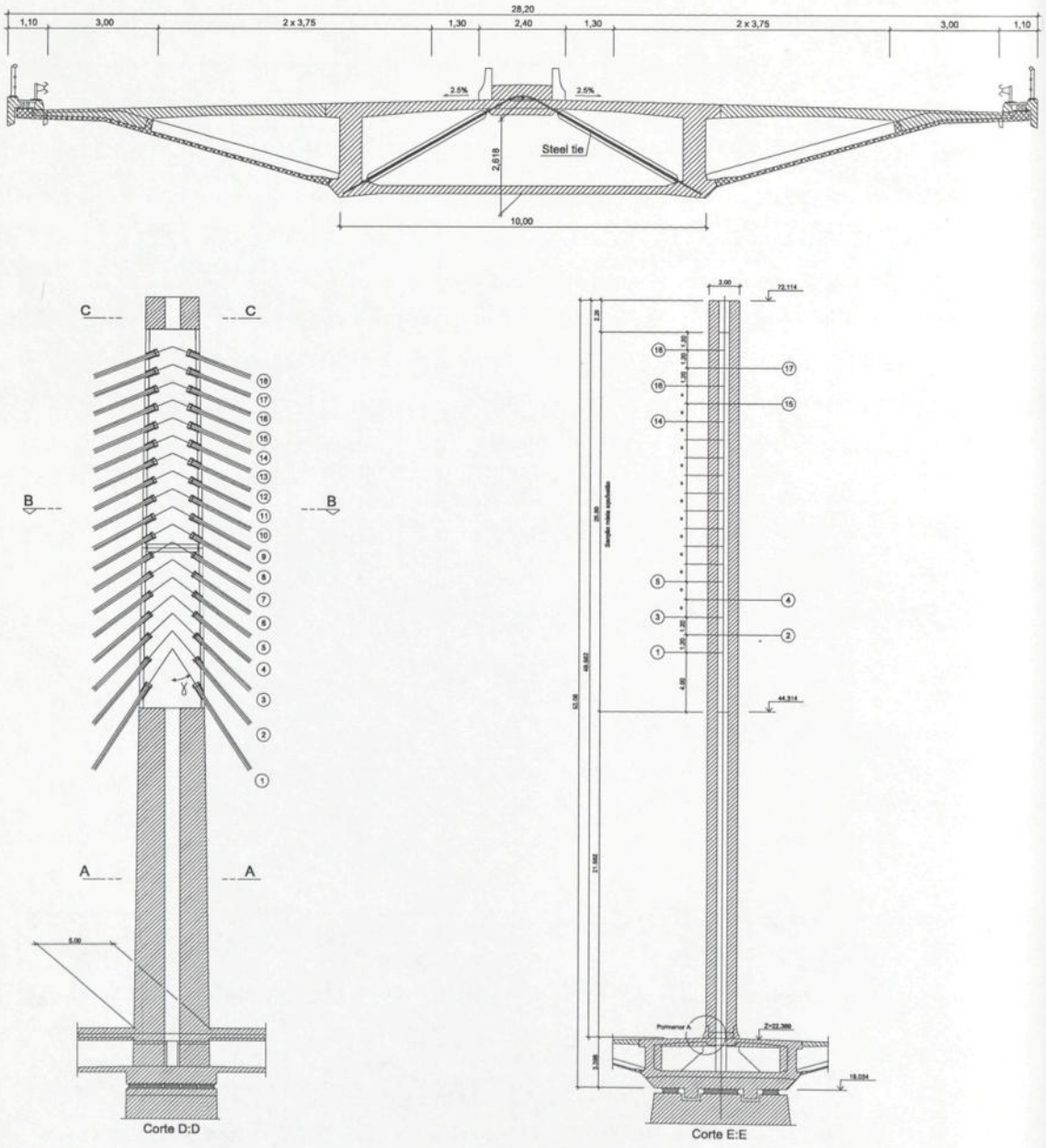
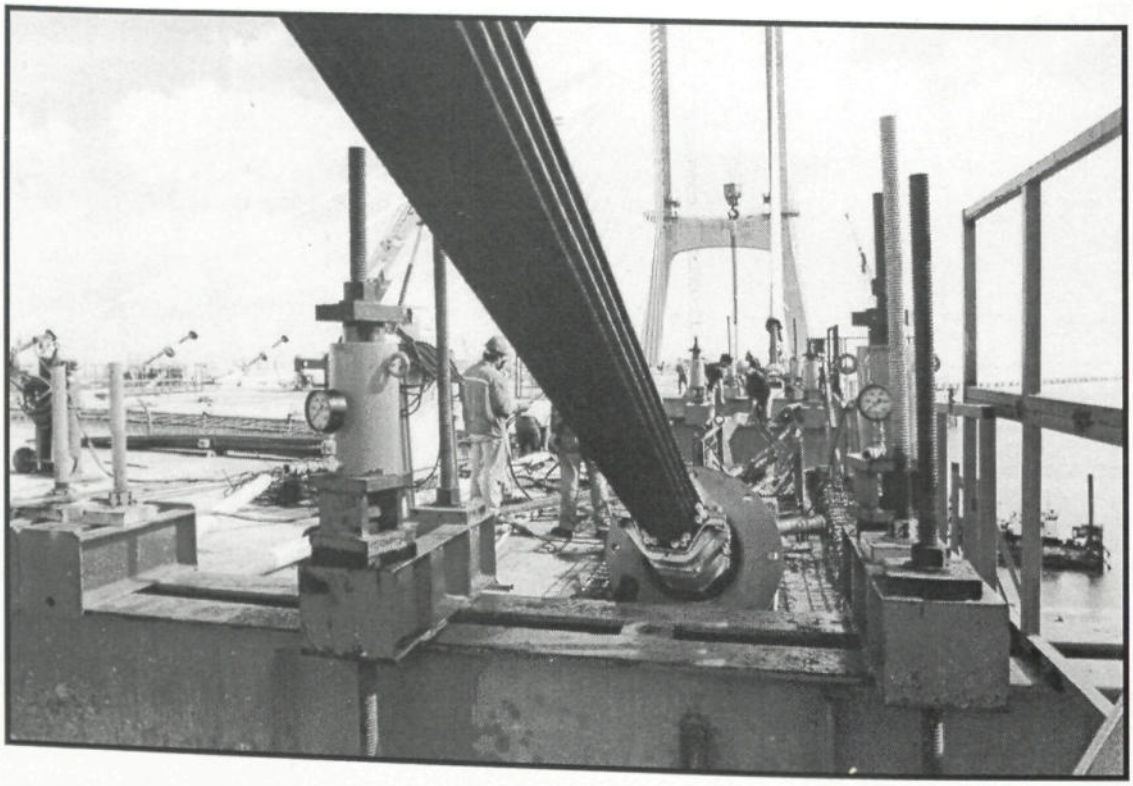


Figure 2.92. The Salgueiro Maia Bridge: (a) Deck cross-section; (b) Longitudinal section of mast; (c) Transversal section of mast.

CHAPTER 3

THEORY OF CABLE DYNAMICS



CHAPTER THREE

THEORY OF CABLE DYNAMICS

3.1 GENERAL

The single cable is the basic element of cable-stayed bridges. Understanding the corresponding deformational and vibrational characteristics is therefore essential for the analysis of these structures.

The present Chapter begins providing a basic introduction to the statics of a suspended cable, by presentation of the nonlinear problem of an horizontal suspended cable subject to dead weight under the assumption that the cable acts as a completely flexible string and can only resist tensile forces. The particular case of shallow cables is investigated, leading to the parabolic approach for the cable profile, which is further extended to inclined cables. In this description, extensive use is made of the text and papers presented by Irvine and companion authors (Irvine & Caughey, 1974; Irvine, 1977; Irvine, 1981).

In dealing with structures composed of a number of cables, analytical approaches for the static analysis become impracticable and so convenient simplifications have to be adopted. The *Equivalent Modulus of Elasticity*, which includes both the Young's Modulus and the effect of change of sag and tensile force, is widely used in the static analysis of cable supported structures, allowing for the treatment of the cable element as a simple truss element. A derivation of the *Equivalent Modulus of Elasticity* is thus presented, based on the approach by a parabola of the cable profile, and the effects of cable tension and length in the reduction of cable stiffness are analysed.

In addition to the high flexibility, another important characteristic of stay cables, is the very low intrinsic damping. These properties lead to a high sensitivity to dynamic excitations induced under certain circumstances, such as traffic, earthquakes, wind and the combination of rain with wind. The dynamics of a suspended cable is a major topic in the study of cable-stayed bridges. A brief historical review on the most important developments in this subject is therefore presented, followed by the derivation of the basic equations of the motion on the basis of the linearized theory. These equations are extended to the more general case of inclined cables, employing in a first case the simplified approach from Irvine (1981), which proved valid in the practical applications associated with cable-stayed bridges, and then using a more precise solution from Triantafyllou (1984). Finally, using a two-degree-of-freedom approach according to the assumptions of Rao and Iyengar (1991) and Perkins (1992), the nonlinear dynamic equilibrium equations of a small sag cable subject to a most general excitation constituted by vertical and transverse forces along the length and harmonic longitudinal motion of one support are established. The solution of these equations in the particular case of *parametric excitation*, i.e., excitation induced by the harmonic longitudinal oscillations of one support at twice the cable's natural frequency, will be analysed in Chapter six.

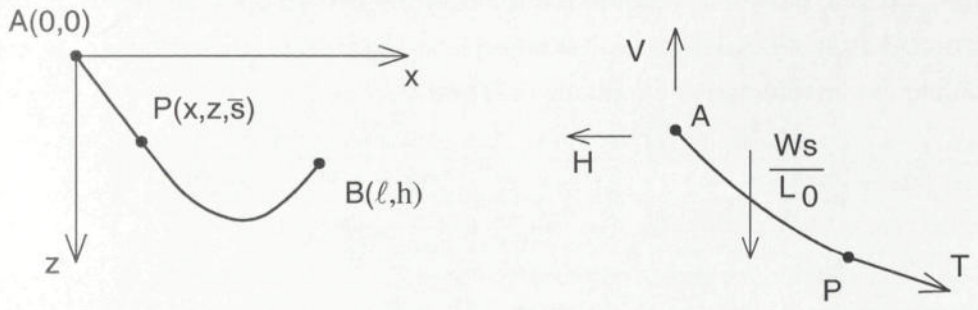
3.2 GEOMETRY AND STATICS OF A SUSPENDED CABLE

The catenary

Consider the cable presented in Figure 3.1 (a), suspended between two fixed points A and B, which have Cartesian coordinates $(0,0)$ and (ℓ, h), respectively. Assuming the cable is perfectly flexible, elastic and extensible, the tension T at an arbitrary point P with Cartesian coordinates (x,z) and Lagrangian coordinate $\bar{s}$ in the strained profile can be related with reactions H and V at the support, by balancing of the horizontal and vertical forces of the cable segment limited by the support and point P, as represented in Figure 3.1 (b). In this Figure, L_0 represents the unstrained length of the cable, s is the Lagrangian coordinate of point P in the unstrained profile, and W represents the weight of the cable, defined by $W=mgL_0$, where m is the mass per unit length and g is the acceleration of gravity. Accordingly

$$T \cdot \frac{dx}{d\bar{s}} = H$$

$$T \cdot \frac{dz}{d\bar{s}} = V - \frac{W s}{L_0} \tag{3.1}$$



(a) (b)

Figure 3.1 (a) Cable suspended between two fixed points (b) Forces on a segment of the strained cable profile.

The constitutive relation describing the Hooke's law is

$$T = EA_0\left(\frac{d\bar{s} - ds}{ds}\right) = EA_0\left(\frac{d\bar{s}}{ds} - 1\right) \tag{3.2}$$

where E is the Young's Modulus of the material, and A_0 is the uniform cross-sectional area in the unstrained profile. The introduction of the geometric constraint

$$\left(\frac{dx}{d\bar{s}}\right)^2 + \left(\frac{dz}{d\bar{s}}\right)^2 = 1 \tag{3.3}$$

into equations (3.1) allows for the calculation of the cable tension according to the expression

$$T(s) = \left[H^2 + \left(V - \frac{W s}{L_0}\right)^2\right]^{1/2} \tag{3.4}$$

Substituting equations (3.2) and (3.4) into (3.1) and integrating, the following expressions for the Cartesian coordinates of a generic point P along the cable are obtained

$$x(s) = \frac{Hs}{EA_0} + \frac{HL_0}{W}\cdot\left[\sinh^{-1}\left(\frac{V}{H}\right) - \sinh^{-1}\left(\frac{V - W s/L_0}{H}\right)\right] \tag{3.5}$$

$$z(s) = \frac{Ws}{EA_0}\left(\frac{V}{W} - \frac{s}{2L_0}\right) + \frac{HL_0}{W}\left\{\left[1 + \left(\frac{V}{H}\right)^2\right]^{1/2} - \left[1 + \left(\frac{V - W s/L_0}{H}\right)^2\right]^{1/2}\right\}$$

These expressions, that characterize the profile of the so-called *elastic catenary*, depend on the values H and V of the reactions at the cable supports, which can themselves be determined by introduction of the boundary conditions in (3.5): ($s=0$: $x=0$, $z=0$; $s=L_0$: $x=\ell$, $z=h$), leading to transcendental equations in H and V

$$\ell = \frac{HL_0}{EA_0} + \frac{HL_0}{W} \cdot \left[\sinh^{-1}\left(\frac{V}{H}\right) - \sinh^{-1}\left(\frac{V-W}{H}\right) \right] \tag{3.6a}$$

$$h = \frac{WL_0}{EA_0}\left(\frac{V}{W} - \frac{1}{2}\right) + \frac{HL_0}{W} \cdot \left\{ \left[1 + \left(\frac{V}{H}\right)^2 \right]^{1/2} - \left[1 + \left(\frac{V-W}{H}\right)^2 \right]^{1/2} \right\} \tag{3.6b}$$

Based on the above expressions and equations, a few important results can be established. The first case considered here corresponds to the *symmetric elastic catenary* that results from the consideration of a cable hanging from supports at the same level. In this case, $h=0$ and $V=W/2$. Substituting into (3.6a) comes

$$\sinh\left(\frac{W\ell}{2HL_0} - \frac{W}{2EA_0}\right) = \frac{W}{2H} \tag{3.7}$$

Considering the case of an inextensible cable, equation (3.7) results in

$$\sinh\left(\frac{W\ell}{2HL_0}\right) = \frac{W}{2H} \tag{3.8}$$

which is the well-known form of a *catenary*.

The elastic parabola

Another important result can be obtained from equation (3.5) and (3.7) for the particular case of a relatively inextensible cable, where the ratio $W/2H$ is small, and ℓ is very close to L_0. By developing (3.5) into a Taylor series and retaining the lower order terms, the profile of the so-called *elastic parabola* can be obtained in the form

$$z(s) = \frac{1}{2} \cdot \frac{W}{HL_0} \cdot \left(1 + \frac{H}{EA_0}\right) \cdot s \cdot (L_0 - s) \tag{3.9}$$

where H can be obtained from the solution of the following cubic equation

$$H^3 + \frac{EA_0}{L_0} \cdot (L_0 - \ell) \cdot H^2 - \frac{EA_0 W^2}{24} = 0 \tag{3.10}$$

For an inextensible cable, the parabola profile reduces to

$$z(s)=\frac{1}{2}\cdot\frac{W}{HL_0}\cdot s\cdot(L_0-s) \tag{3.11}$$

and it can be observed that the sag d at midspan is given by

$$d=\frac{WL_0}{8H}=\frac{mgL_0^2}{8H} \tag{3.12}$$

The same result can be now obtained from a Cartesian description of the cable profile, under the assumption that the cable is shallow and, consequently, the dead weight is assumed uniform along the span.

Figure 3.2 presents a differential cable segment that is part of an extensible cable suspended between two points at the same level. The equilibrium equations of the deformed cable segment are

$$\frac{d}{d\bar{s}}(T\frac{dx}{d\bar{s}})=0 \tag{3.13a}$$

$$\frac{d}{d\bar{s}}(T\frac{dz}{d\bar{s}})=mg\cdot\frac{ds}{d\bar{s}} \tag{3.13b}$$

In a shallow cable, where the sag to span ratio d/ℓ is considered no greater than *1:8*, the ratio between the undeformed and the deformed segment length $ds/d\bar{s}$ is close to unity. In this manner, equations (3.13) can be transformed into

$$T\frac{dx}{d\bar{s}}=constant=H \tag{3.14a}$$

$$H\frac{d^2z}{dx^2}=mg\cdot\frac{d\bar{s}}{dx} \tag{3.14b}$$

where

$$\frac{d\bar{s}}{dx}=\sqrt{1+(\frac{dz}{dx})^2} \tag{3.15}$$

The approach $d\bar{s}/dx\approx 1$ is also valid for a shallow cable. So, the solution of equation (3.14b) is given by

$$z(x) = \frac{1}{2} \cdot \frac{mg}{H} \cdot x \cdot (\ell - x) \tag{3.16}$$

with

$$H = \frac{mg\ell^2}{8d} \tag{3.17}$$

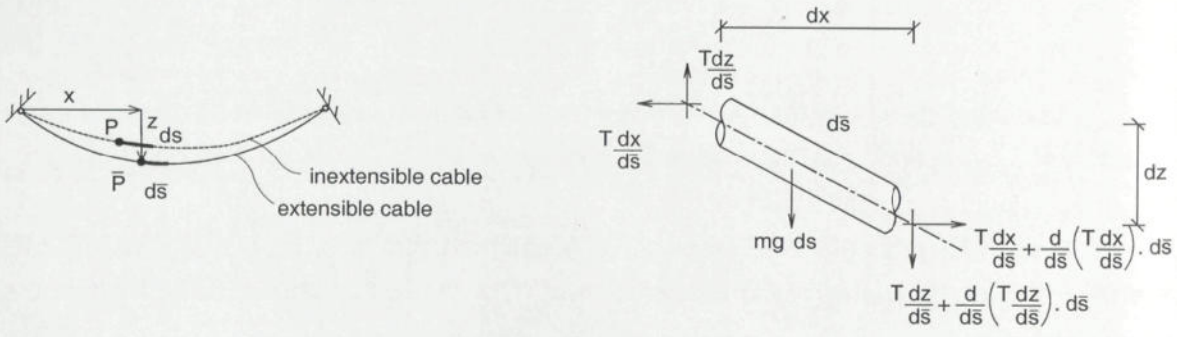


Figure 3.2. Equilibrium of a differential segment of an extensible cable.

The length L of the deformed cable can be now calculated by approximate integration of equation (3.15), which leads to

$$L \approx \ell \left\{ 1 + \frac{8}{3} \left(\frac{d}{\ell}\right)^2 - \frac{32}{5} \left(\frac{d}{\ell}\right)^4 \right\} \tag{3.18}$$

Extension of the theory of horizontal cables to the general case of inclined cables

An important aspect of the statics of cables is the extension of the theory of horizontal behaviour to the general case of inclined cables. Irvine (1977) derived the static profile for inclined cables, by making the assumption that the weight component parallel to the cable chord can be neglected and by performing a transformation of axes.

Consider the cable suspended between two points A and B at different levels represented in Figure 3.3, where the inclined chord makes an angle θ with respect to the horizontal axis. A generic point $\overline{P}$ in the deformed configuration is characterized by the coordinates (x, z), where z represents now the vertical distance from $\overline{P}$ to the inclined chord AB. The equation of equilibrium in the vertical direction can be then written in the form

$$H \frac{d^2 z}{dx^2} = mg \cdot \left[1 + \left(\tan\theta + \frac{dz}{dx} \right)^2 \right]^{1/2} \tag{3.19}$$

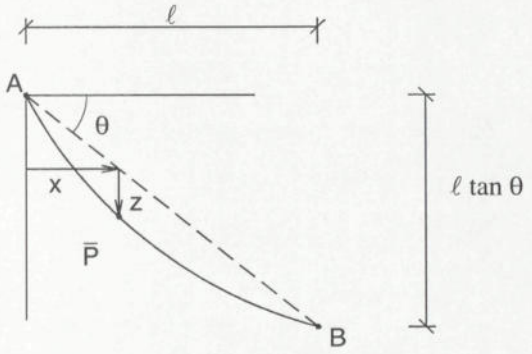


Figure 3.3. Definition of the profile of an inclined cable.

For a shallow cable, where the ratio $(dz/dx)^2$ can be ignored, the expansion of the second member of equation (3.19) in a series, retaining only the first order terms in dz/dx, and the subsequent solution of the differential equation lead to (Irvine, 1977)

$$z(x)=\frac{1}{2}\cdot\frac{mg}{H}\cdot sec\theta\cdot x\cdot(\ell-x)\cdot\left[1+\frac{\varepsilon}{6}\cdot(1-\frac{2x}{\ell})\right] \tag{3.20}$$

where the parameter ε, defined by $\varepsilon=(mg\ell\sin\theta)/H$ represents a small quantity, provided that the cable is shallow. A most convenient form for equation (3.20) can be now obtained by the transformation of axes represented in Figure 3.4, where the coordinates along and perpendicular to the chord, x_* and z_*, respectively, are now defined through

$$x_* = x\sec\theta + z\sin\theta$$

$$z_* = z\cos\theta \tag{3.21}$$

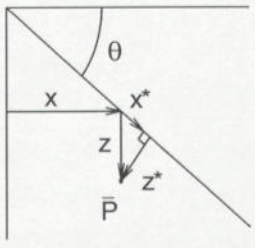


Figure 3.4. Transformation of axes for the definition of the cable profile.

Introducing the quantities $\ell_* = \ell\sec\theta$ and $H_* = H\sec\theta$, which represent, respectively, the chord length of the cable, and the cable tension at an intermediate point of the cable where the tangent is parallel to the chord (H_* is in effect an approximate value of the average tension along the cable), the cable profile can be now defined by

$$z_*(x)=\frac{1}{2}\cdot\frac{mg}{H_*}\cdot\cos\theta\cdot x_*\cdot(\ell_*-x_*)\cdot\left[1-\frac{\varepsilon_*}{3}\cdot(1-\frac{2x_*}{\ell_*})\right] \tag{3.22}$$

with $\varepsilon_* = (mg\ell_*\sin\theta)/H_*$, or, ignoring the correction term ε_*

$$z_*(x)=\frac{1}{2}\cdot\frac{mg}{H_*}\cdot\cos\theta\cdot x_*\cdot(\ell_*-x_*) \tag{3.23}$$

This result, which is in fact equivalent to the one obtained for horizontal cables, is valid for the whole range of interest of the chord inclination, which is $0\le\theta\le\pi/2$.

The Equivalent Modulus of Elasticity

Using the parabola approach for the description of the shallow cable profile, a result of major importance can now be deduced, consisting in the evaluation of an *Equivalent Modulus of Elasticity* E_{eq} of the cable, which allows the treatment of the cable as a simple rod, by relating the elongation along the chord with the increment of the cable force between two different positions of equilibrium (see Figure 3.5)

$$E_{eq}=\frac{\Delta H}{A_0}\cdot\frac{\ell}{\Delta\ell} \tag{3.24}$$

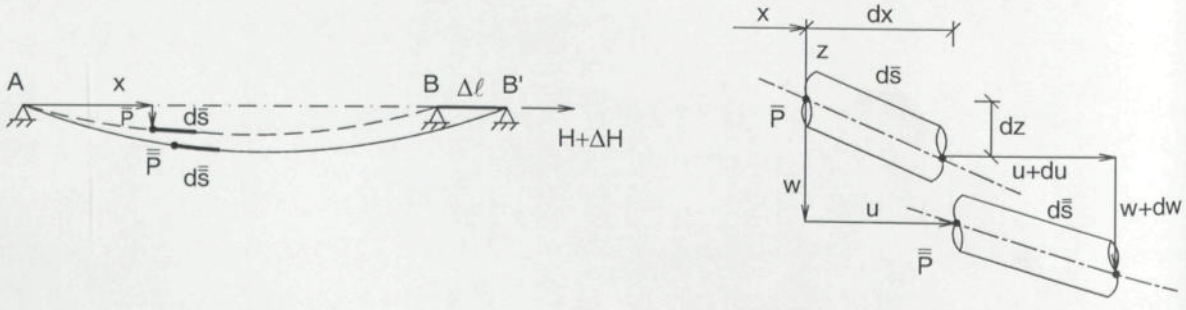


Figure 3.5. Variation of cable profile with elongation $\Delta\ell$ along the chord.

Consider the extensible shallow cable suspended between two points *A* and *B* at the same level, according to the representation of Figure 3.5. By allowing the end *B* to move $\Delta\ell$ along the cable chord, a new equilibrium profile, also assumed parabolic, is attained. A generic point *P*, characterized in the first deformed configuration by the Cartesian coordinates $\overline{P}\,(x,\ z)$, moves to a new position $\overline{\overline{P}}\,(x+u,\ z+w)$, where *u* and *w* represent the small components of motion along the horizontal and vertical directions, respectively. The

equilibrium equations of the differential segment $\overline{\overline{ds}}$ in the last configuration lead to the following expression for the variation of the vertical component of movement

$$w(x) = -\frac{\overline{H}}{1+\overline{H}} \cdot \frac{mg}{2H} \cdot (\ell x - x^2) \tag{3.25}$$

where $\overline{H} = \Delta H / H$. Knowing the length of the differential deformed cable segment in the two configurations, $\overline{ds}$ and $\overline{\overline{ds}}$, given by

$$\begin{aligned} \overline{ds}^2 &= dx^2 + dz^2 \\ \overline{\overline{ds}}^2 &= (dx + du)^2 + (dz + dw)^2 \end{aligned} \tag{3.26}$$

the stretching can be calculated to the second order approximation as

$$\frac{\overline{\overline{ds}} - \overline{ds}}{\overline{ds}} = \frac{du}{\overline{\overline{ds}}} \cdot \frac{dx}{\overline{ds}} + \frac{dz}{\overline{\overline{ds}}} \cdot \frac{dw}{\overline{ds}} + \frac{1}{2} \cdot \left(\frac{dw}{\overline{\overline{ds}}}\right)^2 \tag{3.27}$$

The constitutive relation can be now inserted

$$\frac{\Delta T}{EA_0} = \frac{\overline{\overline{ds}} - \overline{ds}}{\overline{ds}} \tag{3.28}$$

where

$$\Delta T = \Delta H \cdot \frac{\overline{ds}}{dx} \tag{3.29}$$

Substituting (3.29) and (3.27) into equation (3.28), the following fundamental equation is obtained

$$\frac{\Delta H . \left(\frac{\overline{ds}}{dx}\right)^3}{EA_0} = \frac{du}{dx} + \frac{dz}{dx} \cdot \frac{dw}{dx} + \frac{1}{2} \cdot \left(\frac{dw}{dx}\right)^2 \tag{3.30}$$

The integration by parts of equation (3.30) leads to

$$\frac{\Delta H L_e}{EA_0} = u(\ell) - \left(\frac{d^2 z}{dx^2} + \frac{1}{2} \frac{d^2 w}{dx^2}\right) \int_0^{\ell} w \, dx \tag{3.31}$$

where L_e is a virtual length of the cable defined by

$$L_e = \int_0^{\ell} \left(\frac{ds}{dx}\right)^3 dx \approx \ell \cdot \left\{1 + 8\left(\frac{d}{\ell}\right)^2\right\} \tag{3.32}$$

When substituting the second order derivatives of expressions (3.16) and (3.25) with respect to x into (3.31), the following equation is obtained

$$u(\ell) = \Delta\ell = \frac{\overline{H} \cdot H \cdot L_e}{E A_0} + \left(\frac{mg\ell}{H}\right)^2 \cdot \frac{\ell}{12} \cdot \frac{\overline{H}(2+\overline{H})}{2(1+\overline{H})^2} \tag{3.33}$$

Now substituting (3.33) into the expression for the Equivalent Modulus of Elasticity E_{eq} defined in (3.24), results

$$E_{eq} = \frac{E\ell}{L_e\left[1 + \frac{\lambda^2}{12} \cdot \frac{2+\overline{H}}{2(1+\overline{H})^2}\right]} \tag{3.34}$$

Equation (3.34) can be further simplified to

$$E_{eq} = \frac{E}{1 + \frac{\lambda^2}{12}} \tag{3.35}$$

for small increments of the displacement $u(\ell)$ and, consequently, for small variations of the horizontal component of the cable tension $\overline{H}$ in the shallow cable ($L_e \approx \ell$). The quantity λ^2 in equations (3.34) and (3.35) is the fundamental parameter of the extensible cable defined by Irvine (1981) as

$$\lambda^2 = \left(\frac{mg\ell}{H}\right)^2 \cdot \frac{\ell}{\frac{HL_e}{EA_0}} \tag{3.36}$$

This parameter takes account of both the effects of geometry and cable elasticity. Typically λ^2 attains large values ($\lambda^2 > 100$) for cables of suspension bridges, where the sag to span ratio d/ℓ, although appreciable, is small, and the ratio $mg\ell/H$ is relatively large (in the order of unity). In this case, the cable deformation is mainly of geometric nature and the cable reveals a relative inextensibility. Cables from cable-stayed bridges generally attain small values of λ^2 ($\lambda^2 << 1$). In effect, these cables are characterized by a very small sag and, consequently, by a small ratio $mg\ell/H$. Additionally, the cable deformation is achieved mostly by extensibility rather than by geometric change.

Concerning the Equivalent Modulus of Elasticity E_{eq} given by (3.35), Figure 3.6 plots the variation of the ratio E_{eq}/E with λ^2, where it is evident that, compared with the stiffness of a straight bar, the stiffness of the cable may suffer a very significant reduction according to the value of λ^2. Given the definition of this parameter by expression (3.36), it becomes clear that the reduction of the stiffness varies with the third power of the tensile force on the cable and with the second power of the cable span length. Indeed the former derivation of E_{eq} (Ernst, 1965) corresponds to the equivalent formula

$$E_{eq} = \frac{E}{1 + \frac{\gamma^2 \ell^2}{12\sigma^3} E} \tag{3.37}$$

where γ is the specific weight and σ is the tensile stress of the cable.

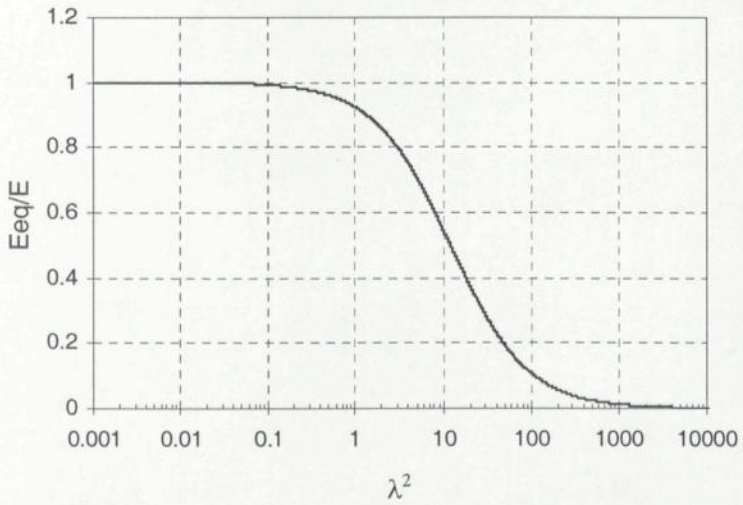


Figure 3.6. Variation of the Equivalent Modulus of Elasticity E_{eq} to Elasticity Modulus E ratio, E_{eq}/E with the cable fundamental parameter λ^2.

In the case of modern cable-stayed bridges, where λ^2 is typically inferior to *1*, and the tensile stress is greater than *500MPa*, the reduction of the cable stiffness does not exceed generally *10%*. The former cable-stayed bridges however employed steel with low admissible stresses. For a cable stressed at *100MPa* with a span of *100m*, this corresponded to a reduction of cable stiffness of *50%*, as can be observed in the graph presented in Figure 3.7, leading to an insufficient stiffness of the global bridge system and to various cases of failures.

As a final note on the calculation of an *Equivalent Modulus of Elasticity*, it should be pointed that both expressions (3.34) and (3.36) apply in the most general case where the cable chord is inclined with respect to the horizontal axis, where λ^2 in expression (3.34) is

now replaced by $\lambda_*^2 = (mg\ell_* \cos\theta / H_*)^2 \ell_* / (H_* L_{e^*} / EA_0)$, L_{e^*} being given by $L_{e^*} \approx \ell_* \left[1 + (1/8)(mg\ell_* \cos\theta / H_*)^2\right]$, and ℓ in expression (3.36) is replaced by ℓ_*.

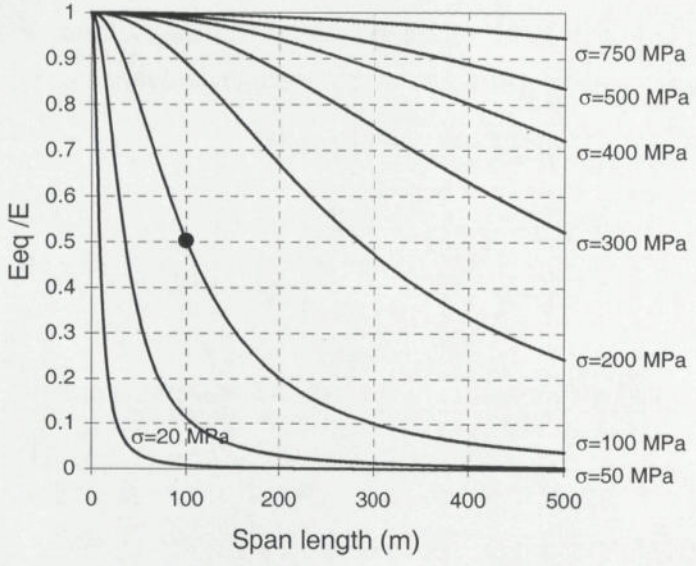


Figure 3.7. Variation of the ratio between the Equivalent Modulus of Elasticity, E_{eq}, and the Elasticity Modulus, E, with the cable span for different levels of cable stress.

3.3 DYNAMICS OF A SUSPENDED CABLE

3.3.1 Brief historic review

The linear theory of vibrations of taut strings was established by 1820. The equations for the natural frequencies of small-sag inextensible and horizontal chain were derived in 1868 by Routh, after preliminary studies by Stokes and Rohrs. Several authors included the effects of elasticity, but it was Simpson (1972) and then Irvine and Caughey (1974) who established an extensive theory for the linear vibrations of a rigidly supported horizontal cable with a small sag to span ratio d/ℓ $(0 \le d/\ell \le 1/8)$, by introducing the basic assumption that the elastic deformation of the cable is quasi-static, i.e., the dynamic cable tension is a function of time only, and by deriving a fundamental system parameter λ^2 that governs the dynamic behaviour of the cable. Subsequently, Irvine extended this linear vibration theory to inclined cables (Irvine, 1978), by simple transformation of axes and by neglecting the weight component parallel to the cable chord. Triantafyllou (1984) presented a more precise solution for the free vibrations of inclined extensible cables, by considering the weight component parallel to the cable chord and assuming a spatial variability of the dynamic tension. The

validity of the Irvine's theory was however confirmed for a wide range of parameters, which include the common parameters in cables from cable-stayed bridges.

Although the linear theory of vibration has been experimentally validated and extensively applied in the dynamic study of cable structures, some phenomena of cable vibrations can only be understood by considering the nonlinear terms in the dynamic equilibrium equations. This is for example the case of vibrations produced by the so-called *parametric excitation*, a matter that will be presented in Chapter six.

Several studies have been developed during the decade of 1980 in order to define the properties of nonlinear vibrations of flat cables. In particular, Hagedorn and Schäfer (1980) investigated the effect of nonlinearities on the first normal modes in free planar vibrations. They showed that in the specific case of a transmission line (with an intrinsic λ^2 parameter of about 500), the frequency of the first modes changed by more than 20% with respect to a linear approach. Considering also free planar nonlinear oscillations, Luongo, Rega and Vestroni (1984) obtained an equation expressing the dependence of the nonlinear frequency Ω on the amplitude of cable vibration. Yamaguchi, Miyata and Ito (1981) deduced nonlinear equilibrium equations for horizontal and inclined cables in the most general situation of three-dimensional oscillations. Takahashi and Konishi (1987) used these equations in the study of the influence of amplitudes and geometric parameters on the nonlinear cable oscillations. Basically, the presence of quadratic and cubic terms in the differential equilibrium equations originates a coupling between in-plane and out-of-plane motion. This coupling has been investigated with different levels of simplification in the analysis of the response to several types of excitation, namely under various external and internal resonance conditions. Benedettini and Rega (1987), for example, employed a single-degree-of-freedom model in the nonlinear analysis of an elastic cable subject to planar excitation. Two-degree-of-freedom models were used both by Rao and Iyengar (1991) and by Perkins (1992), who studied the nonlinear response associated with the harmonic excitation of the cable induced by vortex shedding, and with the harmonic excitation at the cable supports, respectively. Lee and Perkins (1995) introduced a three-degree-of-freedom model in order to capture the interaction of a symmetric in-plane mode with two out-of-plane modes. Benedettini, Rega and Allagio (1995) employed a four-degree-of-freedom algorithm in the study of nonlinear oscillations under multiple internal resonance conditions.

3.3.2 The linear theory of free vibrations of an horizontal cable

Consider the uniform cable represented in Figure 3.8, suspended between two supports at the same level. The cable is in static equilibrium and a generic point P is characterized by the coordinates $\overline{P}(x,0,z)$ in the deformed configuration. An arbitrary small displacement is now applied, originating motion of point P from $\overline{P}$ to $\overline{P'}(x+u,v,z+w)$, where u, v and w

represent the small components of motion along the horizontal (in-plane and out-of-plane) and vertical directions, respectively.

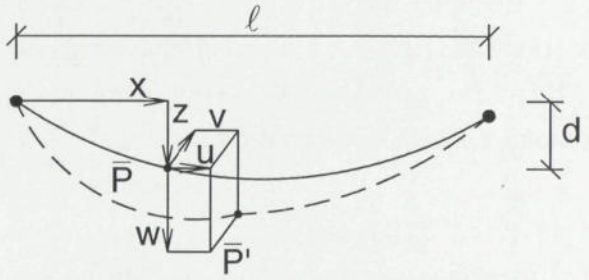


Figure 3.8. Components of displacement of a generic point *P* of an horizontal cable in a disturbed profile.

The equilibrium of a differential segment (Figure 3.9) in this new configuration leads to the following set of equations

$$\frac{\partial}{\partial \bar{s}}\{(T+\tau)\varphi_x\} = m\frac{\partial^2 u}{\partial t^2} \tag{3.38a}$$

$$\frac{\partial}{\partial \bar{s}}\{(T+\tau)\varphi_y\} = m\frac{\partial^2 v}{\partial t^2} \tag{3.38b}$$

$$\frac{\partial}{\partial \bar{s}}\{(T+\tau)\varphi_z\} = m\frac{\partial^2 w}{\partial t^2} - mg \tag{3.38c}$$

where τ is the additional tension generated in the cable, and φ_x, φ_y and φ_z are defined by

$$\varphi_x = \frac{dx+\partial u}{d\bar{s}'};\ \varphi_y = \frac{\partial v}{d\bar{s}'};\ \varphi_z = \frac{dz+\partial w}{d\bar{s}'} \tag{3.39}$$

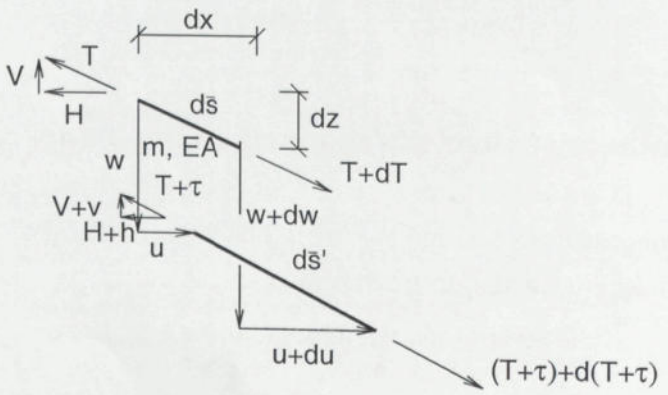


Figure 3.9. Dynamic equilibrium of a differential segment.

Considering that the elastic strain ε is

$$\varepsilon = \frac{d\bar{s}'}{d\bar{s}} - 1$$

The cosines φ_x, φ_y and φ_z given by (3.39) can be expressed as

$$\begin{aligned}\varphi_x &= \frac{dx + \partial u}{d\bar{s}} \cdot \frac{1}{1+\varepsilon} \\ &= \frac{dx + \partial u}{d\bar{s}} \cdot (1 - \varepsilon + \varepsilon^2 - \ldots) \\ &\approx \left(\frac{dx}{d\bar{s}} + \frac{\partial u}{\partial \bar{s}}\right) \cdot (1 - \varepsilon)\end{aligned}$$

$$\varphi_y \approx \frac{\partial v}{\partial \bar{s}} \cdot (1 - \varepsilon) \tag{3.40}$$

$$\varphi_z \approx \left(\frac{dz}{d\bar{s}} + \frac{\partial w}{\partial \bar{s}}\right) \cdot (1 - \varepsilon)$$

The consideration that the cable is shallow and consequently, that the longitudinal component of motion is unimportant, allows to drop equation (3.38a). Furthermore, the inertial forces in the cable direction are very small and, consequently, the variation of the cable tension along the cable can be neglected, i.e., $\partial\tau/\partial x = 0$. This is the so-called *quasi-static* assumption. Using this result, equation (3.38c) expressing the dynamic equilibrium in the vertical direction can now be further simplified, by substitution of expressions (3.40), insertion of the elasticity equation

$$\tau = \varepsilon \cdot EA_0 \tag{3.41}$$

and by replacement of the static equilibrium equalities (3.14a) and (3.14b), which leads to

$$H \cdot \frac{\partial^2 w}{\partial x^2} + h_\tau \frac{d^2 z}{dx^2} \cdot \left[\left(\frac{dx}{d\bar{s}}\right)^2 - \frac{H}{EA_0} \cdot \frac{d\bar{s}}{dx} \right] = m \frac{d\bar{s}}{dx} \cdot \frac{\partial^2 w}{\partial t^2} \tag{3.42}$$

where $h_\tau = \tau \cdot dx/d\bar{s}$. For a small sag ($d/\ell \leq 1/20$), the differentials $dx/d\bar{s}$ and $d\bar{s}/dx$ can be replaced by unity and the quantity H/EA_0, which is assumed very small, can be neglected. Equation (3.42) reduces therefore to the form

$$H\frac{\partial^2 w}{\partial x^2}+h_\tau\frac{d^2 z}{dx^2}=m\cdot\frac{\partial^2 w}{\partial t^2} \tag{3.43}$$

which is the basic equation of dynamic equilibrium in the vertical direction presented by Irvine and Caughey (1974). A procedure of the same type gives the equilibrium equation for the out-of-plane motion

$$H\frac{\partial^2 v}{\partial x^2}=m\cdot\frac{\partial^2 v}{\partial t^2} \tag{3.44}$$

A third equation, providing the elastic and geometric compatibility of the cable element is obtained directly from (3.30), by retaining only the linear terms

$$\frac{h_\tau\cdot(\frac{d\bar{s}}{dx})^3}{EA_0}=\frac{\partial u}{\partial x}+\frac{dz}{dx}\cdot\frac{\partial w}{\partial x} \tag{3.45}$$

where the increment of the horizontal component of tension ΔH corresponds now to the component h_τ. It is important to note that this component is not in effect the dynamic part h of the horizontal force on the cable which is defined, according to Starossek (1990), by

$$h=h_\tau-H\frac{dz}{dx}\cdot\frac{\partial w}{\partial x} \tag{3.46}$$

After integration by parts, equation (3.45) results in

$$\frac{h_\tau L_e}{EA_0}=\frac{mg}{H}\int_0^\ell w\,dx \tag{3.47}$$

where the virtual length L_e is defined by expression (3.32).

Equations (3.43), (3.44) and (3.47) constitute the basic equations of the linear theory of cable vibrations. The solution of these equations is now presented for the particular case of free vibration.

The out-of-plane motion

The first important aspect of the linear theory of cable vibration is the uncoupling of in-plane and out-of-plane motion. In effect, the out-of-plane motion, characterized by the linearized equation (3.44) does not involve an additional cable tension. This means that, to first order, a disturbance with no in-plane components will only induce transverse horizontal motion and vice-versa. Assuming that this out-of-plane vibration is characterized by the product

$$v(x,t) = \tilde{v}(x) \cdot e^{i\omega t} \tag{3.48}$$

where ω is the natural frequency of vibration and $i^2 = -1$, equation (3.44) reduces to

$$H\frac{d^2\tilde{v}}{dx^2} + m\omega^2 \cdot \tilde{v} = 0 \tag{3.49}$$

Introducing the boundary conditions $\tilde{v}(0) = \tilde{v}(\ell) = 0$, the solution of equation (3.49) can be obtained from

$$\omega_n = \frac{n\pi}{\ell} \cdot \sqrt{\frac{H}{m}} \qquad n=1, 2, 3, \ldots$$

$$\tilde{v}_n(x) = A_n \cdot \sin\left(\frac{n\pi x}{\ell}\right) \qquad n=1, 2, 3, \ldots \tag{3.50}$$

where ω_n represents the n_{th} frequency of vibration and $\tilde{v}_n(x)$ is the corresponding modal shape, defined by an arbitrary constant A_n.

The in-plane motion

With regard to the in-plane motion, and considering the assumption on the small sag to span ratio ($d/\ell \leq 1/8$), the longitudinal component of motion is always substantially less than the amplitude of the vertical component of motion. Consequently, the characterization of modal shapes as *symmetric* and *anti-symmetric* is made according to the vertical component of motion.

In the study of in-plane mode shapes, the separation into *symmetric* and *anti-symmetric* modes becomes relevant, as these two types of modes have distinct characteristics. In effect, the observation of equation (3.47) immediately shows that the *symmetric* motion involves a non-zero additional component of tension, while in the *anti-symmetric* case this component vanishes for this linear approach.

(i) Anti-symmetric in-plane modes

Considering now that the in-plane vibration is described by $u(x,t)$ and $w(x,t)$, defined by the products

$$u(x,t) = \tilde{u}(x) \cdot e^{i\omega t} \tag{3.51a}$$

$$w(x,t)=\tilde{w}(x)\cdot e^{i\omega t} \tag{3.51b}$$

the substitution into (3.43) and (3.45) yields, for the case of *anti-symmetric modes*

$$H\frac{d^2\tilde{w}}{dx^2}+m\omega^2\cdot\tilde{w}=0 \tag{3.52a}$$

$$\frac{d\tilde{u}}{dx}+\frac{dz}{dx}\cdot\frac{d\tilde{w}}{dx}=0 \tag{3.52b}$$

Introducing the boundary conditions $\tilde{w}(0)=\tilde{w}(\ell/2)=0$ the solution of equation (3.52a) is obtained

$$\omega_n=\frac{2n\pi}{\ell}\cdot\sqrt{\frac{H}{m}} \qquad n=1, 2, 3, ... \tag{3.53}$$

$$\tilde{w}_n(x)=A_n\cdot sin(\frac{2n\pi x}{\ell}) \qquad n=1, 2, 3, ...$$

where ω_n and $\tilde{w}_n(x)$ represent, respectively, the natural frequency for the nth order *anti-symmetric* in-plane mode, and the corresponding vertical component of the modal shape.

The solution of equation (3.52b) is now determined by substitution of the derivatives of $z(x)$ and $\tilde{w}(x)$ with respect to x, followed by integration and inclusion of the boundary condition $\tilde{u}_n(0)=0$, which leads to

$$\tilde{u}_n(x)=-\frac{1}{2}(\frac{mg\ell}{H})A_n\left\{(1-\frac{2x}{\ell})sin(\frac{2n\pi x}{\ell})+\frac{1-cos(2n\pi x/\ell)}{n\pi}\right\} \tag{3.54}$$

As can be observed from this expression, the amplitude of the longitudinal component of motion is very small for a shallow cable, where the ratio $mg\ell/H$ is small. Another important aspect is the symmetry of this modal component, which is evident from equation (3.52b), considering that the derivative dz/dx vanishes at the midspan and the product $dz/dx\cdot d\tilde{w}/dx$ changes the sign at that location. Also it should be observed that the maximum displacement is reached at the quarter spans for the first modal component. Figure 3.10 presents the longitudinal and vertical configurations for the first three anti-symmetric mode shapes of a shallow cable with a limiting sag to span ratio $d/\ell=1/8$, where a maximum longitudinal amplitude of vibration of *41%* of the vertical amplitude of vibration A_n is attained.

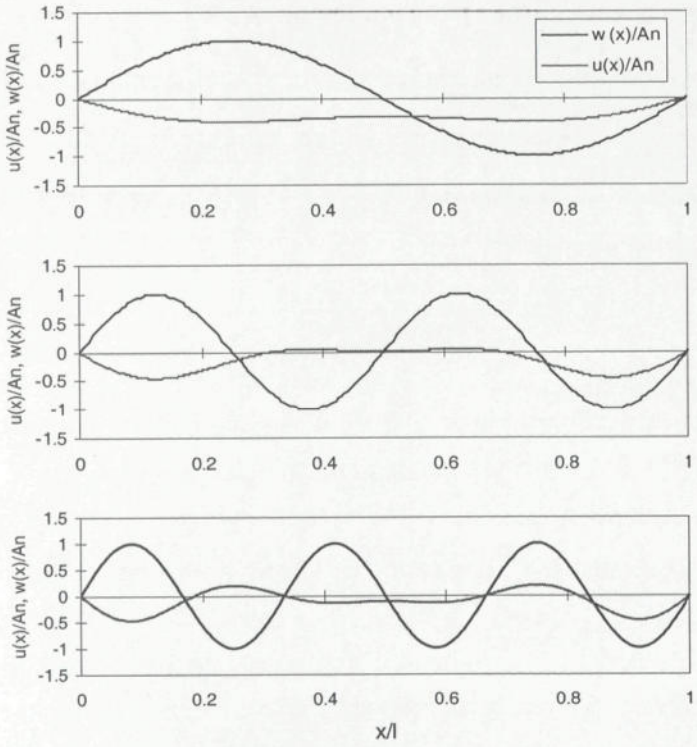


Figure 3.10. Vertical and longitudinal components of the first three anti-symmetric in-plane modes.

(ii) Symmetric in-plane modes

In the case *of symmetric in-plane modes*, an additional cable tension is induced by the motion, which is assumed quasi-static and is characterized by the product

$$h_\tau(t)=\tilde{h}_\tau\cdot e^{i\omega t} \tag{3.55}$$

Substituting expressions (3.51) and (3.55) into equations (3.43) and (3.45) yields

$$H\frac{d^2\tilde{w}}{dx^2}+m\omega^2\,\tilde{w}=\frac{mg}{H}\cdot\tilde{h}_\tau \tag{3.56a}$$

$$\frac{\tilde{h}_\tau\,(d\bar{s}/dx)^3}{EA_0}=\frac{d\tilde{u}}{dx}+\frac{dz}{dx}\cdot\frac{d\tilde{w}}{dx} \tag{3.56b}$$

The solution of the non-homogeneous equation (3.56a) can be now obtained, by introduction of the boundary conditions $\tilde{w}(0)=\tilde{w}(\ell)=0$

$$\tilde{w}(x)=\frac{mg\ell^2}{\bar{\omega}^2H^2}\cdot\tilde{h}_\tau\cdot(1-\tan\frac{\bar{\omega}}{2}\sin\frac{\bar{\omega}x}{\ell}-\cos\frac{\bar{\omega}x}{\ell}) \tag{3.57}$$

where $\overline{\omega}$ is the adimensional natural frequency given by $\overline{\omega} = \omega\ell/(H/m)^{1/2}$, ω being the natural frequency of the cable. Eliminating the term $\tilde{h}_\tau$ in equations (3.56a) and (3.56b), and integrating (3.56b) with inclusion of the boundary conditions $\tilde{u}(0)=\tilde{u}(\ell)=0$, the following transcendental equation in $\overline{\omega}$ is obtained

$$tan\frac{\overline{\omega}}{2}=\frac{\overline{\omega}}{2}-\frac{4}{\lambda^2}(\frac{\overline{\omega}}{2})^3 \tag{3.58}$$

where λ^2 is the fundamental parameter of the cable system defined by expression (3.36).

Equation (3.58) is of utmost importance in the theory of cable vibration. The sole dependence of the natural frequencies of *in-plane symmetric modes* on the independent parameter λ^2 also illustrates the importance of λ^2 as an intrinsic characteristic of the cable system.

Based on equation (3.58), particular solutions can be now obtained for the limiting cases of an *inextensible cable* and a *taut string*.

When the cable is *inextensible*, λ^2 is very large and the deformations are essentially of geometric nature. In this situation, the transcendental equation (3.58) reduces to

$$tan\frac{\overline{\omega}}{2}=\frac{\overline{\omega}}{2} \tag{3.59}$$

The roots of this equation are given by

$$\overline{\omega}_n=(2n+1)\pi-\frac{4}{(2n+1)\pi} \qquad n=1, 2, 3, ... \tag{3.60}$$

So, for large values of λ^2, the numeric solution of (3.58) can be replaced by (3.60).

On the contrary, when λ^2 is very small, the roots of (3.58) approach the roots of the symmetric modes of a *taut string*

$$\overline{\omega}_n=(2n-1)\pi \qquad n=1, 2, 3, ... \tag{3.61}$$

Comparing expressions (3.60) and (3.61), it becomes evident that the transition from the dynamics of a taut string ($\lambda^2 = 0$) to the dynamics of an inextensible cable ($\lambda^2 = \infty$) is marked by a shift of almost 2π in the value of the adimensional frequency $\overline{\omega}_n$ of symmetric modes. This fact can be observed in Figure 3.11, which represents the variation of the quantity $\overline{\omega}_n / \pi$ with λ^2. An important aspect of this Figure is the occurrence of the so-called *crossovers* in the transition regions, corresponding to values of λ^2 beyond which the natural

frequency of the *symmetric modes* becomes higher than the natural frequency of the same order *anti-symmetric* modes.

Generally, the values of λ^2 associated with n^{th} order *crossovers* can be obtained by

$$\lambda^2 = 4(n\pi)^2 \tag{3.62}$$

This results from the substitution into (3.58) of the values $\bar{\omega}_n = 2n\pi$ for the anti-symmetric modes of vibration. Also it can be observed that the configuration associated with the vertical component of symmetric vibration modes varies according to the value of λ^2. Considering the 1st mode of vibration and the corresponding *crossover* value $\lambda^2 = 4\pi^2$, it is shown in Figure 3.12, that for $\lambda^2 < 4\pi^2$, the vertical component of vibration has no internal nodes. For $\lambda^2 = 4\pi^2$, this component is tangential to the cable profile at the supports. Finally, for $\lambda^2 > 4\pi^2$, when the symmetric natural frequency becomes higher than the corresponding order anti-symmetric natural frequency, two internal nodes occur in the symmetric vertical component.

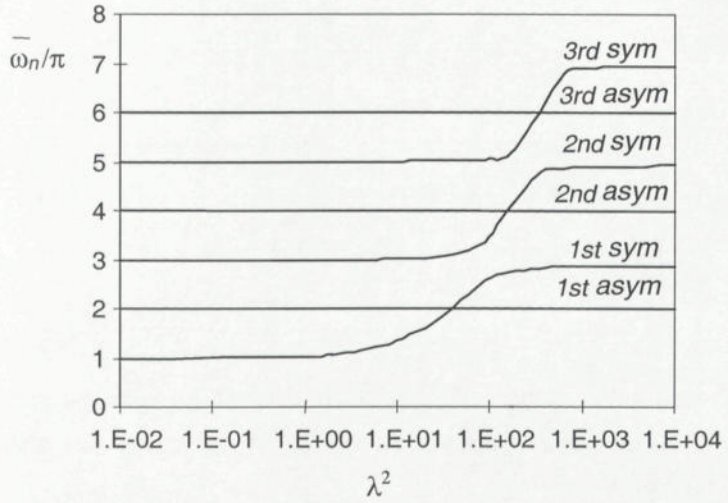


Figure 3.11. Variation of the natural frequencies of the first three *symmetric* and *anti-symmetric* modes of vibration with λ^2.

Finally, the longitudinal component of vibration associated with symmetric modes can be obtained using equations (3.56a), (3.56b) and (3.57), yielding

$$\tilde{u}(x) = \frac{mg\ell}{H} \cdot \frac{mg\ell^2}{\bar{\omega}^2 H^2} \cdot \tilde{h}_\tau \cdot \left[\frac{\bar{\omega}^2}{\lambda^2} \cdot \frac{L_x}{L_e} - \frac{1}{2}(1 - 2\frac{x}{\ell}) \cdot \left\{ 1 - \tan\frac{\bar{\omega}}{2} \cdot \sin(\bar{\omega}\frac{x}{\ell}) - \cos(\bar{\omega}\frac{x}{\ell}) \right\} - \right.$$
$$\left. - \frac{1}{\bar{\omega}} \cdot \left\{ \bar{\omega}\frac{x}{\ell} - \tan\frac{\bar{\omega}}{2} \cdot (1 - \cos(\bar{\omega}\frac{x}{\ell})) - \sin(\bar{\omega}\frac{x}{\ell}) \right\} \right] \tag{3.63}$$

where

$$L_x = \ell\left[\frac{x}{\ell} + \frac{3}{8}\cdot\left(\frac{mg\ell}{H}\right)^2 \cdot\left\{\frac{x}{\ell} - 2\left(\frac{x}{\ell}\right)^2 + \frac{4}{3}\left(\frac{x}{\ell}\right)^3\right\}\right] \tag{3.64}$$

According to Figure 3.12, where this component has been represented for the limiting situation $d/\ell = 1/8$, $\tilde{u}(x)$ is anti-symmetric, the number of internal nodes increasing from the situation where $\lambda^2 < 4\pi^2$ to the case of $\lambda^2 > 4\pi^2$.

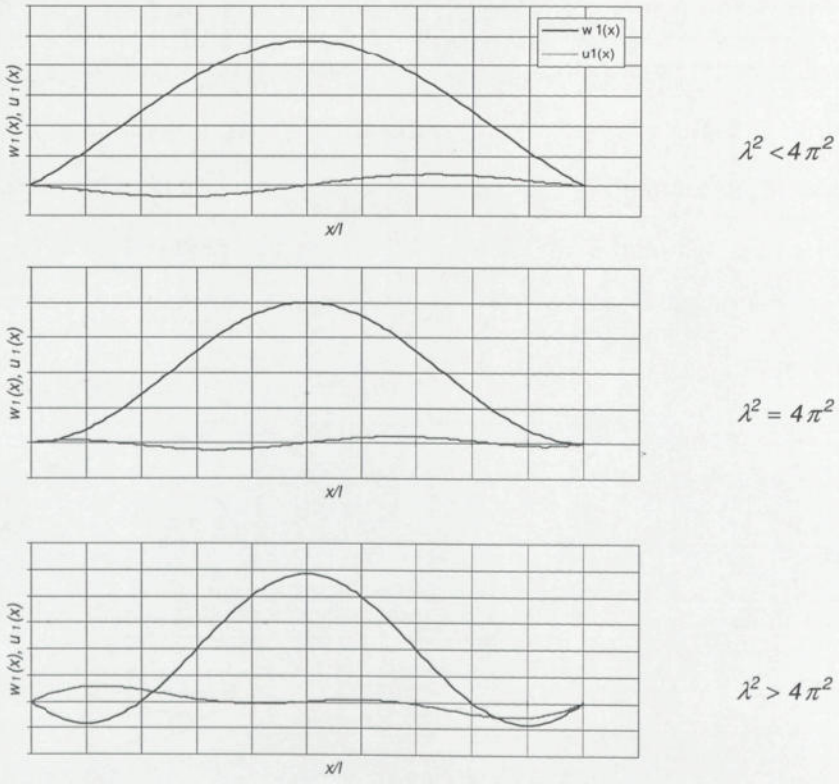


Figure 3.12. Representation of the vertical and longitudinal modal components associated with the first vibration mode for different values of λ^2: $\lambda^2 < 4\pi^2$, $\lambda^2 = 4\pi^2$ and $\lambda^2 > 4\pi^2$.

As a final consideration, it should be noted that the cables employed in cable-stayed bridges are tightly stretched, presenting small values of λ^2 (typically inferior to *1*, as already stated). Therefore, according to the representation in Figure 3.11, the corresponding natural frequencies lie outside the transition ranges and can be obtained using the formulae for taut strings. On the contrary, the cables from suspension bridges are generally in the transition range and, consequently, their vibration characteristics should consider both the cable geometry and elasticity.

3.3.3 The linear theory of free vibrations of an inclined cable

3.3.3.1 The simplified approach from Irvine

As in the case of the definition of the static profile of an inclined cable, Irvine (1981) extended his linearized theory of horizontal cable vibration to inclined flat cables. The methodology employed consisted in performing a transformation of the horizontal/ vertical axes to inclined axes parallel/ perpendicular to the cable chord with the basic assumption that the weight component parallel to the cable chord is neglectable.

Consider the inclined cable presented in Figure 3.3 and the transformation of axes represented in Figure 3.4, corresponding to a new set of coordinates (x_*, z_*) defined according to (3.21).

As in the case of horizontal cables, the out-of-plane motion is, to first order, uncoupled from the in-plane motion. Also the in-plane longitudinal component of motion is much smaller than the in-plane transverse component and does not affect the calculation of natural frequencies. So, defining ω_{*n} as the nth order natural frequency of an inclined cable and $\overline{\omega}_{*n} = \omega_{*n} \ell_* \cdot \sqrt{m/H_*}$ as the corresponding adimensional natural frequency, the out-of-plane modes of an inclined cable are now characterized by

$$\overline{\omega}_{*n} = n\pi \qquad n=1, 2, 3, \ldots \tag{3.65}$$

For in-plane anti-symmetric modes, the natural frequencies are obtained from

$$\overline{\omega}_{*n} = 2n\pi \qquad n=1, 2, 3, \ldots \tag{3.66}$$

while for symmetric in-plane modes, $\overline{\omega}_{*n}$ are the roots of the transcendental equation

$$\tan\left(\frac{\overline{\omega}_{*n}}{2}\right) = \frac{\overline{\omega}_{*n}}{2} - \frac{4}{\lambda_*^2}\left(\frac{\overline{\omega}_{*n}}{2}\right)^3 \tag{3.67}$$

Equations (3.65) to (3.67) are of general applicability and contain, as a particular case, the results corresponding to an horizontal suspended cable. Irvine states however that these equations are not valid for all angles in the range $\left[0, 90^\circ\right]$. In fact, the precision of these equations decreases with the increase of the angle of inclination θ. However, for the common case where θ does not exceed 60°, validity of this theory can be assumed.

3.3.3.2 The asymptotic approach from Triantafyllou

Triantafyllou (1984) developed a more precise solution for the vibration problem of an inclined elastic cable with small sag. In his approach, Triantafyllou considered the spatial variability of the dynamic cable tension (Irvine had assumed only variation with time of this quantity) as well as the effect of the weight component parallel to the cable chord (Irvine had neglected this component).

By establishing the static and dynamic equilibrium of the inclined cable in Lagrangian coordinates and including the compatibility equations, Triantafyllou arrived to a set of four independent linearized first-order differential equations, whose asymptotic solutions were determined by considering two distinct physical mechanisms of cable vibration: (i) the transverse cable dynamics, in which the rate of spatial change of the transverse displacement is large compared with the rate of change of the static solution and; (ii) the axial dynamics of the cable, that results in tangential and transversal vibrations with slow spatial variation. The first physical mechanism led to a so-called *fast solution*, while the later led to a *slow solution*. The total solution is obtained from the sum of the independent solutions, giving the following coupled equations for the transverse and tangential displacements q and p, respectively, relative to the static solution (Triantafyllou and Grinfogel, 1986)

$$q(s,t)=\left\{\frac{1}{\sqrt[4]{T_0\frac{s}{m}}}\cdot[c_1\cdot cosW(s)+c_2\cdot sinW(s)]+\frac{d\phi_0(s)}{ds}[c_3\cdot A_i(-z)+c_4\cdot B_i(-z)]\right\}e^{i\omega t} \tag{3.68a}$$

$$p(s,t)=\left\{\frac{d\phi_0}{ds}\frac{\sqrt[4]{T_0\frac{s}{m}}}{\omega}[c_1\cdot sinW(s)-c_2\cdot cosW(s)]-Q^{1/3}\left[c_3\cdot A_i'(-z)+c_4\cdot B_i'(-z)\right]\right\}e^{i\omega t} \tag{3.68b}$$

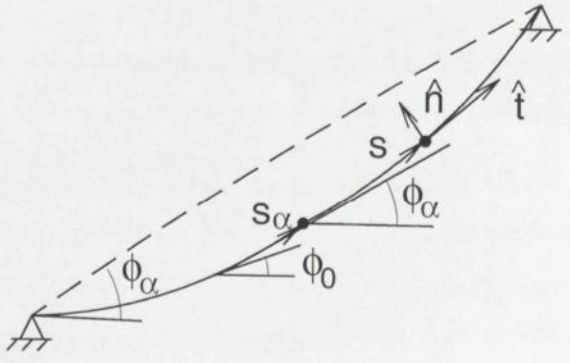


Figure 3.13. Inclined cable in static configuration.

In these expressions, T_0 represents the static tension, $\phi_0(s)$ is the static angle at an arbitrary point defined by the Lagrangian coordinate s (see Figure 3.13), the quantities $W(s)$, Q and z being defined by

$$W(s)=\omega\int_0^s\frac{ds}{\sqrt{T_0\frac{s}{m}}}$$

$$Q=\frac{4(mg)^3\cos^2\phi_\alpha\sin\phi_\alpha}{T_\alpha^3}$$

$$z=Q^{1/3}(s-s_0)$$

where ϕ_α represents the angle of inclination of the chord with respect to the horizontal (Figure 3.13), T_α is the tension at the point whose static angle of inclination is equal to ϕ_α, characterized by the Lagrangian coordinate s_α given by

$$s_\alpha=\frac{-(\frac{mg\cos\phi_\alpha}{T_\alpha})^2+\frac{m\omega^2}{EA_0}}{Q}$$

The constants c_1, c_2, c_3 and c_4 are determined from the boundary conditions, and finally, $A_i(z)$ and $B_i(z)$ are the Airy functions of the first and second kind, respectively, $A_i'(z)$ and $B_i'(z)$ being the corresponding derivatives.

The first two terms in the second member of expressions (3.68a) and (3.68b) are associated with the *fast solution* above referred and are of the same type of the solutions previously obtained by Irvine for the stretched cable. The last two terms are related with the *slow solution* and can be of sinusoidal or exponential type, or of a combination of the two.

A simplifying approach can be now used, if the cable inertia in the longitudinal direction is neglected. This corresponds to a quasi-static assumption for the stretching, leading to the following simplifying equation for the determination of natural frequencies

$$\sin\theta\left[\theta(\frac{4\theta^2}{\lambda^2}-1)\cos\theta+\sin\theta\right]-\frac{49}{64}\varepsilon^2\cdot\sin^2\phi_\alpha\cdot\cos2\theta=0 \qquad (3.69)$$

where

$$\varepsilon=\frac{mgL}{T_\alpha}$$

$$\theta = \frac{kL}{2}$$

$$k = \frac{\omega}{\sqrt{\frac{T_\alpha}{m}}}$$

$$\lambda^2 = \frac{EA_0}{T_\alpha}\left(\frac{mgL}{T_\alpha}\right)^2 \cos^2\phi_\alpha$$

The transverse modes can be found from (Triantafyllou & Grinfogel, 1986)

$$\begin{aligned}
q_n(s) = C_n &\left\{\left\{2\sin^2\left(\frac{kL}{2}\right)\left[\cos\left(\frac{kLs}{L}\right)-1\right]-\sin\left(\frac{kLs}{L}\right)\left[\sin kL + kL\left(\frac{k^2L^2}{\lambda^2}-1\right)\right]\right\}+\right.\\
&+\frac{\varepsilon\sin\phi_\alpha}{4}\left\{2\sin^2\frac{kL}{2}\left[\left(\frac{kLs}{L}\right)\left(\frac{s}{L}-1\right)\sin\left(\frac{kLs}{L}\right)-\left(\frac{s}{L}-\frac{1}{2}\right)\cos\left(\frac{kLs}{L}\right)\right]+\right.\\
&+\frac{1}{2}\cos\left(\frac{kLs}{L}\right)\left(-\cos kL+15\right)+\left[-\sin\left(\frac{kLs}{L}\right)\frac{1}{2}+\left(\frac{s}{L}-1\right)\left(\frac{kLs}{L}\right)\cos\left(\frac{kLs}{L}\right)+\right.\\
&\left.\left.+\left(\frac{s}{L}-\frac{1}{2}\right)\sin\left(\frac{kLs}{L}\right)\right]\cdot\left[\sin kL + kL\left(\frac{k^2L^2}{\lambda^2}-1\right)\right]+4\left[-1-\frac{3}{4}\cos kL+4\sin^2\left(\frac{kL}{2}\right)\left(\frac{s}{L}-\frac{1}{2}\right)\right]\right\}+\\
&+\varepsilon^2\sin^2\phi_\alpha\left[\frac{7}{2}\left(\frac{s}{L}-\frac{1}{2}\right)+\frac{7}{4}\cos\left(\frac{kLs}{L}\right)-\frac{7}{16}\left(\frac{s}{L}-\frac{1}{2}\right)\cos\left(\frac{kLs}{L}\right)-\frac{7}{32}+\right.\\
&\left.\left.+\frac{7}{16}\left(\frac{kLs}{L}\right)\left(\frac{s}{L}-1\right)\sin\left(\frac{kLs}{L}\right)\right]\right\}
\end{aligned} \tag{3.70}$$

in which C_n is an arbitrary amplitude. Finally, the dynamic tension is given by

$$T(s,t) = \frac{m\omega^2 L}{\varepsilon\cos\phi_\alpha} C_n \left(2\sin^2\frac{kL}{2}+\frac{7}{4}\varepsilon\sin\phi_\alpha\right)\varepsilon^{i\omega t} \tag{3.71}$$

Considering now the analogy of the tension component T_α with H_* defined by Irvine for inclined cables and admitting that the cable is flat, in which case the length L is very close to the cable chord ℓ_* and the virtual length L_{e^*} introduced by Irvine, i.e., $L \approx \ell_* \approx L_{e^*}$, the parameters λ^2 and λ_*^2 defined by Triantafyllou and Irvine, respectively, become equivalent. Also it becomes evident that $\theta \approx \bar{\omega}_{n^*}/2$. Replacing this value into equation (3.69), it can be observed that equations (3.67) and (3.69) only differ from the second order term $-98/64 \cdot \varepsilon^2 \cdot \sin^2\phi_\alpha \cdot 1/\tan 2\theta$. So, for the particular case of a horizontal cable, equations (3.67) and (3.69) are identical. For inclined cables however, this second order term produces

a modification in the solutions obtained by Irvine in such a way that the *crossovers* never occur. According to Figure 3.14, representing the variation of the adimensional natural frequencies $\overline{\omega}_{n^*}/\pi$ associated with the first two modes of vibration with λ^2 for different angles of inclination of the cables, the natural frequencies of consecutive modes of vibration become very close in the regions previously defined for the crossovers, i.e., for $\lambda^2 = 4(n\pi)^2$, but they never coincide. This phenomenon of noncrossing curves has no significant implication in terms of the values of the natural frequencies of small sag inclined cables, which differ only by a few percent from the corresponding frequencies obtained under the simplified approach from Irvine (Triantafyllou & Grinfogel, 1986). It has however a significant influence in the determination of the mode shapes, which are totally different from those obtained for horizontal cables over the transition regions. In effect, and according to the representation of Figure 3.15, near the so-called *avoided crossings*, the modes are hybrid, a mixture of symmetric and anti-symmetric forms. This results from the fact that the lower part of the cable is closer to an inextensible chain, while the upper part is closer to a taut string and has major implications in the dynamic cable tension. In fact, according to the theory of Irvine, the anti-symmetric modes don't develop, to first order, any dynamic tension. Consequently, for fatigue and strength analysis purpose, only the symmetric modes are of interest. With the present approach, all modes involve the development of a dynamic component of tension and are now of interest over the transition region.

Finally, it should be noted that for $\lambda^2 < 1$, the range of values of the parameter λ^2 associated with cables from cable-stayed bridges, the theory of Irvine maintains its validity.

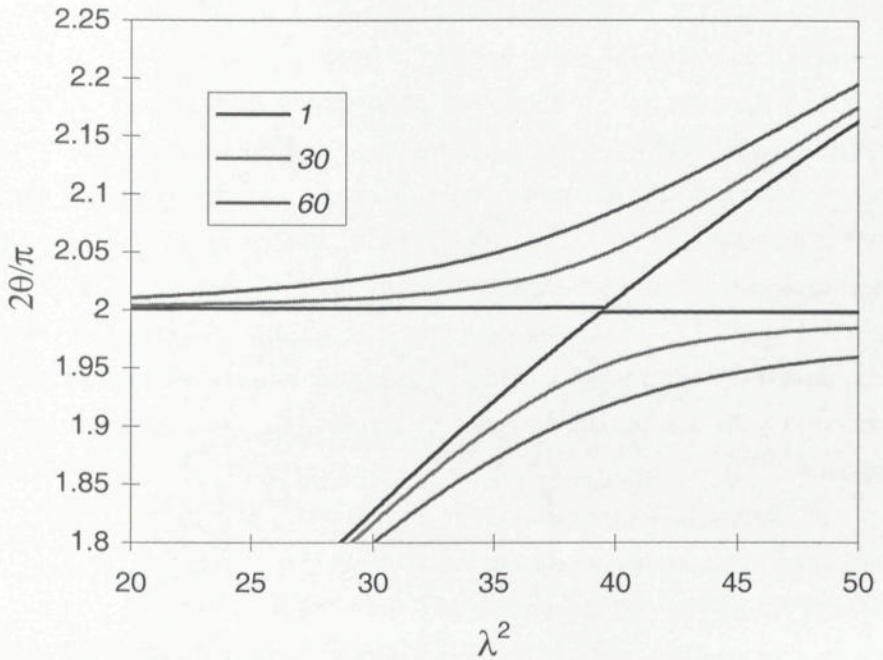


Figure 3.14. Variation of the natural frequency $\overline{\omega}_{n^*=2\theta}$ of the first two modes of vibration with λ^2, for different angles of inclination of the cable: $\phi_\alpha = 1°, 30°, 60°$ and $\varepsilon = 0.3$.

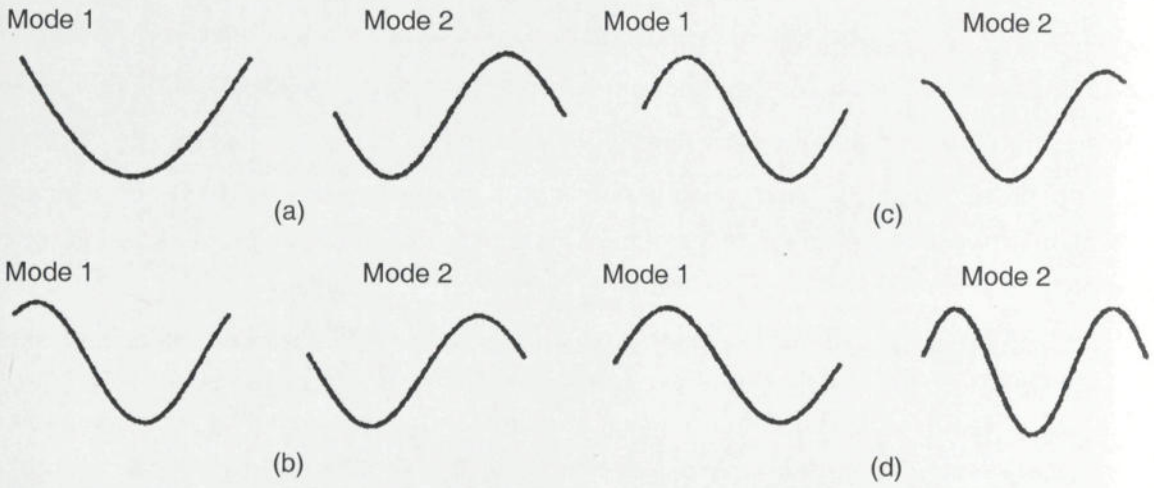


Figure 3.15. Transverse modal configuration of the first two modes of vibration of an inclined cable ($\phi_\alpha = 30^\circ$) for different values of λ^2 and $\varepsilon = 0.3$: (a) $\lambda^2 = 0.01\pi^2$; (b) $\lambda^2 = 3.61\pi^2$; (c) $\lambda^2 = 5.29\pi^2$; (d) $\lambda^2 = 64\pi^2$ (Triantafyllou & Grinfogel, 1984).

3.3.4 Non-linear theory of cable vibration

Both the Irvine (1981) and Triantafyllou (1984) approaches for the theory of cable vibrations are linear theories, in the sense that only first order terms are used in the definition of the elastic strain ε.

It is the purpose of the current Section to show the modifications introduced in the dynamic equilibrium equations by the consideration of nonlinear terms in the definition of ε.

By formulating the problem in a general case where vertical and lateral forces are applied simultaneously with a harmonic longitudinal displacement at one cable end, a coupled system of equations will be obtained, containing quadratic and cubic terms. These terms are associated with the geometric and elastic character of the deformation, respectively, and introduce an enormous complexity in the system of equations.

An important aspect of these equations is also the appearance of first order parametric terms, which will introduce additional resonances into the structural system. This later topic, associated with the particular issue of *parametric excitation,* will be focused in detail in Chapter six.

Consider the flat cable represented in Figure 3.8, whose static configuration is described by the parabola given by expression (3.16). The general equilibrium equations (3.38) for the differential segment represented in Figure 3.9 in a deformed configuration are now transformed, assuming that

$$\varphi_x = \frac{dx + \partial u}{d\bar{s}}$$

$$\varphi_y = \frac{\partial v}{d\bar{s}} \tag{3.72}$$

$$\varphi_z = \frac{dz + \partial w}{d\bar{s}}$$

and retaining the second order terms in the definition of the elastic strain ε, which assumes the form

$$\varepsilon = \frac{\tau}{EA_0} = \frac{\partial u}{\partial x} + \frac{dz}{dx}\cdot\frac{\partial w}{\partial x} + \frac{1}{2}\left(\frac{\partial v}{\partial x}\right)^2 + \frac{1}{2}\left(\frac{\partial w}{\partial x}\right)^2 \tag{3.73}$$

Note that, because of being much smaller than the corresponding terms in v and w, the term in $(\partial u/\partial x)^2$ is not included in (3.73).

The cable is then subjected to external time dependent forces $f_y(s,t)$ and $f_z(s,t)$, and to a harmonic displacement of one end with a natural frequency Ω, as represented in Figure 3.16.

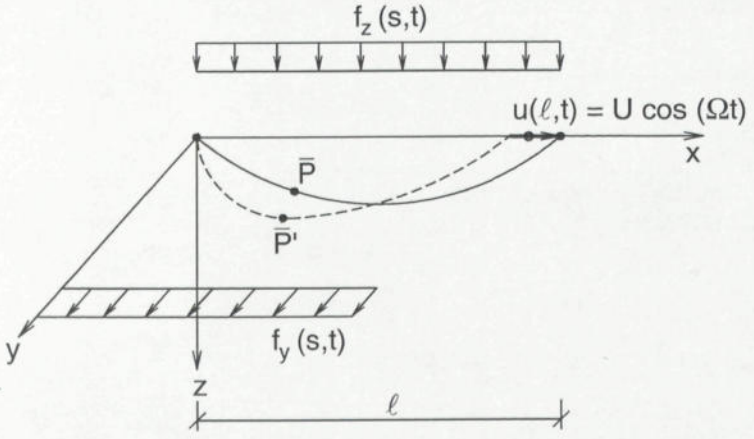


Figure 3.16. Flat cable subjected to time dependent forces along y and z directions and to harmonic displacement of one end.

The equilibrium of one element of cable requires that

$$\frac{\partial}{\partial \bar{s}}\left\{(T+\tau)\cdot\frac{dx+\partial u}{d\bar{s}}\right\} = m\frac{\partial^2 u}{\partial t^2} \tag{3.74a}$$

$$\frac{\partial}{\partial \bar{s}}\left\{(T+\tau)\cdot\frac{\partial v}{\partial \bar{s}}\right\}+f_y=m\frac{\partial^2 v}{\partial t^2} \tag{3.74b}$$

$$\frac{\partial}{\partial \bar{s}}\left\{(T+\tau)\cdot\frac{dz+\partial w}{d\bar{s}}\right\}+f_z=m\frac{\partial^2 w}{\partial t^2}-mg \tag{3.74c}$$

Neglecting the longitudinal inertia, the elastic strain ε becomes a function of time only. Integrating (3.73) including the boundary condition $u(\ell,t)=U\cos\Omega t$ (see Figure 3.16) yields

$$\varepsilon=\frac{U}{\ell}\cos\Omega t+\frac{1}{\ell}\int_0^{\ell}\left[\frac{dz}{dx}\cdot\frac{\partial w}{\partial x}+\frac{1}{2}\left(\frac{\partial v}{\partial x}\right)^2+\frac{1}{2}\left(\frac{\partial w}{\partial x}\right)^2\right]dx \tag{3.75}$$

Replacing (3.75) into equations (3.74), the following two equations of motion are obtained

$$H\frac{\partial}{\partial x}\left[\frac{\partial v}{\partial x}+\gamma\frac{\partial v}{\partial x}\cdot\left(\frac{U}{\ell}\cos\Omega t+\frac{1}{\ell}\int_0^{\ell}\left\{\frac{dz}{dx}\cdot\frac{\partial w}{\partial x}+\frac{1}{2}\left(\frac{\partial v}{\partial x}\right)^2+\frac{1}{2}\left(\frac{\partial w}{\partial x}\right)^2\right\}dx\right)\right]+f_y=m\frac{\partial^2 v}{\partial t^2} \tag{3.76a}$$

$$H\frac{\partial}{\partial x}\left[\frac{\partial w}{\partial x}+\gamma\left(\frac{dz}{dx}+\frac{\partial w}{\partial x}\right)\left(\frac{U}{\ell}\cos\Omega t+\frac{1}{\ell}\int_0^{\ell}\left\{\frac{dz}{dx}\cdot\frac{\partial w}{\partial x}+\frac{1}{2}\left(\frac{\partial v}{\partial x}\right)^2+\frac{1}{2}\left(\frac{\partial w}{\partial x}\right)^2\right\}dx\right)\right]+f_z=m\frac{\partial^2 w}{\partial t^2} \tag{3.76b}$$

where $\gamma=EA_0/H$.

Consider now the non-dimensionalization

$$\bar{x}=x/\ell$$

$$\bar{t}=t/\sqrt{\ell/g}$$

$$\bar{v}(\bar{x},\bar{t})=v(\bar{x},\bar{t})/\ell$$

$$\bar{w}(\bar{x},\bar{t})=w(\bar{x},\bar{t})/\ell$$

$$\bar{f}_y=\frac{f_y}{mg\ell} \tag{3.77}$$

$$\bar{f}_z=\frac{f_z}{mg\ell}$$

$$\bar{U} = \frac{U}{\ell}$$

$$\omega = \Omega \sqrt{\ell / g}$$

and define the quantities k, v_t and v_ℓ as

$$k = \frac{mg\ell}{H}$$

$$v_t^2 = \frac{H}{mg\ell} = \frac{1}{k} \tag{3.78}$$

$$v_\ell^2 = \frac{EA_0}{mg\ell}$$

Assuming that the initial static profile is parabolic and given by equation (3.16), the following expression is obtained for the strain ε

$$\varepsilon = \bar{U}\cos\omega\bar{t} + k\int_0^1 \bar{w}\,d\bar{x} + \frac{1}{2}\int_0^1 \left[\left(\frac{\partial \bar{v}}{\partial \bar{x}}\right)^2 + \left(\frac{\partial \bar{w}}{\partial \bar{x}}\right)^2 \right] d\bar{x} \tag{3.79}$$

and the equations of motion (3.76) are transformed into

$$(v_t^2 + v_\ell^2\,\varepsilon)\cdot\frac{\partial^2 \bar{v}}{\partial \bar{x}^2} + \ell \bar{f}_y = \frac{\partial^2 \bar{v}}{\partial \bar{t}^2} \tag{3.80a}$$

$$(v_t^2 + v_\ell^2\,\varepsilon)\cdot\frac{\partial^2 \bar{w}}{\partial \bar{x}^2} - k v_\ell^2\,\varepsilon + \ell \bar{f}_z = \frac{\partial^2 \bar{w}}{\partial \bar{t}^2} \tag{3.80b}$$

Note that the quantity $(v_t^2 + v_\ell^2\,\varepsilon)$ represents the total cable tension, the component v_t^2 representing the static component and $v_\ell^2\,\varepsilon$ being the dynamic component. This component includes the dynamic tension induced by the support motion, that leads to the so-called *parametric excitation* terms $(v_\ell^2\,\bar{U}\cos\omega\bar{t})\cdot\partial^2\bar{v}/\partial\bar{x}^2$ and $(v_\ell^2\,\bar{U}\cos\omega\bar{t})\cdot\partial^2\bar{w}/\partial\bar{x}^2$ in equations (3.80a) and (3.80b), respectively.

The non-linear system equations are now studied by separation of variables, describing the displacements $\bar{v}(\bar{x},\bar{t})$ and $\bar{w}(\bar{x},\bar{t})$ by the products

$$\bar{v}(\bar{x},\bar{t}) = \theta(\bar{x}) \cdot V(\bar{t}) \tag{3.81a}$$

$$\bar{w}(\bar{x},\bar{t}) = \phi(\bar{x}) \cdot W(\bar{t}) \tag{3.81b}$$

$V(\bar{t})$ and $W(\bar{t})$ in equations (3.81) are the unknown time functions, and the functions $\theta(\bar{x})$ and $\phi(\bar{x})$ in these equations are chosen to be particular out-of-plane and in-plane mode shapes associated with free linear response, with corresponding natural frequencies ω_t and ω_v, respectively. Note that, although this approach has been widely used in the discretization of nonlinear partial-differential equations, recent studies by Pakdemirli *et al.* (1995) have shown that linear mode shapes fail to reproduce accurately the dynamics of a cable that exhibits a nonlinear behaviour in resonance.

Substitution of equations (3.81) into (3.80) and addition of a viscous damping term characterized by a damping ratio ξ, yields the following two-degree-of-freedom discrete model

$$\ddot{V} + 2\xi\omega_t \dot{V} + \omega_t^2 V = 2\bar{U} p_t \cos\omega\bar{t} V + \alpha_1 VW + \beta_1 V^3 + \beta_2 VW^2 + F_y(\bar{t}) \tag{3.82a}$$

$$\begin{aligned} \ddot{W} + 2\xi\omega_v \dot{W} + \omega_v^2 W = {} & 2\bar{U} p_v \cos\omega\bar{t} W - \bar{U} f_v \cos\omega\bar{t} + \alpha_2 V^2 + \alpha_3 W^2 + \\ & + \beta_3 WV^2 + \beta_4 W^3 + F_z(\bar{t}) \end{aligned} \tag{3.82b}$$

whose coefficients are

$$p_t = -\frac{1}{2}\frac{v_\ell^2}{v_t^2}\omega_t^2 \qquad p_v = -\frac{1}{2}\frac{v_\ell^2}{v_t^2} r^2 \qquad f_v = -\frac{v_\ell^2}{v_t^2} \cdot \bar{\phi}$$

$$\alpha_1 = \frac{v_\ell^2}{(v_t^2)^2}\omega_v^2 \cdot \bar{\phi} \qquad \alpha_2 = \frac{1}{2}\alpha_1 \qquad \alpha_3 = \frac{3}{2}\frac{v_\ell^2}{(v_t^2)^2} r^2 \cdot \bar{\phi}$$

$$\beta_1 = -\frac{1}{2}\frac{v_\ell^2}{(v_t^2)^2}\omega_t^4 \qquad \beta_2 = \beta_3 = -\frac{1}{2}\frac{v_\ell^2}{(v_t^2)^2} r^2 \omega_t^2 \qquad \beta_4 = -\frac{1}{2}\frac{v_\ell^2}{(v_t^2)^2} r^4$$

with

$$r^2 = \omega_v^2 - \frac{v_\ell^2}{v_t^2} \cdot \overline{\phi^2}$$

and

$$\bar{\phi} = \int_0^1 \phi(\bar{x}) \cdot d\bar{x}$$

The modal components of the external forces $F_y(\bar{t})$ and $F_z(\bar{t})$ in equations (3.82) are given by

$$F_y(t) = \int_0^1 \bar{f}_y(\bar{x},\bar{t}) \Big/ \theta(\bar{x}) d\bar{x} \tag{3.83a}$$

$$F_z(t) = \int_0^1 \bar{f}_z(\bar{x},\bar{t}) \Big/ \phi(\bar{x}) d\bar{x} \tag{3.83b}$$

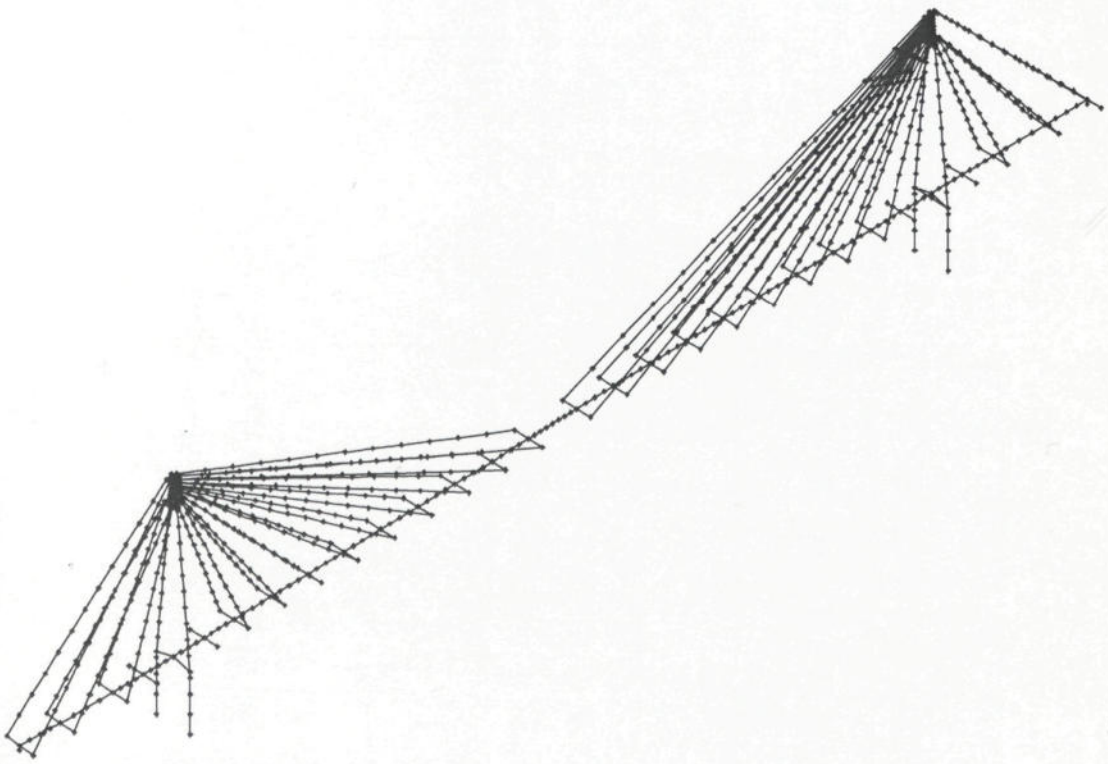
Equations (3.82) evidence the appearance of quadratic and cubic terms which couple the movement. Quadratic non-linear terms are associated with the cable curvature, i.e., with geometric type of deformation, while cubic terms reflect the non-linearity due to the stretching of the cable. For the case of a taut string, where typically $k \to 0$, the coefficients associated with quadratic terms also approach *0*, leaving only cubic nonlinearities in the equations of motion. Even in this simplified case, analytical solutions to the differential equations are difficult to obtain and consequently most authors develop numerical solutions based in perturbation methods, namely the method of multiple scales (Nayfeh & Mook, 1979).

In the context of the present research, the most important situation to analyse is related with *parametric excitation* of a taut cable, that is the phenomenon of cable vibration motivated by longitudinal oscillation of the supports. This topic will be focused in Chapter six.

CHAPTER 4

DYNAMIC ANALYSYS OF CABLE-STAYED BRIDGES:

Design loads and numerical formulation



CHAPTER FOUR

DYNAMIC ANALYSYS OF CABLE-STAYED BRIDGES: DESIGN LOADS AND NUMERICAL FORMULATION

4.1 GENERAL

Although the principal design loads for cable-stayed bridges are of static nature, it is recognized that both during and after construction dynamic loads have a determinant role in the behaviour of these structures. This is particularly valid for modern long span bridges which, in virtue of the efficient use of high strength materials, combined with technical improvements in the design and construction procedures, have a reduced dead weight and damping when compared with early cable-stayed bridges.

The most significant dynamic effects on a cable-supported structure are due to (i) wind loads; (ii) moving loads along the girder and (iii) earthquake excitation. It is the purpose of the current Chapter to present an overview of the main aspects related with the definition of design loads associated with each of these effects. The procedures of assessment of the dynamic behaviour of the bridge are then systematized, with particular relevance to the numerical modelling of the bridge using a finite element analysis. Considering the geometrical nonlinearity as the primary source of nonlinearity present in the analysis of a cable-stayed bridge, the basic governing finite element equations are derived, and the finite element matrices associated with particular elements employed in the discretization of the bridge components are presented.

4.2 THE LOADS

The definition of design loads includes, in a first step, the characterization of the wind loads on the structure. This involves the construction of a wind model, by assessing the main climate characteristics and features of the site, and by specifying a law for the variation of mean wind velocity with height, accompanied by a probabilistic definition of wind turbulence. The main load components are then identified, considering both the static (mean wind velocity) and dynamic effects (fluctuating component of wind), the later being divided into motion-dependent (*aeroelastic*) and motion-independent (*buffeting*) effects. Reference is made in particular to specific phenomena of instability motivated by the interaction of the structure motion with the air flow (*torsional divergence*, *flutter*, *galloping*, vortex-shedding/*lock-in*). A few guidelines for the control of these phenomena are presented based on the Eurocode 1 (*EC1).*

With respect to moving loads, two general categories are considered: *traffic and railway* loads, and *pedestrian* loads. Considering the dynamic effects of these loads, their main characteristics are presented.

For traffic and railway loads, the simplified procedure of evaluating dynamic effects based on the definition of static load models, which are amplified by appropriately defined dynamic factors, is referred. The main variables involved in the specification of these factors are presented, namely those related with the definition of the traffic composition, with the particular type of bridge under analysis, with the surface roughness, and even the variability of the dynamic factors according to the type of measured quantity they are based on and the type of structural element they respect. Numerical simulations, involving some or all of these parameters and considering the vehicle-structure interaction, are referred as a valid form of assessing dynamic amplification factors, particularly when validated and complemented with results from *in-situ* measurements.

For pedestrian loads, which are of interest for small and medium span cable-stayed bridges, time load functions are defined and a simplified methodology is presented towards the assessment of the dynamic effect associated with the simultaneous presence of a number of pedestrians on the bridge. Tolerable limits for serviceability expressed in terms of maximum allowed acceleration are defined according to British (BS 5400, 1978) and Canadian (OHBDC, 1983) codes.

Seismic loads are then characterized using three different alternative approaches, based on response spectra, power spectra and acceleration time series. The issue of spatial variability of earthquake loads is then discussed. This topic is of particular importance for long span bridges, where the ground motion at the different supports varies as a consequence of the phase delay, amplitudes and types of the seismic waves, considering the scale of ground heterogeneities corresponding to the structural frequencies involved. The methodologies for the seismic analysis are then reviewed, combined with each form of seismic representation.

4.2.1 Wind loads

The large flexibility of cable-supported bridges makes these structures prone to undergo large dynamic motions induced by wind loads. In the past, several cases of damage or even failure of cable-supported bridges occurred in consequence of wind forces. The most well-known example is the Tacoma Narrows Bridge which, under a mild gale, begun to oscillate and dramatically increased the vibration till the collapse, in a period of about three hours. Figure 4.1 shows some well-known pictures taken during this period of time, evidencing the incredible large motions and the level of destruction resultant from wind action (Smith, 1974).

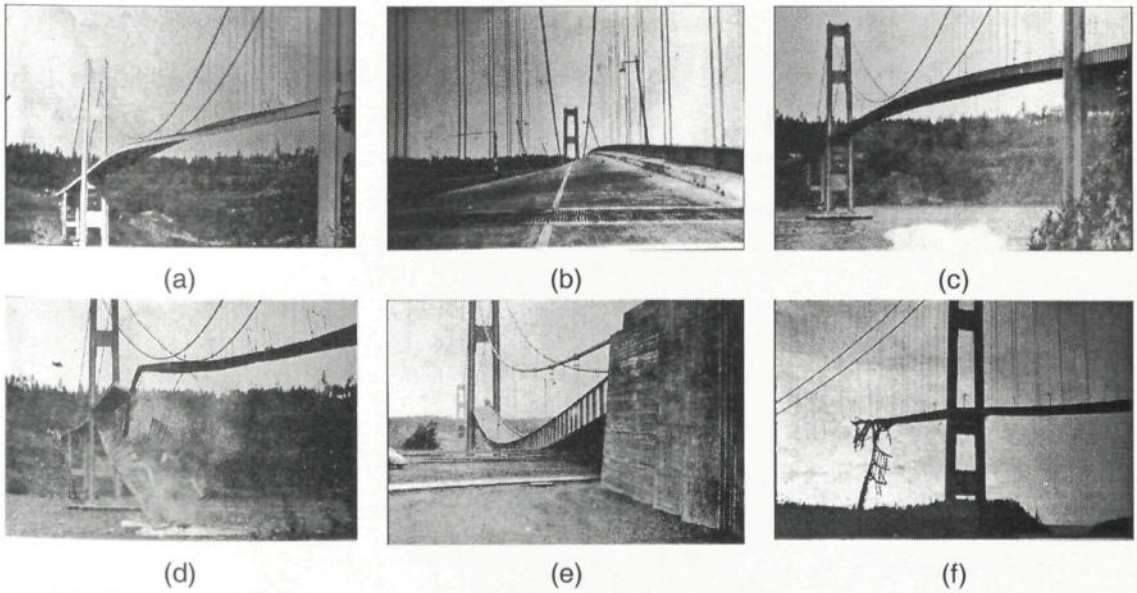


Figure 4.1. Collapse of the Tacoma Narrows Bridge: (a) Twisting motion at centre span prior to failure; (b) Twisting motion, maximum inclination of approximately 45° to static position; (c) First concrete dropped out of the roadway; (d) Break of the suspension span; (e) Sag in east side span after failure (13.7m); (f) Shortly after the failure (Smith, 1974).

The failure of Tacoma Narrows Bridge on 7 November 1940 has brought a new conscience on the importance of aerodynamics of bridges and motivated the intensive research that has been done during the last decades. For being more recent than suspension bridges, cable-stayed bridges have benefited from the experience acquired with the former system type. Although cable-stayed bridges are indeed stiffer than suspension systems and, to the knowledge of the author, there is no reported failure of a cable-stayed bridge, wind effects in this type of structures are also important and should be considered with care.

A first aspect in the characterization of the bridge resistance to wind loads, is the definition of a suitable *wind model*. This model comprehends the definition of the mean wind and turbulence of the site, the characterization of these parameters with height, and of the

spatial structure of the turbulent component. Additionally, knowledge of the wind climate, extreme winds, directional pattern and types of storms are of interest (Davenport, 1994).

4.2.1.1 Definition of mean wind

A basic definition of wind is given in the literature (Podolni & Scalzi, 1976; Simiu & Scanlan, 1996; Dyrbye & Hansen, 1999) as the air movement caused by atmospheric pressure differentials that occur over the surface of the earth. At a sufficient distance from earth, the air flow is unaffected by friction at the ground surface and it is assumed horizontally homogenous, being characterized by an universal velocity, defined as the *gradient velocity* U_G.

Close to the earth surface, ground obstructions retard the movement of air. Figure 4.2 represents the effect of the surface roughness on the wind velocity, evidencing that the rougher the terrain is, the more reduced the wind speed is. The height at which the gradient velocity is attained is defined as the *gradient height* h_G. Table 4.1 resumes typical values of h_G according to the surface roughness for the categories considered in *EC1.*

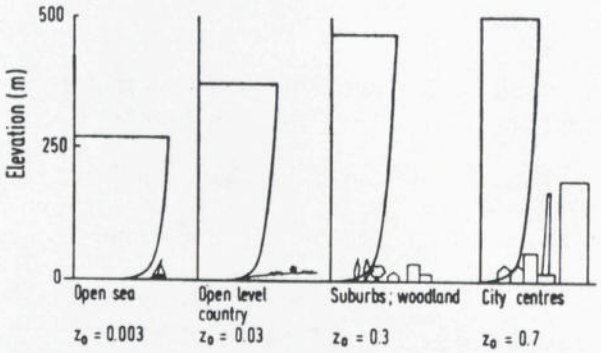


Figure 4.2. Effect of the surface roughness on the wind velocity (Balendra, 1993).

The interaction of the natural wind with the surface topography produces turbulence. Turbulence or gusts are associated with wind velocity fluctuations, which are spatial and temporal in character.

So, in the so-called *atmospheric boundary layer*, the region limited by the gradient height h_G, the wind field is characterized by the following components

in the longitudinal direction: $U(x,y,z,t)=\overline{U}(z)+u(x,y,z,t)$ (4.1a)

in the lateral direction: $v(x,y,z,t)$ (4.1b)

in the vertical direction: $w(x,y,z,t)$ (4.1c)

The longitudinal component of the wind velocity is characterized by the sum of a mean wind velocity $\overline{U}(z)$ that depends only on the height above the ground z, with a fluctuating component $u(x,y,z,t)$ that is spatial in nature. Figure 4.3 illustrates the evolution of the wind velocity (solid curve) with height at a particular time instant.

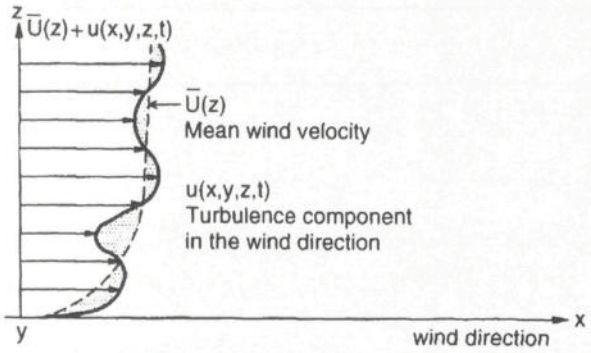


Figure 4.3. Evolution of wind velocity with height above the ground (Dyrbye & Hansen, 1999).

The mean wind velocity $\overline{U}(z)$, also represented in that Figure, has a variation with height that can be approached by a logarithmic profile. *EC1* adopts the following definition for $\overline{U}(z)$

$$\begin{aligned} &\overline{U}(z) = U_{ref} \cdot c_r \cdot c_t \cdot ln(\frac{z}{z_0}), && \text{if } z_{min} \le z \le 200\,m \\ &\overline{U}(z) = U(z_{min}), && \text{if } z < z_{min} \end{aligned} \tag{4.2}$$

The coefficient $c_r(z)$ in these equations is a coefficient that accounts for the variability of the mean wind velocity at the site due to the height above the ground level, and to the roughness of the terrain, depending on the wind direction. This coefficient is defined by

$$\begin{aligned} &c_r(z) = k_r \cdot ln(z/z_0), && \text{if } z_{min} \le z \le 200m \\ &c_r(z) = c_r(z_{min}), && \text{if } z < z_{min} \end{aligned} \tag{4.3}$$

where k_r is a *terrain factor* whose values are indicated in Table 4.1, and the quantity z_0, designated as the *roughness length*, can be interpreted as the size of a characteristic vortex formed as the result of the friction between the air and the earth surface. *EC1* specifies values of z_0 for each category of terrain, according to Table 4.1. This Table also shows values for the minimum height above the ground or water level z_{min} below which the wind speed is considered constant.

The coefficient $c_t(z)$ in equations (4.2) accounts for the increase of mean wind speed over isolated hills and escarpments. This coefficient is appropriately defined in *EC1*.

Table 4.1. *Gradient height* h_G, *terrain factor* k_r, *roughness length* z_0 and *minimum height* z_{min} as a function of the terrain roughness

	Type of terrain	h_G (m)	k_r	z_0 (m)	z_{min} (m)	ε
I	Rough, open sea, lakes with at least *5km* fetch upwind and smooth flat country without obstacles	*250*	*0.17*	*0.01*	*2*	*0.13*
II	Farmland with boundary hedges, occasional small farm structures, houses or trees	*300*	*0.19*	*0.05*	*4*	*0.26*
III	Suburban or industrial areas and permanent forests	*400*	*0.22*	*0.3*	*8*	*0.37*
IV	Urban areas in which at least *15%* of the suraface is covered by buildings with an average height exceeding *15m*	*500*	*0.24*	*1*	*16*	*0.46*

Finally, the quantity U_{ref} in equations (4.2) is the so-called *reference wind velocity*. This velocity is defined by *EC1* as the expected value of a maximum mean wind velocity of *10* minute duration at an height above the water or ground of *10m*, considering a *roughness length* z_0 of *0.05m*, and an annual probability of exceedence of *0.02*, corresponding to a recurrence period of *50* years. According to *EC1*, U_{ref} is determined from the product

$$U_{ref} = c_{DIR} \cdot c_{TEM} \cdot c_{ALT} \cdot U_{ref,0} \tag{4.4}$$

where $U_{ref,0}$ is a basic value of the *reference wind velocity*, defined for each country according to the particular location and climate, based on systematic measurements taken during a period of several years. For the countries covered by the *Eurocode 1*, $U_{ref,0}$ varies in the range *19m/s* to *50m/s*, for certain parts of Sweden and Norway, respectively. In Portugal, for example, the *EC1* defines two different values of $U_{ref,0}$, in association with the two national zones considered in the *Portuguese Code on Safety and Actions*: the *zone B*, covering the archipelagos of Azores and Madeira, and the continental territory, the coastal areas from the coast line to *5km* inland, the estuaries and regions with altitudes above *600m*; and the *zone A*, covering all the territories not included in *zone B*. For *zone A*, $U_{ref,0} = 28\,m/s$, while for *zone B*, $U_{ref,0} = 31\,m/s$.

The weighting coefficients c_{DIR}, c_{TEM}, and c_{ALT} in equation (4.4) introduce additional corrections in the definition of the reference wind velocity, taking into consideration the change of extreme winds with direction of incidence, the temporary character of particular structures, or the influence of altitude, respectively.

In all cases these coefficients are taken as *1.0* whenever not specified for the particular location of the structure.

The *EC1* allows a correction of the reference wind velocity U_{ref}, considering an annual probability of exceedence *p* different from *0.02*

$$U_{ref}(p) = U_{ref} \cdot \left(\frac{1 - K_1 \cdot ln[-ln(1-p)]}{1 - K_1 \cdot ln[-ln(0.98)]} \right)^n \tag{4.5}$$

where U_{ref} is the wind velocity above defined, corresponding to $p = 0.02$, K_1 is a shape parameter, with a representative value of *0.2*, and *n* is an exponent, taken as *0.5* when not specified.

In effect, return periods of *100* years (*p=0.01*) have been considered in the definition of wind action for certain long span bridges. This was for example the case of the Skarnsundet Bridge, in Norway (Hansvold, 1994).

4.2.1.2 Definition of the site turbulence

Reference is now made to the fluctuating components of wind velocity, *u*, *v* and *w*, in equations (4.1). In view of their nature, these components are characterized probabilistically by parameters that depend on the standard deviation and on integral length scales, and by power spectral density functions and normalized co-spectra (Dyrbye & Hansen, 1999).

Assuming that the terrain is homogeneous, the air flow is horizontal and consequently the standard deviation of the wind fluctuations only varies with height. Up to a height of about *100m-200m* above ground, the standard deviations associated with *u*, *v* and *w*, σ_u, σ_v and σ_w respectively, are related through (Dyrbye & Hansen, 1999)

$$\sigma_v \approx 0.75\,\sigma_u \qquad \sigma_w \approx 0.5\,\sigma_u \tag{4.6}$$

A measure of the wind turbulence in the along-wind direction is obtained from the *turbulence intensity* $I_u(z)$, defined by

$$I_u(z) = \frac{\sigma_u(z)}{\overline{U}(z)} \tag{4.7}$$

and given in *EC1* by

$$I_u(z) = \frac{k_r}{c_r(z) \cdot c_t(z)} \tag{4.8}$$

where $c_r(z)$ and $c_t(z)$ are the *roughness* and *topography coefficients* previously defined.

The frequency content of the fluctuating along-wind component of turbulence is generally represented by the *nondimensional power spectral density* $R_N(z,f)$, defined as (Dyrbye & Hansen, 1999)

$$R_N(z,f) = \frac{f \cdot S_u(z,f)}{\sigma_u^2(z)} \tag{4.9}$$

where f is the frequency in Hertz, $S_u(z,f)$ is the power spectrum, and σ_u is the standard deviation of the along-wind turbulence component.

The proposal from *EC1* to the definition of $R_N(z,f)$ is the function represented in Figure 4.4 for a height above the ground of *10m*, given by

$$R_N(z,f) = \frac{6.8 f_L}{(1+10.2 f_L)^{5/3}} \tag{4.10}$$

where the non-dimensional frequency f_L is defined as

$$f_L = f \cdot \frac{L_u^x(z)}{\overline{U}(z)} \tag{4.11}$$

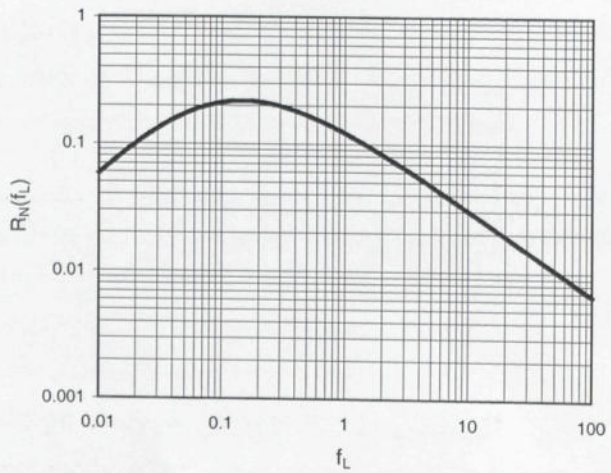


Figure 4.4. Frequency distribution of along-wind component of turbulence. Proposal from *EC1*.

The quantity $L_u^x(z)$ in equation (4.11) is designated as an *integral length scale*, a function that measures the average size of an eddy (in this case, in the *x*-direction, for the

along-wind direction), which is calculated from the cross correlation $R_u(\Delta x)$ between the turbulence component u in two points separated by a distance Δx and measured simultaneously

$$L_u^x(z) = \int_0^\infty R_u(\Delta x) \cdot d(\Delta x) = \frac{E\{u(x,y,z,t) \cdot u(x+\Delta x,y,z,t)\}}{\sigma_u^2(z)} \tag{4.12}$$

The *EC1* gives the following formula for calculation of $L_u^x(z)$

$$L_u^x(z) = \begin{cases} 300 \cdot (z/300)^{\varepsilon} & \text{if } z_{min} \le z \le 300m \\ 300 \cdot (z_{min}/300)^{\varepsilon} & \text{if } z \le z_{min} \\ 300 & \text{if } z > 300m \end{cases} \tag{4.13}$$

in which ε is a parameter defined according to the terrain category (Table 4.1).

With regard to the frequency content of the lateral and vertical turbulence components, the following approaches given by Simiu and Scanlan (1986) can be used

$$\frac{f \cdot S_v(z,f)}{u_*^2} = \frac{15 f_z}{(1+9.5 f_z)^{5/3}} \tag{4.14}$$

$$\frac{f \cdot S_w(z,f)}{u_*^2} = \frac{3.36 f_z}{1+10 f_z^{5/3}} \tag{4.15}$$

where u_* is the friction velocity, that can be related with the standard deviation of the turbulence component σ_u through the relation

$$\sigma_u = A u_* \tag{4.16}$$

with the constant $A \approx 2.5$ if $z_0 = 0.05m$, and $A \approx 1.8$ if $z_0 = 0.3m$ (Dyrbye & Hansen, 1999), the non-dimensional frequency f_z, known as the *Monin similarity coordinate*, being given by

$$f_z = \frac{f z}{\bar{U}(z)} \tag{4.17}$$

Many other proposals have been presented in the literature for the description of the spectral content of the wind turbulence. These are summarized and compared in an extensive research by Mendes (1994).

Finally, a measure of the *spatial correlation* of the turbulence content can be obtained from a *normalized cross-spectrum* $S_N(P_1,P_2,f)$, that describes the probabilistic dependence between the turbulent component at two points P_1 and P_2 at a frequency f and is given by

$$S_N(P_1,P_2,f)=\frac{S_{uu}(P_1,P_2,f)}{S_u(P_1,f)\cdot S_u(P_2,f)} \tag{4.18}$$

$S_{uu}(P_1,P_2,f)$ is the cross-spectrum between the longitudinal turbulence components at points P_1 and P_2, and $S_u(P_i,f)$ is the power spectrum of the longitudinal turbulence component in the point P_i.

The normalized cross-spectrum S_N defined by equation (4.18) is a complex function, whose real part Ψ_u is called the *normalized co-spectrum*, and the imaginary part, the *normalized quad-spectrum*. Ψ_u is the quantity normally used in the calculation of the response. Depending on the size of the vortices generated in the wind field, Ψ_u decreases as the distance between P_1 and P_2 increases. This decrease has been described empirically by exponential functions by several authors. The proposal from *EC1* is based on a formula by Davenport (1967, 1977) and applies to two points $P_1(x,y,z)$ and $P_2(x,y+\Delta y,z+\Delta z)$ located in a plane orthogonal to the mean wind direction x

$$\Psi_u(\Delta y,\Delta z,f)=exp(-\frac{2f\cdot\sqrt{(c_y\cdot\Delta y)^2+(c_z\cdot\Delta z)^2}}{\overline{U}(z)+\overline{U}(z+\Delta z)}) \tag{4.19}$$

The coefficients c_y and c_z are non-dimensional decay constants that are assumed to be *11.5* in average.

4.2.1.3 Characterization of wind loads on a bridge structure

The information above obtained on the wind velocities and fluctuations should now be converted either on pressures, or on resultant forces and moments over the structure under analysis.

The most common procedure in the analysis of bridges is the adoption of force-based formulations. In these formulations, the *total wind force* F_t on the bridge can be obtained from the sum of three components, namely the *mean wind load* $F_{\overline{U}}$, the *fluctuating wind load* due to turbulence F_u and a *motion-induced wind load* F_m

$$F_t=F_{\overline{U}}+F_u+F_m \tag{4.20}$$

The later component F_m is only relevant for flexible structures, and results from the interaction between the air flow and the motion of the structure. This component is of major importance in suspension and cable-stayed bridges.

Mean wind load

The *mean wind load* $F_{\bar{U}}$ on a bridge deck is the static component of the wind load, which can be evaluated on the assumption that the mean wind velocity $\bar{U}$ and the corresponding angle of incidence are constant along a flat plate cross section. Three components describe the force $F_{\bar{U}}$: the *drag force* $F_{\bar{U}}^{D}(y)$, in the direction of the mean wind load, the *lift force* $F_{\bar{U}}^{L}(y)$, in the direction perpendicular to $F_{\bar{U}}^{D}(y)$, and the *moment* $F_{\bar{U}}^{M}(y)$. These forces, represented in Figure 4.5, are defined for a unit length of the deck by

$$F_{\bar{U}}^{D}(y) = \frac{1}{2}\rho \bar{U}^{2}(y) B C_{D}(\alpha(y)) \tag{4.21a}$$

$$F_{\bar{U}}^{L}(y) = \frac{1}{2}\rho \bar{U}^{2}(y) B C_{L}(\alpha(y)) \tag{4.21b}$$

$$F_{\bar{U}}^{M}(y) = \frac{1}{2}\rho \bar{U}^{2}(y) B^{2} C_{M}(\alpha(y)) \tag{4.21c}$$

in which ρ is the air density, $\bar{U}(y)$ is the *mean wind velocity* at a coordinate *y* along the deck, *B* is a typical reference dimension of the structure, and C_D, C_L and C_M are non-dimensional *aerodynamic coefficients* or *shape factors*, that depend on the angle of incidence of the wind α, and are obtained experimentally from wind tunnel tests. Note that, for the most part of deck cross-sections, the shape factors are actually time dependent. This is a consequence of the *signature turbulence* generated by the deck cross-section when immersed in the uniform flow (Scanlan, 1993). The constant values usually adopted for C_D, C_L and C_M must be then interpreted as mean values.

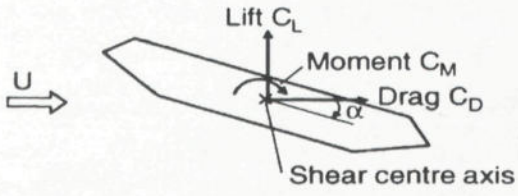


Figure 4.5. Components of mean wind load on a bridge deck.

Both the *turbulence* (motion independent) and the *motion-induced* forces, F_u and F_m, designated respectively as *buffeting* and *aeroelastic* forces, can be described either in the frequency domain (Scanlan & Jones, 1990; Jain *et al.*, 1995), the most conventional procedure, or in the time domain, according to most recent formulations (Kovàcs *et al.*, 1992; Fujino *et al.*, 1995; Grillaud *et al.*, 1997; Mendes & Branco, 1997; Boonyapinyo *et al.*, 1999). A

frequency domain approach will be used here, in which the Fourier Transform of a generic force component $F_i^j(y,t)$ is defined by

$$\overline{F}_i^j(y,K) = \int_0^\infty F_i^j(y,s)\cdot e^{-iKs} ds \tag{4.22}$$

where $K = B\omega/U$ is a *reduced frequency* of the system when oscillating at the circular frequency ω, and $s = Ut/B$ is a *reduced time instant.* Note that the mean wind velocity $\overline{U}$ is now designated simply by *U*, the symbol " $\bar{}$ " being used to designate a Fourier Transform.

Buffeting forces

The three components of the *buffeting forces* can be then defined by the following formulae (Scanlan, 1994), for a particular angle of incidence of wind α_0

$$\overline{F}_u^D(y,K) = \frac{1}{2}\rho U^2(y)B\cdot\left\{2C_D(\alpha_0)\frac{\overline{u}}{U}\chi_u + C_D'(\alpha_0)\frac{\overline{w}}{U}\chi_w\right\} \tag{4.23a}$$

$$\overline{F}_u^L(y,K) = \frac{1}{2}\rho U^2(y)B\cdot\left\{2C_L(\alpha_0)\frac{\overline{u}}{U}\chi_u + \left[C_L'(\alpha_0) + C_D(\alpha_0)\right]\frac{\overline{w}}{U}\chi_w\right\} \tag{4.23b}$$

$$\overline{F}_u^M(y,K) = \frac{1}{2}\rho U^2(y)B^2\cdot\left\{2C_M(\alpha_0)\frac{\overline{u}}{U}\chi_u + C_M'(\alpha_0)\frac{\overline{w}}{U}\chi_w\right\} \tag{4.23c}$$

The quantities C_D', C_L' and C_M' are the *aerodynamic coefficient* derivatives with respect to the angle of incidence of wind, and are obtained experimentally. The functions χ_u and χ_w are complex *aerodynamic admittance functions*, that express the relationship between the fluctuating wind velocity and the fluctuating wind load acting on the structure (Dyrbye & Hansen, 1999). These functions are determined experimentally and have unit values in *quasi-steady formulations.* According to Grillaud *et al.* (1997), the assumption of unit values for these functions either in the spectral, or in the time domain approach, can lead to an overestimation of the response by about *50%.*

Aeroelastic forces

The *aeroelastic forces* depend on the three-dimensional motion, with components $h(y)$, $p(y)$ and $\alpha(y)$ defined according to Figure 4.6, and can be evaluated based on the model introduced by Scanlan (1994) from

$$\bar{F}_m^D(y,K)=\frac{1}{2}\rho U^2(y)BK^2\cdot\left[(iP_1^*+P_4^*)\frac{\bar{p}}{B}+(iP_2^*+P_3^*)\bar{\alpha}\right] \tag{4.24a}$$

$$\bar{F}_m^L(y,K)=\frac{1}{2}\rho U^2(y)BK^2\cdot\left[(iH_1^*+H_4^*)\frac{\bar{h}}{B}+(iH_2^*+H_3^*)\bar{\alpha}\right] \tag{4.24b}$$

$$\bar{F}_m^M(y,K)=\frac{1}{2}\rho U^2(y)B^2K^2\cdot\left[(iA_1^*+A_4^*)\frac{\bar{h}}{B}+(iA_2^*+A_3^*)\bar{\alpha}\right] \tag{4.24c}$$

where P_i^*, H_i^* and A_i^* are non-dimensional functions of reduced velocity ($=1/K$) known as *flutter derivatives*. These functions can be determined experimentally (Sarkar *et al.*, 1994).

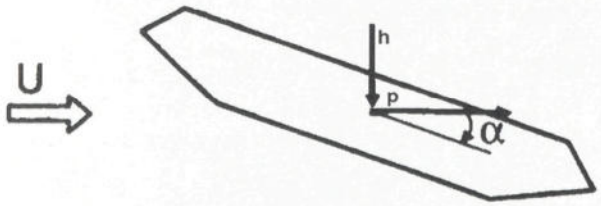


Figure 4.6. Displacement coordinates of cross-section.

4.2.1.4 Instability phenomena

The above mentioned formulae can be used to evaluate the response to both the static and dynamic components of the wind. In this procedure, that requires the development of a finite element model of the structure and the solution of an eigenvalue problem for the determination of the modal response (spectral approach) (Scanlan, 1994; Jain *et al.*, 1995), or the evaluation of the structural response by direct integration methods (Fujino *et al.*, 1995; Boonyapinyo *et al.*, 1999), a series of instability phenomena can be identified: *torsional divergence*, *flutter*, *galloping* and *vortex shedding/lock-in*. Although it is out of the scope of this dissertation to present a thorough description of each phenomenon, a brief insight and some guidelines towards the assessment of the critical conditions for instability will be presented.

A first aspect to refer is the concept of *instability*. *Torsional divergence*, *flutter* and *galloping* are instability phenomena in the true assessment of the term, as they provoke a divergent structural response that, in the limit, leads to the collapse. On the contrary, *vortex shedding* produces limited amplitude oscillations in a specific range of the wind velocity.

The *torsional divergence*, *flutter* and *galloping* are *aeroelastic phenomena* that result from the generation of motion-dependent forces on the structure. The components of the *aeroelastic forces* that depend on the bridge displacements will affect its stiffness, while those that depend on the velocity will modify the damping.

Torsional divergence

The *torsional divergence*, also called *divergence*, is a non-oscillatory phenomenon that occurs in virtue of non-balanced moment forces on the bridge deck. The condition for the occurrence of *divergence* is that the structural modal torsional stiffness K_α equals the aerodynamic modal torsional stiffness K_M. This leads to a critical wind velocity U_{div} given by

$$U_{div} = \sqrt{\frac{2K_\alpha}{\frac{dC_M}{d\alpha}\rho B^2}} \tag{4.25}$$

and a limiting criterion, given by *EC1*, is that the mean wind velocity at the site U defined by equations (4.2) satisfies the condition

$$U_{div} > 2U \tag{4.26}$$

Galloping

The phenomenon of *galloping* is also due to non-balanced drag and lift forces, but in this case along the vertical direction. The consequence is the generation of a negative aerodynamic damping that cancels the structural damping, leading to growing vibrations in a direction almost perpendicular to the wind direction. The Glauert-Den Hartog criterion for *galloping instability* will be deduced in Chapter six for the specific case of cable vibration (see equation (6.26)), as well as the onset velocity for the occurrence of galloping and the criterion from EC1 to avoid this phenomenon. This criterion applies equally to bridge decks, provided that appropriately chosen parameters are employed.

Flutter

Flutter is the most serious phenomenon of instability in cable-supported structures. The mathematical condition for the occurrence of *flutter* is that the determinant of an impedance complex matrix containing both stiffness and damping terms vanishes (Scanlan, 1994). In physical terms, this corresponds to the following: Assume that the bridge deck is immersed in an air flow (turbulent or not), the mean velocity of which is increasing slowly. The motion of the deck generates increasing aerodynamic damping and stiffness that may be positive or negative, depending on the vibration mode. If the aerodynamic stiffness and / or the aerodynamic damping are negative, a limit condition occurs when the mean wind velocity attains a value that originates the vanishing of the total stiffness or damping of the system. Experience has shown (Dyrbye & Hansen, 1999) that in general, the aerodynamic damping associated with the vertical bending modes is positive for long span bridge decks, while it can

actually have negative values for torsional modes of non-streamlined decks. So, for single-mode approaches (Scanlan &Jones, 1990), *flutter* is expected to occur only for torsional modes. This is in practice a phenomenon of *torsional galloping.* But even in the case of positive aerodynamic damping associated with all modes *flutter instability* can occur. This situation arises in consequence of the coupling between two vibrational modes. According to Dyrbye & Hansen (1999), some aeroelastic terms associated with specific aerodynamic derivatives will tend to increase the vertical stiffness and reduce the torsional stiffness. So, when the torsional natural frequency is only slightly larger than the vertical natural frequency (in still air), a significant risk of coupled oscillations exists and it is important to assure that the *critical flutter velocity* $U_{Flutter}$, determined either from wind tunnel tests on sectional models of the deck, or from the numerical solution of the above referred vanishing determinant (Scanlan, 1994), satisfies a criterion of the type

$$U_{Flutter} > A \cdot U \tag{4.27}$$

An indicative value for the constant *A,* given by BS5400, is *1.3.*

Vortex excitation/ Lock-in

Finally, the phenomenon of vortex excitation is directly motivated by the presence of a non-streamlined section in the flow. Independently of the body being fixed or not, the generation of opposite vortices in the upper and lower faces at a particular shedding frequency originates crosswind harmonic forces. In the presence of flexible bodies, these harmonic forces will enhance the crosswind vibration. The situation is particularly critical when the structural frequency of vibration coincides with the vortex shedding frequency, generating an aeroelastic phenomenon designated as *lock-in.* The phenomenon of *vortex-shedding/ lock-in* is described with some detail in Chapter six, and a methodology based on the simplified *vortex-resonance model* as prescribed by the *EC1* is presented for the assessment of the maximum amplitude of vibration of cables, which may be equally applied to the deck cross-section, provided that the parameters are conveniently chosen.

4.2.2 Moving loads

4.2.2.1 Traffic loads

In addition to the static response, traffic loads induce dynamic effects. These effects are conditioned by a significant number of variables, such as those related with vehicle characteristics (type of suspension, weight and spacing between the axles), the traffic flow (type of vehicle and distribution along the stream, velocities and relative distances), the road

roughness, and the dynamic behaviour of the bridge structure (natural frequencies, structural damping).

The permanent actuation of traffic loads poses the problem of fatigue, which is of crucial importance when assessing the remaining service life of existing roadway and railway bridges, and particularly old steel railway bridges, or when defining maintenance and retrofit measures to allow for increased traffic loads. In the case of cable-stayed bridges, particular attention should be addressed to the assessment of the fatigue life of stay cables of both newly built and existing bridges. Cables are, in effect, very flexible elements characterized by a very low structural damping. The fact that the corresponding fundamental vibration modes have natural frequencies in the range associated with traffic loads, i.e., *1.5Hz* to *4.5Hz*, makes these elements very prone to vibrations and sensitive to ruptures by fatigue.

For design purposes, the procedure adopted by national codes worldwide to determine the effects produced by traffic loads consists in employing simplified models of static loads whose effects are amplified by appropriately defined factors designated differently according to the author and country as *dynamic amplification factors DAF*, *dynamic amplifications DA*, or *impact factors* I. These factors relate the maximum dynamic response R_{dyn} and the static response R_{sta}, and are defined as follows

$$DAF = \frac{R_{dyn}}{R_{sta}} \tag{4.28a}$$

$$DA = \frac{R_{dyn} - R_{sta}}{R_{sta}} \qquad \Rightarrow \; DAF = 1 + DA \tag{4.28b}$$

$$I(\%) = \left(\frac{R_{dyn}}{R_{sta}} - 1 \right) \cdot 100\% \qquad \Rightarrow I = (DAF - 1) \cdot 100\% \tag{4.28c}$$

Most of the codes used to specify the dynamic amplification factors as a function of the bridge fundamental natural frequency or the span length, in order to contemplate the resonance effect that results from the closeness between a fundamental bridge frequency and an exciting frequency. Figure 4.7, developed by Karoumi (1996), presents a comparison of *DAF*s specified by different codes as a function of the bridge natural frequency. For the codes that define the *DAF* as a function of the span length *L*, the fundamental natural frequency f_0 was evaluated based on the function

$$f_0 = 82\, L^{-0.9} \tag{4.29}$$

which was estimated by Paultre *et al.* (1992), based on experimental tests (see Figure 4.8). Although it is a fact that the static loads are also defined differently from code to code, great discrepancies can be found amongst the different *DAF* proposals.

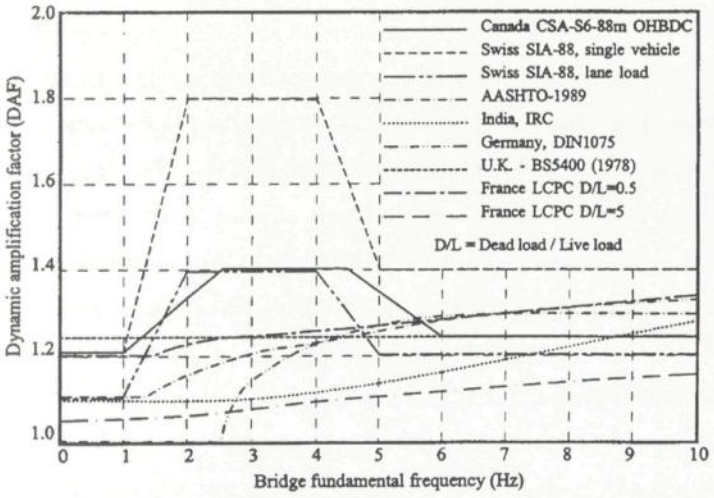


Figure 4.7. Comparison of *DAF*s as functions of fundamental frequency for different codes (Karoumi, 1996).

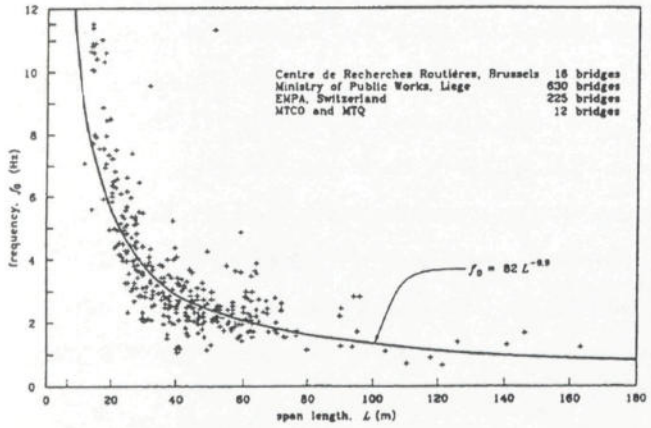


Figure 4.8. Fundamental frequency of bridges as function of maximum span length, based on hundreds of experimental tests (Kirkegaard, 1997).

Recently, several codes adopted a single value for such dynamic factor, in order to simplify the evaluation of traffic loads at the conception stage (Broquet, 1999). In *EC1*, the *DAF* is implicitly included in the formulation of the live loads.

It is important to note that the above presented definitions of the dynamic amplification factors (see equations (4.28)) are quite general and allow different interpretations and forms of evaluation. Moreover, *DAF*s, *DA*s and *Is* depend on quantities that are random in nature and should therefore be treated statistically.

Considering the different factors that influence the evaluation of dynamic effects on a bridge, the following comments should be addressed:

- First of all, the design loads and amplification factors adopted by codes do not generally apply to long-span bridges, i.e., bridges with span lengths greater than

200m. In effect, the design loads defined for a small bridge correspond to the heaviest truck or trucks that can travel over it. In a long-span bridge, the deck won't be entirely covered by the heaviest vehicles and in fact, as the loaded length of the bridge increases, the average load per unit length will decrease, as cars and light vehicles are injected in the traffic stream (Buckland et al., 1980). So, the application of load models prescribed by national codes in the design of a long span bridge would lead to an extremely conservative design. This information has been corroborated by Kirkegaard (1997), who compared simulated traffic load effects with those calculated with the Swiss design traffic load model. Note however that some codes, like the BS 5400 (1978), already consider a decrease of the uniform live load with the loaded length (see Figure 4.9);

- Another aspect is that the density of traffic varies according to the importance of the road. Hence, the design of a long span bridge integrated in a particular type of road should incorporate a study of the traffic flow and composition for that particular location. In this respect, reference should be made to the studies of Bakht and Jaeger (1990), who proposed multipresence reduction factors to be used in conjunction with AASHTO codes (1992) for different classes of highways. It is also worth mentioning the probabilistic models used to represent the natural variation of traffic developed by Bailey (1996), which incorporate the traffic composition, the distance between vehicles, axle group weights and vehicle geometry, and the preparatory works for *EC1* (Bruls & Sedlacek, 1989; Mathieu *et al.*, 1991), which present a synthesis of traffic data available in the EU countries involved, namely in terms of traffic flow, vehicle classification and silhouettes, inter-vehicles spacings and axles and lorries weights.

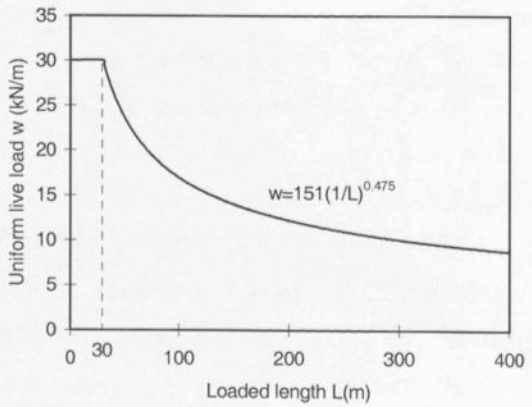


Figure 4.9. Uniform live load, according to BS 5400 (1978), including dynamic effects.

- Assuming that static load models are defined for a particular long span cable-stayed bridge, the quantification of dynamic amplification factors needs to be addressed. Although many studies have been performed for conventional small and medium size bridges, only few authors dedicated considerable effort to the

study of the effect of traffic loads to this particular type of bridges. These studies involve two main components, numerical and experimental. Numerical simulations of the bridge response are the most common. Examples of such studies are those from: Alessandrini *et al.* (1984) and Brancaleoni *et al.* (1987), who investigated the train-structure interaction in cable-stayed railway bridges; Wang and Huang (1992), who analysed the effect of the road roughness in the dynamic response of a cable-stayed bridge; Khalifa (1993), who performed parametric studies on different 3D models considering trains of moving standard trucks and investigated the effect of moving loads in the vibration of cables; Chatterjee *et al.* (1994), who performed parametric time domain analyses of cable-stayed bridges, considering both the vehicle-structure interaction and the roughness of the road surface; Fuheng (1996), who equally investigated the dynamic response of a cable-stayed bridge under moving loads using vehicle-structure interaction models and considering the dynamics of cables; Karoumi (1998), who developed methods for time domain linear analysis by modal superposition or non-linear analysis by direct integration considering the vehicle-structure interaction. With regard to experimental investigation of the effect of moving vehicles in cable-stayed bridges, reference should be made to the tests performed by the team of Walther on a physical model of a *200m* span cable-stayed bridge at a scale of *1:20* under the moving load of a model vehicle (Walther *et al.*, 1988). In the particular issue of cable vibration, reference should be made to the work of Sugianto (1990), who used fatigue analysis procedures to assess the fatigue life of a stay cable of a newly built cable-stayed bridge, the Rama IX bridge, in Thailand, modelling the speed, mass of the trucks and the roughness of the surface using a probabilistic approach. Another interesting study on this particular bridge (Wieland & Lukkunaprasit, 1990) refers to the analysis of cable and deck vibrations partly motivated by significant roughness of the bridge pavement, leading to rather violent secondary vibrations of the lamp posts. A final reference to the numerical/ experimental evaluation of dynamic amplification factors and assessment of fatigue in cables of cable-stayed bridges, is the ongoing project for the monitoring of a cable-stayed bridge recently constructed in Portugal, the Salgueiro Maia Bridge, at Santarém, in which the author is directly involved, and that comprehends an extensive instrumentation of the bridge deck and cables (Calçada & Cunha, 2000);

- As referred above, an important factor in the evaluation of dynamic effects is the roughness of the pavement. Three different types of roadway roughness may be found on road bridges: local extreme unevenesses (e.g. transition joints, road holes or artificial obstacles), regular unevenesses (e.g. surface waves due to fabrication) and irregular unevenesses. The two first unevenesses are deterministic and may be described geometrically. However, irregular

unevenesses have a random character and so must be idealized on the basis of stochastic processes.

Measurements of road surface roughness on bridges (Honda *et al.*, 1982) permitted to conclude that all kinds of roadway pavements have very similar power spectral densities of surface roughness, and that a single parameter shifts the power density up and down, depending on the overall level of roughness.

An approximation of this power spectral density is usually taken in the form of an exponential function, as it happened in preparatory studies of *EC1* (Drosner and Sedlacek, 1989), in which the values of the exponent variable depend on the quality of the pavement (very good, good, average, poor and very poor), according to limits defined in ISO-TC 108 standard for the classification of roadway roughness. These power density functions can also be used to generate artificial pavement profiles to be used in deterministic analyses based on the Monte-Carlo simulation technique (Calçada & Cunha, 1998).

In the case of railway bridges, it is of interest to simulate different types of track irregularities, as it is evidenced in Report 2 on Question D160 from the Office for Research and Experiments of the International Union of Railways (UIC). Among these irregularities, the following can be considered: dishing or deflection of the bridge caused by the weight of the bridge itself and/or initial static load; deflection of the rail bearers and cross-girders; isolated track irregularities; longitudinal track curvature over the bridge ends.

With respect to the measurement of road surface irregularities, two techniques can be followed, either employing inverse identification methods, in which the surface roughness is calculated from vibrational data of a vehicle whose dynamic properties are well-established, or by a more recent technology based on a laser profilometer mounted on a particular vehicle running over the surface;

– In the studies for the assessment of amplification factors, the modelling of the vehicle dynamics has been considered with different degrees of sophistication (Fryba, 1971; Akin & Mofid, 1989; Humar & Kashif, 1995). An example of a simple one-axle vehicle model is represented in Figure 4.10. This model was considered by Drosner and Sedlacek (1989) in the preparatory studies of *EC1*, consisting in a discrete rigid multi-body system with non-linear behaviour for which the mass of the wheels and the axle structure are represented by a concentrated mass between the tyre spring and the suspension structure, the suspension structure being idealized as a parallel system consisting of a linear elastic spring for the suspension, a friction element and a viscous damper, and the body mass being considered as a rigid element with translatory mass inertia.

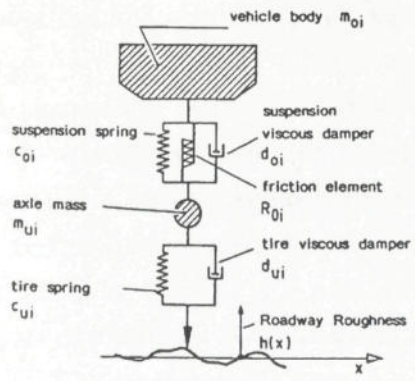


Figure 4.10. One-axle vehicle model (Drosner & Sedlacek, 1989).

- A final remark, concerning the evaluation of dynamic amplification factors, is the evidence of variation of these coefficients with the location of the measurements and the type of efforts under consideration (Broquet, 1999). In general, in situ measurements are reported in terms of dynamic amplification of vertical displacements. As the design stresses are not proportional to the displacements, it is understandable that a more efficient measurement of *DAFs* should be obtained in terms of strains. Another important aspect reported by Broquet (1999) is that different structural elements on the bridge should incorporate different *DAF*s. This is particularly important when the retrofit of a bridge is being considered, as not all the structural elements have the same safety reserve.

4.2.2.2 Pedestrian loads

The dynamic effects caused by pedestrian actions in footbridges constitute another interesting topic in the analysis of cable-stayed bridges. In general, the actions induced by people do not affect the fatigue behaviour and safety of structures. They may however pose problems of serviceability associated with excessive vibrations.

The modelling of dynamic actions associated with pedestrians must consider three different possibilities: *walking*, *running* or *skipping*. The loading associated with each category is characterized by the following parameters: *pacing rate*, *forward speed* and, particularly, by the *time function* of the loading. This function depends on many other variables, which will be referred subsequently.

Pacing rate

The *pacing rate* f_s is the fundamental parameter of the dynamic load. Studies by Matsumoto *et al.* (1978) and Schulze (1980) have shown that f_s is characterized by a Gaussian normal distribution with an average walking rate of *2Hz*, and a standard deviation of *0.13Hz* and

0.18Hz, respectively. From this fact, it can be inferred that *50%* of pedestrians walk at rates between *1.9Hz* and *2.1Hz*, while *95%* pedestrians walk at rates between *1.65Hz* and *2.35Hz* (Pretlove *et al.*, 1997). Table 4.2 indicates average values of the pacing rate for different forms of motion. An important note is the necessity of considering equally the frequency of the second and third harmonic of the normal walking rate at *4Hz* and *6Hz* for vertical motion, as well as the frequency of the first sub-harmonic at *1Hz* for lateral motion. The proximity between a bridge natural frequency and some of these particular frequencies may cause resonance effects, as reported by Fujino *et al.* (1993) in a cable-stayed bridge.

Table 4.2. Average values of *pacing rate* f_s, *forward speed* v_s and *stride length* l_s for *walking* and *running* (Bachmann & Ammann, 1987).

	$f_s(Hz)$	$v_s(m/s)$	$l_s(m)$
slow walk	~1.7	1.1	0.60
normal walk	~2.0	1.5	0.75
fast walk	~2.3	2.2	1.00
slow running (jog)	~2.5	3.3	1.30
fast running (sprint)	~3.2	5.5	1.75

Forward speed

Medical reports indicate that the *forward speed*, or velocity of pedestrian propagation v_s, varies in the range 0.5m/s to 10m/s. The former velocity corresponds to slow walking, while the later is associated with fast running and can only be attained by well-trained sportsmen. This velocity is coupled with the rate of walking through the stride length l_s, according to the representation of Figure 4.11. Table 4.2 includes the average values of the *forward speed* and *stride length* associated with each category of motion.

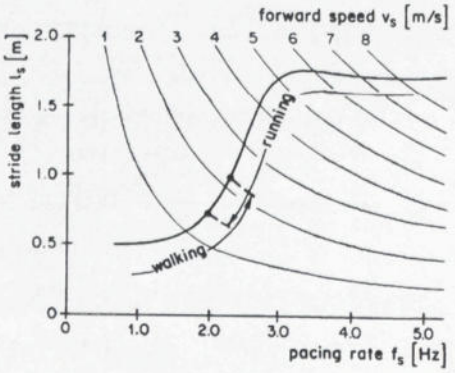


Figure 4.11. *Forward speed* v_s and *stride length* l_s during *walking* and *running* (Bachmann & Ammann, 1987).

Load time function

The load exerted by a pedestrian on the pavement is characterized by a main vertical and secondary lateral components, which depend on a series of factors, like the *walking rate*, the person's *weight* and *sex*, *stepping particularities* (which modify the contribution of the heel and ball), the type of *footwear* (or lack of it) and the *softness of the pavement*. Of these, the most important is the *walking rate*, which determines the form and duration of the loading.

The typical load time function for the vertical component has the approximate form of a saddle, as represented in Figure 4.12, where the two maxima occur as the result of footfall overlap, i.e., when the ball of the foot is pushing off and the heel is stepping forward. The intensity and time duration of the load are dependent on the walking rate, according to the representation of Figure 4.13. When increasing this rate, the intensity of the force applied to the ground increases and the two peaks of the loading function leak. A limit situation is attained at *running*, in which case only one foot is in contact with the floor at time. The loading function is then transformed in a pulse, whose magnitude is around three times the person's weight (see Figure 4.13 (f)).

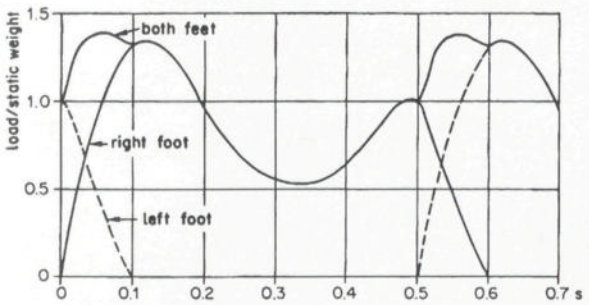


Figure 4.12. Load time function for normal walking (Bachmann & Amman, 1987).

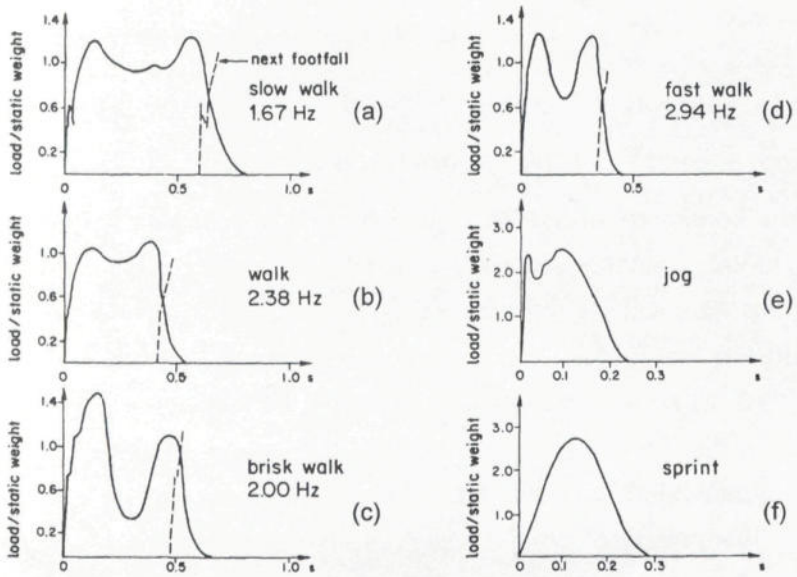


Figure 4.13. Modification of load time function with the pacing rate (Bachmann & Amann, 1987).

The load time function $F_p(t)$ can be modelled analytically, considering the two distinct situations of *walking* and *running*. For *walking*, the following model holds

$$F_p(t) = G + \Delta G_1 \cdot \sin(2\pi f_s t) + \\ + \Delta G_2 \cdot \sin(4\pi f_s t - \varphi_2) + \Delta G_3 \cdot \sin(6\pi f_s t - \varphi_3) \tag{4.30}$$

where G is the weight of a person (normally assumed to be *800N*), ΔG_i is the amplitude of the load component in the ith harmonic, and φ_i is the phase angle of the ith harmonic with respect to the first harmonic.

The values specified for the load components and for the phase angles are (Bachmann & Ammann, 1987)

$$\Delta G_1 = 0.4G, \text{ for } f_s = 2Hz$$

$$\Delta G_1 = 0.5G, \text{ for } f_s = 2.4Hz$$

$$\Delta G_2 \approx \Delta G_3 \approx 0.1G, \text{ for } f_s \approx 2Hz$$

$$\varphi_2 \approx \varphi_3 \approx \pi/2$$

The load time function for running is normally expressed as a sequence of semi-sinusoidal pulses according to the representation of Figure 4.14(a), which are characterized by the formula

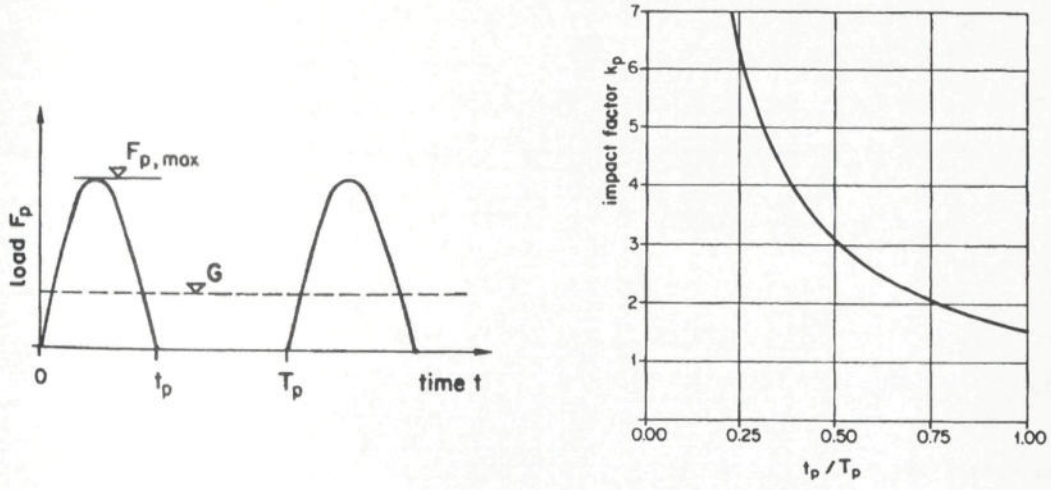
$$F_p(t) = \begin{cases} k_p \cdot G \cdot \sin(\pi t / t_p) & \text{for} \quad t \le t_p \\ 0 & \text{for} \quad t_p < t < T_p \end{cases} \tag{4.31}$$

The quantity $k_p = F_{p,max}/G$ in this equation is designated as *dynamic impact factor*, t_p is the *contact duration*, and T_p is the *pace period* ($T_p = 1/f_s$). The *impact factor* is defined in Figure 4.14(b) as a function of the relative *contact duration* t_p/T_p. The variation of this quantity and of the *contact duration* with the *pacing rate* is illustrated in Figure 4.15.

The horizontal component of the load time function is generally much smaller than the vertical component. This component cannot be neglected however when the bridge is very flexible in the lateral direction, situation in which resonance may produce excessive vibrations.

Figure 4.16 illustrates the vertical dynamic loading and the resulting horizontal vibration displacements for a pedestrian walking with a pacing rate of *2Hz* (Bachmann & Ammann, 1987). It is evident from this Figure that the lateral sway caused by the motion of a person has a dominant frequency that is half the *pacing rate*, while the longitudinal component is dominated by a frequency equal to the vertical *pacing rate*. As for the magnitude of these

components, no values are established in the literature to the knowledge of the author, although the studies of Schulze (1980) gave a lateral force component in the first harmonic (which is dominant) of less than *5%* the person's weight.



(a) (b)

Figure 4.14. Idealized load time function for *jogging* and *skipping* (a) half-sine model; (b) variation of the *impact factor* k_p with the relative *contact duration*, t_p/T_p (Bachmann & Ammann, 1987).

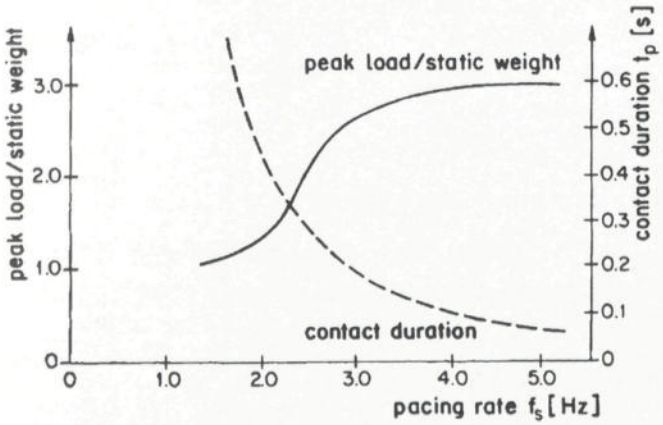


Figure 4.15. Variation of the *contact duration* and *impact factor* with the *pacing rate* (Bachmann & Ammann, 1987).

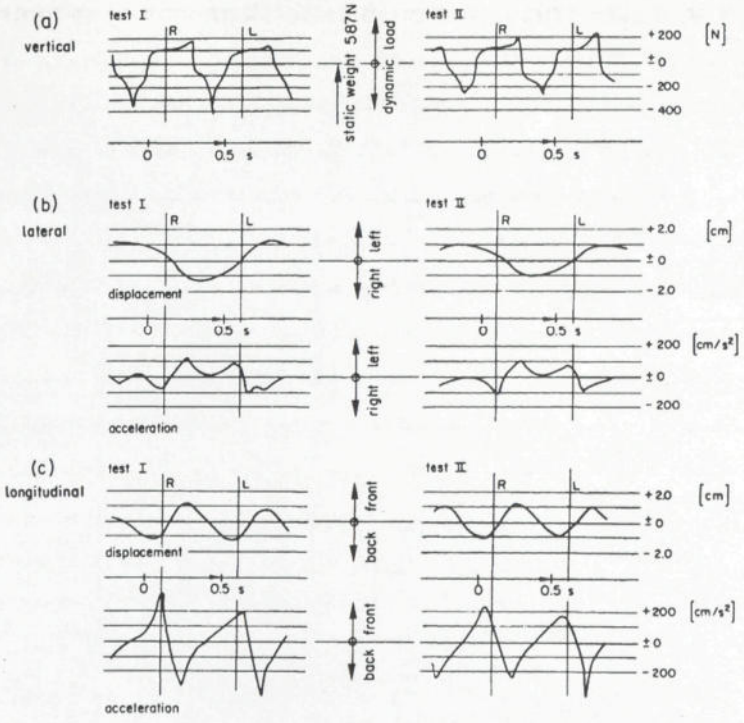


Figure 4.16. Time function of the vertical dynamic loading with resulting horizontal vibration displacements and accelerations for a pedestrian walking with *2Hz* pacing rate (Bachmann & Ammann, 1987).

Influence of the number of persons

For design purpose, it is also necessary to describe the load time function associated with the presence of a number of persons on the bridge. Although the density of pedestrians can be estimated with a certain precision, the characterization of the global response to the ensemble is a more complex issue.

The quantification of static loads is generally based on the assumption of a maximum density of *1.6-1.8 persons/m²*, which leads to a maximum load of *1100-1400N/m²* (Bachmann & Ammann, 1987). For the evaluation of dynamic effects, one can understand that the assumption of a perfect synchronization of the motion of all persons would lead to an extremely conservative analysis. Reference should be made to the studies of Matsumoto *et al.* (1978) who, assuming that the probability of arrival of pedestrians on a bridge is described by a Poisson law, derived an *enhancement factor m* to apply to the vibration amplitude caused by a single pedestrian in the centre span of the bridge. This factor is defined by

$$m = \sqrt{\lambda T_0} \tag{4.32}$$

where λ is the *mean flow rate* (*persons/s* over width of the deck) for a certain period of time (maximum λ : $\lambda_{max} \approx 1.5\, persons/s \cdot m$) and T_0 is the time necessary to cross the bridge

length L at speed v_s ($T_0 = L/v_s$). The quantity $\lambda \cdot T_0$ means then the number of persons simultaneously present on the bridge at the given mean flow rate and m represents the number of persons in synchronized oscillation. Equation (4.32) may be applied to pedestrian bridges with a fundamental natural frequency in the range *1.8Hz* to *2.2Hz*. For the ranges *1.6Hz* to *1.8Hz* and *2.2Hz* to *2.4Hz*, it is suggested that m is reduced to a minimum value of *2*, which corresponds to the walking of two persons in step.

Particular care should be taken with flexible bridges subjected to crowds. The studies of Fujino *et al.* (1993) have shown that when large structural vibrations are attained, the pedestrians tend to subconsciously adjust their step and synchronize to the bridge vibration, yielding increased vibrations. Measurements with a video camera on a *134m* main span cable-stayed bridge in a congested situation evidenced that about 20% of the pedestrians on the bridge main span were completely synchronized to the girder vibration. Thus, instead of an equivalent number $\sqrt{n}$ of persons on the bridge, $0.20\,n$ persons should have been considered in the design. Considering a total number of persons on the bridge n of *2000* persons, this would give an enhancement factor of *400* instead of *45*, as predicted by formula (4.32).

Design measures against man-induced vibrations in footbridges

The best form of preventing the occurrence of vibrations due to pedestrian actions consists in assuring that the bridge fundamental natural frequencies are distant from the typical range of frequencies induced by pedestrians and from the corresponding harmonics. Both the British Standards (BS 5400, 1978) and the Canadian code (OHBDC, 1983) define a threshold natural frequency for the fundamental mode of vibration above which no further verification is needed, which is of *5Hz* for the former, and *6Hz* for the later. Below this frequency, it is necessary to define limits of acceptability for the induced vibrations, which are expressed by these codes in terms of accelerations. The BS 5400 specifies the limit vibration acceleration as

$$0.5 f_1^{0.5} \ (m/s^2) \tag{4.33}$$

while for the OHBDC, this limit is given by

$$0.25 f_1^{0.78} \ (m/s^2) \tag{4.34}$$

The quantity f_1 in equations (4.33) and (4.34) is the fundamental frequency of the bridge. Considering a critical value $f_1 = 2Hz$, equations (4.33) and (4.34) give limit acceleration values of $0.7 m/s^2$ and $0.43\ m/s^2$, respectively. Note that these limits are stated for the excitation of a single pedestrian.

4.2.3 Earthquake loads

Modern seismic codes have well established the main requirements for the economical and safe design of earthquake resistant buildings and standard bridges. However, the knowledge of the dynamic behaviour of long span cable-supported bridges under earthquake loads is still limited and records of the earthquake response of this type of bridges are very scarce (Kawashima & Unjoh, 1991; Abdel-Ghaffar, 1994). In fact, to the author's knowledge, no case has been reported in the literature concerning the effect of a strong earthquake on a cable-stayed bridge, and only one case is known of damage induced possibly by a medium magnitude earthquake on a relatively short cable-stayed bridge in Canada (Filiatrault *et al.*, 1993). Yet, a significant number of these structures have been constructed in zones of high seismic risk during the last years.

A general idea regarding long span suspension bridges is that these structures are exempted from the effects of earthquakes, in virtue of their flexibility. In effect, long span suspension bridges are characterized by very low fundamental vibration frequencies, which have a very low contribution to the seismic response. Some components of these structures, like the towers, are however quite stiff. The motion of these elements is characterized by higher frequency vibration modes, which may have high participation factors and, consequently, be subjected to significant stresses. Emphasis should also be put on certain structural components that connect subsystems of different stiffnesses, like cable saddles, cable bents, wind locks and deck joints, and that need to be designed to accommodate large seismic demands (Ketchum & Cheng, 1994).

Two other aspects that enhance the seismic vulnerability of long span suspension bridges are related to the propagation of seismic waves on the soil. First of all, it is known that the intensity of the ground motion attenuates with the distance from the causative fault more rapidly in the high frequency range than in the low frequencies. So, at long distances from the fault, suspension bridges will actually be subjected to more severe seismic effects than other stiffer structures.

The second point is that, when the bridge is very long, the seismic waves arrive at the piers with an eventually significant delay. Moreover, if the foundation conditions are different, then the amplitudes and phases of the seismic waves will be different for the various piers and abutments. The spatial variability of the seismic action is thus an important topic in the study of long span bridges.

Compared with suspension bridges, long span cable-stayed bridges present an additional complexity, which relates to the marked three-dimensionality of their behaviour. In effect, on the contrary to suspension bridges, where the vibration modes can be classified as torsional, sway and bending modes, cable-stayed bridges exhibit complex three-dimensional modes. Many of these modes are characterized by high participation factors and need to be considered in the analysis.

The present Section addresses the main issues associated with the seismic analysis of cable-stayed bridges. These comprehend the characterization of the seismic action through alternative approaches, like response spectra, power spectra and artificial time histories, the consideration of the corresponding spatial variability for long-span bridges, and the definition of methodologies and strategies for the analysis of seismic effects in these bridges.

Characterization of the seismic action

One of the major causes of earthquakes is the occurrence of movements along faults in the earth's crust. During these movements, two types of body waves are generated, dilational waves and shear waves. The former are designated as *P* (Primary) waves, and travel faster than the later, the *S* (Secondary) waves. These waves propagate along the earth at very long distances and may generate significant ground motion, depending on the soil condition and distance to the causative fault. Additionally, low frequency surface waves (of Rayleigh and Love types), confined to the skin of the earth's crust, are also generated.

The time variation of the ground motion is the most useful form of defining the movement of the ground during an earthquake. The installation of a network of strong-motion accelerographs in regions of high seismic risk, namely in certain parts of the US, Mexico and Japan, has allowed the recording of a progressively growing number of earthquakes since 1933, date when the first strong motion accelerogram was recorded during the Long Beach earthquake (Chopra, 1995).

Generally three components of acceleration are recorded at sample intervals of *1/100* or *1/50* second. These records are available to researchers from international databases. Figure 4.17 represents an example of an accelerogram recorded during the Valparaiso Chile earthquake, in 1985, an earthquake with a surface magnitude of *7.8*. This record was obtained at the Valparaiso Chile Station, about *125km* distant from the earthquake epicentre, and presents a peak acceleration of $121.3 cm/s^2$.

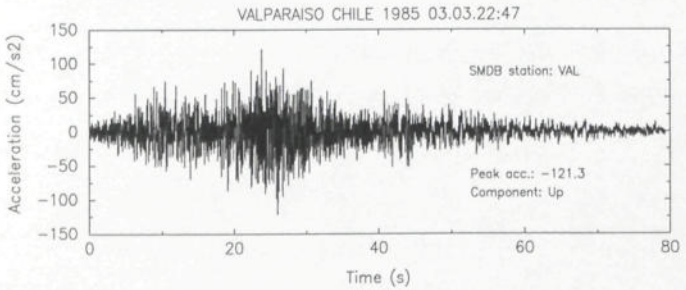


Figure 4.17. Vertical component of Valparaiso Chile Earthquake (1985) recorded at the Valparaiso Chile Station, *124.9* km distant from the earthquake epicenter (http://smdb.crustal.ucsb.edu/).

Once the three components of the ground motion are recorded, a complete description of the earthquake can be obtained at that specific recording station. From these records, three main characteristics of the earthquake are known, namely the amplitude, the

frequency content and the duration of the earthquake. The amplitude is generally characterized by the peak value of acceleration. The predominant frequency content can be roughly approximately by the number of zero crossings per second. Finally, the duration is evaluated by the interval of time between the first and the last peaks exceeding a certain fixed threshold level.

It is important to note that these measures do characterize a particular event of a random process, whose probabilistic nature can only be established from detailed statistic analysis of an ensemble of events.

A convenient description of the earthquake action at a particular location can be obtained from any of the following approaches: response spectra, power density spectra and artificial time histories.

Response spectra

Response spectra constitute the most widely used form of definition of the ground motion in the analysis of structures. The concept, introduced by Biot in 1932 (Chopra, 1995), consists in performing a graphical representation of the approximate peak response of a linear single-degree-of-freedom system subjected to a seismic action, characterized by an accelerogram. From the study of the response spectra associated with a number of earthquake records, it is possible to define an envelope function around the major peaks, which has a typical shape for a specific region and is designated as the *design response spectrum.*

A systematic description of the different available procedures for the definition of response spectra and design response spectra is presented in (Barbat *et al.,* 1994).

The idealization of the seismic action through response spectra is particularly suited to design applications and for this reason this type of representation is adopted by most of the design codes. In effect, using a modal analysis approach, the seismic response associated with each vibrational mode can be evaluated from the consideration that the system responds in that particular mode as a single-degree-of-freedom system, the total structural response being then obtained from the combination of the responses in the different modes of the system.

Within the scope of *Eurocode 8* (*EC8*), the earthquake motion is generally represented by an elastic acceleration response spectrum $S_e(T)$ defined by branches in the following form

$$S_e(T)=\begin{cases} a_g \cdot S \cdot \left[1+\dfrac{T}{T_B}\cdot(\eta\beta_0-1)\right] & , \quad 0\le T\le T_B \\ a_g \cdot S \cdot \eta \cdot \beta_0 & , \quad T_B\le T\le T_C \\ a_g \cdot S \cdot \eta \cdot \beta_0 \cdot \left[\dfrac{T_C}{T}\right]^{k_1} & , \quad T_C\le T\le T_D \\ a_g \cdot S \cdot \eta \cdot \beta_0 \cdot \left[\dfrac{T_C}{T_D}\right]^{k_1}\cdot\left[\dfrac{T_D}{T}\right]^{k_2} & , \quad T\ge T_D \end{cases} \tag{4.35}$$

The symbol T in these equations represents the structural vibration period of a linear single-degree-of-freedom system; a_g is the design ground acceleration for the reference return period; β_0 is the spectral acceleration amplification factor for 5% viscous damping; T_B and T_C are the limits of the constant spectral acceleration branch; T_D is the value that defines the beginning of the constant displacement range of the spectrum; k_1 and k_2 are exponents that influence the shape of the spectrum for a vibration period greater than T_C and T_D, respectively; S is a soil parameter, and η is a damping correction factor with reference value $\eta = 1$ for 5% viscous damping.

The values of the parameters β_0, T_B, T_C, T_D, k_1, k_2 and S are given in Table 4.3 for the three classes A, B and C in which the subsoil is classified (type A corresponds to stiff subsoil, while type C corresponds to soft subsoil). The damping correction factor η can be evaluated from the following expression

$$\eta = \sqrt{7/(2+\xi)} \geq 0.7 \tag{4.36}$$

where ξ is the value of the viscous damping ratio of the structure (%).

A representation of the elastic response spectrum according to equations (4.35) is given in Figure 4.18. This response spectrum characterizes any two independent components of ground motion along the horizontal direction, and can also be used to represent the vertical motion, provided that an appropriate scaling is performed.

Table 4.3. Values of the parameters describing the elastic response spectrum.

Subsoil class	S	β_0	k_1	k_2	$T_B(s)$	$T_C(s)$	$T_D(s)$
A	1.0	2.5	1.0	2.0	0.10	0.40	3.0
B	1.0	2.5	1.0	2.0	0.15	0.60	3.0
C	0.9	2.5	1.0	2.0	0.20	0.80	3.0

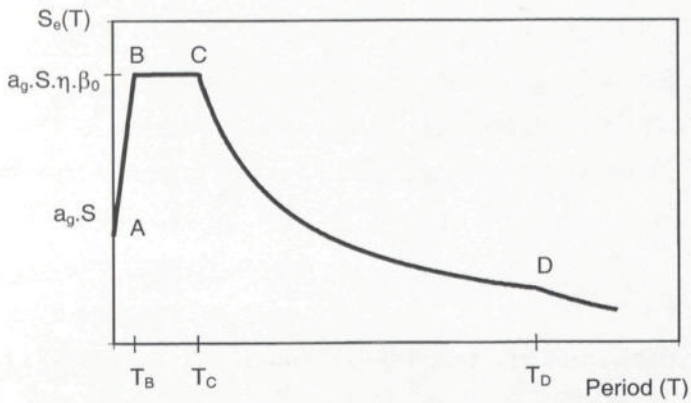


Figure 4.18. Elastic response spectrum: definition according to Eurocode 8.

Power spectra

The representation of the earthquake loads through *power spectra* is indicated by the *EC8* as an alternative to response spectra, providing a deeper analysis. This approach is based on a stochastic description of the seismic action, in which the ground motion is idealized as a sample of given duration of a stationary Gaussian vectorial random process defined by a power spectral density matrix.

The definition of this power spectral density $S_u(f)$ should consider the seismic characteristics of the region under analysis. This approach is adopted for example by the Portuguese Code for Safety and Design Loads (RSA, 1986), which introduces a multi-linear description of $S_u(f)$, considering two types of seismic action (Type *1*: moderate magnitude, short focal distance; Type *2*: larger magnitude, longer focal distance) and a classification of the subsoil condition similar to the one used in *EC8*. Figure 4.19 represents the power spectral density function defined by *RSA* for a seismic action of type *1* and a subsoil condition in correspondence with class *A* from *EC8*. Note that the quantity *f* designates the frequency expressed in Hertz.

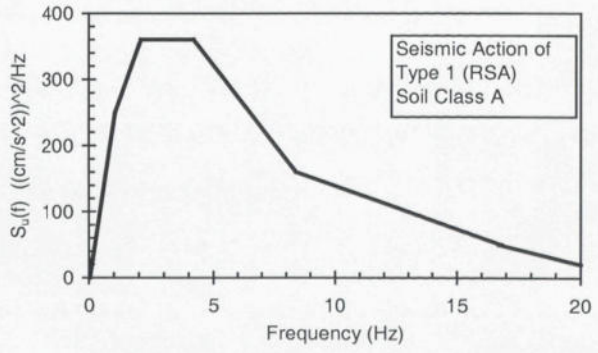


Figure 4.19. Multi-linear power spectral density defined by the Portuguese code *RSA* for a moderate magnitude earthquake at short focal distance and soil condition equivalent to class *A* (*EC8*).

Other possibilities for the representation of the power spectral density of the seismic action consist in defining either an analytical function $S_u(f)$ according to a particular model (for example, the Kanai-Tajimi description), or a function $S_u(f)$ consistent with a given elastic response spectrum. The later approach is adopted by the *EC8*. The two approaches will be referred later in the text, in the context of generation of artificial time series.

The representation of the seismic action through a power spectral density function is adequate for a stochastic structural analysis in the frequency domain. It is then possible to obtain probabilistic information for design, like mean maximum values of different control variables of the response, or the expected time for a given response to exceed a certain two-sided barrier level (first passage problem), which can be used to assess the structural reliability.

Artificial time histories

The performance of a direct time integration analysis of the structural response to input ground motions properly scaled to represent long return period earthquakes (typically *475* years, corresponding to *0.2%* probability of exceedence in one year) is the most detailed form of analysis to seismic excitation. A sufficient number of earthquake records need however to be used in order to give a stable probabilistic measure of the response. The *EC8* specifies the use of a minimum of five recorded samples representing adequately the seismic characteristics of the region where the bridge is located.

Because in many cases earthquake records are not available, it is also of interest to generate artificial time histories that are compatible either with given response spectra or with power spectra.

The first contribution to the generation of artificial accelerograms was given by Housner (1947), who interpreted the earthquake record as a series of pulses randomly occurring in time, obeying some specified laws for frequencies and amplitudes. Accordingly, Housner defined the input acceleration time history by

$$\ddot{u}(t) = \sum_{j=1}^{n} A_j \sin(\omega_j t + \phi_j) \tag{4.37}$$

The coefficients ϕ_j in this equation represent the phase angles associated with the jth frequencies ω_j. These coefficients are a sample obtained from n independent random variables uniformly distributed in the interval $[0,2\pi]$. The amplitude coefficients A_j can be calculated from the power spectral density of the earthquake random process, discretized in the increments of frequency $\Delta\omega_j$, as

$$A_j \approx \sqrt{2 S_{\ddot{u}}(\omega_j)\Delta\omega_j} \tag{4.38}$$

The first approach for the generation of artificial accelerograms consisted in modelling earthquake records as segments of band-limited white noise. The analysis of existing accelerograms showed however that the Fourier amplitude spectra are not generally constant with frequency, but instead are characterized by peaks that are associated with a filtering of the generated motion along several layers of soil. This suggested the use of a stationary filtered white noise of limited duration to represent the ground motion, and led to one of the most widely used models of representation of the seismic action, the model of Kanai and Tajimi (Kanai, 1957; Tajimi, 1960). This model defines the power spectral density associated with an earthquake $S_{\ddot{u}}(\omega)$ from the response of a single degree-of-freedom system with natural frequency ω_g and damping factor ξ_g, in terms of absolute accelleration, to an earthquake defined by a white noise with spectral density S_0. $S_{\ddot{u}}(\omega)$ is then given by

$$S_{\ddot{u}}(\omega) = S_0 \cdot \frac{1 + 4\xi_g^2 \cdot \omega_g^2 \cdot \omega^2}{(\omega_g^2 - \omega^2)^2 + 4\xi_g^2 \cdot \omega_g^2 \cdot \omega^2} \tag{4.39}$$

The parameters ω_g and ξ_g are defined considering the seismic characteristics of each site and are determined through the identification of the first spectral moments of the accelerogram. Although the first approaches used the first three moments (*j=0, 1, 2*), it is considered presently that a larger number should be used (*3n, n=1, 2, 3*) in order to better describe the frequency content of the earthquake (Barbat *et al.*, 1994). The spectral moment of order j, λ_j, is defined as

$$\lambda_j = \int_0^\infty \omega^j \cdot S_{\ddot{u}}(\omega) d\omega \tag{4.40}$$

The Kanai-Tajimi model has however a major drawback, that corresponds to the inclusion of a finite acceleration response at zero frequency, which represents an infinite ground displacement. In order to overcome this difficulty, Clough and Penzien (1986) introduced a high-pass filter so as to remove the low frequency content, and obtained the following description for the spectral density function

$$S_{\ddot{u}}(\omega) = S_0 \cdot \left[\frac{1 + 4\xi_g^2 \cdot \omega_g^2 \cdot \omega^2}{(\omega_g^2 - \omega^2)^2 + 4\xi_g^2 \cdot \omega_g^2 \cdot \omega^2}\right] \cdot \left[\frac{\omega^4}{(\omega_f^2 - \omega^2)^2 + 4\xi_f^2 \cdot \omega_f^2 \cdot \omega^2}\right] \tag{4.41}$$

The frequency ω_f and the damping ξ_f are parameters that characterize the filter.

The idealizations of the power spectral density by Kanai and Tajimi and by Clough and Penzien are represented in Figure 4.20 in terms of the natural frequency ω, for the values of $\omega_g = 15.6\ rad/s$ and $\xi_g = 0.6$ suggested by Kanai to represent firm soil conditions, and for the second filter parameters $\omega_f = 1.64\ rad/s$ and $\xi_f = 0.6$.

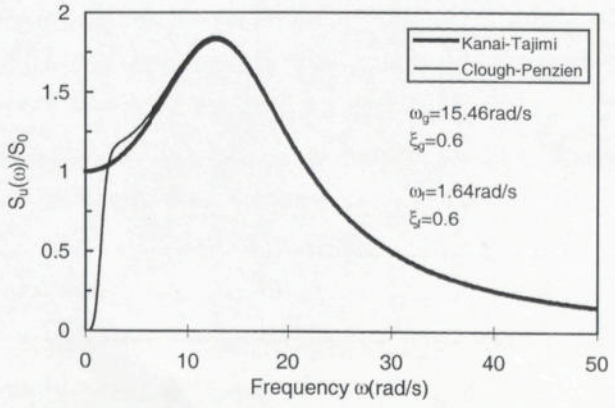


Figure 4.20. Power spectral density representation of earthquake action: models of Kanai-Tajimi and Clough-Penzien.

The models above described are based on a stationary description of the earthquake action. It is well known at present that real accelerograms represent realizations of a non-stationary random process, not only in terms of amplitude, but also in terms of the frequency content (Cunha *et al.*, 1997).

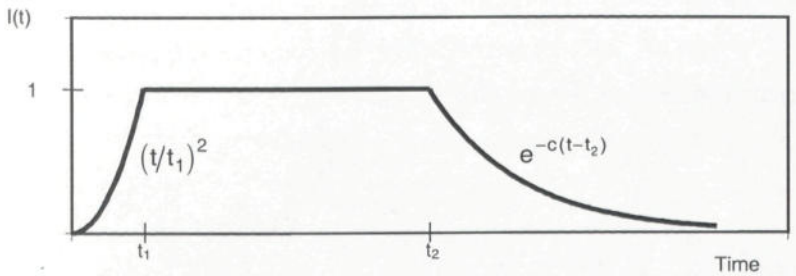
The former representations of the non-stationary character of the ground motion considered only the time variation of the amplitude through a time modulation of the random stationarity process $x(t)$, using an intensity function $I(t)$, the evolutionary power spectral density of the non-stationary process being then given by $I^2(t)\cdot S_{\ddot{u}}(\omega)$.

An example of a well-known modulating function is that suggested by Amin and Ang, defined by

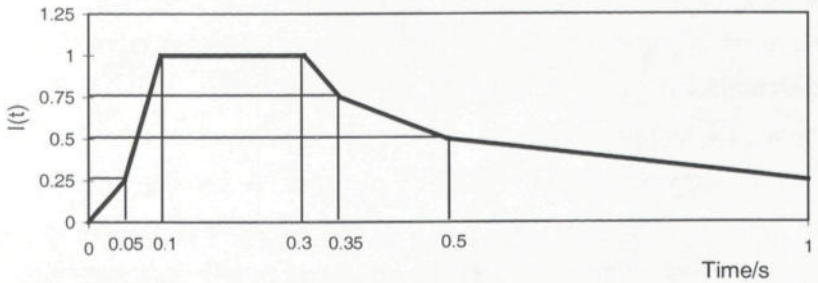
$$I(t)=\begin{cases}0 & , \quad t<0\\ (t/t_1)^2 & , \quad 0\le t\le t_1\\ 1 & , \quad t_1\le t\le t_2\\ e^{-c(t-t_2)} & , \quad t\ge t_2\end{cases} \tag{4.42}$$

Equations (4.42) depend on various constants, namely c, t_1 and t_2, that are defined as a function of the ground motion characteristics at the specific region under analysis. The general form of this intensity function is depicted in Figure 4.21(a).

Figure 4.21(b) presents the function suggested in *EC8*, defined by branches as a function of the total earthquake duration *s*. When no information is available concerning the characteristics of past earthquakes, this duration is established in *EC8*, varying in the range *10s* to *25s*.



(a)



(b)

Figure 4.21. General form of the intensity function $I(t)$: (a) introduced by Amin and Ang; (b) suggested by *EC8*.

The frequency non-stationarity of earthquake ground motion can also be introduced through the theory of the evolutionary spectra presented by Priestley (1971). A particularly well suited model for the stochastic assessment of the linear and nonlinear seismic response of structural systems has been developed by Yeh (1989), and was subsequently used by Hurtado *et al.* (1996) in the context of Base Isolated structures. Detailed formulations concerning this topic can be found in (Barbat *et al.,* 1994).

Reference is now made to the generation of artificial accelerograms compatible with given response spectra. This procedure, followed by *EC8,* departs from the definition of the accelerogram as an expansion in a series of harmonics according to equation (4.37). Introducing the amplitude non-stationarity in terms of the intensity function I(t), a modified accelerogram $\ddot{u}_I$ is obtained

$$\ddot{u}_I(t) = I(t) \cdot \sum_{j=1}^{n} A_j \sin(\omega_j t + \phi_j) \tag{4.43}$$

where the coefficients A_j are defined by equation (4.38) as a function of the power spectral density $S_{\ddot{u}}(\omega)$. It is thus necessary to relate $S_{\ddot{u}}(\omega)$ with the specified response spectrum, what can be done using the approximate recursive relationship developed by Gasparini and Vanmarcke (1976). An algorithm developed by Taylor (1991) based on this approach was used in the generation of the earthquake records used in the experiments described in Chapter eight.

Spatial variability of earthquake motion

According to *EC8*, a spatial variability model of the earthquake motion must be used when either the length of the bridge is greater than *600m*, or when there exist discontinuities or marked topographical features that can introduce significant variations in the characteristics of the ground motion.

The spatial variation of the earthquake motion can be attributed to the following three main causes: (i) difference in the arrival times of seismic waves; (ii) loss of coherence due to reflection and refraction; (iii) difference in local soil conditions. The effects associated with these causes are designated respectively as *wave passage*, *incoherence* and *local effects.*

Several forms of representation of these effects have been used in the past, involving different levels of simplification.

A simplified approach regarding the consideration of the *wave passage effect,* consists in defining a constant value of the velocity of wave propagation, which is assigned to the entire seismic disturbance. Several authors, like Abdel-Ghaffar (1984), who studied the wave passage effect in suspension bridges, used this approach. Applying the same methodology to cable-stayed bridges, and considering additionally different input motions recorded at different stations during an earthquake, Nazmy (1987) concluded that significant

effects can be produced in the response, particularly for more rigid cable-stayed bridges (with reinforced or prestressed concrete decks, or with closely spaced stay cables). Parametric studies developed by Dumanoglu *et al.* (1986) on the Bospurus and Humber suspension bridges considering the *wave passage effect* for different velocities of propagation of the seismic waves also showed that the asynchronous seismic excitations can lead to greater displacements and bending moments than conventional seismic analysis. It is important however to question whether the velocity of propagation of the seismic waves used in the calculations can be considered representative or not of the velocity of propagation of the seismic waves at the bedrock.

But one of the most important steps in the investigation of spatial variations of earthquake motion was the installation of the *SMART1* array at Lotung, Taiwan. This array consists of a central strong-motion recorder plus 12 stations arranged at three concentric rings. Based on studies of data collected from this array, Loh (1985) constructed a stochastic model to describe the spatial variability of ground motion, developing analytical expressions for the spatial correlation coefficient. This model considered both the wave passage effect and incoherency effects. In more recent formulations (Barbat *et al.*, 1994), the concept of random process depending upon a single variable, the time, has been extended to the more general concept of *random field*, as a process that depends upon two or more variables.

For the evaluation of correlation functions of the absolute ground motion at the level of the bridge foundations, modern techniques tend to perform a finite element modelling of the soil basin. This approach allows a detailed characterization of the vibration of the different layers of the soil, requiring however a detailed knowledge of the spatial variation of the soil profile and its mechanical characteristics. Also, as the spatial variability is frequency dependent, its correlation functions may be characterized, in a first approximation, by bands of frequency. This means that, based on the design spectral densities of ground motion at the bedrock, spectral density functions for any number of points in the soil layers, and namely for the supports of the structure, can be established. This methodology was employed by Vaz *et al.* (1987) in the seismic study of the Arade cable-stayed bridge, in Portugal. These authors concluded that the influence of spatial variability on the earthquake response was not significant, when comparing with results from rigid base models. This conclusion supports some more simplified analysis performed for example by Taylor *et al.* (1985) and Khalil (1996) on the Annacis, and on the Skytrain Fraser River Crossing, respectively. In both analyses the spatial variability was addressed only in terms of the *wave passage* and *local effects*. The model employed considered, in a first step, the spatial variability associated with the soil profile through a one-dimensional shear-wave propagation analysis based on a computer code developed by Schnabel (1972). For this purpose, sets of *6* accelerograms (obtained from earthquake records at locations with similar site characteristics) were introduced as input at the bedrock, and the corresponding response spectra were evaluated in correspondence with each foundation profile. Based on the response spectra obtained at the two piers, a smoothed design response spectrum was defined. The wave passage effect was introduced through a

simplified static analysis in which one of the foundations suffered an horizontal displacement calculated as twice the relative displacement at the period of the first longitudinal mode of vibration.

For design purposes, the *EC8* presents two alternatives. The first proposed methodology consists in the construction of spectral density matrices that relate the different components of the ground motion at two different stations. This approach, however, requires a model for the generation and propagation of the seismic waves, and the establishment of a scenario with the relative position (distance and orientation) between site and earthquake fault. After the characteristics of the site are established, the computation of the spectral density functions is relatively simple (Ravara *et al.*, 1984). It is also possible to use another approach, which does not require the characteristics of the seismic waves at the site. This approach is based in a partition of the motion into several frequency bands and in defining the spatial variability for each band. The spatial variability is based on stochastically independent motions defined for the nodes of a square mesh, one mesh for each frequency band. Inside each square, the motion is a weighted average of the motion at the four nodes; weights are selected to obtain a constant spectral content if motion at the nodes has the same spectral content. The process is described in some detail in (Ravara *et al.*, 1984).

Seismic behaviour of cable-stayed bridges

Considering the complexity and damaging effects of earthquake loads, particularly for structures located in zones of high seismic risk, one of the main important aspects is to develop a bridge design with reduced seismic demands. In this respect, it is important to note that the type of connection between the deck and the towers affects significantly the seismic demands. The total suspension system, i.e., the system in which the deck is swinging freely at the towers, leads to a more flexible solution and, consequently, attracts less earthquake loads. The inconvenience is the possibility of occurrence of large displacements under service loads, whose control requires the use of specific mechanical devices. This solution was adopted at the recently constructed Vasco da Gama cable-stayed bridge, in Lisbon, which was designed for a soil acceleration of *0.5g*. Innovative steel damper devices were installed connecting the deck and towers (see Figures 2.87 and 2.89), in order to control the horizontal displacements (Capra & Leveille, 1997; Guerreiro *et al.*, 1997). A more radical solution has been devised for the Salgueiro Maia Bridge at Santarém (Figure 2.90). In this case, both the deck and masts, which are rigidly connected, lay on special damping devices made of a high damping rubber.

In terms of the design criteria, different possibilities can be followed, depending both on the structural design requirements and on the importance of the structure. A common approach consists in defining two levels of requirements in correspondence with two different intensity ground motions. So, for example, it may be required that the structure behaves elastically without damage for a moderate earthquake (with a *100* year return period, i.e., a

probability of exceedence of *1%* in one year), while for a strong-motion earthquake (with a *475* years return period, i.e., a probability of exceedence of *0.2%* in one year) some repairable damage may occur. Very long span bridges may however be designed in the elastic range.

With regard to the methodologies of analysis of seismic effects, two categories of methods can be employed, *static* and *dynamic*. The *static* methods, are based on the definition of equivalent static forces dependent on the design response spectra, which can be used in a preliminary analysis of the bridge in order to obtain a rough estimate of the order of magnitude of stresses and displacements induced by earthquake loads. Dynamic methods can be further classified into two level methods: (i) the multi-mode spectral method and; (ii) the general dynamic methods. The multi-mode spectral method is based on an eigenvalue analysis of the structure and on a mode-by-mode estimation of the maximum response through design response spectra. The total response of the bridge is calculated after convenient combination of modal contributions. The more accurate dynamic methods can be further divided into frequency and time domain methods. Frequency domain methods are associated with a representation of the earthquake excitation in the frequency domain, through power spectral density functions. Although these methods have the inconvenience of requiring the performance of linear or equivalent linear analyses, they provide important statistical information regarding the seismic behaviour of the bridge at a relatively low cost (Cunha, 1990; 1994). The most general time domain methods, based on the application of direct integration techniques, provide a more realistic approach for the study of the seismic behaviour of a cable-stayed bridge, and allow the incorporation of material and geometric non-linearity, the introduction of spatial variability of earthquake loads, the consideration of soil-structure interaction, and the adequate modelling of special damping devices. The necessity of employing a significant number of earthquake records in order to obtain reliable enough estimates of stresses and displacements leads however to much more time consuming and complex analyses.

4.3 NUMERICAL FORMULATIONS

4.3.1 General

Much of the progress associated with the construction of cable-stayed bridges owes to the development and application of powerful numerical methods of structural analysis, which took place during the last decades as a consequence of the increase of computer potentialities. This is particularly evident when comparing the relatively simple structural systems adopted in the former cable-stayed bridges with the extremely complex cable-stayed bridges constructed during the late 1990's, satisfying ever demanding criteria for safety, comfort and efficient use of materials.

Cable-stayed bridges exhibit a very complex static and dynamic behaviour, which is marked by a three-dimensional character and by nonlinearities of different types. The increase of span achieved during the last years and the adoption of progressively more slender aerodynamic cross-sections has led to an increase of the flexibility and consequently of the degree of nonlinearity of the bridge behaviour.

An important source of nonlinearity in a long span cable-stayed bridge is the sag caused by the cable weight. In effect, when a stay cable is tensioned, a nonlinear force-displacement relation is established, according to the curve represented in bold in Figure 4.22. This is due to the fact that only one part of the end movements is associated with material deformation (elastic), the remaining motion resulting from a change in the cable sag. As the cable tension increases, the change in the cable sag becomes smaller and smaller, and an increasing component of the movement of the cable ends occurs due to the material deformation, i.e., the apparent stiffness increases with the tensile force in the cable. This type of behaviour is designated as of *hardening type*, as opposed to the *softening behaviour* exhibited by conventional non-cable structures composed of stiffness degrading materials (characterized by a force-displacement relation of the type represented by the light solid curve in Figure 4.22). As one can understand, longer cables are characterized by higher sag and consequently exhibit a higher degree of nonlinearity.

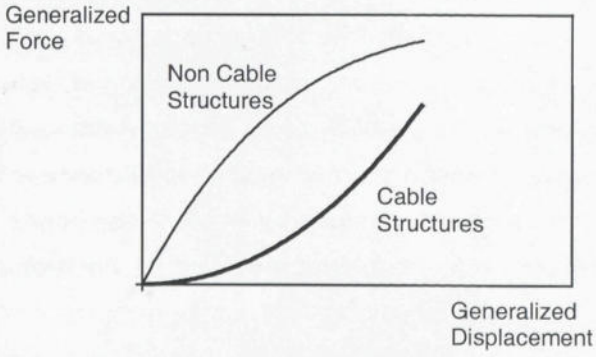


Figure 4.22. Nonlinear force-displacement relationships for structural systems.

The other source of nonlinearity that assumes higher importance in long span cable-supported bridges is the geometric change caused by large displacements. This change may enhance the axial force-bending moment interaction, the corresponding effect being particularly significant for cable-stayed bridges in consequence of the high axial compression forces installed in the deck and towers.

In fact, the interaction between axial force and bending moment of structural members is generally neglected when small displacements are assumed. When the structure undergoes large displacements, second order effects should be considered, namely the additional end moments $N \cdot x_2$ (see the representation in Figure 4.23 for two-dimensional bending moment-axial force interaction), and the axial force $\frac{EA}{L} \cdot u_b$ produced by an apparent

shortening u_b of these members, caused by bending deformations. The former is designated as *beam-column effect*, while the later is the *bowing effect*.

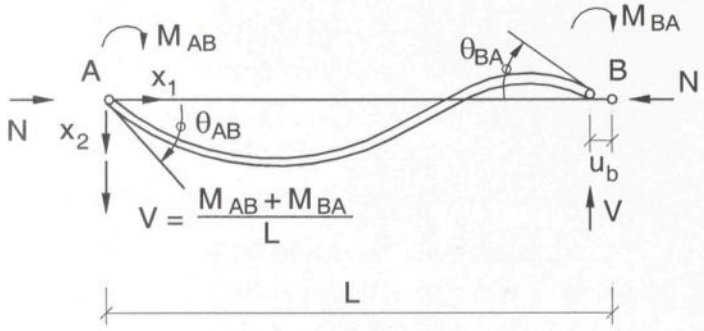


Figure 4.23. Nonlinear elastic beam-column and bowing effects for two-dimensional analysis.

The consideration of the effects of large displacements in long span cable-stayed bridges requires that the stiffness of the bridge is calculated from the deformed configuration instead of the original undeformed geometry, as is the procedure for conventional linear structural analysis. Since the deformed configuration of the bridge is unknown, an iterative process of analysis is required.

The sources of nonlinearity above referred are all related to the bridge geometry, and their analysis requires the use of so-called *geometric nonlinear formulations*.

Physical nonlinearity associated with material properties is another source of non-linearity that may deserve consideration.

In general, due to the economic and social importance of cable-stayed bridges (particularly for long-span bridges), it is required that these structures behave elastically and actually work at relatively low stresses under service loads. For exceptional load conditions, which is the case of strong-ground motion and large return period wind loads, material nonlinear behaviour is allowed under specific requirements. Furthermore, when concrete is employed, it is of utmost importance that both creep and shrinkage effects, which are of nonlinear nature, are incorporated in the static analysis for the different stages of construction so that the final geometry and cable tensions are assessed accurately.

The present Section starts with a presentation of a brief state-of-art of the structural analysis of these structures, considering the assessment of the different sources of nonlinearity present in the problem, in the perspective of a dynamic analysis.

The basic governing equations for a finite element analysis of a geometrically nonlinear problem are then established in incremental form and applied to the modelling of a cable-stayed bridge. The general two-node and four-node truss elements are described as two possibilities for discretization of the stay cables. For discretization of the deck and towers, the beam-column element is considered the most adequate. The formulation of this element is presented both based on the 'exact' theory, and using a finite element approach.

4.3.2 Brief state-of-the-art of static and dynamic analysis of cable-stayed bridges

Early studies of the static analysis of cable-stayed bridges considered the bridge as a linear two-dimensional structural system where the cables acted equally as linear tension members (Thul, 1966, Smith, 1968). This approach was considered inadequate by several authors, such as Tung and Kudder (1968), Leonhardt and Zellner (1970), Tang (1971), Podolny (1971), Lazar (1972), Baron & Lien (1973) and Morris (1974). Tung and Kudder, for example, referred that errors of up to *15%* could be produced when the cable sag was not accounted for, particularly for long cables. Lazar referred that for the particular case of the North Bridge, at Düsseldorf, the error produced by neglecting in the analysis the geometric nonlinear behaviour of the bridge attained up to *12.4%*.

According to Narayanan *et al.* (1987), the earliest contribution for the development of nonlinear analysis of cable-stayed bridges is due to Schreier (1961) who, employing a continuous model, obtained the solution of the differential equations of equilibrium expressed in the deformed configuration of the bridge. This solution consisted of a sum of two parts, one corresponding to the initial undeformed state (equivalent to the linear elastic solution), and another part determined iteratively as a function of the unknown displacements, which introduced additional secondary moments along the bridge girder.

Although continuous formulations have been recently employed as simplified methods of analysis of cable-supported bridges (Como *et al.*, 1985; Bruno & Leonardi, 1986), the discrete approaches based either on frame or on finite element analysis constitute the most efficient and powerful methods and are therefore the most widely used. These methods incorporate geometric and material nonlinearities in different forms and at different levels of approximation, as will be discussed below.

4.3.2.1 Geometric nonlinearities

Nonlinearity due to cable sag

A simplified method for considering the nonlinearity due to the cable sag consists in substituting the curved cable by a straight chord member with an *equivalent modulus of elasticity* E_{eq}. This modulus, deduced in Chapter three and given by equation (3.37), combines the effect of material and geometric deformations, hence depending on the cable tension.

The concept of *equivalent modulus of elasticity* was introduced by Ernst (1965) and has been used by many researchers, such as Leonhardt and Zellner (1970), Tang (1971), Lazar (1972), Troitsky (1988), Fleming (1979), Podolny and Scalzi (1986), Nazmy (1987), Wang and Yang (1996) and Schemmann and Smith (1997). The impossibility of assessing the

lateral behaviour of the cable is the main inconvenient associated with this approach, which is relevant for the dynamic analysis of cable-stayed bridges. Another inconvenience has to do with the difficulty in evaluating the unstrained length of the cable.

Alternatively, the stay cable can be discretized into several finite elements. The simplest of these elements is the truss element, a linear two-node bar that was employed for static analysis by Baron and Lien (1973) and Yiu and Brotton (1987), and for dynamic studies by Abdel-Ghaffar and Khalifa (1991), Tuladhar (1995) and by the author in the context of the present dissertation. Applying the loads and the self-weight at the nodes used to discretize the cable, the corresponding deformed geometry can be calculated by a geometrically nonlinear analysis and the dynamic behaviour of the cable can be captured, provided that a sufficient number of finite elements is employed. Since the two-node truss element is implemented in most commercial finite element packages, its use is of high interest in the context of bridge design, even if a relatively high number of elements need to be employed in the modelling of each cable.

Other more sophisticated finite element models of cable have been employed, such as (i) the family of geometric nonlinear finite elements developed by Henghold and Russell (1976), which allow the expression of the displacement as any polynomial expansion; (ii) the two-node curved finite element developed by Gambhir and Batchelor (1977), that employs cubic polynomial interpolation functions and enforces the continuity of nodal displacements and corresponding derivatives; (iii) the two-node curved finite element proposed by Ozdemir (1979), which employs Lagrangian functions for the interpolation of element geometry and enforces displacement continuity; (iv) the elastic catenary element of Jayaraman and Knudson (1981), later implemented also by Fuheng (1996); and the four-node isoparametric truss element implemented by Ali (1991).

A last alternative for the representation of the nonlinear behaviour of a stay cable consists in the analytical description of a dynamic stiffness matrix. This approach was introduced by Davenport & Steels (1965) and further developed by Veletsos and Darbre (1983). A more accurate solution for the study of highly tensioned cables was developed by Starossek (1991), who employed the differential continuum equations derived by Irvine (1981). A main drawback associated with this approach is the validity only for small displacements. Another difficulty that arises is the frequency dependence of the dynamic stiffness matrix, which requires the solution of multiple eigenvalue problems in the iterative process towards the evaluation of the bridge response. Starossek (1993) overcame this problem by developing a reduction of the dynamic cable stiffness coefficients to linear polynomials.

Nonlinearity due to large deflections

In addition to flexural forces, the deck and towers of a cable-stayed bridge are subjected to large compressions introduced by the inclined stay cables. Due to the possibility of large

deflections, the beam-column elements suffer second order effects caused by the interaction of these force components. The formulation of the geometric nonlinear behaviour of these members can be developed according to two main approaches, one based on the *beam-column theory*, and another based on *finite element modelling*.

The beam-column method is the classical method of analysis, and is based on the definition of *stability functions*, which are multiplication functions used to modify the stiffness coefficients associated with the elastic problem. *Stability functions* for a two-dimensional analysis are presented in (Livesley & Chandler, 1965). Oran (1973a) included additionally the bowing effect, and extended these functions to the three-dimensional problem. Several authors have employed formulations based on the use of *stability functions*, as for example Lazar (1972), Fleming (1979), Fleming and Egeseli (1980), and Nazmy (1987). It should be pointed however that the stability functions are nonlinear functions that depend on the axial force in the beam-column member, which depends itself on the state of deformation of the member. Thus an iterative scheme is necessary for the updating of the beam-column stiffness matrix, which may be subjected to numerical problems.

The finite element method considers the geometric nonlinearity through the use of *geometric stiffness matrices*. These matrices are linear functions of the member axial force and need to be updated during an iterative cycle. Conventionally, two approaches can be used in an incremental nonlinear finite element analysis, the *Updated Lagrangian* (*UL*), and the *Total Lagrangian* (*TL*) Formulations. The two formulations are well established in the literature (Bathe, 1982). The *UL* formulation is considered the most efficient for the problem under analysis and will be briefly reviewed in the text. Due to the immense range of applications, finite element formulations are very widely used and constitute the basis of most of the applications developed in the topics of numerical analysis of cable-stayed bridges. It should be noted however that finite element formulations using *geometric stiffness matrices* lead to approximate results and require consequently a finer mesh of finite element discretization than the exact beam-column method. In this respect, it is interesting to refer the paper by Dumir *et al.* (1993), who actually showed that the *geometric stiffness matrix* is the first term of the expansion of the "exact" beam-column stiffness matrix into a Taylor series.

A final consideration on the *beam-column / bowing nonlinearities* is that, provided that a geometric nonlinear analysis is performed, the simple introduction of intermediate nodes along the beam-column members may avoid the necessity of accounting for such type of second order effects. In effect, by reducing the distance between the end nodes, relative displacements are reduced and second order effects are also reduced. An approximate expression derived by Bunce and Brown (1973) can be used in order to determine the maximum length ℓ of beam-column element to use, as a function of the allowed percentage of error ε and the axial load P applied to the element

$$\ell = \left(\frac{EI\,\varepsilon}{10\,P} \right)^{1/2} \tag{4.44}$$

The quantities E and I in equation (4.44) represent the modulus of elasticity and the moment inertia of the element, respectively.

It's still worth noting that the consideration of the effects due to large displacements is performed from the definition of the equilibrium equations in the deformed configuration of the bridge. This requires that both the bridge geometry and the transformation matrices are updated for each increment of load.

4.3.2.2 Geometric and material nonlinearities

In addition to geometric nonlinearities, some authors have included in the mathematical model the nonlinear characteristics of the material, what allows the determination of the ultimate bearing capacity of the bridge. Reference should be made to the works of (i) Seif and Dilger (1987), who introduced the nonlinear stress-strain relationships for the concrete and steel, and evaluated the effects of geometric and material nonlinearities on the distribution of stresses for several types of loading; (ii) Khalil *et al* (1983), who considered the creep and shrinkage of concrete, and the relaxation of prestressing steel in the analysis of prestressed concrete cable-stayed bridges; Abbas (1993), who performed identical calculations on the basis of a finite element modelling, using multi-slice fiber beam-column elements; and of Adheli and Zhang (1995), who studied composite girder cable-stayed bridges under different levels of loading, considering simplified nonlinear moment-curvature relationships.

4.3.2.3 Dynamic analysis of cable-stayed bridges

Due to the complexity of the problem, the research on the dynamic analysis of cable-stayed bridges has received a relatively small number of contributions during the sixty and seventy decades. In effect, it was only during the eighties, with the well-establishment of the finite element analysis and the boom in computer technology, that the dynamic analysis became an important component in the design of cable-stayed bridges.

The early approaches for the dynamic analysis of cable-stayed bridges were based on continuous energy methods. According to Nazmy (1987), the first reported investigation on the dynamic behaviour of cable-stayed bridges is due to Goschy (1961), who employed the Ritz method in the evaluation of the bridge natural frequencies. This method was also employed by Troitsky (1988).

A lumped mass approach was employed by Baron and Lien (1973) in the investigation for the Southern Crossing Bridge, in California. Using a three-dimensional model composed of beam-column and elastic catenary members, these authors developed extensive aerodynamic and seismic studies at various stages of construction and at closure. Basically, the dynamic analysis was performed linearly by modal superposition considering the contribution of the

first ten modes, employing however the tangent stiffness matrix at the dead load deformed state obtained from a geometric nonlinear analysis.

From a comparative study between the linear and nonlinear dynamic analysis of two planar cable-stayed bridges, Morris (1974; 1977) concluded that the linear and nonlinear responses did not differ significantly. He also showed that the damping effect was much more important than geometric nonlinearities. These conclusions should however be faced with reservation, as they apply to relatively short span cable-stayed bridges.

Several studies of static and dynamic analysis of cable-stayed bridges are then reported in the literature, which consider either linear or geometric nonlinear analysis for dead loads, and linear dynamic analysis for the wind and traffic loads. Some examples are the studies developed by Lu (1979) and by Persoon and van Nunen (1979), on the Ruck-A-Chucky and on the Waal Bridges, respectively, which were validated by experimental tests performed on a physical model, and on the bridge prototype.

One of the most clarifying papers concerning the necessity of performing linear or nonlinear static / dynamic analysis of cable-stayed bridges is that from Fleming and Egeseli (1980), who investigated the dynamic response of the North Bridge, at Düsseldorf, under traffic, wind and seismic loads. Two main conclusions were obtained from these studies. The first was that almost the same results were obtained when performing a nonlinear static analysis followed by a linear dynamic analysis using the tangent stiffness matrix evaluated at the dead load deformed state, or a nonlinear static analysis followed by a nonlinear dynamic analysis. The second conclusion was that the values adopted for the damping factors can affect significantly the bridge dynamic response.

At this point two aspects should be noted. First of all, all of the dynamic analyses above referred, except those from Baron and Lien, considered the sag effect through the use of an equivalent straight chord member with an equivalent modulus of elasticity. This means in practice that the cable dynamics was not included in the bridge model and so the actual nonlinear effects associated with cable sag could have been underestimated by these authors. Another aspect is that the bridges above referred don't represent the actual trend in terms of span length and cable arrangement, but instead are characterized by small and medium size spans and, in most cases, by relatively stiff decks and a small number of stay cables. These bridges are clearly stiffer systems than the ones employed presently.

Considering the later point, Nazmy (1987) and Nazmy and Abdel-Ghaffar (1990a; 1990b; 1990c) extended the research from Fleming and Egeseli to large span cable-stayed bridges. By performing different types of three-dimensional analyses on two bridge models, one with a centre span of *335m* (model of Fleming and Egeseli) and the other with a span of *670m*, these authors confirmed the conclusions from Morris and from Fleming and Egeseli, that, for centre spans up to *420m*, linear dynamic analysis is adequate, as long as it employs the tangent stiffness matrix calculated at the end of a geometric nonlinear static analysis. However, both static and dynamic nonlinear analyses are required for large centre spans, i.e., greater than *600m*.

Subsequent numerical modelling of the Quincy Bridge, in the US (a composite cable-stayed bridge with a centre span of *274m*), by Wilson and Gravelle (1991), and experimental validation from full scale ambient vibration tests (Wilson & Liu, 1991) showed that performing both linear static and linear dynamic analyses was adequate to represent that particular bridge behaviour under service loads.

More recently, Kanok-Nukulchai *et al.* (1992, 1993) discussed different methodologies for modelling the different components of the bridge, namely the deck, pylons, cables, joints, as well as their assembly into a concrete bridge, using finite element analysis.

With respect to the inadequacy of modelling the dynamic behaviour of the stay cables using an equivalent straight chord member with equivalent modulus of elasticity, reference should be made to the paper by Causevic and Sreckovic (1987), who stated that the vibration of stay cables affects significantly the response of cable-stayed bridges to general dynamic loading, specially when the eigenfrequencies of the bridge approach some eigenfrequency of a stay cable, and proposed the modelling of these elements as associations of linear springs and lumped masses. By discretizing each stay cable as a series of truss links, Abdel-Ghaffar and Khalifa (1991) emphasized the necessity of accounting for the interaction between cable vibrations and bridge vibrations in the analysis of the earthquake behaviour. Tuladhar (1995) and Tuladhar *et al.* (1995) employed the same methodology in the parametric studies of conventional and multi-span cable-stayed bridges, arriving at identical conclusions.

4.3.3 Finite element approach for the geometric nonlinear problem

The essence of matrix methods of analysis consists in idealizing the continuous structures by equivalent discrete-element models with a finite number of degrees-of-freedom. The elastic and inertial properties of the individual structural elements of the discrete model are expressed through matrices, which are derived from energy considerations assuming specific forms of displacement, and which are conveniently assembled to obtain a representation of the full model of the continuous structure. Depending on the type of structure and loading, and on the assumptions employed for the description of displacements, exact or approximated representations of the original structural system can be achieved.

The current Section attempts to describe the approximate representation given by the finite element method in the particular context of cable-stayed bridges. Given the characteristics of the problem above defined, the finite element formulation will be presented on the basis of the large defection theory, i.e., considering that the deflections are large enough to cause significant changes in the geometry of the structure, what requires that the equations of equilibrium are formulated for the deformed configuration. This leads to the presence of nonlinear terms in the governing system of equations, the so-called geometrically nonlinear terms. The strains are however assumed small and thus linear elastic material analysis is considered.

The formulation presented is based mainly on the book of Bathe (1982). Other supportive bibliography includes the following references: Fung (1965), Przemieniecki (1968), Harrison (1973), Martin and Carey (1973) and Barbosa (1992).

4.3.3.1 Incremental equations of motion for static analysis

Consider the generic point P of a volume ${}^{0}V$ (see Figure 4.24), whose coordinates, expressed in a Cartesian coordinate system are, at time *0*, ${}^{0}x_1$, ${}^{0}x_2$, ${}^{0}x_3$. Adopting a Lagrangian formulation of the problem, in which the motion is expressed on the basis of a fixed referential, the coordinates of P' at time t, ${}^{t}x_1$, ${}^{t}x_2$, ${}^{t}x_3$, are given by

$$ {}^{t}x_i = {}^{0}x_i + {}^{t}u_i, \text{ with } \quad i = 1, 2, 3 \tag{4.45} $$

where ${}^{t}u_i$ represents the total displacement component along the axis x_i at time t.

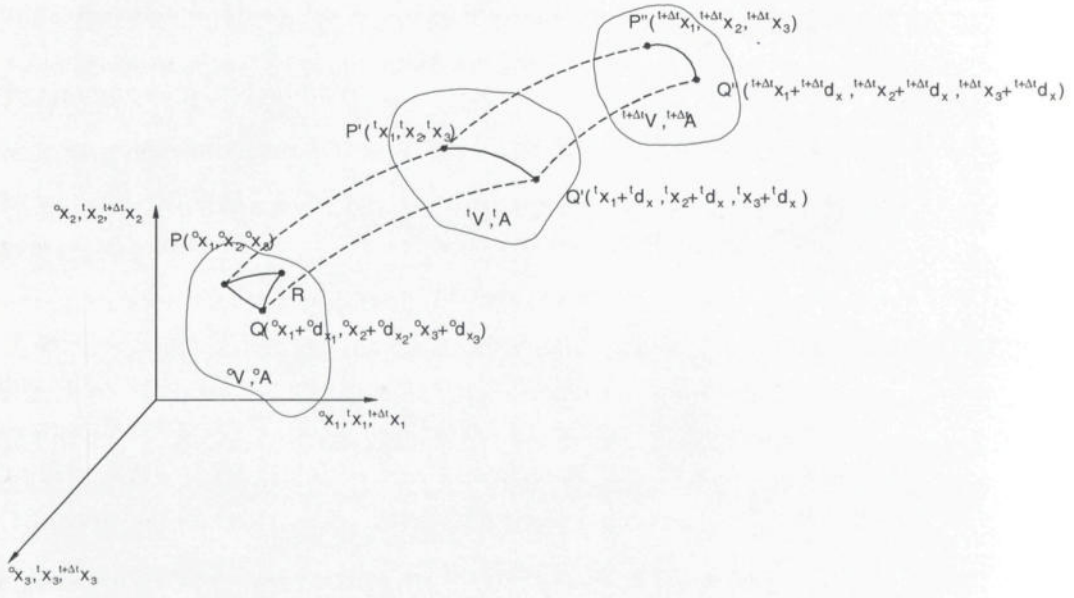


Figure 4.24. Motion of the body in a fixed Cartesian coordinate system.

The hypothesis of large deflections requires that the variations of the surface area, of the volume and of the mass density of the body are taken into consideration. However, when formulating the equilibrium equations at a generic time t, these quantities are unknown. An efficient form of dealing with this problem consists in defining auxiliary strain and stress measures which, when used to define the system energy, lead to integrals over the original area and volume of the structure (at time *0*). Among the different possibilities, the *Green-Lagrange* and the *2nd Piola-Kirchhoff strain* and *stress tensors*, respectively, will be used for description of strains and stresses.

The Green-Lagrange strain tensor

The deformations of the body represented in Figure 4.24 will be assessed considering three different neighbouring points *P, Q, R*, forming a triangle in the original configuration. The deformed configuration of the triangle *P'Q'R'* at time *t* will be determined if the change in length of the sides of the triangle is known.

Consider the infinitesimal line element connecting points *P* and *Q*, whose length ${}^0ds$ at the undeformed configuration is obtained from

$$\left({}^0ds\right)^2 = d^0x_i \cdot d^0x_i \tag{4.46}$$

When *PQ* is deformed to *P'Q'* at time *t*, the square of the length ${}^tds$ of the new segment is given by

$$\left({}^tds\right)^2 = d^tx_i \cdot d^tx_i \tag{4.47}$$

using an indicial notation.

Assuming that the change of configuration is continuous, it follows that the generic components d^tx_k of the deformed segment *P'Q'* relate with the original components d^0x_i in the undeformed configuration by

$$d^tx_k = \frac{\partial\, {}^tx_k}{\partial\, {}^0x_i} d\,{}^0x_i \tag{4.48}$$

Substituting (4.48) into (4.47) yields

$$\left({}^tds\right)^2 = \frac{\partial\, {}^tx_k}{\partial\, {}^0x_i} \cdot \frac{\partial\, {}^tx_k}{\partial\, {}^0x_j} \cdot d\,{}^0x_i \cdot d\,{}^0x_j \tag{4.49}$$

The difference between the squares of the length of the segment *PQ* in the deformed and undeformed configuration is then

$$\begin{aligned} \left({}^tds\right)^2 - \left({}^0ds\right)^2 &= \left(\frac{\partial\, {}^tx_k}{\partial\, {}^0x_i} \cdot \frac{\partial\, {}^tx_k}{\partial\, {}^0x_j} - \delta_{ij}\right) \cdot d\,{}^0x_i \cdot d\,{}^0x_j = \\ &= \left({}^tC_{ij} - \delta_{ij}\right) \cdot d\,{}^0x_i \cdot d\,{}^0x_j \end{aligned} \tag{4.50}$$

The quantity ${}^tC_{ij}$ in this equation is defined as the *Green's strain tensor*, and δ_{ij} is the *Kronecker delta*. Another possible definition for a strain tensor is the so-called *Green-Lagrange strain tensor* E_{ij}, which is defined at time *t* by

$$ {}^{t}E_{ij} = \frac{1}{2} \cdot ({}^{t}C_{ij} - \delta_{ij}) \tag{4.51} $$

This tensor can be expressed in terms of the displacement components ${}^{t}u_i$ defined in equation (4.45), considering the following relation

$$ \frac{\partial\, {}^{t}x_k}{\partial\, {}^{0}x_i} = \frac{\partial\, {}^{0}x_k}{\partial\, {}^{0}x_i} + \frac{\partial\, {}^{t}u_k}{\partial\, {}^{0}x_i} = \delta_{ki} + \frac{\partial\, {}^{t}u_k}{\partial\, {}^{0}x_i} \tag{4.52} $$

Substituting (4.52) into (4.50) and using this result in equation (4.51), the well-known expression for the Green-Lagrange strain tensor as a function of the displacement components is obtained

$$ {}^{t}E_{ij} = \frac{1}{2} \left(\frac{\partial\, {}^{t}u_i}{\partial\, {}^{0}x_j} + \frac{\partial\, {}^{t}u_j}{\partial\, {}^{0}x_i} + \frac{\partial\, {}^{t}u_k}{\partial\, {}^{0}x_i} \cdot \frac{\partial\, {}^{t}u_k}{\partial\, {}^{0}x_j} \right) \tag{4.53} $$

Two important properties of the strain tensors C_{ij} and E_{ij} are (i) the symmetry, and (ii) the vanishing of all terms in the absence of strain, i.e., when only rigid body motion occurs.

The 2nd Piola-Kirchhoff stress tensor

Consider a cubic element of a strained solid, whose centre is characterized by the coordinates ${}^{t}x_1$, ${}^{t}x_2$, ${}^{t}x_3$, according to the representation of Figure 4.25.

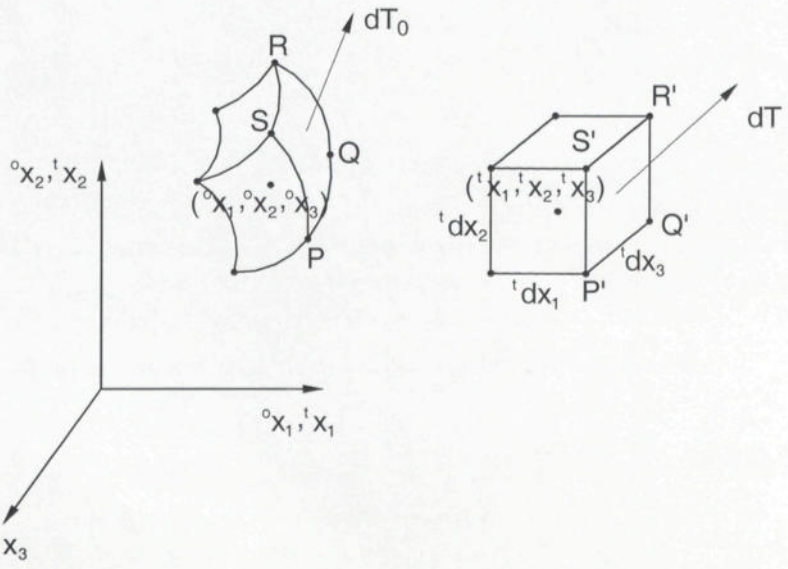


Figure 4.25. Representation of a volume element in the undeformed and deformed state, and corresponding vector forces acting on a particular surface.

In general, the stresses on a particular external surface of a volume element are referred to the strained configuration of the solid, and are characterized by the well-known Cauchy tensor σ_{ij}. So, the force vector $\boldsymbol{d}^t\boldsymbol{T}$ acting on a surface element *P'Q'R'S'* of area $d\,^tS$ characterized by a unit outer normal vector $^t\hat{n}$, can be obtained through the Cauchy's relation by

$$d\,^tT_i = \sigma_{ji} \cdot {}^tn_j \cdot d\,^tS, \text{ with } i=1, 2, 3 \tag{4.54}$$

Since strains are referred here to the undeformed state of the solid, it is convenient that the same criterion is adopted for the definition of stress tensors. So, the force vector $\boldsymbol{d}^t\boldsymbol{T}$ acting on the strained surface *P'Q'R'S'*, must be related with the force vector $\boldsymbol{d}^0\boldsymbol{T}$ acting on the corresponding undeformed surface *PQRS*, characterized by a unit outer normal vector $^0\hat{n}$ (note that in the undeformed state, the cubic element is a curved solid centred at a point with coordinates $^0x_1$, $^0x_2$, $^0x_3$, as represented in Figure 4.25).

Adopting the Kirchhoff rule (Fung, 1965), the following correspondence between $\boldsymbol{d}^t\boldsymbol{T}$ and $\boldsymbol{d}^0\boldsymbol{T}$ is obtained

$$d\,^0T_i = \frac{\partial\,^0x_i}{\partial\,^tx_j} \cdot d\,^tT_j \tag{4.55}$$

The force vector $\boldsymbol{d}^0\boldsymbol{T}$ will then be obtained, relating a tensor S_{ij} with the unit outer normal $^0\hat{n}$ and the area $d\,^0S$ of the undeformed surface *PQRS* through

$$d\,^0T_i = {}^tS_{ji}\,{}^0n_j d\,^0S \tag{4.56}$$

where $^tS_{ij}$ is defined as the *Kirchhoff tensor*, or the *2nd Piola-Kirchhoff tensor*, and expresses the stress state at time *t* in terms of the original undeformed referential. Equating equations (4.55) and (4.56), a relationship between $^tS_{ij}$ and σ_{ij} can be established, which requires however that the relation between the quantities $^tn_j\,d\,^tS$ and $^0n_j\,d\,^0S$ is known.

Considering the hypothesis of conservation of the mass, and defining $^t\rho$ and $^0\rho$ as the densities of the material in the deformed and in the original state, respectively, this relation is given by (Fung, 1965)

$$\frac{\partial\,^0x_i}{\partial\,^tx_\gamma} \cdot {}^0n_i \cdot d\,^0S = \frac{^t\rho}{^0\rho} \cdot {}^tn_\gamma \cdot d\,^tS \tag{4.57}$$

So, the *2nd Piola-Kirchhoff stress tensor* ${}^{t}S_{ij}$ relates with the *Cauchy tensor* σ_{ij} through

$$ {}^{t}S_{ji} = \frac{{}^{0}\rho}{{}^{t}\rho} \cdot \frac{\partial\, {}^{0}x_i}{\partial\, {}^{t}x_\alpha} \cdot \frac{\partial\, {}^{0}x_j}{\partial\, {}^{t}x_\beta} \cdot \sigma_{\beta\alpha} \tag{4.58} $$

This tensor can also be expressed in terms of the displacement components ${}^{t}u_i$ as

$$ {}^{t}S_{ji} = \frac{{}^{t}\rho}{{}^{0}\rho} \cdot \left[\sigma_{ji} - \left(\delta_{j\beta} \frac{\partial\, {}^{t}u_i}{\partial\, {}^{t}x_\alpha} + \delta_{i\alpha} \frac{\partial\, {}^{t}u_j}{\partial\, {}^{t}x_\beta} - \frac{\partial\, {}^{t}u_i}{\partial\, {}^{t}x_\alpha} \cdot \frac{\partial\, {}^{t}u_j}{\partial\, {}^{t}x_\beta} \right) \cdot \sigma_{\beta\alpha} \right] \tag{4.59} $$

Note that the relation between the mass densities at times *0* and *t*, ${}^{0}\rho$ and ${}^{t}\rho$, can be established using again the hypothesis of conservation of mass, yielding

$$ {}^{t}\rho = {}^{0}\rho \cdot det\left(\frac{\partial\, {}^{0}x_i}{\partial\, {}^{t}x_j} \right) \tag{4.60} $$

The *2nd Piola-Kirchhoff stress tensor* has also some important properties, namelly (i) the symmetry, and (ii) the invariance of its components under rigid body motion of the structure.

Another important property relating the *2nd Piola-Kirchhoff stress tensor* and the *Green-Lagrange strain tensor*, is that the two tensors are energetically conjugate. This means that when applying the principle of virtual displacements at time *t*, the virtual work expression can be equally written in terms of these tensors, referred to the original configuration of the structure, or in terms of the stress and strain tensors referred to the strained configuration (the *Cauchy stress tensor* ${}^{t}\sigma_{ij}$, and the *infinitesimal strain tensor* ${}^{t}e_{ij}$), i.e.

$$ \int_{{}^{0}V} {}^{t}S_{ij}\, \delta\, {}^{t}E_{ij}\, {}^{0}dV = \int_{{}^{t}V} {}^{t}\sigma_{mn}\, \delta\, {}^{t}e_{mn}\, {}^{t}dV \tag{4.61} $$

The symbol δ in equation (4.61) means "*variation in*", and the strain tensor ${}^{t}e_{mn}$ is defined by

$$ {}^{t}e_{mn} = \frac{1}{2} \left(\frac{\partial\, {}^{t}u_m}{\partial\, {}^{t}x_n} + \frac{\partial\, {}^{t}u_n}{\partial\, {}^{t}x_m} \right) \tag{4.62} $$

General incremental continuous mechanics equations

The equilibrium equations are now presented, considering an incremental formulation and assuming that for all discrete time instants between *0* and *t* the equilibrium position is known.

The application of the Principle of Virtual Work at time $t+\Delta t$ requires that

$$\int_{{}^{t+\Delta t}V} {}^{t+\Delta t}\sigma_{ij}\,\delta\,{}^{t+\Delta t}e_{ij}\;{}^{t+\Delta t}dV = {}^{t+\Delta t}\Re \tag{4.63}$$

In this equation ${}^{t+\Delta t}\sigma_{ij}$ and ${}^{t+\Delta t}e_{ij}$ represent the Cauchy stress tensor and the infinitesimal strain tensor, respectively, at time $t+\Delta t$. The quantity ${}^{t+\Delta t}\Re$ represents the external virtual work, and is given by

$${}^{t+\Delta t}\Re = \int_{{}^{t+\Delta t}V} {}^{t+\Delta t}f_i^B\,\delta u_i\;{}^{t+\Delta t}dV + \int_{{}^{t+\Delta t}S} {}^{t+\Delta t}f_i^S\,\delta u_i^S\;{}^{t+\Delta t}dS \tag{4.64}$$

where ${}^{t+\Delta t}f_i^B$ and ${}^{t+\Delta t}f_i^S$ are the components of the externally applied body and surface forces, respectively, and δu_i are the components of the virtual displacement vector.

As the volume and surface configurations are unknown at time $t+\Delta t$, equation (4.63) needs to be expressed in terms of a previously known configuration. In principle, since the equilibrium equations have already been solved for all time instants *0*, Δt, $2\Delta t$, ..., between *0* and *t*, any of the corresponding configurations could be used. In practice, however, only two alternatives are normally chosen, one that corresponds to refer the system of equations to the original configuration at time *0*, and another, that refers the system of equations to time *t*, i.e., to the previous increment of load considered. These possibilities lead to the so-called *Total Lagrangian* (*TL*) and *Updated Lagrangian* (*UL*) formulations, respectively. Although these formulations are equivalent in terms of final results, it is generally considered that the *UL* method is more effective numerically. For this reason, this formulation is normally adopted in the solution of geometrically nonlinear problems and will be described here.

Using the property described by equation (4.61) associated with the *2nd Piola-Kirchhoff stress tensor* and the *Green-Lagrange strain tensor*, but referring these tensors now to time *t*, the following relation holds

$$\int_{{}^{t}V} {}^{t+\Delta t}_{t}S_{ij}\,\delta\,{}^{t+\Delta t}_{t}E_{ij}\;{}^{t}dV = {}^{t+\Delta t}\Re \tag{4.65}$$

where the *2nd Piola-Kirchhoff stress tensor* ${}^{t+\Delta t}_{t}S_{ij}$ at time $t+\Delta t$ referred to time *t* is now defined as

$$ {}^{t+\Delta t}_{t}S_{ji} = \frac{{}^{t}\rho}{{}^{t+\Delta t}\rho} \cdot \frac{\partial\, {}^{t}x_i}{\partial\, {}^{t+\Delta t}x_\alpha} \cdot \frac{\partial\, {}^{t}x_j}{\partial\, {}^{t+\Delta t}x_\beta} \cdot {}^{t+\Delta t}\sigma_{\beta\alpha} \tag{4.66} $$

and the *Green-Lagrange strain tensor* ${}^{t+\Delta t}_{t}E_{ij}$ referred to the same time is

$$ {}^{t+\Delta t}_{t}E_{ij} = \frac{1}{2}\left(\frac{\partial u_i}{\partial\, {}^{t}x_j} + \frac{\partial u_j}{\partial\, {}^{t}x_i} + \frac{\partial u_k}{\partial\, {}^{t}x_i} \cdot \frac{\partial u_k}{\partial\, {}^{t}x_j} \right) \tag{4.67} $$

Note that u_i represents the components of the increment of displacement at time $t + \Delta t$ referred to time t, i.e.

$$ u_i = {}^{t+\Delta t}u_i - {}^{t}u_i \tag{4.68} $$

The quantities ${}^{t}u_i$ and ${}^{t+\Delta t}u_i$ in this equation are the components of the total displacement associated with point P above described at times t and $t + \Delta t$, respectively. The coordinates of P at time $t + \Delta t$ are then

$$ {}^{t+\Delta t}x_i = {}^{0}x_i + {}^{t+\Delta t}u_i = {}^{0}x_i + {}^{t}u_i + u_i = {}^{t}x_i + u_i \tag{4.69} $$

As for the second member of equation (4.65), and assuming that the loading is deformation-independent, the external virtual work ${}^{t+\Delta t}\Re$ can be evaluated using

$$ {}^{t+\Delta t}\Re = \int_{{}^{0}V} {}^{t+\Delta t}f_i^B \delta u_i \, {}^{0}dV + \int_{{}^{0}S} {}^{t+\Delta t}f_i^S \delta u_i^S \, {}^{0}dS \tag{4.70} $$

The solution of equation (4.65) is now obtained approximately by linearization of the stress and strain tensors at time t.

The stress tensor is incrementally decomposed as

$$ {}^{t+\Delta t}_{t}S_{ij} = {}^{t}_{t}S_{ij} + {}_{t}S_{ij} = {}^{t}\sigma_{ij} + {}_{t}S_{ij} \tag{4.71} $$

whereas the incremental strain tensor ${}_{t}E_{ij}$ can be assigned to

$$ {}^{t+\Delta t}_{t}E_{ij} = {}_{t}E_{ij} \tag{4.72} $$

and divided into two components

$$ {}_{t}E_{ij} = {}^{t}e_{ij} + {}^{t}\eta_{ij} \tag{4.73} $$

with

$$ {}^{t}e_{ij} = \frac{1}{2}\left(\frac{\partial u_i}{\partial {}^{t}x_j} + \frac{\partial u_j}{\partial {}^{t}x_i} \right) \tag{4.74} $$

and

$$ {}^{t}\eta_{ij} = \frac{1}{2} \cdot \frac{\partial u_k}{\partial {}^{t}x_i} \cdot \frac{\partial u_k}{\partial {}^{t}x_j} \tag{4.75} $$

Substituting equations (4.71) to (4.73) into (4.65) results

$$ \int_{{}^{t}V} {}_{t}S_{ij}\, \delta\, {}_{t}E_{ij}\, {}^{t}dV + \int_{{}^{t}V} {}^{t}\sigma_{ij}\, \delta\, {}^{t}\eta_{ij}\, {}^{t}dV = {}^{t+\Delta t}\Re - \int_{{}^{t}V} {}^{t}\sigma_{ij}\, \delta\, {}^{t}e_{ij}\, {}^{t}dV \tag{4.76} $$

Equation (4.76) is now linearized using the following approximations

$$ {}_{t}S_{ij} = {}_{t}C_{ijrs} \cdot {}^{t}e_{rs} \tag{4.77} $$

$$ \delta\, {}_{t}E_{ij} = \delta\, {}^{t}e_{ij} \tag{4.78} $$

where ${}_{t}C_{ijrs}$ is the incremental material property tensor at time t referred to the configuration of the structure at that instant. The following result is then obtained

$$ \int_{{}^{t}V} {}_{t}C_{ijrs}\, {}^{t}e_{rs}\, \delta\, {}^{t}e_{ij}\, {}^{t}dV + \int_{{}^{t}V} {}^{t}\sigma_{ij}\, \delta\, {}^{t}\eta_{ij}\, {}^{t}dV = {}^{t+\Delta t}\Re - \int_{{}^{t}V} {}^{t}\sigma_{ij}\, \delta\, {}^{t}e_{ij}\, {}^{t}dV \tag{4.79} $$

In the present problem, a linear elastic material is considered, which leads to constant components of the tensor ${}_{t}C_{ijrs}$, given by

$$ {}_{t}C_{ijrs} = \lambda\, \delta_{ij}\, \delta_{rs} + \mu\, (\delta_{ir}\, \delta_{js} + \delta_{is}\, \delta_{jr}) \tag{4.80} $$

The quantities δ_{mn} in this equation represent the Kronecker delta, while λ and μ are the Lamé constants, which depend on the Poisson coefficient ν according to

$$ \lambda = \frac{E\nu}{(1+\nu)(1-2\nu)}, \quad \mu = \frac{E}{2(1+\nu)} \tag{4.81} $$

Equation (4.79) can now be used to calculate the incremental displacements u_i, and consequently to obtain a first estimate of the total displacements, strains and stresses at time $t + \Delta t$.

Due to linearization, the external virtual work ${}^{t+\Delta t}\Re$ will slightly differ from the internal virtual work. As the Cauchy stress tensor and the strain tensor have now been estimated at time $t+\Delta t$, the error in the approximation can be evaluated from

$$Error = {}^{t+\Delta t}\Re - \int_{{}^{t+\Delta t}V} {}^{t+\Delta t}\sigma_{ij}^{(1)}\,\delta\,{}^{t+\Delta t}e_{ij}^{(1)}\;{}^{t+\Delta t}dV \tag{4.82}$$

Note that the symbol "$.^{(1)}$" in equation (4.82) refers to the first iteration. In order to reduce the out-of-balance virtual work, an iteration procedure can be developed which leads, for the iteration of order *(k)*, to the following equation

$$\begin{aligned}\int_{{}^{t}V} {}_{t}C_{ijrs}\,\Delta\,{}^{t}e_{rs}^{(k)}\,\delta\,{}^{t}e_{ij}\;{}^{t}dV + \int_{{}^{t}V} {}^{t}\sigma_{ij}\,\delta\,\Delta\,{}^{t}\eta_{ij}^{(k)}\;{}^{t}dV = {}^{t+\Delta t}\Re - \\ - \int_{{}^{t+\Delta t}V} {}^{t+\Delta t}\sigma_{ij}^{(k-1)}\,\delta\,{}^{t+\Delta t}e_{ij}^{(k-1)}\;{}^{t+\Delta t}dV\end{aligned} \tag{4.83}$$

The total displacements at time $t+\Delta t$ are then updated according to

$${}^{t+\Delta t}u_i^{(k)} = {}^{t+\Delta t}u_i^{(k-1)} + u_i^{(k)} \qquad {}^{t+\Delta t}u_i^{(0)} = {}^{t}u_i \tag{4.84}$$

4.3.3.2 Governing finite element equations for static analysis

The continuous structure is now discretized into an assembly of finite elements, which are connected with each other at a discrete number of nodal points along the element boundaries. An approximation of the value of a generic variable inside each element can be obtained from the corresponding value at the element nodes, using appropriately chosen interpolation functions.

In particular, the incremental displacement components $u_i^{(m)}$ of a point of coordinates x_j inside a generic finite element *(m)*, will be given approximately as a function of the incremental nodal displacements ΔU_i^k associated with node *k* by

$$u_i^{(m)}(x_j) = \sum_{k=1}^{N} H_k^{(m)}(x_j)\cdot\Delta U_i^k \text{ , with } \quad i = 1,2,3 \text{ and } \quad k = 1,2,...,N \tag{4.85}$$

The functions $H_k^{(m)}(x_j)$ in this equation are the interpolation functions associated with the m_{th} finite element, *N* being the number of nodal points of the finite element.

Using isoparametric finite elements, which employ the same interpolation functions to describe the variation of displacements and coordinates, the following relation yields for the coordinates x_i

$$x_i^{(m)} = \sum_{k=1}^{N} H_k^{(m)} \cdot X_i^k \,, \quad \text{with} \quad i=1, 2, 3 \tag{4.86}$$

where X_i^k are the coordinates of the finite element nodal point k.

For simplicity, the symbol $.^{(m)}$ will be dropped in the subsequent text. It should be noted however that the incremental equilibrium equation derived herein respects this generic finite element.

Equations (4.85) and (4.86) can be expressed in matrix notation as

$$\underset{(3x1)}{\boldsymbol{u}(x_j)} = \underset{(3x3N)\cdot(3Nx1)}{\boldsymbol{H} \cdot \boldsymbol{\Delta U}} \tag{4.87}$$

and

$$\boldsymbol{x}(x_j) = \boldsymbol{H} \cdot \boldsymbol{X} \tag{4.88}$$

where the matrix $\boldsymbol{H}$ is defined as a function of the identity matrix of third order $\boldsymbol{I_3}$ as

$$\mathbf{H} = [H_1 \boldsymbol{I_3} \mid H_2 \boldsymbol{I_3} \mid \ldots \mid H_N \boldsymbol{I_3}] \qquad \boldsymbol{I_3} = \begin{bmatrix} 1 & 0 & 0 \\ 0 & 1 & 0 \\ 0 & 0 & 1 \end{bmatrix} \tag{4.89}$$

and the incremental nodal displacement vector is formed by the ith components associated with node k, ΔU_i^k

$$\boldsymbol{\Delta U}^T = \left[\Delta U_1^1 \quad \Delta U_2^1 \quad \Delta U_3^1 \mid \Delta U_1^2 \quad \Delta U_2^2 \quad \Delta U_3^2 \mid \ldots \mid \Delta U_1^N \quad \Delta U_2^N \quad \Delta U_3^N \right] \tag{4.90}$$

In view of their symmetry, the components of the incremental strain tensor ${}_tE_{ij}$ and of the Cauchy stress tensor ${}^t\sigma_{ij}$ can be expressed in vectorial form respectively as

$$\boldsymbol{\varepsilon}^T = [{}_tE_{11} \quad {}_tE_{22} \quad {}_tE_{33} \quad 2{}_tE_{12} \quad 2{}_tE_{23} \quad 2{}_tE_{31}] \tag{4.91}$$

and

$$\boldsymbol{\tau}^T = \left[{}^t\sigma_{11} \quad {}^t\sigma_{22} \quad {}^t\sigma_{33} \quad {}^t\sigma_{12} \quad {}^t\sigma_{23} \quad {}^t\sigma_{31} \right] \tag{4.92}$$

Establishing the same indicial correspondence for the components of ${}^te_{ij}$ and ${}^t\eta_{ij}$ (see equation (4.73)), the following vectors can be formed

$$\boldsymbol{\varepsilon}_l^T = \left[\begin{array}{cccccc} {}^t e_{11} & {}^t e_{22} & {}^t e_{33} & 2^t e_{12} & 2^t e_{23} & 2^t e_{31} \end{array} \right] \tag{4.93}$$

and

$$\boldsymbol{\varepsilon}_{nl}^T = \left[\begin{array}{cccccc} {}^t \eta_{11} & {}^t \eta_{22} & {}^t \eta_{33} & 2^t \eta_{12} & 2^t \eta_{23} & 2^t \eta_{31} \end{array} \right] \tag{4.94}$$

which represent, respectively, the linear and nonlinear components of the incremental strain tensor $\boldsymbol{\varepsilon}$, i.e.

$$\boldsymbol{\varepsilon} = \boldsymbol{\varepsilon}_l + \boldsymbol{\varepsilon}_{nl} \tag{4.95}$$

Considering now relations (4.74) and (4.75), the components of the vectors $\boldsymbol{\varepsilon}_l$ and $\boldsymbol{\varepsilon}_{nl}$ can be expressed as functions of the nodal displacement vector $\boldsymbol{\Delta U}$ as

$$\boldsymbol{\varepsilon}_l = \boldsymbol{B}_l \cdot \boldsymbol{\Delta U} \tag{4.96}$$

and

$$\boldsymbol{\varepsilon}_{nl} = \frac{1}{2} \boldsymbol{B}_{nl} \cdot \boldsymbol{\Delta U} \tag{4.97}$$

The matrix $\boldsymbol{B}_l$ is independent of the nodal displacements, and is formed by the derivatives of the interpolation functions according to

$$\boldsymbol{B}_l = \left[\begin{array}{ccc|ccc|ccc} \frac{\partial H_1}{\partial x_1} & 0 & 0 & \cdots & \cdots & \cdots & \frac{\partial H_N}{\partial x_1} & 0 & 0 \\ 0 & \frac{\partial H_1}{\partial x_2} & 0 & \cdots & \cdots & \cdots & 0 & \frac{\partial H_N}{\partial x_2} & 0 \\ 0 & 0 & \frac{\partial H_1}{\partial x_3} & \cdots & \cdots & \cdots & 0 & 0 & \frac{\partial H_N}{\partial x_3} \\ \frac{\partial H_1}{\partial x_2} & \frac{\partial H_1}{\partial x_1} & 0 & \cdots & \cdots & \cdots & \frac{\partial H_N}{\partial x_2} & \frac{\partial H_N}{\partial x_1} & 0 \\ 0 & \frac{\partial H_1}{\partial x_3} & \frac{\partial H_1}{\partial x_2} & \cdots & \cdots & \cdots & 0 & \frac{\partial H_N}{\partial x_3} & \frac{\partial H_N}{\partial x_2} \\ \frac{\partial H_1}{\partial x_3} & 0 & \frac{\partial H_1}{\partial x_1} & \cdots & \cdots & \cdots & \frac{\partial H_N}{\partial x_3} & 0 & \frac{\partial H_N}{\partial x_1} \end{array} \right] \tag{4.98}$$

On the contrary, the matrix $\boldsymbol{B}_{nl}$ depends on the nodal displacements and can be defined as the product of two matrices $\boldsymbol{A}$ and $\boldsymbol{G}$

$$\boldsymbol{B}_{nl} = \boldsymbol{A} \cdot \boldsymbol{G} \tag{4.99}$$

The matrix $\boldsymbol{A}$ depends on the displacement field and is defined as

$$\boldsymbol{A}=\left[\begin{array}{ccc|ccc|ccc}
\frac{\partial u_1}{\partial x_1} & 0 & 0 & \frac{\partial u_2}{\partial x_1} & 0 & 0 & \frac{\partial u_3}{\partial x_1} & 0 & 0 \\
0 & \frac{\partial u_1}{\partial x_2} & 0 & 0 & \frac{\partial u_2}{\partial x_2} & 0 & 0 & \frac{\partial u_3}{\partial x_2} & 0 \\
0 & 0 & \frac{\partial u_1}{\partial x_3} & 0 & 0 & \frac{\partial u_2}{\partial x_3} & 0 & 0 & \frac{\partial u_3}{\partial x_3} \\
\frac{\partial u_1}{\partial x_2} & \frac{\partial u_1}{\partial x_1} & 0 & \frac{\partial u_2}{\partial x_2} & \frac{\partial u_2}{\partial x_1} & 0 & \frac{\partial u_3}{\partial x_2} & \frac{\partial u_3}{\partial x_1} & 0 \\
0 & \frac{\partial u_1}{\partial x_3} & \frac{\partial u_1}{\partial x_2} & 0 & \frac{\partial u_2}{\partial x_3} & \frac{\partial u_2}{\partial x_2} & 0 & \frac{\partial u_3}{\partial x_3} & \frac{\partial u_3}{\partial x_2} \\
\frac{\partial u_1}{\partial x_3} & 0 & \frac{\partial u_1}{\partial x_1} & \frac{\partial u_2}{\partial x_3} & 0 & \frac{\partial u_2}{\partial x_1} & \frac{\partial u_3}{\partial x_3} & 0 & \frac{\partial u_3}{\partial x_1}
\end{array}\right] \tag{4.100}$$

The matrix $\boldsymbol{G}$ contains only derivatives of the interpolation functions and is

$$\boldsymbol{G}=\left[\begin{array}{ccc|ccc|ccc}
\frac{\partial H_1}{\partial x_1} & 0 & 0 & \cdots & \cdots & \cdots & \frac{\partial H_N}{\partial x_1} & 0 & 0 \\
\frac{\partial H_1}{\partial x_2} & 0 & 0 & \cdots & \cdots & \cdots & \frac{\partial H_N}{\partial x_2} & 0 & 0 \\
\frac{\partial H_1}{\partial x_3} & 0 & 0 & \cdots & \cdots & \cdots & \frac{\partial H_N}{\partial x_3} & 0 & 0 \\
0 & \frac{\partial H_1}{\partial x_1} & 0 & \cdots & \cdots & \cdots & 0 & \frac{\partial H_N}{\partial x_1} & 0 \\
0 & \frac{\partial H_1}{\partial x_2} & 0 & \cdots & \cdots & \cdots & 0 & \frac{\partial H_N}{\partial x_2} & 0 \\
0 & \frac{\partial H_1}{\partial x_3} & 0 & \cdots & \cdots & \cdots & 0 & \frac{\partial H_N}{\partial x_3} & 0 \\
0 & 0 & \frac{\partial H_1}{\partial x_1} & \cdots & \cdots & \cdots & 0 & 0 & \frac{\partial H_N}{\partial x_1} \\
0 & 0 & \frac{\partial H_1}{\partial x_2} & \cdots & \cdots & \cdots & 0 & 0 & \frac{\partial H_N}{\partial x_2} \\
0 & 0 & \frac{\partial H_1}{\partial x_3} & \cdots & \cdots & \cdots & 0 & 0 & \frac{\partial H_N}{\partial x_3}
\end{array}\right] \tag{4.101}$$

The linearized incremental equations of equilibrium (4.79) can now be expressed in terms of the incremental nodal displacement vector $\boldsymbol{\Delta U}$. For this purpose, the variations in the linear and nonlinear components of the strain tensors, $\boldsymbol{\delta \varepsilon_l}$ and $\boldsymbol{\delta \varepsilon_{nl}}$, need to be addressed.

Considering the definition of $\boldsymbol{\varepsilon_l}$ in terms of the nodal displacement vector $\boldsymbol{\Delta U}$ given by equation (4.96), it results that

$$\boldsymbol{\delta \varepsilon_l = B_l \cdot \delta \Delta U} \tag{4.102}$$

where $\boldsymbol{\delta \Delta U}$ represents the variation in the nodal displacements $\boldsymbol{\Delta U}$.

For the nonlinear component $\boldsymbol{\varepsilon_{nl}}$, the displacement dependence of $\boldsymbol{B_{nl}}$ leads to the following result

$$\delta \varepsilon_{nl} = \frac{1}{2} (\delta B_{nl} \cdot \Delta U + B_{nl} \cdot \delta \Delta U) \tag{4.103}$$

Given the definition of B_{nl} by equation (4.99), and considering that

$$\delta B_{nl} \cdot \Delta U = \delta A \cdot G \cdot \Delta U = A \cdot G \cdot \delta \Delta U \tag{4.104}$$

it results that

$$\delta \varepsilon_{nl} = B_{nl} \cdot \delta \Delta U \tag{4.105}$$

Introducing the matrix notation and the results above obtained in equation (4.79), it follows that

$$\int_{{}^tV} \delta \varepsilon_l^T \cdot D \cdot \varepsilon_l \, {}^tdV + \int_{{}^tV} \delta \varepsilon_{nl}^T \cdot \tau \, {}^tdV = {}^{t+\Delta t}\Re - \int_{{}^tV} \delta \varepsilon_l^T \cdot \tau \, {}^tdV \tag{4.106}$$

where the matrix D is derived from the tensor C_{ijrs} considering linear elastic material. This matrix is given on the basis of the Lamé parameters by

$$D = \begin{bmatrix} \lambda+2\mu & \lambda & \lambda & 0 & 0 & 0 \\ \lambda & \lambda+2\mu & \lambda & 0 & 0 & 0 \\ \lambda & \lambda & \lambda+2\mu & 0 & 0 & 0 \\ 0 & 0 & 0 & \mu & 0 & 0 \\ 0 & 0 & 0 & 0 & \mu & 0 \\ 0 & 0 & 0 & 0 & 0 & \mu \end{bmatrix} \tag{4.107}$$

Introducing (4.102) and (4.105) in equation (4.106) yields

$$\int_{{}^tV} \delta \Delta U^T \cdot B_l^T \cdot D \cdot B_l \cdot \Delta U \, {}^tdV + \int_{{}^tV} \delta \Delta U^T \cdot B_{nl}^T \cdot \tau \, {}^tdV = {}^{t+\Delta t}\Re - \int_{{}^tV} \delta \Delta U^T \cdot B_l^T \cdot \tau \, {}^tdV \tag{4.108}$$

and given the equality

$$B_{nl}^T \cdot \tau = G^T \cdot \sigma \cdot G \cdot \Delta U \tag{4.109}$$

in which the matrix σ is formed by the components of the Cauchy stress tensor ${}^t\sigma_{ij}$ according to

$$\sigma = \begin{bmatrix} \tilde{\sigma} & \tilde{0} & \tilde{0} \\ \tilde{0} & \tilde{\sigma} & \tilde{0} \\ \tilde{0} & \tilde{0} & \tilde{\sigma} \end{bmatrix}, \quad \text{with} \quad \tilde{\sigma} = \begin{bmatrix} {}^t\sigma_{11} & {}^t\sigma_{12} & {}^t\sigma_{13} \\ {}^t\sigma_{21} & {}^t\sigma_{22} & {}^t\sigma_{23} \\ {}^t\sigma_{31} & {}^t\sigma_{32} & {}^t\sigma_{33} \end{bmatrix} \tag{4.110}$$

$$\text{and} \quad \tilde{0} = \begin{bmatrix} 0 & 0 & 0 \\ 0 & 0 & 0 \\ 0 & 0 & 0 \end{bmatrix}$$

equation (4.108) reduces to

$$\int_{{}^tV} \boldsymbol{\delta \Delta U}^T \cdot \boldsymbol{B}_l^T \cdot \boldsymbol{D} \cdot \boldsymbol{B}_l \cdot \boldsymbol{\Delta U}\, {}^tdV + \int_{{}^tV} \boldsymbol{\delta \Delta U}^T \cdot \boldsymbol{G}^T \cdot \boldsymbol{\sigma} \cdot \boldsymbol{G} \cdot \boldsymbol{\Delta U}\, {}^tdV = \\ = {}^{t+\Delta t}\Re - \int_{{}^tV} \boldsymbol{\delta \Delta U}^T \cdot \boldsymbol{B}_l^T \cdot \boldsymbol{\tau}\, {}^tdV \tag{4.111}$$

The external virtual work ${}^{t+\Delta t}\Re$ defined above by equation (4.70) can also be established as a function of the incremental nodal displacement vector $\boldsymbol{\Delta U}$ and of the interpolation function matrices $\boldsymbol{H}^S$ (surface) and $\boldsymbol{H}$ (volume)

$${}^{t+\Delta t}\Re = \int_{{}^0V} \boldsymbol{\delta \Delta U}^T \cdot \boldsymbol{H}^T \cdot \boldsymbol{f}^B\, {}^0dV + \int_{{}^0S} \boldsymbol{\delta \Delta U}^T \cdot \boldsymbol{H}^{S^T} \cdot \boldsymbol{f}^S\, {}^0dS \tag{4.112}$$

The vectors $\boldsymbol{f}^B$ and $\boldsymbol{f}^S$ in this equation contain the components of the body and surface forces per unit volume and area, respectively.

Note that the integrals in the equations presented above respect the volume and surface of the generic finite element of order *m*. The extension to the full structure is straightforward.

The general equilibrium equations for the incremental load at time $t+\Delta t$ in the i_{th} iteration can now be obtained from (4.111) and (4.112) as

$$({}^t_t\boldsymbol{K}_L + {}^t_t\boldsymbol{K}_{NL})\boldsymbol{\Delta U}^{(i)} = \boldsymbol{R}^{t+\Delta t} - {}^{t+\Delta t}_{t+\Delta t}\boldsymbol{F}^{(i-1)} \tag{4.113}$$

with

$${}^t_t\boldsymbol{K}_L = \int_{{}^tV} \boldsymbol{B}_l^T \cdot \boldsymbol{D} \cdot \boldsymbol{B}_l\, {}^tdV \tag{4.114}$$

$${}^t_t\boldsymbol{K}_{NL} = \int_{{}^tV} \boldsymbol{G}^T \cdot \boldsymbol{\sigma} \cdot \boldsymbol{G}\, {}^tdV \tag{4.115}$$

$${}^{t+\Delta t}\boldsymbol{R} = \int_{{}^0V} \boldsymbol{H}^T \cdot \boldsymbol{f}^B\, {}^0dV + \int_{{}^0S} \boldsymbol{H}^{S^T} \cdot \boldsymbol{f}^S\, {}^0dS \tag{4.116}$$

$${}^{t+\Delta t}_{t+\Delta t}\boldsymbol{F}^{(i-1)} = \int_{{}^tV} \boldsymbol{B}_l^T \cdot \boldsymbol{\tau}^{(i-1)}\, {}^tdV \tag{4.117}$$

These quantities have the following significance:

${}_t^t\boldsymbol{K}_L$ - Linear strain incremental stiffness matrix calculated at time t;

${}_t^t\boldsymbol{K}_{NL}$ - Nonlinear strain incremental stiffness matrix calculated at time t.This matrix is also designated as geometric or initial incremental stiffness matrix;

${}^{t+\Delta t}\boldsymbol{R}$ - Vector of the externally applied nodal point loads at time $t+\Delta t$;

${}_{t+\Delta t}^{t+\Delta t}\boldsymbol{F}^{(i-1)}$ - Vector of the nodal point forces equivalent to the element stresses at time $t+\Delta t$ associated with the previous iteration *(i-1);*

$\boldsymbol{\Delta U}^{(i)}$ - Vector of the incremental nodal point displacements in iteration *(i).* The nodal displacement vector at time $t+\Delta t$ in iteration *(i)* is then

$$ {}^{t+\Delta t}\boldsymbol{U}^{(i)} = {}^{t+\Delta t}\boldsymbol{U}^{(i-1)} + \boldsymbol{\Delta U}^{(i)} $$

The matrix ${}_t^t\boldsymbol{K}_S$ obtained by

$$ {}_t^t\boldsymbol{K}_S = {}_t^t\boldsymbol{K}_L + {}_t^t\boldsymbol{K}_{NL} \tag{4.118} $$

represents actually a secant incremental stiffness matrix associated with the finite element/ volume under consideration. This matrix is obtained as the result of the linearization of the general nonlinear incremental stiffness matrix.

4.3.3.3 Governing finite element equations for dynamic analysis

The set of finite element equations derived above for static analysis can now be extended to the dynamic problem, assuming that a implicit time integration is performed .The general system of equations is then

$$ \boldsymbol{M}\,{}^{t+\Delta t}\ddot{\boldsymbol{U}}^{(i)} + \boldsymbol{C}\,{}^{t+\Delta t}\dot{\boldsymbol{U}}^{(i)} + ({}_t^t\boldsymbol{K}_L + {}_t^t\boldsymbol{K}_{NL})\boldsymbol{\Delta U}^{(i)} = \boldsymbol{R}^{t+\Delta t} - {}_{t+\Delta t}^{t+\Delta t}\boldsymbol{F}^{(i-1)} \tag{4.119} $$

The first term in this equation represents the inertia force vector, which is given by the product of a mass matrix $\boldsymbol{M}$ by the vector of nodal point accelerations at time $t+\Delta t$, in iteration *(i)*, ${}^{t+\Delta t}\ddot{\boldsymbol{U}}^{(i)}$. The matrix $\boldsymbol{M}$ is independent of the time instant of analysis and is defined as a function of the interpolation matrix $\boldsymbol{H}$ as follows

$$ \boldsymbol{M} = {}^0\rho\left(\int_{{}^0V} \boldsymbol{H}^T \cdot \boldsymbol{H}\; {}^0dV\right) \tag{4.120} $$

where ${}^0\rho$ is the material density.

The second term in equation (4.119) represents the damping force vector, which is for simplicity considered proportional to the velocity vector ${}^{t+\Delta t}\dot{\boldsymbol{U}}^{(i)}$. In this case, $\boldsymbol{C}$ is a consistent

damping matrix that can be expressed as a function of the interpolation functions matrix $\boldsymbol{H}$, and of a viscous damping matrix $\boldsymbol{\mu}$ as

$$\boldsymbol{C} = \int_{{}^0V} \boldsymbol{H}^T \cdot \boldsymbol{\mu} \cdot \boldsymbol{H}\, {}^0dV \tag{4.121}$$

The determination of the matrix $\boldsymbol{C}$ is in practice very difficult, as the knowledge of the viscous damping matrix $\boldsymbol{\mu}$ is lacking. Simplificative assumptions are therefore employed, one possibility being to express this matrix as a linear combination of the stiffness and mass matrices, i.e.

$$\boldsymbol{C} = \alpha \boldsymbol{M} + \beta \boldsymbol{K} \tag{4.122}$$

This is the so-called *Rayleigh-damping model*. The coefficients α and β of the decomposition above presented need to be defined based on experimental data. Note that the stiffness matrix $\boldsymbol{K}$ referred in equation (4.122) can be chosen as the linear stiffness matrix calculated for the original configuration of the structure. This leads to a time independent damping matrix and simplifies considerably the problem.

4.3.4 Finite element modelling of a cable-stayed bridge

The general incremental equilibrium equations for a three-dimensional body with a nonlinear geometric behaviour were derived in the previous Section. It is now the purpose of the present section to describe a finite element discretization procedure for dynamic analysis of a cable-stayed bridge. Given the two basic components of the bridge, which are the stay cables and the girders and towers, finite element matrices associated with a possible discretization of these elements will be presented in the current Section.

An important aspect to consider here is that the modelling of the bridge is usually performed at a number of different levels. These levels are not absolutely defined and may overlap with each other. However, a primary division into three different levels is possible. According to Kanok-Nukulchai *et al.* (1992), the modelling at the first level consists, in general, in performing a global analysis of the complete bridge. At a second level, all or some of the bridge components, namely the deck, towers or cables are studied individually. Finally, at a third level, particular details of the bridge can be studied, such as a cable socket, or a bearing device.

For the purpose of performing dynamic analysis over the cable-stayed bridge, a global model of the bridge will be considered in the context of the present Section.

4.3.4.1 Modelling of the stay cables

In the brief state-of-the-art presented above, it was referred that one of the major causes of nonlinearities in cable-stayed bridges is due to the cable sag. Historically, the geometric nonlinearity of the stay cables has been treated in three different ways: (i) modelling each stay cable as a single truss element characterized by an equivalent modulus of elasticity; (ii) modelling each stay cable as a series of truss elements; (iii) modelling each stay cable using curved cable elements. The first two possibilities involve the definition of the simplest element, the two-node finite element, which is presented below. The third alternative comprehends the use of more sophisticated cable elements, which incorporate some particular aspects of the nonlinear geometric stay cable behaviour, like the geometry and more approximate nonlinear stress-strain relations.

The present section derives the basic matrices associated with the two-node truss finite element. As an example of a more efficient finite element for description of the dynamic behaviour of the stay cable, the four-node truss finite element matrices are also presented.

The same assumptions will be made herein in the derivation of the two finite elements, namely: (i) the element develops stress only in the direction normal to its cross-section; (ii) the normal stress is uniform along the cross-sectional area; (iii) the cross-sectional area remains constant during deformation.

The two-node truss element

Consider the two-node truss element represented in Figure 4.26, with undeformed length ${}^0L$ (time *0*). The strain-displacement matrices at time *t* are established, for simplicity, in a local reference system ${}^t\tilde{x}_1 - {}^t\tilde{x}_2$. The transformation of these matrices into the global stationary system ${}^0x_1 - {}^0x_2$ is straightforward and won't be discussed here.

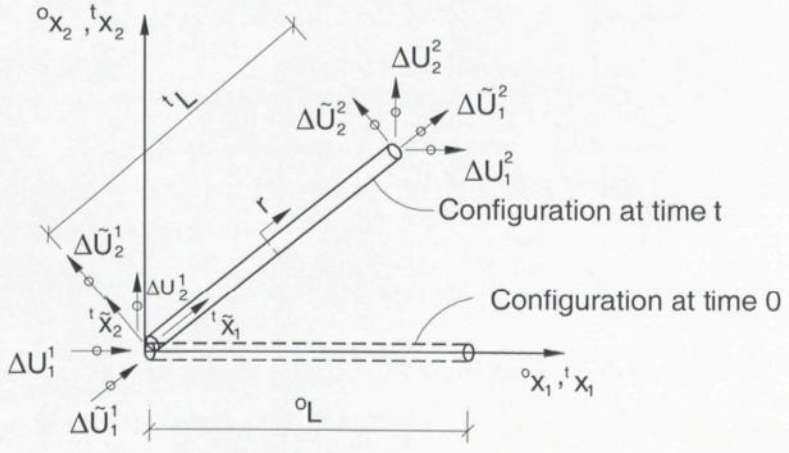


Figure 4.26. Two-node truss element: representation in the global and natural coordinate system.

Given the deformed configuration of the truss element at time *t*, the coordinates x_i of a generic point along the element are established as functions of the nodal coordinates X_i^k *(k=1, 2)*, using a natural coordinate system with variable *r*, where $-1 \le r \le 1$. The equation (4.86) applies, with *N=2*, the interpolation functions H_k being

$$H_1(r) = \frac{1}{2}(1-r)$$

$$H_2(r) = \frac{1}{2}(1+r)$$

and the nodal coordinate vector $\boldsymbol{X}$

$$\boldsymbol{X}^T = \left[0 \;\; 0 \;\; 0 \;\middle|\; {}^tL \;\; 0 \;\; 0 \right]$$

Considering an isoparametric formulation, the same interpolation functions are used to define the incremental displacement vector at the point characterized by coodinates x_i.

Now, for the calculation of the element stiffness matrix, only the first component of the vectors $\boldsymbol{\varepsilon}$ and $\boldsymbol{\tau}$ (equations (4.91) and (4.92)) are non nul. The matrices $\boldsymbol{B_l}$ and $\boldsymbol{G}$ used in the evaluation of the stiffness matrices are then formed from the matrices given in (4.98) and (4.101), retaining only the terms of interest. Noting that the generic quantities $\partial F / \partial x_i$ can be expressed by

$$\frac{\partial F}{\partial x_i} = \frac{\partial F}{\partial r} \cdot \frac{\partial r}{\partial x_i} \tag{4.123}$$

where $\partial r / \partial x_i = 2 / {}^tL$, the following relations hold

$$\boldsymbol{B_l} = \frac{1}{{}^tL} \cdot [-1 \;\; 0 \;\; 0 \,|\, 1 \;\; 0 \;\; 0]$$

$$\boldsymbol{G} = \frac{1}{{}^tL} \cdot \left[\begin{array}{ccc|ccc} -1 & 0 & 0 & 1 & 0 & 0 \\ 0 & -1 & 0 & 0 & 1 & 0 \\ 0 & 0 & -1 & 0 & 0 & 1 \end{array} \right]$$

The linear and geometric stiffness matrices of the truss element at time *t*, ${}^t_t\tilde{\boldsymbol{K}}_L$ and ${}^t_t\tilde{\boldsymbol{K}}_{NL}$, expressed in the local reference system ${}^t\tilde{x}_1 - {}^t\tilde{x}_2$ are then calculated as

$$ {}_t^t\tilde{\boldsymbol{K}}_L = \int_{-1}^{1} \boldsymbol{B}_l^T \cdot \boldsymbol{D} \cdot \boldsymbol{B}_l \cdot A \cdot \frac{{}^tL}{2} dr = \frac{EA}{{}^tL} \cdot \left[\begin{array}{ccc|ccc} 1 & 0 & 0 & -1 & 0 & 0 \\ 0 & 0 & 0 & 0 & 0 & 0 \\ 0 & 0 & 0 & 0 & 0 & 0 \\ \hline -1 & 0 & 0 & 1 & 0 & 0 \\ 0 & 0 & 0 & 0 & 0 & 0 \\ 0 & 0 & 0 & 0 & 0 & 0 \end{array}\right] \tag{4.124} $$

and

$$ {}_t^t\tilde{\boldsymbol{K}}_{NL} = \int_{-1}^{1} \boldsymbol{G}^T \cdot \boldsymbol{\sigma} \cdot \boldsymbol{G} \cdot A \cdot \frac{{}^tL}{2} dr = \frac{{}^tP}{{}^tL} \cdot \left[\begin{array}{ccc|ccc} 1 & 0 & 0 & -1 & 0 & 0 \\ 0 & 1 & 0 & 0 & -1 & 0 \\ 0 & 0 & 1 & 0 & 0 & -1 \\ \hline -1 & 0 & 0 & 1 & 0 & 0 \\ 0 & -1 & 0 & 0 & 1 & 0 \\ 0 & 0 & -1 & 0 & 0 & 1 \end{array}\right] \tag{4.125} $$

where the elasticity matrix $\boldsymbol{D}$ is given by $\boldsymbol{D}=E$, and A is the area of the truss element cross section. The matrix $\boldsymbol{\sigma}$ in equation (4.125) is given by

$$ \boldsymbol{\sigma} = \begin{bmatrix} \sigma_{11} & 0 & 0 \\ 0 & \sigma_{11} & 0 \\ 0 & 0 & \sigma_{11} \end{bmatrix} $$

The terms σ_{11} in this matrix represent the axial stress at time t, which is simply given by the ratio between the installed tension ${}^tP$, and the cross-sectional area of the element, $\sigma_{11} = {}^tP/A$.

Finally, the vector of the nodal point forces ${}_t^t\tilde{\boldsymbol{F}}$ at time t is calculated as

$$ {}_t^t\tilde{\boldsymbol{F}}^{(i-1)} = \int_{-1}^{1} \boldsymbol{B}_l^T \cdot \boldsymbol{\tau}^{(i-1)} \cdot A \cdot \frac{{}^tL}{2} dr = {}^tP \cdot \begin{bmatrix} -1 \\ 0 \\ 0 \\ 1 \\ 0 \\ 0 \end{bmatrix} \tag{4.126} $$

For dynamic analysis, a mass matrix $\boldsymbol{M}$ can be calculated according to (4.120), yielding

$$ \boldsymbol{M} = \frac{{}^0\rho \, A \, {}^0L}{6} \cdot \left[\begin{array}{c|c} 2\boldsymbol{I}_3 & \boldsymbol{I}_3 \\ \hline \boldsymbol{I}_3 & 2\boldsymbol{I}_3 \end{array}\right] \tag{4.127} $$

This matrix is consistent. For simplicity, a lumped mass matrix is frequently employed, which considers the element mass concentrated at the element nodes and is thus defined as

$$\boldsymbol{M} = \frac{{}^{0}\rho\, A\, {}^{0}L}{2} \cdot \left[\begin{array}{c|c} \boldsymbol{I}_3 & \tilde{\boldsymbol{0}} \\ \hline \tilde{\boldsymbol{0}} & \boldsymbol{I}_3 \end{array}\right] \tag{4.128}$$

Employing the Rayleigh damping model above described, a consistent damping matrix $\boldsymbol{C}$ can be formed according to equation (4.122), the coefficients α and β being determined by prescribing the modal damping factor ξ_i for two particular modes of vibration of the bridge and solving the equations (Clough & Penzien, 1986)

$$\xi_i = \frac{\alpha}{2\omega_i} + \frac{\beta}{2}\omega_i, \quad \text{with } i=1, 2 \tag{4.129}$$

The four-node isoparametric finite element

The assessment of the dynamic behaviour of the stay cables requires that each stay cable is discretized into a series of two-node finite elements, the number of links varying according to the number of modes that need to be assessed. Considering that a sinusoidal arcade is fully characterized by three points, the representation of the first four vibration modes would require the discretization of each stay cable into something as twelve truss elements. This approach has been adopted in the present dissertation, although the author recognises a major drawback, which is the very large number of degrees of freedom required to model the bridge. This is particularly important for large cable-stayed bridges, which employ a significant number of stay cables.

A more efficient modelling of the stay cable can be achieved using more sophisticated finite elements. The four-node isoparametric truss element, employed for example by Ali (1991), is described here as an alternative.

Consider the four-node truss element represented in Figure 4.27 at the undeformed and at a deformed configuration (times *0* and *t*, respectively).

The incremental displacement components within the element are obtained as functions of the nodal incremental displacements according to equation (4.86), considering *N=4*. The interpolation functions H_k are expressed using once more the natural coordinate system with variable *r*, and are given by

$$H_1(r) = \frac{1}{16}(-9r^3 + 9r^2 + r - 1)$$

$$H_2(r) = \frac{1}{16}(9r^3 + 9r^2 - r - 1)$$

$$H_3(r)=\frac{1}{16}(27r^3-9r^2-27r+9)$$

$$H_4(r)=\frac{1}{16}(-27r^3-9r^2+27r+9)$$

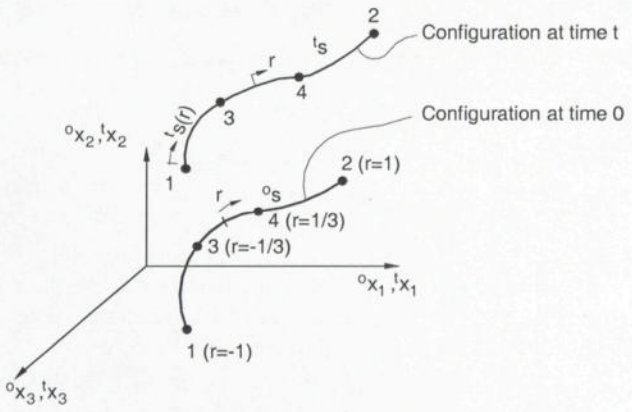


Figure 4.27. Four-node truss element representation in the undeformed configuration, at time *0*, and in a deformed configuration, at time *t*.

The same equation (4.86) applies to the evaluation of the arc length $^ts(r)$ as function of the nodal arc lengths $^tS^k$, i.e.,

$$^ts(r)=\sum_{k=1}^{N}H_k(r)\cdot{}^tS^k \tag{4.130}$$

The local element strain $\tilde{e}_{ss}$ is now defined as function of the arc length at time *t*, $^ts(r)$, associated with the material point characterized by coordinates $^tx_i(r)$ at that time, according to

$$\tilde{e}_{ss}=\frac{d\,{}^tx_i}{{}^tds}\cdot\frac{du_i}{{}^tds} \tag{4.131}$$

Accordingly, the nonlinear component of the strain $^t\tilde{\eta}_{ss}$ expressed in the same local reference system is

$$^t\tilde{\eta}_{ss}=\frac{1}{2}\cdot\frac{du_k}{{}^tds}\cdot\frac{du_k}{{}^tds} \tag{4.132}$$

The evaluation of $\tilde{e}_{ss}$ and ${}^{t}\tilde{\eta}_{ss}$ as functions of the nodal coordinates and incremental displacement components requires that the relation between the local and natural coordinate derivatives is known. This relation is given by

$$ {}^{t}J = \frac{{}^{t}ds}{dr} = \sum_{k=1}^{N} \frac{dH_k}{dr} \cdot {}^{t}S^{k} \tag{4.133} $$

The linear and nonlinear components of the local element strain can then be written as

$$ {}^{t}\tilde{e}_{ss} = \frac{1}{{}^{t}J^{2}} \cdot {}^{t}\boldsymbol{X}^{T} \cdot \boldsymbol{H}_{,r}^{T} \cdot \boldsymbol{H}_{,r}\, \boldsymbol{\Delta U} \tag{4.134} $$

and

$$ 2\,{}^{t}\tilde{\eta}_{ss} = \left(\frac{1}{{}^{t}J} \cdot \boldsymbol{H}_{,r}\, \boldsymbol{\Delta U}\right)^{T} \cdot \left(\frac{1}{{}^{t}J} \cdot \boldsymbol{H}_{,r}\, \boldsymbol{\Delta U}\right) \tag{4.135} $$

The matrix $\boldsymbol{H}_{,r}$ in these equations contains the derivatives with respect to the natural coordinate r of the interpolation functions

$$ \boldsymbol{H}_{,r} = \left[\frac{dH_1}{dr}\boldsymbol{I}_3 \;\middle|\; \frac{dH_2}{dr}\boldsymbol{I}_3 \;\middle|\; \frac{dH_3}{dr}\boldsymbol{I}_3 \;\middle|\; \frac{dH_4}{dr}\boldsymbol{I}_3 \right] \tag{4.136} $$

The vectors ${}^{t}\boldsymbol{X}$ and $\boldsymbol{\Delta U}$ contain the nodal coordinates and the incremental components of displacement, respectively, at time t, as previously defined.

The linear strain-displacement matrix $\boldsymbol{B}_l$ is then given by

$$ \boldsymbol{B}_l = \frac{1}{{}^{t}J^{2}} \cdot {}^{t}\boldsymbol{X}^{T} \cdot \boldsymbol{H}_{,r}^{T} \cdot \boldsymbol{H}_{,r} \tag{4.137} $$

and the matrix $\boldsymbol{G}$ is

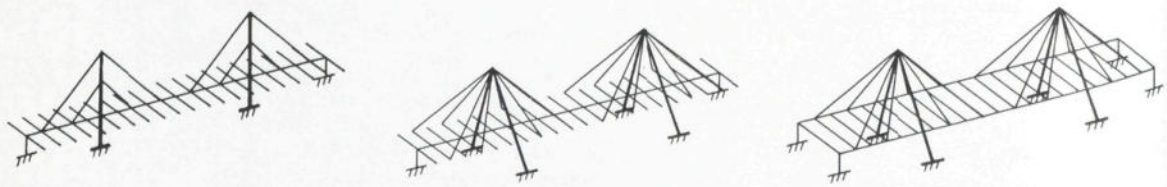
$$ \boldsymbol{G} = \frac{1}{{}^{t}J} \cdot \boldsymbol{H}_{,r} \tag{4.138} $$

Substituting (4.137) and (4.138) into equations (4.114) to (4.117), the linear and geometric stiffness matrices can be obtained, as well as the equivalent nodal force vector. The mass and damping matrices are obtained, as for the previous case, using equations (4.120) and (4.122). Lumped mass matrix schemes are also common procedure.

4.3.4.2 Modeling of the girders and towers

In the perspective of building a general model of the bridge for dynamic analysis, the most common approach consists in idealizing the deck and towers as systems of uniform skeletal elements that are able to resist bending, shear, torsion and axial forces (Kanok-Nukulchai *et al.*, 1992).

Figure 4.28 shows different possible discretizations for use in a global model of a cable-stayed bridge.



(a) (b) (c)

Figure 4.28. Full model of a cable-stayed bridge. Different discretization procedures: (a) Single-plane cable-stayed bridge; (b) Two-inclined plane cable-stayed bridge with deck box cross-section; (c) Two-inclined plane cable-stayed bridge with a deck cross-section composed of two main longitudinal girders braced at intervals.

For the single-cable plane bridge (Figure 4.28(a)), the deck box section is modelled as a series of equivalent beam elements. Stiff fictious cantilever elements, here designated as rigid links, are added, in order to allow for the application of eccentric loads. The same hypothesis can be employed to model a double plane cable-stayed bridge (Figure 4.28(b)). In this case, the rigid links provide also displacement compatibility between the cable ends and the deck. If the bridge deck is composed of two main longitudinal girders braced at intervals, the model presented in Figure 4.28(c) can also be employed. In this model, the deck is idealized by two parallel series of beam elements connected by rigid links. Thin-walled deck cross-sections may require the use of more complex elements, such as plate, shell or three-dimensional elements, in order to adequately model the distorsion of the cross-section.

So, although other possibilities exist in the modelling the deck and towers of a cable-stayed bridge, the basic element employed in the modelling of these components is the beam element. The matrices associated with this element are derived in the current Section, considering the second order effects associated with the high compressions that are usually present in cable-stayed bridges.

In effect, the simultaneous presence of bending moments and axial forces in a beam element originates interaction effects. The lateral deflection of a beam subjected to an axial load causes additional bending moments. Equally, the bending deformations associated with the presence of bending moments originate an apparent shortening of the beam, which leads to a reduction of its axial stiffness. When the displacements are small, the interaction between bending and axial forces can be neglected and linear force-displacement relations can be

established. However, if the displacementss are large, the force-displacement relations are no longer linear. This is the essence of the geometrical nonlinear problem in the so-called *beam-column* element that will be established here.

The formulation of the geometrically nonlinear *beam-column element* can be based either on the 'exact' *beam-column theory*, which employs the continuum equations, or on the finite element approach, that approximates the nonlinear stiffness matrix by the sum of a *linear stiffness matrix* with a *geometric stiffness matrix*. The two approaches are presented in this section, in order to assess the errors associated in the finite element modelling using a conventional beam element in the context of a geometric nonlinear formulation, the methodology employed in the current dissertation.

The beam-column theory

Consider the beam-column represented in Figure 4.29, subjected to the distributed loads $q_2(x_1)$ and $q_3(x_1)$, in the directions of the principal axes of the cross-section x_2 and x_3, respectively.

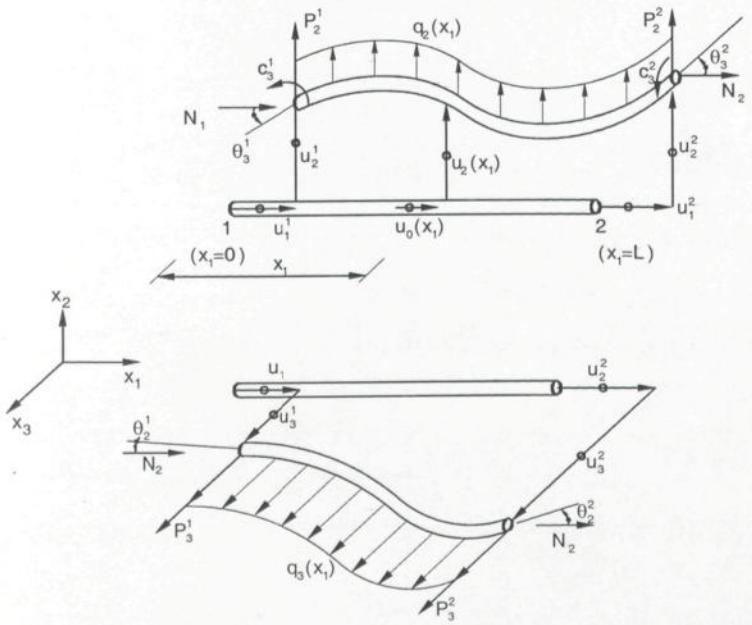


Figure 4.29. Loads and displacement components on a beam-column element.

The axial force along the beam-column is defined as $N(x_1)$, and the bending moments with respect to the axes x_2 and x_3, $M_2(x_1)$ and $M_3(x_1)$, respectively, are established as functions of the displacement components under the following assumptions: the transverse shear strains E_{12} and E_{23} are neglected, and the transverse displacement components u_2 and u_3 depend only on the coordinate along the longitudinal axis x_1.

The axial displacement u_1 at a point along the beam-column characterized by coodinates x_i $(i=1, 2, 3)$ is then defined as

$$u_1(x_1,x_2,x_3)=u_0(x_1)-x_2\cdot\frac{du_2}{dx_1}-x_3\cdot\frac{du_3}{dx_1} \tag{4.139}$$

where $u_0(x_1)$ is the axial displacement at the neutral axis for the cross-section associated with the longitudinal coordinate x_1, and the derivatives du_2/dx_1 and du_3/dx_1 represent the angular rotations of the cross section for the same coordinate.

The axial strain ε_1 along the longitudinal direction is now defined according to equation (4.67) by

$$\varepsilon_1=E_{11}=\frac{du_1}{dx_1}+\frac{1}{2}\cdot\left[\left(\frac{du_1}{dx_1}\right)^2+\left(\frac{du_2}{dx_1}\right)^2+\left(\frac{du_3}{dx_1}\right)^2\right] \tag{4.140}$$

Considering only the nonlinear components due to the rotations du_2/dx_1 and du_3/dx_1 yields

$$\varepsilon_1\approx\frac{du_1}{dx_1}+\frac{1}{2}\cdot\left[\left(\frac{du_2}{dx_1}\right)^2+\left(\frac{du_3}{dx_1}\right)^2\right] \tag{4.141}$$

Introducing now the the stress-strain relation and the definition of $u_1(x_1)$ given by (4.139), the following expression is obtained for the axial stress σ_1

$$\sigma_1=E\varepsilon_1=E\cdot\left[\frac{du_0}{dx_1}+\frac{1}{2}\cdot\left(\frac{du_2}{dx_1}\right)^2+\frac{1}{2}\cdot\left(\frac{du_3}{dx_1}\right)^2-x_2\cdot\frac{d^2u_2}{dx_1^2}-x_3\cdot\frac{d^2u_3}{dx_1^2}\right] \tag{4.142}$$

Finally, the forces $N(x_1)$, $M_2(x_1)$ and $M_3(x_1)$ are established as functions of the displacement components according to the following relations

$$N(x_1)=\int_A\sigma_1\,dA=EA\cdot\left[\frac{du_0}{dx_1}+\frac{1}{2}\cdot\left(\frac{du_2}{dx_1}\right)^2+\frac{1}{2}\cdot\left(\frac{du_3}{dx_1}\right)^2\right] \tag{4.143}$$

$$M_2(x_1)=\int_A x_3\cdot\sigma_1\,dA=-EI_2\cdot\frac{d^2u_3}{dx_1^2} \tag{4.144}$$

$$M_3(x_1)=\int_A -x_2\cdot\sigma_1\,dA=EI_3\cdot\frac{d^2u_2}{dx_1^2} \tag{4.145}$$

in which the quantities I_2 and I_3 represent the moments of inertia of the cross-section about the principal axes x_2 and x_3.

Introducing these expressions in the equilibrium equations, the following relations are obtained

$$N(x_1) = constant \tag{4.146}$$

$$EI_3 \cdot \left[\frac{d^4 u_2}{d x_1^4} + \alpha_3^2 \frac{d^2 u_2}{d x_1^2} \right] = q_2(x_1) \tag{4.147}$$

$$EI_2 \cdot \left[\frac{d^4 u_3}{d x_1^4} + \alpha_2^2 \frac{d^2 u_3}{d x_1^2} \right] = q_3(x_1) \tag{4.148}$$

with $\alpha_3^2 = -N/EI_3$ and $\alpha_2^2 = -N/EI_2$.

The solution of the fourth-order differential equations (4.147) and (4.148) can be then obtained. The inclusion of the boundary conditions leads to the following system of equations

$$\overline{\boldsymbol{K}}\,\boldsymbol{U} = \overline{\boldsymbol{P}} \tag{4.149}$$

where $\overline{\boldsymbol{K}}$ is the stiffness matrix associated with the beam-column element, $\boldsymbol{U}$ is the displacement vector, characterized by the components

$$\boldsymbol{U}^T = \left[u_1^1 \;\; u_2^1 \;\; u_3^1 \;\; \theta_1^1 \;\; \theta_2^1 \;\; \theta_3^1 \;\middle|\; u_1^2 \;\; u_2^2 \;\; u_3^2 \;\; \theta_1^2 \;\; \theta_2^2 \;\; \theta_3^2 \right] \tag{4.150}$$

and $\overline{\boldsymbol{P}}$ is an equivalent force vector. The definition of the coefficients of matrix $\overline{\boldsymbol{K}}$ and of the vector $\overline{\boldsymbol{P}}$ depend on the sign of the parameters α_3^2 and α_2^2. In effect, the differential equations (4.147) and (4.148) can have three different types of solutions according to the values of these parameters. The case of nul α_3^2 and α_2^2 corresponds to the absence of axial force, therefore to a beam element subjected to transverse loads only. For this situation, the system of equations (4.149) is linear and the resulting stiffness matrix is the conventional three-dimensional linear stiffness matrix associated with the beam element. For the cases where $\alpha_3^2, \alpha_2^2 > 0$ (the beam-column is subjected to compressive forces), or $\alpha_3^2, \alpha_2^2 < 0$ (the beam-column is subjected to tensile forces), the resulting stiffness matrix is nonlinear and given by (Nazmy, 1987)

$$\overline{\boldsymbol{K}} = \begin{bmatrix} k(1,1) & k(1,2) & \ldots & k(1,12) \\ k(2,1) & k(2,2) & \ldots & k(2,12) \\ \ldots & \ldots & \ldots & \ldots \\ k(12,1) & k(12,2) & \ldots & k(12,12) \end{bmatrix} \tag{4.151}$$

in which

$$k(1,1)= k(7,7)= -k(1,7)= -k(7,1)= \frac{EA}{L}\cdot S_5 \tag{4.152a}$$

$$k(2,2)= k(8,8)= -k(2,8)= -k(8,2)= \frac{12EI_3}{L^3}\cdot S_{13} \tag{4.152b}$$

$$k(3,3)= k(9,9)= -k(3,9)= -k(9,3)= \frac{12EI_2}{L^3}\cdot S_{12} \tag{4.152c}$$

$$k(2,6)= k(6,2)= k(2,12)= k(12,2)= -k(6,8)=$$
$$= -k(8,6)= -k(8,12)= -k(12,8)= \frac{6EI_3}{L^2}\cdot S_{23} \tag{4.152d}$$

$$k(3,5)= k(5,3)= k(3,11)= k(11,3)= -k(5,9)=$$
$$= -k(9,5)= -k(9,11)= -k(11,9)= -\frac{6EI_2}{L^2}\cdot S_{22} \tag{4.152e}$$

$$k(4,4)= k(10,10)= -k(4,10)= -k(10,4)= \frac{GI_1}{L} \tag{4.152f}$$

$$k(5,5)= k(11,11)= \frac{4EI_2}{L}\cdot S_{32} \tag{4.152g}$$

$$k(6,6)= k(12,12)= \frac{4EI_3}{L}\cdot S_{33} \tag{4.152h}$$

$$k(5,11)= k(11,5)= \frac{2EI_2}{L}\cdot S_{42} \tag{4.152i}$$

$$k(6,12)= k(12,6)= \frac{2EI_3}{L}\cdot S_{43} \tag{4.152j}$$

The quantities L, I_1 and G in the coefficients expressed by (4.152) represent the beam-column length, the torsional moment of inertia of the cross-section, and the material shear modulus.

The coefficients $k(i,j)$ of matrix $\overline{\boldsymbol{K}}$ are obtained as the well-known linear stiffness matrix coefficients multiplied by a set of functions S_{ij} called *stability functions*. The functions S_{i2} modify the bending stiffness coefficients associated with bending about the axis x_2, while the functions S_{i3} modify the bending stiffness coefficients associated with bending about the axis x_3. Finally, the function S_5 modifies the axial stiffness. These highly nonlinear functions actually reflect the second order contribution associated with the interaction between bending

moments and axial forces, and are defined as functions of the axial force and of the bending moments at the beam-column element nodes according to (Nazmy, 1987)

- $\alpha_2^2, \alpha_3^2 < 0$ (tension member):

$$S_{1i} = \omega_i^3 \frac{\sinh \omega_i}{12 R_t} \tag{4.153a}$$

$$S_{2i} = \omega_i^2 \frac{(\cosh \omega_i - 1)}{6 R_t} \tag{4.153b}$$

$$S_{3i} = \omega_i \frac{(\omega_i \cosh \omega_i - \sinh \omega_i)}{4 R_t} \tag{4.153c}$$

$$S_{4i} = \omega_i \frac{(\sinh \omega_i - \omega_i)}{2 R_t} \tag{4.153d}$$

$$S_5 = \frac{1}{1 - \frac{EA(R_{tm2} + R_{tm3})}{4N^3 L^2}} \tag{4.153e}$$

where

$$\omega_i = \mu_i L \quad , \quad \mu_i^2 = \frac{N}{EI_i} \text{ and } i=2, 3 \tag{4.154}$$

and the quantities R_t, R_{tmi} $(i=2,3)$ are given by

$$R_t = 2 - 2\cosh \omega_i + \omega_i \sinh \omega_i \tag{4.155a}$$

$$R_{tmi} = \omega_i((M_i^1)^2 + (M_i^2)^2)(\coth \omega_i + \omega_i \operatorname{cosech}^2 \omega_i) - 2(M_i^1 + M_i^2)^2 + \\ + (M_i^1 M_i^2)(1 + \omega_i \coth \omega_i)(2\omega_i \operatorname{cosech} \omega_i) \tag{4.155b}$$

- $\alpha_2^2, \alpha_3^2 > 0$ (compression member):

$$S_{1i} = \omega_i^3 \frac{\sin \omega_i}{12 R_c} \tag{4.156a}$$

$$S_{2i} = \omega_i^2 \frac{(1 - \cos \omega_i)}{6 R_c} \tag{4.156b}$$

$$S_{3i} = \omega_i \frac{(\sin \omega_i - \omega_i \cos \omega_i)}{4 R_c} \tag{4.156c}$$

$$S_{4i} = \omega_i \frac{(\omega_i - \sin\omega_i)}{2R_c} \tag{4.156d}$$

$$S_5 = \frac{1}{1 - \dfrac{EA(R_{cm2} + R_{cm3})}{4N^3L^2}} \tag{4.156e}$$

where

$$\omega_i = \mu_i L \quad , \quad \mu_i^2 = -\frac{N}{EI_i} \text{ and } i=2, 3 \tag{4.157}$$

and

$$R_c = 2 - 2\cos\omega_i - \omega_i \sin\omega_i \tag{4.158a}$$

$$R_{cmi} = \omega_i((M_i^1)^2 + (M_i^2)^2)(\cot\omega_i + \omega_i \operatorname{cosec}^2\omega_i) - 2(M_i^1 + M_i^2)^2 + \\ + (M_i^1 M_i^2)(1 + \omega_i \cot\omega_i)(2\omega_i \operatorname{cosec}\omega_i) \tag{4.158b}$$

Figure 4.30 contains a representation of the *stability functions* associated with the bending stiffness coefficients, as a function of the ratio between the axial force on the beam-column element and the *critical Euler load*, defined as $N_E = -\pi^2 EI_i / L^2$. As can be observed in this Figure, unit values are obtained for $N/N_E = 0$, i.e., when $(\alpha_3^2 = \alpha_2^2 = 0)$. For compressive loads $(\alpha_2^2, \alpha_3^2 > 0, \omega_i^2 > 0)$, significant variations can be observed in the stability functions, meaning that numerical difficulties may be found in the solution of the nonlinear system of equations (4.149).

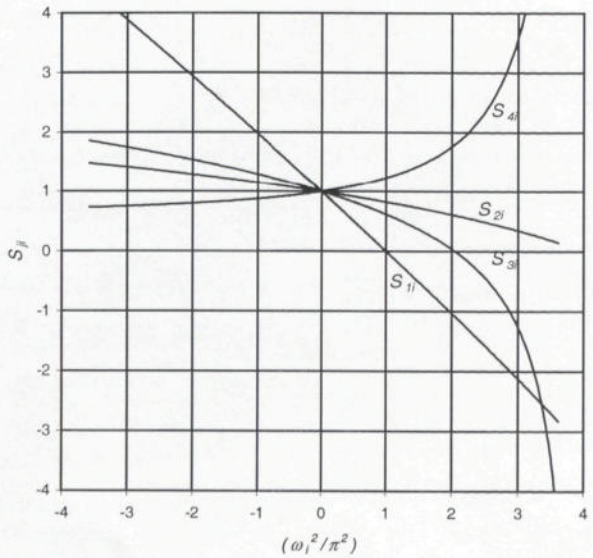
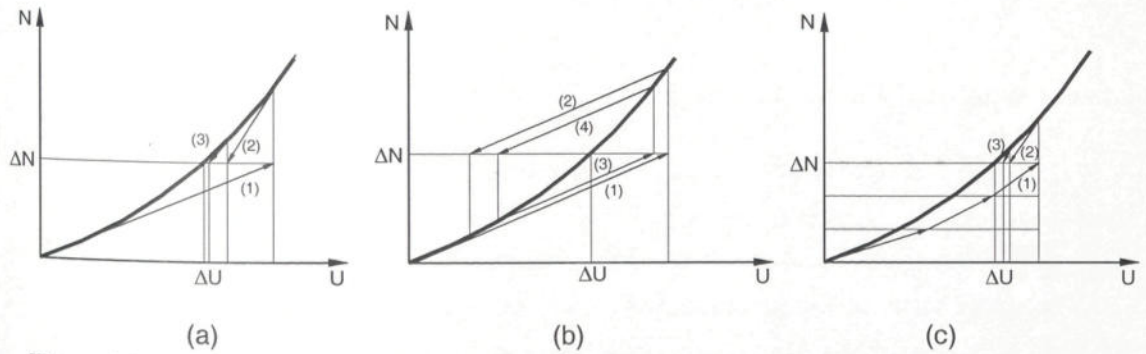


Figure 4.30. Stability functions as functions of the ratio.

The nonlinear stiffness matrix $\overline{\boldsymbol{K}}$ associated with the beam-column element defined in terms of the stability functions S_{ij} is considered the exact stiffness matrix of the beam-column element, since its derivation results from direct integration of the differential equations. Note however that this matrix has been established considering the undeformed configuration of the beam-column element. Thus, the nonlinearities here considered are actually due only to large rotations. The inclusion of a so-called exact formulation in the nonlinear geometric analysis of a cable-stayed bridge, where large translational displacements are expected, requires then an incremental formulation of the problem, so that the conditions of validity of the above defined stiffness matrix are met.

As the matrix $\overline{\boldsymbol{K}}$ depends nonlinearly on the axial force N, which is undetermined until the incremental displacements are known for each increment of applied load, an iterative process is required. Several methods are available (Harrison, 1973; Nazmy, 1987), which are in general variations of the well-known Newton-Raphson method. Figure 4.31 represents the converging procedure for a cable-stayed bridge analysis according to three different procedures: the Newton-Raphson, the modified Newton-Raphson and a hybrid method developed by Nazmy (1987).



(a) (b) (c)

Figure 4.31. Iterative procedures for cable-stayed bridges: (a) Newton-Raphson method; (b) Modified Newton-Raphson; (c) Hybrid method (Nazmy, 1987).

A common requirement to all these methods is the calculation of a tangent stiffness matrix at a certain known load position, which is in general obtained from a linearization of the general stiffness matrix $\overline{\boldsymbol{K}}$. Dumir *et al.* (1993) expanded this matrix in the Taylor's series for the two-dimensional beam-column problem, arriving at the following decomposition for the coordinates considered in Figure 4.32

$$\overline{K} = \frac{EI_3}{L^3}\cdot\begin{bmatrix} 12 & 6L & -12 & 6L \\ 6L & 4L^2 & -6L & 2L^2 \\ -12 & -6L & 12 & -6L \\ 6L & 2L^2 & -6L & 4L^2 \end{bmatrix} + \frac{N}{30L}\cdot\begin{bmatrix} 36 & 6L & -36 & 3L \\ 3L & 4L^2 & -3L & -L^2 \\ -36 & -3L & 36 & -3L \\ 3L & -L^2 & -3L & 4L^2 \end{bmatrix} -$$

$$-\frac{N^2L}{12600\,EI_3}\cdot\begin{bmatrix} 18 & 9L & -18 & 9L \\ 9L & 22L^2 & -9L & -13L^2 \\ -18 & -9L & 18 & -9L \\ 9L & -13L^2 & -9L & 22L^2 \end{bmatrix} + \qquad (4.159)$$

$$+\frac{N^3L^3}{756000\,(EI_3)^2}\cdot\begin{bmatrix} 12 & 6L & -12 & 6L \\ 6L & 28L^2 & -6L & -22L^2 \\ -12 & -6L & 12 & -6L \\ 6L & -22L^2 & -6L & 28L^2 \end{bmatrix}$$

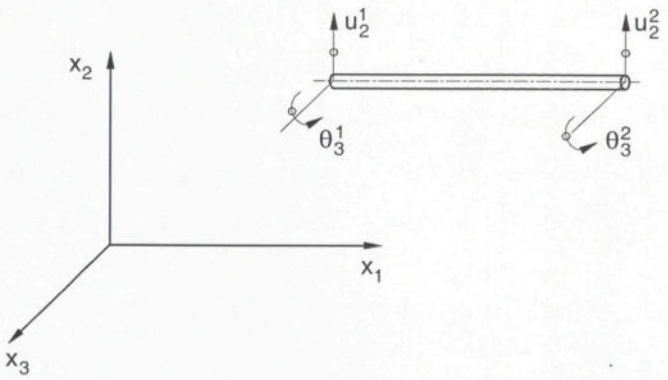


Figure 4.32. Beam-column element: coordinates for two-dimensional analysis.

The first term of the expansion in the Taylor's series is the linear stiffness matrix associated with a beam element. The second term in equation (4.159) depends linearly on the axial force N and constitutes the consistent geometric stiffness matrix $\boldsymbol{K}_{NL}$ that will be derived for the finite element approach subsequently.

The finite element approach

As for the case of the truss members, an isoparametric formulation can be employed to model the nonlinear beam element. The four-node curved beam element represented in Figure 4.33 is the most general beam finite element for nonlinear geometric analysis. This element has been formulated by Bathe (1982) for the case of large displacements and rotations, although with small strains. In this formulation, Bathe used the Lagrangian interpolation functions above presented for the four-node truss element and the current assumption that plane sections originally normal to the centre line axis remain plane and undistorted under deformation, although not necessarily normal to the axis (possibility of shear deformation).

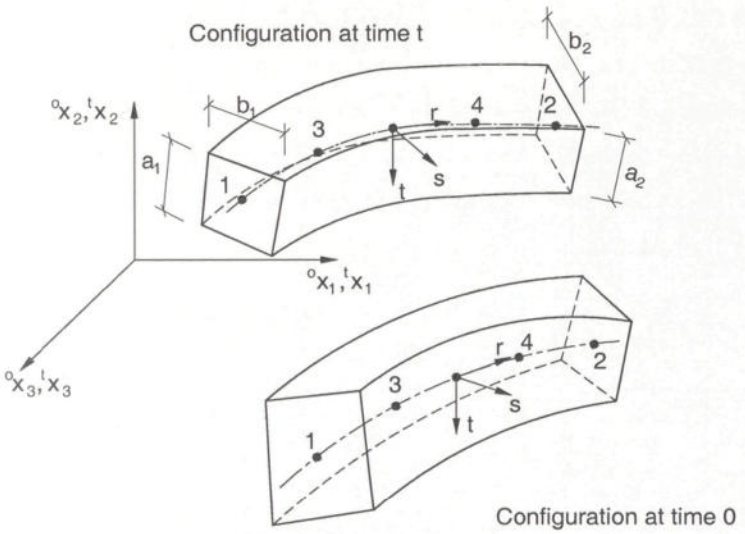


Figure 4.33. Four-node general curved beam element at undeformed and deformed configuration.

For the sake of comparison with the beam-column theory, the current Section derives the simple two-node plane beam-column element, neglecting the shear deformations and employing Hermitian interpolation functions.

Consider the prismatic beam element represented in Figure 4.34, with symmetric cross-section and undeformed length ${}^0L$, loaded in the plane $x_1 - x_2$. The same element is represented in the deformed configuration at time t, characterized by the nodal displacement vector ${}^t\boldsymbol{U}$, given by

$$ {}^t\boldsymbol{U}^T = \left[{}^tU_1^1 \quad {}^tU_2^1 \quad {}^t\theta^1 \;\middle|\; {}^tU_1^2 \quad {}^tU_2^2 \quad {}^t\theta^2 \right] \tag{4.160} $$

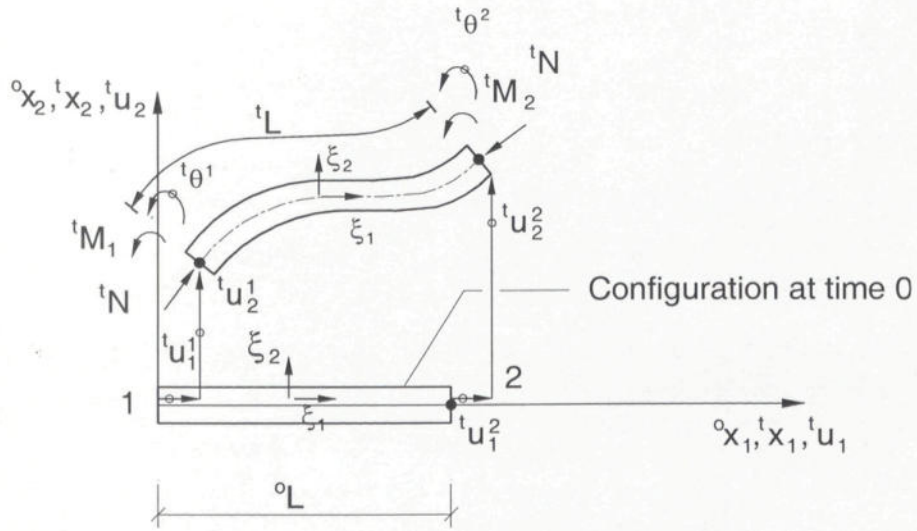


Figure 4.34. Two-node plane beam column element in undeformed and deformed configuration.

Under the assumptions of small displacements and strains, the "exact" stiffness matrix of the beam element can be obtained, provided that the chosen interpolation functions correspond to the "exact" displacements of the beam element. Note that the stiffness matrix is not exact in the truth assessement of the term, as the shear deformations are neglected.

Defining the interpolation functions as the bending deformations associated with unit nodal displacements of the beam column element, the displacement distribution along the element can be written as

$$^{t}\boldsymbol{u} = \boldsymbol{H} \cdot {}^{t}\boldsymbol{U} \tag{4.161}$$

with

$$^{t}\boldsymbol{u}^{T} = \left[\begin{array}{cc} {}^{t}u_1(x_1, x_2) & {}^{t}u_2(x_1, x_2) \end{array} \right] \tag{4.162a}$$

and

$$\boldsymbol{H} = \left[\begin{array}{ccc|ccc} 1-\xi_1 & 6(\xi_1 - \xi_1^2)\cdot\xi_2 & (-1+4\xi_1 - 3\xi_1^2)\cdot{}^{t}L\cdot\xi_2 & \xi_1 & -6(\xi_1 - \xi_1^2)\cdot\xi_2 & (2\xi_1 - 3\xi_1^2)\cdot{}^{t}L\cdot\xi_2 \\ 0 & 1-3\xi_1^2+2\xi_1^3 & (\xi_1 - 2\xi_1^2 + \xi_1^3)\cdot{}^{t}L & 0 & 3\xi_1^2 - 2\xi_1^3 & (-\xi_1^2 + \xi_1^3)\cdot{}^{t}L \end{array} \right] \tag{4.162b}$$

The quantities ξ_1 and ξ_2 in equation (4.162b) are adimensional variables, defined as

$$\xi_1 = x_1 / {}^{t}L \quad \text{and} \quad \xi_2 = x_2 / {}^{t}L \tag{4.162c}$$

Identical equations apply when the problem is formulated incrementally. In this case, the vector containing the incremental displacement components associated with the time increment Δt at time t, $\boldsymbol{u}$, is given as function of the incremental nodal displacements $\boldsymbol{\Delta U}$

$$\boldsymbol{u} = \boldsymbol{H} \cdot \boldsymbol{\Delta U} \tag{4.163}$$

Neglecting the shear deformations, only one component of the strain and of the stress vectors $\boldsymbol{\varepsilon}$ and $\boldsymbol{\tau}$, ε_1 and σ_{11}, respectively, are of interest.

For the case of large deformations, the strain-displacement matrices $\boldsymbol{B_l}$ and $\boldsymbol{G}$ are defined as

$$\boldsymbol{B_l} = \frac{1}{{}^{t}L} \cdot \left[\begin{array}{cc|cc} -1 & 6(1-2\xi_1)\cdot\xi_2 & (4-6\xi_1)\cdot{}^{t}L\cdot\xi_2 & 1 & -6(1-2\xi_1)\cdot\xi_2 & (2-6\xi_1)\cdot{}^{t}L\cdot\xi_2 \end{array} \right] \tag{4.164a}$$

and

$$\boldsymbol{G} = \frac{1}{{}^{t}L} \cdot \left[\begin{array}{ccc|ccc} -1 & 6(1-2\xi_1)\cdot\xi_2 & (4-6\xi_1)\cdot{}^{t}L\cdot\xi_2 & 1 & -6(1-2\xi_1)\cdot\xi_2 & (2-6\xi_1)\cdot{}^{t}L\cdot\xi_2 \\ 0 & -6\xi_1 + 6\xi_1^2 & (1-4\xi_1+3\xi_1^2)\cdot{}^{t}L & 0 & 6\xi_1 - 6\xi_1^2 & (-2\xi_1 + 3\xi_1^2)\cdot{}^{t}L \end{array} \right] \tag{4.164b}$$

The linear and nonlinear stiffness matrices at time t, ${}^t_t\boldsymbol{K}_L$ and ${}^t_t\boldsymbol{K}_{NL}$, to use in the updated Lagrangian incremental formulation presented above are then given, according to equations (4.114) and (4.115), respectively, by

$$
{}^t_t\boldsymbol{K}_L = \frac{EI_3}{{}^tL^3}
\left[\begin{array}{ccc|ccc}
\frac{A\,{}^tL^2}{I_3} & 0 & 0 & -\frac{A\,{}^tL^2}{I_3} & 0 & 0 \\
0 & 12 & 6\,{}^tL & 0 & -12 & 6\,{}^tL \\
0 & 6\,{}^tL & 4\,{}^tL^2 & 0 & -6\,{}^tL & 2\,{}^tL^2 \\
\hline
-\frac{A\,{}^tL^2}{I_3} & 0 & 0 & \frac{A\,{}^tL^2}{I_3} & 0 & 0 \\
0 & -12 & -6\,{}^tL & 0 & 12 & -6\,{}^tL \\
0 & 6\,{}^tL & 2\,{}^tL^2 & 0 & -6\,{}^tL & 4\,{}^tL^2
\end{array}\right]
\tag{4.165a}
$$

$$
{}^t_t\boldsymbol{K}_{NL} = \frac{{}^tN}{30\,{}^tL}\cdot
\left[\begin{array}{ccc|ccc}
0 & 0 & 0 & 0 & 0 & 0 \\
0 & \frac{360I_3}{A\,{}^tL^3} & \frac{180I_3}{A\,{}^tL^2} & 0 & -\frac{360I_3}{A\,{}^tL^3} & \frac{180I_3}{A\,{}^tL^2} \\
0 & \frac{180I_3}{A\,{}^tL^2} & \frac{120I_3}{A\,{}^tL} & 0 & -\frac{180I_3}{A\,{}^tL^2} & \frac{60I_3}{A\,{}^tL} \\
\hline
0 & 0 & 0 & 0 & 0 & 0 \\
0 & -\frac{360I_3}{A\,{}^tL^3} & -\frac{180I_3}{A\,{}^tL^2} & 0 & \frac{360I_3}{A\,{}^tL^3} & -\frac{180I_3}{A\,{}^tL^2} \\
0 & \frac{180I_3}{A\,{}^tL^2} & \frac{60I_3}{A\,{}^tL} & 0 & -\frac{180I_3}{A\,{}^tL^2} & \frac{120I_3}{A\,{}^tL}
\end{array}\right] +
\tag{4.165b}
$$

$$
\frac{{}^tN}{30\,{}^tL}\cdot
\left[\begin{array}{ccc|ccc}
30 & 0 & 0 & -30 & 0 & 0 \\
0 & 36 & 3\,{}^tL & 0 & -36 & 3\,{}^tL \\
0 & 3\,{}^tL & 4\,{}^tL^2 & 0 & -3\,{}^tL & -{}^tL^2 \\
\hline
-30 & 0 & 0 & 30 & 0 & 0 \\
0 & -36 & -3\,{}^tL & 0 & 36 & -3\,{}^tL \\
0 & 3\,{}^tL & -{}^tL^2 & 0 & -3\,{}^tL & 4\,{}^tL^2
\end{array}\right]
$$

As expected, the matrix ${}^t_t\boldsymbol{K}_L$ is the conventional linear stiffness matrix associated with bending deformations of the beam element. As for the nonlinear matrix ${}^t_t\boldsymbol{K}_{NL}$, the stress matrix $\boldsymbol{\sigma}$ used in its calculation is given by

$$
\boldsymbol{\sigma} = \begin{bmatrix} \sigma_{11} & 0 \\ 0 & \sigma_{11} \end{bmatrix}
\tag{4.166}
$$

where $\sigma_{11} = {}^tN/A$.

Note that ${}^t_t\boldsymbol{K}_{NL}$ is obtained as the sum of two matrices ${}^t_t\boldsymbol{K}_\theta$ and ${}^t_t\boldsymbol{K}_G$ that depend linearly on the axial force of the beam element. In general, the matrix ${}^t_t\boldsymbol{K}_\theta$, given by

$$ {}^{t}_{t}\boldsymbol{K}_{\theta} = \frac{{}^{t}N}{30\,{}^{t}L} \cdot \left[\begin{array}{ccc|ccc} 0 & 0 & 0 & 0 & 0 & 0 \\ 0 & \frac{360I_3}{A\,{}^{t}L^3} & \frac{180I_3}{A\,{}^{t}L^2} & 0 & -\frac{360I_3}{A\,{}^{t}L^3} & \frac{180I_3}{A\,{}^{t}L^2} \\ 0 & \frac{180I_3}{A\,{}^{t}L^2} & \frac{120I_3}{A\,{}^{t}L} & 0 & -\frac{180I_3}{A\,{}^{t}L^2} & \frac{60I_3}{A\,{}^{t}L} \\ \hline 0 & 0 & 0 & 0 & 0 & 0 \\ 0 & -\frac{360I_3}{A\,{}^{t}L^3} & -\frac{180I_3}{A\,{}^{t}L^2} & 0 & \frac{360I_3}{A\,{}^{t}L^3} & -\frac{180I_3}{A\,{}^{t}L^2} \\ 0 & \frac{180I_3}{A\,{}^{t}L^2} & \frac{60I_3}{A\,{}^{t}L} & 0 & -\frac{180I_3}{A\,{}^{t}L^2} & \frac{120I_3}{A\,{}^{t}L} \end{array}\right] \tag{4.167} $$

is neglected, by comparison of the corresponding terms with the terms of matrix ${}^{t}_{t}\boldsymbol{K}_{G}$. The nonlinear geometric stiffness matrix ${}^{t}_{t}\boldsymbol{K}_{NL}$ is then given approximately by

$$ {}^{t}_{t}\boldsymbol{K}_{NL} = {}^{t}_{t}\boldsymbol{K}_{\theta} + {}^{t}_{t}\boldsymbol{K}_{G} \approx {}^{t}_{t}\boldsymbol{K}_{G} = \frac{{}^{t}N}{30\,{}^{t}L} \cdot \left[\begin{array}{ccc|ccc} 30 & 0 & 0 & -30 & 0 & 0 \\ 0 & 36 & 3\,{}^{t}L & 0 & -36 & 3\,{}^{t}L \\ 0 & 3\,{}^{t}L & 4\,{}^{t}L^2 & 0 & -3\,{}^{t}L & -{}^{t}L^2 \\ \hline -30 & 0 & 0 & 30 & 0 & 0 \\ 0 & -36 & -3\,{}^{t}L & 0 & 36 & -3\,{}^{t}L \\ 0 & 3\,{}^{t}L & -{}^{t}L^2 & 0 & -3\,{}^{t}L & 4\,{}^{t}L^2 \end{array}\right] \tag{4.168} $$

This matrix depends only on the axial force and deformed length of the beam, and corresponds in fact to the linear term that resulted from the expansion in the Taylor's series of the beam-column "exact" stiffness matrix (see equation (4.159)). Note that an additional component of the nonlinear stiffness matrix could have been obtained, dependent on the bending moments at the beam-column element ends, ${}^{t}M_1$ and ${}^{t}M_2$, if the stress term had included the nonlinear effects associated with bending, i.e.,

$$ \sigma_{11} = \frac{{}^{t}N}{A} + ({}^{t}M_1 \cdot (1-\xi_1) + {}^{t}M_2 \cdot \xi_2) \cdot \frac{x_2}{I_3} \tag{4.169} $$

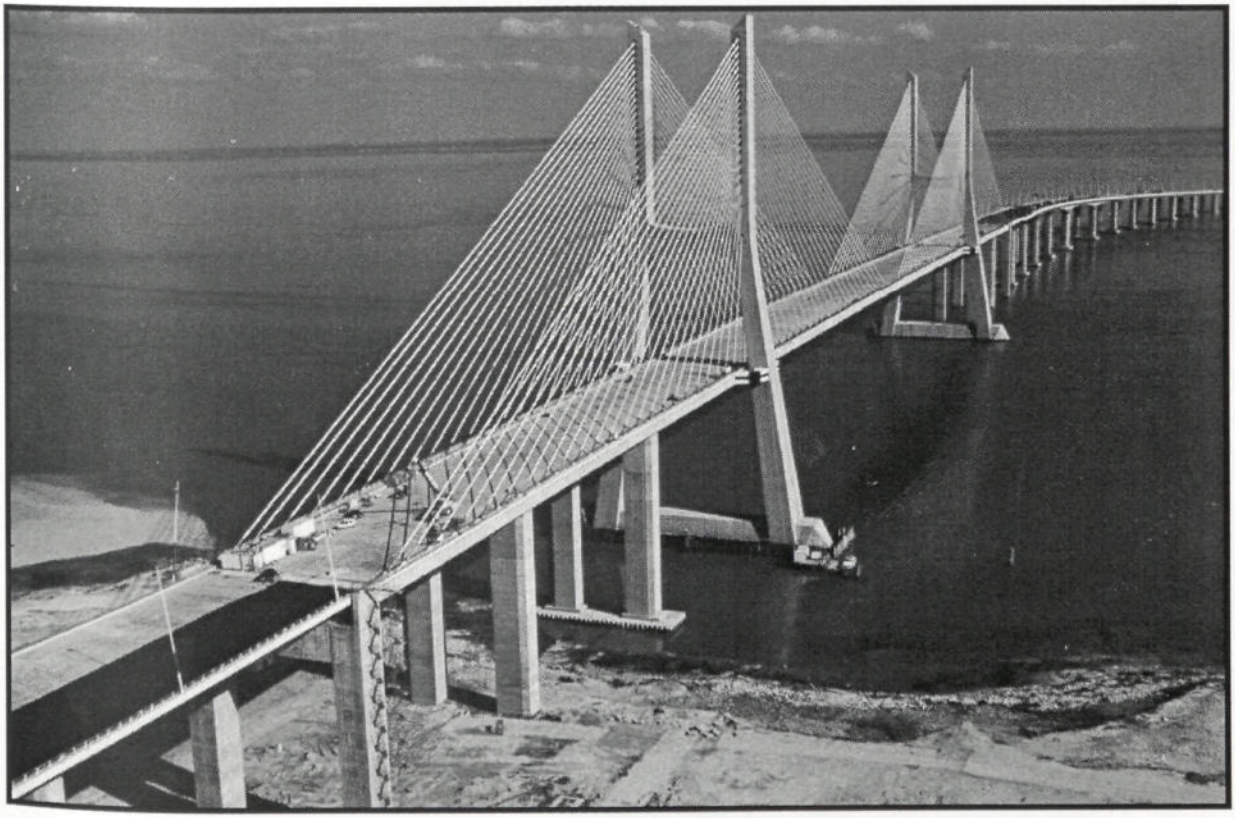
This later component is normally neglected also.

Conclusion

The main conlusion that can be extracted from the two methods presented in the text for the numerical modelling of beam-column elements is that the incremental finite element approach relies on a second order effect matrix that is the linear component of the more general nonlinear stiffness matrix derived on the basis of the beam-column theory. So, the adequate precision is attained in a finite element analysis, whenever a significant number of finite elements are used to discretize the girders and towers. For the beam-column theory, the discretization is only conditioned by the general assumption of the method that displacements are small.

CHAPTER 5

EXPERIMENTAL IDENTIFICATION OF THE DYNAMIC BEHAVIOUR OF CABLE-STAYED BRIDGES



CHAPTER FIVE

EXPERIMENTAL IDENTIFICATION OF THE DYNAMIC BEHAVIOUR OF CABLE-STAYED BRIDGES

5.1 GENERAL

The progress in the design of modern cable-stayed bridges has been accompanied by a marked development in three different areas, namely: (i) the analysis methods, based on powerful numerical techniques; (ii) the use of new constructional materials, such as light weight concrete and high strength steel; and (iii) the performance of full-scale observation programs, through use of advanced instrumentation devices and acquisition systems. The current Chapter deals with the last topic in the perspective of observation of dynamic properties.

The basis for modern *Experimental Stress Analysis* was established in the 1940's with the introduction of strain gauges (Sabnis *et al.*, 1983). Experimental analysis on physical models constructed at reduced scales was used then on particularly complex structures that could not be solved using the existing analytical tools, or which were important in terms of involved investment and risk of failure (case of dams and nuclear reactors, for example).

The advance in computer methods of analysis during the 1960's and 1970's conjugated with experimental observation on reduced models allowed a better insight into the behavior of structures and led in particular to an increase of the span length in cable-stayed bridges.

Due to the considerable time and cost associated with experimental observation of reduced scale structures by comparison with numerical analysis, tests on these models have been gradually abandoned, or at least employed in a narrower range of structures. It should be noted however that physical models are still employed intensively in certain areas, like Aerodynamics and Wind Engineering.

As a counterpart, the development of instrumentation devices and acquisition systems allowed the instrumentation of prototypes since the late 1960's, which provided more valuable information on the structural behavior in terms of material properties, boundary conditions, stress distribution, deformation, vibration and damping.

Although the former instrumentation systems were limited in terms of precision and reliability, they overcame several limitations associated with physical model testing, like the impossibility of reproducing at a given scale all the properties of interest of the structure, as well as the boundary conditions, and lack of knowledge of the load characteristics. Moreover, these systems rapidly gained a new purpose, related with the assessment of the time evolution of the structural performance and damage detection.

The development of monitoring programs for large-scale structures is at the current state-of-the-art a normal procedure, the degree of sophistication varying as a function of the relative importance of the structure. The most common instrumentation programs are of short duration and comprehend sensors and equipments for measuring displacements, rotations, strains, accelerations, temperatures, and the wind speed and direction. Static measurements are performed during the bridge construction and at spaced time intervals after completion, while dynamic measurements are performed at the end of construction. Some sensors are however left at the bridge, which trigger particular events, like earthquakes and severe wind condition, or send alarm signals whenever excessive vibrations or displacements are attained. More sophisticated *Health Monitoring Systems* perform continuous measurements, storing statistical information and particular records. These systems incorporate communications with a Central Station, which may be located several hundreds of kilometers away, and from where specific commands concerning the signal acquisition and processing can be issued, such as data transfer or change of the signal acquisition parameters (Nigbor & Diehl, 1997; Myrvoll *et al.*, 2000). According to Chong (1997), the current trend is the evolution towards the concept of *Smart Structure*, which is a structure provided with a series of sensors and actuators that, by analogy with a biological system, monitors its own condition, detecting certain damage threshold conditions and commanding the actuators, in order to adapt to changing environments (see Figure 5.1). In this system, the sensors play the role of the *nervous system*, while the acquisition and system processors are understood as the *brain system*, the *muscular system* being materialized by the actuators.

Considering the particular issue of experimental dynamic testing on full-scale bridges, the current Chapter starts to present a brief state-of-the-art of the problem for the two major groups of techniques, the *Forced Vibration Tests* (*FVT*), and the *Ambient Vibration Tests* (*AVT*). In Section 5.3, some considerations are presented concerning available instrumentation equipments and data acquisition systems. The basic system identification techniques employed for *FVT* and *AVT* are then reviewed in Section 5.4. The last Section comprehends a description and presentation of the main results obtained on the dynamic tests of the Vasco da Gama Bridge (Delgado *et al.*, 1998; Cunha *et al.*, 2000), in which the author participated actively.

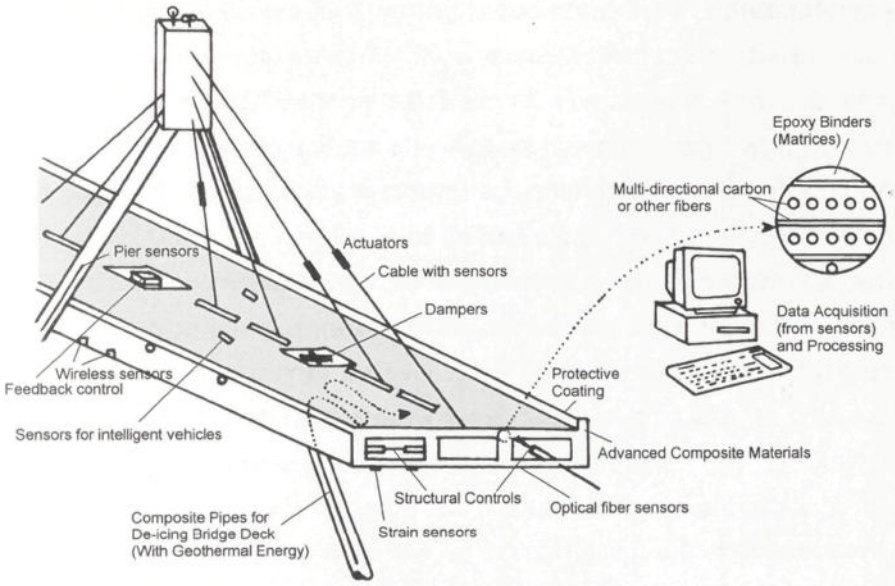


Figure 5.1. An intelligent and integrated bridge system (Chong, 1997).

5.2 BRIEF STATE-OF-THE-ART ON THE EXPERIMENTAL DYNAMIC ANALYSIS OF CABLE SUPPORTED BRIDGES

As referred above, the experimental dynamic tests on full-scale Civil Engineering structures can be classified into two major groups, the *FVT* and the *AVT* techniques.

Forced Vibration Testing Techniques

The *Forced Vibration Testing* techniques employed in Civil Engineering structures constitute straight applications of the so-called *Modal Analysis Techniques*, which were born in the areas of Mechanical and Aeronautic Engineering some decades ago. These techniques are based on the application of a controlled excitation, and measurement of the response at a set of locations. From the set of excitation and response time histories, estimates of *Frequency Response Functions* (*FRF's*) or of *Impulse Response Functions* (*IRF's*) can be obtained (for frequency or time domain analysis, respectively) and *System Identification* algorithms applied, in order to extract the most relevant dynamic parameters of the structure, i.e., the natural frequencies, modal shapes and damping coefficients (Caetano, 1992).

The former application of *FVT* to Civil Engineering structures dates back from the 1960's. One of the most traditional applications, refers to the testing of dams, for which large mechanical shakers have been designed and operated, either on an individual base (Pedro *et al.*, 1986; Portugal & Caetano, 1992), or in combinations of two to four shakers applied at selected locations, in order to enhance particular vibrational modes (Keightley *et al.*, 1961; Severn *et al.*, 1980, 1981; Clough *et al.*, 1982; Deinum *et al.*, 1982; Ellis *et al.*, 1984). Eccentric Mass, hydraulic and other types of shakers have also been used in the *FVT* of

buildings (Paquet, 1990) and in diverse highway bridges (Flesch, 1990; Agardh, 1991; Cantieni *et al.*, 1994). The application of *FVT* to large cable supported bridges is very uncommon, as the very low natural frequencies of these bridges require more powerful devices, which need adequate transportation and particular safety measures for operation, hence constituting very expensive methods of analysis. Only four applications of this type of tests are known, concerning one cable-stayed bridge in Sweden (Ohlsson, 1987), and three other cable-stayed bridges in Japan (Hoshino *et al.*, 1997; Okauchi *et al.*, 1997; Yamaguchi *et al.*, 1999). For the test on the Tjörn bridge, in Sweden, a mechanical device was designed which excited a concrete block of *3tf* in a swept-sine ranging from *0.4Hz* to *1.6Hz*. For the three other cases, two eccentric mass shakers were employed at different locations along the bridge deck (typically, the mid-span and about ¼ span), in order to excite a wider range of vibration modes. Also for the three cases the shakers were operated both vertically and horizontally, allowing the identification of a significant number of vibration modes and associated damping factors. Figure 5.2 refers to the field vibration tests performed on the Tatara Bridge (Yamaguchi *et al.*, 1999), where two exciters with a total weight of 370kN each were used, and a maximum vibration amplitude of *30.5cm* was measured in correspondence with the first vertical vibration mode, at a natural frequency of *0.23Hz*. For the Histuishijima Bridge (Okauchi *et al.*, 1997), a truss cable-stayed bridge with a main span of *420m*, a maximum vibration of *10cm* was measured during vibration tests.



Figure 5.2. FVT tests on the Tatara Cable-Stayed Bridge (www.hsbp.go.jp/bridge/tata_inf.htm).

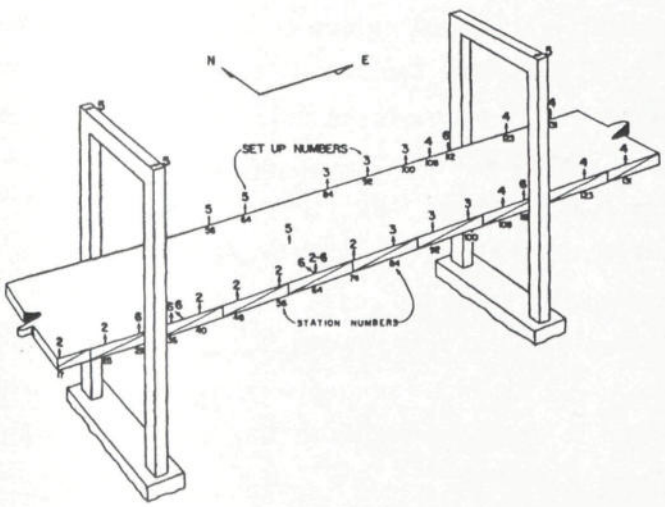
Although recognizing that the *FVT* tests performed by the above referred teams on long span bridges provide very valuable information, it is also evident that these tests are extremely demanding in terms of involved costs and practical feasibility, specially when a cheap alternative can be followed based on *Ambient Vibration Testing* techniques.

Ambient Vibration Testing techniques

AVT techniques constitute a derivation of the conventional *Modal Analysis Techniques* in which environmental actions (wind, vehicle traffic and micro seismic tremors) are considered as input and only the ambient vibration response is measured.

In effect, the random nature of environmental actions for diverse simultaneous and independent sources of vibration allows the assumption of the input excitation as a band limited white noise defined in the frequency range of interest. So, the amplitude of *FRFs* is proportional to the spectral density of the response functions and, consequently, natural frequencies, modal shapes and damping coefficients can be estimated from spectral analysis of the response measurements solely (Bendat & Piersol, 1980).

According to McLamore *et al.* (1971), the first proposal for extracting structural dynamic properties from ambient response is due to Crawford and Ward (1964), who applied the methodology to determine natural frequencies in buildings. The tests on the Newport Bridge and on the William Preston Lane Memorial Bridge (two suspension bridges in the USA with main spans of about *480m*) performed by McLamore and companion authors (1971), together with those performed on the Cheasapeake Bay Bridge (Mason & Carder, 1967), another suspension bridge in the USA with similar main span, are among the former applications of *AVT* to long span bridges. It is interesting to note that, although sensors and acquisition systems have developed a lot in terms of precision, signal acquisition and processing capabilities of measured signals, the procedure of testing defined in these former experiences is actually very similar to the current test procedures for *AVT*. Figure 5.3 represents the instrumentation plan and setups defined for the *AVT* of the Newport Bridge with a set of seven seismometers.



Setup 2: Vertical motion on south side of roadway on the western half of the bridge
Setup 3: Vertical motion on both sides of the roadway in the eastern half of the center span
Setup 4: Vertical motion on both sides of the roadway, primarily on the eastern side span
Setup 5: Horizontal motion in the east-west direction at tops of towers, and vertical motion at two points on the northern side of the roadway on the western half of the center span
Setup 6: Vertical motion of roadway at the towers and transverse horizontal motion at the reference location and western tower

Figure 5.3. Instrumentation locations for *AVT* of Newport Bridge (MacLamore *et al.*, 1971).

In terms of results, it is relevant to refer the paper by Trifunac (1972) who performed a comparison between *FVT* and *AVT* techniques, concluding that both methods yield similar results whenever applied correctly.

In view of the relative easiness of application, *AVT* techniques have become very popular in dynamic testing of bridges and, in particular, of cable supported bridges. Several applications all over the world concerning bridges of this type deserve reference: Abdel-Ghaffar & Housner, 1978; Buckland *et al.*, 1979; van Nunen & Persoon, 1982; Abdel-Ghaffar & Scanlan, 1985ab; Ohlsson, 1987; Ostenfeld & Langsoe, 1987; Brownjohn *et al.*, 1987, 1989; Stiemer *et al.*, 1988; Kumarasena *et al.*, 1989; Jones & Spartz, 1990; Murià-Vila *et al.*, 1991; Wilson & Liu, 1991; LNEC, 1992a, 1992b; Fujino *et al.*, 1993; Paultre *et al.*, 1994; Casas, 1995; Jakobsen *et al.*, 1995; Felber & Cantieni, 1996; Felber & Ventura, 1996; Owen *et al.*, 1996; Gentile & Cabrera, 1997; Xu *et al.*, 1997; MacDonald *et al.*, 1998; Hoshino *et al.*, 1999; Main & Jones, 1999; Cunha *et al.*, 2000.

The publications above referred respect to *AVT* performed on both suspension and cable-stayed bridges of very different characteristics and spans. Although different sensors and test procedures are employed, a common ensemble of characteristics can be found: (i) the existence of a low level of vibration, in general inferior to *0.5g*; (ii) the existence of a very high number of modes of vibration in a narrow frequency range (dependent on the bridge span, but always in the range *0-10Hz*), some of which with very close natural frequencies; (iii) a marked three-dimensional character of vibration modes, particularly for cable-stayed bridge structures; (iv) a significant variation in the damping coefficient estimates; (v) the need for measuring very long duration records for each instrumented location, in general for periods longer than *10* minutes.

These characteristics evidence two main difficulties associated with the *AVT* techniques: the lack of resolution (i) in amplitude, and (ii) in frequency.

The lack of resolution in amplitude is the consequence of the low level of environmental excitation, which may not be sufficient to induce certain higher modes of vibration to a measurable level of response. If, in addition, two or more modes are very closely spaced in frequency, the corresponding identification may become difficult.

In this respect, it is important to refer that the significant improvements both in sensors' sensibility and in data acquisition systems, that took place during the last few decades, have allowed the performance of vibration measurements at extremely low levels of response.

The lack of resolution in frequency is an important aspect in case of existence of vibration modes closely spaced in frequency. In principle, any two close vibration modes can be separated, provided that they are not coupled and an adequate frequency resolution is adopted. This resolution is defined as a function of the time record and can be as small as required, the inconvenience being the large acquisition time and length of the records. It is generally accepted that a minimum frequency resolution of *0.01Hz* should be used in the test of flexible structures, and that the recorded length of the response should be of about *30* to *40* times the highest structural period, times a number of averages varying between *8* and *32*.

The lack of resolution in both time and amplitude constitute possible explanations for the dispersion found in the damping estimates. Another aspect that contributes to that dispersion relates to the presence of a varying amount of the *aerodynamic damping*.

In effect, the aeroelastic coupling between the bridge deck and the wind may originate a modification of the bridge dynamic characteristics. Depending on the average wind velocity and on the intensity of turbulence, a viscous damping component, designated as *aerodynamic damping*, adds to the typically low *mechanical damping* (according to Jones and Spartz (1990), this damping varies in the range *0.5%* to *1%*). So, the estimates of damping obtained from ambient vibration tests incorporate the two components, aerodynamic and mechanical, the first of which varying in a great deal according to the weather conditions.

In face of the above listed issues, it is of particular interest the adoption of certain strategies for observation, which include the performance of ambient vibration tests under measured more or less uniform weather conditions, the choice of particular instrument locations where the level of the signal is higher or coincident with nodes of particular mode shapes, or even the separation of modal components by direct operation of signals (summing and subtracting signals measured on opposite sides of the deck, for example, allows for a separation of purely torsional from bending vibrational modes).

In addition to the above referred, two other possible directions of actuating can be followed to improve the quality of dynamic estimates, one based on the application of simplified excitation techniques that enhance the level of the response, and the other based on the application of recently developed powerful techniques of system identification from output measurements (*AVT*).

Simplified excitation techniques

With regard to the first issue, it is interesting to refer the free vibration tests performed in several bridges using specific devices, such as masses suspended from the bridge deck, or loads released from barges.

One of the former tests of this type was performed during the field observation of the Tagus suspension Brigde, in Lisbon, in 1966. In an attempt to measure the fundamental bending and torsional frequencies and the corresponding damping factors, Marecos *et al.* (1969) applied an impulsive vertical force of about *100kN* at midspan by breaking a calibrated steel bar attached to the main downstream cable on the upper end, and to a winch carried on a floating crane on the other end.

Tests of the same type were performed more recently at the Tjörn, Normandy and Vasco da Gama Bridges. For the Tjörn Bridge (Ohlsson, 1987), a floating barge weighting about *600kN* was released from midspan through fire explosions that cut off the connecting wires. For the Normandy Bridge (Bietry & Jan, 1995), the free vibration test comprehended two sequences, releasing in one of them a mass of *50t* vertically and eccentrically at about the third span and, in the other, a mass of *100t* inclined *14°* with horizontal. With these tests, the fundamental vertical, transversal and torsional modes were excited, and the corresponding

damping factors estimated. Finally for the Vasco da Gama Bridge, a barge weighting *600 kN* hanging eccentrically from one third the span at low tide was released by forced failure of a Diwidag rope (see Figure 1.11) (Cunha *et al.*, 1999).

Another test procedure has also been used in the past, which consists of hanging a weight from a crane in the form of a pendulum, whose length can be varied in such a form that the swinging frequency of the mass (excited manually by ropes) is tuned to the excited vibration mode. After several minutes of oscillation, the concrete block is placed back on the deck, and the response measured. The procedure was employed by Buckland *et al.* (1979) during the field tests of the Lion's Gate suspension bridge, in Canada, employing a weight of about *5kN*. It was later employed in the tests of the Annacis cable-stayed bridge, in Canada (Stiemer *et al.*, 1988), and in the tests of the Arade Bridge, in Portugal (Fernandes *et al.*, 1996), employing a concrete block weighting *20kN*.

Finally, it is of interest to refer a simpler test, based on the repeated passage of a heavy loaded truck on a plank at a given velocity. Buckland *et al.* (1979) performed tests of this type on the Lion's Gate suspension bridge, using a timber *15cm* thick plank and a truck full of wet sand. He also tried to induce torsional motion, by driving the truck across the lanes at about *45°* and suddenly applying the brakes. The plank tests were also performed recently on the Vasco da Gama Bridge (Cunha *et al.*, 1999), employing trucks weighting *300kN*, and a timber plank *4cm* thick at different positions on the deck (see Figure 1.12). Several passage velocities were tested. Although a great number of mode shapes were induced, which required more sophisticated data processing techniques and the acquisition of longer records to separate the modes and extract damping coefficients, it was possible to observe from these tests that an intermediate level of signal was measured, between the ambient vibration tests and the free vibration tests using the *600kN* barge, and rather good results were obtained.

System identification techniques from output measurements

The application of system identification algorithms to extract modal parameters from forced vibration tests has suffered a great evolution during the last decades, leading to well-established and widely used methods of identification (Maia & Silva, 1997). In the context of Civil Engineering applications, the technique of identification of modal parameters from output measurements described by Bendat and Piersol (1980) and later systematized by Felber (1993) has been employed for a long time, despite the inconveniences above referred. More recently, a set of algorithms for ambient vibration measurements have been implemented, idealizing the input as a stochastic process, and employing special techniques that are able to deal with the low level of response and noise (James *et al.*, 1995; Andersen *et al.*, 1996; Van Overschee *et al.*, 1996; Hermans *et al.*, 1998; Peeters & Roeck, 1999). One of the main advantages attributed to the application of this new generation of algorithms is an increased efficiency and accuracy in the estimation of damping factors. A recent benchmark study of the ambient measurements on a tall building seems to indicate this fact (Horyna & Ventura, 2000).

However, the author has no knowledge of any applications of these methods to measurement data from more flexible structures at the present state-of-the-art.

5.3 RECENT TRENDS IN INSTRUMENTATION SYSTEMS FOR DYNAMIC TESTING OF CABLE SUPPORTED BRIDGES

The instrumentation systems employed for dynamic testing of structures comprehend the following main components: (i) a subsystem for excitation; (ii) a subsystem for measurement of applied forces and responses; (iii) a data acquisition modulus, for control of excitation, and for recording and analyzing the measured data. A great diversity of solutions exist for instrumentation of Civil Engineering structures, the main characteristics of which were compiled by the author in a previous work (Caetano, 1992).

The current Section attempts to update that work, restraining however the field of applications to large cable supported bridges. The general characteristics that should be expected in the testing of these structures are then discussed, and the most recent trends in instrumentation systems are presented.

5.3.1 Excitation devices

As referred above, most dynamic tests performed on large cable supported bridges use ambient excitation as input, and so the subsystem for excitation is not normally present. For the few cases where forced vibration tests have been performed, quite impressive excitation devices have however been employed, which should be referred in the current dissertation. This is the case of the large scale synchronous exciters designed by the Japanese Company Kajima Corporation for dynamic testing of large structures, such as nuclear power plants, high-rise buildings and long span prestressed concrete buildings (Kajima Corporation, 1985). The Company owns a set of three units, two of which for horizontal excitation, and the other for vertical excitation. These shakers are composed of two eccentric masses rotating synchronously in a plane and generating a sinusoidal force, which varies in amplitude with the excitation frequency (see the working principle in Figure 5.4). The maximum exciting force is *100kN/unit* in the horizontal direction, and *50kN* in the vertical direction, the frequency range of sinusoidal force being for the former *0.2Hz* to *20Hz*, and for the later *0.2Hz* to *30Hz*. The two horizontal exciters can operate synchronously.

The major characteristics of the horizontal and vertical exciters and corresponding force properties are presented in Table 5.1 and Figure 5.5, the later Figure including also a view of the two horizontal shakers. Relevant aspects are the shakers' weight, which are about *100kN* and *50kN* for each of the horizontal and vertical units, respectively, and the corresponding dimensions (*3.7x2.18x1.95* m^3 and *1.84x1.80x1.80* m^3 for horizontal and vertical shakers, respectively).

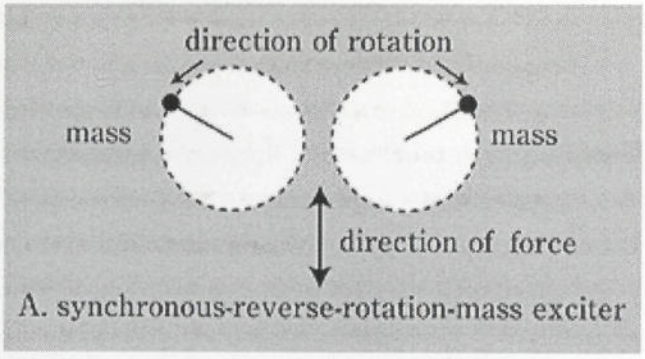
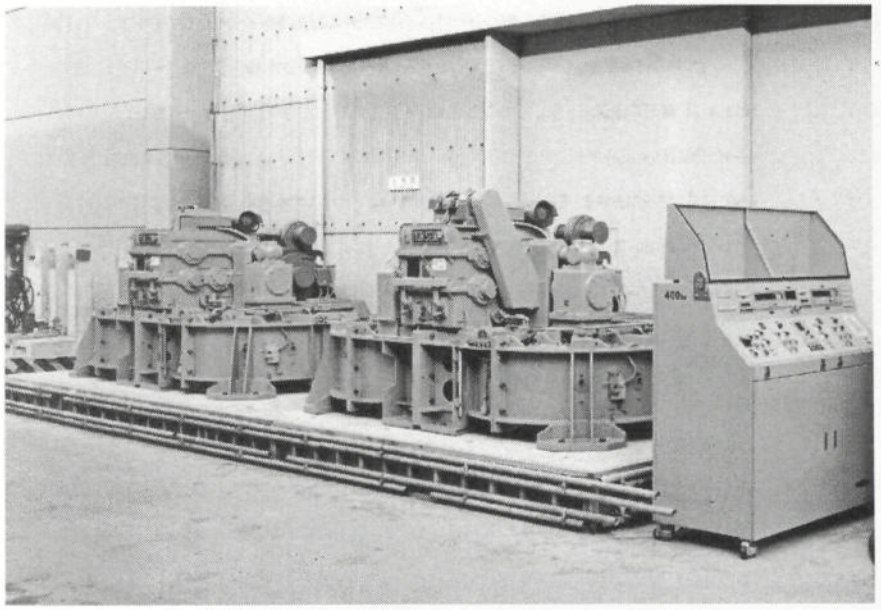


Figure 5.4. Generation of sinusoidal force in an eccentric mass exciter.

Table 5.1. Specifications for the mechanical exciters of Kajima Corporation (Courtesy of Kajima).

	Horizontal exciters	Vertical exciter
Exciting mechanism	2 eccentric masses in synchronous coplanar rotation	
Direction of Excitation	2 horizontal (X and Y) axes	Vertical (Z) axis
Exciting waveform	Sinusoidal	
Maximum exciting force	10,000 kg.f (2Hz or more)	5,000 kg.f (6.43Hz or more)
Eccentric moment	0.63~630kg.m (low and middle ranges) 0.26~260kg.m (high range) Successive variable operation possible	0.03~30kg.m Successive variable operation possible
Accuracy of moment setting	± 0.1% of maximum value	
Range of vibration frequency	Low range: 0.2~2Hz Middle range: 0.8~8Hz High range: 2.0~20Hz	Low range: 0.2~2Hz Middle range: 0.8~8Hz High range: 3.0~30Hz
Accuracy of vibration frequency setting	Below ± 0.5% of maximum vibration frequency of each range	
Accuracy of synchronous operation	Below 1 degree at each range (using synchronous BL motor)	
Dimensions	Width 3,700 mm Depth 2,180 mm Height 1,950 mm	Width 1,840 mm Depth 1,800 mm Height 1,800 mm
Weight	Approx. 10t	Approx. 5t
Power supply	200V, 3ϕ, 70kVA	



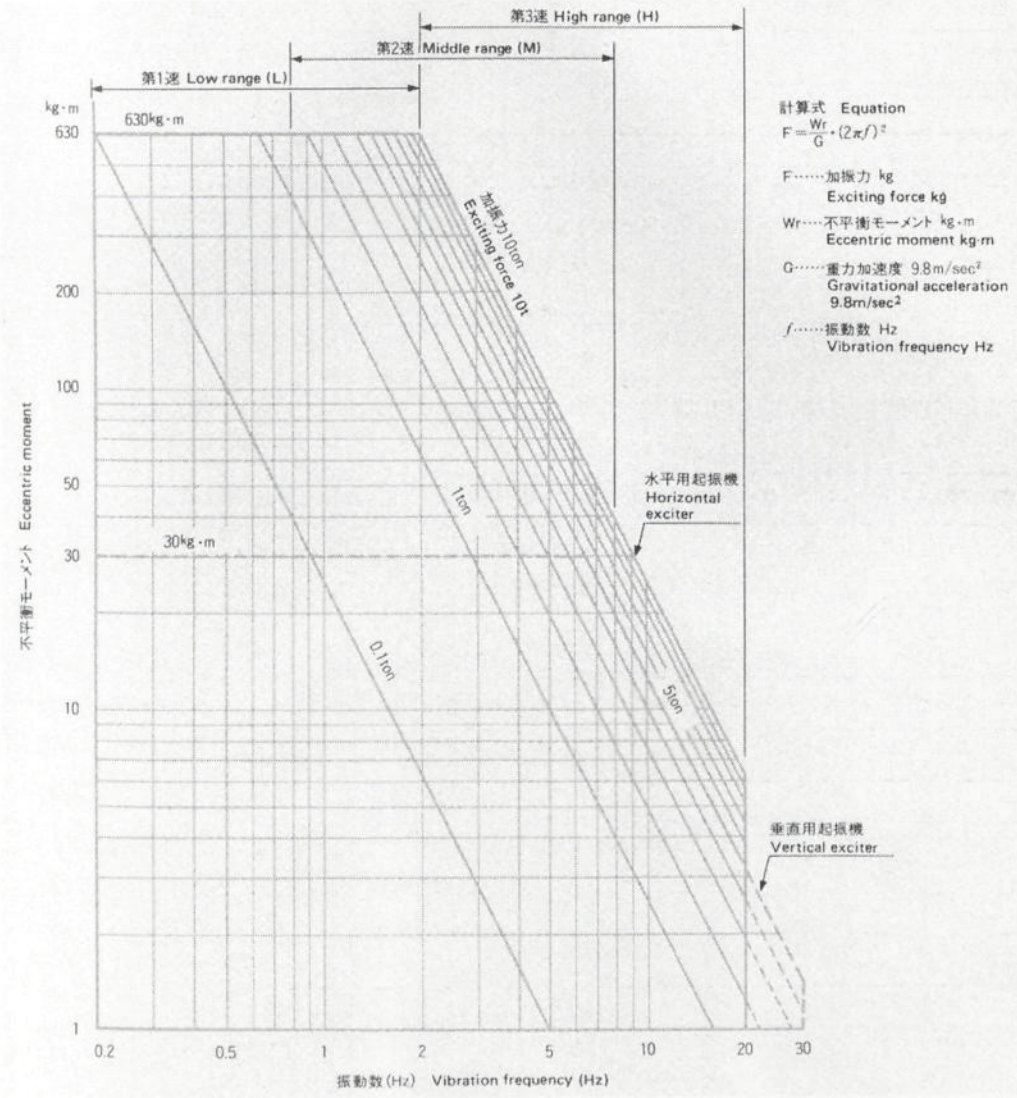


Figure 5.5. Large scale eccentric mass exciters: General view of horizontal devices and properties of the delivered force. Courtesy of Kajima Co..

The shakers above described were employed on the *FVT* of the Ikara Bridge (Hoshino *et al.*, 1997), in Japan, a prestressed concrete cable-stayed bridge with a main span of *260m*. During the tests, maximum forces of *4.9kN* and *19.6kN* were applied in the vertical, and in the horizontal direction, respectively, achieving a maximum girder displacement of about *4mm*. Note that the fundamental transversal, vertical and torsional frequencies of the bridge were respectively of *0.36Hz*, *0.37Hz*, and *0.48Hz*.

5.3.2 Input and response measurement devices

The subsystem for measurement includes a component associated with the quantification of applied forces, and another component that respects the structural response, i.e., the bridge motion.

5.3.2.1 Input devices

Starting with input measurement, two different types of devices are of interest, one associated with the control of sinusoidal forces applied by mechanical shakers, and another that respects to the quantification of particular ambient conditions for correlation with the bridge response, namely by measurement of wind speed and direction.

Control of sinusoidal forces applied by mechanical shakers

Although force cells are adequate for interposition between the shaker and the structure in the case of vertically applied forces, the same option is not easily available for the horizontal direction. However, the mechanical exciters above described are based on the opposite rotation of two perfectly known masses M with perfectly known strokes S. So, the magnitude of the generated sinusoidal force F at natural frequency f can be accurately evaluated through

$$F(f) = 4\pi^2 f^2 M(S/2) \tag{5.1}$$

As for the phase control, it is expected that the exciter control system generates a reference signal for operation with the measured response, allowing for the evaluation of the phase-lag associated with the later.

Devices for measuring the wind speed and direction

The time and spatial variation of the wind can be characterized at different levels employing a wide range of sensors.

Two major categories of sensors can be identified, (i) the in-situ sensors, and (ii) the remote sensors. The in-situ sensors are the traditional instruments employed for accurate

measurements at the lower boundary layer. These instruments are normally mounted on towers and masts and constitute the only category described in the text.

For the purpose of Civil Engineering applications, two main types of measurements are of interest, related with the evaluation of the mean and fluctuating properties of the wind. The measurement of these properties presents different types of requirements. Sensors for measurement of average wind properties are required to have a high degree of absolute accuracy and long term stability, providing good averages for time intervals of *10* minutes or longer. Sensors for measurement of the wind turbulence are required to have a frequency response broad enough to cover all the eddy scales that contribute to the process, although the accuracy needs only to be relative with respect to a working mean.

According to Kaimal and Finningan (1994) the accuracy required for both absolute and relative amplitudes of wind velocity is $\pm$ *0.05m/s*. The response time for mean sensors can be as large as *1 minute*. For fluctuating sensors, it should be no greater than *0.1s*.

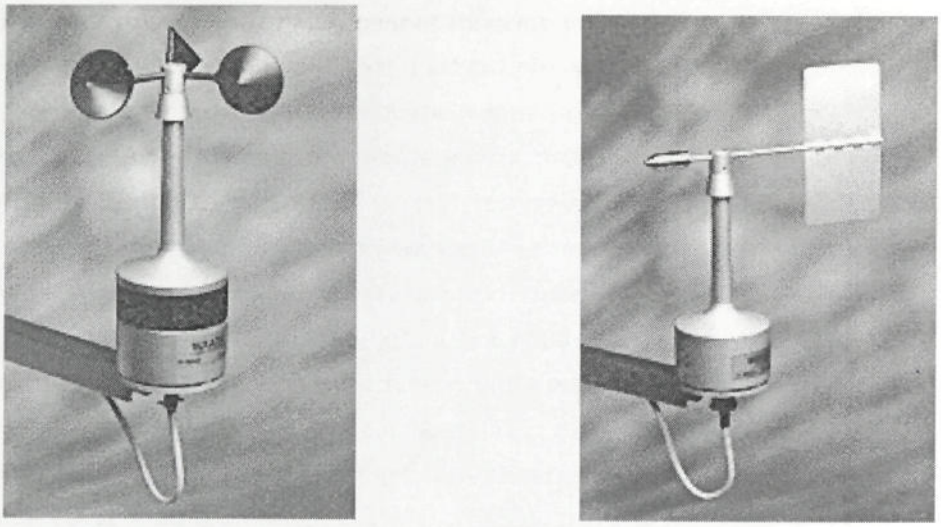
Mean wind sensors

The sensors most commonly used for the measurement of wind profiles are cup anemometers, propeller anemometers and vanes. The three types of sensors have been used for over one century (Kaimal, 1986) and are in general characterized for their simple working principle, ruggedness, dependability and low cost.

Figure 5.6 represents one of the most well-known configurations for a cup and vane system, consisting in a three-cup wind speed sensor (Figure 5.6(a)) and a direction vane (Figure 5.6(b)) that can be installed side by side on a common mounting arm.

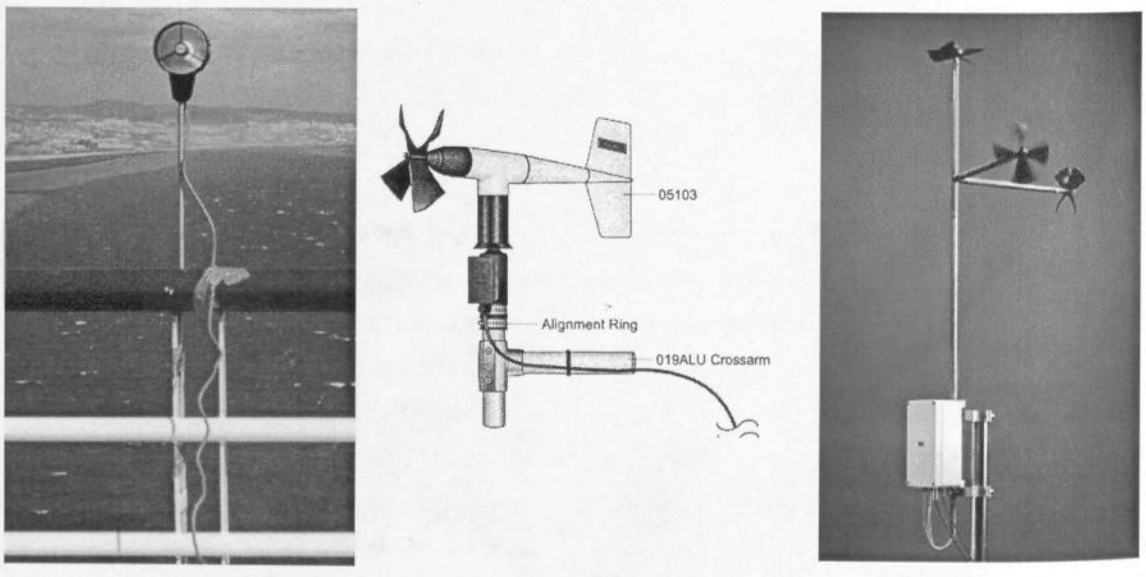
According to Figure 5.6(a), the three cups are mounted around a vertical shaft. Air striking the concave sides of the cups causes rotation, the number of rotations per unit time being a measure of the wind speed. In some modern devices, the rotation of the cups generates an electric tension that is proportional to the wind speed. The same principle applies to the vane represented in Figure 5.6(b). Because of the inertia of the mechanical components, the time response of these sensors is relatively large and consequently they are not adequate for measuring wind fluctuations. Typically, a standard cup anemometer measures the horizontal wind speed and fluctuations up to about *0.5Hz* (Sorbjan, 1989). In terms of amplitude range, the available devices cover in general the interval *0.5m/s* to *75m/s*. Although the cup anemometers tend to overestimate the wind speed by *5%* to *10%*, a rather good accuracy of *±1%* can be achieved in the measurements, provided that the sensor is properly calibrated in wind tunnel.

Most propeller anemometers have helicoid rotors with two or four blades, the later type working in the lower wind ranges, i.e., from *0.5m/s* to about *35m/s*. When used in the single configuration represented in Figure 5.7(a), these sensors have the inconvenience of demanding to be aligned along the wind direction. Alternatives are the propeller-vane combination represented in Figure 5.7(b), or the two- or three-component orthogonal configuration as represented in Figure 5.7(c).



(a) (b)

Figure 5.6. Example of (a) cup anemometer (b) direction vane (http://www.vaisala.com).



(a) (b) (c)

Figure 5.7. Example of propeller anemometers in: (a) single configuration; (b) combined with vane (http://www.campbellsci.com); (c) in three-component orthogonal configuration (http://www.meteolabor.ch/e/wnz.htm).

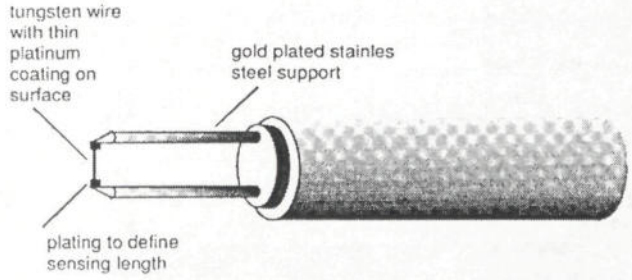
In terms of accuracy and response time, propeller anemometers have characteristics that are comparable with the cup anemometers, requiring also appropriate wind tunnel calibration.

Velocity fluctuation sensors

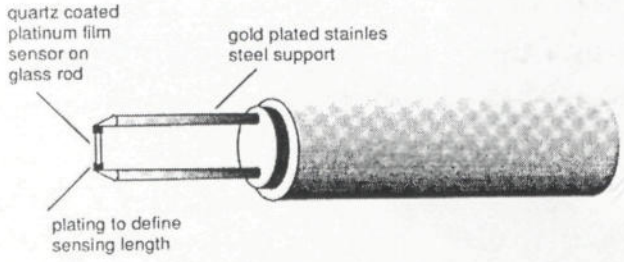
Two main categories of sensors can be employed for measurement of the fluctuating properties of the wind, (i) the hot-wire and hot-film anemometers and (ii) the sonic

anemometers. The first category comprehends sensors that have been in use for several decades, which are relatively economic and have a high frequency response (on the order of *10kHz*). These sensors are not however so adequate for *in-situ* measurements and are essentially used for laboratory and wind tunnel studies, in view of a few major drawbacks: susceptibility to calibration shifts from atmospheric contamination, fragility and narrow wind acceptance angle.

Figure 5.8(a) represents a hot-wire sensor whose working principle is the following: a very small resistance wire typically *0.004* to *0.005mm* in diameter and *1* to *2mm* long is electrically heated relative to the surrounding fluid. In the constant temperature method, the wire is kept at constant temperature in a Wheatstone bridge with a feedback circuit. As the magnitude of wind velocity in the plane perpendicular to the direction of the wire varies, the heat transfer varies and the power required to keep the wire at constant temperature varies. By combining wires inclined at different angles, the three components of the wind vector can be addressed. The same principle applies to the hot-film sensor represented in Figure 5.8(b), which employs a film sensor instead of a wire sensor.



(a)



(b)

Figure 5.8. Hot-wire and hot-film anemometers: (a) tungsten hot-wire sensor and support (b) cylindrical hot-film sensor and support (Sorbjan, 1989).

The sonic anemometers, developed in the 1950s, employ the propagation of sound waves to measure the velocity and temperature of a gas flow. These devices have none of the problems of both the cup and propeller anemometers, or of the hot-wire and hot-film anemometers. However, they have an extremely high cost and for this reason other simplified techniques have been used in the measurement of wind turbulence based on indirect measurements. This is the case of the dynamic anemometers, which sense pressure or the drag force of an object immersed in the flow.

The sonic anemometer can measure the wind velocity in one, two and three axes. The principle of operation consists in transmitting and receiving acoustic pulses along fixed directions. The time of propagation of the received impulses is then related with the sound velocity and the wind velocity through microcomputer electronics. The sensors have a high frequency response, producing measurable signals at up to *60Hz* frequency with extreme accuracy (about *±0.03m/s*). Several configurations are available in the market according to the manufacturer. Figure 5.9 represents two possible configurations for wind measurements along two and three axes from Gill Instruments, as well as one configuration for three-axes measurement from Applied Technologies.

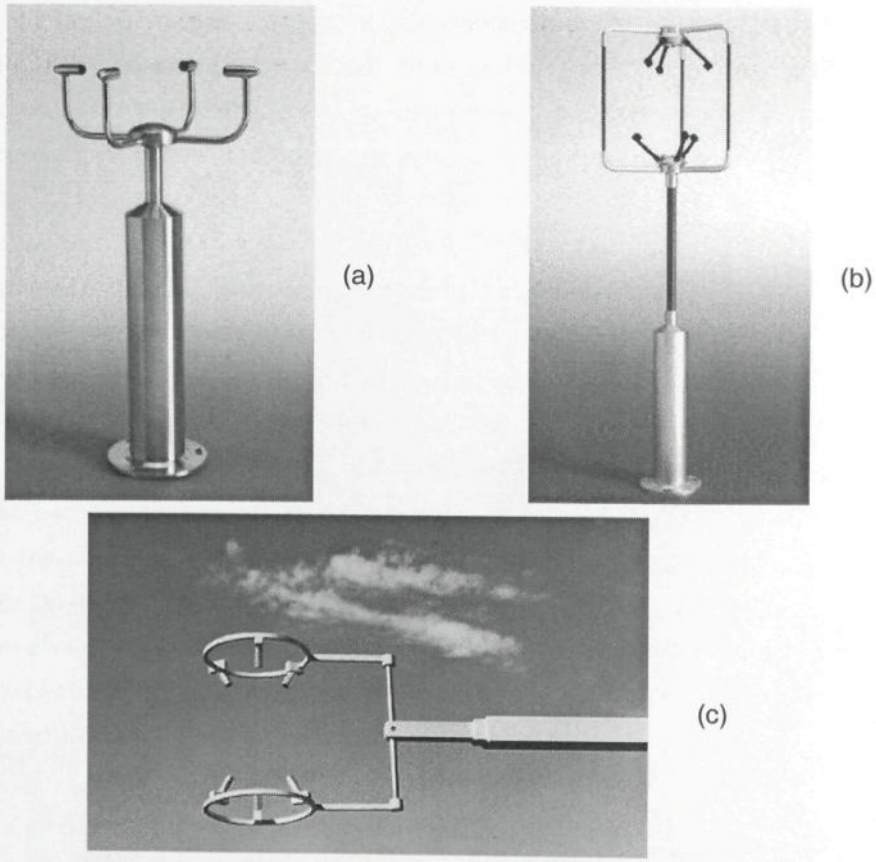


Figure 5.9. Example of sonic anemometers: (a) Two-axis; (b) three-axis wind measurement (http://www.gill.co.uk/Products/Met.htm); (c) Three-axis configuration "*A*"-style probe (http://apptech.com/aprobe.htm).

5.3.2.2 Response measurement devices

The dynamic response of a cable-supported bridge in an ambient vibration test can be assessed in terms of the motion, deformation or force at particular locations along the bridge.

The most common measurements in dynamic testing of structures respect the motion, which can be expressed in terms of displacement, velocity or acceleration. Theoretically, it is irrelevant which of these three parameters is measured. It is known however that displacement

measures give more weight to the low frequency component of the response, and acceleration measures stress the high frequencies. So, it is expected that the low level of response of a cable-supported structure, characterized by very low natural frequencies, can be captured with more accuracy using displacement transducers.

The practice with use of accelerometers in dynamic testing has however shown that rather accurate results can be obtained with this type of transducers at a relatively low cost. The additional fact that electronic integration of a signal is more reliable than differentiation and so that it is easier to obtain displacement records from acceleration time histories than the contrary, has led to a general use of accelerometers in dynamic testing of large structures.

The current Section describes some of the main types of *accelerometers* for dynamic testing of large flexible structures. Besides accelerometers, a series of other less conventional transducers that have been employed lately in dynamic testing of this type of structures are described. This is for example the case of *strong motion accelerographs*, which are actually integrated units that include an accelerometer and a data acquisition system each and that allow the suppression of electrical cables during the measurements. *Strain transducers*, which provide a straight assessment to the stress state of a structure, are conventional transducers in static measurements and have been also increasingly used in dynamic testing. *Non-contact transducers* are of interest for light structures or for remote measurements in large structures. In terms of Civil Engineering applications, the first situation can only concern the laboratory test of physical models for which *magnetic transducers* are a relatively cheap and accurate option. *Optical systems* have been developed for large applications, either based on light beam or laser displacement sensors, or on laser velocity transducers. In applications to cable supported structures, the dynamic measurement of the forces installed in the stays may be of interest. For this application, conventional *load cells* can be employed or else recently developed sensors based on the magnetoelastic principle. The Section ends with reference to a new generation of transducers and measurement systems that are still under investigation and that have enormous potential in the dynamic testing of full-scale structures, the *optical fiber sensors*, and the measurement systems based on the *GPS*.

Accelerometers

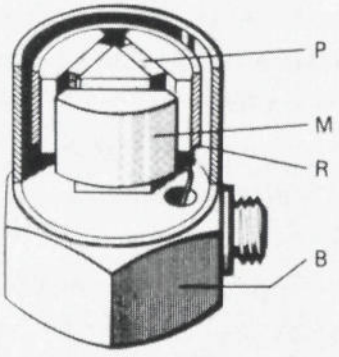
Accelerometers are devices constituted by spring-mass-damper systems that produce signals proportional to the acceleration in a frequency band well bellow their resonance.

Different systems and working principles can be employed in the construction of an accelerometer. The following three main categories can be identified: (i) *piezoelectric*; (ii) *piezoresistive* and *capacitive*; (iii) *force-balanced*.

(i) Piezoelectric accelerometers

Figure 5.10 represents schematically the mechanical components of a piezoelectric accelerometer for a particular configuration designated as *delta-shear* (other configurations

are available, such as the *planar-shear*, *compression* and *annular*). The active elements of the accelerometer are the piezoelectric elements, which act as springs and connect the seismic masses to the base of the accelerometer through a rigid centre, suffering therefore slight shear deformations (for this configuration) when moving with the structure. These deformations produce a charge that is proportional to the acceleration of the seismic masses and, consequently, proportional to the acceleration of the surface onto which the accelerometer is mounted.



P - Piezoelectric element
M - Seismic mass
R - Clamping ring
B - Base

Figure 5.10. Schematic representation of *delta-shear* piezoelectric accelerometer (Serridge & Licht, 1987).

Compared with other types of accelerometers, piezoelectric accelerometers have several advantages, such as: (i) not needing external power source (the accelerometers are designated as *self-generating*); (ii) being rugged and stable in the long term and relatively insensitive to the temperature; (iii) being characterized by high signal-to-noise ratios; (iv) being linear over a wide frequency and dynamic range.

These transducers present however a serious inconvenience in applications involving large flexible structures with low level and frequency response, which has to do with a limitation in the lower frequency range. Piezoelectric transducers are not in effect capable of a true *DC* response, as the piezoelectric elements only produce charge when acted by dynamic forces. The actual low frequency limit is determined by the preamplifier to which the sensor is connected and is in general greater than *1Hz*. A few manufacturers have however produced near-*DC* response piezoelectric sensors. The *PCB* model *393C*, which has been employed by the author in the tests at the Vasco da Gama Bridge (see Section 5.5), has a nominal sensitivity of *1V/g* and is claimed to operate in the range *0.025Hz* to *800Hz* with *5%* maximum deviation. The *ENDEVCO* accelerometer *model 7754-1000* has identical sensitivity and operates, according to the manufacturer, in the range *0.2Hz* to *400Hz* with *5%* maximum deviation. Finally, the *B&K model 8318* has a sensitivity of *680pC/g* and operates in the range *0.1Hz* to *1000Hz* with *10%* deviation.

(ii) Piezoresistive and capacitive accelerometers

Piezoelectric accelerometers were above defined as *self-generating transducers*, in the sense that they generate an electrical charge proportional to the mechanical energy which is then conveniently amplified and transformed into an electrical energy. These devices can also be designated as *active transducers*.

As opposed to *piezoelectric* accelerometers, *piezoresistive* and *capacitive* are defined as *passive transducers*, requiring the supply of electrical energy. This energy modifies with the change of mechanical energy, the difference to the input energy being proportional to the structural acceleration.

Piezoresistive accelerometers are composed of a bending beam with bonded strain-gages forming part or all of an active Wheatstone bridge. The beam supports a seismic mass (see Figure 5.11). As the beam deforms under acceleration of the seismic mass, the Wheatstone bridge is unbalanced and the differential output (proportional to the beam strain) is a measure of acceleration.

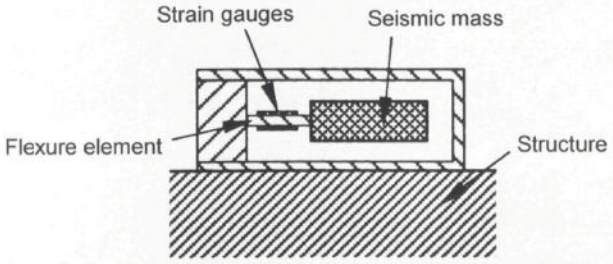


Figure 5.11. Schematic cross-section of a piezoresistive accelerometer (Maia & Silva, 1998).

Capacitive accelerometers comprehend a bending beam supporting a seismic mass in a scheme similar to *piezoresistive* transducers. In this case, the seismic mass moves from its central support between two electrodes (see Figure 5.12). The measuring elements form a half-capacitive bridge which is unbalanced whenever the seismic mass moves, the differential output measured being proportional to the structural acceleration.

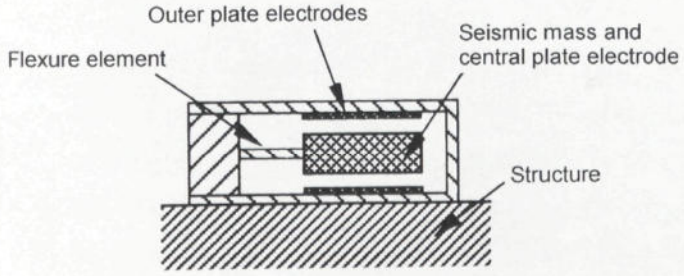
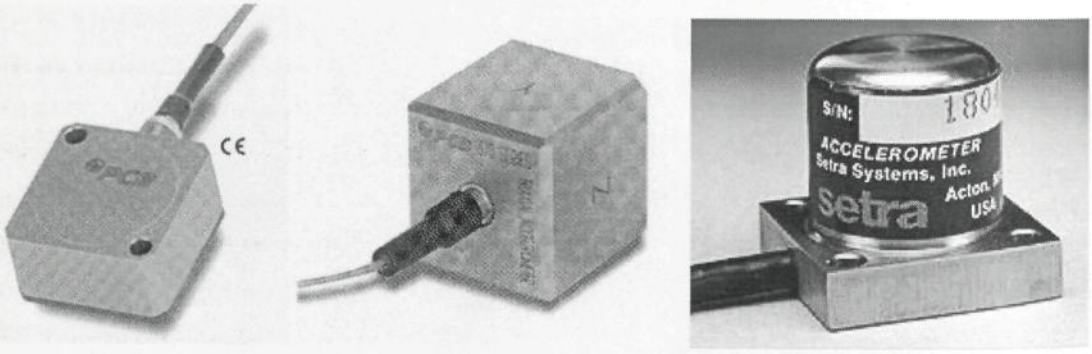


Figure 5.12. Schematic cross-section of a capacitive accelerometer (Maia & Silva, 1998).

Piezoresistive and *capacitive* accelerometers are adequate for Civil Engineering applications to flexible structures and, in particular, cable supported bridges, since they can measure accelerations from *DC*. An example of a *capacitive* transducer is the *PCB* accelerometer model *M3701G3FA3G* (see Figure 5.13(a)), which weights *15gram*, operates in the range *DC* to *150Hz*, has a sensitivity of *1V/g*, and a measurement range of *±0.00012g* to *±3g*. The triaxial version of this sensor is also available (see Figure 5.13(b)). These sensors require an external *5VDC* excitation for operation. The *SETRA* accelerometer *model 141A* is another extremely high precision *capacitive* accelerometer that can operate in the range *DC* to *200Hz-3000Hz*, depending on the selected measuring range. So, for a *±2g* amplitude range, the transducer operates from *DC* to *200Hz*. The required excitation voltage varies in the range *5VDC-15VDC* and the mass of the accelerometer is only *30gram*.



(a) (b) (c)

Figure 5.13. Examples of *capacitive* transducers: (a) *PCB* model *M3701G3FA3G;* (b) *PCB* model *M3703D3FA3G (http://www.pcb.com);* (c) *SETRA* model *141A* (http://www.setra.com).

(iii) Force-balance accelerometers

These transducers pertain to the category of *passive transducers* and are composed, similarly to the *piezoresistive* and *capacitive* accelerometers, by mass-spring systems whose motion generates modification of the DC voltage fed as input. Figure 5.14 represents schematically the main components of a force-balance accelerometer. For the particular case represented in Figure 5.14(a), a central plate (mass) is supported on four suspension beams that are anchored on their tips (springs). When the transducer experiences acceleration, the central plate moves causing unequal capacitances between the central multi-plate electrode and two fixed electrodes (see Figure 5.14(b)). The changes in capacitance are sensed and conditioned to generate a DC voltage that is fed back to the capacitor plates and electrostatically forces the central plate back to the equilibrium position. The voltage required to hold the central plate in equilibrium provides the output signal. This signal is proportional to the structural acceleration (Maia & Silva, 1998).

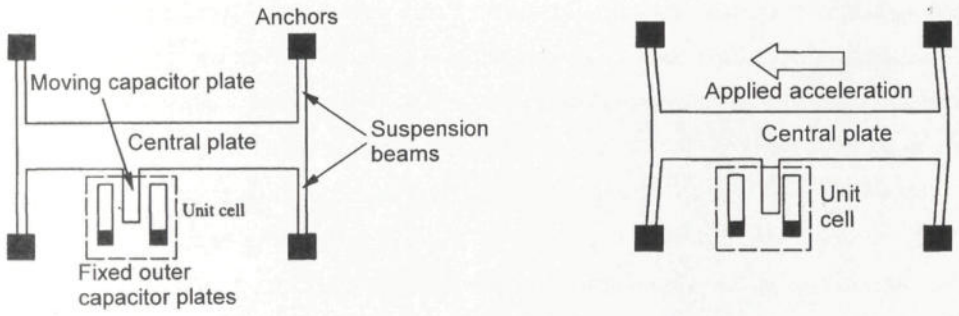


Figure 5.14. Schematic view of a force-balance type accelerometer: (a) accelerometer in the equilibrium position; (b) acceleration in a transient condition due to an external acceleration (Maia & Silva, 1998).

Force-balance accelerometers have been available for a long time and constitute at present one of the most employed types of transducers for Civil Engineering applications to large flexible structures. These transducers have a set of characteristics that fit well the requirements for ambient vibration testing of flexible structures, such as the ruggedness, the high sensitivity, the operation in the low frequency range (from *DC* to as much as *100Hz*), and a significant dynamic range.

A well-known accelerometer of force-balance type is the *KINEMETRICS model FBA-11* (or *FBA-23*, the three-axial version), which has been in use since 1971 and has suffered, according to the manufacturer, significant improvements. This model of sensor was used in 1985 by Abdel-Ghaffar and Scanlan (1985a; 1985b) in the tests of the Golden Gate Bridge, and by Wilson and Liu (1990) in the tests of the Quincy Bayview Bridge. Recent tests in large cable supported bridges have employed the same type of sensor. This is the case of the Halkis Bridge, a cable-stayed bridge with a centre span of *215m* in Greece, which was instrumented by *KINEMETRICS* in 1994, and where among other devices, thirty-six *FBA-11* and four *FBA-23* force-balance accelerometers were employed. In 1996 *KINEMETRICS* installed a monitoring system on the Namhae bridge, a suspension bridge with a main span of *400m* in South Korea, employing a total of twelve *FBA-11* and two *FBA-23* accelerometers.

Figure 5.15 displays a triaxial mounting using three FBA-11 units on a leveling plate.

The main characteristics of *FBA-11* accelerometers are as follows: a sensitivity of *5V/g* for the standard sensor, with a full-scale range of *±1g*, a dynamic range of *135dB* in the range *0.01Hz* to *50Hz*, or *145dB* in the range *0.01Hz* to *20Hz*, a resonant frequency of about *50Hz* (or *100Hz*, optionally), a damping factor of *70%*, a mass of *0.7kg* and a supply voltage of *12VDC*. The plot of the gain functions for a set of three transducers *FBA-11* is represented in Figure 5.16. It can be concluded from the analysis of the gain functions that the adequate range of operation of these sensors is the *DC* to *10Hz*, although the gain of the accelerometers actually departs no more than *5%* from unity in the range *DC* to *30Hz* for the set of transducers analysed.

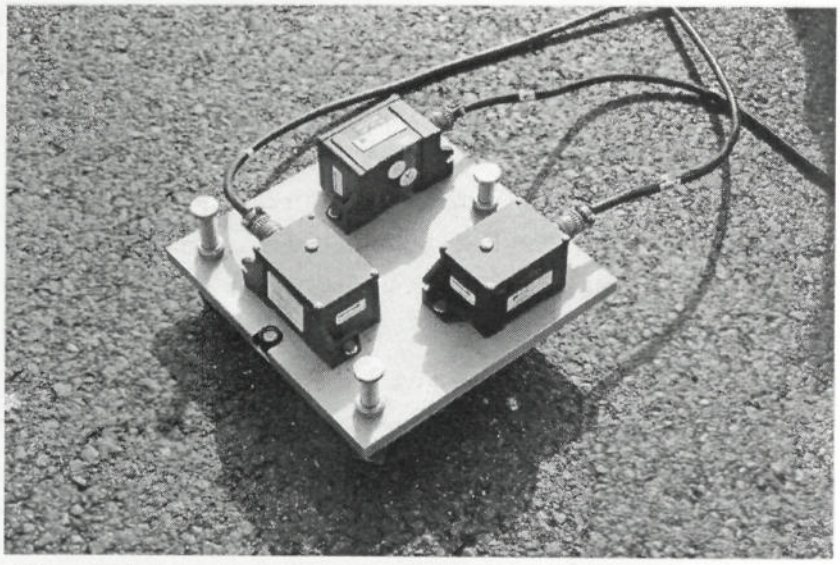


Figure 5.15. Triaxial mounting on a leveling plate of three units *KINEMETRICS* model *FBA-11*.

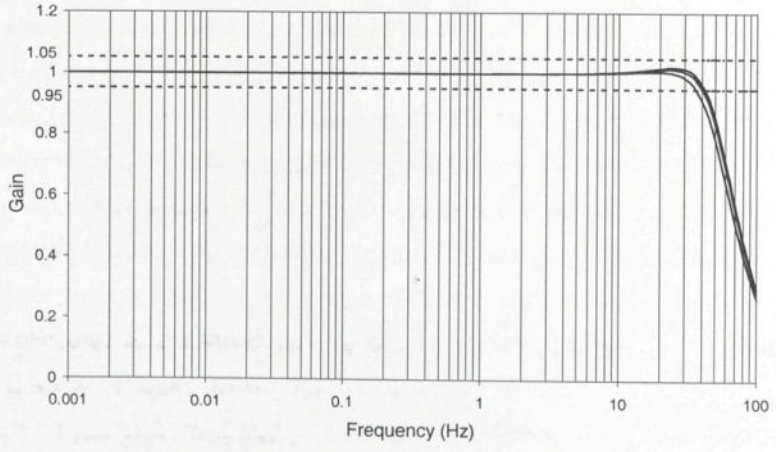


Figure 5.16. Gain of three standard *FBA-11* accelerometers.

It should also be noted that, although the *DC-10Hz* frequency range of operation covers most of the applications to large cable-supported bridges, it is normally of interest that accelerometers cover a wider range of frequencies and can be used in other stiffer structures. In this respect, it is of interest to refer the optional resonant frequency of *100Hz* for the *FBA-11* model, or even a more recent force balance sensor, the *EPISENSOR*, also from *KINEMETRICS*, which performs full scale recording in user selectable ranges varying from *±0.25g* to *±4g*, operating in the frequency range *DC* to *200Hz*, and having a dynamic range of *155dB* or more.

Strong Motion Accelerographs

Modern strong motion accelerographs are devices that incorporate a triaxial force-balance or piezoelectric accelerometer, as well as signal conditioning modules, data acquisition and

memory cards, allowing for an integrated signal acquisition with adequate filtering and pre-amplification. These devices are designed for the purpose of earthquake recording, and operate on the basis of a software programmable trigger. The possibility of synchronizing these accelerographs using either the GPS or simply the personal computer clock, and the fact that these devices need no cabling to a central data acquisition system, gives them an advantage over conventional measurement systems based on a set of transducers, each one connected to a conditioning unit, and then to a central data acquisition system using some kilometers of cable. In this respect, it is interesting to refer the tests performed by Rodrigues and Campos Costa (1998) on the Figueira da Foz Bridge (see Figures 2.76 and 2.77) and on the Arrábida Bridge, a reinforced concrete arch bridge at Porto, with a centre span of *225m*. The tests were performed on a very short time using six accelerographs *GEOSYS GSR-16*, which employed triaxial force-balance accelerometers with characteristics similar to the *FBA-11* (having however a lower dynamic range), and which had a *16-bit* digitizer. Accelerographs of the same type were used by the author in the tests of the Vasco da Gama Bridge (Delgado *et al.*, 1998), allowing the recording of the time histories at *58* locations (top and intermediate level sections of both towers included), using five units in as much as two and a half days. Figure 5.17 presents a view of one accelerograph during those tests. More recent devices enlarge the sensitivity, available memory, digitizing resolution and frequency range. This is the case of the *GEOSIG* model *GSR-18*, which uses a *18-bit* digitizer, or the *KINEMETRICS* model *ETNA*, with identical resolution, but employing a triaxial accelerometer *EPISENSOR*. The *GSR-18* weights *7.2kg*, while the *ETNA* weights *9kg* (including in both cases the battery and charger).

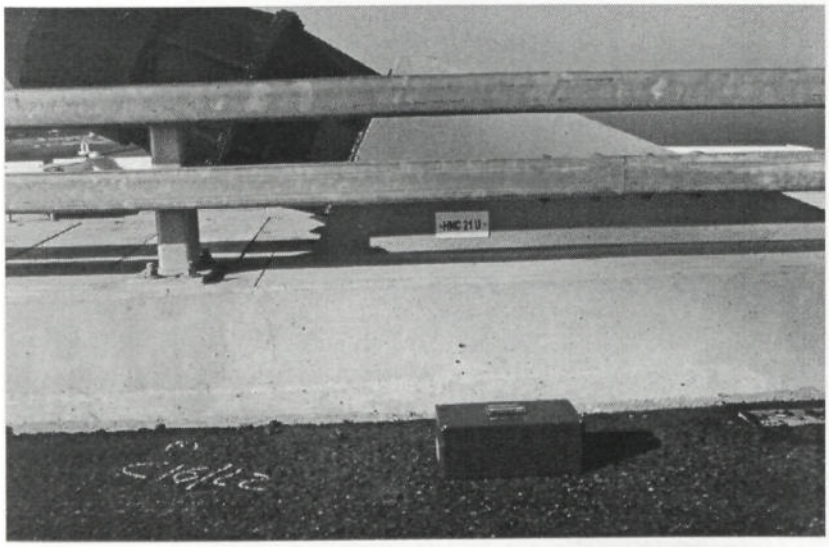


Figure 5.17. Strong ground motion accelerograph *GSR-16* used in ambient vibration tests at the Vasco da Gama Bridge.

When using strong ground motion accelerographs for ambient vibration tests, the amount of available memory of each accelerograph is a matter of interest, as a considerable

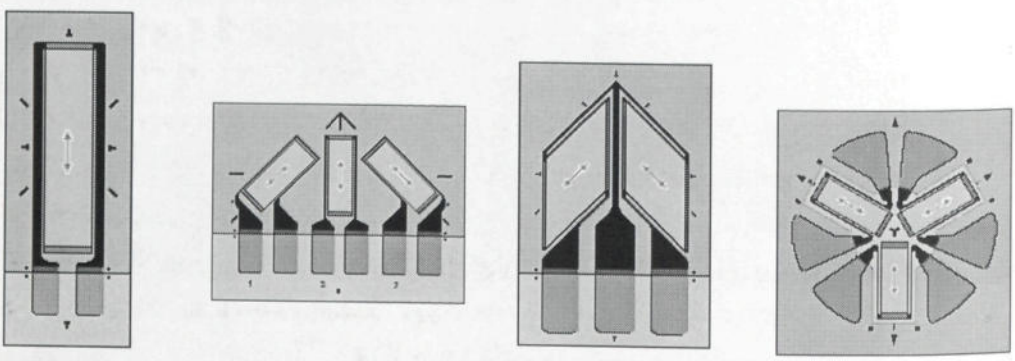
amount of time is needed to download data from each device to the computer. In the tests at the Vasco da Gama bridge, where *16minute* records were sampled at *50Hz*, only three records could be obtained at a time with the standard memory of *2Mb*.

In this respect, it is interesting to refer that the future trend in terms of data transmission will be certainly a complete suppression of electrical cables connecting the transducers to the data acquisition and processing system, communicating instead and transmitting data using modern technologies associated to the remarkable developments recently occurred in the area of mobile phones.

Strain transducers

Strain measurements provide a straight assessment of the stress state of structures and constitute thus one of the most suited transducers for characterizing the static and dynamic structural behaviour. The fact that the installation and operation of strain transducers requires particular care (in terms of mounting the transducers, executing adequate cabling connections and conditioning the signal) compared with the relative easiness of installation of other dynamic transducers above referred, has led in practice to almost exclusive use of strain sensors in static testing of structures. Note however that strain transducers are on the base of several types of dynamic sensors, like the piezoresistive accelerometers above referred, or load cells.

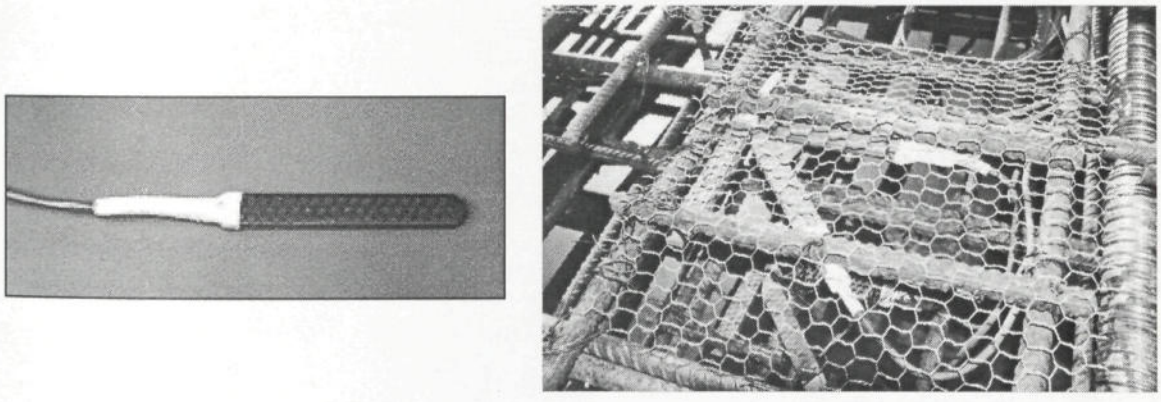
Strain transducers can be designed according to three main principles. The simplest are the well-known *resistance strain gauges*. These transducers are composed of a conducting element whose resistance changes when they are strained. The variation of resistance is proportional to the strain at the measuring surface through a constant, the *gauge factor*. A strain gauge of this type consists of a sensitive wire bonded onto an insulated backing sheet, which is cemented to the surface where the strain is to be measured. A wide range of configurations and sizes are available for different types of applications. Figure 5.18 shows some examples.



(a) (b) (c) (d)

Figure 5.18. Examples of resistance strain gauges: (a) Uniaxial; (b) Rectangular rosette; (c) Shear pattern; (d) Delta rosette (http://measurementsgroup.com).

A particular type of strain gauges has been designed for measuring the mechanical strain inside concrete structures. These are so-called *embedment strain gauges*, which are covered by a rugged outer body of proprietary polymer concrete that resists mechanical damage during concrete pouring and provides protection against corrosive attack. Figure 5.19(a) displays one sensor of this type, the *EGP* from *Measurements Group*. Figure 5.19(b) illustrates the mounting setup for a sensor of this type in the concrete.



(a) (b)

Figure 5.19 (a) Embedment strain gauge: EGP-5-120 (http://measurementsgroup.com);
(b) Mounting setup of a rosette for concrete embedment (Calçada *et al.*, 2000).

Another category of *embedment strain gauges* are those based on the *vibrating wire principle*. These transducers are constituted of steel tubes with flanges at the ends (see Figure 5.20(a)). Inside each tube there is a steel strip that is held in tension between the flanges and is plucked and set into vibration by a magnetic coil. Strain in the concrete is transferred through the flanges to the body and the steel strip, which changes tension and, consequently, its natural frequency, producing a frequency signal that is proportional to the strain.

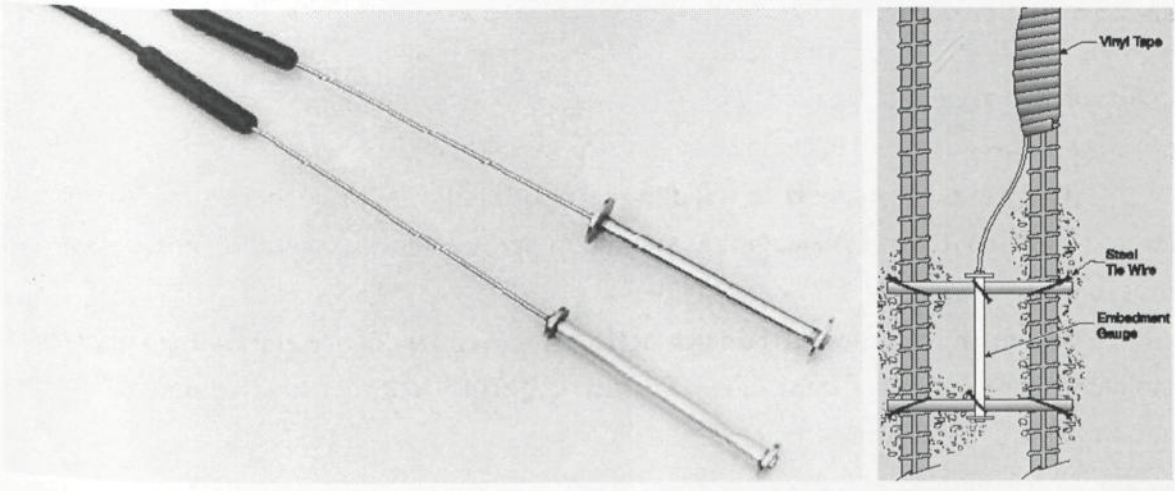


Figure 5.20. Example of embedment vibrating wire strain gage and mount setup
(http://www.slopeindicator.com).

The *piezoelectric strain sensors* constitute a third category of strain transducers. These sensors integrate a piezoelectric sensing element and provide high sensitivity and fast response measurements. Figure 5.21 represents the *PCB model* 740B02 Dynamic ICP *sensor*, which has a sensitivity of *50mV/μE ± 20%* and operates in the range *0.5Hz* to *100000Hz*.

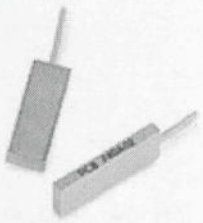


Figure 5.21. *Piezoelectric strain sensor PCB model 740B02.*

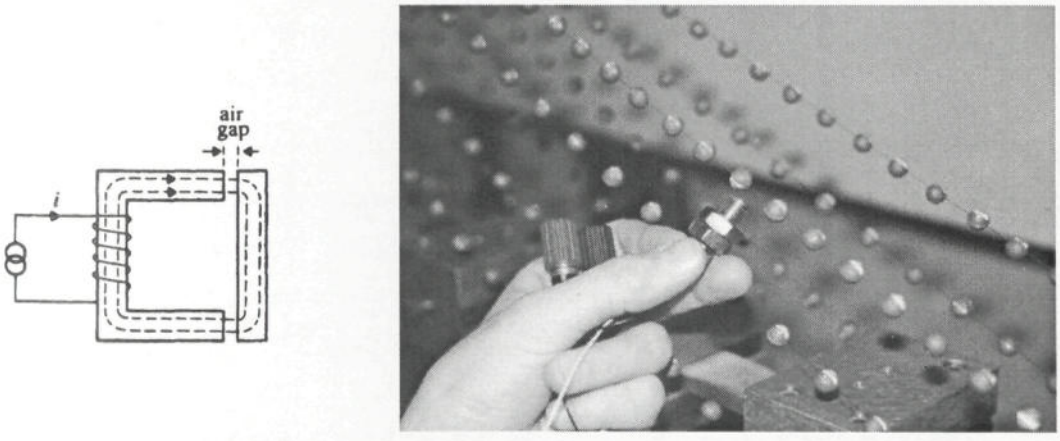
Non-contact motion transducers

Non-contact motion transducers are of interest for applications to small structures where (i) the mass of an attached sensor can modify the dynamic characteristics or else (ii) for large structures where absolute measurements are required or where the installation of instrumentation is difficult. The first issue does not constitute a problem in Civil Engineering applications, except for tests performed on physical models as the ones described in Chapters seven and eight of this work. For this particular case and, provided that the measuring surface is electrically conductive, magnetic pickups are of interest. These transducers are based on the inductive proximity principle whereby a variation of the air gap between the measuring surface and the transducer (due to structural vibration) changes the magnetic flux in the transducer, which is detected as a variation of inductance. Figure 5.22(a) illustrates this working principle, while Figure 5.22(b) represents the use of a magnetic transducer in the detection of the natural frequency of a wire (this wire actually represents a stay cable of the physical model described in Chapter seven).

The two other aspects referred in (ii) associated with the response measurement of large structures have constituted a motivation for the development of non-conventional measuring techniques.

A former reference in non-contact transducers for long distance measurement of structural motion is the measuring system designed and constructed at the National Laboratory of Civil Engineering (LNEC) for the measurement of displacements at the suspension bridge over the Tagus River (see Figure 2.75) during the 1960's. Figure 5.23 schematically illustrates the working principle of this system which was the following (Marecos et al., 1969): Spotlights were placed at the points of the structure that were to be measured (in

that case, two points at ¼ span, and two points at the midspan). These spotlights were low-tension lamps with a concentrated beam and a high efficiency near the infrared. Optical systems fitted with servo-controls were mounted on a fixed base (at the bridge tower, as represented in Figure 5.24). Each optical system was composed of an optical device and two motors that displaced this device along vertical and horizontal directions. The movements were then converted into an electrical signal that was recorded on magnetic tape recorder or directly plotted. According to Marecos and companion authors, this system was stable and was not disturbed by fog or other occasional obstructions, such as masts, being able to detect a minimum displacement of about *0.5cm*.



(a) (b)

Figure 5.22. Magnetic transducer: (a) inductive proximity principle (Heylen *et al.*, 1991); (b) scheme of measurement for detection of wire natural frequency.

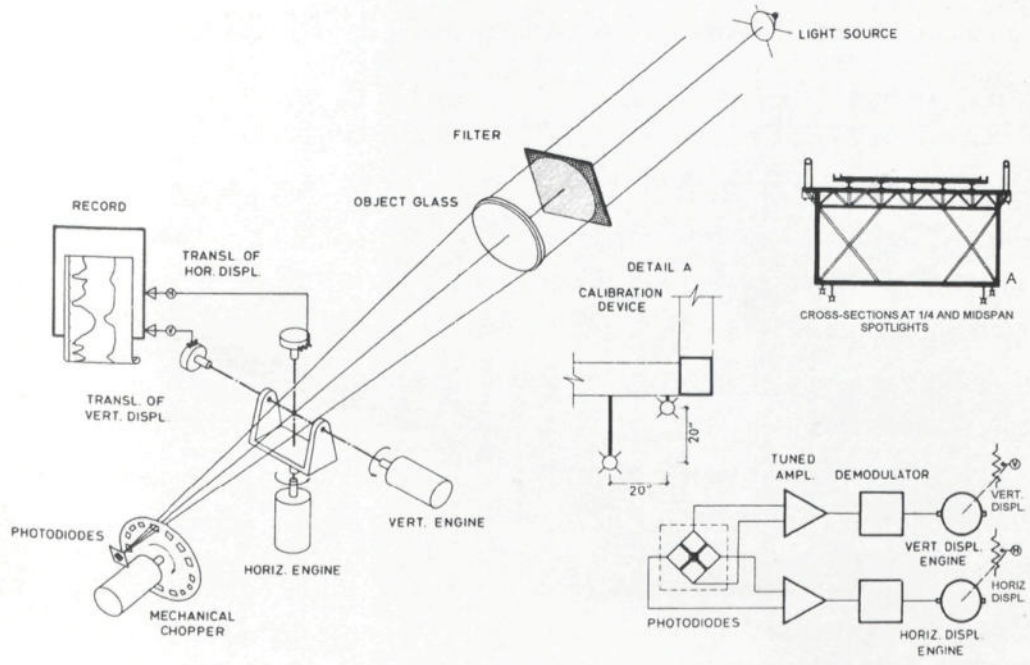


Figure 5.23. Automatic device for remote measurement of the displacements (Marecos *et al.*, 1969).

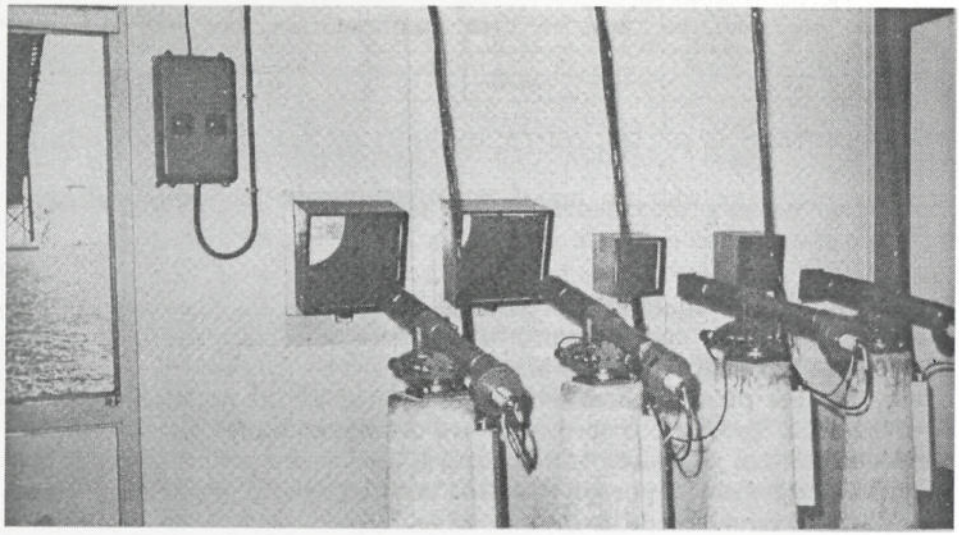
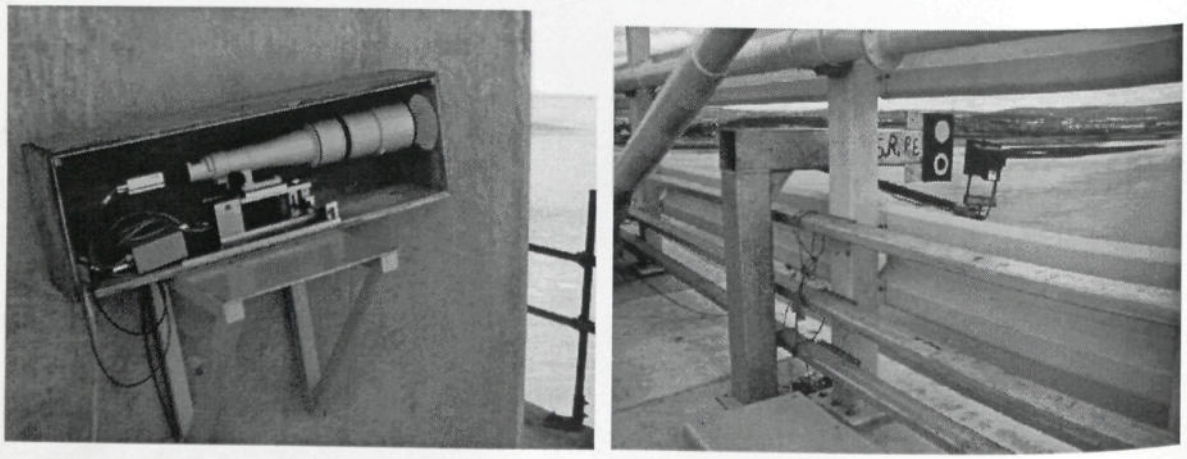


Figure 5.24. Optical systems in operation at the recording station on the Tagus Bridge (Marecos *et al.*, 1969).

A more recent and sophisticated device for remote measurement of displacements is the computer vision system of the University of Bristol (Stephen *et al.*, 1993; Macdonald *et al.*, 1997). The system was initially developed at ISMES and then improved and modified at the University of Bristol, the purpose being the development of a remote displacement sensor for assessing static displacements of large structures.

The computer vision system digitizes images from standard video cameras sighted on linear images of high contrast using image intensity thresholding software to determine the coordinates of targets at points of interest. Figure 5.25(a) shows a video camera mounted at the base of a pylon on the Second Severn Crossing cable-stayed bridge. The target represented in Figure 5.25(b) comprises simple circles of rings of reflective material on a black background.



(a) (b)

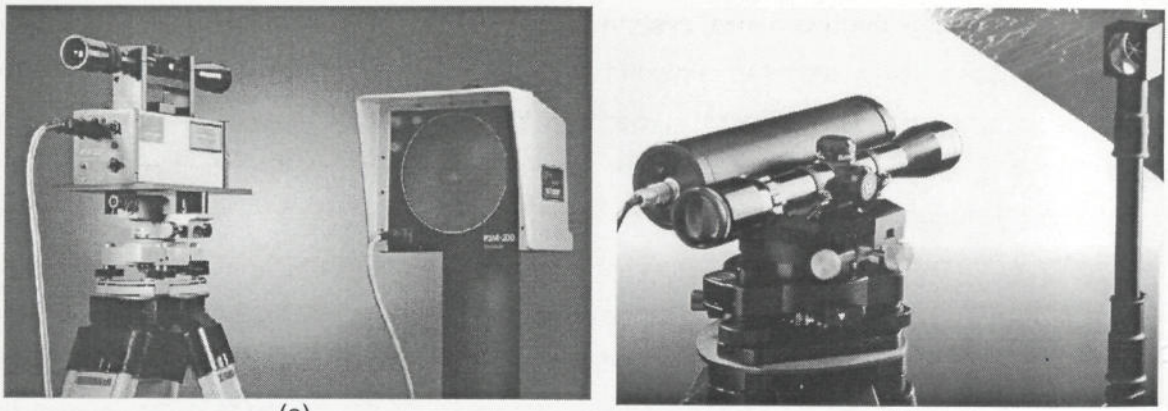
Figure 5.25. Computer vision system from the University of Bristol: (a) Camera mounted at the base of the pylon; (b) Target on the bridge deck. Courtesy of J. Macdonald.

According to Macdonald and companion authors (1997) a displacement measurement accuracy of *0.5mm* was achieved with this system at a distance over *200m*. The system incorporates other interesting features, such as the possibility of full synchronization with conventional measurement equipment and the possibility of sampling at a frequency of *12.5Hz*.

Laser systems constitute another category of devices that can be currently used for remote displacement measurements. The system developed and commercialized by NOPTEL is based on the two components represented in Figure 5.26(a), a laser diode transmitter, and a position-sensitive detector. The two elements are installed so that the laser beam forms a reference line from the transmitter to the centre of the receiving target area. When the receiver moves with the structure, the position of the laser beam on the optical target changes in correspondence. This position is continuously measured to PC or data logger.

According to the manufacturer, this optical system can be applied for remote measurements at a maximum practical operating distance of about *300m*, and can be affected by external interference, like background radiation, temperature, fog, rain, snow. For that reason, moderate weather conditions are desired for optimal results. The laser beam is eye safe (according to *EN60825*, corresponds to a *Laser Class 2*). The system provides fast measurements at a maximum sample rate of *500 samples/s* and has a resolution lower than *0.1mm* (that depends on the measurement distance). The maximum range of measurable displacements goes to *4m* for the standard receiver with a diameter of *200mm*. Examples of application of this measurement system are referred in (www.noptel.fi/nop_eng/ms_ap_a.html) and comprehend the dynamic tests of the Kemijoki Bridge, in Finland, an asymmetrical cable-stayed bridge with a main span of *125m*, performed in 1989, and more recently, in 1997, the tests on the Raippaluoto Bridge, a cable-stayed bridge with with a centre span of *250m*. Figure 5.27 illustrates the setup used for the Kemijoki Bridge, which employed two *PSM-100* instruments, the transmitters being installed at the base of the pylon, and the receivers on top of the tower and at about midspan on the deck.

Because in some cases an active receiver cannot be used, other type of optical devices are proposed by *NOPTEL*, like the model *PSM-R* (see Figure 5.26(b)). These devices are based on combined led transmitters and optoelectronic receivers that measure the movement of the reflector or prism attached to the target. Figure 5.28 illustrates the working principle, which is as follows: the operator directs the laser beam at the target and locks it in a steady position. The beam is reflected from the target back to the receiver, so that its position is evaluated, at a sample rate not greater than *100samples/s*. The *PSM-R* systems are meant for long distance measurements, in the range *0* to *600m*. In practice, however, the resolution of these devices increases with the distance and attains values of *30mm* for measurement distances of *600m* and distances longer than *100m* should be avoided (Resolution of *1mm* to *3mm* for *100m* operating distance, according to the manufacturer).



(a) (b)

Figure 5.26. *NOPTEL* laser system model: (a) *PSM-200;* (b) *PSM-R* for dynamic assessment of large structures at long distances (*NOPTEL*).

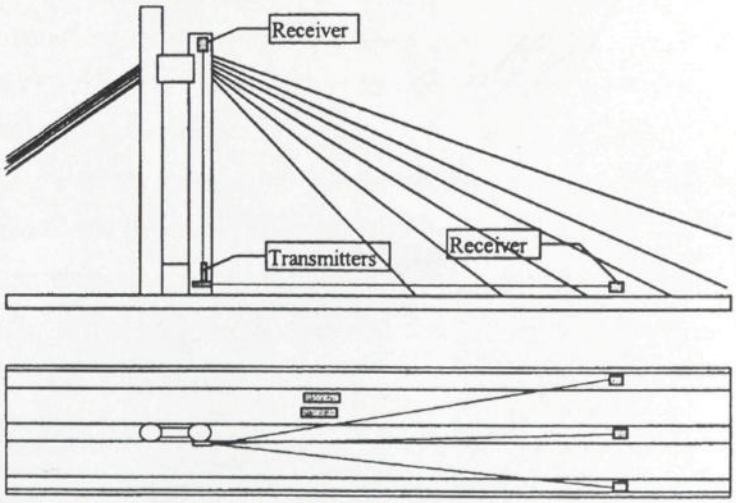


Figure 5.27. Installation of optical PSM-90 instruments on the Kemijoki cable-stayed bridge.

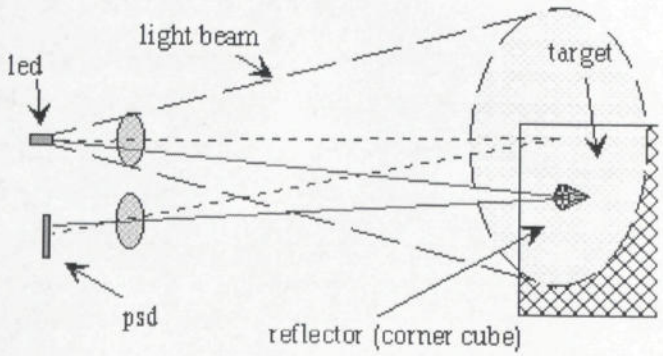
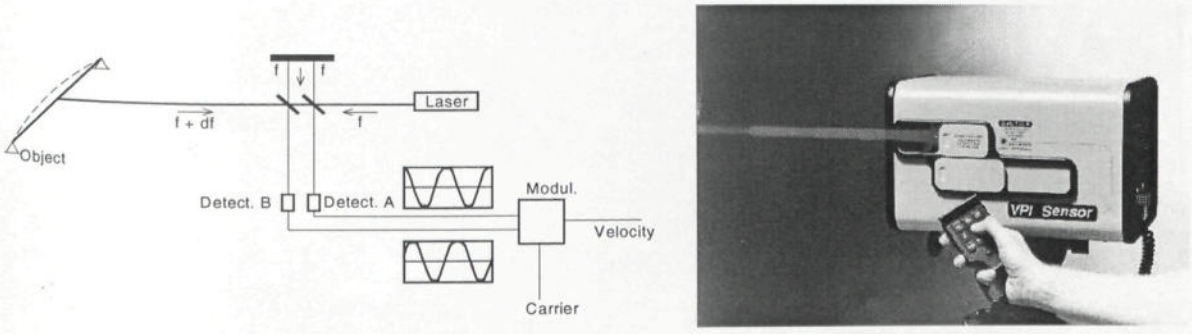


Figure 5.28. Principle of working of a PSM-R displacement sensor (http://noptel.fi/nop_eng/msp_pr1.htm).

Still regarding the two optical systems above described (based on direct or reflected analysis of a laser beam), a final note should be added that relates to the practical application of these systems. According to experienced users, these systems actually perform well for relatively low distance measurements as they are very much affected by light reflection and weather and light conditions. Another criticism respects the signal digitizing which still requires improvement.

Laser systems can still be employed for non-contact measuring of velocities. These sensors are also available commercially for different purposes. Reference is made here to the *OMETRON, VPI system A* vibrometer, which is an industrially engineered Doppler-based interferometer that has been employed at the Faculty of Engineering of Porto in the dynamic testing of some Civil Engineering structures. The basic principle behind the laser Doppler technique used is that when a beam of coherent light is reflected from a moving surface, its frequency changes according to the well-known Doppler effect. This change of frequency can be measured very accurately using optical interferometry in conjunction with electronic frequency measurement equipment, the velocity of the moving surface in the direction of the Laser beam being directly derived from the frequency changes. Figure 5.29 illustrates the working principle of a Laser interferometry system and shows an image of the *OMETRON VPI* sensor, whose main features are as follows: (i) measurement of relative velocities at maximum distances of about *200m*; (ii) possibility of operation in a wide frequency range (*DC to 300kHz*); (iii) three user selectable measuring ranges: low *0-10mm/s*, medium *0-100mm/s* and high *0-1000mm/s*; (iv) an optional built-in scanning beam positioning system with capability for multipoint measurements (this is of particular interest in the performance of forced vibration tests, as it allows for an almost instantaneous picture of vibrational modes of a structure, using a mesh with a maximum of *512x512 points)*.



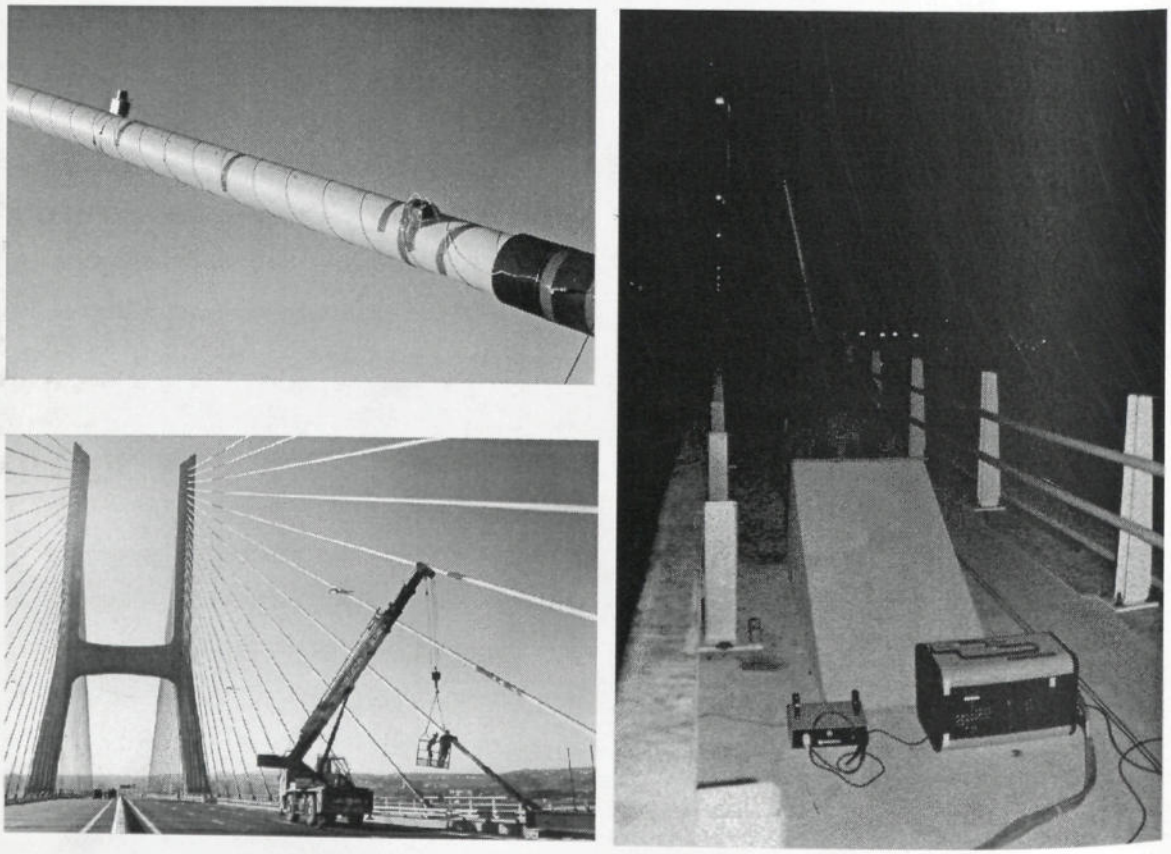
(a) (b)

Figure 5.29. Laser interferometry system (a) Scheme of velocity measurement (b) *OMETRON VPI* sensor (http://www.imageautomation.com/ometron/default.htm).

A few considerations should be made concerning the practical use of the *VPI* Laser system. First of all and, as other Laser systems, the *VPI* sensor is affected by weather and light conditions, as well as by the reflection characteristics of the measured surfaces (no

targets are required) and consequently the possibility of operation of distances of about *200m* referred by the manufacturer can give good results only in some particular conditions. Practical operation with the *VPI* sensor has shown however that provided that the measurement surfaces are relatively smooth and the level of vibration is not too low, a measurement accuracy similar to that of conventional accelerometers can be achieved.

The *VPI* sensor can meet a quite interesting application in the testing of cables from cable-stayed bridges. In effect, stay cables have in general metallic or polyethylene coatings, hence providing flat measurement surfaces, and have a vibration level that is superior to the deck and towers vibration, even for cables that apparently have no motion at all. On the other side, the installation of accelerometers at points sufficiently apart from the anchorages requires specific means of access which are not normally available after the bridge construction, while the use of a Laser sensor is quite straightforward. Figure 5.30 illustrates this point, showing the operation of mounting a conventional accelerometer on a stay cable, and the measurement of velocity vibration using the *VPI* sensor on the same location on the cable. Details of instrumentation and comparison of results will be presented in Section 5.5.



(a) (b)

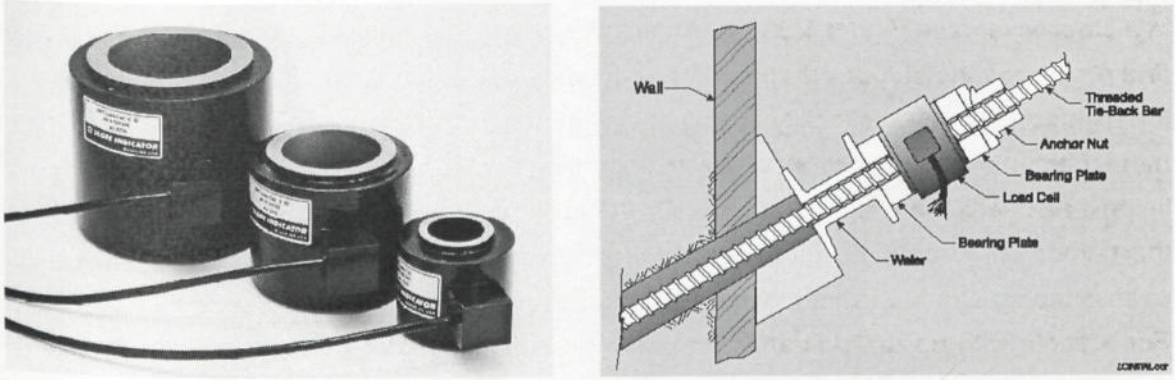
Figure 5.30. Dynamic tests on the stay cables at the Vasco da Gama Bridge: (a) Mounting of conventional accelerometer on a stay cable; (b) Use of *VPI* sensor for measurements at the same location on the cable.

Force transducers

One of the major motivations in the dynamic testing of stay cables is the assessment of the tension installed in these elements. The measurement of velocities or accelerations along the cables gives not only a measure of the level of cable vibrations, but also the possibility of indirectly determining that tension using the vibrating string theory, eventually complemented with specific corrections for the bending of the stay cable or for the sag-extensibility (Meharabi & Tabatabai, 1998).

Direct measurement of the tension variation on the stay cable is another possibility, through the use of load cells.

Conventional load cells are used for measuring loads on cables and rods in very different applications. The so-called *center-hole load cells* from *Slope Indicator* represented in Figure 5.31(a) are mounted at one of the cables' anchorages between two bearing plates (see the scheme of Figure 5.31(b)). The load-bearing element of these cells is a spool of heat-treated steel alloy. Evenly spaced around the periphery of the spool are bonded strain gauge rosettes in a number of at least four units, so that eccentricity effects are avoided. The rosettes are composed of two strain gauges, one for axial and the other for tangential strain measurement. A strong aluminum housing filled with a high-density resin protects the strain gauges from moisture and impact damage.



(a) (b)

Figure 5.31 (a) Example of center-hole load cell and; (b) Scheme of installation (http://www.slopeindicator.com/instruments/loadcell-bondedsg.html).

The standard load cells from *Slope Indicator* exist in inner diameters of *42mm* to *102mm* and have a capacity of *450kN* to *2700kN*. However other sizes and capacity cells are available in the market, which allow the measurement of the cable tension either strand by strand, or by ensemble of strands. Figure 5.32 shows the mounting of a load cell on a strand of a stay cable. This is part of the instrumentation plan of the Salgueiro Maia Bridge (Figure 2.90) which involves the Freyssinet (who supplied and installed load cells on sixteen of the stay cables), the University of Porto and the LNEC.

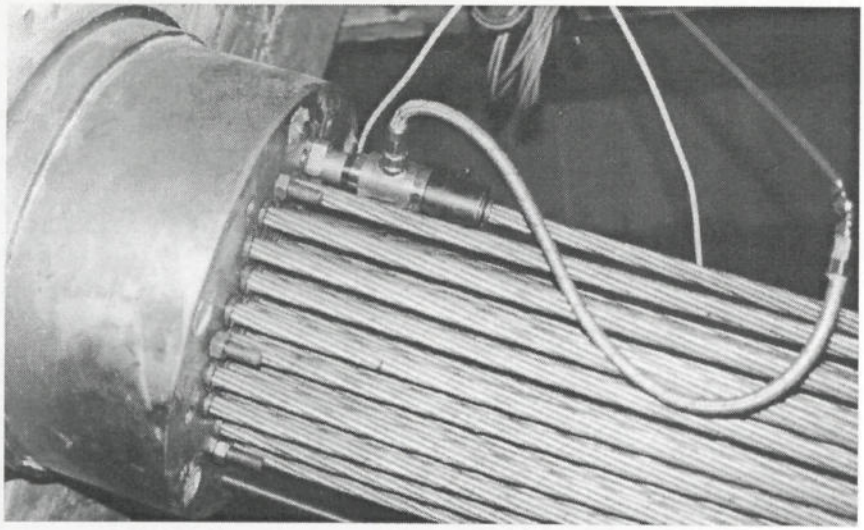
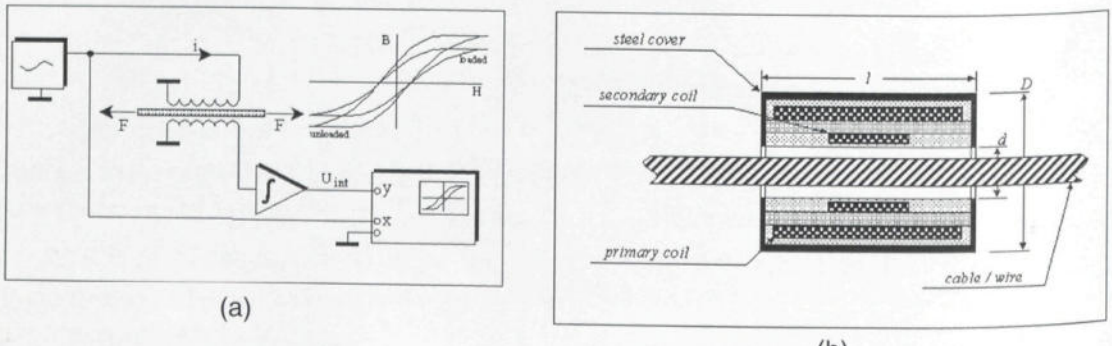


Figure 5.32. Installation of a load cell on a strand of one stay cable of the Salgueiro Maia Bridge.

A final reference is made to another system for measurement of forces and tensions in cables based on the magnetoelastic phenomenon, designated as *DYNAMAG* system (Jarosevic & Chandoga, 1994). This system has been developed at the Comenius University, at the Slovak Republic and is based on the principle represented in Figure 5.33(a), according to which the modification of the mechanical load (compression, tension, torsion and bending) leads to a modification of the magnetic hysteresis loop. The system employs two coils housed in a steel cover (see Figure 5.33(b)). An electronic device supplies the primary coil with current and processes the output voltage of the secondary coil. Interesting features of this system are the high accuracy and reliability specified by the manufacturer and the possibility of performing measurements through the steel cover, mounting the transducer at any instance. The main inconvenience is the weight and naturally the cost that these devices attain for large cables, if the purpose is to obtain a measure of the stress at the whole cable instead of the stress at each or some strands (a transducer for a *15.5mm* strand, for example, would weight *0.35kg*. For a cable with up to *70* strands, i.e., with an outer diameter of *225mm*, the sensor would reach *100kg*).



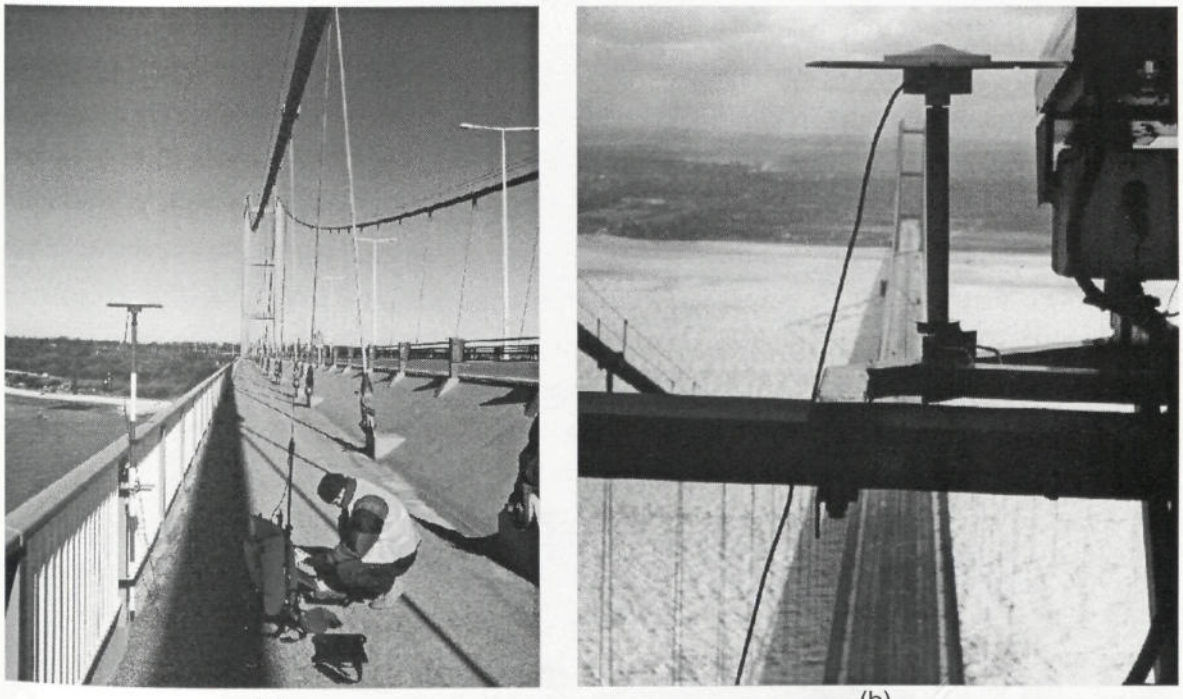
(a) (b)

Figure 5.33. The DYNAMAG system (a) Working principle; (b) Transducer components (http://dynamag.sk).

GPS measurement systems

The idea of employing the Global Positioning System (*GPS*) of navigation of satellites for real-time monitoring of large scale-structures has been used by Ashkenazi and Roberts (1997) in the instrumentation of the Humber Bridge, a suspension bridge in the UK with a main span of *1410m*. By installing two *GPS* receivers on the bridge (see Figure 5.34) and specific software, the authors collected a set of time records, which showed resolutions of *±1mm* and *±3mm* for horizontal and vertical motions, respectively.

In principle, this precision is not sufficient for performance of dynamic measurements of structures that undergo rather small displacements, like cable-stayed bridges. However, the technique reveals a large interest for the testing of suspension bridges.



(a) (b)

Figure 5.34. *GPS* monitoring equipment at the Humber Bridge: (a) *GPS* antenna at midpsan; (b) *GPS* antenna on top of one tower (Ashkenazi & Roberts, 1997).

Fiber optic transducers

Fiber optic transducers constitute possibly one of the most recent innovations in the Civil Engineering domain, which definitely have contributed to an effectiveness of the concept of *Smart Structure* previously referred. According to this concept, the structural behaviour would be measured through an array of optical fiber sensors which would allow the monitoring of different parameters that are critical for security (like deformations, temperatures and penetration of chemicals), playing the role of a nervous system.

At the current state-of-the-art different sensing systems have been developed at different investigation Centres which have been employed essentially in the performance of static measurements. An interesting characteristic of these systems is the widening of the conventional concept of point sensing to the point multiplexed, integrating or distributed configurations (Culshaw, 2000). The use of fiber optic sensing in dynamic measurements is currently under investigation and only a few experimental applications are known. This is the case of the dynamic load tests performed by Kim and Paik (1997) on a bridge in Korea, where the strain was measured on a steel girder at midspan using both conventional strain gauges and Fabry-Peyrot sensors for different velocities of passage of a loaded truck.

5.3.3 Measurement and analysis systems

The systems for data acquisition and analysis are required to perform three main tasks: (i) the recording of the electrical signals generated by the transducers (force and response); (ii) the processing of this information in order to obtain estimates of frequency and/or time responses; (iii) the derivation of modal parameters from the later estimates.

A wide variety of systems for data acquisition and analysis are available at present, which can be grouped into three main categories.

The first category comprehends the PC-based systems with plugged in acquisition boards and corresponds to the lowest level of sophistication, lowest cost and a relatively high flexibility.

An intermediate category corresponds to the use of a Fourier Analyzer or the combination of a Fourier Analyzer with a PC or workstation. In this case the Fourier Analyzer performs the tasks of acquisition and signal processing, the control of the data sampling and storage of data being performed by the PC, when existing. An important aspect to note concerning the use of Fourier Analyzers in ambient vibration testing is the memory limit associated with these devices. In effect Fourier Analyzers have been developed with the purpose of applying conventional Experimental Modal Analysis techniques for solving Mechanical Engineering problems, which typically involve high sampling frequencies and short acquisition times. On the contrary, Civil Engineering structures are characterized by low natural frequencies and their test requires rather long acquisition periods, which are not compatible with most Fourier Analyzer models. Some of these devices have however optional modules that allow direct sampling to a hard disk and so overcome this difficulty. But even with this option the on-line processing of signals is compromised and so full use of the analyzer capabilities is not possible.

The later category of systems for data acquisition and analysis comprehends powerful workstations provided with acquisition frontend modules. This solution is the most versatile in terms of memory, number of channels of measurement and signal conditioning. It is also the most expensive solution and it is essentially dedicated to the very large applications, that

involve a very significant number of measurement channels (for example in aeronautic applications).

The current Section describes the main features of the *KINEMETRICS* model *VSS-3000* Vibration survey system, a recent data acquisition and analysis system that has been developed for ambient and forced vibration tests of Civil Engineering structures. Note that this system, that is being used at FEUP, is not the only one available in the market or even the better solution for performance of this type of tests. Its main features can however be used to emphasize the characteristics that should be required in terms of acquisition and signal processing in a measuring system dedicated to the performance of tests on large Civil Engineering structures.

The *VSS-3000* is a system that belongs to the first category above referred, although being supplied with analysis software that performs a series of signal processing functions that are typical of a Fourier Analyzer. The system actually comprehends a laptop computer, an acquisition board and an interface panel for connecting up to *16* transducers. This panel together with the PC, the acquisition board and two *6V DC* batteries for powering the transducers (for example the *FBA* accelerometers above referred) are housed in an aluminum box (see Figure 5.35).



Figure 5.35. The KINEMETRICS model VSS-3000 Vibration Survey System (http://www.kinemetrics.com/vss3000.html).

The main features of the *VSS-3000* are as follows:

- The data acquisition board has a *16-bit A/D* converter and a speed of conversion of *100kHz*, allowing for a maximum sampling rate of *1000Hz* for the set of *16* transducers. The allowed voltage range is the common *0* to *10V*, or *±5V and gains of 1, 2, 4 or 8* can be programmed;
- The system does not include any analogue amplifiers or filters. So, in order to avoid *aliasing* errors, it is recommended that preliminary tests are performed with a high sampling frequency, say *1000Hz*, so that the frequency content of the measured signal is determined. The signal should then be sampled at four times

the maximum frequency and, if required, digitally filtered (lowpass and highpass) and decimated to a narrower band of interest (available digital filters are of Bessel, Butterworth and Chebyshev types);

- The signal acquisition and processing is performed through software from the laptop computer. This software runs under Windows-95 operating system and allows for the definition of the acquisition parameters (sampling frequency, gain, size of records), as well as for the operation over the signals and graphical representation. Basically, all the operations performed by conventional Fourier Analyzers are available, which include mathematical functions (from fundamental arithmetics to integral and differential calculus), statistics, digital filters of the types above referred, frequency analysis including windowing of different types (Bartlet, Hamming, Hanning, Cosine taper, Blackman, Blackman-Harris, Tukey, Poisson, Hanning-Poissson, Cauchy and Gauss), signal generators and scopes for graphic display of the results;
- The possibility of performing continuous data transfer from the data acquisition device to the PC hard disk while performing real-time on-screen display of the signal is one of the most remarkable characteristics of the *VSS-3000* system. This allows, on the one hand, that long records are stored and, on the other hand, the on-line processing for a quick analysis of the data on site.

As a final note, it is worth mentioning the availability of interesting modules for signal processing based on *MATLAB* or *LABVIEW* software that can be integrated in a self-created environment for acquisition and processing, when complemented with an acquisition board and corresponding software supplied by the manufacturer. This environment may inclusively integrate a module for system identification, another toolbox from *MATLAB*, which allows for a straight identification of modal parameters from the recorded signals. This task is not performed by the *VSS-3000* system, requiring the use of dedicated software.

5.4 SYSTEM IDENTIFICATION TECHNIQUES

5.4.1 General

The last step in the structural dynamic testing corresponds to the processing of the measured data in order to extract the most relevant dynamic properties of the structure. This is known as the *System Identification Problem.*

In effect, assuming that the structure is linear and time invariant, the characterization of any two of the blocks represented in Figure 5.36(a) yields information on the properties of the third block. The most straightforward problem is designated as the *Analysis* or *Direct Problem* and consists in the calculation of the structural response based on the known input and structural system properties (see Figure 5.36(b.1)). The *Inverse Problem* is less common

and consists in determining the input based on the known response and structural properties (see Figure 5.36(b.2)). Finally, the *System Identification (SI) Problem* requires the knowledge of the input and structural response (see Figure 5.36(b.3)). These are characterized by time series of specific quantities, like forces, strains, accelerations, velocities or displacements.

SI techniques were born in the context of Mechanical Engineering in the decade of *50* (Curtis, 1980) and received a major impulse with the advent of the *Fast Fourier Transform* (*FFT*) algorithm (Cooley & Tuckey, 1965), that led to the development of the *Theory of Digital Signal Processing* and to the appearance of *Fourier Analyzers*.

The combination of these tools with powerful computers has contributed to the development of a wide range of identification methods during the last decades. The particular application of these techniques to Civil Engineering Structures only took place during the 1970's. Some of the first known applications to large structures are due to Crawford and Ward (1964), McLamore *et al.* (1971), Trifunac, (1972), Hart and Yao (1977), Abdel-Ghaffar and Housner (1978), Beck and Jennings (1980) and Abdel-Ghaffar and Scanlan (1985ab).

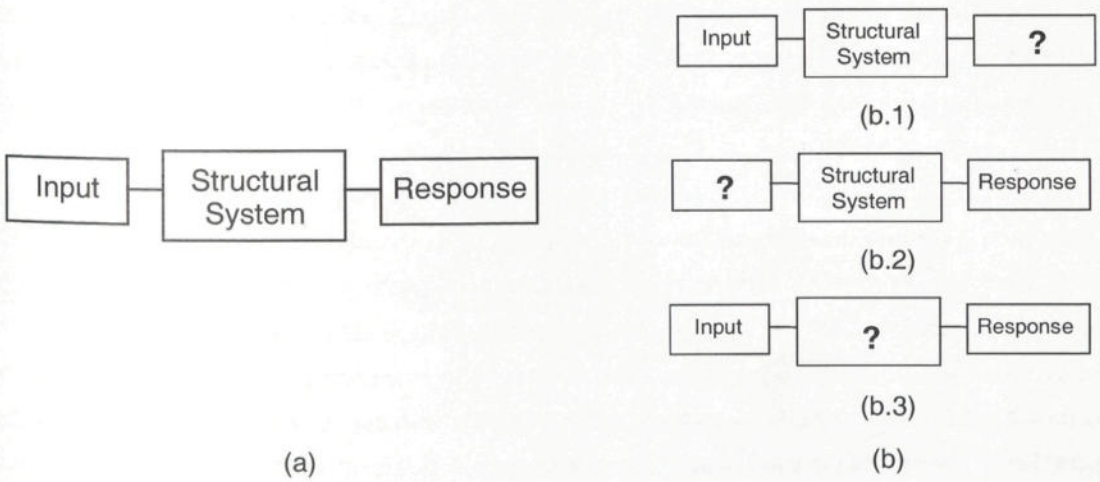


Figure 5.36 (a) General formulation of a dynamic system (b) Possible problems: (b.1) The *Direct Problem*; (b.2) The *Inverse Problem*; (b.3) The *System Identification Problem*.

The numerous available *SI* methods can be classified according to different criteria. For the purpose of *SI* on Civil Engineering structures, it is relevant the division in two main categories, which correspond to (i) the classical *SI* techniques, based on measured input and output on the analyzed system, and (ii) the so-called *Output-Only SI* techniques.

The former category comprehends most of the techniques developed in the Mechanical Engineering domain, that assume that the system excitation is controlled. Although significant developments are still in progress in this particular topic, it can be considered that a mature state of technique has already been reached, which allowed the implementation of some of the most powerful identification algorithms in commercial software packages. This is the case for example of the *CADA* software from LMS (LMS CADA-PC, 1992).

The *Output-Only SI* methods are exclusively based on the measured response of the structural system, naturally requiring some assumptions concerning the external excitation. Although these techniques have also been used in the context of Mechanical Engineering and

Aeronautics, they are of utmost importance in Civil Engineering applications, considering the difficulty in applying an excitation to a large structure within an acceptable level (greater than ambient excitation's).

One of the former applications of the concept of output-only identification is due to Crawford and Ward (1964), who developed a procedure based on the concept of the power spectral density function for the identification of dynamic parameters in building structures. The methodology was explored by Bendat and Piersol (1966), who established the conditions of validity, and has been employed widely in Civil Engineering applications ever since. In this context, reference should be made to the research of Felber (1993), that systematized the technique using specific spectral and coherence functions. Recognizing some limitations in the method, particularly in the estimation of modal damping coefficients, other *SI* methods were developed and applied, but once more mostly in the Mechanical Engineering and Aeronautics domain. This is the case of a time domain technique developed by Cole (1968) at NASA with the purpose of identifying the dynamic characteristics and detecting damage in space structures subjected to ambient loads, the *Random Decrement Technique.* It is interesting to refer that applications of the *Random Decrement Technique* or other time or frequency domain techniques to large Civil Engineering structures only deserved attention during the last few years (Brincker *et al.*, 1990; De Roeck et al., 1995; Andersen, 1997; Asmussen, 1997; Peeters *et al.*, 1999).

Considering the two main *SI* groups of methods above referred, the current Section starts presenting a classification and brief description of the most well-known and widely used *SI* techniques for *Forced Vibration Tests* of Civil Engineering structures, which will be employed in Chapter 7, in the analysis of the Jindo Bridge physical model. These will be designated as *Input-Output* identification techniques. More emphasis will be put however on the topic of *Output-Only* identification techniques, used in the processing of data from *Ambient Vibration Tests*, considering the recently developed methods and relatively limited application in practical cases. In this context, the traditional power spectrum based technique will be described, as well as the main principles of two methods that are presently considered to be among the most efficient for Civil Engineering applications: the *Frequency Domain Decomposition* (*FDD*) and the *Stochastic Subspace Identification* (*SSI*) methods.

5.4.2 Input-Output identification methods

The application of classical *Input-Output Identification methods* involves the simultaneous measurement of the system excitation and response time histories. From the collection of time histories, a set of functions can be estimated either in the frequency, or in the time domain, the *Frequency Response Functions* (*FRF*s) and *Impulse Response Functions* (*IRF*s), respectively. These functions are characteristic of the structural system under analysis, i.e., they are independent of the type and level of excitation (provided that the structure has been excited in

all the frequency range of interest and behaves linearly), and are used in the extraction of system parameters.

The different available *SI* methods based on *FRF* or *IRF* measurements employ different formulations or optimization procedures, and different levels of simplification. In order to have an overview of the possibilities, a general classification of *SI* techniques is presented, which comprehends the following criteria: (i) domain of application; (ii) type of formulation; (iii) number of degrees of freedom; (iv) type of estimates; (v) number of inputs.

Domain of application

This criterion classifies the *SI* methods according to their domain of application. In general, frequency domain methods employ *FRF* estimates, while time domain methods apply to *IRF* estimates.

The former *SI* techniques were developed in the frequency domain, which in general provides a more intuitive understanding of the fitting procedure and errors. Frequency domain techniques have however a few disadvantages, which are associated with the frequency resolution. In effect, the discrete and finite character of time records is responsible for the limited frequency resolution of *FRF* estimates, originating leakage errors. These errors can be limited provided that higher frequency resolutions are employed, what basically means sampling longer time series. This may be a limitation in very flexible structures, which are characterized by very low natural frequencies, requiring hence that very long time series are sampled (note that the *FRF* or *IRF* estimates are obtained averaging over a number of records, in order to reduce the noise effect). If, in addition, mode shapes are very closely spaced in frequency, the required resolution is increased and frequency domain methods may be no longer efficient.

According to Maia and Ewins (1989), frequency domain methods produce best results when applied to systems where the number of modes to identify is relatively limited, the corresponding frequency range being relatively narrow. On the contrary, time domain methods are considered of interest for systems whose natural frequencies are distributed in a wide frequency range and where the number of modes of interest is significant. When compared with frequency domain methods, time domain *SI* techniques have a major inconvenience that relates to the impossibility of taking into consideration the residual contribution of mode shapes that lie outside the frequency band of interest.

Taking into account these considerations and the nature of Civil Engineering problems, the author tends to conclude that for most structures, like buildings, slabs, dams and medium size bridges, frequency domain methods would produce the best results. For large cable supported bridges, characterized by a very significant number of mode shapes in a relatively narrow frequency range, it is not so clear whether one or the other type of method yields better results.

Type of formulation

The *SI* methods can be established according to two different types of formulations. These are the *Direct* and *Indirect* (*Modal*) formulations.

Direct SI methods operate directly on the differential dynamic equilibrium equations, providing estimates of the constant coefficients of those equations. These methods can be formulated in both the time and frequency domain, approaching for the former case the second order differential equations by difference equations that incorporate the input and output time values, while for the last case the input-output relationships are established in the form of ratios between polynomials (Leuridan *et al.*, 1991).

Some of the *Direct SI* methods are based on the formulation of the dynamic equilibrium equations using a state space approach. Once more the problem can be formulated in both the time and frequency domains. Frequency domain formulations are in general fitting algorithms that yield dynamic parameters of the system model, namely natural frequencies, modal shapes and damping coefficients. The fact that modal shapes are complex makes these formulations more general. On the other side, time domain state space formulations using modern numerical techniques, like the projection in subspaces and *Singular Value Decomposition* (*SVD*) may or may not employ specific models of the system. The algorithms based on these formulations are considered to be quite powerful and also time consuming, and can be applied both to the classic input-output data problem, or simply to output-only data (see Section 5.4.3).

Direct formulations constitute the most general methods of identification, in the sense that no specific simplifications are introduced in order to uncouple the differential dynamic equilibrium equations.

On the contrary, *Modal* formulations are based on modal descriptions of the structural system. These formulations assume the validity of certain assumptions, namely the linearity of the system, and the orthogonal property of the mode shapes not only with respect to the mass $\boldsymbol{M}$ and stiffness $\boldsymbol{K}$, but also with respect to the damping $\boldsymbol{C}$ matrix, which is considered proportional with regard to the stiffness and mass matrices ($\boldsymbol{C} = \alpha \boldsymbol{M} + \beta \boldsymbol{K}$).

Modal formulations start to apply coordinate transformations in order to transform the coupled second order differential equations into sets of uncoupled differential equations that are expressed in terms of the well-known modal parameters of the system (natural frequencies, mode shapes and modal damping coefficients). The theoretical *FRF*s and/or *IRF*s (in frequency or time domain formulations, respectively) can be then expressed as functions of the modal parameters, the later being estimated from a fitting to the measured data using specific algorithms. A wide range of fitting algorithms have been developed, in such a way that *Experimental Modal Analysis* has constituted a domain of research. In this respect, it is relevant to refer two major publications in the topic, the book from Ewins (1984), that constitutes one of the former and most well-known references in the domain, and a recent book from Maia and Silva (1997) that presents an updated state-of-the-art of the most powerful *SI* techniques in the context of Mechanical Engineering applications.

Number of degrees of freedom

This criterion applies only to modal formulations in the frequency domain, which have the remarkable property of uncoupling the structural response in modal contributions, allowing for the consideration of only a few of them in the curve-fitting algorithm.

In effect, and assuming that the damping coefficients are small and the mode shapes are well-spaced in frequency, a valid simplifying assumption is that in the vicinity of a resonance (a structural natural frequency) the structural response is dominated by the corresponding mode shape. The fitting algorithms will consist then in adjusting a function that depends on one only natural frequency and damping coefficient to the measured data in a narrow frequency range. These algorithms are designated as *Single-Degree-Of-Freedom* (*SDOF*) algorithms, providing a simple and quick means of assessing the most dominant modal contributes to the structural response. On the contrary, *Multi-Degree-Of-Freedom* algorithms (*MDOF*) consider the simultaneous contribution of several mode shapes, allowing for the identification of closely spaced mode shapes. These methods are obviously more powerful and also more time consuming and will have to be inevitably employed in almost every Civil Engineering application, either in simplified versions, or in more complex formulations.

Type of estimates

Once more this criterion applies only to frequency domain modal formulations and has to do with the procedure adopted in the extraction of the mode shapes, which can be based either on the separate fitting of each *FRF*, or on the fitting at a time of the ensemble of *FRF*s.

The first procedure yields the so-called *local* estimates, which are sets of natural frequencies, damping factors and modal constants for each *FRF*. The presence of noise and errors in the curve fitting leads to variations in the estimates of natural frequencies and damping factors and so these parameters will have to be averaged over the set of *FRF*s, eventually weighted by the coherence function estimates (these functions measure the level of correlation between the input and output).

Global methods yield estimates of natural frequencies and damping coefficients that are representative of the set of *FRF*s under analysis. Because the contribution of some mode shapes is residual for particular *FRF*s, the signal-to-noise ratio in the vicinity of the corresponding natural frequency may be very low, leading to errors in the estimates. So, the fitting algorithm should weight equally the *FRF* estimates according to the coherence functions that are associated.

It is the author's opinion that in general best results are obtained from *local* rather than from *global* estimates, as the visual inspection of the quality of each separate fitting allows for the rejection of particular estimates, allowing for a better control of the fitting procedure.

Number of inputs/outputs

In the process of application of an excitation to the structural system in order to mobilize its dynamic behaviour, dynamic forces can be applied at one or more points, simultaneously or not.

The objective of simultaneous *Multi-Input* excitation is obviously the achievement of an appropriate distribution of the applied energy throughout the whole structure, in such a way that the highest number of modal contributions are induced and measured. The demands in terms of equipment and possible synchronization difficulties make this type of tests less common than *Single-Input* excitation methods. However, as single point excitation may not induce all the modes of interest, different input locations can be selected and single point tests performed at different times. The measured responses, which for *Multi-Input* tests comprehend generally a number of locations, may then be treated simultaneously or not, the first case leading to the so-called *Multi-Input-Multi-Output* (*MIMO*) identification algorithms, and the later to the *Single-Input-Multi-Output* (*SIMO*) algorithms. The simplest algorithms are those that apply to *Single-Input* tests and to one location only of the measured response, being designated as *Single-Input-Single-Output* (*SISO*) algorithms.

General classification of SI methods

Based on the above described criteria, a general classification of input-output SI methods can be presented, which is schematically represented by Figure 5.37.

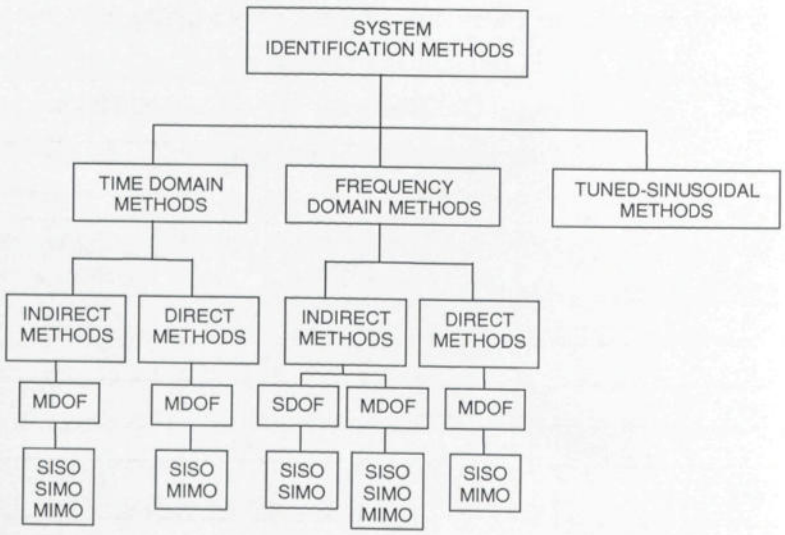


Figure 5.37. Classification of input-output system identification methods (Maia & Silva, 1997).

This classification comprehends two major groups of algorithms, one that respects to *time domain* methods, and the other referring to *frequency domain* methods. A third group is designated by Maia and Silva (1997) as the *tuned-sinusoidal force* methods, corresponding to the particular type of tests that are based on the application of a sinusoidal force at successive

natural frequencies close to the structural resonances, and measurement of the sinusoidal response at several locations. The tests performed with eccentric mass shakers in Civil Engineering applications are typical examples of *tuned-sinusoidal force* tests. Although the input and output are measured for each excitation frequency, the *FRF* estimates are obtained point by point in a quite lengthy process and not at once from the ratio between output and input spectral measurements. In principle, once the *FRF* estimates are obtained, any frequency or time domain algorithm of the other two groups can be applied. It should be noted however that, in this case, certain particularities of the problem may prevent a straightforward application of those algorithms. One aspect is for example the definition of *FRF* estimates in only certain ranges of frequency (and not at all the frequency lines of the range of interest). Another issue is the unequal frequency spacing between successive *FRF* point estimates (a closer spacing is ususally adopted near the resonance frequencies). Finally, it is not always possible to measure the phase components of the *FRF*'s. This topic has been discussed by the author (Caetano, 1992), who implemented and applied *SI* algorithms for this particular situation.

Going back to Figure 5.37, *Direct* or *Indirect* (*Modal*) formulations can be employed in both the time and frequency domain algorithms. Indirect formulations in the frequency domain can then employ simplifying assumptions for the description of the *FRF*s, leading to the *SDOF* methods, while the other formulations generally employ *MDOF* algorithms. All these algorithms are then classified according to the number of input and output locations in which they are based, ranging from the simplest *SISO* methods to the more complex *MIMO SI* methods.

Table 5.1 presents some of the most widely used *SI* algorithms and corresponding characteristics, some of which will be briefly revised in the text, based on the book of Maia and Silva (1997) and on a previous survey by the author (Caetano, 1992).

Table 5.1. Classification of some *SI* algorithms.

	Method	Type of formulation	SDOF or MDOF	Type of estimates	Number of inputs/outputs
Frequency domain	Peak Peaking	Modal	SDOF	LOCAL	SISO
	Circle-Fit				
	Inverse				
	Dobson				SISO/SIMO
	Nonlinear LSFD		MDOF	LOCAL GLOBAL	SIMO MIMO
	Orthogonal Polynomials				
Tuned-sinusoid	Mau		SDOF	LOCAL	SISO
	Asher's		MDOF	GLOBAL	MIMO
Time domain	Complex Exponential		SDOF	LOCAL	SISO
	LSCE		MDOF	GLOBAL	SIMO/MIMO
	Ibrahim				MIMO
	ERA				
	ARMA	Direct			

A common characteristic of these methods is the use of least-squares techniques for minimizing an error function. It is important however to refer that some direct *SI* techniques employ other methods, namely the *Instrumental Variable* and the *Maximum Likelihood* methods. These are however out of the scope of this work.

5.4.2.1 Frequency domain methods

The frequency domain methods presented in Table 5.1 are all based on modal formulations, hence on the application of fitting algorithms to measured *FRF*s. It is then necessary first to express the theoretical *FRF*s as functions of the modal parameters, then define the process of measuring these functions and finally to distinguish the different *SI* methods according to the directions followed in the extraction of modal parameters.

Theoretical definition of an FRF

The *Frequency Response Function* $H_{ij}(\omega)$ is defined as a function of two specific locations *i* and *j*, the first index *i* referring to the location where the response is to be calculated, while the second index *j* refers to the location where the excitation is applied. $H_{ij}(\omega)$ is then obtained as the ratio between the Fourier spectrum of the response $X_i(\omega)$ at location *i*, and the Fourier spectrum of the applied excitation at location *j*, $F_j(\omega)$

$$H_{ij}(\omega)=\frac{X_i(\omega)}{F_j(\omega)} \tag{5.2}$$

As the response can be expressed in terms of displacements, velocities and accelerations, the *FRF* can assume three different forms, which are designated as *Receptance* $\alpha_{ij}(\omega)$, *Mobility* $Y_{ij}(\omega)$ and *Accelerance* $A_{ij}(\omega)$ (or *Inertance*), respectively, and are related through the following equations

$$Y_{ij}(\omega)=i\omega\alpha_{ij}(\omega) \tag{5.3a}$$

$$A_{ij}(\omega)=-\omega^2\alpha_{ij}(\omega) \tag{5.3b}$$

where $i^2=-1$.

Formulating the dynamic equilibrium problem as a state-space problem and assuming that the modal shapes are orthogonal with respect to the damping matrix, the *Receptance* $\alpha_{ij}(\omega)$ of a linear viscously damped system can be expressed by

$$\alpha_{ij}(\omega)=\sum_{r=1}^{r=N}\left(\frac{{}_rA_{ij}}{\omega_r\xi_r+i\left(\omega-\omega_r\sqrt{1-\xi_r^2}\right)}+\frac{{}_rA_{ij}^*}{\omega_r\xi_r+i\left(\omega+\omega_r\sqrt{1-\xi_r^2}\right)}\right) \tag{5.4}$$

where N is the total number of mode shapes, ω_r and ξ_r are the angular natural frequency and damping coefficient, respectively, associated with mode r, and ${}_rA_{ij}$ are the residues associated with the same mode shape, which are defined as functions of the i_{th} and j_{th} modal components, ϕ_{ir} and ϕ_{jr} respectively, according to

$$ {}_rA_{ij} = \phi_{ir} \cdot \phi_{jr} \tag{5.5} $$

Note that the symbol " * " denotes "complex conjugate of", and the mode shapes $\boldsymbol{\varphi}_r$ are complex, so the quantities ${}_rA_{ij}^*$ are given by

$$ {}_rA_{ij}^* = \phi_{ir}^* \cdot \phi_{jr}^* \tag{5.6} $$

Measurement of FRF functions

Given the measured time histories $x_i(t)$ and $f_j(t)$of the response and excitation on a structural system, respectively, the function $H_{ij}(\omega)$ can in principle be obtained directly from the application of equation (5.2), by application of a Fourier Transform to the time series.

Other possibilities for the evaluation of $H_{ij}(\omega)$ are based on the stochastic input-output relations in terms of the cross-spectral density functions between the input and output, $S_{ij}(\omega)$, and the power spectral density functions of the input or the response, $S_{jj}(\omega)$ and $S_{ii}(\omega)$, respectively, leading to the following equations

$$ \left|H_{ij}(\omega)\right|^2 = \frac{S_{ii}(\omega)}{S_{jj}(\omega)} \tag{5.7} $$

$$ H_{ij}(\omega) = \frac{S_{ij}(\omega)}{S_{jj}(\omega)} \tag{5.8} $$

A first aspect should be pointed here, which has to do with the discrete character of the measurements. So, in practice the functions indicated in equations (5.2), (5.7) and (5.8) can only be estimated at discrete frequency values ω_k with a spacing $\Delta\omega$ defined as a function of the sampling frequency f_S and of the size of the time series (n samples) by

$$ \Delta\omega = \frac{2\pi}{n f_S} \tag{5.9} $$

leading to the following estimators (the symbol " ^ " denotes "estimate")

$$ \hat{H}_{ij}(\omega_k) = \frac{\hat{X}_i(\omega_k)}{\hat{F}_j(\omega_k)} \tag{5.10} $$

$$ \left|\hat{H}_{ij}(\omega_k)\right|^2 = \frac{\hat{S}_{ii}(\omega_k)}{\hat{S}_{jj}(\omega_k)} \tag{5.11} $$

$$ \hat{H}_{ij}(\omega_k) = \frac{\hat{S}_{ij}(\omega_k)}{\hat{S}_{jj}(\omega_k)} \tag{5.12} $$

Unfortunately the issue of estimating *FRF*s is not that simple, as the time histories measured are in fact finite series of the response and force sampled at equally spaced time instants. The combination of the finite and discrete character of the records leads to leakage errors in the spectral estimates, which can be reduced (although not eliminated) by appropriate time windowing and acquisition of long time series. An additional source of errors in the measurements is due to noise. Noise is present in both the input and response measurements and can only be reduced by averaging the estimates over a number of records.

The two main sources of errors, bias (due to leakage) and random errors (due to measurement noise) are responsible for a different level of confidence in the calculation of the *FRF* estimates according to the formulae (5.2) or (5.10) to (5.12). For the particular case of Civil Engineering problems, it is generally considered that formula (5.12), designated as the estimator H_1, is the one that leads to smaller bias and random errors in the *FRF* estimates.

SDOF SI algorithms

These are the simplest and also the most widely used *SI* methods. Their formulation starts from the hypothesis that in the vicinity of a resonance the response is dominated by the resonant mode shape. Also it is assumed that the mode shapes are real. So, the *Receptance* given for the general case by equation (5.4) is defined, in the vicinity of a resonance by

$$\alpha_{ij}(\omega) \approx \frac{\phi_{ir} \cdot \phi_{jr}}{(\omega_r^2 - \omega^2) + i(2\xi_r \omega_r \omega)} \tag{5.13}$$

This function is characterized by a series of properties in which several *SI* algorithms are based.

(i) The Peak Peaking method

The *Peak Peaking* or *Peak Amplitude* method (Pendered & Bishop, 1963), for example, is based on the fact that the magnitude of the *FRF* (*Receptance* or other) has peaks at the resonant frequencies (in reality very close, but not exactly at these frequencies). The natural frequencies are then the frequencies that are associated with the peaks of the *FRF* magnitude. The *Half-Power Bandwidth* method can then be employed in the estimation of the damping coefficients. The procedure consists in determining the natural frequencies ω_1 and ω_2 for which

$$\left|\alpha_{ij}(\omega)\right|^2 = \frac{1}{2}\left|\alpha_{ij}(\omega_r)\right|^2 \tag{5.14}$$

Using the definition given by (5.13), the damping estimate is given approximately by

$$\xi_r \approx \frac{\omega_2 - \omega_1}{2\omega_r} \tag{5.15}$$

Figure 5.38 shows an example of a *SDOF* fitting of an *FRF* at a particular resonance. The estimation of the damping coefficient using the *Half-Power Bandwidth* method is exemplified in Figure 5.39.

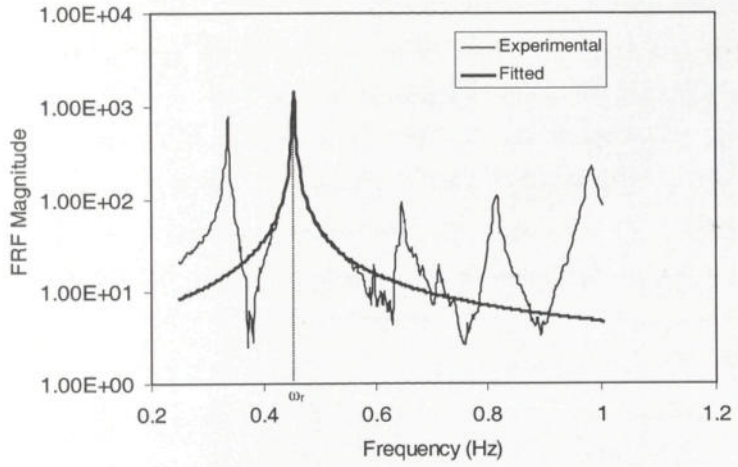


Figure 5.38. Application of a *SDOF SI* algorithm in the fitting of a mode shape.

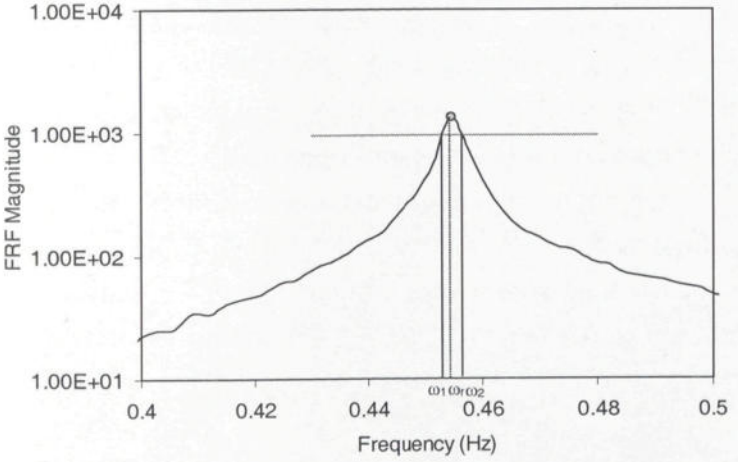


Figure 5.39. Estimation of the damping coefficient using the *Half-Power Bandwidth* method.

The modal components can now be estimated for the set of *FRF*s, taking the peak values of those functions at resonance. These are given according to equation (5.13) by

$$|\alpha_{ij}(\omega_r)| \approx \frac{\phi_{ir} \cdot \phi_{jr}}{2\xi_r \omega_r^2} \tag{5.16}$$

So, starting with the diagonal terms, i.e., with the *FRF*s relating input and response measured at the same location, the following components are obtained

$$\phi_{ir} = \sqrt{2\xi_r \omega_r^2 \cdot |\alpha_{ii}(\omega_r)|} \qquad \phi_{jr} = \sqrt{2\xi_r \omega_r^2 \cdot |\alpha_{ij}(\omega_r)|} \Big/ \phi_{ir} \tag{5.17}$$

Recalling that the mode shapes were assumed to be real, the phase of the components can only be *0°* or *180°* (positive or negative components, respectively). The sign is then determined comparing the phase of each *FRF* at resonance with the corresponding phase of the diagonal *FRF*.

An important aspect concerning the *Peak Peaking* method is that all the estimates concerning a mode shape are based only on three points from each *FRF* estimate. It is evident that this method is very sensitive to noise and also to the level of damping present in the system. On the other hand, very low modal damping originates extremely sharp *FRF* peaks and consequently a very low precision in the damping estimates. A final difficulty can be expected in the application of the *Peak Peaking* method when mode shapes are very closely spaced in frequency, as the significant modal interference may then prevent the accurate identification of resonances.

Several procedures can be followed in order to obtain higher quality estimates of the modal parameters, such as the separation of signal components (torsion and bending, for example) or the successive elimination of the identified modal components.

(ii) The Circle-Fit method

The *Circle-Fit* method (Kennedy & Pancu, 1947; Klosterman, 1971) employs another interesting property of the *SDOF FRF* approach, which is the fact that the *Mobility* function describes a circle in the Nyquist diagram (i.e. real part versus imaginary part), the influence of the other modes being approximated by a complex constant.

Note that the *SDOF* approach is only valid in the neighborhood of a resonance, hence the complete *FRF* will not be a complete circle around each resonance, but will be constituted by sections of near-circular arcs around those frequencies as shown in Figure 5.40 (Maia & Silva, 1997).

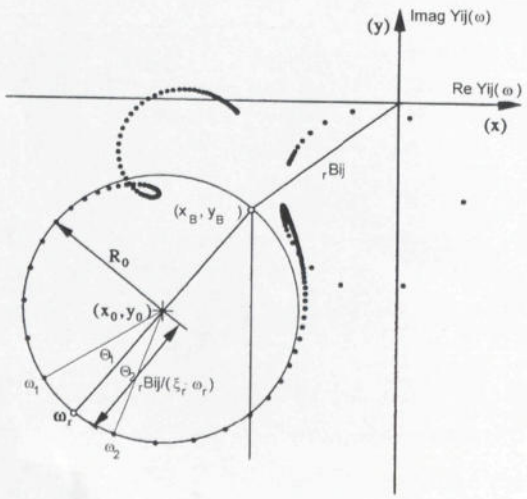


Figure 5.40. Nyquist plot of the *Mobility*, showing the circle-fit approach (Maia & Silva, 1997).

The fitting algorithm is then based on a least-squares approach of a set of measured *Mobility* lines around a resonance ω_r by a circle expressed according to

$$Y_{ij}(\omega) \approx \frac{i\omega \cdot (\phi_{ir} \cdot \phi_{jr})}{(\omega_r^2 - \omega^2) + i(2\xi_r \omega_r \omega)} + {}_rB_{ij} \tag{5.18}$$

The different alternatives concerning the fitting procedure will in practice lead to a number of variations of the general method that will not be discussed in the text.

Once the circle has been fitted, the modal parameters can be extracted directly. The resonant frequency ω_r will be estimated as the frequency associated to the point on the circle of maximum rate of angle change between data points. Then, selecting two frequency lines ω_1 and ω_2 at both sides of ω_r, the damping estimate will be given by

$$\xi_r = \frac{1}{2\omega_r}\left[\frac{\omega_2^2 - \omega_1^2}{\omega_1 \tan(2\theta_1) + \omega_2 \tan(2\theta_2)}\right] \tag{5.19}$$

The angles θ_1 and θ_2 in this equation are the angles between the radius of the frequency points ω_1 and ω_2, respectively, and the radius of ω_r, as represented in Figure 5.40. These angles can be calculated from

$$\tan(2\theta_1) = \frac{\omega_r^2 - \omega_1^2}{2\xi_r \omega_r \omega_1} \qquad \tan(2\theta_2) = \frac{\omega_2^2 - \omega_r^2}{2\xi_r \omega_r \omega_2} \tag{5.20}$$

The complex constant ${}_rB_{ij}$ can be then estimated as the intersection of the line connecting the center of the circle and the natural frequency point with the circle (see Figure 5.40).

The knowledge of ω_r, ξ_r and ${}_rB_{ij}$ allows finally for the estimation of the modal constant ${}_rA_{ij} = \phi_{ir} \cdot \phi_{jr}$ as

$${}_rA_{ij} = 2\xi_r \omega_r \cdot (Y_{ij}(\omega_r) - {}_rB_{ij}) \tag{5.21}$$

Because of depending on a larger number of points around a resonance, the *Circle-Fit* method is expected to produce better results than the *Peak Peaking* method. This method is in effect very widely employed and, if combined with specific strategies for elimination of the already fitted modes, very good results are indeed obtained.

(iii) The Inverse Methods

The *Inverse Methods* are relatively recent (Dobson, 1984; 1987) and use another interesting property of an *FRF*, that is the fact that both the real and the imaginary parts of the inverse of the *Receptance* are linear functions in the frequency squared and in the frequency, respectively, provided that a number of assumptions are employed. These are: (i) the mode shapes are real; (ii) the damping is assumed to be of hysteretic type; and (iii) the mode shapes are well separated in frequency.

BIBLIOTE F.E. PO

In terms of hypotheses the *Inverse* methods are equivalent to the *Circle-Fit* method and constitute an interesting alternative to the former method, with the advantage of leading to the fitting of a set of points by straight lines instead of circles, which is obviously a simpler task. The so-called Dobson method (1987) is simply an extension of the Inverse method to complex modes, with the possibility of compensating for the effects of neighbouring modes, leading thus to a higher level approach to the *SDOF* problem.

It is still worth mentioning that the Inverse and Dobson's methods were also the basis for the development of a new *SISO* method (Maia *et al.*, 1994), based on the interesting concept of *Characteristic Response Function* (*CRF*). This function, that can be obtained from several measured *FRFs* has the important property of being independent from the location of the points of measurement, in the vicinity of the several natural frequencies. It is independent of the residual terms, as well as of the modal constants, depending only on the global parameters of the structure.

MDOF SI algorithms

Considering the characteristics of Civil Engineering structures, it becomes evident that *SDOF* algorithms are generally insufficient to provide an accurate extraction of modal parameters. The adoption of more sophisticated *MDOF* algorithms does not invalidate however the use of SDOF methods, which are in effect extremely quick and simple to use. Moreover many *MDOF SI* algorithms require initial estimates of the modal parameters that are normally obtained from the application of *SDOF* methods.

(i) Nonlinear Least Squares Algorithm (LSFD)

The nonlinear *Least Squares Frequency Domain* (*LSFD*) method is a *MDOF* algorithm that is based on the approach of the *FRF*s by sets of N_m modes according to

$$\alpha_{ij}(\omega)=\sum_{r=1}^{N_m}\left(\frac{\phi_{ir}\cdot\phi_{jr}}{\omega_r\xi_r+i\left(\omega-\omega_r\sqrt{1-\xi_r^2}\right)}+\frac{\phi_{ir}^{*}\cdot\phi_{jr}^{*}}{\omega_r\xi_r+i\left(\omega+\omega_r\sqrt{1-\xi_r^2}\right)}\right)+UR_{ij}+\frac{LR_{ij}}{\omega^2} \qquad (5.22)$$

where UR_{ij} and LR_{ij}/ω^2 are the upper and lower residual terms. Note that in general $N_m < N$, what means that only the modes in a frequency band of interest are identified. The residual terms are added with the purpose of approaching the effect of the modes with natural frequencies below and above that frequency band of interest.

The *SI* algorithm consists then in fitting the measured *FRF*s by functions of the type of the indicated on the right hand side of equation (5.22), which will be designated by $G_{ij}(\omega)$ and depend on the modal parameters and residual terms, i.e.

$$G_{ij}(\omega)=G_{ij}(\omega,\omega_r,\xi_r,\phi_{ir},\phi_{jr},UR_{ij},LR_{ij})\Big|_{r=1,N_m} \qquad (5.23)$$

The least-squares approach follows from the definition of an error function E_{ij} as the difference between the measured and the theoretical response function. This error function is estimated over the frequency range of interest, i.e., it is calculated for all the N_S frequency lines of the frequency range of interest and is given by

$$E_{ij} = \sum_{0}^{N_S} [\hat{\alpha}_{ij}(\omega) - G_{ij}(\omega)] \cdot [\hat{\alpha}_{ij}(\omega) - G_{ij}(\omega)]^* \tag{5.24}$$

Note that the error function E_{ij} defined for the fitting of a particular FRF estimate (relating in this case the response at location *i* with the force applied at location *j*) can be extended to the set of measured *FRF*s (N_i input locations and N_o locations of the measured response) yielding then global estimates of the modal parameters, using

$$E = \sum_{j=1}^{N_i} \sum_{i=1}^{N_o} E_{ij} \tag{5.25}$$

The development of the least-squares approach leads to a set of equations of the type

$$\begin{aligned} &\frac{\partial E}{\partial r_1} = 0 \\ &\cdots \\ &\frac{\partial E}{\partial r_k} = 0 \end{aligned} \tag{5.26}$$

which are highly nonlinear equations in the unknowns r_i (representing the modal parameters and residuals). The solution of these equations is obtained iteratively by linearizing the system of equations around a modal model whose parameters are the user-supplied initial estimates.

The *LSFD* classical formulation is not a commonly employed method due to several difficulties in its application, one of the main aspects being the need for a good initial estimate of all the modal parameters in order to avoid divergence.

(ii) The Rational Fraction Polynomial Method (RFP)

The *Rational Fraction Polynomial* (*RFP*) method (Richardson & Formenti, 1982) constitutes a development of the *LSFD* method which employs the following three main concepts: (i) the formulation of the *FRF* in the rational fraction form instead of the partial fraction form; (ii) the definition of an error function in such a way that the resulting system of equations is linear and does not require initial estimates for the modal parameters, and (iii) the expression of the rational fraction form in terms of orthogonal Forsythe polynomials, in order to avoid ill-conditioned matrices.

The rational form of a *Receptance* function $\alpha(\omega)$ is given as

$$\alpha(\omega) = \frac{\sum_{k=0}^{2N_m - 1} a_k (i\omega)^k}{\sum_{k=0}^{2N_m} b_k (i\omega)^k} \tag{5.27}$$

where a_k and b_k are the unknown coefficients of the polynomials.

The error function is defined for each measured frequency ω_j as

$$e_j' = e_j \sum_{k=0}^{2N_m} b_k \cdot (i\omega_j)^k \tag{5.28}$$

where e_j is the error between the experimental FRF value at frequency ω_j and the corresponding value obtained from (5.27)

$$e_j = \frac{\sum_{k=0}^{2N_m-1} a_k (i\omega_j)^k}{\sum_{k=0}^{2N_m} b_k (i\omega_j)^k} - \hat{\alpha}(\omega_j) \tag{5.29}$$

Making $b_{2N_m} = 1$ and using (5.29), equation (5.28) is transformed into

$$e_j' = \sum_{k=0}^{2N_m-1} a_k (i\omega_j)^k - \hat{\alpha}(\omega_j) \cdot \left[\sum_{k=0}^{2N_m-1} b_k (i\omega_j)^k + (i\omega_j)^{2N_m} \right] \tag{5.30}$$

The general error function J is then formed, including the errors associated with all the N_S measured frequencies, and is given by

$$J = (\boldsymbol{E}^*)^T \cdot \boldsymbol{E} \tag{5.31}$$

with

$$\boldsymbol{E}^T = \left[e_1' \quad \ldots \quad e_{N_S}' \right] \tag{5.32}$$

The minimization of J yields, as already referred, a linear system of equations whose matrix of coefficients is however ill-conditioned. The problem can be reduced if the polynomials of equation (5.27) are expressed as combinations of complex orthogonal polynomials φ and θ like, for example, the Forsythe polynomials. So, instead of determining the coefficients a_k and b_k, the problem reduces to the determination of c_k and d_k, such that

$$\alpha(\omega) = \frac{\sum_{k=0}^{2N_m-1} c_k \varphi_k}{\sum_{k=0}^{2N_m} d_k \theta_k} \tag{5.33}$$

The development of the procedure for the identification of modal parameters is fully described by Maia & Silva (1997) and won't be further detailed in the present text.

5.4.2.2 Tuned-Sinusoidal SI methods

The Asher's method

The basis for the application of *SI* algorithms to the results from tuned-sinusoidal tests was established by Asher in 1958. The so-called Asher's method (Asher, 1958) assumes that a set of shakers is applied to the structure at specific locations and, by establishing the dynamic

equilibrium equations, allows for the extraction of the undamped natural frequencies, of the force distribution required to induce the vibration modes and, finally, of the undamped (real) modes.

The Asher's method has been widely used in Mechanical Engineering and Aeronautics applications since 1974. The application to Civil Engineering problems is not so popular, as the use of several shakers is very uncommon.

The Mau's method

The difficulty in measuring the *FRF* phases in large applications leads to a practical impossibility of direct application of any of the above described *SI* algorithms, but the *Peak Amplitude* method. In this respect, it is relevant to refer a simple method developed by Mau and Wang (1989), here designated as the Mau's method. This *SDOF* method is based on the fitting of a set of points in the neighbourhood of a resonance by an *FRF* function defined in terms of amplitude as a function of the modal parameters associated to the mode of vibration under analysis, i.e.

$$|\alpha(\omega)| = \frac{P_r}{\sqrt{(\omega_r^2 - \omega^2) + (2\xi_r\omega_r\omega)^2}} \tag{5.34}$$

The modal participation factor P_r, the natural frequency ω_r and the damping coefficient ξ_r are then estimated by defining an error function as

$$E = \sum_{k=1}^{N_k} (-\omega_k^4 + \hat{\omega}_k^4)^2 \tag{5.35}$$

where $\hat{\omega}_k$ is the estimated natural frequency associated with each measured *FRF* amplitude $|\overline{\alpha}(\hat{\omega}_k)|$ and N_k is the number of points used in the fitting, which should ideally by of *5*, according to Mau and Wang (1989). The minimization of this error function leads to a linear system of equations in the modal parameters, which can be found in the reference above indicated.

5.4.2.3 Time domain methods

Time domain *SI* algorithms include not only those algorithms that apply a least-squares fitting of the measured data by a particular model (the modal model, for example), but also methods that employ other minimization techniques.

The Complex Exponential Method (CE)

This method is one of the most simple time domain methods and is based on the fitting of an *Impulse Response Function* (*IRF*) by a modal *MDOF* model. The measured *IRF* is calculated

directly from the *FRF* estimate by application of an inverse Fourier Transform. As for the modal model of the *IRF* $h_{ij}(t)$, it is expressed in the form (Spitznogle & Quazi, 1971)

$$h_{ij}(t) = \sum_{r=1}^{2N_m} {}_rA_{ij} e^{s_r t} \tag{5.36}$$

where ${}_rA_{ij}$ is the modal constant defined above in equation (5.4) and s_r is given by

$$s_r = -\omega_r \xi_r + i\omega_r^d \tag{5.37}$$

with the damped frequency ω_r^d being defined by

$$\omega_r^d = \omega_r \sqrt{1-\xi_r^2} \tag{5.38}$$

Considering a number L of equally spaced points of the measured $h_{ij}(t)$ which, for the sake of simplicity will simply be defined as h_0, h_1, ..., h_L and given by

$$\begin{aligned} h_0 &= h_{ij}(0) = \sum_{r=1}^{2N_m} {}_rA_{ij} \\ h_1 &= h_{ij}(\Delta t) = \sum_{r=1}^{2N_m} {}_rA_{ij} e^{s_r \Delta t} = \sum_{r=1}^{2N_m} A_r' \cdot V_r \\ &\cdots \\ h_L &= h_{ij}(L \cdot \Delta t) = \sum_{r=1}^{2N_m} {}_rA_{ij} e^{s_r (L\Delta t)} = \sum_{r=1}^{2N_m} A_r' \cdot V_r^L \end{aligned} \tag{5.39}$$

with

$$V_r = e^{s_r \Delta t} \qquad A_r' = {}_rA_{ij} \tag{5.40}$$

a system of equations is formed that depends on the unknowns V_r and A_r'.

The quantities V_r, which appear in complex conjugate pairs, can be obtained as the roots of a polynomial defined by (Prony, 1975)

$$\beta_0 + \beta_1 V_r + \beta_2 V_r^2 + \ldots + \beta_L V_r^L = 0 \tag{5.41}$$

whose coefficients β_k, designated as autoregressive coefficients, are obtained from the solution of a system of equations defined as follows

$$\begin{bmatrix} h_0 & h_1 & \ldots & h_{2N_m-1} \\ h_1 & h_2 & \ldots & h_{2N_m} \\ \ldots & \ldots & \ldots & \ldots \\ h_{2N_m-1} & h_{2N_m} & \ldots & h_{4N_m-2} \end{bmatrix} \cdot \begin{Bmatrix} \beta_0 \\ \beta_1 \\ \ldots \\ \beta_{2N_m-1} \end{Bmatrix} = - \begin{Bmatrix} h_{2N_m} \\ h_{2N_m+1} \\ \ldots \\ h_{4N_m-1} \end{Bmatrix} \tag{5.42}$$

Note that for convenience the number of points was made equal to $2N_m$ and β_{2N_m} will be set to *1*.

The roots V_r of (5.41) are finally related with the modal constants A_r' through the system of equations

$$\begin{bmatrix} 1 & 1 & \dots & 1 \\ V_1 & V_2 & \dots & V_{2N_m} \\ \dots & \dots & \dots & \dots \\ V_1^{2N_m-1} & V_2^{2N_m-1} & \dots & V_{2N_m}^{2N_m-1} \end{bmatrix} \cdot \begin{Bmatrix} A_1' \\ A_2' \\ \dots \\ A_{2N_m}' \end{Bmatrix} = - \begin{Bmatrix} h_0 \\ h_1 \\ \dots \\ h_{2N_m-1} \end{Bmatrix} \tag{5.43}$$

The procedure above indicated shows that the *CE* method is rather simple and does not require the use of initial estimates. It requires however that the number of fitting modes is specified, what eventually leads to an iterative identification process.

Another aspect associated with this method is that the number of time values employed in the identification procedure is only four times the number of identified modes, hence it is expected that the method exhibits some sensitivity to noise. In order to avoid this problem, some extensions of the algorithm have been derived, namelly the so-called *Least Squares Complex Exponential* (*LSCE*) method, which departs from the hypotheses above formulated, but applies the technique simultaneously to several *IRF*s at a time, leading to systems of equations with rectangular matrices. These are solved via the pseudo-inverse technique.

The Ibrahim Time Domain (ITD) method

The *Ibrahim Time Domain* (*ITD*) method described in the current Section is a modified version from the original method derived by Ibrahim (Ibrahim & Mikulcik, 1976;1977).

The method employs free decay responses instead of *FRFs* and establishes the relationship between two sets of *L* data points shifted by one interval of time Δt, which depends on a system square matrix from which the modal parameters can be extracted.

The free response $x_i(t_j)$ measured at location *i* for a generic time instant t_j can in effect be expressed as a summation of the modal responses as

$$x_i(t_j) = \sum_{r=1}^{2N_m} \phi_{ir} \cdot e^{s_r t_j} \tag{5.44}$$

where ϕ_{ir} is the i_{th} component of the complex mode shape $\boldsymbol{\varphi}_r$.

The time response data at *L* time instants and q locations can be gathered in a matrix $\boldsymbol{X}$ according to

$$\boldsymbol{X} = \begin{bmatrix} x_1(t_1) & x_1(t_2) & \dots & x_1(t_L) \\ x_2(t_1) & x_2(t_2) & \dots & x_2(t_L) \\ \dots & \dots & \dots & \dots \\ x_q(t_1) & x_q(t_2) & \dots & x_q(t_L) \end{bmatrix} \tag{5.45}$$

Accordingly, the shifted time data matrix $\hat{\boldsymbol{X}}$ is given by

$$\hat{\boldsymbol{X}} = \begin{bmatrix} x_1(t_1+\Delta t) & x_1(t_2+\Delta t) & \dots & x_1(t_L+\Delta t) \\ x_2(t_1+\Delta t) & x_2(t_2+\Delta t) & \dots & x_2(t_L+\Delta t) \\ \dots & \dots & \dots & \dots \\ x_q(t_1+\Delta t) & x_q(t_2+\Delta t) & \dots & x_q(t_L+\Delta t) \end{bmatrix} \tag{5.46}$$

The matrices $\boldsymbol{X}$ and $\hat{\boldsymbol{X}}$ are related through a square (qxq) matrix $\boldsymbol{A}_S$ according to

$$\boldsymbol{A}_S \cdot \boldsymbol{X} = \hat{\boldsymbol{X}} \tag{5.47}$$

The next step consists in evaluating this matrix, what requires the use of the pseudo-inverse technique and leads to (Maia & Silva, 1997)

$$\boldsymbol{A}_S = \frac{1}{2} \cdot \left[\left(\hat{\boldsymbol{X}} \cdot \hat{\boldsymbol{X}}^T \right) \cdot \left(\boldsymbol{X} \cdot \hat{\boldsymbol{X}}^T \right)^{-1} + \left(\hat{\boldsymbol{X}} \cdot \boldsymbol{X}^T \right) \cdot \left(\boldsymbol{X} \cdot \boldsymbol{X}^T \right)^{-1} \right] \tag{5.48}$$

The modal parameters can be then extracted directly from the formulation of the following eigenvalue problem

$$\left[\boldsymbol{A}_S - e^{s_r \Delta t} \boldsymbol{I} \right] \cdot \boldsymbol{\varphi}_r = \boldsymbol{0} \tag{5.49}$$

where $\boldsymbol{I}$ is the identity matrix.

The Eigensystem Realization Algorithm (ERA)

This method was developed by Juang and Pappa (1985) based on the state-space formulation of a viscously damped system and can be described in a very summarized form according to the following steps:

- Evaluation of a so-called *Hankel* matrix $\boldsymbol{H(0)}$, containing the shifted time series (Maia & Silva, 1997);
- The application of a *Singular Value Decomposition* (*SVD*), which allows for a recalculation of $\boldsymbol{H(0)}$ using a reduced number of lines and columns (corresponding to the rank of $\boldsymbol{H(0)}$). This process of reconstruction of the *Hankel* matrix through a *SVD* allows for the separation of the true response from noise and is designated as a *Realization*;
- The construction of a shifted Hankel matrix $\boldsymbol{H(1)}$, and calculation of a set of three *Realized* matrices, which are related with the state-space matrices;
- The solution of an eigenvalue problem from the matrices above referred, from which the modal parameters are extracted.

Further details of this method can be found in (Maia & Silva, 1997).

The AutoRegressive Moving Average (ARMA) method

This method starts from the idea that the output *y(t)* of a system is contaminated with a zero mean sequence of additive noise and that the set of input time series *f(t)* is a zero mean uncorrelated history (Gersch, 1970).

Writing the system of differential equations of motion in a linear difference form, the current observation $y(t)$ can be expressed as the sum of its own past (the autoregressive part) plus a linear combination of uncorrelated terms (the moving average terms) plus a prediction error *e(t)*

$$y(t) = -\sum_{k=1}^{2N_m} \alpha_k\, y(t-k) + \sum_{k=0}^{2N_m-1} \beta_k\, f(t-k) + e(t) \tag{5.50}$$

where the unknown coefficients α_k and β_k are designated as the *autoregressive* and *moving-average* parameters respectively.

The input and output sets can be used in the formation of a system transfer function in a rational fraction polynomial form, in terms of the z-variable ($z = e^{s\,\Delta t}$)

$$H(z) = \frac{Y(z)}{F(z)} = \frac{\sum_{k=0}^{m} \beta_k\, z^{-k}}{\sum_{k=0}^{n} \alpha_k\, z^{-k}} \tag{5.51}$$

The knowledge of the parameters α_k and β_k allows for the determination of the roots of the polynomials $Y(z)$ and $F(z)$ in equation (5.51), which are related, respectively, with the natural frequencies and damping coefficients, and with the modal components (residues).

Going back to equation (5.50), a vector of future observations of the response at the time instants $t = 2N_m + 1, 2N_m + 2, \ldots, 2N_m + L$ can be formed, which will accordingly depend on the parameters α_k and β_k as follows

$$\begin{Bmatrix} y(2N_m+1) \\ y(2N_m+2) \\ \vdots \\ y(2N_m+L) \end{Bmatrix} = \begin{bmatrix} -y(2N_m) & \ldots & -y(1) & f(2N_m+1) & \ldots & f(2) \\ -y(2N_m+1) & \ldots & -y(2) & f(2N_m+1) & \ldots & f(3) \\ \vdots & \ldots & \vdots & \vdots & \ldots & \vdots \\ -y(2N_m+-1) & \ldots & -y(L) & f(2N_m+L) & \ldots & f(L+1) \end{bmatrix} \cdot \begin{Bmatrix} \alpha_1 \\ \vdots \\ \alpha_{2N_m} \\ \beta_1 \\ \vdots \\ \beta_{2N_m-1} \end{Bmatrix} + \begin{Bmatrix} e(2N_m+1) \\ e(2N_m+2) \\ \vdots \\ e(2N_m+L) \end{Bmatrix} \tag{5.52}$$

or in a more compact form

$$\boldsymbol{y} = \boldsymbol{X}\,\boldsymbol{\theta} + \boldsymbol{e} \tag{5.53}$$

By minimizing the squared error $J = \boldsymbol{e}^T \cdot \boldsymbol{e}$, the following expression is obtained for the vector $\boldsymbol{\theta}$ containing the autoregressive and the moving average coefficients

$$\boldsymbol{\theta} = \left(\boldsymbol{X}^T \cdot \boldsymbol{X}\right)^{-1} \cdot \boldsymbol{X}^T \cdot \boldsymbol{y} \tag{5.54}$$

The coefficients α_k of this vector are then used to determine the natural frequencies and damping coefficients, the modal components being determined from the components β_k.

It should be pointed that there exist several variations of the *ARMA* method. Of particular interest are the extensions of the method to the case where the excitation is not known and is assumed to be a white noise. This leads to the so-called *output-only* identification problem, which will be introduced in the next Section.

5.4.3 Output-Only SI methods

The methods presented in this Section apply to the particular case of *AVT* described in Section 5.2, when the structural response to ambient loads (e.g. wind action, traffic, earthquake excitation, machinery and human activity) is measured.

A certain number of particularities associated with *AVT* should be noted:

- The first aspect has to do with the characteristics of the input. Given the different sources of ambient excitation, it is in practice impossible to characterize the input on the structural system. On the other hand, the consideration of the several sources of random excitation as a whole allows for the assumption of certain properties, like the stochastic and Gaussian character of the input;
- A second aspect is the fact that in general ambient excitation originates a structural response of low intensity, leading in general to a signal to noise ratio of the measured data smaller than the one obtained from *FVT*. This also means that *AVT* usually provides poorer estimates of dynamic parameters than *FVT*;
- One consequence of the impossibility of controlling the input and of the low level of excitation is that some structural modes may not be induced to a measurable level and eventually won't be identified. On another hand, the identified parameters do not necessarily correspond to structural parameters, as the analysed measured response may eventually contain the response to some particular input that does not fit the general assumptions adopted by the *SI* algorithm.

From the general aspects above referred it is well evident that the classical *SI* algorithms previously described, based on the simultaneous measurement of the input and output, cannot apply directly to *AVT*. Two main possibilities can then be followed in the derivation of estimation algorithms, namely: (i) the assumption of certain characteristics for the input, which allow for an alternative formulation of the *SI* problem in the frequency domain; (ii) the understanding of the measured response time series as structural responses of the system to an input uncorrelated noise added by the system noise. The different time domain techniques employed in the minimization of this noise are the basis for a variety of time domain *SI* methods.

The present Section starts to present and discuss the classical output-only identification approach, based on the application of the *Peak Peaking* method to the response spectral estimates. The author extensively employed this methodology in the processing of

AVT data (in particular, the data from the *AVT* of the Vasco da Gama cable-stayed bridge presented in Section 5.5), obtaining in general very good natural frequency and modal shape estimates.

A brief description of some recent algorithms for the purpose of output-only identification of Civil Engineering structures is then presented considering the latest developments in the topic. These are summarized in Table 5.2.

It should be noticed that some of these methods derive from algorithms previously developed for the input-output *SI* in the context of Mechanical Engineering and Aeronautics.

As for the practical experience of application of the most recent methods to the results from *AVT* on large Civil Engineering structures, it should be referred that very few publications are known, what is due in large extent to the mathematical complexity of most algorithms.

Table 5.2. Some relevant output-only *SI* methods.

	Type of methods	Characteristics
Frequency domain	Peak Peaking	Classical SDOF method
	Frequency Domain Decomposition (FDD)	MDOF method; application of SVD to reduce noise
Time domain	Random Decrement (RD)	Operates on time domain series, leading to a free-decay curve analysis
	Recursive Techniques (ARMA)	Time series modelling using recursive algorithms
	Maximum Likelihood Methods	Stochastic methods based on the minimization of a covariance matrix
	Stochastic Subspace methods	Stochastic methods based on the projection of a state vector on a vector of past realizations

5.4.3.1 Frequency domain methods

The extension of the Peak Peaking Method to Output-Only Identification

The major assumption employed in classical data processing from *AVT* is the consideration of the ambient excitation as a stationary Gaussian white noise stochastic process in the frequency band of interest. Under this assumption, the power spectral density of the input is considered constant, i.e., $S_{jj}(\omega) = C$, and so equation (5.11) is transformed into

$$\left|H_{ij}(\omega)\right|^2 = \frac{S_{ii}(\omega)}{C} \tag{5.55}$$

wich means that the *FRF* peaks (corresponding to system natural frequencies) are given directly from the peaks of the power spectral density functions of the measured response.

It is also necessary to define a spectral function from which the modal components are extracted. For this purpose, the dynamic equilibrium equations can be formulated in terms of modal coordinates, which leads to the uncoupled system of equations

$$M_r \ddot{y}_r(t)+C_r \dot{y}_r(t)+K_r y_r(t)=F_r(t) \tag{5.56}$$

where the modal mass M_r, the modal damping C_r, the modal stiffness K_r and modal force F_r associated with the r_{th} vibration mode $\boldsymbol{\varphi}_r$ are defined respectively as functions of the mass matrix $\boldsymbol{M}$, the damping matrix $\boldsymbol{C}$, the stiffness matrix $\boldsymbol{K}$ and the force vector $\boldsymbol{f(t)}$ by

$$M_r = \boldsymbol{\varphi}_r^T \cdot \boldsymbol{M} \cdot \boldsymbol{\varphi}_r \tag{5.57a}$$

$$C_r = \boldsymbol{\varphi}_r^T \cdot \boldsymbol{C} \cdot \boldsymbol{\varphi}_r \tag{5.57b}$$

$$K_r = \boldsymbol{\varphi}_r^T \cdot \boldsymbol{K} \cdot \boldsymbol{\varphi}_r \tag{5.57c}$$

$$F_r = \boldsymbol{\varphi}_r^T \cdot \boldsymbol{f(t)} \tag{5.57d}$$

and $y_r(t)$ is the corresponding modal contribution.

The response at location *i* can then be expressed in terms of displacements $x_i(t)$ by the linear combination of mode shapes

$$x_i(t)=\phi_{i1} y_1(t)+\phi_{i2} y_2(t)+...+\phi_{iN_m} y_{N_m}(t) \tag{5.58}$$

Applying the Fourier Transform to both members of equation (5.58) yields

$$X_i(\omega)=\phi_{i1} Y_1(\omega)+\phi_{i2} Y_2(\omega)+...+\phi_{iN_m} Y_{N_m}(\omega) \tag{5.59}$$

where the Fourier Transform $Y_r(\omega)$ of the modal coordinate $y_r(t)$ can be obtained applying also the Fourier Transform to equation (5.56), which gives

$$Y_r(\omega)=\frac{F_r(\omega)}{-\omega^2 M_r + i\omega C_r + K_r}=H_r(\omega)\cdot F_r(\omega) \tag{5.60}$$

The function $H_r(\omega)=\dfrac{1}{-\omega^2 M_r + i\omega C_r + K_r}$ in equation (5.60) can be viewed as a frequency response function associated with a single-degree-of-freedom system, presenting amplitude peaks close to the resonance frequencies ω_r, as well as sudden phase variations of 180° at the vicinity of those frequencies.

Introducing (5.60) into (5.59) yields

$$X_i(\omega)=\phi_{i1} H_1(\omega)\cdot F_1(\omega)+\phi_{i2} H_2(\omega)\cdot F_2(\omega)+...+\phi_{iN_m} H_{N_m}(\omega)\cdot F_{N_m}(\omega) \tag{5.61}$$

The Peak Amplitude hypothesis can be now employed, assuming that in the vicinity of a resonance ω_r the response is dominated by the mode $\boldsymbol{\varphi}_r$, the contribute of the other modes being neglected, i.e.

$$X_i(\omega) \approx \phi_{ir} H_r(\omega)\cdot F_r(\omega), \qquad \omega \in \left[\omega_r \pm \delta_{\omega_r}\right] \tag{5.62}$$

If the response is measured simultaneously at a different location *j*, the ratio between the Fourier Transforms of the response at both locations can be given approximately by

$$\frac{X_j(\omega_r)}{X_i(\omega_r)} = \frac{\phi_{jr} \cdot H_r(\omega_r) \cdot F_r(\omega_r)}{\phi_{ir} \cdot H_r(\omega_r) \cdot F_r(\omega_r)} = \frac{\phi_{jr}}{\phi_{ir}} \tag{5.63}$$

This means that the mode shape components associated with the vibration mode $\boldsymbol{\varphi}_r$ at any location can be obtained simply by calculating the ratio between the Fourier Transform amplitudes of the response at that location and at a particular location *i* taken as a reference.

Note that equation (5.63) is valid even when the responses are measured in terms of velocities or accelerations, given that $\dot{X}_j(\omega) = i\omega X_j(\omega)$ and $\ddot{X}_j(\omega) = -\omega^2 X_j(\omega)$. Note also that the validity of (5.63) relies on the assumptions employed in the application of the Peak Peaking method, which are the following: (i) the mode shapes are well separated in frequency and are lightly damped; (ii) the structure is characterized by a proportional damping and so the mode shapes are real. The later hypothesis leads to mode shape components that are only in phase (positive) or out-of-phase (negative) with respect to the reference components.

Given the errors associated to the finite and discrete character of the response time series used in the *SI* process, the mode shapes must be obtained from power spectral estimates instead of the Fourier Transforms (equation (5.63)). By analogy with equation (5.12), a response transfer function estimator $\hat{\overline{H}}_{ji}(\omega_r)$ can be then defined, relating the cross-power spectral, $\hat{S}_{ji}(\omega_r)$, and the power spectral, $\hat{S}_{ii}(\omega_r)$, density estimators of the response at two locations *j* and *i* as

$$\hat{\overline{H}}_{ji}(\omega_r) = \frac{\hat{S}_{ji}(\omega_r)}{\hat{S}_{ii}(\omega_r)} \tag{5.64}$$

Using the approach from equation (5.62), it comes that

$$\hat{\overline{H}}_{ji}(\omega_r) = \frac{\hat{\phi}_{jr} \cdot \hat{\phi}_{ir} \cdot \left|\hat{H}_r(\omega_r)\right|^2 \cdot \hat{S}_{ii}(\omega_r)}{\hat{\phi}_{ir} \cdot \hat{\phi}_{ir} \cdot \left|\hat{H}_r(\omega_r)\right|^2 \cdot \hat{S}_{ii}(\omega_r)} = \frac{\hat{\phi}_{jr}}{\hat{\phi}_{ir}} \tag{5.65}$$

It is important to refer that the power spectral estimators employed in the formation of the ficticious transfer function relating two simultaneous outputs at locations *j* and *i* must incorporate averaging over a number of series in order to reduce the negative effect of the noise present in the signals.

In parallel with the transfer function estimator, a coherence function estimator $\hat{\gamma}^2_{ji}(\omega_k)$ relating the output signals at a generic frequency ω_k can also be defined according to the equation

$$\hat{\gamma}^2_{ji}(\omega_k) = \frac{\left|\hat{S}_{ji}(\omega_k)\right|^2}{\hat{S}_{jj}(\omega_k) \cdot \hat{S}_{ii}(\omega_k)} \tag{5.66}$$

This function gives a measure of the degree of statistical correlation between the measured structural responses and should approach *1* in the vicinity of the natural frequencies, provided that the signal to noise ratio is high enough.

Finally, modal damping coefficient estimates can be obtained directly by application of the half-power bandwidth method previously described. Bendat and Piersol (1966) suggested that the cross-power spectral estimator should be employed for this purpose, as this estimator is the one that contains a lower influence of noise.

Recognizing that the application of the half-power bandwidth method encloses significant errors, particularly when the damping coefficients are very small and the mode shapes are not well separated in frequency, Brownjohn (1988) developed some peak fitting techniques. This author verified however that the damping estimates may vary by more than *100%* depending on the analysis technique employed. Damping coefficients also vary as a function of the amplitude of vibration and of the temperature, as was observed by Okauchi *et al.* (1992) in the dynamic testing of three suspension bridges. The author could prove the first issue with the dynamic tests performed on the physical model of the Jindo Bridge described in Chapter seven.

A final remark concerning the application of the Peak Peaking method in the identification of modal parameters on large structures has to do with the necessity of processing a large amount of data. In this respect, the task of identifying natural frequencies from each measured ficticious transfer function or power spectral estimate becomes very demanding and so it is of interest the definition of a unique function that contains all the information of the natural frequencies present in the set of measured signals. This function was introduced by Felber (1993) and is designated as the *Average Normalized Power Spectral Density* (*ANPSD*) function, being defined as the average of a group of ℓ *Normalized Power Spectral Densities* (*NPSD*s)

$$ANPSD(\omega_k) = \frac{1}{\ell} \sum_{m=1}^{\ell} NPSD_m(\omega_k) \tag{5.67}$$

The *NPSD* functions are calculated from the *Power Spectral Estimates* (*PSD*s) as follows

$$NPSD_m(\omega_k) = \frac{PSD_m(\omega_k)}{\sum_{k=1}^{n} PSD_m(\omega_k)} \tag{5.68}$$

where ω_k is a generic frequency and n is the number of discrete frequencies of the m_{th} *PSD* estimator.

The Frequency Domain Decomposition (FDD) method

The limitations of the *Peak Peaking* method were already referred and become naturally increased when the measured signals are contaminated by a significant level of noise. This is clearly the case of *AVT*.

The *Frequency Domain Decomposition* (*FDD*) method is an interesting alternative that can be viewed as an extension of the *Peak Peaking* method, that enables the treatment of closely spaced modes and eventually the extraction of better damping estimates. This method employs a process of noise reduction of a cross-power matrix of the output measurements $\hat{\boldsymbol{S}}(\omega)$ through the solution of a *Single Value Decomposition* (*SVD*) problem. The formulation described here was developed at Aalborg University by Brincker *et al.* (2000), although the concept of principal spectral analysis on which it is based has been previously employed by Corrêa and Campos Costa (1992) and by Otte *et al.* (1994).

The first step of the method consists in forming the cross-power spectra matrix $\hat{\boldsymbol{S}}(\omega)$ for each frequency line ω_k and applying the Single Value Decomposition, which is a numerical process of transformation of a matrix (complex, in the present case) into the product of three matrices

$$\hat{\boldsymbol{S}}(\omega_k) = \boldsymbol{U}_k \cdot \boldsymbol{\Lambda}(\omega_k) \cdot \boldsymbol{U}_k^H \tag{5.69}$$

The matrix $\boldsymbol{\Lambda}(\omega_k)$ is a diagonal matrix that contains the singular values, which are the positive and real eigenvalues of the matrix $\hat{\boldsymbol{S}}(\omega_k)$ organized in descending order, that can be considered as the principal component autospectra $\hat{\boldsymbol{S}}'(\omega_k)$ (Otte *et al.*, 1994). These components are mutually uncorrelated and are related with the observed power and cross-power spectra by a set of linear combinations expressed by the matrix $\boldsymbol{U}_k$. On another hand, $\boldsymbol{U}_k$ is a unitary matrix, i.e., a matrix of complex values that respects the relation

$$\boldsymbol{U}_k \cdot \boldsymbol{U}_k^H = \boldsymbol{U}_k^H \cdot \boldsymbol{U}_k = \boldsymbol{I} \tag{5.70}$$

the superscript "^{H}" denoting "complex conjugate (Hermitian) matrix". The columns of this matrix contain the singular vectors, which represent mode shapes for each of the spectral peaks.

The *SI* procedure adopted by Brincker *et al.* (2000) consists in selecting segments of the principal autopower spectra around the peaks of these functions, apply these segments an inverse *FFT* so that time domain data is obtained, and perform the identification of the natural frequency and damping coefficient from the crossings and logarithmic decrement of the corresponding *SDOF* autocorrelation function.

5.4.3.2 Time domain methods

The Random Decrement (RD) method

The *Random Decrement* (*RD*) method was introduced by Cole at NASA during the late 60s (Cole, 1968) in the context of the dynamic analysis of space structures under ambient loads. The large variations of damping estimates obtained from the application of the half-power bandwidth technique and the impossibility of assessing damage from spectral analysis

motivated the introduction of this time domain technique. The idea on which it is based is the possibility of transforming a random time series into a free decay response of the structure under analysis. This is naturally a form of extracting noise from the time series, and allows for a simple extraction of the damping ratios, by analysis of the decay.

The question is then how to transform a random time series into a free decay.

According to Cole, the random response of a structure at the time $t_0 + \Delta t$ is composed of three parts: (i) the step response from the initial displacements at the time t_0; (ii) the impulse response from the initial velocity at time t_0; (iii) a random part, which is due to the load applied to the structure in the time interval $[t_0, t_0 + \Delta t]$.

By selecting time segments out of the time record every time *x(t)* equals a specified value, say *x(t)=a,* and by averaging, the following conclusions can be extracted:

- The initial velocity is expected to vary randomly with time, so the average processing will eventually cancel the associated structural response components;
- The averaging of the time segments will also tend to cancel the random component of the response;
- The resulting component of the averaged time segments, which is designated as the *Random Decrement* (*RD*) function and is defined according to

$$\hat{D}_{XX}(\tau) = \frac{1}{N} \sum_{i=1}^{N} x(t_i + \tau) | x(t_i) \tag{5.71}$$

where N is the number of averaged time segments, will be the free decay response from the initial displacement $x(t_i) = a$.

Although the concept associated with the *RD* method is very simple, the corresponding practical implementation has a few problems. These are, for example, the choice of the triggering level *a*, the discrete character of the time series, that prevents an accurate choice of the time instant t_k where $x(t_k) = a$, the choice of the number of averaging segments or the amplitude of these segments.

These aspects have motivated research on the *RD* method until the present time. An important result obtained by Vandiver *et al.* (1982), and further extended by Brincker *et al.* (1990) and explored by Asmussen (1997), is the proportionality between the *RD* functions and the auto and cross correlation functions, which allows the conjugation of the *RD* method with the application of *FFT* techniques.

With regard to the methodology for the extraction of modal parameters from the free decay responses, it's still worth mentioning that the *Ibrahim Time Domain* technique described in Section 5.4.2.2 is also fully applicable.

Recursive Techniques (ARMA)

The recursive techniques discussed in Section 5.4.2.2 for the input-output problem can also be applyed to output-only data, under the assumption that the inputs generating the response are white noise.

The input functions $f(t-k)$ in equation (5.50) represent then white noise sequences $w(t-k)$ that drive the system to the response $y(t)$, i.e.

$$y(t)=-\sum_{k=1}^{2N_m}\alpha_k\, y(t-k)+\sum_{k=0}^{2N_m-1}\beta_k\, w(t-k)+e(t) \tag{5.72}$$

The identification of the coefficients α_k and β_k from equation (5.72) can be performed by minimization of a specified error function, which leads to a non-linear optimization process (Maia & Silva, 1997).

Although the *ARMA* models are very well known and have an important range of applications in control problems, they can also lead to a number of difficulties, which are associated with the calculation time, the necessary amount of computer memory and convergence.

Although some innovative strategies have been recently introduced, like the formulation of the *ARMA* problem in the modal space (Andersen, 1997), the *ARMA* methods have not yet shown to be of great interest in applications to Civil Engineering structures, as far as known by the author.

Maximum Likelihood (ML) methods

An inconvenience associated with the least-squares technique is related with the fact that significant errors can be obtained in the estimated structural parameters when the measurement errors are not uniformly distributed.

Knowing that a large number of engineering random quantities can be idealized by normal distributions, a more reliable method of estimation of structural parameters relies on the assumption that the errors between the measured and the model response also respect a distribution of that type, the identification problem reducing then to a maximization of the joint probability density of the errors.

The *Maximum Likelihood* (*ML*) method was introduced as a *SI* method by Ljung (1987). This method can be applied both in the time (Ren *et al.*, 2000) and in the frequency domain (Guillaume *et al.*, 1999), and is based on the definition of a so-called *Likelihood* function $L(\boldsymbol{\theta})$, which is no more than the joint probability density function of a set of p random vectors $\boldsymbol{Y}=[\boldsymbol{y}_1,\boldsymbol{y}_2,...,\boldsymbol{y}_p]$, the generic variable $\boldsymbol{y}_k$ representing a time series of the response associated with the location k.

Assuming that each of the time responses $\boldsymbol{y}_k$ is composed of a sequence of m independent repetitions, i.e.

$$\boldsymbol{y}_k^T = [y_k(1) \quad y_k(2) \quad \ldots \quad y_k(m)] \tag{5.73}$$

and that the probability distribution of a repetition $y_k(j)$ referred to a parameter vector $\boldsymbol{\theta}$ (related with the structural properties to identify) is given by $f(y_k(j) \mid \boldsymbol{\theta})$, the joint probability density of $\boldsymbol{y}_k$ conditional to the vector $\boldsymbol{\theta}$ is then

$$f(\boldsymbol{y}_k \mid \boldsymbol{\theta}) = L(\boldsymbol{\theta}) = \prod_{j=1}^{m} f(y_k(j) \mid \boldsymbol{\theta}) \tag{5.74}$$

It is then possible to maximize the function $L(\boldsymbol{\theta})$ by adjusting the components of vector $\boldsymbol{\theta}$.

It should be noticed that the definition of the joint probability density function associated with the random variables $\boldsymbol{Y}$ involves the calculation of covariance matrices. So, when a great number of observations are present, the process becomes extremely complicated and lengthy. Although some strategies can be adopted to improve the method, like the expression of the *Likelihood* function in the logarithmic form (that leads to the transformation of the product in (5.74) in a sum), the application of the *ML* method to large amounts of data may encounter some difficulties at the current state-of-the-art. It is important however to refer that the *ML* method yields confidence intervals for the estimated parameters, information that is particularly valuable for the quantification of damping coefficients.

Stochastic Subspace (SS) methods

Stochastic Subspace methods are currently at a forefront position in the chapter of *SI* from output-only measurements. These methods were born in the context of control problems and have been developed at both the Katholieke University of Leuven, in Belgium (Overschee & De Moor, 1996; Peeters *et al.*, 1999), and at the University of Aalborg, in Denmark (Andersen & Brincker, 2000), in the context of Civil Engineering applications.

An important aspect that deserves reference here is the current availability of robust software based on these methods and developed at both Centres for the purpose of applying *SI* methods to *AVT* data. The Leuven University has developed the *SI* toolbox *MACEC* for *MATLAB* (Peeters *et al.*, 1999) and the commercial software package *ARTEMIS* was developed by Andersen & Brincker (2000), at the Aalborg University.

The main ideas employed by the *SS* methods are that the structure (i) is excited by a white noise, and; (ii) is described by a stochastic state-space model. Accordingly, the *n*-second order differential equations of motion can be described by *2n*-first order differential equations, which can be then written in difference form as

$$\boldsymbol{x}_{k+1} = \boldsymbol{A}\,\boldsymbol{x}_k + \boldsymbol{w}_k \tag{5.75}$$

$$\boldsymbol{y}_k = \boldsymbol{C}\,\boldsymbol{x}_k + \boldsymbol{v}_k \tag{5.76}$$

where the vectors and matrices have the following designation and meaning:

$\boldsymbol{x}_k$ - is the state vector associated with the time instant characterized by the k_{th} sample;

$\boldsymbol{A}$ - is the state matrix, which is assumed constant, since the system is considered linear and time invariant;

$\boldsymbol{y}_k$ - is the observation vector, which contains the sampled measurements;

$\boldsymbol{C}$ - is designated as the output matrix, and relates the observation vector with the state vector;

$\boldsymbol{w}_k$ - is the process noise vector, i.e., the input that drives the dynamics of the system;

$\boldsymbol{v}_k$ - is the measurement noise vector.

The purpose of the *SS* method is then to identify the state-space matrices $\boldsymbol{A}$ and $\boldsymbol{C}$, based on the measurements. Following a *Stochastic Subspace Covariance-Driven* approach, a *Single Value Decomposition* is applied to a *Toeplitz* output covariance matrix. Introducing a convenient splitting of the diagonal singular values matrix, the so-called *Observability* and *Controlability* matrices, whose product regenerates the *Toeplitz* covariance matrix, are identified, the matrices $\boldsymbol{A}$ and $\boldsymbol{C}$ being easily extracted from some of their internal blocks. Knowing matrices $\boldsymbol{A}$ and $\boldsymbol{C}$, the solution of an eigenvalue problem yields the natural frequencies, damping coefficients and the mode shapes estimates.

It's worth noting that an alternative *Data-Driven SS* aproach, involving the concepts of subspace projection and QR-factorization can be also used (Peeters, 2000).

5.4.3.3 Comparison of Output-Only SI methods

Having described the basis of the most relevant output-only *SI* methods, the main question that arises is naturally: - Which method leads to the best estimates in a specific application?

This problem was recently studied by Andersen *et al.* (1999), who applied several *SI* algorithms to the ambient vibration data from the tests on a Swiss highway bridge. The authors concluded that most of the employed *SI* algorithms (*Peak Peaking*, *Polyreference LSCE*, *ARMA* and *SS*) produced reasonable estimates of the natural frequencies and mode shapes, although only the later three methods led to comparable damping coefficients estimates.

An identical conclusion was extracted from the benchmark study of a 15-storey building structure organized in the context of the XVIII IMAC Conference by Ventura and Horyna (2000), in which the author participated (integrated in a team from the University of Porto (UP)) (Cunha *et al.*, 2000).

In effect, it was proven that the several methods employed yielded in general identical estimates of the natural frequencies and mode shapes, although the Peak Peaking technique revealed more difficulty in identifying closely spaced modes. It should be noticed that the remarkably good estimates obtained from the application of the *Peak Peaking* method by the UP team resulted in a great deal from the strategy of: (i) separating the bending and torsional components of the measured signals from simple operations on the time series; (ii) carefully

choosing the frequency resolution and number of averaging of the time series for determination of spectral estimates.

With regard to the damping estimates, a great dispersion was found among the estimates from the several participating teams, even when the same method was employed by two different teams. However, the application of the *FDD* and *SS* tecnhiques in similar conditions (Brincker *et al.*, 2000) could lead to rather similar estimates.

The major conclusion the author can take is then that *SS* methods are probably the most robust methods for output-only *SI*. However, the quality of the estimates obtained from the application of a specific method depends very much on the characteristics of the data and so a good practice may be the combination of several identification methods, whenever possible. Beyond that, the author's experience shows that the use of conventional *Peak Peaking* method can lead in general to very good estimates, provided that its application is made with appropriate physical sense.

With regard to the damping coefficients, the author considers that research should be incremented using the more robust *SS* methods, in the perspective of increasing the degree of confidence in the obtained estimates, although it is recognised that without a proper control of the test conditions (vibration levels, wind characteristics) the enormous dispersion of values will continue to be an evidence.

5.5 DYNAMIC TESTS ON THE VASCO DA GAMA CABLE-STAYED BRIDGE

The current Section presents a description of a series of tests and corresponding results obtained from the dynamic testing of the Vasco da Gama Bridge (Figure 5.41).



Figure 5.41. The Vasco da Gama cable-stayed bridge. General view.

Given the characteristics of the structure already described in Chapter two, and the high seismic risk of the Southern part of Portugal, where the bridge is located, extensive numerical and experimental studies were performed (Grillaud *et al.*, 1997; Branco *et al.*, 1998). The final dynamic reception tests were developed by a team from the University of Porto (UP), in which the author actively participated.

These tests had the purpose of identifying the most relevant dynamic parameters of the bridge for validation of the numerical model employed in the structural analysis at the design stage and, in particular, estimate the modal damping coefficients associated with the first torsional vibration mode, whose knowledge was of utmost importance for the evaluation of the response to the wind action.

Although an extension of about *5km* of Bridge was tested by the UP, only the procedures and main results from the tests on the cable-stayed bridge, presented in Figure 5.41, are discussed here.

The dynamic tests involved the following main components: (i) preliminary measurements for evaluation of the levels of acceleration and identification of an appropriate reference section; (ii) an ambient vibration test to identify global natural frequencies and mode shapes of the bridge, measuring the structural response at 58 different points along the deck and towers; (iii) the performance of response measurements during the passage of heavy trucks, passing over a wood plank, to increase the vertical accelerations; (iv) a free vibration test, based on the sudden release of a *60t* mass eccentrically suspended from the deck, in order to accurately identify modal damping factors; (v) dynamic measurements on stay cables in order to identify either global natural frequencies of the whole structure or local frequencies of the stay cables, using both conventional piezoelectric accelerometers and an interferometry laser sensor; (vi) experimental evaluation of dynamic amplification factors (DAFs) associated to the passage of heavy traffic at different speeds and along several lanes.

Starting with a brief presentation of the equipment employed in the dynamic tests, the main phases of the tests will then be described.

5.5.1 Instrumentation system

The testing equipment and procedure were defined considering the following main conditions: (i) the low values of the natural frequencies; (ii) the significant modal interference at the fundamental frequencies of vibration; (iii) the low level of vibrations; (iv) the very short time available for the performance of the dynamic tests.

In effect, and according to the numerical results provided by the contractor and confirmed in preliminary tests on the bridge, the lowest natural frequency was about *0.3Hz*, the most significant modes of the structure lying in the range *0.3Hz* to *1Hz*. These mode shapes were very closely spaced in frequency and thus a significant modal interference was expected.

Preliminary tests indicated also that the vibration level was very low, even for relatively strong winds, what required the use of very sensitive transducers for the performance of accurate measurements.

A final and also determinant condition was the availability of less than three weeks to test the main cable-stayed bridge and about *5km* of viaducts. This condition obliged to a very careful planning of the tests and motivated the use of a less conventional measurement and

acquisition system, essentially based on a set of *6* accelerographs that were programmed and synchronized from a laptop.

The list of equipment employed for the tests was as follows:

- *1* testing van;
- *1* pentium laptop *TOSHIBA*, model *460CDT*;
- *6* triaxial acceleropgraphs *GEOSYS*, model *GSR-16*;
- *3* uniaxial force-balance accelerometers *KINEMETRICS*, model *FBA-11*, and portable recorder *KINEMETRICS*, model *SSR-1;*
- *3* piezoelectric accelerometers *Brüel & Kjær*, model *4379S* and corresponding conditioning units;
- *4* piezoelectric accelerometers *PCB*, model *393C* and corresponding conditioning units;
- *1* Laser-doppler sensor *OMETRON*, model *VPI* system *A*;
- *1* propeller anemometer;
- *1* eight-channel spectral analyzer *HP*, model *3566A* connected to a PC *HP-VECTRA.*

Given the main characteristics of the structure, and knowing that force-balance accelerometers are probably the most adequate sensors for ambient vibration tests of large flexible bridges (see Section 5.3.2.2), it was decided to employ sensors of this type for the performance of the tests. So, both the accelerographs and the uniaxial *KINEMETRICS* accelerometers above listed are of the force-balance type.

With regard to the digitization, and considering the small levels of vibration, it is important that ambient vibration tests are performed using at least a *16-bit A/D* converter.

The choice of the accelerographs used for the performance of the main measurements along the bridge deck and tower considered the two above referred aspects and attempted, in addition, to avoid difficulties that are usually associated with the need of a large amount of electrical cable and cable connections. The synchronization, control and data transfer from the memory units installed in the accelerographs was made through the laptop. Because the dynamic range of the *FBA-11* accelerometers is higher than the corresponding to the accelerographs, three of these accelerometers were mounted additionally on a reference location and measured continuously in order to obtain high resolution spectral estimates at that location. Figure 5.42 shows five of the accelerographs, the force-balance accelerometers, the laptop, the recorder and a propeller anemometer mounted on the bridge parapet.

The performance of dynamic measurements on the stay cables involved the use of the piezoelectric accelerometers and also the Laser system above listed. Both types of sensors are well adequate for measurements on stay cables, since the level of oscillation of the stays is much higher than that of the deck and towers. The Laser sensor has a major advantage, which results from the fact that no contact with the structure is required, hence the time and

effort necessary for the attachment of sensors and electrical cables to the stay cables at a considerable height can be saved.

The piezoelectric sensors, the Laser sensor and the propeller anemometer were connected to the *HP*-spectral analyzer. Figure 5.43 shows the spectral analyzer and associated PC, and Figure 5.44 shows the *PCB* and *B&K* accelerometers and corresponding conditioning units. The mounting of an accelerometer on a stay cable is shown in Figure 5.30(a). Figure 5.30(b) illustrates the Laser sensor in operation for stay cable response measurement.

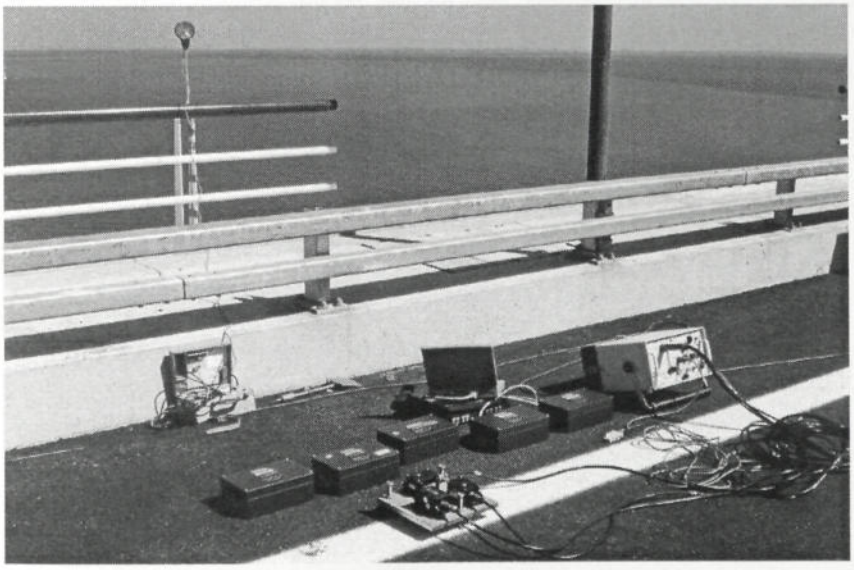


Figure 5.42. Some sensors employed in the instrumentation of the bridge deck and towers: *5 GSR-16* accelerographs, *3 FBA-11* accelerometers, recorder *SSR-1*, laptop and propeller anemometer.

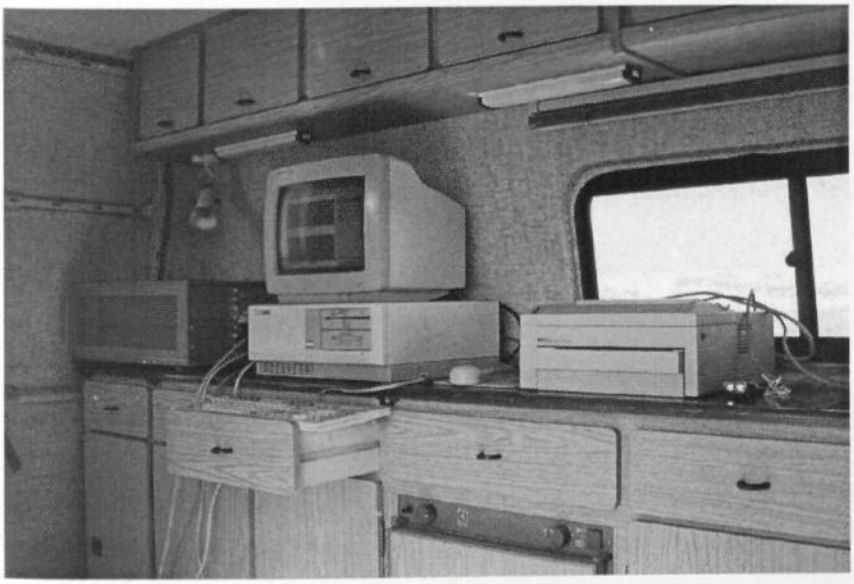


Figure 5.43. HP-3566A spectral analyzer in the testing van.

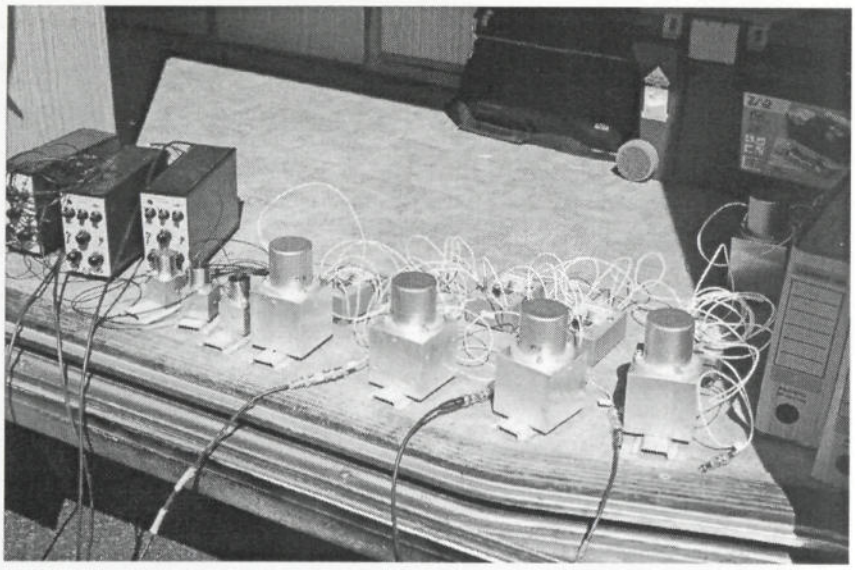


Figure 5.44. Piezoelectric accelerometers and associated conditioning units.

5.5.2 Ambient vibration test

5.5.2.1 Test procedure

The ambient vibration test was developed using the six accelerographs above referred according to the following scheme: two of the accelerographs were installed at a reference cross-section (section 10, at about 1/3 span North), while the other accelerographs were successively placed at 28 different mobile sections along the deck and towers (see Figure 5.45).

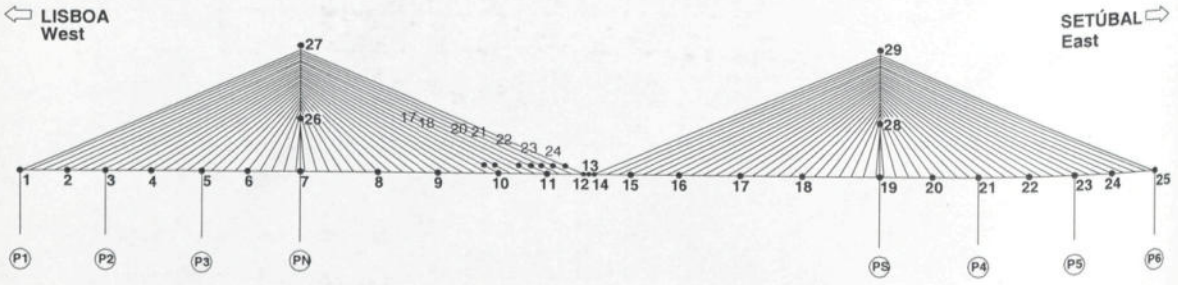


Figure 5.45. Schematic representation of the Vasco da Gama Bridge with indication of the measurement sections during the ambient vibration tests.

In all sections, the pairs of sensors were located laterally, upstream and downstream, always oriented according to the orthogonal referential X (longitudinal direction), Y (transversal) and Z (vertical) (Figure 5.17). These accelerographs were appropriately programmed before each sequence of measurements, in order to begin the acquisition simultaneously every twenty minutes, in principle. Taking into account the very low frequency

range of interest (*0-1Hz*), the time of acquisition for each setup was always *16* minutes, with a sampling frequency of *50Hz*, so as to obtain average spectral estimates with a frequency resolution inferior to *0.01Hz*. The time left to change the position of the accelerographs between successive setups was of *4* minutes, except for the case of measurements along the towers. A longer standby time between successive setups was programmed for these specfic measurements, due to the necessity of climbing the stairs till the top, transporting the accelerographs in rock-bags.

The *2Mb* of available memory for each accelerograph allowed for a maximum recording of *3* time series, i.e., about *48* minutes of sampling. It was then necessary to periodically download the data from the six accelerographs to the laptop and this was the lengthiest step of the measurements.

Due to the relatively low level of signal captured, appropriate amplification factors were used, leading to a precision superior to $0.015mg$ ($1g/2^{16}$), in consequence of the use of *16-bit A/D* converters. With the purpose of increasing the signal level in the vertical component, vibration measurements were also carried out during the passage of a heavy truck, with a mass of *30t*, over a timber plank *4cm* thick placed at *1/3* span (see Figure 5.46).

It is worth emphasizing that the measurement system used revealed to be quite practical and efficient, permitting the development of the whole ambient vibration test in *2.5* days. During this time the propeller anemometer above referred was employed for assessment of the average wind velocity, mounted at the bridge parapet by the midspan (Figure 5.42).



Figure 5.46. Loaded truck passing over a timber plank.

5.5.2.2 Levels of vibration

Before proceeding to the identification of modal parameters, preliminary analysis of the recorded time series was done in order to characterize the levels of response measured.

Tables 5.3 and 5.4 display the maximum and minimum, respectively, peak and root mean square values (r.m.s) of the response measured at the reference station *10*, expressed in terms of accelerations, velocities and displacements.

The considerable oscillation of the level of the response that can be observed in these tables results in a great deal from the variation of the wind speed, whose average value varied during the observation period in the range *1m/s* to *22m/s*. Figure 5.47 characterizes the correlation between the average velocity and direction of the wind at the midspan and the peak vertical response at the reference station *10*.

Table 5.3. Maximum peak and *r.m.s.* values of the response at reference station *10*.

Response	Acceleration (mg)			Velocity (mm/s)			Displacement (mm)		
	X	Y	Z	X	Y	Z	X	Y	Z
Peak	2.30	2.56	12.5	1.87	9.53	31.34	1.10	4.54	14.95
r.m.s.	0.13	0.35	1.69	0.30	1.43	5.62	0.19	0.73	2.38

Table 5.4. Minimum peak and *r.m.s.* values of the response at reference station *10*.

Response	Acceleration (mg)			Velocity (mm/s)			Displacement (mm)		
	X	Y	Z	X	Y	Z	X	Y	Z
Peak	0.19	0.20	0.36	0.30	0.20	0.54	0.16	0.19	0.18
r.m.s.	0.03	0.03	0.06	0.05	0.05	0.09	0.04	0.04	0.05

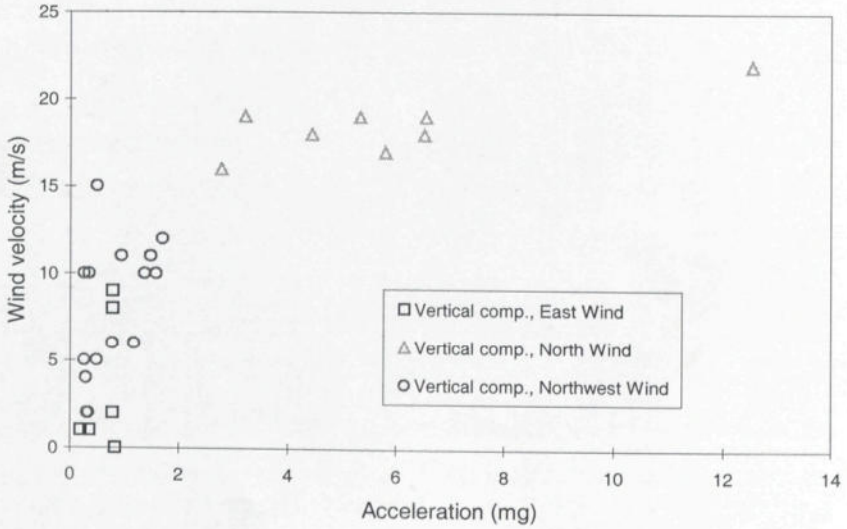


Figure 5.47. Correlation between the average wind speed at midspan and the peak vertical response at the reference station *10*.

Table 5.5 displays the maximum peak and *r.m.s.* values of the acceleration measured at some particular locations, and establishes the correspondence with the values measured simultaneously at the reference station.

Table 5.5. Maximum peak and r.m.s. values of the response at reference station *10*.

Location	Peak value (mg)			r.m.s. (mg)		
	X	Y	Z	X	Y	Z
10		1.11	6.74		0.126	0.655
13		0.93	5.57		0.115	0.663
10		1.30	6.71		0.187	1.29
16		1.36	7.16		0.200	1.37
10		0.90	2.30		0.050	0.131
27	1.75	2.58		0.128	0.072	
10		0.84	5.78		0.075	0.332
29	4.91	0.65		0.393	0.110	

5.5.2.3 Identification of natural frequencies

The identification of natural frequencies was based on the peak values of *Normalized Power Spectral Density* functions (*NPSD*) corresponding to the acceleration response at each section (downstream, upstream, half-sum and half-difference signals), as well as on the peak values of *Normalized Cross-Power Spectral Density* functions (*NCPSD*) relating the acceleration response at each section and at the reference section, and also on the coherence values associated to the simultaneous measurements at the several pairs of points (Felber,1993).

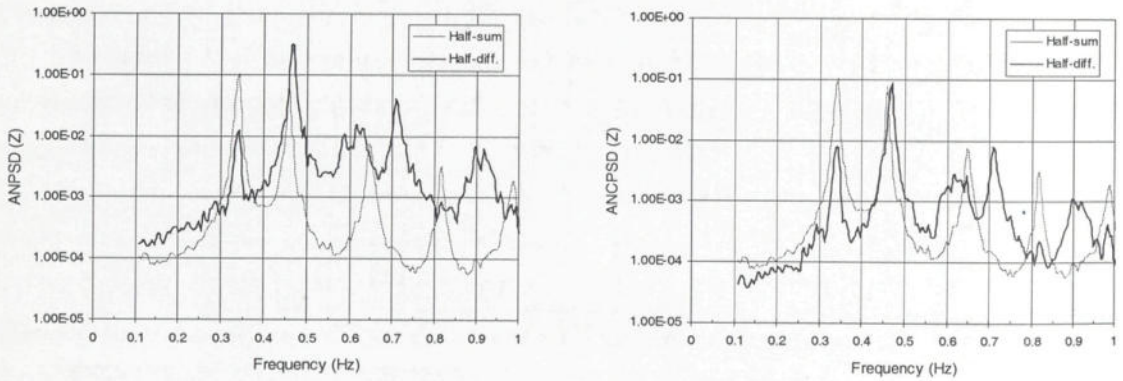
Each of the *NPSD* and *NCPSD* estimates was calculated based on the division of the 16-minute time records into *8* segments, with about *30%* overlapping. A linear trend removal was then applied to each segment, as well as a *Hanning* window. Finally the power spectral estimates were calculated using the *FFT* algorithm and then normalized in terms of the associated variance. The spectral resolution achieved with this procedure was of *0.006Hz*.

In order to better emphasize the natural frequencies to identify, the so-*called Averaged Normalized Power Spectral Density* (*ANPSD*) and *Averaged Normalized Cross-Power Spectral Density* (*ANCPSD*) function estimates were evaluated, obtained as the average of *NPSDs* and *NCPSDs*, respectively, associated with the measurements in *23* different sections, taking into account both the half-sum and the half-difference signals (upstream-downstream).

Figures 5.48 and 5.49 show the average normalised auto spectra (*ANPSD*) and cross-spectra (*ANCPSD*), corresponding to vertical (*Z*), transversal (*Y*) and longitudinal (*X*) acceleration components.

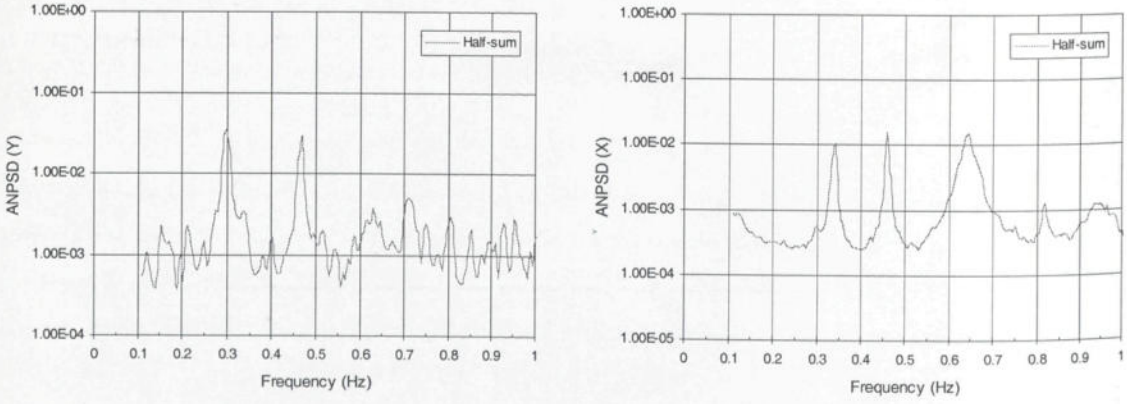
Figures 5.50 to 5.52 show the amplitudes and phases of *NCPSD* spectra and the corresponding coherence functions associated to simultaneous measurements at sections *10* and *16*, considering once more the separation of the bending and torsional components using

the half-sum and half-difference of the measured upstream-downstream signals, respectively, for the vertical components of motion.



(a) (b)

Figure 5.48. Average Normalized: (a) Power and; (b) Cross-Power Spectral Density functions associated to the vertical acceleration (half-sum and half-difference signals, upstream-downstream).



(a) (b)

Figure 5.49. Average Normalized Power Spectral Density functions associated to the: (a) transversal (*Y*) and; (b) longitudinal (*X*) acceleration components (half-sum signals, upstream-downstream).

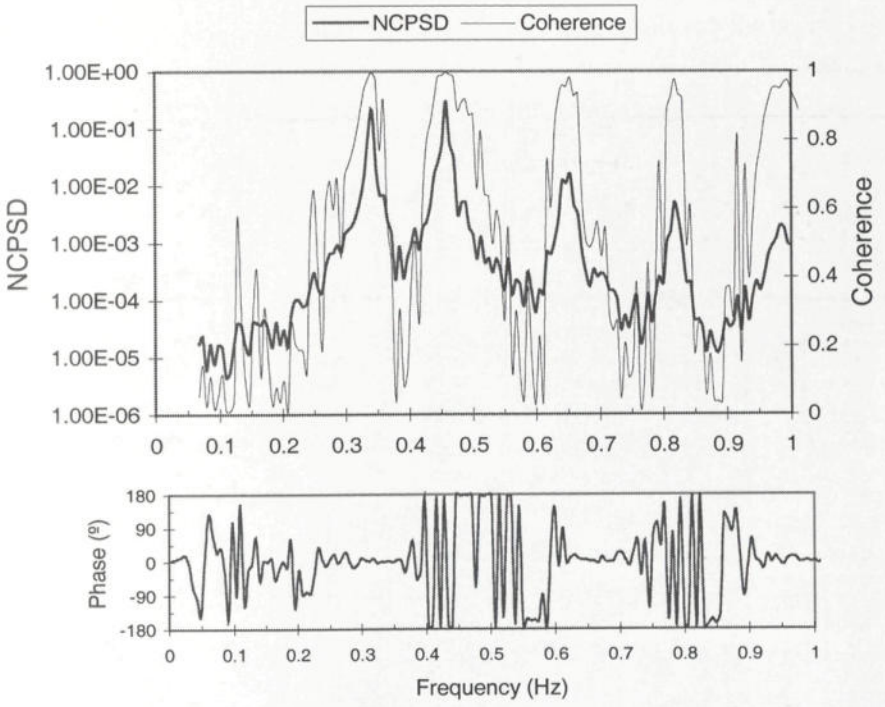


Figure 5.50. *NCPSD* (amplitude and phase) of the half-sum signal of vertical acceleration at sections *10* and *16*, and associated coherence.

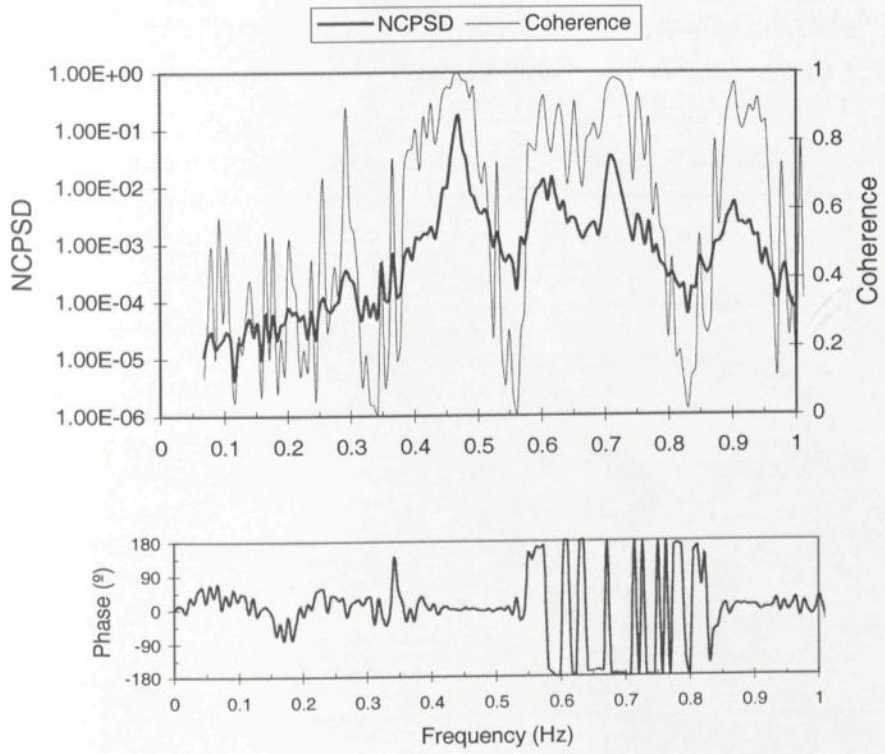


Figure 5.51. *NCPSD* (amplitude and phase) of the half-difference signal of vertical acceleration at sections *10* and *16*, and associated coherence.

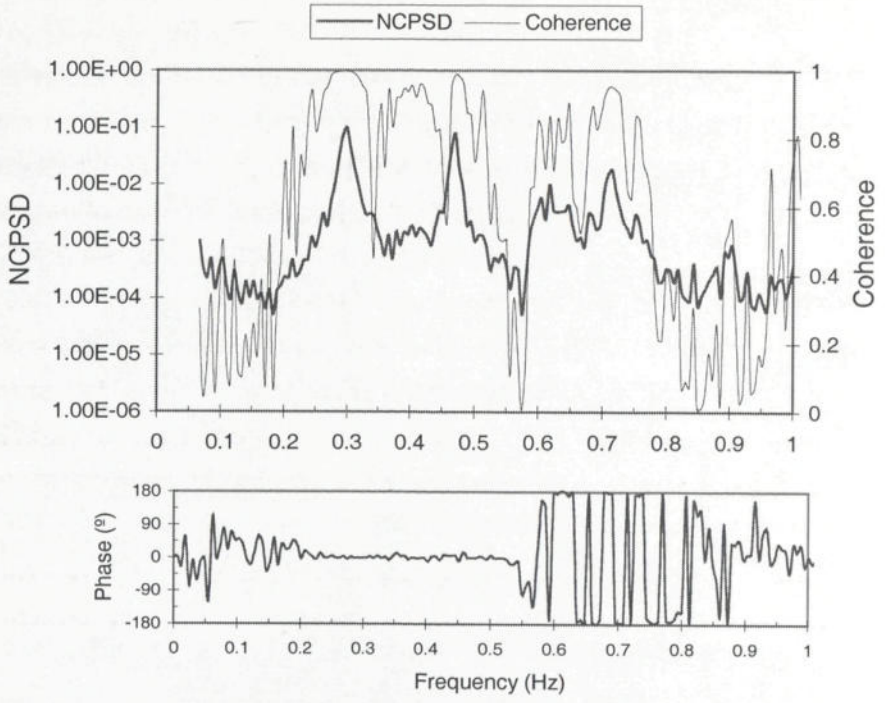


Figure 5.52. *NCPSD* (amplitude and phase) of the half-sum signal of transversal acceleration at sections *10* and *16*, and associated coherence.

Inspection of all the average spectral estimates obtained (Delgado *et al.*, 1998) permitted to identify the values of natural frequencies summarized in Table 5.6, in the range *0-1.15Hz*, in correspondence with the natural frequencies provided by the numerical model.

Table 5.6. Identified and calculated natural frequencies.

Calculated frequencies (Hz)	Identified Frequencies (Hz)	Type of mode of vibration
0.2624	0.298	1st transversal bending
0.3185	0.341	1st vertical bending
0.4287	0.437	2nd vertical bending
0.4386	0.471	1st torsion + transversal bending
0.6268	0.572*/0.590*/0.599*/0.619*/0.624*	2nd torsion + transversal bending
0.6077	0.651	3rd vertical bending
0.6268	0.693*/0.707*/0.718*/0.755*	2nd torsion + transversal bending
0.7600	0.817*	4th vertical bending
(**)	0.895*/0.917*	3rd torsion
(**)	0.985	5th vertical bending
(**)	1.129*	4th vertical bending

(*) – multiple modes, low signal level; (**) – uknown

5.5.2.4 Identification of modes of vibration

The identification of modes of vibration associated with the identified natural frequencies was based on the estimates of transfer functions (using estimator H_1) and corresponding coherences, relating the ambient response at the reference section (half-sum and half-difference signals, upstream-downstream) with the response at the other measurement sections along the deck and towers. The ratios between the values of those transfer functions related to each natural frequency (linear magnitude) associated to the several sections led to the absolute value of the modal components, the corresponding signal having been evaluated on the basis of the phase evolution, according to the procedure described in Section 5.4.3.1.

It should be noted that all the tasks related with the signal processing and identification of modal parameters were performed using software previously developed by the author (Caetano, 1992) and further developed in the context of the current tests.

Figure 5.53 shows some of the identified modal shapes of the deck, as well as the corresponding numerical modes and some modal components identified using the free vibration test that will be described in the next Section.

Figure 5.54 shows some of the identified modal components for the two sections along the towers, as well as the corresponding numerical components.

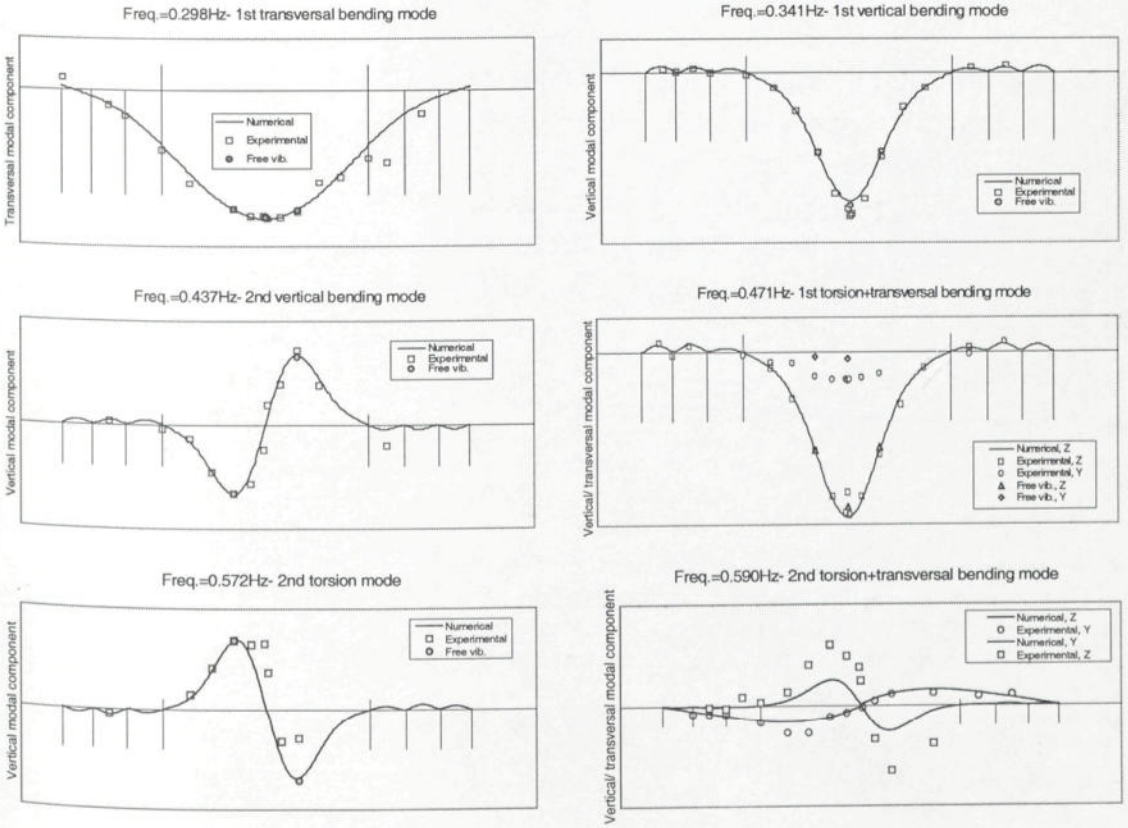


Figure 5.53 (a) Some modal shapes of the deck.

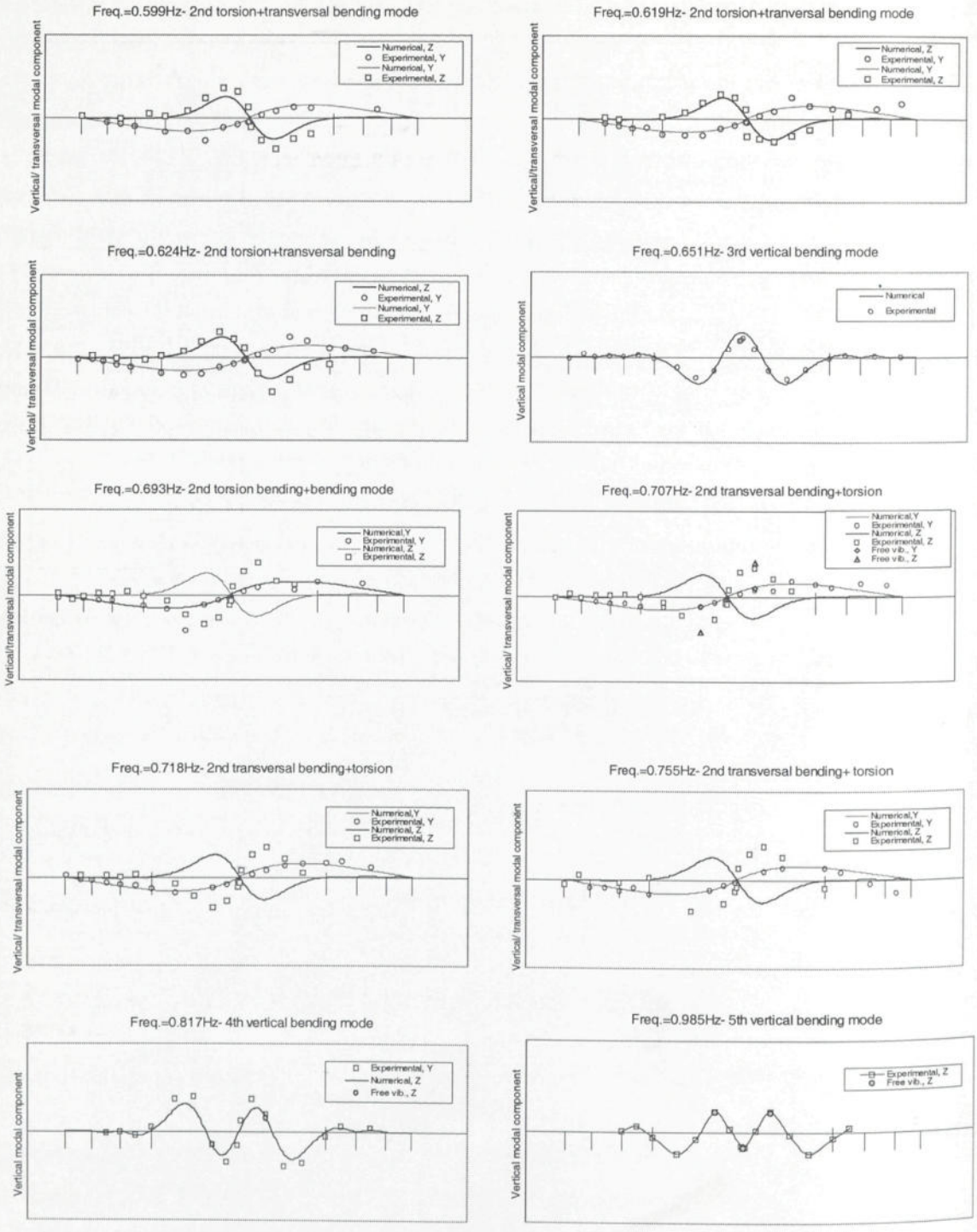


Figure 5.53 (b) Some modal shapes of the deck.

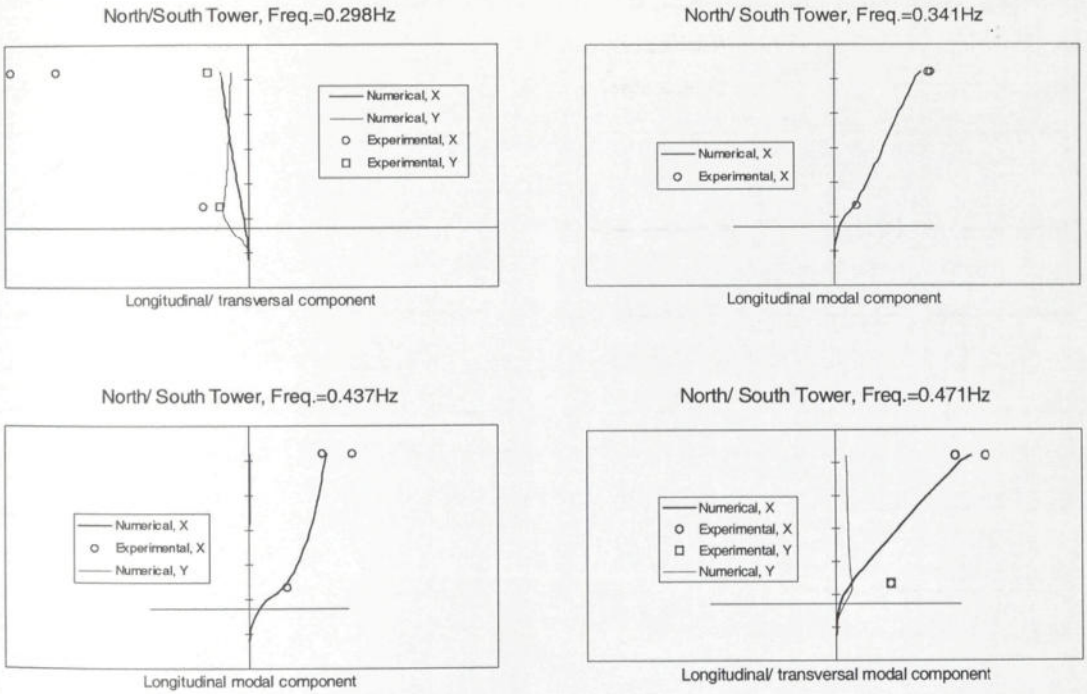


Figure 5.54. Some modal components along the towers.

5.5.3 Free vibration test

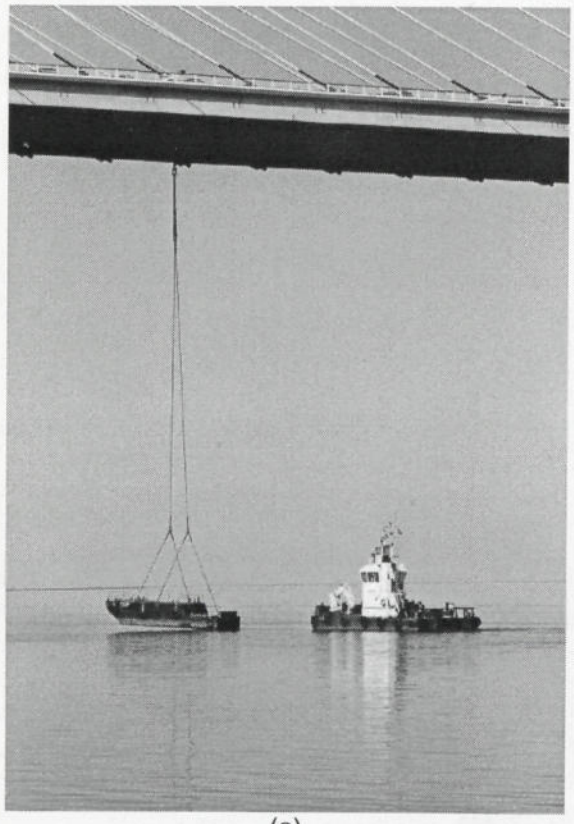
The free vibration test was performed with two main purposes: (i) to check the main results of the ambient vibration test previously developed, and (ii) to identify the damping factors associated with the fundamental modes of vibration. The last objective was however the essential motivation for the performance of this test, considering that the first torsional mode has a determinant contribution for the wind response of the bridge. In effect, given that the aerodynamic damping of torsional modes is null, the small amount of structural damping associated with this particular mode needed to be accurately evaluated.

5.5.3.1 Test procedure

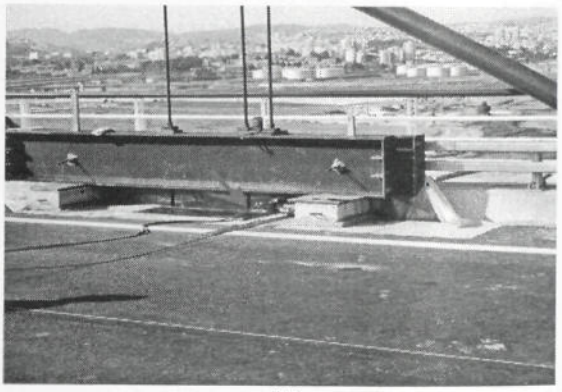
A barge weighting *60t* was attached at one point of the deck close to the section *1/3* span North, near the upstream border. The barge became suspended with the low tide (Figure 5.55(a)), and was subsequently released (Figure 5.55(c)) by cut of the suspension Dywidag bar at the deck level (Figure 5.55(b)). A vibratory phenomenon was then generated, which was recorded during *16* minutes by *6* triaxial accelerographs, located at the sections *1/3* and *1/2* span (upstream and downstream).

In order to verify that the wind would not affect the accuracy of evaluation of the structural modal damping factors, introducing a component of aerodynamic damping, it was necessary to perform the tests under low wind velocity. The wind speed was thus permanently

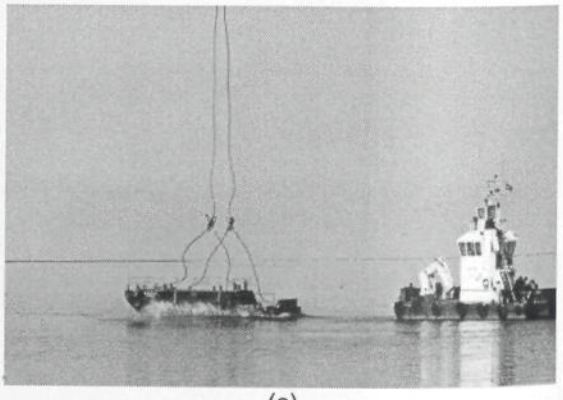
measured at midspan during the test, connecting the anemometer to a spectral analyzer. The maximum wind velocity did not in effect exceed *2.5m/s*.



(a)



(b)



(c)

Figure 5.55. Free vibration test: (a) Eccentrically suspended *60t* barge; (b) Starting cut of hanging Dywidag bar; (c) Release of barge.

Figure 5.56 presents two of the six time series recorded along the deck, as well as the wind speed record. These series are formed by *32768* points, sampled at *50Hz*, what corresponds to a total acquisition time of *655s*.

Figure 5.57 presents the displacement series associated with the records presented in Figure 5.56. These were obtained from the former by numerical integration.

The maximum displacements recorded during the free vibration test are synthesized in Table 5.7. As can be observed from this table, the maximum displacement occurred at the upstream *1/3* span stations, and was of about *25mm*.

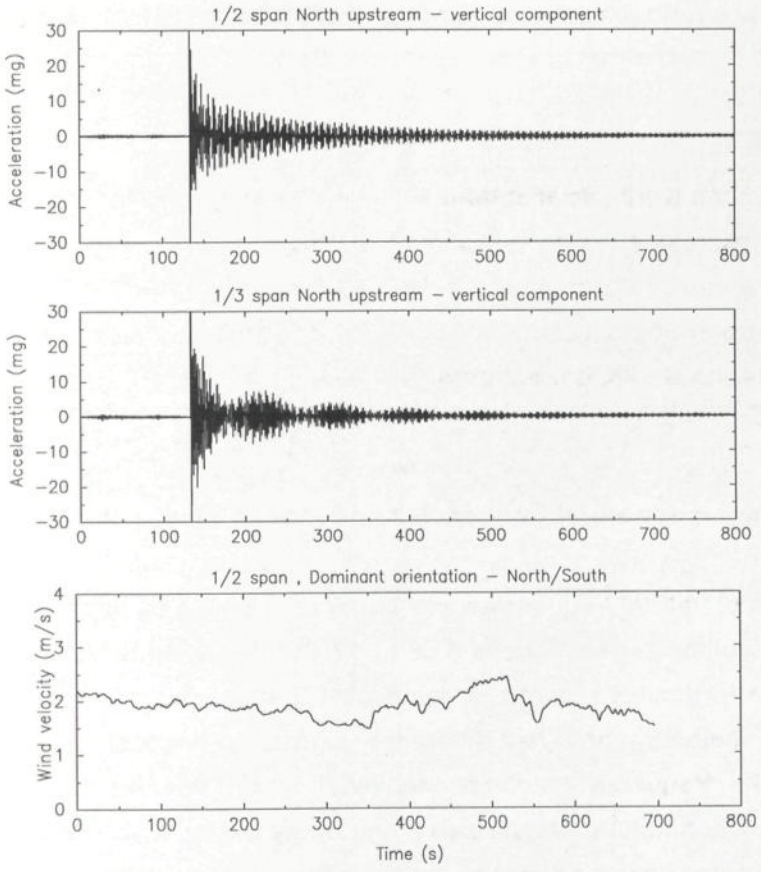


Figure 5.56. Vertical component of acceleration at *1/2* span (upstream) and at *1/3* span North (upstream) and temporal evolution of the wind speed at *1/2* span (upstream).

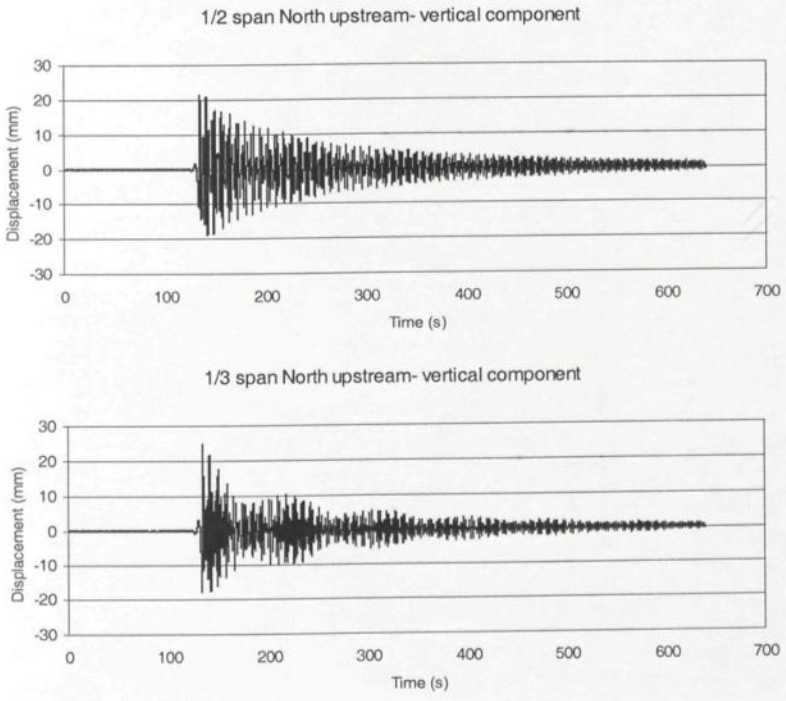


Figure 5.57. Vertical component of displacement at *1/2* span (upstream) and at *1/3* span North (upstream).

Table 5.7. Maximum displacement recorded during the free vibration test.

Station	Maximum displacement (mm)
1/3 span North, upstream	24.6
1/3 span North, downstream	14.7
1/2 span, upstream	21.5
1/2 span, downstream	19.6
1/3 span South, upstream	24.8
1/3 span South, downstream	20.9

5.5.3.2 Identification of natural frequencies and modes of vibration

The identification of natural frequencies was then made on the basis of the peaks of the *FFTs* of the acceleration time series. Figures 5.58 and 5.59 represent the *FFT* amplitudes obtained at two of the instrumented sections, located at *1/2* span and *1/3* span North, considering respectively the half-sum and half-difference signals of vertical acceleration (upstream-downstream). The frequency resolution achieved was *0.0015Hz*. Table 5.8 resumes the values of the identified natural frequencies in the range *0-1Hz*, which show a good agreement with the corresponding values obtained from the ambient vibration test (see Table 5.6).

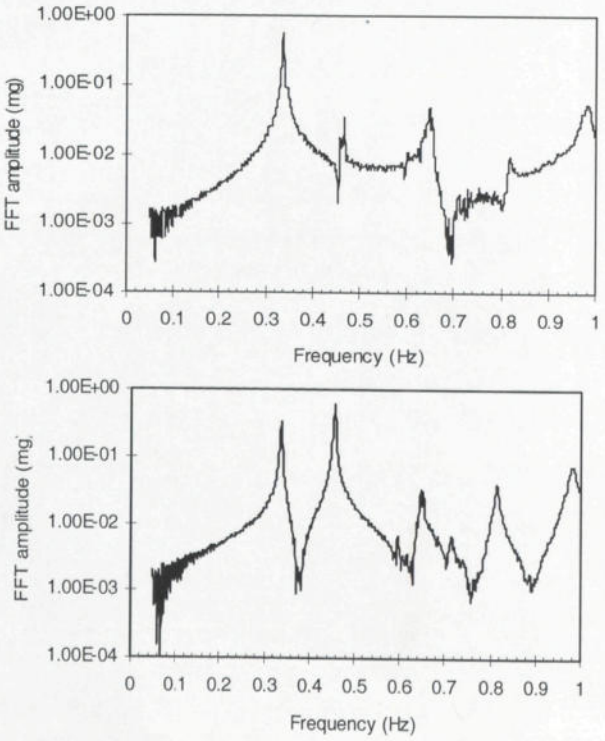


Figure 5.58. Amplitude of the *FFT* of the half-sum signal of vertical acceleration (upstream-downstream) at: (a) *1/2* span; (b) *1/3* span North.

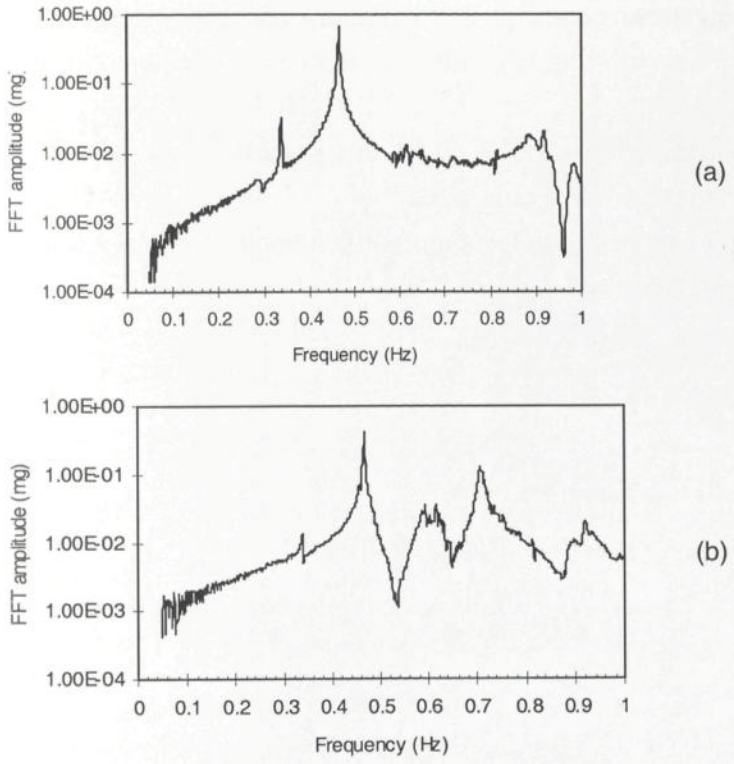


Figure 5.59. Amplitude of the FFT of the half-difference signal of vertical acceleration (upstream-downstream) at: (a) *1/2* span; (b) *1/3* span North.

Table 5.8. Natural frequencies identified from the free vibration test

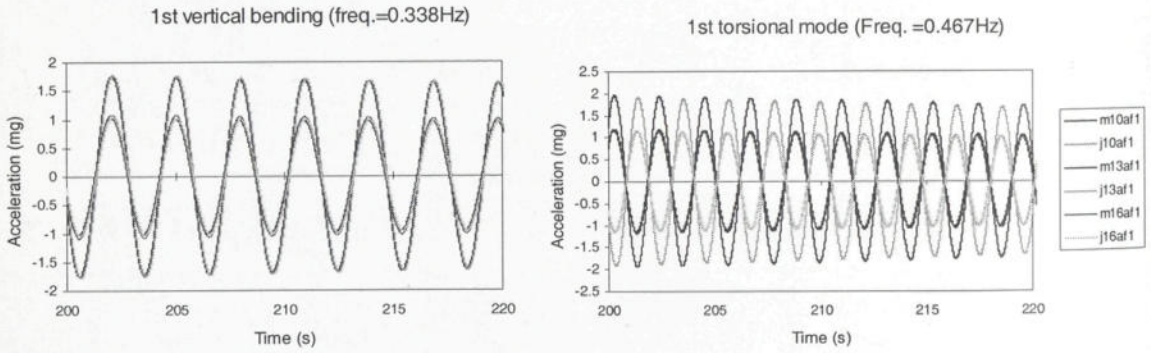
Identified frequencies (Hz)	Type of mode of vibration
0.295	1st transversal bending
0.338	1st vertical bending
0.456	2nd vertical bending
0.467	1st torsion + transversal bending
0.591*/0.62*	2nd torsion + transversal bending
0.647	3rd vertical bending
0.707*	2nd torsion + transversal bending
0.814	4th vertical bending
0.982	5th vertical bending

(*) – multiple modes, low signal level

The procedure adopted for the identification of the mode shapes consisted in the application of a band-pass Butterworth digital filter with *10* poles around each of the natural frequencies identified, followed by a comparison between the amplitudes and phases of the

filtered signals at different points of measurement. Figure 5.60 shows a superposition of filtered time series measured at the three-instrumented sections for two particular mode shapes.

The modal components identified by this procedure are also represented in Figure 5.54, together with the numerical and experimental components obtained from the ambient vibration test. It can be observed in this Figure that a good agreement with both types of modal components has been achieved.

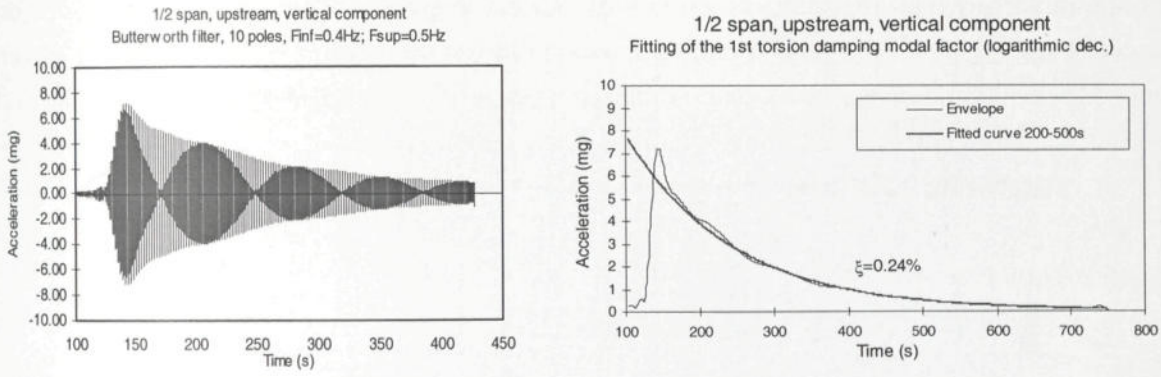


(a) (b)

Figure 5.60. Superposition of filtered signals for: (a) the *1st* vertical bending mode; (b) the *1st* torsional mode (m10af1- station *10*, upstream (up); j10af1- station *10*, downstream (dw); m13af1- station *13*, up; j13af1-station *13*, dw; m16af1- station *16*, up; j16af1- station *16*, dw).

5.5.3.3 Identification of modal damping factors

At last, the identification of the modal damping factors was done on the basis of the decay of the envelope of the filtered signals obtained applying also a band-pass *10* poles Butterworth digital filter around each natural frequency in the range *0-1.0Hz*. Figure 5.61 illustrates the procedure for the filtered vertical time series measured at *1/2* span upstream. The series was filtered with low and high cutoff frequencies of *0.4Hz* and *0.5Hz*, respectively, and an exponential function of the type $a(t) = Ue^{-\xi_i \omega_i t}$ was fitted to the resulting envelope, the parameter ξ_i being the damping factor to identify. As the estimates of the modal damping factors depend on the level of vibration, different exponential regressions were performed in correspondence with different time intervals of the free response. Table 5.9 shows the average estimates obtained, as well as the respective intervals of variation.



(a) (b)

Figure 5.61. Identification of the modal damping factor associated with the natural frequency *0.467Hz*. Analysis based on the measured response at *1/2* span upstream.

Table 5.9. Identified natural frequencies and modal damping factors from the free vibration test.

Identified natural frequency (Hz)	Modal damping factor (%)		Type of mode
	Mean value	Int. of variation	
0.295	1.23	0.87-1.73	1st transversal bending
0.338	0.21	0.16-0.40	1st vertical bending
0.456	0.23	0.19-0.27	2nd vertical bending
0.467	0.24	0.14-0.36	1st torsion + transversal bending
0.591	0.34	0.30-0.39	2nd torsion + transversal bending
0.647*	0.37		3rd vertical bending
0.653*	0.20		
0.707	0.78	0.71-1.12	2nd torsion + transversal bending
0.814	0.48	0.45-0.54	4th vertical bending
0.982	0.74	0.67-1.24	5th vertical bending

(*) – Multiple modes; identification based on the half-power bandwidth method due to the difficulty of application of digital filters

It is worth mentioning that, beyond the application of the logarithmic decrement method, the frequency domain *MDOF* identification algorithm *RFP* (*Rational Fraction Polynomial* method (Han and Wicks, 1989)) was still used, based on transfer functions relating the response measured at each point with the excitation. As the excitation was not actually measured when the mass of *60t* was suddenly released from the deck, the transfer functions were evaluated assuming the input as an impulsive load with unit magnitude, applied during a very short period of time, and hence characterized by a spectral content with an almost

constant intensity over the frequency range of interest. Figure 5.62 shows two of the transfer functions obtained following this procedure, as well as the corresponding synthesized transfer functions, evaluated on the basis of the modal parameters identified using the *RFP* algorithm.

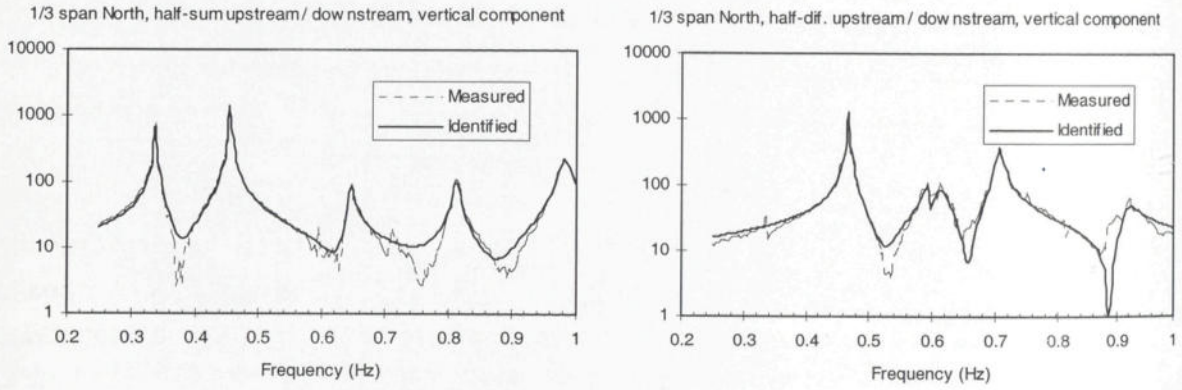


Figure 5.62. Identification of modal parameters using the *RFP* method. Measured and synthesized transfer functions.

5.5.4 Dynamic Measurements on Stay Cables

Dynamic measurements on stay cables are often required to assess different problems of great interest in the context of the design, construction and maintenance of cable-stayed bridges, such as: (i) the evaluation of cable tensions, whose knowledge is critical to the correct alignment and distribution of internal forces in the finished bridge, and whose change in time can provide interesting indications concerning the structural health; (ii) the evaluation of damping characteristics of damping devices installed close to the cable anchorages (iii) the assessment of fatigue problems in stay cables caused by long-term traffic loads; (iv) the evaluation of the level of importance of cable vibrations, that can occur due to vortex-shedding phenomena, parametric or rain-wind excitation, and that have affected the behaviour of several important cable-stayed bridges, as will be referred in Chapter 6; (v) the experimental identification of local and global natural frequencies, which may contribute to validate and update finite element numerical models used to simulate the dynamic behaviour of the bridge under wind or seismic loads.

The most common way of making such dynamic measurements is based on the use of accelerometers conveniently attached to the external cable surface, which involves a rather hard and tedious setup when dealing with the large number of stay cables, common in modern cable-stayed bridges. Therefore, in terms of practical applications, it is of utmost importance to develop and apply new measurement systems that enable systematic and accurate dynamic measurements on stay cables in a simple and comfortable way.

Under these circumstances, some measurements of vibrations in some of the longest cables of Vasco da Gama Bridge were also developed on the basis of the *OMETRON* laser Doppler velocimeter already described, in order to clarify the reliability and practical interest of this alternative measurement technique, which presents the remarkable advantage of avoiding

the direct contact with the structure. The dynamic measurements on stay cables were carried out simultaneously with piezoelectric accelerometers. The results obtained showed clearly that the use of this laser system provided an excellent accuracy in comparison with conventional accelerometers. Furthermore an enormous simplicity in terms of practical application could be also verified.

5.5.4.1 Instrumentation and setup

For the purpose of measuring vibrations in some of the longest stay cables, the accelerometers were screwed on small metallic cubes (Figure 5.44), conveniently attached to the external surface of the stay cables with the help of metallic belts. This relatively boring preparatory operation, only possible as the bridge was not open to the normal road traffic yet, was systematically repeated in all the stay cables observed, placing the accelerometers *5m* above the deck by means of a crane, and measuring vibrations in the vertical plane (Figure 5.30(a)). The use of the laser transducer became however incomparably easier, the only operation needed being the control of the position of the laser head, simply placed on the deck under each cable, in order to produce a laser beam hitting the cable surface at the section of application of the corresponding accelerometer (Figure 5.30(b)). Due to the significant inclination of the cables observed, the laser beam could be positioned vertically, and the output signal of the laser sensor was directly connected with a spectral analyzer. No special targets were used for the laser beam, in order to improve the signal to noise ratio. It is still worth noting that, although a distance of observation of *5m* has been used to permit a correct comparison of results with the accelerometer, larger distances of observation of the laser sensor, of the order of several tenths of meters, can be used without considerable loss of accuracy, as previously shown by Cunha *et al.* (1995).

5.5.4.2 Identification of natural frequencies

Figure 5.63 presents a direct comparison between the acceleration average power spectra associated to the ambient response of one of the longest stay cables of the bridge, obtained with simultaneous measurements at the same point on the basis of the two types of sensors mentioned, averaging over *16* records, using a frequency resolution of *0.0078Hz* and performing a digital differentiation of the laser velocity signal, using a *FFT* algorithm. This comparison shows the excellent agreement achieved in terms of the identification of the local natural frequencies of the cable, characterized by equally spaced well-pronounced peaks, and the lower noise level of the laser system. Moreover, some global natural frequencies of the bridge, corresponding to main peaks of the spectra in the range *0-1Hz*, are also apparent, though not so clearly in the case of the laser sensor, as this transducer measures the relative velocity between the deck and the stay cable. The same conclusion can also be drawn when

comparing the natural frequencies identified using the laser sensor with those obtained with conventional equipment in the free vibration test (Figure 5.64). In this last case, the peaks related to global natural frequencies are still more evident, due to the much higher level of global vibrations recorded during the free vibration test.

The values of the first *5* natural frequencies of the stay cable observed, identified on the basis of these spectra using the two measurement systems referred, are virtually coincident (*0.594, 1.180, 1.766, 2.367, 2.953Hz*), the only difference noted in one of the natural frequencies being equal to the frequency resolution (*0.0078Hz*).

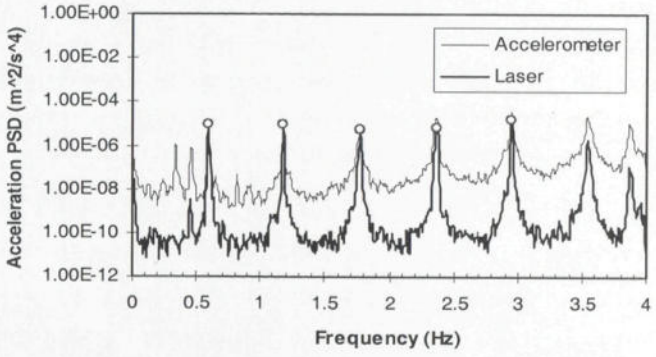


Figure 5.63. Comparison of acceleration average power spectra of the ambient response of a stay cable measured with a conventional accelerometer and a Laser sensor.

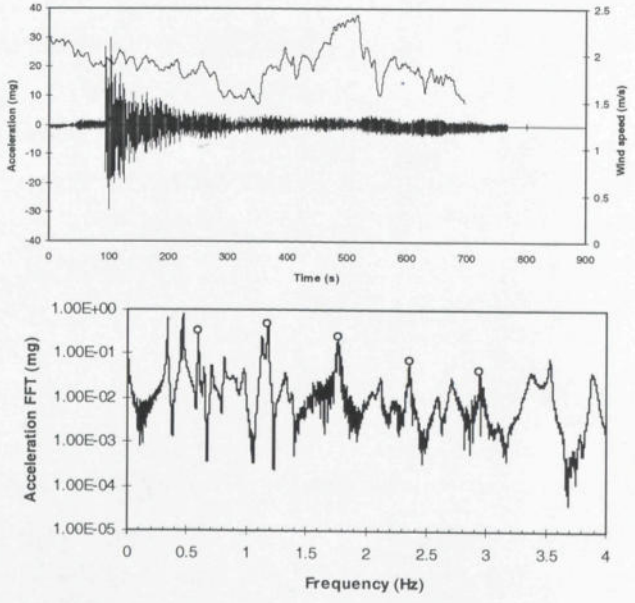


Figure 5.64. Response of the stay cable during the free vibration test of the bridge: (a) Cable response and wind speed at *1/2* span; (b) *FFT* of the cable response.

5.5.4.3 Evaluation of cable tensions

Several techniques can be employed to evaluate cable forces, namely measurement of the force in a tensioning jack, application of a ring load-cell, topographic measurements,

elongation of the cables during tension and installation of strain gauges in the strands. As referred by Casas (1994), in spite of their simple theoretical bases, each of these methods is complex in its practical application and, in some cases, the level of accuracy is insufficient.

A relatively simple and less expensive method to estimate cable tensions in cable-stayed bridges is based on the vibrating chord theory, taking into consideration the identified values of natural frequencies of the stay cables, which leads to the following relation:

$$T = \frac{4mf_n^2L^2}{n^2} \tag{5.77}$$

where T is the cable tension, f_n is the n_{th} natural frequency, L is the distance between fixed cable ends and m represents the mass of the cable per unit length.

This approach was applied in the evaluation of the tension installed in the seven instrumented stay cables (see Figure 5.45), employing the first five natural frequencies identified for each stay cable, which are summarized in Table 5.10.

Table 5.11 resumes the stay cable properties, as well as the estimates of the average tension measured on the seven stay cables, and the minimum and maximum design tensions.

It should be noted that the length L employed in equation (5.77) was taken as the chord length measured between the cable anchorages. It is known actually that the points of the cable with null displacement are located somewhere between the anchorages and the cable dampers, which are located within *10m* from the former. So, the evaluated cable tensions are expected to be lower than the real tensions installed in the cables, the error in the estimation being however inferior to *10%*. This aspect is in fact the largest inconvenience of tension evaluation through vibration measurements. In order to reduce the margin of error of the tension estimation, a calibration of the installed tension could have been performed, making the vibration measurements during the operation of cable tension, and comparing the tension measured by load cells with the tension estimated from vibrating chord theory.

Table 5.10. Natural frequencies identified on the stay cables.

Stay	HNC24U	HNC23U	HNC22U	HNC21U	HNC20U	HNC18U	HNC17U
1st Freq.(Hz)	0.609	0.594	0.633	0.648	0.664		0.766
2nd Freq.(Hz)	1.211	1.172	1.25	1.289	1.312	1.539	1.523
3rd Freq.(Hz)	1.812	1.773	1.867	1.938	1.977	2.312	2.289
4th Freq.(Hz)	2.414	2.359	2.492	2.578	2.633	3.078	3.047
5th Freq.(Hz)	3.031	2.945	3.117	3.227	3.289	3.844	3.797

Table 5.11. Stay cables properties and estimated installed tension.

Stay	HNC24U	HNC23U	HNC22U	HNC21U	HNC20U	HNC18U	HNC17U
m(kg/ml)	96.9	96.9	90.2	90.2	90.2	80.9	80.9
*L(m)**	223.77	214.97	206.18	197.42	188.68	171.3	.66
Average estimated tension (kN)	**7119.0**	**6234.2**	**5998.2**	**5862.5**	**5578.4**	**5624.4**	**4975.8**
Minimum design tension (kN)	7336.5	6823.5	6009.5	5687	5372	5193	5153
Maximum design tension (kN)	7501	6959.5	6171	5821	5496	5243.5	5186.5

5.5.5 Conclusions

The dynamic tests above described permitted the creation of a quite large data base and provided the UP team a unique opportunity to apply and enhance the experience and knowledge acquired during the many years of dedication to the application of experimental techniques in Civil Engineering structures. The main conclusions extracted from the processed data can be listed as follows:

- The measurement system used in the ambient and free vibration tests, based on the use of independent triaxial accelerographs conveniently programmed and synchronized by a laptop, revealed to be a very efficient and comfortable solution, avoiding the use of several hundred meters of electric cables and permitting the integral data acquisition within a relatively short period of time;
- The ambient vibration test provided a very accurate estimate of natural frequencies and mode shapes, despite the rather low level of signal captured (between 0.36 and 12.5mg of maximum vertical acceleration at the reference section in the several records), the low range of natural frequencies of interest (*0-1Hz*) and the relatively high number of modes of vibration in that range;
- The free vibration test, based on the sudden release of a *60t* mass suspended from the deck, seemed to be quite useful as a complementary test that permitted not only to check the previous identification of natural frequencies and mode shapes, but essentially the very accurate identification of modal damping factors, whose knowledge is particularly relevant in terms of the study of the aerodynamic stability of the bridge;
- There is, in general, a very good correlation between modal parameters identified and the corresponding parameters calculated on the basis of the *3D*-finite element model developed at the design stage, though some small differences can be found, as it is the

case of the multiple modes identified associated to the *2nd* torsion + transversal bending numerical mode, related with local stay cable frequencies, or of the 3rd torsion mode, in which no transversal bending component was experimentally detected;

- Although no force measurement has been performed during the free vibration test, a standard MDOF identification algorithm (*RFP – Rational Fraction Polynomial* method) in the frequency domain could be applied with success, assuming the input as an impulsive load, with unit magnitude, acting during a very short period of time, leading to a spectral content of the excitation with an almost constant intensity over the frequency range of interest;
- The application of a laser Doppler velocity transducer revealed to be a rather accurate and easy to use non-contact vibration measurement technique, particularly appropriate to perform dynamic measurements in stay cables of cable-stayed bridges. In effect, the use of this sensor provided a powerful form of systematic and accurate evaluation of natural frequencies and cable tensions, which is a factor of significant importance, in particular, in terms of the long term health monitoring of this type of bridges.

5.6 SUMMARY

This Chapter covered the main issues associated with the experimental identification of the dynamic behaviour of cable-stayed bridges.

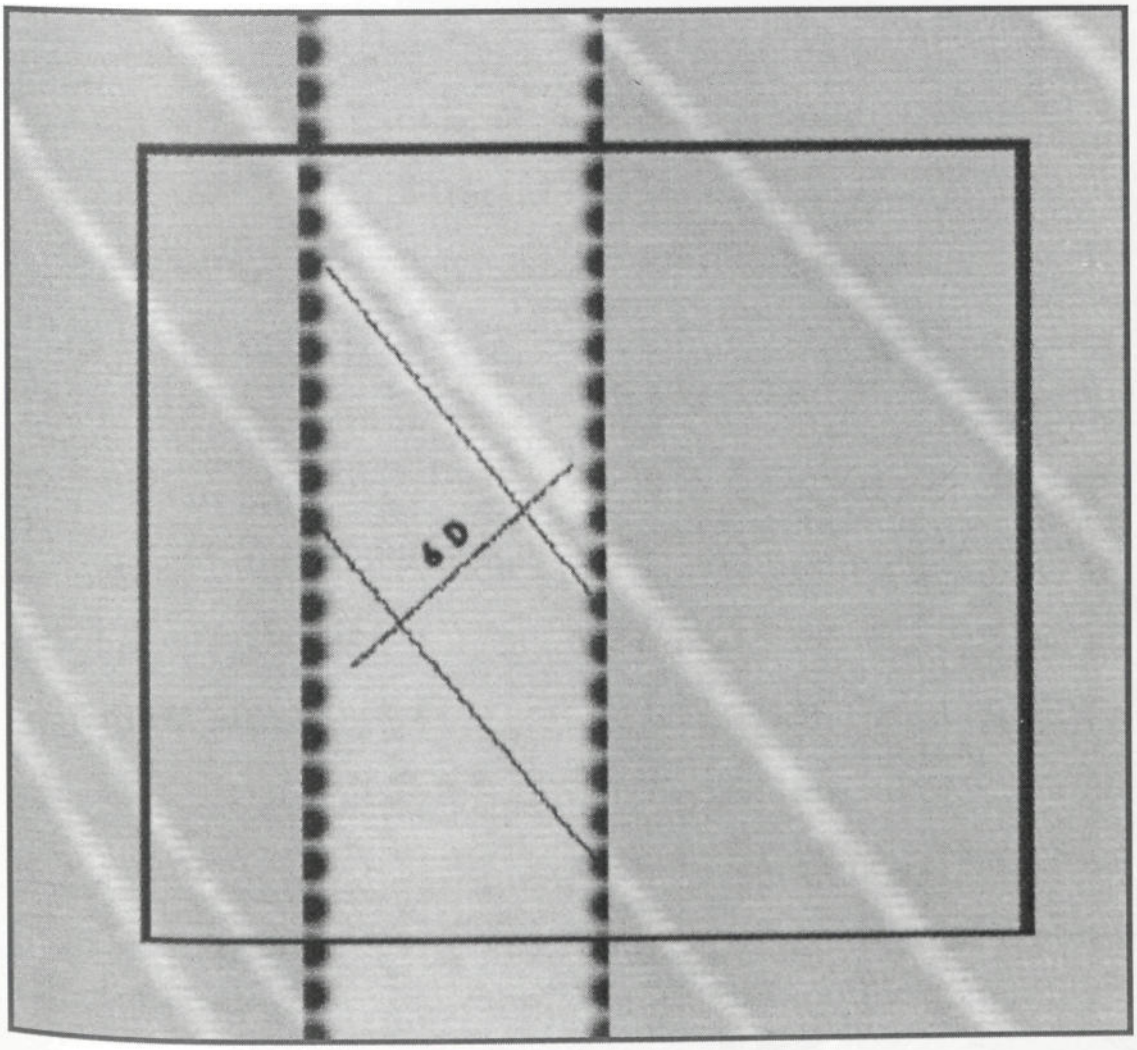
Starting with a brief presentation of the current state-of-the-art in dynamic testing of cable-supported bridges, the current trends in instrumentation systems were then reviewed, in the perspective of testing large bridges. The review comprehended excitation devices and sensors, and emphasized particular advantages and potential interest in the use of non-conventional sensors.

A survey on the numerous existing system identification techniques was subsequently presented. These methods were classified according to diverse parameters and the fundamentals of some of the most widely used techniques were described, considering both the cases of input-output and output-only identification methods.

The final Section of the Chapter was dedicated to the presentation of the methodology and main results obtained during a campaign of dynamic observation of the Vasco da Gama Bridge.

CHAPTER 6

CABLE VIBRATIONS



CHAPTER SIX

CABLE VIBRATIONS

6.1 GENERAL

Brotonne Bridge, France, October 1976: End of construction. On a rainy day, with winds of about *15m/s* blowing athwart at *20°* to *30°* with regard to the longitudinal axis of the bridge, important vibrations of the stays up to the third mode were observed (Wianecki, 1979). The oscillations were so large, that the longest cables, which were almost parallel and *1957mm* apart at the centre shocked against one another (Stiemer *et al.*, 1988). For higher wind velocities, the vibrations decreased down to zero. Each time, the oscillations lasted for about *30* minutes. The problem was solved after installation of dampers near the lower socket of all the cables.

Farø Bridge, Denmark, 1985: Both during and after construction, stay cable vibrations occurred, with a maximum amplitude of about *1.5m*. These oscillations were attributed both to the motion of the anchorages and to rain vibrations (Langsoe & Larsen, 1987). By interconnecting the stays with steel wires, the problem was minimized. However, after about four years of service, the first wire in the interconnecting system ruptured. A more robust design for the connecting wires was then devised, which suffered identical problems after seven years of service, requiring further improvement. In addition to this measure, the stay cables were spirally wrapped with a *16mm* polyethylene duct, what proved to reduce the vibrations to an acceptable level (Bloomstine & Stoltzner, 1999).

Ben-Ahin Bridge, Belgium, March 1988: For a period of about three hours, nine to ten of the stay cables vibrated at a peak-to-peak amplitude of about *1m*. A slight vibration was observed on the deck. At the time of occurrence of vibrations, the mean wind speed was about *10m/s*, the wind direction was almost constant with an angle of incidence of about *50°* to the longitudinal axis of the bridge, and there was drizzle. The vibrations stopped when the wind direction changed (Dumortier, 1990). As a remedial measure, the cables were interconnected with steel wire.

Erasmus Bridge, Netherlands, November 1996: Less than two months after its opening, the stay cables vibrated heavily, the bridge deck also oscillating significantly. The bridge was temporarily closed to the traffic as a safety measure. The weather conditions at the time were characterized by a mean wind speed of about *14m/s* and rain. As soon as the rain stopped, the vibrations disappeared (Geurts *et. al.*, 1998). As in the previous case, interconnecting cables were employed to restrain cable vibrations.

Guazú Bridge, Argentina, November 1996: A stay cable broke. The Guazú Bridge is one of the two almost identical Zárate-Brazo Largo Bridges in Argentina, with a main span of *300m* and carrying combined highway and railway traffic. After inspection, it was concluded that a combination of corrosion and fatigue was in the origin of the failure. Fatigue, in particular, was considered to take place, not only as a consequence of larger traffic loads than accounted for in the original design that was almost *20* years older, but also due to large amplitude cable vibrations (Andersen *et al.*, 1999). In effect, significant cable vibrations of a number of cables had been previously observed, indicating from visual inspection amplitudes of about *1m*. This was consistent, according to Andersen and companion authors (1999), with the pressure marks in the PE pipes close to the anchorages. These vibrations were attributed to large motion of the bridge deck at certain wind speeds (*10m/s* to *20m/s*) and directions (vertical component angles of attack in the range *2.5°* to *5°*).

The examples presented above are only a few amongst many cases of reported and non-reported problems of stay cable vibrations in cable-stayed bridges all over the world.

Cables are in effect very flexible elements, which additionally are characterized by a very low damping. Their proneness to vibration is thus a major aspect in the study of cable supported structures and particularly of cable-stayed bridges. Considering the typical natural frequencies of stay cables, which are, for the fundamental mode, in the range *0.3Hz* to *3Hz*, it is evident that during their lifetime an enormous quantity of cycles of tension variation will occur. When the amplitudes of oscillation are significant, the degradation of the cable properties is accelerated, as happened in the Guazú Bridge above referred.

The main causes of cable vibration can be divided into two main groups: *direct* and *indirect* actions on the cables. The first encloses essentially the effects of wind and/or rain

action, namely the *vortex-shedding*, *galloping*, *wake interference* and *rain-wind induced vibrations*. As for *indirect* actions, they include all the excitations that can originate the motion of the cable anchorages associated to a global motion of the structure (e.g. wind, pedestrian actions, traffic or earthquakes), and that can indirectly induce particularly large vibrations in the cables. This phenomenon is commonly designated as *parametric* excitation, and incorporates two types of components, one comprehending cable vibrations motivated by harmonic motion of the supports in the direction perpendicular to the cable chord, and the second respecting to cable vibrations motivated by harmonic motion of the supports in the longitudinal direction.

All the above referred topics have been traditionally analysed considering the stay cables isolated from the rest of the structure. Several authors however stressed the importance of evaluating a possible dynamic interaction between the cable and the bridge structure, topic here defined as *cable-structure interaction*.

This Chapter attempts to present an extensive state-of-art of the phenomenon of cable vibration in cable-stayed bridges, including a component developed by the author on the topics of *parametric excitation* and *cable-structure interaction*.

Starting with the *direct excitation* of stay cables by wind and rain, the phenomena of *vortex-shedding*, *galloping*, *wake interference* and *combined action of wind and rain* are described and illustrated with examples of particular problems of cable vibration reported in the literature.

For the case of *vortex-shedding*, empirical formulae specified by *EC1* and based on the vortex resonance model are presented for estimation of maximum amplitude of cable oscillations.

With regard to the phenomenon of *galloping*, the Glauert-Den Hartog criterion for incipient galloping instability is presented, evidencing the possibility of occurrence of this type of instability for non-circular cross sections.

Wake interference phenomena are then described, emphasizing the possibility of occurrence of *galloping / interference galloping* for associations of cables. Simple formulae specified by *EC1* for the evaluation of critical wind velocities are presented for each case.

As for the combined action of *rain and wind*, a complex phenomenon that was only identified in 1986 for cable-stayed bridges, a full description of the main characteristics and conditions of occurrence of vibration are presented, and an analytical model developed to describe the corresponding main features, based on a modified galloping mechanism, is presented.

With regard to the *indirect excitation* of the stays, both perpendicular and longitudinal excitations on a horizontal stay cable are investigated. The nonlinear differential equation of motion is characterized in both cases by quadratic and cubic terms, which are responsible by the existence of secondary resonances. For the particular case of vibration motivated by motion of the anchorage in the direction perpendicular to the chord of a taut cable, here designated as *external excitation*, a nonlinear differential equation with non-zero second

member is obtained, for which the fundamental resonance is the most critical. In the case of *parametric excitation*, the nonlinear differential equation of motion is the equation of a parametrically excited system, i.e. a system characterized by a sinusoidal term in the stiffness coefficient and null second member. For this system, the second resonance, called the principal parametric resonance, is the most critical.

Considering these two fundamental resonances, and based on mathematical solutions of differential equations of each type, the author develops expressions for the following results:

- the threshold amplitude of support oscillations for the occurrence of instability;
- the maximum steady-state amplitude of oscillation at resonance;
- the maximum increment of cable tension in steady-state vibration.

A numerical analysis of a medium size stay cable (a cable from the Ben-Ahin Bridge), is then performed for different amplitudes of support *external / parametric excitation*, based on the finite element software SOLVIA (1995). The numerical results are compared with the values obtained from the application of the above described formulae.

The final topic of *cable-structure interaction* is introduced with a state-of-art of the research. A small numerical example is then presented, comprehending the analysis of the above referred stay cable when connected to a mass-spring system with properties equivalent to the modal properties of a bridge at fundamental / parametric resonance, in order to stress the importance of considering the effect of dynamic interaction with the bridge.

6.2 DIRECT EXCITATION BY WIND AND RAIN

Wind is one of the most severe actions in the design of a cable-stayed bridge and particularly in the design of the stay cables, which suffer both from direct excitation along the surface and from indirect action on the deck and towers, by oscillation at the supports. In this Section, the main phenomena associated with direct actuation of the wind are analysed, namely the *vortex shedding*, *galloping*, *wake interference* and *rain-wind induced vibrations*, the issue of indirect action by wind and other sources being discussed in Section 6.3.

As referred in Chapter four, the action of wind can be divided into a static component, associated with the mean wind speed, and a dynamic part, related with the atmospheric turbulence. Only the later component will be addressed in this Section. It should however be noted that the shape of the cross section affects significantly the drag and lift forces associated with the static component of wind. Considering that the wind load on the stays can be close or even more than *50%* of the total transverse loads on the bridge structure (Virlogeux, 1992), the choice of the cable cross section becomes a matter of utmost importance. Wind tunnel tests have shown in particular that the drag coefficient C_D for

bunches of auto-protected cables arranged in an hexagonal cross-section (Figure 6.1) attain values of *1.2*, while for the cross-section achieved by encasing the cables in circular ducts made of high density polyethylene, C_D does not exceed normally *0.7* (Virlogeux, 1992). For this reason, and also for additional advantages in terms of corrosion protection and wind stability, only the circular cross section will be considered in the geometric definition of the stay cables.

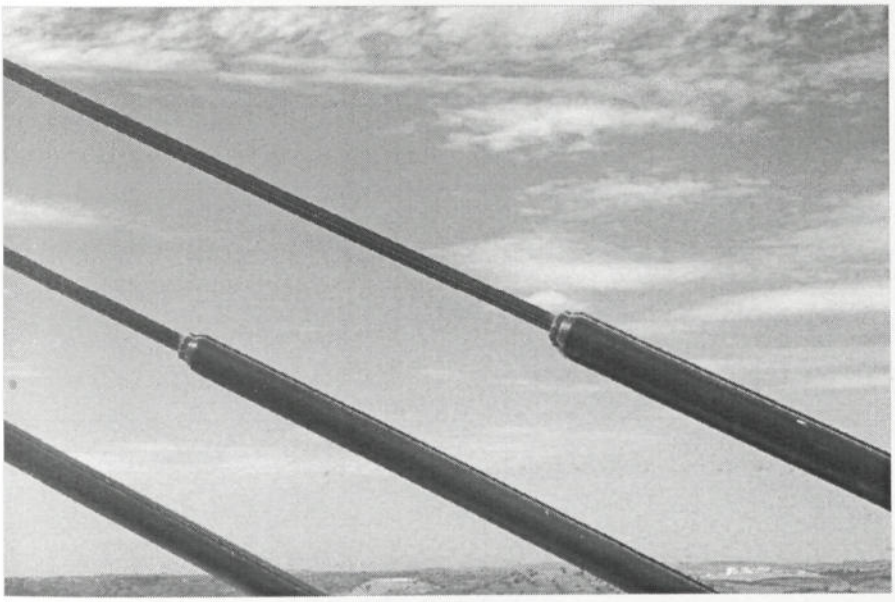


Figure 6.1. Bunches of auto-protected cables arranged in hexagonal cross-section.

6.2.1 Vortex shedding

The *vortex shedding* is a phenomenon of turbulence provoked by a structure, designated as a *bluff body*, when immersed in a flow.

Consider a two-dimensional smooth flow around the circular cylinder presented in Figure 6.2 (Simiu & Scanlan, 1996). The characteristic of the flow around the bluff body is governed by a nondimensional parameter, the Reynolds number ***Re***, that expresses the relative magnitude between the two most important effects present in the flow, associated with inertial and viscous forces, being defined by

$$\boldsymbol{Re} = \frac{UD}{\nu} \tag{6.1}$$

The symbol U in equation (6.1) represents the uniform wind velocity, D is a representative length of the body, and ν is the kinematic viscosity of the air, whose value is $0.15cm^2/s$ at $20^\circ C$.

At low Reynolds number (***Re*** $\approx$ *1*), the viscosity forces are dominant in the flow. So, according to Figure 6.2(a), the flow around a cylinder remains attached to the cylinder throughout its complete periphery. By increasing the velocity of the flow, the Reynolds number increases. At ***Re*** $\approx$ *20* the flow separates, creating two symmetrical vortices that reside near the downstream surface of the cylinder (Figure 6.2(b)). At an increased Reynolds number of *30*, the symmetrical vortices are broken and replaced by cyclic alternating vortices that form by term at the top and bottom surfaces and are swept downstream to form a vortex trail, defined as the *Von Karman vortex trail* (Figure 6.2 (c)). Figure 6.3 presents a visualization of the phenomenon by emission of dye from the cylinder immersed in a water tunnel (Simiu & Scanlan, 1996).

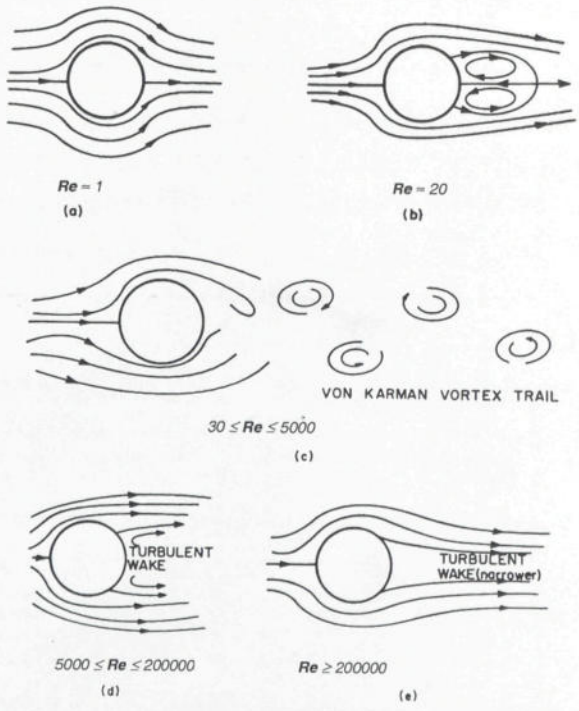


Figure 6.2. Flow past circular cylinder: (a) at ***Re*** $\approx$ *1;* (b) ***Re*** $\approx$ *20;* (c) *30* $\leq$ ***Re*** $\leq$ *5000;* (d) *5000* $\leq$ ***Re*** $\leq$ *200000;* (e) ***Re*** $\geq$ *200000* (Simiu & Scanlan, 1996).



Figure 6.3. Vortex trail for a circular cylinder immersed in a water tank (Simiu & Scanlan, 1996).

As the Reynolds number increases into the range $5000 \leq \boldsymbol{Re} \leq 200000$, the attached flow upstream of the separation point remains laminar, while transition to turbulent flow occurs in the wake (Figure 6.2 (d)), further downstream from the cylinder for the smaller ***Re*** number, and closer to the cylinder surface for the higher ***Re***. Finally, for very large ***Re*** number, i.e., $\boldsymbol{Re} \geq 200000$, the wake narrows (Figure 6.2 (e)).

The cyclic formation of vortices can be described by the *Strouhal number* ***S***, a nondimensional parameter defined as

$$\boldsymbol{S} = \frac{N_S D}{U} \tag{6.2}$$

where N_S is the frequency of full cycles of *vortex-shedding* and D is a characteristic dimension of the body projected on a plane normal to the mean flow velocity.

The Strouhal number ***S*** depends upon the cross section shape and is approximately constant with the Reynolds number for a wide range of ***Re***, as can be observed in Figure 6.4, that resumes measurements on circular cylinders for different values of the roughness *k/D* (Shi *et al.*, 1993). For practical applications, a constant value of ***S*** of *0.2* can be considered for circular cylinders.

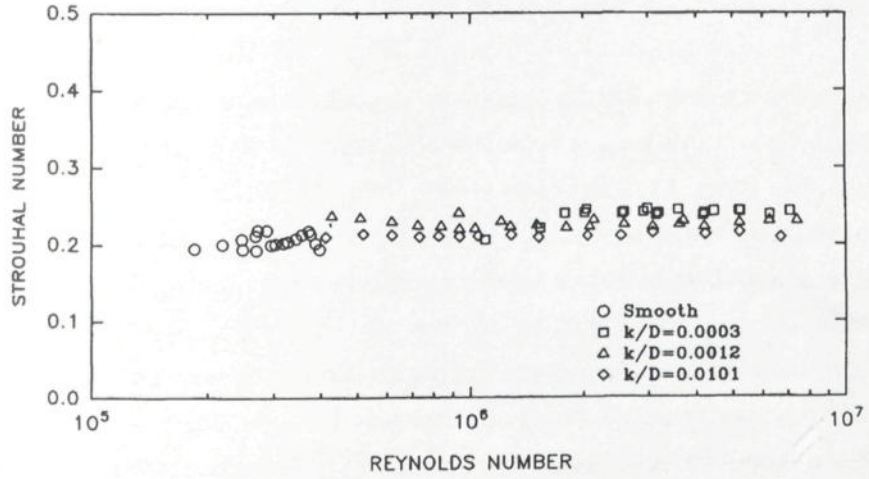


Figure 6.4. Relation between the Strouhal number and the Reynolds number for circular cylinder (Shi *et al.*, 1993).

An important aspect associated with the oscillatory character of the wake is the generation of a crosswind force with the same frequency of the vortex shedding, N_S. If the cylinder is elastically supported in the cross flow direction, it will deflect in this direction, influencing the cross flow. In general, the response will be of small amplitude, except in the case where the cylinder natural frequency is close to N_S. In this situation, the body interacts strongly with the flow and controls the vortex-shedding mechanism for a certain range of variation of the wind velocity, i.e., an increase of the flow velocity by a few percent won't change the shedding frequency, which coincides with the cylinder natural frequency. This

aeroelastic phenomenon, illustrated by Figure 6.5, is commonly known as *lock-in* or *synchronization*, and originates additional crosswind loads, which are characterized by an inertial component, proportional to the accelerations of the structure, and an aerodynamic damping component, proportional to the velocity. In Civil Engineering applications, the inertial component associated with the "added mass of air" is normally disregarded, in view of its small value. The aerodynamic damping component is however of great importance, as it may reduce the effective damping force for negative aerodynamic damping coefficients, and lead to significant *vortex-induced* vibrations.

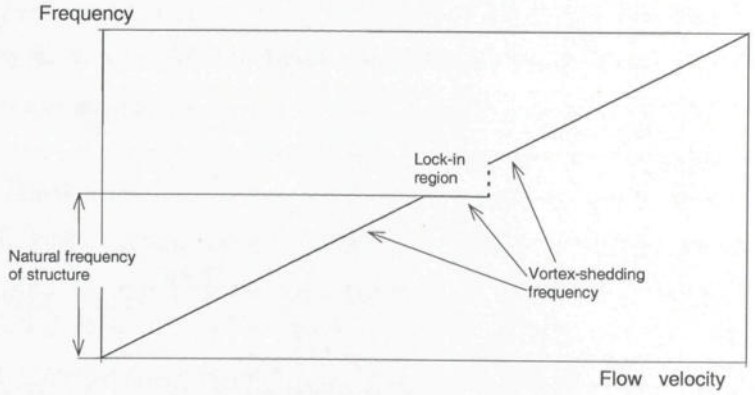


Figure 6.5. Evolution of vortex-shedding frequency with wind velocity over elastic structure.

The *vortex-shedding* phenomenon was described for a uniform wind flow. It is now interesting to know how turbulence affects the occurrence of vibrations.

According to Dyrbye and Hansen (1999), two turbulence conditions can enhance the risk of *vortex-induced* vibrations, one corresponding to locations where the air flow is smooth, and the other, characterized by an increased small-scale turbulence. The first situation occurs typically for isolated structures located by the sea, for which the negative aerodynamic damping is increased. The later condition occurs for structures located in the wake of slender nearby structures of similar size, which have increased lift coefficients. On the contrary, large-scale turbulence reduces the aerodynamic damping characterized by the logarithmic decrement δ_a^T. This effect can be observed in Figure 6.6 (a), which illustrates the variation of the ratio δ_a^T/δ_a^S with the intensity of the turbulence, δ_a^S being the logarithmic damping decrement in smooth flow.

The occurrence of violent *vortex-induced* vibrations depends on the intensity of large-scale turbulence, as well as of the intrinsic structural damping, which is characterized by the *Scruton number* $\mathbf{S_c}$, a nondimensional parameter defined by

$$\mathbf{S_c} = \frac{2\delta m}{\rho D^2} \tag{6.3}$$

where δ is the logarithmic decrement of structural damping, m is the generalized mass associated with the mode of vibration considered and ρ is the density of the air.

High intensity of large-scale turbulence and/or high *Scruton numbers* reduce the risk of violent vortex-induced vibrations, as illustrated in Figure 6.7. According to Dyrbye and Hansen (1999), no risk of *lock-in* exists for S_c values greater than about *20*. On the contrary, the risk of *lock-in* is very significant if S_c is less than *10*.

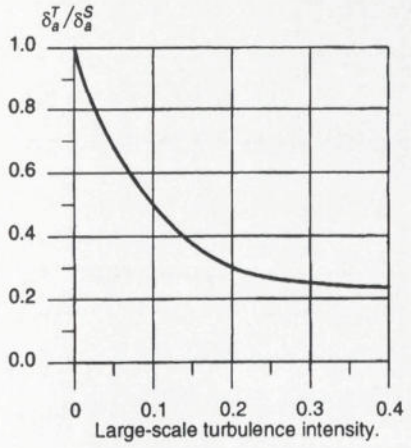


Figure 6.6. Variation of the ratio δ_a^T/δ_a^S with the intensity of large-scale turbulence (Dyrbye & Hansen, 1999).

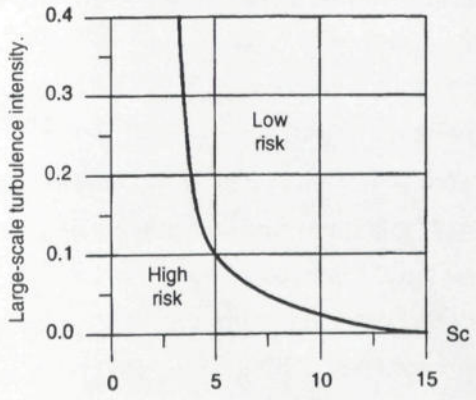


Figure 6.7. The risk of vortex-induced vibrations of circular cylinders: variation with the intensity of large-scale turbulence and S_c number (Dyrbye & Hansen, 1999).

Figure 6.8 illustrates the *Scruton number* values obtained by Yamada (1997) for a set of cables from different types of cable-stayed bridges in Japan, assuming a logarithmic decrement of 0.01 as a representative value for oscillations in the first mode (Yamaguchi & Fujino, 1998). According to this Figure, the S_c number is above *20* for most of the cables and, consequently, vortex-induced vibrations of cables from cable-stayed bridges is not normally a

matter of great concern. In effect, for the normal range of wind speed, *vortex-shedding* occurs at high frequencies, affecting essentially higher modes of the shortest bridge stays.

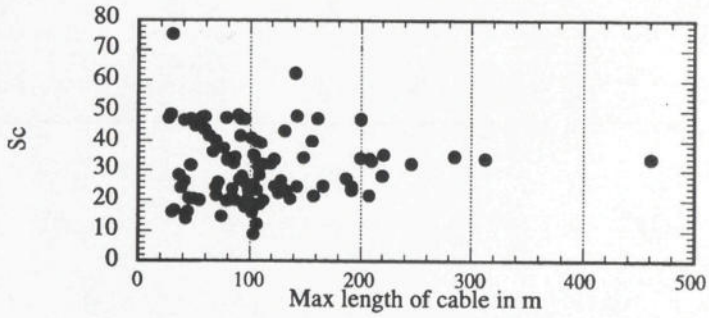


Figure 6.8. *Scruton number* vs cable length for cable-stayed bridges in Japan (Yamada, 1997).

Consider as an example the stays of the Vasco da Gama Bridge, in Portugal (see Figure 2.87), with diameters of *160mm* to *250mm*, lengths varying in the range *35m* to *226m*, and associated first natural frequencies of *3Hz* to *0.6Hz*, respectively. Assuming a constant ***S*** value of *0.2* and a wind velocity of *12m/s* (which could affect the deck response), the shedding frequency for the shortest cable would be *15Hz*, according to equation (6.2), which is clearly distant from the first mode's natural frequency and consequently no coupling would be expected.

As for the possibility of occurrence of *lock-in* in the fundamental mode of vibration, and according to equation (6.2) and to the assumed S value of *0.2*, the critical velocity U_{cr} can be calculated by

$$U_{cr} = 5 N_S D \tag{6.4}$$

So, for the shortest stay at the Vasco da Gama Bridge, the critical velocity associated with the occurrence of *lock-in* in the first mode would be *2.4m/s*. This velocity is clearly too low to provide a significant energy input for the occurrence of cable oscillations.

With regard to the characterization of the *vortex-shedding* phenomenon in terms of the definition of wind forces and evaluation of the response, no completely successful analytical method has been developed to represent the full range of response behaviour of a bluff body under the action of *vortex shedding* yet. Instead, several empirical analytical models have been developed to represent the *vortex-induced* response of bluff cylinders, whose parameters are obtained from experimental data (Simiu & Scanlan, 1996). These models are either governed by two differential equations, one to characterize the structure, and another for its wake or, by more limited single-degree-of-freedom models that predict the largest sustained response amplitude at *lock-in*. This is for example the case of the formula obtained by Griffin, Skop and Ramberg (1975), which gives the maximum relative amplitude of vibration y_0/D by

$$\frac{y_0}{D} = \frac{1.29}{\left[1 + 0.43(2\pi S^2 S_c)\right]^{3.35}} \tag{6.5}$$

Equation (6.5) is plotted in Figure 6.9 for S equal to *0.2*.

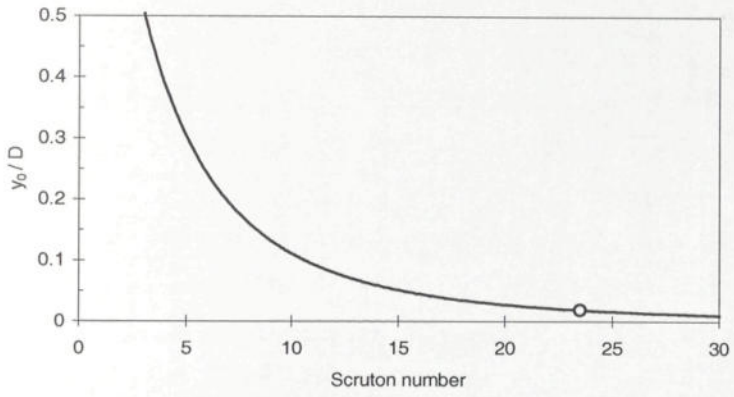


Figure 6.9. Maximum amplitude of *vortex-induced* vibration at *lock-in* vs S_c number according to the formula of Griffin, Skop and Ramberg (1975).

Considering the usual values found for the S_c numbers for cables of cable-stayed bridges (see Figure 6.8), it becomes evident that the amplitudes of vibration are generally very small. Davenport (1994), for example, states that the amplitude of *vortex-shedding* vibration rarely attains half the cable diameter.

In the case of the Vasco da Gama Bridge, where the measured logarithmic decrement damping of the shortest stays is about *0.085* (without damping devices) and the S_c number is *23.5*, the maximum amplitude of vortex-induced vibration would be *0.02D*, as marked in Figure 6.9, corresponding to a *3mm* amplitude of oscillation. Although irrelevant for vortex-induced vibration, damping devices were installed in all stays, leading to a S_c number of *233* for the shortest stays.

A more complete model for the evaluation of the resonance amplitude at *lock-in*, y_0, is the so-called *vortex resonance model*, on which the specifications of *EC1* (CEN, 1991) are based. The *vortex resonance model* is specifically dedicated to flexible structures and has been thoroughly applied in the study of tall chimneys and stacks. This model considers in particular the fact that the vortex-shedding mechanism is not uniformly distributed along the cylinder axis, the cross correlation of the exciting force $F_{y\sigma}$ decreasing along the cylinder axis. Figure 6.10 represents the typical variation of the exciting force coefficient $c_{y\sigma}$ ($F_{y\sigma} = \frac{1}{2} \cdot c_{y\sigma} \cdot \rho \cdot U_{cr}^2 \cdot D$) along the cylinder for two different end conditions. The *vortex resonance model* considers a simplified distribution of vortex loading along the cylinder, which is characterized by a constant value c_{lat}, the maximum value of $c_{y\sigma}(z)$, and is distributed in a specific zone of the structure defined by a correlation length L' given as

$$L' = \frac{1}{c_{lat}} \int_0^h c_{y\sigma}(z)\,dz \tag{6.6}$$

where h represents the cylinder length and c_{lat} is obtained from measurements on model tests from full-scale measurements.

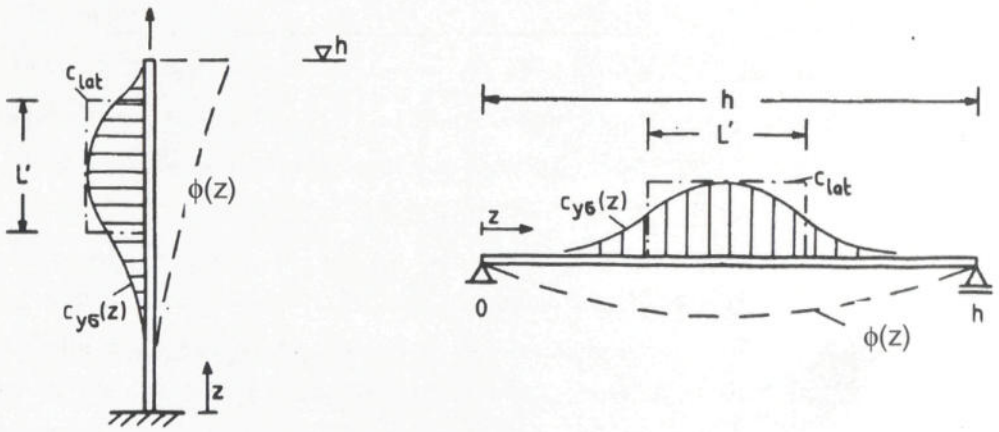


Figure 6.10. Cross-correlation of vortex-exciting force along the cylinder axis (Ruscheweyh, 1994).

According to Ruscheweyh (1994), if the cylinder starts to vibrate in resonance with *vortex-shedding*, the correlation length L' increases with the increasing relative amplitude y_0/D. This effect can be observed in Figure 6.11.

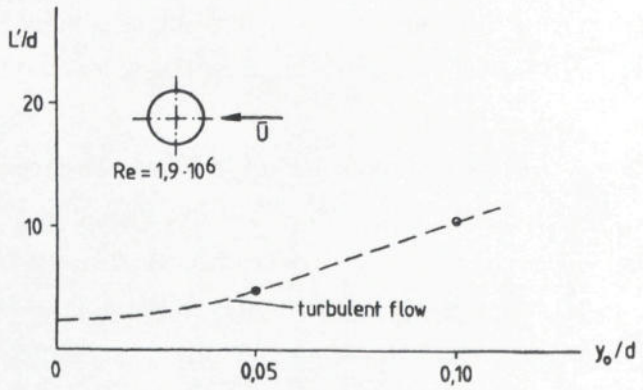


Figure 6.11. Increase of correlation length L' with increase the relative amplitude of oscillation, y_0/D (Ruscheweyh, 1994).

In a simplified manner, Ruscheweyh approached the curve of Figure 6.11 by three linear branches (see Figure 6.12), defining an *effective correlation length* L_e according to the table 6.1, also adopted by *EC1*.

Table 6.1. Definition of an effective correlation length L_e.

$\frac{L_e}{D} = 6$	$\frac{y_0}{D} \leq 0.1$
$\frac{L_e}{D} = 4.8 + 12 \cdot \frac{y_0}{D}$	$0.1 \leq \frac{y_0}{D} \leq 0.6$
$\frac{L_e}{D} = 12$	$\frac{y_0}{D} \geq 0.6$

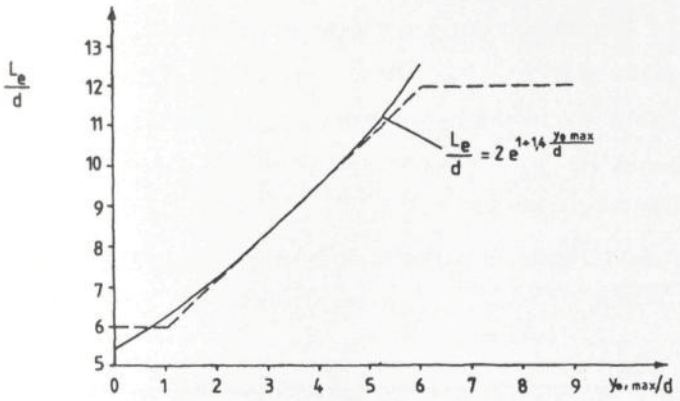


Figure 6.12. Effective correlation length vs relative amplitude of oscillation, y_0/D. Approach by three linear branches (Ruscheweyh, 1994).

On the other side, assuming a modal exciting force with sinusoidal character actuating along the length L_e, the maximum deflection amplitude can be obtained from the formula

$$\frac{y_0}{D} = K_\phi \, K_w \, c_{lat} \, \frac{1}{S_c} \cdot \frac{1}{S^2} \tag{6.7}$$

in which K_ϕ and K_w are a *mode shape constant* and a *correlation length factor*, respectively, defined by

$$K_\phi = \frac{\int_0^h \phi(z)\,dz}{4\pi \int_0^h \phi^2(z)\,dz} \tag{6.8}$$

and

$$K_w = \frac{\int_0^{L_e} \phi(z)\,dz}{\int_0^h \phi(z)\,dz} \tag{6.9}$$

The function $\phi(z)$ in (6.8) and (6.9) represents the amplitude of the mode shape. For the particular case of a stay cable, the constant K_ϕ associated with the first mode shape ($\phi(z) = sin(\pi z / h)$) is *0.101* and the constant K_w is given by

$$K_w = cos\left[\frac{\pi}{2}(1 - \frac{L_e/D}{h/D})\right] \tag{6.10}$$

As for the value of c_{lat}, a base value $c_{lat,0}$ is obtained from measurements and a reduction correction is subsequently applied, considering that high wind speeds have a limited duration, which is not normally sufficient to overcome the transient phase of the response at vortex resonance, i.e., the maximum amplitude at resonance may not be attained. The correction to apply is defined in *EC1* according to Table 6.2, based in the difference between the mean wind velocity at the centre of the effective correlation length U_m, and the critical wind velocity U_{cr}, obtained by (6.4).

Table 6.2. Aerodynamic exciting force coefficient c_{lat} versus U_{cr}/U_m.

$\frac{U_{cr}}{U_m} \leq 0.83$	$c_{lat} = c_{lat,0}$
$0.83 \leq \frac{U_{cr}}{U_m} \leq 1.25$	$c_{lat} = (3 - 2.4 \cdot \frac{U_{cr}}{U_m}) \cdot c_{lat,0}$
$\frac{U_{cr}}{U_m} \geq 1.25$	$c_{lat} = 0$

With regard to the definition of the base aerodynamic exciting force coefficient $c_{lat,0}$ for circular cylinders, the following values are proposed by *EC1*

$$c_{lat,0} = \begin{cases} 0.7 & , \ \mathbf{Re} \leq 3x10^5 \\ 0.2 & , \ 5x10^5 \leq \mathbf{Re} \leq 4x10^6 \\ 0.3 & , \ \mathbf{Re} \geq 10^7 \end{cases}$$

In each of the intervals $3x10^5 < \mathbf{Re} < 5x10^5$ and $4x10^6 < \mathbf{Re} < 10^7$, it is assumed that $c_{lat,0}$ varies linearly with $\ell n(\mathbf{Re})$. Figure 6.13 represents the variation of $c_{lat,0}$ with the Reynolds number according to this proposal, as well as experimental values obtained by different authors.

A final comment concerning the *vortex-shedding* is that the phenomenon, as described and modelled above, is essentially two-dimensional in nature. A new type of so-called *vortex-shedding* has been introduced more recently by Matsumoto *et al.* (1992) in the course of wind tunnel investigations of rain-wind vibration. This complex three-dimensional

phenomenon caused by the presence of an axial flow along the stay cable and enhanced by the presence of rain will be described later in the section and occurs for high wind velocities.

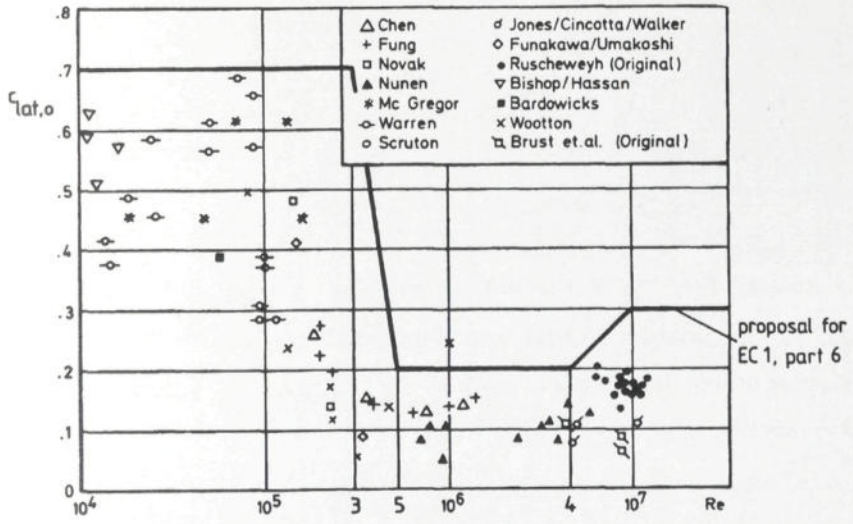


Figure 6.13. Basic exciting force coefficient $c_{lat,0}$ versus *Reynolds number* for circular cylinders (Ruscheweyh, 1994).

6.2.2 Galloping

Galloping is an instability phenomenon typical of slender structures with rectangular or "D" cross-sections, which is characterized, in a similar manner to *vortex-shedding*, by oscillations transverse to the wind direction, that occur at frequencies close to some natural frequency of the structure. The phenomenon is however quite different from *vortex-induced* vibration. In effect, while the later originates small amplitudes of oscillation in restricted ranges of wind velocity, *galloping* occurs for all wind speeds above a critical value and produces high amplitude vibrations, which may be ten times or even more the typical body dimension. In the case of ice-coated power line cables, where the phenomenon was first reported, the amplitude of vibration can be one hundred times this length (Sockel, 1994).

Consider a section of a prismatic body in a smooth oncoming flow (Figure 6.14).

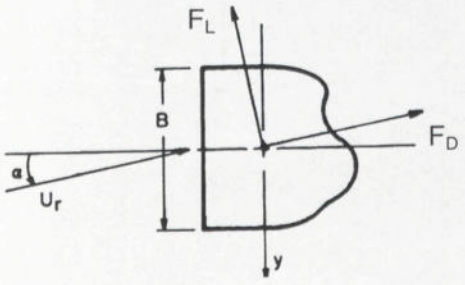


Figure 6.14. Lift and drag forces on a fixed bluff object (Simiu & Scanlan, 1996).

Assuming that the body is fixed and that the angle of attack of the flow velocity U_r is α, a drag and lift forces $F_D(\alpha)$ and $F_L(\alpha)$ develop along and across the wind direction, respectively, whose mean value are

$$F_D(\alpha)=\frac{1}{2}\rho U_r^2 BC_D(\alpha) \tag{6.11}$$

$$F_L(\alpha)=\frac{1}{2}\rho U_r^2 BC_L(\alpha) \tag{6.12}$$

where $C_D(\alpha)$ and $C_L(\alpha)$ represent the drag and lift coefficients, respectively, associated with the particular cross section and angle of wind attack.

Considering these two components of wind force, the vertical force $F_y(\alpha)$ can be obtained by

$$F_y(\alpha)=-F_D(\alpha)\sin\alpha-F_L(\alpha)\cos\alpha \tag{6.13}$$

Introducing (6.11) and (6.12) into (6.13), the following relation is obtained

$$F_y(\alpha)=\frac{1}{2}\rho U^2 BC_y(\alpha) \tag{6.14}$$

where

$$U=U_r\cos\alpha \tag{6.15}$$

and the force coefficient along the vertical direction $C_y(\alpha)$ is

$$C_y(\alpha)=-[C_L(\alpha)+C_D(\alpha)\tan\alpha]\sec\alpha \tag{6.16}$$

In a second situation, assume that the bluff body is vibrating in the across wind direction y in a flow with velocity U (Figure 6.15).

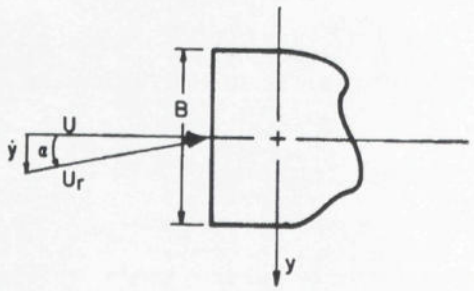


Figure 6.15. Effective angle of attack on an oscillating bluff body (Simiu & Scanlan, 1996).

The relative velocity of the flow with respect to the moving body is now obtained from the vectorial sum represented in Figure 6.15, whose amplitude is

$$U_r = \sqrt{U^2 + \dot{y}^2} \tag{6.17}$$

and whose angle of attack is

$$\alpha = a\tan\frac{\dot{y}}{U} \tag{6.18}$$

The dynamic equation of the motion of the bluff body is then characterized by

$$m\ddot{y} + 2\xi m\omega\,\dot{y} + m\omega^2 y = F_y(\alpha) \tag{6.19}$$

where m is the mass of the body per unit length, ξ is the damping ratio, ω is the natural frequency of the body and $F_y(\alpha)$ is given by (6.13).

In the case of small motions, the angle of attack can be neglected, i.e.

$$\alpha \approx \frac{\dot{y}}{U} \approx 0 \tag{6.20}$$

So, an expansion of $F_y(\alpha)$ about $\alpha = 0$ followed by a linearization leads to

$$F_y(\alpha) \approx \left.\frac{dF_y}{d\alpha}\right|_{\alpha=0} \cdot \alpha \tag{6.21}$$

Considering that

$$\frac{dF_y}{d\alpha} = \frac{1}{2}\rho U^2 B \frac{dC_y}{d\alpha} \tag{6.22}$$

and the derivative of the force coefficient C_y with respect to the angle of attack α is

$$\left.\frac{dC_y}{d\alpha}\right|_{\alpha=0} = -\left(\frac{dC_L}{d\alpha} + C_D\right)_{\alpha=0} \tag{6.23}$$

equation (6.19) can be transformed into

$$m\ddot{y} + 2\xi m\omega\,\dot{y} + m\omega^2 y = -\frac{1}{2}\rho U^2 B\left(\frac{dC_L}{d\alpha} + C_D\right)_{\alpha=0}\frac{\dot{y}}{U} \tag{6.24}$$

As can be observed from equation (6.24), the aerodynamic force on the bluff body is a damping force that modifies the overall system damping to a net value d of

$$d = 2m\omega\xi + \frac{1}{2}\rho UB\left(\frac{dC_L}{d\alpha} + C_D\right)_{\alpha=0} \tag{6.25}$$

By analogy with the first component of d, known as *mechanical damping*, the second component of the net damping is defined as *aerodynamic damping*.

Considering now the stability of the single-degree-of-freedom system characterized by (6.24), which is guaranteed provided that the viscous damping d is positive, and given the fact that the mechanical damping is always positive, a necessary condition for instability is

$$\left(\frac{dC_L}{d\alpha}+C_D\right)_{\alpha=0}<0 \tag{6.26}$$

This is the so-called *Glauert-Den Hartog* criterion for *incipient galloping instability* (Simiu & Scanlan, 1996).

From (6.26) it becomes clear that circular cross-sections are never subject to instability by *galloping*, as the derivative $dC_L/d\alpha$ is always null in view of the symmetry. So, except for the cases where the external shape has been altered, either by the presence of ice or of water rivulet (see Section 6.2.4), instability of the cables by *galloping* is not generally expected in cable-stayed bridges, that generally employ circular cross sections for these elements. The only reported case of *galloping* in a cable-stayed bridge (Matsumoto *et al.*, 1989a) respects a cable-stayed bridge in Japan whose cables cross section was an octagonal cylinder for which the variation of the drag and lift coefficients with the angle of attack is depicted in Figure 6.16, evidencing regions of wind approach angle $-5^\circ<\alpha<5^\circ$ to the faces of the octagonal section that are susceptible to instability.

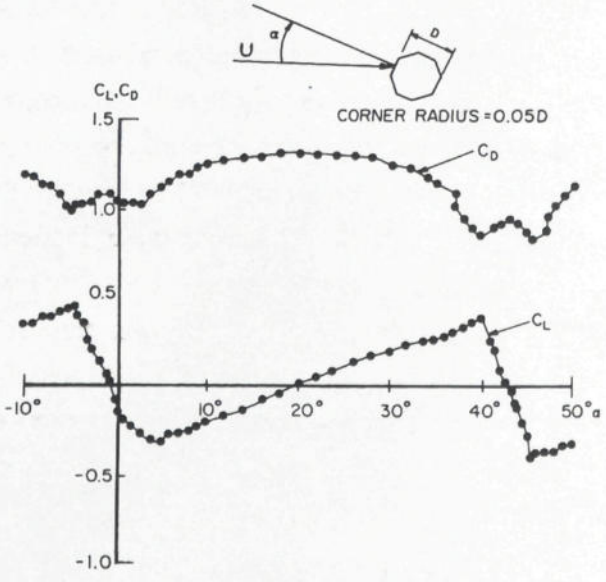


Figure 6.16. Force coefficients on an octogonal cylinder (Simiu & Scanlan, 1996).

6.2.3 Wake interference

The phenomenon of *wake interference* occurs when a stay cable lies in the wake of another stay or structural element, or of a construction equipment. The perturbing element affects the wind flow creating local turbulent conditions that originate oscillations of the cable. These

oscillations, that may be associated to *vortex resonance*, *galloping* or to another specific phenomenon that will be described subsequently, designated as *interference galloping*, occur more easily in locations of low turbulence and cannot be easily anticipated in design phase, the most effective counter-measure being the addition of damping into the cable in order to balance any negative aerodynamic damping. The most common situations that originate cable vibrations due to *wake effects* are described bellow:

(i) Bridges with two planes of cables subject to oblique winds

Some of the downstream cables that are in the wake of the upstream leg of the towers (specially for *H*-shaped towers) may exhibit vibrations. According to Virlogeux (1998), this problem was reported in the Evripos Bridge in Greece (see Figure 2.30) and may have also occurred at the Normandy Bridge (see Figure 1.2) during construction for some of the shortest cables behind a tower leg;

(ii) Bridges with twin or triple cables

In order to restrain the size of the cables, multiple parallel stay cables have been used in several cable-stayed bridges, particularly in Japan. These multiple cables are distant from each other by a few diameters only and are anchored at the same level in the tower and deck.

It has been observed that, under particular conditions, the cable assembly may undergo vibrations. These oscillations are due to *vortex resonance*, to *galloping* of the cable assembly, or to a so-called *interference* or *wake galloping*. The later phenomenon is no more than a *galloping* that occurs on the downstream cable(s) induced by the turbulent wake of the upstream cable(s). The oscillation of the downstream cable(s) induces also a perturbation of the flow around the upstream cable(s).

The *EC1* proposes some conservative formulae for the evaluation of instability by *wake effects*;

- With respect to the *vortex resonance* effects, the *EC1* proposes the definition of an amplitude of *vortex resonance* of the cable assembly using the model previously described for *lock-in* of a single cable (see section 6.2.1), with an increased exciting force coefficient equal to $1.5\,c_{lat}$;
- With regard to the possibility of occurrence of *galloping* of the cable assembly, it is assumed that braces or stringers connecting the twin or triple cables at certain locations along the cables establish a certain degree of coupling of the assembly. For a situation of coupled cables, a critical velocity U_{cG} is defined as

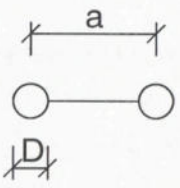
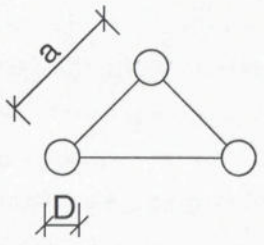
$$U_{cG} = \frac{2\,S_c}{a_G} \cdot f \cdot D \tag{6.27}$$

where f is the frequency of vibration of the cable and a_G is a quantity defined in Table 6.3, that depends on the type of cable assembly and on the value of the relative cable spacing. This critical velocity should satisfy the relation

$$U_{cG} > 1.25 U_m \tag{6.28}$$

where U_m is the mean wind velocity calculated at the point of maximum amplitude of oscillation.

Table 6.3. Constant a_G for the estimation of the critical velocity of *galloping* in associations of cables (*EC1*).

Type of association	a_G	
	$a \leq 1.5D$	$a \geq 2.5D$
	$a_G = 1.5$	$a_G = 3$
	$a_G = 6$	$a_G = 3$

- Finally, for *interference galloping*, which is the most common type of instability referred in the literature for associations of cables, the *EC1* proposes the estimation of the critical wind velocity U_{clG} by the following formula

$$U_{clG} = 3.5 \cdot f \cdot D \cdot \sqrt{\frac{\frac{a}{D} \cdot S_c}{a_{IG}}} \tag{6.29}$$

where a_{IG} is a combined stability parameter with a value of *3.3*, if not otherwise specified. This formula is valid if $a/D < 3$ and the angle of wind attack is in the range of the critical wind direction β_k, as defined in Figure 6.17. As in the previous case of instability of the cable assembly by *galloping*, the critical velocity should satisfy a relation of the type of (6.28).

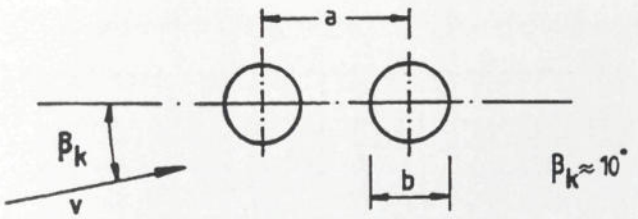


Figure 6.17. Critical wind direction range for *interference galloping*.

Referring to practical cases of occurrence of *interference galloping*, Miyata (1991) defined the main aspects of the phenomenon: it generally originates vibrations in the first mode, it occurs when the wind direction is about 0° to 45° from transverse direction of the bridge axis and it is very much conditioned by the adopted spacing between the cables. The phenomenon of *wake galloping* was observed in several cable-stayed bridges in Japan, such as the Hitsuishijima, Iwakurojima, Yobuko and Shima Maruyama Bridges (Narita & Yokoyama, 1991). For the particular case of the Yobuko Bridge, amplitudes of oscillation of *2.5D* were reported.

Based on observations of cable-stayed bridges in Japan, Matsumoto *et al.* (1989b) refer the range *1.2D* to *4.3D* (measured from the centres of cables) as the critical range of cable spacings for occurrence of wake galloping (see Figure 6.18). These values are consistent with the results from wind tunnel observations of twin circular cylinders reported by the same authors and presented in Figure 6.19.

In a more recent research, Kubo (1994; 1997) showed that the mechanism of *wake galloping* changes at a spacing around *3.6D* between circular cylinders, and proposed in particular the following measures to prevent this form of instability: adopt a close spacing between cables in the range *1.2D* to *1.3D*, which proved to show no *galloping* at reduced wind velocity $U_r = U/f\,D$ (f is the vibration frequency) of *200* (an increase of that spacing to more than *5D* would produce equivalent effects, although not so convenient for practical reasons); connect parallel cables by spacers or stringers at lengths defined by a deflection of the connecting points no greater than *0.2D*. Another alternative has been suggested by Yoshimura *et al.* (1993, 1995b), consisting in the use of a pair or three cables stranded helically.

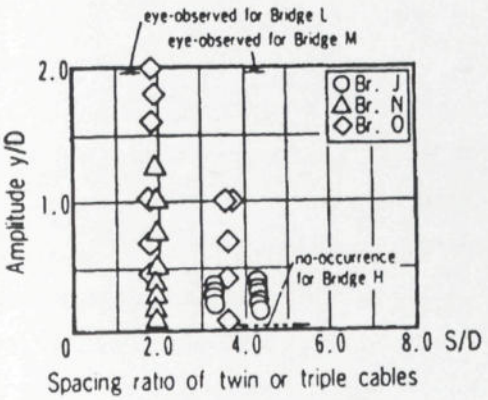


Figure 6.18. Amplitude vs spacing of twin or triple cables associated with instability by *wake galloping*: observations on prototypes (Matsumoto *et al.*, 1989b).

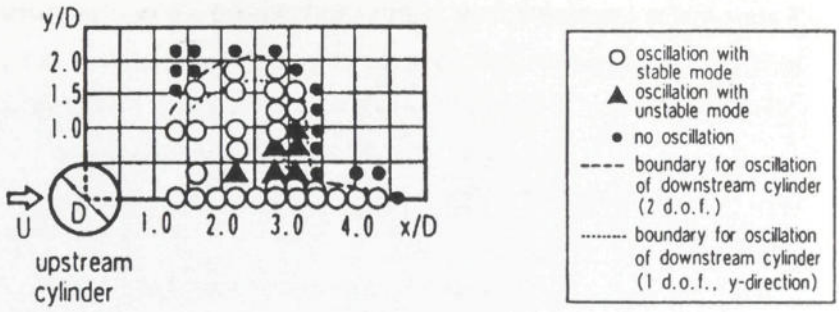


Figure 6.19. Amplitude vs spacing of twin circular cylinders associated with instability by *wake galloping*: results from wind tunnel tests (Matsumoto *et al.*, 1989b).

(iii) Cables made of a bunch of parallel individually protected cables

An interference phenomenon of similar type of the previously described may occur due to the aerodynamic interaction between strands, which shock against each other, generating global vibration of the cable and producing a significant and disagreeable rattling noise. Virlogeux (1998) defines these movements as *breathing of strands*. The author of the current work has recently eye-observed this type of vibrations on the Guadiana Bridge, in Portugal (see Figure 2.78). These occurred under a small wind velocity estimated in *5m/s* to *8m/s* for an average angle of attack of about *20°* to *40°* to the bridge axis. Many of the cables suffered vibrations, apparently mainly in the first and second mode, with maximum amplitude estimated in about *0.50m*. Although other vibration mechanisms might be present at that time, this *breathing* of the cables was clearly noticed and showed to have produced damage, as several of the braces that connected the strands at about the thirds of the cables were missing.

6.2.4 Rain-wind induced vibrations

Identification of the phenomenon

Although *rain-wind induced vibration* of power lines, designated as *rain vibration*, had been reported in the literature *10* years earlier (Hardy *et al.*, 1975; Hardy & Bourdon, 1979), it was only in 1986 that Hikami identified the phenomenon of cable vibration in cable-stayed bridges induced by the combined action of wind and rain, during the construction of the Meiko-Nishi Bridge (Hikami, 1986; Hikami & Shiraishi, 1988). This conventional three-span cable-stayed bridge with a main span of *405m* and side spans of *176.5m*, whose cables were manifestly stable under dry condition, exhibited strong cable vibrations with a peak to peak amplitude of *55cm* under combined action of rain and wind at a relatively low wind velocity of *14m/s*. The impossibility of classifying the observed vibrations according to existing theories, such as *vortex-induced oscillations*, or *wake galloping*, motivated the development of a five month

observation program on the bridge prototype in which all the *24* cables of one cable plane connected to one of the towers were instrumented (see Figure 6.21), allowing the measurement of transverse oscillations in the vertical plane. Wind speed and direction were also measured simultaneously and damping factors were identified from the set of observations. The following main observations were made:

- The logarithmic decrement of the cables varied between *0.007* and *0.028*, depending on the vibration mode, cable length (*65m* to *200m*) and constructed situation;
- The occurrences of cable vibration were in all the cases accompanied by rain. This can be observed in Figure 6.22, representing the time variation of wind speed, direction and maximum amplitude of vibration in a *10*-hour record for three of the vibrating cables;
- The occurrence of cable vibration was limited to the cables that geometrically declined in the direction of the wind;
- All the observed cable motions occurred in the vertical plane for wind speeds in the range *5-15m/s*. These vibrations were composed mostly of a single mode, although some associations of two modes were found, always characterized by natural frequencies in the range *1Hz* to *3Hz;*
- During vibration of a cable, a water rivulet was formed at the lower cable surface, which oscillated circumferencially.

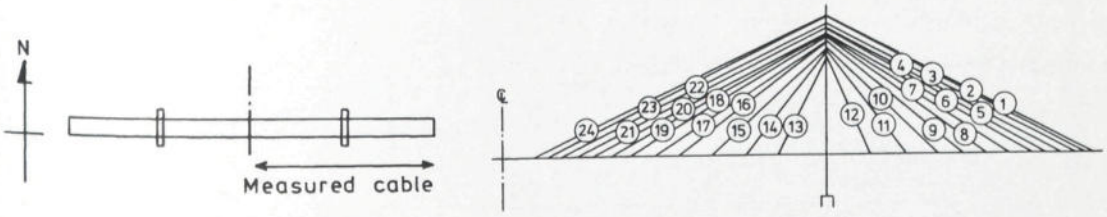


Figure 6.21. Instrumentation of cables at the Meiko-Nishi Bridge (Hikami & Shirashi, 1988).

Additional wind tunnel tests with reproduction of the rain condition were performed by Hikami and Shiraishi (1988), in order to better understand the generating mechanism of *rain-wind induced vibration*, investigating in particular the formation and role of the water rivulet along the cable. The tests were performed on a *2.6m* segment of a prototype polyethylene pipe which was mounted with an inclination angle α to the horizontal plane of 45° and an angle to the wind direction β of $\pm 45^\circ$, according to the setup and scheme presented in Figure 6.23, so as to reproduce as much as possible the prototype motion. The rain condition was achieved by spraying water.

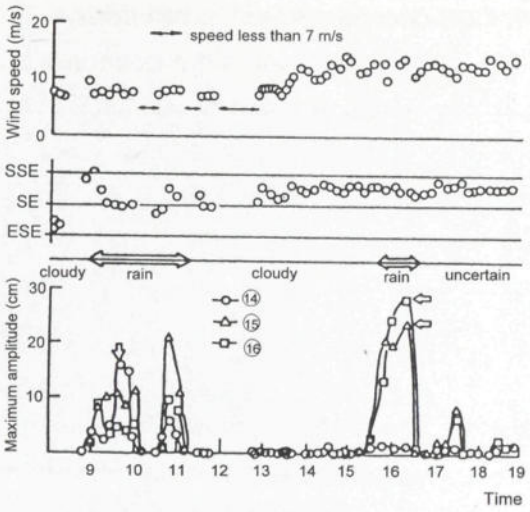


Figure 6.22. *10*-hour-record of vibration amplitudes and weather conditions at the Meiko Nishi Bridges (Hikami & Shirashi, 1988).

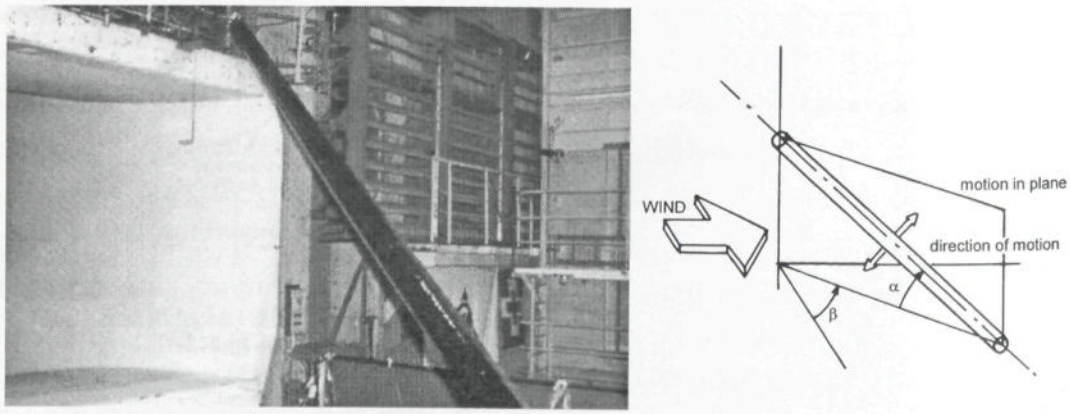


Figure 6.23. Example of the mount setup for the wind tunnel test of a stay cable (Yamada *et al.*, 1991). Scheme of setup.

In addition to the confirmation of the set of observations previously reported from full scale measurements on the bridge, the wind tunnel tests evidenced the formation of another water rivulet along the upper windward surface of the cable in the mount associated with an angle β of $45°$, that is, for a cable geometrically declining in the wind direction. In effect, for a small wind velocity, a raindrop falling on the windward surface of the cable slides down the surface. For a wind velocity greater than a certain value (*9m/s* in this case), a drag force of flow acting on the rain drop overcomes the gravity and friction forces, so that the rain drop climbs up the surface and becomes part of the rivulet. As the wind velocity increases, the angle θ of formation of the upper rivulet represented in Figure 6.24 decreases, i.e., the rivulet moves up. Moreover, when the cable vibrates, both the upper and the lower rivulets oscillate in circumferencial direction at the same frequency of the cable oscillation. A maximum angular oscillation of about $20°$ has been measured for the upper rivulet, according to the

representation of Figure 6.25. It can be also observed in this Figure that the increase in the wind velocity produces a gradual shift of the bottom boundary of the rivulet. When this shift reached up to 40°, at a wind velocity of *14m/s*, the rivulet was disorganized and the vibration ceased.

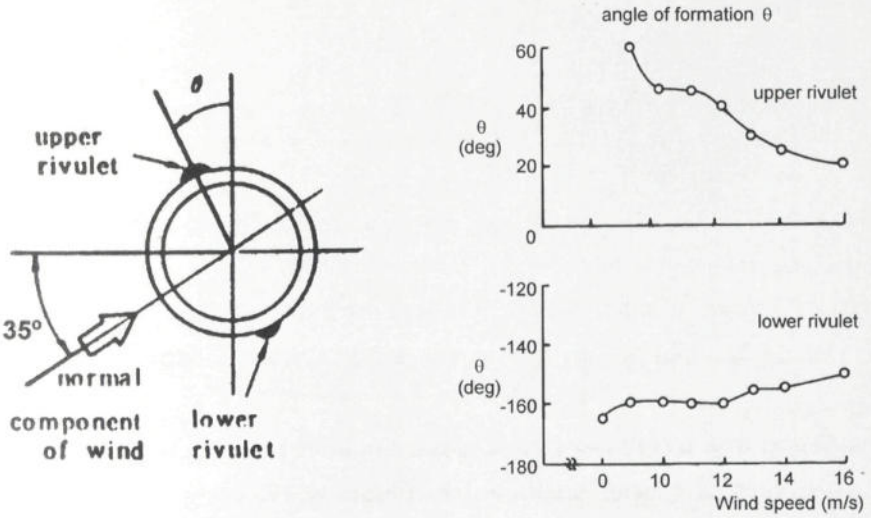


Figure 6.24. Variation of the angle of formation of the water rivulet with wind speed for $\alpha = 45^{\circ}$, $\beta = 45^{\circ}$ (Hikami & Shirashi, 1988).

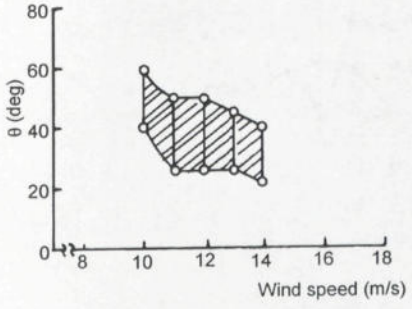


Figure 6.25. Variation of the upper rivulet circumferential oscillation region with wind speed (Hikami & Shirashi, 1988).

By measuring the drag force associated with the upper and lower rivulet formed separately at different wind speeds (Figure 6.26), Hikami and Shiraishi showed that the lower rivulet has a stabilizing role, as its formation produces aerodynamic forces in opposition to the cable motion, i.e., damping forces. On the contrary, the upper rivulet generates exciting forces and is responsible for the unstable behaviour of the cable. Hikami and Shiraishi explained this type of behaviour based on the analogy to the phenomenon of instability of an iced overhead conductor by "torsional" galloping.

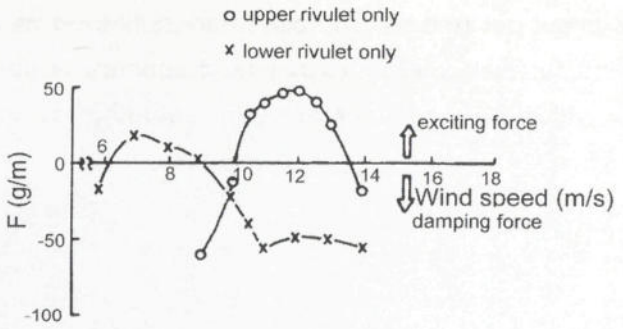


Figure 6.26. Unsteady aerodynamic force with rivulet formed separately (Hikami & Shirashi, 1988).

The analytical model of Yamaguchi

In an attempt to further explain the generation mechanism of rain-wind induced vibration, Yamaguchi (1990) developed an analytical study investigating this form of "torsional" galloping.

Considering that the upper rivulet is the origin of rain vibration, Yamaguchi based his studies on an analytical model described in Figure 6.27, comprehending the cable cross section, with diameter D, and an upper cylinder simulating the water rivulet, with diameter d, located at an angle β to the vertical axis (with respect to the wind direction).

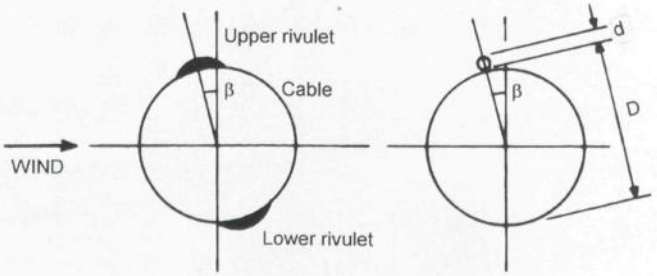


Figure 6.27. Model of cable with rivulet.

Given the reported oscillation of the rivulet in the circumferencial direction during cable vibration, a two-degree-of-freedom galloping model (Blevins & Iwan, 1974) was adopted, considering for degrees of motion both the rotation θ and the vertical motion y, according to the representation of Figure 6.28.

Designating by F_y and M the vertical component and moment per unit length of the unsteady aerodynamic force, respectively, the dynamic equilibrium equations are

$$m\ddot{y} + k y = F_y \qquad (6.30)$$

$$I\ddot{\theta} = M$$

where m is the cable mass per unit length, k the generalized stiffness of the normal mode under consideration, and I is the polar moment of inertia per unit length of the rivulet about the cable axis. It should be noted that both the mass of rivulet and the damping force on the cable are neglected for simplification.

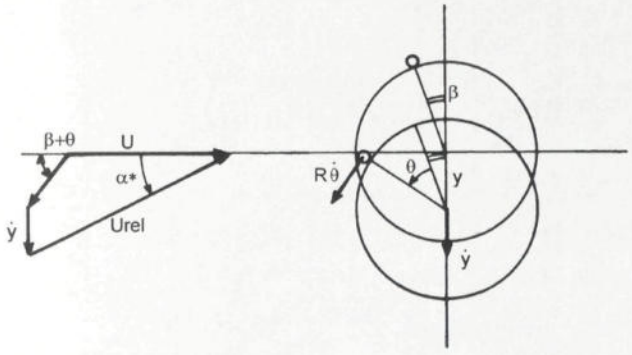


Figure 6.28. Relative flow for translation of cable with rotation of the rivulet (Yamaguchi, 1990).

The unsteady aerodynamic forces F_y and M are now evaluated introducing a quasi-steady assumption that allows the quantification of a relative wind velocity U_{rel} and relative angle of attack α^* based on the velocity of vertical translation $\dot{y}$ and on the angular velocity of rotation of the rivulet $\dot{\theta}$, as represented in Figure 6.28. According to the geometric construction presented in this Figure, U_{rel} and α^* are

$$U_{rel} = \frac{U + R\dot{\theta}\cos(\beta+\theta)}{\cos\alpha^*} \tag{6.31}$$

$$\alpha^* = \tan^{-1}\frac{\dot{y} + R\dot{\theta}\sin(\beta+\theta)}{U + R\dot{\theta}\cos(\beta+\theta)}$$

In these equations, U represents the free-stream wind velocity and R is given by $(d+D)/2$.

Considering that a bluff body in a quasi-steady flow characterized by average wind velocity and angle of attack U_{rel} and α^*, respectively, generates a drag force F_D, lift force F_L and a moment M as represented in Figure 6.29, given by

$$\begin{aligned} F_D &= \frac{1}{2}\rho U_{rel}^2 (d+D) C_D(\alpha) \\ F_L &= \frac{1}{2}\rho U_{rel}^2 (d+D) C_L(\alpha) \\ M &= \frac{1}{2}\rho U_{rel}^2 (d+D) C_M(\alpha) \end{aligned} \tag{6.32}$$

in which ρ is the air density, and C_D, C_L and C_M are, respectively, adimensional drag, lift and moment aerodynamic coefficients measured in wind tunnel, the force components F_y and M are

$$F_y = -\frac{1}{2}\rho U_{rel}^2 (d+D)\cdot\left\{C_D(\alpha)\sin\alpha^* + C_L(\alpha)\cos\alpha^*\right\}$$

$$M = \frac{1}{2}\rho U_{rel}^2 (d+D)\cdot C_M(\alpha) \tag{6.33}$$

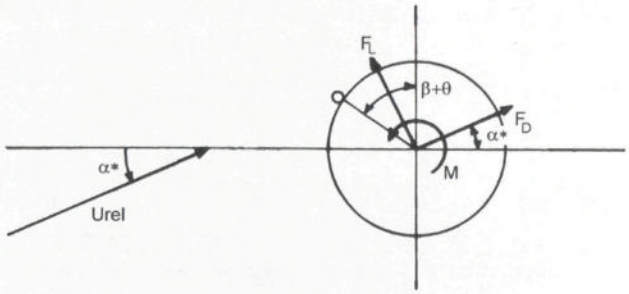


Figure 6.29. Action of quasi-steady wind force (Yamaguchi, 1990).

Now, assuming that the maximum velocities of the cable and rivulet are much less than the free-stream velocity U, the following relations hold

$$U_{rel} \approx U;\ \alpha = -\theta + \alpha^* \approx -\theta + \frac{\dot{y}}{U} + \frac{R\sin\beta\dot{\theta}}{U} \tag{6.34}$$

For small angles of attack α, the expansion of the aerodynamic coefficients and trigonometric functions in (6.33) about $\alpha = \theta = 0$ followed by a linearization and substitution into (6.30) yields the following equations of motion

$$\underline{M}\begin{Bmatrix}\ddot{y}\\ \ddot{\theta}\end{Bmatrix} + \underline{C}\begin{Bmatrix}\dot{y}\\ \dot{\theta}\end{Bmatrix} + \underline{K}\begin{Bmatrix}y\\ \theta\end{Bmatrix} = \begin{Bmatrix}0\\ 0\end{Bmatrix} \tag{6.35}$$

with

$$\underline{M} = \begin{bmatrix}1 & 0\\ 0 & 1\end{bmatrix};\quad \underline{K} = \begin{bmatrix}\omega_y^2 & -\frac{1}{m}\cdot\frac{1}{2}\rho(d+D)U^2\frac{dC_L}{d\alpha}\\ 0 & \frac{1}{I}\cdot\frac{1}{2}\rho(d+D)^2U^2\frac{dC_M}{d\alpha}\end{bmatrix} \tag{6.36}$$

$$\underline{C} = \frac{1}{2}\rho(d+D)U\begin{bmatrix}\frac{1}{m}\left\{C_D + \frac{dC_L}{d\alpha}\right\} & \frac{(d+D)\sin\beta}{2m}\left\{C_D + \frac{dC_L}{d\alpha}\right\}\\ -\frac{(d+D)}{I}\frac{dC_M}{d\alpha} & -\frac{(d+D)^2\sin\beta}{2I}\frac{dC_M}{d\alpha}\end{bmatrix} \tag{6.37}$$

The quantity ω_y in (6.36) represents the natural frequency of vertical translation of the cable. Figure 6.30 illustrates the variation of C_L, C_D and C_M with the angle of attack α obtained from wind tunnel tests for a *d/D* ratio of *0.1*.

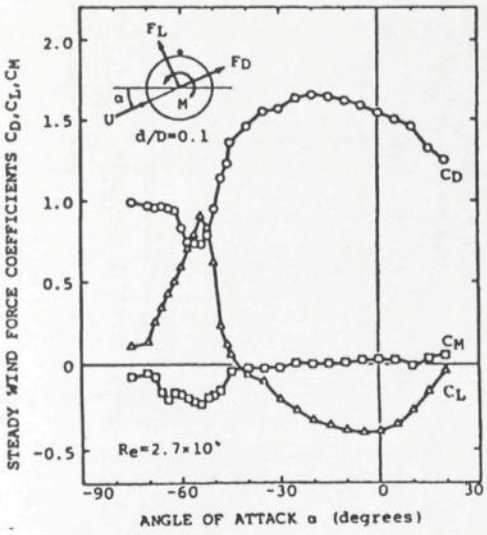


Figure 6.30. Steady wind force coefficients of figure *8*-section at various angles of wind attack for a *d/D* ratio of *0.1* (Yamaguchi, 1990).

Based on the above defined equations, Yamaguchi performed a complex eigenvalue analysis, assuming that the rivulet was located at an angle β of *10°* (with regard to the vertical) and the ratio *d/D* was *0.1*. Figures 6.31 to 6.33 illustrate the main results of this analysis which can be summarized in the following points:

- The natural frequency of circumferencial motion is proportional to the wind velocity, while the natural frequency of vertical motion is independent of this quantity (see Figure 6.31);

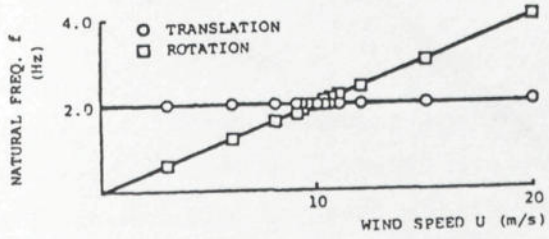


Figure 6.31. Change of natural frequency with wind speed (Yamaguchi, 1990).

- The modal aerodynamic damping exhibits a strong variation with wind speed (Figure 6.32). In particular, for a wind speed around *10m/s*, the logarithmic decrement attains significant negative values, indicating the generation of self-exciting forces. These

results are qualitatively consistent with the estimates of damping obtained previously by Hikami (1986), also represented in Figure 6.32. It can still be observed in this Figure that a conventional single-degree-of-freedom galloping analysis would provide positive damping in the full range of wind speeds and is not consequently sufficient to explain the mechanism of rain-wind induced vibration;

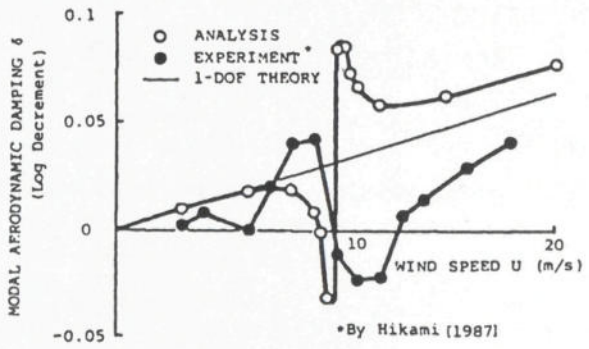


Figure 6.32. Change of modal aerodynamic damping with wind speed (Yamaguchi, 1990).

- The amplitude of rotation is strongly coupled with vertical motion at a wind speed close to 10m/s (Figure 6.33). Considering that the oscillation of the rivulet motivated by the aerodynamic stiffness can only occur when $dC_M/d\alpha$ is positive, as given by (6.36), then it is evident from (6.37) that this coupled motion of the rivulet generates the negative aerodynamic damping that causes instability

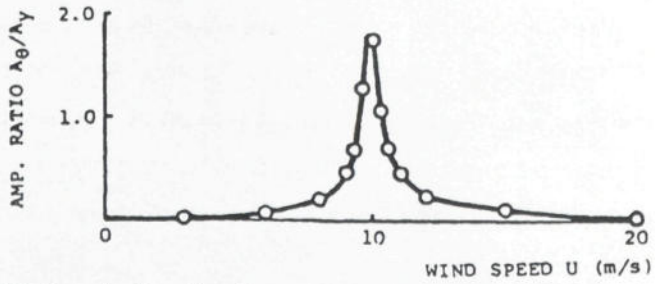


Figure 6.33. Coupled torsional amplitude *vs* wind speed (Yamaguchi, 1990).

The study of Yamaguchi seems therefore conclusive in terms of the indispensability of circumferencial oscillation of the upper rivulet to the generation of rain vibration in a stay cable. And this result was indeed confirmed by other authors that performed wind tunnel tests on prototype segments of cables, such as Flamand (1993, 1994) and Verwiebe (1998). Flamand, in particular, developed wind tunnel tests using false fixed rivulets glued on the cable surface at the position observed of formation of the real rivulet, and he concluded that instability did not occur. These results are not however in agreement with other reported wind tunnel observations, namely by Matsumoto and co-workers (1989a), who also installed false

rivulets near the separation points on an inclined cylinder and concluded that the resulting modified cross-section was already unstable, the presence of rain acting as an amplifier of that instability. Therefore, the *rain-wind induced vibration* would be no more than a particular case of the most general *inclined cable aerodynamic instability* phenomenon.

Experimental findings from Matsumoto

Based on the results of numerous wind tunnel tests performed under different conditions and models (Matsumoto *et al.*, 1989b, 1992, 1995), Matsumoto (1998) classified the generating mechanisms of this instability into three main types: *conventional Karman vortex excitation*, *galloping instability* and *high speed vortex excitation*.

(i) Conventional Karman vortex excitation

The *conventional Karman vortex excitation* phenomenon was already discussed in Section 6.2.1, occurring for relatively small values of the reduced velocity $U_r = U/f\,D$ (U- wind velocity; f- vibration frequency; D- Cable diameter) around *5*, and being characterized by relatively small amplitudes, which don't exceed normally *0.3D*.

(ii) Galloping instability

The instability by *galloping* is motivated not only by the coupled circumferencial oscillation of the water rivulet with the cable vibration as described by Hikami (1986) and Yamaguchi (1990), but also by an axial flow generated in the wake of the inclined cable. The axial flow was identified from wind tunnel tests, and is evidenced in the visualization by light flag presented in Figure 6.34. According to the representation of Figure 6.35, the axial flow velocity U_a increases with oncoming velocity U and with the yawing angle β of the cable (see Figure 6.23). Galloping instability occurs when the axial flow velocity reaches more than *30%* of the approaching velocity, for yawing angles greater than 25°, situation where the lift coefficient designated by C_F in Figure 6.36 attains a negative slope. The presence of an artificial rivulet originates an extension of the instability regions, as shown in Figure 6.37, which summarizes the response characteristics of a yawed cable in smooth flow with and without artificial rivulet. It is however considered that the rivulet may have a stabilizing role. In effect, by increasing the velocity of the flow, the rivulet moves leeward to a region where the lift coefficient slope is positive, thus "erasing" the galloping instability. Matsumoto characterized this phenomenon as a *velocity restricted type galloping*.

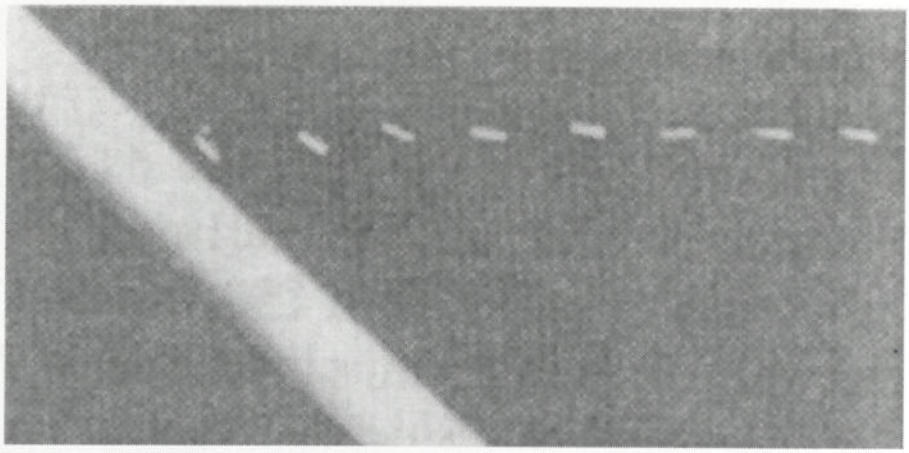


Figure 6.34. Visualized axial flow by light flag (yaw angle β of 45°) (Matsumoto, 1998).

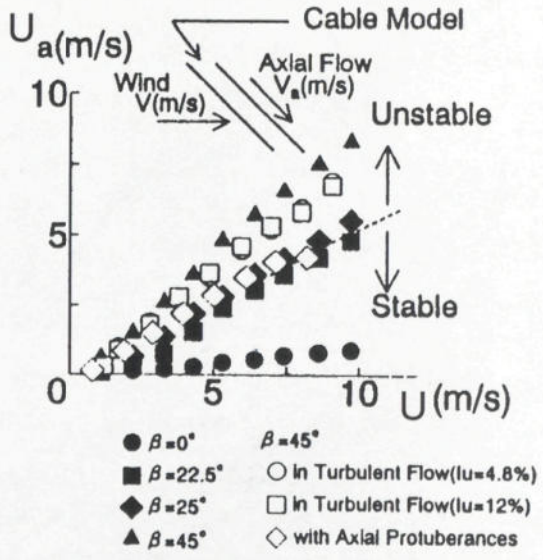


Figure 6.35. Intensity of axial flow for yawed cables. (Matsumoto, 1998).

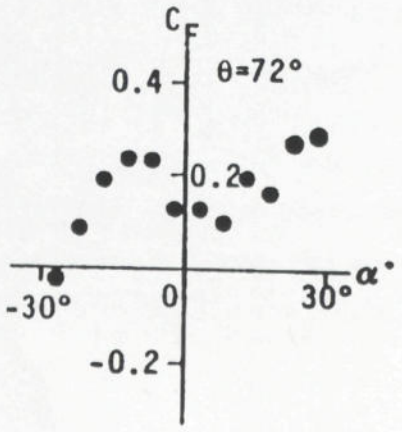


Figure 6.36. Lift coefficient of yawed cable ($\beta = 45^\circ$) with artificial water rivulet (Matsumoto, 1998).

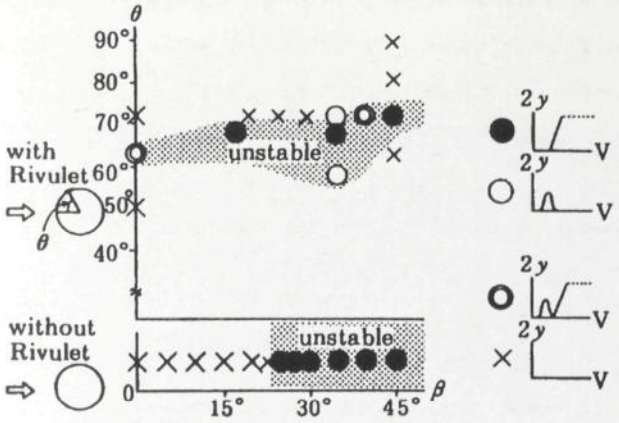


Figure 6.37. Response characteristics of yawed cable with and without rivulet in smooth flow (Matsumoto, 1998).

(iii) High speed vortex excitation

The third cause of aerodynamic instability of an inclined cable, as described by Matsumoto, the *high speed vortex excitation*, is directly associated with the formation of the axial flow in the wake of the cable. According to Matsumoto (1998), the conventional two-dimensional Karman vortex interact with the axial flow, generating an amplified vortex, which sheds every once three Karman vortex shed, as illustrated in Figure 6.38. Figure 6.39 presents a visualization of this phenomenon using the liquid paraffin method.

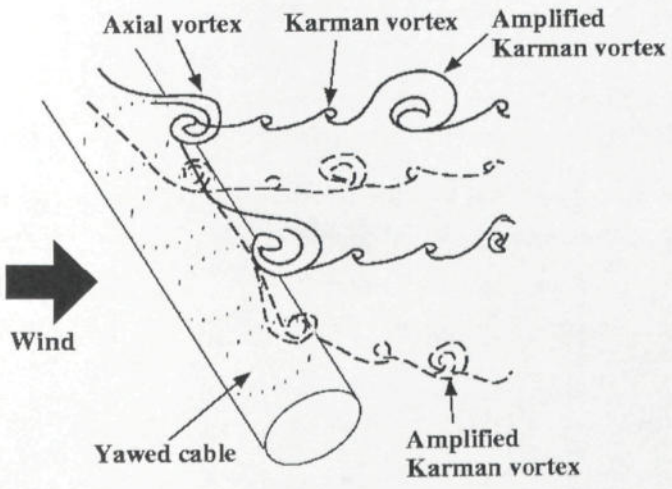


Figure 6.38. Illustration of the axial vortex and Karman vortex around the yawed inclined cable (Matsumoto, 1998).

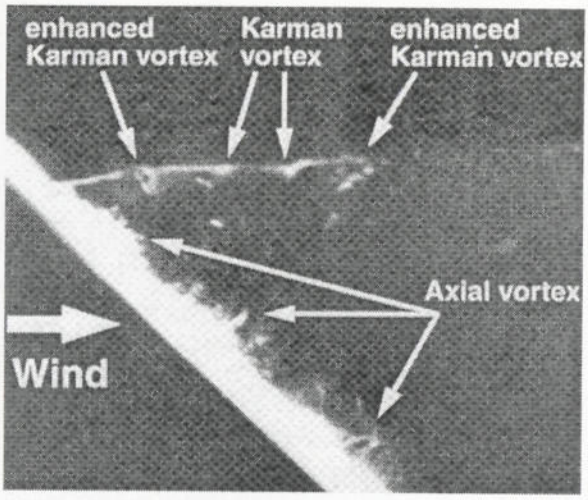


Figure 6.39. Visualized axial vortex and intermittently enhanced Karman vortex for the yawed cable ($\beta = 45^{\circ}$) in smooth flow (by liquid paraffin method (Matsumoto, 1998).

Though the characteristics of this *axial vortex* are not entirely identified yet, the frequency of the shedding seems to be about one-third the conventional Karman frequency, depending on factors such as the yawing of the cable, the location of the upper rivulet and the frequency of cable vibration. The occurrence of this type of instability is associated with reduced velocities that are integer times of about *20* and is very much affected by the intensity of turbulence. These facts are consistent with the observations at the Higashi Kobe Bridge (Saito *et al.*, 1994), where despite the use of protuberated cable (see Figure 1.11) preventing the formation of water rivulets, the cables became unstable with small amplitude oscillations at a high wind velocity of *40m/s*, corresponding to reduced velocities of *161*, *241* and *468* for the fundamental vibrating modes (Matsumoto, 1998).

Other variables to the rain-wind induced vibration problem

The results presented above suggest that the phenomenon of rain-wind induced vibration may enclose different excitation mechanisms acting simultaneously. The complexity of the phenomenon is evident and can still be enhanced when considering other variables to the problem, like the adhesion property of the cable coating material, or the intensity of the rainfall.

The first topic has been thoroughly investigated by Flamand (1994). Noting that the cable instability usually occurred with standard polyethylene smooth casing of the cable, this author tested the influence of the characteristics of several materials and surface types in the formation of the rivulet, realizing for example that a stable smooth surface became unstable when covered by a coating of soot resulting from fuel-oil combustion (which is alike atmospheric pollution).

With regard to the second topic, reference should be made to the studies of Ohshima and Nanjo (1987) and more recently of Main and Jones (1999). The first authors developed

wind tunnel tests based on a prototype cable model of the Ajigawa cable-stayed bridge, in Japan, subject to different rates of rainfall, concluding that the higher this rate is, the lower is the onset wind velocity for the occurrence of cable vibrations. These results seem consistent with the observations on the Fred Hartman and East Huntington cable-stayed bridges by Main and Jones.

Prediction of the possibility of occurrence of rain-wind induced vibrations

In view of the extreme complexity of this phenomenon and as far as known by the author, no general model has been established for the prediction of the possibility of occurrence and amplitude of rain-wind induced vibrations yet. Reference should be made however to the work of Geurts *et al.* (1998), who developed a model based on a modified galloping mechanism whose parameters, namely the lift coefficient, were adjusted based on the amplitudes and frequencies of vibration measured on the bridge prototype. The model was useful in the numerical simulation of the bridge behaviour for selecting and tuning the final measures (hydraulic dampers installed at the cable ends) to prevent further vibrations on the bridge.

In a more recent paper, and based on the same model, Geurts and Staalduinen (1999) developed formulae for a rough estimation in design stage of the critical wind speed U_{cr} associated with the occurrence of rain-wind vibration and of the maximum amplitude of vibration y_0 given by

$$U_{cr} = \frac{8m\pi f_e}{-\rho\left(\frac{dC_y(\alpha)}{d\alpha} + C_D\right)\cdot D} \tag{6.38}$$

and

$$\left(\omega_e \cdot \frac{y_0}{U}\right)^2 = \frac{8}{\frac{d^3 C_y}{d\alpha^3}}\left(-\frac{dC_y}{d\alpha} - \frac{2\xi m\omega_e}{\frac{1}{2}\rho U D}\right) \tag{6.39}$$

where f_e is the natural frequency of the cable in *Hz*, ω_e is the corresponding value in *rad/s*, U is the wind velocity, C_y is the coefficient for loading in the vertical direction and α is the relative angle of attack.

According to Geurts and Staalduinen, these formulae don't attempt to describe the exact generating mechanism of rain-wind induced vibration, but consider instead the main features that were extracted from wind tunnel observations. A particular care should be taken in the choice of the derivatives of the lift coefficient, which are in fact the key values of equations (6.38) and (6.39), and should be obtained from wind tunnel tests on a model of the cable to be used for a worst case scenario. Geurts and Staalduinen adopted values of *-0.8*

and *54* for the quantities $dC_y/d\alpha$ and $d^3C_y/d\alpha^3$ respectively, based on a wind tunnel test of a smooth cable model with an artificial upper rivulet.

The application of equation (6.39) to a particular cable of a cable-stayed bridge leads to a series of curves of variation of the maximum amplitude of oscillation with wind speed for different possible damping ratios, as depicted in Figure 6.40. Fixing acceptable limits for y_0, the necessary damping ratio can be estimated from this Figure.

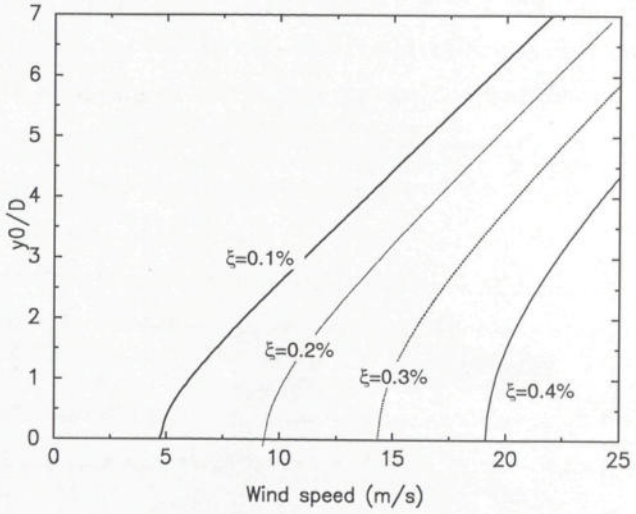


Figure 6.40. Estimation of maximum amplitude of vibration as a function of the wind velocity and damping ratio ξ of a stay cable with a smooth cable coating.

Practical cases of occurrence of rain-wind induced vibrations

With regard to the status of occurrence of rain-wind induced vibration in cable-stayed bridges, it is important to note that, since the identification of the phenomenon in 1986 until the present days, many unanticipated vibration problems in prototypes have been reported all over the world. As far as known by the author, the first report of cable oscillations dates back from 1979 and respects the Brotonne Bridge (Wianecki, 1979). It is thought presently that these vibrations were caused by rain and wind. The experience of the phenomenon in Europe has been also reported for the Farø Bridge, in Denmark (Langsoe & Larsen, 1987), the Ben-Ahin and Wandre Bridges, in Belgium (Cremer *et al.*, 1995), and more recently, for the Second Severn Bridge in UK (Virlogeux, 1998) and the Erasmus Bridge, in Netherlands (Geurts *et al.*, 1998). In Japan, and besides the Meiko-Nishi Bridge (West Meiko), the Aratsu (Yoshimura, 1989), the Higashi Kobe (Matsumoto, 1998), the Tempozan (Matsumoto, 1998) and the Central Meiko Bridges (Ito, 1998) have experienced rain-wind vibration. In the US, rain vibration occurred at the Weirton-Steubenville Bridge, in West Virginia (Thiele, 1996), and at the Fred Hartman and East Huntington Bridges, located in Texas and West Virginia,

respectively (Main & Jones, 1999). And in Australia, rain vibration amplitudes of several meters have been been observed at the Glebe Island Bridge.

Conclusions

Based upon the experience gathered from the observation of rain vibration in prototypes of cable-stayed bridges, the main conditions and characteristics associated with the occurrence of the phenomenon can be summarized as follows (Hikami & Shiraishi, 1988; Matsumoto, 1998; Main & Jones, 1999; Sarkar *et al.*, 1999):

- The wind speed and direction vary in the ranges of *5m/s* to *20m/s*, and *30°* to *50°* to the longitudinal axis of the bridge, respectively;
- Existence of rain, heavy, light or drizzle;
- The cable surface is smooth, such as polyethylene or painted metal cased cables;
- The cable diameter is in the range *80mm* to *200mm*;
- Typical vibration frequencies are in the range *0.3Hz-3Hz*;
- Typical amplitudes of vibration are about twice the cable diameter. However, amplitudes of *7D* have already been observed;
- The structural damping of the cables is very low (logarithmic damping decrement less than *0.01*);
- The cable is located behind the bridge pylon and declines in the direction of the wind;
- The cable-stayed bridge is located in an area where the intensity of turbulence is expected to be low, such as in a seaside area;
- The vibration orbit varies according to the intensity of the rainfall: for light rain and drizzle, vibration occurs essentially in the vertical plane, while for heavy rainfall the orbit may exhibit significant two-dimensionality.

The state-of-art report on wind-induced cable vibration of cable-stayed bridges in Japan presented in 1989 (Matsumoto et al, 1989) indicated that, from an enquiry to concerned bridge authorities in Japan, a total of sixteen out of fifty-five cable-stayed bridges had suffered from wind-induced cable vibration. From these, five or six had experienced rain-wind vibrations.

6.3 INDIRECT EXCITATION

6.3.1 General

The vibration of cables may be motivated by harmonic oscillation of their supports, corresponding to harmonic movement of the deck and /or towers. This indirect type of cable

excitation results from any type of action on the bridge structure, such as wind, traffic, pedestrian loads, or earthquake. Considering that the displacement of the cable anchorages allows an energy transfer from the deck and towers to the cables, and given the relative mass ratio of the former to the later, it is expected that small oscillations at the supports originate large amplitude vibrations of the cables. According to Clement and Cremona (1996), these can be up to *30* times larger than the vibrations at the supports.

Another aspect is the fact that a harmonic excitation at one or two of the supports (see Figure 6.41) comprehends both an excitation along the chord, and an excitation perpendicular to that direction. This excitation is generally designated for both cases as *parametric excitation*, due to the fact that when establishing the differential equation of motion, the excitation term appears as a coefficient. In the current text the term *parametric excitation* will be used only to characterize the excitation associated with longitudinal motion of the anchorage, while the excitation induced by motion of the anchorage perpendicular to the cable chord will be designated as *external excitation.* In fact, it will be observed that for taut cables, on the contrary to the *external excitation*, which mostly generates large responses whenever the excitation frequency is close to one of the natural frequencies of the system (*primary resonance*), a small excitation along the longitudinal direction originates large amplitude response when the excitation frequency is about twice the natural frequency of the system. This is the so-called *principal parametric resonance.*

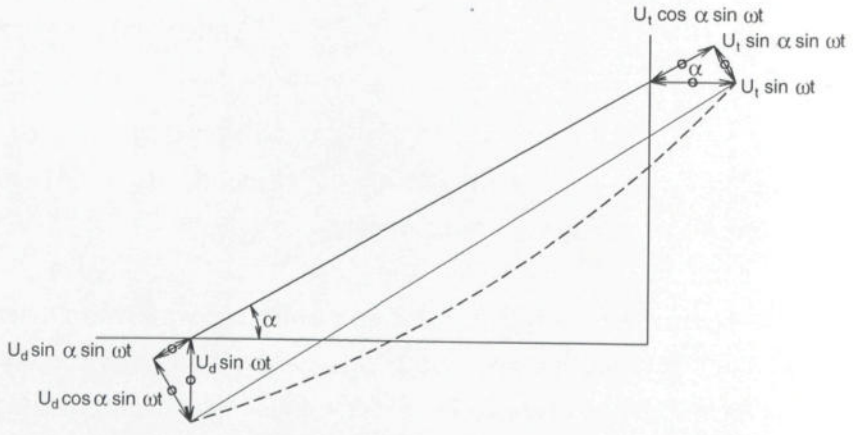


Figure 6.41. Stay cable subjected to harmonic motion at the anchorages.

From an engineering point of view, the goal is to quantify the amplification of the deck /tower motion and define the amount of damping necessary to prevent the cable system to undergo large vibrations.

The current Section analyses the problem of harmonic oscillation of the supports considering separately the *external* and *parametric excitations.*

For the case of *external excitation*, and in a first approach, a linear model is employed to characterize the motion of the stay cable, according to Virlogeux (1998). The comparison between the linear response and the response calculated numerically for a particular stay cable using a finite element model and a nonlinear geometric formulation shows an important departure from the linear model for relatively small amplitudes of support oscillation and, consequently, analytical solutions obtained for specific types of nonlinear differential equations by Nayfeh and Mook (1979) are applied, namely the response of a system with small viscous damping characterized by small quadratic and cubic nonlinearities to an harmonic excitation. This allows the estimation of maximum amplitudes of the steady-state response associated with the *primary resonance*.

The nonlinear differential equation that governs the in-plane motion of a *parametrically excited* cable is then investigated, employing general solutions developed by Nayfeh and Mook (1979), Tagata (1977) and Pinto da Costa *et al.* (1996), and experimentally validated by the last two authors. Considering the instability regions that are associated with parametrically excited systems, threshold amplitudes of support oscillation for the occurrence of instability are defined, and the limit cycle response calculated, for the principal parametric resonance. The analytical solution is compared with the numerically calculated response of a particular stay cable.

The issue of *cable-structure interaction* is then introduced through a finite element analysis of a very simple system that is composed by an association of a stay cable and a spring/ mass system whose dynamic characteristics are conveniently chosen. It is shown that the nonlinear character of vibration may enhance the global bridge/ cable vibrations, for large oscillations at the deck/ towers. For small amplitudes of oscillation, the cable-structure interaction may lead to a decrease of the global bridge response.

6.3.2 External excitation

Consider the horizontal cable represented in Figure 6.42, whose anchorage B is subjected to an harmonic oscillation $z_B(t)$ given by

$$z_B(t) = z_B \cdot \sin\omega t \tag{6.40}$$

Accordingly, the position $z(x, t)$ of a generic point is given by the sum

$$z(x,t) = z_g(x) + z_0(x,t) + w(x,t) \tag{6.41}$$

where $z_g(x)$ is the cable deformation due to dead weight, approximated by the parabola defined by equation (3.16), $z_0(x,t)$ is the solid movement produced by the oscillation at the anchorage B, which is given by

$$z_0(x,t) = z_B(t) \cdot \frac{x}{\ell} \tag{6.42}$$

and *w(x,t)* is the intrinsic vibration of the cable.

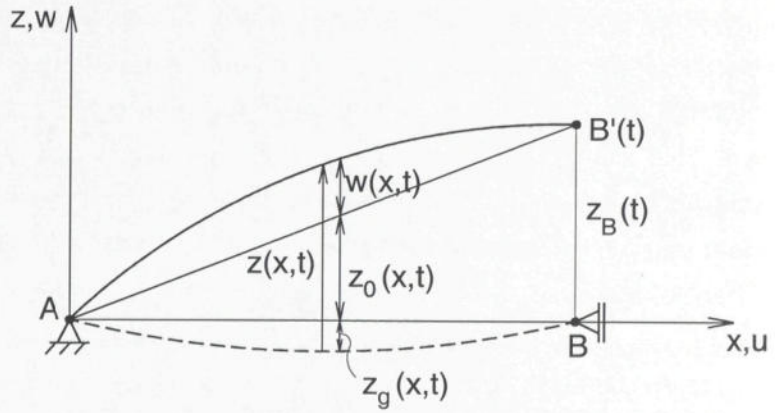


Figure 6.42. Stay cable subjected to transverse motion at one anchorage.

The linear model

Assuming that the cable is a taut string and neglecting the additional component of tension τ by comparison with the initial tension in the cable T, the dynamic equilibrium equation of the cable in the vertical direction (3.38c) can be simplified into

$$T\frac{\partial^2 z}{\partial x^2} = m\frac{\partial^2 z}{\partial t^2} - mg \tag{6.43}$$

The substitution of (6.41) and (6.42) into (6.43) yields

$$T\frac{\partial^2 w}{\partial x^2} = m\frac{\partial^2 w}{\partial t^2} + m \cdot \frac{x}{\ell} \cdot \frac{\partial^2 z_B}{\partial t^2} \tag{6.44}$$

Equation (6.44) can now be solved by decomposition of *w(x, t)* into a Fourier series, whose coefficients $\alpha_k(t)$ represent the contribution of the kth mode shape, with an assumed sinusoidal configuration

$$w(x,t) = \sum_{k=1}^{n} \alpha_k(t) \cdot \sin\left(\frac{k\pi x}{\ell}\right) \tag{6.45}$$

Introducing (6.45) into (6.44), the following equation is obtained

$$\sum_{k=1}^{n}\left[m\frac{\partial^2 \alpha_k(t)}{\partial t^2} + T\left(\frac{k\pi}{\ell}\right)^2 \alpha_k(t)\right] \cdot \sin\left(\frac{k\pi x}{\ell}\right) = -m \cdot \frac{x}{\ell} \cdot \frac{\partial^2 z_B(t)}{\partial t^2} \tag{6.46}$$

Making use of the property of orthogonality of the sinusoidal modal shapes, a set of n equations in the coefficients $\alpha_k(t)$, $(k=1, 2, ..., n)$, associated with the n modes of vibration considered can now be obtained. Multiplying the two terms of equation (6.46) by the generic function $sin(\frac{j\pi x}{\ell})$ and integrating over the length of the cable, equation (6.46) is transformed into

$$\sum_{k=1}^{n}\left[m\frac{\partial^2\alpha_k(t)}{\partial t^2}+T(\frac{k\pi}{\ell})^2\,\alpha_k(t)\right]\cdot\int_0^{\ell} sin(\frac{k\pi x}{\ell})\cdot sin(\frac{j\pi x}{\ell})\,dx = \\ =-m\,\frac{\partial^2 z_B(t)}{\partial t^2}\cdot\int_0^{\ell}\frac{x}{\ell}\cdot sin(\frac{j\pi x}{\ell})\,dx \tag{6.47}$$

For $j=k$ equation (6.47) reduces to

$$\frac{\partial^2\alpha_k(t)}{\partial t^2}+\frac{T}{m}(\frac{k\pi}{\ell})^2\,\alpha_k(t)=\frac{2}{k\pi}(-1)^k\,\frac{\partial^2 z_B(t)}{\partial t^2} \tag{6.48}$$

From the taut string theory (see Chapter three), the natural frequency ω_k associated with the k_{th} mode of vibration is

$$\omega_k=\frac{k\pi}{\ell}\sqrt{\frac{T}{m}} \tag{6.49}$$

Considering that the anchorage motion is the sinusoid of amplitude z_B and frequency ω given by equation (6.40) and introducing into (6.48) a viscous damping term characterized by a damping coefficient ξ_k, the following equation of motion is obtained

$$\frac{\partial^2\alpha_k(t)}{\partial t^2}+2\xi_k\omega_k\frac{\partial\alpha_k(t)}{\partial t}+\omega_k^2\cdot\alpha_k(t)=\frac{2}{k\pi}(-1)^k\,\omega^2 z_B\cdot sin(\omega t) \tag{6.50}$$

whose solution $\alpha_k(t)$ is the response of a damped single-degree-of-freedom oscillator to a sinusoidal excitation, given by (Clough & Penzien, 1986)

$$\alpha_k(t)=\frac{\frac{2}{k\pi}(-1)^k\,\beta_k^2\,Z_B}{\sqrt{(1-\beta_k^2)^2+(2\xi_k\beta_k)^2}}\cdot sin(\omega t-\theta_k) \tag{6.51}$$

with $\beta_k=\omega/\omega_k$ and

$$\theta_k=tan^{-1}\,\frac{2\xi_k\beta_k}{1-\beta_k^2} \tag{6.52}$$

The vibration of a generic point along the cable is then given by

$$\bar{z}(x,t) = z_B \cdot \frac{x}{\ell} \cdot \sin(\omega t) + \sum_{k=0}^{n} \left[\frac{\frac{2}{k\pi}(-1)^k \beta_k^2 z_B}{\sqrt{(1-\beta_k^2)^2 + (2\xi_k \beta_k)^2}} \cdot \sin(\omega t - \theta_k) \cdot \sin\frac{k\pi x}{\ell} \right] \quad (6.53)$$

Equation (6.53) evidences that the contribution of a mode of kth order depends both on the ratio β_k between the excitation frequency ω and the cable frequency ω_k, and on the damping coefficient ξ_k. $\alpha_k(t)$ is maximum whenever β_k is unit, that is, when the excitation frequency is in resonance with one of the natural frequencies of the cable and, in particular, when *k=1*. This is the so-called *primary resonance*, the maximum amplitude of oscillation in the first mode being

$$(\alpha_1)_{max} = \frac{z_B}{\pi \xi_1} \quad (6.54)$$

Considering the small amount of damping associated with stay cables, which, in the absence of other mechanical devices and aerodynamic influence varies in the range *0.1%* to *0.2%* for the majority of the stays, it is evident from (6.54) that the amplification of the support oscillation may be enormous. The validity of the linear approach above presented to evaluate the amplitude of cable vibration should then be questioned.

Numerical example

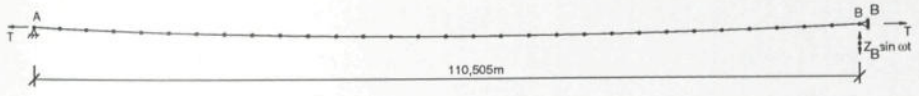
In order to have a perception of the degree of nonlinearity in the stay cable vibration associated with external excitation, the response of a medium size stay cable to harmonic oscillation at the support was evaluated numerically, using a finite element formulation based on the software SOLVIA (1995).

The characteristics of the stay cable presented in Figure 6.43 correspond approximately to one of the stay cables of the Ben-Ahin Cable-Stayed Bridge (Belgium, 1987) and were obtained from (Lilien & Pinto da Costa, 1994). According to Figure 6.43, the *110.5m* long stay cable was analysed in an horizontal layout and divided into a total of thirty truss elements. These elements were subjected both to dead weight and to an initial strain that lead to the installed tension *T* of *4902.7kN*. Fixing the vertical displacement at anchorage *B*, and considering the stiffness matrix derived in the deformed position, the linear eigenvalue problem was solved, which lead to the first natural frequencies of in-plane vibration presented in Table 6.4.

In a second step, the response to a vertical harmonic displacement at anchorage *B* was evaluated based on a nonlinear geometric formulation (SOLVIA, 1995), considering different amplitudes and an excitation frequency of *1.25Hz* (situation of *primary resonance*). In this analysis, a Rayleigh damping matrix proportional to the mass matrix was used, with an assumed damping coefficient of *1%* for the first mode of vibration (this coefficient can be

considered an average value of the damping coefficient in a stay cable after mechanic devices are added).

Figure 6.44 represents the time response at the central span expressed in terms of the vertical displacements for the first *50s*, considering an amplitude of oscillation at the supports of *0.10m*. The variation of the cable tension at anchorage *B* associated with this amplitude of motion is presented in Figure 6.45 for the same time interval.



$\ell = 110.505m$

$m = 64.841kg/m$

$E = 210x10^9 N/m^2$

$A_0 = 0.00826m^2$

$T = 4902.7x10^3 N$

$\lambda^2 = 0.0727$

Figure 6.43. Stay cable of Ben-Ahin Cable-Stayed Bridge. Discretization for *FEM* analysis and main characteristics.

Table 6.4. First natural frequencies of vibration for in-plane motion of stay cable.

Order	Frequency (Hz)
1st	1.25
2nd	2.49
3rd	3.75
4th	5.01
5th	6.29

Figures 6.44 and 6.45 exhibit a pattern that is common to all levels of induced excitation, consisting of the following aspects:

- Vibration of the stay cable in the fundamental mode (which is coincident, in this case, with the excitation frequency);
- Convergence of the response to a limit cycle, after a transition region in which the oscillation may exceed the steady-state response;
- Development of a double frequency content in the stay cable tension which becomes apparent and significant whenever the amplitude of cable vibration exceeds the initial amplitude of deformation due to cable sag.

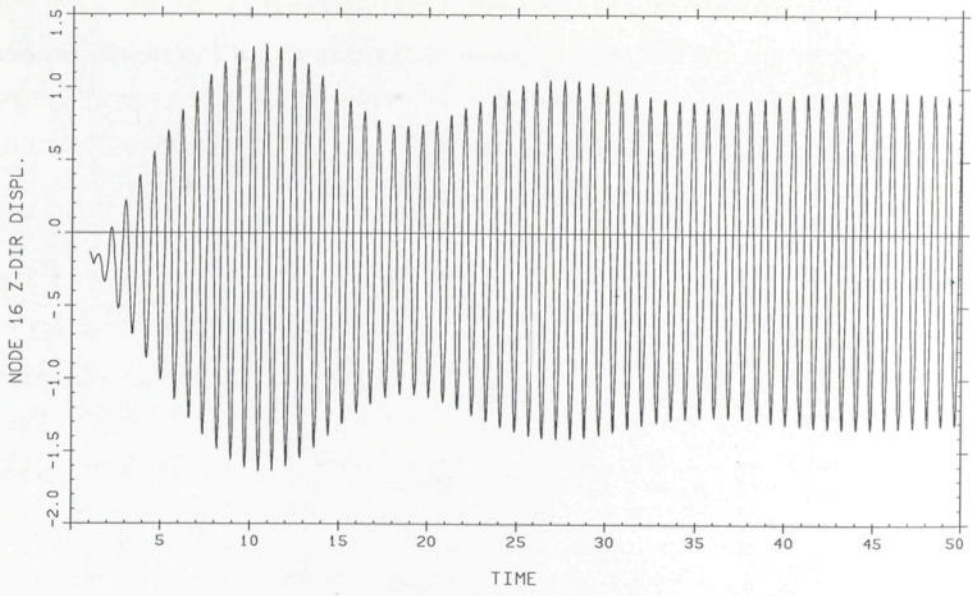


Figure 6.44. Vertical displacement at the central span for a vertical oscillation at anchorage *B* of $0.10\sin(2\cdot\pi\cdot1.25\cdot t)$.

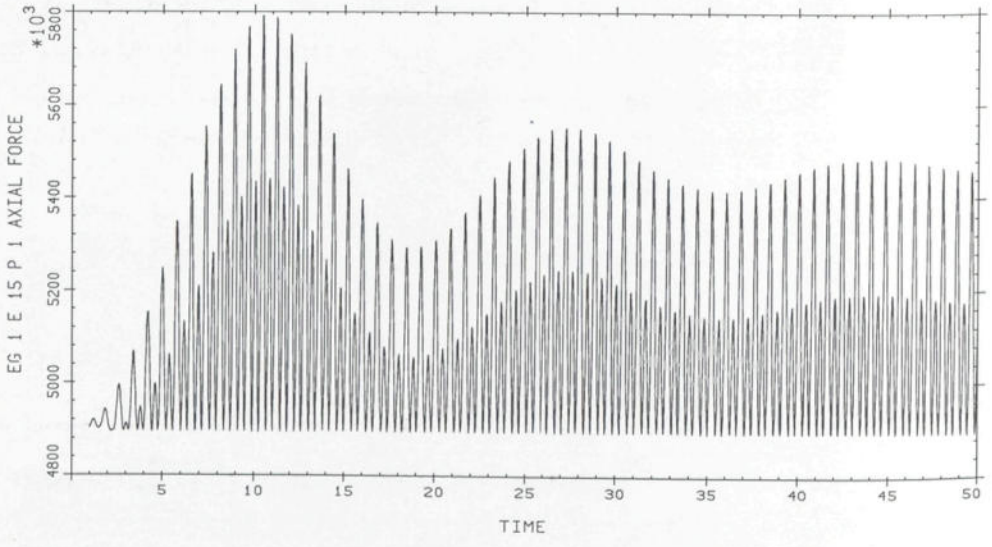


Figure 6.45. Cable tension at anchorage *B* associated with vertical oscillation at that point of $0.10\sin(2\cdot\pi\cdot1.25\cdot t)$.

Figure 6.46 summarizes the limit cycle response and the increment of tension calculated for several amplitudes of support oscillation in the range *0.005m* to *0.2m*, considering two different damping coefficients for the first vibration mode, *0.5%* and *1%*. Superimposed in graphs (a) and (b) of that Figure are solid straight lines that represent the maximum response calculated on the basis of the linear model above described, which is

given by equation (6.54). A bold curve in those graphs describes the results obtained under an analytical nonlinear formulation that will be explained subsequently.

The graphs of Figure 6.46 clearly evidence a deviation of the numerically calculated response from the linear model, which starts at an amplitude of *0.01m* when $\xi = 0.5\%$, and at an amplitude of *0.02m*, when $\xi = 1\%$. For a support oscillation of *0.05m* of amplitude, for example, the numerical response is actually *30%* of the linear response for $\xi = 0.5\%$ and *59%* for $\xi = 1\%$. An interesting aspect is the very slight dependence of the numerical response on the damping coefficient for larger amplitudes of oscillation (see Figure 6.46 (c)). This phenomenon is however specific of very small λ^2 parameters, as will be illustrated hereafter. It can be also observed that for larger amplitudes of vibration, the increment of cable tension attains significant values and should not be neglected (see Figure 6.46(d)).

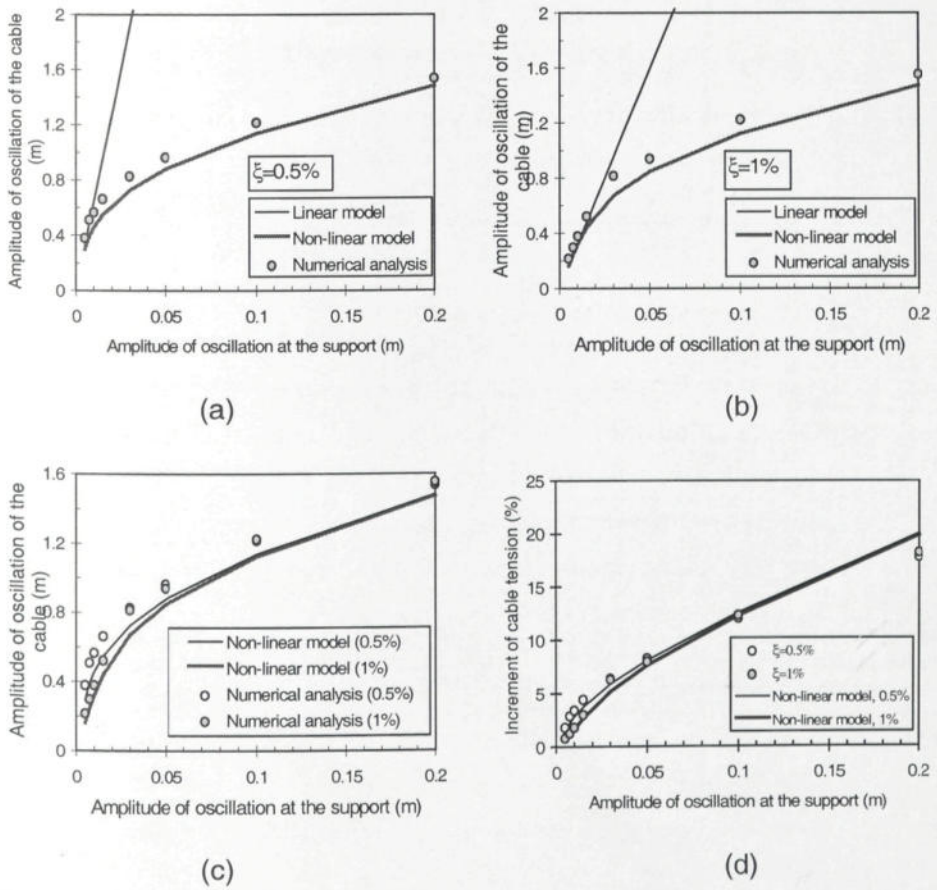


Figure 6.46. Variation of the amplitude of oscillation / increment of cable tension with the amplitude of harmonic oscillation at the anchorage at *primary resonance*, considering $\xi = 0.5\%$ and $\xi = 1\%$: Linear model, numerical response, and nonlinear model.

Another important fact to discuss is the maximum amplitude of the transient response. Although the graphs presented above respect the steady-state response, it should be noted that, for large amplitudes of support oscillation, the transient vibration may exceed the steady-

state response (see Figure 6.44). Figure 6.47 illustrates the variation of the ratio between maximum transient and steady-state response for the two damping coefficients above considered of *0.5%* and *1%* and evidences the significant dependence of this ratio both on the damping coefficient and on the amplitude of oscillation.

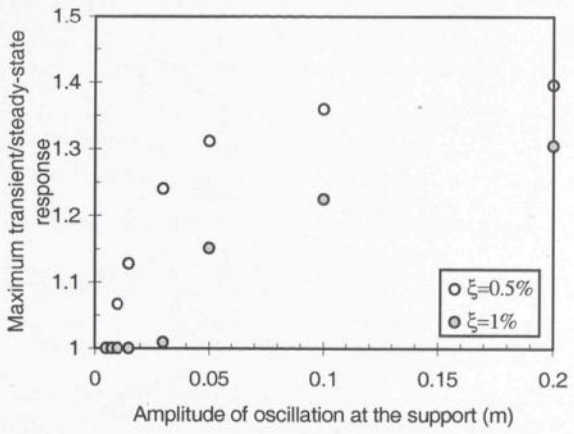


Figure 6.47. Variation of the ratio between maximum transient and steady-state response with amplitude of oscillation for $\xi = 0.5\%$ and $\xi = 1\%$.

Nonlinear model

In an attempt to obtain a nonlinear correction for the maximum amplitude of oscillation in a stay cable, the author adapted the nonlinear differential equations developed by Pinto da Costa *et al.* (1996) for an inclined cable subjected to vertical harmonic motion of one support and obtained the solution associated with primary resonance.

Assuming that the static configuration of the cable is a parabola, neglecting the longitudinal inertia forces, employing a nonlinear geometric formulation in the evaluation of the potential energy according to Perkins (1992) (see Chapter three), and approaching the transverse displacement by a function containing the first two linear free-oscillation modes of a taut cable

$$w(x,t) = z_B \frac{x}{\ell} \sin(\omega t) + \alpha_1(t) \sin\frac{\pi x}{\ell} + \alpha_2(t) \sin\frac{2\pi x}{\ell} \qquad (6.55)$$

Pinto da Costa and companion authors applied the Galerkin method and derived two coupled partial differential equations in the functions $\alpha_1(t)$ and $\alpha_2(t)$. Neglecting the coupling terms in $\alpha_2(t)$ and the terms associated with smaller order of magnitude, the equation in $\alpha_1(t)$ reduces, for the particular case of an horizontal cable, to

$$\ddot{\alpha}_1(t)+2\xi_1\omega_1\dot{\alpha}_1(t)+\omega_1^2\cdot\left[1+\frac{1}{2}(\frac{2}{\pi})^4\cdot\lambda^2-\frac{\lambda z_B}{2\sqrt{X_0\ell}}sin(\omega t)\right]\alpha_1(t)-$$
$$-\frac{3\omega_1^2}{\pi\sqrt{X_0\ell}}\cdot\lambda\cdot\alpha_1^2(t)+\frac{\pi^2}{4}\frac{\omega_1^2}{X_0\ell}\alpha_1^3(t)=2\frac{\omega_1^2}{\pi}\cdot z_B\cdot\left[1-(\frac{\lambda}{\pi})^2\right]\cdot sin(\omega t) \qquad (6.56)$$

where X_0 is the elastic elongation of the cable, $X_0=T\ell/(EA_0)$, and ω_1 is the linear natural frequency associated with the first vibration mode of a taut string, given by $\omega_1=\frac{\pi}{\ell}\sqrt{T/m}$.

Considering the application to taut cables, for which λ^2 is very small (say $\lambda^2\leq 0.5$), the periodic component term in $\alpha_1(t)$, named the *parametric term*, has generally a lower order of magnitude than the other terms and will consequently be neglected. In this case, the differential equation in $\alpha_1(t)$

$$\ddot{\alpha}_1(t)+2\xi_1\omega_1\dot{\alpha}_1(t)+\omega_1^2\cdot\left[1+\frac{1}{2}(\frac{2}{\pi})^4\cdot\lambda^2\right]\alpha_1(t)-\frac{3\omega_1^2}{\pi\sqrt{X_0\ell}}\cdot\lambda\cdot\alpha_1^2(t)+$$
$$+\frac{\pi^2}{4}\frac{\omega_1^2}{X_0\ell}\alpha_1^3(t)=2\frac{\omega_1^2}{\pi}\cdot z_B\cdot\left[1-(\frac{\lambda}{\pi})^2\right]\cdot sin(\omega t) \qquad (6.57)$$

can be viewed as the governing equation of a system with quadratic and cubic nonlinearities subjected to a harmonic excitation.

An important characteristic of nonlinear systems is the existence of *secondary resonances*. A system with quadratic nonlinearities only (taut string) possesses a so-called *subharmonic resonance* of order *1/2* and a *superharmonic resonance* of order *2*, in addition to the primary resonance, of order *1*. A system with cubic nonlinearities only (inextensible cable) possesses a *subharmonic resonance* of order *1/3* and a *superharmonic resonance* of order *3*. In any of the cases, the existence of *secondary resonances* means that, if the system is subjected to an harmonic excitation characterized by a frequency ω that is in the vicinity of the natural frequency ω_1, then in addition to the steady-state response in the frequency ω_1, a component in a *subharmonic / superharmonic* frequency ($\frac{1}{2}\omega_1$, $\frac{1}{3}\omega_1$, $2\omega_1$, $3\omega_1$) occurs. This component either vanishes with time, or converges to a finite value, according to the initial conditions.

In the present system, where both quadratic and cubic nonlinearities are present, both *subharmonic* and *superharmonic resonances* of order *1/3*, *1/2*, *2* and *3*, respectively, exist. Additionally, other so-called *combination resonances* may exist, if the system is excited by a combination of harmonics with particular values (Nayfeh & Mook, 1979).

The present study will only focus on the *primary resonance*, which dominates the steady-state response. Nayfeh and Mook (1979) developed a solution for equation (6.57) in a vicinity of the resonance ω_1, using a perturbation method, the *method of multiple scales*. This solution, given by

$$\alpha_1(t) = a\sin(\omega t - \gamma) + \frac{3\lambda}{2\pi\sqrt{X_0 \ell}} a^2 \cdot \left[1 - \frac{1}{3}\sin(2\omega t - 2\gamma)\right] \tag{6.58}$$

depends on the parameters a and γ, which have maximum values given by

$$a = \frac{z_B}{\pi\xi_1} \frac{1 - (\frac{\lambda}{\pi})^2}{\left[1 + \frac{1}{2}(\frac{2}{\pi})^4 \lambda^2\right]^{1/2}} \cdot \sin\gamma \tag{6.59a}$$

and by the solution of

$$\sin^2\gamma \cdot \tan\gamma = \frac{32}{3} \cdot X_0 \ell \frac{\left[1 + \frac{1}{2}(\frac{2}{\pi})^4 \cdot \lambda^2\right]^4}{\left[1 - (\frac{\lambda}{\pi})^2\right]^2 \cdot \left[1 - 32\frac{\lambda^2}{\pi^4}\right]} \cdot \frac{\xi_1^3}{z_B^2} \tag{6.59b}$$

Noting that for very small values of λ^2 (say $\lambda^2 < 0.2$)

$$\frac{1 - (\frac{\lambda}{\pi})^2}{\left[1 + \frac{1}{2}(\frac{2}{\pi})^4 \lambda^2\right]^{1/2}} \approx 1$$

the maximum value of the amplitude of the steady-state response a in the frequency ω reduces to

$$a = \frac{z_B}{\pi\xi_1} \cdot \sin\gamma \tag{6.60}$$

This is no more than the linear amplitude of the response weighted by a function $\sin\gamma$ that reflects the nonlinear character of the system and whose value is obtained by numerical solution of equation (6.59b). Figure 6.48 illustrates the variation of $\sin\gamma$ with the amplitude of support oscillation at *primary resonance* for different damping coefficients, for the cable described in Figure 6.43. It is clear from that Figure that for small damping coefficients significant nonlinearities in the response occur at very small amplitudes of oscillation.

Another aspect is evidenced by equation (6.58), which consists in the appearance of a drift in the steady-state response, that grows with the amplitude of oscillation. For the cable under analysis, this drift is no greater than *2%* of the maximum response.

The maximum amplitude of oscillation was calculated for the stay cable above described using equations (6.58) and (6.59) (equation (6.59b) was solved using the commercial software *MAPLEV*) and is plotted in bold solid line in Figure 6.46 for the two values of the damping coefficient considered, *0.5%* and *1%*. The analysis of this Figure shows a small deviation between the numerical and theoretical model, the later producing however smaller response than the first one. Another characteristic evidenced both by the numerical

and analytical responses, is the relatively slight dependence of the amplitude of vibration on the damping coefficient for large amplitudes of vibration. This phenomenon can be observed in Figure 6.46(c), considering the two damping coefficients of *0.5%* and *1%*, and is framed by the shaded area of Figure 6.49 both for this cable ($\lambda^2 = 0.0727$) and for the longest cable of the Vasco da Gama Bridge ($\lambda^2 = 0.4321$), for damping coefficients in the range *0.1%* to *1.5%*.

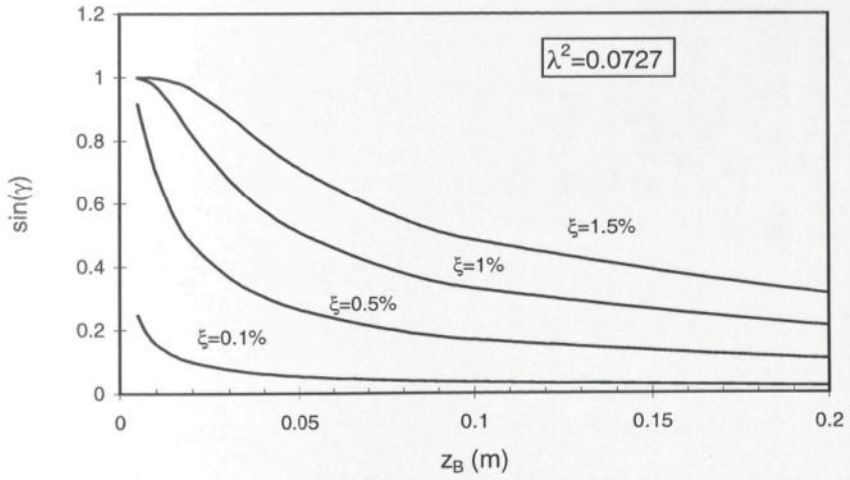


Figure 6.48. Variation of $sin\gamma$ with the amplitude of support oscillation for different damping coefficients and $\lambda^2 = 0.0727$.

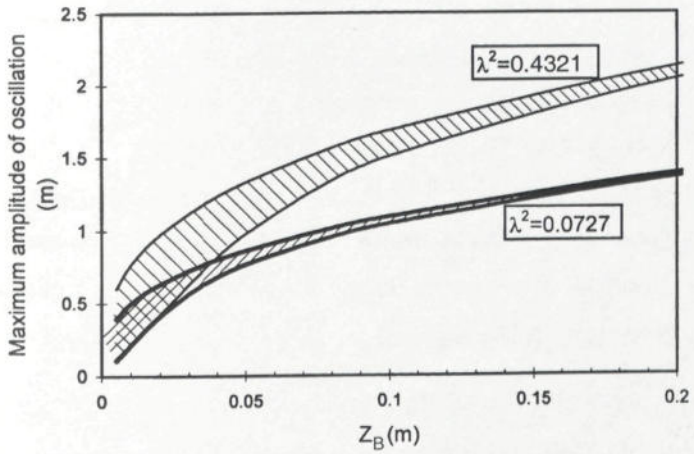


Figure 6.49. Variation of maximum steady-state amplitude of oscillation at primary resonance with amplitude of support oscillation for damping coefficients within the range *0.1%* to *1.5%*.

Finally, based on a second order definition of the elastic strain ε of the cable given by equation (3.73) and considering only motion in the plane, the dynamic increment of tension τ in the cable can be obtained from

$$\tau(t) = \frac{EA_0}{\ell} \cdot \left[u(\ell,t) - u(0,t) + \int_0^\ell \frac{dz}{dx} \cdot \frac{\partial w}{\partial x} dx + \frac{1}{2} \cdot \int_0^\ell \left(\frac{\partial w}{\partial x}\right)^2 dx \right] \tag{6.61}$$

Given the parabolic profile of the cable in the static configuration, and the definition of w(x, t) according to (6.55), where the component in the second mode is neglected ($\alpha_2 = 0$), the partial derivatives reduce to

$$\frac{dz}{dx} = \frac{mg}{2T} \cdot (\ell - 2x) \tag{6.62a}$$

$$\frac{\partial w}{\partial x} = \frac{z_B}{\ell} \cdot \sin(\omega t) + \alpha_1(t) \frac{\pi}{\ell} \cos\left(\frac{\pi x}{\ell}\right) \tag{6.62b}$$

Substituting (6.62a) and (6.62b) into (6.61) and introducing the boundary conditions $u(\ell,t) = u(0,t) = 0$ yields

$$\tau(t) = \frac{EA_0}{\ell} \cdot \left[2\frac{\ell}{\pi} \cdot \frac{mg}{T} \alpha_1(t) + \frac{1}{2} \frac{z_B^2}{\ell} \sin^2 \omega t + \frac{\pi^2}{4\ell} \cdot \alpha_1^2(t) \right] \tag{6.63}$$

Considering that for the primary resonance $\alpha_1(t)$ is approximately given by a sinusoid of frequency ω_1 and amplitude a (see equation (6.60), the maximum increment of cable tension can be approximated by

$$\tau_{max} \approx \frac{EA_0}{\ell} \left[2\frac{\ell}{\pi} \cdot \frac{mg}{T} \cdot a + \frac{z_B^2}{2\ell} + \frac{\pi^2}{4\ell} \cdot a^2 \right] \tag{6.64}$$

The variation of the increment of cable tension with the amplitude of oscillation was calculated for the stay cable analysed above, using equation (6.64). Figure 6.46(d) shows the good agreement between the nonlinear estimates and the numerical response for the two damping coefficients of *0.5%* and *1%* considered in the analysis.

An important aspect associated with the nonlinear evaluation of the increment of cable tension, is the appearance of a double frequency component (2nd and 3rd terms in equation (6.63)), which is the result of the integration of the second order component of the elastic strain (equation (6.61)). Although the component in z_B^2 that corresponds to the solid motion of the cable is generally very small, the component in α_1^2 grows with the amplitude of oscillation and may attain significant values. This is particular relevant for the shorter stays, as illustrated in Figure 6.50 for the two cables discussed in this Section, the cable from Ben-Ahin Bridge ($\ell = 110.505m; \lambda^2 = 0.0727$), and the longest cable from Vasco da Gama Bridge ($\ell = 225.97m; \lambda^2 = 0.4321$). The nonlinear component of cable tension attains, for the first of these, *80%* of the total increment of cable tension. Also, for large amplitudes of support oscillation, the dependence on the damping coefficient is almost non-significant.

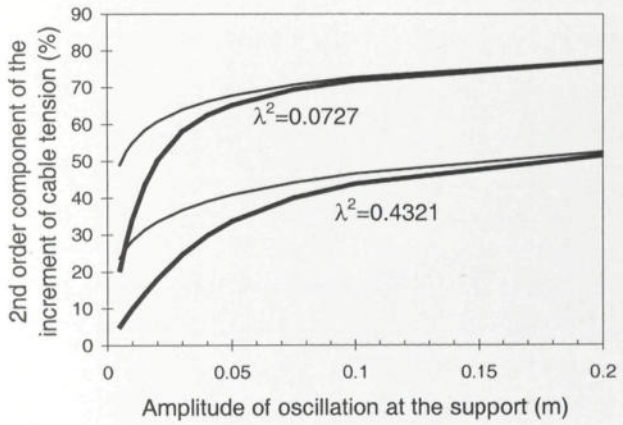


Figure 6.50. Variation of the weight of the second order component of the increment of cable tension with the amplitude of support oscillation for two stay cables, considering (a) $\xi = 0.1\%$ - solid line; (b) $\xi = 1.5\%$ - bold solid line.

6.3.3 Parametric excitation

The horizontal cable represented in Figure 6.51 is now subjected to a harmonic oscillation at anchorage B along the longitudinal axis $x_B(t)$ given by

$$x_B(t) = x_B \sin 2\omega t \tag{6.65}$$

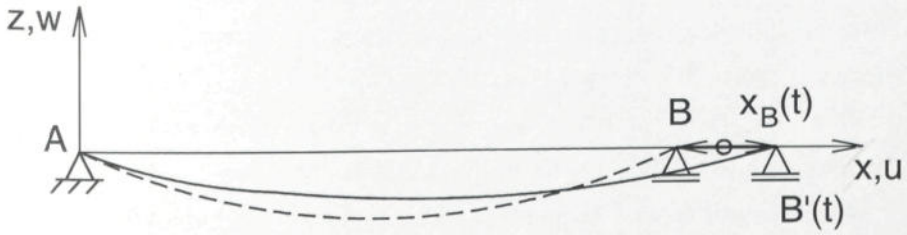


Figure 6.51. Horizontal cable subjected to longitudinal harmonic motion at one anchorage.

The equation of motion in the transverse direction can be obtained directly from (3.74c), considering a parabolic profile for the static configuration of the cable, and admitting that the sag is very small, that is $d\bar{s} \approx dx$. Neglecting the longitudinal inertia, the increment of cable tension τ becomes a function of time only and the following relation is obtained

$$(T+\tau)\cdot\frac{\partial^2 w}{\partial x^2} + \tau\frac{d^2 z}{dx^2} = m\frac{\partial^2 w}{\partial t^2} \tag{6.66}$$

Considering a second order definition of the elastic strain ε according to (3.75), where the boundary condition is $u(\ell,t)=x_B sin2\omega t$ and assuming that the motion is confined to the plane of the cable, the increment of tension $\tau(t)$ comes

$$\tau(t)\approx\frac{EA_0}{\ell}\left[x_B sin2\omega t+\int_0^{\ell}\frac{dz}{dx}\frac{\partial w}{\partial x}dx+\frac{1}{2}\int_0^{\ell}(\frac{\partial w}{\partial x})^2 dx\right] \tag{6.67}$$

Equation (6.66) can be solved by separation of variables, describing the spatial variation of motion by the first vertical mode of vibration, assumed sinusoidal

$$w(x,t)=\alpha_1(t)\cdot sin\frac{\pi x}{\ell} \tag{6.68}$$

Introducing equation (6.67) and the partial derivatives of (6.68) into (6.66), and including a viscous damping term characterized by a damping coefficient ξ_1 for the first mode of vibration yields

$$\begin{aligned}&\ddot{\alpha}_1(t)+2\xi_1\omega_1\dot{\alpha}_1(t)+\omega_1^2\cdot(1+\frac{\lambda^2}{\pi^2}+\frac{x_B}{X_0}sin2\omega t)\cdot\alpha_1(t)+\\&+2\frac{\omega_1^2}{\pi\sqrt{X_0\ell}}\cdot\lambda\cdot(1+\frac{\pi^2}{16})\cdot\alpha_1^2(t)+\frac{\pi^2}{4}\frac{\omega_1^2}{X_0\ell}\cdot\alpha_1^3(t)=\frac{\omega_1^2\cdot\ell}{2\pi\sqrt{X_0\ell}}\cdot\lambda\cdot x_B sin2\omega t\end{aligned} \tag{6.69}$$

The differential equation (6.69) is, as in the case of *external excitation* (see equation (6.57)), the governing equation of a system with quadratic and cubic nonlinearities subjected to an harmonic excitation. A peculiar aspect of this system is the presence of a non-negligible harmonic term in $\alpha_1(t)$, that is, the excitation does not appear only as an inhomogeneity in the differential equation, but also as a coefficient of that equation. Since, when it is time independent, the excitation appears as a parameter in the governing equation of motion, it is called *parametric excitation* (Nayfeh & Mook, 1979).

On the contrary to *external excitation*, for which a small excitation only produces large responses when its frequency is close to some linear natural frequency of the system, small *parametric excitations* can produce large responses when the frequency of excitation is away from the linear natural frequencies of the system.

Equation (6.69) is a so-called *modified Mathieu equation*, which has the following general form

$$\ddot{u}+(\delta^2+2\varepsilon sin2\bar{t})u=\varepsilon f(u,\dot{u}) \tag{6.70}$$

where $\varepsilon<<1$. This is the equation of a system characterized by small nonlinearities subjected to a small excitation. Particular solutions of this equation have been obtained in the past (Nayfeh & Mook, 1979) using perturbation methods. A case of interest is the *Duffing equation* with *small damping*, for which the function f in equation (6.70) is $f=-\alpha u^3-2\mu\dot{u}$ resulting in

$$\ddot{u}+2\varepsilon\mu\dot{u}+(\delta^2+2\varepsilon sin2\bar{t})u+\varepsilon\alpha u^3=0 \tag{6.71}$$

This type of equation represents for example the governing equation of motion of a weightless taut string, and can be obtained directly from (6.69), after a convenient normalization, neglecting the contribution of both the quadratic term and the second member, which are of the same order of magnitude

$$\bar{t} = \omega t; \qquad u(\bar{t}) = \frac{\alpha_1(\bar{t})}{K}; \qquad K = \frac{4}{\pi} \cdot \sqrt{\frac{X_0 \ell}{3}} \tag{6.72}$$

$$\delta = \omega_1 / \omega; \qquad \varepsilon = \delta^2 \frac{x_B}{2X_0}; \quad \alpha = \frac{4}{3} \cdot \frac{\delta^2}{\varepsilon}; \qquad \mu = \xi_1 \cdot \frac{\delta}{\varepsilon}$$

In order to understand the characteristics of this equation, the assessment of the solution will depart from the simplest situation where both $\alpha = 0$ and $\mu = 0$ (linear undamped system). The resulting equation is then a *Mathieu equation*

$$\ddot{u} + (\delta^2 + 2\varepsilon \sin 2\bar{t})u = 0 \tag{6.73}$$

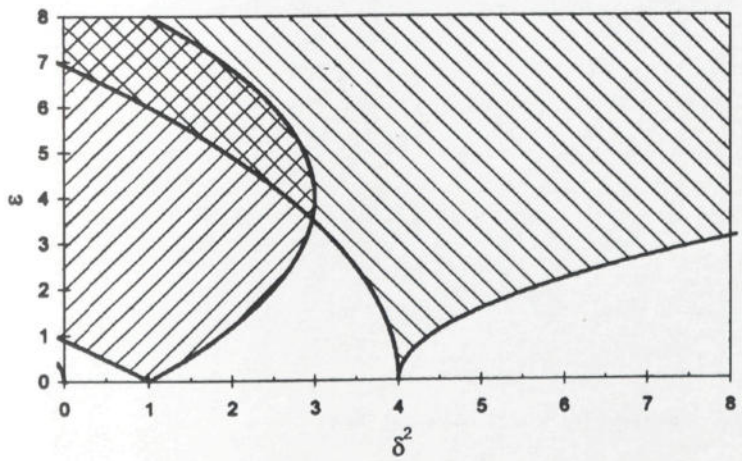


Figure 6.52. Stable and unstable (shaded) regions in the parameter plane for the *Mathieu* equation.

It is known (Tagata, 1977; Nayfeh & Mook, 1979) that the solutions of this equation may be bounded or unbounded, according to the combination of parameters δ and ε. A set of so-called transition curves divide the $\varepsilon\delta$-plane into regions that correspond either to unstable or to stable motions, as represented in the diagram of Figure 6.52, called a *Strutt diagram.*

These curves emanate from $\delta^2 = n^2$ $(n = 1,2,...)$ for each instability region of order n^{th}, and are defined to third order for the first two instability regions by (Nayfeh & Mook, 1979)

$$\delta^2 = 1 \pm \varepsilon - \frac{1}{8}\varepsilon^2, \quad \delta^2 \approx 1$$

(6.74)

$$\delta^2 = 4 + \frac{1}{6}\varepsilon^2 \pm \frac{1}{4}\varepsilon^2, \quad \delta^2 \approx 4$$

It is evident from Figure 6.52 and equations (6.74) that whenever the frequency of excitation is close to a resonance of nth order ($\delta^2 \approx n^2$), the system will respond in the nth harmonic with a diverging amplitude, as long as the amplitude of support oscillation exceeds a certain limit. Considering for example $\delta^2 \approx 1$, and using equations (6.74), instability will be reached for a support oscillation given by

$$\frac{x_B}{2X_0} \geq \left| \frac{4 - 2\sqrt{6 - 2\delta^2}}{\delta^2} \right| \tag{6.75}$$

By including the dissipation term in the *Mathieu equation*, the first and second transition regions will be defined to third order by (Nayfeh & Mook, 1979)

$$\delta^2 = 1 \pm (\varepsilon^2 - 4\mu^2)^{1/2} - \frac{1}{8}\varepsilon^2, \quad \delta^2 \approx 1 \tag{6.76a}$$

$$\delta^2 = 4 + \frac{1}{6}\varepsilon^2 \pm (\frac{1}{16}\varepsilon^4 - 16\mu^2)^{1/2}, \quad \delta^2 \approx 4 \tag{6.76b}$$

These curves are represented in Figure 6.53 for different values of the damping coefficient. The effect of the linear viscous damping term is a lift of the unstable regions from the δ-axis. This means that higher amplitude of support oscillations is required to attain instability, for a given excitation frequency ratio δ. As indicated in Figure 6.53, this effect is more pronounced for the second order resonance ($\delta^2 \approx 4$).

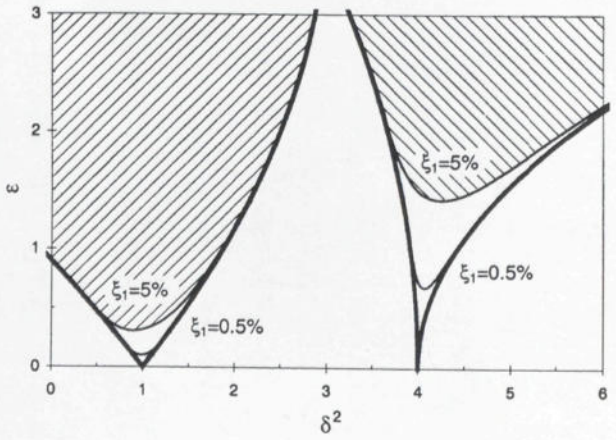


Figure 6.53. Transition curves for different values of the damping coefficient ξ_1: *0* (in bold), *0.5%* and *5%*.

Considering the *first parametric resonance* $\delta^2 \approx 1$, the threshold amplitude for the occurrence of instability is, according to equation (6.76a), given by

$$\delta^6 \cdot (\frac{x_B}{2X_0})^4 - 4\xi_1^2 = (\frac{x_B}{2X_0})^2 \cdot \left[\delta^3 - 1 + \frac{\delta^5}{8} \cdot (\frac{x_B}{2X_0})^2\right]^2 \tag{6.77}$$

For $\delta^2 = 1$, equation (6.77) reduces to

$$(\frac{x_B}{2X_0})^6 - 64(\frac{x_B}{2X_0})^4 + 256\xi_1^2 = 0 \tag{6.78}$$

The roots of this equation are presented in Figure 6.54 for different values of the damping coefficient ξ_1. These values can be compared with the values obtained using the criterion deduced by Kovács (1982)

$$(\frac{x_B}{2X_0})_{min} = \sqrt{\left[1 - (\frac{\omega}{\omega_1})^2\right]^2 + 4\xi_1^2 \cdot (\frac{\omega}{\omega_1})^2} \tag{6.79}$$

with $\frac{\omega}{\omega_1} \approx 1$, which are represented by the solid line in the Figure.

The criterion defined by Kovács and later used by Labeeuw (1990) was adopted by the Belgium Standard NBN N03-002 and was deduced on the assumption that the increment of cable tension is exclusively due to the harmonic variation of the cable length

$$\tau = \frac{EA_0}{\ell} \cdot x_B \tag{6.80}$$

This hypothesis is extremely conservative for the case under analysis, according to the representation in Figure 6.54.

Note that Figure 6.54 also contains the threshold amplitudes of oscillation associated with the second resonance ($\delta^2 = 4$), which are as expected higher than those associated with *primary resonance*.

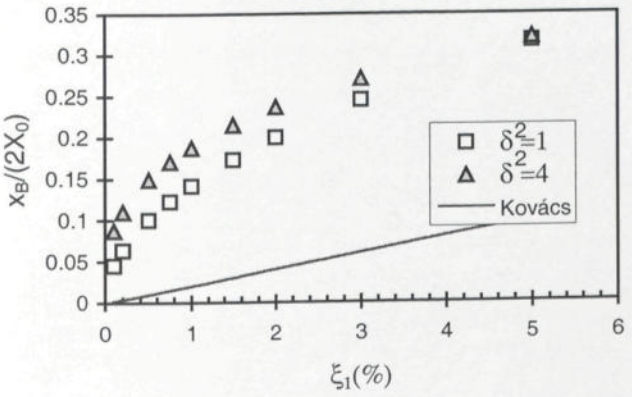


Figure 6.54. Threshold amplitudes of support oscillation for instability in the first ($\delta^2 = 1$) and second ($\delta^2 = 4$) resonances.

In a last step, the cubic nonlinearity term will be accounted for in the dynamic equilibrium equation, what is essential whenever the amplitude of oscillation builds up. The presence of this term does not affect the definition of the transition regions, according to Nayfeh & Mook (1979). Therefore, the threshold values defined above for the beginning of instability will hold. In fact, the effect of adding this cubic term, is that the amplitude of oscillation will not grow unlimitedly inside an instability region, but will converge instead to a finite-amplitude value. Tagata (1977), Pinto da Costa *et al.* (1996) and Clement and Cremona (1996), employing the method of harmonic balance, and Nayfeh and Mook (1979), using the method of multiple scales, obtained an approximation of the steady-state response in the vicinity of the first resonance ($\delta \approx 1$), which can be expressed as

$$\alpha_1(t) = a \sin(\omega t - \frac{1}{2}\psi) \tag{6.81}$$

where

$$a = \frac{4}{\pi} \cdot \sqrt{\frac{X_0 \ell}{3}} \cdot \frac{1}{\delta} \cdot \left\{ 1 - \delta^2 \pm \left[\delta^4 \cdot (\frac{x_B}{2X_0})^2 - 4\delta^2 \xi_1^2 \right]^{1/2} \right\}^{1/2} \tag{6.82}$$

and

$$\tan\psi = -\frac{2\,\xi_1\,\delta^2}{2\,(1-\delta) - \delta^4\,a^2} \tag{6.83}$$

Equation (6.82) is plotted in Figure 6.55 for the cable studied in the previous section (see Figure 6.43), considering two values of the relative support motion $x_B/(2X_0)$, of *0.05* and *0.3*, and a damping coefficient of *1%*. The nonlinearity of the differential equation induces, as can be observed in this Figure, a bending of the frequency-response curves into the right (the cable behaves as a hardening spring), which leads to multivalued responses and, consequently, to a so-called *jump* phenomenon. The evolution of the amplitude of the response is represented by the arrows in Figure 6.55, where it can be observed that in a vicinity of the first parametric resonance ($\delta \approx 1$) the trivial solution is not stable.

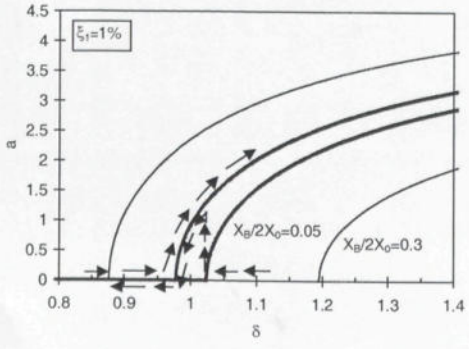


Figure 6.55. Frequency-response functions for a stay cable subjected to two different amplitudes of support motion: $x_B/(2X_0)=0.05$, and $x_B/(2X_0)=0.3$.

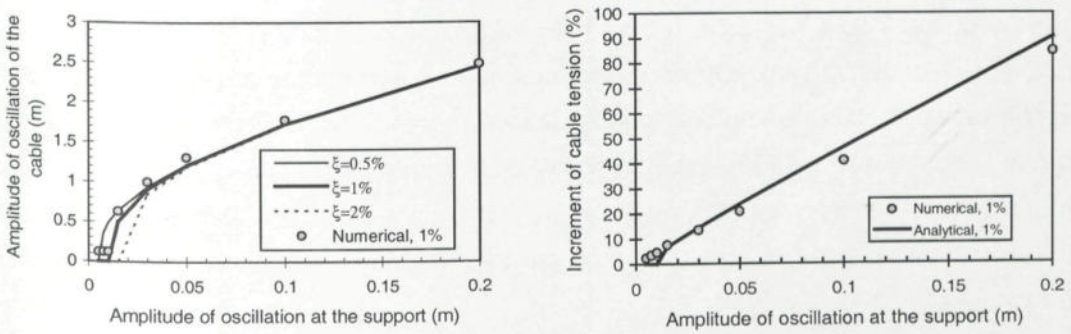
Numerical example

Using the model described by Figure 6.43 for the stay cable of the Ben-Ahin Bridge and the SOLVIA software, the amplitude of steady-state response was calculated for a longitudinal harmonic motion at the anchorage at twice the linear natural frequency of the cable, considering different amplitudes of support motion and a damping coefficient of *1%*. Both the analytical (equation (6.82)) and the numerically calculated amplitude of the steady-state oscillation are represented in Figure 6.56(a). The agreement between the two estimates of steady-state response is very good. Also, it can be observed, by comparison with the *external excitation* response represented in Figure 6.46, that *parametric excitation* induces amplitudes of vibration that almost double the amplitude of oscillations induced by *external excitation* for the cable under analysis.

As for the increment of cable tension, the following expression can be obtained

$$\tau(t)=\frac{EA_0}{\ell}\cdot\left[x_B \sin 2\omega t+\frac{\sqrt{2}\ell}{\pi}\frac{mg}{T}\cdot\alpha_1(t)+\frac{\pi^2}{8\ell}\cdot\alpha_1^2(t)\right] \tag{6.84}$$

with $\alpha_1(t)$ given by equation (6.81). In addition to the excitation term, this expression encloses, as in the case of *external excitation*, a non-negligible term in the double frequency. The variation of the maximum value of $\tau(t)$ with the amplitude of support oscillation is represented in Figure 6.56(b), assuming that the quantity ψ in equation (6.81) is very small. The comparison with the corresponding numerical response shows a rather good agreement, the theoretical response leading in general to greater values of the increment of cable tension for high amplitudes of support oscillation.



(a) (b)

Figure 6.56. Numerical *vs* analytical amplitude of the steady-state response at the *principal parametric resonance:* (a) amplitude of cable oscillation; (b) maximum increment of cable tension.

Reference should be made to the transient component of the response, that may exceed, for certain amplitudes of oscillation, the limit-cycle response and that, depending on the frequency and damping coefficient, may last for a few minutes. Figure 6.57 depicts the ratio between the maximum transient and steady-state response, expressed both in terms of

displacements and increments of cable tension, for the numerically calculated response of the stay cable under analysis, considering damping coefficients of *0.5%* and *1%*. In this case, for a damping coefficient of *1%*, the transient response is observable in a period of about *1* minute. Dependence both on the amplitude of support oscillation and damping coefficient is evident.

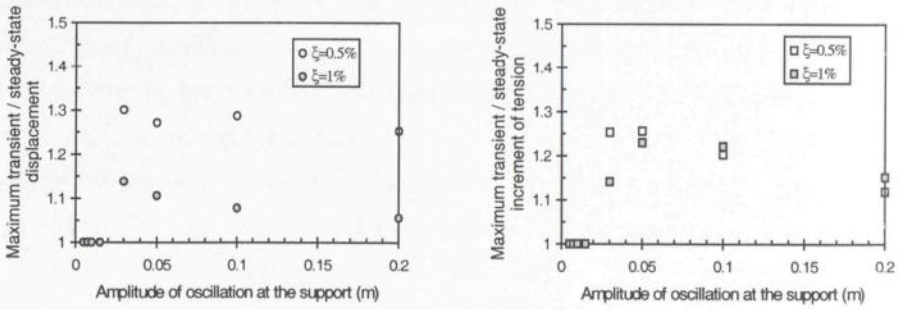


Figure 6.57. Variation of the ratio between the maximum transient and steady-state response with amplitude of oscillation for $\xi = 0.5\%$ and $\xi = 1\%$.

Practical occurrences of vibrations due to external/ parametric excitation

With regard to the practical occurrence of vibrations in cable-stayed bridges motivated by *parametric / external excitation*, and although it has not always been possible to identify with certainty the real causes of instability observed in some bridges, even because several causes may be present together in many circumstances, some examples reported in the literature can be cited. In the Ben-Ahin and Wandre bridges, in Belgium, amplitudes of vibration of *0.50m* and *0.30m*, respectively, were observed, accompanied by a slight vibration of the deck. Although attributed to the combined action of rain and wind, it is also thought that the motion of the cable supports (deck) may have enhanced these vibrations (Dumortier, 1990; Cremer *et al.*, 1995). Other cases where support motion or, more precisely, an interaction between cable and deck/ towers vibration were observed, are the Annacis Bridge, in Canada (Stiemer *et al.*, 1988), the Farø Bridges, in Denmark (Langsoe & Larsen, 1987), the Helgeland Bridge, in Norway (Jakobsen *et al.*, 1995), the Erasmus Bridge, in Netherlands (Geurts *et al.*, 1998), and the Burlington and the Second Severn Crossing Bridges, in US and UK, respectively (Virlogeux, 1998).

6.4 CABLE-STRUCTURE INTERACTION

6.4.1 General

The issue of cable vibration in cable-stayed bridges has been almost exclusively investigated in terms of isolated stay cables. According to the Sections presented above, two basic types

of studies have been performed in the past, one considering the forces (mainly caused by the wind action) that act directly on the stay cable, which is assumed to remain fixed at the ends, and the other, that attempts to evaluate the possible effect of harmonic displacements at the cable supports in the dynamic behaviour of the cable.

Another aspect to consider is the possible influence of the dynamic behaviour of the bridge in the cable response and vice-versa, i.e., the importance of cable response in the global behaviour of the cable-stayed bridge.

The possible interaction between the dynamic behaviour of the cable and the structure has been referred and studied by some authors in the past. One of the first known references to the problem is due to Davenport and Steels (1965), who obtained expressions for the dynamic stiffness of a cable which allowed the inclusion of the cable dynamics in the study of a guyed mast system. Davenport and Steels validated experimentally the derived expressions for small oscillations of the cable. For large amplitude vibrations, these authors observed a significant nonlinearity at resonance, marked by the appearance of higher harmonic components in the cable response. They observed in particular the transverse swaying in half the vertical frequency of vibration for the first and third resonances, which is the phenomenon of *parametric excitation* described in the previous section.

In the specific topic of cable-stayed bridges, it is interesting to refer the concept of *system damping*, introduced by Leonhardt and Zellner (1980), stating that cables can play a favourable role in terms of the dynamic behaviour of cable-stayed bridges subjected to wind or earthquake excitation, contributing to the development of an additional damping of the structural response. This damping is due both to the nonlinear behaviour of the cable (sag effect), and to the interference of cable oscillations at different natural frequencies. Maeda *et al.* (1983) newly defined the concept of *system damping*, based on a beating phenomenon motivated by internal resonance. Kovács (1982) introduced the concept of *parametric excitation* in cable-stayed bridges, as described in the previous Sections, and from linear considerations derived expressions for the maximum amplitude of cable oscillation as a function of the ratio between the natural frequencies of the stay cable and the bridge.

Using the numerical model of a railway cable-stayed bridge in which the stay cables were modelled as assemblages of linear springs and masses, Causevic and Sreckovic (1987) stressed the importance of the nonlinearity of cable behaviour that results from the closeness between a cable natural frequency and a natural frequency of the global structure. Furthermore, these authors stated that the eigenfrequencies of the global bridge structure should not approach the vicinity of natural frequencies of any of the cable-stayed bridge cable.

It was however a paper by Abdel-Ghaffar and Khalifa (1991) that motivated the present research. Considering the evidence of large vibrations in certain cable-stayed bridges and the consequent fatigue and corrosion problems that may determine the premature rupture of wires in a stay cable, and given the trend to an increase in the span length, situation that may increase the vibration problems, Abdel-Ghaffar and Khalifa stressed the importance of evaluating the influence of the stay cables' vibrations into the overall dynamics of cable-stayed

bridges. Starting from a three-dimensional finite element model of a large span (*671m*) cable-stayed bridge in which the stays were discretized into series of small truss elements (instead of being idealized as single truss elements with reduced modulus of elasticity for consideration of the sag effect, the usual procedure in the design of cable-stayed bridges), these authors performed a dynamic analysis based on the tangent stiffness matrix of the bridge in the dead-load deformed state and compared the calculated natural frequencies/ mode shapes/ modal participation factors for seismic excitation with the corresponding quantities calculated for the single element traditional model, showing that cable vibrations affect the mode shapes of the deck/ tower system and the corresponding participation factors. The inadequacy of using single truss elements to model the cables and the necessity of considering a convenient discretization of the cables into several finite elements was also stressed by Tuladhar *et al.* (1995), who concluded that the interaction between cable vibrations and deck vibrations can have a significant influence on the seismic response of the bridge, especially when the first natural frequencies of cables overlap with the first fundamental frequencies of the bridge. To complement the above mentioned numerical investigations, the author conducted an experimental study on an existing physical model of a cable-stayed bridge, the Jindo Bridge (in South Korea), which was modified for the purpose of studying the dynamic behaviour of the cables (Caetano *et al.*, 2000a; Caetano *et al.*, 2000b). The procedures and main results of this research will be described in Chapters seven and eight of the current dissertation.

A last reference should be made to the research of Fujino *et al.* (1993), who distinguished the so-called *local vibrations* from *global vibrations*, according to the designation of Gimsing (1983). The former correspond to cable vibrations, while the later respect the girder / towers vibrations. Fujino and companion authors stated that the separate treatment of *local* and *global vibrations* was not sufficient when the corresponding natural frequencies became nearly equal to each other. In addition, for large amplitudes of vibration, the coupling between local and global vibrations could be also nonlinear. Quadratic coupling, in particular, caused *autoparametric interaction* when two of the natural frequencies were in the ratio of one to two.

Considering a simplified model of a cable-stayed bridge constituted by a cantilevered beam and a taut cable for which the ratios between the natural frequency of vibration of the cable and of the first and second horizontal modes of vibration of the cantilever were respectively of *1:1* and *1:2*, Fujino *et al.* (1993) developed an analytical three-dimensional model and calculated the steady-state response to an harmonic excitation at parametric resonance. They checked the results experimentally, using a small physical model of the cantilever / cable system. A major aspect evidenced by the phenomenon was a nonlinear character of the interaction between the structural members.

Although recognizing the complexity of the phenomenon of *cable-structure interaction* and the necessity of studying the overall bridge structure, the present section aims to introduce the main aspects of the problem, through a finite element analysis of a very simple

structure, that consists of an horizontal taut cable connected to a mass-spring system in two distinct conditions, according to the representation of Figure 6.58.

The characteristics of the horizontal cable correspond to those of the Ben-Ahin stay cable previously studied and described by Figure 6.43. As for the mass/ spring system, the following values were used: a mass of *15000t* for both structures ($M_1 = M_2$); a stiffness K_1 of *3.70GN/m* for the case represented in Figure 6.58(a), corresponding to a frequency of the spring/ mass system that is twice the fundamental frequency of the cable, and K_2 of *0.612GN/m* for the case represented in Figure 6.58(b), leading to a frequency of the spring/ mass system that is equal to the fundamental frequency of the cable. The two cases will be analysed separately.

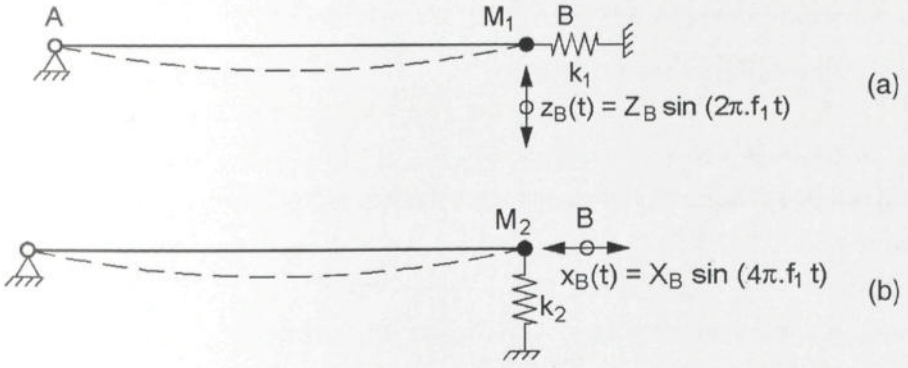
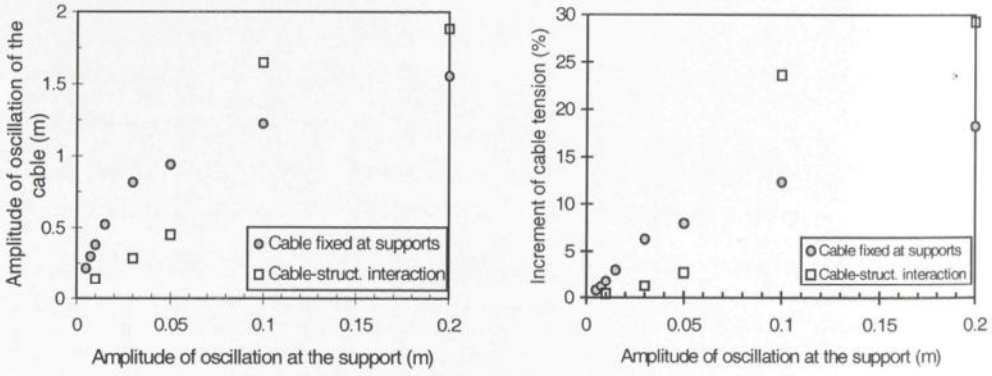


Figure 6.58. Examples of simplified systems for the study of cable-structure interaction: (a) External excitation (b) Parametric excitation.

6.4.2 Effect of cable-structure interaction in external excitation

The idea that supported the present test is that the steady-state increment of cable tension for external excitation at fundamental resonance (see expression (6.63)) is characterized essentially by a component in the resonance frequency and by a component in the second harmonic, which depends on the square of the amplitude of cable oscillation. For large amplitudes of support oscillations, the later component may be significant. If, additionally, the cable is connected to a system whose frequency is in resonance with this second harmonic, then an amplification of the tension will occur and will induce *parametric excitation*, with the effect of magnifying the amplitudes of oscillation of the stay cable. On the contrary, for small amplitudes of oscillation, the *parametric excitation* term will be very small. A phase delay in the term $\alpha_1(t)$ defined both for *external* (see expression (6.58)) and *parametric* (see expression (6.81) excitations, may inclusively reduce the amplitudes of oscillation. The two contradictory effects are well evident in the representations of Figures 6.59(a) and 6.59(b), which show the variation of the maximum steady-state amplitude of vibration and increment of cable tension, respectively, with the amplitude of support excitation at fundamental resonance,

calculated either neglecting the effect of cable-structure interaction (cable horizontally fixed at supports), or considering that interaction (system of Figure 6.58(a)). The values in these Figures were obtained from a finite element nonlinear geometric analysis of the systems represented in Figures 6.42 and 6.58(a) subjected to harmonic displacement in the fundamental frequency of the cable, considering a viscous damping coefficient of *1%*.

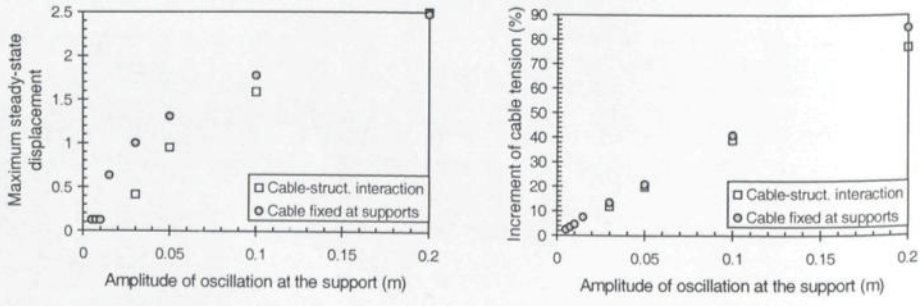


(a) (b)

Figure 6.59. Variation of the: (a) amplitude of oscillation and; (b) increment of cable tension with the amplitude of support excitation for the system represented in Figure 6.58(a).

6.4.3 Effect of cable-structure interaction in parametric excitation

In this case, it is the effect of vertical interaction in the fundamental resonance that may amplify or decrease the vibration of the cables. Note that, for a given amplitude of oscillation, a phase shift exists between the vertical oscillations due to parametric and external excitations (see expressions (6.81) and (6.58), respectively). Consequently, the effect of *cable-structure interaction* may be either an increase or a decrease of the amplitude of oscillations that would occur for the isolated cable vertically fixed at the supports (see Figure 6.51). Comparing the results from the calculations performed both for the isolated cable and for the system represented in Figure 6.58(b), which are summarized in Figures 6.60(a) and 6.60(b), one can see that for this situation an improve in the dynamic behaviour of the structure occurs.



(a) (b)

Figure 6.60. Variation of the (a) amplitude of oscillation and (b) increment of cable tension with the amplitude of support excitation for the system represented in Figure 6.58(b).

6.5 CONCLUSIONS

This Chapter presented a survey on the various causes of cable vibration in the context of cable-stayed bridges.

Starting by a description of a few cases of vibrations reported in the literature, showing the various characteristics of observed oscillations, conditions of occurrence and consequences, the various sources of vibration were grouped into two main categories, *direct* and *indirect excitation*.

The *direct excitation* sources respect the phenomena motivated by direct actuation of wind and rain on the stay cables, which are *vortex-shedding*, *galloping*, *wake interference* and *rain-wind* induced excitation. All these phenomena were described and, whenever possible, empirical or analytical expressions for prediction of amplitudes of oscillation or for the definition of threshold conditions for the occurrence of instability were presented.

Particular emphasis was put on the *rain-wind induced* vibration phenomenon, which was identified recently on cable-stayed bridges, and which has not been completely assessed yet.

With regard to the *indirect excitation* of the stays, which is produced by motion of the cable anchorages, two particular cases were identified, one corresponding to oscillations of the anchorages perpendicularly to the cable chord, designated as *external excitation*, and the other corresponding to oscillations of the anchorages in the direction of the chord, designated as *parametric excitation*. The two cases were studied analytically, departing from the nonlinear equations of Perkins derived in Chapter three, and simplifying for the particular case of taut cables.

Analysing the nonlinear character of these equations, it was possible to observe that the quadratic and cubic terms are responsible for the appearance of secondary resonances. It was also observed that the primary resonance was critical for the case of external excitation, while for parametric excitation the second resonance is more important.

So, based on mathematical solutions of differential equations of the same type, the author derived expressions for characterizing the external and parametric vibrations, namely: (i) the threshold amplitude of support oscillations for the occurrence of instability; (ii) the maximum steady-state amplitude of oscillation at resonance; (iii) the maximum increment of cable tension in steady-state vibration.

The obtained expressions were used in the analysis of a medium–size stay cable, and the results compared with corresponding values obtained numerically from a nonlinear geometric *FEM* analysis.

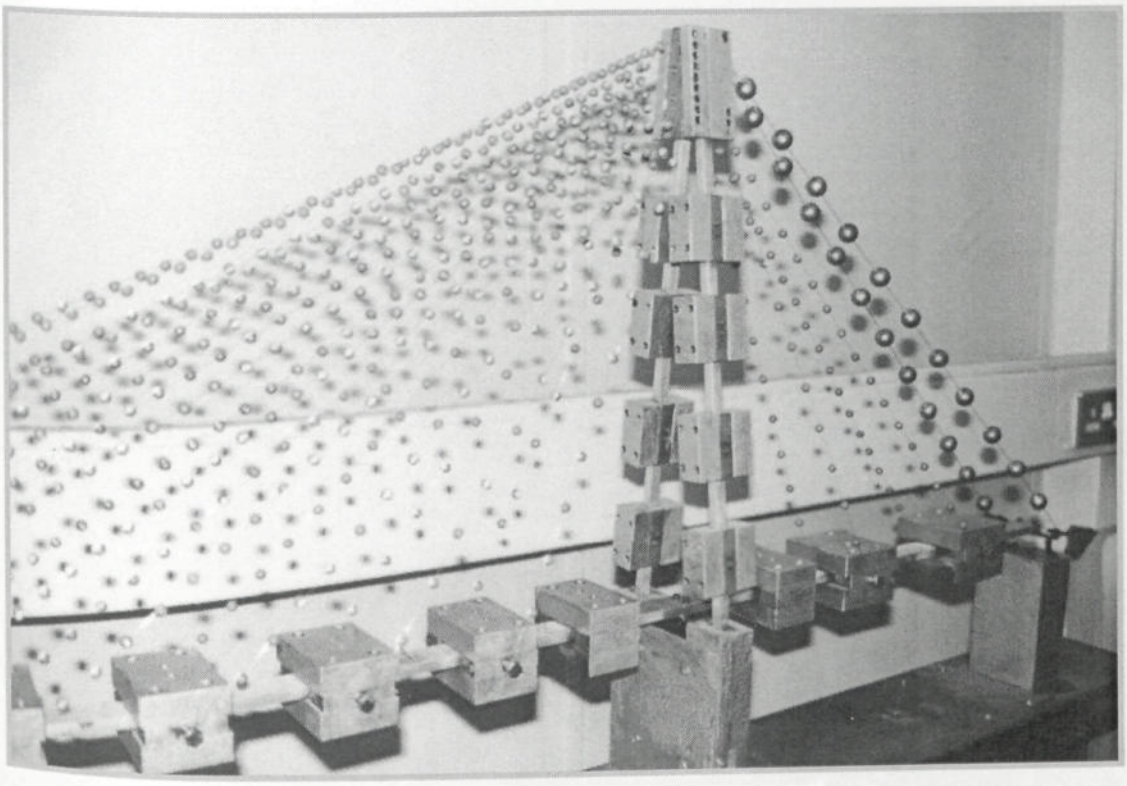
A final topic was introduced in this Chapter, concerning the issue of *cable-structure interaction*. Starting by a literature survey concerning the topic, a numerical example of a stay cable connected at one anchorage to a spring-mass system simulating a cable-stayed bridge was presented.

External and *parametric* excitations were then introduced and the interaction effect was analysed. Although the obtained results cannot be generalized to all stay cables, they present an indication that *cable-structure interaction* may lead to increased oscillation of the stays for large amplitudes of anchorage excitation, particularly for the case of *external excitation*, and should thus be investigated more thoroughly. This study served as an introduction to the experimental *cable-structure interaction* that will be presented in Chapter seven.

CHAPTER 7

THE JINDO BRIDGE

Experimental and numerical survey



CHAPTER SEVEN

THE JINDO BRIDGE: EXPERIMENTAL AND NUMERICAL SURVEY

7.1 GENERAL

The previous Chapter described the several sources of cable vibration in cable-stayed bridges. These were grouped in two different categories, designated respectively as *direct* and *indirect* excitation phenomena, and were characterized considering an isolated analysis of the stay cables.

Complementary, the topic of *dynamic cable-structure Interaction* was introduced (see Section 6.4), the main aspects being characterized through a simplified numerical study comprehending an horizontal cable connected at one end to a mass-spring system, which represented the effect of the bridge structure.

The analysis of the state-of-art presented in Section 6.4 and of the main results of this numerical preliminary study evidenced the two following points:

- First of all, although several practical occurrences of cable vibrations have shown the existence of *dynamic cable-structure interaction*, the research in this particular issue has been relatively scarce. In fact, the deeper studies on this topic, presented by Abdel-Ghaffar and Khalifa (1991), were exclusively numerical. And though some experimental research studies were also performed (Maeda *et al.*, 1984; Fujino *et al.*, 1993), mostly simplified models were employed (in the later case, consisting in a combination of a cantilever, representing the bridge deck, with an inclined cable, representing a stay cable);

- The occurrence of *Cable-Structure Interaction* may lead to an increase of the cable tensions, as well as of the displacements and stresses along the bridge.

Having these aspects into consideration, two main objectives were defined for the current research: (i) the experimental identification of the *dynamic cable-structure interaction* phenomenon on a cable-stayed bridge; (ii) the evaluation of the significance of that interaction in terms of the bridge response.

The first topic is covered in the current Chapter, while the later will be presented in Chapter eight, considering in particular the response to seismic excitation.

Ideally the experimental validation of the results obtained by Abdel-Ghaffar and Khalifa should consider: (i) a bridge prototype, with (ii) large span, where (iii) the phenomenon of cable-structure interaction had already been observed.

Gathering the three conditions would be however an almost impossible task. In effect, the performance of dynamic tests on a prototype would require the control of the excitation and test conditions (e.g. temperatures, wind, traffic) in order to produce unambiguous results. These objectives would clearly be extremely difficult to attain with *in-situ* testing of a prototype, and so the performance of laboratory tests on the physical model of a bridge was considered. Moreover, since an already constructed physical model of a cable-stayed bridge existed at the Earthquake Engineering Research Centre (*EERC*) of the University of Bristol, that required minor modifications for the purposes here designated, it was decided to concentrate the current studies on this particular model. Note however that this model represented a bridge (the Jindo Bridge, in South Korea) with a not so large span (*344m* centre span), relatively rigid due to the box cross section of the deck and corresponding support conditions, and so eventually not so prone to cable-structure effects as desired.

The studies performed on this physical model involved a numerical and an experimental component. The experimental component, in particular, comprehended a long series of modal tests of the modified Jindo model, which were performed at the University of Bristol, using both an electrodynamic shaker and the six-degree-of-freedom shaking table from that University. These measurements were complemented with a series of tests performed at the same shaking table, measuring the response to a set of artificial accelerograms. A second series of tests with identical characteristics were later conducted on the Jindo model, conveniently modified in order to suppress the effect of the mass distribution of the cables. Due to lack of availability of the *EERC* shaking table, the tests were performed at the Structural Dynamic Testing Laboratory of *ISMES*, in Italy.

More recently, the author had access to some data collected on the Jindo Bridge prototype by an American consulting company, *CTL*, which installed a monitoring system on the bridge.

The current Chapter starts with a description of the Jindo Bridge prototype and of the corresponding physical model, which was conceived by Garevski (1990). The similarity requirements and adopted simplifications are discussed, and a set of cable masses are

designed for the purpose of adequately representing the effect of mass distribution along the stay cables.

The results of a numerical analysis are then presented, considering both a two-dimensional numerical model (whose results were used in the preparation of the experimental tests), and a three-dimensional model. In both cases the effect of *dynamic cable-structure interaction* was investigated, by addition of the correct distribution of mass along the stay cables in the numerical model, and by comparison with a simplified model that considers exclusively the stiffness characteristics of the stay cables behaviour.

The results from the numerical modelling are experimentally validated, by performance of the experimental modal survey. Both the tests performed at the *EERC* and at *ISMES* are described, and the main results presented and discussed. The evidence of *cable-structure interaction* and of the corresponding pattern is shown.

Although the purpose of the current work was not to analyse the capacity of the physical model to reproduce the actual prototype characteristics, it was considered of interest to complementary analyse the ambient vibration data collected by *CTL* on the prototype, and compare the identified characteristics with those obtained from numerical and experimental analysis of the physical model, applying appropriate scale factors. Unfortunately, the available data was rather limited in terms of frequency resolution and number of instrumented locations for the purpose of identifying cable-structure interaction on the bridge prototype and no further conclusions were thus possible to extract in that particular issue.

7.2 THE JINDO BRIDGE PROTOTYPE

The Jindo Bridge, designed by Rendel Palmer & Tritton and built in South Korea (Tappin, 1985), is a three span steel cable-stayed bridge with a continuous stiffening girder, having a total length of *484 m*. The main span is *344 m* and the side spans are *70 m*, according to the scheme of Figure 7.1. The boundary conditions of the main girder are achieved by two rocker supports at the ends, one pinned support at one of the towers and a roller at the other tower.

The deck cross section, represented in Figure 7.1, has a hexagonal shape with main average properties and loading characteristics summarized in Table 7.1.

The *A*-framed towers are cantilevers reaching a height of *69m*, the corresponding steel legs' cross section being of rectangular box shape with average properties also listed in Table7.1.

The stays are arranged in a form of a fan converging at the top of each *A*-frame tower. Each tower carries *24* stays. The cables are locked coil ropes with diameters varying in the range *56 mm* to *87 mm*, according to the representation of Table 7.2. According to this table, that summarizes the cable properties, each of the backstays is constructed of six ropes with a diameter of *87mm*.

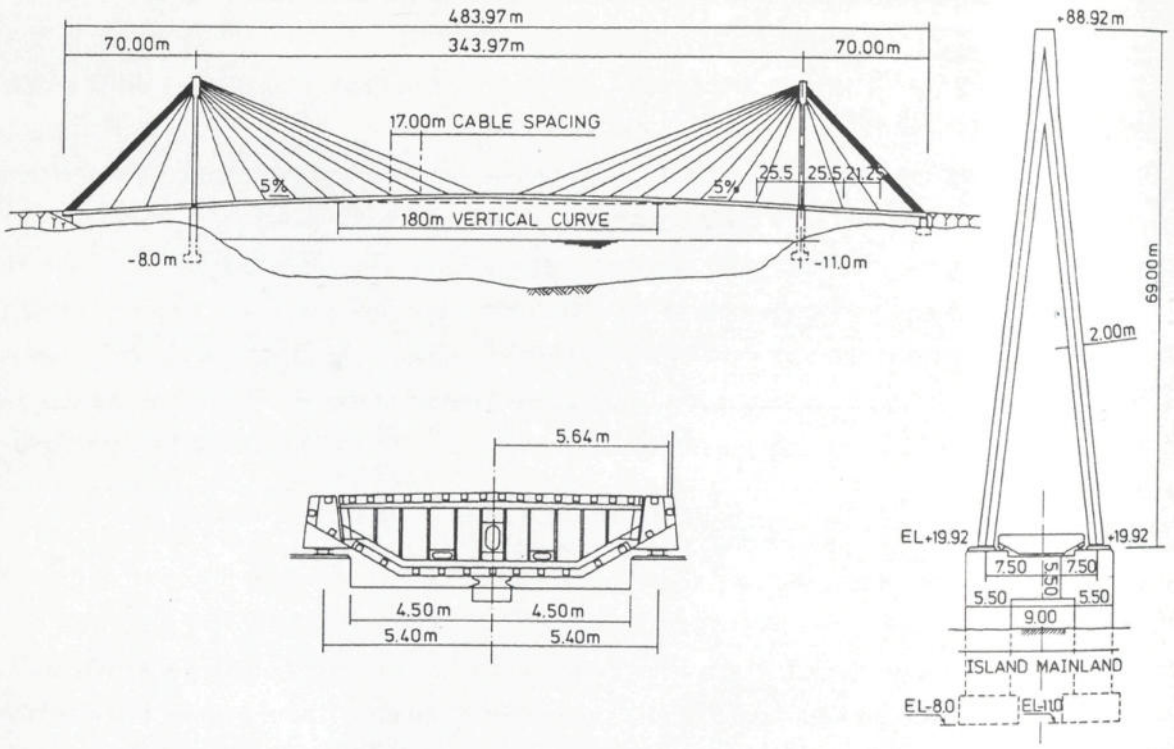
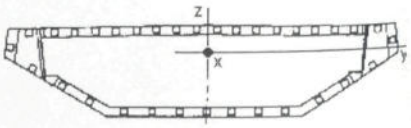


Figure 7.1. General characteristics of Jindo Bridge.

Table 7.1. Jindo Bridge: average properties and loading characteristics of the deck and tower legs' cross-section.

DECK	Area	0.464 m^2
	Moment of inertia I_y	0.54 m^4
	Moment of inertia I_z	5.4 m^4
	Torsional inertia moment I_x	1.2 m^4
	Dead Weight	40 kN/m
	Super Dead Weight	20 kN/m
TOWERS	Area	0.237 m^2
	Moment of inertia I_x	0.230 m^4
	Moment of inertia I_y	0.276 m^4



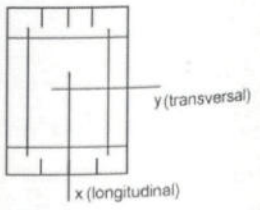
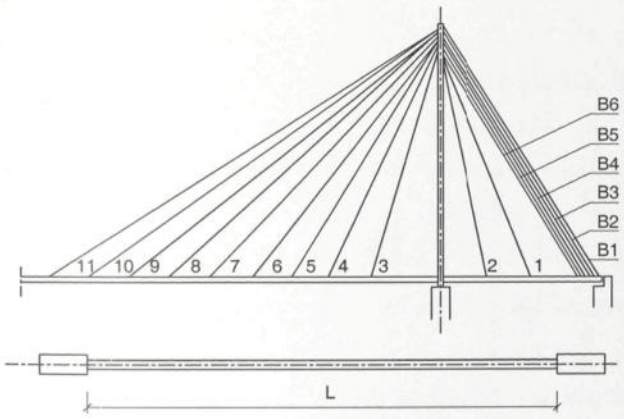


Table 7.2. Jindo Bridge: cable properties and design tensions.



Modulus of Elasticity: 157Mpa

Filling Factor f for Area Calculation: 0.84

(Area= $\frac{\pi D^2}{4} \cdot f$)

Rope No.	Dia. of Rope D (mm)	Approx. Metallic Area (mm^2)	Approx. Weight (N/m)	Final Tension (kN)
1	66.5	2990	240	904
2	56	2130	171	663
3	56	2130	171	583
4	56	2130	171	550
5	66.5	2990	240	756
6	66.5	2990	240	826
7	76	3810	305	912
8	76	3810	305	1019
9	76	3810	305	1126
10	76	3810	305	1203
11	87	4990	400	1488
B1	87	4990	400	1417
B2	87	4990	400	1417
B3	87	4990	400	1417
B4	87	4990	400	1417
B5	87	4990	400	1417
B6	87	4990	400	1417

7.3 THE PHYSICAL MODEL OF THE JINDO BRIDGE

The physical model of Jindo Bridge, built at the Earthquake Engineering Research Center of the University of Bristol, can be described as a distorted small-scale model with artificial mass simulation. This model was designed by Garevski (1990), who performed damping and seismic response measurement tests, and was slightly modified by the author (Caetano & Cunha, 1995), in order to study appropriately the problem of coupled cable-deck motions.

In order to reduce the total weight and cost of the structure, different materials were employed in the construction. An aluminum alloy was used for the main girder and the tower

legs, steel was used for the cable stays and for the masses added to the girder, towers and cables, and lead was used for the masses added to the back stays.

The model was designed to satisfy similarity for the bending stiffness of the girder and towers and for the axial stiffness of the cable stays, so as to reproduce accurately the most important characteristics of the structural dynamic behaviour. With these assumptions, it was not possible to correctly scale the axial stiffness for the deck and towers, although it was considered that these properties would not affect significantly the global behaviour of the model. It was also not possible to conveniently scale the torsional behaviour of the deck. This may naturally have implications in terms of the accuracy of the reproduction of the prototype bridge behaviour, and also in terms of identification of *cable-structure interaction* associated with torsional vibration modes. It should be noted however that, according to the three-dimensional numerical modelling performed by Garevski and Severn (1993), the bridge presents a significant torsional stiffness, the first torsional mode being actually of seventh order and occurring at a frequency of about *1.5Hz,* while the fundamental bending modes associated with the lateral and vertical motion of the deck occur at frequencies of about *0.32Hz* and *0.50Hz*, respectively. Therefore, comparing with the contribution from the vertical and transversal modes, the response associated with the torsional modes of the bridge is expected to be relatively low.

One specific aspect of the construction of this model concerns the form of construction of the masses to add to the cables. The imposition of similarity with regard to the axial stiffness of the cables led to very small diameters for the steel cables of the model (piano wires). On another hand, the simulation of the dead weight of the stays implied the addition of a considerable amount of mass. Garevski designed steel and lead cylinders that were attached to the cables (with diameters ϕ of *0.23mm* and *0.66mm*) by means of two *2mm* bolts touching the piano wire very slightly. This arrangement would prevent the addition of damping and bending stiffness to the cable. However, it revealed not to be very efficient, due to the difficulty of fixing the cylinders to the cables. Moreover, the use of a relatively small number of cylinders per cable (varying from *3* to *10* in a length of *0.50m* to *1.20m*) would not reproduce correctly the dynamic behaviour of a continuous cable, compromising the present investigation on the dynamic interaction of the cables-deck/towers system. For these reasons, the author decided to redesign the stay cables.

The current Section presents some considerations related with the similitude requirements and simplifications adopted in the definition of the scale factors. The physical model is then described, with particular emphasis to the stay cable design and tuning of the tensions.

7.3.1 Definition of scale factors

The construction of a physical model requires an appropriate definition of scale factors, so that the results from the testing of this model can be related with the corresponding to the prototype structure. It is thus necessary to satisfy a number of so-called *similitude requirements*, which are defined based on the *theory of modeling* and can be deduced from a dimensional analysis of the physical phenomena involved in the behaviour of the structure (Sabnis *et al.*, 1983).

The idea is then to characterize the governing equations of the phenomena involved in the testing of the physical model in terms of a set of dimensionless terms, designated as the *Pi* terms (π_i). These terms depend on a number r of independent variables, which are chosen according to specific criteria, such as restrictions of the testing devices, instrumentation, weight or cost. By equating all the *Pi* terms (or combinations of terms) for the prototype ($_p$) and for the physical model ($_m$), i.e. making $(\pi_i)_p = (\pi_i)_m$, a set of similitude relations are derived, and *scale factors* are defined for all the physical quantities that govern the behaviour of the structure.

In many situations it is not however possible to satisfy all the *similitude requirements* and construct a so-called *true model* as defined above. A simplified model, designated as *distorted model*, can then be constructed satisfying only some of the similarity conditions, namely those that are most important to characterize the problem under analysis.

For the present case, which consists of the study of the dynamic behaviour of a bridge model with elastic properties, a significant number of physical quantities can be defined, which can be divided in the following groups: (i) geometrical variables; (ii) mechanical variables; (iii) loading variables; (iv) response variables. Table 7.3 systematizes the most significant of those. It is important to note that only three of these variables are independent from the dimensional point of view and these have to be carefully chosen, for example, the *Mass M*, the *Length L* and the *time t*.

The *scale factors* S_X, i.e., the ratios between the prototype ($_p$) and physical model ($_m$) quantities X

$$S_X = \frac{(X)_p}{(X)_m} \tag{7.1}$$

will be now defined, establishing appropriate relations for the most relevant characteristics of the problem and fixing scale factors for three of the variables in the physical model.

Table 7.3. Physical variables that govern a dynamic analysis problem with materials behaving in the linear elastic range.

Group	Physical Variable	Symbol
Geometry	Length	L
	Area	A
	Inertia	I
Material Properties	Modulus of Elasticity	E
	Mass	M
	Poisson's ratio	ν
Loading	Force	F
	Gravitational acceleration	g
	Time	t
	Frequency	f
Response	Displacement	δ
	Strain	ε
	Acceleration	$\ddot{\delta}$
	Stress	σ

The most important characteristics to reproduce for an accurate simulation of the dynamic behaviour of a cable-stayed bridge are the axial stiffness of the stay cables, the bending stiffness of the deck and towers, and naturally the ratio between gravity forces and elastic forces. These can be evaluated forming at a first instance dimensionless *Pi terms* for the force-displacement relations

$$F = \frac{E_c A_c}{L} \cdot \delta \tag{7.2}$$

$$F = k \cdot \frac{E_b I}{L^3} \cdot \delta \tag{7.3}$$

where the subscrits "$_c$" and "$_b$" designate the stay cable and the deck/ towers properties, respectively, and k represents a constant.

The *Pi term* associated with the *axial stiffness* is given from equation (7.2) as

$$(\pi)_{axial\ stiffness} = \frac{E_c A_c \delta}{F L} \tag{7.4}$$

while the term associated with the *bending stiffness* is given from equation (7.3) as

$$(\pi)_{bending\ stiffness} = \frac{E_b I \delta}{F L^3} \tag{7.5}$$

A dimensionless term can also be formed associated with the gravity forces

$$F = M \cdot g \tag{7.6}$$

which can be expressed as

$$(\pi)_{gravity} = \frac{M g}{F} \tag{7.7}$$

Note the symbols that appear in equations (7.2) to (7.7) are conveniently characterized in Table 7.3.

The similitude requirements are now established from the following dimensional ratios between *Pi terms:*

(i) Ratio between axial stiffness and bending stiffness terms

$$\frac{(\pi)_{axial\ stiffness}}{(\pi)_{bending\ stiffness}} \doteq \frac{E_c A_c L^2}{E_b I} \tag{7.8}$$

(ii) Ratio between gravity and axial stiffness terms

$$\frac{(\pi)_{gravity}}{(\pi)_{axial\ stiffness}} \doteq \frac{M g}{E_c A_c} \tag{7.9}$$

(iii) Ratio between gravity and bending stiffness terms

$$\frac{(\pi)_{gravity}}{(\pi)_{bending\ stiffness}} \doteq \frac{M g L^2}{E_b I} \tag{7.10}$$

The symbol "$\doteq$" in equations (7.8) to (7.10) means "dimensional equivalent to".

Now, equating the relations (7.8) to (7.10) defined for the physical model and the prototype, and fixing *three scale factors*, the *scale factors* for all other physical variables are defined.

Fixed scale factors

In the present case, a *length scale factor* $S_L = (L)_p / (L)_m$ was preliminary fixed, considering the dimensions (*3m x 3m*) of the shaking table available for the tests (Blakeborough *et al.*, 1986). Given the total length of the prototype of about *484m*, a length scale factor $S_L = 150$ led to a length of *3.22m* for the physical model. This length exceeded slightly the dimensions of the shaking table, but an overhanging of *11cm* on each side of the platform was feasible.

A second restriction concerned the gravity scale factor, which was naturally fixed as unitary ($S_g = 1$). The last restriction consisted in specifying the materials to employ in the construction of the model, fixing thus the scale factor associated with the modulus of elasticity. For the stay cables, where piano wire was employed, the scale factor was calculated as $S_E^c = 0.748$. For the deck and towers, constructed in aluminum, $S_E^b = 3.07$.

Scale factor for the stay cables' area S_A^c

Equating the relations defined by (7.8) for the prototype and the physical model yields

$$\left(\frac{E_c A_c L^2}{E_b I}\right)_p = \left(\frac{E_c A_c L^2}{E_b I}\right)_m \tag{7.11}$$

Considering that $S_L = (L)_p/(L)_m$, $S_E^b = (E_b)_p/(E_b)_m$ and $S_E^c = (E_c)_p/(E_c)_m$ are known, and assuming that the scale factor for the moment of inertia $S_I = (I)_p/(I)_m$ is given directly from dimensional analysis as $S_I = S_L^4$, equation (7.11) leads to

$$S_A^c = \frac{(A_c)_p}{(A_c)_m} = \frac{S_E^b}{S_E^c} \cdot S_L^2 \tag{7.12}$$

Scale factor for the stay cables' mass S_M^c

Equating the relations defined by (7.9) for the prototype and the physical model yields

$$\left(\frac{M_c g}{E_c A_c}\right)_p = \left(\frac{M_c g}{E_c A_c}\right)_m \tag{7.13}$$

Considering now that S_E^c and S_g are known, and S_A^c is given by equation (7.12), equation (7.13) leads to

$$S_M^c = S_E^c \cdot S_A^c \tag{7.14}$$

Scale factor for the deck/ towers' mass S_M^b

Equating the relations defined by (7.10) for the prototype and physical model yields

$$\left(\frac{M_b g L^2}{E_b I}\right)_p = \left(\frac{M_b g L^2}{E_b I}\right)_m \tag{7.15}$$

Considering that S_L, S_I, S_E^b and S_g are known, equation (7.15) leads to

$$S_M^b = S_E^b \cdot S_L^2 \tag{7.16}$$

Scale factors for other physical quantities

The evaluation of scale factors for other physical quantities, such as force or time, can now be performed based on a dimensional analysis, considering the scale factors that were preliminary fixed, and those that are defined according to equations (7.12), (7.14) and (7.16). Table 7.4 resumes the obtained definitions of scale factors, as well as the corresponding values for the present physical model.

Table 7.4. Definition and values of the scale factors for several physical quantities.

Group	Physical Variable	Scale Factor	Value
Geometry	Length, L	S_L	150
	Area, A	$S_A^b = S_L^2$,	$(150)^2$,
		$S_A^c = S_E^b \cdot S_L^2 / S_E^c$	$4.1 \cdot (150)^2$
	Inertia, I	$S_I^b = S_L^4$	$(150)^4$
Material Properties	Modulus of Elasticity, E	S_E^b,	3.07,
		S_E^c	0.748
	Mass, M	$S_M^{b,c} = S_E^b \cdot S_L^2$	$3.07 \cdot (150)^2$
	Poisson's ratio, ν	S_ν	1
Loading	Force, F	$S_F^{b,c} = S_E^b \cdot S_L^2$	$3.07 \cdot (150)^2$
	Gravitational acceleration, g	S_g	1
	Time, t	$S_t = S_L^{1/2}$	$\sqrt{150}$
	Frequency, f	$S_f = S_L^{-1/2}$	$(150)^{-1/2}$
Response	Displacement, δ	$S_\delta = S_L$	150
	Strain, ε	$S\varepsilon$	1
	Acceleration, $\ddot{\delta}$	$S_{\ddot{\delta}} = S_g$	1
	Stress, σ	$S_\sigma^{b,c} = S_E^b$	3.07

7.3.2 Description of the physical model

The total length of the bridge model was *3.22m*, according to the length scale factor $S_L = 150$. The choice of such a small scale, conditioned by the dimensions of the shaking table, prevented the correct scaling of all aspects of the prototype. The box cross sections of the

girder and tower legs were substituted by solid rectangular cross sections with correctly scaled bending stiffness (but not axial stiffness), maintaining the *A*-shape of the towers. These components, constructed in an aluminum alloy (Young's modulus $E_b = 72GPa$), had the following dimensions: girder, $25.4x7.92mm$, tower legs, $9.2x8.4mm$. The stay cables were simulated with piano wires (Young's modulus $Ec = 210GPa$). Their axial stiffness was correctly scaled and the only difference to the prototype was on the back stays, that were made of *6* cables in the real structure, and were constituted by one piano wire with equivalent scaled area in the model. To compensate for the dead weight of such a light model, additional masses were added. Small steel plates were attached to the towers and girders by two bolts, without any further contact to minimize any stiffening effects. These masses were designed respecting the scale factors defined in Table 7.4. A general description of the overall bridge model can be found in Figure 7.2, while a more detailed characterization of the model is presented in (Garevski, 1990).

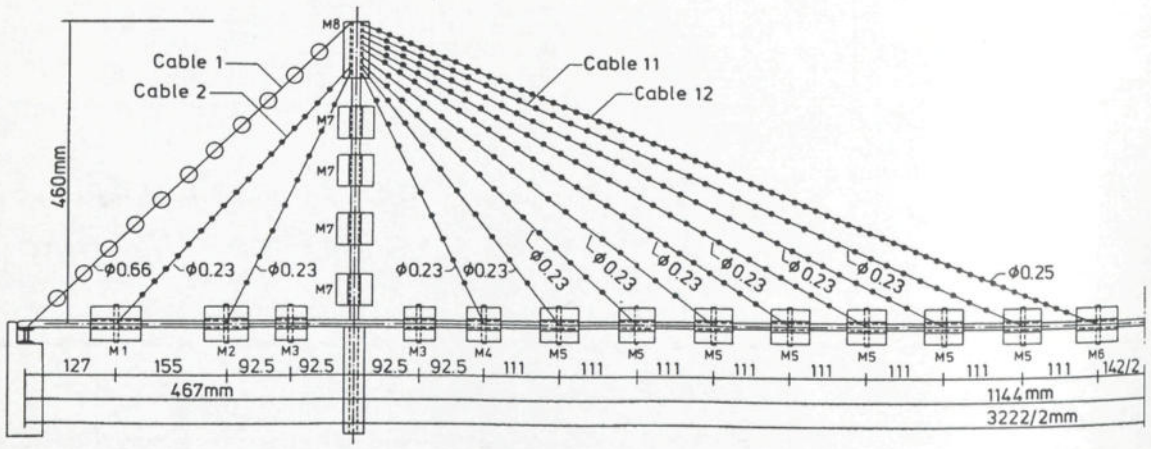


Figure 7.2. Overall characteristics and dimensions of the Jindo Bridge physical model.

The cables presented in Figure 7.2 were redesigned by the author (Caetano & Cunha, 1995), employing different types of masses and using also a different form of fixation of those masses to the piano wires.

For the back stays, represented by piano wires with a diameter of *0.66mm*, small lead spheres ($\phi = 12mm$, $weight \approx 30.6gr$) were glued directly to the wires. For the other stay cables, represented by piano wires with diameters of *0.23mm* and *0.25mm*, smaller masses ($\phi = 6.5mm$, $weight \approx 4.4gr$) made of a zinc alloy usually used as angling weights were attached to the cables simply by pressure. Table 7.5 summarizes the characteristics of the masses added both to the stay cables and to the deck and towers, defined according to the scale factors presented in Table 7.4. Figure 7.3 shows a general view of the physical model mounted on a steel beam, while some specific details are presented in Figure 7.4.

Note that the cable numbers used in Table 7.5 and onwards respect the designation of Figure 7.2.

Table 7.5. Characteristics of the added masses.

Location	Type of mass	Number of masses / cable	Total mass (kg)
Cable 1	Lead	11	0.306
Cable 2	Zinc	17	0.0267
Cable 3	Zinc	10	0.0157
Cable 4	Zinc	10	0.0157
Cable 5	Zinc	11	0.0173
Cable 6	Zinc	18	0.0283
Cable 7	Zinc	22	0.0348
Cable 8	Zinc	32	0.0505
Cable 9	Zinc	35	0.0552
Cable 10	Zinc	40	0.0631
Cable 11	Zinc	44	0.0694
Cable 12	Zinc	64	0.1009

Location	Type of mass	Total mass (kg)
Girder	Steel (M1)	1.83
Girder	Steel (M2)	1.63
Girder	Steel (M3)	1.20
Girder	Steel (M4)	1.31
Girder	Steel (M5)	1.45
Girder	Steel (M6)	1.68
Tower	Steel (M7)	2 x 0.4545
Tower	Steel (M8)	1.007

Total mass of superstructure: $\approx 50kg$

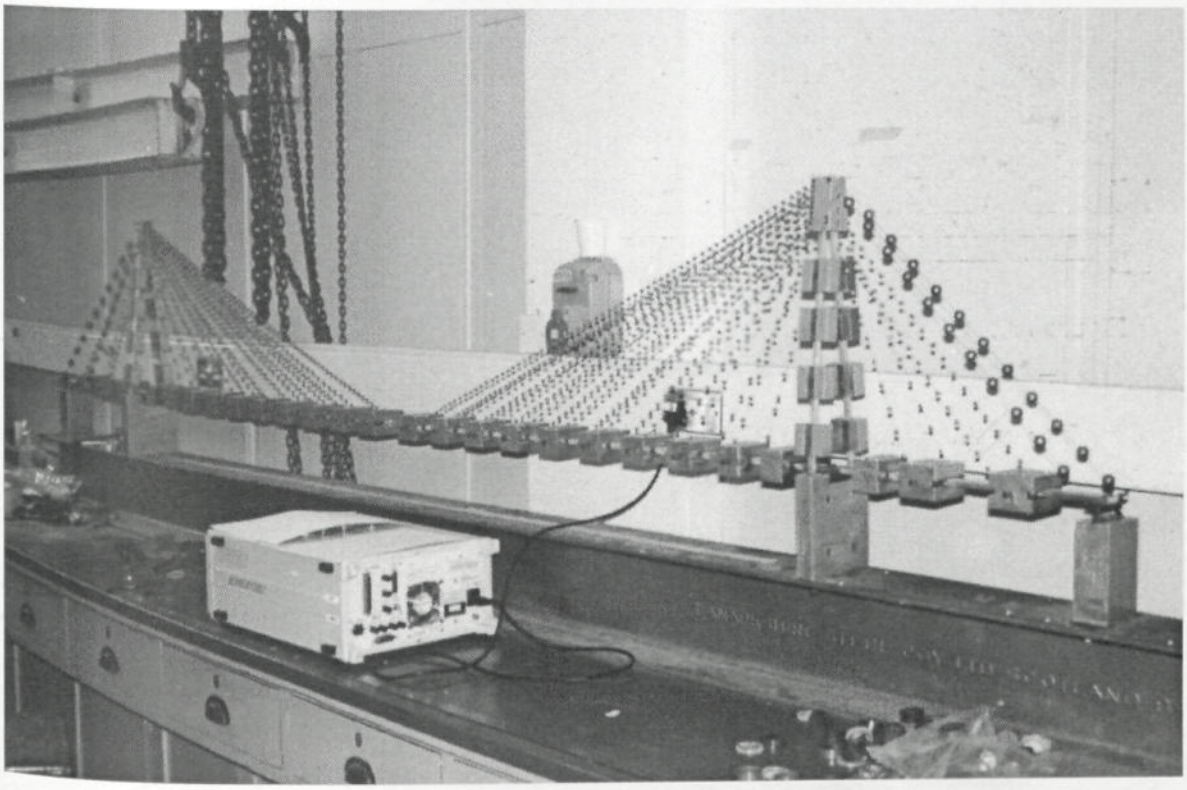
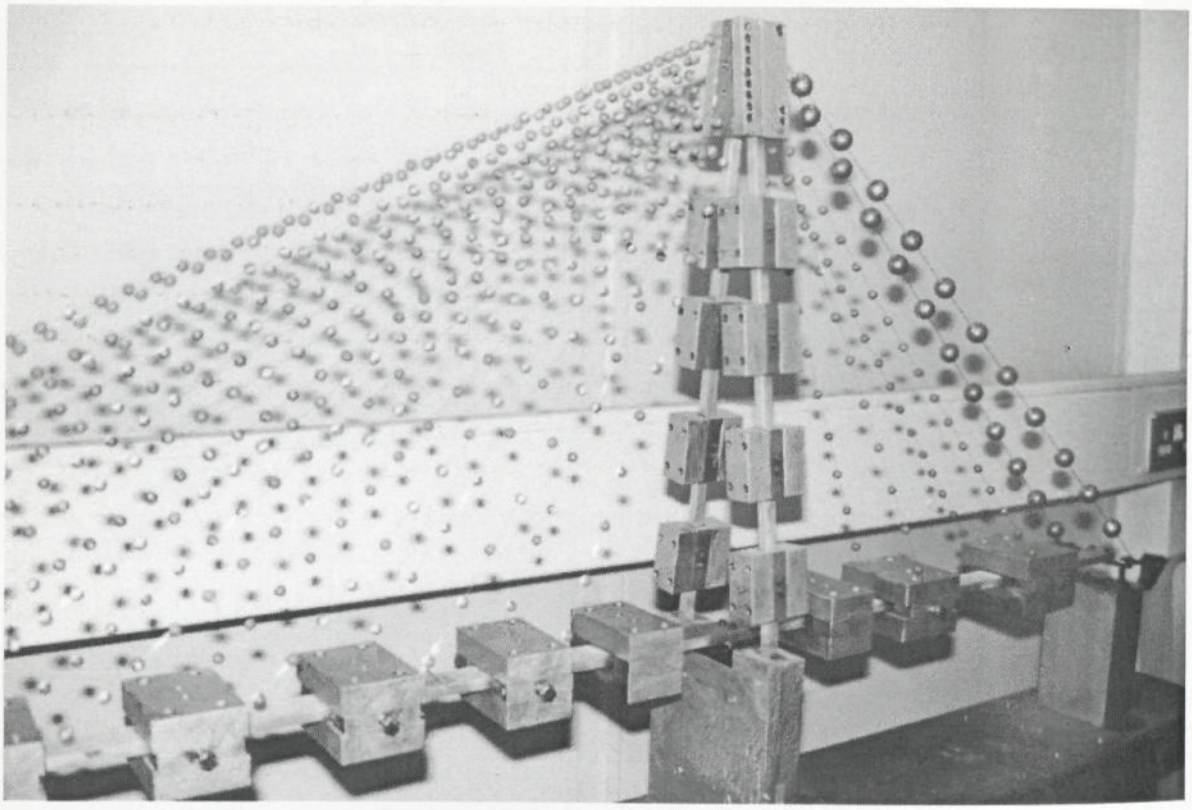
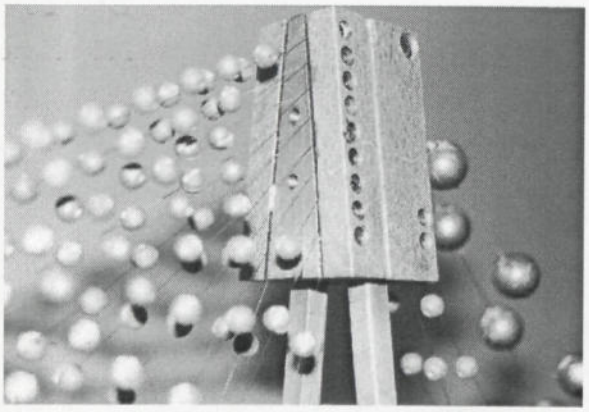


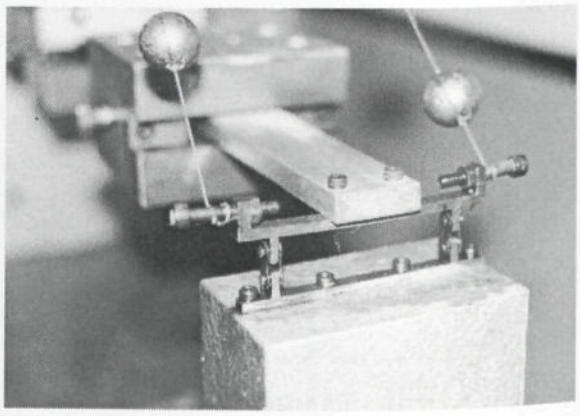
Figure 7.3. General view of the physical model after redesign of the stay cables.



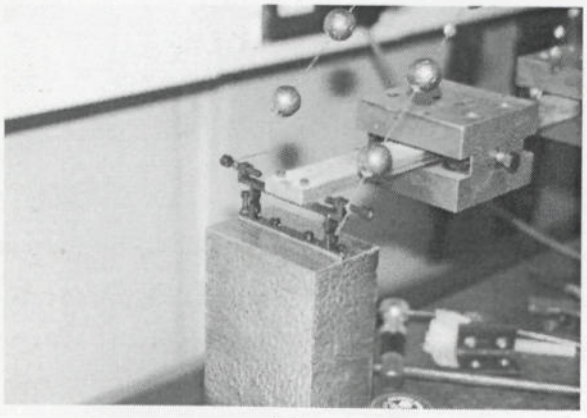
(a)



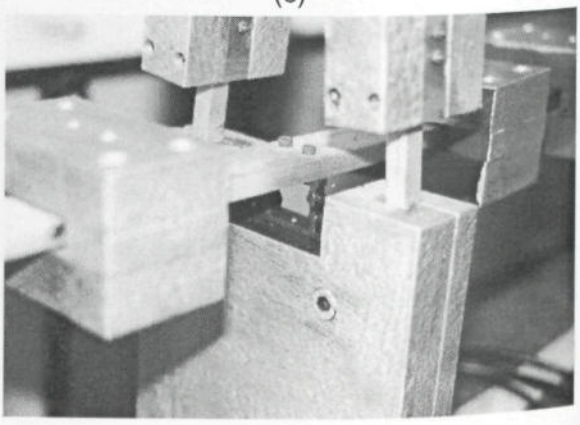
(b)



(c)



(d)



(e)

Figure 7.4. Partial view of the physical model (a) and specific details: (b) Top of tower; (c) Back stay connection at abutment; (d) Pinned support at abutment; (e) Pinned support at one tower.

7.3.3 Tuning of cable tensions

The set of final tensions on the cables from the bridge prototype was scaled according to the similitude theory, leading to the values of the prestress to be developed in the wires of the model presented in Table 7.6. This prestress was achieved by turning bolts, around which the ends of the cables were wrapped, in the manner of tuning a violin. The tension in each cable was tuned indirectly using a magnetic sensor (see Figure 5.22(b)) and a Fourier analyzer (see Figure 7.3), taking into account the relation between the natural frequencies of the cables and the corresponding tensions, according to the vibrating chord theory (Irvine, 1978). This relation is expressed by equation (3.66) and by the roots of equation (3.67) derived in Chapter three for very small λ^2 values, and can be written simply as

$$f_n = \frac{n}{2L} \cdot \sqrt{\frac{T}{m}} \tag{7.17}$$

where f_n is the natural frequency of nth order, expressed in *Hz*, L is the total length of the cable, T is the tension and m is the distributed mass of the cable. Table 7.6 summarizes the frequencies of the first three harmonics of the stay cables calculated using equation (7.17) (assuming thus a continuous idealization of the cables), and calculated from a finite element formulation (*FEM*), dividing each cable into several truss elements with lumped masses at the nodes. As can be observed from this Table, the continuous and *FEM* analysis of the cables produced quite similar results, the differences between first natural frequencies not exceeding *5.4%* (with respect to the frequencies calculated using the continuous model).

Table 7.6. Jindo Bridge model: natural frequencies of the stay cables.

Cable No.	Length (mm)	Mass (kg/m)	Tension (N)	1st Freq. (Hz) FEM (Irvine)	2nd Freq.(Hz) FEM (Irvine)	3rd Freq. (Hz) FEM (Irvine)	1st Freq. (no mass)
1	643.5	0.5258	123.1	11.46 (11.89)	22.61 (23.78)	33.42 (35.67)	166.03
2	513.0	0.05205	13.1	14.72 (15.46)	29.30 (30.93)	43.82 (46.39)	194.96
3	424.3	0.03724	9.6	17.90 (18.92)	35.46 (37.84)	52.35 (56.76)	201.79
4	424.4	0.03723	8.4	16.94 (17.70)	33.57 (35.39)	49.56 (53.09)	188.71
5	486.4	0.03577	8.0	14.64 (15.37)	29.06 (30.74)	43.00 (46.12)	160.69
6	558.7	0.05076	10.9	12.89 (13.11)	25.39 (26.23)	37.92 (39.34)	163.29
7	646.5	0.05375	12.0	11.22 (11.56)	22.40 (23.11)	33.53 (34.67)	148.97
8	740.7	0.06816	13.2	9.14 (9.39)	18.26 (18.79)	27.39 (28.18)	135.54
9	839.1	0.06581	14.8	8.95 (8.94)	17.44 (17.87)	26.15 (26.81)	126.69
10	940.3	0.06711	16.3	8.20 (8.29)	15.90 (16.57)	23.84 (24.86)	118.65
11	1043.6	0.06652	17.4	7.90 (7.75)	15.37 (15.50)	23.04 (23.25)	110.45
12	1148.4	0.08788	21.5	7.05 (6.81)	13.76 (13.62)	20.95 (20.43)	102.65

Figure 7.5 shows the instantaneous response and corresponding power spectrum measured using the magnetic pick up and a *2*-channel Fourier analyzer while tuning the cable number *9*.

In general, the errors in the frequency adjustment to the design natural frequencies were no greater than *5%*, what led to errors in the installed design tension lower than *10%*.

Note however that the tuning of the stay cables was actually a relatively lengthy process, requiring several iterations. The first iteration was performed during the mounting of the piano wires, before application of the zinc masses. In order to achieve the required geometry, the wires were tuned to the design tensions, the corresponding natural frequencies being however calculated from equation (7.17) considering only the wire mass. The last column in Table 7.6 summarizes the first natural frequencies obtained from this consideration, which are obviously much higher than the final frequencies.

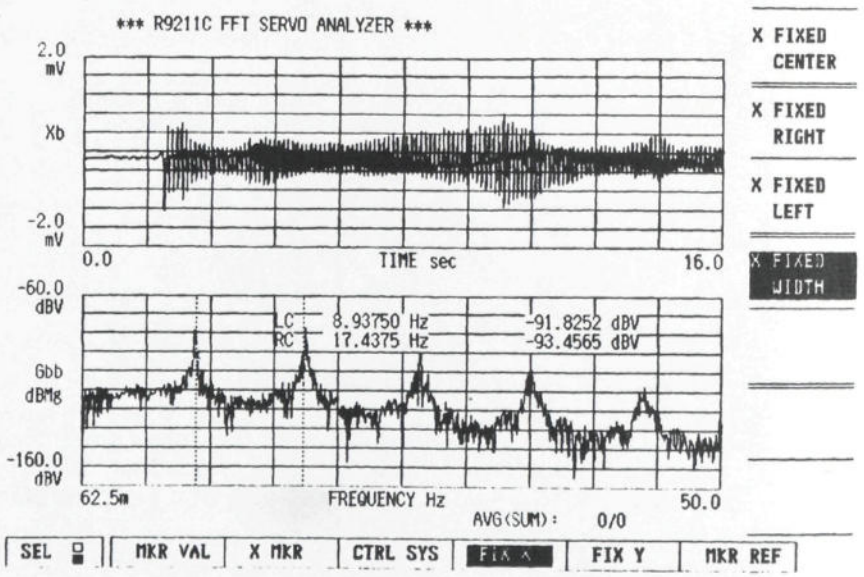


Figure 7.5. Tuning of cable *9* (left, front) using a magnetic pick up: instantaneous response and corresponding power spectrum.

7.4 NUMERICAL EVALUATION OF MODAL PARAMETERS OF THE MODEL

Although it is recognized that the behaviour of cable-stayed bridges is clearly three-dimensional and so a valid numerical analysis requires, in principle, a *3-D* mathematical model, it was decided to develop, for simplicity in the first instance, a *2-D* finite element analysis. The results obtained, which will be summarized in the current Section, were used to prepare the experimental tests and to extract preliminary conclusions about the effect of the vibration of the cables on the global dynamic response of the bridge.

In a second phase, a *3-D* finite element analysis was developed, employing a richer description of the physical model. This study will be also presented in the current Section.

Two models of the Jindo Bridge physical model were developed in both the *2-D* and *3-D FEM* analyses. These models were designated, according to Abdel-Ghaffar and Khalifa (1991), as *OECS* (*One-Element Cable System*) and *MECS* (*Multi-Element Cable System*) models.

The *OECS* model discretized the deck and towers into a number of *2-D* or *3-D* beam elements and idealized each stay cable as a simple truss element with an equivalent Modulus of Elasticity, reproducing in this way the most common type of formulation employed in the numerical modeling of cable-stayed bridges. This corresponds in practice to neglect the mass distribution of the stay cables, and hence in not accounting for the corresponding dynamic behaviour.

The *MECS* model adopted the same discretization of the deck and towers, but discretized each stay cable into a total number of *12* truss elements, what corresponded actually to the consideration of a lumped mass distribution and so to the introduction in a simplified form of the continuous character of the mass distribution.

The results of a modal analysis employing the two models will be also presented and discussed in this Section, considering in particular the identified pattern for *dynamic cable-structure interaction.*

7.4.1 Preliminary 2-D FEM analysis

The *2-D* finite element models discretized the deck and towers into *76* beam elements, according to the representation of Figure 7.6. This Figure also shows the assumptions employed in the idealization of the supports at the abutments and towers. As referred above, the *OECS* idealized each stay cable as a single truss element with an equivalent Modulus of Elasticity, while the *MECS* model idealized each stay cable as a series of *12* truss elements.

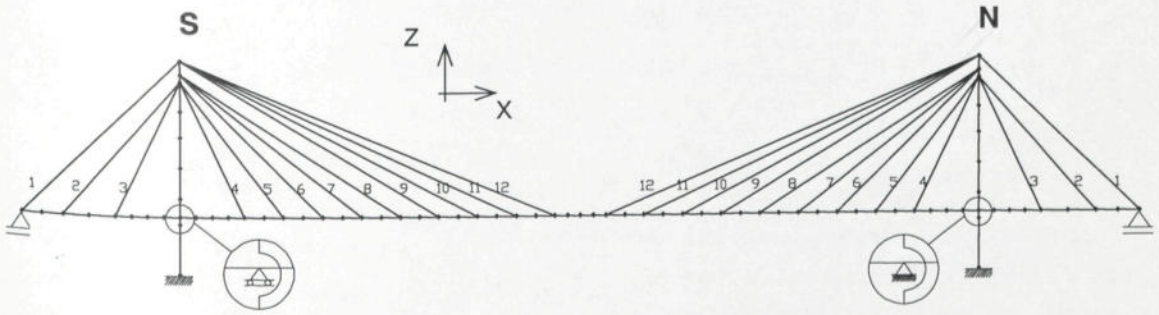


Figure 7.6. Structural discretization used in the *OECS 2-D* model.

Using the two models, dynamic analyses were performed based on the stiffness matrices obtained under a previous application of the static loads in a nonlinear geometric calculation, using the software package SOLVIA (1995). This preliminary static analysis was actually performed iteratively, given that it was necessary to impose the design cable tensions

at the dead-load configuration. The simplified procedure adopted consisted in departing from the "non-deformed" bridge structure subject to dead-weight, by applying vertical supports at all the cable connections to deck points, and horizontal supports at the tower connections, conducting then a static analysis of the modified bridge model under dead-weight. The reactions at the supports were then transferred into the stay cables, applied as equivalent initial strains, and the supports were de-activated. The response of the final bridge models to dead-weight was then calculated, what led to a tension distribution slightly different from the imposed in the beginning of the analysis, as well as to slight deformations, which were not controlled due to their relatively small value. Introducing small corrections in the initial-strains of the stay cables, the dead-weight response was again calculated, and the new tensions were compared with the corresponding design tensions. The analysis was repeated iteratively until errors lower than *10%* with respect to the design tension were achieved. This required *8* iterations.

As for the dynamic analysis, the lowest *20* natural frequencies in the range *0-100Hz* and the corresponding modal shapes were evaluated for the *OECS*. Table 7.7 summarizes these natural frequencies and the type of the corresponding modal shapes (*SYM*-mode shape of the girder and towers is symmetric with respect to the axis of symmetry of the bridge; *ASM*-mode shape of the girder and towers is anti-symmetric; *LTW*- mode shape involves essentially the movement of the left (South) tower; *RTW*- mode shape involves essentially the movement of the right (North) tower; *AXG*- mode shape involving essentially the axial deformation of the girder). Some of these modal shapes are represented in Figure 7.7.

Table 7.7. Calculated natural frequencies of Jindo Bridge model (*2-D OECS* numerical model).

Mode number	Natural frequency (Hz)	Type of Mode	Mode number	Natural frequency (Hz)	Type of Mode
1	6.21	1st SYM	11	41.36	1st RTW
2	9.16	1st ASM	12	48.50	5th ASM
3	13.68	2nd SYM	13	59.37	6th SYM
4	18.14	2nd ASM	14	63.04	2nd LTW
5	22.66	3rd SYM	15	64.18	2nd RTW
6	26.13	3rd ASM	16	66.77	6th ASM
7	28.79	4th SYM	17	71.85	7th SYM
8	32.68	4th ASM	18	76.65	7th ASM
9	40.19	5th SYM	19	90.04	8th SYM
10	41.13	1st LTW	20	99.29	1st AXG

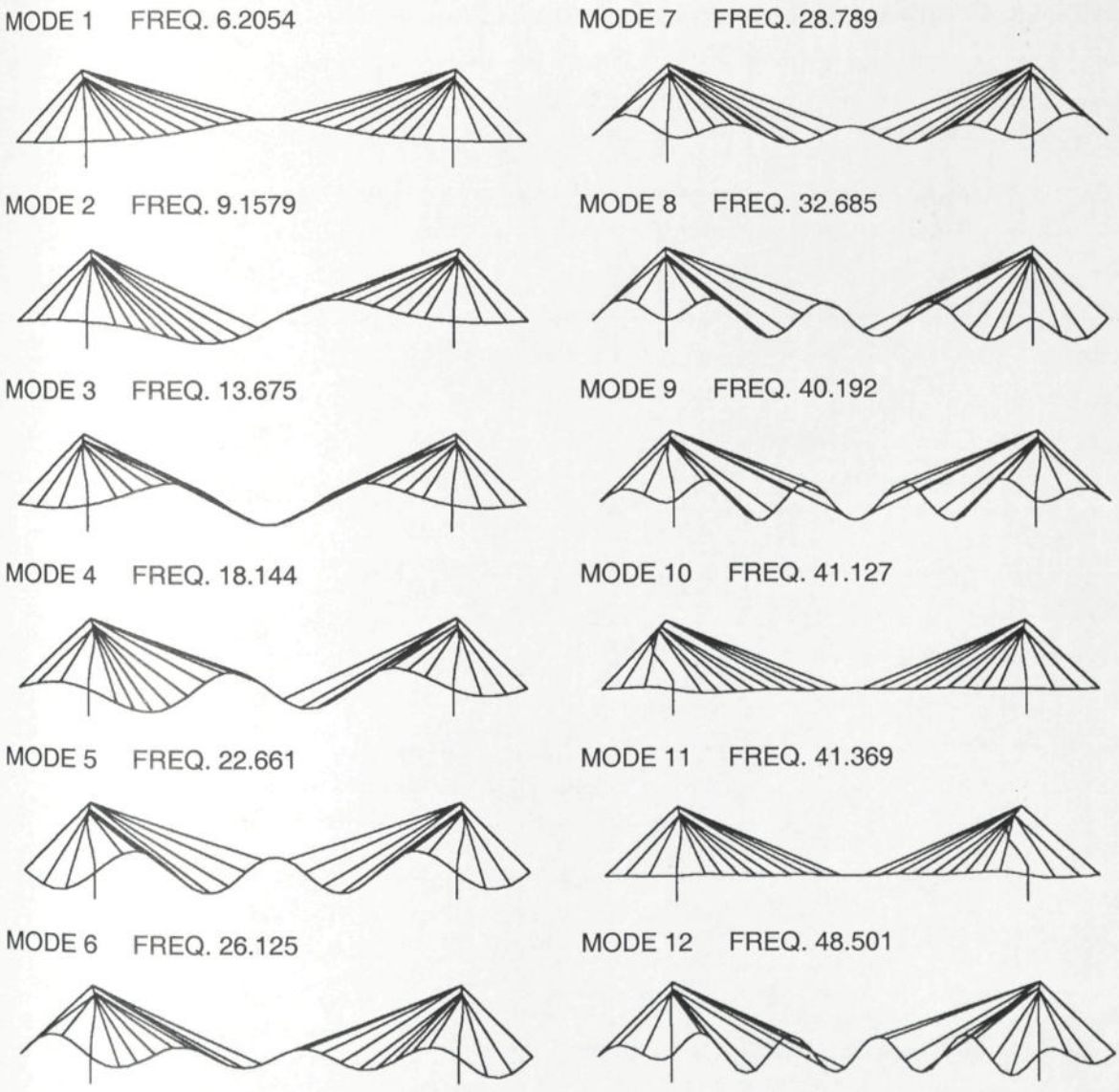


Figure 7.7. Calculated modal shapes (*OECS* analysis).

For the *MECS*, the lowest *100* natural frequencies in the range *0-48 Hz* and the corresponding modal shapes were calculated. Table 7.8 summarizes the values of some of these natural frequencies, while Figure 7.8 represents some of the obtained modal shapes.

Note that the natural frequencies presented in Tables 7.7 and 7.8 respect the physical model characteristics. These can be extrapolated to the bridge prototype by adequate application of the frequency scale factor S_f presented in Table 7.4. So the *OECS* analysis, for example, leads to a fundamental frequency of $6.21/\sqrt{150} = 0.51Hz$ on the prototype.

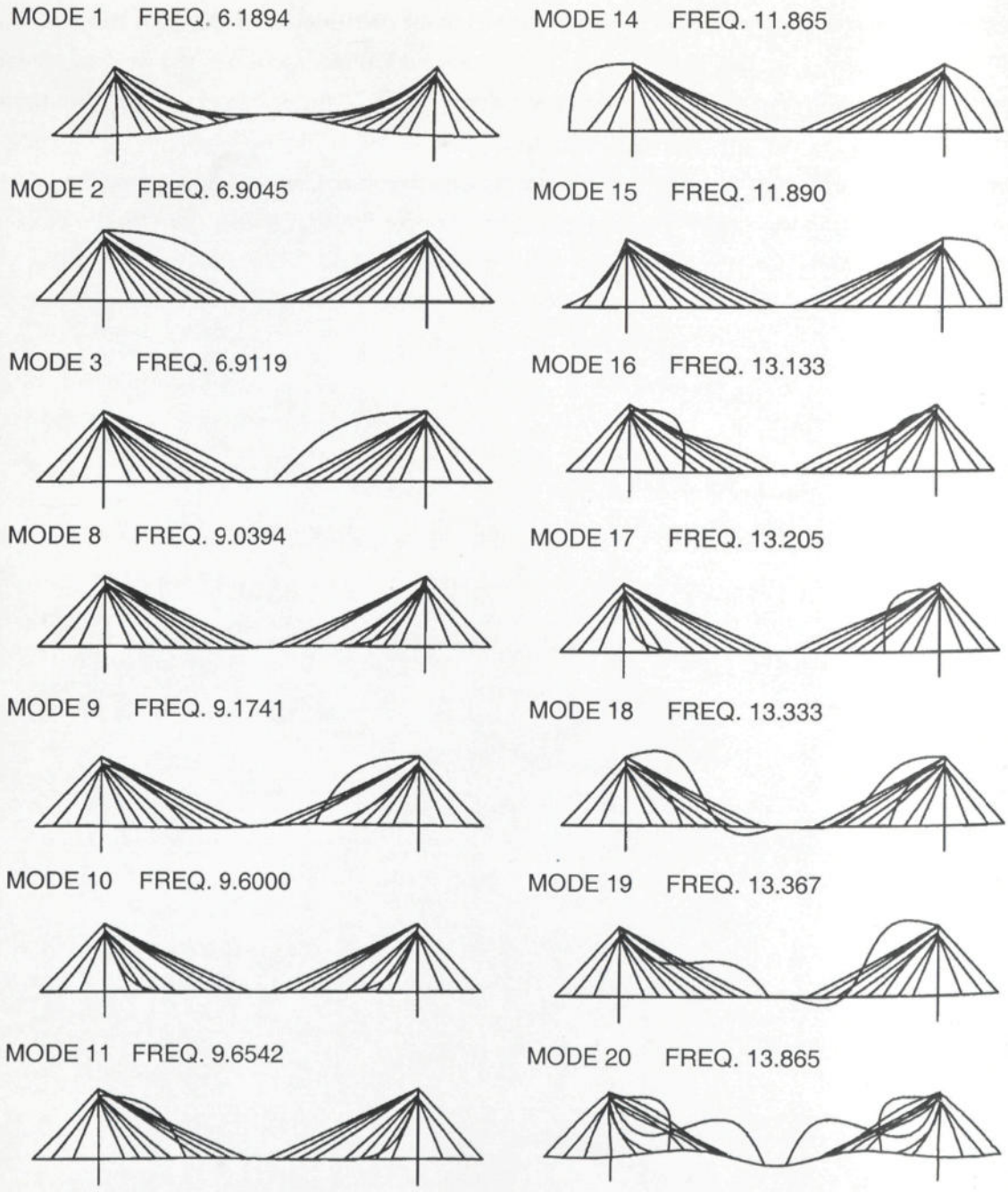


Figure 7.8. Calculated modal shapes (*MECS* analysis).

The analysis of Tables 7.7 and 7.8 and the observation of the modal shapes (Figures 7.7 and 7.8) lead to the conclusion that the *MECS* analysis, based on the discretization of the cables into several truss elements, produce many new modes of vibration. Most of the new modes simply involve local vibrations of the cables and so are not important in terms of the contribution to the global response of the bridge. Others of these new modes, however, involve simultaneous motion of the cables and of the deck and towers. In most cases, several of these modes of vibration have close natural frequencies and similar mode shapes for the deck/towers system, but different movements of the cables, the relative order of magnitude of the motion also varying (see the representation at different scales in Figure 7.9). The

importance of the coupling can be quantified by a factor obtained from the ratio between the maximum normalized modal displacements of the group of cables and of the deck/towers system (Table 7.8). In the present analysis, for the set of *100* natural frequencies, this factor varies from *1.3* to *566.9*. Small ratios (indicated in bold type in Table 7.8) denote a very clear interaction between the cables and the girder/towers movement. High ratio values are typical of modal shapes that involve essentially vibration of one or more cables, here designated as *local modes*.

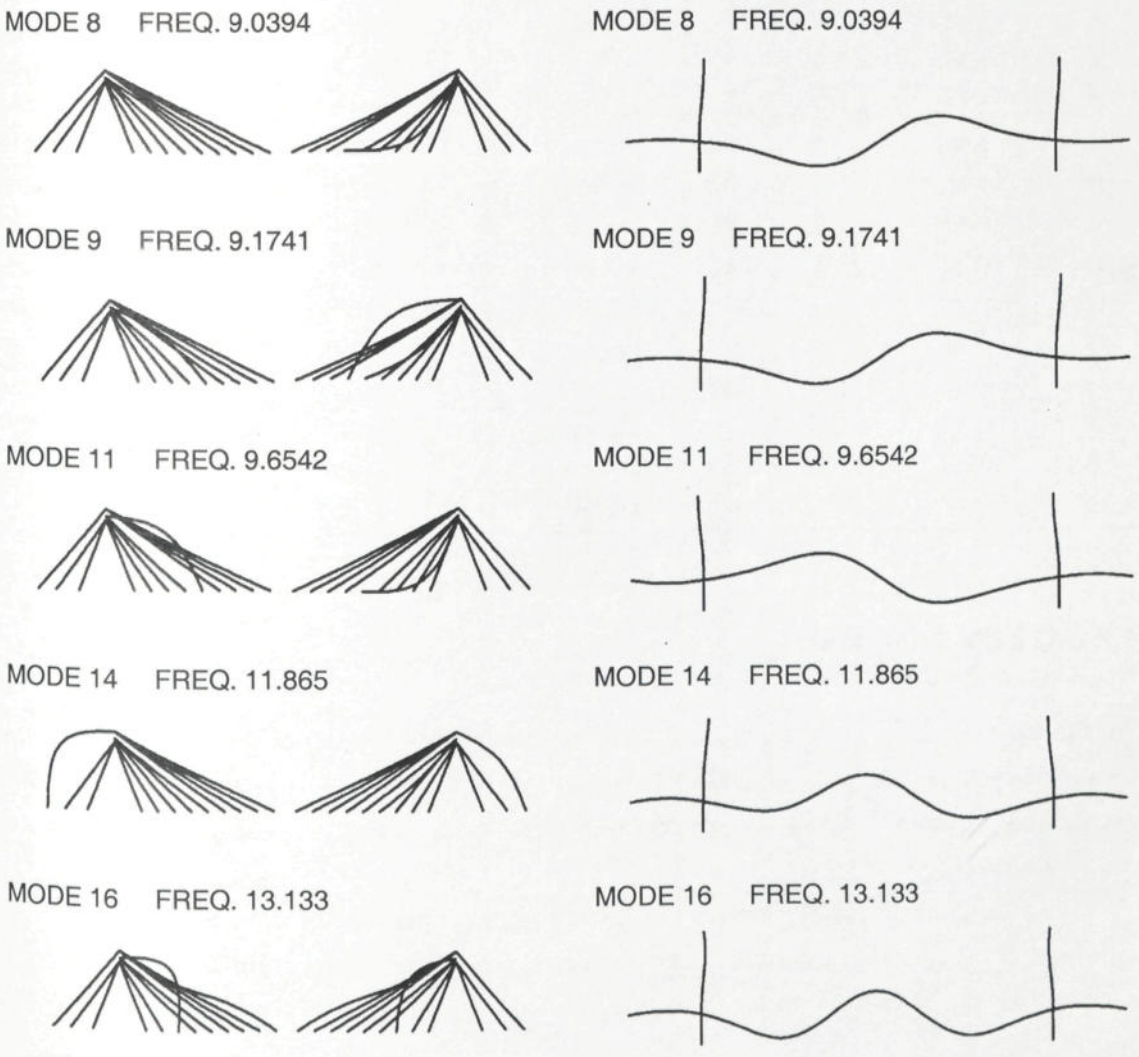


Figure 7.9. Calculated modal shapes (*MECS* analysis): separated representation of cables and deck/towers motion at different scales.

Table 7.8. Calculated natural frequencies of Jindo Bridge Model (*2-D MECS* numerical model).

Mode number	MECS natural frequency (Hz)	Associated OECS frequency (Hz)	Ratio truss/beam max. displ.	Type of mode	Mode number	MECS natural frequency (Hz)	Associated OECS frequency (Hz)	Ratio truss/beam max. displ.	Type of mode
1	6.19	6.21	**1.97**	1st SYM	20	13.86	13.68	**3.4**	2nd SYM
2	6.90		276.7	LOCAL	29	17.81		**48.8**	2nd ASM
3	6.91		285.4	LOCAL	32	18.29	18.14	**15.9**	2nd ASM
4	7.78		566.9	LOCAL	41	22.81	22.66	**3.5**	3rd SYM
5	7.78		282.6	LOCAL	44	23.30		**43.3**	3rd SYM
6	8.35		254.3	LOCAL	45	23.34		**30.6**	3rd SYM
7	8.36		325.0	LOCAL	50	26.33	26.13	**1.3**	3rd ASM
8	9.04		**17.7**	1st ASM	52	26.70		**49.5**	3rd ASM
9	9.17	9.16	**10.6**	1st ASM	53	26.73		**46.8**	3rd ASM
10	9.60		161.4	LOCAL	56	28.88	28.79	**3.2**	4th SYM
11	9.65		**31.8**	1st ASM	58	29.63		**28.6**	4th SYM
12	11.62		162.9	LOCAL	65	32.94	32.68	**3.8**	4th ASM
13	11.65		225.4	LOCAL	83	39.93		**44.0**	5th SYM
14	11.86		**45.1**	2nd SYM	85	40.45	40.19	**10.2**	5th SYM
15	11.89		**49.2**	1st ASM	87	40.77		**11.5**	5th SYM
16	13.13		**32.6**	2nd SYM	88	41.69	41.13	**1.0**	1st LTW
17	13.20		134.6	LOCAL	89	41.88	41.36	**1.0**	1st RTW
18	13.33		**35.1**	2nd SYM	93	44.73		**19.1**	2nd LTW
19	13.37		92.7	LOCAL	94	44.80		**18.5**	2nd RTW

7.4.2 3-D FEM analysis

Both the deck and towers were represented by three-dimensional beam elements with rectangular cross sections, identical to those corresponding to the physical model. A total of *216 3-D* beam elements were employed (*120, 80* and *16*, to represent the deck, towers and piers, respectively).

In order to adequately model the geometric arrangement of the stay cables, fifty-six infinitely rigid cross beam elements, designated as *rigid links*, were connected to the central line of the deck, in correspondence with added masses and cable end attachments (see Figure 7.10).

Forty-eight *rigid links* were also added at the top of the towers, in order to simulate the accurate length of the cables.

Eleven additional stiff beam elements, connecting horizontally the two legs of each A-tower at the top, were also included, in order to obtain compatible displacements in conformance with the physical model.

As in the *2-D* modeling, the *OECS* idealized each stay cable as a single truss element, while the *MECS* adopted a discretization into a total number of *12* truss elements.

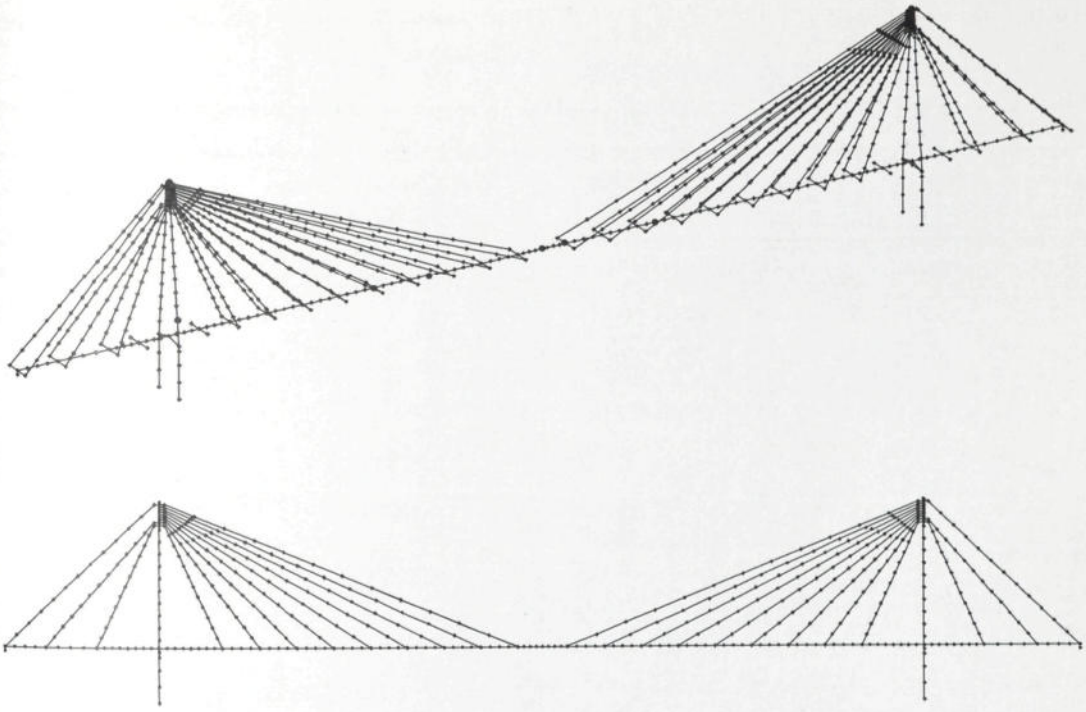


Figure 7.10. Structural discretization used in the *MECS* model. Perspective and elevation.

The following boundary conditions were assumed in both models: (i) the piers were clamped to the soil; (ii) the vertical displacements, as well as the rotations around the longitudinal and vertical axes were precluded at the end supports of the deck; (iii) the transversal motion of the deck at the end and left (South) tower supports was constrained by appropriate spring elements; (iv) additional constraints at the intermediate supports of the deck over the piers were introduced in order to ensure compatibility of the deck and pier motions, imposing equal vertical displacements at the left support (Figure 7.10) and equal transversal and vertical displacements at the right one. The introduction of the design initial cable tensions was achieved iteratively by successive adjustment of the initial strain of the stay cables, using the procedure described for the *2-D* analysis.

Dynamic analyses were then performed with the software SOLVIA already referred, using again the global stiffness matrices obtained at the end of geometric nonlinear static analyses under permanent loads and using also consistent mass matrices, which included in particular the rotational mass moments associated with the steel added masses along the deck and tower legs.

The lowest *20* natural frequencies in the range *0-46 Hz* and the corresponding modal shapes were evaluated for the *OECS*. Table 7.9 summarizes the values of these frequencies and the type of the corresponding modal shapes. Figure 7.11 shows these modal shapes in elevation and plan.

For the *MECS*, the lowest *150* natural frequencies in the range *0-21.3 Hz* and the corresponding modal shapes were calculated. Table 7.10 summarizes the values of some of these natural frequencies. Figure 7.12 shows these modal shapes in elevation and plan.

Table 7.9. Calculated natural frequencies of Jindo Bridge model (*3-D OECS* numerical model).

Mode number	Natural freq. (Hz)	Type of Mode	Mode number	Natural freq. (Hz)	Type of Mode
1	4.28	1st transversal SYM	11	24.95	1st torsion SYM
2	6.21	1st vertical SYM	12	26.00	3rd vertical ASM
3	9.12	1st vertical ASM	13	28.61	4th vertical SYM
4	11.71	1st transversal ASM	14	30.33	2nd LTW+ 2nd RTW in phase
5	13.74	2nd vertical SYM	15	30.45	transversal
6	18.26	2nd vertical ASM	16	30.46	2nd LTW+ 2nd RTW opp. phase
7	22.10	2nd transv.SYM+1st torsion SYM	17	32.52	4th vertical ASM
8	22.70	3rd vertical SYM	18	38.80	transversal
9	23.42	1st LTW	19	39.69	5th vertical SYM
10	23.42	1st RTW	20	45.11	1st torsion ASM

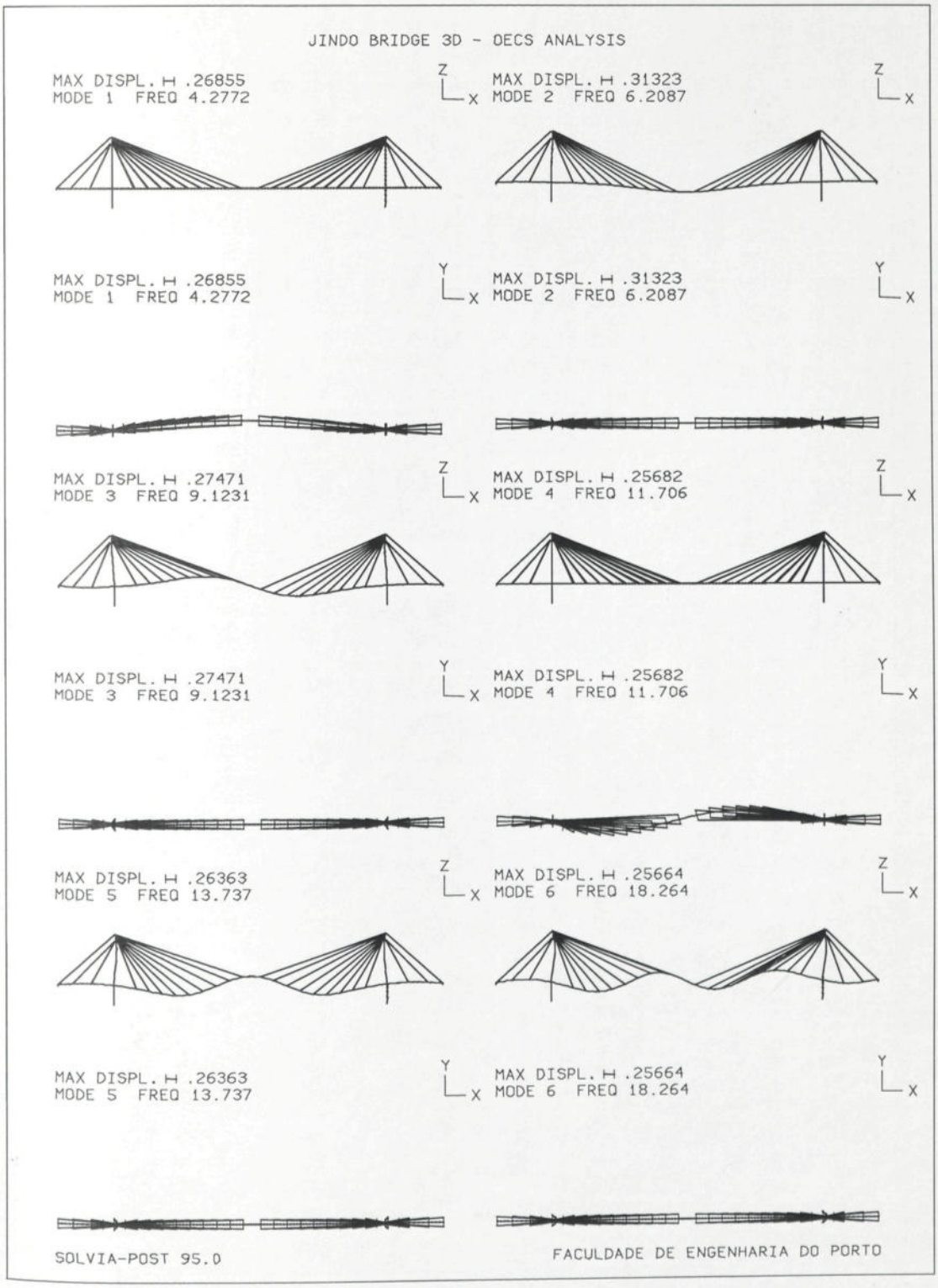


Figure 7.11. Calculated modal shapes (*OECS* analysis): (a) Modes *1* to *6*.

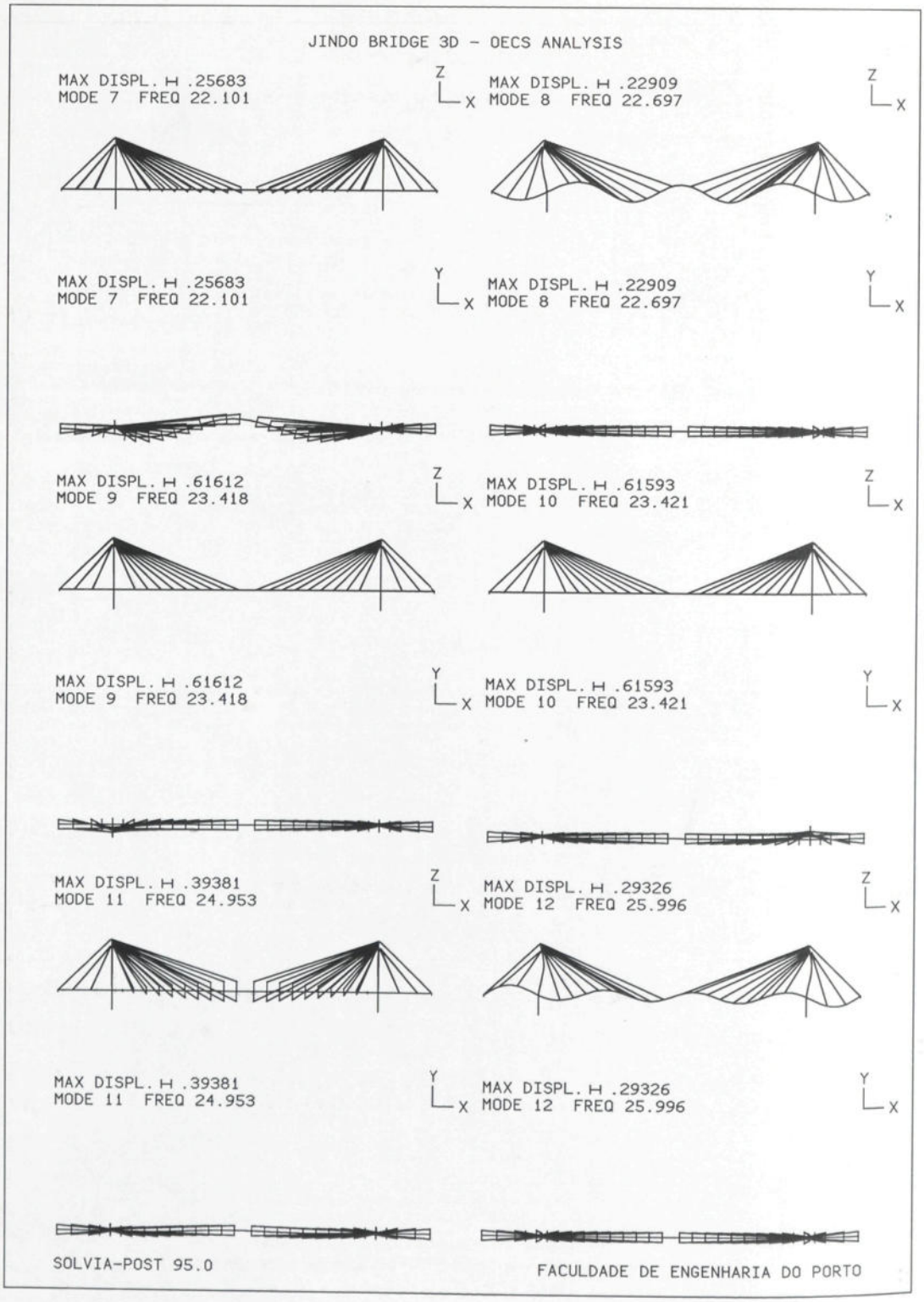


Figure 7.11. Calculated modal shapes (*OECS* analysis): (b) Modes *7* to *12*.

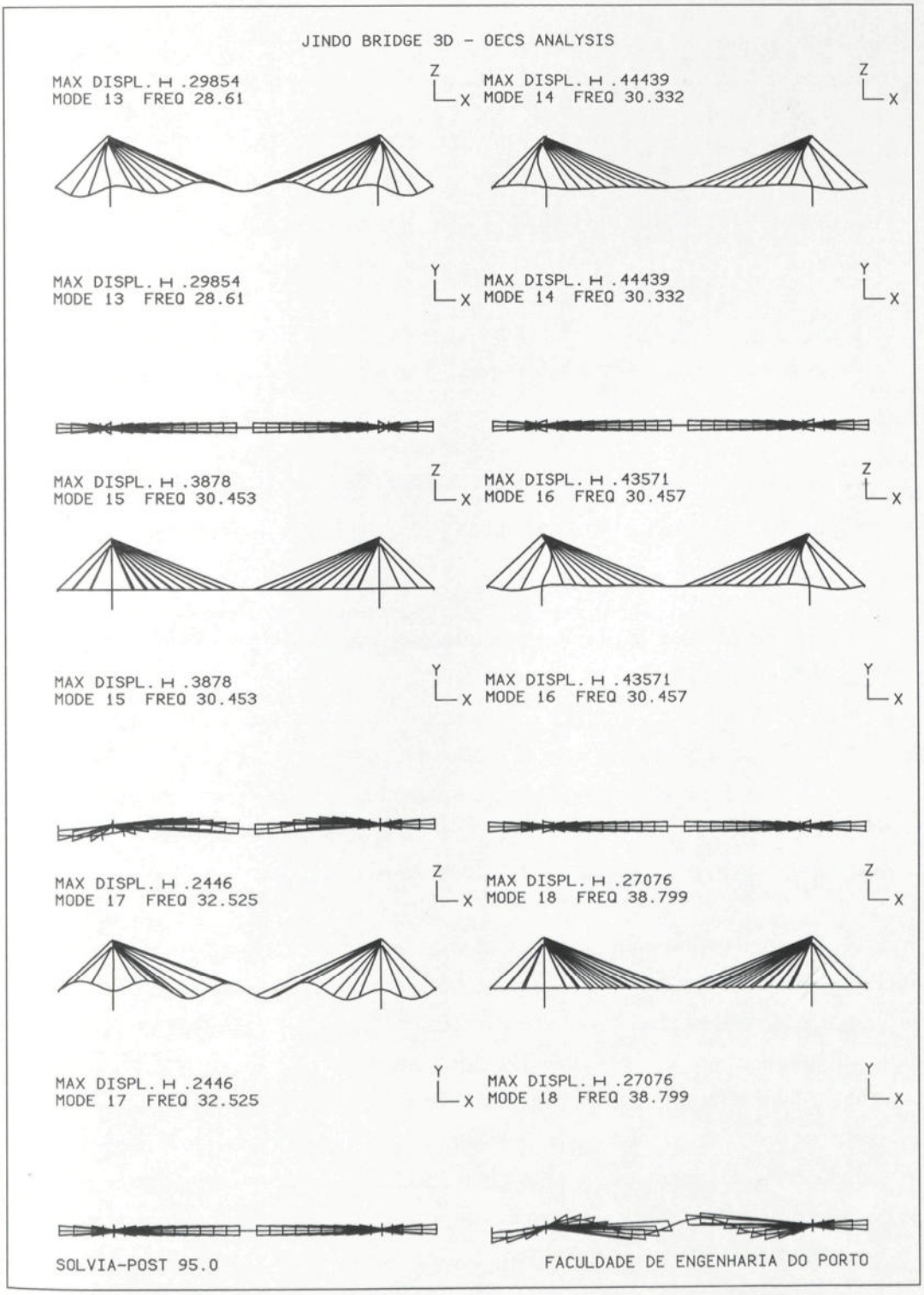


Figure 7.11. Calculated modal shapes (*OECS* analysis): (c) Modes *13* to *18*.

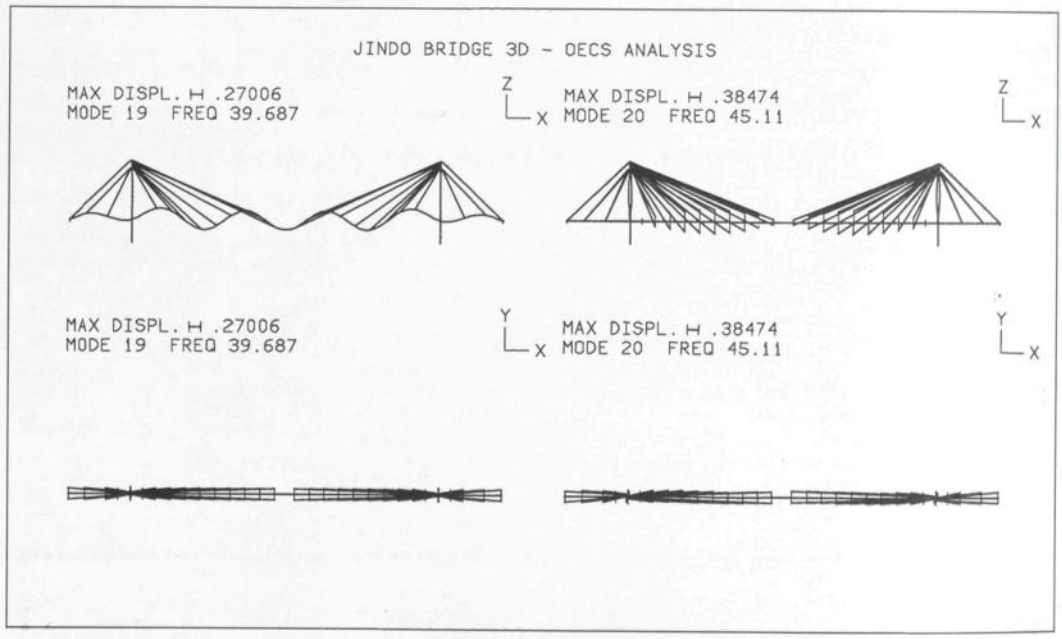


Figure 7.11. Calculated modal shapes (*OECS* analysis): (d) Modes *19* to *20*.

The analysis of the sets of natural frequencies and modal shapes shows that, as in the case of the *2-D* study, the *MECS* analysis produces many new modes of vibration (many more, in fact, than the *2-D* analysis). A pattern similar to the *2-D* analysis was found, consisting in the appearance of groups of modes closely spaced in frequency, which involves similar mode shapes for the deck and towers system, but different movements of the cables, the relative order of magnitude also varying. This effect is illustrated in Figure 7.13, representing the motion of stay cables and deck/ towers at different scales for four groups of modes.

With respect to the quantification of the degree of cable-structure interaction, it is observed that the ratio between maximum modal vectorial displacements associated with stay cables and with the deck and towers nodes (as calculated for the 2-D analysis) is not an adequate measure of degree of cable-structure interaction. In effect, the analysis of mode shapes shows that, although a significant cable-structure interaction may occur either in the vertical plane or for transversal motion for in-plane or out-of-plane modes, respectively, these modes may also involve local lateral or in-plane motion of the stay cables, respectively, which lead to global ratios between truss/ beam elements displacements rather high.

So, it was decided to establish the following criterion for evaluation of the degree of cable-structure interaction: (i) define a *Z-ratio*, as the ratio between the maximum vertical modal components of displacement associated with the stay cables and the deck and towers nodes, and a *Y-ratio*, as the ratio between the maximum lateral modal components of displacement associated with the stay cables and the deck and towers nodes; (ii) compare the modal participation factors in the *Y* (lateral) and *Z* (vertical) directions, calculating the

corresponding ratio (Z-part./Y-part.); (iii) when the ratio between participation factors is lower than *1*, i.e., the mode shape involves essentially lateral movements, select the *Y-ratio* as the ratio that quantifies the level of cable-structure interaction. Otherwise, select the *Z-ratio* value to quantify this effect.

The modes of vibration listed in Table 7.10 were selected among the first *100* modes of vibration as those that, according to this criterion, exhibited the highest cable-structure interaction.

Table 7.10. Calculated natural frequencies of Jindo Bridge model (*3-D MECS* numerical model).

Mode number	MECS natural frequency (Hz)	Associated OECS frequency (Hz)	Ratio of participation factors (Z/Y)	Ratio of cable/beam max. displ (Z-ratio).	Ratio of cable/beam max. disp (Y-ratio).	Type of mode
1	4.26	4.28	<1	532.1	**1.1**	1st transv. SYM
2	6.14	6.21	>1	**1.0**	1066.4	1st vert. SYM
4	6.94	6.21	>1	**6.1**	205509.8	1st vert. SYM
5	6.94	6.21	>1	**5.8**	1845228.0	1st vert. SYM
9	7.15	11.71	<1	77919.0	**3.3**	1st transv. ASM
10	7.16	4.28	<1	83074.8	**16.2**	1st transv. SYM
12	7.93	9.12	>1	**8.4**	148279.8	1st vert. ASM
13	7.93	9.12	>1	**8.0**	2257478.0	1st vert. ASM
17	8.11	11.71	<1	76110.7	**8.3**	1st transv. ASM
18	8.11	11.71	<1	77946.7	**19.9**	1st transv. ASM
20	8.42	9.12	>1	**3.8**	114344.9	1st vert. ASM
21	8.42	9.12	>1	**3.7**	3830175.0	1st vert. ASM
25	8.61	11.71	<1	69048.1	**3.2**	1st transv. ASM
26	8.61	11.71	<1	65279.4	**17.3**	1st transv. ASM
27	9.04	9.12	>1	**1.6**	2673.4	1st vert. ASM
29	9.63	9.12	>1	**7.3**	77529.4	1st vert. ASM
30	9.63	9.12	>1	**7.3**	9995453.0	1st vert. ASM
33	9.69	9.12	>1	**12.9**	36454.3	1st vert. ASM
38	9.79	11.71	<1	42457.2	**28.6**	1st transv. ASM
39	9.79	11.71	<1	60449.4	**30.4**	1st transv. ASM
41	9.90	11.71	<1	51944.1	**19.4**	1st transv. ASM
42	9.90	11.71	<1	35404.6	**11.7**	1st transv. ASM
46	11.36	13.74	>1	**5.8**	1065667.0	2nd vert. SYM
47	11.36	13.74	>1	**6.4**	118704.9	2nd vert. SYM
48	11.45	13.74	>1	**37.2**	29824.1	2nd vert. SYM
49	11.47	13.74	>1	**35.2**	17452.5	1st vert. ASM
50	11.48	11.71	<1	6395.6	**7.8**	1st transv. ASM
51	11.49	11.71	<1	5927.5	**24.9**	1st transv. ASM
52	11.66	11.71	<1	696.4	**11.3**	1st transv. ASM
55	12.00	13.74	>1	**12.4**	248350.0	2nd vert. SYM
57	12.13	11.71	<1	12735.4	**26.4**	1st transv. ASM
59	12.14	11.71	<1	14815.6	**17.7**	1st transv. ASM
60	12.16	11.71	<1	5180.5	**23.4**	1st transv. ASM
61	13.55	13.74	>1	**6.4**	8786.0	2nd vert. SYM
63	13.75	13.74	>1	**18.6**	795354.8	2nd vert. SYM
69	13.91	13.74	>1	**35.3**	42291.0	2nd vert. SYM
77	14.12	13.74	>1	**12.3**	19593.1	2nd vert. SYM

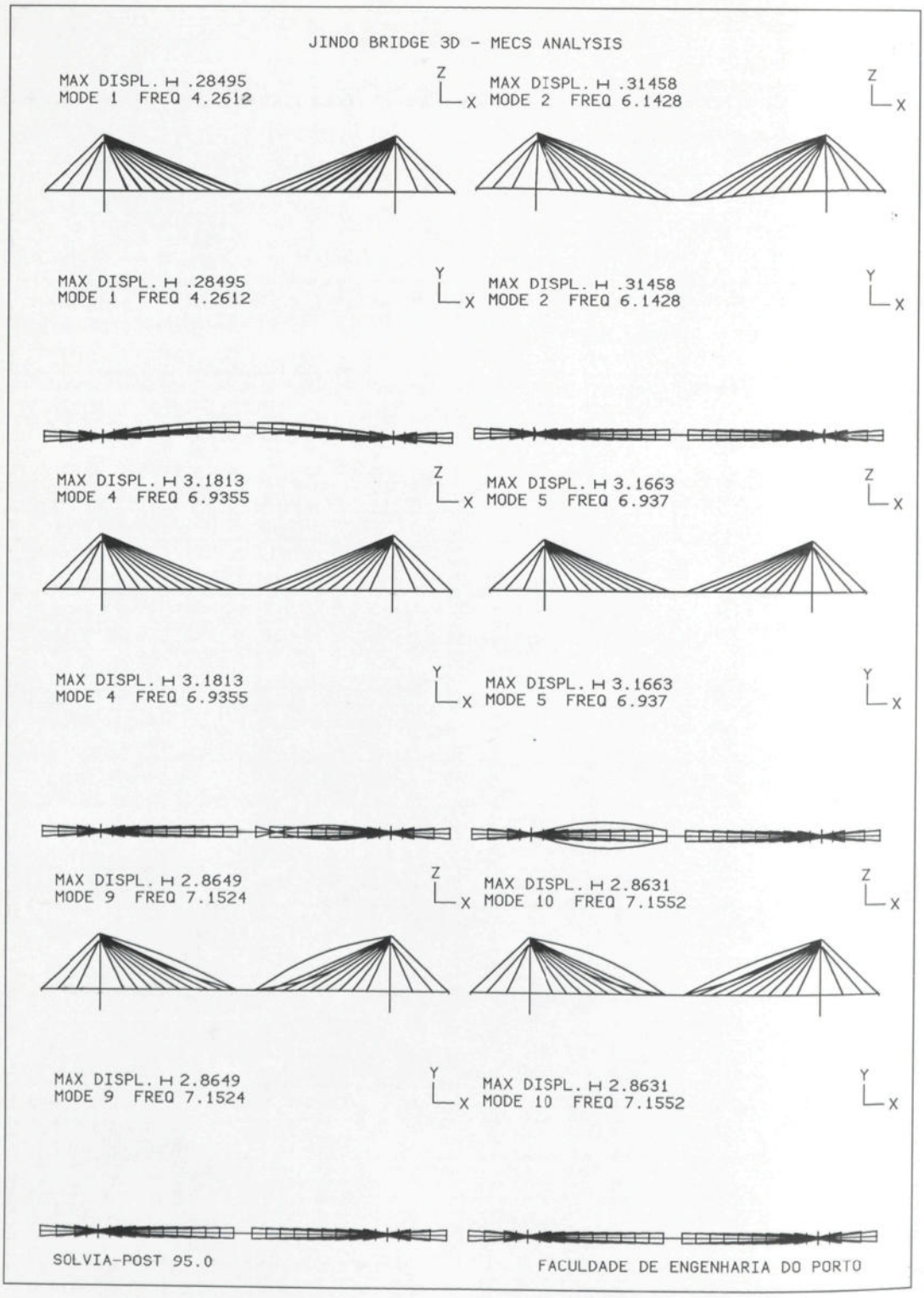


Figure 7.12. Calculated modal shapes (*MECS* analysis): (a) Frequency range *4.26-7.16Hz.*

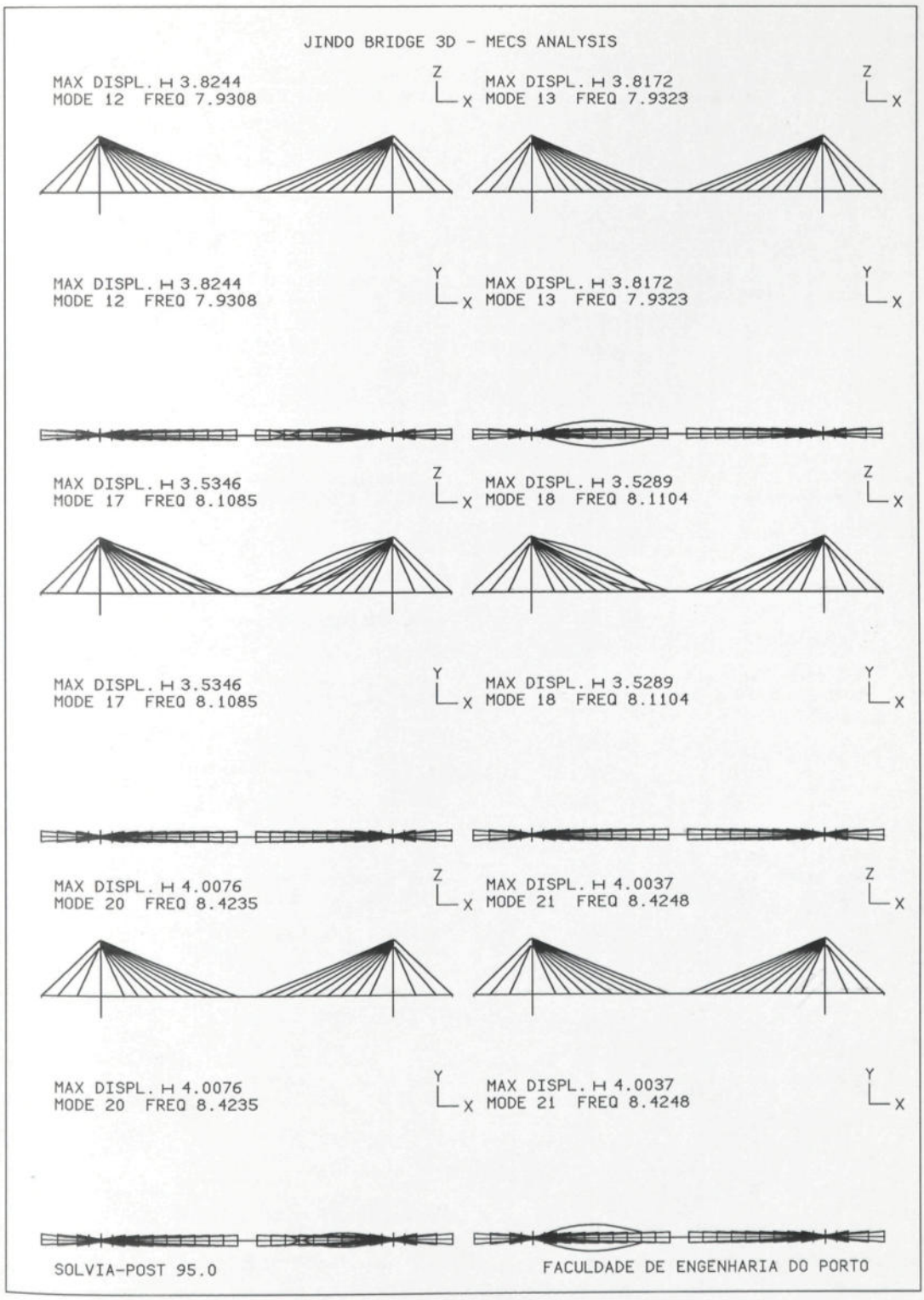


Figure 7.12. Calculated modal shapes (*MECS* analysis): (b) Frequency range *7.93-8.42Hz.*

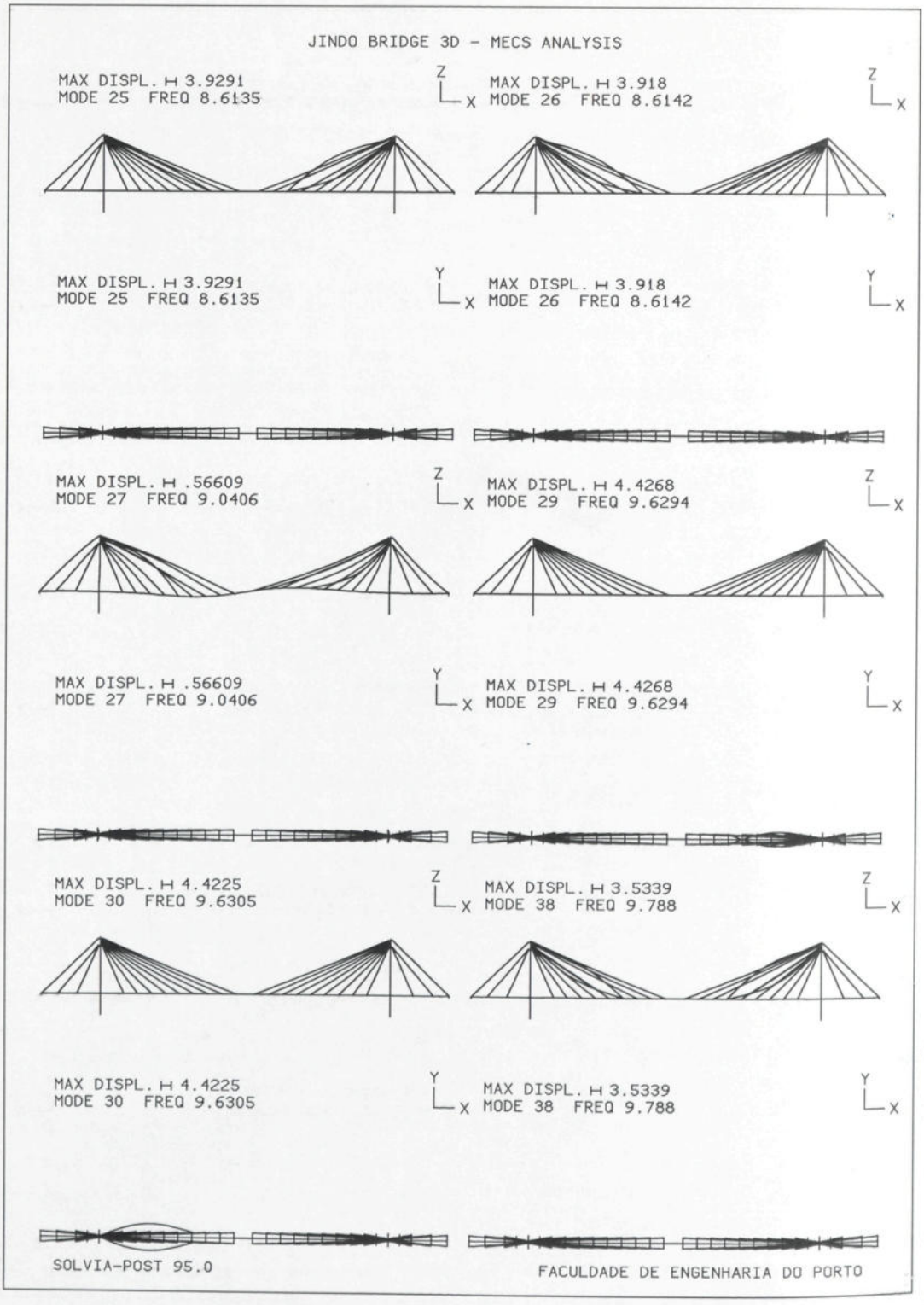


Figure 7.12. Calculated modal shapes (*MECS* analysis): (c) Frequency range *8.61-9.79Hz*.

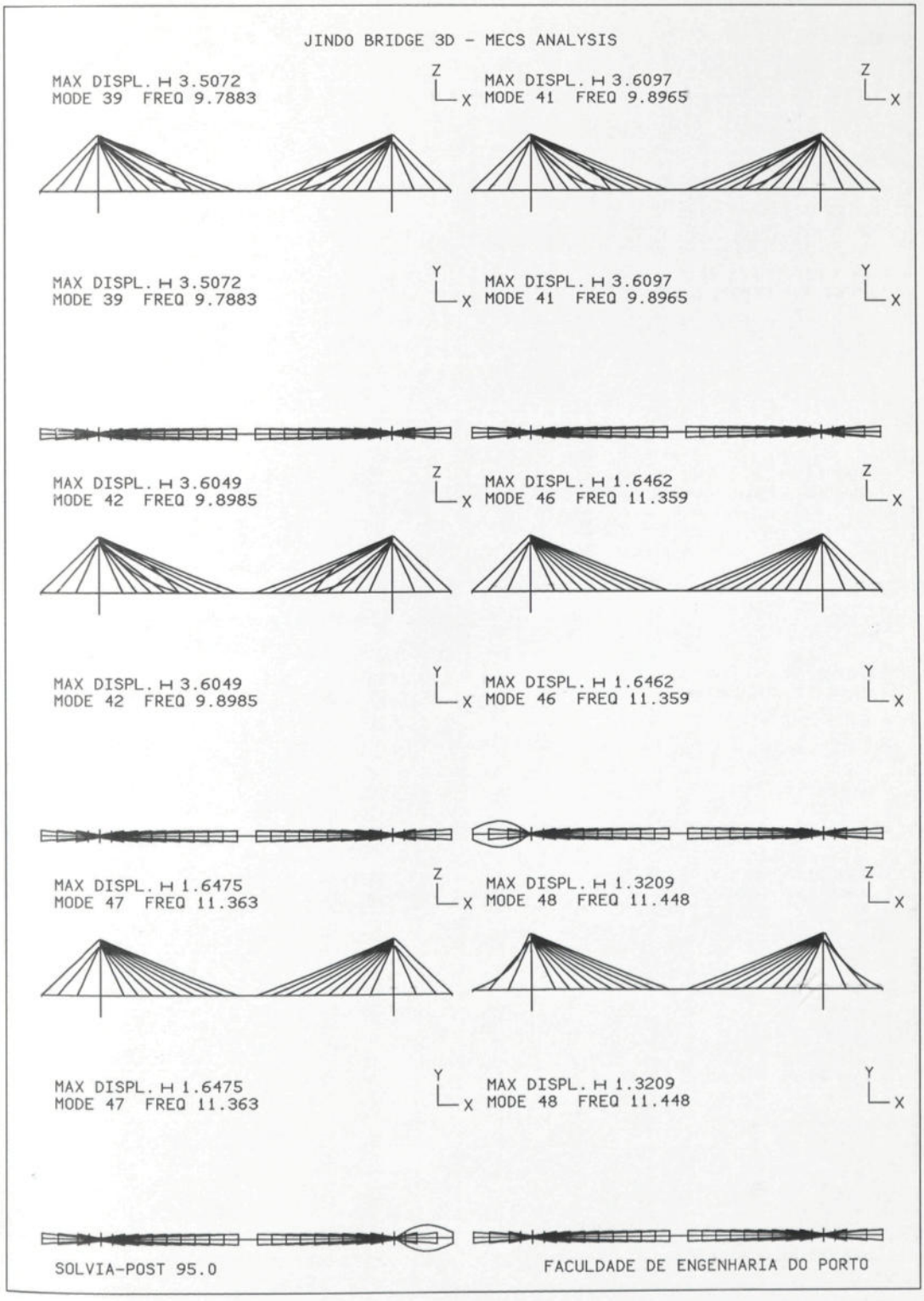


Figure 7.12. Calculated modal shapes (*MECS* analysis): (d) Frequency range *9.79-11.45Hz.*

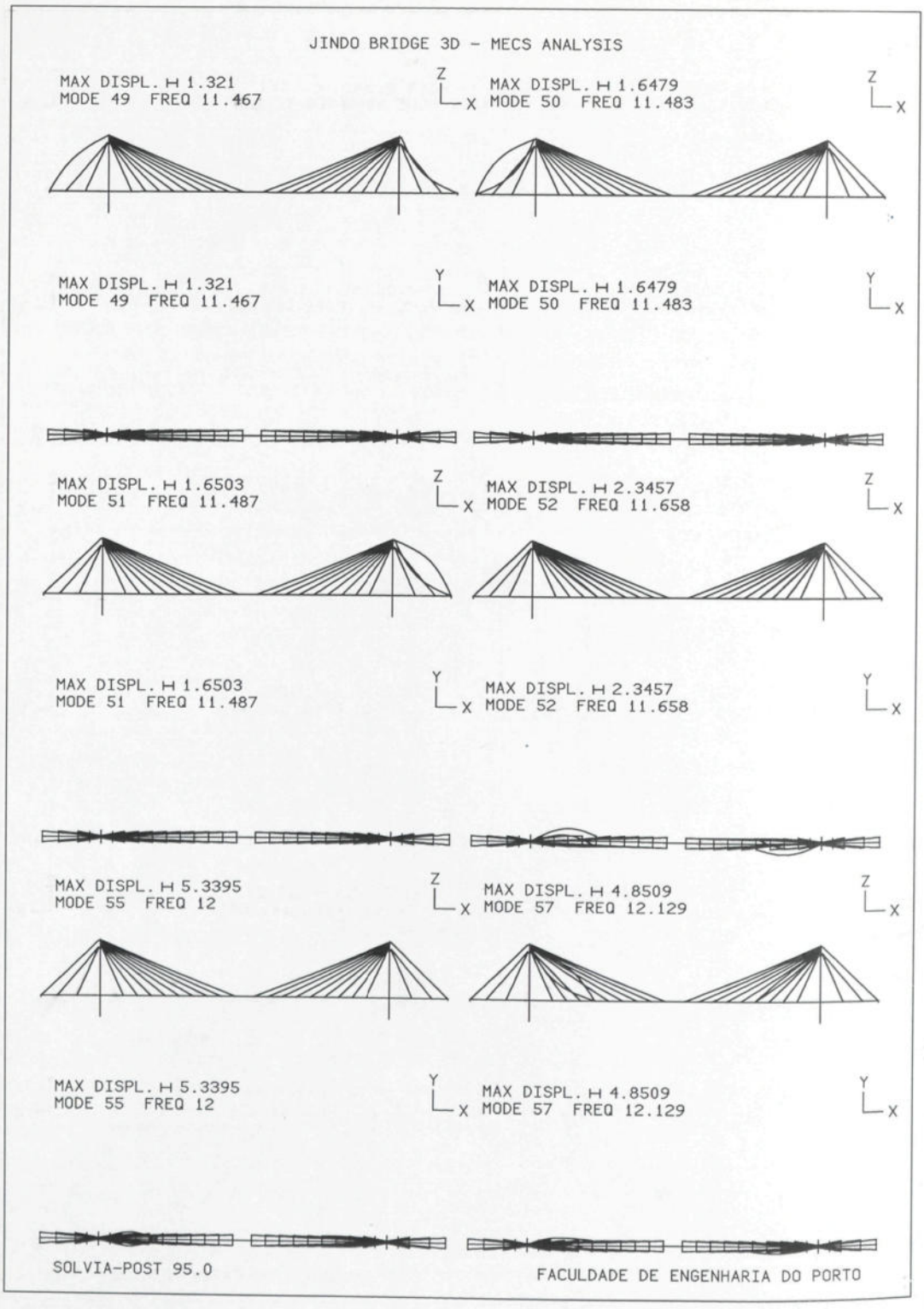


Figure 7.12. Calculated modal shapes (*MECS* analysis): (e) Frequency range *11.47-12.13Hz*.

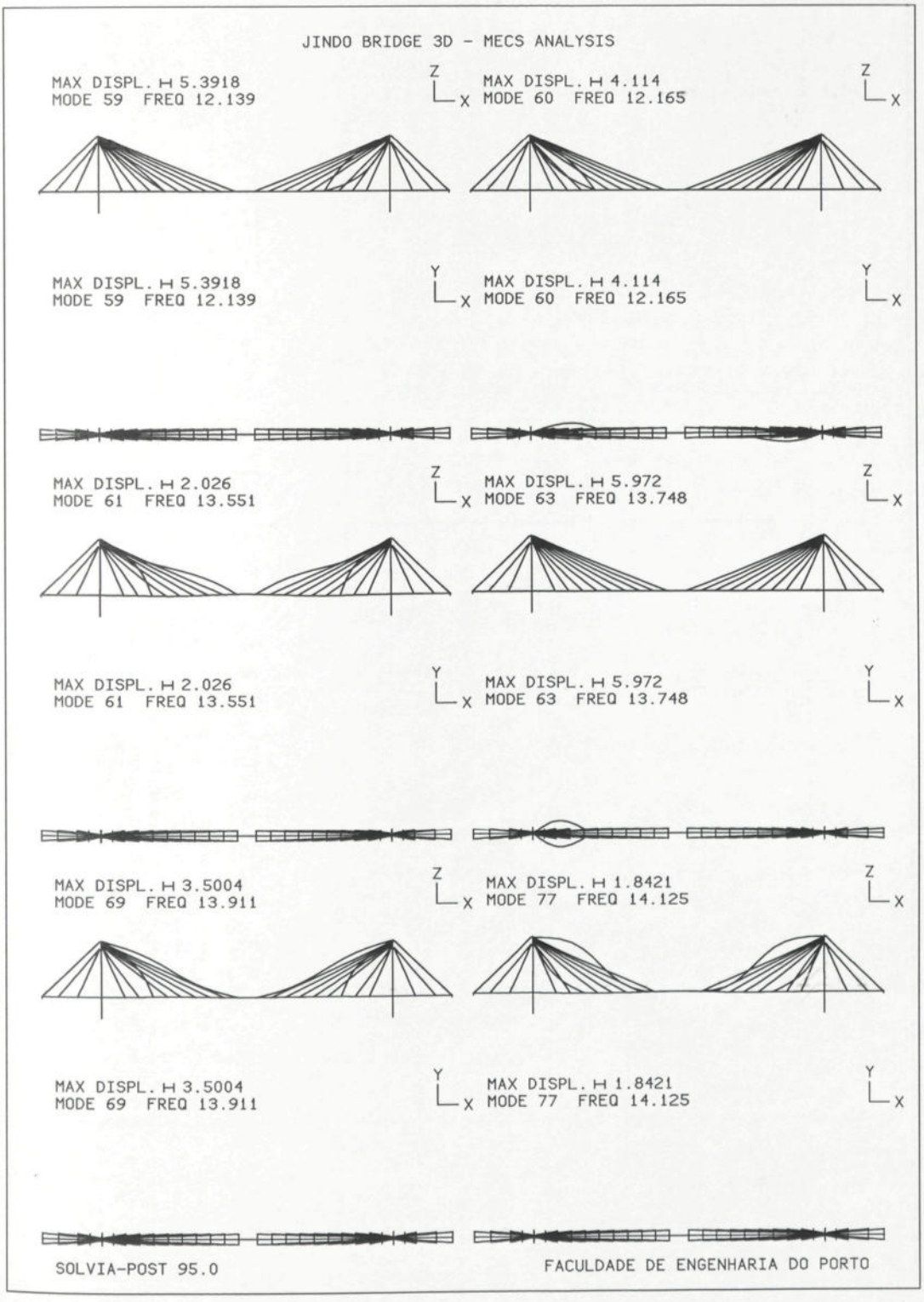


Figure 7.12. Calculated modal shapes (*MECS* analysis): (f) Frequency range *12.14-14.12Hz.*

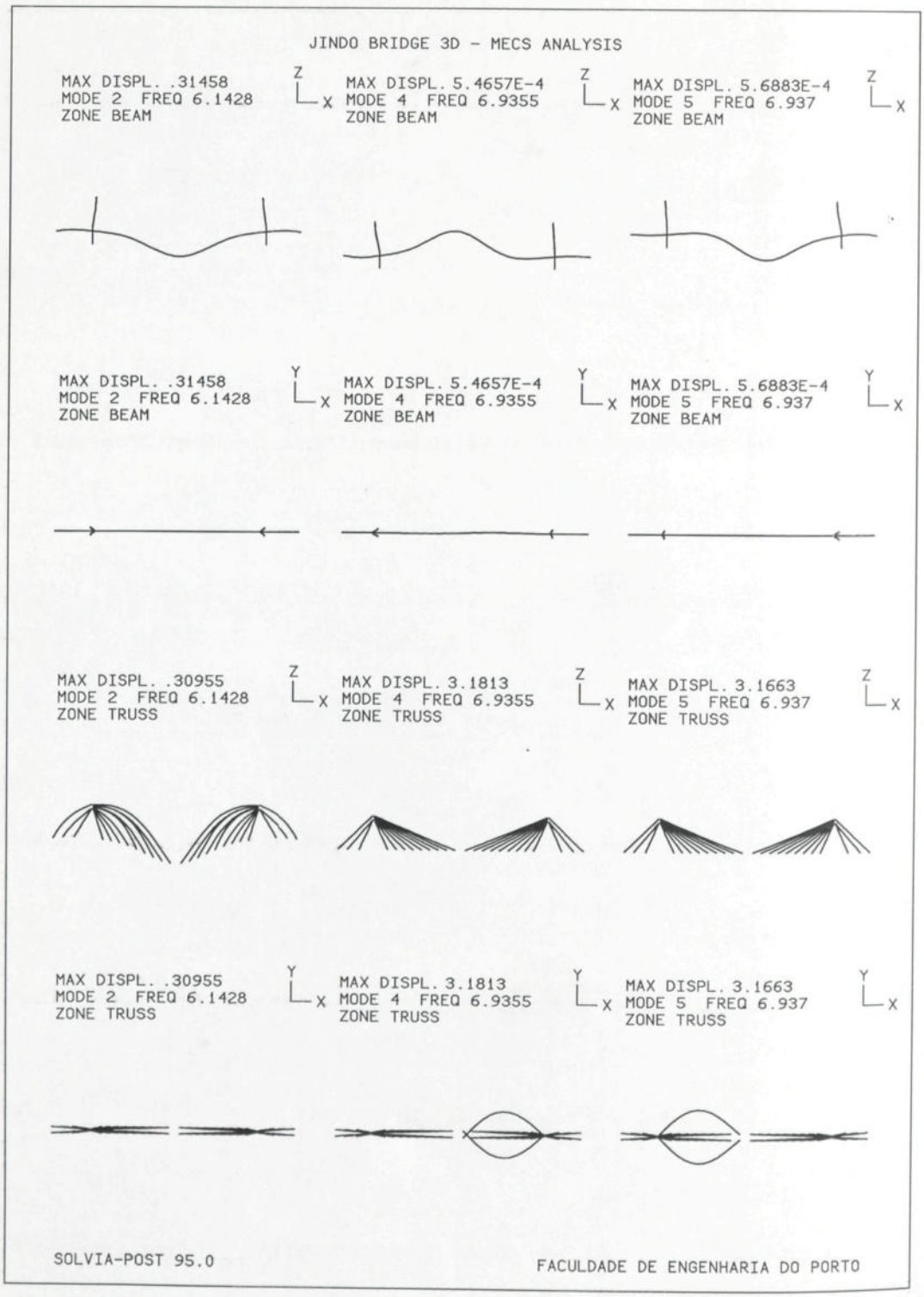


Figure 7.13. Some calculated modal shapes (*MECS* analysis), separate representation of cables and deck: (a) *1st* vertical symmetrical mode shapes.

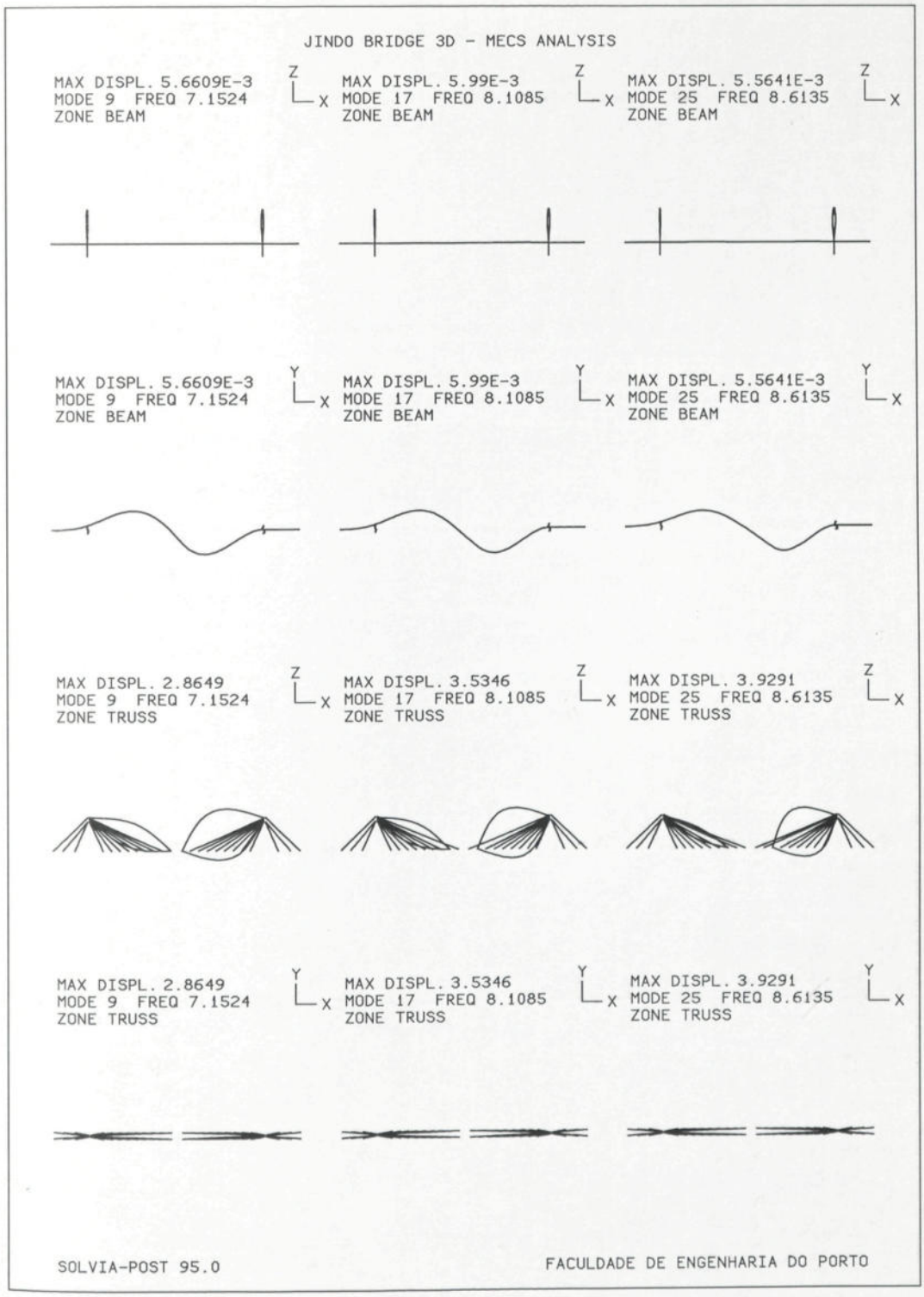


Figure 7.13. Some calculated modal shapes (*MECS* analysis), separate representation of cables and deck: (b) 1st transversal anti-symmetrical mode shapes.

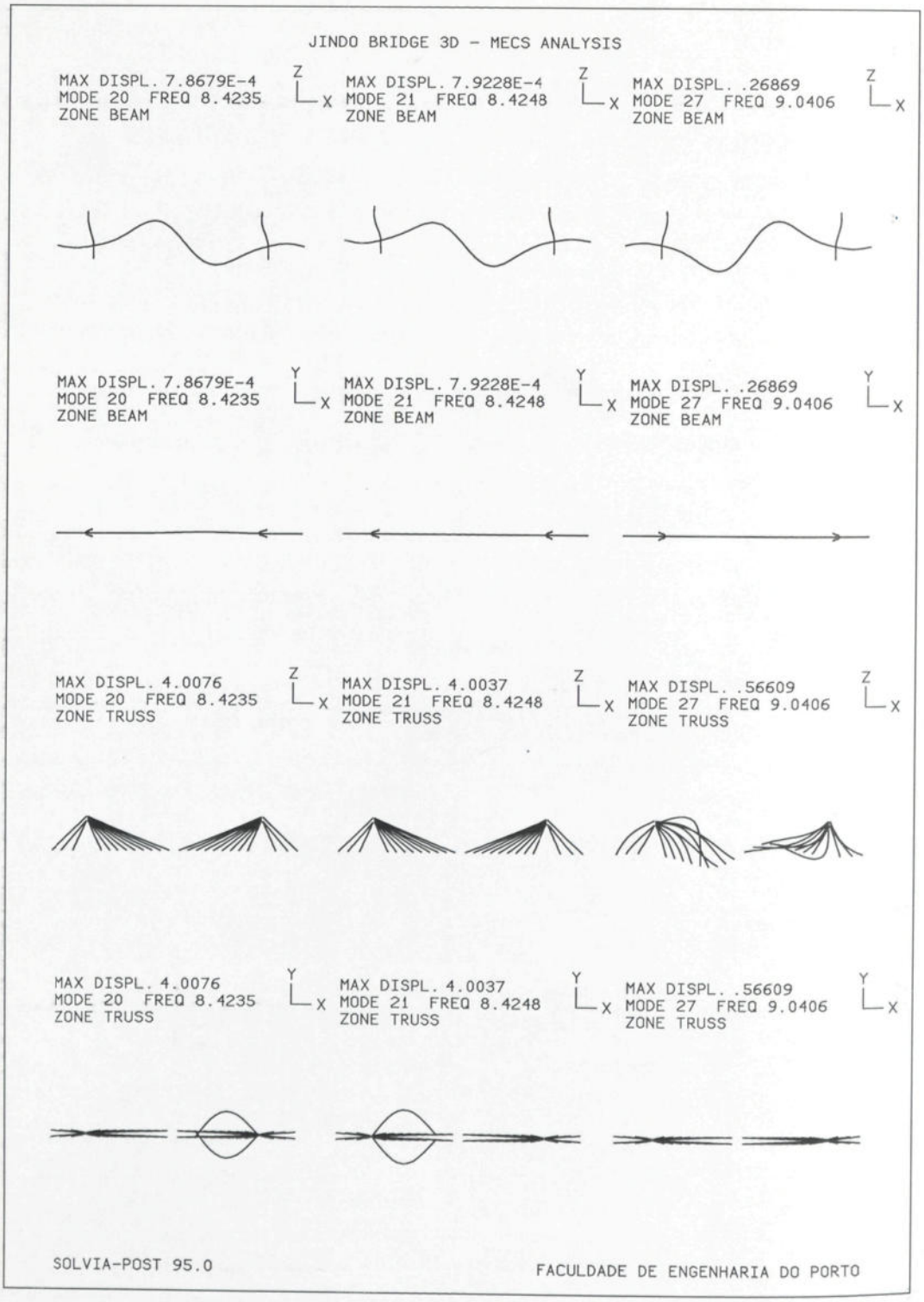


Figure 7.13. Some calculated modal shapes (*MECS* analysis), separate representation of cables and deck: (c) *1st* vertical anti-symmetrical mode shapes.

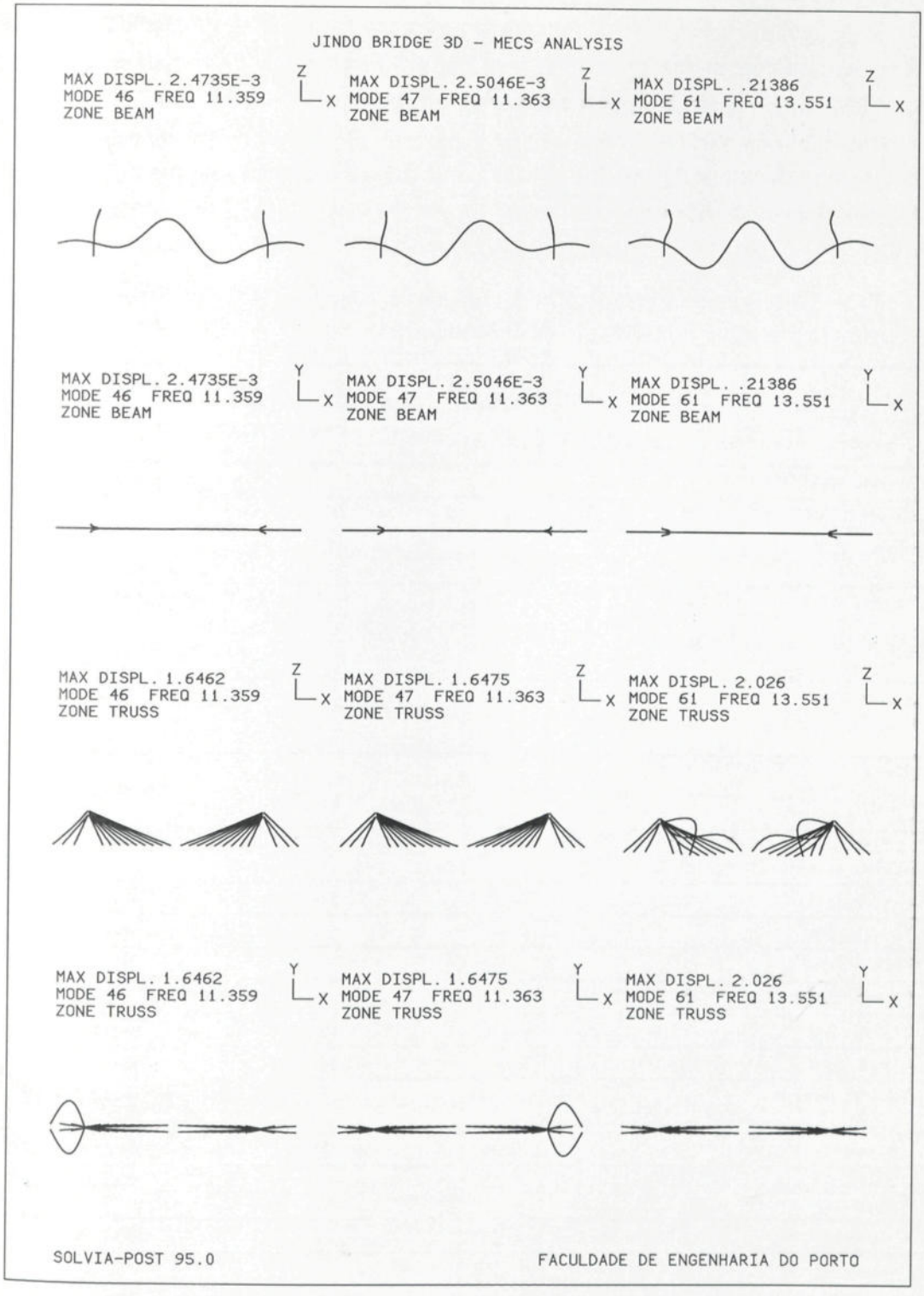


Figure 7.13. Some calculated modal shapes (*MECS* analysis), separate representation of cables and deck: (d) 2nd vertical symmetrical mode shapes.

7.4.3 Comparison between numerical analyses

In order to extract the most relevant information from the results of the *2-D* and *3-D* numerical modeling, the values of the most important natural frequencies and characteristics of the corresponding modal shapes were summarized in Table 7.11.

Note that only the *MECS* modes that exhibited ratios between modal displacements of stay cables and deck and towers lower or equal to *35* were selected for the *2-D* analysis, the same criterion being adopted with respect to the *Y-ratio* or *Z-ratio* for the *3-D* analysis.

Table 7.11. Summary of natural frequencies calculated from *2-D* and *3-D* analyses (*OECS* and *MECS*).

Type of mode	OECS-2D: calculated natural frequency (Hz)	OECS-3D: calculated natural frequency (Hz)	MECS-2D: calculated natural frequency (Hz)	MECS-3D: calculated natural frequency (Hz)
1st transv. SYM		4.28		4.26/ 7.16
1st vert. SYM	6.21	6.21	6.19	6.14/ 6.94/ 6.94
1st vert. ASM	9.16	9.12	9.04/ 9.17/ 9.65	7.93/ 7.93/ 8.42/ 8.42/ 9.04/ 9.63/ 9.63/ 9.69/ 11.47
1st transv. ASM		11.71		7.15/ 8.11/ 8.11/ 8.61/ 8.61/ 9.79/ 9.79/ 9.90/ 9.90/ 11.48/ 11.49/ 11.66/ 12.13/ 12.14/ 12.16
2nd vert. SYM	13.68	13.74	13.13/ 13.33/ 13.68	11.36/ 11.36/ 11.45/ 12.00/ 12.00/ 13.55/ 13.75/ 13.75/ 13.91/ 14.12/
2nd vert. ASM	18.14	18.26	18.29	15.70/ 15.70/ 16.38/ 16.39/ 18.26/ 18.69/ 18.79/ 18.86/ 18.98
2nd transv. SYM+torsion		22.10		Not calculated
3rd vert. SYM	22.66	22.70	22.81/ 23.34	Not calculated
1st lateral LTW		23.42		Not calculated
1st lateral RTW		23.42		Not calculated
1st torsion SYM		24.95		Not calculated
3rd vert. ASM	26.13	26.00	26.33	Not calculated
4th vert. SYM	28.79	28.61	28.88/ 29.63	Not calculated
2nd LTW+ 2nd RTW in phase		30.33		Not calculated
transversal		30.45		Not calculated
2nd LTW+ 2nd RTW in opp. phase		30.46		Not calculated
4th vert. ASM	32.68	32.52	32.94	Not calculated
transversal		38.80		Not calculated
5th vert. SYM	40.19	39.69	40.45/ 40.77	Not calculated
1st LTW	41.13		41.69	Not calculated
1st RTW	41.36		41.88	Not calculated
1st torsion ASM		45.11		Not calculated

The analysis of Table 7.11 permitted to extract the following conclusions:

- There is no coupling between in-plane and out-of-plane motion for the first *6* modes obtained on the basis of the *OECS* model, the first torsional mode occurring only at *22.1Hz*. This led, in this case, to a significant proximity of the results provided by the *2-D* and *3-D* numerical models used to analyze the structural dynamic response. However, the value of *22.1Hz* is not really representative of the prototype torsional fundamental frequency, as the physical model did not respect the similarity requirements for the torsional behaviour. In fact, and according to the numerical modeling of the bridge prototype performed by Garevski (1990), the first torsional frequency occurred at a natural frequency of *1.5Hz*, what would correspond for the physical model, if scaled properly, to a frequency of about *18.4Hz*;
- The *3-D* analysis of the *MECS* yielded a very long set of natural frequencies and modal shapes when compared with the *2-D* analysis. In fact, the *2-D MECS* analysis produced *100* natural frequencies and modal shapes in the range *0-48Hz*, while the corresponding *3-D* analysis yielded *150* natural frequencies and modal shapes in the range *0-21.3Hz*;
- Both the *2-D* and *3-D MECS* analyses showed the appearance of groups of modes with identical configurations of the deck and towers, but different movements of the cables. These modes occur predominantly in the frequency range associated with the fundamental frequency of the stay cables (*6.8Hz –18.9Hz*, according to the Table 7.6).

7.5 EXPERIMENTAL MODAL SURVEY

The primary purpose of the modal survey described in this Section was the experimental identification of the phenomenon of *dynamic cable-structure interaction*, already described and evidenced with appropriate numerical modelling of the Jindo Bridge model.

A long series of tests was performed on the physical model described in Section 7.3, using as source of excitation both a small electrodynamic shaker attached to the physical model at different locations, applying forces vertically or laterally, and the shaking table of the University of Bristol.

For the sake of completeness, it was considered of interest to repeat the tests on a modified physical model, where the cable mass was lumped at the cable anchorages. This is the usual hypothesis adopted in the numerical modeling of cable-stayed bridges, and corresponds to the model designated here as *OECS*.

The Jindo Bridge model was then modified by a Master student from the University of Bristol, B. Wainwright, who designed magnetic masses equivalent to the distributed masses of

the cables to apply at the cable anchorages, and substituted the mass distributed stays by single piano wires with the same area, and with an identical distribution of tensions.

After a complex process of unassemblage, package and transportation to Italy, the Jindo model was assembled again and tested at the *ISMES* shaking table, with participation of the author.

Three groups of modal analysis tests will thus be described in the current Section, and the corresponding results discussed: (i) tests performed on the physical model using the electrodynamic shaker; (ii) tests performed on the physical model using the Bristol shaking table; tests performed on the modified model using the *ISMES* shaking table.

The presentation herein follows the chronology of the events, in order to explain better the decisions taken at each step.

7.5.1 Electrodynamic shaker tests

7.5.1.1 Instrumentation

Classical modal analysis tests were performed on the Jindo model using the following equipment:

- A small piezoelectric accelerometer *DYTRAN*, model *3101AG*, for the measurement of the response along the deck and towers, and for measurement of accelerations on the back stays. This accelerometer weights *5gr*, has a sensitivity of *10mV/g*, and operates in the frequency range *2Hz-5000Hz*. Due to its reduced weight, it was mounted on the bridge using simply bee wax;
- A magnetic pick-up transducer *RS*, model *285-756*, only used to evaluate the frequency content of the stay cable vibration;
- A small electrodynamic shaker *LING*, equivalent to model *V201/3*, that can deliver a maximum force of *17.8N* in a broad frequency range;
- A dynamic force sensor *DYTRAN*, model *1051V6*. This piezoelectric load cell has a sensitivity of *1mV/LbF*, and compression and tension ranges for *+5V* output of *5000LbF* and *500LbF*, respectively. It was interposed between the shaker and the bridge model, in order to measure the applied dynamic force;
- A *2*-channel Fourier analyzer *ADVANTEST*, model *R9211C*. This analyzer played a key role in the development of the modal analysis tests, by generating the input signal to drive the shaker (after convenient amplification), and building the *Frequency Response Functions* (*FRFs*) from the applied force (input, force transducer) and the measured response (output, piezoelectric accelerometer).

Figures 7.14 and 7.15 show some details of the mounting of the *DYTRAN* accelerometers on the bridge deck, on a tower and on a stay cable. Figure 7.16 shows the *RS* magnetic transducer measuring the vibration of a taut wire mounted on a small uni-directional shaking table (instrumented with a high precision accelerometer *SETRA, model 141)*, during an attempt to obtain a calibration chart for the former sensor.

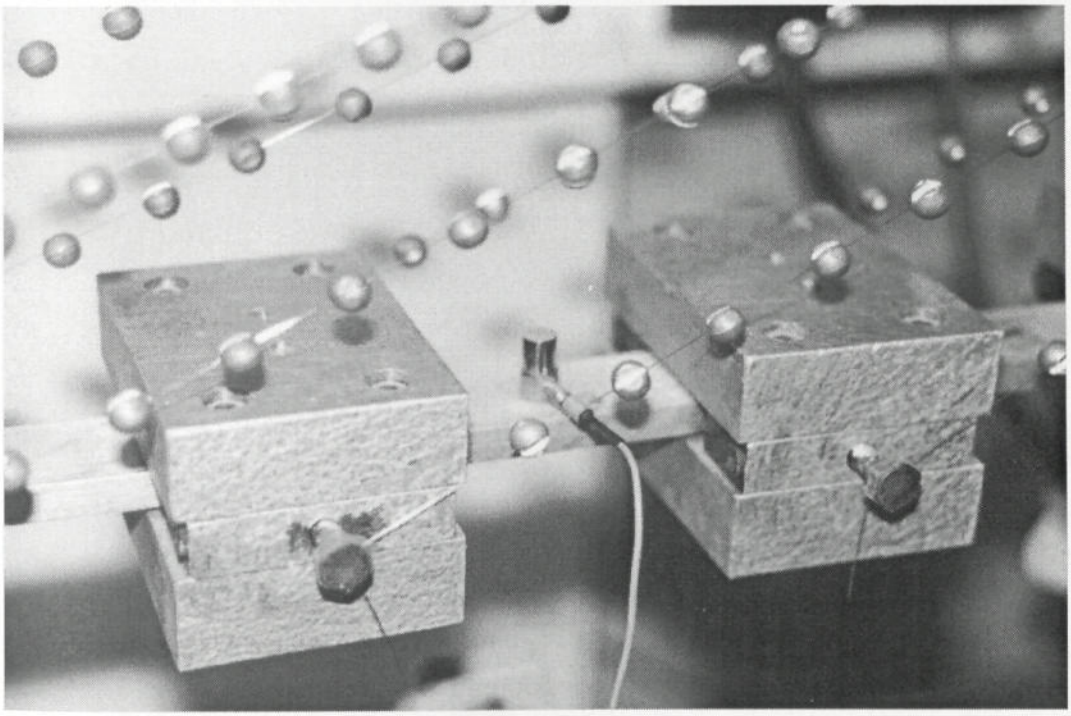


Figure 7.14. Mounting of *DYTRAN* accelerometer on the bridge girder.

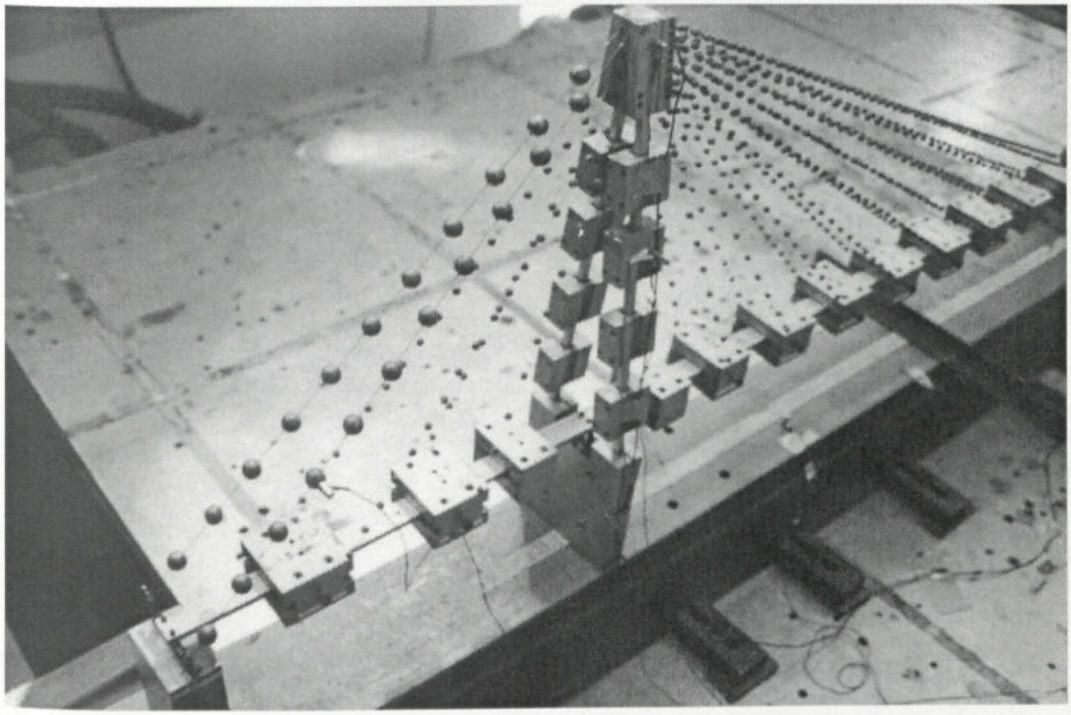


Figure 7.15. Mounting of *DYTRAN* accelerometers on a back stay and on the top of one tower.

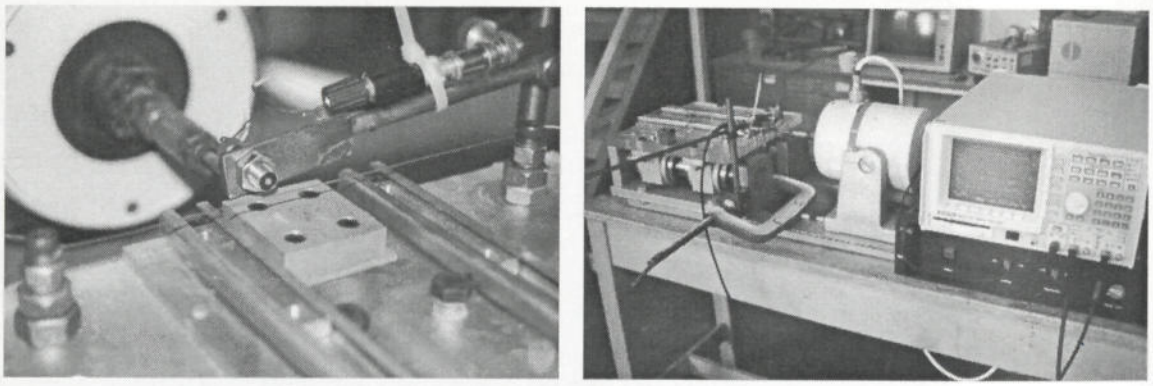


Figure 7.16. Magnetic pick-up transducer in calibration operation using a Fourier analyzer and a small uni-directional shaking table instrumented with a high precision accelerometer.

Figure 7.17 shows one of the tested schemes of attachment of the electrodynamic shaker to the bridge model. As can be observed in that Figure, a small rod was interposed between the shaker and the structure, in order to ensure that the applied force was vertical (for the current mounting scheme). The load cell was screwed to the rod and then attached to the bridge.

It should be noted that the scheme presented in Figure 7.17 was not actually employed in the model tests, as it was observed that, due to the reduced weight of the model, a certain degree of restraint was introduced by the shaker during vibration. So, it was decided to suspend the shaker from a spring both for application of vertical and lateral dynamic forces. Unfortunately no pictures were taken of the adopted suspension scheme.

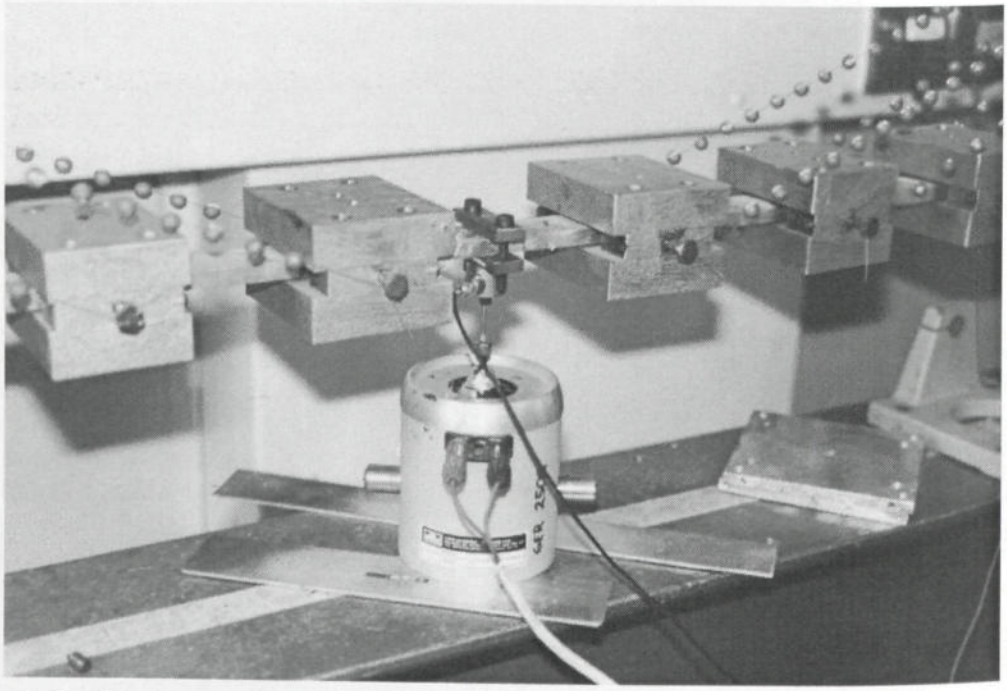


Figure 7.17. Attachment of electrodynamic shaker to the bridge model, with interposition of force transducer.

7.5.1.2 Multi-sine excitation tests

The identification of modal parameters from the physical model was based on the use of the electrodynamic shaker, which was suspended from a spring and attached to the bridge deck at different locations and directions. Figures 7.18 to 7.21 summarize the different setups, employing the node numbering adopted for the *2-D OECS* analysis: (i) mounting of the shaker at about one third span, in correspondence with node *38* (Figure 7.18), applying vertical forces; (ii) mounting of the shaker at the midspan, in correspondence with node *31* (Figure 7.19), applying vertical forces; (iii) mounting of the shaker at about one third span, in correspondence with node *24* (Figure 7.20), applying lateral forces; (iv) mounting of the shaker at the midspan, in correspondence with node *31* (Figure 7.21), applying lateral forces.

Preliminary tests were developed in order to select the most adequate type of excitation and the general procedure for the modal survey. It was then decided to build at a first instance a general set of *FRFs* relating the response measured with the accelerometer (or eventually, the magnetic transducer) at selected locations, with the applied force (measured with the force transducer), in a relatively wide frequency range.

The small lozenges and the circles in Figures 7.18 to 7.21 indicate the locations selected for measuring the response.

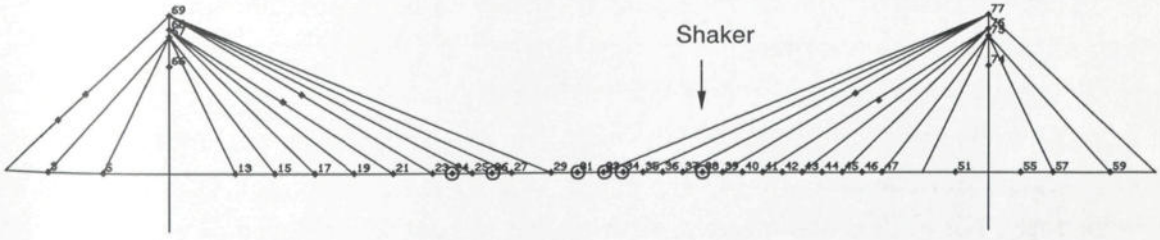


Figure 7.18. Shaker mounted at node *38*, applying vertical forces. Lozenges indicate instrumented locations. Circles indicate instrumented locations where higher resolution measures were taken.

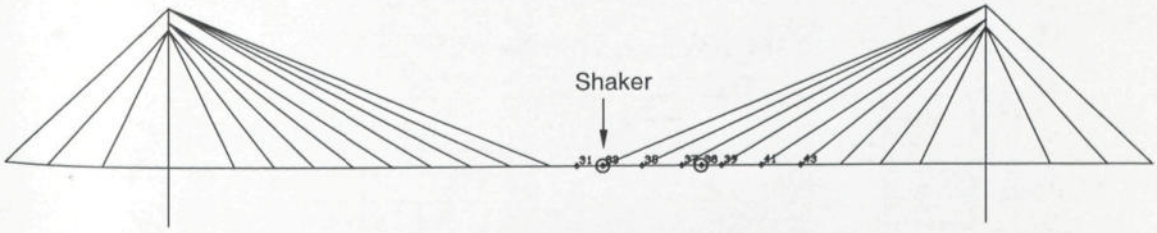


Figure 7.19. Shaker mounted at node *31*, applying vertical forces. Lozenges indicate instrumented locations. Circles indicate instrumented locations where higher resolution measures were taken.

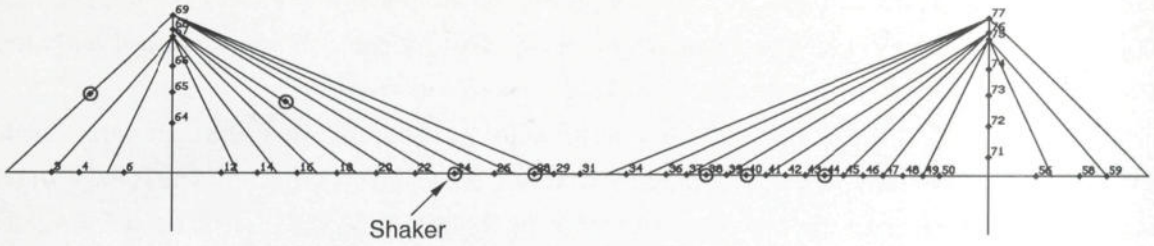


Figure 7.20. Shaker mounted at node *24*, applying lateral forces. Lozenges indicate instrumented locations. Circles indicate instrumented locations where higher resolution measures were taken.

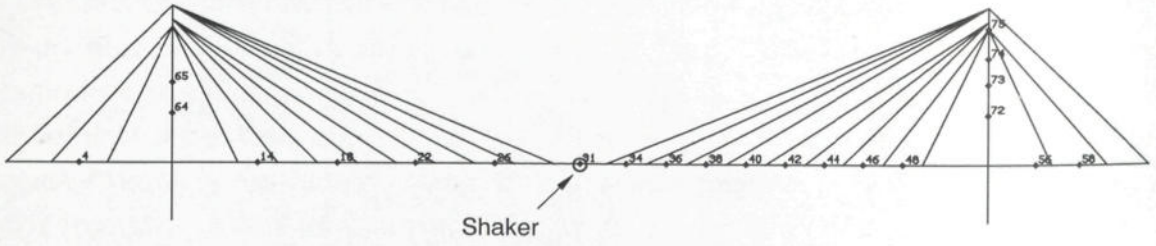


Figure 7.21. Shaker mounted at node *31*, applying lateral forces. Lozenges indicate instrumented locations. Circles indicate instrumented locations where higher resolution measures were taken.

Except for the fourth setup (Figure 7.21), where all measurements were performed within a *15-30Hz* frequency range, the frequency range selected for these preliminary tests was *0-100Hz*, with a resolution of *0.125Hz*, the maximum allowed by the Fourier analyzer (*800* lines). The excitation employed was of the *multi-sine* type in the same frequency range. This is no more than a *swept-sine* type of input signal, where the harmonic frequency does not vary continuously, but at discrete intervals, equal to the frequency resolution. This type of signal introduces no leakage effects, and so it was not necessary to apply any specific time window to the measured signals. Figure 7.22 illustrates the time variation of the input signal during a sweep in the range *0-50HZ*.

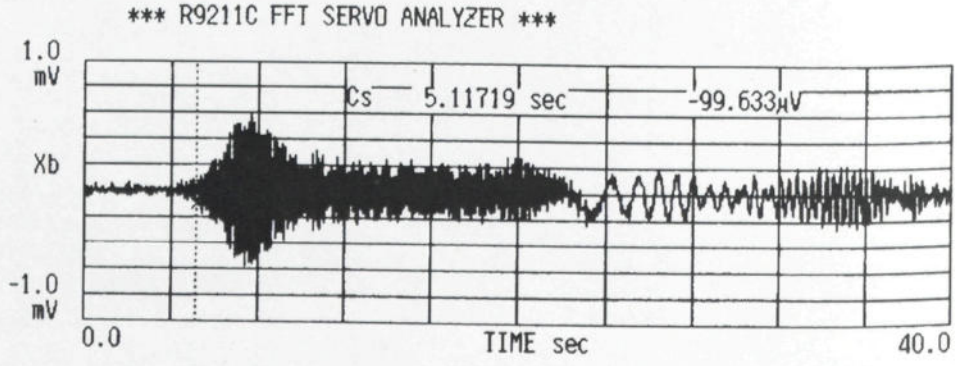


Figure 7.22. Time variation of applied force during a sweep, for a multi-sine excitation type in the range *0-50Hz*.

The *FRFs* were thus obtained using the estimator H_1, and averaging over *16* to *32* raw estimates of auto and cross-spectra. Modal parameters were extracted from the set of *FRFs* using a least squares frequency domain algorithm (Han & Wicks, 1989) based on the *Rational Fraction Polynomial Method* (see Chapter five).

Figures 7.23 to 7.25 present some examples of *FRF* and coherence function estimates, relating the excitation applied at nodes *38V* (*Vertical*), *31V* and *24L* (*Lateral*), with the response measured at some selected locations. These are designated by a point number and a symbol that indicates the direction of measurement: "*V*" for *Vertical*, "*H*" for in-plane *Horizontal*, and "*L*" for *Lateral* (horizontal, transversal to the bridge axis). The synthesized *FRFs* based on the mentioned identification algorithm are also represented in correspondence with the measured *FRFs*.

Except for the range *0-10Hz*, where the noise to signal ratio was more significant, high coherence values were generally achieved, giving evidence of high quality measurements.

The quality of the *FRF* fitting is also generally very good, and so a high level of confidence can be obtained from the performed tests in the frequency range *10Hz-100Hz*.

Given that the level of induced energy was rather small for the low frequency range when exciting the structure with a multi-sine input signal in the range *0-100Hz*, it was decided to repeat the tests for a number of points of higher significance considering the frequency range *0-20Hz*. This allowed in particular an increase of the level of applied signal by a factor of two, and led to a better frequency resolution, of *0.05Hz*. The inconvenience of this procedure was naturally the time necessary to obtain *FRF* estimates, averaging over *16* to *32* raw estimates. In some locations where a high number of modes were observed at very close natural frequencies, or where a better frequency resolution was desired (a maximum of *0.0125Hz* was achieved), it was even decided to perform high quality zoom measurements in lower frequency ranges, such as *0-5Hz* (identification of the fundamental transversal mode of vibration), *4-7Hz* (identification of the fundamental vertical mode of vibration), *8-12Hz* (identification of a large number of *1st* vertical anti-symmetric modes of vibration), *8-12.5Hz* (identification of a large number of *1st* transversal anti-symmetric modes of vibration) or *15-30Hz* (identification of a large number of *2nd* transversal symmetric +torsion modes of vibration). It should be noticed that each zoom *FRF*, depending on the frequency range considered, could take more than one hour to be evaluated.

Figures 7.26 to 7.29 show some of the *FRF* zooms obtained for the four setups defined by Figures 7.18 to 7.21. The circles in the later Figures indicate all the locations where zoom measurements were performed.

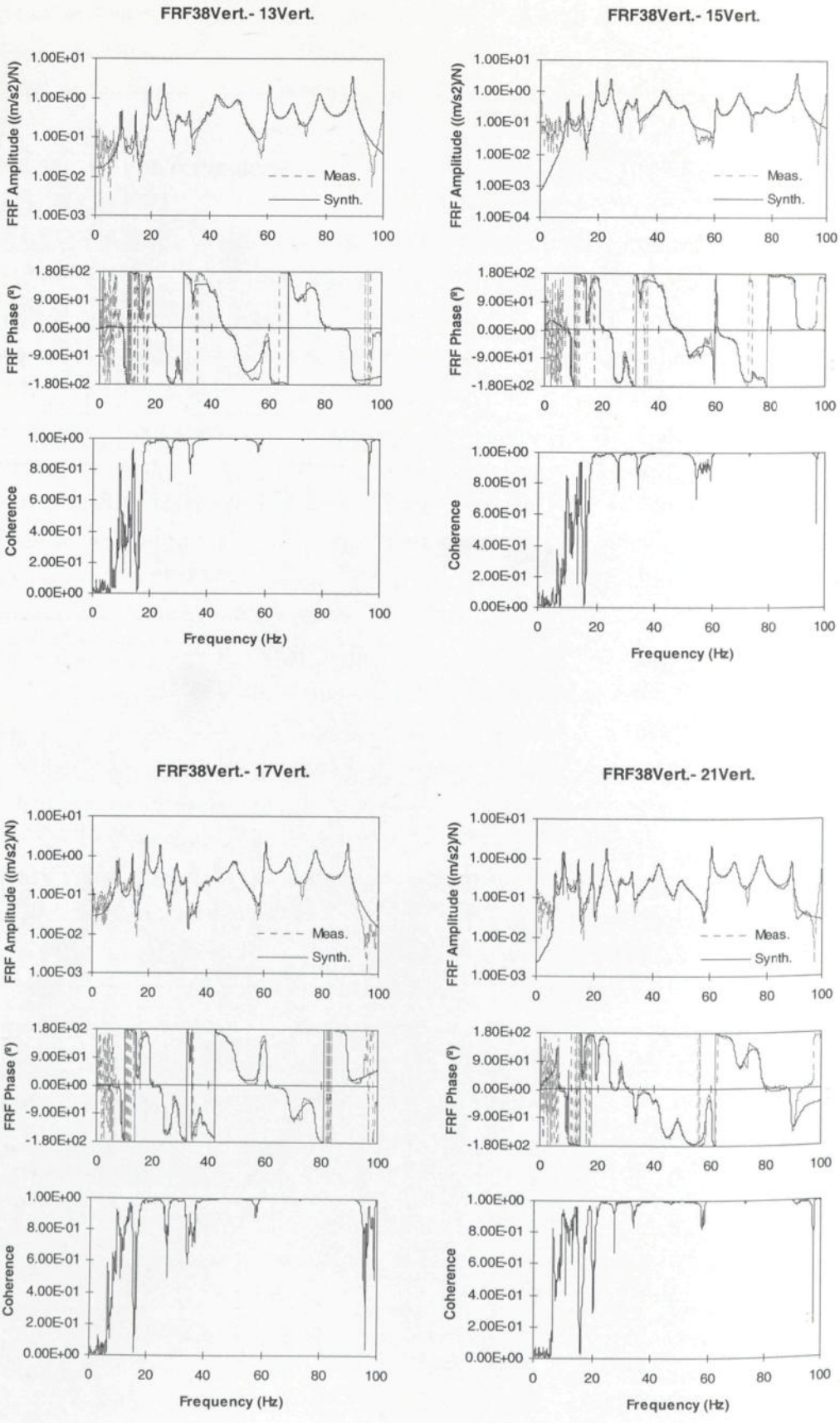


Figure 7.23 (a) Coherence and *FRF* measured/ synthesized from node *38V* (excitation) to nodes *13V*, *15V*, *17V* and *21V* (response).

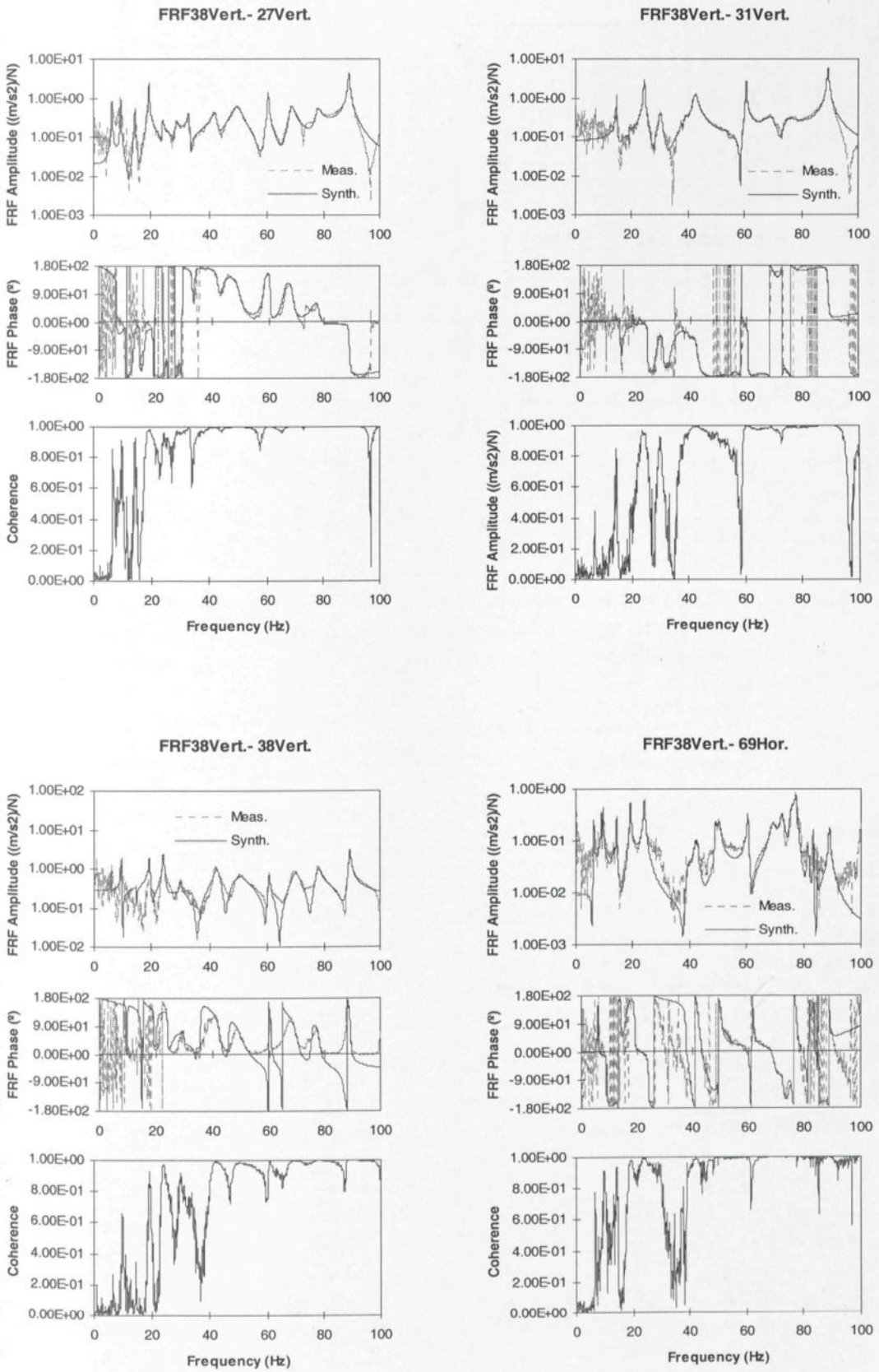


Figure 7.23 (b) Coherence and *FRF* measured/ synthesized from node *38V* (excitation) to nodes*27V*, *31V*, *38V* and *69H* (response).

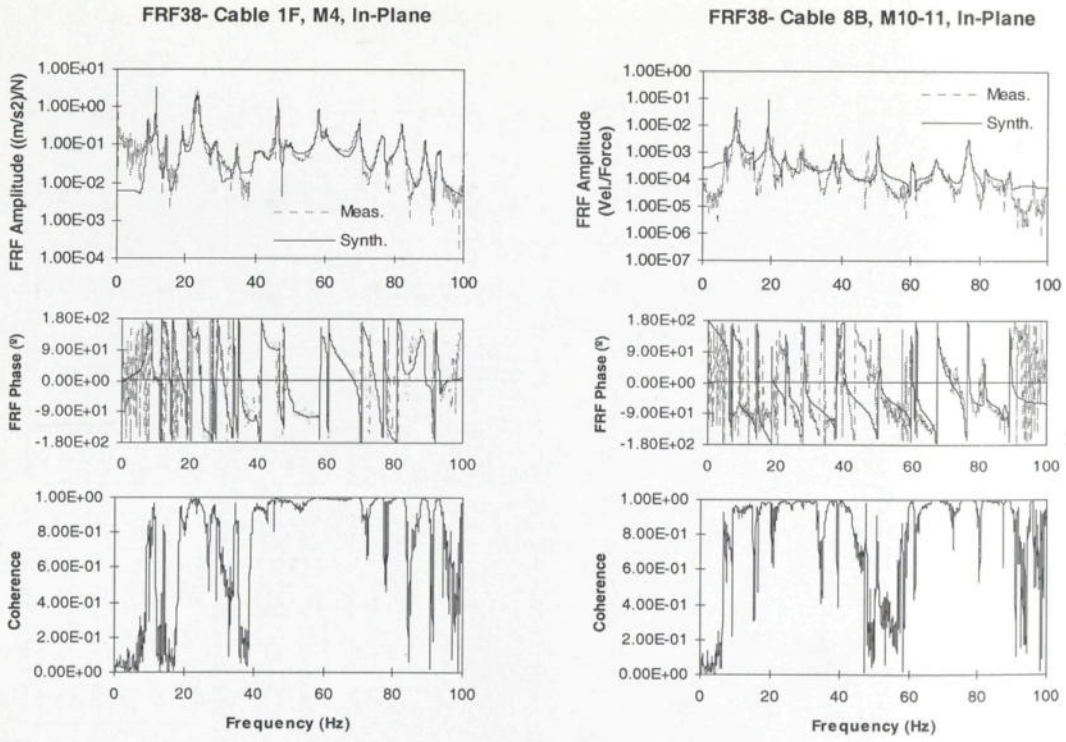


Figure 7.23 (b) Coherence and *FRF* measured/ synthesized from node *38V* (excitation) to *Cable 1,* (left tower, front cable, on 4th mass from bottom), and to *Cable 8*, (left tower, backward cable, between 10th and 11th mass from bottom) (response).

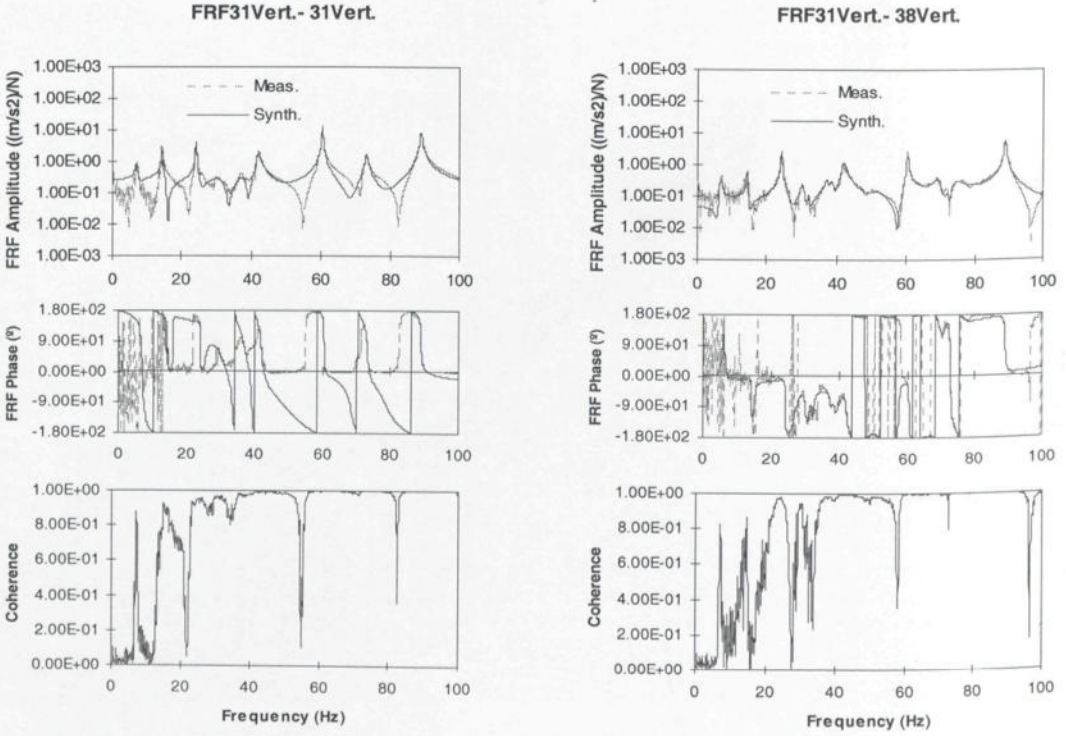


Figure 7.24. Coherence and *FRF* measured/ synthesized from node *31V* (excitation) to nodes *31V*, and *38V* (response).

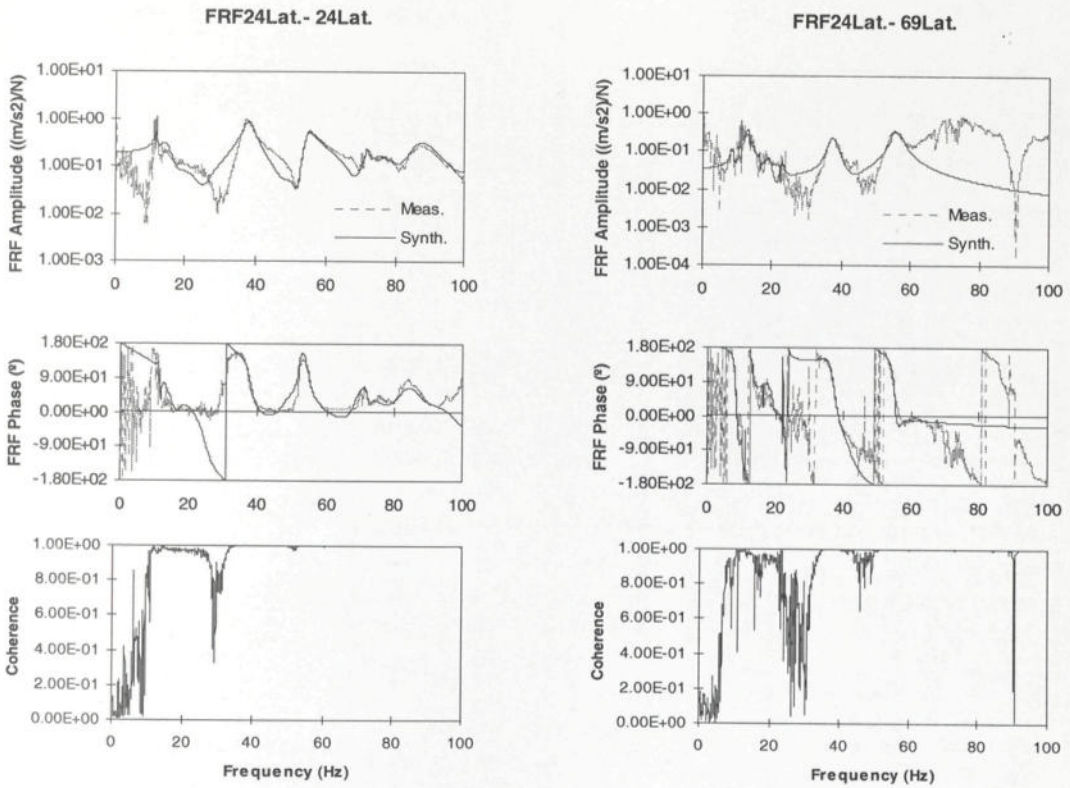


Figure 7.25. Coherence and *FRF* measured/ synthesized from node *24L* (excitation) to nodes *24L*, and *69L* (response).

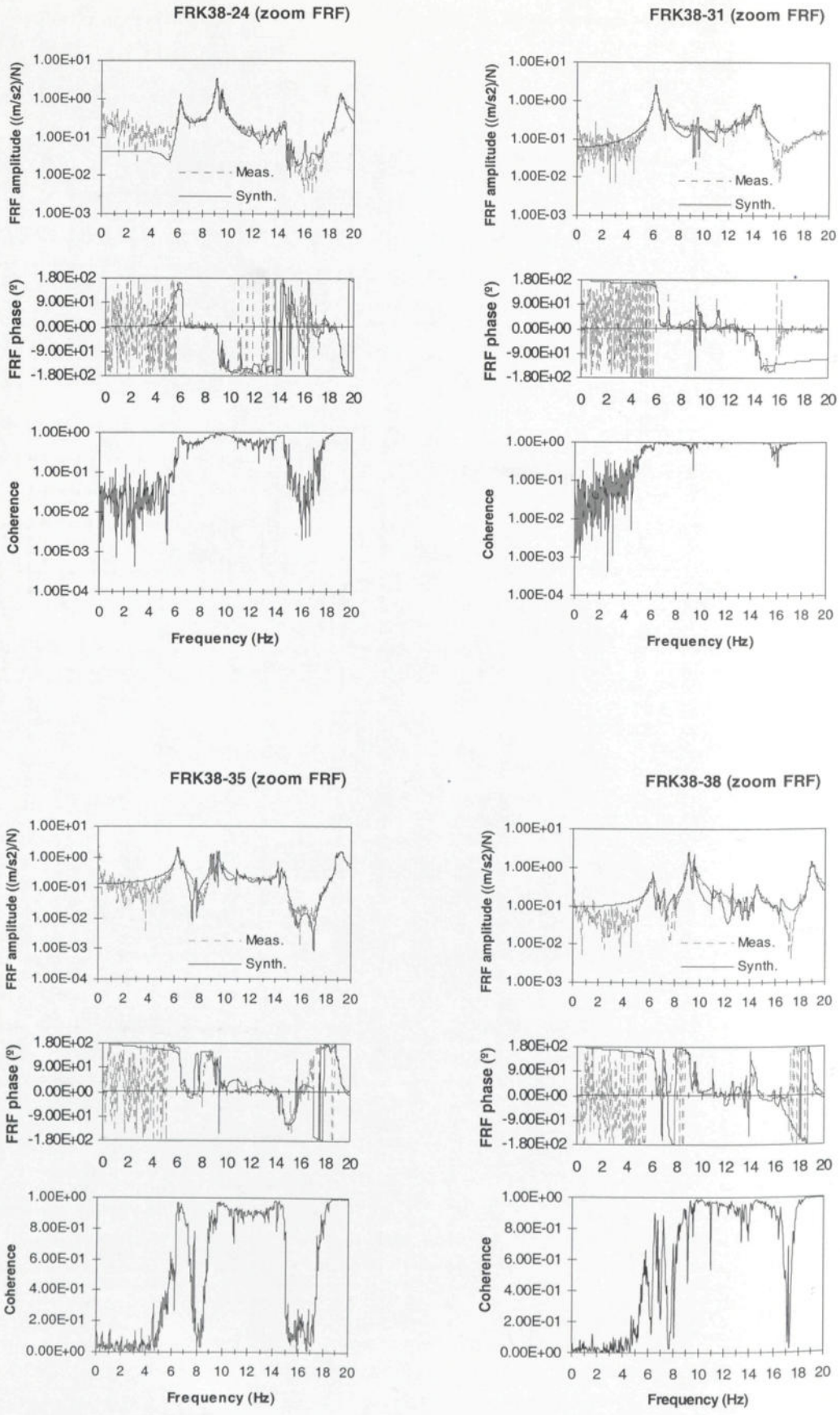


Figure 7.26. Coherence and *FRF* measured/ synthesized from node *38V* (excitation) to nodes *24V*, *31V*, *35V* and *38V* (response). Excitation in the frequency range *0-20Hz*.

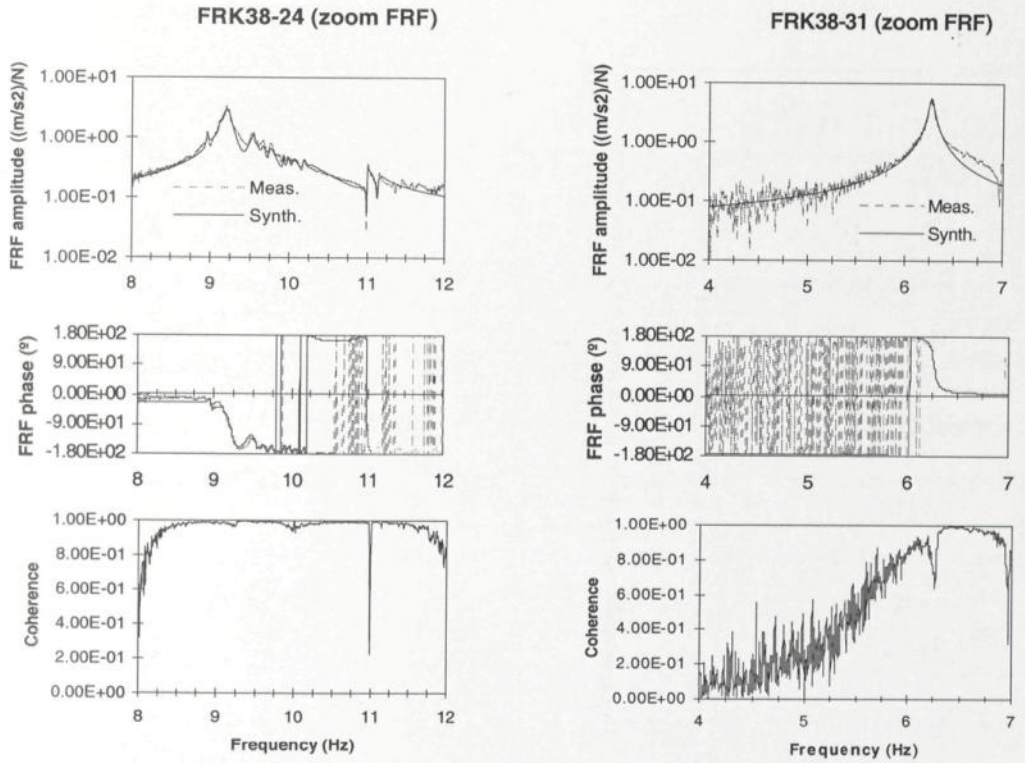


Figure 7.27. Coherence and *FRF* measured/ synthesized from node *38V* (excitation) to nodes *24V* and *31V* (response). High quality zooms in the frequency ranges *8-12Hz* and *4-7Hz*, respectively.

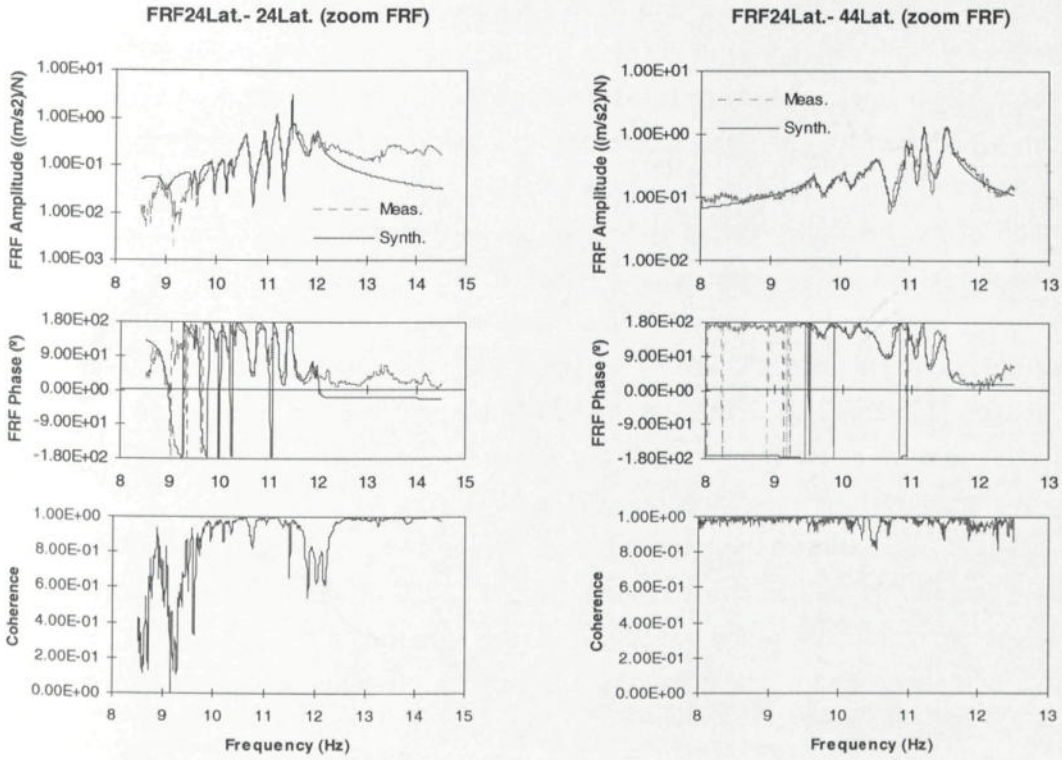


Figure 7.28. Coherence and *FRF* measured/ synthesized from node *24L* (excitation) to nodes *24L* and *44L*(response). High quality zooms in the frequency ranges *8-14.5Hz* and *8-12.5Hz*, respectively.

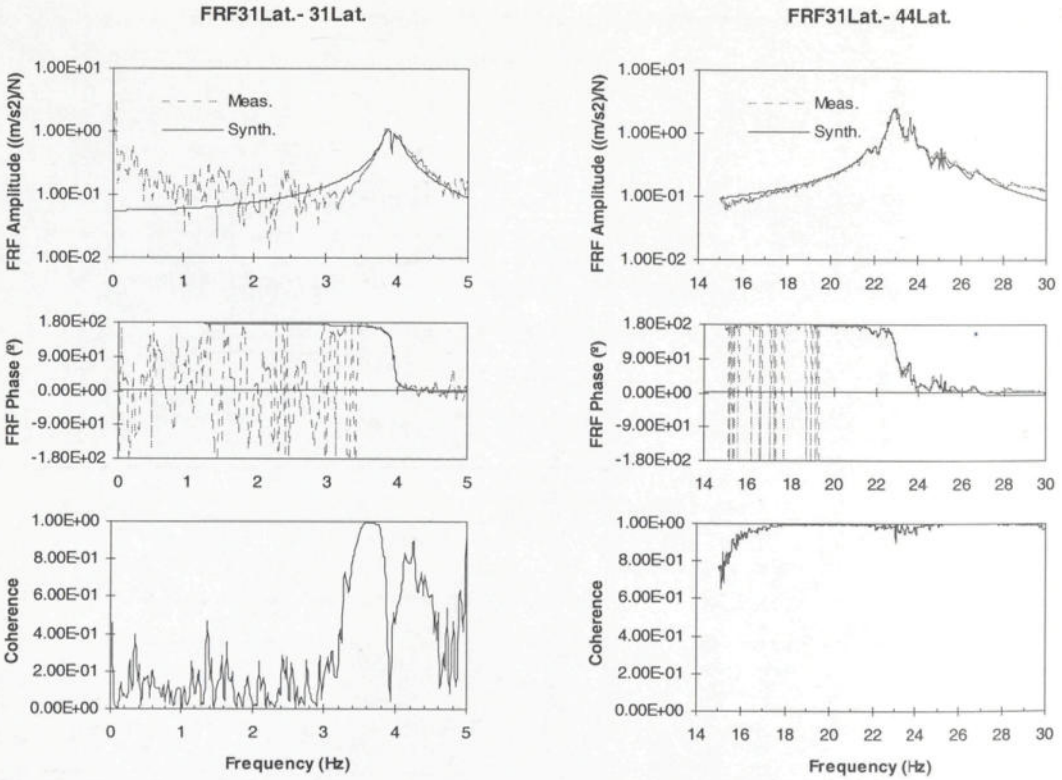


Figure 7.29. Coherence and *FRF* measured/ synthesized from node *31L* (excitation) to nodes *31L* and *44L*(response). High quality zooms in the frequency ranges *0-5Hz* and *15-30Hz*, respectively.

The analysis of Figures 7.26 to 7.29 shows that the narrow range excitation produced generally very high coherences in the vicinity of the resonances. An exception respects the *0-5Hz* zoom for the lateral direction represented in Figure 7.29. The relatively poor quality of the measured FRF can be attributed essentially to a perturbation induced by the shaker in the lateral direction, where the bridge is rather flexible. It is also possible to observe that, with exception of the frequency range *0-7Hz*, where only two modes of vibration exist (the *1st* transversal and *1st* vertical symmetric modes), a very significant number of vibration modes occur for the ranges of frequency analyzed. This is naturally consistent with the results from the *MECS* numerical analysis. The rather good fitting achieved by the application of the *RFP* identification algorithm is also evident. It should be noted that the *RFP* algorithm was applied individually to each of the measured *FRFs*, the natural frequencies and damping coefficients being averaged over the set of analyzed *FRFs*.

Table 7.12 resumes the most important values of the identified natural frequencies and damping factors, as well as the corresponding intervals of variation for the set of analyzed *FRFs*. The characteristics of the associated vibration modes are also indicated, based on the analysis of the identified modal components associated with the configuration of the deck and towers.

The existence of groups of modes with identical configuration of the deck and towers, but involving different motion of the cables is one of the most interesting aspects evidenced by the performed tests. In effect, while the bridge was excited, it was possible to observe that, as

the harmonic frequency varied, the vibration of certain stay cables stopped, while other cables started oscillating and successively stopped vibrating. This issue will be further investigated in Section 7.5.1.3.

Table 7.12. Identified natural frequencies and damping factors.

Type of mode	Identified natural frequency (Hz)	Measured damping factor (%)
1st transv. SYM	3.95± 0.10	1.80
1st vert. SYM	6.25± 0.08	0.42-1.33
1st vert. SYM	6.69± 0.06	0.60-0.87
1st vert. SYM	7.12± 0.06	0.52-0.91
1st vert. ASM	8.96± 0.02	0.13-0.16
1st vert. ASM	9.16± 0.06	0.15-1.18
1st vert. ASM	9.52± 0.11	0.15-0.78
1st vert. ASM	9.62± 0.09	0.36-0.62
1st vert. ASM	9.74± 0.01	0.19-0.22
1st vert. ASM	10.08± 0.16	0.14-0.30
1st vert. ASM	11.00± 0.01	0.15-0.17
1st vert. ASM	11.14± 0.01	0.10-0.14
1st transv. ASM	9.62± 0	0.58-0.59
1st transv. ASM	10.10± 0.08	0.60-0.90
1st transv. ASM	10.27± 0.02	0.28-0.30
1st transv. ASM	10.58± 0.06	0.18-1.08
1st transv. ASM	10.95± 0.01	0.08-0.12
1st transv. ASM	11.00± 0.03	0.10-0.33
1st transv. ASM	11.18± 0.11	0.03-0.82
1st transv. ASM	11.48± 0.03	0.02-0.25
1st transv. ASM	11.52± 0.01	0.21-0.32
1st transv. ASM	11.88± 0.03	0.05-0.45
2nd vert. SYM	14.44± 0.12	0.24-0.61
2nd vert. SYM	14.75± 0.09	
2nd vert. ASM	18.74± 0.05	0.46-0.92
2nd vert. ASM	19.05± 0.02	0.16-0.25
2nd vert. ASM	19.23± 0.07	0.14-1.09
2nd transv.SYM+1st torsion SYM	23.24± 0.09	0.14-0.47
3rd vert. SYM	24.10± 0.33	
1st torsion SYM	25.19± 0.01	
1st torsion SYM	25.49± 0.01	
3rd vert. ASM	29.61± 0.67	0.16-1.51
4th vert. SYM	30.48± 0.52	0.24-1.80
4th vert. ASM	32.99± 0.12	0.57-0.86
5th vert. SYM	39.33± 1.73	0.96-2.06
5th vert. SYM	42.18± 1.58	0.87-2.29
5th vert. ASM	49.35± 0.38	0.28-2.91

7.5.1.3 Sinusoidal tests

Given that a relatively small number of points were instrumented for the low frequency range, it was decided to identify the modal components associated with the fundamental vibration modes using tuned–sinusoidal excitation.

The sinusoidal tests were developed according to the following steps: (i) application of the shaker at the midspan for the symmetrical modes (*1st* transversal *SYM* and *1st* vertical *SYM*), and at one third span for the anti-symmetrical modes (*1st* transversal *ASM* and *1st* vertical *ASM*); (ii) application of sinusoidal forces at different closely spaced frequencies centered at the resonance frequencies predicted by the *FRF* analysis, and measurement of the response to each sinusoid at a location close to the point of maximum modal amplitude; (iii) selection of the frequencies associated with the maximum level of response as the resonance frequencies; (iv) acquisition of time series of input and response to harmonic excitation in the resonance frequencies for a number of points along the bridge deck.

Five vibration modes were identified using this procedure, at the resonance frequencies listed in Table 7.13. Each of the recorded input and response time series comprehended *2048* points sampled at *19.5ms* intervals, hence having a duration of *40s*.

Table 7.13. Characteristics of tuned-sinusoidal excitation.

Type of mode	Shaker location / direction	Resonance frequency (Hz)
1st transversal SYM	31L	3.95
1st vertical SYM	31V	6.20
1st vertical ASM	38V	9.20
1st vertical ASM	38V	9.50
1st transversal ASM	24L	11.20

The procedure for extraction of modal components comprehended the following operations for each pair of input/output time series: (i) trend removal; (ii) band-pass filtering in a narrow frequency range centered at the excitation frequency (for removal of noise); (iii) extraction of the amplitude and phase of the modal component, relating the input and output amplitudes and phases.

A final step in the processing of experimental data consisted in an operation of scaling of the modal components for subsequent comparison with numerical data, using conventional least-squares techniques.

Figures 7.30 to 7.32 present a superposition of the numerical and experimental modal components for three identified vertical modes of vibration, showing a rather good agreement between experimental and numerical data. The accuracy of the fitting can be better analyzed by a separate representation of the deck and towers modal configurations, which is presented in Figures 7.33 to 7.37 for all the identified modes of vibration.

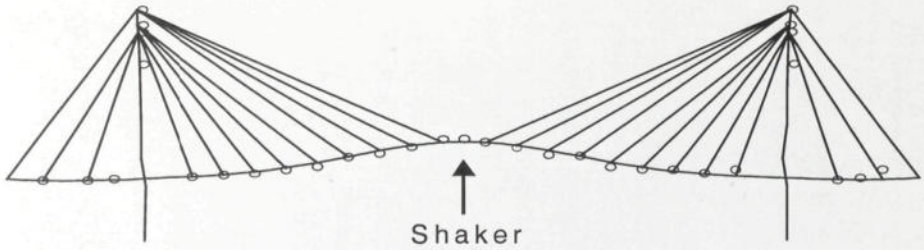


Figure 7.30. First vertical symmetric mode, resonance frequency of *6.2Hz*: numerical and experimental (o) components.

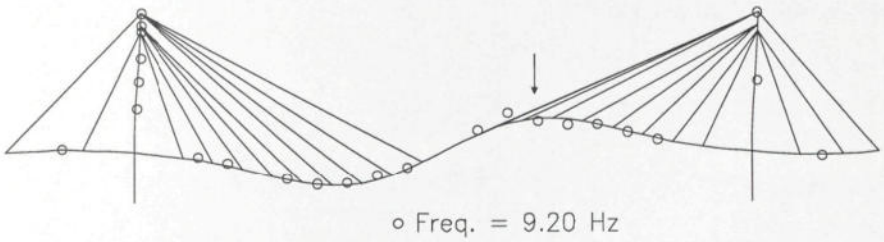


Figure 7.31. First vertical anti-symmetric mode, resonance frequency of *9.2Hz*: numerical and experimental (o) components.

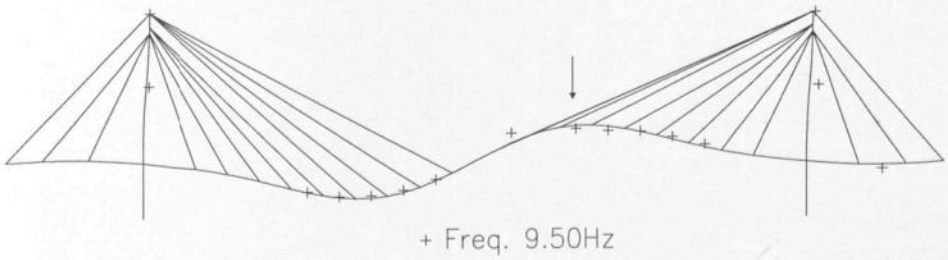


Figure 7.32. First vertical anti-symmetric mode, resonance frequency of *9.5Hz*: numerical and experimental (+) components.

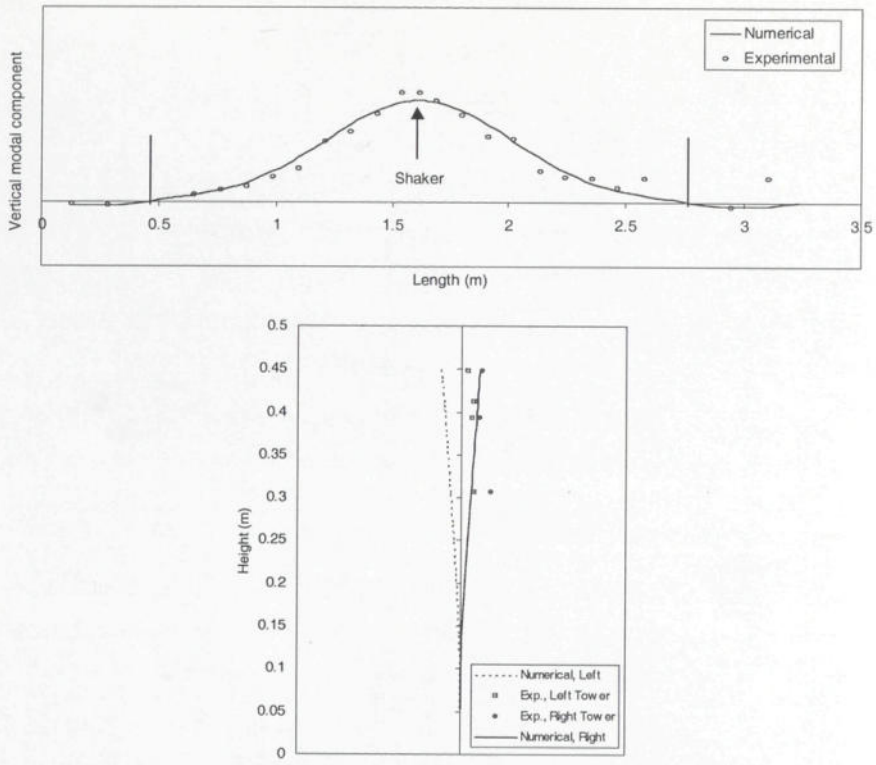


Figure 7.33. First vertical symmetric mode, resonance frequency of *6.2Hz*. Separate representation of numerical and experimental components: (a) Deck; (b) Towers.

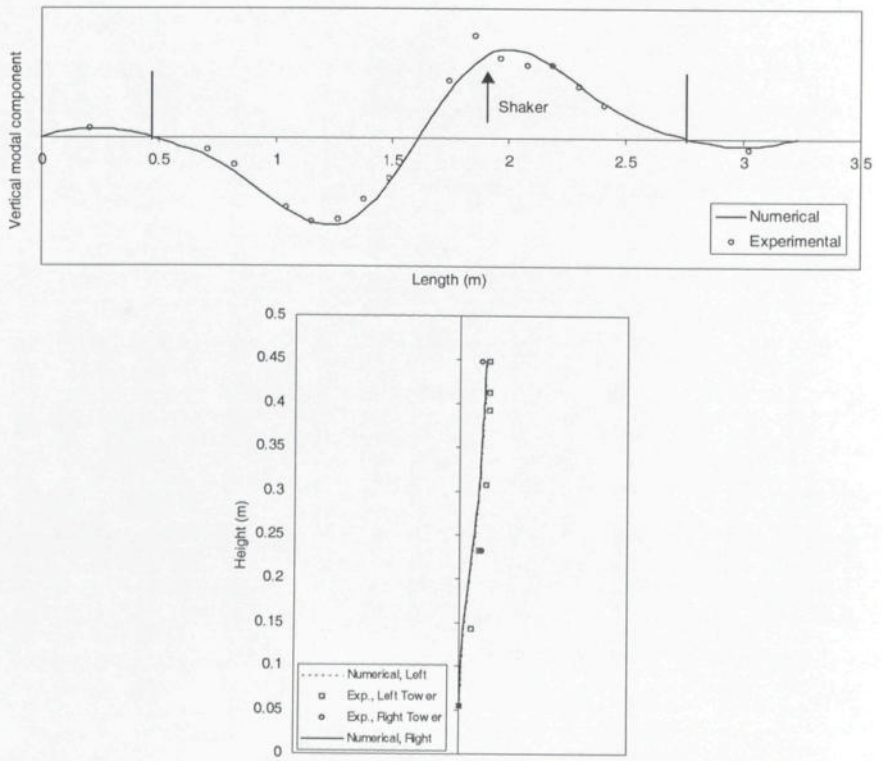


Figure 7.34. First vertical anti-symmetric mode, resonance frequency of *9.2Hz*. Separate representation of numerical and experimental components: (a) Deck; (b) Towers.

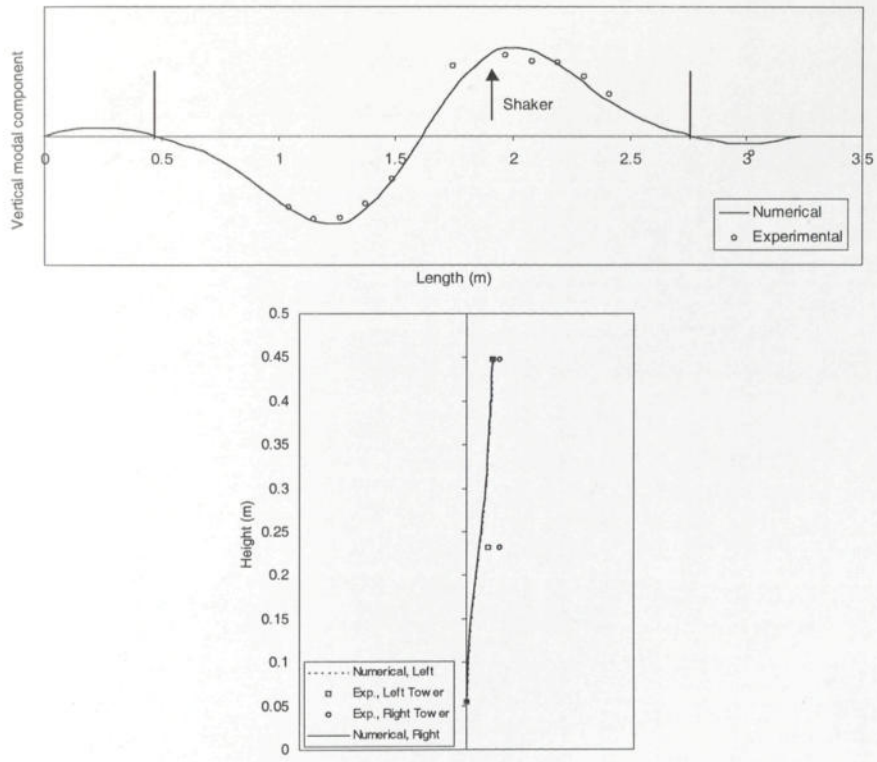


Figure 7.35. First vertical anti-symmetric mode, resonance frequency of *9.5Hz*. Separate representation of numerical and experimental components: (a) Deck; (b) Towers.

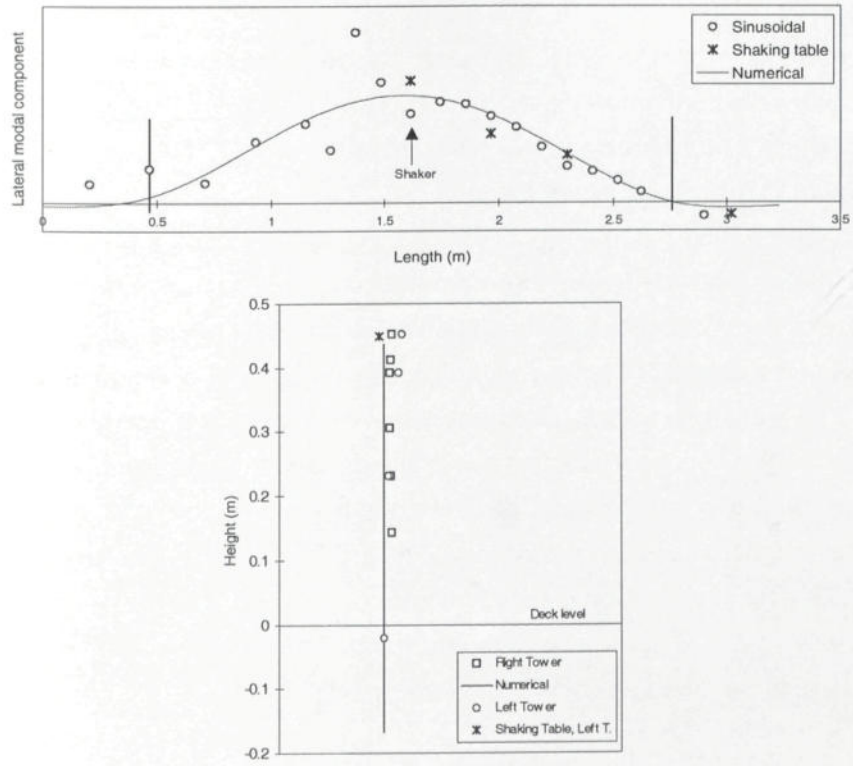


Figure 7.36. First transversal symmetric mode, resonance frequency of *3.95Hz*. Separate representation of numerical and experimental components: (a) Deck; (b) Towers.

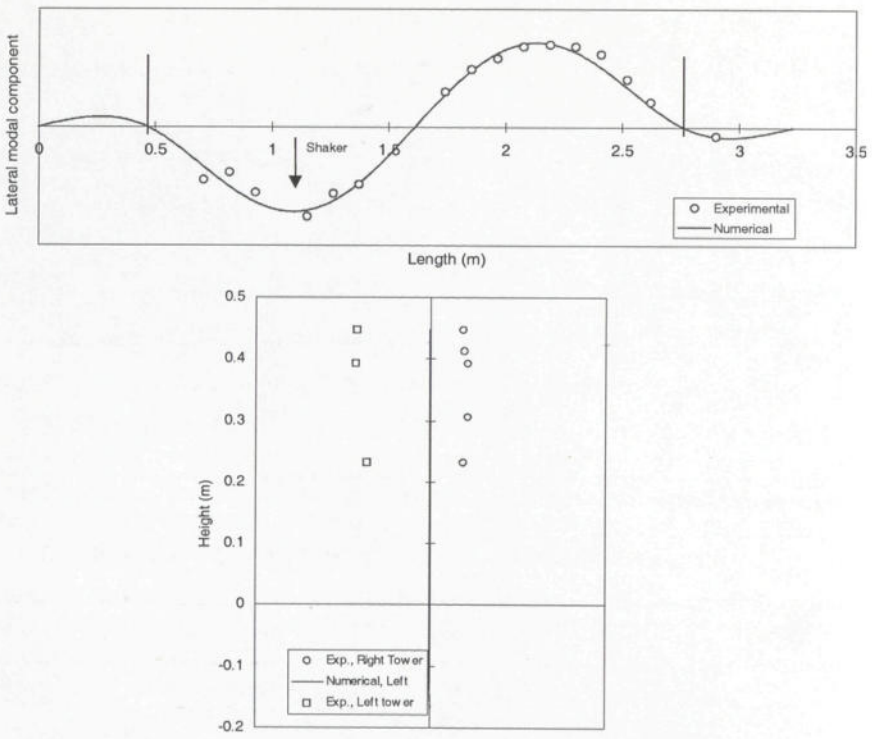


Figure 7.37. First transversal anti-symmetric mode, resonance frequency of *11.2Hz*. Separate representation of numerical and experimental components: (a) Deck; (b) Towers.

The analysis of Figures 7.33 to 7.37 shows a very good agreement between experimental and numerical components. However, higher agreement can in general be observed for the deck modal configurations than for the towers, what evidences some difficulty in adequately modeling the support devices of the physical model. This fact is particularly evident for the lateral modal components of the towers.

The analysis of the modal components associated with the configuration of the girder also shows that the shaker possibly induced some perturbation in the bridge behaviour.

A final consideration respects the identification of the two vertical modes associated with the first vertical anti-symmetric configuration. The observation of a significant number of modes of vibration at very close natural frequencies motivated the identification of the corresponding modal configurations. Selecting two of the dominant resonances and applying a sinusoidal excitation at the corresponding natural frequencies (*9.2Hz* and *9.5Hz*), it was possible to verify that the identified modal configurations are in effect very similar, as shown by Figures 7.34 and 7.35. This fact is even clearer in Figures 7.38 and 7.39, where the identified modal components associated with the two resonant frequencies are represented against the numerical configuration of the first vertical anti-symmetric *OECS* mode.

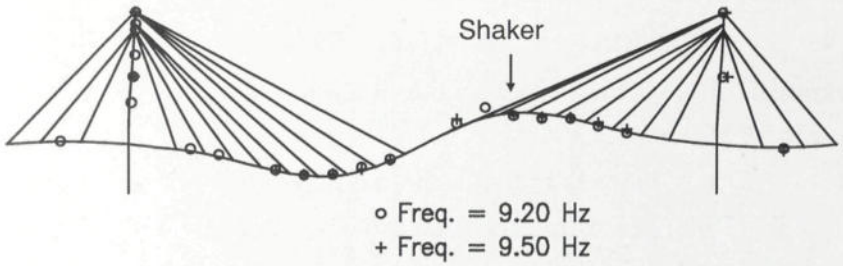


Figure 7.38. First vertical anti-symmetric modes, resonance frequencies of *9.2Hz* and *9.5Hz*: experimental and numerical.

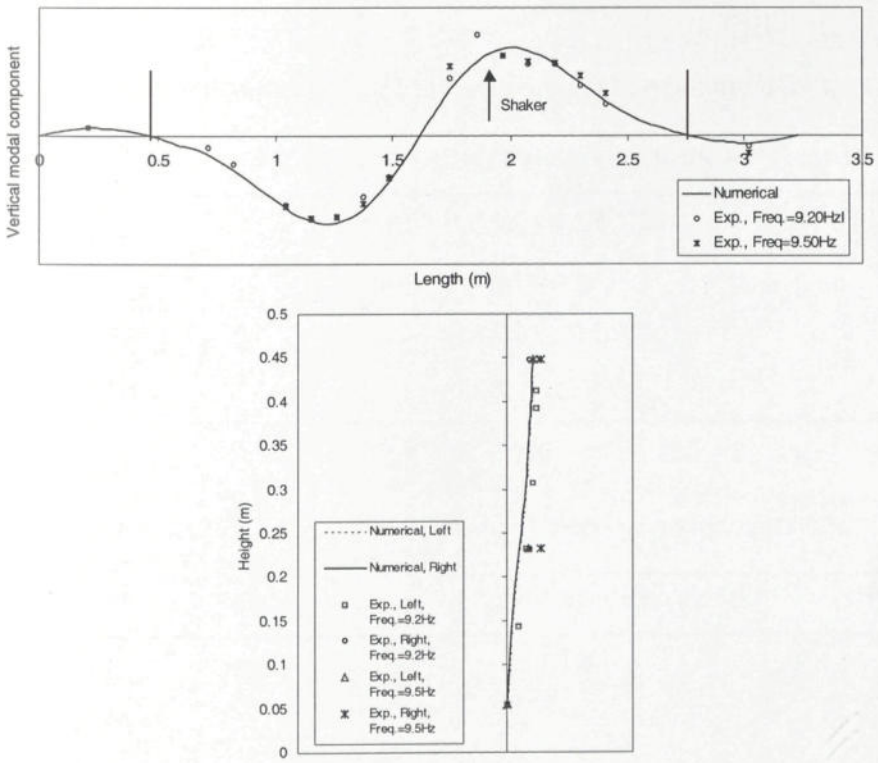


Figure 7.39. First vertical anti-symmetric modes, resonance frequencies of *9.2Hz* and *9.5Hz*. Separate representation of numerical and experimental components: (a) Deck; (b) Towers.

As for the cable motion, it was visually observed that sinusoidal excitations applied at the two natural frequencies induced different movements of the cables. Moreover, for the levels of vibration induced, the persistence of the excitation showed no evidence of inducing a modification of the configurations of vibration (either of the girder/towers or of the cables) into other configurations (for instance, the configuration of adjacent modes of vibration). It was also observed that the repetition of some sinusoidal excitations at different times and with different initial conditions did not induce different movements of the cables. This fact could be noticed for other frequencies rather than the *9.2Hz* and *9.50Hz*. Table 7.14 reports the observed movement of the cables for different frequencies of excitation close to *9Hz*. To distinguish the

two pairs of cables connected to the upstream and downstream side of the same tower, symbols *D* (downstream cable) and *U* (upstream cable) have been employed. The relative amplitude of the cable movement is represented by $i, \underline{i}$ or $\underline{\underline{i}}$, the first meaning that the amplitude of vibration of cable *i* was low and the last meaning that this amplitude was quite high.

It is noteworthy that there is in fact a three-dimensional character of the vibration, as the *4* equal stay cables with similar tensions associated with each cable number (e.g.: *8U left*, *8D left*, *8U right*, *8D right*) behave differently. As a consequence, one can not expect a perfect agreement either of the number and value of the identified frequencies or of the corresponding modal shapes with those that resulted from the *2-D MECS* analysis. It is clear however, from Tables 7.14 and 7.15, that the cables with major vibrations are the same.

Table 7.14. Observation of cable movement during sinusoidal excitation.

Frequency (Hz)	Cables connected to left tower	Cables connected to right tower
9.20	$\underline{8}D,\underline{\underline{8}}U,\underline{9}D,9U,\underline{3}U$	$\underline{\underline{8}}U,\underline{9}D,\underline{\underline{9}}U,\underline{5}D,\underline{5}U$
9.25	$\underline{8}D,\underline{\underline{8}}U,9D,9U$	$\underline{8}D,\underline{\underline{8}}U,\underline{9}D,\underline{\underline{9}}U,\underline{5}D,\underline{5}U$
9.50	$\underline{\underline{8}}D,9D,9U,10D,10U$	$\underline{8}D,\underline{\underline{8}}U,\underline{9}D,\underline{\underline{9}}U,\underline{5}D,\underline{5}U,12D,12U$
9.55	$\underline{\underline{8}}D,\underline{9}U,10D,10U$	$8U,9U,9D,\underline{5}D$

Table 7.15. Description of cable movement using a *2-D MECS* analysis.

Frequency (Hz)	Cables connected to left tower	Cables connected to right tower
9.04	*8*	$8,\underline{\underline{9}}$
9.17	$\underline{8}$	$\underline{8},\underline{\underline{9}},11,12$
9.65	$\underline{\underline{8}}$	$\underline{\underline{8}}$
11.89	$\underline{\underline{1}}$	$\underline{\underline{1}}$

A comparison of the observed cable vibration with the results obtained on the basis of the *3-D MECS* analysis (see Table 7.16 and Figure 7.40) also evidences a qualitative agreement, as the same cable numbers are involved in the most significant vibration. However, it is also clear that the symmetry of the numerical results is not reproduced by experimental data, and the correspondence between experimental and numerical modes is not perfect. Two explanations can be found for this difference of dynamic behaviour: (i) a practical difficulty of achieving an accurate numerical model of certain local features, like the effective cable anchorages, and the connection devices at the towers; (ii) the existence of slight imperfections in the physical model.

An example associated with the second listed issue is the existence of a very slight difference in the installed tensions on the upstream and downstream cables. This aspect might lead to some asymmetry of the bridge behaviour and explain thus why different levels of vibration were observed on the upstream and downstream cables, sometimes one of them vibrating in an inclined plane, or even rotating during vibration, in perfect disagreement with numerical evidence.

Note that these slight differences occur also for bridge prototypes and are not particular aspects of the physical model under analysis. In effect, an analysis of certain cable vibrations reported in the literature for some prototypes shows similar patterns to those found on the physical model, i.e., non-symmetry of vibration, successive vibrations of different cables at different wind velocities, etc.

Table 7.16. Description of cable movement using a *3-D MECS* analysis.

Frequency (Hz)	Mode no.	Cables connected to left tower	Cables connected to right tower
7.93	12		*11U,11D*
7.93	13	*11U,11D*	
8.42	20		*10U,10D*
8.42	21	*10U,10D*	
9.04	27	*1U,1D,8U,8D,9U,9D,10U,10D, 11U,11D,12U,12D*	*1U,1D,8U,8D,9U,9D,10U,10D, 11U,11D,12U,12D*
9.63	29		*9U,9D*
9.63	30	*9U,9D*	
9.69	33		*8U,8D*
11.47	49	*1U,1D*	*1U,1D*
11.48	50	*1U,1D*	

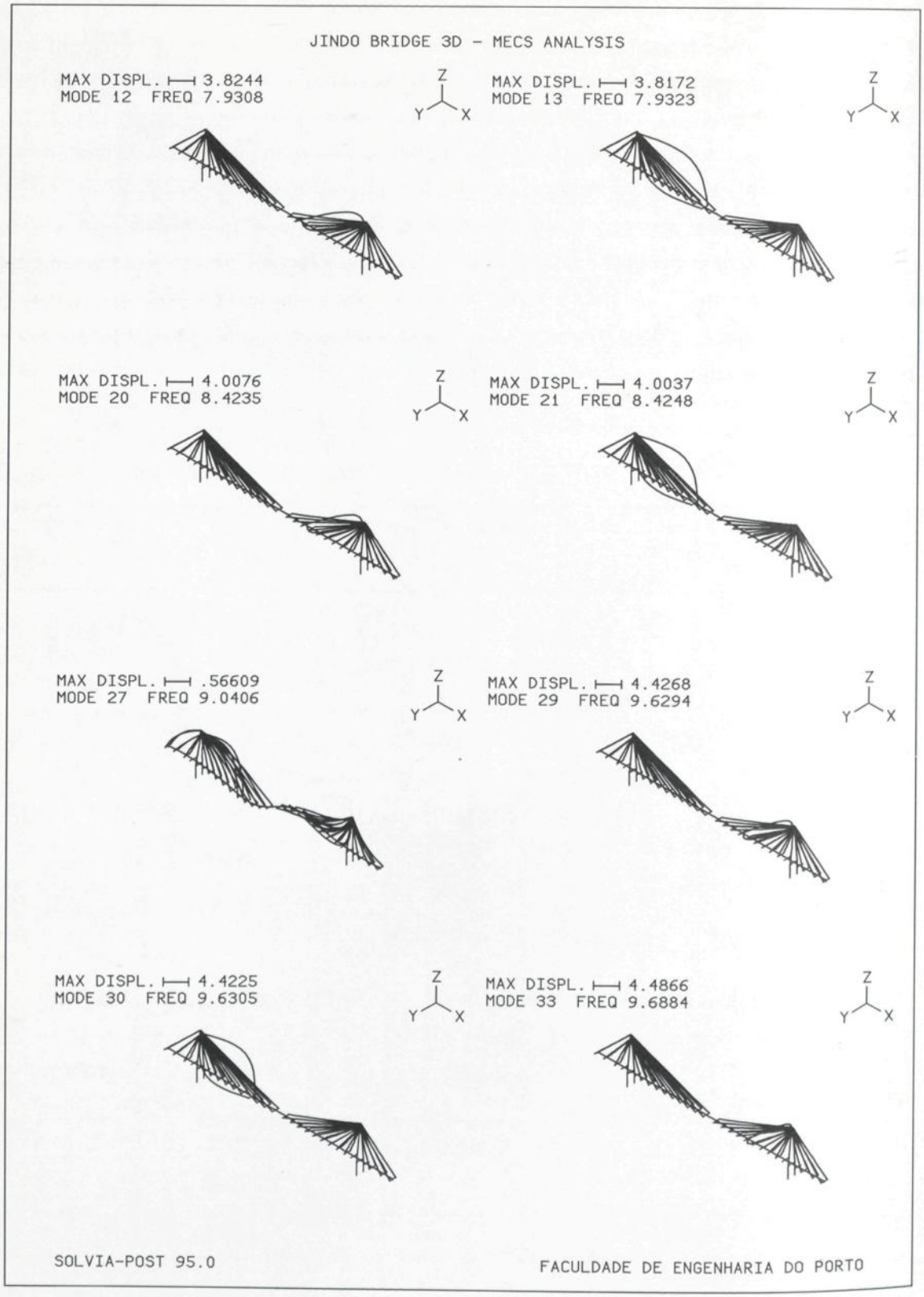


Figure 7.40. Cable vibration in some *3-D MECS* vibration modes.

7.5.2 Tests at the EERC shaking table

The current Section describes a set of preliminary tests conducted at the shaking table of the University of Bristol, which aimed at a first instance to confirm and enhance the evidence of *dynamic cable-structure interaction* in the bridge behaviour.

The fact that the shaking table motion leads to more distributed forces applied to the bridge model than the ones produced by a shaker mounted at some location along the bridge allows, on one side, to identify with a higher accuracy the modal characteristics of the physical model. On the other hand, because no device is directly attached to the physical model, the shaking table excitation guarantees that no external perturbation is introduced in the bridge behaviour.

A second objective of the tests was the identification of damping factors for the fundamental vibration modes at different levels of vibration of the bridge. This was achieved by measurement of the free response of the bridge after being excited at particular resonance frequencies.

7.5.2.1 Instrumentation

The tests on the shaking table involved the following transducers:

- *11* piezoelectric *DYTRAN* accelerometers, model *3101AG*;
- *3* capacitive transducers *SETRA*, model *141A* (see Figure 5.13(c)). The characteristics of these accelerometers were already described in Chapter five;
- *1* magnetic displacement transducer *INDICON*.

All the transducers employed were connected to a conditioning system *FERN*, model *EF6*, which filtered the measured signals at *80Hz* cutoff frequency and adequately amplified the instruments to produce a signal of *1V/g*.

The first series of tests comprehended the measurement of *FRF*s relating the response measured at specific locations with the base acceleration along the direction of excitation, measured using one of the three *SETRA* accelerometers that were mounted directly on the platform. For these tests the platform was driven by the *ADVANTEST* analyzer already described, which was also used to obtain the *FRF* estimates.

The sinusoidal tests were performed using the shaking table control system and software, and employing two eight-channel acquisition boards. The main characteristics of the shaking table and of the corresponding control system are described in (Blakeborough *et al.*, 1986).

Figure 7.41 shows a general view of the physical model mounted on the shaking table and instrumented with the *DYTRAN* and *SETRA* accelerometers, as well as with the *INDICON* transducer. Some closer details of the instruments can be found in Figures 7.15 and 7.42.

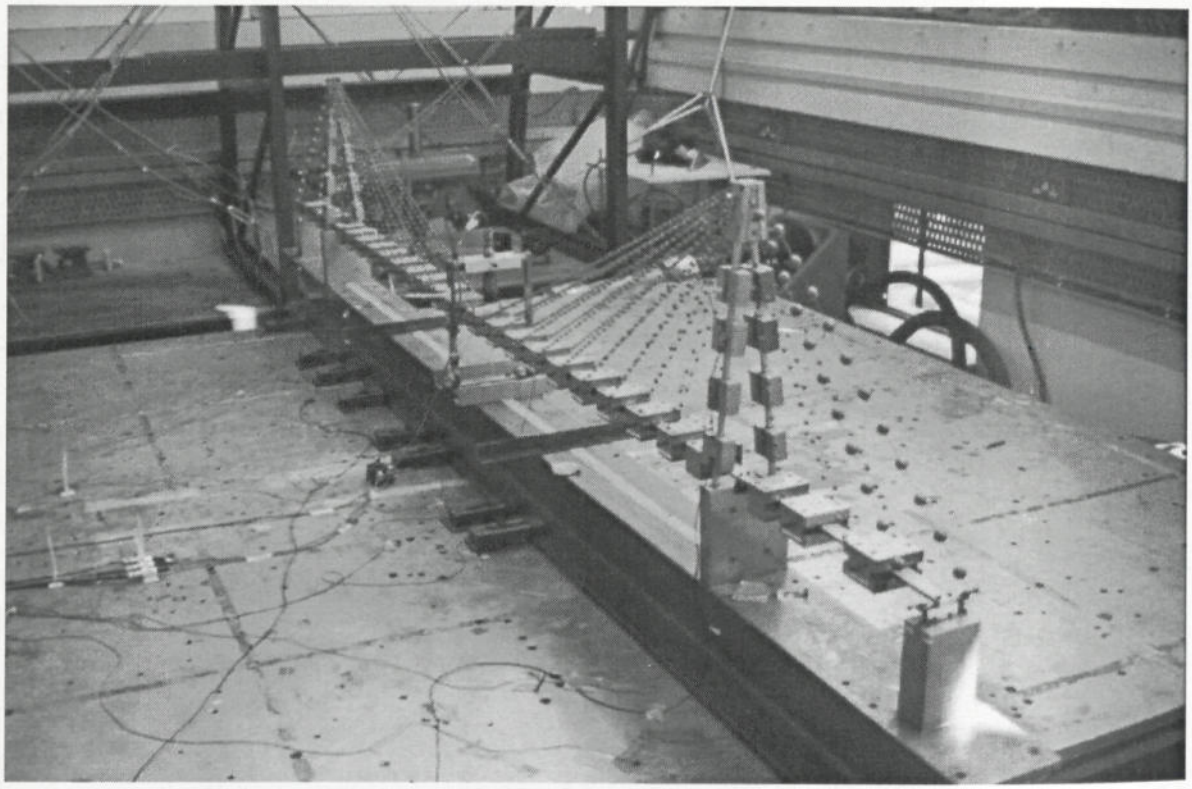


Figure 7.41. Mounting of the Jindo Bridge model on the shaking table.

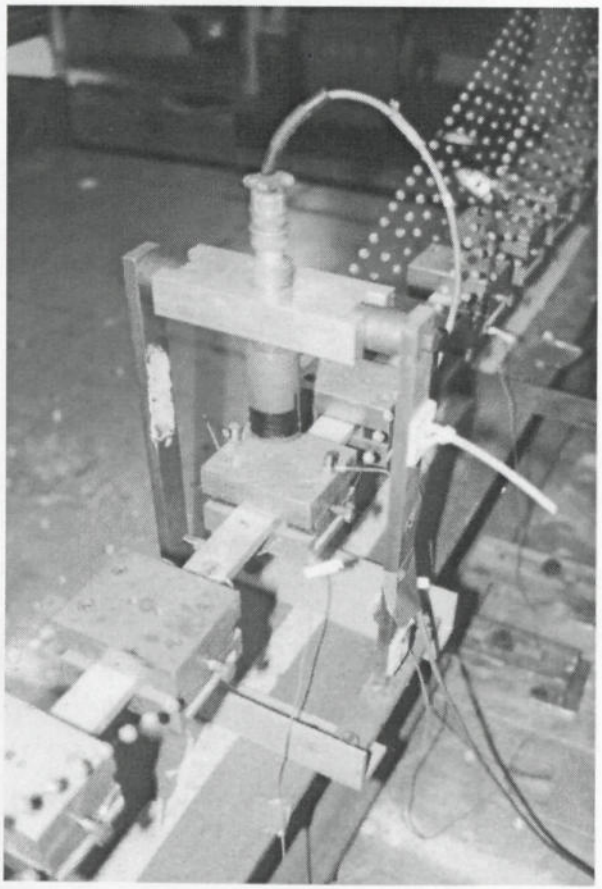


Figure 7.42. Detail of the scheme of fixation of the displacement transducer.

7.5.2.2 Multi-sine excitation tests

The first operation after mounting the Jindo model on the shaking table, was a re-tuning of the tensions on the stay cables. Then a series of modal analysis tests were performed using the *ADVANTEST* analyzer, and applying a base excitation of multi-sine type. The "*Frequency Response Function*" estimates were generally calculated for the frequency range *0-50Hz*, relating the structural response measured in terms of acceleration or displacements with the acceleration measured at the platform. The frequency resolution achieved was then *0.0625Hz*.

Figure 7.43 indicates the points and directions in which *FRF* estimates were obtained for the frequency range *0-50Hz* (arrows), and where some high-quality zooms were performed, in the ranges *5Hz-14Hz* and *8Hz-14Hz* (circles in the arrows). The three directions will be designated as *X* (*longitudinal*), *Y* (*transversal*) and *Z* (*Vertical*).

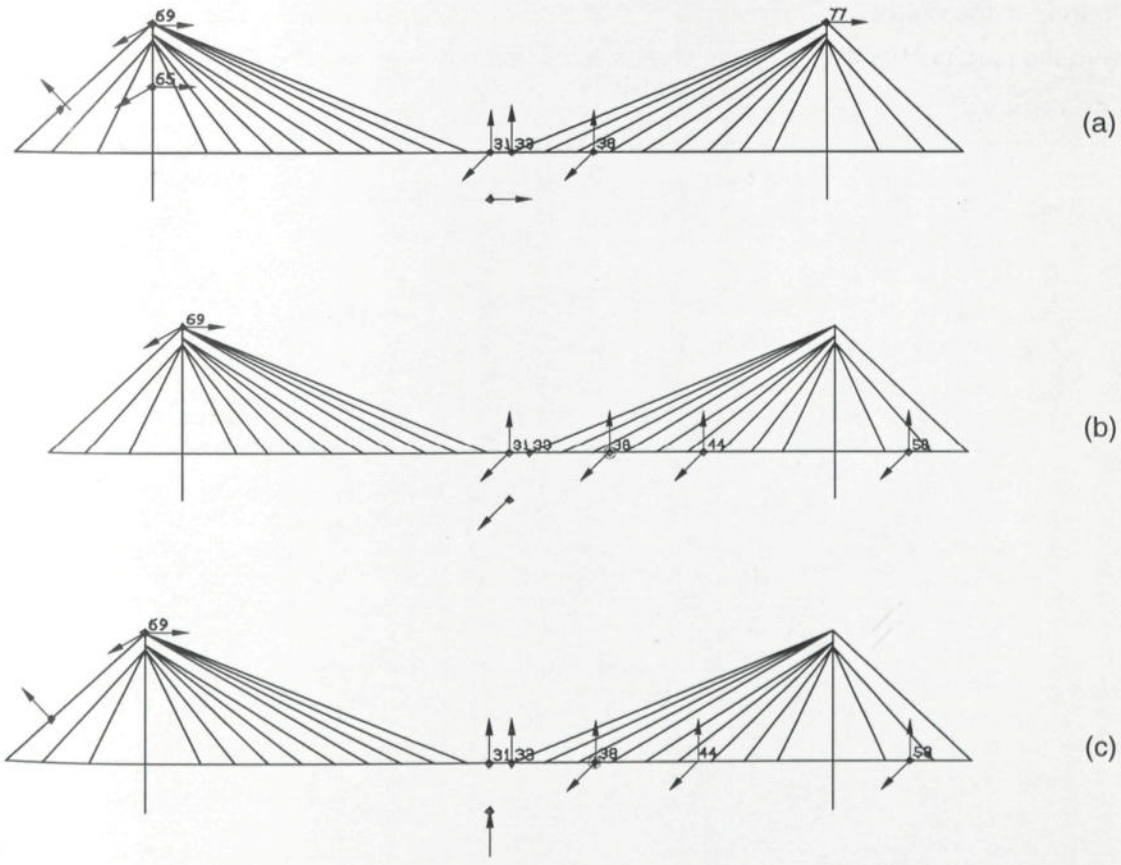


Figure 7.43. Locations of instruments for multi-sine tests on the shaking table in the direction: (a) *X*; (b) *Y*; (c) *Z*. Arrows indicate the direction of *FRF* measurement for the range *0-50Hz*. Circles in the arrows indicate further zoom analysis in the range *5Hz-14Hz*.

Figure 7.44 presents some examples of *FRF* and coherence function estimates, relating the acceleration measured at the platform along directions *X* (Figure 7.44(a)), *Y*

(Figure 7.44(b)) and *Z* (Figure 7.44(c)), with the response measured at some selected locations. The synthesized *FRFs* based on the mentioned identification algorithm are also represented in correspondence with the measured *FRFs*.

The analysis of Figures 7.44 shows that generally very good coherences have been achieved in correspondence with the vibration modes, even for the lower frequency range. Most important, a high consistency between the data obtained on the basis of the types of excitation employed (shaker and shaking table) exists.

In order to improve the frequency resolution for the ranges of frequency where the fundamental modes of vibration existed, some high quality zoom FRF estimates were also obtained. Figure 7.45 presents two examples that relate the acceleration at the platform along directions *Y* and *Z* with the transversal and vertical responses, respectively, measured at node 38. The same pattern associated with the existence of groups of closely spaced modes with similar configurations of the deck and towers, but involving different motions of the cables was also identified. Table 7.17 resumes the average values and associated intervals of variation found for the natural frequencies and damping coefficients, establishing the correspondence with the results obtained from the shaker tests (already presented in Table 7.12).

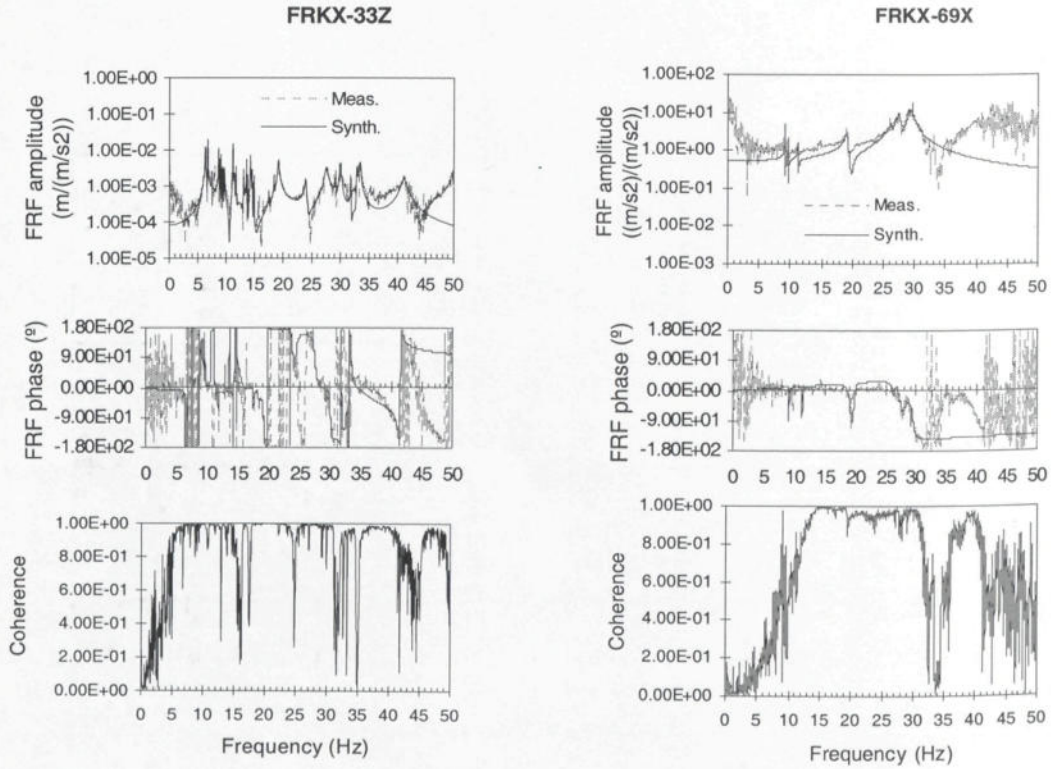


Figure 7.44 (a) Coherence and *FRF* measured/ synthesized from the platform acceleration in the *X*-direction (excitation) to nodes *33Z* and *69X* (response). Excitation in the frequency range *0-50Hz*.

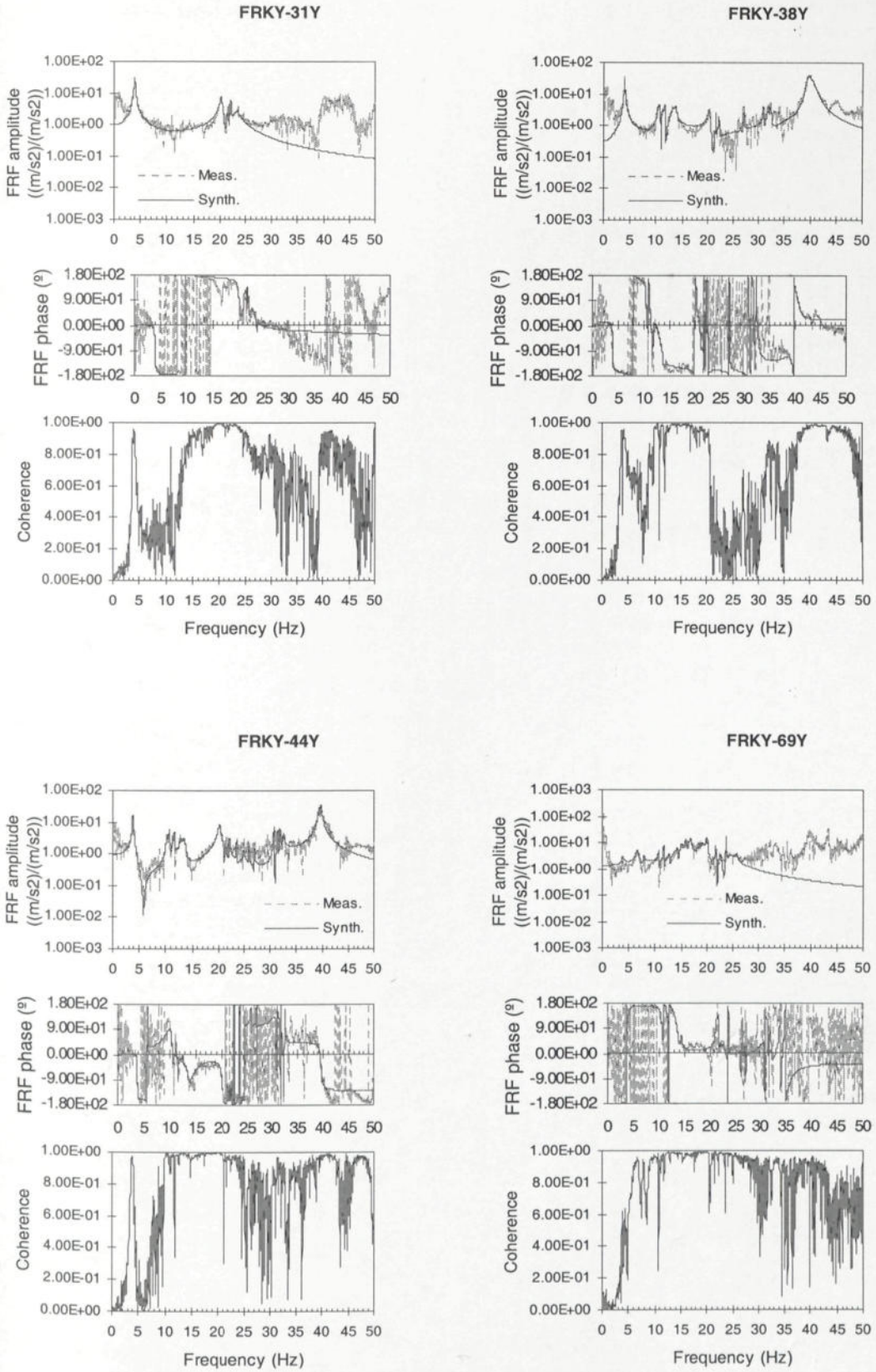


Figure 7.44 (b) Coherence and *FRF* measured/ synthesized from the platform acceleration in the *Y*-direction (excitation) to nodes *31Y, 38Y, 44Y* and *69Y* (response). Excitation in the frequency range *0-50Hz*.

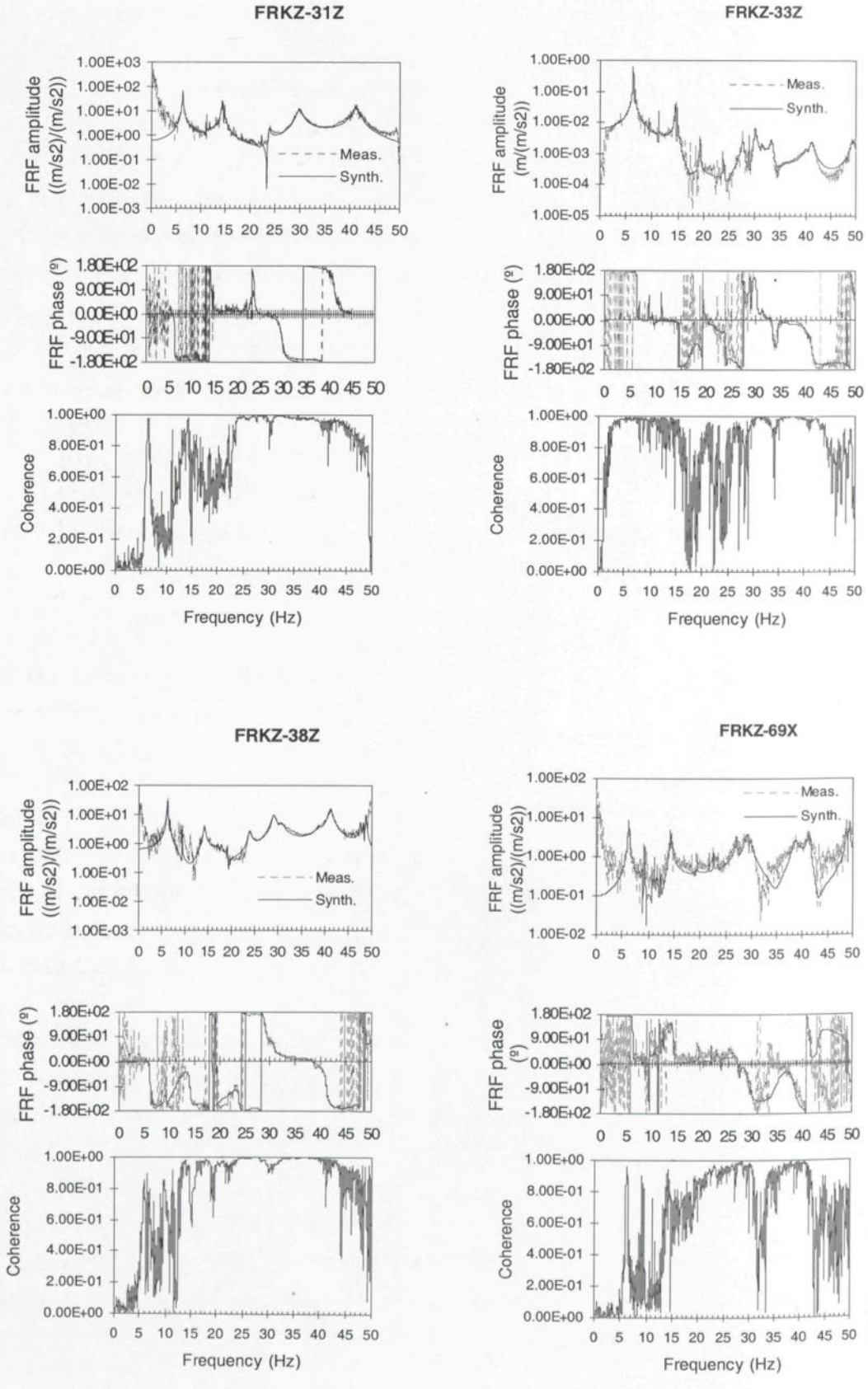


Figure 7.44 (c) Coherence and *FRF* measured/ synthesized from the platform acceleration in the *Z*-direction (excitation) to nodes *31Z, 33Z, 38Z* and *69X* (response). Excitation in the frequency range *0-50Hz.*

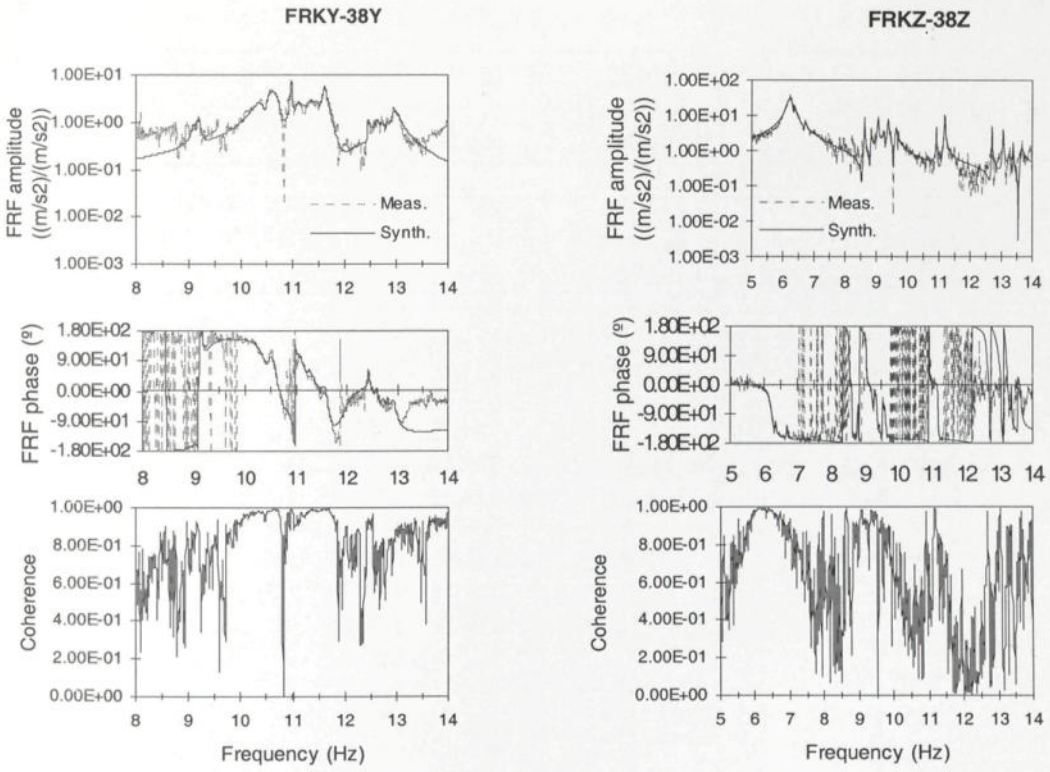


Figure 7.45. Coherence and *FRF* measured/ synthesized from the platform acceleration in the Y and Z-directions (excitation) to node *38Z* (response). High quality zooms in the frequency ranges *8Hz-14Hz* and *5Hz-14Hz*, respectively.

Inspection of Table 7.17 evidences the consistency between measurements performed under excitation from the electrodynamic shaker and on the shaking table. Some slight differences obtained may be explained by perturbations induced by the shaker. In certain cases it was not possible to identify accurately some of the multiple modes simultaneously with both excitation techniques, due to high modal interference and insufficient amplitude and/or frequency resolution of the *FRF* estimates.

It is important to note the significant variation of the identified damping factors, which seem to be highly dependent on the amplitude of vibration. This fact is particularly relevant for the damping factors associated to the first transversal and vertical bending modes of vibration, whose magnitudes also attained values much superior to other modes.

Finally, for a comparison between experimental and numerical data, the average values of the identified natural frequencies, obtained from the shaking table measurements, and the corresponding calculated values based on the *3-D OECS* and *MECS* models are resumed in Table 7.18. These frequencies are grouped according to the deck/towers configuration of the associated mode shapes.

Table 7.17. Identified natural frequencies and damping factors.

Type of mode	Identified natural frequency (Hz)		Measured damping factor (%)	
	Shaker	Shaking table	Shaker	Shaking table
1st transv. SYM	3.95± 0.10	3.91± 0.09	1.80	1.65-2.08
1st vert. SYM	6.25± 0.08	6.27± 0.10	0.42-1.33	0.35-1.67
1st vert. SYM	6.69± 0.06	6.73± 0.03	0.60-0.87	0.11-0.43
1st vert. SYM	7.12± 0.06		0.52-0.91	
1st vert. ASM	8.96± 0.02	8.63± 0	0.13-0.16	0.060-0.069
1st vert. ASM		8.82± 0.01		0.092-0.097
1st vert. ASM	9.16± 0.06	9.05± 0.01	0.15-1.18	0.14-0.18
1st vert. ASM		9.25± 0.01		0.18-0.25
1st vert. ASM	9.52± 0.11	9.37± 0.06	0.15-0.78	0.19-0.25
1st vert. ASM	9.62± 0.09	9.49± 0.04	0.36-0.62	0.11-0.15
1st vert. ASM	9.74± 0.01	9.63± 0.03	0.19-0.22	0.15-0.29
1st vert. ASM	10.08± 0.16		0.14-0.30	
1st vert. ASM	11.00± 0.01	10.90± 0.02	0.15-0.17	0.043-0.049
1st vert. ASM	11.14± 0.01	11.18± 0.01	0.10-0.14	0.037-0.099
1st transv. ASM		9.10		0.34
1st transv. ASM		9.19		0.25
1st transv. ASM	9.62± 0		0.58-0.59	
1st transv. ASM	10.10± 0.08		0.60-0.90	
1st transv. ASM	10.27± 0.02	10.35± 0.11	0.28-0.30	0.52-1.73
1st transv. ASM	10.58± 0.06	10.54± 0.08	0.18-1.08	0.65-1.16
1st transv. ASM		10.73		0.60
1st transv. ASM	10.95± 0.01	10.98	0.08-0.12	0.094
1st transv. ASM	11.00± 0.03		0.10-0.33	
1st transv. ASM	11.18± 0.11	11.17± 0.03	0.03-0.82	0.81-1.13
1st transv. ASM	11.48± 0.03	11.49	0.02-0.25	0.12
1st transv. ASM	11.52± 0.01		0.21-0.32	
1st transv. ASM		11.62± 0.01		0.13-0.53
1st transv. ASM	11.88± 0.03		0.05-0.45	
1st transv. ASM		12.45		0.14
1st transv. ASM		12.66		0.11
1st transv. ASM		12.79		0.17
1st transv. ASM		12.82		0.61
1st transv. ASM		12.96		0.64
2nd vert. SYM	14.44± 0.12	14.36± 0.04	0.24-0.61	0.041-0.69
2nd vert. SYM	14.75± 0.09	14.51± 0.01		0.097-0.21
2nd vert. SYM		14.80± 0.02		0.16-0.24
2nd vert. ASM	18.74± 0.05		0.46-0.92	
2nd vert. ASM	19.05± 0.02	19.16± 0.08	0.16-0.25	0.039-0.47
2nd vert. ASM	19.23± 0.07	19.29± 0.09	0.14-1.09	0.16-0.41
2nd transv.SYM+1st torsion SYM		20.24± 0.08		0.86-1.24
2nd transv.SYM+1st torsion SYM		21.61± 0.03		0.07-0.32
2nd transv.SYM+1st torsion SYM		21.97± 0.15		0.06-0.16
2nd transv.SYM+1st torsion SYM		22.26± 0		0.01-0.28
2nd transv.SYM+1st torsion SYM	23.24± 0.09	23.62± 0.17	0.14-0.47	0.038-0.098
3rd vert. SYM	24.10± 0.33	23.89± 0.12		0.51-1.35
1st torsion SYM	25.19± 0.01			0.14-0.15
1st torsion SYM	25.49± 0.01			0.42-0.45
3rd vert. ASM	29.61± 0.67	27.59± 0.06	0.16-1.51	0.13-0.87
4th vert. SYM	30.48± 0.52	29.68± 0.56	0.24-1.80	0.33-1.88
4th vert. ASM	32.99± 0.12	33.42± 0.09	0.57-0.86	0.32-0.67
5th vert. SYM	39.33± 1.73	41.08± 0.53	0.96-2.06	0.63-1.22
5th vert. SYM	42.18± 1.58		0.87-2.29	
5th vert. ASM	49.35± 0.38		0.28-2.91	

Table 7.18. Identified and calculated natural frequencies: Experimental *vs* calculated *3-D*.

Type of mode	OECS: Calculated natural frequency (Hz)	MECS: Calculated natural frequency (Hz)	Identified natural frequency (Hz)
1st transv. SYM	4.28	4.26/ 7.16	3.95/ 6.81/ 7.94
1st vert. SYM	6.21	6.14/ 6.94/ 6.94	6.27 / 6.73
1st vert. ASM	9.12	7.93/ 7.93/ 8.42/ 8.42/ 9.04/ 9.63 / 9.63 / 9.69/ 9.69/ 11.47	8.63 / 8.82 / 9.05 / 9.25 / 9.37 / 9.49 / 9.63 /10.90 / 11.18
1st transv. ASM	11.71	7.15/ 8.11/ 8.11/ 8.61/ 8.61/ 9.79/ 9.79/ 9.90/ 9.90/ 11.48/ 11.49/ 11.66/ 12.13/ 12.14/ 12.16	9.10/ 9.19/ 10.35/ 10.54/ 10.73/ 10.98/ 11.17/ 11.49/ 11.62/ 12.45/ 12.66/ 12.79/ 12.82/ 12.96
2nd vert. SYM	13.74	11.36/ 11.36/ 11.45/ 11.47/ 12.00/ 12.00/ 13.55/ 13.75/ 13.75/ 13.91/ 14.12	14.36 / 14.51 / 14.80
2nd vert. ASM	18.26	17.81 / 18.29	19.16 / 19.29
2nd transv. SYM + 1st torsion SYM	22.10	*	20.24/ 21.61/ 21.97/ 22.26/ 23.62
3rd vert. SYM	22.70	*	23.89
1st torsion SYM	24.95	*	25.19/ 25.49

* - Not calculated

It can be observed from Table 7.18 that, with exception of the first transversal mode, the identified natural frequencies were in general very slightly higher than those obtained from the numerical model.

The existence of cable-structure interaction was proven both by numerical calculations and by an extensive series of tests. However, it was not possible to establish a perfect correspondence between experimental and numerical data. This fact results from a first aspect that is indeed the very slight differences in the several vibration modes present in the system, associated with two distinct types of components: a main structural system with relatively stiff characteristics, composed by the deck and towers, and a secondary flexible system, composed by the cables, which interacts with the former system. The characteristics of the deck and towers subsystem govern the dynamic behaviour of the whole bridge, in the sense that they basically define the order of magnitude of the global system's natural frequencies, while the cables subsystem produces a significant number of new vibration modes that dictate their interaction with the former subsystem, whose significance in terms of global bridge response will be investigated in Chapter eight. A second aspect already referred explains the differences found between numerical and experimental, which is the possibility of existence of small imperfections in the physical model that dictate a loss of symmetry and consequent appearance of different sets of vibration modes.

7.5.2.3 Damping tests

The damping coefficients identified on the basis of both the shaker and shaking table excitation exhibited significant variations, as evidenced in the previous Section.

Given the interest in adequately characterizing damping coefficients for the purpose of calculation of the bridge response to seismic excitation, it was decided to perform a set of additional tests in which each fundamental vibration mode was isolated, assessing then the variation of damping coefficients with the amplitude of oscillation.

Tests procedure

The tests were performed on the shaking table and consisted in the measurement of the vibration response at several locations, after exciting the bridge model at specific resonances, by application of a sinusoidal excitation.

The tests started with the generation of a *10Hz* sinusoid sampled at *256Hz* by the *16* available channels, according to the setup presented in Figure 7.46, and recording time histories with *4096* points. This signal was windowed using a trapezoidal time window defined in an extension of about *25%* the full record length. A re-scaling of the time values allowed for a successive variation of the sinusoid frequency, which was then applied to the shaking table for the following frequencies and directions: (i) *3.95Hz, Y* (*1st* transversal *SYM* vibration mode); (ii) 6.24Hz, Z (1st vertical *SYM* vibration mode); (iii) *9.20Hz, Z* (1st vertical *ASM* vibration mode); (iv) *9.50Hz, Z* (1st vertical *ASM* vibration mode); (v) *10.90Hz, Y* (1st transversal *ASM* vibration mode) (vi) *11.20Hz, Y* (1st transversal *ASM* vibration mode) (vii) *14.25Hz, Z* (2nd vertical *SYM* vibration mode); (viii) 1*9.25Hz, Z* (2nd vertical *ASM* vibration mode). For each of these frequencies two sinusoidal tests were performed, setting two different amplitudes of oscillation.

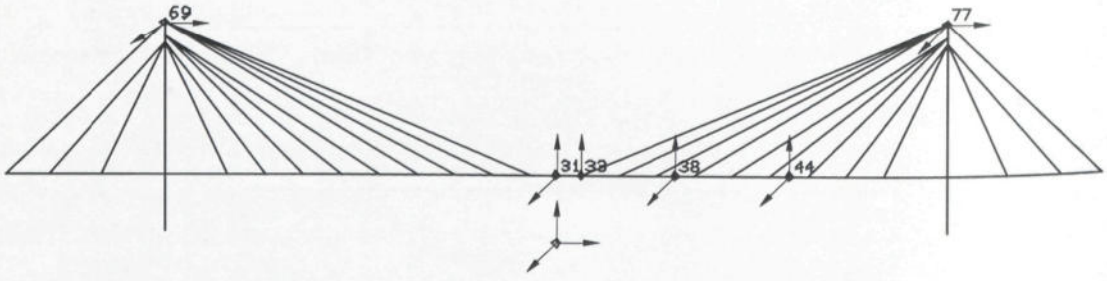


Figure 7.46. Setup employed in the sinusoidal tests. The arrows indicate directions of measurement.

Figures 7.47 and 7.48 show some of the time series collected for the first transversal and vertical symmetric modes, excited at frequencies of *3.95Hz* and *6.24Hz*, respectively.

It should be noted that the level of signal applied was relatively low, particularly for the first transversal vibration mode, as the bridge model was in effect very flexible and the

resonant excitation produced very significant levels of vibration. The consequence of this was the presence of a significant level of noise in the signal, which was removed by digital filtering in narrow frequency ranges. Figures 7.49 and 7.50 represent the results of this operation for the signals represented in Figures 7.47 and 7.48.

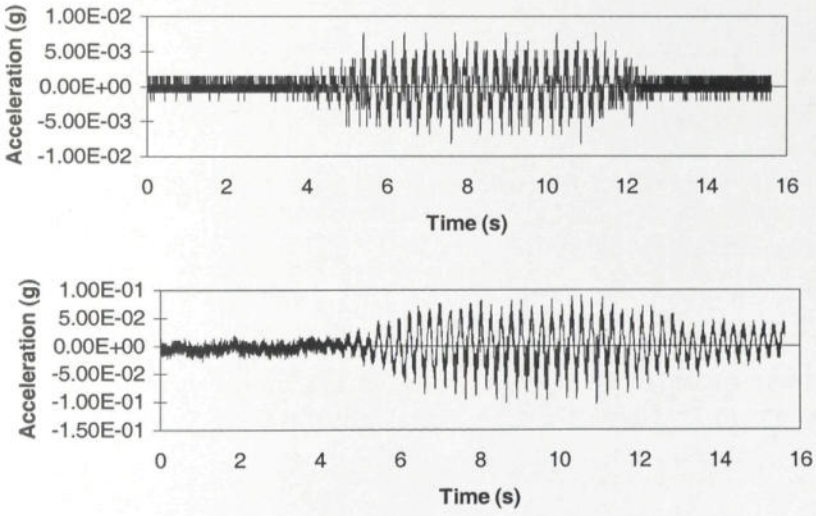


Figure 7.47. Sinusoidal excitation in transversal direction (*Y*), frequency of *3.95HZ*: (a) Acceleration at the platform (*Y*); (b) Acceleration at node *31* (*Y*).

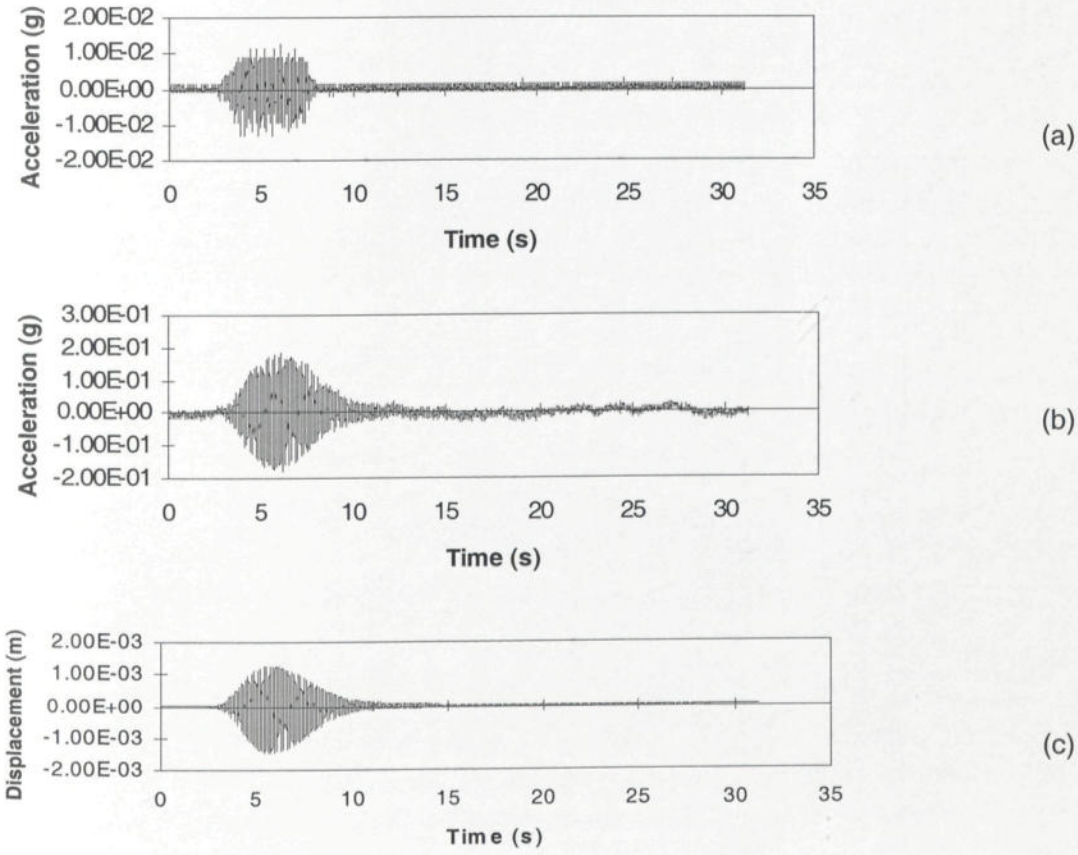


Figure 7.48. Sinusoidal excitation in vertical direction (*Z*), frequency of *6.24HZ*: (a) Acceleration at the platform (Z); (b) Acceleration at node *31* (*Z*); (c) Displacement at node *33* (*Z*).

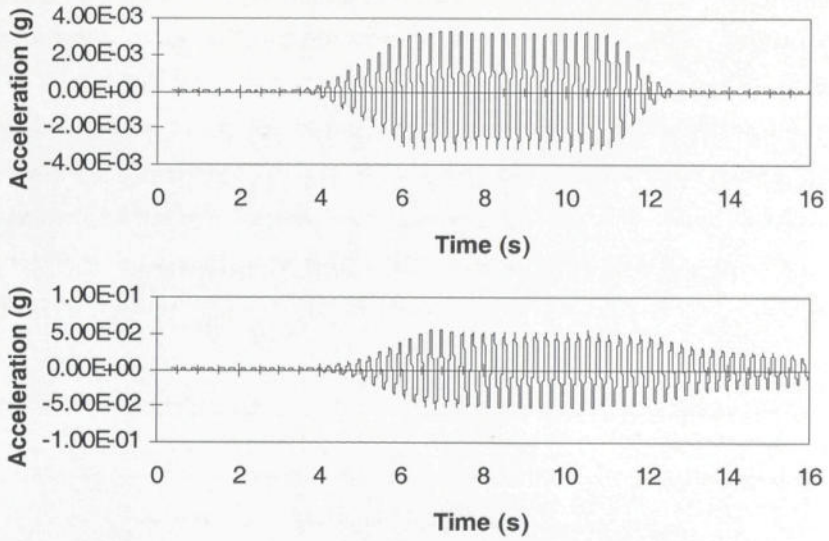


Figure 7.49. Sinusoidal excitation in transversal direction (*Y*), frequency of *3.95HZ*: (a) Acceleration at the platform (*Y*); (b) Acceleration at node *31* (*Y*). Signals filtered in the range *3.35Hz-5Hz*.

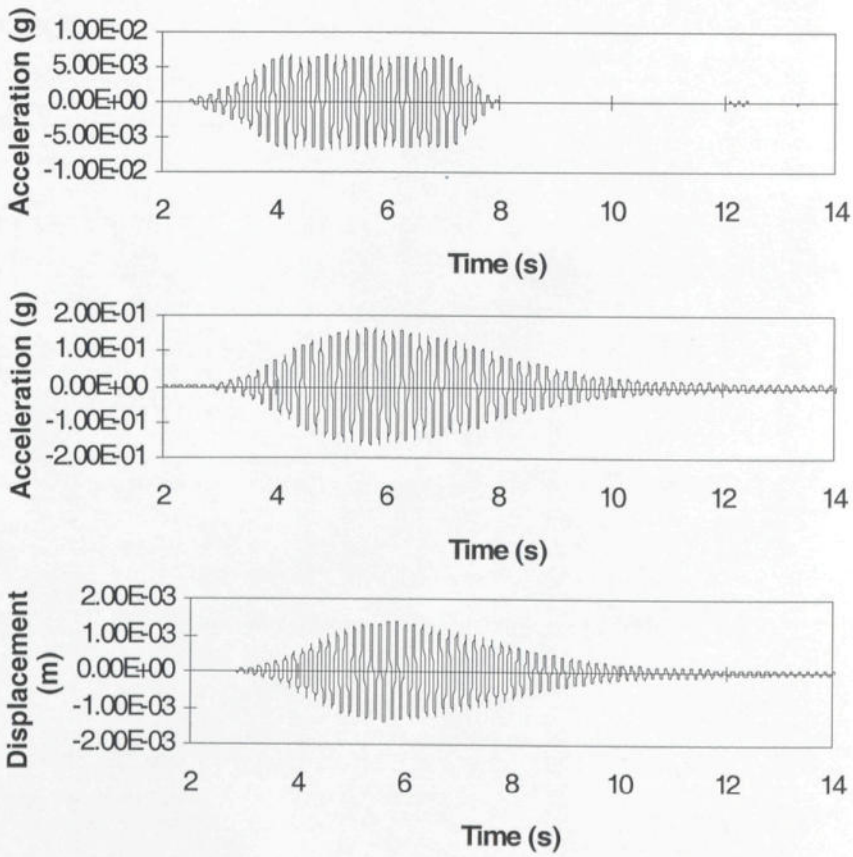


Figure 7.50. Sinusoidal excitation in vertical direction (*Z*), frequency of *6.24HZ*: (a) Acceleration at the platform (Z); (b) Acceleration at node *31* (*Z*); (c) Displacement at node *33* (*Z*). Signals filtered in the range *5Hz-7Hz*.

The identification of damping coefficients was then performed using a single-degree-of-freedom complex exponential fitting of the time series. Average damping coefficients were obtained considering a "large" time segment of free response, as for example the *8s-14s* segment of the vertical response at node *31* (Figure 7.51), for the case of vertical excitation at *6.24Hz*. Damping coefficient estimates were also extracted for shorter time segments (for example, *8s-9s*, *9s-10s*,etc) and were associated with the average amplitude of response during the periods considered. Figure 7.52 resumes the values of identified damping coefficients and associated natural frequencies and their variation with the amplitude of response at the midpoint (node *31*) for the first transversal and vertical vibration modes.

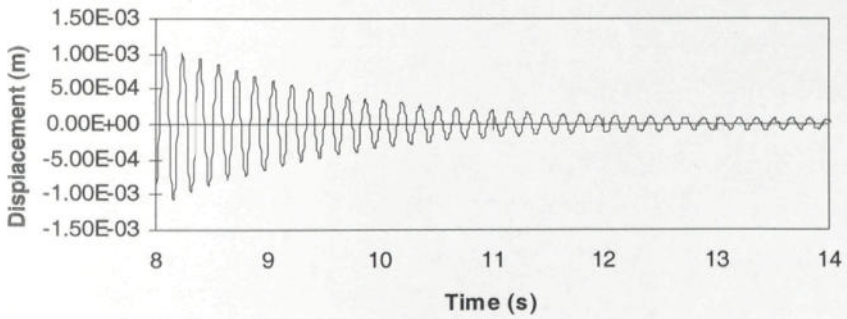


Figure 7.51. Free vibration response at node *33(Z)* after sinusoidal excitation at *6.24Hz*.

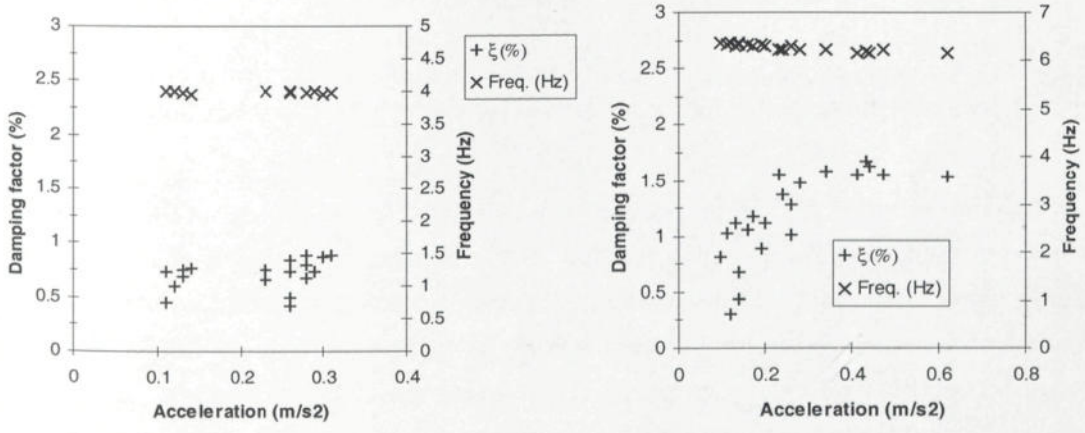


Figure 7.52. Variation of damping coefficient and natural frequency with the amplitude of vibration for the: (a) *1st* transversal; (b) *1st* vertical symmetric vibration modes (sinusoidal tests).

Although the maximum amplitudes of oscillation for the transversal mode are only about half the amplitudes of vertical vibration, the damping coefficients identified for this mode of vibration do not show variation with amplitude of oscillation, as do the damping coefficients associated with the vertical vibration mode. The later achieve in particular a significant level for high amplitudes of vibration.

It is also interesting to notice that a large discrepancy exists between damping coefficients identified for the transversal mode using sinusoidal or multi-sine excitation. Table

7.17 shows in effect that both the shaker and shaking table tests produced much higher damping coefficients (*1.65%-2.08%)* than the sinusoidal tests (*0.42%-0.89%*). Since the level of induced excitation is not comparable for the different types of tests, no clear conclusions could be extracted with respect to this fact.

On the contrary, the damping coefficients identified for the vertical vibration mode on the basis of sinusoidal and multi-sine tests show a good agreement (varying in the range *0.31%-1.67%* for the sinusoidal tests, and *0.35%-1.67%* for the multi-sine tests*)* and an identical type of variation with the amplitude of oscillation (Figures 7.52(b) and 7.53), even if the levels of vibration are not comparable for the two types of tests.

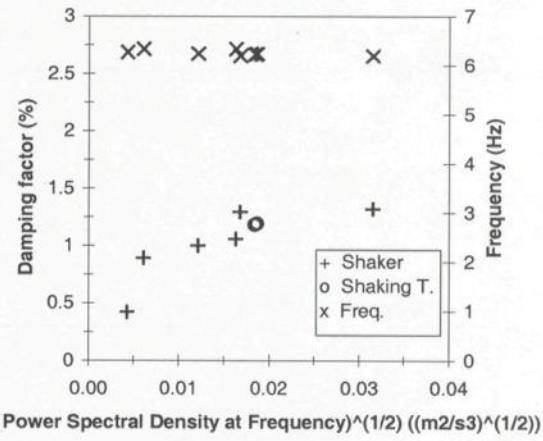


Figure 7.53. Variation of damping coefficient and natural frequency with the amplitude of power spectral density of the response for the 1st vertical symmetric vibration mode (multi-sine tests).

The identification of damping coefficients of mode shapes for higher frequencies using the sinusoidal tests was not possible, in view of the significant beating that appeared in the measured signals. In effect, when exciting the bridge at *9.20HZ*, for example, it was observed that the response occurred not only in the *9.20Hz*, but also in a range of frequencies around this resonance. This was one more prove of the existence of *cable-structure interaction* and the result is very clear in the response *FFTs* represented in Figure 7.54, corresponding to the excitation of the bridge at *9.20Hz* and *9.50Hz*. The argument that *9.20Hz* might not correspond to a bridge resonance could for example justify that the bridge responded in *9.50HZ*. But the inverse would not then occur. It is interesting to note that precisely this type of results were met and reported during the test of other physical models, as for example the Ruck-A-Chucky (Godden & Aslam, 1978) and the Zarate-Brazo Largo bridges (Castoldi *et al.*, 1972). For the later bridge, in particular, it is reported that cable vibrations occurred and the tests had to be performed at very low amplitudes of vibration in order to avoid the observed interaction.

It should also be noted that the filtering of the measured signals in narrow frequency ranges did not eliminate the beating, as shown in Figure 7.55, and so no confidence existed in the results provided by the sinusoidal tests for the higher frequency vibration modes.

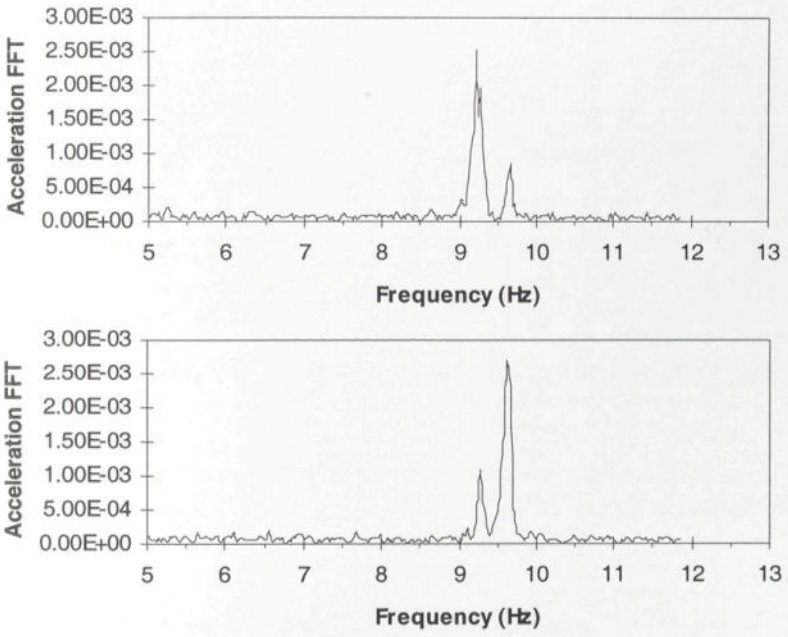


Figure 7.54. *FFT* amplitudes of the vertical response measured at node *38* when exciting the bridge in the vertical direction at: (a) *9.20Hz*; (b) *9.50Hz*.

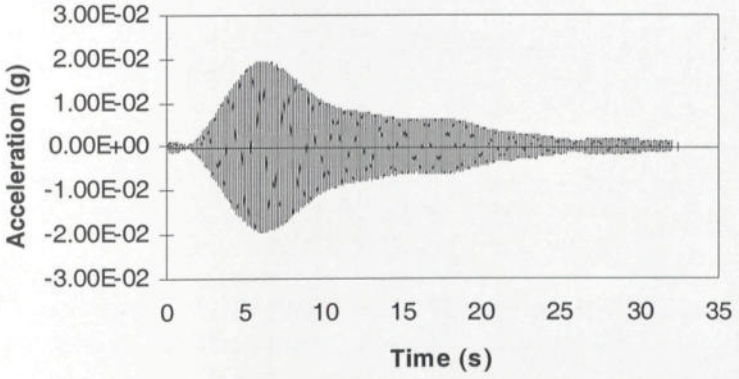


Figure 7.55. Vertical response measured at node *38*, under vertical excitation at *9.50Hz*. Signal filtered in the band *9.45Hz-9.80Hz*.

In order to understand the form of variation of the damping coefficients with the amplitude of vibration, it was decided to employ the results previously obtained from the multi-sine tests. The variation of damping coefficients with the square root of the amplitude of the response power spectrum for a specific node is represented for some groups of vibration modes in Figures 7.56 to 7.58. The different symbols employed in those figures respect the several identified natural frequencies based either on the shaker, or on the shaking-table tests.

The results presented in Figures 7.56 to 7.58 show a certain trend for an increase of the damping coefficients, but evidence also a large dispersion.

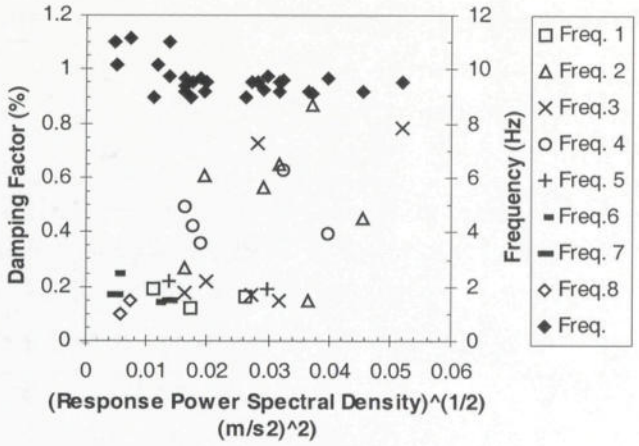


Figure 7.56. Variation of identified damping coefficients with the amplitude of response power spectrum for the group of *1st* vertical anti-symmetrical vibration modes.

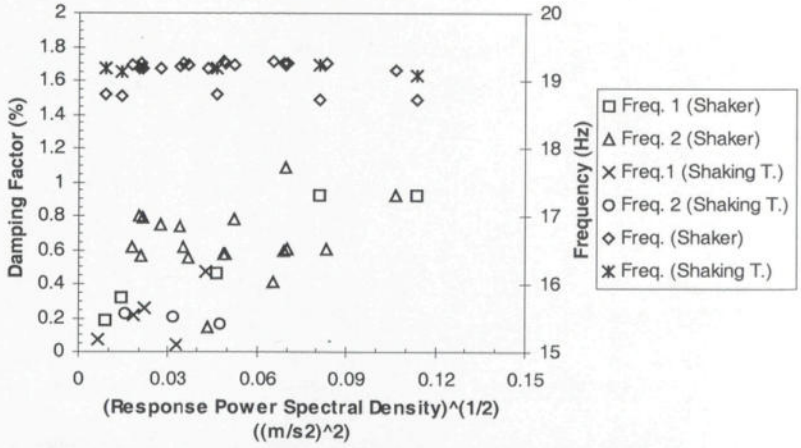


Figure 7.57. Variation of identified damping coefficients with the amplitude of response power spectrum for the group of *2nd* vertical anti-symmetrical vibration modes.

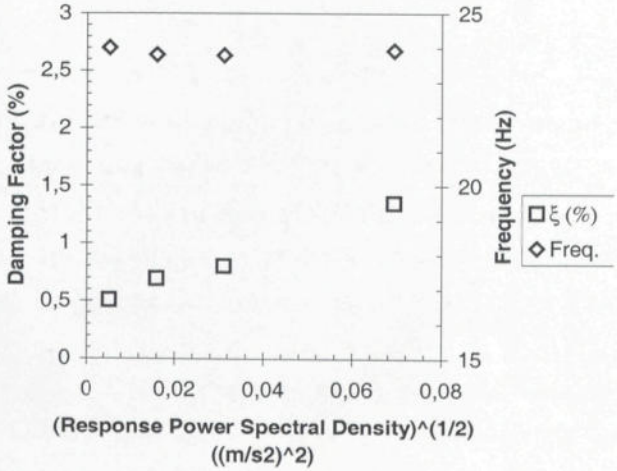


Figure 7.58. Variation of identified damping coefficients with the amplitude of response power spectrum for the group of *3rd* vertical symmetrical vibration modes.

7.5.3 Tests at the ISMES shaking table

The current Section describes a set of complementary tests conducted on a modified version of the Jindo Bridge physical model.

By suppressing the distributed mass of the stay cables and applying equivalent lumped masses at the associated anchorages, the dynamic interaction between cables and structure was eliminated, and a model equivalent to the numerical *OECS* was obtained. This model was fully tested on the largest of the *ISMES* shaking tables (*4x4m*), according to the following steps: (i) exploratory phase, multi-sine tests for assessment of dynamic properties; (ii) sinusoidal tests, for identification of damping coefficients; (iii) seismic tests, evaluation of the response to artificial accelerograms.

The main results of the first two steps of the tests will be summarized in this Section.

7.5.3.1 Modification of the Jindo Bridge model

The physical model of the Jindo Bridge was assembled, using piano wire for the stay cables of the same type of the described for the original model (see Section 7.3.2). The mass of each stay cable was lumped at the anchorages, using pieces of magnetic material with equivalent weight, as represented in Figures 7.59 and 7.60 for a section of the bridge deck, and for the anchorage at the tower, respectively.

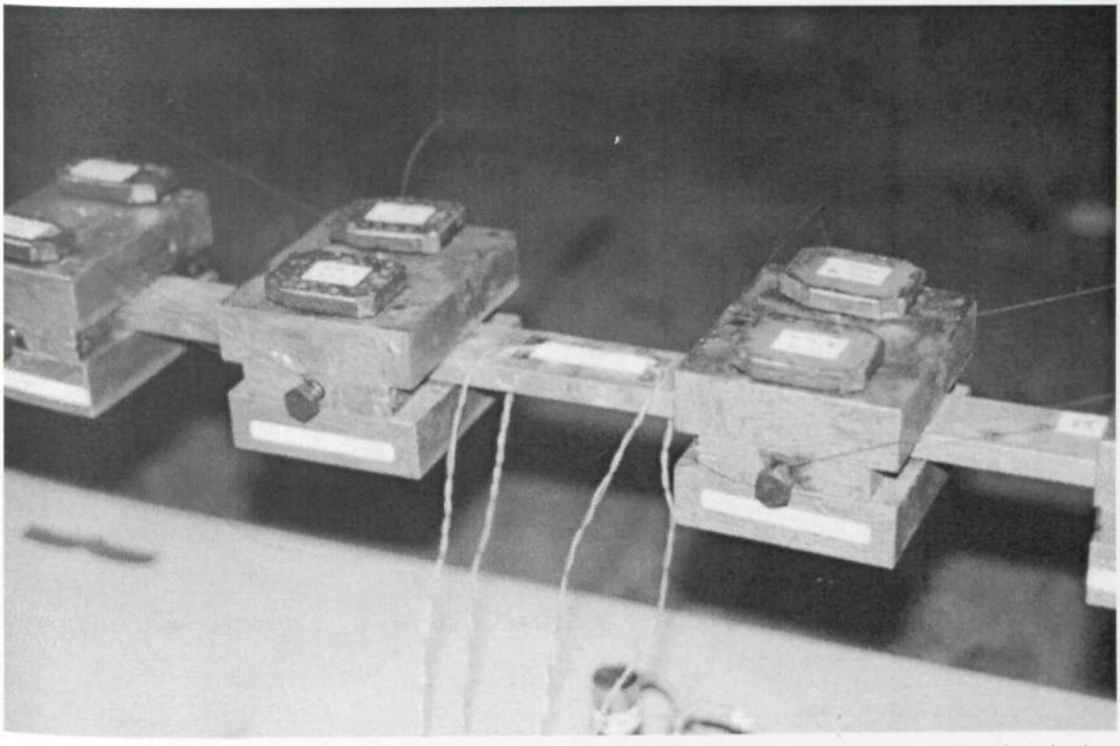


Figure 7.59. Jindo Bridge modified model. Lumping of the stay cables' masses at the deck anchorages.

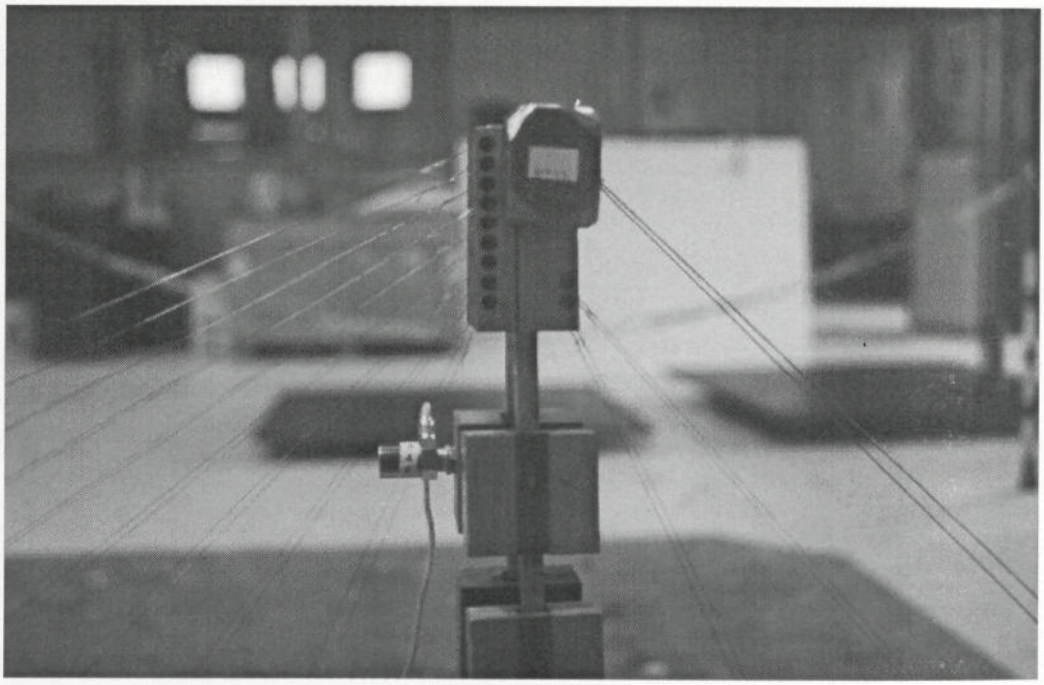


Figure 7.60. Jindo Bridge modified model. Lumping of the stay cables' masses at the tower anchorages.

7.5.3.2 Instrumentation

The only source of excitation employed during the tests was the base excitation provided by the six-degree-of-freedom shaking table at *ISMES*. The main characteristics of the facility are described in (Severn, 1998).

Figure 7.61 shows the mounting of the Jindo model on the shaking table, before application of the transducers.

A total of *32* transducers were used for vibration measurement, which were of the following types:

- *18* accelerometers *ENDEVCO*, model *2262c-25*. These are piezoresistive accelerometers, which have a sensitivity of *10mV/g* and operate in the frequency range *DC-650Hz*. The corresponding weight is *28gr*;
- *6* strain gauges *HBM*, model *1.5/120LY11*, with a resistance of *120 Ohm*. These gauges were used for measurement of both axial and bending strains;
- *8* inductive displacement transducers *HBM*, model *W20K*, with a nominal displacement of *± 20mm*. These transducers were connected to the structure using springs, in order to reduce the influence from transversal displacements;
- *1* magnetic pick-up transducer *RS*, model *285-756*. This sensor was employed for tuning the cables tensions;
- A *2*-channel Fourier analyzer *ADVANTEST*, model *R9211C*. This analyzer was employed only for the multi-sine tests.

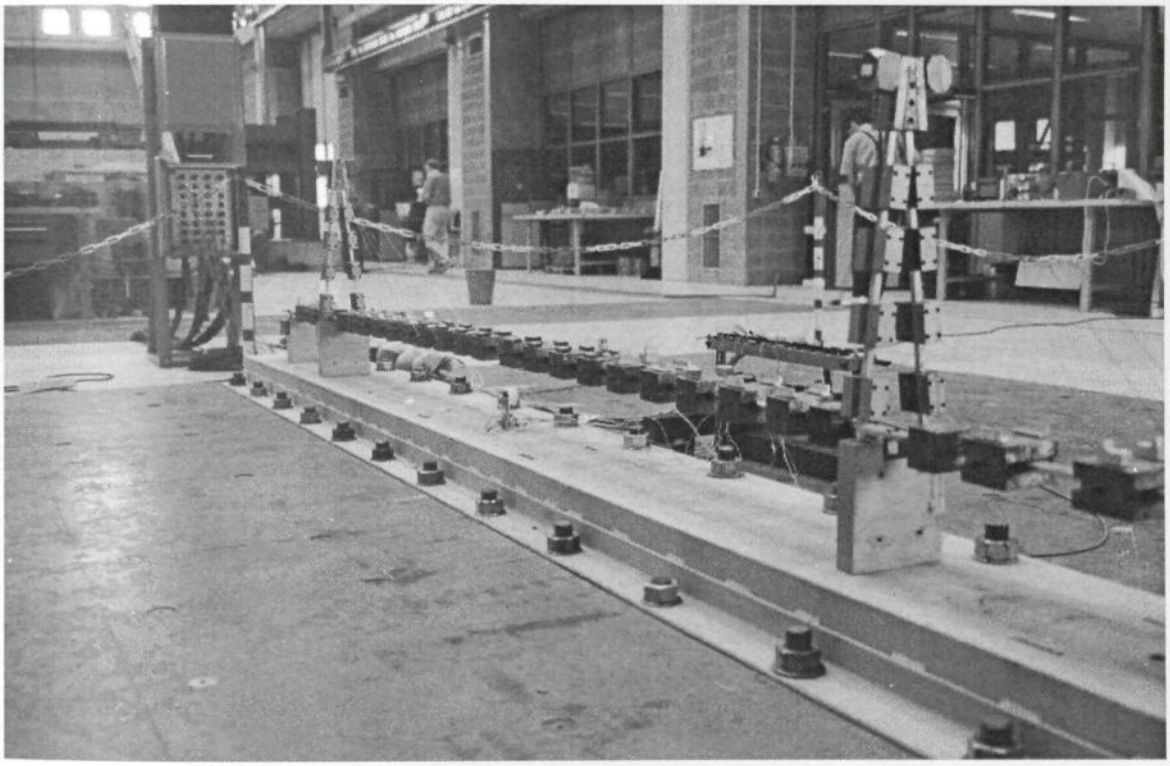


Figure 7.61. The modified Jindo Bridge model. Mounting on the shaking table.

Figure 7.62 shows the setup employed for the damping and seismic tests, indicating the different directions of measurement and types of transducers employed for each location.

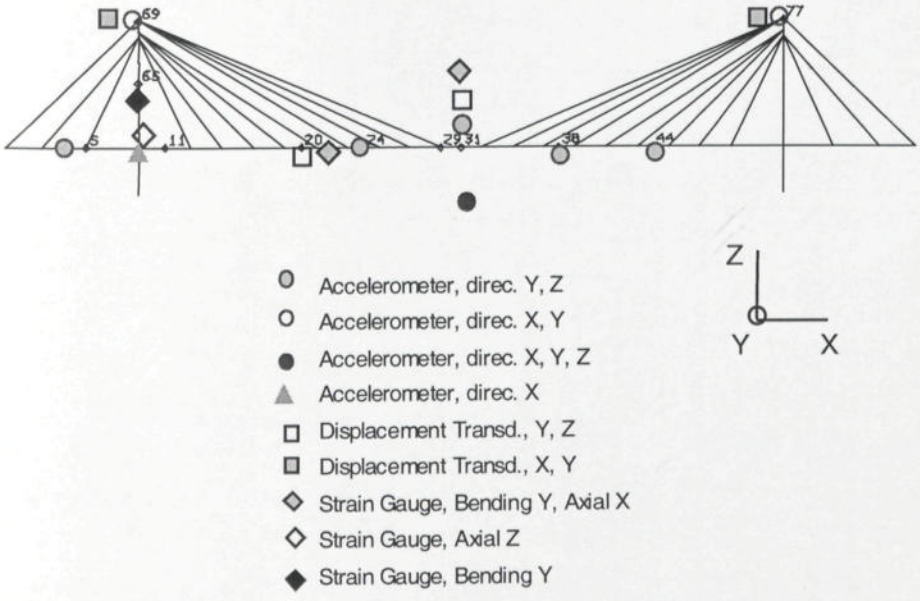


Figure 7.62. Setup employed for the tests performed at the ISMES shaking table.

Some details of the instrumentation are also presented in Figures 7.63 and 7.64. It should be noted that, because the transducers had a relatively large mass compared with the bridge model's, some of the adjacent magnetic pieces with equivalent weight were suppressed.

The data acquisition for the *32* measurement channels and the control of the shaking table were performed using the *ISTAR* system (Severn, 1998).

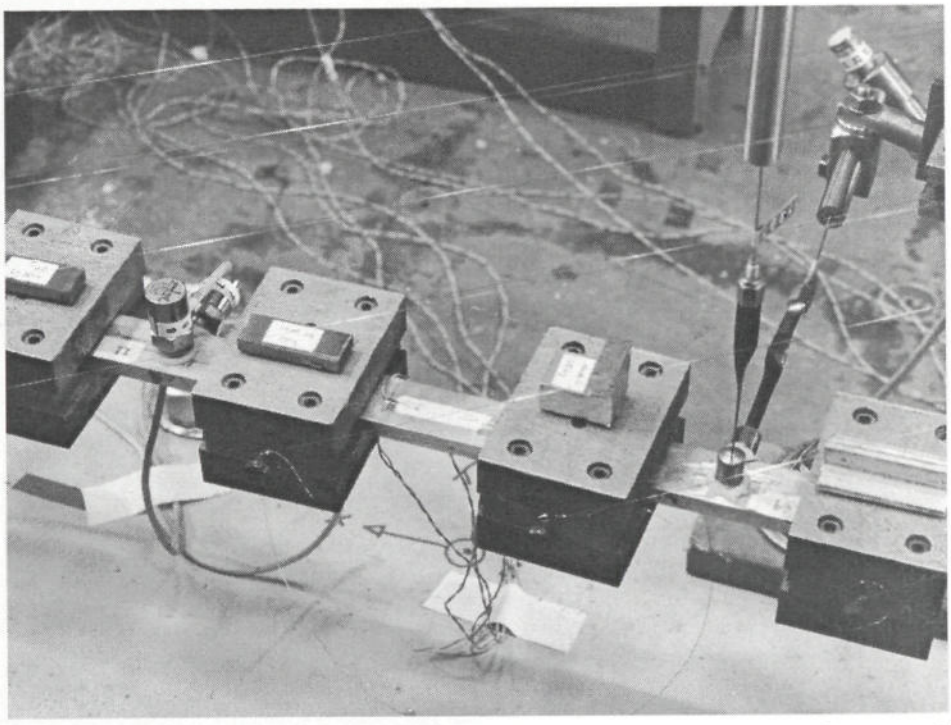
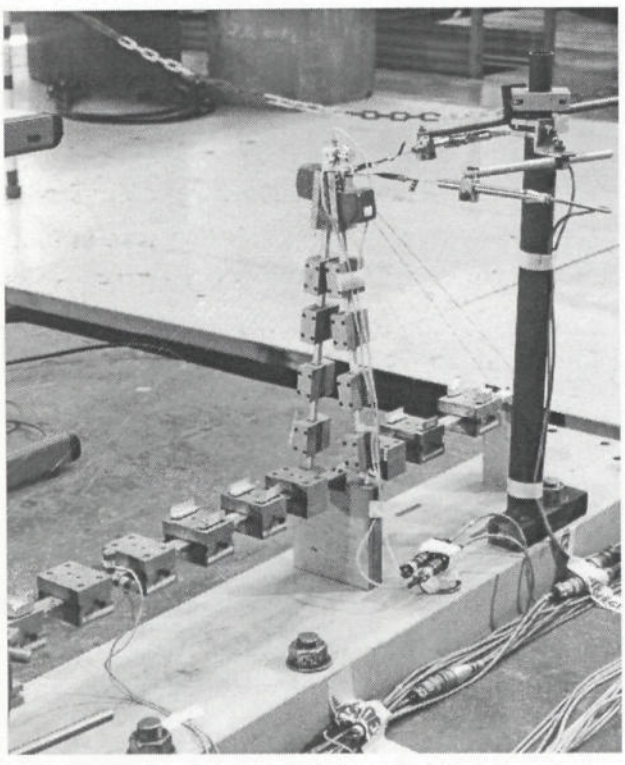
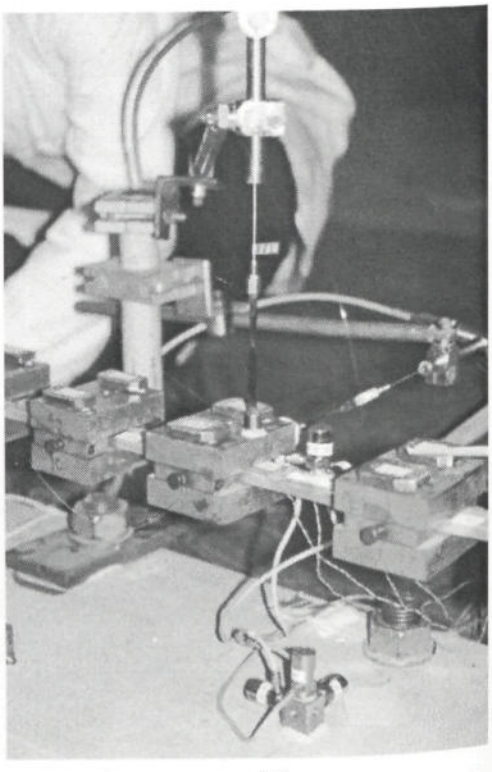


Figure 7.63. Mounting of accelerometers, strain gauges and displacement transducers on the bridge deck.



(a)



(b)

Figure 7.64. Mounting of: (a) accelerometers and displacement transducers on the bridge deck and on the top of one tower; (b) accelerometers on the frame connected to the seismic platform.

7.5.3.3 Multi-sine excitation tests

After a preliminary operation of tuning the cables tensions, using the magnetic pick-up transducer and the technique already described in Section 7.3.3, a set of multi-sine tests were performed.

The multi-sine signal generated by the *ADVANTEST* analyzer fed the shaking table along separate directions (*X*-longitudinal; *Y*-transversal; *Z*-vertical), and the *FRFs* relating the response at the base of the platform (*X*, *Y* or *Z*) and the response at particular locations and directions along the bridge deck and tower were measured, using the *ENDEVCO* accelerometers.

Some of the obtained *FRFs* and associated coherence functions are shown in Figure 7.65. The synthesized *FRFs* based on the *RFP* identification algorithm are also represented in this Figure.

The observation of Figure 7.65 shows at a first instance, that the obtained measurements were slightly noisier than the corresponding measurements obtained at the Bristol shaking table. This reveals a difficulty of exciting certain modes of vibration that was not felt with the former Jindo model. In effect, on the contrary to the Bristol tests, the excitation in the vertical and lateral directions was unable to induce at a significant level the *first* anti-symmetrical vibration modes. And the excitation in the longitudinal direction failed to induce vibrations in the first symmetrical vibration mode.

It is also well evident that no longer mode shapes appear in groups of closely spaced modes, as in the case of the model tested at Bristol, as the cable vibration effect was eliminated with the modification of the model. This aspect is very clearly observed in Figure 7.66, representing the amplitude of the measured/synthesized *FRFs* relating the lateral excitation with the response measured at the top of one tower on the original Jindo model, against the corresponding *FRF* amplitude measured on the modified model. The only vibration mode induced at the top of the tower of the later model by a lateral excitation was in fact a local mode of the tower. Figure 7.67 shows the consistency between the later *FRF* and the *FRFs* measured at points at about mid-height (node *65Y*) of the same tower and the other tower (node *73Y*) with respect to the characterization of the lateral vibration modes of the towers.

As for the quality of the *FRF* fitting, it can be observed that generally good approximation between measured and synthesized *FRFs* was obtained for the range of frequencies associated with high coherence values. Moreover, the values of identified natural frequencies are very well correlated with the corresponding values obtained on the basis of the *3-D* numerical analysis using the *OECS* model, as can be observed in Table 7.19.

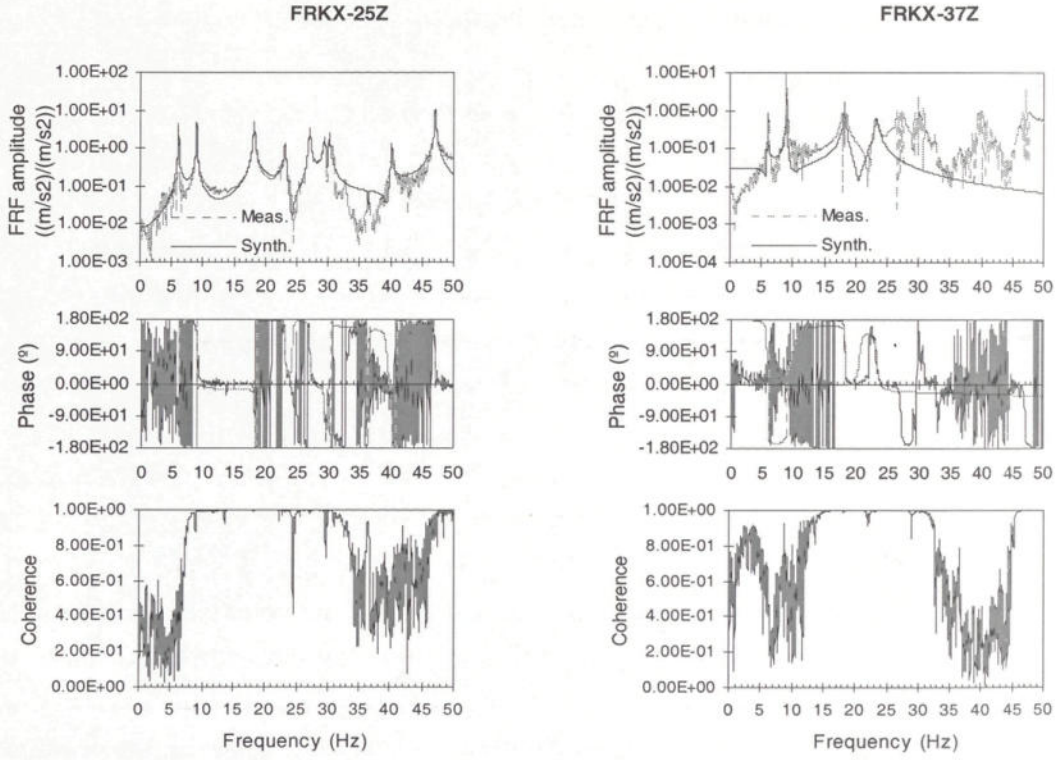


Figure 7.65 (a) Coherence and *FRF* measured from the platform acceleration in the *X*-direction (excitation) to the nodes *25Z* and *37Z* (response). Excitation in the frequency range *0-50Hz*.

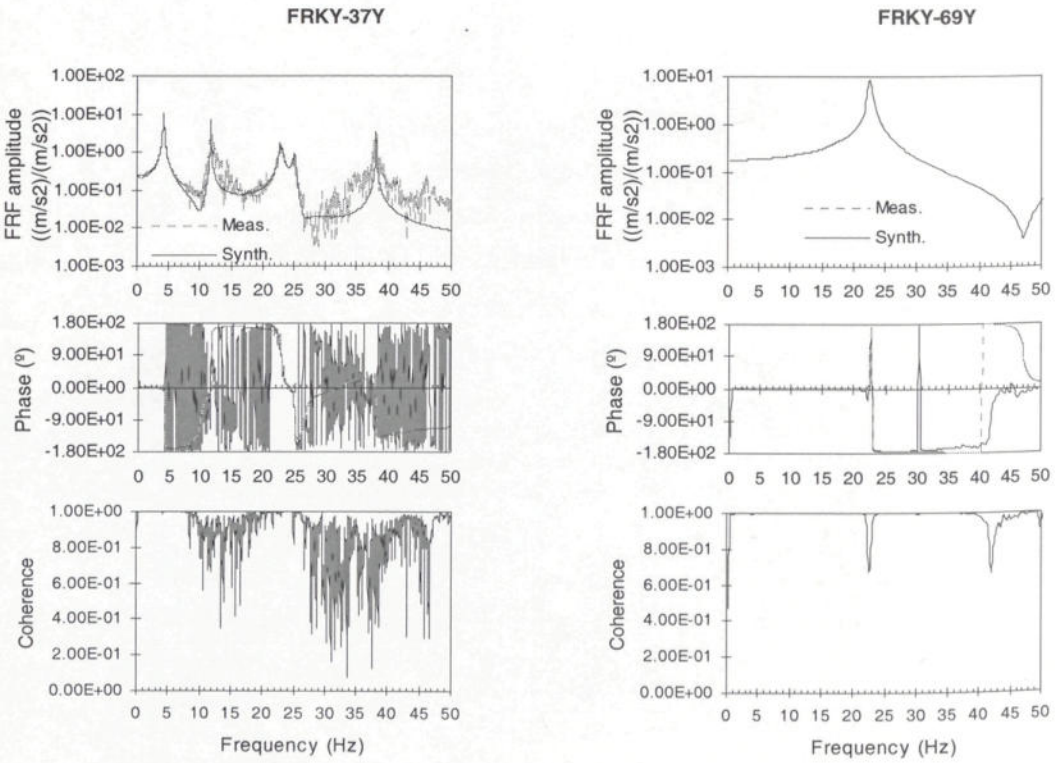


Figure 7.65 (b) Coherence and *FRF* measured from the platform acceleration in the *Y*-direction (excitation) to the nodes *37Y* and *69Y* (response). Excitation in the frequency range *0-50Hz*.

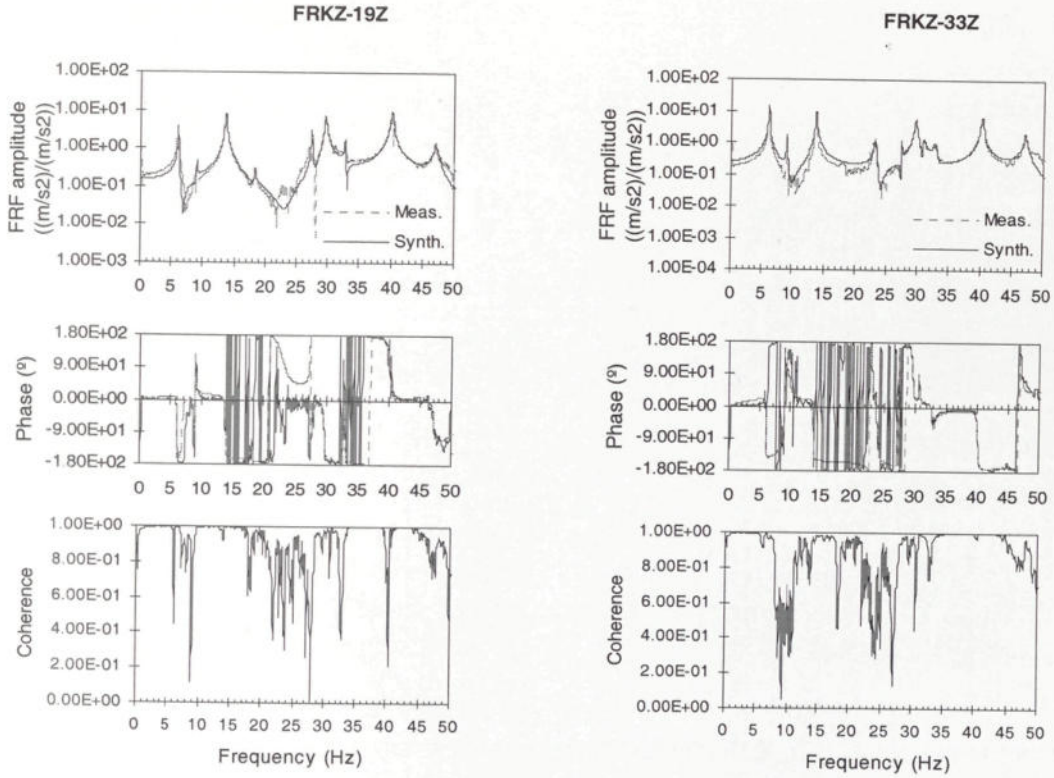


Figure 7.65 (c) Coherence and *FRF* measured from the platform acceleration in the *Z*-direction (excitation) to the nodes *19Z* and *33Z* (response). Excitation in the frequency range *0-50Hz*.

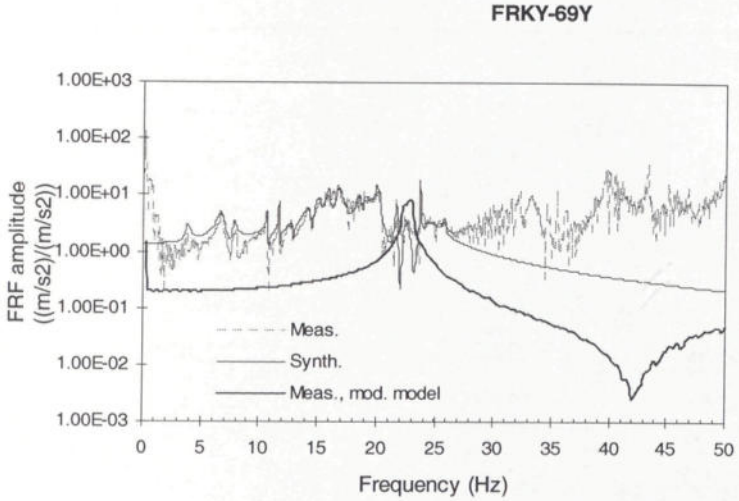


Figure 7.66. Amplitude of measured/synthesized *FRF vs* measured *FRF*, relating the lateral excitation (*Y*) with the response at node *69Y*, for the original and modified physical models, respectively.

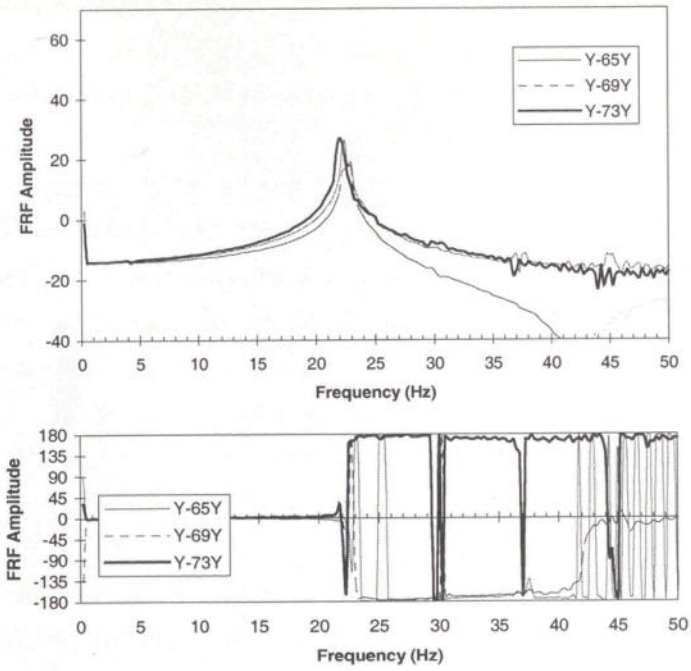


Figure 7.67. Coherence and measured *FRF* from the platform acceleration in the *Y*-direction (excitation) to the nodes *65Y, 69Y and 73Y* (response). Excitation in the frequency range *0-50Hz.*

Table 7.19. Natural frequencies identified/ calculated on the modified Jindo model.

Type of mode	Identified natural frequency (Hz)	Identified damping coefficient (%)	Calculated natural frequency (OECS, 3-D) (Hz)
1st transversal SYM	4.2	1.08	4.28
1st vertical SYM	6.00	0.32-0.69	6.21
1st vertical ASM	9.02	0.46-0.49	9.12
1st transversal ASM	-		11.71
2nd vertical SYM	13.7	0.44-0.60	13.74
2nd vertical ASM	18.3	0.34-0.45	18.26
1st LTW, 1st RTW, transversal	22.9	0.73-1.02	23.42
2nd transversal ASM	23.2	0.38-0.45	22.69

7.5.3.4 Damping tests

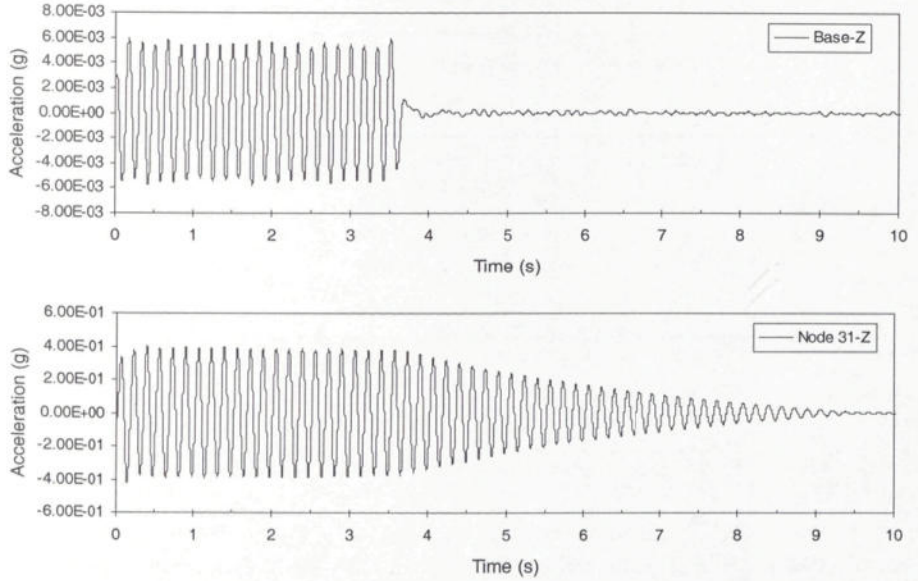
Sinusoidal tests of the type described in Section 7.5.2.3 were also performed in the modified physical model of the bridge. The response was measured using *32* transducers installed at the locations defined in Figure 7.62 for the following frequencies and directions: (i) *4.25Hz, Y* (*1st* transversal *SYM* vibration mode); (ii) *6.0Hz, Z* (*1st* vertical *SYM* vibration mode); (iii) *9.02Hz, X* (*1st* vertical *ASM* vibration mode); (iv) *13.75Hz, Z* (*2nd* vertical *SYM* vibration mode).

The time series were sampled at *500Hz*, collecting a total of *8192* points, i.e., about *16s* long records. A difference to the test performed at Bristol was that no time window was applied to the sinusoidal input, which was suddenly stopped after about *20* cycles of sine excitation.

Figures 7.68 to 7.70 show the acceleration records at some locations for three of the excitation frequencies: vertical direction (*Z*), frequencies of *6.0Hz* (Figure 7.68) and *9.02Hz* (Figure 7.69), and lateral direction (*Y*), frequency of *4.25Hz* (Figure 7.70).

It should be noted that the measured responses were filtered in relatively large frequency ranges (*8Hz-9Hz* wide), as there was no significant noise or resonance in the vicinity of the first few vibration modes. And, naturally, no beating was detected for the 1st vertical anti-symmetric mode (*9.02Hz*), as in the tests performed at Bristol on the original physical model.

The average identified damping coefficients for the first four vibration modes are resumed in Table 7.20, and attain a rather significant value, compared with the corresponding values identified on the basis of the multi-sine tests (see Table 7.19). The only explanation found for this fact is that the frames that supported the displacement transducers introduced some additional damping into the bridge vibration. In effect, these frames had not been installed when the multi-sine excitation tests were performed. For this reason, the damping coefficients identified on the basis of these tests will be considered more representative of the behaviour of the bridge.



(a)

(b)

Figure 7.68. Sinusoidal excitation in vertical direction (*Z*), frequency of *6.0Hz*: (a) Acceleration at the platform (*Z*); (b) Acceleration at node *31(Z)*. Signals filtered in the range *2Hz-10Hz*.

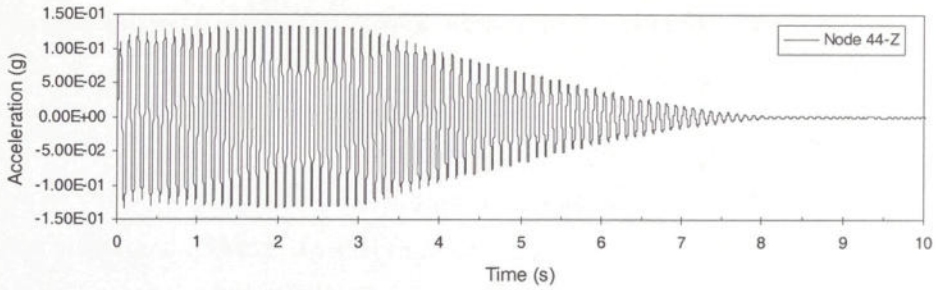


Figure 7.69. Sinusoidal excitation in vertical direction (*X*), frequency of *9.02Hz*: Acceleration at node *44(Z)*. Signal filtered in the range *3Hz-15Hz*.

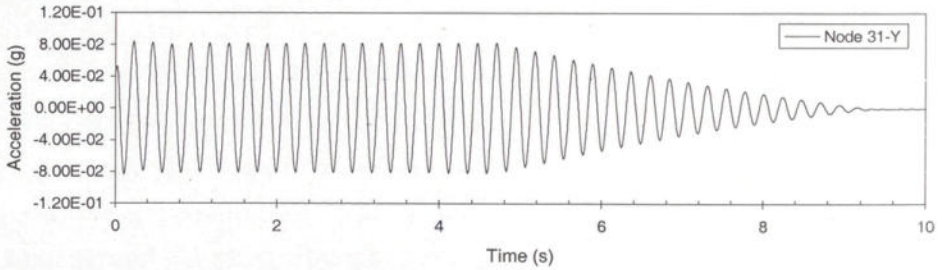


Figure 7.70. Sinusoidal excitation in vertical direction (*Y*), frequency of *4.25Hz*: Acceleration at node *31(Y)*. Signal filtered in the range *1Hz-10Hz*.

Table 7.20. Identified damping coefficients from sinusoidal tests.

Natural frequency (Hz)	Average identified damping coefficient (%)
4.25	1.36
6.0	1.29
9.02	1.22
13.75	0.86

7.6 AMBIENT VIBRATION TESTS ON THE BRIDGE PROTOTYPE

This Section presents the results of a set of ambient vibration tests performed by an American Consulting Company, *Construction Technology Laboratories, Inc. (CTL)*. The data was collected in the context of the installation of a monitoring system on the bridge, and was kindly supplied to the author. Unfortunately, as the purpose of the tests was checking the instruments and data acquisition system, only a few time series were collected in a relatively short time. So, it was not possible to perform a full identification of dynamic parameters of the bridge

prototype. However, it was considered of interest to compare the main observed results with the corresponding results from the tests on the physical model.

7.6.1 Monitoring system

The monitoring system installed on the Jindo Bridge comprehends two separate data acquisition systems, one installed on the North side of the bridge (right tower), and another installed on the South side (left tower). Each of these systems has *16* channels for data acquisition, although only *15* channels were available for measurements.

Figure 7.71 represents the location of the several instruments on the bridge, which are: (i) *3* triaxial accelerometers, located at each of the bridge abutments and at the deck support on the North tower; (ii) *20* uniaxial accelerometers, *4* of which are installed at the midspan (*2*) and top of towers, while the others are installed at specific stay cables; (iii) *2* anemometers, located at each of the towers, one at the deck level and the other at the top of a tower.

It should be noted that all the uniaxial instruments were installed in such a way that only in-plane measurements were performed.

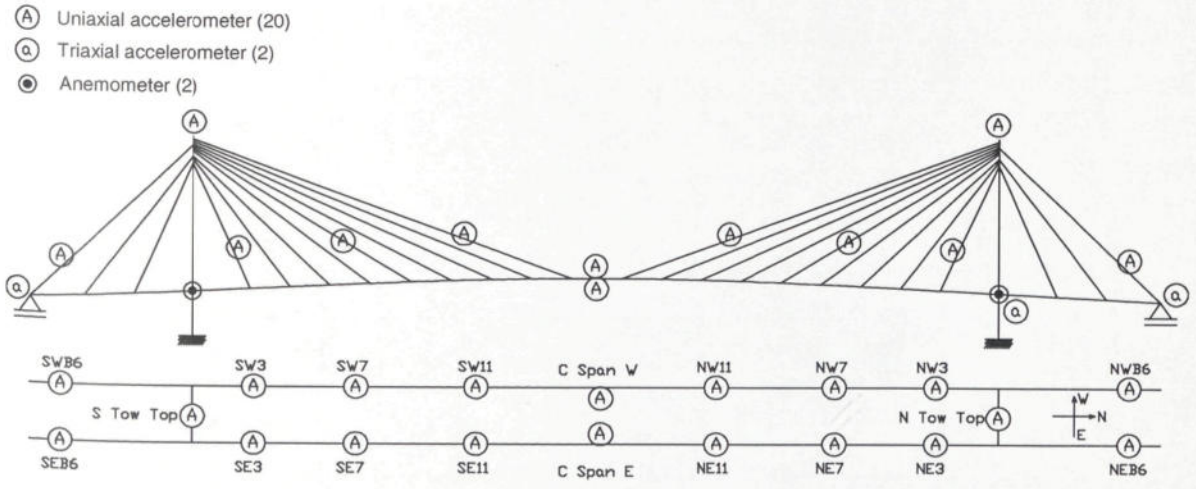


Figure 7.71. Type and location of instruments employed in the monitoring system of the Jindo Bridge prototype.

7.6.2 Ambient vibration tests

The time series supplied to the author comprehended two scans. These involved measurements taken at all the locations shown in Figure 7.71, except the abutments. All the time series were sampled at *20Hz* for *100s*, so each record contained a total of *2000* points.

Figure 7.72 shows some of the measured time records during the first scan for transducers connected to the data acquisition system installed in the North tower. The first two

records in that Figure represent the wind speed expressed in *m/s*, and the corresponding direction with respect to the North.

It is clear from both Figures that the wind speed kept rather low and stationary during the *100s* measured. Spatial stationarity did not exist, however, as shown by the graphic presented in Figure 7.73, concerning the variation of wind speed with direction at the two towers. Note that the two records were not obtained simultaneously, but the delay was only of a few seconds.

The observation of the simultaneous response at various locations shows the three-dimensional character of the response and significant differences between measurements performed on the East and West pairs of stay cables.

It is also observed that some of the stay cables occasionally vibrate at higher levels of vibration. This is for example the case of cable *NE-7* (Figure 7.72(i)). The amplification of the response in that stay cable is not however simultaneous with the perturbation induced on the deck and towers, but occurs some time later.

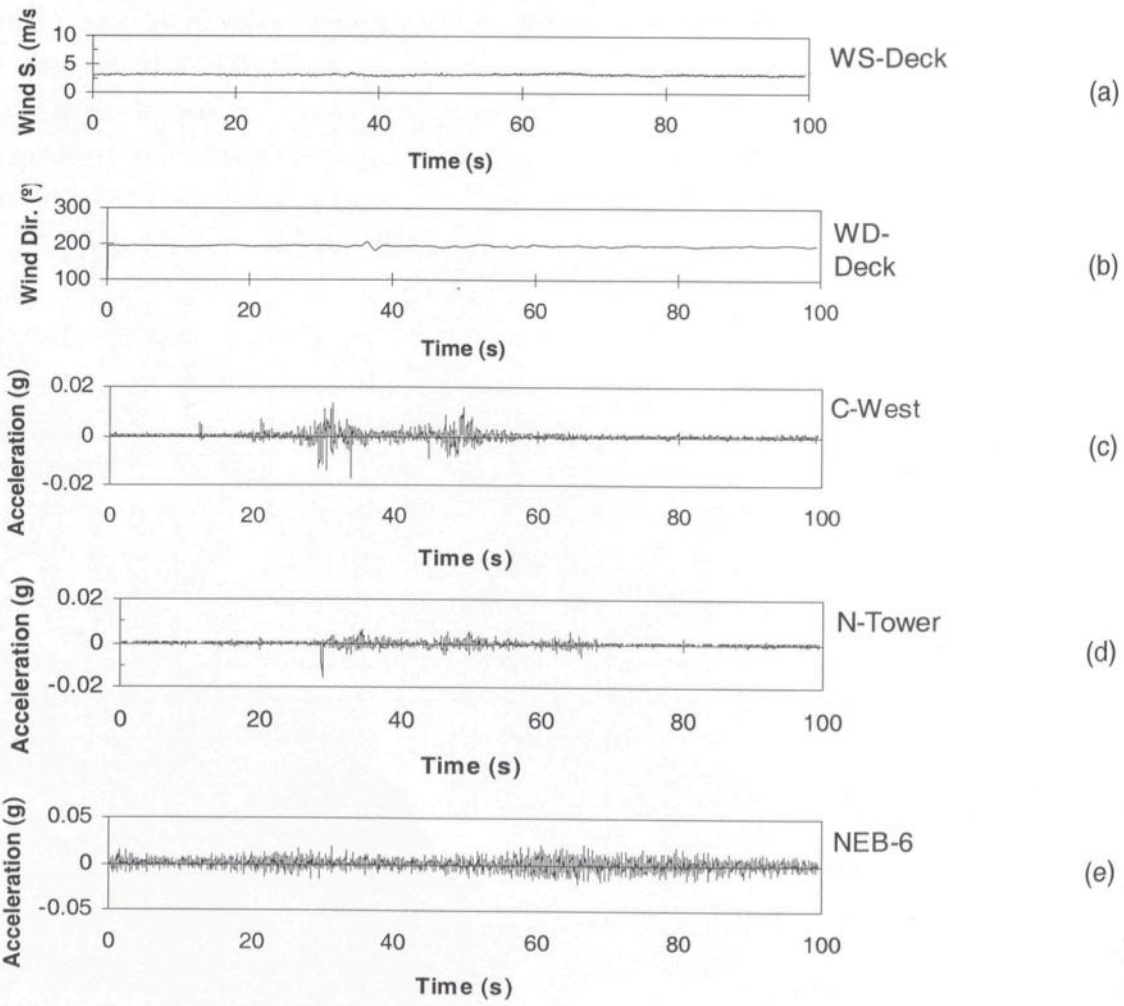


Figure 7.72. Time series recorded with the data acquisition system installed on the North tower. Scan 1.

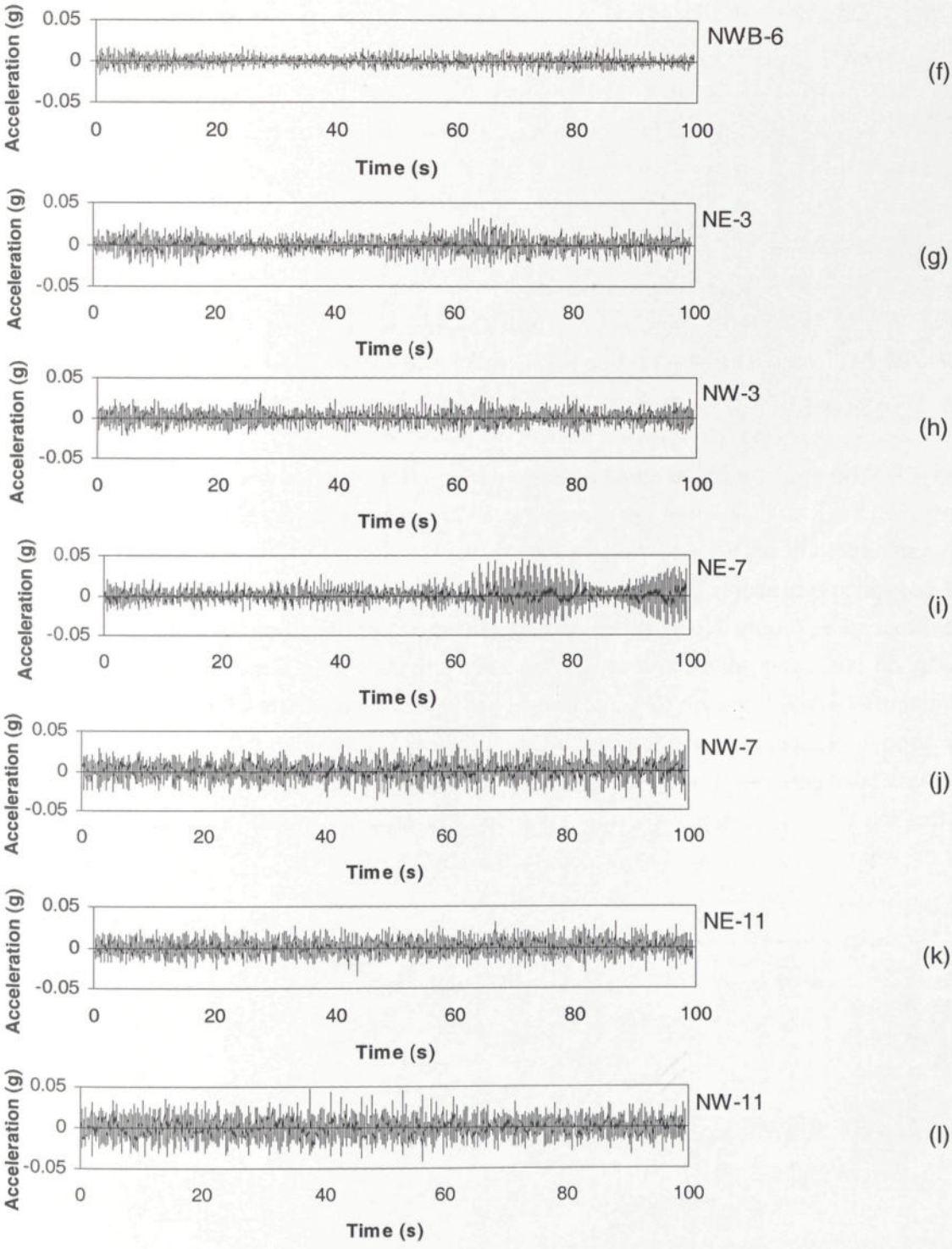


Figure 7.72 (continuation). Time series recorded with the data acquisition system installed on the North tower. Scan 1.

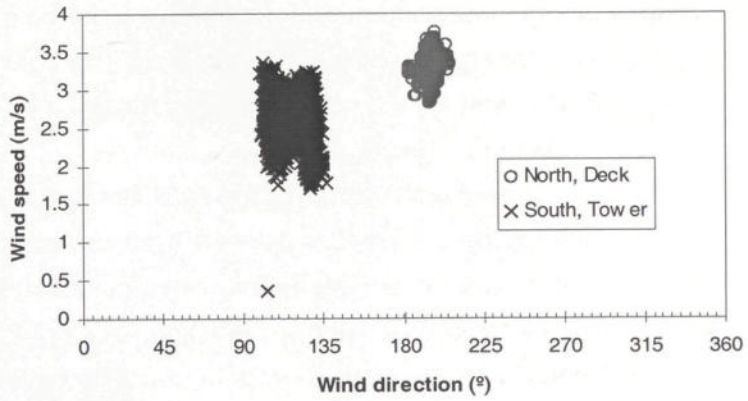


Figure 7.73. Variation of wind speed with direction at the North (deck level) and South (top) towers. Scan 1.

The analysis of the spectral content of the responses at midspan and top of the towers allowed the identification of systematic peak values that are very close to the scaled values of the natural frequencies identified for the physical model. An example of this is shown in Figure 7.74, which represents the *Power Spectral Density* estimates (*PSDs*) at locations C-East and *S-Tower* (see Figure 7.70). These were obtained simply based on the *2000* points time series, with no smoothing of estimates, as the available data was rather restricted. The response measured at the midspan (*C-East*) shows two relevant peaks at *0.51Hz* and *1.04Hz*, while the response measured at the top of the South tower (*S-Tower*) shows a peak at *0.72Hz*. These values are consistent with the first two symmetric and the first anti-symmetrical vertical vibration modes, respectively, measured on the physical model, and summarized in Table 7.21, after appropriate scaling.

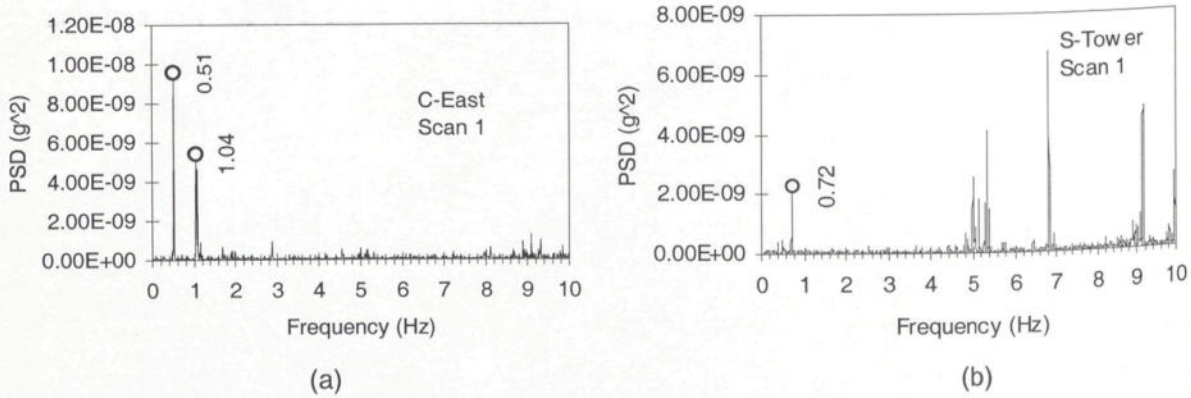


Figure 7.74. *PSD* estimates of the time responses measured at: (a) *C*-East; (b) *S*-Tower.

Table 7.21. Natural frequencies identified on the physical model, scaled to the bridge prototype.

Type of mode	Identified natural frequency (Hz)	Peak of *PSD* on the prototype (Hz)
1st vertical SYM	0.51	0.51
1st vertical ASM	0.70-0.91	0.72
2nd vertical SYM	1.17-1.21	1.04

Finally, the analysis of the spectral content of the records measured at the stay cables allowed the estimation of the tensions installed in the stay cables. The comparison of these values with the corresponding design values can give an idea of the state of degradation and possible occurrence of damage in some of the stay cables.

Figure 7.75(a) represents the Fourier spectrum of the response measured at stay *SE-7* (Figure 7.70). Among the various harmonics associated with the cable vibration, a peak at *0.72Hz* is also visible, that should correspond to the *first* anti-symmetrical vibration mode of the bridge, given the configuration of this mode. On another hand, it is also observed that the successive cable harmonics lie very closely to a straight line in the representation of Figure 7.75(b). This clearly evidences the fact that nonlinear effects due to sag or bending are not significant and so the use of the vibrating chord theory is adequate for identification of cable tensions.

Table 7.22 resumes the values estimated for the cable tensions at the stays that were instrumented, providing a comparison with the corresponding design values. A rather good agreement between those values can be in general observed, with differences in the tensions lower than *10%*, except for the pair of stays *SE-7*, *SW-7* (Figure 7.71), where the measured tensions exceed by about *20%* the design tensions.

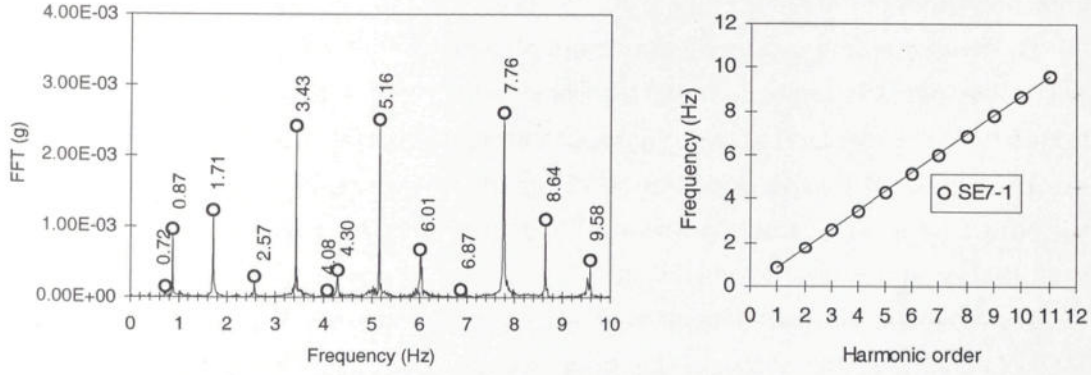


Figure 7.75. Response measured at stay *SE-7*, Scan 1: (a) Fourier spectrum; (b) Frequency vs harmonic order.

Table 7.22. Comparison between estimated and design tensions in some stay cables.

Stay	Design tension (kN)	Estimated tension (kN)	Relative difference (%)	Stay	Estimated tension (kN)	Relative difference (%)
SE-B6	1417	1493	5.4	NE-B6	1492	5.3
SW-B6		1550	9.4	NW-B6	1521	7.3
SE-3	583	601	3.1	NE-3	540	-7.4
SW-3		585	0.34	NW-3	547	-6.2
SE-7	912	1096	20.2	NE-7	1024	12.3
SW-7		1096	20.2	NW-7	977	7.1
SE-11	1488	1541	3.6	NE-11	1593	7.0
SW-11		1541	3.6	NW-11	1593	7.0

7.7 CONCLUSIONS

The main objective of this Chapter was to describe an experimental investigation developed by the author at the Earthquake Engineering Research Centre of the University of Bristol, concerning the study of the dynamic behaviour of the physical model of an existing cable-stayed bridge, the Jindo Bridge (South Korea, 1995).

Starting with a brief description of the bridge prototype and of an already existing physical model, the Chapter describes the modifications introduced in this model so that the effect of mass distribution of the stay cables might be dully accounted.

The main dynamic characteristics of the new physical model were then evaluated numerically. A preliminary analysis considered only *2-D* formulations, while more refined models were used later in *3-D* analyses. In both cases two types of numerical models were developed, which were designated as *OECS* and *MECS*. The *OECS* was a finite element model of the physical model that idealized each stay cable as a single truss element, not considering thus the effect of mass distribution, i.e., the dynamic behaviour of the stay cables. The *MECS* idealized each stay cable as a series of *12* truss elements and so assumed the distributed mass of the stays lumped at *11* nodes along the cables, i.e., considered the dynamic behaviour of the stays in the global dynamics of the bridge.

By comparing the dynamic parameters obtained on the basis of the *OECS* and *MECS* models, it was possible to observe that the consideration of the cable dynamics in the study of the bridge behaviour yielded a very numerous set of vibration modes. These modes defined a pattern characterized by the appearance of groups of modes closely spaced in frequency, characterized by a similar configuration of the deck and towers, but involving motions of different cables, and different levels of cable-structure interaction.

An extensive series of tests was then conducted on the physical model with the purpose of confirming this finding, using both an electrodynamic shaker and the shaking table from the University of Bristol. Generally rather high coherences were obtained for the set of measured *FRFs*, and a great consistency between results obtained on the basis of the two different excitation systems was also found, proving that the formed data base was of very good quality. Moreover, it was also possible to confirm the existence of dynamic interaction between the stay cables and the deck and towers, and a pattern similar to the one identified from numerical analysis was found. The appearance of the groups of closely spaced modes proved to be conditioned by the closeness between a natural frequency of the global structure and the natural frequencies of some cables.

Comparing the experimental data with the results from the numerical analysis, generally good agreement was found in terms of the values of natural frequencies and corresponding modal shapes associated with the deck and towers. There was not however a perfect correspondence between the cable motion observed and the corresponding motion that resulted from finite element analysis. This was attributed to the following two main reasons: (i) the difficulty in accurately reproducing in the numerical model all the features of

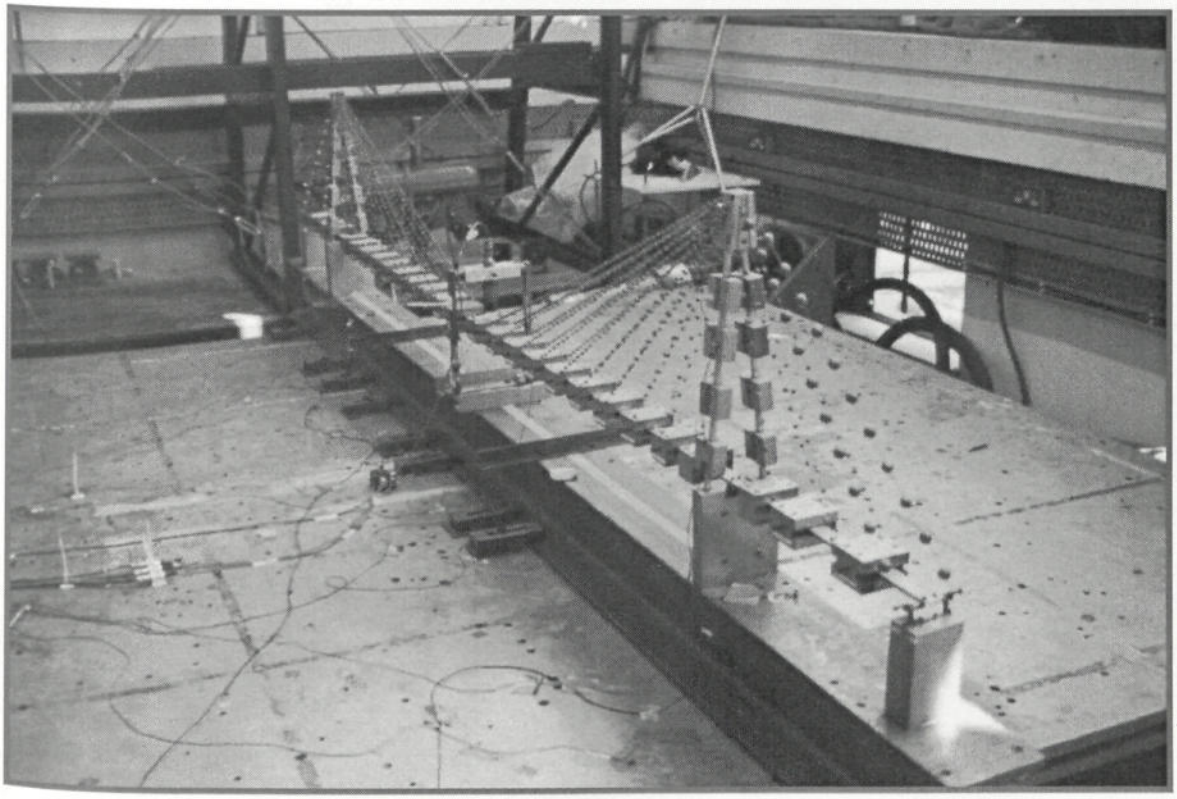
the physical model; (ii) the existence of slight imperfections in the numerical model, which might have resulted in a certain loss of symmetry with respect to the numerical results.

An additional proof of existence of cable-structure interaction was obtained with another series of tests performed at the *ISMES* shaking table on a modified version of the physical model previously employed, where the effect of mass distribution along the stay cables was eliminated. This was an experimental version equivalent to the *OECS* studied numerically. The modal survey developed on this later structure showed an extremely good correlation between experimental and numerical results, and showed also no evidence of the groups of closely spaced vibration modes around each global resonance, as the former model.

Finally, and as curiosity, the data obtained recently from a set of ambient vibration tests on the Jindo Bridge prototype was analyzed. The available time series had very short durations, not allowing thus the averaging of spectral estimates, nor a sufficient frequency resolution for possible identification of cable-structure interaction. However, it was possible to identify the main global natural frequencies, which correlated very well with the corresponding to the physical model, and it was also possible to estimate the tensions installed in eight pairs of stay cables. These tensions showed in general relatively small discrepancies with regard to the design tensions, what is a good indicator of the proper behaviour of the bridge prototype *10* years after construction.

CHAPTER 8

THE EFFECT OF DYNAMIC CABLE-STRUCTURE INTERACTION IN THE GLOBAL RESPONSE TO SEISMIC EXCITATION



CHAPTER EIGHT

THE EFFECT OF DYNAMIC CABLE-STRUCTURE INTERACTION IN THE GLOBAL RESPONSE TO SEISMIC EXCITATION

8.1 GENERAL

In the previous Chapter the phenomenon of *dynamic cable-structure interaction* was identified and characterized on the basis of the physical model of the Jindo Bridge.

A question that arises now is to know how this interaction phenomenon affects the response to dynamic excitations.

Starting to search in the literature survey presented in Section 6.4.1, two apparently contradictory opinions have been sustained by different authors: (i) the idea that the stay cable vibration contributes to the development of an additional damping (*system damping*) in the structural response (Leonhardt & Zellner, 1980), therefore having a favourable role with respect to the global dynamic bridge behaviour; (ii) the idea that the vibration of the stay cables may induce vibrations of the deck and /or towers, being thus unfavorable to the global bridge behaviour. The later theory was supported by Abdel-Ghaffar and Khalifa (1991), who performed a numerical modeling of a long-span cable-stayed bridge and realized that the vibration of the stay cables originated the appearance of a numerous set of vibration modes involving simultaneous motion of the stays, deck and towers, and having non-neglectable participation factors for seismic excitation. Moreover, Abdel-Ghaffar and Khalifa emphasized the risk of premature damage of the stay cables in consequence of fatigue caused by vibration of the cables.

It is interesting to note that the practical observation of the phenomenon of cable-structure interaction is not more conclusive, as both theories seem to find support. In effect, several cases reported in the literature refer the observation of significant vibration of the deck induced by the oscillation of the stay cables. On another hand, Virlogeux (1998) reports the case of a bridge that experienced significant cable vibrations where, in an attempt to reduce these oscillations, cross-cables were installed in the staying system. This measure was effective in mitigating the cable vibrations, but led to a significant increase of the deck vibrations. Virlogeux considered that the original vibration of the stay cables was, at least partially, due to the effect of deck vibrations produced by wind, i.e., was due to indirect excitation by wind. But it was the cables, through intense vibrations that acted as dampers for the deck movements.

The present Chapter attempts to present a deeper insight into the importance of the *cable-structure interaction* phenomenon in terms of the response to seismic excitation. The study involved an experimental component that consisted of a series of shaking table tests of the Jindo Bridge physical model, using different types of artificial accelerograms as input. The measured response was then used to validate finite element models previously developed, in which the cables were idealized either as simple truss elements, or as sets of several truss elements (multiple link method).

The analysis and comparison of the experimental and calculated responses obtained under each of the two finite element models developed, *OECS* (*One-Element Cable System*) and *MECS* (*Multi-Element Cable System*), showed, as will be demonstrated later, the following main aspects: (i) a relatively good correlation between the experimental and calculated responses predicted by both numerical models; (ii) some slight differences between the *OECS* and *MECS* responses, which did not reveal however any significant "system damping" effect for the type of excitation considered.

Two different numerical simulations were subsequently performed, in order to enhance and better understand this situation. The first consisted of modifying the natural frequency of the fundamental mode of vibration to the range of the first frequency of the cables. The second corresponded to the analysis of the response of the Jindo model to a severe high amplitude base excitation defined in a narrow frequency range, containing both a natural frequency of the structure, and the *first* frequencies of some cables. It was found that the cable interference with global oscillations may cause a significant decrease of the bridge response (with regard to standard *OECS* analysis, where the local behaviour of the cable is not modelled). However, this "system damping" may not develop in the case where a narrow band excitation is applied. In this case, the large amplitude of vibration of some cables may cause significant nonlinearity and induce higher order modes, causing therefore an increase of the response.

8.2 THE JINDO BRIDGE MODEL

8.2.1 Modal participation factors

The physical model of the Jindo Bridge was already described in Section 7.3.2 and the corresponding dynamic properties were identified based on experimental tests. Moreover, the experimental data was used to validate two numerical finite element models: the *OECS* (*One-Element Cable System*) and the *MECS* (*Multi-Element Cable System*). The two models idealize the structure as an assemblage of beam and truss elements and differ only in the number of truss elements used to represent the stay cables. The *OECS* employs a simple truss element to describe each stay cable, while the *MECS* idealizes each cable as a set of several truss elements.

The calculation of natural frequencies and mode shapes presented in Section 7.4.2 was based on a tangent stiffness matrix, obtained at the end of a geometric nonlinear static analysis of the structure under permanent load, and on a lumped mass matrix. A subspace iteration algorithm, integrated in a structural analysis software, SOLVIA (1995), was used to extract the first *20* modes associated with the *OECS* model, in the range *0-46 Hz*, and the first *150* modes related with the *MECS* model, lying in the range *0-21.3 Hz*. The natural frequencies and characteristics of some of these modes are listed in Table 7.11.

A plot of the calculated frequencies obtained from the *3-D MECS* analysis against the order of the mode is presented in Figure 8.1. The frequencies associated with the *OECS* analysis are also represented in this Figure, in correspondence with the mode of closer characteristics obtained in the *MECS* analysis (*VSYM* and *VASM*- vertical symmetric and anti-symmetric bending modes; *TSYM* and *TASM*- transversal symmetric and anti-symmetric bending modes). It is clear from this Figure that the numerous modes of vibration that resulted from the modeling of local cable behaviour are separated by flat regions, which can generally be associated with a common configuration of the deck and towers. These sets of modes involve different movements of the cables, with a varying intensity level (relative to the girder/towers movement), and occur at an almost identical natural frequency.

Figure 8.2 presents the participation factors calculated for both the *OECS* and *MECS* models. It is evident, from the analysis of these figures and of the mode shape configurations, that: (i) the structural response along the vertical (*Z*) and transversal (*Y*) directions is clearly dominated by one mode of vibration (the 1st *VSYM* and the 1st *TSYM* modes, respectively); (ii) the structural response along the longitudinal (*X*) direction is strongly conditioned by two vertical anti-symmetric modes (the 1st *VASM* and the 2nd *VASM*). Another aspect to refer to is that although the highest participation factors associated with the *OECS* modes are in some cases slightly higher than the corresponding to modes obtained from the *MECS* analysis, the participation factors associated with the new mode shapes may have some significance for the response evaluation. This fact justifies the importance of the present investigation.

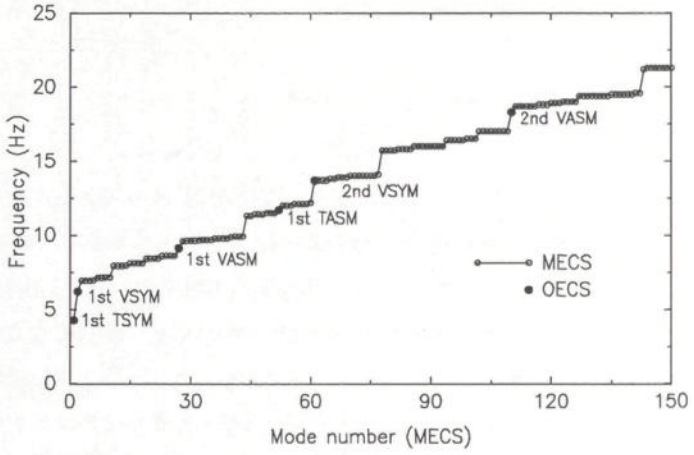


Figure 8.1. *OECS* vs *MECS* natural frequencies.

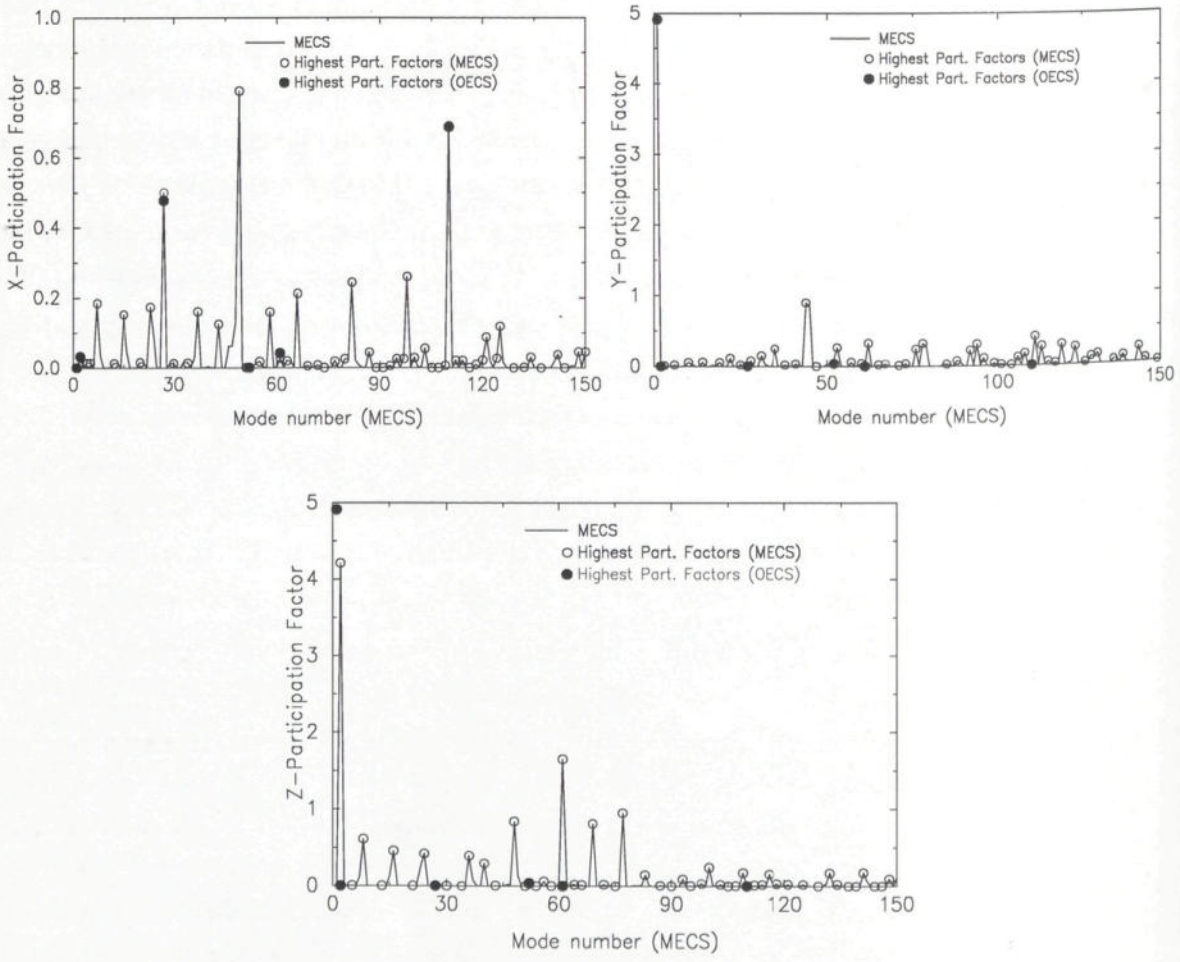


Figure 8.2. Participation factors associated with models *OECS* and *MECS*.

8.2.2 Response to seismic excitation

8.2.2.1 Generation of artificial accelerograms

The shaking table tests of the Jindo Bridge physical model were conducted at the *Earthquake Engineering Research Centre* of the University of Bristol. Two different ground acceleration time histories were generated using the program *EQSIM* (Taylor, 1991), based on the algorithm developed by Gasparini and Vanmarke (1976). According to this software, the time histories can be fitted to a specified acceleration, velocity or displacement response spectrum, or to a power spectral density. The nonstationarity of the seismic excitation can be then introduced in terms of amplitude by the application of a time modulation function that simulates the usual three phases of a common accelerogram. In the present case, the time histories were generated based on two different target response spectra which were defined attempting, in a first instance (records *RRS1*), to excite predominantly the fundamental modes of the cables, whereas in a second situation (records *RRS2*), the objective was to excite essentially the first mode shapes of the structure. These criteria were established under the purposes of (i) inducing the vibration of the stay cables at the fundamental resonance, forcing the occurrence of *cable-structure interaction* (records *RRS1*), and (ii) inducing excitation in the most harmful frequency range, containing the fundamental lateral and vertical frequencies of vibration (records *RRS2*). All the time series were generated with an approximate duration of *30s* for the prototype, and appropriately scaled to the model, according to a scale factor of $S_t = \sqrt{150}$ (see Table 7.4), what corresponded to input time records about *2.5s* long. A trapezoidal time window was then applied to all records, in order to simulate the nonstationarity of the earthquake excitation.

Graphical representations of two acceleration time series measured at the seismic platform and of the corresponding Fourier spectra are represented in Figure 8.3 for longitudinal records with about *10%g* peak value. The dashed lines in the Fourier spectrum plots define the frequency ranges of maximum target spectral content. It can be clearly observed that the final signals measured on the shaking table do not actually respect the criteria defined in their generation, although it is also evident from the observation of the two *FFT* plots that the records *RRS1* are indeed characterized by a spectral content richer in high frequencies than the record *RRS2*. The difficulty in generating records satisfying a specific requirement is related with the control mechanism of the shaking table available at the time when the tests were performed.

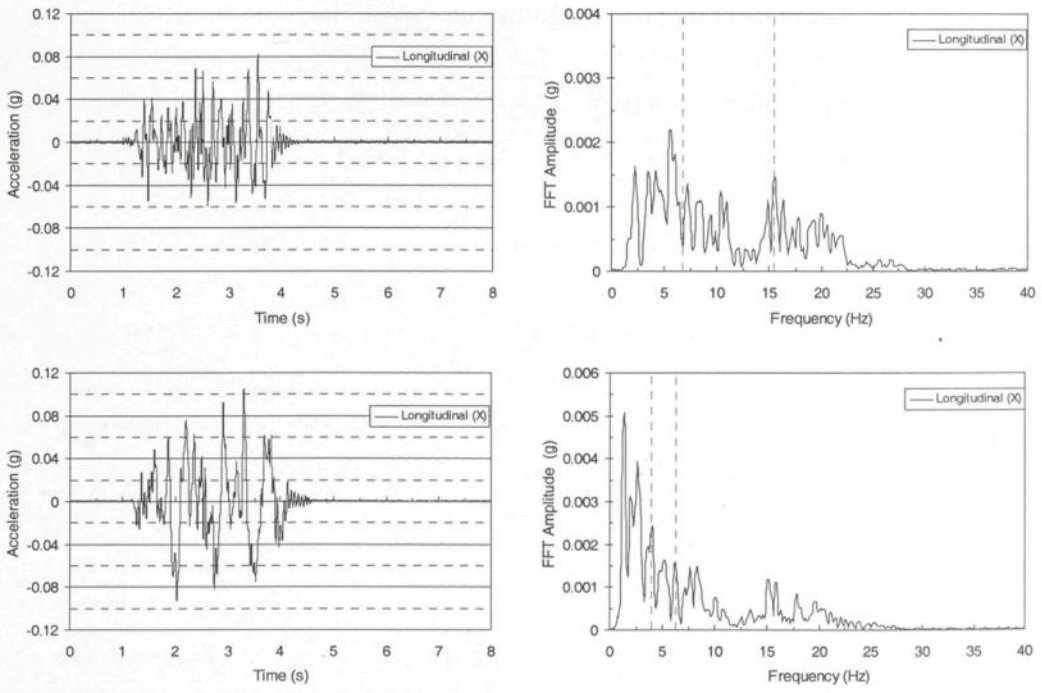


Figure 8.3. Examples of acceleration time series and corresponding Fourier spectra: (a) record *RRS1*; (b) record *RRS2*.

8.2.2.2 Measured response

The response of the physical model was measured for three input directions, *X* (longitudinal), *Y* (transversal) and *Z* (vertical), and for the combinations *XZ* and *XYZ*, with about *5%g* and *10%g* peak values along the two horizontal directions, and about *3%g* and *6%g* in the vertical direction. A final set of responses was measured for a combination *XYZ* of records *RRS1*, with about *20%g* peak value along the two horizontal directions and about *12%g* in the vertical direction. A total of *13* small piezoelectric accelerometers *DYTRAN*, model *3101AG* and *1* non-contact displacement transducer *INDIKON* (see Section 7.5.2.1) were used to obtain simultaneous measurements along the bridge, according to the various setups indicated in Figure 8.4. The node numbering used in that Figure corresponds to the adopted for the *2-D OECS* analysis.

Table 8.1 resumes the characteristics of the signals selected to be presented in this dissertation, which comprehend the input and response to the combinations *XZ*, *Y* and *XYZ* with different intensity levels of records *RRS1* and *RRS2*. Figures 8.5 to 8.7 show the input signals measured at the platform, as well as the response at some representative locations associated with the various setups presented in Figure 8.4.

It should be noted that, although it was the purpose of the author to generate input excitations with *5%g* and *10%g* peak values along the horizontal directions, and *3%g* and *6%g* peak values along the vertical direction, the actual signals measured on the platform showed slightly different values.

In order to facilitate the analysis of the measured signals, the peak values associated with the various records described by Table 8.1 were extracted and are presented in Tables 8.2, 8.3 and 8.4, for the combinations of signals *XZ*, *Y* and *XYZ*. The spectral content of these signals was also analyzed. Figures 8.8 to 8.11 represent the *FFT* amplitude plots obtained on some of the most representative locations.

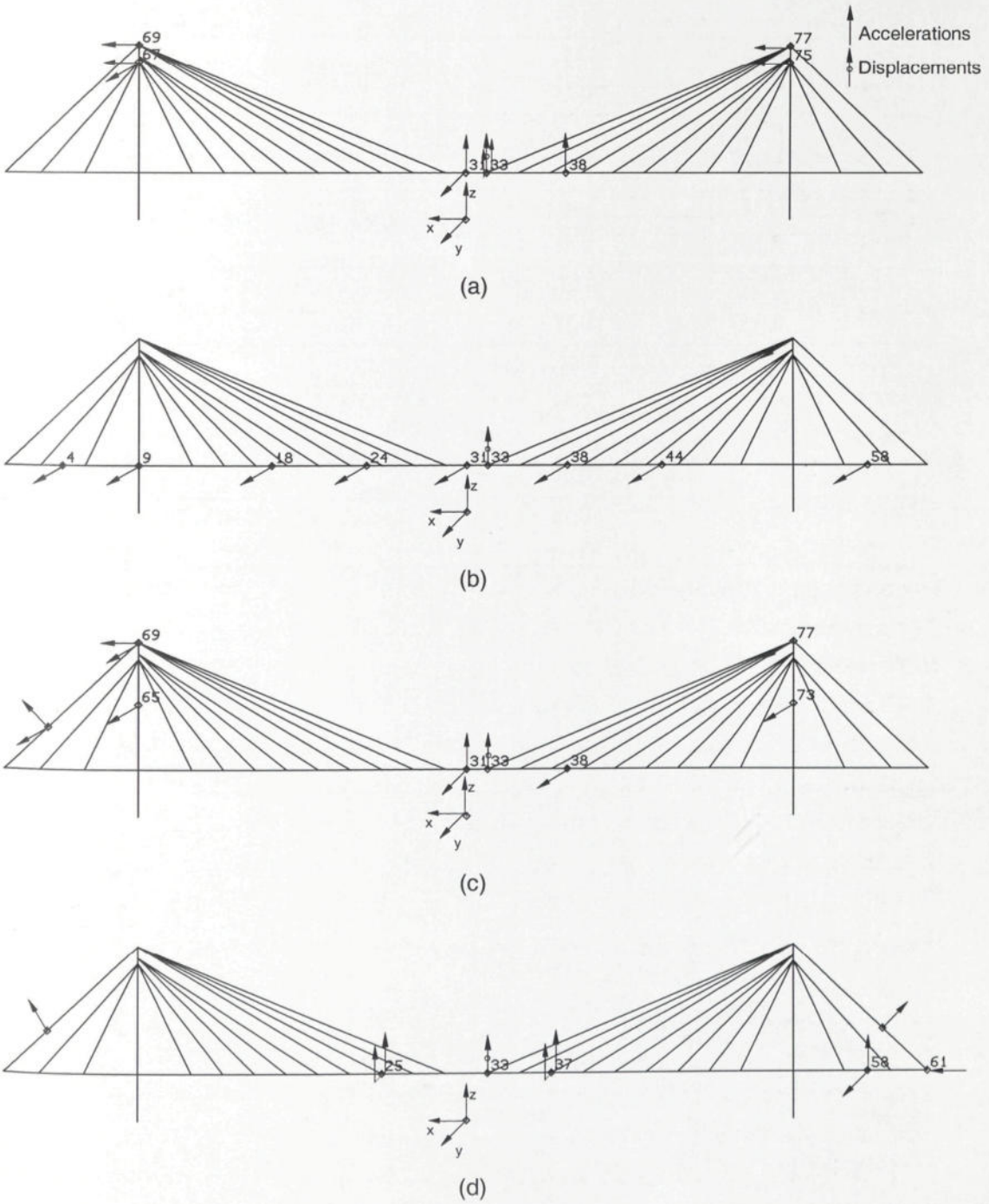


Figure 8.4. Locations of sensors in the seismic tests: (a) Setup *1*, excitation along *X*, *Z* and combined *XZ* directions; (b) Setup *2*, excitation along *Y* and combined *XYZ* directions; (c) Setup *3*, excitation along combined *XYZ* directions; (d) Setup *4*, excitation along combined *XYZ* directions.

Table 8.1. Characteristics of some seismic measurements.

Record name	Type of record	Amplitude of input			Locations of response measurement	Representation in Figure
		X (g)	Y (g)	Z (g)		
AQ40	RRS1	0.063		0.032	X, Z, 31Z, 33Z, 38Z, 69X	8.5(a)
AQ41	RRS1	0.11		0.073		8.5(b)
AQ48	RRS2	0.052		0.033		8.5(c)
AQ49	RRS2	0.12		0.061		8.5(d)
AQ56	RRS1		0.022		Y, 9Y, 18Y, 24Y, 31Y, 33Z	8.6(a)
AQ63	RRS1		0.11			8.6(b)
AQ79	RRS1		0.056		Y, 77Y, Cable1 Y Left	8.6(c)
AQ80	RRS1		0.11			8.6(d)
AQ66	RRS2		0.037		Y, 9Y, 18Y, 24Y, 31Y, 33Z	8.6(e)
AQ69	RRS2		0.13			8.6(f)
AQ84	RRS2		0.070		Y, 77Y, Cable1 Y Left	8.6(g)
AQ85	RRS2		0.11			8.6(h)
AQ92	RRS1	0.067	0.057	0.038	X, Y, Z, 33Z, 37Z, Cable1 Plane Left, Cable 1 Y Left, Cable 1 Y Right	8.7(a)
AQ93	RRS1	0.11	0.11	0.076		8.7(b)
AQ94	RRS2	0.048	0.063	0.038		8.7(c)
AQ95	RRS2	0.12	0.10	0.062		8.7(d)
AQ121	RRS1	0.20	0.19	0.12	X, Y, Z, 31Z, 33Z, 38Y, 38Z, 44Y, 69X, 69Y	8.7(e)

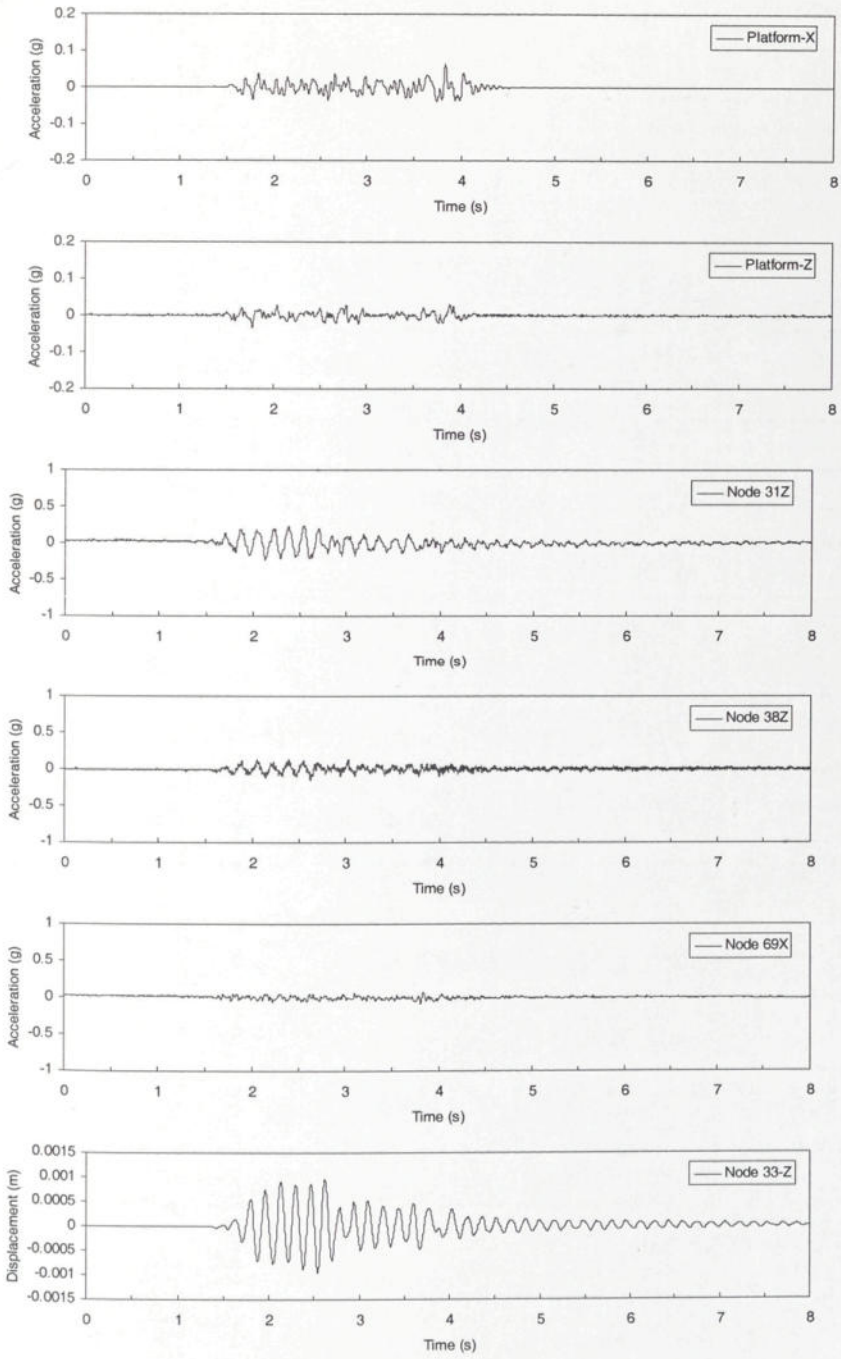


Figure 8.5. Input and response measurements: (a) Record *RRS1, 6%g (X), 3%g(Z) (AQ40).*

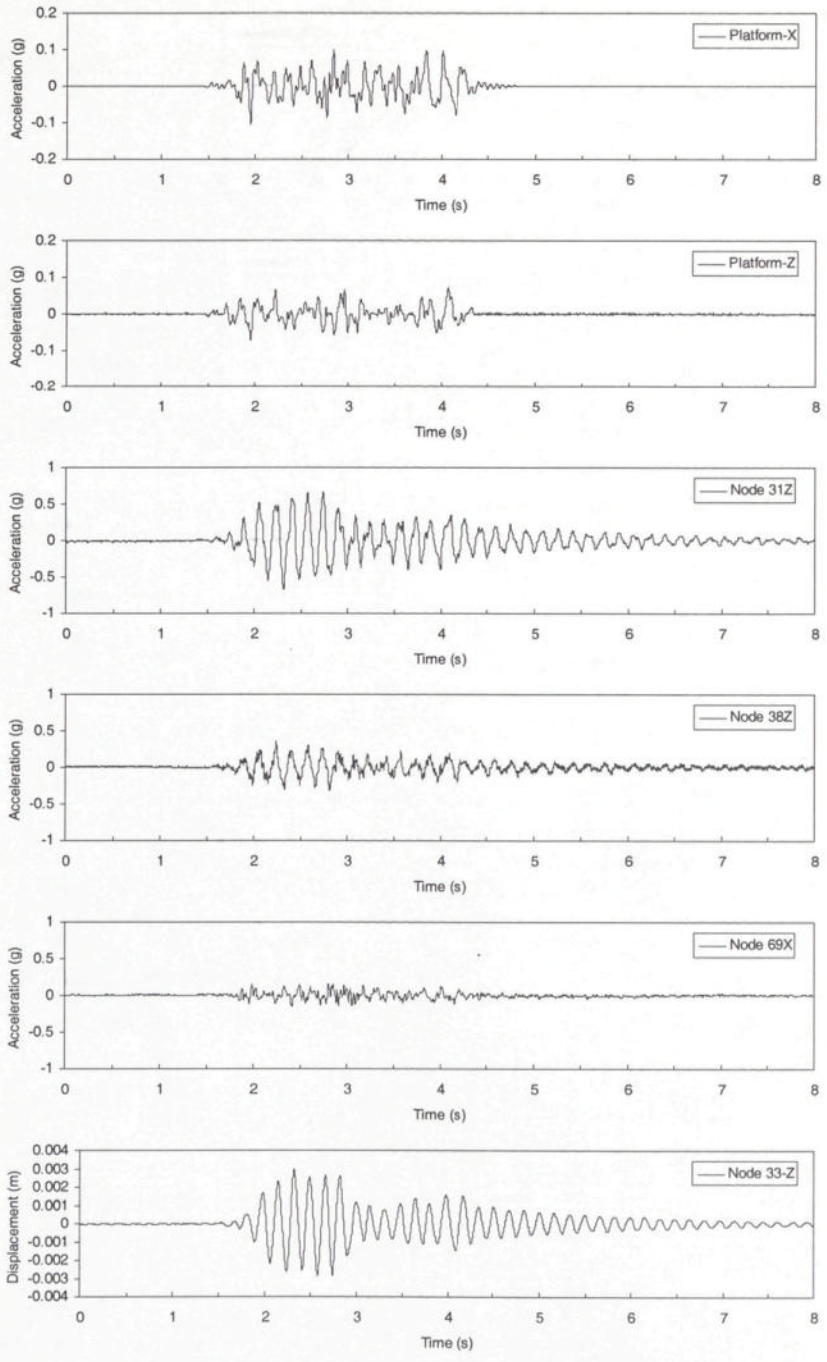


Figure 8.5. Input and response measurements: (b) Record *RRS1, 11%g (X), 7%g(Z) (AQ41).*

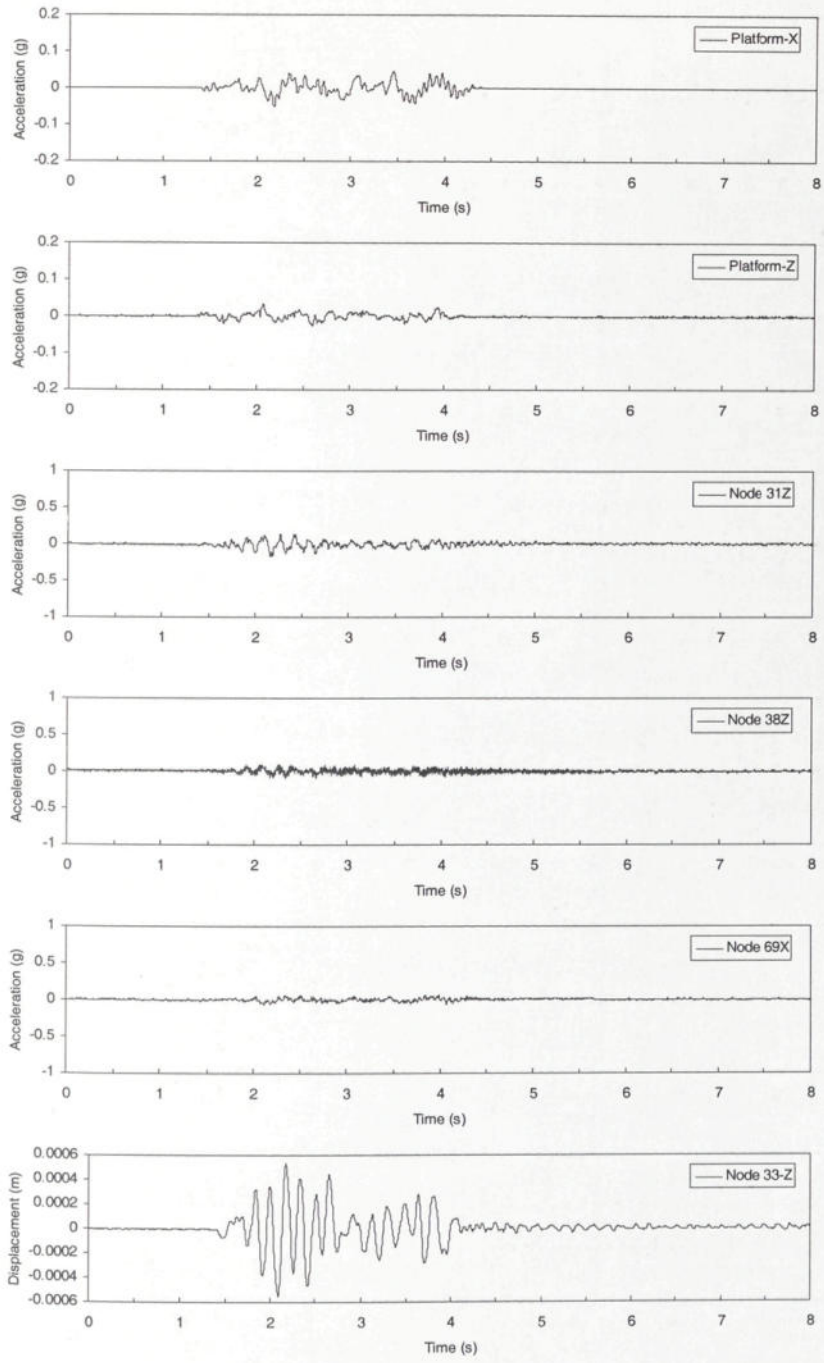


Figure 8.5. Input and response measurements: (c) Record *RRS2, 5%g (X), 3%g(Z) (AQ48).*

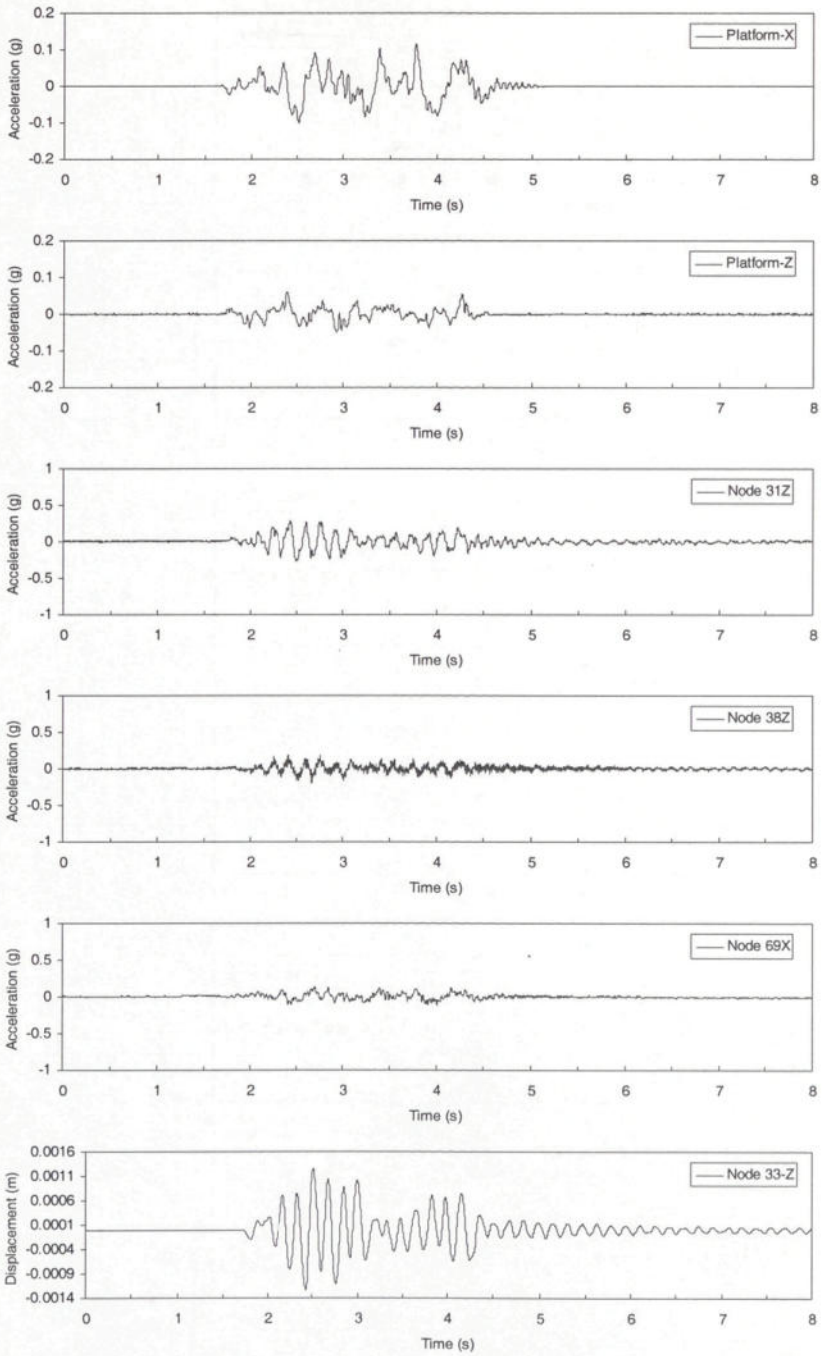


Figure 8.5. Input and response measurements: (d) Record *RRS2, 12%g (X), 6%g(Z) (AQ49).*

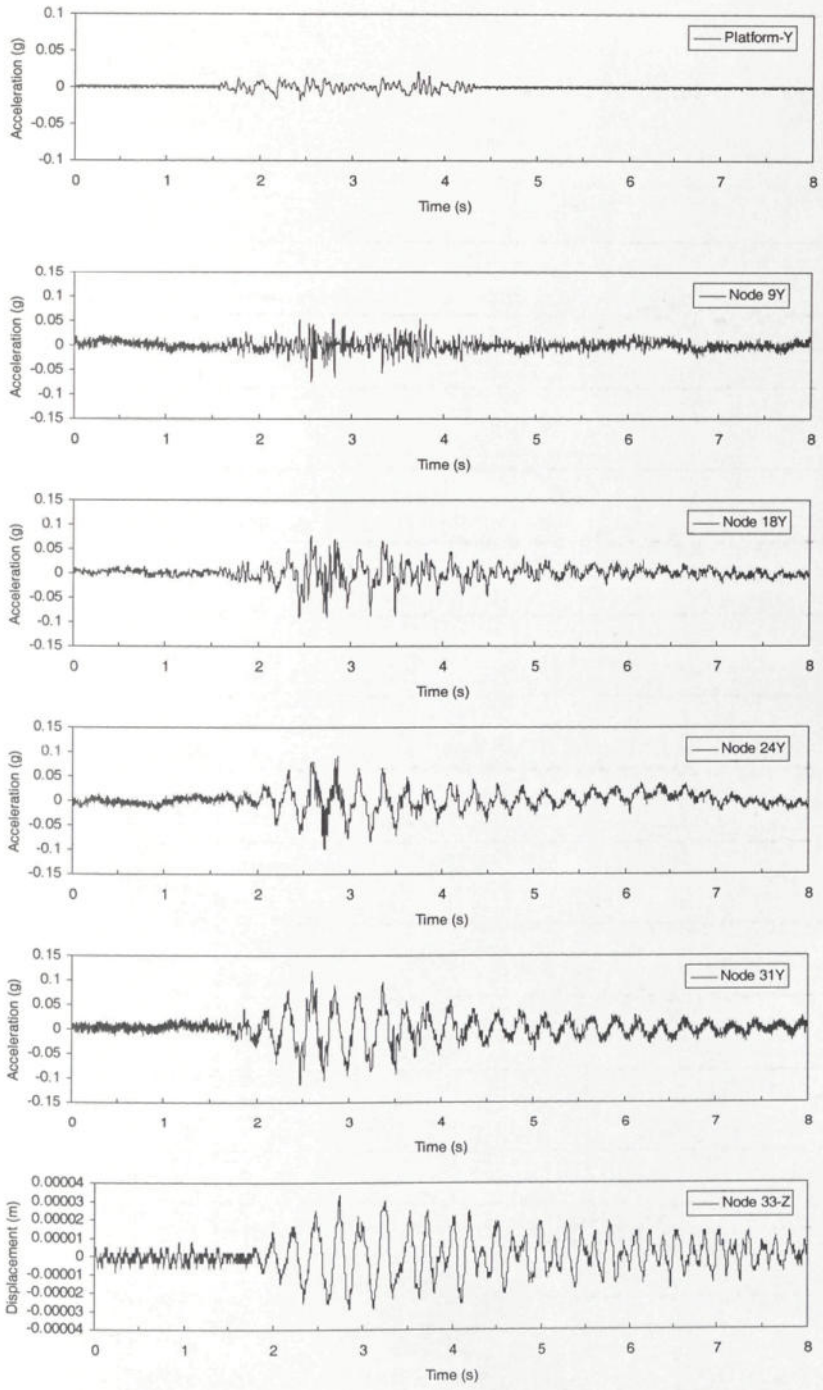


Figure 8.6. Input and response measurements: (a) Record *RRS1, 2%g (Y) (AQ56).*

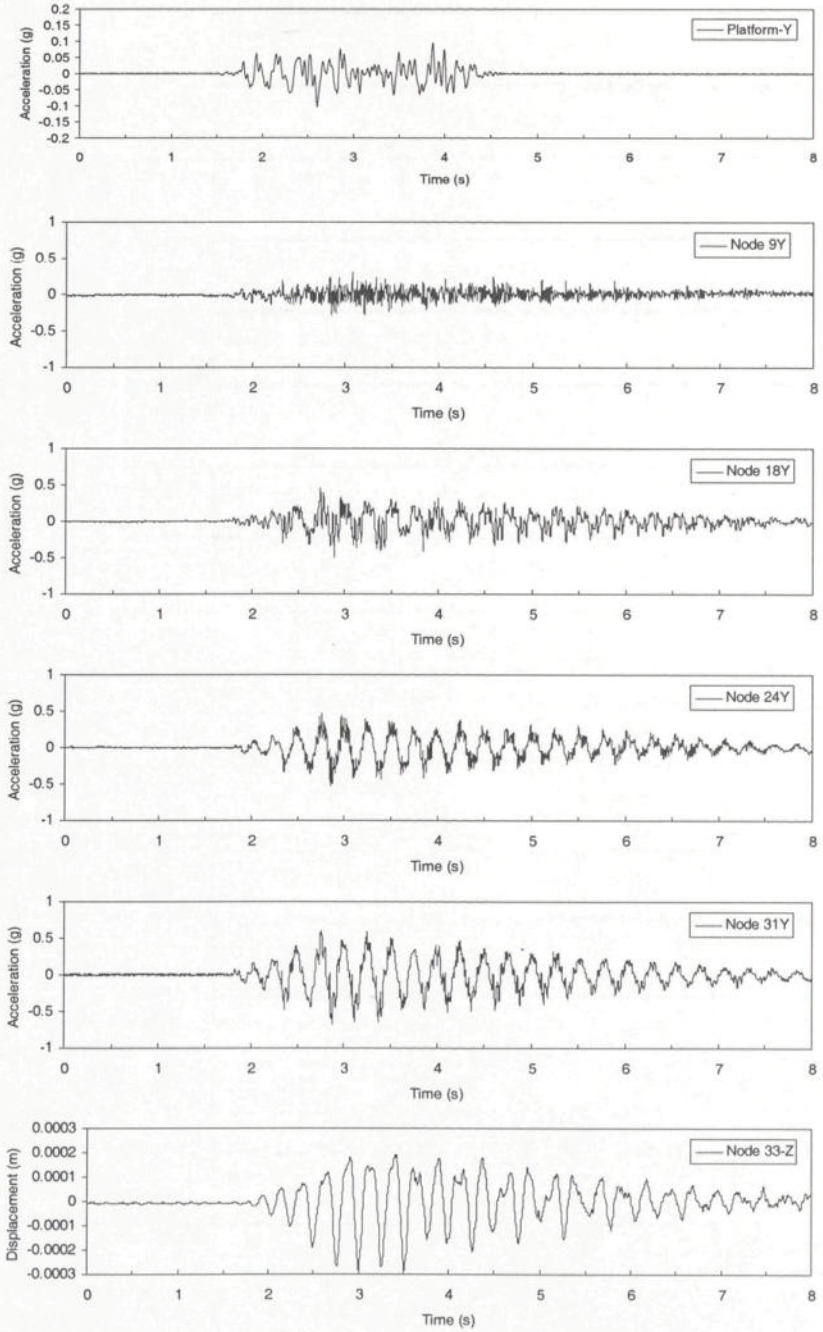
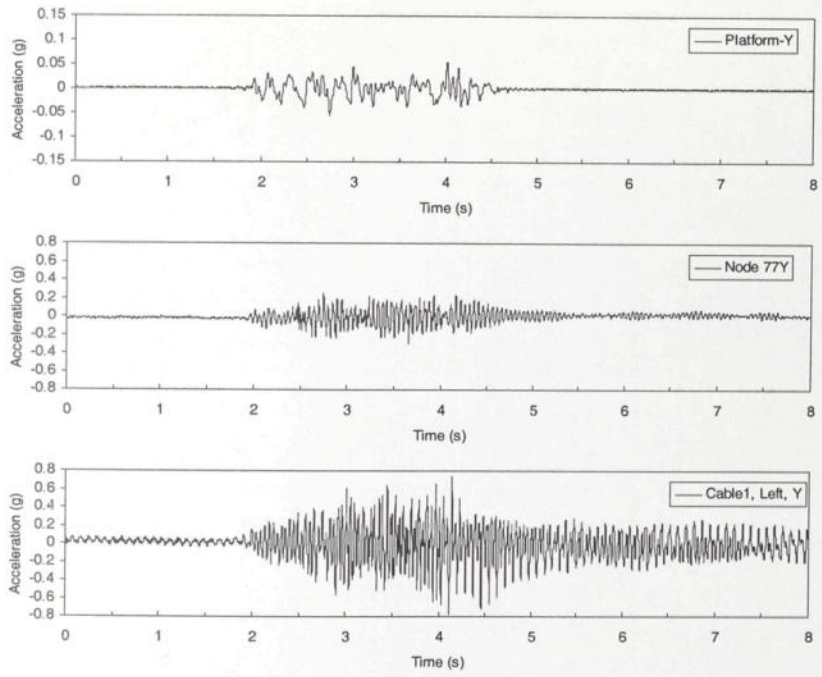


Figure 8.6. Input and response measurements: (b) Record *RRS1, 11%g (Y) (AQ63).*

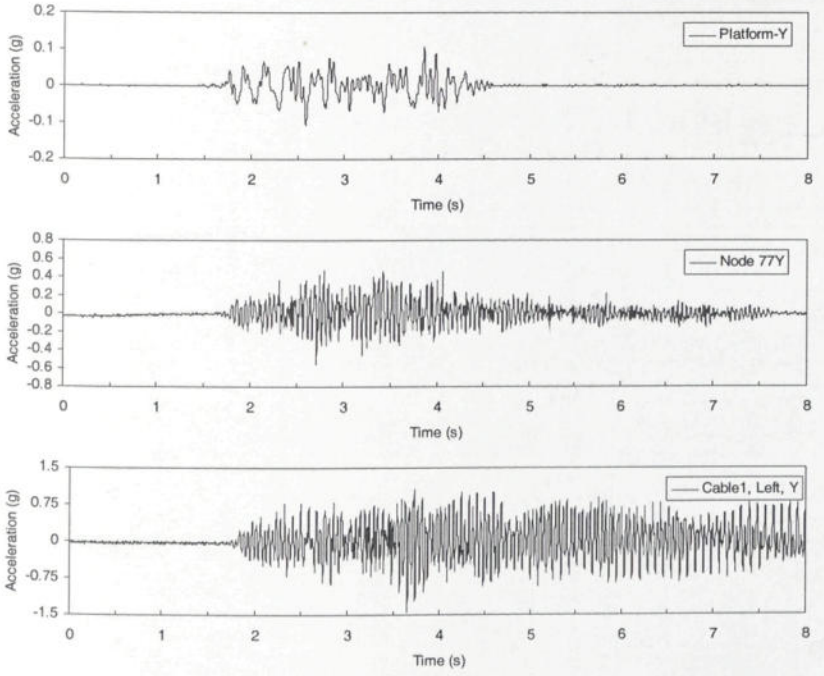


Peak: 0.056g

Peak: -0.29g

Peak: -0.79g

Figure 8.6. Input and response measurements: (c) Record *RRS1, 6%g (Y) (AQ79).*



Peak: -0.11g

Peak: -0.55g

Peak: -1.45g

Figure 8.6. Input and response measurements: (d) Record *RRS1, 11%g (Y) (AQ80).*

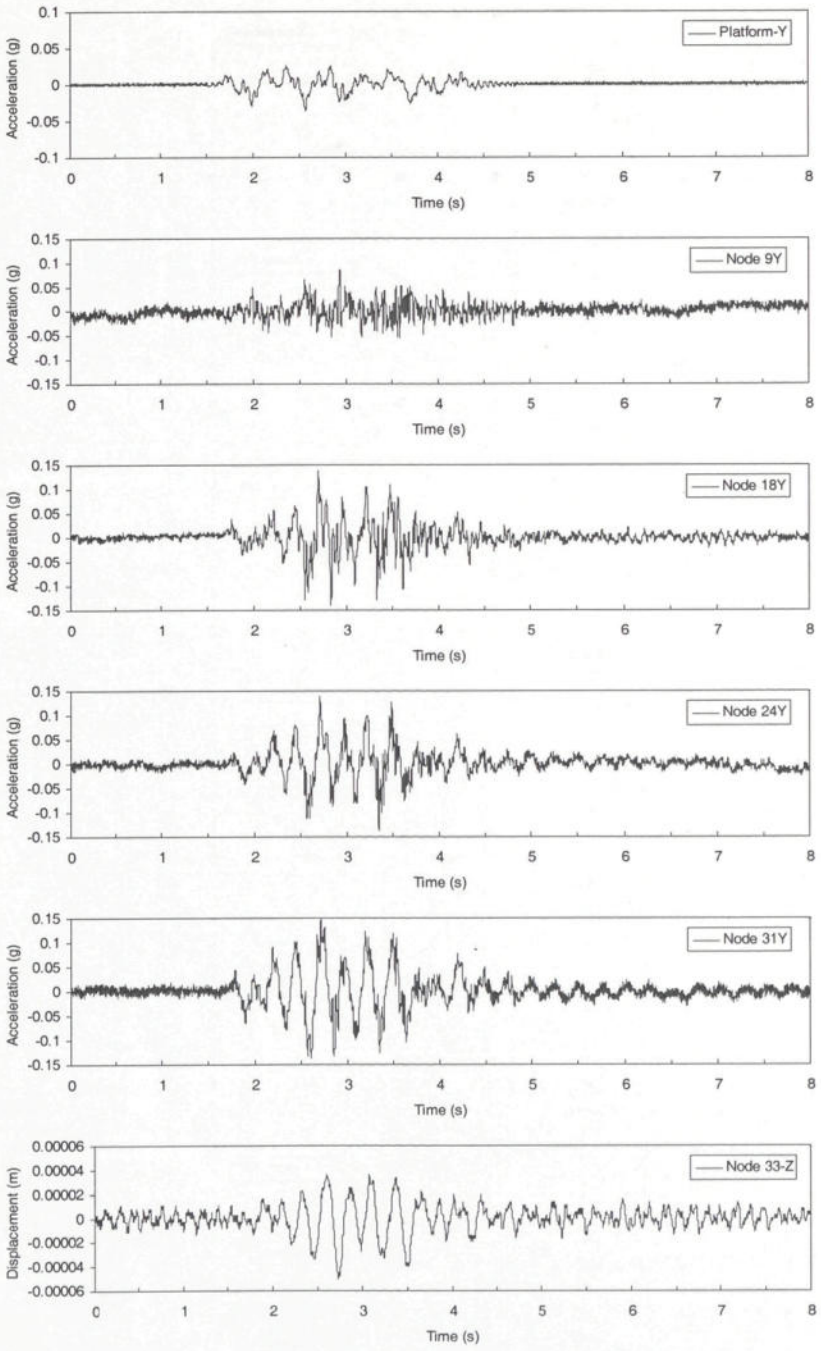


Figure 8.6. Input and response measurements: (e) Record *RRS2, 4%g (Y) (AQ66).*

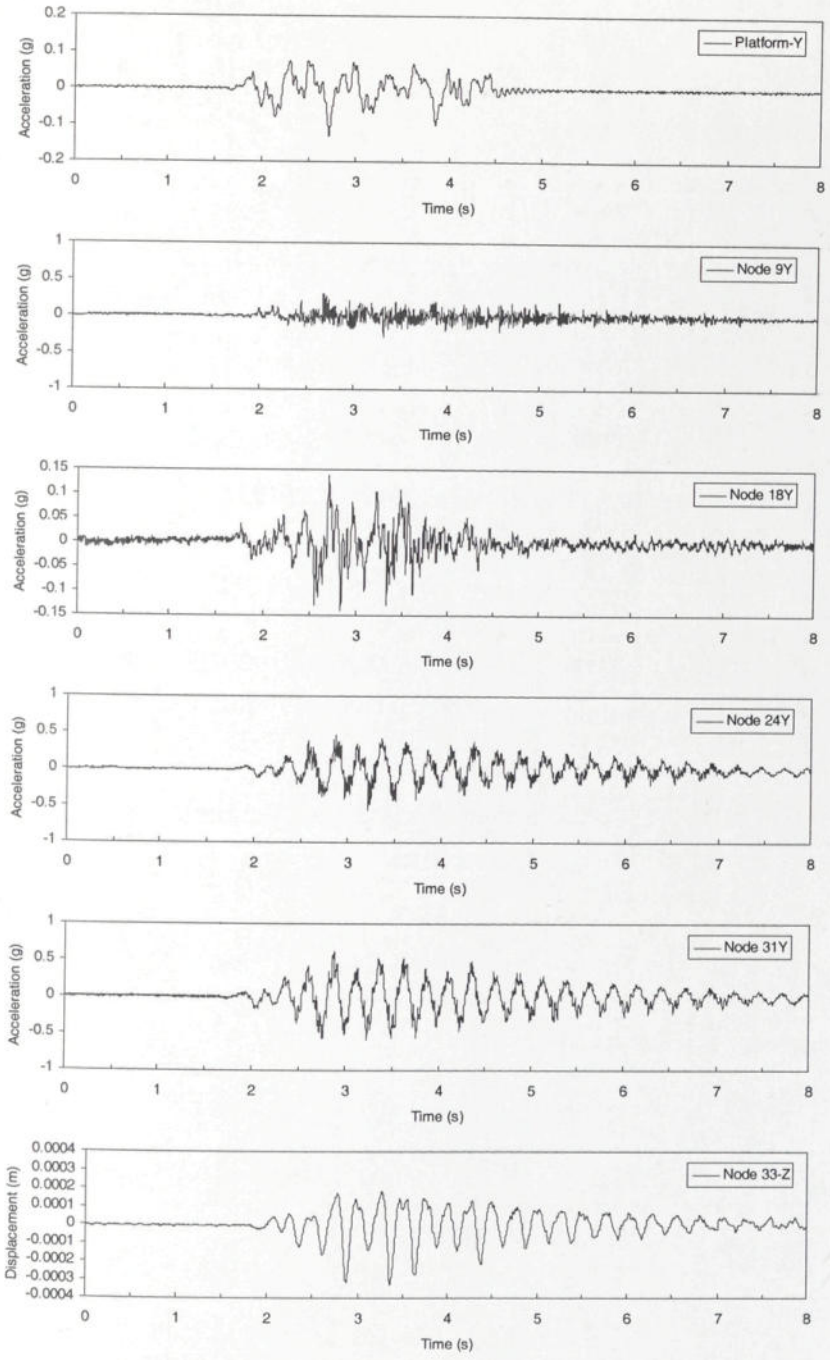
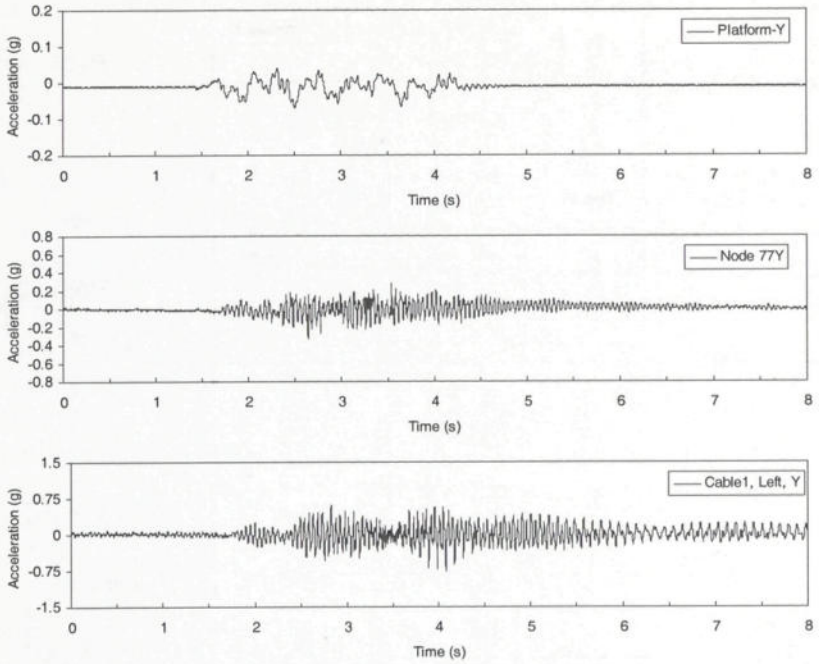


Figure 8.6. Input and response measurements: (f) Record *RRS2, 13%g (Y) (AQ69).*

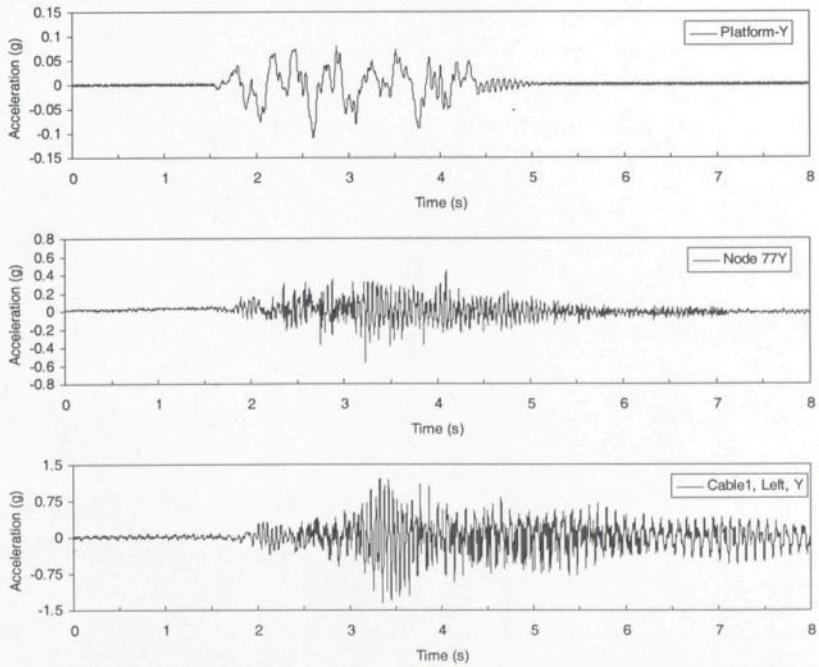


Peak: -0.070g

Peak: -0.34g

Peak: -0.77g

Figure 8.6. Input and response measurements: (g) Record *RRS2, 7%g (Y) (AQ84).*



Peak: -0.11g

Peak: -0.55g

Peak: -1.37g

Figure 8.6. Input and response measurements: (h) Record *RRS2, 11%g (Y) (AQ85).*

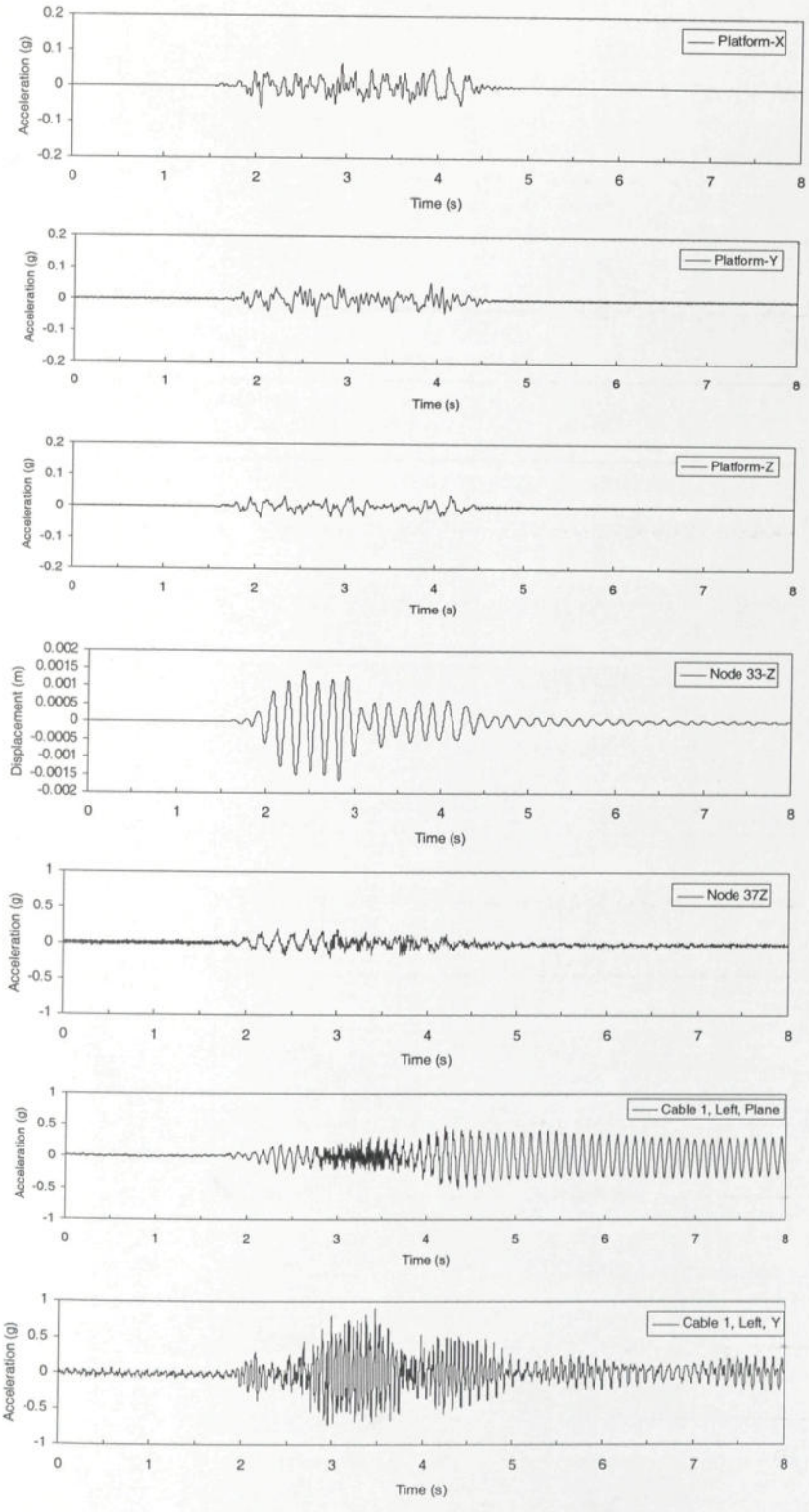


Figure 8.7. Input and response measurements: (a) Record *RRS1, 7%g (X), 6%g (Y), 4%g (Z) (AQ92).*

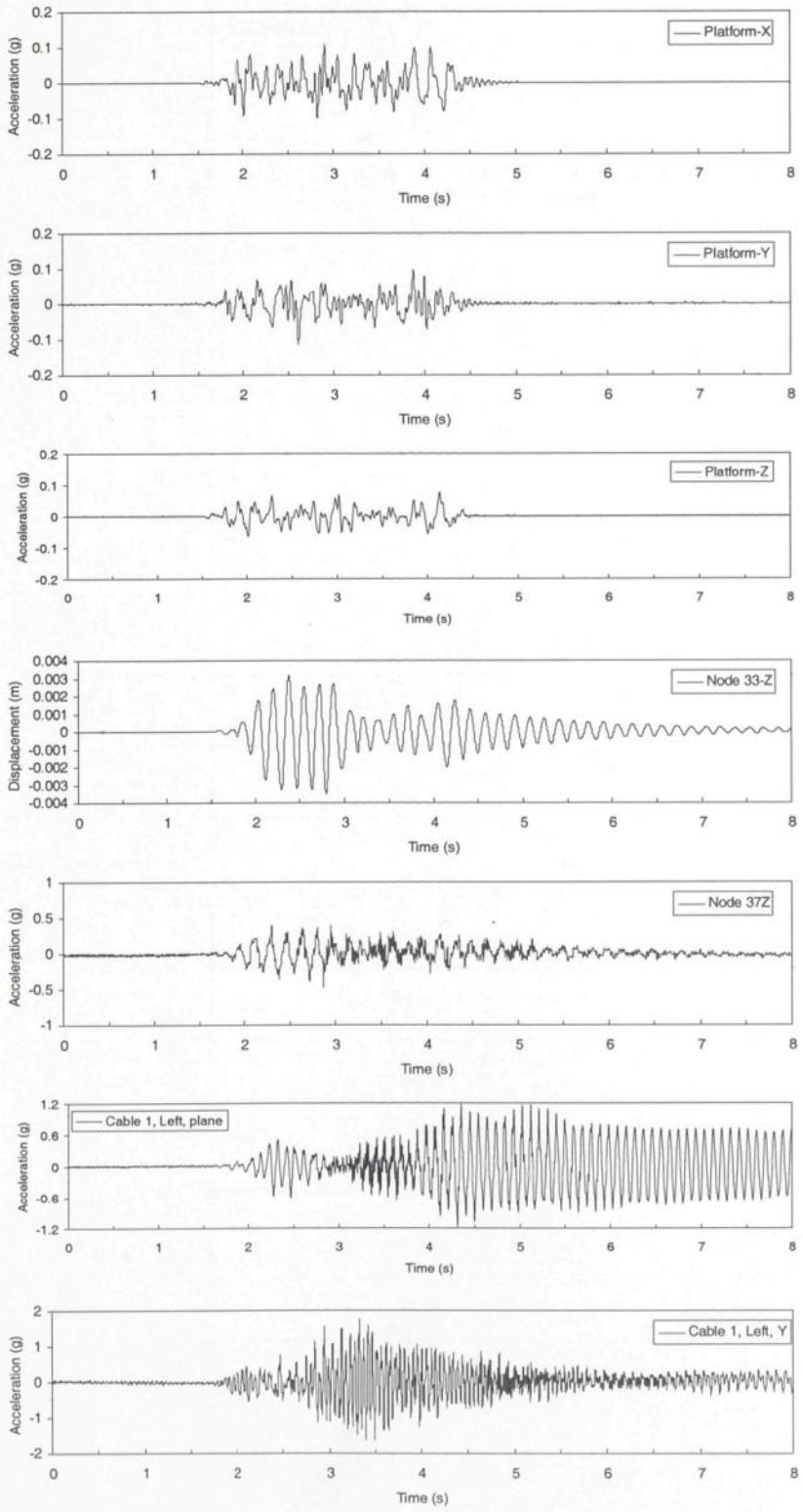


Figure 8.7. Input and response measurements: (b) Record *RRS1, 11%g (X), 12%g (Y), 8%g (Z) (AQ93).*

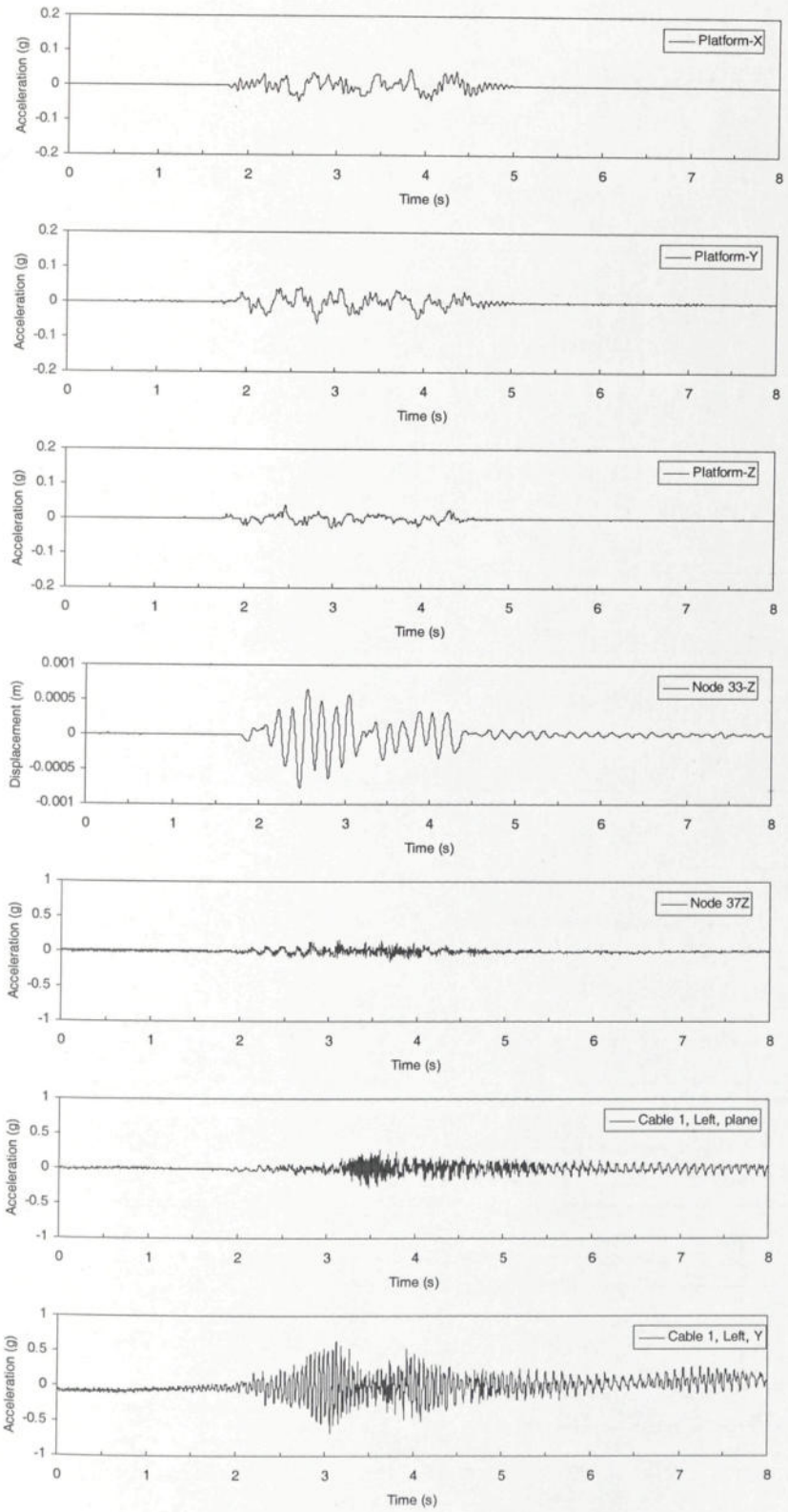


Figure 8.7. Input and response measurements: (c) Record *RRS2, 5%g (X), 6%g (Y), 4%g (Z) (AQ94).*

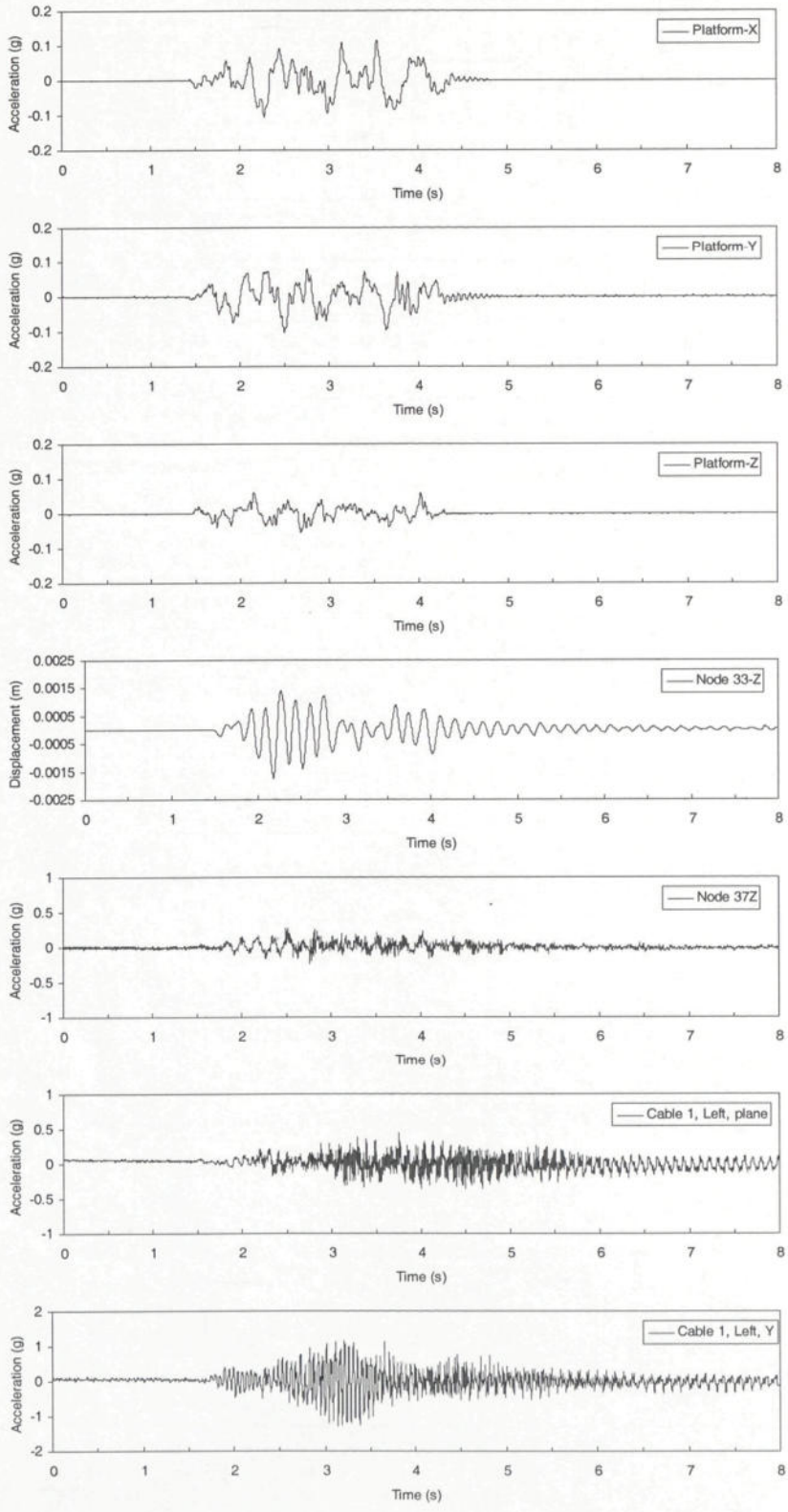


Figure 8.7. Input and response measurements: (d) Record *RRS2, 12%g (X), 10%g (Y), 6%g (Z)(AQ95).*

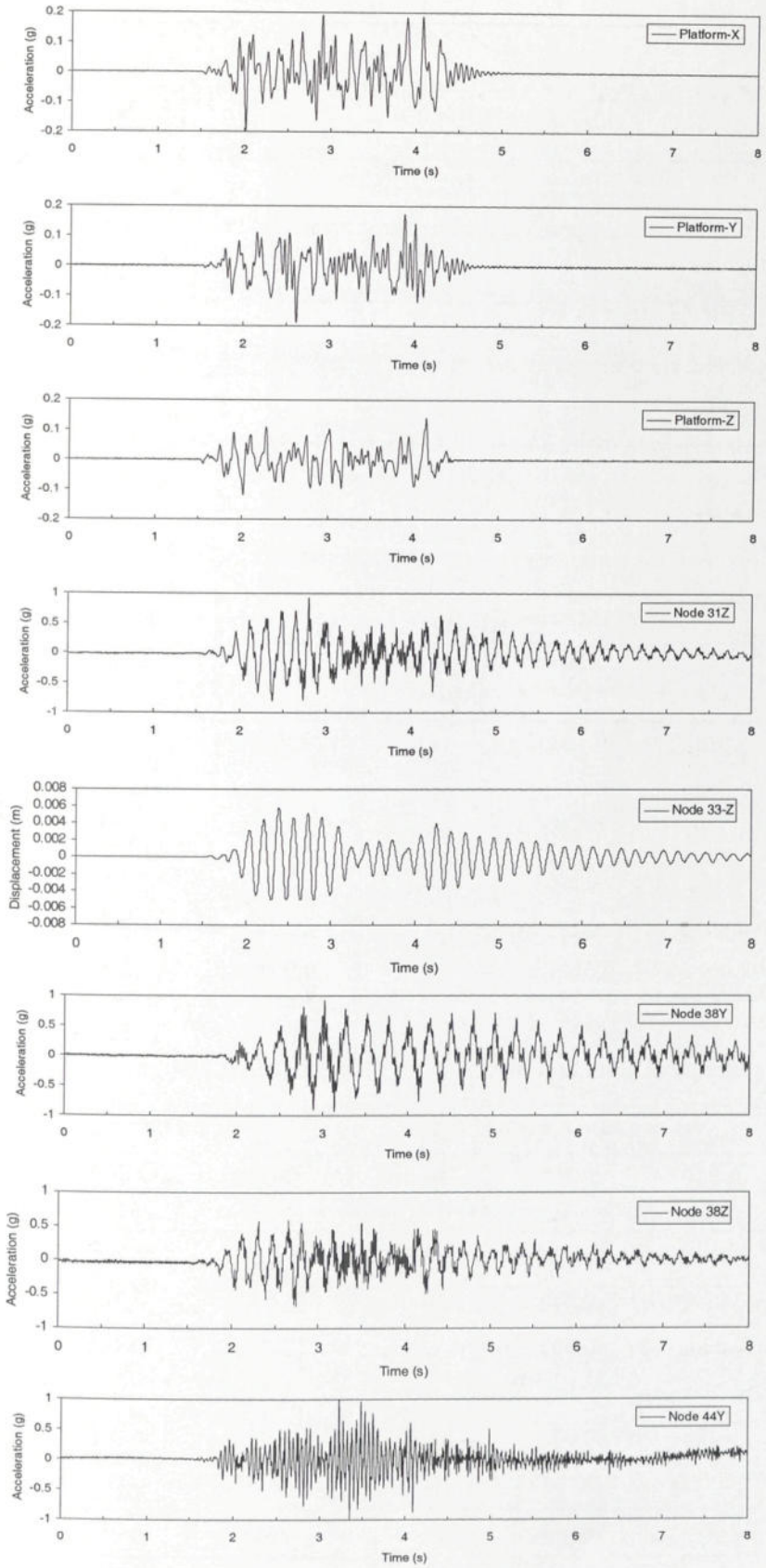


Figure 8.7. Input and response measurements: (e) Record *RRS1, 20%g (X), 19%g (Y), 12%g (Z) (AQ121).*

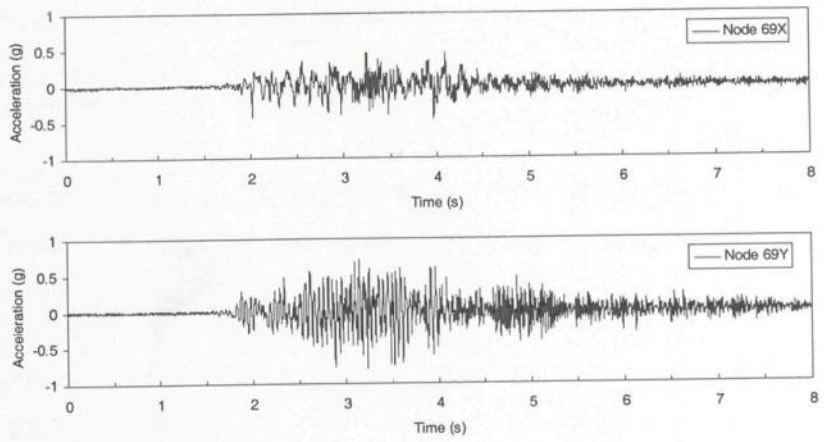


Figure 8.7. Input and response measurements: (e) Record *RRS1, 20%g (X), 19%g (Y), 12%g (Z)(AQ121)* (continuation).

Table 8.2. Peak values of input and response for base excitation along the directions *X* and *Z*.

Location, type of measurement	Record **RRS1**, excitation (XZ)			Record **RRS2**, excitation (XZ)		
	AQ40	**AQ41**	**Ratio** (AQ41/AQ40)	**AQ48**	**AQ49**	**Ratio** (AQ49/AQ48)
X, acceleration	0.063g	0.106g	1.7	0.052g	0.12g	2.3
Z, acceleration	0.032g	0.073g	2.3	0.033g	0.061g	1.9
31Z, acceleration	0.25g	0.67g	2.7	0.17g	0.29g	1.7
38Z, acceleration	0.15g	0.36g	2.4	0.097g	0.19g	2.0
69X, acceleration	0.087g	0.16g	1.8	0.063g	0.13g	2.1
33Z, displacement	0.00096m	0.0029m	3.0	0.00055m	0.0013m	2.4

Table 8.3. Peak values of input and response for base excitation along the direction *Y*.

Location, type of measurement	Record **RRS1**, excitation (Y)			Record **RRS2**, excitation (Y)		
	AQ56	**AQ63**	**Ratio** (AQ63/AQ56)	**AQ66**	**AQ69**	**Ratio** (AQ69/AQ66)
Y, acceleration	0.022g	0.105g	4.8	0.037g	0.13g	3.5
9Y, acceleration	0.074g	0.30g	4.0	0.090g	0.34g	3.8
18Y, acceleration	0.090g	0.50g	5.6	0.14g	0.44g	3.1
24Y, acceleration	0.10g	0.54g	5.4	0.14g	0.56g	4
31Y, acceleration	0.12g	0.69g	5.75	0.15g	0.63g	4.2
33Z, displacement	0.000033m	0.00028m	8.5	0.000051m	0.00033m	6.5
	AQ79	**AQ80**		**AQ84**	**AQ85**	
Y, acceleration	0.056g	0.11g	2.0	0.070g	0.11g	1.6
77Y, acceleration	0.29g	0.55g	1.9	0.34g	0.55g	1.6
Cable 1, Left, Y, acceleration	0.79g	1.45g	1.8	0.77g	1.37g	1.8

Table 8.4. Peak values of input and response for base excitation along the directions *X*, *Y* and *Z*.

Location, type of measurement	Record **RRS1**, excitation (XYZ)					Record **RRS2**, excitation (XYZ)		
	AQ92	**AQ93**	**Ratio** (AQ93/AQ92)	**AQ121**	**Ratio** (AQ121/AQ93)	**AQ94**	**AQ95**	**Ratio** (AQ95/AQ94)
X, accel.	0.067g	0.11g	1.6	0.20g	1.8	0.048g	0.12g	2.5
Y, accel.	0.057g	0.12g	2.1	0.19g	1.9	0.063g	0.10g	1.6
Z, accel.	0.038g	0.076g	2	0.12g	1.6	0.038g	0.062g	1.6
31Z, accel.				0.93g				
33Z, displ.	0.0017m	0.0035m	2.1	0.0059m	1.7	0.00077m	0.0017m	2.2
37Z, accel.	0.21g	0.49g	2.3			0.16g	0.28g	1.8
38Y, accel.				0.93g				
38Z, accel.				0.68g				
44Y, accel.				1.09g				
69X, accel.				0.49g				
69Y, accel.				0.79g				
Cable 1, Left, Plane, accel.	0.50g	1.18g	2.4			0.28g	0.44g	1.6
Cable 1, Left, Y, accel.	0.91g	1.77g	1.9			0.69g	1.31g	1.9

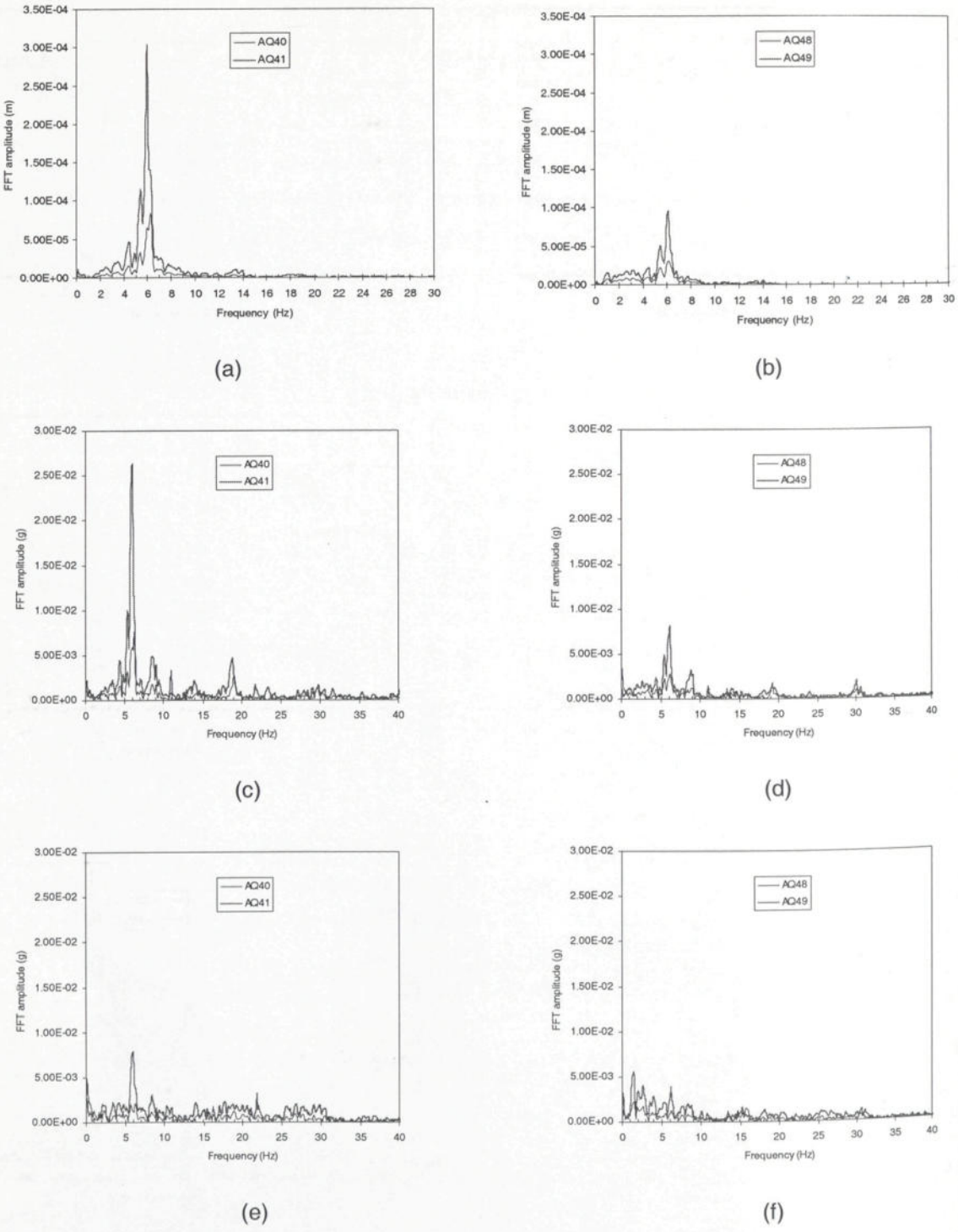


Figure 8.8. Excitation ***XZ***, response at node: (a) ***33Z***, *RRS1*; (b) ***33Z***, *RRS2*; (c) ***38Z***, *RRS1*; (d) ***38Z***, *RRS2*; (e) ***69X***, *RRS1*; (f) ***69X***, *RRS2*.

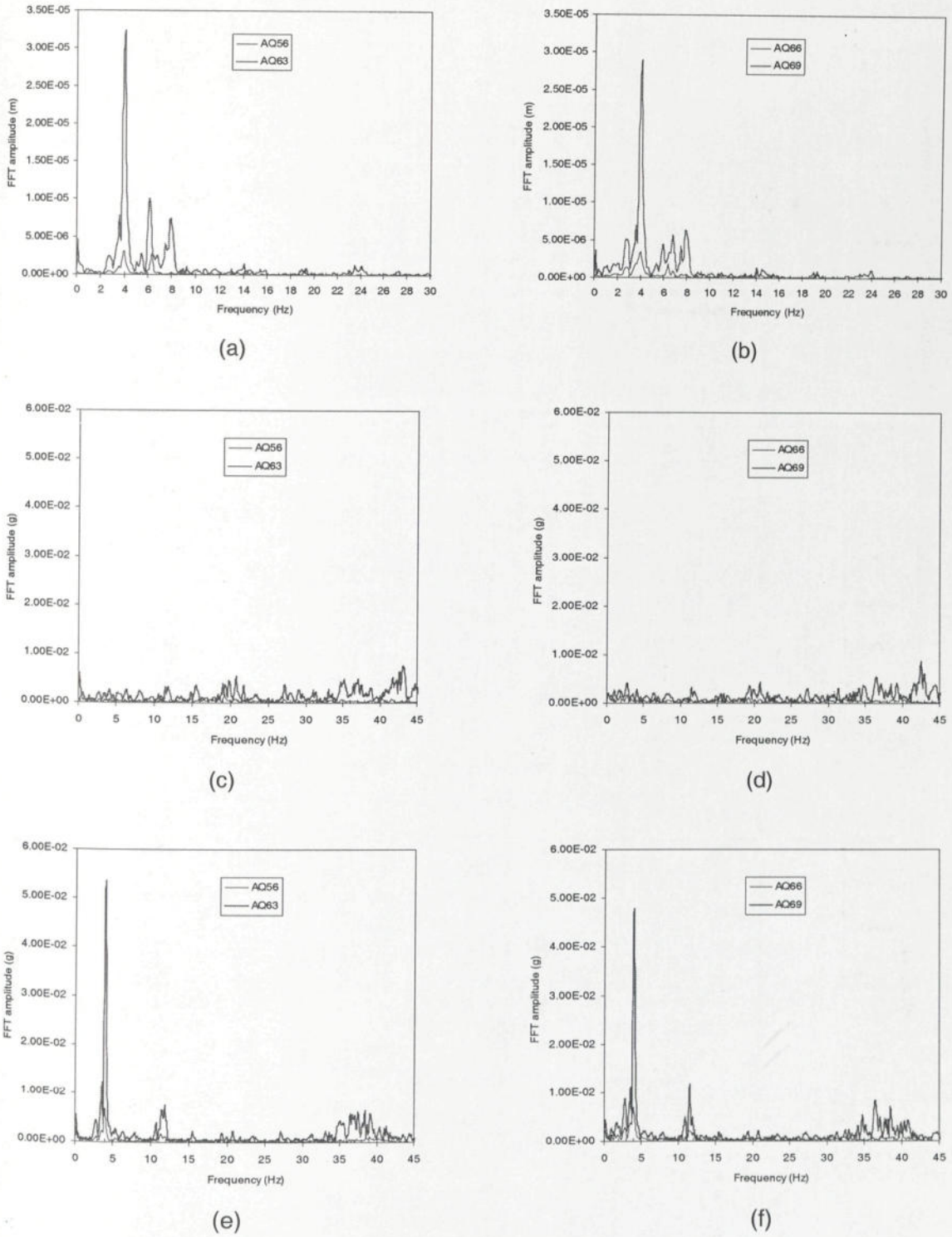


Figure 8.9. Excitation ***Y***, response at node: (a) ***33Z***, *RRS1*; (b) ***33Z***, *RRS2*; (c) ***9Y***, *RRS1*; (d) ***9Y***, *RRS2*; (e) ***24Y***, *RRS1*; (f) ***24Y***, *RRS2*.

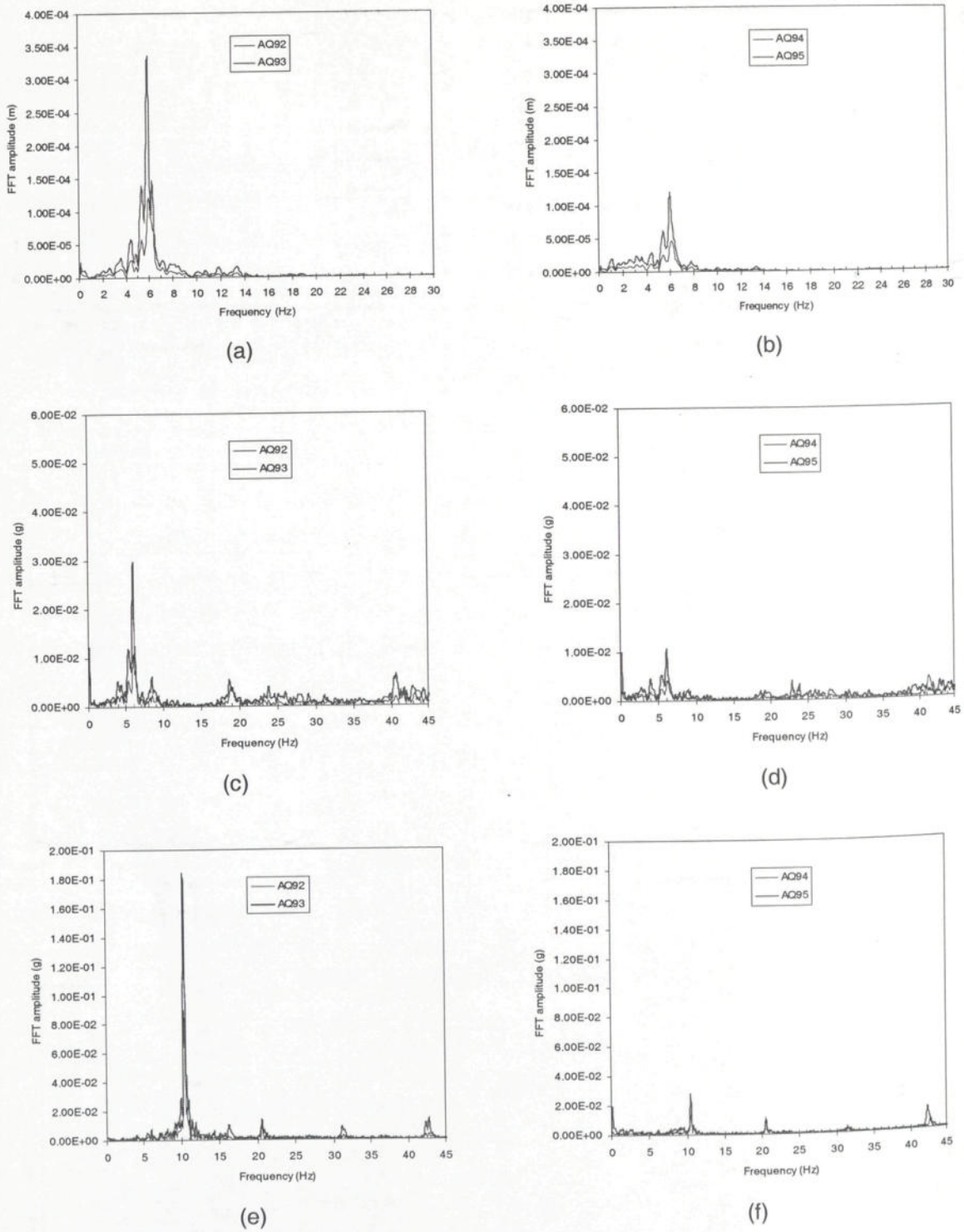
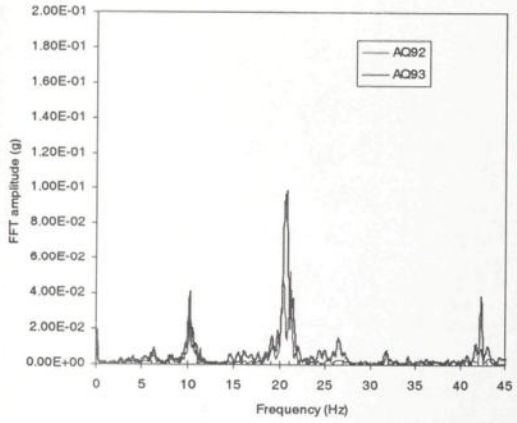
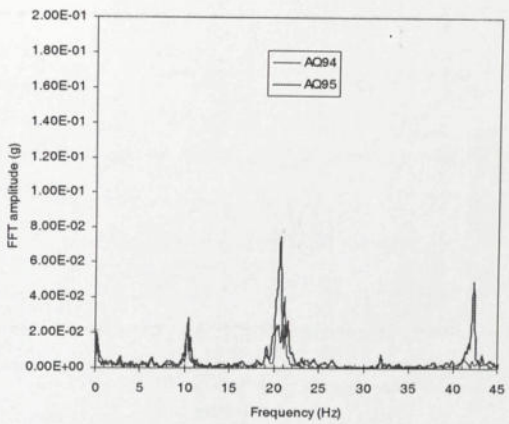


Figure 8.10. Excitation ***XYZ***, response at node: (a) ***33Z***, *RRS1*; (b) ***33Z***, *RRS2*; (c) ***37Z front***, *RRS1*; (d) ***37Z front***, *RRS2*; (e) ***Cable 1 Left Plane***, *RRS1*; (f) ***Cable 1 Left Plane***, *RRS2*.

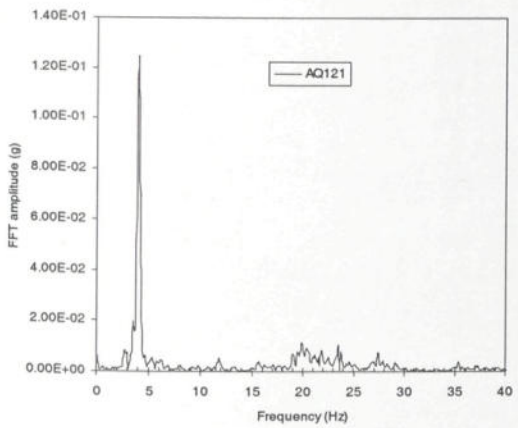


(g)

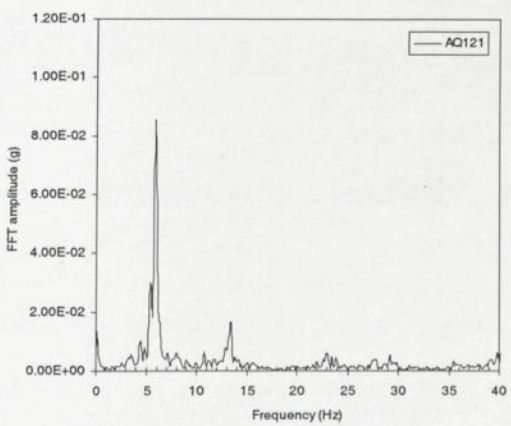


(h)

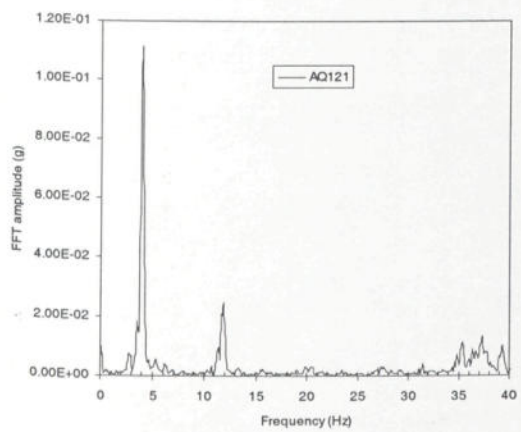
Figure 8.10 (continuation). Excitation ***XYZ***, response at node: (g) ***Cable 1 Left Y,*** *RRS1*; (h) ***Cable 1 Left Y,*** *RRS2.*



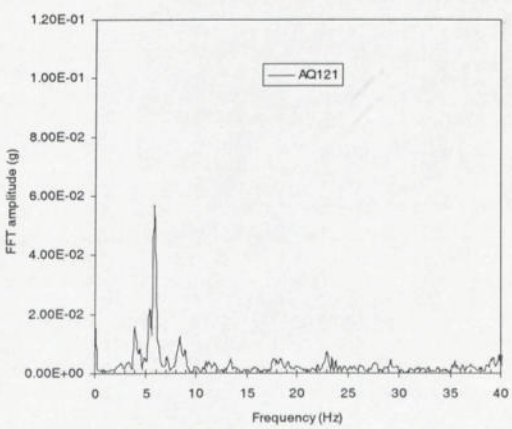
(a)



(b)



(c)



(d)

Figure 8.11. Excitation ***XYZ***, record *RRS1,* large amplitude, response at node: (a) ***31Y***; (b) ***31Z***; (c) ***38Y***; (d) ***38Z***.

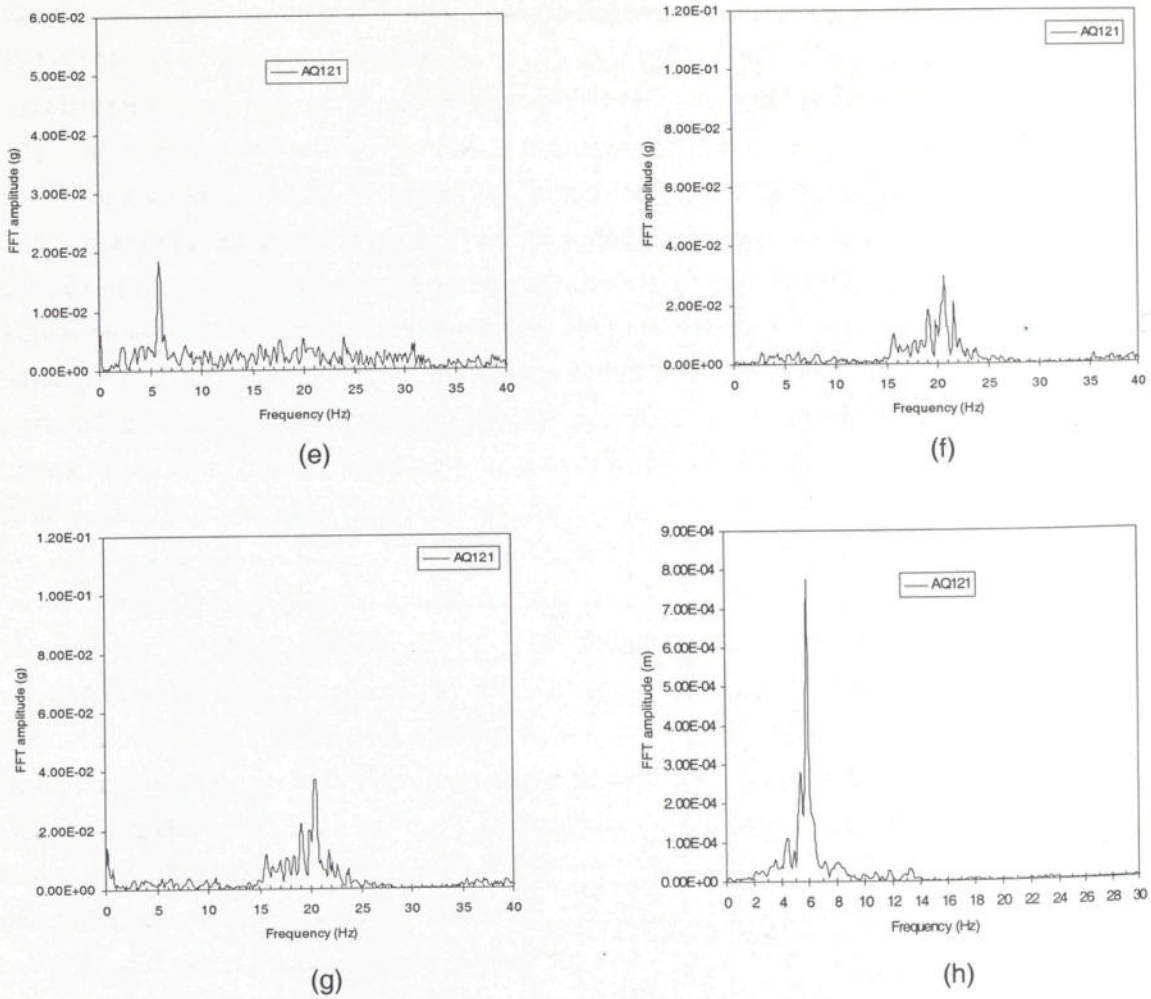


Figure 8.11(continuation). Excitation ***XYZ***, record *RRS1,* large amplitude, response at node: (e) ***69X***; (f) ***69Y***; (g) ***48Y***; (h) ***33Z***.

The analysis of Figures 8.5 to 8.11 illustrates the major aspects associated with the measured signals, which can be synthesized in the following points:

- Both the vertical and lateral responses are clearly dominated by the first vertical and lateral vibration modes, respectively;
- In general, the input records *RRS1* produce higher levels of response than the records *RRS2* for similar input peak values;
- The structure exhibits some nonlinear behaviour, which can be observed in terms of the peak response and also of the spectral content of the measured signals. In effect, by calculating the ratio between the peak response measured for two different amplitudes of excitation, an approximate measure of the nonlinearity involved can be obtained. It can be observed in Tables 8.2, 8.3 and 8.4 that this nonlinearity is more pronounced for the signals associated with the records *RRS1*. An interesting aspect associated with the structural nonlinearity can be observed in

Figures 8.9(a) and 8.9(b), which show that the vertical displacement induced by a lateral excitation (with *2%g* and *4%g* peak values, for records *RRS1* and *RRS2*, respectively) is characterized by two dominant contributions in the lateral (*3.95Hz*) and vertical (*6.2Hz*) natural frequencies. For higher amplitude excitation (*11%g*, for record *RRS1*, and *12%g*, for record *RRS2*), an additional contribution appears in the displacement response, associated with a dominant natural frequency of about *8Hz*, and, for the record *RRS2*, with other additional frequencies in the vicinity. Since some of the largest stay cables have natural frequencies close to *8Hz*, about the second order harmonic of the lateral fundamental frequency, it is expected that the deck displacements in the lateral direction are responsible by *external/ parametric* excitation in some of the stay cables, the vertical motion of the deck being the result of the *dynamic cable-structure interaction*. Note that the appearance of oscillations in frequencies higher than the fundamental natural frequencies, namely close to the frequencies of some stay cables, is not confined to the lateral excitation or to node *33*.

- One particular aspect of the displacement signals, associated with the vertical response to in-plane and three-dimensional excitation, is the occurrence of a sudden decrease of the response after about half the base acceleration record has been applied. This effect is well evident for example in Figures 8.5 and 8.7 for both records *RRS1* and *RRS2* and cannot be associated with the excitation characteristics, since it occurs for the two types of records and the signals measured at the platform don't show any local perturbation. A closer look at the acceleration records measured at other points and, in particular, associated with the backstay response (Figure 8.7) shows the development of a high frequency response component by the same time when the response decreases, which results in a damping of the deck response. The effect of this high frequency oscillation on the stay cable response is however different. Figures 8.7(a) and 8.7(b), for example, show that the high frequency content of the response at one backstay led to a temporary amplification of the out-of-plane response, followed by a decay marked by beating in the successive harmonics of the stay cable (see Figures 8.7(a), 8.7(b), 8.10(g) and 8.10(h)). As for the in-plane response, it is very clear that the oscillation in the high harmonics at significant amplitudes motivated a resonance in the fundamental frequency (see Figures 8.7(a), 8.7(b) and 8.10(e)), leading to a clear phenomenon of parametric excitation;
- Finally, it should be referred that, on the contrary to the design purpose, the deck support on the left tower (see Figure 7.4(e) and the node *9*, in Figure 8.4(b)) showed some mobility in the lateral direction. This fact could be observed visually and was due to a certain degree of flexibility of the connection in that particular direction.

8.2.2.3 Numerical response, OECS *vs* MECS

In an attempt to reproduce numerically the results obtained from the seismic tests, and obtain additional information concerning the stay cables tensions and internal forces on the deck and towers, a set of numerical analyses of the Jindo Bridge model were conducted, in which the response to the set of base accelerograms measured on the shaking table was determined. The Jindo model was idealized alternatively by the two models *OECS* and *MECS* described in Section 7.4.2, and the time domain analyses were performed based on a direct integration algorithm (Newmark method) and using a geometric nonlinear formulation available in the SOLVIA (1995) software package. A few particularities of the numerical analyses must be referred:

- The lateral mobility of the deck support at one of the towers was considered in both the *OECS* and *MECS* models, by interposition of a spring element between the pier and the deck. The stiffness of this element was iteratively adjusted, comparing the first lateral frequency calculated numerically with the corresponding measured natural frequency;
- After some trials based on the *2-D* numerical models, it was decided to perform the time integration of the *8s* seismic records with a time step of *0.002s* , which led to response records with *4000* points;
- A key point in the numerical analysis is the model employed to describe the structural damping. The SOLVIA software package allows for the definition of modal damping coefficients to be used in a mode superposition analysis in the decoupled modal equation, or else for a definition of a consistent damping matrix proportional to the mass and stiffness matrices. If the stiffness matrix is evaluated from a nonlinear formulation, which is the current case, the consistent damping matrix is only proportional to the mass matrix. This means in practice that the consistent damping matrix is defined as a function of one quantity only, i.e., only one damping coefficient of the structure can be fixed. This is a very limiting hypothesis, if one considers that the identified damping coefficients exhibit a very distinct variation with frequency from the one that results from the application of the mass-proportional model. Figure 8.12 shows the ranges of variation of the identified damping coefficients for some of the vibration modes identified on the Jindo model, as well as the variation with frequency of the damping coefficients associated with the mass-proportional model for three selected parameters. These parameters were chosen by fixing the damping coefficient of the fundamental vertical mode, at *6.2Hz,* as *0.35%, 1%* and *1.5%.*

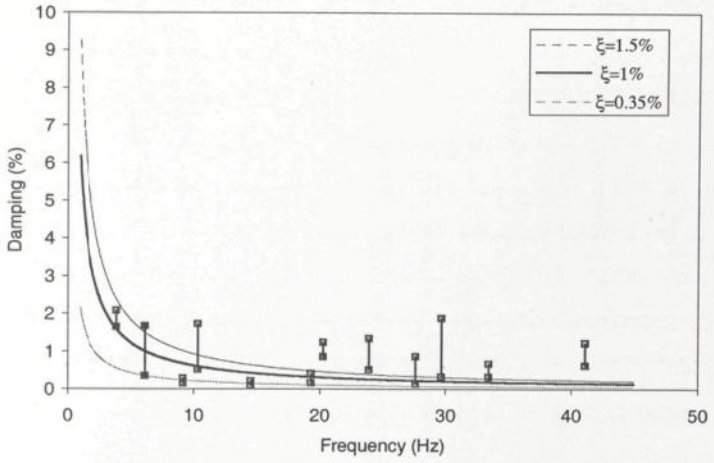


Figure 8.12. Variation of damping with frequency, mass-proportional model *vs* experimental data.

- One of the first questions was to decide whether to employ a mode superposition or a direct integration analysis. In any circumstance the calculus is rather lengthy, as a significant number of degrees of freedom exists, the number of time steps is large, and also a very large number of vibration modes is required when considering the effect of cable vibration. The mode superposition analysis has a major advantage, which is the possibility of defining the damping coefficients more in accordance with the damping coefficients measured on the physical model. However, once the vibration modes are calculated on the basis of the tangent stiffness matrix obtained at the end of a static analysis of the bridge under permanent loads, a linear dynamic calculation of the response is performed. On the contrary, the direct time integration can be performed using the nonlinear geometric analysis, though the available damping model is then rather limited to describe the real damping characteristics. In order to have an insight into the differences of the results that might be obtained from each type of analysis, some preliminary calculations were performed, testing different damping coefficients and the two methods of analysis. Figure 8.13 shows a comparison between the vertical displacement measured at node *33* (Figure 8.4) and the corresponding displacement that resulted from the *3-D* analysis using the *MECS* model and the two alternative dynamic analyses, direct integration and mode superposition. This displacement is the response to an in-plane excitation along the directions *X* and *Z* (record *AQ41*, Table 8.1). For the direct integration, the mass-proportional model was defined fixing the damping coefficient of the first vertical vibration mode as *1%,* which led to a variation of damping with frequency represented by the bold curve in Figure 8.12. The mode superposition analysis was performed using, for the *MECS* model, *125* vibration modes, and the damping coefficients presented in Table 8.5.

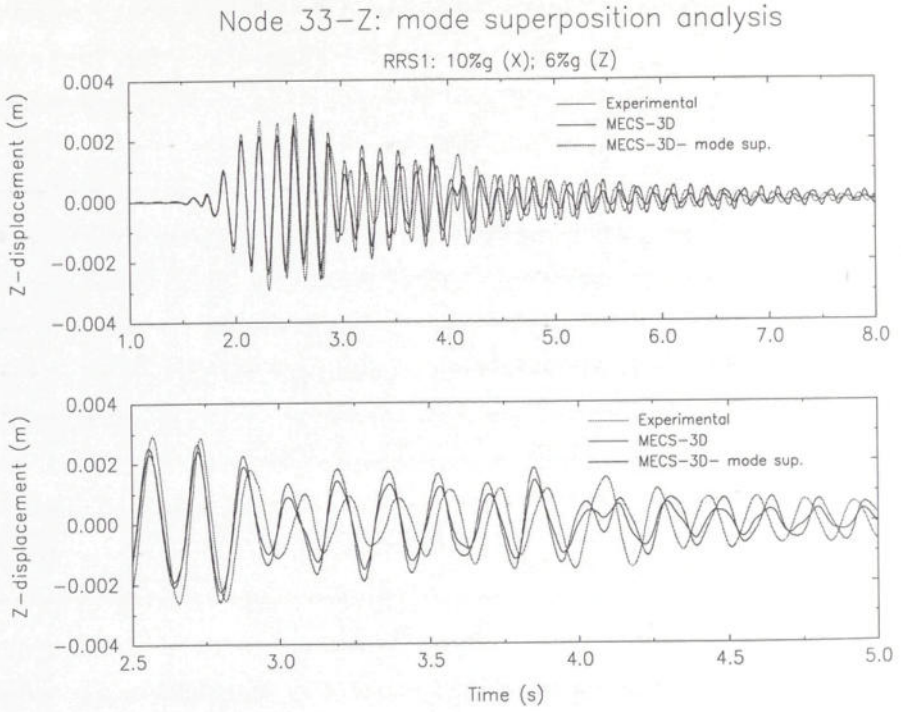


Figure 8.13. Vertical displacement at node *33*, response to seismic excitation *XZ*, record *AQ41*: measured response *vs* direct integration /mode superposition analyses.

Table 8.5. Damping coefficients employed in mode superposition analysis.

Mode numbers	Natural frequencies (Hz)	Modal damping coefficient (%)	Characteristics of vibration modes
1, 2	4.26, 6.14	1	1st transv. SYM, 1st vert. SYM
3, ..., 26	6.85, ..., 8.61	0.3	Local modes, 1st transv. ASM, 1st vert. ASM
27	9.04	0.6	1st vert. ASM
28, ..., 76	9.15, ..., 13.84	0.6	Local modes, 1st vert. ASM, 1st transv. ASM, 2nd vert. SYM
77	14.12	0.5	2nd vert. SYM
78, 79	15.68, 15.69	0.3	2nd vert. SYM
80, 81	15.70, 15.70	0.5	2nd vert. SYM
83, ..., 125	15.77, ..., 19.01	0.6	Local modes, 2nd vert. ASM, 3rd vert. SYM, In-plane tower modes

The analysis of Figure 8.13 shows that the response at node *33* is essentially dominated by the contribution of the first vertical vibration mode. The comparison between experimental and numerical responses during the first part of the excitation, say from *1.5s* to *2.8s*, shows a rather good approximation, although the measured displacement is slightly higher than the obtained numerically. Moreover, the two numerical methods produce very similar results. It is then possible to observe a short period of time, say from *2.8s* to *3.8s*, in which the measured response suffers a sudden decrease (see the zoom in Figure 8.13). During this part of the record the two numerical responses follow a similar path, which differs significantly from the experimental response, the direct integration analysis leading to slightly lower amplitudes. Finally, the later part of the record looks as a sinusoid of similar amplitude for the experimental and mode superposition response, and with slightly lower amplitude for the direct integration response. The two numerical responses are almost in-phase, but are out-of-phase with the measured response, what shows that some phenomenon occurred in the intermediate part of the record that could not be explained by any of the developed numerical models. The previous analysis of measured responses (see Section 8.2.2.2) pointed to the development of a high frequency contribution into the response in an intermediate part of the excitation records, which was due to vibration of the stay cables, and which apparently damped the deck response. Beyond that, the damping studies presented in Section 7.5.2.3 showed that the damping coefficients associated with the fundamental vibration modes varied strongly with the amplitude of oscillation. These two aspects are quite difficult to reproduce with the two types of numerical analyses above described. The option for direct integration analysis was due then to the interest in simulating numerically a stronger nonlinearity than the one observed on the Jindo Bridge model in subsequent studies.

Response to lateral excitation (Y)

This Section analyses the response to a seismic excitation in the lateral direction (*Y*) characterized by the *RRS1* record and by a peak value of *11%g* (record *AQ63*, Table 8.1). Figures 8.14 and 8.15 resume the input time record measured on the seismic platform and applied as a base excitation to the structures described by the *OECS* and *MECS* models, as well as the corresponding responses calculated at some of the instrumented locations along the structure. The peak values associated with the dynamic experimental and numerical response at some selected locations are summarized in Table 8.6. Figure 8.16 superimposes the experimental and numerical responses at some selected locations, namely the lateral acceleration at nodes *18* and *24*, and the vertical displacement at node *33* (see Figure 8.4).

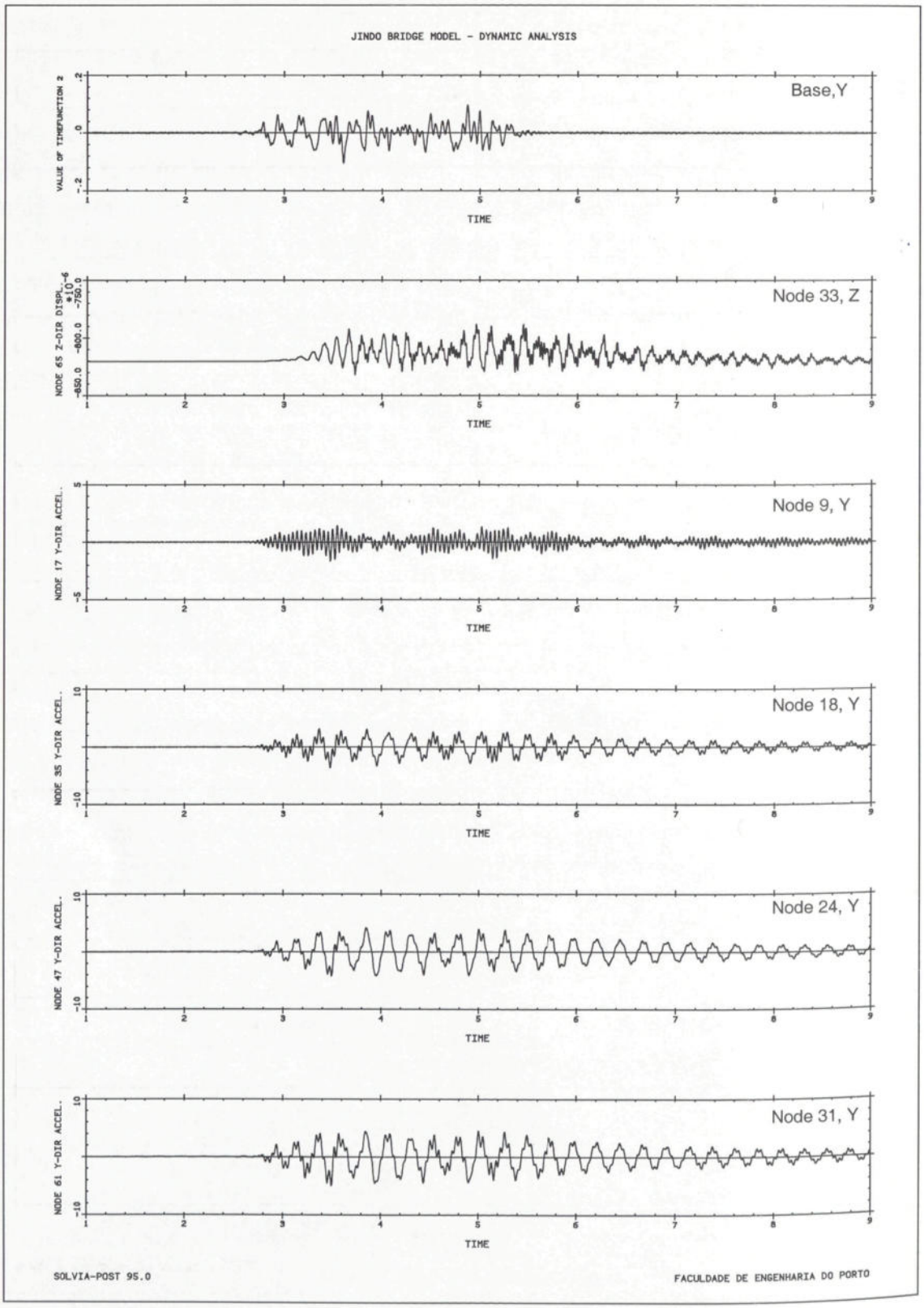


Figure 8.14. Input record along direction *Y* (record *AQ63*) and numerical response calculated using the *MECS* model.

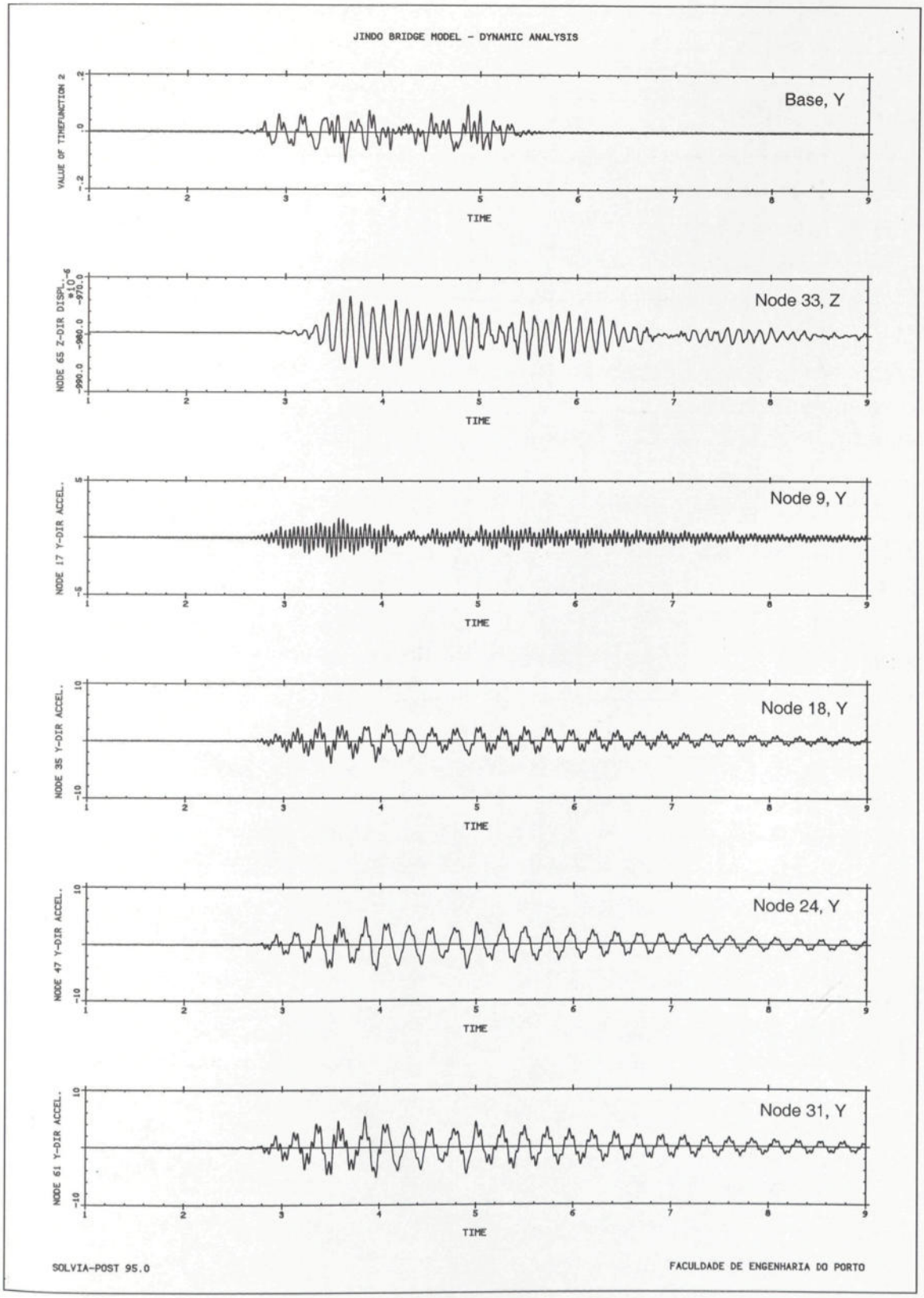


Figure 8.15. Input record along direction *Y* (record *AQ63*) and numerical response calculated using the *OECS* model.

Table 8.6. Excitation in ***Y*** direction, record *RRS1* (*AQ63*). Peak values of measured/calculated response.

Location, Type of Measure	Experimental	OECS-3D	MECS-3D
9Y, acceleration	0.30g	0.17g	0.17g
18Y, acceleration	0.50g	0.39g	0.37g
24Y, acceleration	0.49g	0.49g	0.43g
31Y, acceleration	0.54g	0.54g	0.50g
33Z, displacement	0.00028m	0.000006m	0.000012m

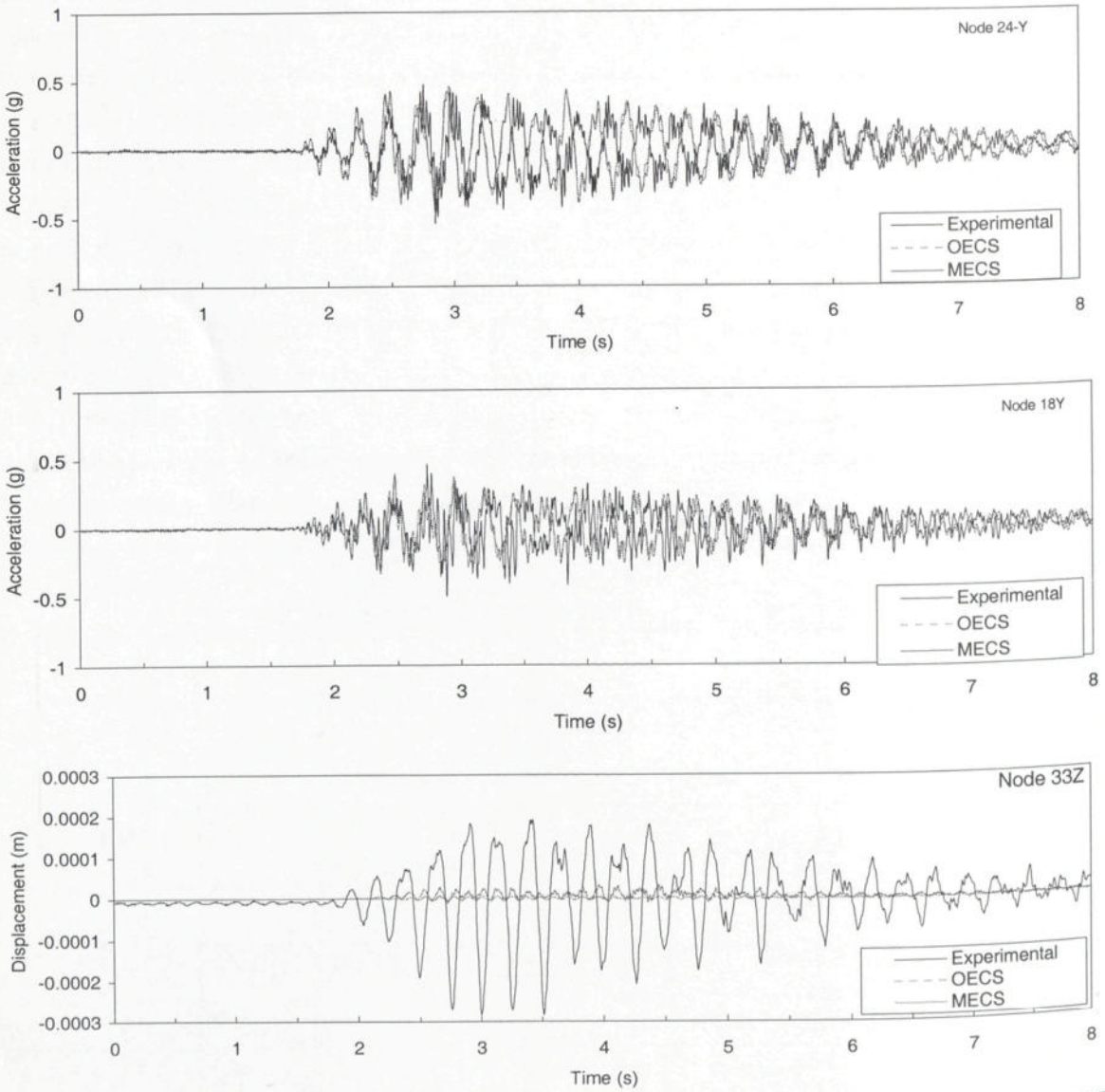


Figure 8.16. Experimental *vs* numerical response (*OECS* and *MECS*) at nodes *18Y*, *24Y* and *33Z*.

The comparison between the numerical response calculated on the basis of the two numerical models shows, at first, that minor differences exist between the two types of analysis, except for the vertical displacement at node *33* (close to the midspan). Although this displacement is very small, there is clear evidence that the consideration of the cable dynamics led to an amplification of the response. This means basically that the vibration of the stay cables increases the coupling between the responses in two different planes, accentuating the three-dimensional character of the bridge behaviour.

With respect to the comparison between the experimental and numerical responses, and although no major differences can be found between the experimental and numerical amplitudes for the lateral response, the numerical models are unable to reproduce accurately the full response time histories. The following points can be noticed: (i) the numerical response fits rather well the measured response during a first part of the record, say from *1.5s* to *2.8s*; (ii) in a second segment, say from *2.8s* to *5s*, a frequency and phase shift between numerical and experimental signals occur, which attenuate during a time interval from about *5.3s* to *6.2s*, but increase again in the final part of the records; (iii) the envelope of the experimental and numerical responses are nevertheless very close, proving that the damping properties employed in the numerical analyses are adequate to represent the average path of the structural response; (iv) the experimental response exhibits a stronger composition in the higher frequencies than the numerical response. This aspect is evident from the observation of Figure 8.17, which plots the *FFT* amplitudes associated with the lateral acceleration at node *24* (at about *1/3* span) for the measured and calculated responses. This Figure shows in fact a relevant frequency content of the measured response in the range *35Hz* to *40Hz*. The slight difference between experimental and numerical natural frequencies associated with the first transversal mode is also evident from this Figure.

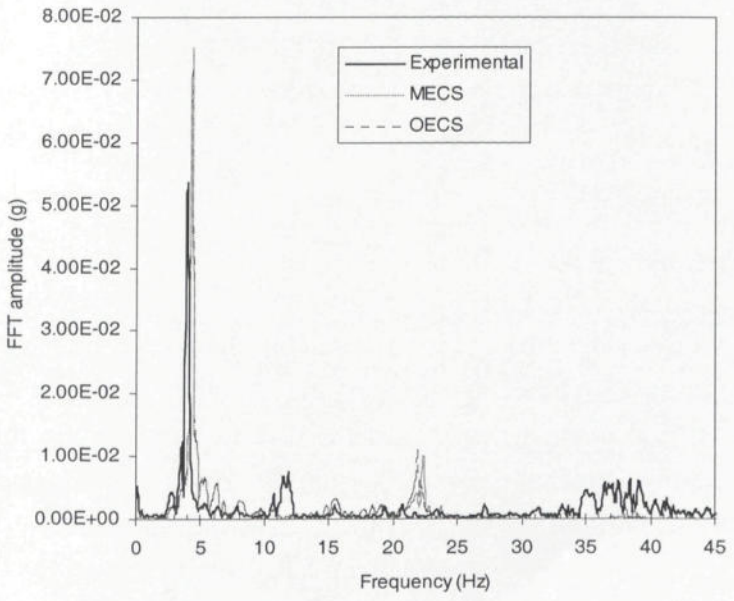


Figure 8.17. *FFT* amplitude of the lateral response at node *24*. Experimental *vs* numerical *OECS/MECS* analyses.

The comparison between the experimental and numerical displacements along the vertical direction at node *33* shows very significant differences in terms of amplitude and frequency (Figure 8.16). Figure 8.18 shows the FFT amplitude associated with the measured and numerical displacements at node *33*. The major aspect that can be inferred from the observation of this Figure is that the bridge oscillates vertically at the fundamental transversal frequency, at about *4Hz*, and also at about *8Hz*, which is an harmonic of that frequency. In addition, a contribution in the fundamental in-plane vibration mode, at about *6.2Hz*, exists. The numerical response exhibits essentially vibration in this mode, but not on the lateral mode, and not at *8Hz*. The parametric excitation effect, as explained previously, cannot therefore be reproduced by the numerical model, what is attributed to the fact that the cable modes with lower frequencies are much more damped than the real cables, in virtue of the restrictions associated with the damping properties. In effect, the selected damping model leads to a damping coefficient of *0.77%* for a cable mode with natural frequency at *8Hz*, whereas the real measured damping is less than *0.3%*.

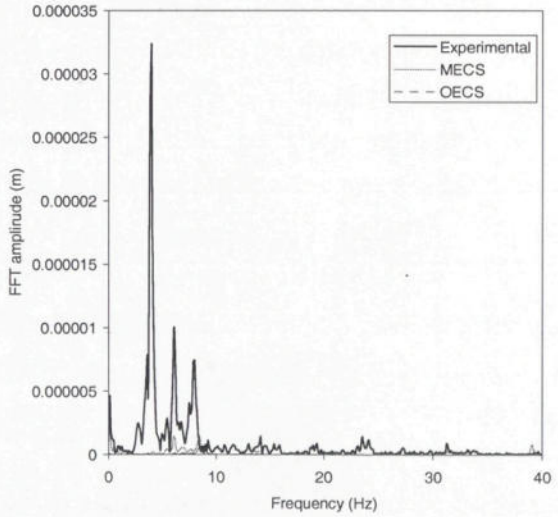


Figure 8.18. *FFT* amplitude of the vertical response at node *33*. Experimental *vs* numerical *OECS/MECS* analyses.

Response to three-dimensional excitation (XYZ)

The response to a three-dimensional excitation, consisting in a combination of *RRS1* records with *11%g*, *12%g* and *8%g* peak values along the directions *X*, *Y* and *Z*, respectively (record *AQ93*, Table 8.1), is now analysed. Figures 8.19 and 8.20 resume the input time records measured on the seismic platform along directions *X*, *Y* and *Z*, as well as the response to this base excitation calculated on the basis of the *OECS* and *MECS* models for some particular locations along the structure. The peak values associated with the measured and numerical response at these locations are summarized in Table 8.7.

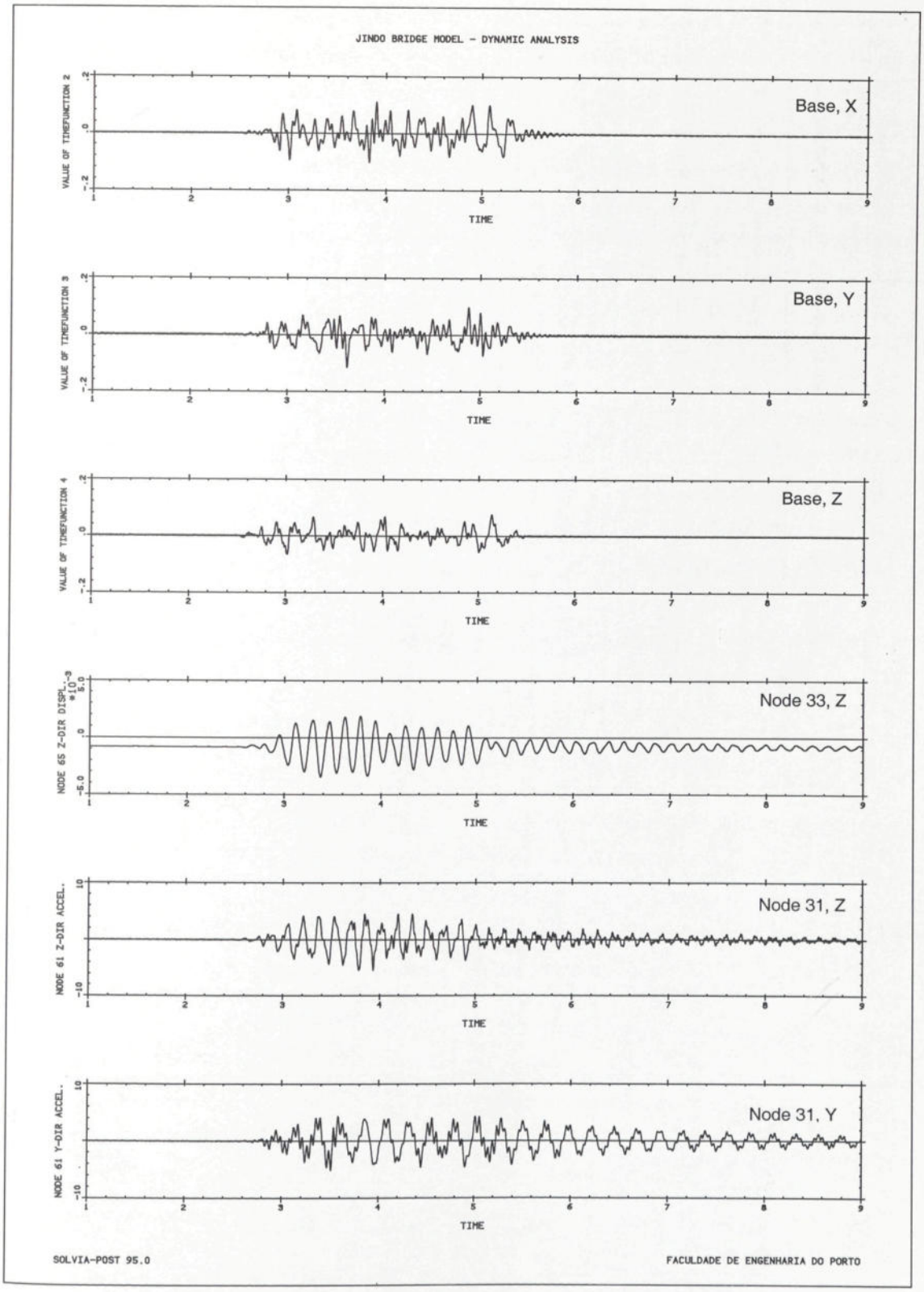


Figure 8.19. Input record along the directions *X, Y* and *Z* (record *AQ93*), and numerical response calculated using the *MECS* model.

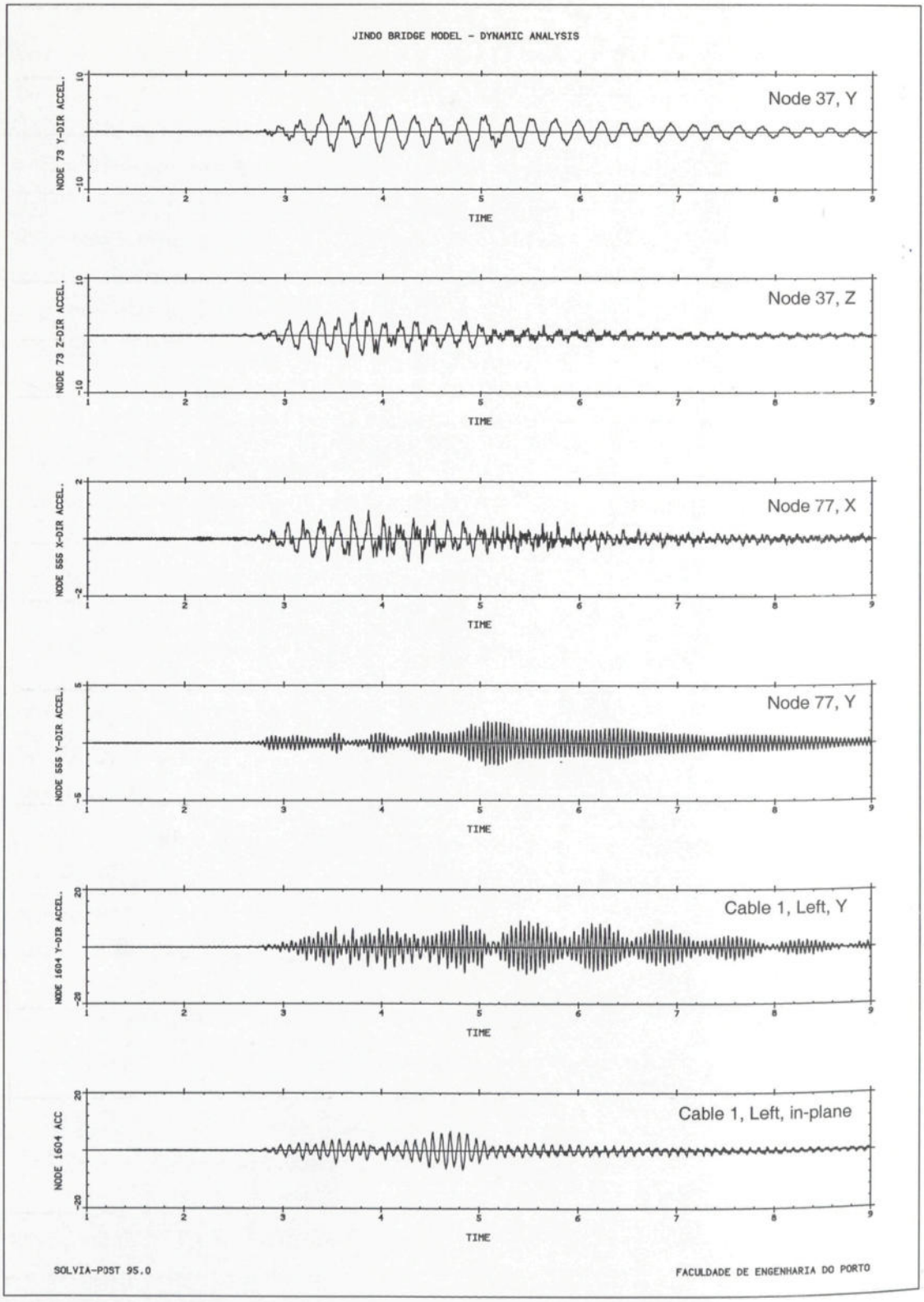


Figure 8.19 (continuation). Input record along the directions *X, Y* and *Z* (record *AQ93*), and numerical response calculated using the *MECS* model.

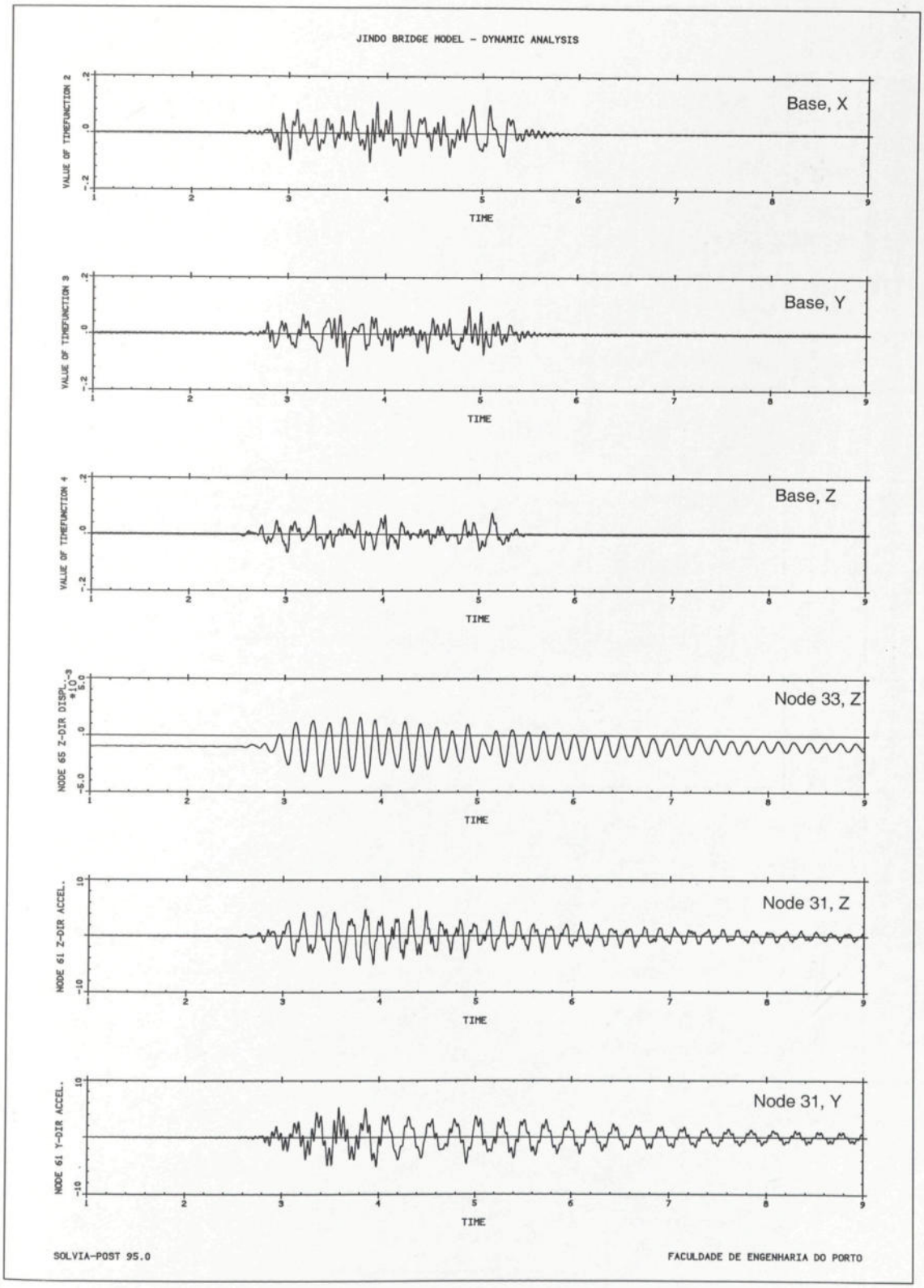


Figure 8.20. Input record along the directions *X, Y* and *Z* (record *AQ93*), and numerical response calculated using the *OECS* model.

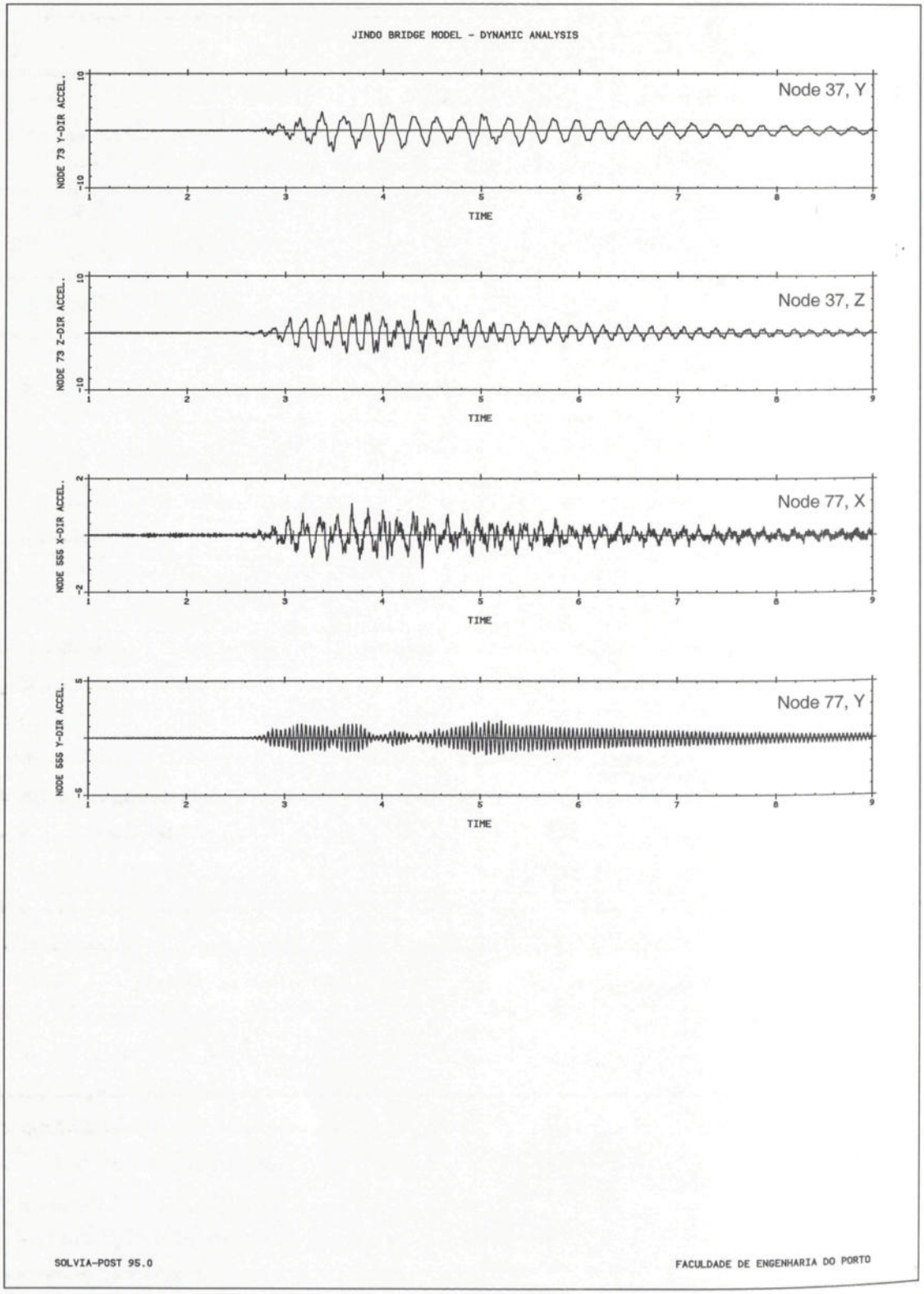


Figure 8.20 (cont.). Input record along the directions *X, Y* and *Z* (record *AQ93*), and numerical response calculated using the *OECS* model.

Table 8.7. Excitation in **X Y Z** directions, record *RRS1* (*AQ93*). Peak values of measured/calculated response.

Location, Type of Measure	Experimental	OECS-3D	MECS-3D
31Y, acceleration		0.53g	0.52g
31Z, acceleration		0.52g	0.54g
33Y, acceleration		0.48g	0.47g
37Y, acceleration		0.38g	0.37g
37Z, acceleration	0.49g	0.54g	0.40g
77X, acceleration		0.12g	0.10g
Cable 1, Left, in-Plane, acceleration	1.18g	-	0.69g
Cable 1, Left, Y, acceleration	1.77g	-	0.94g
33Z, displacement	0.0035m	0.0027m	0.0026m

The comparison between the numerical response calculated on the basis of the two numerical models shows that very similar peak values are in general obtained. Looking at the plots presented in Figure 8.21, which superimpose the experimental and numerical *OECS/MECS* time histories at some selected locations, it can be observed that the *OECS* response attenuates more slowly than the *MECS*. The effect of added damping introduced by the stay cables is therefore identified, even if no apparent difference occurs in the peak response.

With respect to the comparison between the experimental and numerical responses, a close approximation can be found during the first part of the response records either in terms of displacements or accelerations along the deck (Figure 8.21). The vertical displacements measured at node *33* have however higher amplitudes than the corresponding numerical displacements. The second part of the response records, say from *2.8s* to *4.8s* shows some discrepancies between numerical and measured displacements, in amplitude, frequency and phase. These discrepancies are of the same type of those already referred in correspondence with the excitation in the *Y* direction. Finally, the last part of the signals shows again proximity between the experimental and the *MECS* response, both in amplitude and frequency, but a slight phase shift. As for the comparison between the in-plane and out-of-plane response at *1/3*rd span of a left backstay, more significant discrepancies can be noticed. Although some differences in the lateral and in-plane accelerations exist already during the first part of the records, the amplitudes are identical in the first *3.8s* and *2.8s*, for the in-plane and out-of-plane responses, respectively. The major differences can be observed afterwards, as an amplification of the response takes place in both directions. A resonance in the fundamental mode occurs for the in-plane response. Although the *MECS* shows an identical behaviour, the

cable response is attenuated very quickly, in consequence of the higher damping of the numerical model for this range of frequencies.

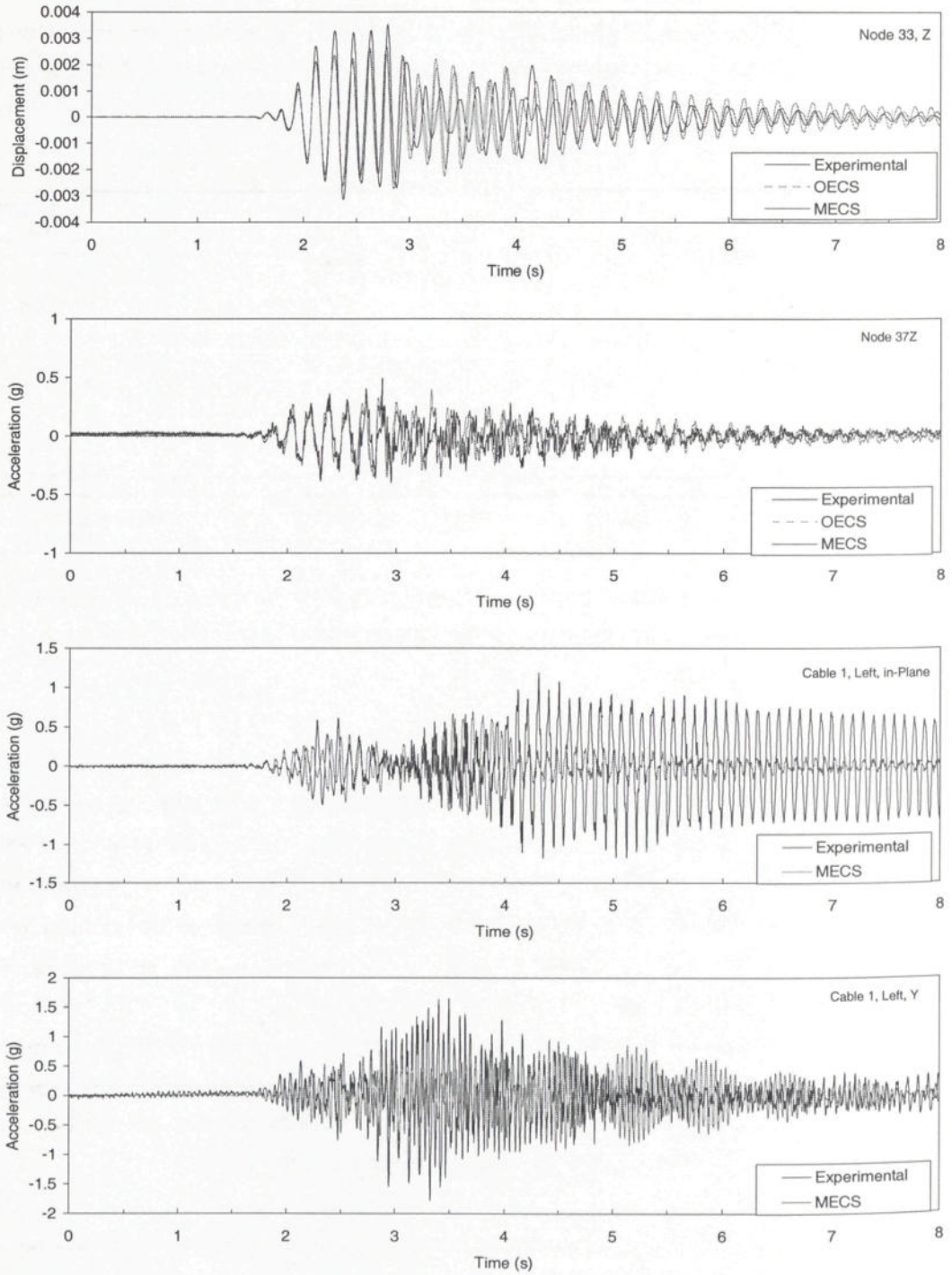
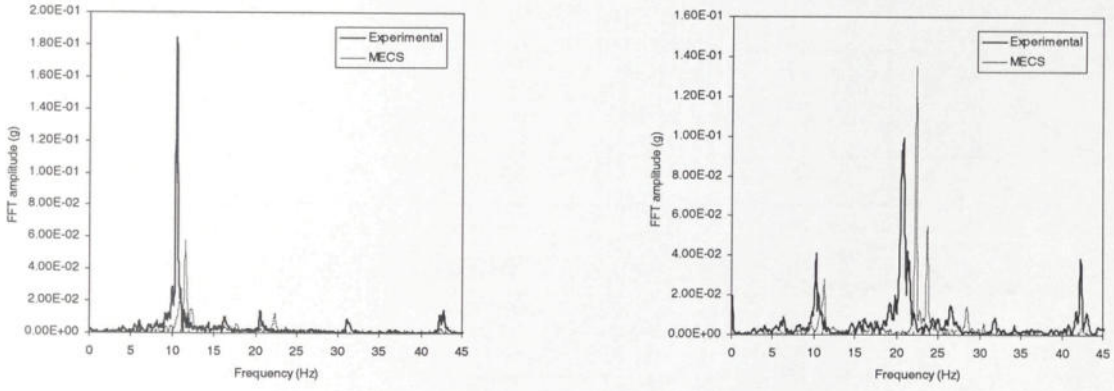


Figure 8.21. Experimental *vs* numerical response (*OECS* and *MECS*) at nodes *33Z, 37Z* and at 1/3rd span of a left backstay, in-plane and in direction *Y*.

Figures 8.22(a) and 8.22(b) represent the *FFT* amplitudes of the measured and calculated accelerations in the backstay for the in-plane and lateral (*Y*) directions, respectively.

A major conclusion that results from the observation of the Figure is the difference in measured and calculated natural frequencies (the measured natural frequency associated with the first mode is *10.25Hz*, while the corresponding calculated frequency is *11.23Hz*). These differences were not expected, as the errors in the installed tension were rather small (the tuned tension led to a natural frequency of *11.9Hz*). It is therefore possible that the variation in the cable natural frequency is due to the large amplitudes of vibration of the stay cable.



(a) (b)

Figure 8.22. *FFT* of the accelerations at the left back stay. Experimental *vs* numerical *MECS* analysis: (a) in-plane response; (b) lateral (*Y*) response.

Response to in-plane excitation (XZ)

This Section analyses the response to seismic excitation applied simultaneously along the directions *X* and *Z*, characterized by signals *RRS1* with peak values of *11%g* and *7%g* along the directions *X* and *Z*, respectively (record *AQ41*). As in the previous cases, this record was used as base excitation in the numerical evaluation of the response on the basis of the models *OECS* and *MECS*, leading to similar conclusions in terms of the comparison between experimental data and the *MECS/ OECS* analyses. This fact is illustrated by Figure 8.23, representing the experimental and numerical vertical displacement at node *33*, and by Table 8.8, which summarizes some measured and calculated absolute peak values on some of the most significant nodes of the structure (mid-span, node *31Z*; attachment of longest cable, node *33Z*; third of span, node *38Z*; top of left tower, node *69X*).

Figure 8.24 presents the Fourier spectra associated with the experimental and calculated response at node *33*. It can be observed that, although the modal analysis performed with the *OECS* and *MECS* models has led to a fundamental frequency for vertical motion almost identical to the corresponding measured frequency, the spectral content associated with the seismic response is now marked by a slight shift in that frequency. Dividing the displacement history into three segments for both the experimental and *MECS* records, it can be observed that in the middle part of the time response, the measured

displacements show a slight decrease of the frequency, which is not observed with the numerical model.

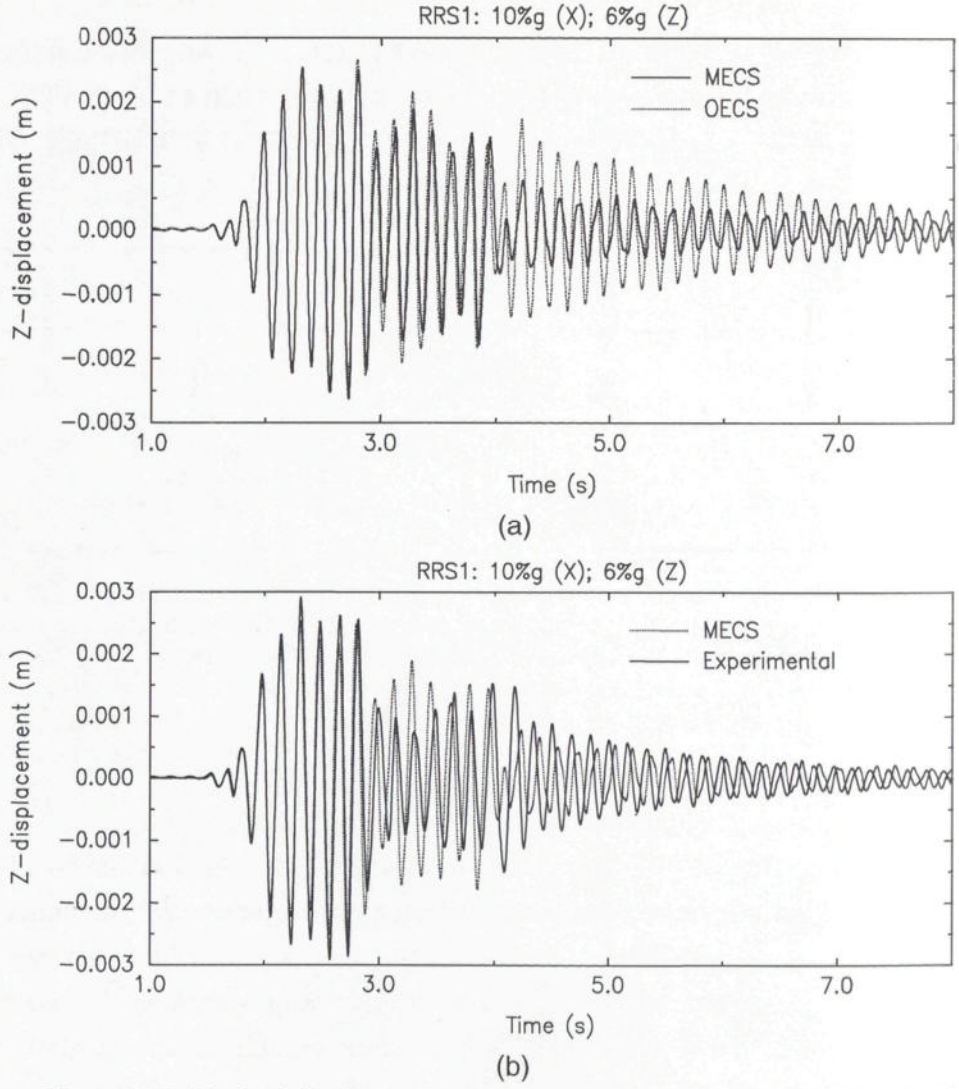


Figure 8.23. Vertical displacement at node *33:* (a) calculated, *OECS vs MECS*; (b) experimental *vs* calculated response, *MECS*.

Table 8.8. Excitation in ***XZ*** directions, record *RRS1* (*AQ41*). Peak values of meas./calc. response.

Location, Type of measure	Experimental	OECS-3D	MECS-3D
33Z, Displacement (m)	-0.0029 / 0.0029	-0.0026 / 0.0025	-0.0025 / 0.0026
31Z, Acceleration (m/s²)	-6.6 / 6.5	-4.8 / 4.1	-5.7 / 4.4
33Z, Acceleration (m/s²)	-4.2 / 4.6	-4.5 / 4.0	-5.3 / 4.3
38Z, Acceleration (m/s²)	-2.9 / 3.2	-3.1 / 3.0	-3.1 / 3.7
69X, Acceleration (m/s²)	-1.5 / 1.5	-1.2 / 1.2	-1.0 / 0.9

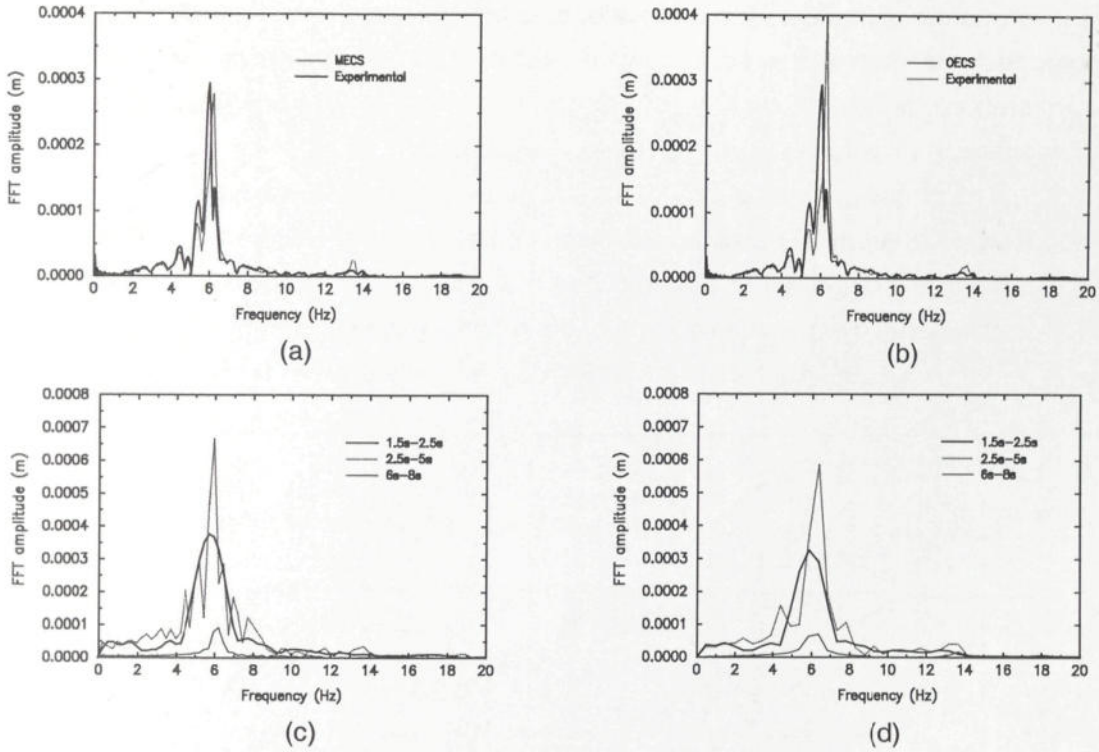


Figure 8.24. Fourier spectra at node *33Z* (displacement): (a) experimental *vs MECS*; (b) experimental *vs OECS*; (c) experimental, segment analysis; (d) *MECS*, segment analysis.

Validation of numerical models

The general conclusion from the comparison between experimental and numerical responses to seismic excitation is that the numerical models lead to a rather good agreement of results in global terms, although they cannot indeed represent several particularities observed on the physical model. The major differences found are precisely attributed to the difficulty in modeling accurately the damping associated with the stay cables, although it is recognized that some local aspects of the physical model may not have been represented by the numerical models as well. Because the seismic response is in general dominated by the contribution of the fundamental lateral and vertical modes, the differences in terms of peak response along the deck and towers are in fact not so significant.

Global analysis of the Jindo model, OECS vs MECS models

Although the exaggerated damping attributed to the fundamental cable modes has actually led to an attenuation of the effect of cable vibration, it was possible to observe that the free vibration response at low amplitudes (the final part of the seismic response records) obtained on the basis of the *MECS* analysis indeed showed a quicker decay than the *OECS* response. This is the evidence of the so-called "*system-damping effect*". It is important to note however that no appreciable differences were found between peak accelerations and displacements for the selected locations analysed using the two numerical models. The current Section assumes

that the numerical models are validated, and provides additional information concerning the peak response along the deck, towers and stay cables, expressed not only in terms of accelerations and displacements, but also in terms of other important quantities, like bending moments and axial forces.

The global peak response of the bridge to the in-plane excitation characterized by the record *AQ41* in terms of maximum displacements, accelerations, bending moments and axial forces along the deck, the cables and one of the towers is depicted in Figures 8.25 to 8.27. Note that only the dynamic component of the response is analysed here.

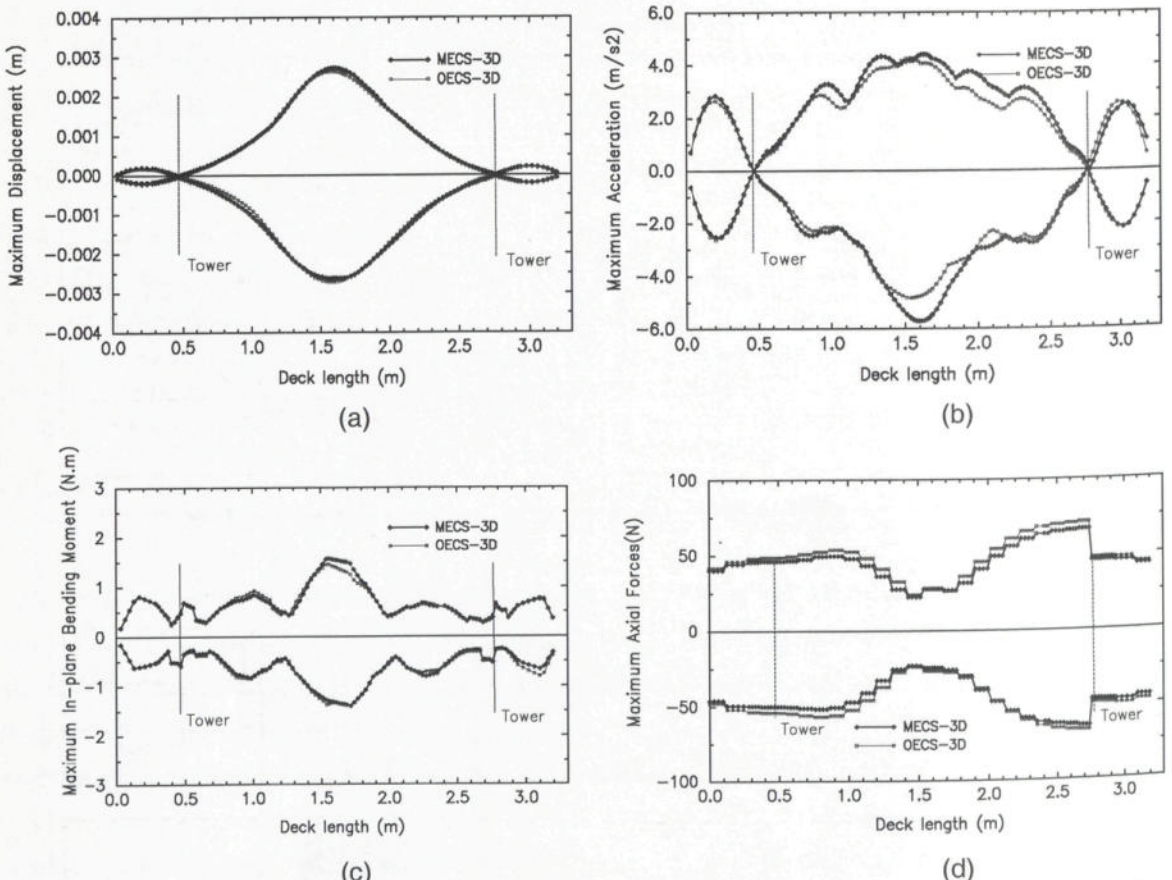


Figure 8.25. Peak values of the calculated response along the girder, *OECS vs MECS* analysis: displacements, accelerations, bending moments and axial forces.

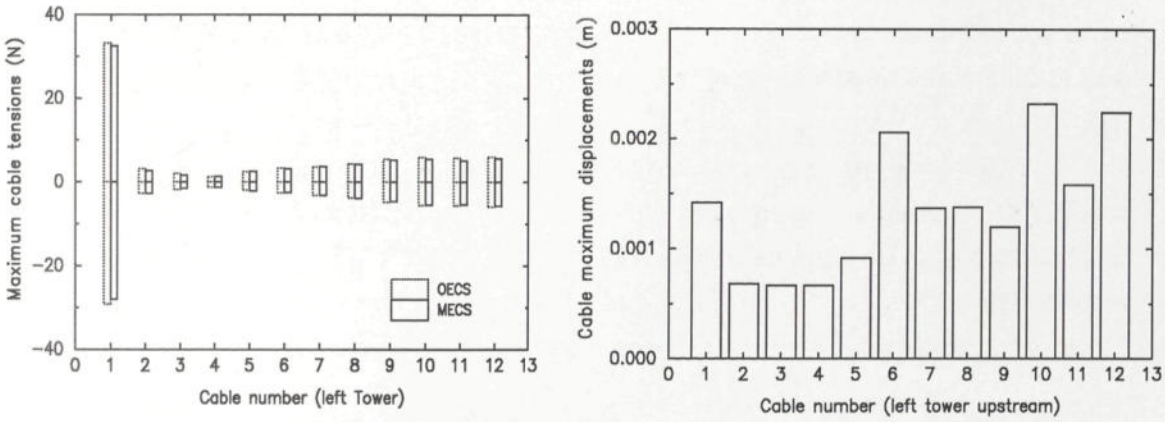


Figure 8.26. Peak values of cable response: (a) tension, *OECS vs MECS* analysis; (b) peak displacements at the midpoint of cables.

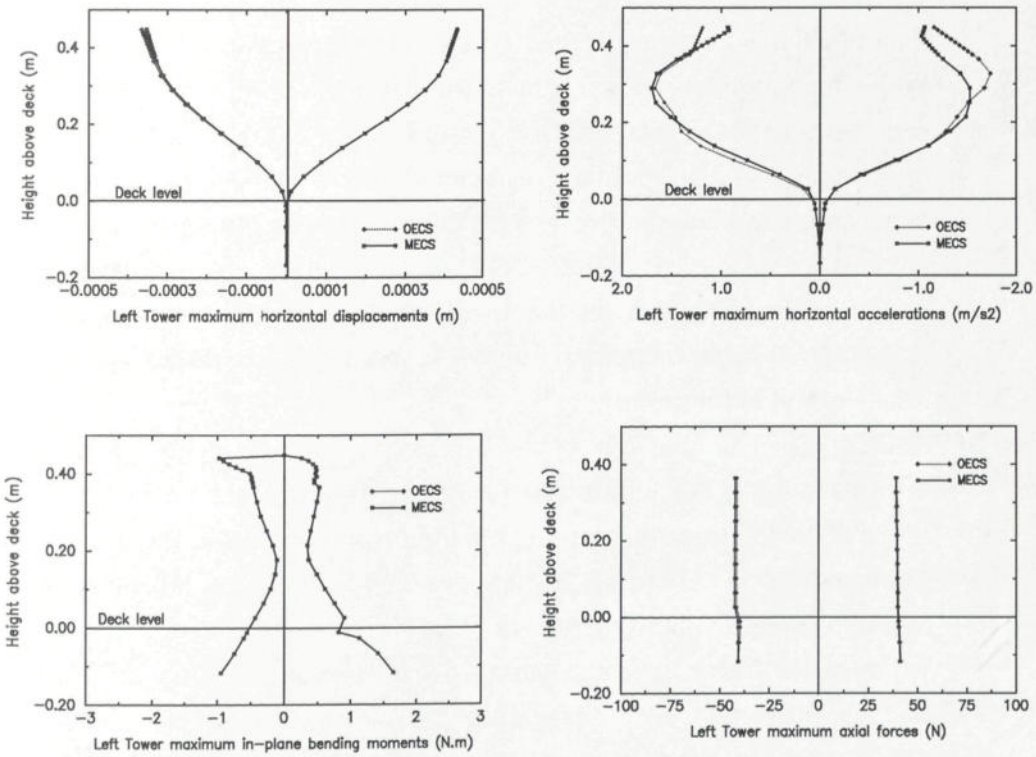


Figure 8.27. Peak values of the calculated response along one tower, *OECS vs MECS* analysis: displacements, accelerations, bending moments and axial forces.

Inspection of Figures 8.25 to 8.27 suggests that the *MECS* analysis led to very slight modification of the peak response. Table 8.9 resumes some values of the most significant changes in the negative and positive peak response that resulted from a *MECS* analysis, with regard to a standard *OECS* analysis. The major differences are found for accelerations, which are more affected by the higher frequency content of the signals.

Table 8.9. Change of peak response, MECS vs *OECS* analysis.

Type of response	Change of peak response (*MECS / OECS*) (%)			
	Deck	Node no.	Towers	Node no.
Displacement	105.9 / 115.7	**33Z**	96.4 / 99.8	**69X**
Acceleration	122.1 / 106.2	**33Z**	91.4 / 78.6	**65X**
Bending moment	100.0 / 115.4	**33**	98.9 / 100.4	**67**
Axial force	103.4 / 89.5	**38**	102.4 / 98.6	**67**

It is important to note that the slight peak differences in the analysis are by no means an indication that the effect of *dynamic cable-structure interaction* is negligible. In fact, the following aspects need to be pointed out:

- First of all, it is evident that the seismic response is dominated by the contribution in the fundamental modes, due to the important frequency content of the input excitation used in this analysis, in the vicinity of the corresponding natural frequencies. These modes, the vertical mode in particular, do not involve a significant cable interaction, and so the differences obtained between responses calculated on the basis of the *OECS* and *MECS* models are relatively small;
- A second issue is that the numerical model employed damps excessively the fundamental cable modes and so the resonant effects do not result in significant amplification of the response;
- Another point is that the cable damping/resonance does not in fact develop instantaneously, but only some time after the structure starts vibrating. So, the effect of cable-structure interaction in the peak response is limited;
- The observation of Figure 8.26(b) shows that some of the cables (cables *6*, *10* and *12*, with fundamental frequencies of *13.11Hz*, *9.39Hz* and *6.81Hz*, respectively) experienced higher levels of vibration than the others. Considering that the first three in-plane natural frequencies of the structure, obtained on the basis of the *OECS* analysis, associated with vertical bending modes, are *6.21Hz*, *9.12Hz* and *13.74Hz*, it seems clear that major cable effects occur when a global natural frequency lies in the range of the first natural frequencies of some cables.

The issues listed above prompt two main questions:

- How magnified would be the effect of *dynamic cable-structure interaction* if the fundamental modes interacted in a higher extent with the cable modes, i.e., if for example the fundamental in-plane natural frequency lied in the range of the first frequency of the stay cables (*6.81Hz* to *18.92Hz*, according to Table 7.6)?

- How would the *cable-structure interaction* develop if the structure were excited by an intense force defined in a narrow frequency range that contained, for example, a global natural frequency of the bridge and the natural frequency of some cables?

In order better to understand these points, and taking into account the existence of a significant number of stay cables with fundamental frequencies close to the frequency of the first vertical anti-symmetric bending mode (*9.12Hz*), two different numerical simulations were performed. The first consisted of modifying the mechanical characteristics of the structure, in order to increase the natural frequency of the first mode of vibration to the range of the first natural frequency of those cables. The second consisted of the application of a new artificially generated input signal, based on an almost rectangular power spectrum defined in a narrow frequency band that contains both the frequency of the third global mode of vibration (first vertical anti-symmetric) and the first natural frequency of some cables.

With these tests, whose results will be presented in the next Sections, the author intended to frame the effects of dynamic cable-structure interaction, considering, on the one hand, the possibility of development of an added damping effect, in consequence of the vibrations of the various cables at different natural frequencies and, on the other hand, the possibility of magnification of the response, in consequence of a resonance at one particular mode of vibration.

8.3 NUMERICAL SIMULATIONS

8.3.1 Internal resonance at the fundamental mode of vibration

The current Section describes the numerical simulations developed with the purpose of achieving a resonance at the fundamental vertical vibration mode. These simulations were based on an artificial modification of the mechanical properties of the materials, maintaining the bridge geometry and employing the same excitation records in directions *XZ* (*AQ41*).

8.3.1.1 Modified model

The numerical models of the Jindo bridge physical model were modified, by increasing the Young's modulus of the materials that constitute the deck/towers and the stay cables, by factors of *2.8* and *2*, respectively. This led to an increase of the frequency of the first vertical bending mode from *6.21Hz* to *9.01Hz*, while the fundamental frequencies of the cables increased from *6.81Hz-18.92Hz* to *7.73Hz-23.69Hz*.

The analysis of mode shape configurations for the new *OECS* and *MECS* models shows that, as for the previous analysis, groups of symmetric mode shapes alternate with groups of anti-symmetric modes (note that this designation is applied to describe only the configuration of the deck and towers). It is also evident, according to Table 8.10, which

presents the minimum ratio between the maximum normalized modal displacement components (along the three orthogonal directions *X*, *Y* and *Z*) of the group of cables and of the deck/towers, that the *MECS* analysis produced many new modes of vibration associated with the same first symmetric vertical configuration. These modes involve significant interference with cables.

Table 8.10. Calculated natural frequencies of modified models.

Mode number	MECS natural frequency (Hz)	Associated OECS frequency (Hz)	Min.ratio of cable/beam max. displ .	Type of mode
1	6.62	6.72	2.2	1st transv. SYM
3	7.78	9.01/6.72	4.9	1st vert. SYM+1st transv.ASM
4	7.78	9.01/11.71	4.3	1st vert. SYM+1st transv.ASM
8	8.02	11.71	15.6	1st transv. ASM
9	8.03	6.72	13.7	1st transv. SYM
11	8.46	9.01	6.0	1st vert. SYM
12	8.46	9.01	7.5	1st vert. SYM
13	8.46	9.01	6.2	1st vert. SYM
14	8.46	9.01	6.1	1st vert. SYM
15	8.46	9.01	6.0	1st vert. SYM
16	8.46	9.01	6.2	1st vert. SYM
17	8.47	9.01	6.1	1st vert. SYM
21	8.72	9.01	16.2	1st vert. SYM
25	8.83	6.72	17.0	1st transv. SYM
27	8.98	9.01	12.0	1st vert. SYM
28	8.98	9.01	11.9	1st vert. SYM
29	8.98	9.01	11.7	1st vert. SYM
44	11.2	9.01/6.72	13.0	1st vert. SYM+1st transv.SYM
45	11.2	9.01/6.72	10.5	1st vert. SYM+1st transv.SYM
53	12.0	13.72	12.5	1st vert. ASM
54	12.0	13.72	12.0	1st vert. ASM
55	12.0	13.72	14.9	1st vert. ASM
56	12.1	13.72	17.7	1st vert. ASM
57	12.2		5.9	tranversal
59	13.6	13.72	11.8	1st vert. ASM
61	13.6	13.72	13.9	1st vert. ASM
63	13.6	13.72	14.0	1st vert. ASM
67	14.1	13.72	12.0	1st vert. ASM
77	15.8	13.72	10.2	1st vert. ASM
79	15.8	13.72/6.72	10.1	1st vert. ASM+1st transv.SYM
85	16.4	13.72/11.71	21.2	1st vert. ASM+1st transv.ASM
87	16.4	13.72/11.71	25.0	1st vert. ASM+1st transv.ASM

The participation factors along the longitudinal (*X*) and vertical (*Z*) directions, presented in Figure 8.28, show the contribution of a significant number of modes (from the *MECS* analysis) to the response.

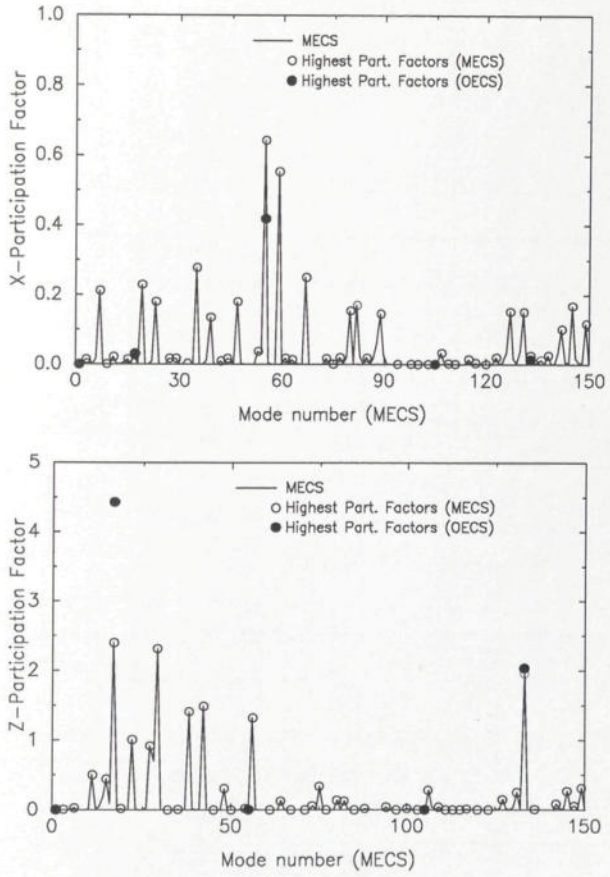


Figure 8.28. Participation factors associated with models *OECS* and *MECS*.

8.3.1.2 Numerical response, *OECS vs MECS*

The calculation of the response of the *OECS* and *MECS* models of the new structure to the combination *XZ* (*11%g (X), 7%g (Z)*) of accelerograms *AQ41* from record *RRS1* above described, was based on a geometric nonlinear formulation, using the direct integration method of Newmark and the same mass-proportional damping matrix (f=6.20Hz, $\xi = 1.0\%$). Figures 8.29 and 8.30 show the peak dynamic response along the deck and one of the towers, and along the cables, respectively, expressed in terms of displacements, accelerations and bending moments.

Figure 8.31 represents the time history of the bending moment response at node *33* and the corresponding Fourier spectrum. The relative difference between the peak response calculated at some significant locations, based on the *OECS* and *MECS* analyses, is presented in Table 8.11.

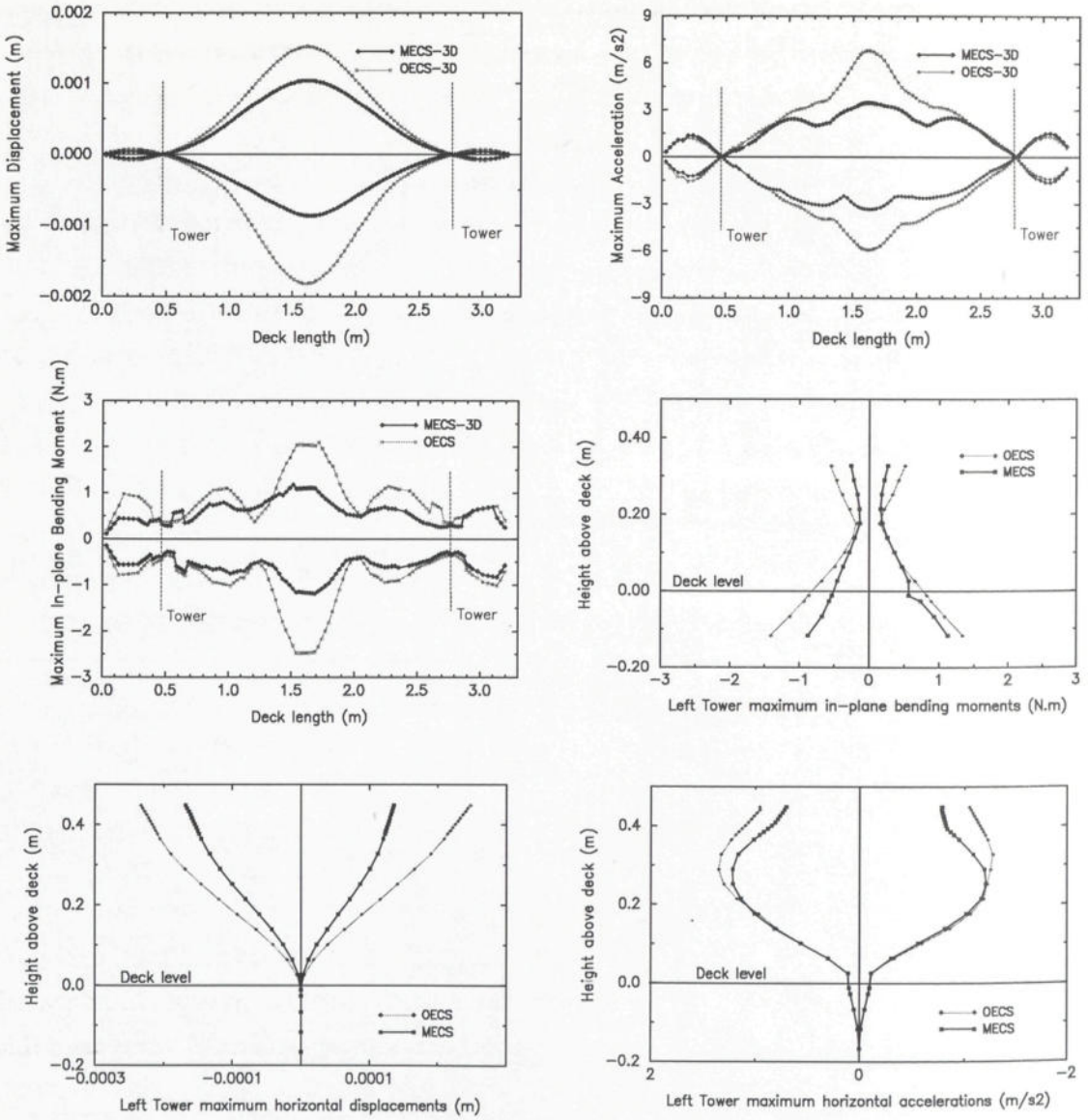


Figure 8.29. Peak response along the deck and left tower: displacements, accelerations and bending moments.

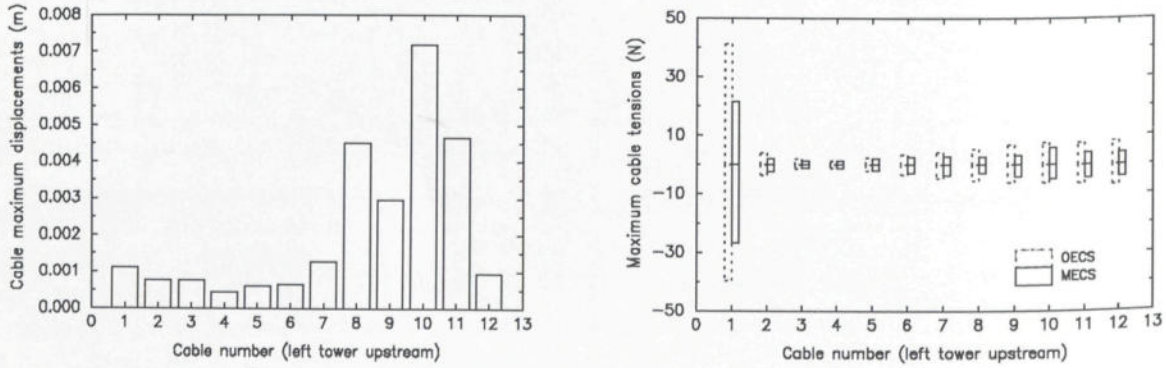


Figure 8.30. Peak response along the cables: displacements and tensions.

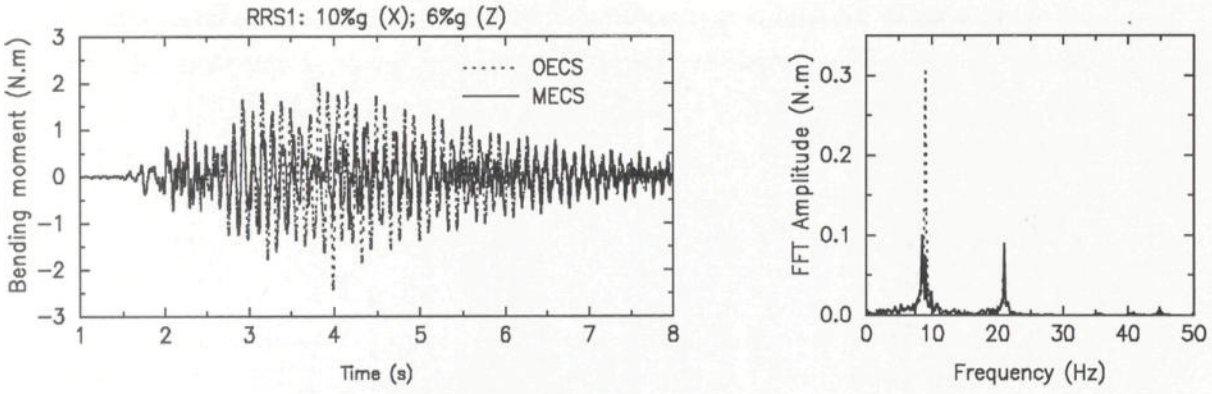


Figure 8.31. Bending moment at node *33*, *MECS vs OECS* analysis.
Time history and Fourier spectrum.

Table 8.11. Change of peak response, *MECS vs OECS* analysis.

Type of response	Change of peak response (*MECS / OECS*)			
	Deck	**Node no.**	**Towers**	**Node no.**
Displacement	48.2 %	**33Z**	54.8 %	**69X**
Acceleration	51.9 %	**33Z**	72.8 %	**69X**
Bending moment	54.5 %	**33**	67.4 %	**61**

The analysis of this table and of Figures 8.29 to 8.31 illustrates that, except for small extensions along the deck, the response obtained on the basis of the *MECS* analysis is much lower than the corresponding response obtained from the *OECS* analysis. This effect constitutes the so called "system damping". The damping of the response is due mostly to the contribution of the several new modes of vibration associated with the *1st* symmetric vertical configuration. These modes, occurring at close frequencies (*7.78Hz*, *8.46Hz*, *8.47Hz*, *8.72Hz*, *8.98Hz*) involve exclusively the movement of cables that have similar natural frequencies (e.g. mode *17*, *freq.=8.47Hz*, involves vibration of cables *8, 9, 10* and *11*, whose first natural frequencies are *9.39Hz, 8.94Hz, 8.29Hz* and *7.75Hz*, respectively).

It can be then concluded that the existence of resonance in the fundamental mode of vibration accentuates the effect of dynamic cable-structure interaction, leading to a significant decrease of the global bridge response. It is important to note also that the levels of oscillation of the stay cables *8*, *9*, *10* and *11* increased significantly.

8.3.2 Effect of severe cable excitation

The current Section describes the numerical simulations developed with the purpose of testing the effect of an intense excitation defined in a narrow frequency band containing both a global

natural frequency of the bridge and some cables natural frequencies. The simulations employ the former Jindo Bridge physical models, and define a new input signal to apply in the directions *XZ*.

8.3.2.1 Generation of input accelerograms

The new accelerograms were generated artificially, based on a narrow-band target power spectrum, defined in the range *8.5-12 Hz*, that includes the frequency of the second vertical mode of vibration (according to the *OECS* analysis) and the first natural frequency of a few stay cables that participate in the modes of vibration obtained from the *MECS* analysis. Figure 8.32 presents the generated time history and the corresponding Fourier spectrum.

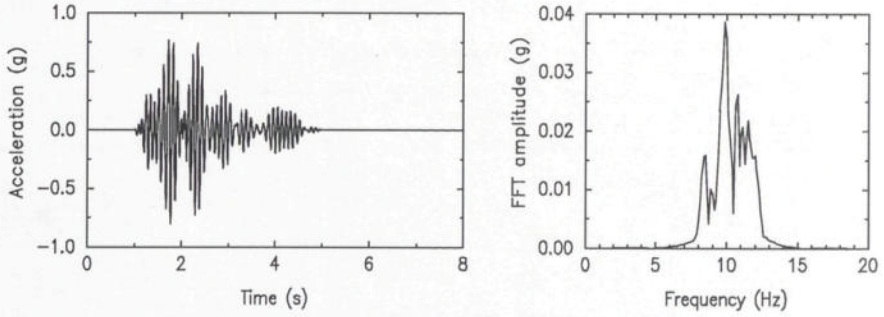


Figure 8.32. Artificial record of ground motion. Acceleration time history and Fourier spectrum.

8.3.2.2 Numerical response, *OECS vs MECS*

Considering a combination of two time histories from the generated record with *60%g* and *30%g* peak values along *X* and *Z* directions, respectively, and imposing a damping factor $\xi_1 = 1.0\%$ for the first mode of vibration ($f_1 = 6.20Hz$) in order to generate a mass-proportional damping matrix, the system response has been calculated for the *OECS* and *MECS* models (using a geometric nonlinear formulation and the direct integration method of Newmark). Figures 8.33 to 8.35 summarize the global response of the bridge in terms of the following extreme values: displacements, accelerations, bending moments and axial forces.

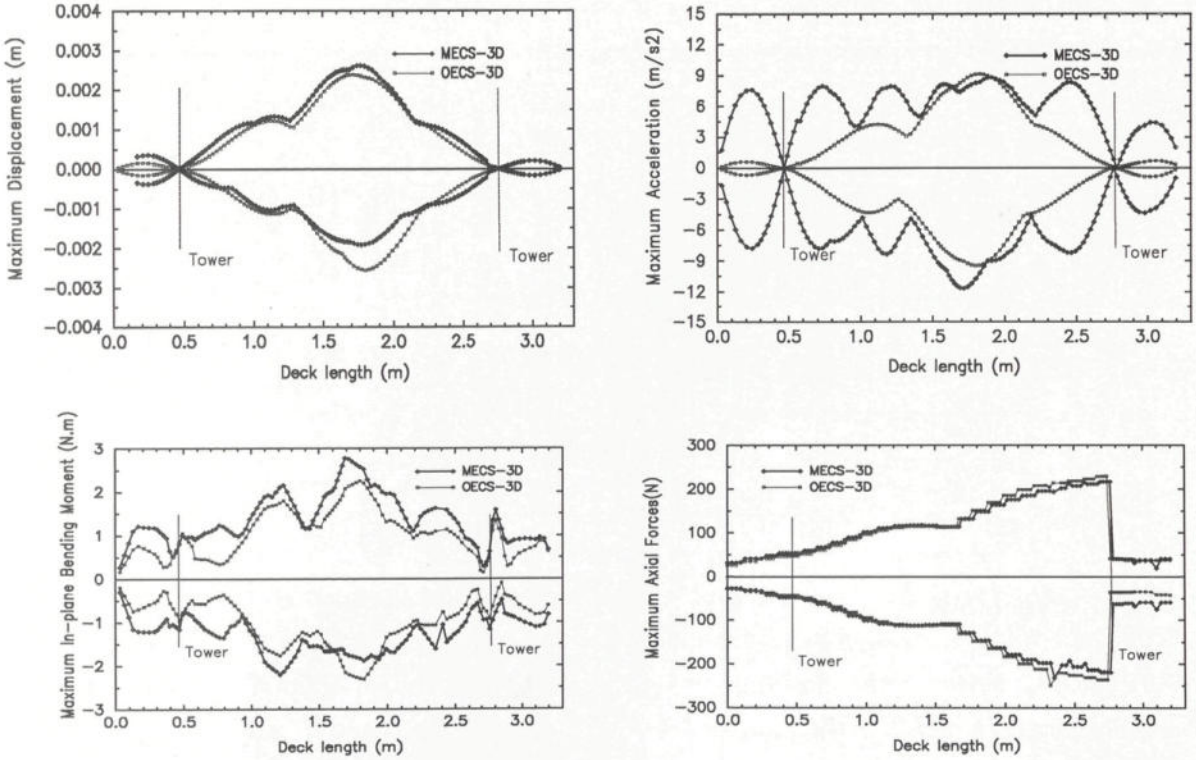


Figure 8.33. Peak responses along the deck: *OECS vs MECS* displacements, accelerations, bending moments and axial forces.

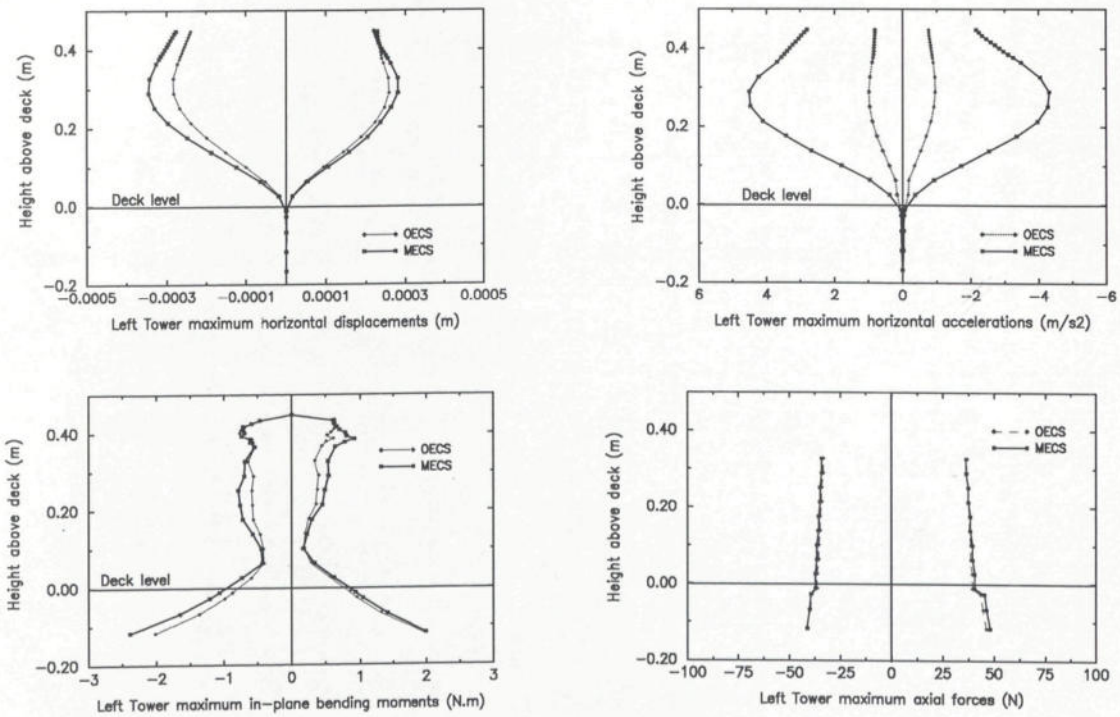


Figure 8.34. Peak responses along the left tower: *OECS vs MECS* displacements, accelerations, bending moments and axial forces.

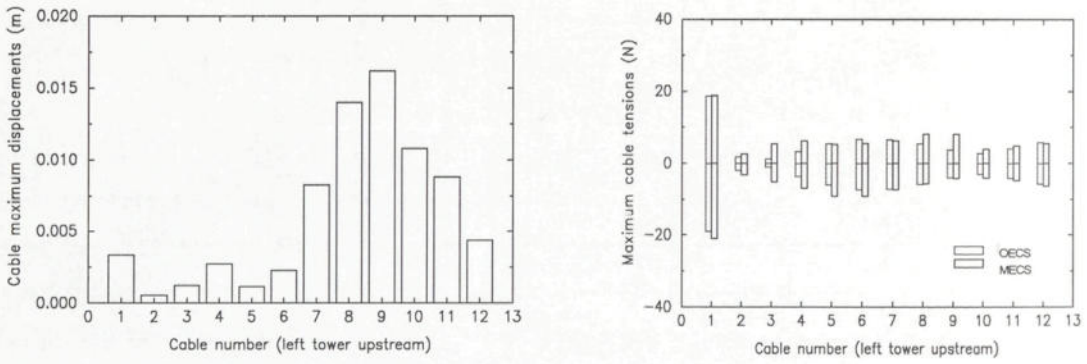


Figure 8.35. Peak responses along the cables: *OECS vs MECS* displacements at midpoint and tensions.

Figures 8.36 to 8.38 represent the time and frequency response in terms of displacement, acceleration and bending moment at nodes *33Z*, *38Z* and *65*, respectively. Table 8.12 summarizes the negative and positive peak values obtained on some of the most representative nodes of the structure.

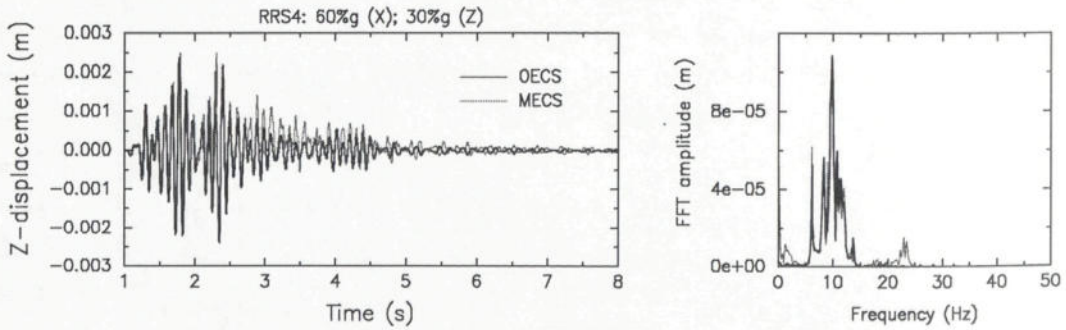


Figure 8.36. Displacement calculated at node *33Z* and corresponding Fourier spectrum, *OECS vs MECS*.

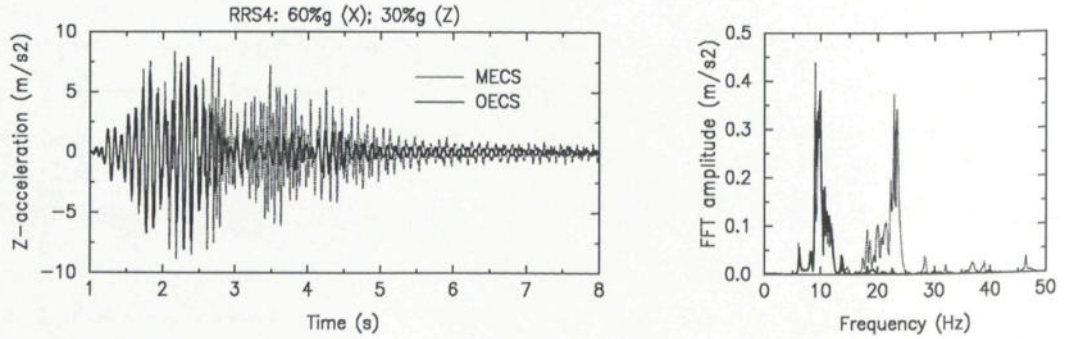


Figure 8.37. Acceleration calculated at node *38Z* and corresponding Fourier spectrum, *OECS vs MECS*.

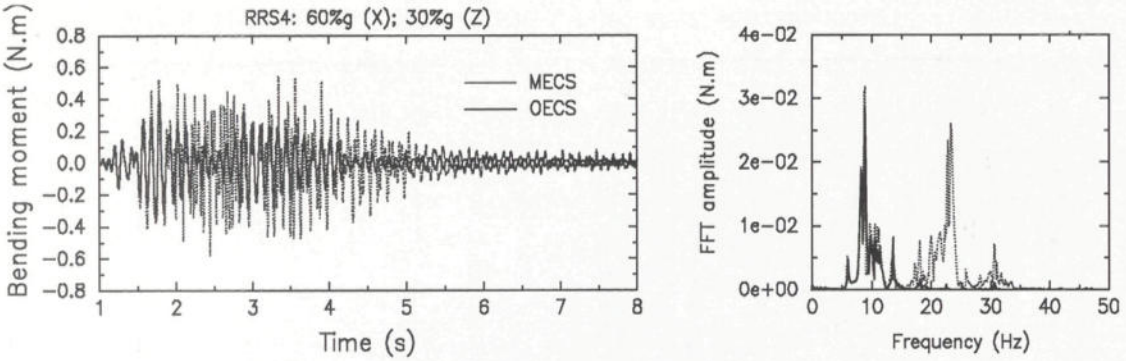


Figure 8.38. Bending moment calculated at node *65* and corresponding Fourier spectrum in the range *2-8s*, *OECS vs MECS.*

Table 8.12. Peak response for input *RRS4 - 60%g (X), 30%g (Z).*

Response	OECS	MECS	Change (MECS / OECS) (%)
33Z, accel. (m/s2)	-8.97 / 8.29	-11.6 / 7.41	129.3 / 89.4
38Z, accel. (m/s2)	-8.00 / 8.24	-8.81 / 8.52	110.1 / 103.4
69X, accel. (m/s2)	-0.80 / 0.76	-2.81 / 2.16	351.2 / 284.2
33Z , displ. (m)	-0.00237 / 0.00238	-0.00184 / 0.00251	77.6 / 105.5
38Z, displ. (m)	-0.00219 / 0.00199	-0.00154 / 0.00212	70.3 / 106.5
69X, displ. (m)	-0.000239 / 0.000231	-0.000276 / 0.000221	115.5 / 95.7
33, bend. mom. (N.m)	-2.15 / 2.08	-2.72 / 2.78	126.5 / 133.7
38, bend. mom. (N.m)	-1.56 / 1.47	-1.73 / 2.00	110.9 / 136.0
67, bend. mom. (N.m)	-0.591 / 0.559	-0.733 / 0.622	124.0 / 112.7
38, axial force (N)	-165.1 / 169.9	-163.1 / 163.6	98.8 / 96.3
67, axial force (N)	-36.2 / 39.4	-37.1 / 40.6	102.5 / 103.0
Cable 1, left, tension (N)	-19.1 / 18.6	-21.0 / 18.8	109.9 / 101.1
Cable 8, left, tension (N)	-5.8 / 5.5	-5.7 / 8.1	98.3 / 122.7
Cable 9, left, tension (N)	-3.9 / 3.7	-4.2 / 8.1	107.7 / 218.9

Inspection of this table and Figures shows that, except for the axial force, the inclusion of the local cable behaviour in the analysis (*MECS*) leads to a significant increase of the peak response. This occurs in consequence of a high spectral content of the response at high frequencies (Figures 8.36 to 8.38), which develops only about *2s* after the excitation has been applied.

It was also possible to observe that, during the excitation period, cables *8* and *9* experienced relatively high levels of vibration. Figure 8.39, representing the ratio between the maximum amplitude of displacement at the cable mid-point and the corresponding length for the cables attached to the left tower, illustrates the relative importance of cable motion for the three analyses performed. The significant cable movement associated with the narrow band excitation (input *RRS4*) may be responsible for a marked nonlinear character of the

oscillations, evidenced by the translation upwards of the curves that represent peak displacements along the deck, and by a certain loss of regularity of the curves that represent the peak response along the deck (Figure 8.33).

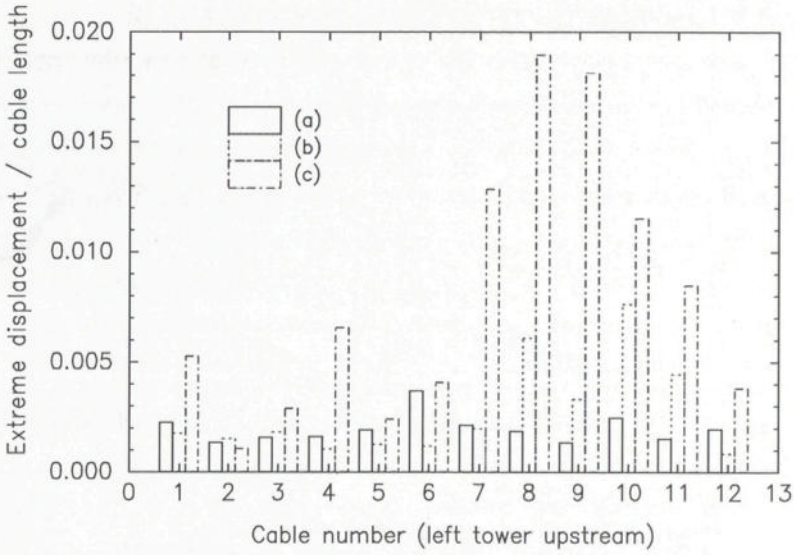


Figure 8.39. Cable motion associated to: (a) Jindo model, input *RRS1*; (b)Jindo modified model, input *RRS1*; (c) Jindo model, input *RRS4.*

An important effect associated with the large oscillations of the cables is the appearance of non-negligible high frequency contributions (see Figures 8.36 to 8.38). In effect, when a stay cable oscillates, the corresponding anchorages apply to the bridge forces at twice the corresponding vibration frequency (see Chapter six, Sections 6.3.2 and 6.3.3). When the cable oscillations are important, these forces may induce a global vibration of the bridge with a close natural frequency, which naturally communicates the cable oscillations in the second harmonic, which themselves may induce some global mode characterized by a natural frequency in the third harmonic, and so on. So, if the cable damping is very small, it is very likely that it suffers large levels of vibration, and it is therefore very likely that the global bridge response is also amplified.

8.4 CONCLUSIONS

The investigation described in this Chapter involved the following topics:

1- Shaking table tests on the physical model of the Jindo Bridge, using artificial accelerograms applied along one direction (*X*, *Y*, *Z*), or combinations in two/three directions (XZ, XYZ) (records *RRS1* and *RRS2*);
2- Numerical analysis of the seismic response of the Jindo Bridge physical model to earthquake excitation characterized by the records *RRS1* and *RRS2*, applied

alternatively along direction *X* and *XYZ*, and by record *RRS1* applied along the directions *XZ* (RRS1 analysis), using both the *OECS* and *MECS*;

3- Numerical simulation of the seismic response of the physical model under the same input excitation, simulating a modification of the structural properties, in order to induce a global cable-deck-towers resonance (*RRS1M* analysis);
4- Numerical simulation of the seismic response of the physical model to a severe narrow-band cable excitation, using *OECS* and *MECS* models (*RRS4* analysis).

From the set of results presented, it is possible to draw in particular the following conclusions:

- The results from tests performed on the shaking table for different artificially generated input actions present a reasonable correlation with the numerical response calculated on the basis of the *OECS* and *MECS* analysis. The main discrepancies that were found correspond to a slight change of frequency and to a complex variation of the damping with the amplitude and frequency of the measured response. These aspects reflect some imprecision related with the difficulty of accurately modelling the real damping characteristics and some local details of the structure;

- Concerning the *RRS1* analysis, it was observed that, due to the relatively high frequency content of the input excitation in the range of the natural frequency of the first vertical bending mode, the response was strongly dominated by this mode of vibration. For the type of excitation employed, involving a relatively low excitation of the stay cables, it was possible to observe that these cables didn't provide significant damping of the structural response in terms of maximum peak values. However, this damping developed some time after the excitation started, leading then to a considerable decrease of the response. It is noteworthy that the increase of some peak response values in the *MECS* analysis reflects the non-linear character induced by the vibration of the cables during an initial period of oscillation, before "system damping" effects occur;

- The modification of the structural properties considered in the *RRS1M* analysis led to a magnification of this effect of "system damping". In fact, the increase of the frequency of the fundamental vertical bending mode to the range of the first natural frequencies of the cables, resulted, for the *MECS* analysis, in the appearance of a very significant number of modes of vibration at very close frequencies, having the same first symmetric configuration of the deck and towers, and involving different movements of the cables. The contribution of these modes tends to cancel and, as a result, the response decreases significantly with regard to the *OECS* analysis;

- Both *RRS1* and *RRS1M* analyses involved a relatively small level of cable vibration and a small degree of nonlinearity. The *RRS4* analysis was intended to evaluate the effect of strong cable motion in the response. So, the excitation was generated artificially, defined in a frequency range that included only the third global mode of vibration (according to the *OECS* model) and the first natural frequency of a few stay cables. It was possible to observe that some of the cables experienced an important level of vibration. This caused significant non-linearity, and a significant increase of the upwards vertical deck displacements. Also, it was observed that high frequency vibration was induced, causing very high increase of acceleration at the deck and towers. The fact that high frequency components only develop some time after the start of the excitation indicates that the peak response increase is not so significant as the increase of the global response.

In view of these results, the author believes that, for relatively small levels of vibration, the cables may act favourably in the reduction of the global response of the cable-stayed bridge. This *damping effect* is more important if the natural frequencies of the fundamental modes of vibration lie in the range of the first natural frequency of the cables. But for high levels of cable vibration, like those caused by an excitation defined in a narrow frequency band that contains the first natural frequency of the cables, significant nonlinearity may cause high frequency vibration to occur. This vibration is associated with higher cable modes and can induce contributions of higher order global modes of the structure, resulting in an unfavourable behaviour of the bridge.

CHAPTER 9

CONCLUSIONS

Mode 1 Freq. 6,1894 Hz



Mode 2 Freq. 6,9045 Hz



Mode 8 Freq. 9,0394 Hz



Mode 9 Freq. 9,1741 Hz



Mode 20 Freq. 13,865 Hz



Mode 16 Freq. 13,133 Hz



Mode 29 Freq. 17,807 Hz



Mode 41 Freq. 22,805 Hz



Mode 88 Freq. 41,687 Hz



CHAPTER NINE

CONCLUSIONS

9.1 SUMMARY

The major purpose of the current dissertation was to experimentally assess the dynamic cable-structure interaction in cable-stayed bridges, i.e., identify a pattern of dynamic cable-structure interaction and analyse the corresponding effect in terms of the global bridge behaviour to some dynamic excitation.

The research was centred on the physical model of an existing cable-stayed bridge, the Jindo Bridge, in South Korea, which was adequately modified by the author and tested using an electrodynamic shaker and a seismic platform. As a result of the various series of tests performed on the bridge model, a very large high quality database was created, which was used to validate numerical models. Further numerical simulations were developed in order to identify the main characteristics of the phenomenon of cable-structure interaction.

Although the theme of the thesis is rather specific, the path followed in the development of the various tasks ended up involving the knowledge and work in several domains associated with the *Dynamics of Cable-Stayed Bridges*, namely the *Theory of Cable Dynamics*, the *Numerical Formulations of Analysis*, the *Experimental Testing and System Identification Techniques*, and the various *Cable Vibrations Phenomena*. The actual research comprehended therefore experimental, numerical and theoretical components.

Under these circumstances, the current Dissertation can be viewed as a proposal of revisiting the *Dynamics of Cable-Stayed Bridges* in the optics of the *Cable Dynamics* and *Vibrations*. The thesis was organized in two main parts. The first part, including Chapters one, two, three, four and part of Chapter five, introduced the Thesis and systematized the main

available information and tools in the topics above referred. The second part included the major author contributions, comprehending a practical example of instrumentation and identification of dynamic parameters on a cable-stayed bridge, the Vasco da Gama Bridge, a complete survey and investigation of particular issues on the various phenomena associated with *Cable Vibrations* in Cable-Stayed Bridges and, finally, the applications to the physical model of the Jindo Bridge above referred.

The following paragraphs describe with further detail the contents of the various Chapters, specifying the particular contributions from the author.

Chapter one

This Chapter introduced the Thesis by identifying the various issues associated with the *Dynamics of Stay Cables*, and briefly describing the current state-of-art associated with the various topics that frame the Dissertation. The motivation for the developed research was then presented, followed by a detailed description of the corresponding organization.

Chapter two

The objective was to present a picture of the historical development and current trends in the construction of cable-stayed bridges all over the world, discussing also the various structural components and proportions adopted in the design. The enormous progress in this particular field during recent years required an updating of the well-known historical reviews by Podolny and Scalzi (1976), Gimsing (1983), Leonhardt (1986), Troitsky (1988), Walther *et al.* (1988) and Mathivat (1994). An extensive survey was therefore developed by the author, incorporating information of newly constructed bridges located in Europe, Asia and America, and comprehending in particular a Section on the most relevant cable-stayed bridges constructed in Portugal.

Chapter three

Chapter three systematized the basic aspects associated with the deformational and vibrational characteristics of cables. The objective was to evaluate natural frequencies and components of the vibration modes of a stay cable, as well as to understand the major characteristics of the response to dynamic excitations. For this purpose, the linear theory of Irvine was first introduced, and the equations for evaluation of natural frequencies and vibration mode components derived. More recent refinements were then presented, namely the nonlinear theory of Perkins, which is relevant for the study of cables subjected to large levels of vibrations, in particular the *parametric* and *external excitation* phenomena.

Chapter four

The definition of dynamic design loads and the development of numerical models for dynamic analysis constitute the topics covered by Chapter four.

The first part of the Chapter presented an updated state-of-art on the description of wind, moving and earthquake loads, systematizing the most relevant specifications and recommendations adopted by the Eurocodes or alternative codes. The second part of the Chapter introduced the nonlinear geometric formulation of the dynamic analysis problem using either the classical beam-column theory or a finite element approach and establishing a comparison between the corresponding assumptions.

Chapter five

This Chapter was dedicated to the experimental and system identification issues that are on the basis of the dynamic tests on bridges and general large Civil Engineering structures.

Three main parts integrated the text, one comprehending instrumentation devices, a second part respecting System Identification methods, and a later component describing the main results obtained from a practical application based on the free and ambient vibration tests of a large cable-stayed bridge, the Vasco da Gama Bridge. The Section on instrumentation devices covered the most relevant sensors and analysis systems available currently for the dynamic testing of large and flexible structures, and comprehended a survey on less conventional sensors and measurement systems that have been developed in the last few years and that seem to have some potential in future applications. The second part of the Chapter addressed the System Identification techniques. The classical System Identification techniques based on Experimental Modal Analysis were briefly reviewed, and the most recent trends in Identification based on output-only measurements were presented and discussed. The description of the tests on the Vasco da Gama Bridge showed finally how the knowledge and experience on Measurement and Signal Processing and Identification techniques can be combined to extract high quality information from the dynamic analysis of a large structure. Although the devices and techniques employed in the performance of the tests are already known, they have seldom been combined and used in a large Civil Engineering structure to produce such an important level of information (in terms of amount and quality of data).

Chapter six

The Chapter started with the report of the various cases of vibration problems observed in cable-stayed bridges associated with the oscillation of stay cables, in order to stress the importance and, unfortunately, the significant frequency of occurrence of this type of problems. The various sources of cable vibrations were then addressed and a very extensive survey on the research and available analysis methodologies was presented. This survey has the merit of gathering very recent results and techniques of analysis and interventions which are very

disperse in the literature. A particular contribution from the author is added in the topic of Indirect Excitation. The phenomenon, associated with the oscillation of a stay cable motivated by the motion of the end anchorages had been previously studied as a linear problem for the component of motion perpendicular to the chord (designated in the current text as *external excitation phenomenon*), and as a nonlinear problem for the longitudinal component, which led to the so-called *parametric excitation*. By presenting a small numerical example corresponding to the analysis of a stay cable, the author showed that the *external excitation* phenomenon is highly nonlinear, even for very small amplitudes of oscillation and, employing an already developed theoretical formulation of the *Cable Dynamics* and well-established mathematical solutions of the differential equations, derived the maximum amplitudes of oscillation at resonance. Finally, the *cable-structure interaction* phenomenon was introduced with a simplified numerical analysis of a cable-structure association, showing that the interaction may have an unfavourable role in terms of the global bridge behaviour.

Chapter seven

The phenomenon of dynamic *cable-structure interaction* was investigated and experimentally identified and characterized in Chapter seven. Although a few papers had already been published in this topic before and a few experiments had been done employing very simplified models of cable-stayed bridges, the phenomenon had never been clearly identified and characterized on a cable-stayed bridge.

The current study was based on an existing physical model of a cable-stayed bridge, the Jindo Bridge, that was adequately modified by the author for the purpose of including the cable dynamics in the overall bridge behaviour. The research comprehended both numerical and experimental components, and involved the experimental and numerical analysis of two models of the same bridge, one that included the cable dynamic effects through an approximate idealization of the mass distribution along the stay cables, and another model, that neglected this effect by concentrating the distributed cable mass at the anchorages. The long series of modal analysis and seismic tests were used to validate the numerical models and allowed in particular for an identification of the dynamic cable-structure interaction phenomenon, as well as for a characterization of the corresponding pattern.

Chapter eight

Once the dynamic cable-structure interaction has been identified and characterized, it is the purpose of any designer to know the corresponding effect on the global response to some dynamic excitation. The study developed for the present Dissertation employed for simplicity the seismic excitation, and attempted to evaluate the dynamic cable-structure interaction effect on the Jindo Bridge behaviour through a series of tests of the physical model conducted on a shaking table, complemented with numerical evaluation of the response using nonlinear geometric direct integration techniques. Additional numerical simulations were developed

considering either a modification of the structural properties, or a severe excitation, in order to frame the possible effects of dynamic cable-structure interaction for a general cable-stayed bridge.

9.2 GENERAL CONCLUSIONS

At the end of this Dissertation, it is the author's belief that a deep and coherent overview of the various issues associated with the vibratory problems related to the stay cables in a cable-stayed bridge has been achieved. An updated state-of-art on the construction and concepts in the design of cable-stayed bridges, a solid knowledge of the cable dynamics, an understanding of the basic geometric nonlinear aspects associated with the dynamic behaviour of cable-stayed bridges and a thorough review and sistematization of experimental issues for the dynamic testing of large and flexible bridges constitute the desired background for the development of the research. As for the research itself, a set of general main conclusions can be extracted, covering: (i) the dynamic testing of the Vasco da Gama Bridge; (ii) the theoretical and numerical studies on the indirect excitation phenomenon, and (iii) the dynamic testing and analysis of the Jindo Bridge physical model. These will be stated in the following Sections.

9.2.1 Dynamic testing of the Vasco da Gama Bridge

Using ambient vibration excitation and a set of accelerographs, a very extensive database of the bridge response was created during the two and a half days of *in-situ* testing. Although the level of the response was generally rather low, it was possible to identify a very large number of vibration modes in the frequency range *0-1Hz*. The success of the tests was naturally determined by the high sensitivity of the sensors, by the high resolution of the digital converter and also by the high frequency resolution analysis achieved using long series of collected data. But it was also conditioned by the combination of classical strategies for separation of the various components of the signal, namely the bending and torsional modes, that are characterized by very close natural frequencies.

Since the classical System Identification techniques are not very efficient in the evaluation of damping coefficients, and given that the knowledge of the damping coefficient associated with the first torsional mode was of utmost importance for the validation of the numerical calculations adopted in the bridge design, a free vibration test was conducted on the bridge, which allowed the identification of damping coefficients for the fundamental vibration modes.

The comparison between the identified modal parameters and the corresponding design parameters showed generally an extremely good agreement. Evidence was found of dynamic cable-structure interaction, through the identification of various vibration modes at

very closely spaced frequencies, with identical deck configuration. The levels of deck and cable vibration were however rather low, even for high wind velocities, what is certainly due to an adequate aerodynamic behaviour of the bridge deck, as well as to the efficiency of the damper devices installed at the cable anchorages and other adequate measures against vibration, such as the helical rib in the polyethylene sheath of the stay cables, or the smooth surface of the road pavement.

9.2.2 Indirect excitation

Although it is a common practice to designate as *parametric excitation* any vibratory phenomenon associated with motion of the anchorages, the manipulation of the differential equations of motion of a stay cable showed that for taut cables of the type employed in cable-stayed bridges, the motion of the anchorage perpendicularly to the cable chord produces a neglectable parametric term. The dynamic equilibrium equation reduces therefore to a nonlinear differential equation with quadratic and cubic terms, which have shown to have an important contribution for the global cable response. The phenomenon of cable vibration motivated by this type of motion of the anchorage is designated in the current text as *external excitation*. In order to evaluate the risk of instability and fatigue caused by the vibration of the stay cable, the maximum amplitudes of oscillation and associated increments of tension at the fundamental resonance were deduced. The numerical analysis of a particular stay cable showed a good agreement with the theoretical solution, and it was in particular possible to observe that the influence of the damping coefficient on the amplitude of oscillation tends to decrease with the amplitude of motion of the anchorage, particularly for taut cables, i.e., for very small values of λ^2. An identical study was developed for the case of anchorage motion in the direction of the chord, leading to the known *parametric excitation* problem and to also known theoretical solutions for the maximum amplitude of vibration and increment of cable tension at the first parametric resonance. It was possible to observe in particular that the maximum amplitudes of oscillation for the same stay cable for *external* and *parametric excitation*s are actually of the same order of magnitude, and so the two phenomena should be considered in the design of a cable-stayed bridge.

9.2.3 Dynamic cable-structure interaction

The phenomenon of cable-structure interaction was first addressed through a simplified numerical study of a cable-structure assembly, which clearly showed that both beneficial and unfavourable dynamic effects of the interaction with the overall bridge behaviour can be achieved, depending on the amplitude of anchorage motion and on the global dynamic properties of the bridge.

This same effect could be observed with the tests on the Jindo Bridge physical model. It is relevant to notice that this study provided an extremely large high quality database, part of which is still to be processed. The modal analysis tests performed either using the electrodynamic shaker, or the shaking table allowed for the estimation of highly coherent frequency response functions from which modal parameters were identified applying classical System Identification algorithms. In addition to the very good agreement achieved between the experimental data and numerical results, it was possible to identify a pattern for the dynamic cable-structure interaction, which is one of the major results of the dissertation, and which consists in the following:

- Whenever a fundamental frequency of a stay cable lies in the vicinity of a global bridge frequency, a coupled vibration may occur. It is very likely that several stay cables in a cable-stayed bridge have close fundamental frequencies and that these are also similar to some global frequency of the bridge. The overall result is the appearance of a new set of vibration modes, which are very closely spaced in frequency and are also characterized by similar deck and towers configurations, but different cable motions. The phenomenon has been clearly observed by tuning of a sinusoidal excitation applied with the electrodynamic shaker at various close natural frequencies. And it was clearly not observed in the modal analysis tests of a modified version of the Jindo Bridge physical model, where the cable mass was concentrated at the anchorages, hence the cable dynamics not considered.

Another interesting result obtained from the seismic tests on the Jindo Bridge model and from the complementary numerical simulations was the evaluation of the effects of the dynamic cable-structure interaction in terms of the global bridge response to seismic excitation. The following main conclusions could be established:

- The effects of cable-structure interaction are more important whenever the cable natural frequencies lie close to a fundamental global frequency of the bridge;

- For small levels of excitation, the cables act generally as dampers of the global bridge response and lead to a general decrease of the response (with respect to the response obtained on the basis of models that neglect the dynamics of the stay cable). However, the damping effect only occurs some time after the excitation is applied and so, an analysis of the response in terms of peak values may lead to a misleading evaluation of the real damping effect associated with the vibration of the stay cables;

- For high levels of excitation, and particularly for narrow band excitations, it was observed that the vibration of the stay cables becomes highly nonlinear, leading eventually to an amplification of the global bridge response. In effect, when the stay cables vibrate at high amplitudes, the nonlinear components, which are

responsible for the appearance of response contributions in the various cable harmonics and sub-harmonics, become non-negligible. So, additional resonances may occur with the global bridge frequencies. In addition, knowing from the previous studies on indirect excitation that when the cables oscillate at their fundamental natural frequency, the corresponding dynamic tensions are characterized by components at twice that frequency, and knowing also that these components increase significantly with the amplitude of oscillation, it results that the cable anchorages end up applying forces to the deck and towers at twice the fundamental frequency. In a situation where another global mode exists at this frequency, it is very likely that the deck vibrates at this new frequency, inducing other cable modes, or amplifying the high frequency contribution of the original vibrating cables;

- The question that naturally arises is then to know how to avoid resonant amplification effects when designing a cable-stayed bridge, or how to suppress these effects in an already constructed bridge. Modifying the design in order to guarantee that resonance effects do not occur at a fundamental vibration mode is in principle a safe measure, although not easy to accomplish in a large bridge comprehending a large number of stay cables. A second alternative is to introduce damping into the structure. This damping may affect the bridge deck, the towers, and/or the stay cables. An important aspect that should be retained is that, according to the theoretical and numerical studies on the *indirect excitation* phenomena, the vibration amplitudes for *parametric resonance* are almost independent of the damping coefficient, the effect of damping being essentially to increase the input threshold for occurrence of instability. A slight dependence on the damping coefficient was observed for the *external excitation* case, which reduces however with the amplitudes of anchorage oscillation. So, it can be stated that, although the installation of damper devices in the stay cables may be an important measure against vibration induced by direct actions on the cables, the same does not happen with respect to indirect excitation. In that particular case, the best solution seems to introduce damper devices along the deck and/or towers in order to reduce the anchorage motion.

9.3 PERSPECTIVES OF FUTURE RESEARCH

The study presented herein showed that despite the enormous progress associated with the implementation of methods of analysis, construction techniques and structural observation, many issues associated with the dynamic behaviour of cable-stayed bridges are still to understand and deserve specific development. A few lines of research are indicated in the current Section for the areas that are of particular interest to the author, concerning: (i) the

instrumentation of large structures; (ii) the application of newly developed System Identification techniques, and; (iii) the control of vibrations in cable-stayed bridges.

9.3.1 Instrumentation of large structures

The several vibration problems reported along the Dissertation have shown that several complex phenomena of vibration are yet to be fully dominated by scientists and designers and require therefore a thorough observation, not only using laboratory models, but also, and most particularly, using the prototypes. Although more and more bridges have been instrumented during the last few years, very few of the bridges that experienced problems have been conveniently observed prior and after retrofit. Moreover, in most cases the observation reports have been kept confidential, for protection of the designers and construction companies.

Instrumenting bridges for assessment of their dynamic behaviour, for identification of the causes of specific problems and, at a higher level, for damage detection, is therefore one of the first goals in future research developments.

Considering that the sensors and measuring systems have also attained such an important development in terms of sensitivity and possibilities for data acquisition, on-line processing and data transfer, it is essential to test the potential of certain configurations of the instrumentation and measurement systems. In this particular topic, reference is made to the use of optical measurement systems, and to the possibility of data transfer using the mobile communications network.

Optical measurement systems based on the Laser technology have been in the market for one or two decades. Application of these systems to in-situ measurements of large Civil Engineering Structures is however a very recent concept and very few applications at present have used this technology. The potential and interest in the use of Laser sensors to assess the dynamic behaviour of a cable-stayed bridge has been shown with the application of a Laser sensor to the dynamic testing of the stay cables of the Vasco da Gama Bridge. In effect, stay cables vibrate at amplitudes that are much superior to the deck and towers, what leads in principle to less noisy signals. The consequence is that, even when using no specific target, the quality of the measurements is rather good for relatively significant distances of measurement, what means that no difficulty in assessing the cables at significant heights needs to be experienced, as well as no cabling problems. The technique can be therefore very useful for a periodic assessment of the tensions installed in the stay cables.

As for the improvements in data transfer technology, it is relevant to stress the importance of developing monitoring programs for bridges, by permanent installation of sensors. These sensors continuously measure the structural response and other critical quantities, like wind speed and direction, temperature, ice condition, or intensity of traffic, which, after a convenient statistical treatment, are able to send resumed information and the most relevant response data to a central station, making use of modern mobile communication technology. The use of this technology is gaining more and more interest and has already

been applied in the instrumentation of bridges. One such example is the Salgueiro Maia Bridge, which was instrumented by a team from this University (Cunha, 1998) using embedment strain gages, and a set of load cells installed at several stay cables. The purposes are the assessment of the fatigue effects associated with traffic loads on the bridge, as well as the evaluation of dynamic amplification factors for the several structural elements.

Still related with the monitoring of bridges are the new fiber optic sensors. These sensors have already been used with success for static applications and are at an experimental phase of development for dynamic sensing. It is thought that in the near future fiber optic sensors will be integrated in a complex measurement system, which will continuously measure the bridge condition and activate specific devices for certain threshold parameters, contributing therefore for an effectiveness of the concept of *Smart Structure* referred in the text (see Figure 5.1). In this respect, it should also be noted that an ongoing project constituted by a multidisciplinary team from the University of Porto is working on the static and dynamic measurement using fiber optic sensors (Figueiras, 1999).

9.3.2 Application of System Identification techniques

One of the most recent innovations in this particular topic respects the development and implementation of new mathematical algorithms for identification of modal parameters obtained from ambient vibration tests, i.e., respecting output-only measurements. It was seen that dynamic testing of the Vasco da Gama Bridge using classical System Identification (*SI*) techniques and specific strategies for separation of closely frequency spaced modal components, led to very good estimates of natural frequencies and vibration modes. The damping estimates were however obtained from free vibration tests, as the values extracted from ambient vibration response showed a significant dispersion. Although this dispersion may be attributed in part to the significant variation of damping with the amplitude of the response, it is expected that the application of more powerful *SI* algorithms, which are more efficient in eliminating noise from measurements, may produce more accurate estimates. Another advantage of these methods is the requirement of a more reduced intervention from the operator to achieve identical or even higher quality modal parameters than using the classical approach.

With respect to the state-of-art of implementation and application of the newly developed output-only identification algorithms, it can be said that, although commercial software is already available, very few practical applications are reported in the literature. One such example respects a benchmark study of a fifteen-storey building (Ventura & Horyna, 2000), in which the author participated. It is also expected that the database obtained from the tests on the Vasco da Gama Bridge can be processed using these new algorithms in order to evaluate their efficiency by comparison with the classical methods.

An additional task that is thought to have a great interest consists in employing more general versions of the new estimators in order to assess not only the structural properties, but

also the characteristics of the input associated with the wind excitation from ambient vibration data. It is required for that purpose that a state estimator is employed, and that a model is employed to extract the wind characteristics from the measurements performed with anemometers along the bridge. The only developments known in this particular area are due to Jones *et al.* (1995) and Pan (1998), who have developed a frequency domain procedure based on the Kalman filter and made some numerical and laboratory applications.

9.3.3 Control of vibrations in cable-stayed bridges

The research described herein identified the major sources of vibration in cable-stayed bridges, presenting whenever possible procedures for evaluation of the amplitudes of vibration and/or for calculating the risk of occurrence of instability phenomena in cable-stayed bridges. The next step and, naturally, the ultimate goal of this study will be the definition of measures for controlling vibrations in these structures.

The introductory Chapter of the Dissertation showed the various possibilities available for vibration control, based either on aerodynamic, structural or mechanical modification. The author is mostly concerned to develop research in mechanical control. In effect, *passive dampers*, in particular, have been widely used in cable-stayed bridges. These devices can provide extremely good results, as long as their design is optimized. On another hand, the *active damping* concept, which is already frequently employed in several areas of Engineering, is arriving at a point where practical implementation to large structures should be tested. Recent studies in this topic have involved a large physical model of a cable-stayed bridge where active tendon control was successfully implemented (Dumoulin *et al.*, 2000; Bossens & Preumont, 2000) and should be pursued in order to evaluate the interest in application to real structures.

A possibly more promising control strategy is based on the so-called *semi-active control*. *Semi-active* devices are based on the use of new materials, whose properties vary dynamically. Besides being stable, these devices are claimed to be much cheaper than active devices, as they have very low power requirements. Magnetorheological dampers (*MR*) have been studied in the last few years at the University of Notre Dame (Johnson *et al.*, 1999) and should also be investigated with experiments on prototypes.

REFERENCES



BIBLIOTECA F.E. PORTO

REFERENCES

A

AASHTO 1992. Standard Specification for Highway Bridges, Section 3: Loads. *American Association of State Highway and Transportation Officials. 15th Edition. Washington D.C.*

Abbas, S. 1993. Nonlinear Geometric, Material and Time Dependent Analysis of Segmentally Erected, Three Dimensional Cable Stayed Bridges, *Ph.D. Thesis, University of California at Berkeley. USA.*

Abdel-Ghaffar, A. M. 1991. Cable-Stayed Bridges under Seismic Action. In M. Ito, Y. Fujino, T. Myiata & N. Narita (eds), *Cable-Stayed Bridges: Recent Developments and their Future:* 171-192. Elsevier.

Abdel-Ghaffar, A. M. 1994. Seismic Behaviour of Cable-Stayed and Suspension Bridges. *Proc. IABSE/ FIP Int. Conference on Cables-Stayed and Suspension Bridges, Deauville, 12-15 Oct. 1994*: 211-221.

Abdel-Ghaffar, A. M. & Housner, G. W. 1978. Ambient Vibration Tests of Suspension Bridge. *Journal of the Engineering Mechanics Division, vol. 104, EM5*: 983-999. ASCE.

Abdel-Ghaffar, A. M. & Khalifa, M. A. 1991. Importance of Cable Vibration in Dynamics of Cable-Stayed Bridges. *Journal of Engineering Mechanics, Vol. 117, No. 11*: 2571-2589. ASCE.

Abdel-Ghaffar, A. M. & Scanlan, R.H. 1985a. Ambient Vibration Studies of Golden Gate Bridge: I. Suspended Structure. *Journal of the Engineering Mechanics Division, vol. 111, EM4*: 463-482. ASCE.

Abdel-Ghaffar, A. M. & Scanlan, R.H. 1985b. Ambient Vibration Studies of Golden Gate Bridge: II. Pier-Tower Structure. *Journal of the Engineering Mechanics Division, vol. 111, EM4*: 483-499. ASCE.

Abdel-Ghaffar, A.M. & Stringfellow, R. 1984. Response of Suspension Bridges to Travelling Earthquake Excitation: Part I. Vertical Response; Part II. Lateral Response. *International Journal of Soil Dynamics and Earthquake Engineering, Vol. 3, No. 2.*

Agardh, L. 1991. Modal Analysis of Two Concrete Bridges in Sweden. *Structural Engineering International, Vol. 1, Issue 4*: 35-39. IABSE.

Akin, J. E. and Mofid, M.1989. Numerical Solution for Response of Beams with Moving Mass, *Journal of Structural Engineering, Vol. 115, No. 1*: 120-131. ASCE.

Alessandrini, L., Brancaleoni, F. & Petrangeli, M. 1984. On the Dynamic Response of Cable-Stayed Bridges Under Moving Loads. *Costruzioni Metalliche, No. 2, October.*

Ali, H. 1991. Nonlinear Seismic Analysis of Cable-Stayed Bridges With Passive Energy Dissipation Devices. *Ph.D. Thesis, University of Southern California. USA.*

Andersen, P. 1997. Identification of Civil Engineering Structures Using Vector ARMA Models. *Ph.D. Thesis, Aalborg University. Denmark.*

Andersen, P., Brincker, R. & Kirkegaard, P. 1996. Theory of Covariance Equivalent ARMAV Models of Civil Engineering Structures. *Proceedings of IMAC14, The 14th International Modal Analysis Conference, 12-15Feb., Michigan*: 260-277.

Andersen, P., Brincker, R., Peeters, B., De Roeck, G., Hermans, L. & Krämer, C. 1999. Comparison of System Identification Methods Using Anbient Bridge Test Data. *Proceedings of IMAC17, The 17th International Modal Analysis Conference, Kissimee, Orlando.*

Andersen, H., Hommel, D. & Veje, E. 1999. Emergency Rehabilitation of the Zárate-Brazo Largo Bridges, Argentina. *IABSE Conference on Cable-Stayed Bridges- Past, Present and Future.* IABSE.

Andersen, P. & Brincker, R. 2000. The Stochastic Subspace Identification Techniques. *In Lecture notes from the course on Modal Identification of Output-Only Systems, 6-9 June, Madrid. SVIBS.*

Aparicio, A. & Casas, J. 1997. The Alamillo Cable-Stayed Bridge: Special Issues Faced in the Analysis and Construction. *Proc. of the Institution of Civil Engineers, Structures & Buildings, No. 122, Nov.*: 432-450.

Appleton, J. & Rito, A. 1998. Inspecção da Ponte da Figueira de Foz e dos Viadutos de Acesso. *Jornadas Portuguesas de Engenharia de Estruturas, 25-28 Nov. 1998*: 527-536. Lisbon. LNEC (in Portuguese).

Asher, G. 1958. A Method of Normal Mode Excitation Utilizing Admittance Measurements. *Proceedings of the National Specialists' Meeting in Dynamics and Aeroelasticity, Institute of the Aeronautical Sciences*: 69-76.

Ashkenazi, V. & Roberts, G. 1997. Experimental Monitoring of the Humber Bridge using GPS. *Proc. Instn. Civil Engineers, Civil Engineering, Vol. 120, Nov.*: 177-182. ICE.

Asmussen, J. 1997. Modal Analysis Based on the Random Decrement Technique: Application to Civil Engineering Structures. *Ph.D. Thesis. Aalborg University. Denmark.*

B

Bachmann, H. & Ammann, W. 1987. Vibrations in Structures Induced by Man and Machines. *Structural Engineering Documents, 3e. IABSE.*

Bailey, S. 1996. Basic Principles and Load Models for the Structural Safety Evaluation of Existing Road Bridges. *Ph..D Thesis no. 1467. École Polytechnique Fédérale de Lausanne. Switzerland.*

Bakht, B. and Jaeger, L.G.1990. Bridge Evaluation for Multipresence of Vehicles. *Journal of Structural Engineering, Vol. 116, No. 3*: 603-618. ASCE.

Balendra, T. 1993. Vibration of Buildings to Wind and Earthquake Loads. *Springer-Verlag, London.*

Barbat, A., Orosco, L., Hurtado, J. & Galindo, M. 1994. Definición de la Acción Sísmica. *Monografía CIMNE IS-10. Centro International de Metodos Numericos en Ingenieria (in Spanish).*

Barbosa, J. 1992. Análise Não Linear por Elementos Finitos de Placas e Cascas Reforçadas: Aplicação a Laminados Anisotrópicos. *Ph.D. Thesis, University of Porto, Portugal* (in Portuguese).

Baron, F. & Lien, S. 1973. Analytical Studies of a Cable-Stayed Girder Bridge. *Computers & Structures, Vol. 3*: 443-465. Pergamon Press.

Bathe, K. 1982. Finite Element Procedures in Engineering Analysis. *Prentice-Hall, Inc. ISBN 0-13-317305-4.*

Beck, J. & Jennings, P. Structural Identification Using Linear Models and Earthquake Engineering Records. *International Journal of Earthquake Engineering and Structural Dynamics, Vol. 8, No. 2*: 145-160. Wiley Interscience.

Bendat, J.S. & Piersol, A. G. 1966. Measurement and Analysis of Random Data. *John Wiley & Sons, Inc., New York, N.Y..*

Bendat, J. S. & Piersol, A. G. 1980. Engineering Applications of Correlation and Spectral Analysis, *Wiley-Interscience.*

Benedettini, F. & Rega, G. 1987. Non-Linear Dynamics of An Elastic Cable Under Planar Excitation. *Int. J. Non-Linear Mechanics, Vol. 22, No. 6*: 497-509. Pergamon Journals.

Bietry, J. & Jan, P. 1995. Essais Dynamiques du Pont de Normandie. *Report of "Mission du Pont de Normandie". EN-D 95.5 C.*

Blakeborough, A., Severn, R. & Taylor, C. 1986. The New UK National Six-Axis Earthquake Shaking Table. *Proceedings of the 8th European Conference on Earthquake Engineering, Vol. 4*: 97-100. Lisbon, Portugal.

Blevins, R. & Iwan, W. 1974. The Galloping Response of a Two-Degree-of-Freedom System. *Journal of Applied Mechanics, Dec. 1974, Paper no. 75-APMW-9*: 1113-1118. Transactions of ASME.

Bloomstine, M. & Stoltzner, E. 1999. The Faroe Cable-Stayed Bridge- Maintenance Experience with Major Components. *IABSE Conference on Cable-Stayed Bridges- Past, Present and Future.* IABSE.

Boonyapinyo, V., Miyata, T. & Yamada, H. 1999. Advanced Aerodynamic Analysis of Suspension Bridges by State-Space Approach. *Journal of Structural Engineering, Vol. 125, No. 12*: 1357-1366. ASCE.

Borges, J. & Delgado, A. 1990. Ensaio Aerodinâmico da Ponte sobre a Ribeira de Socorridos. *Internal Rep. Universidade Nova de Lisboa. Portugal* (in Portuguese).

Bossens, F. & Preumont, A. 2000. Active Tendon Control of Cable-Stayed Bridges: A Large Scale Demonstration. Accepted for publication in the *Journal of Earthquake Engineering and Structural Dynamics.*

Brancaleoni, F., Petrangeli, M. & Villatico, C. 1987. Train-Structure Interaction in Railway Cable-Stayed Bridge Dynamics. In W. Kanok-Nukulchai (ed), *Cable-Stayed Bridges: Experience & Practice, Vol. 1*: 452-463. AIT.

Branco, F., Mendes, P. & Guerreiro, L. 1998. Research Studies for the Vasco da Gama Bridge Project. *IST Science & Technology, No. 2, April*: 2-7. IST. Lisbon.

Bridon. 1998. Structural Systems- Structural Applications. Bridon Catalogue.

Brincker, R., Krenk, S. & Jensen, J. 1990. Estimation of Correlation Functions by the Random Dec Technique. *Proceedings of Skandinavisk Forum for Stokastik Mekanik, Lind, Sweden, Aug. 30-31.*

Brincker, R., Kirkegaard, P. & Rytter, A. 1991. Identification of System Parameters by the Random Decrement Technique. *Proceedings of the 16th International Seminar on Modal Analysis, Florence, Italy, Sept. 9-12.*

Brincker, R., Zhang, L. & Andersen, P. 2000. Modal Identification from Ambient Responses using Frequency Domain Decomposition. *Proceedings of the 18th International Seminar on Modal Analysis, San Antonio, Texas, 7-10 Feb.*

Broquet, C. Comportement Dynamique des Dalles de Roulement des Ponts en Béton Solicités par le Traffic Routier. *Ph.D. Thesis no. 1964. École Polytechnique Fédérale de Lausanne.*

Brown, D. 1993. Bridges: Three thousand Years Defying Nature. *Reed International Books.*

Brownjohn, J. 1988. Assessment of Structural Integrity by Dynamic Measurements. *Ph.D. Thesis. University of Bristol, U.K.*

Brownjohn, J.; Dumanoglu, A. Severn, R. & Taylor, C. 1987. Ambient Vibration Measurements of the Humber Suspension Bridge and Comparison with Calculated Characteristics. *Proc. Instn. Civ. Engrs., Part 2, 83*: 561-600.

Brownjohn, J.; Dumanoglu, A. Severn, R. & Blakeborough, A. 1989. Ambient Vibration Survey of the Bospurus Suspension Bridge. *Earthquake Engineering and Structural Dynamics, 18*: 263-283. John Wiley & Sons.

Bruls, P. and Sedlacek, J.M.. 1989. Traffic data of the European Countries, The final draft. *Eurocodes on actions, No. 9, part 12-W.G.2*: 1-17.

Bruno, D. & Leonardi, A. 1986. Nonlinear Analysis of Cable-Stayed Bridges Eccentrically Loaded. *IABSE Proceedings, P-103/86*: 129-140.

BS 5400. 1978. Steel, Concrete and Composite Bridges: Specifications for Loads. *British Standard BS 5400, Part2.*

Buckland, P., Hooley, R., Morgenstern, B., Rainer, J. & Selst, A. 1979. Suspension Bridge Vibrations: Computed and Measured. *Journal of the Structural Division, Vol. 105, No. ST5, May*: 859-874. ASCE.

Buckland, P., Navin, F., Zidek, J. & McBryde, J. 1980. Proposed Vehicle Loading of Long-Span Bridges. *Journal of the Structural Division, Vol. 106, No. ST4*: 915-932. ASCE.

Bunce, J. & Brown, E. 1973. The Finite Deflection of Plane Frames. *International Journal of Mechanical Science, Vol. 15*: 189-198.

C

Caetano, E. 1992. Experimental Identification of Dynamic Parameters in Structural Systems. *M.Sc. Thesis, University of Porto, Portugal.* (in Portuguese).

Caetano, E. & Cunha, A. 1995. An Investigation Into the Cable Dynamics on Cable-Stayed Bridges. *Report. Earthquake Engineering Research Centre, University of Bristol.*

Caetano, E., Cunha, A. & Taylor, C. 2000. Investigation of Dynamic Cable-Deck Interaction in a Physical Model of a Cable-Stayed Bridge. Part I: Modal Analysis. *International Journal on Earthquake Engineering and Structural Dynamics, Vol. 29*: 481-498. John Wiley & Sons.

Caetano, E., Cunha, A. & Taylor, C. 2000. Investigation of Dynamic Cable-Deck Interaction in a Physical Model of a Cable-Stayed Bridge. Part II: Seismic Response. *International Journal on Earthquake Engineering and Structural Dynamics, Vol. 29*: 499-521. John Wiley & Sons.

Calçada, R. & Cunha, A. 1998. Stochastic Modelling of the Dynamic Behaviour of Bridges under Road Traffic Loads. *XVI World Conference on Computational Mechanics, Buenos Aires, Argentina.*

Calçada. R., Cunha, A. & Delgado, R. 2000. A Project for the Experimental and Numerical Assessment of Dynamic Effects of Road Traffic on Bridges. *European COST F3 Conference on System Identification & Structural Health Monitoring. Madrid.*

Câncio Martins, J. L. 1993. Ponte Internacional sobre o Guadiana em Castro Marim. In Fernandes & Santos (eds), *Pontes Atirantadas do Guadiana e do Arade- Sessão integrada no 4º Encontro Nacional sobre Estruturas Pré-Esforçadas*: 3-15. LNEC (in Portuguese).

Cantieni, R., Deger, Y., Pietrzko, S. 1994. Large Structure Investigation with Dynamic Methods: The Bridge on the River Aare at Aarburg. *Prestressed Concrete in Switzerland, Report of the Swiss FIP Group to the 12th FIP Congress, Washington D.C., 29May-2June: 20-26.*

Capra, A. & Leveille, A. 1997. Vasco da Gama Main Bridge Seismic Design. *Proceedings of the International Conference on New Technologies in Structural Engineering, Lisbon 2-5 July, Session 2.* IABSE.

Cardoso, E. 1977. Projecto da Ponte da Figueira da Foz. *JAE.*

Casas, J. 1994. A Combined Method for Measuring Cable Forces: the Cable-Stayed Alamillo Bridge, Spain. *Structural Engineering International, Vol. 4, No. 4*: 235-240. IABSE.

Casas, J. 1995. Full-Scale Dynamic Testing of the Alamillo Cable-Stayed Bridge in Sevilla (Spain). *Earthquake Engineering and Structural Dynamics, Vol. 24*: 35-51. John Wiley & Sons, Inc..

Castoldi, A., Fumagalli, E. & Oberti, G. 1972. Ponte Zarate-Brazo Largo: Relazione Sulle Prove Statiche e Dinamiche Modello in Scala 1:33.3. *Internal Report, No. 884. ISMES* (in Italian).

Causevic, M. S. & Sreckovic, G. 1987. Modelling of Cable-Stayed Bridge Cables: Effects on Bridge Vibrations. In W. Kanok-Nukulchai (ed), *Cable-Stayed Bridges: Experience & Practice, Vol. 1*: 407-420. AIT.

Chaterjee, P.K., Datta, T.K. and Surana, C.S.1994. Vibration of Cable-Stayed Bridges under Moving Vehicles, *Structural Engineering International, No. 2*:116-121. IABSE.

Chong, K. Health Monitoring of Civil Infrastructures. In F. Chang (ed), *Structural Health Monitoring: Current Status and Perspectives, Proceedings of the International Workshop on Structural Health Monitoring, Stanford, 18-20 September*: 339-350. Technomic.

Chopra, A. Dynamics of Structures: Theory and Applications to Earthquake Engineering. *Prentice-Hall. ISBN 0-13-521063-1.*

Clement, H. & Cremona, C. 1996. Étude Mathématique du Phénomène d'Excitation Paramétrique Appliqué aux Haubans de Pont. *Études et recherches des Laboratoires des Ponts et Chaussées, OA18.* LCPC, Paris.

Clough, R., Stephen, R. & Kuo, J. 1982. Dynamic Response Analysis of Techi Dam. *Report no. UCB/ EERC-82/11. University of California at Berkeley.*

Clough, R. & Penzien, J. 1986. Dynamics of Structures. *McGraw-Hill International Editions. 7th Edition. ISBN 0-07-Y85098-4.*

Cole, H. 1968. On-The-Line Analysis of Random Vibrations. *AIAA Paper No. 68-288.*

Como, M., Grimaldi, A. & Maceri, F. 1985. Statical Behaviour of Long-Span Cable-Stayed Bridges. *International Journal of Solids and Structures, Vol. 21, No. 8*: 831-850. Pergamon Press.

Conti, E., Grillaud, G., Jacob, J. & Cohen, N. 1994. Wind Effects on the Normandy Cable-Stayed Bridge: Comparison Between Full Aeroelastic Model Tests and Quasi-Steady Analytical Approach. *Proc. IABSE/ FIP Int. Conference on Cables-Stayed and Suspension Bridges, Deauville, 12-15 Oct. 1994*: 81-90.

Cooley, J. & Tuckey, J. 1965. An Algorithm for the Machine Calculation of Complex Fourier Series. *Mathematics of Computation, Vol. 19*: 297-301.

Corrêa, M. & Campos Costa, A. 1992. Dynamic Tests of Arade Bridge. In Fernandes & Santos (eds), *Pontes Atirantadas do Guadiana e do Arade- Sessão integrada no 4º Encontro Nacional sobre Estruturas Pré-Esforçadas*: 225-239. LNEC (in Portuguese).

Crawford, R. & Ward, H. 1964. Determination of the Natural Periods of Buildings. *Bulletin of the Seismological Society of America, Vol. 54, Dec.*: 1743-1756.

Cremer, J., Counasse, C., de Ville de Goyet, V., Lotaire, A. & Dumortier, A. 1995. The Stays, their Dynamic Behaviour, their Equipments- Bridges at Ben-Ahin, Wandre and upon Alzette. *Proc. Int. Symposium on Cable Dynamics, 19-21 Oct.*: 489-496. Liège, Belgium.

Cremona, C. 1997. Courbe Universelle pour le Dimensionnement d' Amortisseurs en Pied de Haubans. *Revue Française de Génie Civil. Vol. 1, No. 1*: 137-159.

Culshaw, B. Fibre Optics in Smart Structures- An Introductory Overview. *In Rastogi, P. & Inaudi, D. (eds.), Trends in Optical Nondestructive Testing and Inspection*: 433-446. Elsevier Science.

Cunha, A. 1990. *Dinâmica Estrutural Estocástica; Aplicações à Engenharia Sísmica. Ph.D. Thesis, University of Porto, Portugal* (in Portuguese).

Cunha, A. 1994. The Role of the Stochastic Equivalent Linearization Method in the Analysis of the Non-linear Seismic Response of Building Structures. *Int. Journal Earthquake Engineering and Structural Dynamics, Vol.23, No. 8*:837-857. John Wiley & Sons.

Cunha, A. 1998. Analysis and Monitoring of the Dynamic Effects of Traffic Loads on Bridges. *Praxis Project No. PRAXIS/C/ECM/13251/1998. Portugal.*

Cunha, A., Laje, A., Gomes, A. & Caetano, E. 1995. Accuracy Evaluation of a Laser Interferometry Measurement System in Long Distance Dynamic Measurements. *Proceddings of the 7th International Conference on Computational Methods and Experimental Measurements, CMEM95, Capri, Italy.*

Cunha, A., Caetano, E., Calçada, R. & Delgado, R. 1999. Dynamic Tests on Vasco da Gama Cable-Stayed Bridge. *Cable-Stayed Bridges- Past, Present and Future. IABSE Conference, Malmö, Sweden, 2-4 June.*

Cunha, A., Caetano, E. & Moutinho, C. 2000. Ambient Vibration Data Analysis of Heritage Court Tower. *Contribution of University of Porto to IMAC Benchmark. Proceedings of the 18th International Modal Analysis Conference IMAC-XVIII, San Antonio, Texas.*

Cunha, A., Caetano, E. & Delgado, R. 2000. Dynamic Tests on a Large Cable-Stayed Bridge: An Efficient Approach. *Journal of Bridge Engineering, ASCE. Accepted for publication.*

Cunha, A., Hurtado, A. & Barbat, A. 1997. Análise Estocástica da Resposta Sísmica de Estruturas de Edifícios com Isolamento de Base. *3º Encontro Sobre Sismologia e Engenharia Sísmica, Lisbon*: 505-514.Sociedade Portuguesa de Engenharia Sísmica (in Portuguese).

Curtis, A. 1980. Dynamic Testing- How Far We've Come- How Much Further to Go. *Shock and Vibration Bulletin, No. 50*: 39-44.

D

Davenport, A. G. 1962. Buffeting of a Suspension Bridge by Storm Winds. *Proc. Institution of Civil Engineers, 23*:389-408.

Davenport, A. 1967. Gust Loading Factors. *Journal of the Structural Division, Vol. 93*: 11-34. ASCE.

Davenport, A. 1977. The prediction of the Response of Structures to Gusty Wind. In Holand, Kavlie, Moe & Sigbjörnsson (eds), *Safety of Structures under Dynamic Loading*: 257-284. Tapir, Trondheim.

Davenport, A., 1994. A Simple Representation of the Dynamics of a Massive Stay Cable in Wind. *Proc. IABSE/ FIP Int. Conference on Cables-Stayed and Suspension Bridges, Deauville, 12-15 Oct. 1994, Vol. 2*: 427-438.

Davenport, A. G., King, J. P. C. & Larose, G. L. 1992.Taut Strip Model Tests. *Proc. of the First International Conference on the Aerodynamics of Large Bridges, Copenhagen, Denmark, February 19-21*: 113-124. Rotterdam. Balkema.

Davenport, A. & Steels, G. 1965. Dynamic Behaviour of Massive Guy Cables. *Proceedings of the American Society of Civil Engineers. Journal of the Structural Division, No. ST2*: 43-71. ASCE.

De Roeck, G., Claesen, W. & Van den Brock, P. 1995. DDS-Methodology Applied to Parameter Identification of Civil Engineering Structures. *Proceedings of Vibration and Noise'95: 341-353.*

Deinum, P., Dungar, R., Ellis, B., Jeary, A., Reed, G. & Severn, R. 1982. Vibration Tests on Emossom Arch Dam, Switzerland. *Earthquake Engineering and Structural Dynamics, Vol. 10*: 447-470. John Wiley & Sons, Ltd..

Delgado, R., Cunha, A., Caetano, E. & Calçada, R. 1998. Ensaios Dinâmicos da Ponte Vasco da Gama: Ponte Principal. *Report Instituto da Construção, Faculty of Engineering of the University of Porto. Portugal* (in Portuguese).

Den Hartog, J. P. 1956. Mechanical Vibrations, *4th ed., McGraw-Hill, New York.*

Dobson, B. 1984. Modal Analysis Using Dynamic Stiffness Data. *Royal Naval Engineering College (RNEC), TR-84015. June.*

Dobson, B. 1987. A Straight-Line Technique for Extracting Modal Properties from Frequency Response Data. *Mechanical Systems and Signal Processing*, Vol. 1, No. 1, Jan: 29-40.

Drosner, S. and Sedlacek, G.. 1989. The Dynamic Behaviour of Bridges and its Consideration in the Determination of a loading model in the Eurocode on Actions, *Annales des Travaux Publics de Belgique, Nº3*: 241-254.

Dumanoglu, A., Severn, R. & Brownjohn, J. 1986. Asynchronous Seismic Analysis of Bospurus and Humber Suspension Bridges. *Proceedings of the 8th European Conference on Earthquake Engineering, Vol. 6*: 6.9/1-6.9/8. Lisbon.

Dumir, P., Saha, D. & Sengupta, S. 1993. Beam-Column Method for Frames Under Distributed Loads. *Computers & Structures, Vol. 46, No. 1*: 141-148. Pergamon Press.

Dumortier, A. 1990. Étude Dynamique du Comportement des Haubans de Pont. *Licentiate Thesis, University of Liège, Belgium.*

Dumoulin, C., Försterling, H., Magonette, G. & Bossens, F. 2000. Active Control of Cable-Stayed Bridges: Large Scale Experiments. *1st IFAC Conference MECHATRONICS, Darmstad, September.*

Dyrbye, C. & Hansen, S. 1999. Wind Loads on Structures. *John Wiley & Sons.*

E

Ellis, B., Jeary, A. & Severn, R. 1984. Integrity Monitoring of Dams by Dynamic Tests. *Proceedings of the International Conference on Safety of Dams. Coimbra, Portugal, 23-28 April*: 147-152.

Ernst, H. J. 1965. Der E-Modul von Seilen unter Berücksichtigung des Durchhangers. *Bauingenieur, Vol. 40 (2).*

Ewins, D. 1984. Modal Testing: Theory and Practice. *Research Studies Press, Ltd., Staunton, Somerset, England.* ISBN 0 86380 017 3.

F

Felber, A. 1993. Development of a Hybrid Bridge Evaluation System. *Ph.D. Thesis, University of British Columbia, Canada.*

Felber, A. 1997. Pratical Aspects of Testing Large Bridges for Structural Assessment. In Chang, F. (ed) *Structural Health Monitoring- Current Status and Perspectives*: 577-588. Technomic.

Felber, A. & Cantieni, 1996. Introduction of a New Ambient Vibration Testing System – Description of the System and Seven Bridge Tests. *EMPA Report No. 156'521. Dübendirf, Switzerland.*

Felber, A. & Ventura, C. 1996. Frequency Domain Analysis of Ambient Vibration Data of the Queenborough Bridge Main Span. *14th International Modal Analysis Conference Proceedings*: 459-465. Dearborn. Michigan.

Fernandes, J. A., Branco, F., Santos, L. O. & Santos, T. O. 1996. Load Tests on the Algarve Cable-Stayed Bridges. *Mecânica Experimental, No. 1*: 51-60. APAET (in Portuguese).

Figueiras, J. 2000. Monitoring of Structures using Fibre Optic Bragg Grating Sensors. *PRAXIS Project.*

Filiatrault, A., Tinawi, R. & Massicote, B. 1993. Damage to Cable-Stayed Bridge During 1988 Saguenay Earthquake. I: Pseudostatic Analysis. *Journal of Structural Engineering, 119, No. 5*: 1432-1449. ASCE.

Flamand, O. 1993. Rain-Wind Induced Vibration of Cables. *Structural Dynamics- EURODYN' 93*: 1019-1025. Rotterdam, Balkema.

Flamand, O. 1994. Rain-Wind Induced vibration of Cables. *Proc. IABSE/ FIP Int. Conference on Cables-Stayed and Suspension Bridges, Deauville, 12-15 Oct. 1994*: 523-531.

Fleming, J. 1979. Nonlinear Static Analysis of Cable-Stayed Bridge Structures. *Computers & Structures, Vol. 10*: 621-635. Pergamon Press.

Fleming, J. & Egeseli, E. 1980. Dynamic Behaviour of a Cable-Stayed Bridge. *Earthquake Engineering and Structural Dynamics, Vol. 8*: 1-16. John Wiley & Sons.

Flesch, R. 1990. A Dynamic Method for the Safety Inspection of Large Prestressed Bridges. *Dynamic Actions on Buildings and Structures. CEEC Course, 7-9 March, Aachen, Germany.*

Freyssinet 1994. Cable-stayed Bridges.

Frýba, L.. 1971. Vibration of solids and structures under moving loads. *Nordhoof International Publishing, Groningen, The Netherlands.*

Fuheng, Y. 1996. Vibrations of Cable-Stayed Bridges Under Moving Vehicles. *Ph.D. Thesis. Université de Liège. Belgium.*

Fujino, Y. & Kimura, K. 1997. Cables and Cable Vibration in Cable-Supported Bridges. *International Seminar on Cable Dynamics. Tokyo, 13 October*: 1-11.

Fujino, Y. & Nagai, M. 1994. Steel Cable-Stayed Bridges- With Emphasis on Japanese Bridges. *Proc. IABSE/ FIP Int. Conference on Cables-Stayed and Suspension Bridges, Deauville, 12-15 Oct. 1994*: 173-184.

Fujino, Y., Pacheco, B., Nakamura, S. & Warnitchai, P. 1993. Synchronization of Human Walking Observed During Lateral Vibration of a Congested Pedestrian Bridge. *Earthquake engineering and Structural Dynamics, Vol. 22*: 741-758. John Wiley & Sons, Ltd..

Fujino, Y. & Susumpov, T. 1994. An Experimental Study on Active Control of In-Plane Cable Vibration by Axial Support Motion. *Earthquake engineering and Structural Dynamics, Vol. 23*: 1283-1297. John Wiley & Sons, Ltd..

Fujino, Y., Warnitchai, P. & Pacheco, B. 1993. An Experimental and Analytical Study of Autoparametric Resonance in a 3DOF Model of a Cable-Stayed-Beam. *Nonlinear Dynamics, No. 4*: 111-138. Kluwer Academic Publishers.

Fujino, Y., Wilde, K., Masukawa, J. & Barthia, B. 1995. Rational Function Approximation of Aerodynamic Forces on Bridge Deck and its Application to Active Control of Flutter. *Proc. 9th International Conference on Wind Engineering, New Delhi, India*: 994-1005. Wiley Eastern Ltd.

Fung, Y. 1965. Foundations of Solid Mechanics. *Prentice-Hall.*

G

Gambhir, M. & Batchelor, B. 1977. A Finite Element for 3D Prestressed Cablenets. *International Journal of Numerical Methods in Engineering, Vol. 11*: 1699-1718.

Garevski, M. A. 1990. Dynamic Analysis of cable-Stayed Bridges by Means of Analytical and Physical Modelling. *Ph.D. Thesis, University of Bristol, U.K..*

Garevski, M. & Severn, R. 1993. Damping and Response Measurement on a Small-Scale Model of a Cable-Stayed Bridge. *Earthquake Engineering and Structural Dynamics, Vol. 22*: 13-29. John Wiley & Sons.

Gasparini, D. & Vanmarcke, E. 1976. Simulated Earthquake Motions Compatible with Prescribed Response Spectra. *Evaluation of Seismic Safety of Buildings, Report No. 2, Publication No. R76-4. Massachussets Institute of Technology.*

Gentile, C. & Cabrera, F. 1997. Dynamic Investigation of a Repaired Cable-Stayed Bridge. *Earthquake Engineering and Structural Dynamics, Vol. 26: 41-59.* John Wiley & Sons, Inc..

Gersch, W. 1970. Estimation of the Autoregressive Parameters of a Mixed Autoregressive Moving Average Time Series. *IEEE Transactions on Automatic Control, Vol. AC-15*: 583-588.

Gesner, G. & Jardim, J. 1998. Bridge Within a Bridge. *Civil Engineering, October 1998.* ASCE.

Geurts, C. & Staalduinen, P. 1999. Estimation of the Effects of Rain-Wind Induced Vibration in the Design Stage of Inclined Cables. In Larsen, A., Larose, G. & Livesey, F. (eds) 1999. *Wind Engineering into the 21st Century, Proc. of the Tenth Int. Conference on Wind Engineering*, Vol. 2: 885-892. Copenhagen, 21-24June. Balkema.

Geurts, C., Vrouwenvelder, T., Staalduinen, P. Reusink, J. 1998. Numerical Modelling of Rain-Wind-Induced Vibration: Erasmus Bridge, Rotterdam. *Structural Engineering International, 2*: 129-135. IABSE.

Gimsing, N.J. 1983. Cable Supported Bridges: Concept and Design. *Wiley Interscience.*

Gimsing, N.J. 1991. Design of a Long-Span Cable-Supported Bridge across the Great Belt in Denmark- 25 years of Experience and Evolution. In M. Ito, Y. Fujino, T. Myiata & N. Narita (eds), *Cable-Stayed Bridges: Recent Developments and their Future:* 279-298. Elsevier.

Gimsing, N. & Nissen, J. 1998. The Pylons on the Øresund Bridge. *Structural Engineering International, Vol. 8, No. 4, Nov.*: 263-264. IABSE.

Godden, W. G. & Aslam, M. 1978. Dynamic Model Studies of Ruck-A-Chucky Bridge. *Journal of the Structural Division, 104, ST12*: 1827-1844. ASCE.

Godden, W. G. 1980. Godden Collection. *Earthquake Engineering Library, University of California, Berkeley.*

Goschy, B. 1961. Dynamics of Cable-Stayed Pipe Bridges. *Acier-Stahl-Steel, Vol. 26, June, No. 6: 277-282.*

GPPE & FIP 1994. Prestressed Structures in Portugal.

Griffin, O., Skop, R. & Ramberg, S., 1975. The Resonant Vortex-Excited Vibrations of Structures and Cable Systems, *Offshore Technology Conference,* Paper OTC-2319, Houston.

Grillaud, G., Bourcier, P., Barré, C. And Flamand, O. 1997. Wind Action on the Vasco da Gama Cable-Stayed Bridge. *Proceedings of the 2nd European & African Conference on Wind Engineering, June 22-26, Genova, Italy*: 1449-1456. SGE Editoriali, Padova.

Guerreiro, L., Branco, F. & Azevedo, J. 1997. Seismic Displacement Control of the Vasco da Gama Bridge. *Proceedings of the International Conference on New Technologies in Structural Engineering, Lisbon 2-5 July, Session 2.*

Guillaume, P., Hermans, L. & Van der Auweraer, H. 1999. Maximum Likelihood Identification of Modal Parameters from Operational Data. . *Proceedings of the 17th International Seminar on Modal Analysis, Kissimee, Florida, 8-11 Feb.*

H

Hagedorn, P. & Schäfer, B. 1980. On Non-linear Free Vibrations of an Elastic Cable. *Int. J. of Non-Linear Mechanics, Vol. 15*: 333-340. Pergamon Press.

Han, M-C. & Wicks, A. 1989. On the Application of the Forsythe Polynomials for Global Modal Estimation. *Proceedings of the 7th International Modal Analysis Conference*: 625-630. Las Vegas, Nevada.

Hansvold, C. 1994. Skarnsundet Bridge. *Proc. IABSE/ FIP Int. Conference on Cables-Stayed and Suspension Bridges, Deauville, 12-15 Oct. 1994*: 247-256.

Hardy, C. & Bourdon, P. 1979. The influence of Spacer Dynamic Properties in the Control of Bundle Conductor Motion. *IEEE PES Summer Meeting, Vancouver, British Columbia, Canada, July.*

Hardy, C., Watts, J. A., Brunelle, J. & Clutier, L. J. 1975. Research on the Dynamics of Bundled Conductors at the Hydro-Quebec Institute of Research. *Trans. E. & O. Div., CEA, Vol. 14, Part 4.*

Harrison, H. 1973. Computer Methods in Structural Analysis. *Prentice-Hall, Inc.. ISBN 0-13-166066-7.*

Hart, G. & Yao, J. 1977. System Identification in Structural Dynamics. *Journal of the Engineering Mechanics Division, Vol. 103*: 1089-1104. ASCE.

Henghold, W. & Russell, J. 1976. Equilibrium and Natural Frequencies of Cable Structures (A Nonlinear Finite Element Approach). *Computers & Structures, Vol. 6*: 267-271. Pergamon Press.

Hermans, L., Van der Auweraer, H. & Guillaume, P. 1998. Frequency Domain Maximum Likelihood Approach for the Extraction of Modal Parameters from Output-Only Data. *Proceedings of ISMA23, International Conference on Noise and Vibration Engineering, Vol. 1, 16-18 Sept., Belgium*: 367-376.

Heylen, W., Bielen, P., Sas, P. & Vanherck, P. 1991. On Instrumentation for Experimental Modal Analysis. *Proceedings of the 16th International Seminar on Modal Analysis- Basic Course on Experimental Modal Analysis: Part 1, Firenze, 9-10 Sept. Katholieke Universitit Leuven.*

Hikami, Y. 1986. Rain Vibrations of Cables of a Cable-Stayed Bridge. J. Wind Engineering (Japan), No. 27: 17-28. (In Japanese).

Hikami, Y. & Shirashi, N. 1988. Rain-Wind Induced Vibrations of Cables in Cable-Stayed Bridges. *Journal of Wind Engineering and Industrial Aerodynamics, 29*: 409-418. Amsterdam. Elsevier.

Honda, H., Kajikawa, Y. and Kobori, T.1982. Spectra of Road Surfaces Roughness on Bridges, *Journal of the Structural Division, Vol. 108, No. ST9*: 1956-1966. ASCE.

Horyna, T. & Ventura, C. 2000. Summary of HCT Building Ambient Vibration Data Analyses. *Proceedings of IMACXVIII, A Conference & Exposition on Structural Dynamics, 7-10Feb., San Antonio, Texas*: 1095-1098.

Hoshino, S., Orita, H., Maeda, T., Fujioka, H., Takeda, T. & Ueno, K. 1997. Vibration Test on Ikara Bridge (A Prestressed Concrete Cable-Stayed Bridge). *International Conference on New Technologies in Structural Engineering, 2-5 July, Lisbon. LNEC.*

Housner, G. 1947. Characteristics of Strong Motion Earthquakes. *Bulletin of the Seismologic Society of America, Vol. 37*: 19-31.

Humar, J.L. and Kashif, A. H.1995. Dynamic Response Analysis of Slab-Type Bridges. *Journal of Structural Engineering*, Vol. 121, No. 1: 48-62. ASCE.

Hurtado, J., Barbat, A. & Cunha, A. 1996. Nonlinear Random Vibration of Base Isolated Buildings under Evolutionary Seismic Inputs, *11th World Conference on Earthquake Engineering, Acapulco, Mexico.*

I

Ibrahim, S. 1977. The Use of Random Decrement Technique for Identification of Structural Modes of Vibration. *AIAA Paper, Vol 77*: 1-9.

Ibrahim, S. & Mikulcik, E. 1976. The Experimental Determination of Vibration Parameters from Time Responses. *The Shock and Vibration Bulletin, Vol. 46, No. 5*: 187-196.

Ibrahim, S. & Mikulcik, E. 1977. A Method for the Direct Identification of Vibration Parameters from the Free Response. *The Shock and Vibration Bulletin, Vol. 47, No. 4*: 183-198.

Irvine, H. M. 1977. Free Vibration of Inclined Cables. *Journal of the Structural Division, Proceedings of the American Society of Civil Engineers, Vol. 104, No. ST2*: 343-347. ASCE.

Irvine, H. M. 1981. Cable Structures. *The MIT Press.*

Irvine, H. M. & Caughey, T. K. 1974. The Linear Theory of Free Vibrations of a Suspended Cable. *Proceedings of the Royal Society, London, Series A, Vol. 341*: 299-315.

Irwin, P. A. & Stone, G. K. 1986. Wind Tunnel Tests of the ALRT Fraser River Bridge Steel Design, Vancouver. *RWDI Report 484-1515-1, March 31, Guelph, Ontario.*

Irwin, P. A. 1998. The Role of Wind Tunnel Modelling in the Prediction of Wind Effects Bridges. In Larsen, A. & Esdahl, S. (eds), *Bridge Aerodynamics*: 99-117. Balkema.

Ito, M. 1998a. The Cable-Stayed Meiko Grand Bridges, Nagoya. *Structural Engineering International, Vol. 8, No. 3, Aug.*: 168-171. IABSE.

Ito, M. 1998b. Wind Effects Improve Tower Shape. *Structural Engineering International, Vol. 8, No. 4, Nov.*: 256-257. IABSE.

Ito, M. 1999. Stay Cable Technology: Overview. *Proc. of the Conference on Cable-Stayed Bridges-Past, Present and Future*, 2-4June. Keynote Lecture. IABSE.

J

Jain, A., Jones, N. & Scanlan, R. 1996. Coupled Flutter and Buffeting Analysis of Long-Span Bridges. *Journal of Structural Engineering, Vol. 122, No. 7*: 716-725. ASCE.

Jakobsen, K. A., Jordet, E., Rambjor, S. K. & Jakobsen, A. A. 1995. Full Scale Measurements of the Behaviour of the Helgeland Bridge- A Cable-Stayed Bridge Located in a Harsh Environment. *Proc. of the International Symposium on Cable Dynamics, 19-21 October, Liège*: 473-480. Belgium.

James, G., Came, T. & Lauffer, J. 1995. The Natural Excitation Technique (NexT) for Modal Parameter Extraction from Operating Structures. *International Journal of Analytical and Experimental Modal Analysis, Vol. 10, No. 4*: 260-277.

Jarosevic, A. & Chandoga, M. 1994. Force Measuring of Prestressing Steel. Slovak Report on Prestressed Concrete 1990-1994. XII International congress of FIP. Washington : 56-62.

Jayaraman, H. & Knudson, W. 1981. A Curved Element for the Analysis of Cable Structures. *International Journal of Solids and Structures, Vol. 15*: 424-437.

Johnson, E., Spencer, B. & Fujino, Y. 1999. Semiactive Damping of Stay Cables: a Preliminary Study. *Proc. XVII International Modal Analysis Conference, 8-11Feb., Florida*: 417-423. SEM.

Jones, N., Scanlan, R., Jain, A. & Katsuchi, H. 1998. Advances (and Challenges) in the Prediction of Long-Span Bridge Response to Wind. In Larsen, A. & Esdhal, S. (eds) *Bridge Aerodynamics*: 59-85. Balkema.

Jones, N., Shi, T., Ellis, J. & Scanlan, R. 1995. System-Identification Procedure for System and Input Parameters in Ambient Vibration Surveys. *Journal of Wind Engineering and Industrial Aerodynamics, No. 54/55*: 91-99. Elsevier.

Jones, N. & Spartz, C. 1990. Structural Damping Estimation for Long-Span Bridges. *Journal of Engineering Mechanics, Vol. 116, No. 11*: 2414-2433. ASCE.

Juang, J. & Pappa, R. 1985. Effects of Noise on Modal Parameters Identified by the Eigensystem Realization Algorithm. *Journal of Guidance, Control and Dynamics, Vol. 9, No. 3*: 294-303.

K

Kaimal, J. 1986. Flux and Profile Measurements from Towers in the Boundary Layer. In Lenschow, D. (ed.) *Probing the Atmospheric Boundary Layer*: 19-28. American Meteorological Society, Boston, USA. ISBN 0-933876-63-7.

Kaimal, J. & Finnigan, J. 1994. *Atmospheric Boundary Layer Flows: Their Structure and Measurement. Oxford University Press. ISBN 0-19-506239-6.*

Kajima Corporation 1985. Large-Scale Synchronous Exciters for Vibration Testing. *KICT Leaflet No. 85-8.*

Kajita, T. & Cheung, Y. 1973. Finite Element Analysis of Cable-Stayed Bridges. *International Association of Bridge and Structural Engineering, Publication 33 II.*

Kanai, K, 1957. Semi-empirical Formula for the Seismic Characteristics of the Ground. *University of Tokyo Bulletin of Earthquake Research Institute, Vol. 35*: 309-325.

Kanok-Nukulchai, W. & Hong, G. 1993. Nonlinear Modelling of Cable-Stayed Bridges. *Journal of Constructional Steel Research, Vol. 26*: 249-266. Elsevier.

Kanok-Nukulchai, W. , Yiu, P. & Brotton, D. 1992. Mathematical Modelling of Cable-Stayed Bridges. *Structural Engineering International, Vol. 2*: 108-113. IABSE.

Karoumi, R. 1996. Response of Cable-Stayed Bridges Subjected to Moving Vehicles, *Licentiate Thesis, Structural Engineering, Royal Institute of Technology, Sweden.*

Karoumi, R. 1998. Response of Cable-Stayed Bridges and Suspension Bridges to Moving Vehicules: Analysis Methods and Practical Modelling Techniques. *TRITA-BKN. Bulletin 44. Doctoral Thesis. Depart. Struct. Engineering, Royal Institute of Technology, Sweden.*

Katsuchi, H., Saeki, H., Miyata, T. & Sato, H. 1998. Analytical Assessment in Wind-Resistant Design of Long Span Bridges in Japan. In Larsen, A. & Esdahl, S. (eds), *Bridge Aerodynamics*: 87-98. Balkema.

Kawahito, T., Tsuji, M., Kano, I. & Tsumura, N. 1984. Pendulum-Type Tuned Mass Damper to Suppress Wind-Induced Vibration of the Tower of Meiko-Nishi Bridge Under Construction. *Proc. of the 8th National Symposium on Wind Engineering.*

Kawashima, K. & Unjoh, S. 1991. Seismic Behaviour of Cable-Stayed Bridges. In M. Ito, Y. Fujino, T. Myiata & N. Narita (eds), *Cable-Stayed Bridges: Recent Developments and their Future:* 193-212. Elsevier.

Keightley, W., Housner, G. & Hudson, D. 1961. Vibration Tests of the Encino Dam InTake Tower. *Report. California Institute of Technology.*

Keller, T. 1998. Towers for Cable-Stayed Bridges: An Introduction. *Structural Engineering International, Vol. 8, No. 4*: 248. IABSE.

Kennedy, C. & Pancu, C. 1947. Use of Vectors in Vibration Measurement and Analysis. *Journal of the Aeronautical Sciences, Vol. 14, No. 11*:603-625.

Ketchum, M. & Cheng, K. 1994. Seismic Analysis and Behaviour of Three Major Western-U.S. Suspension Bridges. *Proc. IABSE/ FIP Int. Conference on Cables-Stayed and Suspension Bridges, Deauville, 12-15 Oct. 1994, Vol. 1*: 255-262.

Khalifa, M. A. 1992. Dynamic vibration of cable-stayed bridges using carbon fiber composite cables. *Proc. 1st Conference on Advanced Composite Materials in Bridges and Structures, CSCE*: 465-477.

Khalifa, M. A. 1993. Analysis of Traffic Induced Vibration and Fatigue of Cable-Stayed Bridges. *Ph.D. Thesis. University of Southern California.*

Khalil, M. S. 1996. Seismic Analysis and Design of the Skytrain Cable-Stayed Bridge. *Canadian Journal of Civil Engineering, Vol. 23*: 1241-1248.

Kim, K. & Paik, S. Optical Fiber Monitoring System of Bridges in Korea. In F. Chang (ed), *Structural Health Monitoring: Current Status and Perspectives, Proceedings of the International Workshop on Structural Health Monitoring, Stanford, 18-20 September*: 555-563. Technomic.

Kirkegaard, P.H., Nielsen, S.R.K. and Enevoldsen, I.. 1997. Heavy Vehicles on Minor Highway Bridges - a Literature Review. *Structural Reliability Theory, Paper no. 169, Aalborg University.*

Klosterman, A. 1971. On the Experimental Determination and Use of Modal Representation of Dynamic Characteristics. *Ph.D. Thesis, University of Cincinnati. USA.*

Kovàcs, I. 1982. *Zur Frage der Seilschwingungen und der Seildampfung. Die Bautechnik, October*: 325-332.

Kovàcs, I.; Svensson, H. & Jordet, E. 1992. Analytical Aerodynamic Investigation of Cable-Stayed Helgeland Bridge. *Journal of Structural Engineering, Vol. 118, No. 1*: 147-168. ASCE.

Kubo, Y. 1997. Aeroelastic Instability and Its Improvement of Bundle Cable for Cable-Stayed Bridge. *Proc. of the International Seminar on Cable Dynamics*: 49-56. Tokyo, 13 Oct. JAWE.

Kubo, Y., Kato, K., Maeda, H., Oikawa, K. & Takeda, T. 1994. New Concept on Mechanism and Suppression of Wake Galloping of Cable-Stayed Bridges. *Proc. IABSE/ FIP Int. Conference on Cables-Stayed and Suspension Bridges, Deauville, 12-15 Oct. 1994*: 491-498.

Kumarasena, T., Scanlan, R. & Morris, G. Deer Isle Bridge: Field and Computed Vibrations. *Journal of Structural Engineering, Vol. 115*: 2313-2328. ASCE.

L

Labeeuw, G. 1990. Les Phenomenes Provoques dans les Ponts a Haubans par les Resonances de Couplage des Vibrations au Second Order. *Annales des Travaux Publics de Belgique, No. 2*: 85-94.

Langsoe, H. & Larsen, O. 1987. Generating Mechanism for Cable Stay Oscillations at the Farø Bridges. In W. Kanok-Nukulchai (ed), *Cable-Stayed Bridges: Experience & Practice, Vol. 1*: 1023-1033. AIT.

Law, S. S. & Ko, J. M. 1995. Ambient Vibration Measurements of the Tsing Ma Bridge Towers. *Proc. Conf. on Bridges into the 21st Century, 2-5 October, Hong Kong*: 765-772.

Lazar, B. 1972. Stiffness Analysis of Cable-Stayed Bridges. *Journal of the Structural Division, Vol. 98, No. ST7, July*: 1605-1612.

Lee, C. & Perkins, N. 1995. Three-Dimensional Oscillations of Suspended Cables Involving Simultaneous Internal Resonances. *Nonlinear Dynamics, Vol. 8*: 45-63. Kluwer Academic Publishers.

Leonhardt, F. 1986. Cable-Stayed Bridges. *Keynote Lecture. FIP Congress 1986, New Delhi 16 February. The Institution of Structural Engineers.*

Leonhardt, F. & Zellner, W. 1970. Cable-Stayed Bridges- Report on Latest Developments. *Proceedings of the Canadian Structural Engineering Conference, Toronto.*

Leonhardt, F. & Zellner, W. 1980. Cable-Stayed Bridges. *IABSE Surveys, S-13/80.*

Leonhardt, F. & Zellner, W. 1991. Past, Present and Future of Cable-Stayed Bridges. In M. Ito, Y. Fujino, T. Myiata & N. Narita (eds), *Cable-Stayed Bridges: Recent Developments and their Future:* 1-33. Elsevier.

Leuridan, J., Van Der Auweraer, H. & Mergeay, M. 1991. Review of Parameter Estimation Techniques. *Proceedings of the 16th International Seminar on Modal Analysis: Basic Course on Experimental Modal Analysis, Part 2. Katholieke Universiteit Leuven.*

Lilien, J. L. & Pinto da Costa, A. 1994. Vibration Amplitudes caused by Parametric Excitation of Cable Stayed Structures. *Journal of Sound and Vibration, 174 (1)*: 69-90.

Lin, T. Y. 1996. Arch as Architecture. *Structural Engineering International, Vol. 6, No. 2*: 84-88. IABSE.

Lin, T. Y. & Chow, P. 1991. Gibraltar Strait Crossing- A challenge to Bridge and Structural Engineers. *Structural Engineering International, Vol 1(2)*: 53-58. IABSE.

Livesley, R. & Chandler, D. 1956. Stability Functions for Structural Frameworks. *Manchester University Press, Manchester.*

Ljung, L. 1987. System Identification: Theory for the User. *Prentice Hall Information and System Science Series. ISBN 0-13-881640-9-025.*

LMS CADA-PC. 1992. Modal Analysis Software Package. *LMS International.*

LNEC, 1992a. Ensaios Dinâmicos na Ponte do Arade. *Report LNEC.*

LNEC, 1992b. Ensaios Dinâmicos na Ponte do Guadiana. *Report LNEC.*

Loh, C. 1985. Analysis of the Spatial Variation of Seismic Waves and Ground Movements from SMART-1 Array Data. *Earthquake Engineering and Structural Dynamics, Vol. 13*: 561-581. John Wiley & Sons.

Lu, Z. 1979. Dynamic Analysis of Cable-Hung Ruck-A-Chucky Bridge. *Journal of the Structural Division, Vol. 105, October*: 2009-2018. ASCE.

Luongo, A., Rega, G. & Vestroni, F. 1984. Planar Non-Linear Free Vibrations of an Elastic Cable. *Int. J. of Non-Linear Mechanics, Vol. 19, No. 1*: 39-52. Pergamon Press.

Lundhus, P., Braestrup, M. & Falbe-Hansen, K. 1997. The Øresund Fixed Link Between Denmark and Sweden. *New Tech 97. International Conference on New technologies in Structural Engineering. Lisbon, Portugal, Jul 2-5.* FIP.

M

Macdonald, J., Dagless, E., Thomas, B. & Taylor, C. 1997. Dynamic Measurements of the Second Severn Crossing. *Proc. Instn. Civil Engineers, Vol. 123*: 241-248. Paper no. 11483.

Macdonald, J., Dobinson, N., Macnamara, H. & Taylor, C. 1998. Modal Analysis of a Partially Constructed Cable-Stayed Bridge. *Proc. of the 16th International Modal Analysis Conference, Santa Barbara, California, 3-5 February.* SEM.

MacLamore, V., Hart, G. & Stubbs, I. 1971. Ambient Vibration of Two Suspension Bridges. *Journal of the Structural Division, Vol. 97, No. ST10*: 2567-2582. ASCE.

Maeda, Y., Maeda, K. & Fujiwara, K. 1983. System Damping Effect and its Application to Design of Cable-Stayed Bridge. *Technology reports of the Osaka University, Vol. 33, No. 1699*: 125-135.

Maia, N. & Ewins, D. 1989. New Approach for the Modal Identification of Lightly Damped Structures. *Mechanical Systems and Signal Processing, Vol. 3, No. 2*: 173-193.

Maia, N., Ribeiro, A. & Silva, J. 1994. A New Concept in Modal Analysis: The Characteristic Response Function (CRF). *International Journal of Analytical and Experimental Modal Analysis, Vol. 9, No. 3*: 191-202.

Maia, N. & Silva, J. (Eds.) 1997. Theoretical and Experimental Modal Analysis. *Research Studies Press. ISBN 0 86380 208 7.*

Main, J. & Jones, N. 1999. Full-scale Measurements of Stay Cable Vibration. *Proc. 10th Int. Conference on Wind Engineering, 21-24 June*. Copenhagen.

Malhortra, P. & Wieland, M. 1987. Tuned Mass Damper for Suppressing Wind Effects in a Cable-Stayed Bridge. In W. Kanok-Nukulchai (ed), *Cable-Stayed Bridges: Experience & Practice, Vol. 1*: 557-568. AIT.

Marecos, J., Castanheta, M. & Teixeira Trigo, J. 1969. Field Observation of Tagus River Suspension Bridge. *Journal of the Structural Division, Vol. 95, No. ST4*: 555-583. ASCE.

Martin, H. & Carey, G. 1973. Introduction to Finite Element Analysis: Theory and Application. *McGraw-Hiull, Inc.. ISBN 0-07-040641-3.*

Mason, A. & Carder, D. 1967. Vibration Frequencies of the Cheasapeake Bay Bridge. *Journal of the Structural Division, Vol. 93, No. ST2*: 237-245. ASCE.

Mathieu, H., Calgaro, J.A. & Prat, M.. 1991. Concerning development of models of traffic loading and rules for the specification of bridge loads. *Final Report for the Comision of the European Communities on Contract No. PR2/90/7750/RN/46..*

Mathivat, J. 1983. The Cantilever Construction of Prestressed Concrete Bridges. *John Wiley and Sons Ltd.*

Mathivat, J. 1994. Les ponts a câbles. Des Origines a la Conquête des Grandes Portées. *Proc. IABSE/ FIP Int. Conference on Cables-Stayed and Suspension Bridges, Deauville, 12-15 Oct. 1994*: 3-32.

Mathivat, J. & Lenoir, B. 1984. Evolution des Ponts a Haubans en Béton. *Journée d'étude AFPC-ITBTP de Nov. 1982. Annales de L'ITBTP, Janvier.*

Matsumoto, M. 1998. Observed Behaviour of Prototype Cable Vibration and Its Generating Mechanism. In Larsen, A. & Esdahl, S. (eds), *Bridge Aerodynamics*: 189-211. Balkema.

Matsumoto, M., Knisely, C., Shiraishi, N., Kitazawa, M. & Saitoh, T. 1989a. Inclined Cable Aerodynamics. *Structural Design, Analysis and Testing Proceedings, Structures Congress '89, ASCE*: 81-90. San Francisco, CA.

Matsumoto, Y., Nishioka, T., Shiojiri, H. & Matsuzaki, K. 1978. Dynamic Design of Footbridges. IABSE Proceedings, P-17/78, August.

Matsumoto, M., Yokoyama, K., Miyata, T., Fujino, Y. & Yamaguchi, H. 1989b. Wind-Induced Cable Vibration of Cable-Stayed Bridges in Japan. *Proc. of Canada-Japan Workshop on Bridge Aerodynamics*. Ottawa, Canada.

Matsumoto, M., Shiraishi, H. & Shirato, H. , 1992. Rain-Wind Induced Vibration of Cables of Cable-Stayed Bridges. *Journal of Wind Engineering and Industrial Aerodynamics, Vol. 44*: 2011-2022. Elsevier.

Matsumoto, M., Saitoh, H., Kitazawa, M., T., Shirato & Nishizaki, T. 1995. Response Characteristics of rain-Wind Induced Vibration of Stay Cables of Cable-Stayed Bridges. *Journal of Wind Engineering and Industrial Aerodynamics, Vol. 57*: 323-333. Elsevier Publications.

Mau, S. & Wang, S. 1989. Arch Dam System Identification Using Vibration Test Data. *Earthquake Engineering and Structural Dynamics, No. 18*: 494-505. John Wiley & Sons.

Mehrabi, A. & Tabatabai, H. 1998. A Unified Finite Difference Formulation for Free Vibration of Cables. *Journal of Structural Engineering, Vol. 124, No. 11*: 1313-1322. ASCE.

Mendes, P. 1994. Modelação Numérica do Comportamento Aerodinâmico de Estruturas Esbeltas. *Ph.D. Thesis, Technical University of Lisbon, Portugal* (in Portuguese).

Mendes, P. & Branco, F. 1997. Dynamic Behaviour of Vasco da Gama Bridge Under Wind Gusts. *Proceedings of the International Conference on New Technologies in Structural Engineering, Lisbon 2-5 July, Session 2.*

Menn, C. 1998. Functional Shaping of Piers and Pylons. *Structural Engineering International, Vol. 8, no. 4, November:* 249-251. IABSE.

Morris, N. 1974. Dynamic Analysis of Cable-Stiffened Structures. *Journal of the Structural Division, Vol. 100, No. ST5*: 971-981. ASCE.

Murià-Vila, D., Gomèz, R. & King, C. 1991. Dynamic Structural Properties of Cable-Stayed Tampico Bridge. *Journal of Structural Engineering, 117, No. 11*: 3396-3416. ASCE.

Miyata, T., Yamada, H. & Hojo, T. 1994. Aerodynamic Response of PE Stay Cables with Pattern.Indented Surface. *Proc. IABSE/ FIP Int. Conference on Cables-Stayed and Suspension Bridges, Deauville, 12-15 Oct. 1994*: 515-522.

Miyata, T., Yamada, H., Hojo, T. & Yamazaki, S. 1995. On Aerodynamically Stable PE-Stay-Cables with Decreased Drag Force by Introduction of Newly Developed Lumped Surface Roughness. *Proc. of the International Symposium on Cable Dynamics, 19-21 October, Liège*: 481-488. Belgium.

Morris, N. 1974. Dynamic Analysis of Cable-Stayed Structures. *Journal of the Structural Division, Vol. 100, No. ST5*: 971-981. ASCE.

Morris, N. 1977. The Use of Modal Superposition in Nonlinear Dynamics. *Computers & Structures, Vol. 7*: 65-72. Pergamon Press.

Myrvoll, F., Aarnes, K. & Larssen, R. 2000. Full Scale Measurements for Design Verification of Bridges. *IMAC-XVIII: A Conference & Exposition on Structural Dynamics, 7-10 Feb., San Antonio, Texas, USA. SEM*

N

Narayanan, G., Krishnamoorthy, C. & Rajagopalan, N. 1987. Investigations on Nonlinear Static and Dynamic Response of Cable-Stayed Bridges. In Kanok-Nukulchai (ed), *Cable-Stayed Bridges: Experience & Practice, Vol. 1*: 301-314. AIT.

Narita, N. & Yokoyama, K. 1991. A Sumarized Account of Damping Capacity and Measures Against Wind Action in Cable-Stayed Bridges in Japan. In M. Ito, Y. Fujino, T. Myiata & N. Narita (eds), *Cable-Stayed Bridges: Recent Developments and their Future:* 257-278. Elsevier.

Nayfeh, A. & Mook, D. 1979. Nonlinear Oscillations. John Wiley & Sons.

Nazmy, A. 1987. Nonlinear Earthquake Response Analysis of Cable-Stayed Bridges Subjected to Multiple-Support Excitations. *Ph.D. Thesis. Princeton University. USA.*

Nazmy, A. & Abdel-Ghaffar, M. 1990a. Three-Dimensional Nonlinear Static Analysis of Cable-Stayed Bridges. *Computers & Structures, Vol. 34, No. 2*: 257-271. Pergamon Press.

Nazmy, A. & Abdel-Ghaffar, M. 1990b. Nonlinear Earthquake Response-Analysis of Long-Span Cable-Stayed Bridges: Theory. *Earthquake Engineering and Structural Dynamics, Vol. 19*: 45-62. John Wiley & Sons.

Nazmy, A. & Abdel-Ghaffar, M. 1990c. Nonlinear Earthquake Response-Analysis of Long-Span Cable-Stayed Bridges: Applications. *Earthquake Engineering and Structural Dynamics, Vol. 19*: 63-76. John Wiley & Sons.

NGI; JOHS. HOLT A.S; AAS JAKOBSEN 1994. The Norwegian Road to Improved Bridge Quality: Instrumentation, Documentation and Verification.

Nigbor, R. L. & Diehl, J. G. 1997. Two Year's Experience Using OASIS Real-Time Remote Condition Monitoring System on Two Large Bridges. In F. Chang (ed), *Structural Health Monitoring: Current Status and Perspectives, Proceedings of the International Workshop on Structural Health Monitoring, Stanford, 18-20 September*: 410-417. Technomic.

O

Ohashi, M. 1991. Cables for Cable-Stayed Bridges. In M. Ito, Y. Fujino, T. Myiata & N. Narita (eds), *Cable-Stayed Bridges: Recent Developments and their Future:* 125-250. Elsevier.

OHBDC 1979. Ontario Highway Bridge Design Code. *Ministry of Transportation and Communication, Downsview, Ontario.*

OHBDC 1992. Ontario Highway Bridge Design Code. *Ministry of Transportation and Communication, Downsview, Ontario.*

Ohlsson, S. V. 1987. Dynamic Characteristics of Cable-Stayed Bridges- Nonlinearities and Weakly Coupled Modes of Vibration. In W. Kanok-Nukulchai (ed), *Cable-Stayed Bridges: Experience & Practice, Vol. 1*: 421-431. AIT.

Ohshima, K. & Nanjo, M., 1987. Aerodynamic Stability of the Cables of a Cable-Stayed Bridge Subject to Rain (A Case Study of the Ajigawa Bridge). *Proc. US-Japan Seminar on Natural Resources.*

Okauchi, I., Miyata, T., Tatsumi, M. & Kiyota, R. 1992. Dynamic Field Tests and Studies on Vibrational Characteristics of Long-Span Suspension Bridges. *Structural Engineering, Earthquake Engineering Journal, Vol. 9, No. 1, April*: 89s-100s.

Okauchi, I., Miyata, T., Tatsumi, M. & Sasaki, N. 1997. Field Vibration Test of a Long-Span Cable-Stayed Bridge Using Large Exciters. *Journal of Structural Engineering/ Earthquake Engineering, JSCE, Vol. 14, No. 1*: 83s-93s.

Oran, C. 1973a. Tangent Stiffness in Plane Frames. *Journal of the Structural Division, Vol. 99, No. ST&, June*: 973-983. ASCE.

Oran, C. 1973b. Tangent Stiffness in Space Frames. *Journal of the Structural Division, Vol. 99, No. ST6, June*: 987-1001. ASCE.

Øresund Konsortiet 1998. The Øresund Fixed Link: Design and Construction.

Ostenfeld, K. & Langsoe, H. 1987. Full Scale Measurements and Monitoring of Major Cable-Stayed Bridge. In W. Kanok-Nukulchai (ed), *Cable-Stayed Bridges: Experience & Practice, Vol. 1*: 997-1005. AIT.

Ostenfeld, K. H. & Larsen, A. 1992. Bridge Engineering and Aerodynamics. In Larsen, A. (ed) *Aerodynamics of Large Bridges, Proc. of the First International Symposium on Aerodynamics of large Bridges, 19-21Feb., Copenhagen*: 3-22. Balkema.

Otte, D., Yang, Q. & Sas, P. 1994. Analysis of Multivariate Operating Response Data by Means of ARV Time Series Modelling Techniques. In Sas, P. (ed.) *Proceedings of ISMA 19: Tools for Noise and Vibration Analysis, Vol. III*: 1321-1328. Leuven. Belgium.

Overschee, P. & De Moor, B. 1996. Subspace Identification for Linear Systems: Theory-Implementation- Applications. *Kluwer Academic Publishers.*

Owen, J., Vann, A., Davies, J. & Blakeborough, A. 1996. The Prototype Testing of Kessock Bridge: Response to Vortex Shedding. *Journal of Wind Engineering and Industrial Aerodynamics, Vol. 60*: 91-108. Elsevier Science.

Ozdemir, H. 1979. A Finite Element Approach for Cable Problems. *International Journal of Solids and Structures, Vol. 15*: 424-437.

P

Pacheco, B. & Fujino, Y. 1993. Keeping Cables Calm. *Civil Engineering, October 1993.*

Pakdemirli, M., Nayfeh, S. & Nayfeh, A. 1995. Analysis of One-to-One Autoparametric Resonances in Cables- Discretization vs Direct Treatment. *Non-Linear Dynamics, Vol. 8*: 65-83. Kluwer Academic Publishers.

Pan, K. 1998. System and Excitation for Large Structures. *Ph.D. Thesis, The John Hopkins University. USA.*

Paquet, J. 1990. Building Control with Dynamic Methods. *Dynamic Actions on Buildings and Structures. CEEC Course, 7-9 March, Aachen, Germany.*

Paultre, P., Chaalal, O. and Proulx, J. 1992. Bridge Dynamics and Dynamic Amplification Factors - Review of Analytical and Experimental Findings. *Canadian Journal of Civil Engineering, Vol. 19, No. 2*: 260-278.

Paultre, P., Proulx, J., Bégin, T. & Carbonneau, C. 1994. Étude Expérimentale et Analytique Du Comportement Dynamicque Du Pont Suspendu de Beauharnois. In *Proc. IABSE/ FIP Int. Conference on Cables-Stayed and Suspension Bridges, Deauville, 12-15 Oct.*, Vol. 1: 295-302.

Pedro, J., Silva, A., Pereira, J. Florentino, C., Câmara, R., Silva, H. 1986. Seismic Monitoring of Concrete Dams and Reservoirs. Portuguese Experience. *8th European Conference on Earthquake Engineering, Lisbon. LNEC.*

Peeters, B. 2000. System Identification and Damage Detection in Civil Engineering. *Ph.D. Thesis. Katholieke Universiteit Leuven. Belgium.*

Peeters, B. & De Roeck, G. 1999. Reference Based Stochastic Subspace Identification in Civil Engineering. *Proceedings of the 2nd International Conference on Identification in Engineering Systems, March, Swansea*: 639-648.

Peeters, B., Van den Branden, B., Laquière, A. & De Roeck, G. 1999. Output-Only Modal Analysis: Development of a GUI for MATLAB. *Proceedings of the 17th International Modal Analysis Conference, IMAC, Feb.. Orlando. Florida. SEM.*

Pendered, J. & Bishop, R. 1963. A Critical Introduction to Some Industrial Resonance Testing Techniques. *Journal of Mechanical Engineering Science, Vol. 5, No.4*: 345-367.

Perkins, N. 1992. Modal Interactions in the Non-Linear Response of Elastic Cables Under Parametric /External Excitation. *Int. J. Non-Linear Mechanics, Vol. 27, No. 2*: 233-250. Pergamon Press.

Persoon, A. & Van Nunen, J. 1979. Investigation on the Vibrational Behaviour of a Cable-Stayed Bridge Under Wind Loads. *Proceedings of the International Conference on Environmental Forces on Engineering Structures, Imperial College, London, July*: 107-119.

Pinto da Costa, A., Martins, J., Branco, F. and Lilien, J. 1996. Oscillations of Bridge Stay Cables Induced by Periodic Motions of Deck and / or Towers. *Journal of Engineering Mechanics, vol. 122, No. 7*: 613-622. ASCE.

Podolny, W. 1971. Static Analysis of Cable-Stayed Bridges. *Ph.D. Thesis, University of Pittsburgh.*

Podolny, W., Jr. 1973. Economic Comparisons of Stayed Girder Bridges. *Highway Focus, Vol. 5, No. 2, August.* U. S. Department of Transportation, Federal Highway Administration, Washington D.C.

Podolny, W. & Scalzi, J. 1976. Construction and Design of Cable-Stayed Bridges. *John Wiley & Sons.*

Portugal, A. & Caetano, E. 1992. Experimental Evaluation of the Dynamic Characteristics of Portuguese Dams. *Tenth World Conference on Earthquake Engineering, Madrid*: 3579-3584. Balkema.

Premachandran, R. & Wieland, M. 1994. Optimum Damping of Vibrations of Stay Cables in Cable-Stayed Bridges. *Australasian Structural Engineering Conference, Sydney, 21-23 Sept.*

Pretlove, A., Rainer, J. & Bachmann, H. 1997. Pedestrian Bridges. In Bachmann *et al.* (eds), *Vibration Problems in Structures- Practical Guidelines*: 2-10. Birkhäuser.

Priestley, M. 1971. Some Notes on the Physical Interpretation of Spectra of Nonstationary Stochastic Processes. *Journal of Sound and Vibration, Vol. 17, No. 1*: 51-54.

Prony, R. 1975. Essai Expérimental et Analitique Sur Les Lois de la Dilatibilité des Fluides Élastiques et Sur Celles de la Force Expansive de la Vapeur de L'Eau et de la Vapeur de L'Alkool, À Differentes Temperatures. *Journal de L'École Polytechnique (Paris), Vol. 1, Cahier 2, Flóreal et Prairial, An. III*: 24-76.

Przemieniecki, J. 1968. Theory of Matrix Structural Analysis. *McGraw-Hill, Inc..*

R

Rao, G. V. & Iyengar, R. N. 1991. Internal Resonance and Non-Linear Response of a Cable Under Periodic Excitation. *Journal of Sound and Vibration, Vol. 149, No. 1*: 25-41. Academic Press.

Ravara, A., Duarte, R. & Carvalho, E. 1984. Engenharia Sísmica de Pontes. *ICT Especialização e Aperdeiçoamento, Estruturas, Pub. No. S318. LNEC. Lisbon* (in Portuguese).

Reed, D., Yeh, H., Yu, J. & Gardarsson, S. Tuned liquid Dampers Under Large Amplitude Excutation. *Journal of Wind Engineering and Industrial Aerodynamics, Vol. 74-76*: 923-930. Elsevier.

Reis, A. J. L. & Pereira, A. 1994. Socorridos Bridge: A Cable-Panel Stayed Concept. *Proc. IABSE/ FIP Int. Conference on Cables-Stayed and Suspension Bridges, Deauville, 12-15 Oct. 1994*: 343-350.

Reis, A. J. L., Pereira, A., Pedro, J. J. O., Lopes, N. T. & Sousa, D. 1998. Pontes de Tirantes em Espaços Urbanos. *Jornadas Portuguesas de Engenharia de Estruturas, 25-28 Nov. 1998, Lisbon*: 883-892.

Ren, W., Shen, J. & DeRoeck, G. 2000. Structural Stiffness Identification Using Maximum Likelihood Estimate Method. . *Proceedings of the 18_{th} International Seminar on Modal Analysis, San Antonio, Texas, 7-10 Feb.*

Richardson, M. & Formenti, D. 1982. Parameter Estimation From Frequency Response Measurements Using Rational Fraction Polynomials. *Proceedings of the 1st International Modal Analysis Conference (IMACI), Orlando, Florida*: 167-181. SEM.

Richmond, B. & Sham, R. S.H. 1994. *Proc. IABSE/ FIP Int. Conference on Cable-Stayed and Suspension Bridges, Deauville, 12-15 Oct. 1994*: 79-90.

Rito, A. M. 1993. A Ponte sobre o Rio Arade na Variante à EN 125 em Portimão. In *Pontes Atirantadas do Guadiana e do Arade- Sessão integrada no 4º Encontro Nacional sobre Estruturas Pré-Esforçadas*: 69-96. LNEC.

Rodrigues, J. & Campos Costa, A. 1998. Experimental Modal Analysis of Bridge Structures: Case Studies. *Proc. of the Eleventh European Conference on Earthquake Engineering, 6-11 September, Paris.* Balkema.

Roos, F. & Noisterning, J. 1999.CFRP-Tendons- Development and Testing. *Proc. of the Conference on Cable-Stayed Bridges- Past, Present and Future*, 2-4June. IABSE.

RSA, 1986. Regulamento de Segurança e Acções para Estruturas de Edifícios e Pontes. *Imprensa Nacional- Casa da Moeda. Lisbon.*

Ruscheweyh, H., 1994. Vortex Excited Vibrations. In Sockel, H. (ed), *Wind Excited Vibrations of Structures, CISM Courses and Lectures no. 335*: 51-84. Springer-Verlag.

S

Sabnis, G., Harris, H., White, R. & Mirza, M. 1983. Structural Modeling and Experimental Techniques. *Prentice-Hall, Inc.. ISBN 013853960X.*

Saito, T., Ito, M., Yamaguchi, H., Eya, S. 1988. Use of a Dynamic Damper for Aerodynamic Stability of its Support Tower. *Proc. of $4t^{h}$ U.S.-Japan Workshop on Bridge Engineering, San Diego, USA, 11-12 May.*

Saito, T., Matsumoto, M. & Kitazawa, M. 1994. Rain-Wind Excitation of Cables on Cable-Stayed Higashi-Kobe Bridge and Cable Vibration Control. *Proc. IABSE/ FIP Int. Conference on Cables-Stayed and Suspension Bridges, Deauville, 12-15 Oct. 1994*: 507-514.

Samali, B., Kwok, K. & Facioni, R. 1999. Wind Tunnel Comparison of Active and Passive Tuned mass Dampers. *Proc. of the XVII International Modal Analysis Conference, 8-11Feb. Florida*: 174-180. SEM.

Sarkar, P., Jones, N. & Scanlan, R. 1994. Identification of Aeroelastic Parameters of Flexible Bridges. *Journal of Engineering Mechanics, Vol. 120, No. 8*: 1718-1743. ASCE.

Scanlan, R. 1993. Problematics in Formulation of Wind-Force Models for Bridge Decks. *Journal of Engineering Mechanics, Vol. 119, No. 7*: 1353-1375. ASCE.

Scanlan, R. 1994. Toward Reduction of Empiricism in the Wind Design of Long-Span Bridges. *Proc. IABSE/ FIP Int. Conference on Cables-Stayed and Suspension Bridges, Deauville, 12-15 Oct. 1994, Vol. 2*: 15-28.

Scanlan, R. & Jones, N. 1990. Aeroelastic Analysis of Cable-Stayed Bridges. *Journal of Structural Engineering, Vol. 116, No. 2*: 279-297. ASCE.

Schemmann, A, & Smith, A. 1997. Modeling and Active Control of Cable-Stayed Bridges Subject to Multiple-Support Seismic Excitation. *Report No. 123. The John A. Blume Earthquake Engineering Center, University of Stanford. USA.*

Schlaich, J. 1994. Aesthetics and Structural Performance of Cable-Supported Bridges. *Proc. IABSE/ FIP Int. Conference on Cables-Stayed and Suspension Bridges, Deauville, 12-15 Oct. 1994, Vol. 1*: 43:52.

Schlaich, M. & Bergermann, R. 1998. Monoleg Towers with Transverse Stabilizing Cables. *Structural Engineering International, Vol. 8, No. 4, Nov.*: 252-255. IABSE.

Schnabel, P., Lysmer, J. & Seed, H. 1972. SHAKE - A Computer Program for Earthquake Analysis of Horizontally Layered Sites. *University of California, Berkeley, Report no. EERC 72-12.*

Schreier, G. 1961. Beiträge Zur Anwendung von Baustatischen Methoden auf Probleme der Verformungs Theorie. *Dr. Ing. Thesis, Technical University of Karlsruhe.*

Schulze, H. 1980. Dynamic Effects of the Live Load on Footbridges. *Signal und Schiene, Vol. 24, No. 2*: 91-93, *No. 3*: 143-147 (in German).

Seible, F., Karbhari, V., Burgueno, R. 1999. Kings Stormwater and I-5 Gilman Bridges, USA. *Structural Engineering International, No. 4*: 250-253. IABSE.

Serridge, M. & Licht, T. 1987. Piezoelectric Accelerometer and Vibration Preamplifiers: Theory and Application Handbook. *Brüel & Kjær.*

Sethia, M.R. & Krishna, P. 1987. Modal Tests of a Cable-Stayed Bridge. In W. Kanok-Nukulchai (ed), *Cable-Stayed Bridges: Experience & Practice, Vol. 2*: 927-938. AIT.

Severn, R. 1998. Earthquake Engineering. A European Group of Large-Scale Facilities within the Training and Mobility of Researchers Programme. *European Communities. ISBN: 92-828-4788-8.*

Severn, R., Jeary, A. & Ellis, B. 1980. Forced Vibration Tests and Theoretical Studies on Dams. *Proceedings of the Institution of Civil Engineers, Pt. 2, Vol. 69*: 605-634.

Severn, R., Jeary, A. & Ellis, B. 1981. Forced Vibration Tests and Theoretical Studies on Dams. *Proceedings of the Institution of Civil Engineers, Pt. 2:* 575-595.

Shi, W., Wang, C., Coles, D. & Roshko, A., 1993. Experiments on Flow Past Circular Cylinders at Large Reynolds Numbers. *Journal of Wind Engineering and Industrial Aerodynamics, Vol. 49*: 348-351. Elsevier.

SIA 160. 1989, Actions Sur les Structures Porteuses. *Norme SIA 160. Societé Suisse des ingénieurs et des Architectes.*

Simiu, E. & Scanlan, R., 1996. Wind Effects on Structures: Fundamentals and Applications to Design. *Third Edition. John Wiley & Sons, Inc.*

Simpson, A. Determination of the Natural Frequencies of Multiconductor Overhead Transmission Lines. *Journal of Sound and Vibration, Vol. 20, No. 4*: 417-449.

Smith, B. 1968. A Linear Method of Analysis for Double-Plane Cable-Stayed Bridges. *Proceedings of the Institution of Civil Engineers, Vol. 39, February*: 85-94.

Smith, D. 1974. A Case Study and Analysis of the Tacoma Narrows Bridge Failure. *Internal report, 99.497 Engineering Project, Department of Mechanical Engineering, Carleton University, Canada. (www.civeng.carleton.ca/Exhibits/Tacoma_Narrows/Dsmith/photos.html).*

Sockel, H. 1994. Transverse Galloping Oscillations. In Sockel, H. (ed.), *Wind Excited Vibrations of Structures, CISM Courses and Lectures no. 335*: 181-193. Springer-Verlag.

SOLVIA 95.0 1995. Finite Element System. *SOLVIA Engineering AB. Sweden.*

Soong, T. T. 1988. State-of-the-art Review: Active Structural Control in Civil Engineering. *Engineering Structures, Vol. 19, April*: 74-84. Butterworth & Co.

Sorbjan, Z. 1989. Structure of the Atmospheric Boundary Layer. *Prentice Hall, Inc.. ISBN 0-13-853557-4.*

Spitznogle, F. & Quazi, A. 1971. Representation and Analysis of Time –Limited Signals Using a Complex Exponential Algorithm. *Journal of the Accoustical Society of America, Vol. 47, No. 5 (Part 1)*: 1150-1155.

Starossek, U. 1990. Boundary Induced Vibration and Dynamic Stiffness of a Sagging Cable. *Internal report. Universität Stuttgart. Institut für Statik und Dynamik der Luft- und Raumfahrtkonstruktionen Professor Dr. -Ing. Bernd- H. Kröplin.*

Starossek, U. 1993. Reduction of Dynamic Cable Stiffness to Linear Matrix Polynomial. *Journal of Engineering Mechanics, Vol. 119, No. 10*: 2132-2136. ASCE.

Stephen, G., Brownjohn, J. & Taylor, C. 1993. Measurements of Static and Dynamic Displacement from Visual Monitoring of the Humber Bridge. *Engineering Structures, Vol. 15, No. 3*: 197-208. Butterworth-Heineman Ltd.

Stiemer, S. F., Taylor, P. & Vincent, D. H. C. 1988. Full Scale Dynamic Testing of the Annacis Bridge. *IABSE Periodica, 1*: 1-16.

Sugianto, P. 1990. Simulation of Fatigue Damage in Cables of RamaIX Cable-Stayed Bridge in Bangkok Under Random Truck Loads. *Master of Science Thesis, No. ST-90-11. Asian Institute of Technology.*

Susumpov, T. & Fujino, Y. 1995. Active Control of Multimodal Cable Vibrations by Axial Support Motion. *Journal of Engineering Mechanics, Vol. 121, No. 9, Sept.*: 964-972. ASCE.

T

Tagata, G. 1977. Harmonically Forced, Finite Amplitude Vibration of a String. *Journal of Sound & Vibration, Vol. 51, No. 4*: 483-492.

Tajimi, H. 1960. A Statistical Method of Determining the Maximum Response of a Building Structure During Earthquake. *Proc. of the Second World Conference on Earthquake Engineering, Vol. 2, Tokyo*: 781-798.

Takahashi, K. & Konishi, Y. 1987. Non-Linear Vibrations of Cables in Three Dimensions, Part I: Non-Linear Free Vibrations. *J. of Sound and Vibration, Vol. 118, No. 1*: 69-84. Academic Press.

Takenouchi, K. 1998. Single Pylons for Curved Cable-Stayed Bridges. *Structural Engineering International, Vol. 8, No. 4*: 269-272. IABSE.

Tang, M. 1971. Analysis of Cable-Stayed Girder Bridges. *Journal of the Structural Division, Vol. 97, No. ST5, May*: 1481-1495. ASCE.

Tappin, G. R.. 1985. Jindo and Dolson Bridges. *Proceedings of the Institution of Civil Engineers, Vol. 78, Part I*: 1281-1300.

Taylor, C. 1991. 1991. EQSIM: A Program for Generating Spectrum Compatible Earthquake Ground Acceleration Time Histories. *Reference Manual. University of Bristol.*

Taylor, P. R. 1991. Precast and Composite Concrete Cable-Stayed Bridges. In M. Ito, Y. Fujino, T. Myiata & N. Narita (eds), *Cable-Stayed Bridges: Recent Developments and their Future:* 107-124. Elsevier.

Taylor, P., Selst, A., Hodge, W. & Sexsmith, R. 1985. Annacis Cable-Stayed Bridge-Design for Earthquake. *Canadian Journal of Civil Engineering, Vol. 12*: 472-482.

Thiele, K. 1996. Full-Scale Investigations of Cable Vibrations on Cable-Stayed Bridges and Development of a Cable Damper Using Viscoelastic Material. *Master Science Thesis. The University of Western Ontario, Canada.*

Thul, H. 1966. Cable-Stayed Bridges in Germany. *Proc. of the Conference on Structural Steelwork, Institution of Civil Engineers, 26-28 Sept.*: 69-81. The British Constructional Steelwork Association Ltd., London, England.

Tilly, G., Cullington, D. & Eyre, R. 1984. Dynamic Behaviour of Footbridges. *IABSE Surveys, S-26/84, May.*

Triantafyllou, M. S. 1984. The Dynamics of Taut Inclined Cables. *Quarterly Journal of Mechanics and Applied Mathematics, Vol. 37, Pt. 3*: 421-440.

Trifunac, M. 1972. Comparison Between Ambient and Forced Vibration Experiments. *Earthquake Engineering and Structural Dynamics, Vol. 1*: 133-150. John Wiley & Sons, Inc..

Troitsky, M. S. 1988. Cable-Stayed Bridges: Theory and Design. *2nd ed. BSP Professional Books.*

Troyano, L., Armisen & Suarez, M. 1998. The Inclined Towers of the Ebro and Lérez Bridges. *Structural Engineering International, Vol. 8, No. 4*: 258-260. IABSE.

Tuladhar, R. 1995. Seismic Studies of Conventional and Multi-Span Cable-Stayed Bridges. *Ph.D. Thesis, University of Calgary, Canada.*

Tuladhar, R., Dilger, W. & Elbadry, M. 1995. Influence of Cable Vibration on Seismic response of Cable-Stayed Bridges. *Canadian Journal of Civil Engineering, No. 22*: 1001-1020.

Tung, D. & Kudder, R. 1968. Analysis of Cables as Equivalent Two-Force Members. *AISC Engineering Journal, Vol. 5, No. 1, January*: 12-19.

V

Van Nunen, J. & Persoon, A. 1982. Investigation of the Vibrational Behaviour of a Cable-Stayed Bridge Under Wind Loads. *Engineering Structures, Vol. 4, April*: 99-105. Butherworth & Co. Ltd.

Van Overschee, P. & De Moor, B. 1996. Subspace Identification for Linear Systems: Theory, Implementation and Applications. *Kluwer Academic Publishers, Netherlands.*

Vandiver, J., Dunwoody, A., Campbell, R. & Cook, M. 1982. A Mathematical Basis for the Random Decrement Vibration Signature Analysis Technique. *Journal of Mechanical Design, Vol. 104, April*: 445-460.

Vaz, C., Rito, A. & Duarte, R. 1989. Seismic Studies of the Bridge over the Arade River. *Encontro Sobre Sismologia e Engenharia Sísmica, Nov. 1989*: 193-202. LNEC. Lisbon (in Portuguese).

Veletsos, A. & Darbre, G. 1983. Dynamic Stiffness of Parabolic Cables. *Earthquake Engineering and Structural Dynamics, Vol. 11, No. 3*: 367-401. John Wiley & Sons.

Ventura, C.E. & Horyna, T. 2000. Measured and Calculated Modal Characteristics of the Heritage Court Tower in Vancouver BC. *Proceedings of the 18th International Modal Analysis Conference IMAC-XVIII, San Antonio, Texas.*

Verwiebe, C. 1998. Exciting Mechanisms of Rain-Wind-Induced Vibrations. *Structural Engineering International, No. 2*: 112-117. IABSE.

Verwiebe, C., Ruscheweyh 1998. Recent Research Results Concerning the Exciting Mechanisms of Rain-Wind-Induced Vibrations. *Journal of Wind Engineering and Industrial Aerodynamics, vols. 76-76*: 1005-1013. Elsevier.

Vigouroux, F. 2000. News. Bridge & Engineering. *Second Quarter.*

Virlogeux, 1992. Wind Design and Analysis for the Normandy Bridge. In Larsen, A. (ed.), *Aerodynamics of Large Bridges*:183-216. Balkema. Rottterdam.

Virlogeux, M. 1994. The Normandie Bridge, France: A New Record for Cable-Stayed Bridges. *Structural Engineering International, No. 4*: 208-213. IABSE.

Virlogeux, M.; Foucriat, J.; Lawnicki, J.; Maury, Y.; Paulik, L. 1994. Design of the Normandie Bridge. *Proc. IABSE/ FIP Int. Conference on Cables-Stayed and Suspension Bridges, Deauville, 12-15 Oct. 1994*: 605-630.

Virlogeux, M. 1998. Cable Vibrations in Cable-Stayed Bridges. In Larsen, A. & Esdahl, S. (eds), *Bridge Aerodynamics*: 213-233. Balkema.

Virtual Invention Factory, 1997. The Roebling Online History Archive. *www.inventionfactory.com/history/RHAbridg/.*

X

Xiang, H. & Chen, A. 1998. 21st Century Long-Span Bridges in China. In Larsen, A. & Esdahl, S. (eds), *Bridge Aerodynamics*: 175-186. Balkema.

Xu, Y., Ko, J. & Zhang, W. 1997. Vibration Studies of Tsing Ma Suspension Bridge. *Journal of Bridge Engineering, Vol. 2, No. 4*: 149-156. ASCE.

Xu, Y. & Yu, Z. 1998. Vibration of Inclined Sag Cables with Oil Dampers in Cable-Stayed Bridges. *Journal of Bridge Engineering, Vol. 3, No. 4*: 194-203. ASCE.

W

Wallace, A. A. C. 1985. Wind Influence on Kessock Bridge. *Engineering structures, Vol. 7, January*: 18-22. Elsevier.

Walther, R.; Almeida, J. & Estoppey, R. 1988. Ponts Haubanés a Tablier Mince. *Internal report. IBAP-EPFL. Lausanne.*

Walther, R., Houriet, B., Isler, W. & Moïa, P. 1988. Cable-Stayed Bridges. *Thomas Telford, London.*

Walther, R. 1994. Development of Modern Cable-Stayed Bridges. *Proc. IABSE/ FIP Int. Conference on Cables-Stayed and Suspension Bridges, Deauville, 12-15 Oct. 1994*: 33-41.

Wang, T. L. and Huang, D.Z.. 1992. Cable-Stayed Bridge Vibration due to Road Surface Roughness, *Journal of Structural Engineering, Vol. 118, No. 5*: 1354-1374. ASCE.

Wang, P. & Yang, C. 1996. Parametric Studies on Cable-Stayed Bridges. *Computers & Structures, Vol. 60, No. 2*: 243-260. Elsevier.

Wianecki, J. 1979. Cables Wind Excited Vibrations of Cable-Stayed Bridges. *Proc. of the 5th Int. Conference of Wind Engineering, Colorado, USA*: 1381-1393. Pergamon Press.

Wieland, M. 1987. Instrumentation Aspects of cable-Stayed Bridge. In W. Kanok-Nukulchai (ed), *Cable-Stayed Bridges: Experience & Practice, Vol. 2*: 983-996. AIT.

Wieland, M. & Lukkunaprasit, P. 1990. Dynamic Strain Measurements in Three Stay Cables of Main Span of Rama IX Cable-Stayed Bridge in Bangkok. *Report Dept. Civil Engineering Chulalongkorn University, Bangkok.* Thailand.

Wilde, K. & Fujino, Y. 1998. Aerodynamic Control of Bridge DECK Flutter by Active Surfaces. *Journal of Engineering Mechanics, Vol. 124, No. 7, July*: 718-727. ASCE.

Wilson, J. & Gravelle, W. 1991. Modelling of a Cable-Stayed Bridge for Dynamic Analysis. *Earthquake Engineering and Structural Dynamics, Vol. 20*: 707-721. John Wiley & Sons.

Wilson, J. & Liu, T. 1991. Ambient Vibration Measurements on a Cable-Stayed Bridge. *Earthquake Engineering and Structural Dynamics, Vol. 20*: 723-747. John Wiley & Sons.

Y

Yamada, H. 1997. Control of Wind-Induced Cable Vibrations from a Viewpoint of the Wind Resistant Design of Cable-Stayed Bridges. *Proc. of the International Seminar on Cable Dynamics, 13 Oct.*: 129-138, Tokyo. JAWE.

Yamada, Y., Shiraishi, N., Toki, K., Matsumoto, M., Matsuhashi, K., Kitazawa, M. & Ishizaki, H., 1991. Eatrhquake Resistant and Wind-Resistant Design of the Higashi-Kobe Bridge. In M. Ito, Y. Fujino, T. Myiata & N. Narita (eds), *Cable-Stayed Bridges: Recent Developments and their Future:* 397-416. Elsevier.

Yamaguchi, H. 1990. Analytical Study on Growth Mechanism of Rain Vibration of Cables. *Journal of Wind Engineering and Industrial Aerodynamics, Vol. 33*: 73-80. Elsevier Science Publishers, Amsterdam.

Yamaguchi, H. 1995. Control of Cable Vibrations with Secondary Cables. *Proc. International Symposium on Cable Dynamics, 19-21 Oct., Liège, Belgium*: 445-452. AIM.

Yamaguchi, H. & Dung, N. 1992. Active Wave Control of Sagged-Cable Vibration. *Proc. 1st International Conference on Motion Vibration Control*: 134-139.

Yamaguchi, H. & Fujino, Y. 1998. In Larsen, A. & Esdahl, S. (eds), *Bridge Aerodynamics*: 235-253. Balkema.

Yamaguchi, K., Manabe, Y., Sasaki, N. & Morishita, K. 1999. Field Observation and Vibration Tést of the Tatara Bridge. *Cable-Stayed Bridges- Past, Present and Future. IABSE Conference, 2-4 June, Malmö, Sweden.*

Yamaguchi, H., Miyata, T. & Ito, M. 1981. Time Response Analysis of a Cable under Harmonic Excitation. *Proc. of Japan Soc. of Civil Engineers, Vol. 308*: 37-45.

Yamaguchi, H., Takano, H., Ogasawara, M., Shimosato, T., Kato, M. & Kato, H. 1997. Energy-based Damping Evaluation of Cable-Stayed Bridges and Application to Tsurumi Tsubasa Bridge. *Journal of Structural Engineering/ Earthquake Engineering, JSCE, Vol. 14, No. 2:* 201s-213s.

Yamazaki, S., Nagata, N. & Abiru, H. 1992. Tuned Active Dampers Installed in the Minato Mirai (MM) 21 Landmark Tower in Yokohama. *Journal of Wind Engineering and Industrial Aerodynamics, Vol. 41-44. Elsevier.*

Yang,Q., Bregant, L., Heylen, W. & Sas, P. 1994. Modal Parameter Identification from Operating Response Data. In Sas, P. (ed.) *Proceedings of ISMA 19: Tools for Noise and Vibration Analysis, Vol. III*: 1287-1299. KU Leuven. Belgium.

Yeh, C. 1989. Modelling of Nonstationary Earthquake Ground Motion and Biaxial and Torsional Response of Inelastic Structures. *Ph.D. Thesis, University of Illinois, USA.*

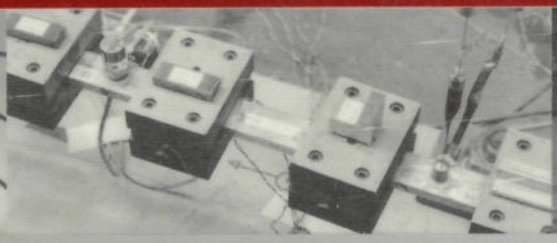
Yiu, P. & Brotton, D. 1987. Mathematical Modelling of Cable-Stayed Bridges for Computer Analysis. In W. Kanok-Nukulchai (ed), *Cable-Stayed Bridges: Experience & Practice, Vol. 1*: 249-260. AIT.

Yoshimura, T., Inoue, A., Kaji, K. & Savage, M. G. 1989. A Study of the Aerodynamic Stability of the Aratsu Bridge. *Canada-Japan Workshop on Bridge Aerodynamics, Ottawa, 25-27 Sept.*

Yoshimura, T., Savage, M. G. & Tanaka, H. 1995a. Wind-Induced Vibrations of Bridge Stay Cables. *Proc. International Symposium on Cable Dynamics, 19-21 Oct., Liège, Belgium*: 437-444. AIM.

Yoshimura, T., Savage, M. G., Tanaka, H. & Wakasa, T. 1993. A Device for Suppressing Wake Galloping of Stay Cables for Cable-Stayed Bridges. *Journal of Wind Engineering and Industrial Aerodynamics, Vol. 49*: 497-506. Elsevier.

Yoshimura, T., Savage, M. G., Tanaka, H. & Urano, D. 1995b. Wind-Induced Oscillations of Groups of Bridge Stay-Cables. *Journal of Wind Engineering and Industrial Aerodynamics, Vol. 54/55*: 251-262. Elsevier.


FACULDADE DE ENGENHARIA
UNIVERSIDADE DO PORTO
BIBLIOTECA
0000056022